

THE JOURNAL of the Acoustical Society of America

Vol. 104, No. 6

December 1998

SOUNDINGS SECTION

ACOUSTICAL NEWS—USA		3137
USA Meetings Calendar		3141
ACOUSTICAL NEWS—INTERNATIONAL		3145
International Meetings Calendar		3146
OBITUARIES		3148
BOOK REVIEWS		3151
REVIEWS OF ACOUSTICAL PATENTS		3152
SELECTED RESEARCH ARTICLES [10]		
Wave decomposition of the vibrations of a cylindrical shell with an automated scanning laser vibrometer	Hyun-Gwon Kil, Jacek Jarzynski, Yves H. Berthelot	3161
Sound absorption in concert halls by seats, occupied and unoccupied, and by the hall's interior surfaces	Leo L. Beranek, Takayuki Hidaka	3169

GENERAL LINEAR ACOUSTICS [20]

An improved moving frame acoustic holography for coherent bandlimited noise	Soon-Hong Park, Yang-Hann Kim	3179
The high-frequency asymptotic description of pulses radiated by a circular normal transducer into an elastic half-space	Dmitri Gridin, Larissa Ju. Fradkin	3190
A fast method for simulating the propagation of pulses radiated by a rectangular normal transducer into an elastic half-space	Dmitri Gridin	3199
The method of fundamental solutions for axisymmetric acoustic scattering and radiation problems	Andreas Karageorghis, Graeme Fairweather	3212
Simple conformal methods for finite-difference time-domain modeling of pressure-release surfaces	John B. Schneider, Christopher L. Wagner, Robert J. Kruhlak	3219
Wave propagation in fluids contained in finite-length anisotropic viscoelastic pipes	Jinghong Yu, Eiichi Kojima	3227
Transient diffraction of a plane step pressure pulse by a hard sphere: Neoclassical solution	H. Huang, G. C. Gaunaurd	3236
Efficiency of a monopole sound source in the vicinity of an elastically suspended, baffled disk	Christiaan Kauffmann	3245
An explicit integral formulation for transient acoustic radiation	Qiang Hu, Sean F. Wu	3251

(Continued)

CONTENTS—Continued from preceding page

AEROACOUSTICS, ATMOSPHERIC SOUND [28]

- | | | |
|--|-------------------------|------|
| Caustic diffraction fields in a downward refracting atmosphere | Erik M. Salomons | 3259 |
| Effects of a background axisymmetric potential flow on vortex ring pairing sound | S. K. Tang, N. W. M. Ko | 3273 |

UNDERWATER SOUND [30]

- | | | |
|--|---|------|
| Propagation in random stratified waveguides—A modal-spectral treatment | Shimshon Frankenthal,
Mark J. Beran | 3282 |
| Modeling of scattering by objects on the seabed | J. A. Fawcett, W. L. J. Fox,
A. Maguer | 3296 |
| Benchmark solutions of plane wave bottom reflection loss | Michael A. Ainslie, Alvin J.
Robins, Mark K. Prior | 3305 |
| Second-order perturbations of peak-arrival times due to sound-speed variations | E. K. Skarsoulis,
G. A. Athanassoulis | 3313 |
| Improved vertical array performance in shallow water with a directional noise field | Kwang Yoo, T. C. Yang | 3326 |
| Time-reversing array retrofocusing in simple dynamic underwater environments | Sunny R. Khosla, David R.
Dowling | 3339 |
| Detection performance of two efficient source tracking algorithms for matched-field processing | Michael J. Wilmut, John M. Ozard | 3351 |

ULTRASONICS, QUANTUM ACOUSTICS, AND PHYSICAL EFFECTS OF SOUND [35]

- | | | |
|--|--|------|
| Elastic constants of the lithium tantalate crystal in the hypersonic range | Tomasz Błachowicz, Zygmunt
Kleszczewski | 3356 |
| Surface-wave modes on soft gels | Y. Onodera, P.-K. Choi | 3358 |

TRANSDUCTION [38]

- | | | |
|---|------------------------------|------|
| Perception of microphone noise in hearing instruments | Lidia W. Lee, Earl R. Geddes | 3364 |
|---|------------------------------|------|

STRUCTURAL ACOUSTICS AND VIBRATION [40]

- | | | |
|---|---------------------------------|------|
| Simplified models of transient elastic waves in finite axisymmetric layered media | Michael El-Raheb | 3369 |
| Use of genetic algorithms for the vibroacoustic optimization of a plate carrying point-masses | Alain Ratle, Alain Berry | 3385 |
| Active structural acoustic control of an infinite ribbed plate under light fluid loading | Nicole J. Kessissoglou, Jie Pan | 3398 |

NOISE: ITS EFFECTS AND CONTROL [50]

- | | | |
|--|--|------|
| Increasing the insertion loss of noise barriers using an active-control system | Jingnan Guo, Jie Pan | 3408 |
| Combined feedback-feedforward active control of sound in a room | Wen-Kung Tseng, B. Rafaely,
S. J. Elliott | 3417 |
| Sound exposure level of railway bridge noise | Rufin Makarewicz, Jun-ichi Koga | 3426 |
| Exposure-response relationships for transportation noise | Henk M. E. Miedema, Henk Vos | 3432 |

ACOUSTICAL MEASUREMENTS AND INSTRUMENTATION [58]

- | | | |
|--|--|------|
| Ultrasonic tomographic imaging of temperature and flow fields in gases using air-coupled capacitance transducers | William M. D. Wright, David W.
Schindel, David A. Hutchins,
Peter W. Carpenter, Dion P. Jansen | 3446 |
|--|--|------|

ACOUSTIC SIGNAL PROCESSING [60]

- | | | |
|---|---|------|
| Maximum likelihood localization of sources propagating in a random media using intensity measurements | Bong-Gee Song, James A. Ritcey,
Terry E. Ewart | 3456 |
|---|---|------|

CONTENTS—Continued from preceding page

PHYSIOLOGICAL ACOUSTICS [64]

- | | | |
|--|------------------------------------|------|
| Measurements and model of the cat middle ear: Evidence of tympanic membrane acoustic delay | Sunil Puria, Jont B. Allen | 3463 |
| Low-level steady-state auditory evoked potentials: Effects of rate and sedation on detectability | Robert A. Dobie, Michael J. Wilson | 3482 |

PSYCHOLOGICAL ACOUSTICS [66]

- | | | |
|--|---|------|
| Nonmonotonicity of informational masking | Eunmi L. Oh, Robert A. Lutfi | 3489 |
| Suppression and the upward spread of masking | Andrew J. Oxenham,
Christopher J. Plack | 3500 |
| Profiling the perceptual suppression of partials in periodic complex tones: Further evidence for a harmonic template | Jeffrey M. Brunstrom, Brian Roberts | 3511 |
| Behavioral assessment of acoustic parameters relevant to signal recognition and preference in a vocal fish | Jessica R. McKibben, Andrew H. Bass | 3520 |
| Effects of ear of entry and perceived location of synchronous and asynchronous components on mistuning detection | Hedwig Gockel, Robert P. Carlyon | 3534 |
| On the source-identification method | William M. Hartmann, Brad Rakerd, Joseph B. Gaalaas | 3546 |

SPEECH PRODUCTION [70]

- | | | |
|--|--|------|
| Methods of interval selection, presence of noise and their effects on detectability of repetitions and prolongations | Peter Howell, Alison Staveley,
Stevie Sackin, Lena Rustin | 3558 |
|--|--|------|

SPEECH PERCEPTION [71]

- | | | |
|--|---|------|
| Role of experience for language-specific functional mappings of vowel sounds | Keith R. Kluender, Andrew J. Lotto, Lori L. Holt, Suzi L. Bloedel | 3568 |
| The recognition of sentences in noise by normal-hearing listeners using simulations of cochlear-implant signal processors with 6–20 channels | Michael F. Dorman, Philipos C. Loizou, Jeanette Fitzke, Zhemin Tu | 3583 |
| Effects of noise and spectral resolution on vowel and consonant recognition: Acoustic and electric hearing | Qian-Jie Fu, Robert V. Shannon,
Xiaosong Wang | 3586 |
| The relation between identification and discrimination of vowels in young and elderly listeners | Maureen Coughlin, Diane Kewley-Port, Larry E. Humes | 3597 |

MUSIC AND MUSICAL INSTRUMENTS [75]

- | | | |
|---|------------------|------|
| A0 and A1 coupling, arching, rib height, and f-hole geometry dependence in the 2 degree-of-freedom network model of violin cavity modes | George Bissinger | 3608 |
|---|------------------|------|

BIOACOUSTICS [80]

- | | | |
|---|--|------|
| Long-range acoustic detection, localization of blue whale calls in the northeast Pacific Ocean | Kathleen M. Stafford,
Christopher G. Fox, David S. Clark | 3616 |
| The neural network classification of false killer whale (<i>Pseudorca crassidens</i>) vocalizations | Scott O. Murray, Eduardo Mercado, Herbert L. Roitblat | 3626 |
| The effect of abdominal wall morphology on ultrasonic pulse distortion. Part I. Measurements | Laura M. Hinkelman, T. Douglas Mast, Leon A. Metlay, Robert C. Waag | 3635 |
| The effect of abdominal wall morphology on ultrasonic pulse distortion. Part II. Simulations | T. Douglas Mast, Laura M. Hinkelman, Michael J. Orr,
Robert C. Waag | 3651 |

(Continued)

CONTENTS—Continued from preceding page

<i>In vitro</i> characterization of a novel, tissue-targeted ultrasonic contrast system with acoustic microscopy	Gregory M. Lanza, Rebecca L. Trousil, Kirk D. Wallace, James H. Rose, Christopher S. Hall, Michael J. Scott, James G. Miller, Paul R. Eisenberg, Patrick J. Gaffney, Samuel A. Wickline	3665
LETTERS TO THE EDITOR		
Does hearing aid benefit increase over time? [10]	Christopher W. Turner, Ruth A. Bentler	3673
Representation of the displacement in terms of scalar functions for use in transversely isotropic materials [20]	A. Rahman, F. Ahmad	3675
Response to “Representation of the displacement in terms of scalar functions for use in transversely isotropic materials” [J. Acoust. Soc. Am. 104, 3675 (1998)] [20]	F. Honarvar, A. N. Sinclair	3677
Observation of flexural Lamb waves (A_0 mode) on water-filled cylindrical shells [40]	J. D. N. Cheeke, X. Li, Z. Wang	3678
Atmospheric propagation transfer function determination using an adaptive filter [60]	Jonathan W. Benson	3681
INDEX TO VOLUME 104		3685
SUBJECT INDEX TO VOLUME 104		3690
AUTHOR INDEX TO VOLUME 104		3720

NOTES CONCERNING ARTICLE ABSTRACTS

1. The number following the abstract copyright notice is a Publisher Item Identifier (PII) code that provides a unique and concise identification of each individual published document. This PII number should be included in all document delivery requests for copies of the article.
2. PACS numbers are for subject classification and indexing. See June and December issues for detailed listing of acoustical classes and subclasses.
3. The initials in brackets following the PACS numbers are the initials of the JASA Associate Editor who accepted the paper for publication.

Document Delivery: Copies of journal articles can be ordered from the new Articles in Physics online document delivery service (URL: <http://www.aip.org/articles.html>).

SOUNDINGS

This front section of the *Journal* includes acoustical news, views, reviews, and general tutorial or selected research articles chosen for wide acoustical interest and written for broad acoustical readership.

ACOUSTICAL NEWS—USA

Elaine Moran

Acoustical Society of America, 500 Sunnyside Boulevard, Woodbury, New York 11797

Editor's Note: Readers of this *Journal* are asked to submit news items on awards, appointments, and other activities about themselves or their colleagues. Deadline dates for news items and notices are 2 months prior to publication.

New Fellows of the Acoustical Society of America



Jan D. Achenbach—For contributions to the understanding of wave propagation in solids.



Peter G. Cable—For contributions to sonar technology.



Oded Ghitza—For contributions to signal-processing techniques for speech.



Frank Henyey—For contributions to fluid dynamics and ocean sound propagation and scattering.



Armin Kohlrausch—For contributions to the understanding of monaural masking and binaural detection.



Kevin J. Parker—For contributions to biomedical ultrasound.

Annual Report of the Editor-in-Chief for the Calendar Year Ending 31 December 1997

This is the annual report to the Executive Council of the Society concerning the activities of the Editor-in-Chief and his colleagues on the Editorial Board of the *Journal* of the Society, as well as other matters related to the *Journal* during the 1997 year.

1. Financial and Pages Published

The total number of *Journal* text pages (articles, letters, front text material and indices) published in 1997 (Volumes 101 and 102) was 7434, a decrease of 2%. This figure includes the indexes of both volumes but does not include the technical programs of meetings in State College, PA and San Diego, CA for which the total number of text pages (abstracts plus author indexes) was 368, nor does it include the 1997 Supplement containing the References to Contemporary Papers in Acoustics, with 612 text pages. The latter appeared as Part 2 of the August 1997 issue. Including all of the above, the total number of text pages published in 1997 was 8414. The corresponding figure for 1996 was 8564, giving a decrease of 2%. Comparing all indexed pages, (pages excluding indexes and References) the number published in 1997 was 7573 and in 1996 was 7793, a 3% decrease. Tardiness in administration by one associate editor probably contributed to the decrease. Table I lists in two columns the number of numbered pages published in the last ten years. Column I gives the total text pages as defined above. Column II gives indexed pages as defined above.

Page charge acceptance was 38%, well below the expected 50% of the total text pages published, exclusive of meeting programs and references. The current page charge is \$80.00 per printed page. Acceptance of page charges is not mandatory. The existence of a mandatory page fee (now \$160.00 per page) for published pages over 12 may have contributed to reduced acceptance of voluntary charges. Some authors have published articles in parts to avoid mandatory fees. Associate editors attempt to discourage this practice.

The Executive Council's budget for 1997 limited total pages for the *Journal* (exclusive of meeting programs and References) to 7700 pages. By month-to-month monitoring of the publication schedule the Editorial Department at AIP and the Editor-in-Chief adhered to this budget, with cooperation from the Associate Editors, totalling 7600 pages.

2. Personnel and Editorial Mechanics

During the year 1997 the following changes in editorial personnel took place, some already reported in the semi-annual report to the Executive Council in December 1997.

Associate Editor Walter Jesteadt for Psychological Acoustics (43.66) asked to be replaced at the end of his three-year term. In consultation with the Technical Committee on Psychological and Physiological Acoustics, the Editor-in-Chief has appointed Robert V. Shannon of the House Ear Institute to be the new Associate Editor.

Associate Editor Raymond H. Dye, Jr. for Psychological Acoustics (43.66) asked to be replaced after three years of service. In consultation with

TABLE I. Number of pages published in the last ten years.

Year	Text total	Indexed
	I	II
1988	5753	5079
1989	5934	5421
1990	6710	6088
1991	7162	6333
1992	7818	6982
1993	7899	7013
1994	8278	7403
1995	8224	7415
1996	8564	7793
1997	8414	7573
Ten-year average	7476	6710

TABLE II. Distribution of articles among categories in JASA, 1997.

Category	Number of articles	Total pages	Pages per article
10. Tutorial	14	150	10.7
20. General Linear Acoustics	122	986	8.1
25. Nonlinear Acoustics, Macrosonics	31	241	7.8
28. Aeroacoustics, Atmospheric Sound	21	184	8.8
30. Underwater Sound	86	872	10.1
35. Ultrasonics, Quantum Acoustics, Physical Effects of Sound	51	436	8.5
38. Transduction	21	187	8.9
40. Structural Acoustics and Vibration	63	544	8.6
50. Noise: Its Effects and Control	24	214	8.9
55. Architectural Acoustics	8	60	7.5
58. Acoustical Measurements	13	96	7.4
60. Acoustic Signal Processing	11	113	10.3
64. Physiological Acoustics	62	650	10.5
66. Psychological Acoustics	91	858	9.4
70,71,72. Speech Communication	72	728	10.1
75. Music and Musical Instruments	18	162	9.0
80. Bioacoustics	36	318	8.8
1997 Total Articles and Letters	744	6799	9.1
1996 Total Articles and Letters (for comparison)	753	6965	9.2

the Chair of the Technical Committee on Psychological and Physiological Acoustics, the Editor-in-Chief appointed D. Wesley Grantham of Vanderbilt University to be the new Associate Editor.

Associate Editor Gilles A. Daigle for Noise, Its Effects, and Control (43.50) asked for replacement after four years of service. In consultation with the Chair of the Technical Committee on Noise, the Editor-in-Chief appointed Michael A. Stinson of the National Research Council of Canada to be the new Associate Editor.

Associate Editor Jeffrey L. Krolik for Acoustic Signal Processing (43.60) asked for replacement at the end of his three-year term. In consultation with the Chair of the Interdisciplinary Technical Group on Signal Processing in Acoustics, the Editor-in-Chief appointed John C. Burgess to be the new Associate Editor.

Being an Associate Editor for our *Journal* requires, in addition to ability and experience in a branch of acoustics, a considerable dedication to the Society and to the field of Acoustics. The Editor-in-Chief expresses his gratitude to both the retiring and the continuing Associate Editors, and to those institutions which support their editorial efforts, on behalf of our contributors, our members, and the Society.

The editorial mechanics of the *Journal* at AIP continues with the able participation of Editorial Supervisor Lin Miller and Rosalind Nissim as Chief Production Editor, with help from Andrea Witt, Connie Nedohon, and Carolyn DeMarco. The Editor-in-Chief is especially grateful to this entire group for their capable, diligent, and cheerful assistance.

3. Subject Coverage and Emphasis in the *Journal*

Table II presents data on the number of articles published in the various categories of our subject classification system (PACS) during the year 1997 together with the number of associated pages, and the average number of pages per article in each category. Note that some categories average over 40% more pages per article than other categories.

From 1996 to 1997 both the number of articles and letters published and the number of pages decreased slightly. The average length decreased to 9.1 pages in 1997 compared to 9.2 in 1996. There was a marked increase in the number of papers published in linear acoustics, ultrasonics, transduction, and noise. There was decreased publication in nonlinear acoustics, architectural acoustics, acoustic signal processing, and speech communication.

In Volumes 101 and 102 published in 1997 there were 497 pages devoted to acoustical news, technical notes, reviews, and indices. Distribution is shown in Table III, which also contains the corresponding figures for 1992 through 1996. The distribution changes little from year to year. However our book reviewers lacked diligence this year.

TABLE III. Page distribution of complementary material for 1992–1997.

	1992	1993	1994	1995	1996	1997
Technical Notes, Research Briefs, and FORUM	11	21	20	25	28	19
Acoustical News—U.S.A.	89	107	89	108	114	122
Acoustical News—International	12	16	12	16	14	12
Standards News	35	29	20	27	31	37
Book Reviews	17	12	19	12	16	1
Patent Reviews	116	121	110	103	102	115
Cumulative Author Indexes	18	20	20	20	18	21
Volume Indexes	207	213	238	220	213	158
Errata	10	6	9	6	12	12
TOTALS	515	535	537	537	548	497

4. Meeting Programs in 1997

The program of the 133rd meeting of the Society in State College, PA (joint with Noise-Con 97) contained 195 pages of abstracts and author index with a total of 825 abstracts. The program appeared as Part 2 of the May issue. All authors of papers in meeting programs are currently indexed in the *Journal*, but the abstracts are not peer reviewed. The program of the 134th meeting of the Society in San Diego contained 161 pages of abstracts and author index with a total of 680 abstracts. The program appeared as Part 2 of the October issue.

5. Acceptance and Rejection of Manuscripts Submitted to the *Journal* for Publication in 1997

The relevant figures are presented in Table IV in the same form as that used previously. Fewer manuscripts were accepted and more were rejected in 1997 than in 1996. The same number of papers are under review currently as a year ago, enough backlog to be entirely adequate for continuity of publication. The overall rejection rate increased to approximately 27%. The largest percentages of rejection in 1997 were musical, noise, speech, structural, and underwater sound.

TABLE IV. Acceptance and rejection of manuscripts submitted to JASA in 1997.

Category	Manuscripts received in 1997	Manuscripts accepted in 1997	Manuscripts rejected in 1997	Manuscripts sent back for revision 1997	Manuscripts under review at end of 1997
10 Martin (Tutorial & Review)	7	4	1	2	1
20 Greenspon	56	54	15	50	73
Norris	86	48	22	23	26
25 Breazeale	38	24	4	24	51
28 Sutherland	28	20	3	2	21
30 Miller	0	53	13	0	0
Bradley	89	19	13	25	32
Chin-Bing	63	22	19	24	20
35 Bass	81	42	10	16	44
38 Ehrlich	21	16	2	23	9
40 Remington	32	14	6	14	14
Burroughs	72	28	16	9	23
50 Daigle-Stinson	30	18	13	13	9
55 Quirt	15	11	2	4	7
58 Ehrlich	21	17	5	20	6
60 Krolik	35	10	3	6	20
64 Frisina	45	49	10	12	13
Lonsbury-Martin	19	6	2	8	2
66 Hall	48	14	3	23	8
Grantham	26	1	2	10	13
Jesteadt	29	19	2	8	0
Shannon	24	1	2	10	11
Dye	25	19	4	12	6
70 Lofqvist	46	25	7	24	12
71 Strange	57	31	27	22	18
72 Hieronymus	14	1	2	2	9
75 Strong	28	11	9	14	17
80 Dunn	46	30	5	26	22
TNRB Ostergaard	3	3	0	2	0
1997 TOTALS	1084	610	222	428	487
1996 Totals (for comparison)	1077	665	200	527	487

The Society owes a continuing debt of gratitude to the Associate Editors who process manuscripts, and to the dedicated reviewers who examine them. A list of 1427 reviewers during the year 1997 was published in the July issue with an expression of appreciation for their services.

6. Outside-U.S.A. Papers Published in the *Journal*

Publication activity in the *Journal* from outside the U.S.A. led in 1997 to the equivalent of 324 articles and letters in the *Journal* compared with 321 in 1996. Forty-three percent of *Journal* authorship was outside U.S.A. The distribution among 35 countries was as follows: United Kingdom 43, Canada 41, France 35, Netherlands 27, Japan 26, Germany 19, Australia 18, Taiwan 11, Russia 9, India 8, Sweden 7, Belgium 7, China 6, Korea 6, Hong Kong 6, Italy 5, Spain 5, Israel 4, Finland 3, Norway 3, Greece 2, Denmark 2, Poland 2, Mexico 2, South Africa 2, Byelorussia 2, with Chile, Yugoslavia, Switzerland, Turkey, New Zealand, Ukraine, Romania, and Singapore also represented.

7. Review and Tutorial Papers

In 1997 every issue contained either a purposely tutorial invited article, or one or more selected research articles "judged (a) to have a subject of wide acoustical interest and (b) to be written for understanding by broad acoustical readership." Titles of these articles are listed on the front cover of the *Journal* in the new format.

8. Technical Notes and Research Briefs

In 1997 this *Journal* section contained 4 brief reports of recent research results in various fields, and also contained 13 abstracts of graduate dissertations in acoustics. This department will be discontinued in 1998, but thesis abstracts will continue to be published.

9. Book Reviews

In 1997 the *Journal* published only one book review, although a number of reviews had been assigned and promised. An attempt will be made in 1998 to convince reviewers to fulfill their responsibility.

10. Patent Reviews

A dedicated corps of 14 patent reviewers published reviews for an average of 55 reviews per reviewer in 1997. These reviews benefit our readers, particularly those who are concerned with new acoustical applications, devices, and instruments.

11. References to Contemporary Papers in Acoustics

The 1997 issue of this document, compiled by computer by Richard Stern, appeared in the summer as Part 2 of the August 1997 issue. It contained 612 text pages. This bibliographical coverage of acoustical information from around the world is a valuable part of the material on acoustics distributed to all members of the Society, and to all non-member subscribers to the *Journal*.

12. Standards News and Standards

This section of the *Journal* continues to provide the essential news of the work of the various standards committees on acoustics, as well as availability of standards in acoustics published by the Society and others. The role of the Society in the publication of standards is very important.

13. News Sections

These sections provide up-to-date information about the work of the Society Office, the activities of the various Society committees and the regional chapters, changes in membership lists, personal notes about members and obituaries, and a calendar of meetings of relevant societies for both the U.S.A. and around the world. The *Journal* is now collecting international information for the ICA.

14. Acoustics 1997

This annual feature has been discontinued because AIP no longer publishes an annual News issue, preferring to learn about and publicize notable advances on a regular basis throughout the year in a timely manner.

15. Time of Appearance of the *Journal*

Release by AIP to the printer has been on schedule consistently. The Editor-in-Chief appreciates the diligent efforts of our publication staff to maintain the schedule during a heavy publication year.

16. Supplementary Publication Media

The *Journal* continued to be available to members bimonthly on CD-ROM in 1997. Back issues through 1961 are also on CD-ROM. Preparations were completed in 1997 for 1998 on-line availability of the *Journal* through the AIP Online Journal Publishing Service, first to institutional subscribers that sign a user agreement, and then to ASA members later in the year. A procedure is being developed by Robert Apfel, with AIP assistance, for the purpose of rapid review and on-line publication of letters of up to 4 published pages in length.

17. Echoes

The Society newsletter was edited by Alice Suter through two issues in 1997, when she retired after six years of outstanding editorial service. She was succeeded in July by Thomas Rossing, who edited the two later issues in 1997. Each issue, in addition to news about the Society, its members and meetings, and press publicity about sound, has a feature article on an acoustical subject. Subjects in 1997 were "Frog Vibrational Communication," "Born to Learn Language," "The Pickering Pickup," and "Robert Bruce Lindsay."

The Editor-in-Chief expresses his deep appreciation for the generous and capable support he has received from all connected with the editing and production of the *Journal*.

DANIEL W. MARTIN

Editor-in-Chief

May 1998

Reports of Technical Committees/Technical Specialty Groups

(See October and November issues for additional reports.)

Signal Processing in Acoustics

The Interdisciplinary Technical Group on Signal Processing in Acoustics (SP) has continued to grow and interact more frequently with various Technical Committees (TC) of the Acoustical Society. Signal and image processing is the underlying technology that encompasses many of the efforts in acoustics through the necessity to model, gather data, analyze data, and extract the required information from noisy measurements. It is for this reason that the Technical Group on Signal Processing has and continues to foster a growing interaction with each of the Technical Committees through the sponsoring of joint sessions and tutorials. This effort was clearly exemplified by the various signal processing related sessions throughout both the San Diego and Seattle meetings.

At the 134th ASA meeting in San Diego SP group sponsored 7 sessions: 2 regular contributed sessions and 5 special sessions. These sessions were entitled:

"Signal Processing for Multichannel Vibrational Analysis" (SA)

"Sound Quality"

"Signal Processing for Microphone Arrays"

"General Signal Processing"

with three special sessions devoted to a topic of high current interest, on "Acoustics in Multimedia."

The 135th ASA meeting in Seattle featured more joint SP group sponsored/co-sponsored sessions with 4 regular and 4 special. These sessions were:

"Speech: Modeling and System Identification" (SC)

"Speech Communication: Non-Stationary and Wavelet Processing Methods" (SC)

"General Topics in Acoustical Signal Processing"

"Implementation Issues of Acoustical Signal Processing in Real Time Systems II"

"Signal Processing for Medical Ultrasound I" (PA)

"Underwater Acoustic Communications" (UW)

"Implementation Issues of Acoustical Signal Processing in Real Time Systems I"

“Multichannel Signal Processing for Acoustic Applications” (AA, SC).

Again the joint effort of the SP group and interactions with various TCs in acoustics is noted by the joint sponsorship of sessions. We plan to encourage even more interactions and joint sessions in the future meetings.

The eighth Meeting of the Technical Group was held in Seattle at which time, the Chair, Gary Wilson had to step down due to time constraints ‘afforded by his new position. James Candy was nominated for the Chair and unanimously elected by the Group. Preparations continue for the Special Sessions of both the Norfolk and Berlin meetings.

JAMES V. CANDY
Chairman

Regional Chapter News

Cincinnati

Following is a summary of the programs and lectures presented in 1997–98 at the Cincinnati Chapter of the ASA meetings and a list of officers.

President: Sharon T. Hepfner
Secretary: Brian C. Thompson
Treasurer: Susan Farrer
Member-At-Large: Ernest M. Weiler

January 1997 lecture: Dr. Robert Dooling (Univ. of Maryland). Topic: “Hearing And Vocal Learning In Birds: A Model For Human Language.”

February 1997 lecture: Dr. Christy Holland. “Demonstration and evaluation of noise exposure during magnetic resonance imaging (MRI).”

April 1997 lecture: Dr. Daniel Martin. “The Singing Voice.” Following the lecture, the group attended a concert by the Knox Presbyterian Church Choir.

May 1997 lecture: Dr. Ernest Weiler. Case study *re:* highway noise barriers. Dr. Roger Adelman described and demonstrated a unique amplification device. Dr. Brian Thompson discussed and demonstrated the Sonatron treatment device.

September 1997 lecture: Christi Themann. “Early data from the NIOSH survey of noise exposure and hearing status in farm families.” Also, Sharon Hepfner presented recent developments in, and new applications for, hearing protection devices.

October 1997: A joint meeting with the Columbus, OH chapter for the guest lecture on the development of an intraoral hearing aid.

December 1997: The Chapter honored Dr. Daniel W. Martin for his outstanding contributions and service to the ASA, and our chapter, with a luncheon. The large gathering heard several speakers, including Dr. Martin’s longtime friend, Dr. Mead Killian.

January 1998 lecture: Michael Hooker. Topic: “Theatrical Acoustics.”

March 1998 lecture: Donald Wasserman. Topic: “Human Aspects of Occupational Exposure to Low Frequency Vibration.”

May 1998 lecture: Leeann Mutzan. Topic: “Music Therapy.”

BRIAN C. THOMPSON
Secretary

USA Meetings Calendar

Listed below is a summary of meetings related to acoustics to be held in the U.S. in the near future. The month/year notation refers to the issue in which a complete meeting announcement appeared.

1999

- 15–19 March Joint meeting: 137th meeting of the Acoustical Society of America/Forum Acusticum, Berlin, Germany [Acoustical Society of America, 500 Sunnyside Blvd., Woodbury, NY 11797, Tel.: 516-576-2360; Fax: 516-576-2377; E-mail: asa@aip.org; WWW: asa.aip.org].
- 10–12 May AIAA/CEAS Aeroacoustics Conference, Bellevue, WA [Belur Shivashankara, The Boeing Company, P.O. Box 3707, MS 67-ML, Seattle, WA 98124-2207; Tel.: 425-234-9551, Fax: 425-237-5247; E-mail: belun.n.shivashankara@boeing.com].
- 6–7 June 1999 SEM Spring Conference, Cincinnati, OH [Katherine M. Ramsay, Conference Manager, Society for Experimental Mechanics, Inc., 7 School St., Bethel, CT 06801; Tel.: 203-790-6373; Fax: 203-790-4472; E-mail: meetings@sem1.com].
- 27–30 June ASME Mechanics and Materials Conference, Blacksburg, VA [Mrs. Norma Guynn, Dept. of Engineering Science and Mechanics, Virginia Tech, Blacksburg, VA 24061-0219; Fax: 540-231-4574; E-mail: nguyenn@vt.edu; WWW: <http://www.esm.vt.edu/mmconf/>]. Deadline for receipt of abstracts: 15 January 1999.
- 6–11 July 1999 Clarinetfest, Ostend, Belgium [International Clarinet Association, Keith Koons, Music Dept., Univ. of Central Florida, P.O. Box 161354, Orlando, FL 32816-1354]. Deadline for receipt of abstracts: 31 January 1999.
- 1–5 Nov. 138th meeting of the Acoustical Society of America, Columbus, Ohio [Acoustical Society of America, 500 Sunnyside Blvd., Woodbury, NY 11797; Tel.: 516-576-2360; Fax: 516-576-2377; E-mail: asa@aip.org; WWW: asa.aip.org].

ACOUSTICAL NEWS—INTERNATIONAL

Walter G. Mayer

Physics Department, Georgetown University, Washington, DC 20057

Statistics—16th ICA/ASA Meeting Seattle

Statistics of the 16th International Congress on Acoustics and the 135th Meeting of the Acoustical Society of America, held in Seattle, Washington, USA 20–26 June 1998, have now been released by the organizers.

The compilation below shows the number of registered participants from the various countries represented at the Seattle ICA/ASA meeting as well as at the six previous congresses, Sydney 1980, Paris 1983, Toronto 1986, Belgrade 1989, Beijing 1992, and Trondheim 1995. The Table reflects the fact that there have been some political changes in the 15 years covered by these statistics.

Country	Sydney	Paris	Toronto	Belgrade	Beijing	Trondheim	Seattle
Algeria	0	1	0	0	0	1	0
Argentina	2	3	5	0	0	0	0
Australia	303	3	19	4	12	19	36
Austria	0	0	0	2	0	6	11
Belgium	2	19	8	9	4	9	15
Brazil	2	1	4	1	3	3	12
Bulgaria	0	3	1	6	0	0	0
Canada	14	30	171	18	10	10	75
Chile	0	1	0	0	1	1	2
China	13	15	19	15	370	4	47
Colombia	0	0	0	0	0	0	1
Croatia					1	0	0
Cuba	0	1	0	0	0	0	0
Czech Republic						4	3
Czechoslovakia	1	6	1	7	0		
Denmark	20	36	23	19	9	28	17
Egypt	1	2	1	1	0	0	1
Estonia						4	2
Finland	0	5	2	4	2	10	7
France	28	350	98	67	35	63	95
Ghana	0	1	0	0	0	0	0
Germany (FRG)	61	100	71	55	32	41	49
Germany (GDR)	0	2	1	3			
Greece	0	3	0	3	0	0	1
Hong Kong	0	2	0	0	2	0	4
Hungary	0	8	3	22	0	11	1
India	8	10	7	8	3	3	9
Indonesia	5	0	0	0	1	0	0
Iran	0	2	0	1	2	0	0
Iraq	1	0	0	0	0	0	0
Ireland	0	0	0	0	0	0	3
Israel	1	4	2	0	3	0	3
Italy	7	20	15	13	8	16	28
Japan	108	97	143	87	106	96	173
Korea	0	0	2	0	21	4	33
Libya	2	0	0	0	0	0	0
Malaysia	1	0	0	0	2	0	0
Morocco	0	0	0	0	1	0	0
Mexico	2	0	0	0	0	0	8
Netherlands	12	24	18	21	8	14	27
New Zealand	12	2	4	1	0	2	9
Nigeria	2	0	1	0	0	0	0
Norway	2	9	8	9	3	89	18
Pakistan	2	0	0	0	0	0	0
Peru	0	0	0	0	0	1	0
Poland	5	17	10	16	2	25	12
Portugal	0	4	1	1	1	3	0
Romania	0	3	0	1	0	1	0
Russia					8	13	27
Singapore	1	2	2	0	3	1	3
Slovak Republic						1	1
South Africa	5	3	8	1	1	0	3

Country	Sydney	Paris	Toronto	Belgrade	Beijing	Trondheim	Seattle
Spain	1	18	16	4	2	7	13
Sweden	10	15	21	16	10	40	25
Switzerland	2	11	3	4	0	7	7
Syria	0	3	0	0	0	0	0
Thailand	0	0	0	0	1	0	0
Turkey	0	0	1	0	0	1	1
Ukraine					0	0	2
United Kingdom	22	75	46	27	20	35	77
U.S.A.	54	117	201	61	64	69	1066
USSR	4	17	12	31			
Venezuela	0	0	0	0	0	0	2
Yugoslavia	5	3	6	169	3	0	3
Total	721	1048	954	707	754	642	1932
Accompanying persons	127	200	133	63	95	98	192

International Commission on Acoustics selects logo

Several months ago the International Commission on Acoustics (ICA) decided that it should have a logo which symbolizes the world-wide role ICA has in the field of acoustics. An international competition was started which came to a close at the time of the Seattle Congress. The design, which



FIG. 1. The logo of the International Commission on Acoustics.

was judged to be the most appropriate, had been submitted by Logan E. Hargrove of Reston, Virginia, USA. His winning entry, which is now the official logo of the International Commission on Acoustics, is shown in Fig. 1.

First Iberoamerican Meeting on Ultrasound

The First Iberoamerican Meeting on Ultrasound was held 25–29 May 1998 in Cartagena de Indias, Colombia. The meeting was organized by the Iberoamerican Network for Ultrasonic Technologies and was sponsored by the Iberoamerican program *Science and Technology for Development (CYTED)*. The 57 participants came from 15 countries: Argentina, Bolivia, Brazil, Colombia, Cuba, Chile, Dominican Republic, Ecuador, El Salvador, Honduras, Mexico, Peru, Portugal, Spain, and Uruguay. Most of the participants were associated with academic institutions but also with industry, hospitals, and consulting firms.

The two main topics of the meeting were transducers and signal processing. The program consisted of tutorials and review lectures (usually during the morning sessions) and contributed papers (usually during the afternoon sessions). The main goal of the meeting was to allow the participants to share their knowledge in order to stimulate cooperation among the different groups working on ultrasound in the Spanish- and Portuguese-speaking areas.

The tutorial and review lectures were given by a team of experienced lecturers who presented the state-of-the-art of the two selected topics of the meeting. Most of the participants also presented papers on the results of their activities. Animated discussions took place after most of the lectures and presentations. The meeting allowed participants to exchange experi-

ences and viewpoints about the present and future research or applications in the two topics of the meeting. As a conclusion, the interaction between academic and industrial groups was strongly recommended.

At the end of the meeting the participants expressed satisfaction and enthusiasm for the goals and the development of the meeting. This positive outcome should also be attributed to the magnificent beauty of the city of Cartagena de Indias, to the charm of the 17th century building of the Spanish House where the conference was held, and especially to the outstanding kindness and efficiency of the team of the Centro Iberoamericano de Formacion who took charge of the local arrangements and coped extraordinarily well with any problem or difficulty.

The review lectures and contributed papers will be published in the Proceedings of the conference. Additional information can be obtained from Lorenzo Leija (lleija@mail.cinvestav.mx), the coordinator of the Iberoamerican Network on Ultrasound.

JUAN A. GALLEGO-JUAREZ
Instituto de Acustica, CSIC
Serrano 144, Madrid 28006, Spain

Papers published in JASJ(E)

A listing of Invited Papers and Regular Papers appearing in the latest issue of the English language version of the *Journal of the Acoustical Society of Japan, JASJ(E)*, was published for the first time in the January 1995 issue of the Journal. This listing is continued below.

The September issue of JASJ(E), Vol. 19, No. 5 (1998) contains the following papers:

- F. Kawakami "Evaluation of initial decay rate of power-law decays for measuring random incident absorption"
- F. Kawakami and T. Sakai "Deep-well approach for canceling the edge effect in random incident absorption measurement"
- K. Tanaka and H. Kojima "Estimation of a degree of speech recognition difficulty for word sets.—An application of between-word distance calculation in a symbolic domain"
- K. Kido, H. Suzuki, T. Ono, and M. Fukushima "Deformation of impulse response estimates by time window in cross spectral technique"
- Y. Shimada, Y. Nishimura, T. Usgawa, and M. Ebata "An adaptive algorithm for periodic noise with secondary path delay estimation"

International Meetings Calendar

Below are announcements of meetings to be held abroad. Entries preceded by an * are new or updated listings with contact addresses given in parentheses. Month/year listings following other entries refer to issues of the *Journal* which contain full calendar listings or meeting announcements.

December 1998

- 9–11 **National Symposium on Acoustics-1998 (NSA-98)**, Calcutta. 10/98
- 15–16 **Sonar Signal Processing**, Loughborough. 4/98

- March 1999**
15–19 **Joint Meeting of EAA Forum Acusticum, and 137th Meeting of the Acoustical Society of America, Berlin.** 6/97
- April 1999**
27–29 **International Conference on Vibration, Noise, and Structural Dynamics, Venice.** 8/98
- May 1999**
10–14 **4th International Conference on Theoretical and Computational Acoustics, Trieste.** 6/98
24–26 **2nd International Conference on Emerging Technologies in NDT, Athens.** 8/98
30–3 ***16th International Evoked Response Audiometry Study Group Symposium, Tromsø, Norway.** (E. Laukli, Otorhinolaryngology, University Hospital, P.O. Box 34, 9038 Tromsø, Norway; Fax: +47 77 62 73 69, e-mail: einar.laukli@rito.no)
- June 1999**
28–30 **1st International Congress of the East European Acoustical Association, St. Petersburg.** 10/97
28–1 **Joint Conference of Ultrasonics International '99 and World Congress on Acoustics '99 (UI99/WCU99), Lyngby.** 6/98
- July 1999**
4–9 **10th British Academic Conference in Otolaryngology, London.** 10/97
5–8 **6th International Congress on Sound and Vibrations, Copenhagen.** 2/98
- September 1999**
1–4 **15th International Symposium on Nonlinear Acoustics (ISNA-15), Göttingen.** 10/97
- 15–17 **British Society of Audiology Annual Conference, Buxton.** 8/98
- October 1999**
20–22 ***Iberian Meeting of the Spanish Acoustical Society and the Portuguese Acoustical Society, Avila, Spain.** (Spanish Acoustical Society, c/Serrano 144, 28006 Madrid, Spain; Fax: +34 91 411 7651; e-mail: ssantiago@fresno.csic.es)
- March 2000**
20–24 **Meeting of the German Acoustical Society (DAGA), Oldenburg.** 10/98
- July 2000**
4–7 ***7th International Congress on Sound and Vibration, Garmisch-Partenkirchen, Germany.** (H. Heller, DLR, Postfach 3267, 38022 Braunschweig, Germany; Fax: +49 531 295 2320; e-mail: hannel.heller@dlr.de; Web: www.iiav.org/icsv7.html)
- October 2000**
3–5 **WESTPRAC VII, Kumamoto.** 6/98
16–18 ***2nd Iberoamerican Congress on Acoustics, 31st National Meeting of the Spanish Acoustical Society, and EAA Tutorium, Madrid, Spain.** (Spanish Acoustical Society, c/Serrano 144, 28006 Madrid, Spain; Fax: +34 91 411 7651; e-mail: ssantiago@fresno.csic.es)
16–20 **6th International Conference on Spoken Language Processing, Beijing.** 10/98
- September 2001**
2–7 **17th International Congress on Acoustics (ICA), Rome.** 10/98

ACOUSTICAL NEWS—INTERNATIONAL

Walter G. Mayer

Physics Department, Georgetown University, Washington, DC 20057

Statistics—16th ICA/ASA Meeting Seattle

Statistics of the 16th International Congress on Acoustics and the 135th Meeting of the Acoustical Society of America, held in Seattle, Washington, USA 20–26 June 1998, have now been released by the organizers.

The compilation below shows the number of registered participants from the various countries represented at the Seattle ICA/ASA meeting as well as at the six previous congresses, Sydney 1980, Paris 1983, Toronto 1986, Belgrade 1989, Beijing 1992, and Trondheim 1995. The Table reflects the fact that there have been some political changes in the 15 years covered by these statistics.

Country	Sydney	Paris	Toronto	Belgrade	Beijing	Trondheim	Seattle
Algeria	0	1	0	0	0	1	0
Argentina	2	3	5	0	0	0	0
Australia	303	3	19	4	12	19	36
Austria	0	0	0	2	0	6	11
Belgium	2	19	8	9	4	9	15
Brazil	2	1	4	1	3	3	12
Bulgaria	0	3	1	6	0	0	0
Canada	14	30	171	18	10	10	75
Chile	0	1	0	0	1	1	2
China	13	15	19	15	370	4	47
Colombia	0	0	0	0	0	0	1
Croatia					1	0	0
Cuba	0	1	0	0	0	0	0
Czech Republic						4	3
Czechoslovakia	1	6	1	7	0		
Denmark	20	36	23	19	9	28	17
Egypt	1	2	1	1	0	0	1
Estonia						4	2
Finland	0	5	2	4	2	10	7
France	28	350	98	67	35	63	95
Ghana	0	1	0	0	0	0	0
Germany (FRG)	61	100	71	55	32	41	49
Germany (GDR)	0	2	1	3			
Greece	0	3	0	3	0	0	1
Hong Kong	0	2	0	0	2	0	4
Hungary	0	8	3	22	0	11	1
India	8	10	7	8	3	3	9
Indonesia	5	0	0	0	1	0	0
Iran	0	2	0	1	2	0	0
Iraq	1	0	0	0	0	0	0
Ireland	0	0	0	0	0	0	3
Israel	1	4	2	0	3	0	3
Italy	7	20	15	13	8	16	28
Japan	108	97	143	87	106	96	173
Korea	0	0	2	0	21	4	33
Libya	2	0	0	0	0	0	0
Malaysia	1	0	0	0	2	0	0
Morocco	0	0	0	0	1	0	0
Mexico	2	0	0	0	0	0	8
Netherlands	12	24	18	21	8	14	27
New Zealand	12	2	4	1	0	2	9
Nigeria	2	0	1	0	0	0	0
Norway	2	9	8	9	3	89	18
Pakistan	2	0	0	0	0	0	0
Peru	0	0	0	0	0	1	0
Poland	5	17	10	16	2	25	12
Portugal	0	4	1	1	1	3	0
Romania	0	3	0	1	0	1	0
Russia					8	13	27
Singapore	1	2	2	0	3	1	3
Slovak Republic						1	1
South Africa	5	3	8	1	1	0	3

Country	Sydney	Paris	Toronto	Belgrade	Beijing	Trondheim	Seattle
Spain	1	18	16	4	2	7	13
Sweden	10	15	21	16	10	40	25
Switzerland	2	11	3	4	0	7	7
Syria	0	3	0	0	0	0	0
Thailand	0	0	0	0	1	0	0
Turkey	0	0	1	0	0	1	1
Ukraine					0	0	2
United Kingdom	22	75	46	27	20	35	77
U.S.A.	54	117	201	61	64	69	1066
USSR	4	17	12	31			
Venezuela	0	0	0	0	0	0	2
Yugoslavia	5	3	6	169	3	0	3
Total	721	1048	954	707	754	642	1932
Accompanying persons	127	200	133	63	95	98	192

International Commission on Acoustics selects logo

Several months ago the International Commission on Acoustics (ICA) decided that it should have a logo which symbolizes the world-wide role ICA has in the field of acoustics. An international competition was started which came to a close at the time of the Seattle Congress. The design, which



FIG. 1. The logo of the International Commission on Acoustics.

was judged to be the most appropriate, had been submitted by Logan E. Hargrove of Reston, Virginia, USA. His winning entry, which is now the official logo of the International Commission on Acoustics, is shown in Fig. 1.

First Iberoamerican Meeting on Ultrasound

The First Iberoamerican Meeting on Ultrasound was held 25–29 May 1998 in Cartagena de Indias, Colombia. The meeting was organized by the Iberoamerican Network for Ultrasonic Technologies and was sponsored by the Iberoamerican program *Science and Technology for Development (CYTED)*. The 57 participants came from 15 countries: Argentina, Bolivia, Brazil, Colombia, Cuba, Chile, Dominican Republic, Ecuador, El Salvador, Honduras, Mexico, Peru, Portugal, Spain, and Uruguay. Most of the participants were associated with academic institutions but also with industry, hospitals, and consulting firms.

The two main topics of the meeting were transducers and signal processing. The program consisted of tutorials and review lectures (usually during the morning sessions) and contributed papers (usually during the afternoon sessions). The main goal of the meeting was to allow the participants to share their knowledge in order to stimulate cooperation among the different groups working on ultrasound in the Spanish- and Portuguese-speaking areas.

The tutorial and review lectures were given by a team of experienced lecturers who presented the state-of-the-art of the two selected topics of the meeting. Most of the participants also presented papers on the results of their activities. Animated discussions took place after most of the lectures and presentations. The meeting allowed participants to exchange experi-

ences and viewpoints about the present and future research or applications in the two topics of the meeting. As a conclusion, the interaction between academic and industrial groups was strongly recommended.

At the end of the meeting the participants expressed satisfaction and enthusiasm for the goals and the development of the meeting. This positive outcome should also be attributed to the magnificent beauty of the city of Cartagena de Indias, to the charm of the 17th century building of the Spanish House where the conference was held, and especially to the outstanding kindness and efficiency of the team of the Centro Iberoamericano de Formacion who took charge of the local arrangements and coped extraordinarily well with any problem or difficulty.

The review lectures and contributed papers will be published in the Proceedings of the conference. Additional information can be obtained from Lorenzo Leija (lleija@mail.cinvestav.mx), the coordinator of the Iberoamerican Network on Ultrasound.

JUAN A. GALLEGO-JUAREZ
Instituto de Acustica, CSIC
Serrano 144, Madrid 28006, Spain

Papers published in JASJ(E)

A listing of Invited Papers and Regular Papers appearing in the latest issue of the English language version of the *Journal of the Acoustical Society of Japan*, JASJ(E), was published for the first time in the January 1995 issue of the Journal. This listing is continued below.

The September issue of JASJ(E), Vol. 19, No. 5 (1998) contains the following papers:

- F. Kawakami "Evaluation of initial decay rate of power-law decays for measuring random incident absorption"
- F. Kawakami and T. Sakai "Deep-well approach for canceling the edge effect in random incident absorption measurement"
- K. Tanaka and H. Kojima "Estimation of a degree of speech recognition difficulty for word sets.—An application of between-word distance calculation in a symbolic domain"
- K. Kido, H. Suzuki, T. Ono, and M. Fukushima "Deformation of impulse response estimates by time window in cross spectral technique"
- Y. Shimada, Y. Nishimura, T. Usgawa, and M. Ebata "An adaptive algorithm for periodic noise with secondary path delay estimation"

International Meetings Calendar

Below are announcements of meetings to be held abroad. Entries preceded by an * are new or updated listings with contact addresses given in parentheses. Month/year listings following other entries refer to issues of the *Journal* which contain full calendar listings or meeting announcements.

December 1998

- 9–11 **National Symposium on Acoustics-1998 (NSA-98)**, Calcutta. 10/98
- 15–16 **Sonar Signal Processing**, Loughborough. 4/98

- March 1999**
15–19 **Joint Meeting of EAA Forum Acusticum, and 137th Meeting of the Acoustical Society of America**, Berlin. 6/97
- April 1999**
27–29 **International Conference on Vibration, Noise, and Structural Dynamics**, Venice. 8/98
- May 1999**
10–14 **4th International Conference on Theoretical and Computational Acoustics**, Trieste. 6/98
24–26 **2nd International Conference on Emerging Technologies in NDT**, Athens. 8/98
30–3 ***16th International Evoked Response Audiometry Study Group Symposium**, Tromsø, Norway. (E. Laukli, Otorhinolaryngology, University Hospital, P.O. Box 34, 9038 Tromsø, Norway; Fax: +47 77 62 73 69, e-mail: einar.laukli@rito.no)
- June 1999**
28–30 **1st International Congress of the East European Acoustical Association**, St. Petersburg. 10/97
28–1 **Joint Conference of Ultrasonics International '99 and World Congress on Acoustics '99 (UI99/WCU99)**, Lyngby. 6/98
- July 1999**
4–9 **10th British Academic Conference in Otolaryngology**, London. 10/97
5–8 **6th International Congress on Sound and Vibrations**, Copenhagen. 2/98
- September 1999**
1–4 **15th International Symposium on Nonlinear Acoustics (ISNA-15)**, Göttingen. 10/97
- 15–17 **British Society of Audiology Annual Conference**, Buxton. 8/98
- October 1999**
20–22 ***Iberian Meeting of the Spanish Acoustical Society and the Portuguese Acoustical Society**, Avila, Spain. (Spanish Acoustical Society, c/Serrano 144, 28006 Madrid, Spain; Fax: +34 91 411 7651; e-mail: ssantiago@fresno.csic.es)
- March 2000**
20–24 **Meeting of the German Acoustical Society (DAGA)**, Oldenburg. 10/98
- July 2000**
4–7 ***7th International Congress on Sound and Vibration**, Garmisch-Partenkirchen, Germany. (H. Heller, DLR, Postfach 3267, 38022 Braunschweig, Germany; Fax: +49 531 295 2320; e-mail: hannel.heller@dlr.de; Web: www.iiav.org/icsv7.html)
- October 2000**
3–5 **WESTPRAC VII**, Kumamoto. 6/98
16–18 ***2nd Iberoamerican Congress on Acoustics, 31st National Meeting of the Spanish Acoustical Society, and EAA Tutorium**, Madrid, Spain. (Spanish Acoustical Society, c/Serrano 144, 28006 Madrid, Spain; Fax: +34 91 411 7651; e-mail: ssantiago@fresno.csic.es)
16–20 **6th International Conference on Spoken Language Processing**, Beijing. 10/98
- September 2001**
2–7 **17th International Congress on Acoustics (ICA)**, Rome. 10/98

OBITUARIES

This section of the Journal publishes obituaries concerning the death of Fellows of the Society and other acousticians eminent in the world of acoustics. When notified, the Editor-in-Chief solicits a summary of the person's life and contributions from an ASA member thoroughly familiar with the details, if possible. If a promised obituary is never received, a brief obituary notice may be published later.

Hugh Guthrie Flynn • 1912–1997



Hugh Flynn, Fellow of the Acoustical Society and grand old man of cavitation acoustics, died 23 May 1997 in Rochester, New York. Hugh was born 8 December 1912 in Lancaster, Ohio, 30 miles from Columbus, to which the family moved when Hugh was ten. During the 1930s he was a crime reporter for the *Ohio State Journal* (Columbus daily newspaper) while at the same time pursuing, off and on, a physics degree at Ohio State University. He graduated in 1939 and a year later took a job with the Navy's Bureau of Ordnance. From 1942 to 1946 he

was a naval officer and saw service in the Pacific aboard a submarine tender. He also made use of the Navy's educational program to get a master's degree in physics from Rensselaer Polytechnic Institute. After separating from the Navy as a lieutenant commander in November 1946, he joined the newly formed National Academy of Science/National Research Council Committee on Undersea Warfare as its first staff member (January 1947 to September 1948). While on a trip for the Committee, he met F. V. Hunt. That encounter subsequently led him to Harvard.

Hugh's graduate and postdoctoral years at Harvard (1948–1960) set the stage for the rest of his life. He became interested in cavitation; it was the beginning of a lifelong love affair with bubbles. He became convinced that modern digital computing techniques were the key to solving cavitation equations and pioneered this approach. After defending his thesis "The Collapse of a Transient Cavity in a Compressible Liquid" in 1956, he continued as one of Hunt's postdoctoral students. Eventually, he became the senior postdoctoral student and served as the Laboratory's Deputy Director (1959–60), a position that gave him valuable experience in the administration of research. In 1960, after joining the faculty of the new Electrical Engineering Department at the University of Rochester in February, he returned to Cambridge in May to marry Prudence Turgeon, with whom he had carried on a long courtship while at Harvard.

Hugh spent the rest of his life in Rochester. He and Prudence raised three children there, Kitty, Molly, and Nathaniel. A remarkable publication, "Physics of Acoustic Cavitation in Liquids," Chap. IX in Vol. 1B of W. P. Mason's series in *Physical Acoustics* (Academic Press, New York, 1964), solidified his international reputation as an authority on cavitation. Years later cavitation colleagues throughout the world still used that chapter as their point of departure and inevitably started out new graduate students with "Go read Flynn's chapter." Hugh's interest in computers, begun at Harvard, grew at Rochester. He played a leading role in founding the University's Computer Science Department and recruiting its first Chair. He retired as Professor Emeritus in 1978.

Hugh's retirement was a signal for rebirth, not slow decay. He became interested in the role of cavitation in medical ultrasound. In the early 1980s he showed that, contrary to beliefs at the time, the short pulses used in diagnostic ultrasound could produce cavitation. His collaboration with Charles Church brought considerable advances in that area. Finally, never afraid of thinking big, Hugh conceived of cavitation as a means of producing nuclear fusion. Awarded a patent in 1982, he continued working on this idea literally as long as he lived. His death on 23 May 1997 came a year and two days after Prudence had died.

In summary, the scientific legacy left us by Hugh Flynn includes (1) a computational approach to cavitation, (2) a widely used classification and terminology for cavitation, (3) the role of cavitation in medical ultrasonics, and (4) the use of cavitation to effect fusion.

Hugh's professional and (to some extent) personal life was celebrated

by two special sessions organized by Charles Church for the Seattle Meeting of the Acoustical Society of America, held jointly with the 16th International Congress on Acoustics. Two-page summaries of the papers given are in the Proceedings, Vol. III, pp. 1905–1920, and Vol. IV, pp. 2275–2292. The celebration was an outpouring of professional respect and personal affection for a colleague we shall sorely miss.

For information and encouragement in the preparation of this article, the author is indebted to Hugh's children Kitty, Molly, and Nathaniel; Mardi Hastings (Ohio State University); and many of Hugh's colleagues at Harvard and at Rochester, particularly Edwin L. Carstensen.

DAVID T. BLACKSTOCK

Russell J. Niederjohn • 1944–1996

Dr. Russell J. Niederjohn, professor in the Department of Electrical and Computer Engineering, Marquette University, Milwaukee, Wisconsin died 17 November 1996 at age 52. He served as chair of the department from 1987 to 1994 and as co-director of the Signal Processing Research Center since 1990. Dr. Niederjohn was a member of the Acoustical Society of America from 1968 until his death. He was very heavily involved in various professional and honorary society activities, particularly in the IEEE. Most recently, he served as president of the IEEE Industrial Electronics Society.

Dr. Niederjohn was born in Schenectady, New York. He received his bachelor's degree in 1967, his master's in 1968, and his doctorate in 1971, all in electrical engineering from the University of Massachusetts. He joined the Marquette faculty in 1971. Early in his career Dr. Niederjohn established several courses in the area of minicomputer and microcomputer hardware and software, at a time when many other universities were simply making plans to do so. In recent years, most of his courses were in digital signal processing and speech processing, areas that he also developed at Marquette.

Dr. Niederjohn was an excellent teacher. In addition to several other teaching awards, he received the Eta Kappa Nu C. Holmes MacDonalld Award as the Outstanding Electrical Engineering Professor in the United States in 1978 and the Marquette University Faculty Award for Teaching Excellence in 1988. For over ten years he served as faculty advisor to the Marquette chapter of Eta Kappa Nu, the national electrical engineering student honorary society. He also carried out an extraordinary amount of scholarly research, especially in the area of digital processing of speech signals. He directed the work of more than fifty master's and doctoral students, published well over one hundred scholarly papers, and was principal or co-principal investigator on grants totaling more than two million dollars. In addition to being recognized many times for his research excellence, in 1996 he received the Marquette University College of Engineering Outstanding Researcher Award. In 1993 he was elected a Fellow of the Institute of Electrical and Electronics Engineers (IEEE), for his "contributions to speech and signal processing."

He is survived by his wife, Susan, and sons, Scott and Jeremy, as well as numerous other relatives and friends.

JIM HEINEN
IGOR V. NABELEK

Antarès Parvulescu • 1923–1998

Antarès Parvulescu, a Fellow of the Society, and a physicist who specialized in ocean acoustics at the Naval Research Laboratory, died of a stroke 15 July 1998 at George Washington University Hospital. A resident of the Washington area off and on since the 1950s, he lived in Alexandria.

Dr. Parvulescu retired from the Navy Department in September 1997. He was a physicist at the Naval Research Laboratory, technical advisor to the Director, Science and Technology, naval technical adviser to the Defense Advanced Research Projects Agency, a consultant to Lockheed Martin Corp., and Principal Scientist at the Applied Physics Laboratory of the Uni-

versity of Washington. Dr. Parvulescu also had an intense interest in marine bioacoustics, and made several fundamental contributions that have had a profound influence on how all studies of fish bioacoustics are done. For his work in theoretical mathematics and physics applied to ocean acoustics, an asteroid was named in his honor in the 1980s by the International Astronomical Union.

Dr. Parvulescu was a native of Ploesti, Romania, and a graduate of the University of Bucharest, where he also received a doctorate in mathematics when he was 19. He had piloted planes since age 14, and he flew small planes as a member of the resistance in German-occupied Romania during World War II.

After the war, he taught mathematics, physics, astronomy, and ocean engineering at the University of Witwatersrand in South Africa. He moved to the United States in 1950 and taught at the University of California at Berkeley. He later taught at Columbia University, Bard and Vassar colleges, the University of Hawaii, and was founding chairman of the physics department at Gallaudet College for the Deaf. He was a senior member of the Institute of Electrical and Electronics Engineers, and a member of two academies of science.

He was a member of St. Mary's Catholic Church in Alexandria. His first wife, Dorothy Parvulescu, died in 1977. Survivors include his wife, Elaine Parvulescu of Alexandria; a son from his first marriage, Constantin Parvulescu of Seattle; and a sister, Dr. Carin Christian of Reston.

ELAINE HICKEY

J. Christian Myers • 1909–1998

Retired Navy Capt. J. Christian Myers, died 25 January 1998, at Rhode Island Hospital in Providence, Rhode Island. He was the husband of Ruth Kennedy Myers who is the founder of "Christmas in Newport." Born in Harrisburg, Pennsylvania on 21 September 1909, he was the son of the late Christian Wissler Myers and the late Ann Henning Myers. Capt. Myers retired from the Navy in 1961 after 30 years of service. He had been deputy and assistant chief of naval research. He later retired from the Raytheon Company as program manager of research and development for the Submarine Signal Division.

He was a 1932 graduate of the U.S. Naval Academy. In his early years, he served on the battleship *Arizona* and the destroyer *Drayton*. He attended the U.S. Navy Postgraduate School in Annapolis, Maryland, and received his master's degree from Harvard University. He was assigned to the USS *SEMME*, a special ship designed for test and evaluation of underwater sound and radar equipment. In 1943, he was selected as the engineering duty officer of the Mine Defense Laboratory in Panama City, Florida. In 1953, he was appointed assistant chief of naval research. Following his retirement from the Navy, he served as vice president of Chesapeake Instrument Corp. In 1964, he joined the Philco-Ford Corp. as program manager in their Marine and Underwater Systems Division later joining Raytheon. Mr. Myers was the recipient of two patents—a signal enhancer and a method of releasing stranded ships.

He was a plank owner and former member of the board of directors of Seaport '76 Foundation where he was one of the project managers in the construction of the Sloop *Providence*. He was a member of the Newport Historical Society, the Preservation Society of Newport County, and the Naval Academy Alumni Association.

Mr. Myers was a senior member of the Institute of Electronic and Electrical Engineers as well as a member of the American Ordinance Association, the American Society of Naval Engineers, and the Acoustical Society of America.

Besides his wife, he leaves a son, Christian W. Myers II of Portsmouth; three grandsons; two granddaughters; and two great-grandchildren.

CHRISTIAN MYERS

Aram Glorig • 1906–1998

Aram Glorig M.D., a Fellow of the Society, and a consultant at the House Ear Clinic, Los Angeles as well as a founder of the American Auditory Society, passed away after a long battle with cancer on 22 June 1998 in San Clemente, California. This forensic and industrial otologist was dedicated to improving the lives of people coping with deafness or a hearing impairment, and further, helped prevent hearing loss to millions of people worldwide. In a career spanning six decades, Dr. Glorig was committed to

providing a forum for the discussion of hearing problems among audiologists, otologists, acoustical and electrical engineers, as well as hearing aid manufacturers and dispensers.

Although he first specialized in pediatrics, he later developed an interest in otolaryngology, completing his second residency on the eve of World War II and promptly joined the army. While at his post in England (his homeland) he observed many cases of severe hearing loss and tinnitus as a result of exposure to bomb and shell blasts. This interest in the effects of noise exposure on hearing prompted Dr. Glorig to learn more about Audiology, the clinical diagnostic science that determines the level of hearing loss and the subsequent rehabilitation of hearing impairment. In 1946, soon after his return to the United States, he first met Howard House, M.D. "It was the first year of the Los Angeles Foundation of Otolaryngology and Aram was one of two students taking my fenestration course," Dr. House reminisced.

A year later, he was recruited from an Assistant Professorship at Yale by the Surgeon General to develop a center to care for military personnel returning with noise-induced hearing at the Walter Reed Army Hospital. Promoted to the rank of Major General, Dr. Glorig became the Director of the Audiology and Speech Correction Center for the Veterans Administration (VA), later duplicated nationwide. As Director of the Army's Technical Research in Hearing he also worked with hearing aid manufacturers to develop smaller, more efficient devices for his patients.

In 1952, Dr. Glorig joined Dr. House on the new Noise Research Center's Subcommittee and conducted scientific surveys of noise in the industrial workplace. The Occupational Safety and Health Administration (OSHA) used the results to set federal standards for protecting workers' hearing which are still in place today. As a Committee member of the National Association of Hearing and Speech Agencies, he helped prepare and promote standards for accrediting hearing and speech agencies throughout the nation and also played a pivotal role in developing the international standards for calibrating hearing-testing equipment.

Another of his finest achievements was the establishment of the Callier Center for Communication Disorders in Dallas, Texas as a result of advice he gave on the treatment and rehabilitation of the deaf and hard-of-hearing. He served as the Center's Director until his retirement in 1977 but retained the title of Director Emeritus for life. A year later, Dr. Glorig accepted an invitation from Dr. House to join the House Ear Clinic as a consultant in Forensic Otolaryngology and over the next twenty years used his expertise to refine the litigation process in cases resulting from all manner of ear injuries in the workplace. During his lifetime Aram Glorig was often recognized for advancing the knowledge and practices of otology and audiology. Among his most prestigious awards are the Presidential Citation from the American Academy of Otolaryngology—Head and Neck Surgery, the American Auditory Society's Lifetime Achievement Award, and the Health Achievement in Occupational Medicine Award from the American College of Occupational and Environmental Medicine.

Aram Glorig is survived by his wife, Bobbi Barras-Glorig, daughters Patti Schiff and Debbie DeVeccia of Dallas, Texas with whom he maintained a close relationship. The eldest, Patricia is well known in Dallas circles as a prodigious fundraiser and continues the family's interest in the Callier Center by serving as a member of its board. She is married to Steve Schiff and has two children, Devon and Denham. His other daughter, Deborah, owns and operates a stable of hunters and jumpers with her husband, Tom DeVeccia. They live in Argyle with their two daughters, Olivia and Maggie and son. His stepchildren Debie Seifert, Tony and Bryan Barras, and seven step-grandchildren all reside in California.

DILYS JONES

Thomas Mariner • 1915–1998

Dr. Thomas Mariner, a Fellow of the Society, formerly of Mount Joy, Pennsylvania, died 7 April 1998 at Moravian Manor in Lititz, Pennsylvania. Born in 17 November 1913 in Blasdale, New York, he was the son of James and Pearl (Gress) Mariner and stepson of Isaac Rowe. He graduated from Newton High School in Newtonville, Massachusetts, receiving National Honor Society recognition and the Boy's Senior Cup for "character, scholarship, athletics, and personality." He obtained his Bachelor of Arts degree from Boston University (1935) with special distinction in physics, general honors, Augustus Howe Buck Scholar recognition, and Phi Beta Kappa honor. His doctoral degree in Physics was earned from Princeton University (1947). Additional honor society memberships included Sigma Xi and the Scientific Research Society of America.

He began his professional career as Physics Group Leader at the American Cyanamid Company of Stamford, Connecticut (1941–1948). He joined the Armstrong Cork Company of Lancaster, Pennsylvania as a manager in the Physics Research Unit (1948–1976), became General Manager of Physics Research (1977–1978), and retired in December 1978. His distinguished career in research includes nine patents and more than 25 technical papers in professional journals. He participated professionally on committees of the Acoustical Society of America, the American Society for Testing Materials, the International Organization for Standardization, the American Standards Association, and the board of editors for “Noise Control” magazine. Dr. Mariner’s civic participation in Lancaster County,

Pennsylvania included school director (1958–1967) of Donegal Union School District, member of Lancaster County Tax Collection Bureau (origin to 1967), and member of the Advisory-Policy Council for Vocational Technical Schools of Lancaster County (1965–1967) as assistant chairman, chairman, and vice-president.

He is survived by his three children, Jacquelyn R. Benner of Upper Black Eddy, Pennsylvania, Dr. Geoffrey R. Mariner of Apalachin, New York, and Dr. Robert W. Mariner of San Diego, California, and his three grandchildren, Sandra J. Benner, Eric A. Benner, and Lisa A. Mariner.

GEOFFREY R. MARINER

BOOK REVIEWS

James F. Bartram

94 Kane Avenue, Middletown, Rhode Island 02842

These reviews of books and other forms of information express the opinions of the individual reviewers and are not necessarily endorsed by the Editorial Board of this Journal.

Editorial Policy: *If there is a negative review, the author of the book will be given a chance to respond to the review in this section of the Journal and the reviewer will be allowed to respond to the author's comments. [See "Book Reviews Editor's Note," J. Acoust. Soc. Am. 81, 1651 (May 1987).]*

Architectural Acoustics: Blending Sound Sources, Sound Fields, and Listeners

Yoichi Ando

Springer-Verlag, New York, NY 10158.
xvi+252 pp. Price: \$49.95.

Professor Yoichi Ando, who is Associate Dean, Graduate School of Science and Technology at Kobe University in Japan, is arguably the most prominent architectural acoustician in that nation. His new text may be considered a followup to his first book, *Concert Hall Acoustics* (Springer-Verlag, Heidelberg, 1985). This new volume goes beyond the Sabine realm of architectural acoustics, which is based on the relatively simple but effective formula $T_{60} = (0.159V)/\Sigma A_i$. Other considerations come into play in determining optimal configurations for listening spaces, and this is what Ando sets out to explain by combining the elements of psychoacoustics, modeling of the auditory-brain system, and mapping of subjective preferences. His text is intended for "both undergraduate and graduate students in various fields including acoustics, psychology and physiology, and musical art, as well as professionals in architecture, engineering, and 'sound coordinators' of concert halls and theaters." The text is not an easy read, especially for those who are not solidly grounded in mathematical techniques and/or are involved more in the artistic aspects (e.g., design or performance) of listening areas rather than in the scientific approach. For these people, the author advises reading of Chaps. 10 and 11 prior to tackling the guidelines described in Chaps. 4 and 6–8.

Following the Introduction and a historical review, Chap. 3 describes the physical properties of source signals and sound fields in a room, in particular the autocorrelation function (ACF) which contains the same information as power density spectrum but it is adjusted to account for hearing sensitivity. Effective duration of the normalized ACF is defined by the delay τ_e at which the envelope of the normalized ACF becomes one-tenth of its maximal value. The response of the ear includes the effects of time delay due not only to the room's acoustical characteristics, but also the spatially-incurred differences in the signals reaching the right ear and the left ear. The chapter would be rendered a bit clearer if the terms IACC (interaural cross-correlation function), IATD (interaural time difference), and IALD (interaural level difference) had been explained beforehand and perhaps in a more elementary fashion.

Chapter 4 deals with the subjective attributes for a sound field in a room. First the simplest sound field is considered, a situation which consists of the direct sound and a single reflection acting in lieu of a set of reflections. The data presented therein are based on tests in anechoic chambers (which allowed for simulation of different concert halls) with normal hearing subjects listening to different musical motifs. From these subjective tests, the optimum design objectives were established, namely the listening level, preferred delay time, preferred subsequent reverberation time (after the early reflections), and dissimilarity of signals reaching both ears (involving IACC). These factors are each assigned scalar values and then combined to yield a subjective preference that can vary from seat to seat in a concert hall. In Chap. 5 on the human hearing system, the first part describes the sensitivity of the human ear to a sound source and the operational principle of the outer and the middle ear. The latter part of the chapter delves into the electrical-physiological responses of the auditory neural passages, even the roles of the right and left cerebral hemispheres, linking the responses to subjective preference. Some rather interesting results of investigations include the statement that the right hemisphere is dominant for "the continu-

ous speech," while the left hemisphere is dominant when variation occurs in the delay time of acoustic reflection. The left hemisphere is usually associated with speech and time-sequential identifications, while the right hemisphere is allied with nonverbal and spatial identifications. A proposed model for the auditory-brain system is also given, which incorporates a subjective analyzer for spatial and temporal criteria and entails the participation of the left and the right hemispheres of the brain.

The auditory system brain model of Chap. 5 provides the basis for the topic of Chap. 6, which deals with the qualities of sound fields in terms of what is occurring in the auditory pathways and in the brain. The power density spectra in the neural processes in the right and left auditory pathways yield sufficient information to establish autocorrelation functions. Chapter 7 treats the subjective effects of sound field on performers. The author suggested in this chapter that music programs be selected for a given concert hall on the basis of their blending into the sound field of the hall, which, of course, would relegate many an acoustically fixed concert facility to rather limited use. Chapter 8 is a "practical" chapter in the sense that it contain design tips to improve the quality of the sound field at each listener's position. These include discussion of side walls, ceilings, diffusers mounted on walls and ceilings (avoidance of image shift is stressed here), scattered reflection by uneven surfaces, fractal geometry for desired sound reflections (yes, based on Mandelbrot's theory), transfer functions for dealing with reflection near the ceiling and for panel arrays, lateral reflection components from canopies, and floor structure and seating including the effects under sub-flooring cavities.

Individual listener subjective preferences and the matter of seat selection comprise the topic of Chap. 9. It is obvious that different individuals are likely to have different subjective preferences with respect to the same musical program, so seating requirements can differ, with respect to the preferred listening level and to the initial time delay, and even lighting. Examples are given of the audience preference, e.g., the performance of Handel's *Water Music* with 106 listeners providing the input on their preferences with respect to listening level, reverberation time, and IACC. Case studies in Chap. 10 illustrate how the acoustical design of a concert hall and a multipurpose auditorium can be accomplished. Procedures for designing sound fields include consideration of temporal factors, spatial factors, the effect of sound field on musicians, the conductor, stage performers, listener and the archetypal problem of fusing acoustical design with architecture. Multi-purpose auditoriums present bigger challenges, some of which have been met very well. The methodologies of acoustical measurements of the sound fields in rooms are discussed in Chap. 11, particularly those dealing with binaural impulse response, reverberation, as well as a recommended method for IACC measurement. An interesting segment is also included on the physical properties of a forest acting as an acoustic space. In the final chapter, a basis for planning physical environments is laid out to take account of time and space in regard to their effects on the specialized hemispheres of the human brain. A number of factors other than acoustical include measurable quantities such as temperature, lighting levels, etc. and other less tangible determinants that can be aesthetically evocative.

In view of the subjective nature of Ando's thesis, a question remains: is aural subjectivity a variant according to culture and nationality? This would constitute an interesting topic for investigation.

DANIEL R. RAICHEL
CUNY Graduate School
Mechanical and Aerospace Engineering Department
City College of New York
New York, New York 10031

REVIEWS OF ACOUSTICAL PATENTS

Daniel W. Martin

7349 Clough Pike, Cincinnati, Ohio 45244

The purpose of these acoustical patent reviews is to provide enough information for a Journal reader to decide whether to seek more information from the patent itself. Any opinions expressed here are those of reviewers as individuals and are not legal opinions. Printed copies of United States Patents may be ordered at \$3.00 each from the Commissioner of Patents and Trademarks, Washington, DC 20231.

Reviewers for this issue:

GEORGE L. AUGSPURGER, *Perception Incorporated, Box 39536, Los Angeles, California 90039*

MAHLON D. BURKHARD, *31 Cloverdale Heights, Charles Town, West Virginia 25414*

RONALD B. COLEMAN, *BBN Acoustic Technologies, 70 Fawcett Street, Cambridge, Massachusetts 02138*

DAVID A. PREVES, *P.O. Box 59124, Minneapolis, Minnesota 55459*

D. LLOYD RICE, *11222 Flatiron Drive, Lafayette, Colorado 80026*

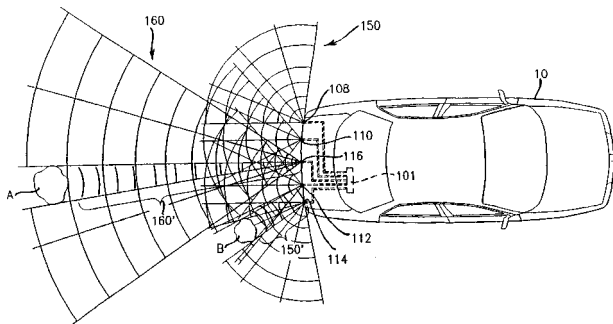
WILLIAM THOMPSON, JR., *The Pennsylvania State University, University Park, Pennsylvania 16802*

5,754,123

43.28.Tc HYBRID ULTRASONIC AND RADAR BASED BACKUP AID

Peter Joseph Nashif *et al.*, assignors to Ford Motor Company
19 May 1998 (Class 340/903); filed 6 May 1996

This backup safety system for automobiles uses ultrasonic transducers 108, 110, 112, 114 to radiate waves and receive reflected waves from nearby object B. Radar source 16 also receives reflected waves from more distant



object A. The two sensing systems are mutually computer controlled to provide warning, speed, and parking signals to the driver.—DWM

5,530,678

43.30.Xm REAL-TIME CALIBRATION ACOUSTIC ARRAY

J. G. Kosalos, assignor to Alliant Techsystems, Incorporated
25 June 1996 (Class 367/13); filed 5 December 1994

The acoustically transparent window of a transducer, or array of transducers, contains a thin PVDF film which can function as either a source or a receiver. Hence, by using preestablished transfer ratios between the input of the transducer proper and the output of the PVDF film, or vice versa, one can perform *in situ* checks or recalibrations of that transducer operating as either source or receiver.—WT

5,499,540

43.35.Yb ELECTROMAGNETIC ACOUSTIC TRANSDUCER FOR BOLT TENSION AND LOAD MEASUREMENT

Hubert L. Whaley *et al.*, assignors to The Babcock & Wilcox Company
19 March 1996 (Class 73/761); filed 15 February 1994

“A device for measuring a load on a part such as a bolt comprises a socket... wherein the socket engages the bolt for transmitting a load to the bolt. An electromagnetic acoustic transducer comprising a magnet and a coil is located in the interior space of the socket near the bolt... A detector is used to detect and measure a change in the ultrasonic signal at the bolt.”—MDB

5,503,020

43.35.Zc ELECTROMAGNETIC ACOUSTIC TRANSDUCER

Efrain A. Mandracchia, assignor to Sonic Force Corporation
2 April 1996 (Class 73/643); filed 1 July 1994

The patent pertains to a method of generating acoustic waves in an electrically conductive structure. It includes establishing a static magnetic field in an electrically conductive structure; positioning a multilayered printed circuit board (PCB) within the static magnetic field in close proximity to the surface of the structure; applying an alternating current to plurality of parallel conductors on the PCB; and detecting acoustic waves in an electrically conductive structure with the same mechanism as a received signal generated by the instantaneous force field in the electrically conductive structure.—MDB

5,752,302

43.35.Zc METHOD AND APPARATUS FOR SIZING AND SEPARATING WARP YARNS USING ACOUSTICAL ENERGY

Shuh-Haw Sheen *et al.*, assignors to the United States of America
19 May 1998 (Class 28/181); filed 23 April 1997

This patent discloses “A slashing process for preparing warp yarns for weaving operations including the steps of sizing and/or desizing the yarns in an acoustic resonance box and separating the yarns...” “The sizing step includes immersing the yarns in a size solution contained in an acoustic resonance box. Acoustic transducers are positioned against the exterior of the box for generating an acoustic pressure field within the size solution.”... “The sized yarns are then separated by passing the warp yarns over and

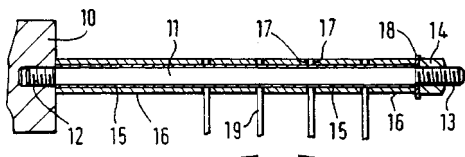
under lease rods. Electroacoustic transducers generate acoustic waves along the longitudinal axis of the lease rods, creating a shearing motion on the surface of the rods for splitting the yarns.”—DWM

5,752,423

43.35.Zc ULTRASONIC CUTTING DEVICE

Francis F. H. Rawson, assignor to Nestee S.A.
19 May 1998 (Class 83/508.3); filed in the United Kingdom 21 March 1995

This ultrasonic cutting device has a “mother” horn **10** to which is attached a solid horn **11** terminated at end **13**. Surrounding horn **11** is a bearing tube **15** surrounded by tubular spacer horns **16** spaced apart by transverse cutting blades **19**. The solid horn has a length that is a multiple of



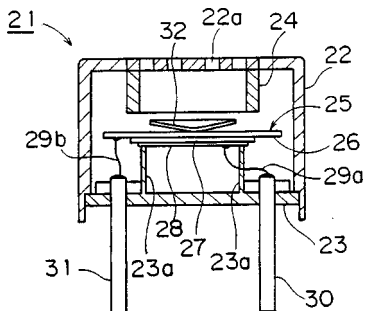
half-wavelengths, and each of the tubular spacer horns is one half-wavelength long so that the cutter blades are positioned at antinodes for maximum cutting efficiency.—DWM

5,495,766

43.38.Fx ULTRASONIC SENSOR

Masaharu Kota and Kazuya Nakatera, assignors to Murata Manufacturing Company
5 March 1996 (Class 73/652); filed in Japan 28 September 1993

The improvement is the addition of a cylindrical element **24** between the sound inlet **22a** and the piezoelectric diaphragm element **25** comprised of metal plate **26** and piezoceramic disk **27**. The inner diameter of element **24** is 1.2 to 1.5 times the diameter of cone **32**. The inner diameter of element



24 is made approximately equal to a wavelength of the ultrasonic signal while the length is less than a wavelength, whereby the coverage angle of the sensor is increased.—MDB

5,497,540

43.38.Fx METHOD FOR FABRICATING HIGH DENSITY ULTRASOUND ARRAY

Subramaniam Venkataramani *et al.*, assignors to General Electric Company
12 March 1996 (Class 29/25.35); filed 22 December 1994

The steps are described for fabricating an array of piezoelectric elements for medical applications requiring focused ultrasound. After an acoustic matching material is applied to two electroded surfaces of a piezoceramic block, the block is cut in two perpendicular planes, which are also perpendicular to the matching material surfaces, into a number of wafers with ends being the acoustic matching material. These wafers are then reassembled,

i.e., bonded together, with a space between the wafers that is filled with a polymer.—MDB

5,526,324

43.38.Fx ACOUSTIC ABSORPTION AND DAMPING MATERIAL WITH PIEZOELECTRIC ENERGY DISSIPATION

W. B. Cushman, assignor to Poiesis Research, Incorporated
11 June 1996 (Class 367/1); filed 16 August 1995

An acoustic absorption or vibration damping material is realized by incorporating lossy, electrically conductive particles or strands into a piezoelectric matrix material such as PVDF. The conductive particles or strands, usually graphite, act as small localized short circuits within the matrix material and dissipate, as heat energy, any electrical charges produced as a result of stressing the piezoelectric material.—WT

5,731,552

43.38.Ja SPEAKER WITH SOUND ABSORBING DIAPHRAGM

Ye-Ming Tsao, Taipei, Taiwan
24 March 1998 (Class 181/156); filed 21 May 1996

It is possible to lower the fundamental resonance of a transmission line loud speaker system by adding a passive radiator to the end of the pipe. Computer modeling suggests that absorptive stuffing is still needed to suppress higher-order harmonics. The patent teaches that sufficient high-frequency attenuation can be achieved by simply designing the passive radiator itself as a “...sound absorbing diaphragm.”—GLA

5,731,553

43.38.Ja SPEAKER SYSTEM

Patrice Ledoux, assignor to Excel Sound & Art
24 March 1998 (Class 181/156); filed 29 January 1997

The patent describes a conventional single-tuned bandpass system having a sealed loudspeaker chamber and a vented sound outlet chamber. The vent tunnel goes through a box filled with sand or other inert material. “The result is extremely clear sound reproduction.”—GLA

5,740,259

43.38.Ja PRESSURE WAVE TRANSDUCING

Charles Dunn, assignor to Bose Corporation
14 April 1998 (Class 381/90); filed 28 April 1995

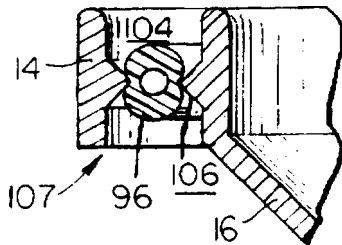
Unwanted resonances in horns or pipes can be attenuated by inserting stubs, expansion or compression chambers, or resistive screens. Claim 1 of the patent puts it in a way that may be easier to understand: “At least one immitance element...is positioned and dimensioned to reduce audible noise and alter the frequency response of said system while allowing said pressure wave waveguide to more efficiently transfer electroacoustical energy between said electroacoustical transducer and said medium as a result of being characterized by a waveguide impedance and effective length that reduces impedance mismatch between said vibratile surface and said medium.”—GLA

5,748,759

43.38.Ja LOUDSPEAKER STRUCTURE

James Joseph Croft and Robert C. Williamson, assignors to Carver Corporation
5 May 1998 (Class 381/193); filed 5 April 1995

A pinched roller **96** can serve as the centering spider or outer cone surround of a loudspeaker while at the same time acting as a negative spring



5,757,942

43.38.Ja SPEAKER UNIT WITH AND IMPROVED ACOUSTIC EQUALIZER

Yoshiteru Kamatani and Nobuo Fuke, assignors to Sony Corporation
26 May 1998 (Class 381/156); filed in Japan 13 November 1995

The loudspeaker unit in question is a high-frequency compression driver and the acoustic equalizer is its phasing plug. In most high-quality drivers the phasing plug is attached rigidly to the center pole piece, which also serves as the outermost member of the multiple-element phasing plug. This patent teaches that this results in a resonant condition that produces distortion. In the improved version, individual elements are resiliently mounted.—GLA

to counteract enclosure air stiffness. A separate sensor and air pump can be used to maintain proper centering.—GLA

5,749,433

43.38.Ja MASSLINE LOUDSPEAKER ENCLOSURE

Michael Jackson, Phoenix, AZ
12 May 1998 (Class 181/156); filed 13 February 1996

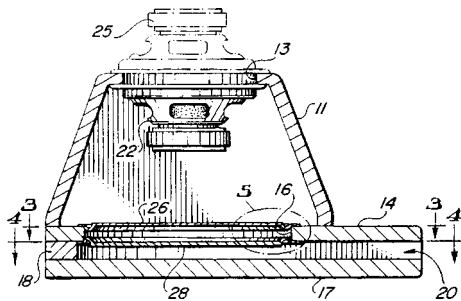
Passive radiators 26, 28 are separated by a small air space. Additional vent mass is supplied by duct 20. Can this arrangement be made to work?—yes. Is the design characterized by "...a significantly reduced volume com-

5,757,946

43.38.Ja MAGNETIC FLUID LOUDSPEAKER ASSEMBLY WITH PORTED ENCLOSURE

Andre John Van Schyndel, assignor to Northern Telecom Limited
26 May 1998 (Class 381/199); filed 23 September 1996

An important feature of Thiele/Small loudspeaker analysis is the observation that electrical and mechanical damping combine to form $Q(ts)$. To realize a desired response curve in a vented enclosure, for example, we can choose between an efficient loudspeaker with high electrical damping or a much less efficient loudspeaker having a highly damped cone suspension. Squirting magnetic fluid into the magnetic gap of a loudspeaker adds considerable damping to the motion of its voice coil. This patent states that the resulting overdamped response curve can be extended by mounting the loudspeaker in a small vented box, exactly as predicted by its Thiele/Small parameters.—GLA



pared with conventional speaker enclosures providing comparable low frequency response"?—no.—GLA

5,750,943

43.38.Ja SPEAKER ARRAY WITH IMPROVED PHASE CHARACTERISTICS

Ralph D. Heinz, assignor to Renkus-Heinz, Incorporated
12 May 1998 (Class 181/152); filed 2 October 1996

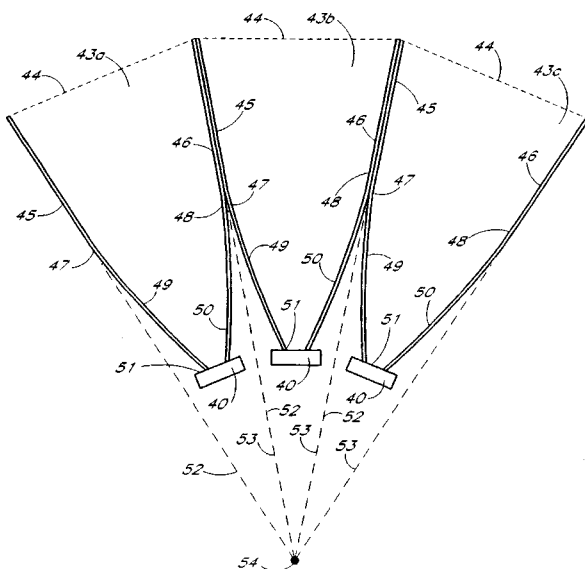
By using a quasi-parabolic flare, an array of horns can share a common acoustic center 54. The patent includes a fair amount of questionable theory,

5,745,585

43.38.Lc DYNAMIC EQUALIZATION METHOD AND DEVICE

Claude Carpentier, assignor to S L X S.A.R.I.
28 April 1998 (Class 381/103); filed in France 12 November 1991

First, we are told that the performance of a loudspeaker system in a room is subject to two kinds of distortion: comb filtering at high frequencies resulting from interference between direct and reflected sound, and broader undulations at low frequencies caused by "non-linearity of the response curve of the enclosure at the listening angle." Because the effects of multiple reflections may take as long as 100 ms to stabilize in an ordinary listening room, it follows that direct and reverberant sound fields can be separated in time and equalized independently. All that is needed is a suitable circuit to discriminate between transient and steady-state conditions and accordingly switch between the two equalization curves.—GLA



but the design appears to offer practical benefits.—GLA

5,751,398

43.38.Md MOTION PICTURE DIGITAL SOUND SYSTEM AND METHOD

Terry D. Beard, assignor to Digital Theater System, Incorporated
12 May 1998 (Class 352/236); filed 29 November 1990

"Both an analog sound track and a digital time code are placed on a motion picture sound film. ... The digital audio data itself is stored in a large capacity high reliability archival storage device rather than on the film." The advantages of this and other separate digital storage schemes include robust, error-free playback and the ability to provide any number of synchronized audio channels. The major disadvantage is that CDs or DATs must accompany each film.—GLA

5,754,664

43.38.Vk VEHICLE AUDIO SYSTEM

David L. Clark and John W. Steuber, assignors to Prince Corporation
19 May 1998 (Class 381/86); filed 1 August 1994

An array of loudspeakers, perhaps eight in all, is mounted in the headliner of an automobile. These are matrixed, delayed, and filtered to provide enhanced stereophonic reproduction.—GLA

5,757,927

43.38.Vk SURROUND SOUND APPARATUS

Michael Anthony Gerzon and Geoffrey James Barton, assignors to Trifield Productions Ltd.
26 May 1998 (Class 381/20); filed in the United Kingdom 2 March 1992

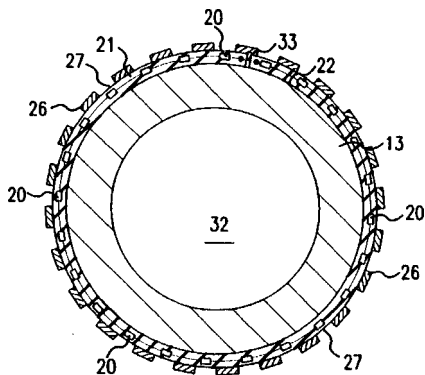
A modified decoder for Ambisonics-encoded recordings provides more stable left/center/right imaging for home theaters and the like.—GLA

5,753,812

43.40.Ph TRANSDUCER FOR SONIC LOGGING-WHILE-DRILLING

Jeffrey B. Aron *et al.*, assignors to Schlumberger Technology
19 May 1998 (Class 73/152.47); filed 7 December 1995

In order to make sonic logging measurements of a subterranean earth formation surrounding a borehole during drilling of an oil well, a horizontal monopole wave (independent of azimuth angle) is generated horizontally by the acoustic wave transducer shown here in cross section at the level of the sonic transmitter. Collar 13 has a central bore 32 through which drilling mud is pumped. Sheath 26 has window openings 27 behind which are piezo-



ceramic transducer elements 20 spaced at equal angular increments. Twenty-four transducer elements are shown, but as large a number as possible should be used to increase the monopole-to-multipole amplitude ratio. In the receiver mode the electrically connected array of elements detects averaged acoustic waves from the surrounding formation.—DWM

5,495,767

43.40.Yq LASER VIBROMETER

Xingwu Wang and James C. Simpson, assignors to Alfred University
5 March 1996 (Class 73/657); filed 26 July 1994

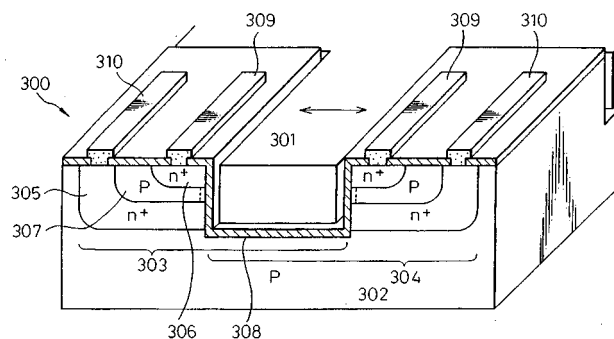
The patent for measuring target vibration rate describes what is essentially a Michelson interferometer with a laser light source with the light intensity variations due to interference being detected by an optical sensor. The optical sensor is comprised of a dual photo-diode, diodes separated by 0.5 to 5000 mm, followed by electronic circuitry for processing the signals from the two diodes.—MDB

5,503,017

43.40.Yq SEMICONDUCTOR ACCELERATION SENSOR

Masahito Mizukoshi, assignor to Nippondenso Company
2 April 1996 (Class 73/514.36); filed in Japan 21 May 1993

The figure is a perspective cross section of the sensor element. There is a pair 303 and 304 of field effect transistors (FETs), one on either side of a movable gate electrode 301. The movable gate electrode is constrained to move in the direction of the arrows. Electrostatic forces on the movable gate



maintain it approximately equidistant between the two FETs at rest condition. Motion of the gate causes modulation of current flow in the FETs in a push-pull mode. The trench recess for the movable gate and the insulating layer 308 are specific features of the construction.—MDB

5,535,177

43.40.Yq MWD SURFACE SIGNAL DETECTOR HAVING ENHANCED ACOUSTIC DETECTION MEANS

W. C. Chin and K. A. Hamlin, assignors to Halliburton Company
9 July 1996 (Class 367/81); filed 7 June 1995

By interposing a one-dimensional waveguide between a pressure transducer and the point in a conduit carrying drilling fluid (mud) in an oil well drilling system, an in-well generated pressure signal that acts on the face of the transducer can be increased (perhaps doubled). Moreover, this waveguide can be filled with a fluid which is lossier than the drilling fluid, thereby damping out high-frequency noise and improving the signal-to-noise ratio. This waveguide should be at least a quarter of a wavelength long at the lowest frequency of interest. The waveguide has been realized using high-pressure, small-diameter ($\frac{1}{4}$ in.) hydraulic hose.—WT

5,748,748

43.50.Ki APPARATUS AND METHOD FOR INFLUENCING OSCILLATIONS IN THE PASSENGER COMPARTMENT OF A MOTOR VEHICLE AND APPARATUS AND METHOD FOR DETECTING DEFECTS IN A MOTOR VEHICLE

Matthias Fischer *et al.*, assignors to Fichtel and Sachs AG
5 May 1998 (Class 381/71.4); filed in Germany 26 August 1995

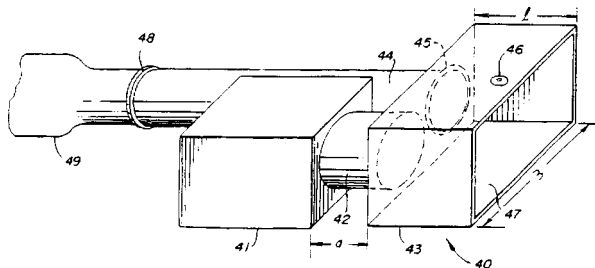
An active control system is described for reducing noise in a passenger compartment of an automobile. As opposed to more traditional approaches that use adapt filter coefficients based on the gradient of the mean-square response of residual sensors, the approach described here uses gain scheduling to select "the best" control filter from a set of stored filters. The selection is based on waveform matching of a set of sensors located throughout the vehicle that are said to characterize the operating condition, and therefore appropriate filter to select. The authors also state that discrepancies between actual sensor responses and stored waveforms can be used to detect operational defects in the vehicle over time.—RBC

5,748,749

43.50.Ki ACTIVE NOISE CANCELLATION MUFFLER

Scott Miller and J. Clay Shipps, assignors to Noise Cancellation Technologies, Incorporated
5 May 1998 (Class 381/71.5); filed 25 June 1996

An active-muffler noise-cancellation system is described having a controller, a loudspeaker housing 41, and a connecting port 42, which enters into a duct extension 43 alongside the exhaust pipe 44. The side-by-side configuration of the exhaust and control piping (44 and 42, respectively) results in a dipole radiation pattern, which is said to be converted into a plane wave by the extension duct 43. The control system uses either a



reference sensor to detect engine RPM, or a microphone located in the exhaust pipe. This signal is filtered to create the drive signal to a loudspeaker located in housing 41. The residual sensor 46 is placed in the duct extension. The authors mention many benefits of this configuration, including improved efficiency and attenuation over other dipole-oriented active-muffler designs.—RBC

5,748,750

43.50.Ki METHOD AND APPARATUS FOR ACTIVE NOISE CONTROL OF HIGH ORDER MODES IN DUCTS

André L'Espérance *et al.*, assignors to Alumax, Incorporated
5 May 1998 (Class 381/71.5); filed 10 June 1997

This patent describes an active noise control system for control of higher-order modes of noise propagating within industrial exhaust stacks. The placement of reference and residual sensors and control loudspeakers is described in relation to reducing radiation of a pure tone at 320 Hz from a 1.8-m-diam stack, which is excited by two fans. The control approach is a Filtered-X LMS algorithm implemented on hardware supplied by commercial vendors. The number and locations of residual sensors are determined using a *k*-mean algorithm described in a reference.—RBC

5,754,662

43.50.Ki FREQUENCY-FOCUSED ACTUATORS FOR ACTIVE VIBRATIONAL ENERGY CONTROL SYSTEMS

Mark R. Jolly *et al.*, assignors to Lord Corporation
19 May 1998 (Class 381/71.4); filed 30 November 1994

This patent discusses how the use of bandpass filters can limit the frequency range of active control systems designed to reduce interior noise in airplanes or helicopters. These bandpass filters (analog and/or digital) are used to send control signals to those actuators (structural or acoustic) in frequency ranges where each is most effective in reducing interior noise, while not significantly increasing structural response.—RBC

5,758,311

43.50.Ki VIBRATION/NOISE ACTIVE CONTROL SYSTEM FOR VEHICLES

Takayuki Tsuji *et al.*, assignors to Honda Giken Kogyo K. K.
26 May 1998 (Class 701/111); filed in Japan 16 March 1994

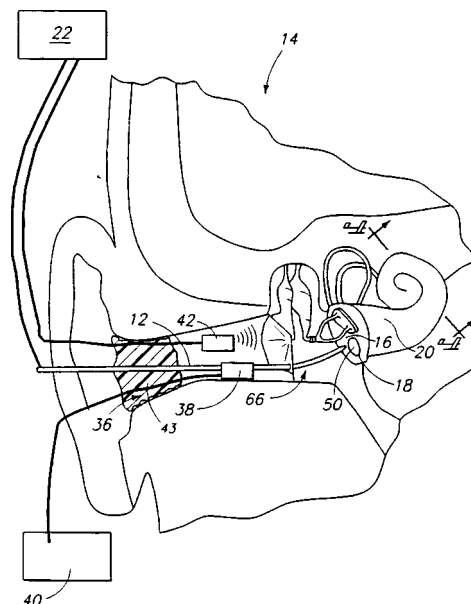
This is another patent describing an active control system for reducing noise within the passenger compartment of an automobile. The approach uses gain scheduling to select nominal control filter coefficient from stored data as a function of suspension-system acceleration levels and vehicle speed. Once these nominal values are selected, a Filtered-X LMS algorithm is used to further adapt the coefficients. The use of gain scheduling is said to allow the control system to respond more rapidly to changes in the transfer characteristics of the vibration/noise transmission, which are speed or road-surface dependent.—RBC

5,776,179

43.64.Me METHOD FOR EVALUATING INNER EAR HEARING LOSS

Tianying Ren and Alfred L. Nuttall, assignors to The University of Michigan
7 July 1998 (Class 607/137); filed 6 October 1995

The patent describes the use of electrically evoked otoacoustic emissions to evaluate the electromotility of hair cells within the mammalian cochlea. For individuals with no middle ear function, the same electrical



stimulation at the round window can also be used to implement a cochlear implant without invasive insertion of electrodes.—DAP

5,771,298

43.66.Yw APPARATUS AND METHOD FOR SIMULATING A HUMAN MASTOID

Larry J. Davis and Robert Chanaud, assignors to Larson-Davis, Incorporated
23 June 1998 (Class 381/60); filed 13 January 1997

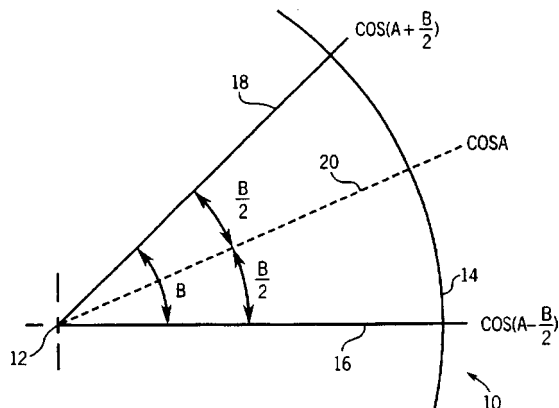
A simulated human mastoid that can be used to test bone conduction hearing aids is described. To reduce cost and complexity, the diaphragm of the device is placed over the opening in an artificial ear. The result is said to be less expensive, easier to use, and to match better the mechanical impedance specified in ANSI S3.26-1981 than previous commercial attempts to do so.—DAP

5,745,648

43.72.Ar APPARATUS AND METHOD FOR ANALYZING SPEECH SIGNALS TO DETERMINE PARAMETERS EXPRESSIVE OF CHARACTERISTICS OF THE SPEECH SIGNALS

Safdar M. Asghar and Mark A. Ireton, assignors to Advanced Micro Devices, Incorporated
28 April 1998 (Class 395/2.13); filed 5 October 1994

The patent describes a method of speech analysis using line spectral frequency (LSF) coding and an efficient mathematical procedure for finding the roots of a polynomial expressed in LSF coefficients. Trigonometric identities



are exploited to scan the arc of the Z plane unit circle in small steps, searching for zero crossings of a trigonometric expression.—DLR

5,751,900

43.72.Ar SPEECH PITCH LAG CODING APPARATUS AND METHOD

Masahiro Serizawa, assignor to NEC Corporation
12 May 1998 (Class 395/2.16); filed in Japan 27 December 1994

This pitch analyzer and the related speech vocoder are able to encode an accurate representation of the pitch value by computing extracted pitch lag values for several subframes of the current frame. The extracted pitch lag values for subframes other than the current or preceding subframe are used to predict a lag for the current subframe.—DLR

5,737,485

43.72.Bs METHOD AND APPARATUS INCLUDING MICROPHONE ARRAYS AND NEURAL NETWORKS FOR SPEECH/SPEAKER RECOGNITION SYSTEMS

James L. Flanagan *et al.*, assignors to Rutgers The State University of New Jersey
7 April 1998 (Class 395/2.41); filed 7 March 1995

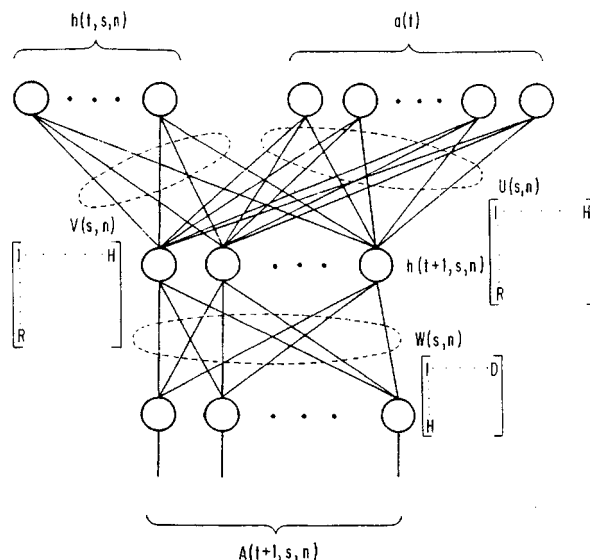
This speech recognition system uses multiple microphones in a linear array to collect speech from a distant talker, for example, from the other side of a room. The microphone signals are processed by a neural network to generate a computed speech signal essentially equivalent to the signal from a single close-talking microphone. A single signal is in fact used to train the neural network.—DLR

5,737,486

43.72.Bs PATTERN RECOGNITION METHOD BY USING REFERENCE PATTERNS EACH OF WHICH IS DEFINED BY PREDICTORS

Ken-Ichi Iso, assignor to NEC Corporation
7 April 1998 (Class 395/2.41); filed 10 May 1990

This speech recognition system uses neural network technology for pattern detection in what is probably the prototypical arrangement of a time-delay neural network for recognition. Past and present feature vectors are



provided as network inputs while network outputs are taken as word or phrase indicators. The input is said to cover a longer time span than a typical hidden Markov model.—DLR

5,745,649

43.72.Bs AUTOMATED SPEECH RECOGNITION USING A PLURALITY OF DIFFERENT MULTILAYER PERCEPTION STRUCTURES TO MODEL A PLURALITY OF DISTINCT PHONEME CATEGORIES

David M. Lubensky, assignor to NYNEX Science & Technology Corporation
28 April 1998 (Class 395/2.41); filed 7 July 1994

This isolated word recognizer uses a combination of HMM and neural network structures to implement phonetic context dependencies while reducing the computational load. Left and right phonetic contexts are grouped into broad classes for which neural networks are trained using a cascade-correlation training procedure. Phonetic segmentation is then performed by HMMs.—DLR

5,749,066

43.72.Bs METHOD AND APPARATUS FOR DEVELOPING A NEURAL NETWORK FOR PHONEME RECOGNITION

Paul A. Nussbaum, assignor to Ericsson Messaging Systems, Incorporated
5 May 1998 (Class 704/232); filed 24 April 1995

This patent describes a development system suitable for designing and testing a speech recognizer using neural network technology. Acoustic analyzer details and segmentation and network training methods may be chosen by the operator and evaluated with respect to system performance.—DLR

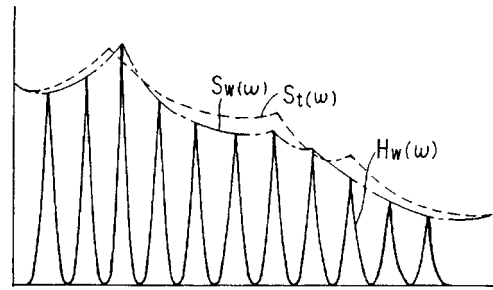
5,749,065

43.72.Gy SPEECH ENCODING METHOD, SPEECH DECODING METHOD AND SPEECH ENCODING/DECODING METHOD

Masayuki Nishiguchi and Jun Matsumoto, assignors to Sony Corporation

5 May 1998 (Class 704/219); filed in Japan 30 August 1994

This CELP vocoder converts the short-term spectral information into line spectral pairs (LSP) representation for transmission. Separate codebooks are provided for voiced and unvoiced portions of the input with separate versions of each for male and female speakers. The waveform during voiced intervals is generated by sine wave synthesis.—DLR



centroid are stored along with a segment of a speech waveform nearest the centroid, but which has been modified so that the spectrum is closer to the centroid target.—DLR

5,751,901

43.72.Gy METHOD FOR SEARCHING AN EXCITATION CODEBOOK IN A CODE EXCITED LINEAR PREDICTION (CELP) CODER

Andrew P. DeJaco and Ning Bi, assignors to Qualcomm, Incorporated

12 May 1998 (Class 395/2.25); filed 31 July 1996

This CELP vocoder uses the mean square error computed over the analysis window (as is typical) to search the excitation codebook. However, the window is extended beyond the current excitation vector by the perceptual filter length into the next subframe. This accounts for the ringing of the code vector into the next subframe and results in a symmetrical autocorrelation matrix, saving memory and computation time.—DLR

5,745,650

43.72.Ja SPEECH SYNTHESIS APPARATUS AND METHOD FOR SYNTHESIZING SPEECH FROM A CHARACTER SERIES COMPRISING A TEXT AND PITCH INFORMATION

Mitsuru Otsuka *et al.*, assignors to Canon Kabushiki Kaisha

28 April 1998 (Class 395/2.69); filed in Japan 30 May 1994

This speech synthesizer stores short-term spectral descriptors to represent the phonetic units. During synthesis, a representative waveform is generated using a sum of cosines method. The input "text" is in the form of a phonetic transcription augmented by pitch indicators, which govern the addition of overlapped fundamental period waveforms.—DLR

5,740,319

43.72.Ja PROSODIC NUMBER STRING SYNTHESIS

Frederick C. Wedemeier, assignor to Texas Instruments, Incorporated

14 April 1998 (Class 395/2.75); filed 24 November 1993

This speech synthesizer for sequences of spoken digits represents the sound of each digit in two forms, a first part, usually just the initial phoneme, and a second form, often the entire word. Stored speech segments for each digit include versions of one or both forms in different contexts, i.e., utterance initial or final or as a digit pair. A total of 13 speech segments are stored for each digit.—DLR

5,748,838

43.72.Ja METHOD OF SPEECH REPRESENTATION AND SYNTHESIS USING A SET OF HIGH LEVEL CONSTRAINED PARAMETERS

Kenneth N. Stevens, assignor to Sensimetrics Corporation

5 May 1998 (Class 395/2.7); filed 24 September 1991

This speech synthesizer control strategy uses models of the human vocal cord dynamics to generate full sets of synthesizer control parameters from a smaller number of high-level parameters. The high-level parameters typically include such items as the glottal fundamental frequency, glottal opening area, and pressure change constraints. The low-level parameters are controls for a formant synthesizer such as the Klatt cascade/parallel model.—DLR

5,740,320

43.72.Ja TEXT-TO-SPEECH SYNTHESIS BY CONCATENATION USING OR MODIFYING CLUSTERED PHONEME WAVEFORMS ON BASIS OF CLUSTER PARAMETER CENTROIDS

Kenzo Itoh, assignor to Nippon Telegraph and Telephone Corporation

14 April 1998 (Class 395/2.76); filed in Japan 10 March 1993

The patent describes a method of speech synthesis based on phoneme clusters. The system is "trained" by a cluster analysis of linear prediction spectra from the training speech. For each cluster, the LPC parameters at the

5,749,071

43.72.Ja ADAPTIVE METHODS FOR CONTROLLING THE ANNUNCIATION RATE OF SYNTHESIZED SPEECH

Kim Ernest Alexander Silverman, assignor to Nynex Science and Technology, Incorporated

5 May 1998 (Class 704/260); filed 19 March 1993

This speech synthesis system performs a linguistic phrase analysis based on specific knowledge of the textual domain, names and addresses taken from a phone book. The phrase structure information is used to construct improved pitch and duration controls, resulting in speech synthesis with improved prosodic patterns and better intelligibility.—DLR

5,734,793

43.72.Ne SYSTEM FOR RECOGNIZING SPOKEN SOUNDS FROM CONTINUOUS SPEECH AND METHOD OF USING SAME

Shay-Ping T. Wang, assignor to Motorola, Incorporated
31 March 1998 (Class 395/2.41); filed 7 September 1994

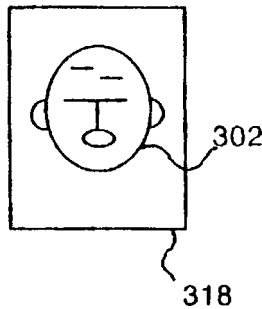
This speech recognizer matches acoustic feature vectors by computing a discriminant function for each of a number of acoustic classes. The discriminant functions may use any orthogonal basis set, but typically consist of low-order polynomials. The set of polynomial discriminant weights constitute the classifier output for each acoustic class.—DLR

5,734,794

43.72.Ne METHOD AND SYSTEM FOR VOICE-ACTIVATED CELL ANIMATION

Tom H. White, Los Angeles, CA
31 March 1998 (Class 395/2.84); filed 22 June 1995

This patent describes an application for a speech recognizer in which the decoded output is used to select animation cells from a set of cartoon facial patterns. The sequence of selected cells results in a film of an ani-



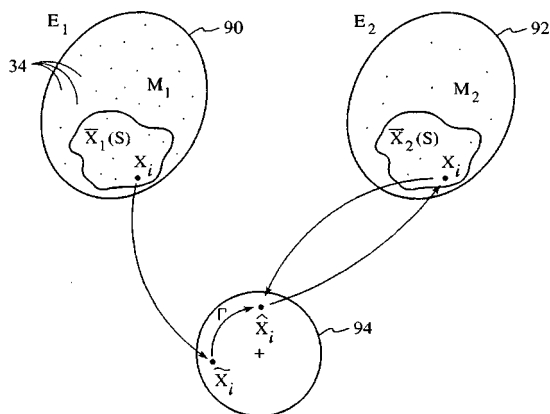
mated speaking character which also can display appropriate emotions or other visual correlates of the processed speech signal.—DLR

5,737,487

43.72.Ne SPEAKER ADAPTATION BASED ON LATERAL TYING FOR LARGE-VOCABULARY CONTINUOUS SPEECH RECOGNITION

Jerome R. Bellegarda *et al.*, assignors to Apple Computer, Incorporated
7 April 1998 (Class 395/25.9); filed 13 February 1996

This technique for speaker adaptation in large vocabulary speech recognition systems uses a sort of mapping between hidden Markov model states corresponding to similar acoustic events from different speakers.



Once a sufficient number of acoustic events has been collected from a new speaker, the mappings can be used in a predictive manner to aid recognition of new items from the new speaker.—DLR

5,737,488

43.72.Ne SPEECH RECOGNIZER

Ken-Ichi Iso, assignor to NEC Corporation
7 April 1998 (Class 395/2.65); filed in Japan 13 June 1994

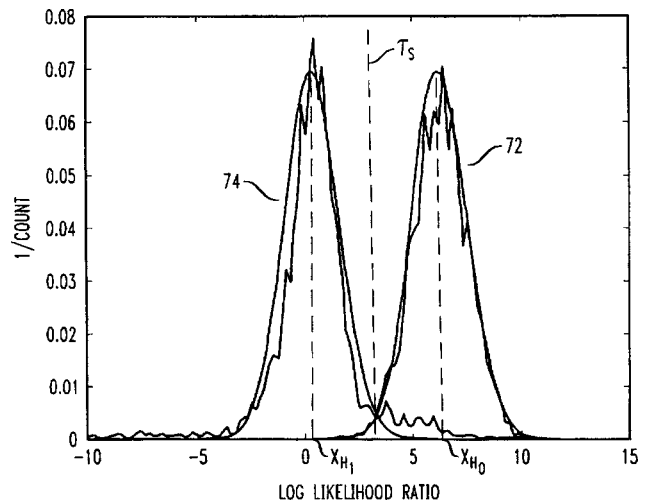
This speech recognition system uses two stages of hidden Markov models, one to "preprocess" the acoustic feature vectors, and the second to perform the usual phonetic sequence matching which leads to decoded output sequences. In order to solve a problem described as "output probability discontinuities," the first HMM stage produces an internal state number which constitutes the input to the second stage.—DLR

5,737,489

43.72.Ne DISCRIMINATIVE UTTERANCE VERIFICATION FOR CONNECTED DIGITS RECOGNITION

Wu Chou *et al.*, assignors to Lucent Technologies, Incorporated
7 April 1998 (Class 395/2.65); filed 15 September 1995

This speech recognizer, designed primarily for connected digit sequences, includes a second hidden Markov model stage trained specifically to verify the digits strings decoded by the first HMM stage. Based on the



recognized candidate sequences, a set of confusable alternates is generated. The verification stage then produces scores for the original and the alternates and computes a recognition confidence rating.—DLR

5,737,490

43.72.Ne METHOD AND APPARATUS FOR CONSTRUCTING CONTINUOUS PARAMETER FENONIC HIDDEN MARKOV MODELS BY REPLACING PHONETIC MODELS WITH CONTINUOUS FENONIC MODELS

Stephen Christopher Austin and Peter Vincent de Souza, assignors to Apple Computer, Incorporated
7 April 1998 (Class 395/2.65); filed 30 September 1993

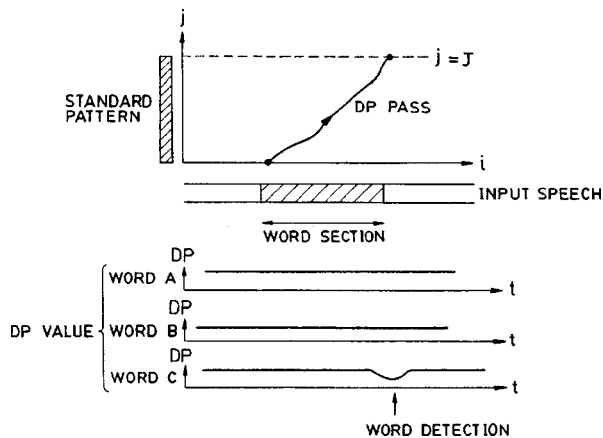
This patent describes the speech recognition process as a compromise between acoustic reality and phonemic classification. In a first training pass, typical phonetic HMMs are produced using a typical phonemic dictionary. In a second retraining pass, new HMM states are created according to the training speech data. Using the coinage of the IBM research group, these new HMMs are called fenonic models.—DLR

5,751,898

43.72.Ne SPEECH RECOGNITION METHOD AND APPARATUS FOR USE THEREIN

Tetsuo Kosaka *et al.*, assignors to Canon Kabushiki Kaisha
12 May 1998 (Class 395/2.5); filed in Japan 3 October 1989

This isolated word speech recognizer is also able to detect the speech signal within a longer input sequence and concentrate the analysis on the speech portion. From the input, speech power, average feature vector, and



covariance matrix are computed. Dynamic programming with the Mahalanobis distance is performed using the average vector and covariance matrix rather than separately testing each stored reference pattern.—DLR

5,753,843

43.75.Wx SYSTEM AND PROCESS FOR COMPOSING MUSICAL SECTIONS

C. Todor Fay, assignor to Microsoft Corporation
19 May 1998 (Class 84/609); filed 6 February 1995

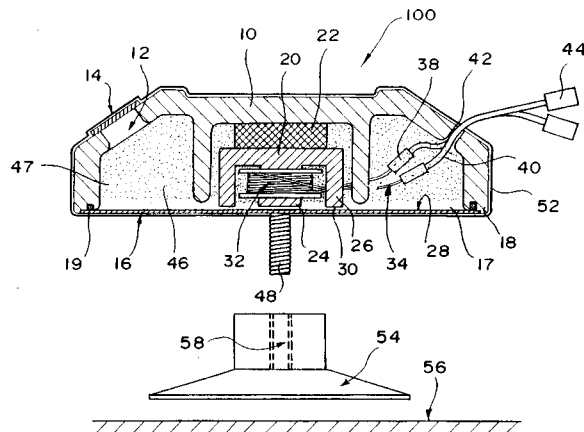
In a multimedia presentation including accompaniment music this system allows the observer to interact with the musical audio portion of the presentation and to vary the style of the musical composition or the shape of musical sequence without requiring the observer to have an extensive knowledge of music. The composition itself may also be modified from one rendition to the next using the controls for the "composition engine." The system diagrams are shown in 20 different figures.—DWM

5,532,980

43.80.Nd VIBRATIONAL ANTI-FOULING SYSTEM

C. E. Zarate *et al.*, assignors to Sciencetech, Incorporated
2 July 1996 (Class 367/139); filed 14 November 1994

A transducer and associated controller are described for producing vibrations of an underwater structure to inhibit the attachment of marine organisms. The transducer consists of housing 10, waterproof coating 52, permanent magnet assembly 20, coil winding 32, flexible diaphragm 16, mounting shaft 48, and mounting fixture 54 which is permanently attached



to underwater structure 56 which one wishes to vibrate. Aperture 12, covered with elastic membrane 14, constitutes a pressure compensation mechanism. Electrical excitation of the coil 32 produces a force which is transmitted to the structure 56 via the mounting shaft 48.—WT

5,774,563

43.80.Qf COMBINED ELECTRONIC ACOUSTICAL STETHOSCOPE

Richard J. DesLauriers, Waterbury, CT and James M. Muskatello, Southington, CT
30 June 1998 (Class 381/67); filed 11 July 1996

A combined electronic and acoustical stethoscope is disclosed in which a microphone, loudspeaker, signal processor, programmable switch, and battery are enclosed in a conventional, spool-like head assembly. The device is said to be able to pick up and digitally record faint heart murmurs while not being unduly different in appearance from a purely acoustical stethoscope.—DAP

Wave decomposition of the vibrations of a cylindrical shell with an automated scanning laser vibrometer^{a)}

Hyun-Gwon Kil,^{b)} Jacek Jarzynski, and Yves H. Berthelot

Woodruff School of Mechanical Engineering, Georgia Institute of Technology, Atlanta, Georgia 30332-0405

(Received 18 August 1997; accepted for publication 23 July 1998)

Elastic waves propagating in a cylindrical shell have been detected by an automated scanning laser vibrometer designed to record both in-plane and out-of-plane surface motion over the surface of the shell (32 points axially and 32 points circumferentially). The structure was freely suspended in air and excited radially by a shaker at a single frequency, either below or above the ring frequency of the shell. A wave vector analysis of the data was performed with a fast Fourier transform and an overdetermined modified extended Prony method. The results clearly show the presence of longitudinal, shear, and flexural waves above the ring frequency. In addition, the Prony method reveals the presence of evanescent waves due to mode conversion of the propagating waves near the ends of the shell. Below the ring frequency, two types of in-plane waves and flexural waves were identified. The results are in excellent agreement with predictions from the dispersion curves for thin shells. © 1998 Acoustical Society of America. [S0001-4966(98)01211-9]

PACS numbers: 43.10.Ln, 43.40.Ey, 43.40.At, 43.40.Yq [CBB]

INTRODUCTION

To fully understand the radiation and scattering of sound from complex elastic structures, it is important to decompose the vibrational wave field on the structure into its basic components (e.g., flexural, extensional, shear, torsional, evanescent, etc.). This requires measurements over a large portion of the structure so as to establish the spatial periodicities that characterize each type of wave. It is in general impractical to load a structure with a large array of accelerometers and, in recent years, laser Doppler vibrometry has emerged as a useful alternative for imaging vibrating structures.¹ Commercially available scanning vibrometers are designed to measure out-of-plane surface motion and, consequently, they are well suited for the detection of flexural waves but they are somewhat insensitive to longitudinal or shear waves.

In this paper, we report experimental results obtained with a fully automated scanning laser vibrometer designed to simultaneously measure in-plane and out-of-plane surface motion over a cylindrical shell. The objectives of the research were (a) to develop a fully automated scanning laser vibrometer, and (b) to establish that longitudinal, shear, flexural waves, and even evanescent waves can be detected separately with a laser vibrometer. This work is an extension of the research presented in Ref. 2. The experimental system is described in Sec. I. The wave vector analysis of the data is summarized in Sec. II, and the results are given in Sec. III.

The optical system described in Sec. I is designed to measure both in-plane and out-of-plane components of surface velocity at the same point on the surface. However, all the dispersion curves presented in Sec. II are based on measurements of the in-plane velocity component only, because

this is the dominant component for both the longitudinal and shear waves in the shell. The flexural waves also have a measurable in-plane velocity component. Measurements of the out-of-plane component of surface velocity on the above cylindrical shell are presented in Ref. 3.

I. EXPERIMENTAL SYSTEMS

A. Laser Doppler vibrometer

The basic operational principle of the laser Doppler vibrometer (LDV) is to detect the change in frequency (or phase) in the light reflected from a vibrating surface. The amplitude and phase of the surface velocity is determined from the measured Doppler frequency shift. The system configuration and signal processing are very similar to those in laser Doppler anemometry.⁴ The incident light is focused to a small spot on the vibrating surface. The surface is rough on an optical scale and reflects light in all directions including specular. The incident light spot is so small that the instantaneous particle velocity is the same for all the illuminated surface particles. The main operational principles of LDV are summarized below. A more detailed description is given in Refs. 3 and 5.

The optical arrangement of the LDV system is shown in Fig. 1. The system is designed so that it can be switched, with a mechanical shutter, from a configuration for measurement of in-plane motion to a configuration for measurement, at the same point on the surface, of the out-of-plane motion. A linearly polarized 10-mW He-Ne laser produces a coherent beam with a wavelength $\lambda = 632.8$ nm. A beamsplitter deflects approximately 4% of the light energy to form a reference beam. The remaining 96% of the light passes through an acousto-optic modulator (Bragg cell) driven by a quartz oscillator at a frequency of 40 MHz. The Bragg cell is adjusted to split the light into two beams of approximately equal amplitude, where the frequency of one of the beams is

^{a)}“Selected research articles” are ones chosen occasionally by the Editor-in-Chief that are judged (a) to have a subject of wide acoustical interest, and (b) to be written for understanding by broad acoustical readership.

^{b)}Present address: Department of Mechanical Engineering, Suwon University, Korea.

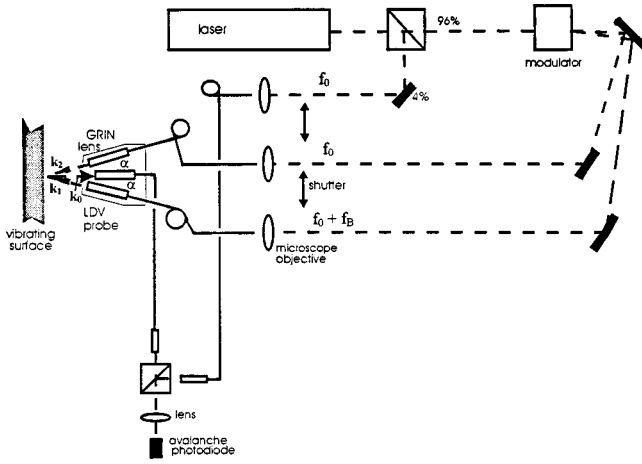


FIG. 1. Optical arrangement of the laser Doppler vibrometer. The two light beams are incident symmetrically on the vibrating surface and 2α is the angle between them. f_0 is the optical frequency and f_B is the additional frequency shift produced by the acousto-optic modulator.

shifted by $f_B = 40$ MHz. The frequency-shifted beam is necessary for heterodyne detection.

The light beams are coupled into polarization maintaining single mode fibers, and carried to the laser probe head. Use of the fibers allows the probe head to be mechanically decoupled from the optical bench, and provides the flexibility needed for the scanning measurement technique. The probe head is designed to take full advantage of optical fiber technology. It is compact (about $4\text{ cm} \times 4\text{ cm} \times 1\text{ cm}$) and it can be scanned along the structure at a distance of about 1.5 cm. The probe head consists of two graded-index (GRIN) cylindrical lenses as transmitting optics, mounted on a Lexan plate. The angle between the incident beams is $2\alpha = 22^\circ$. The two GRIN lenses produce two focused laser beams that are made to overlap on the vibrating surface. The transmitting fibers are oriented and positioned in front of the GRIN lenses so that the same polarization state is kept for the two incident beams. This increases the fringe contrast of the interference pattern and, therefore, the signal-to-noise ratio of the measuring system. A third GRIN lens, placed at the bisector of the two incident beams, is used to collect the light scattered from the vibrating structure. A multimode fiber (graded index, $62.5/125\ \mu\text{m}$) is attached to this lens and transfers the scattered light from the vibrating surface to a photodetector (an avalanche photodiode). The signal output of the photodiode is an FM signal whose carrier frequency is 40 MHz and whose instantaneous phase is proportional to the displacement of the vibrating surface or, alternatively, whose instantaneous frequency deviation from the 40-MHz carrier signal is proportional to the instantaneous surface velocity of the vibrating structure.^{2,4}

The change in frequency (or phase) of the light reflected from the vibrating surface is related to the surface motion as follows. Consider a vibrating surface with the instantaneous displacement

$$\vec{r} = u\vec{e}_x + w\vec{e}_z, \quad (1)$$

where u and w correspond to in-plane and out-of-plane components of displacement vector r . To detect the phase change

due to the in-plane vibration the system is configured as follows. The shutter is moved to block the reference beam. The two laser beams from the Bragg cell are projected into a single spot on the surface with an angle 2α between the corresponding incident wave-number vectors \vec{k}_1 and \vec{k}_2 , which are symmetric with respect to the normal to the surface. The interference of the two speckle fields originating from the incident waves is detected along the direction k_0 normal to the surface. The relative phase change between beam 1 and beam 2 is given by

$$\Delta\phi = (\vec{k}_2 - \vec{k}_1) \cdot \vec{r} = \frac{4\pi}{\lambda} (\sin\alpha)u, \quad (2)$$

where λ is the wavelength of the laser light.

In this paper, the probe with the above configuration was used to measure the in-plane vibration field over the cylindrical shell. However, the probe can also be configured to detect the out-of-plane surfaces vibration as follows. The shutter is now used to block one of the light beams from the Bragg cell (the beam whose frequency was not shifted). For the remaining, frequency-shifted light beam, the light wave scattered along \vec{k}_0 is made to interfere with the reference wave derived directly from the laser as shown in Fig. 1. This configuration allows one to detect the phase change due to a combination of in-plane and out-of-plane surface vibrations, which takes the form

$$\Delta\phi = (\vec{k}_0 - \vec{k}_1) \cdot \vec{r} = \frac{2\pi}{\lambda} [(\sin\alpha)u + (1 + \cos\alpha)w]. \quad (3)$$

Knowing the phase change due to in-plane surface vibration in Eq. (2), one can deduce the phase change due to the out-of-plane surface vibration.

The interference of scattered light generates the electric current at the photodetector. It takes the form

$$i(t) = C[\frac{1}{2}E_1^2 + \frac{1}{2}E_2^2 + E_1E_2 \cos(\omega_B t + \Delta\phi + \Delta\psi)], \quad (4)$$

where C is a constant which includes the quantum efficiency and the gain of the photodetector. E_1 and E_2 are magnitudes of the electric fields of the two scattered light signals for in-plane surface vibration measurement. For the out-of-plane vibration measurements E_1 is the magnitude of the scattered light signal and E_2 is the magnitude of the reference light beam. The frequency $\omega_B = 2\pi f_B$ is an additional frequency shift ($f_B = 40$ MHz), which is required for heterodyne detection⁴ of the surface vibration. $\Delta\psi$ is the phase difference of the two light beams incident into the photodetector due to random fluctuations in environmental conditions, including temperature fluctuations and random vibrations in the optical system.

Equation (4) is based on the assumption that the electric fields of the scattered light are plane and coherent waves. However, in practice the vibrating reflecting surface is rough on the scale of optical wavelength and the scattered waves are not plane. When coherent light waves are scattered from a rough surface, a complex interference pattern of bright and dark spots is formed called the speckle pattern.⁶ It can be shown^{7,8} that the speckle effect reduces the amplitude of the ac signal, and the ac current generated in the photodetector is

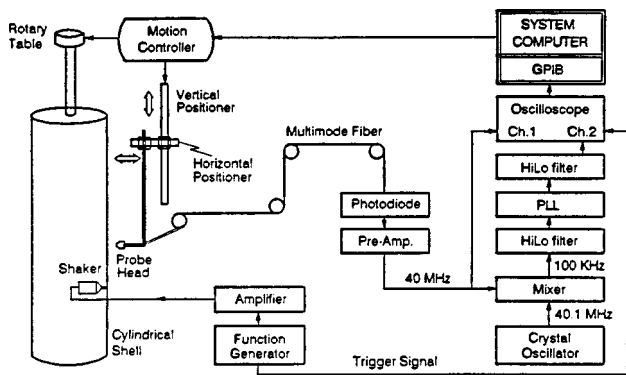


FIG. 2. Electronic system used to detect the vibrating surface velocity.

$$i_{ac} = CF_0 E_1 E_2 \cos(\omega_B t + \Delta\phi + \Delta\psi), \quad (5)$$

where F_0 is the fringe visibility which depends on the statistics of the reflecting surface, and accounts for the speckle effect. Considering harmonic surface vibration at frequency ω_s with in-plane component $u = A \cos(\omega_s t + \phi)$, the ac current takes the form

$$i_{ac} = CF_0 E_1 E_2 \cos(\omega_B t + m(t) + \Delta\psi), \quad (6)$$

where $m(t)$ is the frequency modulation from the vibrating surface, which for the in-plane component takes the form

$$m(t) = \frac{4\pi A}{\lambda} \sin \alpha \cos(\omega_s t + \phi). \quad (7)$$

There are two basic methods to extract information about the modulation index: spectral analysis and FM demodulation. The former has the advantage of being an absolute measurement of the corresponding displacement component. The latter is more appropriate for measurements of transient vibration signals and for wave vector analysis, which requires detection of the phases as well as the amplitudes of the vibration signals. In the present study FM demodulation with a phase locked loop (PLL)⁹ was used to obtain the amplitude A and phase ϕ of the surface vibration.

A schematic diagram for the detection system is shown in Fig. 2. After filtering the low frequencies, the signal is amplified and mixed with a 40.1-MHz signal generated by a crystal oscillator. Mixing the signals produces a downshifted signal at 100 kHz that is still modulated by the phase variations due to the surface vibration. After amplification and filtering of the 100-kHz FM signal, the signal is demodulated by a calibrated phase-locked loop (PLL).⁹ The output signal from the PLL is the vibration signal, proportional to the instantaneous surface velocity at the focal point where the two beams overlap. The vibration signal is displayed on a digital oscilloscope. A GPIB board is used to transfer the vibration signal data from the digital oscilloscope (Tektronix 2430A) to a system computer.

Typical operating conditions for the LDV system are as follows. The light power of each beam incident on the vibrating surface is 1.7 mW. Each beam is focused on the surface (which is rough on the scale of an optical wavelength) to a circular spot with about 50 μm diameter. Light is

reflected diffusively in all directions by the surface. The average light power received by the photodiode is about 2.5 μW . The fringe visibility factor F_0 was measured and found to be $F_0 \approx 0.1$ for a number of rough surfaces including lathe-finished metallic surfaces. The minimum detectable displacement amplitude was determined experimentally to be ~ 1 nm in the frequency range of 200 Hz–20 kHz, with a bandwidth of ~ 1 kHz in the receiving electronics, and with averaging the signal 64 times to reduce noise. The accuracy of the displacement measurement was determined by comparing the LDV data with measurements made using a calibrated accelerometer. The LDV measurements agreed with the accelerometer to within ~ 1 nm. The repeatability of the measurements was also found to be ~ 1 nm. The dynamic range of the system, for displacement measurements, is 50 dB. The lower limit is the minimum detectable displacement of 1 nm. The upper limit is set by the maximum deviation (~ 40 kHz) in frequency which the PLL can track. This corresponds to a displacement of ~ 300 nm at 10 kHz. The frequency range of the system is set by the PLL demodulator. The response of the demodulator used was flat over the range 200 Hz–20 kHz. However, the optical probe has a very wide response, extending from very low frequencies to above 100 MHz. The above probe was used recently to detect Lamb waves in a thin plate at frequencies around 1 MHz (this data will be reported separately). The only change required in the system for these measurements was to replace the PLL demodulator with a broadband FM discriminator. At frequencies below 100-Hz environmental noise (temperature fluctuations and vibration) increases significantly in the system.

The alignment of the optical probe is critical. First the two transmitting GRIN lenses are aligned so that the incident light beams are in the same plane. For each lens this is done with a single, fine-threaded screw which controls the vertical elevation of the lens. During assembly the light from each transmitting lens is focused at a point corresponding to the location of the vibrating surface. This focusing is accomplished as follows. Each GRIN lens is mounted in a metal tube and the optical fiber is mounted in a ferrule which slides in the lens tube. The ferrule is moved in the tube until the end of the fiber is at the right distance from the lens to obtain the desired focal length. The spot size of the incident light at the focal point is about 50 μm . Once the two incident light beams are adjusted to be coplanar the overlap of the incident light spots on the vibrating surface is optimized by moving the optical probe towards or away from the surface until the amplitude of the 40-MHz carrier signal from the photodetector is maximum. After the above alignment of the transmitting lenses, the receiving GRIN lens is aligned. This lens must be aligned both vertically and horizontally. This is most conveniently achieved by sending light down the multimode fiber and using the lens as a transmitting lens during the alignment procedure. First, the distance of the fiber end from the lens is adjusted so that the lens-fiber combination is focused on the vibrating surface. Then, a fine-threaded screw is used to align the lens vertically so that the light beam from this lens is the same (horizontal) plane as the light beams from the transmitting lenses. Finally, a second screw is used

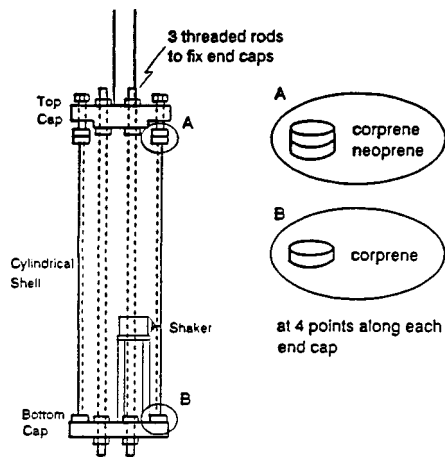


FIG. 3. Mounting, scanning, and driving setup for the cylindrical shell.

for alignment of the lens in the horizontal plane, so that its focal point coincides with the overlapping spots of the transmitting lenses. When the system is used for vibration measurements the above GRIN lens collects light reflected from the vibrating surface. The direction for this reflected light is nonspecular and light is scattered in the direction of the receiving lens only when the surface is rough on an optical scale. The above alignment procedure optimizes the level of light collected into the multimode fiber by the receiving GRIN lens.

B. Cylindrical shell

The experimental model is a thin cylindrical shell made of type 304 stainless steel. The nominal dimensions of the shell, as given by the manufacturer, are as follows: radius $a=7.55$ cm, thickness $h=0.15$ cm, and length $l=93.39$ cm. The tolerances for the above dimensions are stated by the manufacturer to be $\pm 10\%$. Handbook values for the properties of the shell steel are: Young's modulus $E=20.0 \times 10^{10}$ Pa, Poisson's ratio $\nu=0.283$, and density $\rho=7900$ kg/m³. (These values were used to calculate the dispersion curves shown in Figs. 6 and 8.)

In order to approximate the free-free boundary conditions at both ends of the shell, the shell is held between two aluminum end caps with four uniformly spaced pieces of compliant materials such as neoprene and corprene along each end of the shell, as shown in Fig. 3. The two end caps are attached to each other by means of three threaded long rods which passed inside the shell. A brass rod is clamped into the center of the top end cap. It provides vertical suspension from the rotary table. The shell is excited by a piezoelectric shaker driven with a continuous harmonic signal. The shaker is mounted normally to the shell with a 4-40 stud located 30 cm (0.32L) above the bottom of the shell.

C. Automated scanning and focusing algorithm

Wave vector analysis of structural vibrations requires extensive vibration field data over a large portion of the structure. For practical implementation, it is therefore important to design a laser vibrometer with automated scanning capability and automated alignment of the optical head at

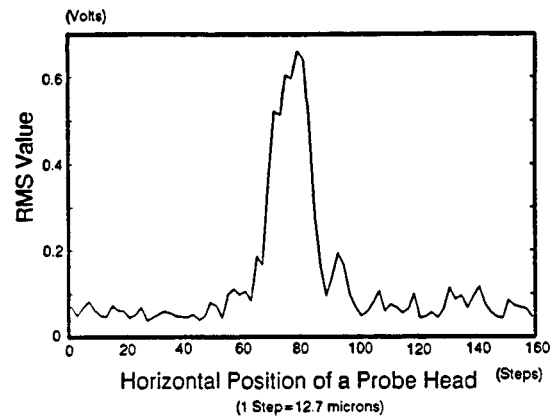


FIG. 4. Amplitude of the 40-MHz frequency modulated carrier signal as a function of the perpendicular distance from the optical probe to the vibrating surface.

each data point. Scanning was accomplished by means of a computer-controlled, stepper motor-driven vertical linear positioner and rotary table which provided two degrees of freedom for the cylindrical geometry as shown in Fig. 2. Motion of the probe head toward or away from the shell (horizontal axis) was accomplished by a computer-controlled stepper motor-driven positioner controlling the overlapping and focusing of the two beams on the surface of the shell. (The angle between the two beams is fixed at 22° and it is not an adjustable parameter in the focusing algorithm). This horizontal positioner has a fine enough step ($12.7\text{-}\mu\text{m}$ advance per step with accuracy within 0.0125 cm/m) to achieve focusing of the two beams.

The key element in the detection system is to obtain a stable FM signal. An FM signal with large and stable amplitude indicates that the two beams overlap well and produce a good fringe contrast, thus ensuring accurate demodulation of the signal to extract the surface velocity data. A good measure of the amplitude and stability of the FM signal is its rms value. Therefore, the automated focusing algorithm is based on measuring the rms value of the FM signals as the probe head moves toward the surface by means of a computer controlled, fine stepping motor. Figure 4 shows typical pattern of the rms value of the 40-MHz FM signal as a function of the distance of the probe to the vibrating surface, clearly indicating the range where one should take the data, i.e., demodulate the FM signal. Alignment is performed manually for the initial data point of the scan over the cylindrical structure and this optimum distance is used as an assumed optimum distance when the probe is repositioned to the next consecutive data point in the scan. After the first point of the scan, the system is fully automated. The probe head moves by steps of $25\ \mu\text{m}$ toward and away from the shell, in a prescribed range (e.g., $\pm 800\ \mu\text{m}$ around the assumed optimum distance). At every step, the rms value of the 40-MHz FM signal is directly acquired from channel 1 on the oscilloscope. The optimum distance is found by comparing the measured rms values and, after scanning the full range, the probe head moves back to the newly determined optimum distance for the probe head. The newly acquired maximum rms value of the FM signal is stored in the computer. If the new amplitude of the FM signal is within some range of the maximum value (e.g., 80%), the FM signal is "accepted"

and demodulated by the phase-locked loop. The demodulated vibration signal is averaged (usually 64 times) to improve the signal-to-noise ratio at the oscilloscope. The signal is then stored as a data file in the system computer. The same procedure is repeated at the next data point in the scan around the cylinder. All those procedures are controlled by a computer program except for the manual alignment at the initial data point.

D. Measurement procedures

In the experiments reported in this paper, the shaker was driven with a continuous single frequency signal. In order to identify the low- and high-frequency characteristics of wave propagation on the shell, two frequencies were chosen, one below and one above the ring frequency of the shell. For a thin cylindrical shell the ring frequency $f_r = c_p/2\pi a$, where a is the radius of the shell and $c_p = (E/[\rho(1-\nu^2)])^{1/2}$ is the plate velocity. The frequencies chosen were 9238 Hz and 18 275 Hz, respectively, because a good signal-to-noise ratio was observed at those frequencies which correspond to $0.84f_r$ and $1.65f_r$, respectively. The circumferential and axial components of the vector displacement were measured at $f = 18\,275$ Hz by positioning the probe head either along a circumferential line or along an axial line, i.e., by rotating the probe by 90° . Measurements were made over an area defined by $z = 40.38$ cm to $z = L = 93.39$ cm, and $\phi = 0$ to 2π , where $z = 0$ refers to the bottom end of the cylinder, and ($z = 30$ cm, $\phi = 0$) refers to the location of the shaker. The axial component of the vector displacement was measured over the surface of the shell, above the shaker, at $f = 9238$ Hz. The spacing of the measurement points over the scanning area was determined so as to avoid spatial aliasing. It led to the choice of 32 points circumferentially and 32 points axially at both frequencies.

II. WAVE VECTOR ANALYSIS

Elastic waves excited at a given frequency travel in the shell at different phase velocities and in different directions, according to the dispersion relation. Each wave belongs to one of three types:¹⁰ (1) a propagating wave with purely real wave number; (2) an evanescent wave with a purely imaginary wave number; (3) an oscillatory decaying wave with a complex wave number. The propagating waves include fast waves (longitudinal, shear) with low wave numbers and slow waves (flexural) with high wave numbers. The wave vector representation of the spatial motion allows the identification of the wave numbers and therefore permits a separation into the contributions from each type of wave to the overall structural vibration.

Consider the displacement field defined by the axial, circumferential, and normal components of the displacement vector $[u(a, \phi, z, f), v(a, \phi, z, f), w(a, \phi, z, f)]$ over the surface of the cylindrical shell of radius a for the cylindrical coordinates (r, ϕ, z) and with the suppressed time dependence $e^{-i2\pi ft}$ at a frequency f . The wave vector decomposition is based on the Fourier transforms of the

displacement components u, v , and w into helical wave components¹¹ U, V , and W . For example, the Fourier transform of $u(a, \phi, z, t)$ is expressed as

$$U(n, k_z, f) = \frac{1}{2\pi} \int_0^{2\pi} d\phi e^{-in\phi} \int_{-\infty}^{\infty} dz e^{-ik_z z} \times \int_{-\infty}^{\infty} dt e^{-i2\pi ft} u(\phi, z, t), \quad (8)$$

where n is the wave number index in the circumferential direction and k_z the wave number in the axial direction. The quantity U physically represents the complex amplitude of a helical wave propagating in the direction defined by the wave vector $\tilde{k} = k_z \tilde{e}_z + (n/a) \tilde{e}_\phi$. Once the spatial distribution of the displacement field $u(\phi, z, t)$ is measured, the complex amplitude $U(n, k_z, f)$ can be predicted by taking the time and spatial Fourier integral transform of $u(\phi, z, t)$. The three dimensional plot of the magnitudes of the complex amplitudes in the wave number plane gives the so-called helical wave spectrum from which the dominant waves can be identified.

The fast Fourier transform (FFT) algorithm is well suited to perform the wave vector representation of Eq. (8) provided that the spatial sampling in the circumferential and axial directions is fine and long enough to detect the periodicities of interest on the shell with good resolution and without any spatial aliasing. In the experiments reported below, the FFT method was appropriate in the circumferential direction but it was inaccurate in the axial direction because of the relatively short length of the shell in terms of the longitudinal wavelength. Furthermore, the FFT algorithm fails to identify the imaginary wave numbers (evanescent waves, or decaying waves) because the vibration signal is represented as a summation of harmonic contributions by propagating waves with real wave numbers. Therefore, for the axial wave number decomposition we have used the extended Prony method.¹² The Prony method models the data with exponentials of arbitrary complex amplitudes (magnitudes and phases) and complex wave numbers (wave numbers and damping terms) which are found by a least-square minimization of the difference between the original and the reconstructed data sets. The detailed algorithm can be found in Ref. 12. The method is well suited for cases where the data are indeed a sum of complex exponentials and when the order of the model (i.e., the number of exponentials) can be correctly guessed. It is then a very effective algorithm, even if the number of original data points is relatively small. However, the method is very sensitive to noise in the data. The overdetermined modified extended (OME) Prony method¹² has been developed precisely to increase the robustness of the method to noise inherent in any real data. The basic idea behind the OME Prony method is to perturb the system and observe the behavior of the poles (wave numbers) in the complex plane. The physical poles remain at a constant location while the noise-induced poles wander in the complex plane. The reader is referred to Refs. 12 and 13 for a more elaborate discussion on the procedure.

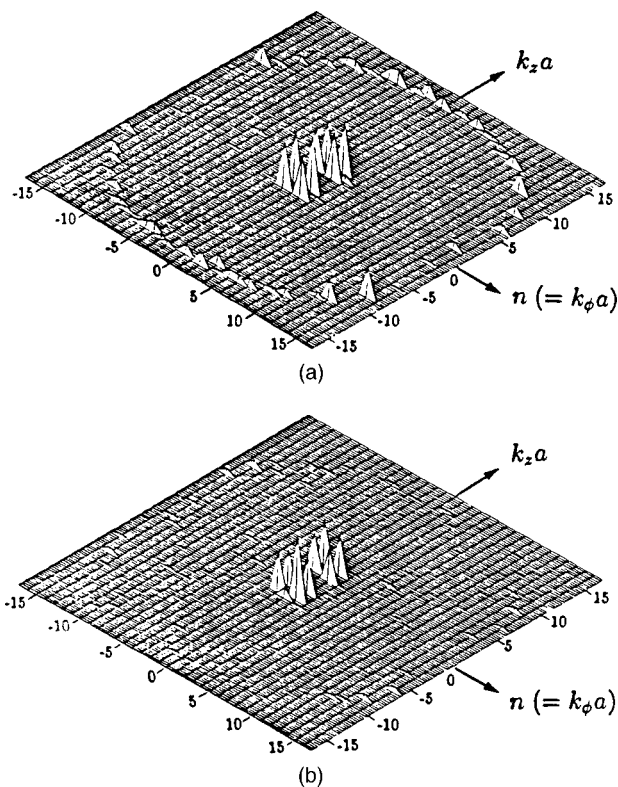


FIG. 5. (a) Helical wave spectrum $U(n, k_z, f)$ of the measured axial displacement field at $f = 18\,275$ Hz, using the FFT for the circumferential detection and the OME Prony method for the axial direction. (b) Helical wave spectrum $V(n, k_z, f)$ of the measured circumferential displacement field at $f = 18\,275$ Hz, using the FFT for the circumferential detection and the OME Prony method for the axial direction.

III. RESULTS

A. Above the ring frequency

Figure 5(a) shows the helical wave spectrum $U(n, k_z, f)$ obtained by the OME Prony decomposition of the axial displacement field $u(r=a, \phi, z, t)$ measured with the laser vibrometer at the frequency 18 275 Hz, or 1.65 times the ring frequency. Similarly, Fig. 5(b) represents the helical wave spectrum $V(n, k_z, f)$ obtained from the measured circumferential displacements $v(r=a, \phi, z, t)$ at that same frequency. Each peak on the helical wave spectrum is associated with the amplitude of a wave propagating in the direction defined by the corresponding wave number vector. Strong peaks appear in the low wave number region while weak peaks appear in the high wave number region. The strong peaks are associated with in-plane waves (longitudinal and shear waves) which dominantly excite the in-plane motion of the shell at that frequency. It should be noted that the OME Prony decomposition allows one to resolve effectively the low wave number peaks, whereas results based on the FFT decomposition (not shown here) were unable to do so. In order to relate the peaks of the helical wave spectra to a given type of wave, it is instructive to plot the predicted dispersion curve of the shell (based on Donnell's¹⁰ shell equations) and compare the result with the measured peaks of the helical wave spectra shown in Fig. 5. The results are shown in Fig. 6 in which the solid lines are the predictions with the outermost line representing the flexural waves, the

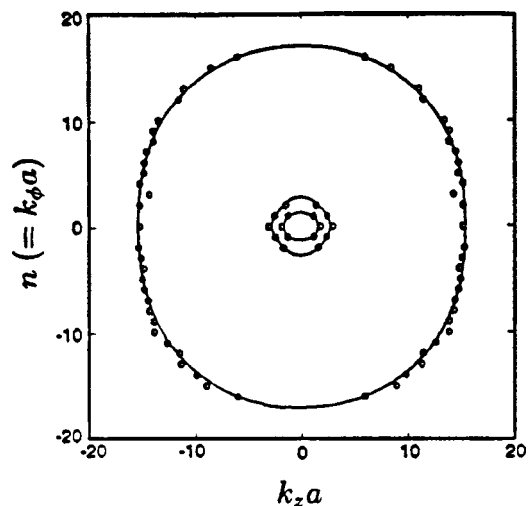


FIG. 6. Comparison between wave number reconstruction from the experimental data (circles) and the theoretical dispersion curves (solid lines) calculated at $f = 18\,275$ Hz.

middle one representing the shear waves, and the innermost one following the longitudinal waves. In Fig. 6, the small circles correspond to the measured wave numbers which are in excellent agreement with the predicted values. Clearly, surface measurements obtained by laser vibrometry can be used to separate the contributions of longitudinal, shear, and flexural waves propagating in a cylindrical shell excited harmonically above its ring frequency.

Analysis of the measurements at 18 275 Hz showed that the helical wave spectra determined from the axial displacement field, $u(a, \phi, z, t)$, and from the circumferential displacement field, $v(a, \phi, z, t)$, were very similar, as shown in Fig. 5(a) and (b), respectively. The only difference is that the amplitudes of the slow, flexural waves are greater in the spectrum determined from the axial displacement. The reason for this difference in amplitudes is not clear. However, the fast wave (extensional and shear) spectra are the same, whether determined from $u(a, \phi, z, t)$ or from $v(a, \phi, z, t)$. Therefore, at the frequency, 9238 Hz, below the ring frequency only the axial displacement field was measured.

B. Below the ring frequency

Figure 7 shows the helical wave spectrum $U(n, k_z, f)$ of the measured axial displacement field at a frequency 9238 Hz (0.84 times the ring frequency of the shell). Four strong peaks are present in the low wave numbers region and weak peaks follow a “figure 8” pattern which is characteristic of waves excited below the ring frequency.¹¹ Figure 8 shows a comparison of the predicted dispersion curves with the measured data. The elliptic curve around the origin of the wave number plane corresponds to in-plane waves (type I) whose characteristics change from longitudinal wave mode to shear wave mode as their propagation directions rotate from the axial direction ($n=0$) to the circumferential direction ($k_z=0$). The “figure 8” curve is associated with two different types of propagating waves. The top and bottom of the “figure 8” curve correspond to flexural waves whereas the dip near small values of n is associated with in-plane waves

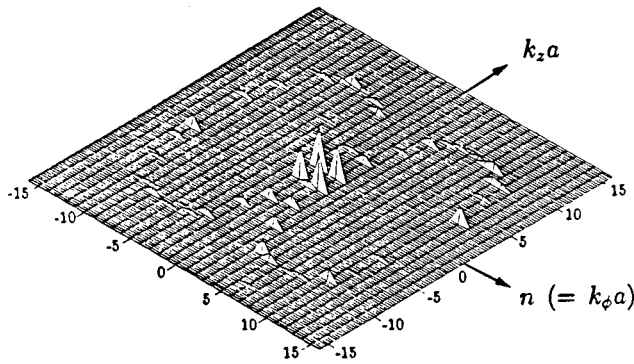


FIG. 7. Helical wave spectrum $U(n, k_z, f)$ of the measured axial displacement field at $f=9238$ Hz, using the FFT for the circumferential direction and the OME Prony method for the axial direction.

(type II) whose phase velocities are smaller than the speed of either longitudinal or shear waves propagating in the axial direction. Again excellent agreement is obtained between theoretical predictions and experimental values.

It should be noted that the characteristics of flexural waves are very sensitive to the thickness of the shell while those of in-plane waves have little dependence on it. Thus the dispersion curves of flexural waves are very sensitive to the variations of the thickness of the shell. Note that the actual thickness of the shell is within the permissible variation of $\pm 10\%$ relative to the thickness h , which has been provided by the manufacturer and satisfies the ASTM (American Society of Testing and Materials) standards. The average value of thickness measured at both ends of the shell was $0.89h$. In Figs. 6 and 8, theoretical dispersion curves were evaluated with the thickness $0.9h$ to fit the experimental results at both frequencies.

C. Evanescent waves

An interesting result occurs when the OME Prony method is used to analyze separately the axial wave field for $n=3$ along the length of the shell, i.e., when evaluating $U(n=3, z, f)$ at $f=9238$ Hz. The result is shown in Fig. 9

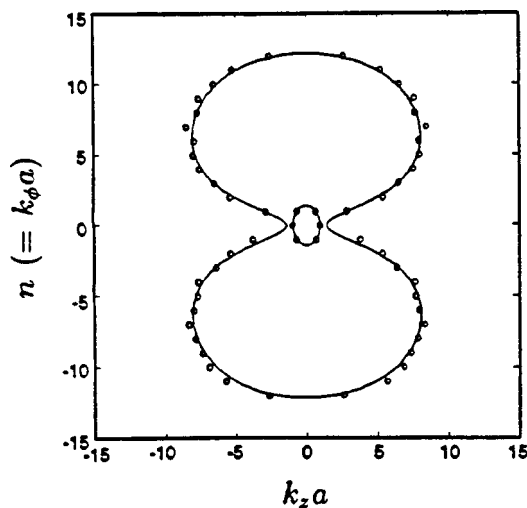


FIG. 8. Comparison between wave number reconstruction from the experimental data (circles) and the theoretical dispersion curves (solid lines) calculated at $f=9238$ Hz.

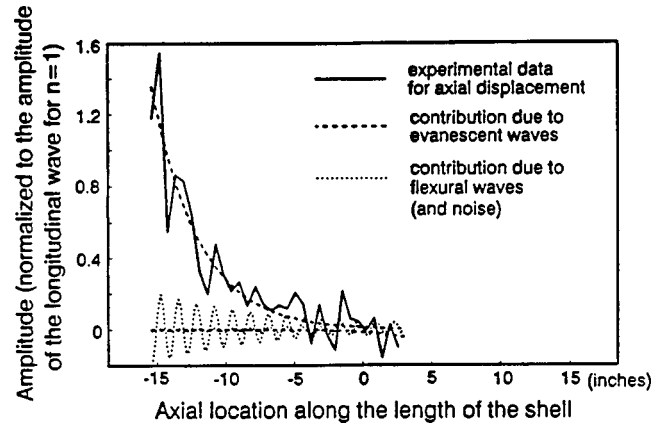


FIG. 9. Decomposition of the axial wave field for $n=3$ from the experimental data by means of the OME Prony method to illustrate the presence of an evanescent wave.

where the horizontal axis is the axial location along the length of the shell and where the vertical axis is the normalized amplitude of the axial wave field for $n=3$. The solid line represents the measured data from one end of the shell to approximately the center of the shell. It clearly reveals the presence of an evanescent wave that extends from one end of the shell to its mid-point. The OME Prony decomposition of the axial data shows the presence of a wavenumber such that $k_z a = -0.11 + 0.92i$. This value is in good agreement with the theoretical value $k_z a = 0.98i$ calculated from the dispersion relations based on Donnell's shell equations. Details of the calculation of these dispersion relations, and of the dispersion curves shown in Figs. 6 and 8, are given in Ref. 3.

These evanescent waves (large imaginary wave number) are the result of the mode conversion of the flexural waves into evanescent waves at the end of the shell. The evanescent waves are usually generated and localized to the region close to the structural discontinuities or the source point. However, the result in Fig. 9 shows that a strong evanescent wave field can be excited along about half the length of the shell.

IV. SUMMARY

An automated scanning laser vibrometer has been designed, built and tested. There have been a number of previous publications on laser Doppler vibrometry, and several Doppler vibrometers are commercially available. Therefore, it is of interest to compare the present design with those previously reported. The new features of the design presented here are the combination of (1) simultaneous measurement, at the same point, of the out-of-plane and in-plane components of surface motion, and (2) the capability to automate these measurements with computer controlled scanning over the vibrating surface. The optical probe described here is a new design developed specifically to achieve the above measurement capabilities. In particular, by positioning the probe close to the vibrating surface it is possible to maintain a relatively large angle (22° in the present design) between the two incident light beams. This improves the accuracy of measurement of the in-plane component of the surface velocity. The majority of commercial vibrometers

measure the component of surface motion along the direction of the incident light. Simultaneous measurements of in-plane and out-of-plane surface velocity components have been recently reported by Vignola *et al.*¹⁴ and Bayon *et al.*¹⁵ However, neither Ref. 14 nor 15 report on any capability to automate these measurements for scanning.

Currently there is interest in the structural acoustics community in extending the laser Doppler vibrometer to underwater operation. However, this extension is not simple. There are design issues because water is a much denser medium than air and the sound field in water can couple strongly to the optical probe. Also, the sound field in the water modulates the refractive index of water and this can lead to a phase shift in the reflected light beam which is added to the phase shift produced by surface vibration. The above design issues are discussed in Ref. 5.

The laser vibrometer was used to measure the axial and circumferential components of the displacement field over the surface of a cylindrical shell freely suspended in air, radially excited by a shaker at a single frequency. The data were collected over a set of 32 points circumferentially and 32 points axially. A wave vector analysis of the data was performed with a fast Fourier transform (for the circumferential direction) and an overdetermined modified extended Prony method (for the axial direction). The results clearly show the presence of longitudinal, shear, and flexural waves above the ring frequency. In addition, the Prony method reveals the presence of evanescent waves due to mode conversion of the propagating waves near the ends of the shell. Below the ring frequency, two types of in-plane waves and flexural waves were identified. The results are in excellent agreement with predictions from the dispersion curves for thin shells.

ACKNOWLEDGMENTS

This work was supported by the Office of Naval Research, Structural Acoustics Program, Code 332. The authors

would like to thank Dr. Philip B. Abraham and Dr. Geoffrey L. Main for insightful comments during the course of this research.

- ¹J. C. L. Dominguez and A. L. Wicks, "Reconstruction of 3-D Structural Velocity Field of a Vibrating Turbine Blade Using a Scanning Laser Doppler Vibrometer," and other papers on laser Doppler vibrometry in *Proceedings of the 13th International Modal Analysis Conference*, Nashville, Feb. 1995.
- ²D. Lee, Y. H. Berthelot, and J. Jarzynski, "A study of wave propagation on a cylindrical shell using fiber optic laser Doppler velocimetry," *J. Acoust. Soc. Am.* **94**, 196–212 (1993).
- ³H-G. Kil, "An automated scanning laser Doppler system for vibration measurements and wave vector analysis of vibration of shells," Ph. D. thesis, Georgia Institute of Technology, School of Mechanical Engineering, 1995.
- ⁴L. E. Drain, *The Laser Doppler Technique* (Wiley, Chichester, 1980).
- ⁵H-G. Kil and J. Jarzynski, "An automated scanning laser probe for underwater measurements of structural vibration," *ASME International Mechanical Engineering Congress and Exposition*, 95-WA/NCA-31 (1995).
- ⁶J. W. Goodman, "Statistical properties of speckle patterns," in *Laser Speckle and Related Phenomena*, 2nd ed., edited by J. C. Dainty (Springer-Verlag, Berlin, 1984).
- ⁷G. A. Massey, "Photomixing with diffusely reflected light," *Appl. Opt.* **4**, 781–784 (1965).
- ⁸C. S. Vikram and T. E. McDevitt, "Illuminated spot size and signal detection in laser Doppler vibrometry," *Opt. Lasers Eng.* **10**, 109–118 (1989).
- ⁹R. E. Best, *Phase-Locked Loops* (McGraw-Hill, New York, 1984).
- ¹⁰A. W. Leissa, *Vibration of Shells* (Acoustical Society of America, Woodbury, NY, 1993).
- ¹¹E. G. Williams, H. D. Dardy, and K. B. Washburn, "Generalized near field acoustical holography for cylindrical geometry," *J. Acoust. Soc. Am.* **81**, 389–407 (1987).
- ¹²K. Grosh and E. G. Williams, "Complex wave number decomposition of structural vibrations," *J. Acoust. Soc. Am.* **93**, 836–848 (1993).
- ¹³S. Braun and Y. M. Ram, "Determination of structural modes via the Prony model: System order and noise induced poles," *J. Acoust. Soc. Am.* **81**, 1447–1459 (1987).
- ¹⁴J. F. Vignola and B. H. Houston, "The design of a three dimensional laser vibrometer," *Winter Annual Meeting of ASME*, 1993-WA/NCA-10 (1993).
- ¹⁵A. Bayon, A. Varade, and F. Gascon, "Elastic characterization of isotropic materials by a single test based on the experimental determination of natural frequencies using laser interferometry," *J. Acoust. Soc. Am.* **101**, 1990–1993 (1997).

Sound absorption in concert halls by seats, occupied and unoccupied, and by the hall's interior surfaces^{a),b)}

Leo L. Beranek

975 Memorial Drive, Suite 804, Cambridge, Massachusetts 02138

Takayuki Hidaka

Takenaka R & D Institute, 1-5 Otsuka, Inzai-machi, Inba-gun, Chiba 270-13, Japan

(Received 10 September 1997; revised 7 July 1998; accepted 20 July 1998)

From experimental data in concert and opera halls, absorption coefficients were determined for audience seating, unoccupied and occupied, of different constructions, and for gypsum, wood, plaster, and concrete interior surfaces of various thicknesses and densities. A total of ten halls were involved in the bare hall (before seats were installed) analysis, yielding "residual" absorption coefficients, i.e., coefficients for those areas not including the areas to be covered by the seating. In ten halls reverberation times were measured after installation of the seats (unoccupied) and in seven of these halls at concerts with seats fully occupied. The seating absorption coefficients are presented for "acoustical" audience areas, i.e., with a 0.5-m-wide edge around each seating block. The results are compared with the data of Appendix 5 in Beranek [*Concert and Opera Halls: How They Sound* (Acoustical Society of America, Woodbury, NY, 1996)]. The sound absorption data presented for interior surfaces and audience areas should permit more accurate estimation of reverberation times as a function of frequency for large halls during the planning stage. © 1998 Acoustical Society of America. [S0001-4966(98)02511-9]

PACS numbers: 43.10.Ln, 43.55.Fw, 43.55.Gx, 43.55.Hy [JDQ]

INTRODUCTION

Although the oldest of the important measurable acoustical attributes of rooms is reverberation time RT (Sabine, 1900), it has been difficult to accurately predict RT as a function of frequency in concert halls. Tables of absorption coefficients for various internal surfaces assembled over the years (Egan, 1988; Fry, 1988; Harris, 1991; Beranek, 1996) have not been applicable to concert halls. Least understood of all is the absorption of chairs and of audiences seated in them in auditoriums, a subject that this paper addresses, and which is receiving increasing attention (Bradley, 1996; Davies *et al.*, 1994; Kirkegaard, 1996; Hidaka *et al.*, 1996; Beranek, 1996). A survey of 30 consulting firms in 1990 revealed that for fully completed large halls, before the chairs were installed, reverberation data were available for only two (Veneklasen, 1964; Commins, unpublished). As part of this study we have assembled data on eight more, one by subtracting the known chair absorption.

In this paper absorption coefficients for seats and audiences in the halls and a table of sound absorption coefficients for a range of interior surfaces are presented. These data are compared with those published in Appendix 5 of Beranek (1996).

I. FORMULAS, DEFINITIONS, AND TERMINOLOGY

A. Sabine or Eyring Formula?

A question unanswered since the derivation of the reverberation equation credited to Eyring (1930) has been which equation to use when calculating room reverberation times, that by Eyring or the earlier one by Sabine? In seeking an answer to which to employ, we have used both a standard reverberation chamber and newly built bare (no seats installed, otherwise fully finished) concert halls as reverberation chambers. It is logical that if either of the formulas is used to derive absorption coefficients from the reverberation times measured in actual concert halls, the same formula

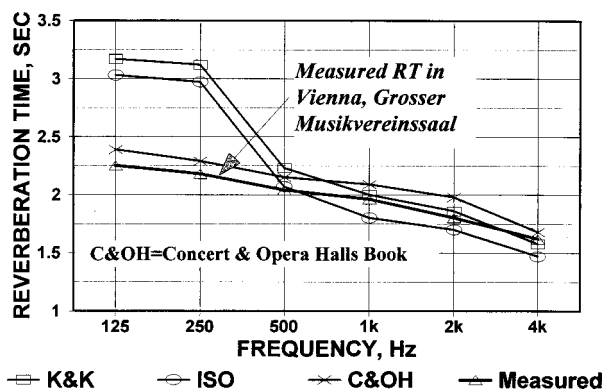


FIG. 1. Application of sound absorption coefficients measured by different methods to the prediction of reverberation times in the Vienna Grosse Musikvereinsaal. Using the Sabine reverberation equation, the K&K and ISO curves for reverberation time were calculated from reverberation chamber measurements using the methods of the ISO and Kath and Kuhl papers in the list of references. The C&OH curve was calculated from the method given in Beranek (1996, Appendix 5). From Hidaka *et al.* (1996).

^{a)}“Selected research articles” are ones chosen occasionally by the Editor-in-Chief that are judged (a) to have a subject of wide acoustical interest, and (b) to be written for understanding by broad acoustical readership.

^{b)}Presented at the 133rd meeting of the Acoustical Society of America, State College, Pennsylvania, 19 June 1997 [J. Acoust. Soc. Am. **101**, 3134(A) (1997)].

must be used when making use of those absorption coefficients in calculating RTs for other concert halls. The rationale is that all concert halls should have similar reverberant fields because their floor surfaces are highly absorbent (by the chairs or the audience) and the walls and ceiling are highly reflective. Also, absorption by the audience is generally 75%–85% of the total. The procedure of deriving absorption coefficients in real concert halls, using the Sabine formula, and then applying them to the prediction of RTs in other concert halls has been presented in Beranek (1996) and was examined in detail earlier (Beranek, 1962, 1969; Kosten, 1965).

There is another need. When consulting on the design of concert halls, where predicting reverberation times is necessary, engineers may be interested in testing a variety of chairs, for example, unoccupied and occupied. Usually, less than 20 chairs are available, so that they must be tested in a standard reverberation chamber for their sound absorbing properties. Which formula is proper for calculating RTs in a concert hall when using the absorption coefficients obtained in a reverberation chamber?

The authors addressed this problem by making measure-

ments of absorption coefficients for 20 chairs, occupied and unoccupied, of 4 different types, in a standard reverberation chamber (ISO 3741) (Hidaka *et al.*, 1996). We employed two methods of test for the chairs, one of which is recommended in ISO 345 and the other was developed by Kath and Kuhl (1965). The coefficients so obtained were then used to determine their efficacy in predicting measured reverberation times in Boston Symphony Hall, Vienna Grosser Musikvereinsaal, Tokyo Hamariky Hall, and Mitaka (Japan) Municipal Hall. The efficacy of Appendix 5 of Beranek (1996) was also evaluated.

The three methods were consistent in their degrees of ability to predict the RTs in all four halls, of which the data of Fig. 1 for the Vienna hall are an example. We found that using the Sabine reverberation equation with the reverberation chamber coefficients, the Kath and Kuhl (K&K) method predicted concert hall RTs satisfactorily for the 500–4000 Hz octave bands. The K&K method was closer than the ISO method. However, for the 125- and 250-Hz octave bands, the reverberation chamber absorption coefficients were much too small, i.e., the predicted RTs for actual halls with them were much too high. The Appendix 5 method predicted the RTs

TABLE I. Sample calculations of residual absorption in concert halls.

1. Calculation of residual sound absorption Munich, Fubertssaal in Schloss Nymphenburg								
Name of area	Area sq m	Alpha or absorp.	Frequency, Hz					
			125	250	500	1k	2k	4k
Ceiling, walls and balcony surfaces 30-mm plaster	1107	alpha absorption	0.140 154	0.123 136	0.084 93	0.063 70	0.061 68	0.041 45
Floor, concrete, no seats <i>S(A)</i>	374	alpha absorption	0.01 4	0.02 7	0.02 7	0.02 7	0.02 7	0.02 7
Total absorption, <i>A</i>	1481 sq m		158	143	100	77	75	52
Av. absorption coefficient, bare hall			0.107	0.097	0.068	0.052	0.051	0.035
Residual coef. (w/o floor)	1107		0.14	0.12	0.08	0.06	0.06	0.04
Calculated and measured RT (bare hall, no seats) 4 <i>mV</i> (24C, 47%)		$V=2614 \text{ m}^3$	0	0	0	14	26	66
Calc. $RT=0.161^*V/(A+4 \text{ mV})$			2.67	2.93	4.19	4.60	4.15	3.55
Measured RT, bare hall			2.69	2.96	4.22	4.61	4.15	3.56
2. Calculation of residual sound absorption in Mitaka, Japan, Concert Hall								
Name of area	Area sq m	Alpha or absorp.	Frequency, Hz					
			125	250	500	1k	2k	4k
Walls, ceiling, balcony surfaces 33-mm heavy gypsum	1934	alpha absorption	0.133 257	0.097 188	0.084 162	0.072 139	0.073 141	0.080 155
Floors, heavy wood, 33 mm <i>S(A)</i>	539	alpha absorption	0.09 49	0.06 32	0.05 27	0.05 27	0.05 27	0.05 27
Doors, wood, 38 mm	48	alpha absorption	0.13 6	0.09 4	0.06 3	0.04 2	0.04 2	0.04 2
Total absorption, <i>A</i>	2521		312	224	192	168	170	184
Av. absorption coefficient, bare hall			0.124	0.089	0.076	0.067	0.067	0.073
Residual coef. (w/o floor)	1982		0.13	0.10	0.08	0.07	0.07	0.08
Calculated and measured RT (bare hall, no seats) 4 <i>mV</i> (20C, 50%)		$V=5500 \text{ m}^3$	0	0	0	35	64	117
Calc. $RT=0.161^*V/(A+4 \text{ mV})$			2.84	3.95	4.61	4.36	3.79	2.95
Measured RT, bare hall			2.85	3.96	4.60	4.39	3.78	2.96

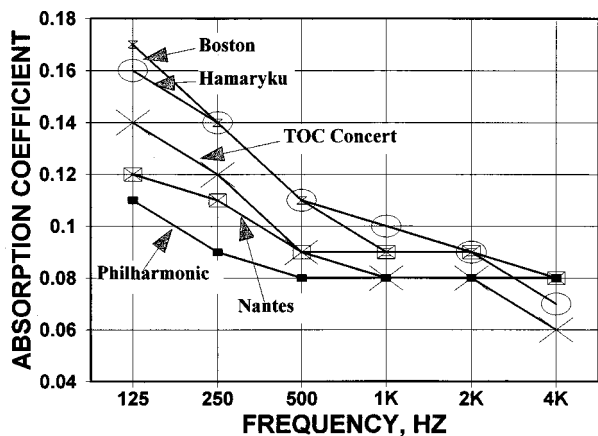


FIG. 2. Residual sound absorption coefficients calculated from measurements made in five concert halls. This is the average α_R for all interior surfaces except those surfaces occupied by audience and orchestra. Heavily absorbent areas and pipe organ absorption were handled by special terms in the reverberation equation. In all but one case, the halls were fully completed and only the seats had not been installed.

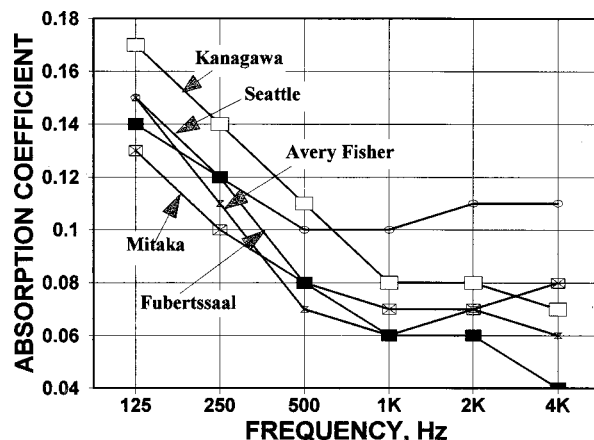


FIG. 3. Same as Fig. 2, except for five other halls.

satisfactorily in all six bands, often better than shown in Fig. 1. Using the reverberation chamber coefficients for the chairs with the Eyring formula to predict the RTs in a concert hall would have led to absurd results in the 500–4000 Hz bands.

To summarize, the Hidaka *et al.* study showed that the Sabine equation is applicable for prediction of RTs in real halls for the 500 Hz or higher octave bands when used with coefficients measured in a reverberation chamber by the K & K method or with coefficients for all six octave bands when derived by the methods of Beranek (1996) and this paper.

The Sabine equation is

$$RT = 0.161V / (A + 4mV) \text{ s.} \quad (1)$$

In a concert hall or opera house, the total room absorption A is

$$A = S_A \alpha_A + S_0 \alpha_0 + \sum S_i \alpha_i + 4mV \text{ m}^2, \quad (2)$$

where S_A is the acoustical audience area, which consists of the sum of (a) floor space, S_a , over which the audience chairs are located and (b) areas of strips 0.5 m wide around each of the separated blocks of the seating area, except that such strips are neither included at the front edge of a balcony where the audience is seated against a balcony rail nor where the seats abut a wall. S_0 is the area of the stage (no added strip is assigned), except that S_0 is the area actually occupied by the players when the entire stage area is not occupied by the players. The S_i 's are the areas of the principal surfaces of the hall, i.e., ceiling, sidewalls, underbalcony soffits, and balcony facia. If any nonseating or nonstage surface has a high absorption coefficient, such as an absorbing material used for echo control, it is designated S_M and is not averaged into the sidewalls/ceiling absorption. V is the volume of the room; and m is the energy attenuation constant for sound traveling through air in units of m^{-1} . The α 's are the sound absorption coefficients associated with their corresponding areas and all are of the α_{sab} type.

When expressing the average sound absorption coefficients for a room, separate from the absorption of the stage

TABLE II. Residual absorption coefficients measured before installation of seats. Group A: Halls lined with wood, less than 3 cm thick, or other thin materials. Group B: Halls lined with heavy materials, e.g., 2.5 cm or more thick plaster or concrete block or cinder block plastered.

Name of hall	Frequency, Hz					
	125	250	500	1k	2k	4k
Group A						
Kanagawa, Chamber Hall	0.17	0.14	0.11	0.08	0.08	0.07
Boston, Symphony Hall	0.17	0.14	0.11	0.09	0.09	0.08
Tokyo, TOC Concert Hall	0.14	0.12	0.09	0.08	0.08	0.06
Tokyo, Hamaryku-Asahi Hall	0.16	0.14	0.11	0.10	0.09	0.07
NY Avery Fisher Hall	0.15	0.11	0.07	0.06	0.07	0.06
Seattle, Opera House	0.15	0.12	0.10	0.10	0.11	0.11
Average	0.16	0.13	0.10	0.09	0.08	0.08
Group B						
Mitaka, City Concert Hall	0.13	0.10	0.08	0.07	0.07	0.08
Nantes (France) Concert Hall	0.12	0.11	0.09	0.09	0.09	0.08
NY Philharmonic Hall	0.11	0.09	0.08	0.08	0.08	0.08
Average	0.12	0.10	0.08	0.08	0.08	0.08
Appendix 5 average: Residual coefficients that are used in the tables that follow for halls not above.						
Other halls in later tables	0.14	0.12	0.10	0.09	0.08	0.07

TABLE III. Sample calculations of seat and audience absorption in concert halls.

	Frequency, Hz					
	125	250	500	1000	2000	4000
1. Calculated sound absorption, unoccupied seats, Mitaka Hall						
Residual coef: Alpha(R) (w/o floors)	0.134	0.096	0.083	0.072	0.074	0.079
4mV (27C; 45%) V = 5500 m³	0	0	0	33	57	133
Measured RT, unoccupied seats, no orchestra	2.02	2.22	2.38	2.60	2.41	2.03
Eq. for calculation of Alpha(A): RT=886/[(1902)*Alpha(R)+413*Alpha(A)+4 mV], or Alpha(A)=886/(RT*413)-1902*Alpha(R)/413-4 mV/413						
Alpha(A), unoccupied seats	0.44	0.52	0.52	0.41	0.41	0.37
2. Calculated sound absorption, occupied seats, Mitaka Hall, no orchestra						
4mV (23C; 53%) V = 5500 m³	0	0	0	29	53	128
Measured RT, occup. seats, without orchestra	1.90	1.99	1.95	1.88	1.74	1.44
Eq. for calculation of Alpha(A): RT=886/[(1902)*Alpha(R)+413*Alpha(A)+4 mV], or Alpha(A)=886/(RT*413)-Alpha(R)*1902/413-4 mV/413						
Alpha(A), seated audience absorption	0.51	0.64	0.72	0.74	0.76	0.82
3. Calculated sound absorption, unoccupied seats, TOC Concert Hall						
Residual coef: Alpha(R) (w/o floors)	0.140	0.115	0.089	0.079	0.075	0.059
4mV (27C; 55%) V = 15 300 m³	0	16	43	97	166	341
Measured RT, unoccupied seats	2.23	2.62	2.86	2.98	3.12	2.92
Eq. for calculation of Alpha(A): RT=2463/[(4791)Alpha(R)+1052Alpha(A)+4 mV], or Alpha(A)=2463/(RT*1052)-4791*Alpha(R)/1052-4 mV/1052						
Alpha(A), unoccupied seats	0.41	0.36	0.37	0.33	0.25	0.21
4. Calculated sound absorption, occupied seats, TOC Concert Hall, no orchestra						
4mV (23C; 63%) V = 15 300 m³	0	14	38	85	147	326
Measured RT, seats occupied, without orchestra	2.17	2.10	2.20	2.11	2.02	1.80
Eq. for calculation of Alpha(A): RT=2463/[(4791)Alpha(R)+1052Alpha(A)+4 mV], or Alpha(A)=2463/(RT*1052)-4791Alpha(R)/1052-4 mV/1052						
Alpha(A), occupied seats	0.44	0.58	0.62	0.67	0.68	0.72

and audience and any strongly absorbing materials, the *residual absorption* is defined in this paper

$$S_R \alpha_R = \sum S_i \alpha_i, \quad (3)$$

where α_R is the *residual absorption coefficient*, and $S_R = \sum S_i$.

II. PROCEDURE

For each hall, fully built but lacking seats, a tabulation was made of the materials used on different interior surfaces. Sample calculations for the unchaired Munich Fubertssaal and Mitaka (Japan) Concert Hall are given in Table I. In part 1 of this table, the Fubertssaal is seen to have only two important sound absorbing surfaces, that over which the audience will sit (floor) and the remaining surfaces. The absorption for chandeliers and ventilation openings are included in the latter. Absorption coefficients for areas that contribute little to the total absorption (i.e., the concrete floor) can be taken from the literature (Beranek, 1996, p. 626, as an example). Because the absorptions for the ceiling and walls will dominate, their values (the first line of absorption coefficients) are obtained by adjusting them until the computed reverberation times, using the Sabine equation,

equal the measured reverberation times (see the last two lines of part 1). The *residual absorption coefficient* is the ratio of the total absorption for the ceiling, walls and balcony surfaces divided by their area, e.g., at 500 Hz, $93 \div 1107 = 0.08$.

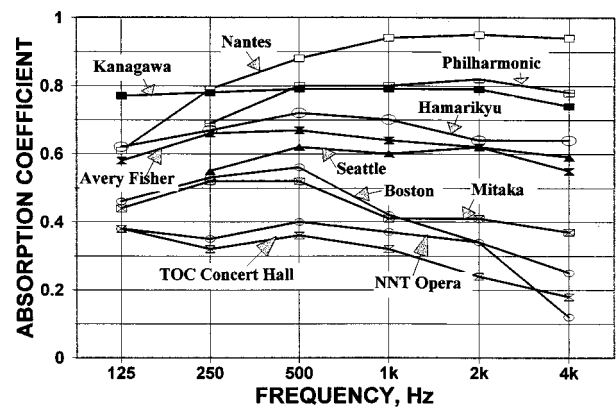


FIG. 4. Absorption coefficients for unoccupied chairs in ten halls determined from measurements before and after their installation. Note that the area S_A associated with these absorption coefficients includes a 0.5-m edge correction around each block of seating area, except for the edge of a seating block when it is adjacent to a wall or a balcony front.

TABLE IV. Unoccupied chair absorption coefficients derived from the acoustical reverberation times presented in Appendix 4 with the use of Eqs. (1)–(3). The halls are grouped according to four degrees of upholstering and were selected because the data were judged reliable and no significant amount of added acoustical materials are known to exist in the halls for which adjustments could not be made. Group 1: Heavily upholstered seats (see Table V). Group 2: Medium upholstered seats (see Table V). Group 3: Lightly upholstered seats (see Table V). Group 4: Extra lightly upholstered seats (see Table V).

Name of hall	Frequency, Hz					
	125	250	500	1k	2k	4k
Group 1						
Berlin, Philharmonie	0.80	0.93	0.84	0.85	0.75	0.69
Cleveland, Severance Hall	0.57	0.74	0.83	0.89	0.91	0.85
Edmonton, Jubilee Hall	0.60	0.72	0.79	0.83	0.93	0.89
N.Y. Philharmonic Hall	...	0.69	0.80	0.80	0.82	0.78
Nantes, Palais des Congres	0.61	0.79	0.88	0.94	0.95	0.94
Rotterdam, De Doelen	0.88	0.94	0.79	0.86	0.75	0.76
Salzburg, Festspielhaus	0.76	0.66	0.71	0.76	0.75	0.74
Average	0.70	0.78	0.81	0.85	0.84	0.81
Average from smoothed curve	0.70	0.76	0.81	0.84	0.84	0.81
Group 2						
Buffalo, Kleinhans Hall	0.31	0.50	0.58	0.71	0.68	0.63
Stuttgart, Liederhalle	0.73	0.80	0.70	0.66	0.60	0.52
Bristol, Colston Hall	0.52	0.77	0.75	0.78	0.74	...
Liverpool, Philharmonic Hall	0.56	0.64	0.74	0.80	0.77	0.75
Hamarikyu Asahi Hall	0.62	0.67	0.72	0.70	0.64	0.64
N.Y. Avery Fisher Hall	0.58	0.66	0.67	0.64	0.62	0.55
Seattle, Opera House	...	0.55	0.52	0.60	0.62	0.59
Boston, Symphony Hall	0.46	0.53	0.56	(includes wooden floor beneath)		
Average	0.54	0.64	0.66	0.70	0.67	0.61
Average from smoothed curve	0.54	0.62	0.68	0.70	0.68	0.66
Group 3						
Basel, Stadt-Casino	0.33	0.41	0.65	0.68	0.62	0.61
Berlin, Konzerthaus	0.36	0.46	0.64	0.72	0.70	0.67
Vienna, Gr. Musikvereinssaal	0.33	0.39	0.46	0.50	0.51	0.56
Amsterdam, Concertgebouw	0.40	0.54	0.60	0.61	0.60	0.62
Average	0.36	0.45	0.59	0.63	0.61	0.62
Average from smoothed curve	0.36	0.47	0.57	0.62	0.62	0.60
Group 4						
Mitaka, Concert Hall	0.44	0.52	0.52	0.41	0.41	0.37
Tokyo, NNT Opera	0.38	0.35	0.40	0.37	0.34	0.25
Tokyo, T.O.C. Concert Hall	0.38	0.32	0.36	0.32	0.24	0.18
Average	0.40	0.40	0.43	0.37	0.33	0.27
Average from smoothed curve	0.35	0.40	0.41	0.38	0.33	0.27

It is apparent that the absorption coefficients for 30-mm plaster (Fubertssaal) and 33-mm heavy gypsum (Mitaka Concert Hall) can be calculated to three decimal places by this procedure because their absorption is 85%–95% of the total absorption and the values for the floors are known within 10%–15%. Obviously, when using these data in other halls, one must allow for the fact that there will be some uncertainty because the structural conditions may not be exactly the same. The inaccuracies in the absorption coefficients for this reason are expected to be less than 10%. We also note that in every hall there are lights, ventilation openings, and doors that are lumped into the values for the ceiling and the walls. Even though these are present in all halls, differing amounts or kinds of them might make a small difference in the coefficients.

For each hall, the residual absorption coefficients as a function of frequency, excluding the acoustical floor area S_A , were determined from a table like Table I. For example

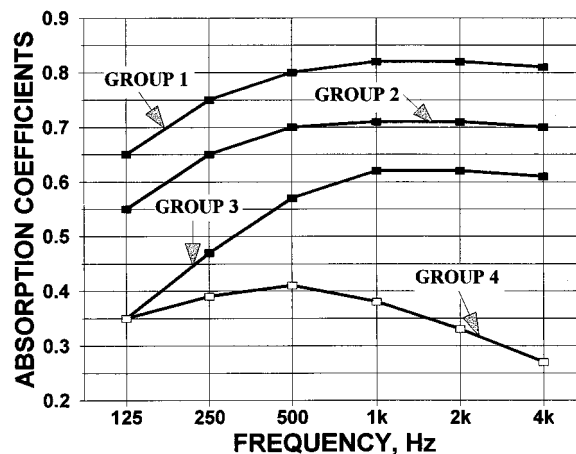


FIG. 5. Unoccupied chair absorption coefficients for 23 halls, plotted from data in Table IV. The average upholstering on the chairs of each group is given in Table V.

TABLE V. Upholstery details on seats in 23 concert halls of Table IV.

Type of seat	Front side of seat Back	Rear side of seat back	Top of seat bottom	Arm rests
Heavily upholstered, group 1	7.5 cm	Sometimes	10 cm	2 cm
Medium upholstered, group 2	2.5 cm	0	5 cm	Solid
Lightly upholstered, group 3	1.5 cm	0	2.5 cm	Solid
Specially upholstered, ^a group 4	65%, 2 cm	0	4–6 cm	Solid

^aUpholstery cushion is covered with a vinyl sheet reducing absorption at high frequencies.

in the Fubertssaal at 250 Hz the residual absorption coefficient is 0.12, and that in the Mitaka hall is 0.10. Thus from the halls analyzed a list of coefficients for plaster, heavy gypsum, wood, and concrete of different thicknesses was developed. In some halls there were two surfaces of large area, e.g., ceiling of plaster and walls of wood. The absorptions for each can be determined by simultaneous equations. If there were more than two such surfaces in a hall, the calculations of their absorption coefficients were not used in the final table.

III. RESIDUAL SOUND ABSORPTION COEFFICIENTS

The residual sound absorption coefficients so obtained for ten halls are plotted in Figs. 2 and 3 and are tabulated, less the Fubertssaal, in Table II. In this table they are divided into two groups: (A) those with interior surfaces of wood (thickness of 3 cm or less) and (B) those with heavy interior surfaces, e.g., concrete block, painted or plastered, porous block, plastered and painted, thick plaster on wire lath, heavy (thick) wood. For comparison, the average residual absorption given in Appendix 5 of Beranek (1996) is shown at the bottom of Table II. The Appendix 5 average is close to the average for these ten halls, provided the Munich Fubertssaal of Fig. 3 is disregarded. This Munich hall has nonporous heavy surfaces throughout. Data for it are included to show the lowest residual absorption to be expected in the higher-frequency bands.

Philharmonic Hall (Fig. 2) was constructed with heavy sidewalls and ceiling, which accounts for the low residual absorption at low frequencies. However, because of a large panel array, the presence of a large pipe organ, and a screen around the stage, the absorption was higher than that of the Fubertssaal at high frequencies. Its successor, the Avery Fisher hall, has higher residual absorption at low frequencies, because of the extensive use of wood, but has lower high-frequency absorption because of the elimination of the absorption of the panels, screen, and pipe organ.

The surprisingly high residual absorption in Boston Symphony Hall is caused by the many open areas in the ceiling and the sidewalls made through the years for lights, air conditioning, and microphones.

IV. ABSORPTION COEFFICIENTS FOR SEATS, UNOCCUPIED

After the seats were installed in these halls, the reverberation times, averaged throughout the rooms, and the relative humidities and temperatures were measured. The computational process for determining the seat absorption is

shown in Table III for the Mitaka and the TOC concert halls. In those halls, the total absorption of the surfaces consisted of only three components, the residual absorption, the air absorption, and the chair absorption. Using the equation for calculation of Alpha (A), given in the table, the absorption coefficients for the chairs, unoccupied or occupied, were determined from the quantities listed above. For example, in the unoccupied Mitaka Hall, the per-unit-area seating absorption coefficient, to be used with the “acoustical area,” at 500 Hz is 0.52 (No. 1), and that in the TOC Hall is 0.36 (No. 3). Occupied, as the Nos. 2 and 4 show, the absorption coefficients at 500 Hz are 0.72 and 0.62, respectively.

The absorption coefficients calculated in this manner for the unoccupied seats in ten halls are shown in Fig. 4. In Table IV the results for 23 unoccupied chairs are listed, divided into four groups. The smoothed averages, made for use in the design stages of a hall, are plotted in Fig. 5. The managers of the concert halls listed in Table IV were asked for details on the upholstering of the seats in their halls, and the averaged responses are shown in Table V.

Boston’s seats are almost unupholstered, but their absorption at low frequencies is high. The reason is that during the regular concert season, the main floor seats are raked, reaching a height of 1.8 m at the rear of the hall, accomplished by constructing a second floor of 19-mm-thick boards on frames which are supported by metal jacks. The absorption of the added wooden floor is assigned to the seats in Fig. 4. The low absorption coefficients at $2k$ and $4k$ Hz for the Boston hall are due to the impervious leather upholstery covering. The upholstery covering in the halls of groups 1–3 is porous cloth. The low coefficients of the chairs for the Japanese halls (group 4 of Fig. 5 at these frequencies) are confirmed by reverberation chamber measurements.

V. ABSORPTION COEFFICIENTS FOR AUDIENCES (SEATS, OCCUPIED)

In Fig. 6 the absorption coefficients for the occupied seats in seven of the halls of this study are presented. The major differences among the curves are in the two lowest-frequency bands. People do not absorb much at low frequencies so that the chair mostly determines the absorption coefficients there. The TOC Concert Hall is discussed in Sec. VII. As in Sec. IV, the calculations for 21 halls are given in Table VI, and the smoothed averages for three groupings are shown in Fig. 7. As already noted, the principal differences among the chairs are at low frequencies.

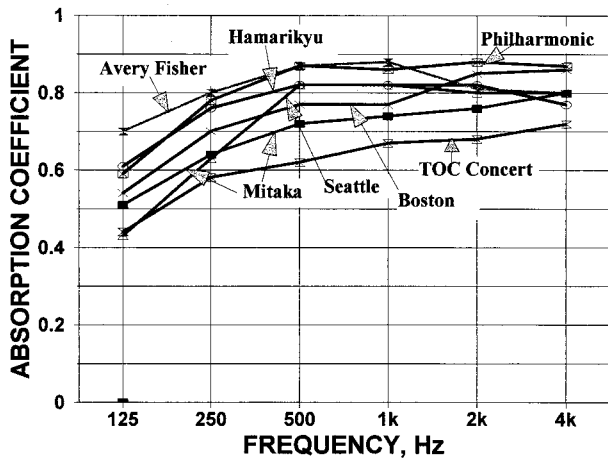


FIG. 6. Absorption coefficients for occupied chairs in seven of the ten halls of Fig. 4 determined from measurements before and after the audience entered the hall. Note that the area S_A associated with these absorption coefficients includes a 0.5-m edge correction around each block of seating area, except for the edge of a seating block when it is adjacent to a wall or a balcony front.

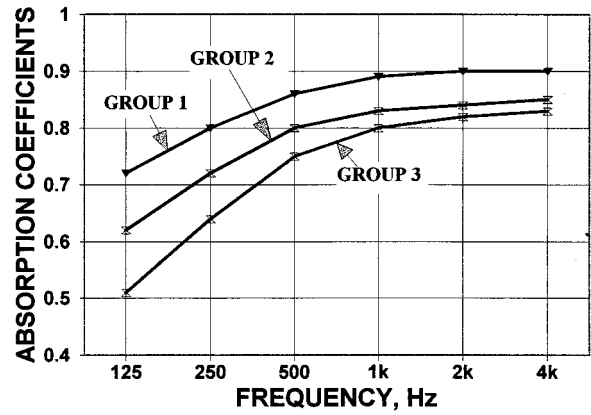


FIG. 7. Occupied chair (audience) absorption coefficients for 21 halls, plotted from data in Table VI.

TABLE VI. Occupied chair (audience) absorption coefficients derived from the reverberation times presented in Appendix 4 with the use of Eqs. (1)–(3). The halls are grouped according to three degrees of upholstery, as listed in Table A5.4 and were selected because the data were judged reliable and no significant amount of added acoustical materials are known to exist in the halls for which adjustments could not be made. Group 1: Heavily upholstered seats (see Table V). Group 2: Medium upholstered seats (see Table V). Group 3: Lightly upholstered seats (see Table V).

Name of hall	Frequency, Hz					
	125	250	500	1k	2k	4k
Group 1						
Berlin, Philharmonie	0.70	0.81	0.88	0.85	0.86	0.87
Cleveland, Severance Hall	0.65	0.78	0.92	0.99	1.02	0.96
Edmonton, Jubilee Hall	0.91	0.83	0.88	0.95	0.93	0.98
Kanagawa, Chamber Hall	0.68	0.74	0.77	0.77	0.84	0.89
N.Y. Philharmonic Hall	0.59	0.78	0.87	0.86	0.88	0.87
Rotterdam, De Doelen	0.85	0.84	0.89	0.86	0.83	0.77
Salzburg, Festspielhaus	0.69	0.78	0.89	0.91	0.92	0.90
Average	0.72	0.79	0.87	0.88	0.90	0.89
Average from smoothed curve	0.72	0.80	0.86	0.89	0.90	0.90
Group 2						
Buffalo, Kleinhans Hall	0.56	0.62	0.85	0.90	0.89	0.95
Stuttgart, Liederhalle	0.73	0.78	0.83	0.82	0.79	0.83
Bristol, Colston Hall	0.62	0.71	0.77	0.81	0.82	0.92
Liverpool, Philharmonic Hall	0.74	0.78	0.82	0.85	0.86	0.90
Tokyo, Hamarikyu Asahi Hall	0.61	0.76	0.82	0.82	0.82	0.77
N.Y., Avery Fisher Hall	0.70	0.80	0.87	0.88	0.81	0.80
Seattle, Opera House	0.43	0.63	0.82	0.82	0.80	0.80
Boston, Symphony Hall	0.54	0.70	0.77	0.77	0.85	0.86
Average	0.62	0.72	0.82	0.83	0.83	0.85
Average from smoothed curve	0.62	0.72	0.80	0.83	0.84	0.85
Group 3						
Amsterdam, Concertgebouw	0.60	0.69	0.81	0.91	0.93	0.99
Basel, Stadt-Casino	0.45	0.6	0.77	0.83	0.87	0.82
Berlin, Konzerthaus	0.56	0.67	0.79	0.82	0.87	0.88
Mitaka, Concert hall	0.51	0.64	0.72	0.74	0.76	0.80
Tokyo, TOC Concert Hall	0.44	0.58	0.62	0.67	0.68	0.72
Vienna, Gr. Musikvereinssaal	0.53	0.63	0.76	0.83	0.86	0.85
Average	0.52	0.64	0.75	0.80	0.83	0.84
Average from smoothed curve	0.51	0.64	0.75	0.80	0.82	0.83

TABLE VII. Sound absorption coefficients for building materials and audience areas. These coefficients must be used in the sabine equation. The measurements were made in the types of diffuse sound fields found in concert halls.

Materials	Frequency						Mass kg/sq m
	125	250	500	1000	2000	4000	
Gypsum, 2 layers, fiberglass reinforced, 25 mm w/lighting and Gypsum, plaster board, not reinforced, mass per sq m equals [thickness in mm]×1.0 kg/sq m, approximately	0.15	0.12	0.10	0.08	0.07	0.06	0
Wood, ceiling, 2 layers, 28 mm w/lighting & ventilation	0.18	0.14	0.10	0.08	0.07	0.06	17
Wood, sidewalls, 1 layer, 20 mm w/doors & lighting	0.25	0.18	0.11	0.08	0.07	0.06	12
Wood, sidewalls, 1 layer, 12 mm w/doors & lighting	0.28	0.22	0.19	0.13	0.08	0.06	6.2
Wood, audience floor, 2 layers, 33 mm on sleepers over concr	0.09	0.06	0.05	0.05	0.05	0.04	N/A
Wood, stage floor, 2 layers, 27 mm over airspace	0.10	0.07	0.06	0.06	0.06	0.06	17
Wood, 19 mm, over 25 mm compressed fiberglass, screwed to 150 mm concrete block w/doors & lighting	0.20	0.15	0.08	0.05	0.05	0.05	N/A
Plaster, ceiling, 60 mm w/lighting & ventilation	0.10	0.08	0.05	0.04	0.03	0.02	60
Plaster, ceiling, 30 mm w/lighting & ventilation	0.14	0.12	0.08	0.06	0.06	0.04	30
Plastic, fiberglass reinforced phenolic foam, filled with aluminum hydroxide, faced with very thin layer plywood, 8 mm (Tokyo, Hamariky-Asahi Concert Hall)	0.25	0.23	0.16	0.12	0.11	0.10	4
Concrete floor, linoleum cemented to it	0.04	0.03	0.03	0.03	0.03	0.02	
Concrete floor, woods boards, 19 mm, secured to it	0.10	0.08	0.07	0.06	0.06	0.06	
Concrete block, plastered	0.06	0.05	0.05	0.04	0.04	0.04	
Organ absorption, case opening 75 m ² (Boston, behind grille)	41	26	19	15	11	11	
Organ absorption, free standing (Tokyo, TOC Concert Hall)	65	44	35	33	32	31	
Audience, seats fully occupied							
Heavily upholstered	0.72	0.80	0.86	0.89	0.90	0.90	
Medium upholstered	0.62	0.72	0.80	0.83	0.84	0.85	
Lightly upholstered	0.51	0.64	0.75	0.80	0.82	0.83	
Seats unoccupied							
Heavily upholstered	0.70	0.76	0.81	0.84	0.84	0.81	
Medium upholstered	0.54	0.62	0.68	0.70	0.68	0.66	
Lightly upholstered	0.36	0.47	0.57	0.62	0.62	0.60	
Absorption power of orchestra (sq m), Tokyo, TOC Concert Hall and NNT Opera House							
Concert Hall (stage 170 sq m, vertical walls, sides (ends) splayed)							
13 string instruments	3	4	6	17	52	64	
44 players (2 brass)	12	21	24	46	74	100	
92 players (4 brass)	22	37	44	64	102	132	
Opera House (pit opening 100 sq m)							
40 players	10	13	17	41	50	57	
80 players	12	17	23	56	67	71	
Note: Surface density values do not include the mass of furring or wooden nailing strips.							
Note: The coefficients following were taken from the literature, references given in text.							
Carpet, heavy, cemented to concrete	0.02	0.06	0.14	0.37	0.6	0.65	
Carpet, heavy, over foamed rubber	0.08	0.24	0.57	0.69	0.71	0.73	
Carpet, thin, cemented to concrete	0.02	0.04	0.08	0.2	0.35	0.4	

VI. SOUND ABSORPTION COEFFICIENTS FOR BUILDING MATERIALS

The sound absorption coefficients for building materials derived from the 11 halls included in this study are listed in Table VII. The values shown are reasonably close to those tabulated in Appendix 5, Beranek (1996, p. 626). At the bottom of the table, total absorptions for orchestras on stage and in pits are shown, as measured in two halls. The data for carpets are from the literature. The values for audiences and chair absorption coefficients are slightly lower than those shown in Appendix 5, p. 626.

VII. NEARLY IDENTICAL SEATS IN DIFFERENT ARCHITECTURAL VENUES

From Fig. 4 we can see the absorption coefficients for nearly identical seats determined in three Japanese halls, Mitaka Concert Hall, NNT Opera, and TOC Concert Hall. The range in absorptions among these three halls is due in part to differences in the thickness of the cushions on the seat bottoms but, we believe, the larger part of the differences is determined by the state of the sound diffusion in these rooms at these reverberation times with most of the sound absorption contributed by horizontal areas. In plan, both the Mitaka

and the TOC halls are rectangular, and both seat less than 1700 persons. The Mitaka ceiling is nearly horizontal, built of three levels, each of smaller area and ascending about 1.3 m per level. The TOC hall has a distorted pyramidal-shaped ceiling, rising at its peak to about 14 m above the level at which it intersects the side walls. The NNT Opera is narrow fan-shaped, with balcony fronts that appear to give the upper part of the hall a rectangular shape. The mid-frequency reverberation time in the NNT Opera House is about 1.5 s, while that in the two concert halls is between 1.85 and 2.0 s, when fully occupied. The absorption coefficients for the occupied seats in the TOC Concert Hall are also lower than those in the Mitaka Hall.

VIII. THE "EDGE EFFECT" SURROUNDING AN ABSORPTIVE AREA

It is well known that the sound absorption of a finite sample of acoustical material measured in a reverberation chamber must have an "edge" correction because of diffraction effects at the edges. As the sample becomes larger, this "edge" correction becomes smaller. It is also known that this effect varies with frequency. Our measurements indicate that a strip of 0.5 m around the actual area of a block of seats is an adequate approximation to this effect, mostly because the "sides" of an audience section as well as its "surface" absorbs sound.

An unexpectedly very large "edge effect" was encountered during our measurements in the NNT Opera House. Measurements of the absorption coefficients in the NNT Opera for the seating areas were performed with the proscenium opening (205 sq m) closed by a fire shutter with a mid-frequency absorption coefficient of about 0.15. In that configuration, the mid-frequency reverberation time was 2.2 s. When the shutter was raised to expose a highly absorbent stage house, the reverberation time decreased to 1.8 s and the calculated *absorption coefficient* for the actual proscenium area was about 1.7 over the entire frequency range from 250 to 4000 Hz! In the drama theater, with the proscenium closed by the fire curtain the RT was 1.5 s. When open it decreased to 1.3 s. The absorption coefficient for this opening calculated to be about 1.2. In both cases, it had been expected that the absorption coefficient would lie close to 1.0, or if the 0.5-m edge was added as for the seating, the ratio of S_A to S_a (actual) would be 1.09. This large an "edge effect" requires further study.

IX. FUTURE DIRECTION

The authors and their colleagues are engaged in a study designed to develop an analytical method for going at all frequencies from sound absorptions of seats measured in a reverberation chamber to the sound absorptions measured in concert halls (Hidaka *et al.*, 1996).

ACKNOWLEDGMENT

The authors wish to thank Noriko Nishihara for her invaluable help with the measurements, with data reduction, and with detailed crosschecking of the tables of absorption coefficients for the 11 halls.

- Beranek, L. L. (1962). *Music, Acoustics, and Architecture* (Wiley, New York).
- Beranek, L. L. (1969). "Audience and chair absorption in large halls," *J. Acoust. Soc. Am.* **45**, 13–19.
- Beranek, L. L. (1996). *Concert and Opera Halls: How They Sound* (Acoustical Society of America, Woodbury, NY).
- Bradley, J. S. (1996). "The sound absorption of occupied auditorium seating," *J. Acoust. Soc. Am.* **99**, 990ff.
- Commins, D. E. (unpublished consultation report).
- Davies, W. J., Orłowski, R. J., and Lam, Y. W. (1994). "Measuring auditorium seat absorption," *J. Acoust. Soc. Am.* **96**, 879ff.
- Egan, M. D. (1988). *Architectural Acoustics* (McGraw-Hill, New York).
- Eyring, C. F. (1930). "Reverberation time in 'dead' rooms," *J. Acoust. Soc. Am.* **1**, 217ff.
- Fry, A. (1988). *Noise Control* (Pergamon, Oxford).
- Harris, C. M. (1991). *Acoustical Measurements and Noise Control* (McGraw-Hill, New York), 3rd ed.
- Hidaka, T., Nishihara, N., and Beranek, L. L. (1996). "Mechanism of sound absorption by seated audiences in concert halls," Presented at the 3rd Joint Meeting: Acoustical Societies of America and Japan, *J. Acoust. Soc. Am.* **100**, 2705(A).
- ISO 345 (1985). "Acoustics: Measurement of sound absorption in a reverberation room," Standards Secretariat, Acoustical Society of America, 120 Wall Street, 32nd floor, New York, NY 10005-3993.
- ISO 3741 (1985). "Precision methods for reverberation rooms," Standards Secretariat, Acoustical Society of America, 120 Wall Street, 32nd floor, New York, NY 10005-3993.
- Kath, U., and Kuhl, W. (1965). "Messungen zur Schallabsorption von Polsterstühlen mit und ohne Personen," *Acustica* **15**, 127–131.
- Kirkegaard, D. L. (1996). "Sound absorption of occupied chairs as a function of chair design and audience clothing," *J. Acoust. Soc. Am.* **99**, 2458.
- Kosten, C. W. (1965/66). "New method for the calculation of the reverberation time of halls for public assembly," *Acustica* **16**, 325–330.
- Sabine, W. C. (1900). "Architectural Acoustics," published in seven parts in April, May, and June, *Am. Arch. Building News* **68**. Available in reprint book, *Collected Papers on Acoustics: Wallace Clement Sabine* (Peninsula Publishing, P.O. Box 867, Los Altos, CA 94023-9912, 1992).
- Veneklasen, P. S., and Christoff, J. P. (1964). "Seattle Opera House—Acoustical Design," *J. Acoust. Soc. Am.* **36**, 903ff.

An improved moving frame acoustic holography for coherent bandlimited noise

Soon-Hong Park and Yang-Hann Kim^{a)}

*Center for Noise and Vibration Control (NOVIC), Department of Mechanical Engineering,
Korea Advanced Institute of Science and Technology (KAIST), Science Town, Taejeon 305-701, Korea*

(Received 24 February 1998; accepted for publication 7 August 1998)

The moving frame acoustic holography method, which can increase the aperture size and spatial resolution of a hologram was recently proposed [H.-S. Kwon and Y.-H. Kim, *J. Acoust. Soc. Am.* **103**, 1734–1742 (1998)]. This method continuously sweeps a stationary sound field by using a line array of microphones so that the hologram of a scanned plane can be obtained. This method enables us to visualize the noise generated by moving noise sources based on near-field acoustic holography. However, a drawback is that it can be applied only to sinusoidal components. This limits its practical application. In practice, bandlimited and transient noise, as well as a sinusoidal component, must be dealt with in order to effectively control the noise generated by the moving noise sources. This paper addresses a way to improve the moving frame acoustic holography method so that it can be applied not only to sinusoidal components, but also to a coherent bandlimited noise. The practical applicability of the improved method is also verified by experiments. © 1998 Acoustical Society of America. [S0001-4966(98)04111-3]

PACS numbers: 43.20.-f, 43.35.Sx, 43.60.Sx [ANN]

INTRODUCTION

Being able to see where noise is generated and how it propagates would simplify the effective control of noise. Although near-field acoustic holography (NAH)¹ is one of the fine visualization methods, it has several limitations. These are mainly due to the aperture size of the hologram, its microphone spacing, and the distance from noise sources. Theoretically, NAH requires a continuous hologram of infinite size, but in practice only a discretized hologram of finite size is obtainable. For stationary sound fields, the aperture size of the hologram and the microphone spacing can be increased and reduced by step-by-step scanning of the sound field over the hologram plane. Several methods of this kind²⁻⁴ have been introduced. However, they cannot visualize moving noise sources, because they assume that noise sources are standing still instead of moving. If we try to apply NAH to the visualization of sound fields generated by moving noise sources, then we must be able to measure sound pressures on the moving plane affixed to the noise sources. This is possible by using a planar array of microphones, which requires a very complex measurement system⁵ and therefore limits the ability of the conventional NAH method¹ to effectively apply to moving noise sources.

Line array methods⁶⁻¹² other than the acoustic holography method have been proposed to localize the noise sources of moving vehicles. Their main application was high speed trains.⁶⁻¹¹ The main objective of line array methods is to find the locations of the noise sources based on a beamforming method. These methods find an equivalent distribution of monopole sources strength over the source surface. This means that they cannot provide the way to describe how the

wavefront of noise propagates. It is also noteworthy that they cannot give us adequate information of sound pressure distribution, particle velocity, and acoustic intensity, all of which are obtainable from the NAH method.

The moving frame acoustic holography (MFAH)¹³ was originally proposed to increase the aperture size of the hologram. In this method a line array of microphones continuously sweeps a sound field. The relative motion between the line array of microphones and the noise sources enables us to visualize the moving noise sources based on the acoustic holography method. This is the major advantage of the method. However, it is noteworthy that this method has an inherent limitation due to the Doppler effect: The frequency band centered at a frequency of interest in the hologram coordinate is broadened as the relative speed between the noise source (hologram) and the line array of microphones is increased. Thus this method is applicable only to tonal components, which do not cause sideband overlapping.¹³ The scope of practical application of this conventional MFAH method is limited due to this drawback. In practice, there exist many noise sources that radiate not sinusoidal noise but bandlimited or transient noise. For example, pass-by or coast-by noise might have various bandlimited or transient noise sources.

This paper explains the way to improve the moving frame acoustic holography so that we can apply it to coherent bandlimited noise. The proposed method is verified both analytically and experimentally.

I. THE MOVING FRAME ACOUSTIC HOLOGRAPHY IN TERMS OF PLANE WAVES AND COMPLEX ENVELOPE

The moving frame acoustic holography (MFAH) enables us to transform the sound pressure of a scanned plane

^{a)}Electronic mail: yhkim@sorak.kaist.ac.kr

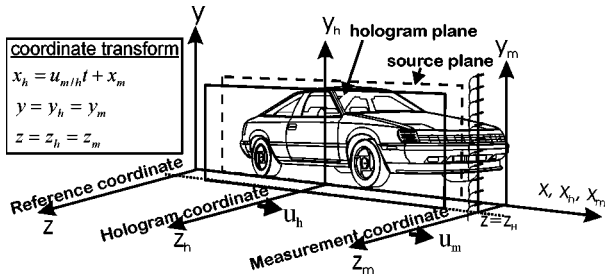


FIG. 1. Three coordinate systems (reference coordinate, hologram coordinate which moves with the vehicle, and measurement coordinate which is attached to a vertical line array of microphones). The coordinate transformation enables us to obtain the hologram on the scanned plane.

measured by a line array of microphones into that of a hologram plane moving with the noise sources. In order to explain the transformation of the sound field, we introduce the measurement coordinate, fixed to the line array of microphones, and the hologram coordinate, fixed to the noise sources. Let us denote the sound pressures on the measurement coordinate $[(x_m, y_m, z_m)]$ and the hologram coordinate $[(x_h, y_h, z_h)]$ as $p_m(x_m, y_m, z_m; t)$ and $p_h(x_h, y_h, z_h; t)$, respectively, as shown in Fig. 1. In this method we assumed that the two coordinates move in parallel and their relative velocity is $u_{m/h} = u_m - u_h$ (See Fig. 1). If we further assume that a line array of microphones is rigidly attached to the measurement coordinate ($u_{m/h} = u_m - u_h$, see Fig. 1), then the sound field measured by the measurement and hologram coordinate will be

$$p_m(0, y_m, z_H; t) = p_h(u_{m/h}t, y_h, z_H; t). \quad (1)$$

Note that Eq. (1) is the exact expression of the relation between the sound pressure on the hologram and the measurement coordinate when the microphone continuously sweeps the sound field induced by the noise sources fixed in space. However, in case of moving noise sources, the pressure on the measurement coordinate represents the sum of the pressure on the hologram coordinate (p_h) and additional pressure due to the source motion.^{14,15} Note that what we want to obtain is only the pressure on the hologram coordinate (p_h). This means that the additional term due to source motion causes an error. However, the effect of this term can be neglected at a low Mach number, because the pressure change due to the source motion is an order of the Mach number.^{14,15}

Equation (1) leads to the basic equation of the MFAH,¹³ that is

$$F_T\{p_h(u_{m/h}t, y_h, z_H; t)\} = \frac{1}{u_{m/h}} \int_{-\infty}^{\infty} \hat{P}_h\left(\frac{2\pi(f_h - f)}{u_{m/h}}, y_h, z_H; f_h\right) df_h, \quad (2)$$

where F_T denotes the temporal Fourier transform and \hat{P}_h denotes an x -directional wave-number spectrum. We denote frequencies in the measurement coordinate and in the hologram coordinate as f and f_h , respectively. Note that p and P denote a time signal and a frequency spectrum, respectively. Equations (1) and (2) mean that the temporal Fourier transform of the pressure signals measured by the measurement

coordinate, or the Doppler shifted spectrum from the line array of microphones [left-hand side of Eq. (2)], is the continuous sum of x -directional wave-number spectra [right-hand side of Eq. (2)]. This has a very significant meaning in practice. It means that we can get the hologram $P_h(x_h, y_h, z_H; f_h)$ from the x -directional wave-number spectrum [Eq. (2)] by filtering the Doppler shifted spectrum centered at f_h with a filter bandwidth.¹³ Note that the desired x -directional wave-number spectrum will be obtained only for the sound field that has discrete frequency components. See the Ref. 13 for the details.

The conventional MFAH [Eq. (2)] can be easily understood by examining the plane wave sound field of frequency f_{h0} and wave vector (k_{x0}, k_{y0}, k_{z0}) , that is

$$p_h(x_h, y_h, z_H; t) = A_0 \exp(j(k_{x0}x_h + k_{y0}y_h + k_{z0}z_H)) \times \exp(-j2\pi f_{h0}t), \quad (3)$$

where A_0 denotes the complex magnitude of the plane wave sound field, and the wave vector satisfies $k_{x0}^2 + k_{y0}^2 + k_{z0}^2 = (2\pi f_{h0}/c)^2$. Note that c denotes the speed of sound.

Recall that the Doppler shifted signal measured by the measurement coordinate is $p_h(u_{m/h}t, y_h, z_H; t)$. The temporal Fourier transform of this signal will be

$$F_T\{p_h(u_{m/h}t, y_h, z_H; t)\} = A_0 \exp(j(k_{y0}y_h + k_{z0}z_H)) \delta\left(\frac{u_{m/h}}{2\pi}k_{x0} - f_{h0} + f\right). \quad (4)$$

Appendix A describes the definitions of Fourier transform pairs, which are frequently used in this paper. From Eq. (4), we can see that the signal measured by the measurement coordinate is Doppler shifted by the frequency, $f = f_{h0} - u_{m/h}k_{x0}/2\pi$. The same spectrum must be observed with regard to the x -directional wave-number (k_x) domain as Eq. (2) implies. The x -directional wave-number spectrum of Eq. (3) is obtained by using the spatial Fourier transform of $P_h(x_h, y_h, z_H; f_h)$, where $P_h(x_h, y_h, z_H; f_h)$ is the temporal Fourier transform of Eq. (3). Therefore the x -directional wave-number spectrum of Eq. (3) will be written as

$$\hat{P}_h(k_x, y_h, z_H; f_{h0}) = 2\pi A_0 \exp(j(k_{y0}y_h + k_{z0}z_H)) \times \delta(k_x - k_{x0}) \delta(f_h - f_{h0}). \quad (5)$$

If we put the right hand side of Eq. (5) to the right hand side of Eq. (2), then we can obtain Eq. (4). This means that the Doppler shifted spectrum of the signal measured by the measurement coordinate $F_T\{p_h(u_{m/h}t, y_h, z_H; t)\}$ expresses the x -directional wave-number spectrum of the measured sound field. Therefore the MFAH provides the way to produce spatial information (x -directional) from temporal information. Figure 2 depicts the relation between the temporal and spatial distribution of the one-dimensional sound field. The frequency and wave-number vector of this sound are f_{h0} and $(k_{x0}, 0, 0)$, respectively. Note that $k_{x0} = 2\pi f_{h0}/c$. The frequency measured by the moving microphone will be $f_{h0} - (u_m/c)f_{h0}$, since we assumed that the moving microphone travels along the positive x -axis. This will be written as

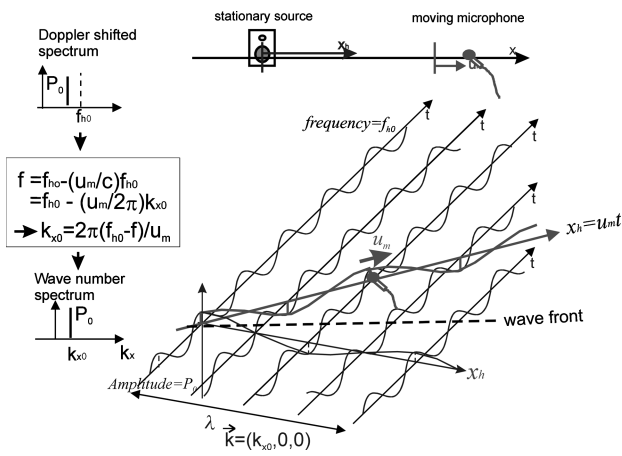


FIG. 2. The illustration of the moving frame acoustic holography for a plane wave sound field whose frequency and wave-number vector are f_{h0} and $(k_{x0}, 0, 0)$. The signal measured by the measurement coordinate has the Doppler shift. From this signal, we can obtain the spatial distribution of the plane wave in the x direction.

$$f = f_{h0} - \frac{u_m}{2\pi} k_{x0} \quad (6)$$

by using the x -directional wave number k_{x0} . Expressing the wave number in terms of the frequency gives

$$k_{x0} = \frac{2\pi(f_{h0} - f)}{u_m}, \quad (7)$$

which is the first argument of the right hand side term of Eq. (2).

This observation can be extended to the general case. Figure 3 illustrates that, in general, a two-dimensional wave can be expressed as the sum of plane waves with regard to an x -directional wave number and a frequency. It is noteworthy

that the moving frame acoustic holography in this case has relative motion in the x direction only; in other words, the moving frame moves in the x direction. Therefore there is no change in the wave number in the y direction. As we can readily see in the figure, the Doppler shifted frequency spectrum has complete information on its wave-number spectrum, therefore pressure distribution in the x direction. This means that we need only one microphone in the x direction to obtain its spatial distribution in the x direction. We only need microphones in the y direction in order to obtain the sound field on the hologram surface. It is interesting to note that the bandwidth of the Doppler shifted spectrum is completely due to the two-dimensional characteristics of sound fields. A one-dimensional sinusoidal wave does not produce any bandwidth. The reason for this is that the Doppler shift is a pure kinematic phenomenon that is associated with the shape of the wavefront. Figure 3 illustrates this fact systematically in terms of plane wave decomposition of the sound field.

Let us summarize the meaning of Eq. (2). The right hand side of Eq. (2) is the Doppler shifted spectrum, and the integrand is the wave-number spectrum which we want to obtain. If a noise source emits the sound of single frequency (f_{h0}), then Eq. (2) will be written as

$$F_T\{p_h(u_{m/h}t, y_h, z_H; t)\} / \Delta f_h = \frac{1}{u_{m/h}} \hat{P}_h\left(\frac{2\pi(f_{h0} - f)}{u_{m/h}}, y_h, z_H; f_{h0}\right), \quad (8)$$

where Δf_h is a spectral bandwidth. From Eq. (8), we can obtain the wave-number spectrum in the x direction with the corresponding frequency f_{h0} . Then taking the inverse Fourier transform with respect to x provides the wavefront distribution in the x direction. If we repeat this procedure for all

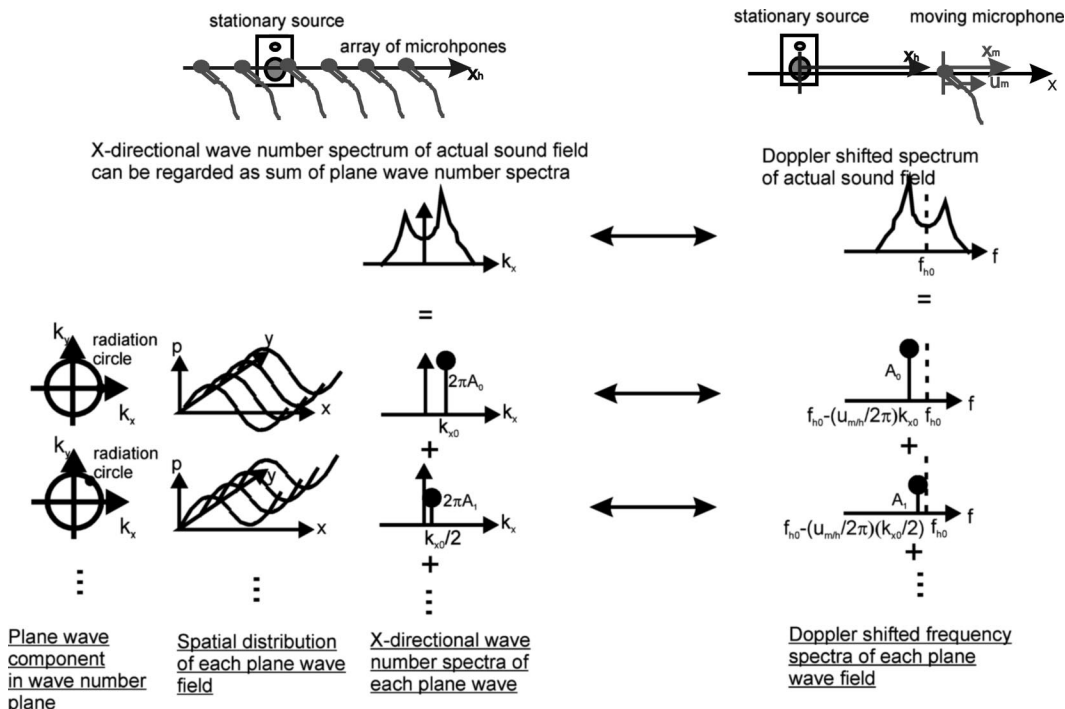


FIG. 3. The interpretation of the MFAH by introducing plane wave decomposition of the general sound field.

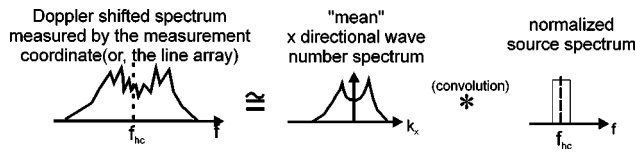


FIG. 4. The modeling procedure of a coherent bandlimited sound field.

y_h 's, which are determined by the positions of microphones in the y direction, then we obtain the required wavefront distribution on the plane of interest (hologram). The temporal inverse Fourier transform of Eq. (8) gives us another interesting feature of the moving frame acoustic holography, that is,

$$\begin{aligned}
 p_h(u_{m/h}t, y_h, z_H; t) / \Delta f_h & \\
 &= \frac{1}{u_{m/h}} F_T^{-1} \left\{ \hat{P}_h \left(-\frac{2\pi f}{u_{m/h}}, y_h, z_H; f_{h0} \right) \right\} e^{-j2\pi f_{h0}t} \\
 &= P_h(x_h, y_h, z_H; f_{h0}) e^{-j2\pi f_{h0}t}. \quad (9)
 \end{aligned}$$

See Appendix B for the detailed derivation of the second part of Eq. (9). Equation (9) expresses that the spatial distribution of sound pressure at f_{h0} is the complex envelope of the complex signal measured by the measurement coordinate. If we know the frequency f_{h0} , then we can obtain the hologram $P_h(x_h, y_h, z_H; f_h)$ by multiplying $e^{j2\pi f_{h0}t}$ by both sides of the equation.

As described in Ref. 13, and also obviously indicated by the above explanations, the moving frame acoustic holography is valid only for discrete frequencies that do not cause the sideband overlapping.

II. THEORETICAL BACKGROUND OF THE MOVING FRAME ACOUSTIC HOLOGRAPHY FOR COHERENT BANDLIMITED NOISE

The conventional MFAH method cannot correctly mimic the sound field of a continuous bandlimited spectrum, simply because the method is valid only for the sinusoids.

In order to apply the MFAH to a continuous bandlimited spectrum, the sideband overlapping¹³ of frequencies within the band must be resolved. Examining a sound field whose spectrum is bandlimited can deal with this problem. We can assume that the sound field generated by bandlimited and coherent noise sources has almost the same spatial distribution of sound pressures at every frequency within the bandwidth. This means that the sound field by the coherent bandlimited noise source can be regarded as having a ‘‘mean sound field’’ whose standard deviation is small if its bandwidth is sufficiently narrow. Mathematically, the Doppler shifted spectrum can be regarded as the convolution of two spectra as illustrated in Fig. 4. The one, a normalized source spectrum, represents the frequency contents of the bandlimited noise of our interest. As we will discuss later, this spectrum can be obtained by normalizing the source spectrum with a spectral value at the center frequency. The other, which we will call by ‘‘mean wave-number spectrum’’ in the x direction, represents the spatial distribution of the sound pressure induced by the bandlimited noise source. Our objective is to find this wave-number spectrum. In practice,

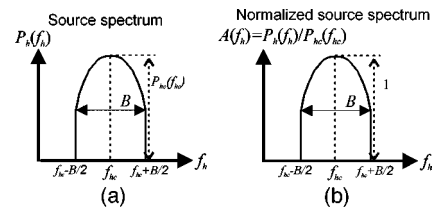


FIG. 5. The notation of the bandlimited spectrum used in the theoretical formulation. (a) Bandlimited noise spectrum emitted by a coherent noise source. (b) Normalized spectrum which represents the ratio of the complex amplitude of the sound field at an arbitrary frequency to that of the center frequency.

when we measure the normalized source spectrum, we obtain the mean wave-number spectrum by deconvolving these spectra. Note that the deconvolution of the two spectra can be easily resolved in a time domain. Now we will present the mathematical derivation associated with this idea in the following.

The center frequency and bandwidth of a bandlimited sound field is denoted as f_{hc} and B , respectively [See Fig. 5(a)]. In practice, a bandpass filter is designed to filter out other frequency components that are not our interest. The bandpass filter will be written as

$$G(f) = \{H(f - f_-) - H(f - f_+)\}, \quad (10)$$

where $f_- = (1 - 2M)(f_{hc} - B/2)$, $f_+ = (1 + 2M)(f_{hc} + B/2)$, $H(\bullet)$ is the unit step function, and M denotes the Mach number. Here we assume that any other neighboring bandlimited spectra do not create the sideband overlapping with the bandlimited spectrum of our interest.

The filtered signal of Eq. (2) by using Eq. (10) is rewritten as

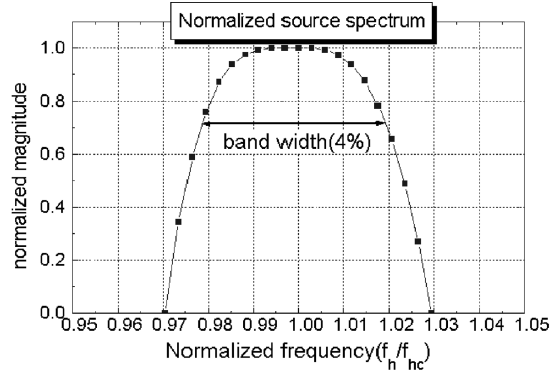
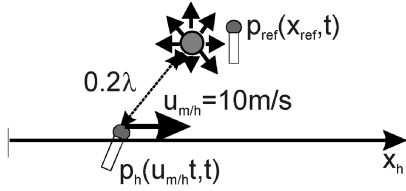
$$\begin{aligned}
 F_T \{ p_h(u_{m/h}t, y_h, z_H; t) \}^{\text{filtered}} & \\
 &= \frac{1}{u_{m/h}} \int_{-\infty}^{\infty} \hat{P}_h \left(\frac{2\pi(f_h - f)}{u_{m/h}}, y_h, z_H; f_h \right) G(f) df_h \\
 &\equiv \frac{1}{u_{m/h}} \int_{-\infty}^{\infty} \hat{P}_{h,B} \left(\frac{2\pi(f_h - f)}{u_{m/h}}, y_h, z_H; f_h \right) df_h. \quad (11)
 \end{aligned}$$

As previously mentioned, if we assume that the bandlimited sound field is produced by the coherent sound sources, then we can express the sound field as

$$P_{h,B}(x_h, y_h, z_H; f_h) \cong A(f_h) P_{hc}(x_h, y_h, z_H; f_{hc}) \quad (f_{h-} \leq f_h \leq f_{h+}), \quad (12)$$

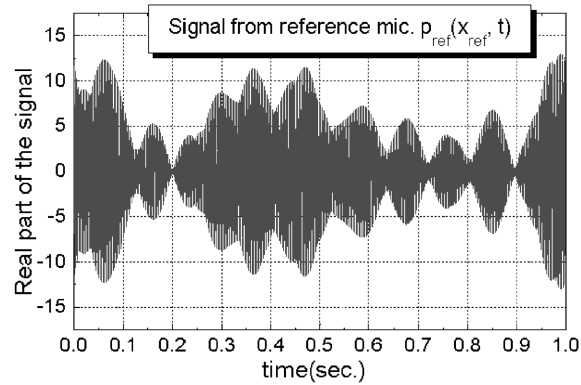
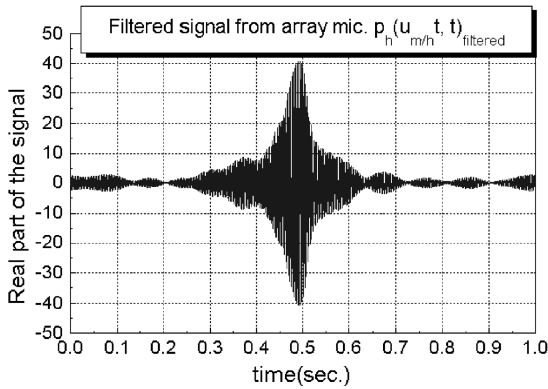
where $A(f_h)$ is the normalized source spectrum that is defined as the ratio of a complex amplitude of sound field at an arbitrary frequency in the band to that of center frequency [See Fig. 5(b)]. We denote $f_{h+} = f_{hc} + B/2$ and $f_{h-} = f_{hc} - B/2$. Note that $A(f_h)$ has zero outside the interval $f_{h-} \leq f_h \leq f_{h+}$. Equation (12) essentially considers that the bandlimited spectrum ($P_{h,B}$) is the product of the spectrum of the band's center frequency (f_{hc}) and the normalized source spectrum.

Point source radiating narrow band noise



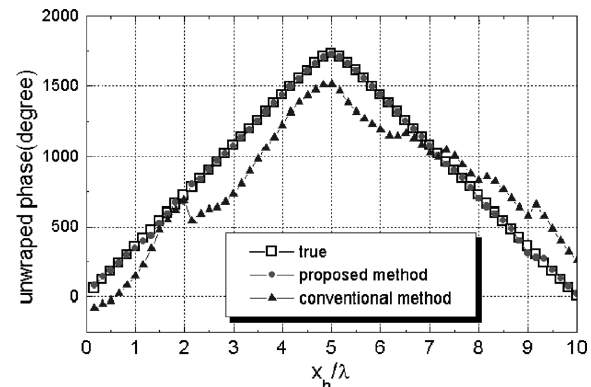
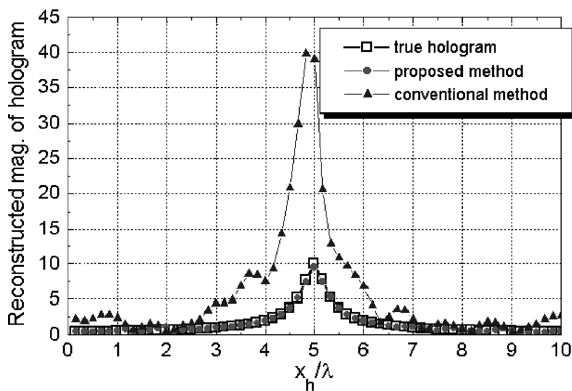
(a)

(b)



(c)

(d)



(e)

(f)

FIG. 6. A numerical simulation to demonstrate the effect of processing [according to Eq. (18)]. (a) Simulation configuration. (b) Normalized frequency spectrum used in the simulation. A narrow-band signal whose bandwidth is 4% of center frequency (343 Hz) was modeled as the sum of sinusoidal components whose initial phase is arbitrary. (c) The real part of the filtered complex signal from the moving microphone. The signal is Doppler shifted. (d) Real part of the reference microphone signal. (e) The magnitude of the reconstructed hologram. This can be obtained by using Eq. (18). The result is compared with the true hologram and the hologram by the conventional method. (f) The phase of the reconstructed hologram.

It is noteworthy that Eq. (12) can be written in terms of an x -directional wave number by utilizing the spatial Fourier transform (see Appendix A), that is,

$$\hat{P}_{h,B}(k_x, y_h, z_H; f_h) \cong A(f_h) \hat{P}_{hc}(k_x, y_h, z_H; f_{hc}). \quad (13)$$

Equations (11) and (13) lead to the result

$$\begin{aligned} F_T\{p_h(u_{m/h}t, y_h, z_H; t)\}_{\text{filtered}} &= \frac{1}{u_{m/h}} \int_{-\infty}^{\infty} A(f_h) \hat{P}_{hc}\left(\frac{2\pi(f_h - f)}{u_{m/h}}, y_h, z_H; f_{hc}\right) df_h \\ &= \frac{1}{u_{m/h}} \int_{-\infty}^{\infty} \hat{P}_{hc}\left(-\frac{2\pi f'}{u_{m/h}}, y_h, z_H; f_{hc}\right) A(f - f') df'. \end{aligned} \quad (14)$$

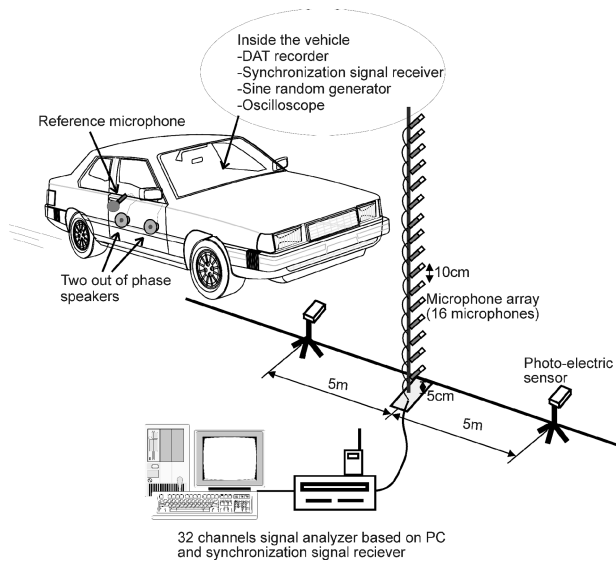


FIG. 7. Experimental setup.

We can easily obtain the second part of Eq. (14) by changing variables, $f' = f - f_h$. We can see that the right hand side of Eq. (14) represents the convolution of the mean wave-number spectrum \hat{P}_{hc} , and the normalized source spectrum $A(f_h)$. The time domain expression of Eq. (14) will be (see Appendix C for the detailed derivation)

$$\begin{aligned}
 &P_h(u_{m/h}t, y_h, z_H; t)_{\text{filtered}} \\
 &= \frac{1}{u_{m/h}} \int_{-\infty}^{\infty} \hat{P}_{hc} \left(-\frac{2\pi f}{u_{m/h}}, y_h, z_H; f_{hc} \right) e^{-j2\pi f t} df \\
 &\quad \times \int_{f_{h-}}^{f_{h+}} A(f_h) e^{-j2\pi f_h t} df_h, \quad (15)
 \end{aligned}$$

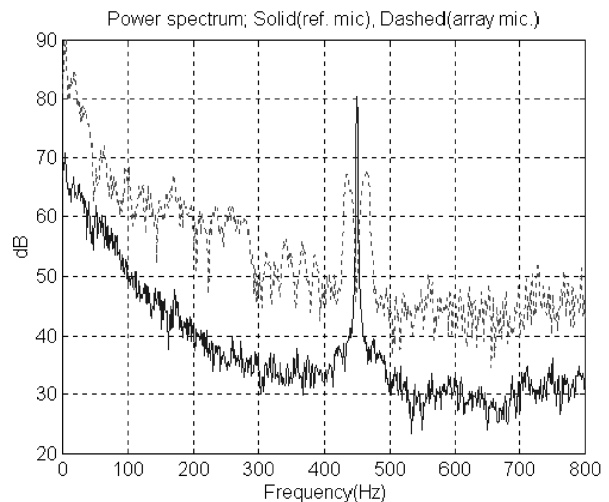
which is easier to interpret.

Note that the second integral of the right-hand side of Eq. (15) must be obtained from actual measurements. This means that we need additional measurement in the hologram coordinate. This can be accomplished by having a reference microphone that is fixed to the noise source. It is also noteworthy that we need only one reference microphone if we can assume that bandlimited noise sources are coherent. From the reference microphone signal, $A(f_h)$ can be obtained as

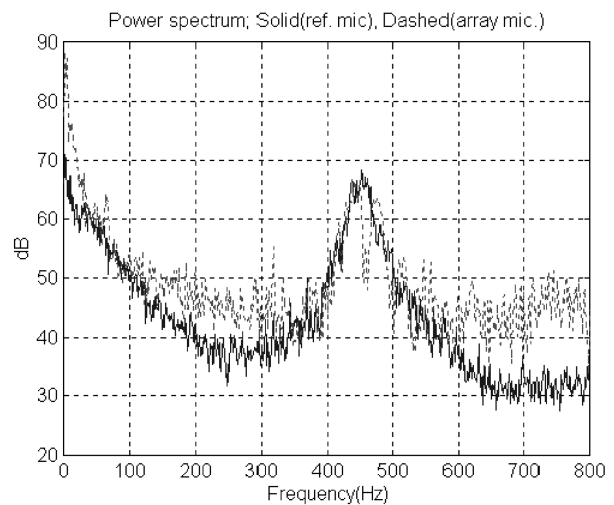
$$A(f_h) = P_{\text{ref}}(x_{\text{ref}}, y_{\text{ref}}, z_{\text{ref}}; f_h) / P_{\text{ref},c}(x_{\text{ref}}, y_{\text{ref}}, z_{\text{ref}}; f_{hc}), \quad (16)$$

where $P_{\text{ref}}(x_{\text{ref}}, y_{\text{ref}}, z_{\text{ref}}; f_h)$ and $P_{\text{ref},c}(x_{\text{ref}}, y_{\text{ref}}, z_{\text{ref}}; f_{hc})$ represent the reference microphone spectrum of an arbitrary frequency f_h and that of center frequency f_{hc} , respectively (see Fig. 5).

If we utilize Eq. (16), then Eq. (15) will be written as



(a)



(b)

FIG. 8. The actual source spectrum measured by the reference microphone (solid line) and the Doppler shifted spectrum by the array microphone (dashed line). (a) A 450 Hz pure tone. (b) A narrow-band noise (450 Hz center frequency and 32 Hz bandwidth).

$$\begin{aligned}
 &P_h(u_{m/h}t, y_h, z_H; t)_{\text{filtered}} \\
 &= \frac{1}{u_{m/h}} \int_{-\infty}^{\infty} \hat{P}_{hc} \left(-\frac{2\pi f}{u_{m/h}}, y_h, z_H; f_{hc} \right) e^{-j2\pi f t} df \\
 &\quad \times \frac{\int_{f_{h-}}^{f_{h+}} P_{\text{ref}}(x_{\text{ref}}, y_{\text{ref}}, z_{\text{ref}}; f_h) e^{-j2\pi f_h t} df_h}{P_{\text{ref},c}(x_{\text{ref}}, y_{\text{ref}}, z_{\text{ref}}; f_{hc})}. \quad (17)
 \end{aligned}$$

Equation (17) can be simplified by using the relation in Appendix B,

$$\begin{aligned}
 &P_h(u_{m/h}t, y_h, z_H; t)_{\text{filtered}} \\
 &= P_{hc}(x_h, y_h, z_H; f_{hc}) \cdot \frac{P_{\text{ref}}(x_{\text{ref}}, y_{\text{ref}}, z_{\text{ref}}; t)_{\text{filtered}}}{P_{\text{ref},c}(x_{\text{ref}}, y_{\text{ref}}, z_{\text{ref}}; f_{hc})}. \quad (18)
 \end{aligned}$$

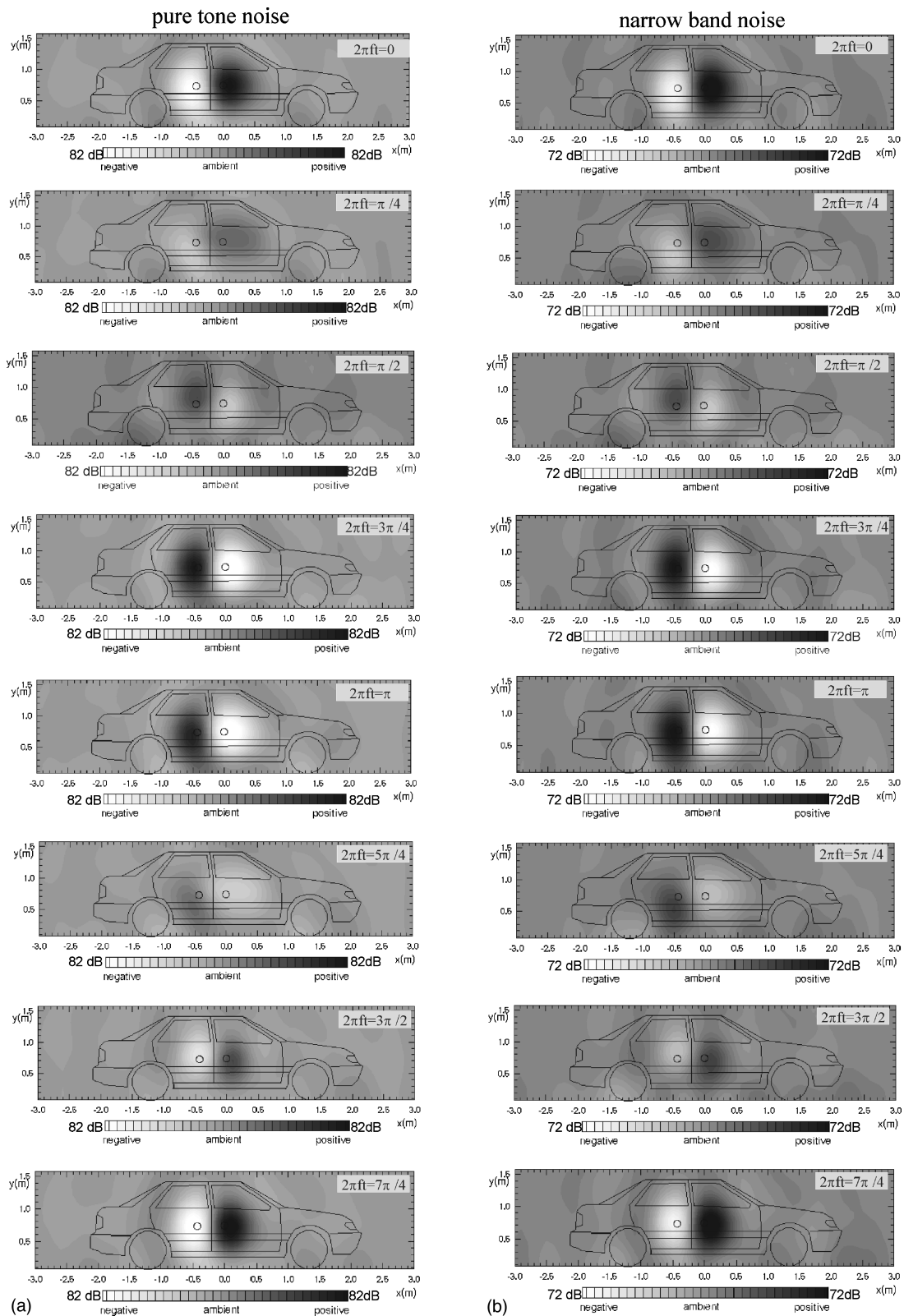


FIG. 9. The animated pictures of the reconstructed phase weighted sound pressure on the source plane by using the proposed method. (a) Two speaker units whose initial phase is 180° out of phase with each other radiate a 450 Hz pure tone. The speed of the vehicle is 14.27 m/s (51.37 km/h) and the distance between the hologram and the source plane is 0.33 m. (b) Two speaker units whose initial phase is 180° out of phase with each other radiate narrow-band noise whose center frequency and bandwidth are 450 and 32 Hz (7% bandwidth of center frequency). The speed of the vehicle is 14.13 m/s (50.87 km/h) and the distance between the hologram and the source plane is 0.33 m.

This equation forms the basis of the improved moving frame acoustic holography for coherent bandlimited noise. The left-hand side of Eq. (18) is the filtered complex pressure signal from the line array of microphones. The first term

of the right-hand side of Eq. (18), $P_{hc}(x_h, y_h, z_H; f_{hc})$, is the mean hologram of the bandlimited noise. Recall that this is obtained from the mean wave-number spectrum in the x direction. The second term is the filtered complex pressure

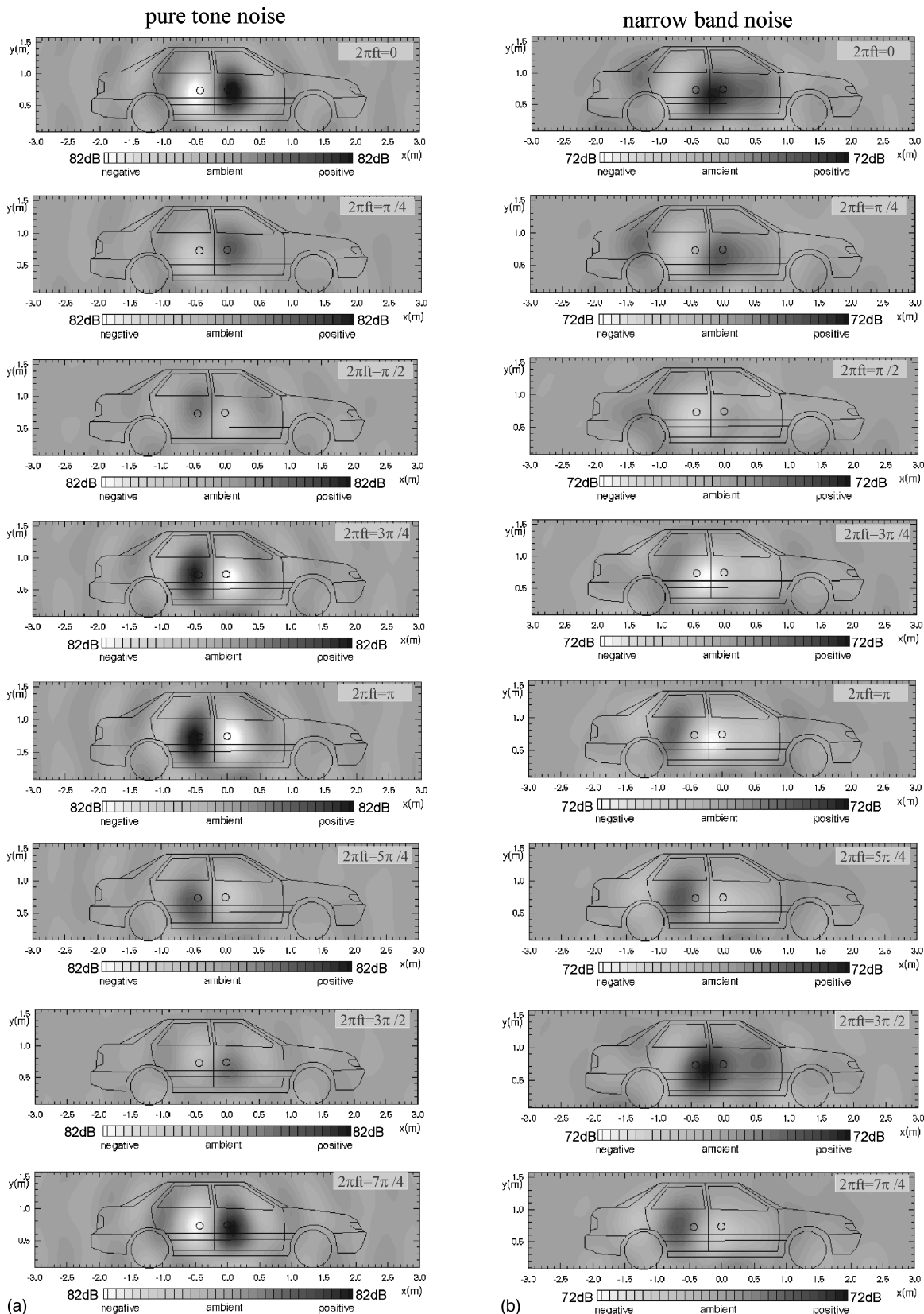


FIG. 10. The animated pictures of the reconstructed phase weighted sound pressure on the source plane by using the conventional MFAH method. The same data in Fig. 9 were used. (a) A 450 Hz pure tone. (b) A narrow-band noise whose center frequency and bandwidth are 450 and 32 Hz (7% bandwidth of center frequency).

signal from the reference microphone that is normalized by the reference microphone spectrum of center frequency $[P_{ref,c}(x_{ref}, y_{ref}, z_{ref}; f_{hc})]$. This equation also informs us that the signals of the line array and those of the reference mi-

crophone must be measured simultaneously.

Figure 6 illustrates the detailed process of the proposed method [Eq. (18)] by means of a numerical simulation. We assumed a point source whose spectrum is bandlimited (See

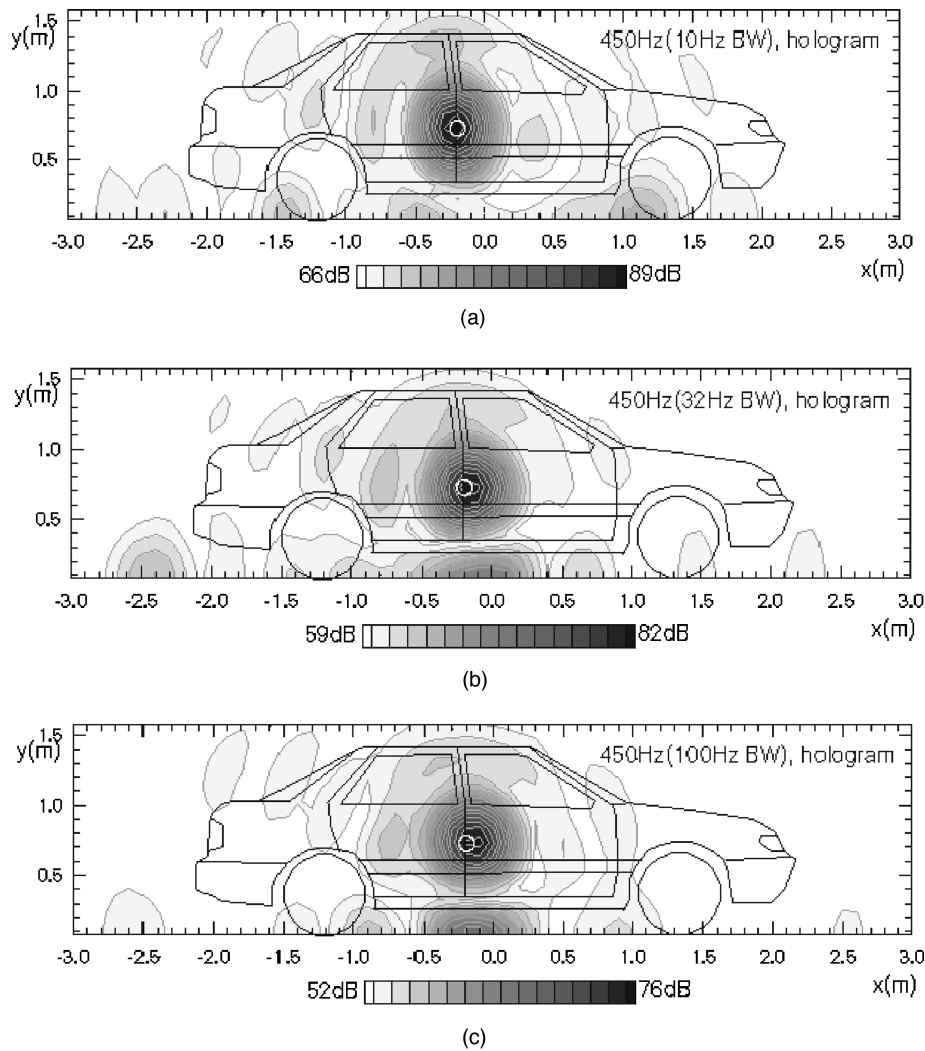


FIG. 11. The magnitude of the reconstructed hologram by using the proposed method. (a) A 450 Hz center frequency and 10 Hz bandwidth bandlimited noise. The speed of the vehicle is 14.32 m/s (51.55 km/h) and the distance between the hologram and the source plane is 0.2 m. (b) A narrow-band noise of 450 Hz center frequency and 32 Hz. The speed of the vehicle is 13.94 m/s (50.18 km/h) and the distance between the hologram and the source plane is 0.26 m. (c) A bandlimited noise of 450 Hz center frequency and 100 Hz. The speed of the vehicle is 13.49 m/s (48.56 km/h) and the distance between the hologram and the source plane is 0.26 m.

Fig. 6). The center frequency is 343 Hz and the bandwidth is 4% of the center frequency. We assumed that the point source was located at $(5\lambda, 0, 0)$ and a microphone was moving 0.2λ away from the noise source at the speed of 10 m/s. According to Eq. (18), we can explicitly show the way to obtain the spatial distribution of the sound field from the measured moving microphone signal and the reference signal. This result was compared with the true hologram as well as the hologram from the conventional method¹⁵ in Fig. 6.

It is noteworthy that the sound pressure level of the hologram can be compensated for by adding the mean squared pressure within the band of interest so that it can represent the overall sound pressure level of the band. It must be emphasized that the scope of this formulation is limited to the coherent bandlimited noise sources.

III. EXPERIMENTAL RESULTS

In order to verify the proposed method, we performed experiments. The experimental setup is illustrated in Fig. 7. The vertical line array of 16 microphones was used to mea-

sure the Doppler shifted signal. The microphone spacing was 0.1 m so that spatial aliasing below 1 kHz could be avoided. The time signal was recorded by using a multichannel signal analyzer that can sample 32 channels simultaneously. Two speaker units of the same kind were used to produce a controlled sound. In order to move the speaker units, we attached them to the right side of a vehicle. The vehicle was specially designed for reducing noises from the vehicle so that they would not affect the controlled sound from the speaker units. The vehicle ran at a constant speed of 50 km/h ($M = 0.04$) during the measurements. Two photoelectric sensors, separated by 10 m, were used to record the relative position between the moving vehicle and the vertical line array by measuring the constant speed of the vehicle.

A reference microphone was installed near the speaker units (Fig. 7) to measure the source signal (or, normalized source spectrum). A 16 channel digital audio tape (DAT) recorder was used to record the reference microphone signal. Recall that signals from the reference microphone and the array microphones must be sampled simultaneously. In prac-

tice, we devised one synchronization signal generator and two receivers: Three walkie-talkies were used: one for generating the synchronization signal and the others for receiving the signal. The received signals were recorded by both the DAT recorder and the signal analyzer during the measurement. They allowed us to synchronize the reference and the array signals.

First, we compared the proposed method with the conventional one. Two speaker units (“O” in the results) whose initial phase was 180° out of phase with each other were used. They were driven by both 450 Hz pure tone and typical narrow-band noise (the center frequency and bandwidth were 450 and 32 Hz, respectively). Figure 8 demonstrates the actual source spectra measured by the reference microphone and the Doppler shifted spectra by the array microphone. The figures explicitly show that the broadening of frequency components of the source spectrum makes the Doppler shifted spectrum. Figures 9 and 10 summarize animated pictures of the results. Figure 9 was created by the proposed method and Fig. 10 by the conventional method. From Figs. 9(a) and 10(a) we can see that both methods are able to visualize the sinusoidal sound field well. However, Figs. 9(b) and 10(b) illustrate that the conventional method cannot visualize the narrow-band sound field, while the proposed method does well.

The effect of the bandwidth of the signal on the visualized image was also demonstrated. One speaker unit, attached to the right side of the vehicle (“O” in Fig. 11), radiated three different kinds of bandlimited noise whose center frequency was 450 Hz. They had a 10 Hz bandwidth (2% of the center frequency), 31.6 Hz bandwidth (7% of the center frequency), and 100 Hz bandwidth (22% of the center frequency), respectively. Figure 11 shows the magnitude of the reconstructed sound field on the hologram plane. The results demonstrate that the proposed method well reconstructs the sound field. However, we can observe that the results have some errors due to bandwidth. Figure 11(b) and

(c) show the lead of the pressure peak (about 1/16λ), whereas Fig. 11(a) does not. Equation (12), which models the coherent bandlimited noise is the source of the error: The uncertainty of a narrow-band random process is represented as a broadening of peak location and shift of the acoustic center.

IV. CONCLUSIONS

The way to improve the moving frame acoustic holography was proposed so that it can be applied not only to discrete frequencies but also to coherent bandlimited noise. The way to apply the method to a practical situation was discussed. The speaker experiment demonstrates the validity of the proposed theory.

ACKNOWLEDGMENTS

The authors would like to thank Dr. Yon-Kyu Park and Dr. Hyu-Sang Kwon for their helpful discussion about the proposed theory. This work is partially supported by HANKOOK TIRE Co., Ltd. and KOSEF (Korea Science and Engineering Foundation).

APPENDIX A: TEMPORAL AND SPATIAL FOURIER TRANSFORM PAIRS

$$P(x, y, z; f) = \int_{-\infty}^{\infty} p(x, y, z; t) \exp(j2\pi ft) dt. \quad (A1)$$

$$p(x, y, z; t) = \int_{-\infty}^{\infty} P(x, y, z; f) \exp(-j2\pi ft) df. \quad (A2)$$

$$\hat{P}(k_x, y, z; f) = \int_{-\infty}^{\infty} P(x, y, z; f) \exp(-jk_x x) dx. \quad (A3)$$

$$P(x, y, z; f) = \frac{1}{2\pi} \int_{-\infty}^{\infty} \hat{P}(k_x, y, z; f) \exp(jk_x x) dk_x. \quad (A4)$$

APPENDIX B: THE DETAILED MATHEMATICAL DERIVATION OF Eqs. (9) AND (18)

$$\begin{aligned} \frac{1}{u_{m/h}} F_T^{-1} \left\{ \hat{P}_h \left(-\frac{2\pi f}{u_{m/h}}, y_h, z_H; f_{h0} \right) \right\} &= \frac{1}{u_{m/h}} \int_{-\infty}^{\infty} \hat{P}_h \left(-\frac{2\pi f}{u_{m/h}}, y_h, z_H; f_{h0} \right) e^{-j2\pi ft} df \\ &= \frac{1}{u_{m/h}} \int_{-\infty}^{\infty} \hat{P}_h(k_x, y_h, z_H; f_{h0}) e^{-j2\pi(-\frac{u_{m/h}/2\pi}k_x)(x_h/u_{m/h})} d \left(\frac{-u_{m/h}}{2\pi} k_x \right) \\ &= \int_{-\infty}^{\infty} \hat{P}_h(k_x, y_h, z_H; f_{h0}) e^{jk_x x_h} dk_x = P_h(x_h, y_h, z_H; f_{h0}). \end{aligned} \quad (B1)$$

APPENDIX C: INVERSE TEMPORAL FOURIER TRANSFORM OF Eq. (14)

$$\begin{aligned} p_h(u_{m/h}t, y_h, z_H; t)_{\text{filtered}} &= \frac{1}{u_{m/h}} \int_{-\infty}^{\infty} \int_{-\infty}^{\infty} \hat{P}_{hc} \left(-\frac{2\pi f'}{u_{m/h}}, y_h, z_H; f_{hc} \right) A(f-f') df' e^{-j2\pi ft} df \\ &= \frac{1}{u_{m/h}} \int_{-\infty}^{\infty} \hat{P}_{hc} \left(-\frac{2\pi f'}{u_{m/h}}, y_h, z_H; f_{hc} \right) \int_{-\infty}^{\infty} A(f-f') e^{-j2\pi ft} df df' \\ &= \frac{1}{u_{m/h}} \int_{-\infty}^{\infty} \hat{P}_{hc} \left(-\frac{2\pi f'}{u_{m/h}}, y_h, z_H; f_{hc} \right) e^{-j2\pi f' t} df' \int_{-\infty}^{\infty} A(\alpha) e^{-j2\pi \alpha t} d\alpha. \end{aligned} \quad (C1)$$

We can replace f' and α with f and f_h without loss of generality, then the above equation can be written as

$$P_h(u_{m/h}t, y_h, z_H; t)_{\text{filtered}} = \frac{1}{u_{m/h}} \int_{-\infty}^{\infty} \hat{P}_{hc} \left(-\frac{2\pi f}{u_{m/h}}, y_h, z_H; f_{hc} \right) e^{-j2\pi f t} df \cdot \int_{f_{h-}}^{f_{h+}} A(f_h) e^{-j2\pi f_h t} df_h. \quad (C2)$$

- ¹J. D. Maynard, E. G. Williams, and Y. Lee, "Near field acoustic holography: I. Theory of generalized holography and development of NAH," *J. Acoust. Soc. Am.* **78**, 1395–1413 (1985).
- ²E. G. Williams, J. D. Maynard, and E. J. Skudrzyk, "Sound source reconstructions using a microphone array," *J. Acoust. Soc. Am.* **68**, 340–348 (1980).
- ³J. Hald, "STSF—A unique technique for scan-based near-field acoustic holography without restrictions on coherence," Brüel & Kjær Technical Review No. 1, 1989.
- ⁴T. Loyau, J.-C. Pascal, and P. Gaillard, "Broadband acoustic holography reconstruction from acoustic intensity measurements. I: Principle of the method," *J. Acoust. Soc. Am.* **84**, 1744–1750 (1988).
- ⁵P. Rasmussen, S. Gade, and G. Ginn, "Tire noise measurement on a moving vehicle," Fourth International Congress on Sound and Vibration (St. Petersburg, Russia, 1996), pp. 599–602.
- ⁶B. Barsikow, W. F. King III, and E. Pfizenmaier, "Wheel/rail noise generated by a high-speed train investigated with a line array of microphones," *J. Sound Vib.* **118**, 99–122 (1987).
- ⁷B. Barsikow and W. F. King III, "On removing the Doppler frequency shift from array measurements of railway noise," *J. Sound Vib.* **120**, 190–196 (1988).
- ⁸Y. Takano, K. Terada, E. Aizawa, A. Iida, and H. Fujita, "Development of a 2-dimensional microphone array measurement system for noise sources of fast moving vehicles," in *Proceedings of Inter Noise 92*, edited by G. A. Daigle and M. R. Stinson (Toronto, Canada, 1992), pp. 1175–1178.
- ⁹S. Brühl and K.-P. Schmitz, "Noise source localization on highspeed trains using different array types," in *Proceedings of Inter Noise 93*, edited by P. Chapelle and G. Vermeir (Leuven, Belgium, 1993), pp. 1311–1314.
- ¹⁰J.-F. Hamet, M.-A. Pallas, and K. P. Schmitz, "DEUFRAKO-I: Microphone array techniques used to locate acoustic sources on ICE, TGV-A and TRANSRAPID 07," in *Proceedings of Inter Noise 94*, edited by M. Koyasu (Yokohama, Japan, 1994), pp. 187–192.
- ¹¹F. Poisson, J. C. Valiere, and P. Herzog, "High speed sound sources localization using bilinear time-frequency transformation," *Appl. Acoust.* **53**, 1–13 (1998).
- ¹²S.-M. Kim, H.-S. Kwon, S.-H. Park, and Y.-H. Kim, "Experimental comparisons of sound visualization methods for moving noise sources," in *Proceedings of Internoise 96*, edited by F. A. Hill and R. Lawrence (Liverpool, UK, 1996), pp. 377–380.
- ¹³H.-S. Kwon and Y.-H. Kim, "Moving frame technique for planar acoustic holography," *J. Acoust. Soc. Am.* **103**, 1734–1742 (1998).
- ¹⁴A. P. Dowling and J. E. Ffowcs Williams, *Sound and Sources of Sound* (Horwood, London, 1983), Chap. 9, pp. 187–192.
- ¹⁵X.-F. Wu and A. Akay, "Sound radiation from vibrating bodies in motion," *J. Acoust. Soc. Am.* **91**, 2544–2555 (1992).

The high-frequency asymptotic description of pulses radiated by a circular normal transducer into an elastic half-space

Dmitri Gridin and Larissa Ju. Fradkin

School of Electrical, Electronic and Information Engineering, South Bank University, 103 Borough Road, London SE1 0AA, United Kingdom

(Received 5 November 1997; accepted for publication 2 September 1998)

A new method for simulating the propagation of pulses radiated by a circular normal ultrasonic transducer which is directly coupled to a homogeneous and isotropic elastic half-space is proposed. Both nonuniform and uniform high-frequency asymptotics inside geometrical regions as well as boundary layers (penumbra, an axial region, and a vicinity of the critical rays) have been used to describe the transient field by means of harmonic synthesis. The nonuniform asymptotic formulas involving elementary or well-known special functions elucidate the physics of the problem and give explicit dependence of the radiated waves upon the model parameters. The formulas are applicable in the radiating near field which is the near-field with the evanescent wave zone excluded. The code based on the uniform asymptotics has been tested in all regions against an exact numerical solution. It is orders of magnitude faster, but in many realistic cases the accuracy does not suffer. The limits of applicability of the model have been established. © 1998 Acoustical Society of America. [S0001-4966(98)03212-3]

PACS numbers: 43.20.Bi, 43.20.Dk, 43.35.Zc [DEC]

INTRODUCTION

Simulating the propagation of pulses radiated by ultrasonic transducers into elastic solids is the first step towards mathematical modeling ultrasonic nondestructive evaluation (NDE) of industrial materials (see for instance Georgiou *et al.*, 1989). It precedes modeling reflection from boundaries, scatter by defects and inclusions, and reception of scattered and reflected pulses. The piston-type normal piezoelectric transducers of several millimeters in radius are commonly employed in industry (e.g., Silk, 1984). Their typical frequency is 5 MHz and thus, the typical compressional wavelength in steels is about 1 mm. The ferritic steels used in construction of high-pressure vessels in nuclear and chemical industry are homogeneous and isotropic on this scale. Consequently, the problem of propagation of pulses radiated by a circular normal transducer directly coupled to a homogeneous and isotropic solid has attracted much attention in the past decade.

The pioneering work in the area of propagation of elastic waves in an homogeneous and isotropic half-space was carried out by Lamb (1904). He studied time-harmonic line and point loads and used harmonic synthesis to deal with pulsed sources. He was particularly interested in the surface waves. The point-source problem is named Lamb's problem after him. In their classical paper, Miller and Pursey (1954) considered several types of time-harmonic loads acting on the surface of a half-space: an infinitely long strip of finite width vibrating normally or tangentially, and a circular disk vibrating normally or performing rotational oscillations about its center. Their solutions were also obtained in the integral form using Fourier and Hankel transforms for a strip and a disk, respectively. The method of steepest descent was applied to evaluate these integrals to describe compressional and shear waves in the far field for the case of a line- or

point-like source. The contribution of the head wave was neglected.

Several authors evaluated solutions obtained using the Hankel transform numerically, and then performed the harmonic synthesis (Kawashima, 1984; Djelouah and Baboux, 1992; Baboux and Kaźys, 1992). This procedure involves evaluating integrals of rapidly oscillating functions, and is, therefore, fairly time-consuming.

The integral transform methods have been extended to deal with pulses using the double Laplace–Fourier and Laplace–Hankel transforms instead of harmonic synthesis (e.g., Achenbach, 1973). This approach is often used in conjunction with the Cagniard–de Hoop method (e.g., Miklowitz, 1978), an analytical technique which allows one to carry out the inverse Laplace–Fourier transform by inspection. Mitra (1964) has applied the Cagniard–de Hoop method to the case of the uniform impulse pressure acting over a circular portion of the surface. Two Bessel functions in the integrands hinder the direct application of the method, and therefore, their integral representations and an integral representation of their product have been used. The final expressions involve double integrals. Note that these expressions are for the impulse load, and thus, a time convolution is needed to obtain the transient field for an arbitrary load. Thus, the whole procedure involves triple integration. This method was used by Bresse and Hutchins (1989) to compute the transient radiation from a *large* circular source (with a radius larger than a wavelength) and they compared their results with experimental data. They did not consider the head wave. Laturelle (1990), who worked with step in time-uniform loads, transformed the inverse Laplace–Hankel integral and separated the contribution of the static solution, the Rayleigh, and other elastic waves.

For the past decade, several direct numerical schemes have been developed to attack the problem of a pulsed cir-

cular source. They include a finite-element method (Ludwig and Lord, 1988) and finite-difference method (Ilan and Weight, 1990) as well as the so-called elastodynamic finite integration technique based on an integral formulation of the elastodynamic equations of motion (Fellinger and Langenberg, 1990). McNab *et al.* (1989) have proposed a numerical approach based on integrating point-load solutions and thus suitable for dealing with apodized loads. The direct numerical schemes are accurate but extremely time consuming. Furthermore, they do not elucidate the physics of the problem and cannot be used to predict easily the dependence of the wave components on the problem parameters.

In order to cut down the run time, several researchers have developed approximate numerical schemes to treat the problem. Weight (1987) has offered a simple phenomenological model based on geometrical acoustics considerations to describe pulse propagation in terms of direct compressional, edge compressional and shear waves. This model incorporates an empirical extension of the impulse-response method developed for fluids (Stepanishen, 1971). Lhémy (1994) has refined Weight's results by introducing an approximate integral formula for transient elastic waves which is closely related to the exact Rayleigh integral for radiation into fluids. The pulse response has been calculated using convolution of the impulse response with the pressure-in-put function. However, for certain observation angles, the Lhémy model produces an overshoot when predicting the edge shear wave. Following the original line of attack proposed by Miller and Pursey (1954), Schmerr and Sedov (1989) have obtained results pertaining to the regions both near and far from the transducer axis but not regions in-between. None of the above approximate models takes into account the head wave.

It has been pointed out in Fradkin *et al.* (1998) that the success of the approximate codes based on geometrical considerations is due to the fact that even the broadband pulses produced by industrial transducers contain mainly high and intermediate frequencies; this means that modern diffraction theory based on high-frequency asymptotics may be employed to refine them (for the asymptotics to be applicable, frequencies have to be only relatively high). Since the relevant formulas involve elementary or well-known special functions (such as Bessel, Fresnel, and parabolic cylinder), the modern asymptotic methods lead to codes which are orders of magnitude faster to run than those based on exact numerical schemes, while remaining practically as accurate. Fradkin *et al.* (1988) have proposed the so-called two-tier approach to describe the radiating near-field of a time-harmonic circular transducer based on the modern diffraction theory (Keller, 1958; Buchal and Keller, 1960; Babič and Kirpichnikova, 1975; Babič and Buldyrev, 1991; Borovikov and Kinber, 1994) and asymptotic approximations of integrals (Fedoryuk, 1977; Wong, 1989; Borovikov, 1994). First, they obtain the far-field asymptotics of a point source acting on the surface of an elastic half-space (Green's function). Then, they integrate these asymptotics over the transducer surface and find the radiating near-field asymptotics of a circular transducer. Gridin (1998a) has complemented these results by applying the uniform stationary phase method

(Bleistein and Handelman, 1986; Borovikov, 1994) to the integral representation of the displacement to obtain both uniform and nonuniform high-frequency asymptotics of the head wave and the field in the vicinity of the critical rays.

In the present paper, the model for simulating the propagation of pulses underneath a circular transducer is proposed. We employ the high-frequency asymptotics of the total field inside both geometrical regions and boundary layers to obtain time-harmonic solutions and then perform harmonic synthesis using the fast Fourier transform.

The paper is organized as follows: First, the physical interpretation of the nonuniform high-frequency asymptotics derived in Fradkin *et al.* (1998) and Gridin (1998a) is briefly discussed and more general, uniform asymptotics are compared with the exact numerical results. Then, the propagation of narrow and wideband pulses is studied. The predictions of the asymptotic model are compared with the exact results obtained by the same numerical integration scheme as in Baboux and Kazýs (1992), as well as exact and approximate results reported in the literature.

I. NORMAL TIME-HARMONIC TRANSDUCER

A. Formulation

Let us consider the forced motion of a homogeneous and isotropic elastic half-space caused by a time-harmonic circular normal transducer. The displacement field \mathbf{u} inside the medium is described by the reduced elasto-dynamic equation

$$b^2 \nabla \times (\nabla \times \mathbf{u}) - a^2 \nabla (\nabla \cdot \mathbf{u}) - \omega^2 \mathbf{u} = 0, \quad (1)$$

where a is a speed of P wave (also known as compressional or longitudinal), b a speed of S wave (also known as shear or transverse), $a > b$, and ω is a circular frequency. The wave numbers of the P and S waves are $k = \omega/a$ and $\kappa = \omega/b$, respectively. The boundary conditions assume that the pressure is uniformly applied over a disk of a radius l and may be written as follows:

$$\begin{aligned} \sigma_{zr}|_{z=0} &= 0, \\ \sigma_{zz}|_{z=0} &= -\frac{Q}{\pi l^2} H(l-r), \end{aligned} \quad (2)$$

where Q has a dimension of force and H is Heaviside's function. The cylindrical coordinates (r, φ, z) are used, where z -axis runs along the transducer axis pointing downwards and $z=0$ on the boundary. The components of the stress tensor are

$$\begin{aligned} \sigma_{zr} &= \rho b^2 \left(\frac{\partial u_r}{\partial z} + \frac{\partial u_z}{\partial r} \right), \\ \sigma_{zz} &= \rho a^2 \frac{\partial u_z}{\partial z} + \rho \frac{a^2 - 2b^2}{r} \frac{\partial (ru_r)}{\partial r}, \end{aligned} \quad (3)$$

where u_r and u_z are the r and z components of the displacement, respectively, and ρ is the density. The problem is axis-symmetrical and, therefore, there is no dependence on φ . We consider the case of a large transducer,

$$kl \gg 1, \quad (4)$$

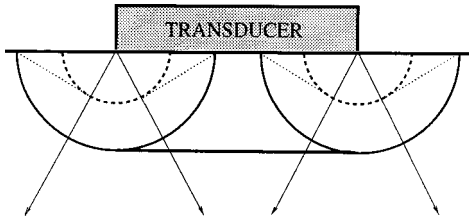


FIG. 1. Fronts of waves underneath a circular transducer acting normally on the surface of an elastic half-space. Thick solid line: the direct P wave; thin solid lines: the edge P wave; dashed lines: the edge S wave; and dotted lines: the edge head wave.

i.e., we assume that the radius of the transducer is larger than the wavelength $\lambda = 2\pi/k$.

B. The high-frequency asymptotics

In this section we summarize the results of Fradkin *et al.* (1998) and Gridin (1998a), who have applied the modern diffraction theory to derive high-frequency asymptotics of the radiating near field radiated by a circular normal transducer into elastic solids. According to this theory, the elastic field of a high frequency consists of the so-called geometrical regions and the boundary layers in-between. The experience shows that frequencies have to be only relatively high, and the theory often works at distances of one- or even one-half-wavelength from a source or scatterer.

The geometrical regions are called that because they may be efficiently modeled using the concept of a ray. The field inside such regions may be represented in the form of a finite number of waves each described by a *ray series*, that is, the asymptotic series in inverse powers of dimensionless wave number k

$$\mathbf{u}(k, \mathbf{s}) = e^{ik\varphi(\mathbf{s})} \sum_{n=0}^{\infty} \frac{A_n(\mathbf{s})}{(ik)^{n+\nu}}, \quad (5)$$

where eikonal (or phase function) $\varphi(\mathbf{s})$ and the amplitude functions $A_n(\mathbf{s})$ all depend on the coordinates of the observation points only, and ν is a different constant for different waves.

This representation breaks down inside boundary layers, which are transitional regions surrounding lines or surfaces of irregularity along which rays of different nature or an infinite number of rays meet. This concept was first introduced by Keller (1958) and Buchal and Keller (1960) by analogy with fluid dynamics and then developed further by Babić and Kirpichnikova (1975). The size and shape of a boundary layer are determined by the condition that the phase difference between the relevant rays is small (usually smaller than π). The fields inside boundary layers are described in terms of asymptotic series involving special functions rather than just inverse powers of dimensionless frequency.

1. Geometrical regions

It is well known (e.g., Weight, 1987) that a compressional circular transducer generates a direct P wave, edge P wave, edge S wave, and edge head wave (see Fig. 1). For every observation point lying inside a geometrical region, there are two arrivals of the edge wave of each type, one

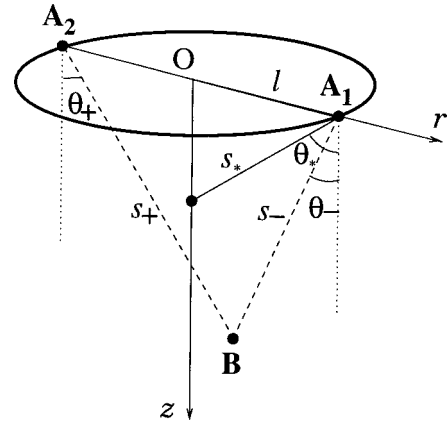


FIG. 2. The nearest (A_1) and farthest (A_2) points on the edge of the transducer. B is the observation point.

from the nearest and the other from the farthest edge point (see Fig. 2). The Rayleigh wave is not taken into account because, when dealing with normal transducers, only body waves are of interest. The leading terms of the corresponding ray series are summarized below. The common factor $\exp(i\omega t)$ is suppressed throughout.

The direct P wave is described by

$$\mathbf{v}^{P(\text{direct})} \propto e^{-ikz} \mathbf{e}_z, \quad (6)$$

where $\mathbf{v}\exp(i\omega t)$ is the particle velocity, which is the first derivative of the displacement with respect to time, and the sign “ \propto ” means “proportional.” The exact constants of proportionality are given in Fradkin *et al.* (1998) and Gridin (1998a). We use the particle velocity, not displacement, because this is the quantity measured by receiving probes (e.g., Weight, 1987). It is easy to show that, for the transducer of infinite radius which exerts the same uniform pressure as our transducer, the above solution is exact. The direct P wave is plane, exists only straight beneath the transducer, and propagates without decay. The S field contains no direct wave.

The edge P and S waves are described by

$$\mathbf{v}_{\pm}^{P(\text{edge})} \propto A^P(\theta_{\pm}) \left[\frac{s_{\pm}}{k(l \pm r)^2} \right]^{1/2} \left(\frac{l}{r} \right)^{1/2} e^{-iks_{\pm}} \mathbf{n}^P, \quad (7)$$

and

$$\mathbf{v}_{\pm}^{S(\text{edge})} \propto A^S(\theta_{\pm}) \left[\frac{s_{\pm}}{\kappa(l \pm r)^2} \right]^{1/2} \left(\frac{l}{r} \right)^{1/2} e^{-i\kappa s_{\pm}} \mathbf{n}^S, \quad (8)$$

where the unit ray vectors are

$$\begin{aligned} \mathbf{n}^P &= \pm \sin \theta_{\pm} \mathbf{e}_r + \text{sgn}(l \pm r) \cos \theta_{\pm} \mathbf{e}_z, \\ \mathbf{n}^S &= \pm \cos \theta_{\pm} \mathbf{e}_r - \text{sgn}(l \pm r) \sin \theta_{\pm} \mathbf{e}_z, \end{aligned} \quad (9)$$

the distances s_{\pm} from the farthest and nearest points as well as associated angles θ_{\pm} are defined by

$$s_{\pm} = [z^2 + (l \pm r)^2]^{1/2}, \quad \sin \theta_{\pm} = |l \pm r|/s_{\pm}, \quad (10)$$

and A^P and A^S are the standard directivities of a point source acting normally on the surface of a homogeneous and isotropic elastic half-space (see, e.g., Miller and Pursey, 1954; Fradkin *et al.*, 1998). It follows from (9) that the relative polarities of the edge P - and S -waves coincide with those in

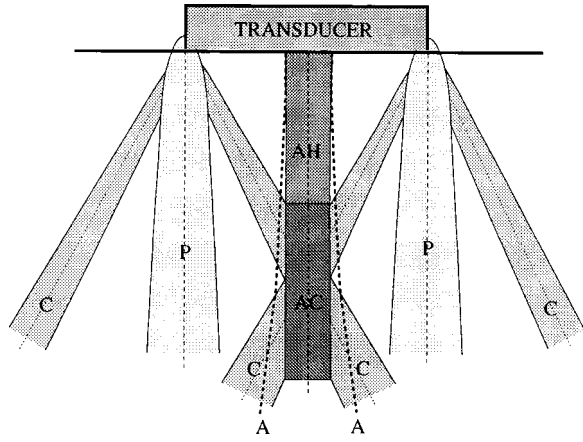


FIG. 3. Boundary layers underneath a circular transducer acting normally on the surface of an elastic half-space: penumbra (P), axial regions (AH, AC and zone between lines marked A) and vicinity of the critical rays (C).

Weight (1987, Fig. 8), and that each of these waves has a toroidal front.

The edge head wave is described by

$$\mathbf{v}_{\pm}^{H(\text{edge})} \propto [\kappa s_{\pm} \sin(\theta_{\pm} - \theta_{\text{cr}})]^{-3/2} \times \left(\frac{l}{r}\right)^{1/2} e^{-i\kappa s_{\pm} \cos(\theta_{\pm} - \theta_{\text{cr}})} H(\theta_{\pm} - \theta_{\text{cr}}) \mathbf{n}^H, \quad (11)$$

where the unit ray vector is

$$\mathbf{n}^H = \pm \sqrt{1 - \gamma^2} \mathbf{e}_r - \text{sgn}(l \pm r) \gamma \mathbf{e}_z, \quad (12)$$

$\theta_{\text{cr}} = \arcsin \gamma$, $\gamma = b/a$, is a critical angle, and H is Heaviside's function. The head wave exists only for $\theta_{\pm} > \theta_{\text{cr}}$. The asymptotics of this wave are of a higher order compared to the P and S wave, i.e., the head wave decays away from the source more rapidly.

2. Boundary layers

The representation of the elastic field as a sum of the above waves breaks down inside the boundary layers. For a circular transducer, these layers are presented in Fig. 3.

There are two boundary layers for the P field—penumbra and the axial region. Inside the penumbra (marked P in Fig. 3), the phase difference between the direct P and edge P arrival from the nearest edge point is small (zero directly underneath the rim). The numerical experiments described below confirm that it is reasonable to choose the phase difference π as a cutoff point. The leading term of the z component of the penumbral asymptotic series is

$$v_z^{P(\text{penumbra})} = F[\text{sgn}(l-r) \sqrt{k(s_- - z)}] v^{P(\text{direct})}, \quad (13)$$

where F is a Fresnel integral. The r -component of the penumbral asymptotic series coincides with the r -component of the edge P wave (7), since the direct P wave has no component in this direction. The shape of the penumbral region is determined by the condition that the phase difference between the direct P and edge P arrival from the nearest edge point is π , that is,

$$k(s_- - z) = \pi. \quad (14)$$

Therefore, it is parabolic.

The asymptotics of the edge P wave fail as $r \rightarrow 0$ when the phase difference between the two edge P arrivals tends to zero, i.e., in the axial region (the area between lines marked A in Fig. 3). In this case, the leading term of the axial asymptotic series involves the Bessel functions of the zeroth and first order, and is given by

$$\mathbf{v}^{P(\text{axial})} \propto A^P(\theta_*) e^{-i\kappa s_*} [J_0(\kappa r \sin \theta_*) \cos \theta_* \mathbf{e}_z + iJ_1(\kappa r \sin \theta_*) \sin \theta_* \mathbf{e}_r], \quad (15)$$

where the distances s_* from the edge to the axis and the corresponding angle θ_* are defined by

$$s_* = (z^2 + l^2)^{1/2}, \quad \sin \theta_* = l/s_*. \quad (16)$$

The shape of the axial region is determined by the condition that the phase difference between the edge arrivals from the nearest and farthest points is equal to π , which is approximately equivalent to

$$\kappa r \sin \theta_* = \frac{\pi}{2}. \quad (17)$$

Therefore, this shape is hyperbolic. Note that these asymptotics are of a lower order compared to the asymptotics of the edge P wave (7), i.e., the focusing of the edge wave near the transducer axis takes place.

There are two types of boundary layers in the total S field: the axial region and the vicinity of the critical rays. There is no penumbra because there is no direct S wave. The leading terms of the axial asymptotic series for the edge S wave are similar to those for the edge P wave and are given by

$$\mathbf{v}^{S(\text{axial})} \propto A^S(\theta_*) e^{-i\kappa s_*} [J_0(\kappa r \sin \theta_*) \sin \theta_* \mathbf{e}_z + iJ_1(\kappa r \sin \theta_*) \cos \theta_* \mathbf{e}_r]. \quad (18)$$

For the head wave in the axial region (marked AH in Fig. 3), we have

$$\mathbf{v}^{H(\text{axial})} \propto (\kappa l)^{1/2} \frac{e^{-i\kappa s_* \cos(\theta_* - \theta_{\text{cr}})}}{[\kappa s_* \sin(\theta_* - \theta_{\text{cr}})]^{3/2}} H(\theta_* - \theta_{\text{cr}}) \times [iJ_1(\kappa r \gamma) \sqrt{1 - \gamma^2} \mathbf{e}_r + J_0(\kappa r \gamma) \gamma \mathbf{e}_z]. \quad (19)$$

Note that for the head wave, the shape of the axial region is determined by the condition that the phase difference between two head arrivals, one from the nearest and the other from the farthest edge point, is π . This is equivalent to

$$\kappa r \gamma = \pi/2. \quad (20)$$

Therefore, this shape is cylindrical.

The representation of the total S field as a sum of the edge S and head waves is not applicable inside the boundary layers surrounding the critical rays (marked C in Fig. 3) where the phase difference between these waves is small. There are two leading terms of the critical-ray asymptotic series: One involves the parabolic cylinder function $D_{1/2}$, and the other differs from the edge S asymptotics (8) only by the directivity function \tilde{A}^S , so that we have

$$\begin{aligned} \mathbf{v}_{\pm}^{S(\text{total})} \propto & \alpha_{\pm} (\kappa s_{\pm})^{-3/4} \left(\frac{l}{r}\right)^{1/2} \\ & \times \exp\left(-i\kappa s_{\pm} \frac{1 + \cos(\theta_{\pm} - \theta_{\text{cr}})}{2}\right) D_{1/2}(w_{\pm}) \mathbf{n}^H \\ & + \beta_{\pm} \tilde{A}^S(\theta_{\pm}) \left[\frac{s_{\pm}}{\kappa(l \pm r)^2}\right]^{1/2} \left(\frac{l}{r}\right)^{1/2} e^{-i\kappa s_{\pm} \mathbf{n}^S}, \end{aligned} \quad (21)$$

where the argument of the parabolic cylinder function is

$$w_{\pm} = -(1+i) \operatorname{sgn}(\theta_{\pm} - \theta_{\text{cr}}) \sqrt{\kappa s_{\pm} [1 - \cos(\theta_{\pm} - \theta_{\text{cr}})]}, \quad (22)$$

and the explicit expressions for constants α_{\pm} and β_{\pm} and function \tilde{A}^S can be found in Gridin (1998a). It follows from (21) that the total S field is not zero on the critical ray where the edge S wave (8) vanishes. The shape of the critical-ray boundary layers is determined by the condition that the phase difference between the edge S and head wave is π , so that we have

$$\kappa s_{\pm} [1 - \cos(\theta_{\pm} - \theta_{\text{cr}})] = \pi. \quad (23)$$

Therefore, this shape is parabolic.

These asymptotics fail inside the axial region (marked AC in Fig. 3) where we have two leading terms: One involves both the parabolic cylinder and Bessel functions, and the other differs from the edge S asymptotics (18) only by the directivity function \tilde{A}^S , so that we have:

$$\begin{aligned} \mathbf{v}^{S(\text{total-axial})} \propto & \alpha_{*} \kappa^{-1/4} s_{*}^{-3/4} e^{-i\kappa s_{*} (1 + \cos(\theta_{*} - \theta_{\text{cr}})/2)} D_{1/2}(w_{*}) \\ & \times [iJ_1(\kappa r \gamma) \sqrt{1 - \gamma^2} \mathbf{e}_r + J_0(\kappa r \gamma) \gamma \mathbf{e}_z] \\ & + \beta_{*} \tilde{A}^S(\theta_{*}) e^{-i\kappa s_{*}} [J_0(\kappa r \sin \theta_{*}) \sin \theta_{*} \mathbf{e}_z \\ & + iJ_1(\kappa r \sin \theta_{*}) \cos \theta_{*} \mathbf{e}_r], \end{aligned} \quad (24)$$

where the argument of the parabolic cylinder function is

$$w_{*} = -(1+i) \operatorname{sgn}(\theta_{*} - \theta_{\text{cr}}) \sqrt{\kappa s_{*} [1 - \cos(\theta_{*} - \theta_{\text{cr}})]}. \quad (25)$$

3. Uniform asymptotics

The nonuniform asymptotics elucidate the physics of the problem by producing description of the structure of the field in terms of geometrical regions and boundary layers. To avoid transition from a boundary layer to a geometrical region, it is often advisable to use *uniform* asymptotics, that is, asymptotics which are applicable both inside and outside the layer (Bleistein and Handelsman, 1986; Borovikov, 1994).

The leading terms of the z -component of the penumbral uniform asymptotics are given by

$$\begin{aligned} v_z^{P(\text{penumbra})} \propto & F[\operatorname{sgn}(l-r) \sqrt{k(s_- - z)}] e^{-ikz} \\ & + (2\pi k r)^{-1/2} \\ & \times \left[\frac{A^P(\sin \theta_-)}{\gamma^2} \frac{z}{r-l} \sqrt{\frac{l}{s_-}} \right. \\ & \left. + \operatorname{sgn}(r-l) \sqrt{\frac{r}{2(s_- - z)}} \right] e^{-i(k s_- - 3\pi/4)}. \end{aligned} \quad (26)$$

The corresponding r component coincides with the nonuniform asymptotic expression (7), since the direct P wave has no component in this direction, and thus no interference of direct and edge wave takes place along the r -axis. Numerical experiments described below show that adding (26) to the edge P wave from the farthest edge point gives a very good description of the z component of the P field everywhere outside the axial region. Outside the penumbra, that is for $k(s_- - z) > \pi$, one can use the large-argument asymptotics of the Fresnel integral to check that (26) produces the leading terms of the nonuniform asymptotics (6) and (7).

To obtain the uniform asymptotics of the total S field, one should add to (21) or (24) the term which involves the parabolic cylinder function $D_{3/2}$ and is the order $(\kappa s)^{1/2}$ higher than the $D_{1/2}$ term. The corresponding expressions can be found in Gridin [1998a, Eqs. (40) and (41)]. Note that numerical experiments have shown, despite the fact that the $D_{3/2}$ term is of a higher order, it still makes a significant contribution.

Strictly speaking, all the above uniform asymptotics are only *locally* uniform since we still have different expressions inside and outside the axial region. Global uniform asymptotics may be obtained by the matching of the inner and outer asymptotics, but we have not derived them because they are too cumbersome.

C. Limits of applicability and numerical results

All the above asymptotics are applicable in the radiating near field of a circular transducer, i.e., for

$$kz \gg 1, \quad z/kl^2 \ll 1. \quad (27)$$

Numerical experiments have confirmed more precise limits as

$$\lambda \leq z \leq l^2/\lambda, \quad (28)$$

where λ is a wavelength of the P wave. For a typical frequency of 5 MHz and the transducer radius $l = 10$ mm, this region extends in steels from about 1 mm to about 80 mm. Numerical experiments have demonstrated further that the asymptotic formulas give a reasonable agreement with an exact numerical solution in the intermediate zone as well, i.e., for

$$l^2/\lambda < z < 8l^2/\lambda. \quad (29)$$

This is the region which, in steels, extends down to about 640 mm, and thus is large enough for most applications of interest.

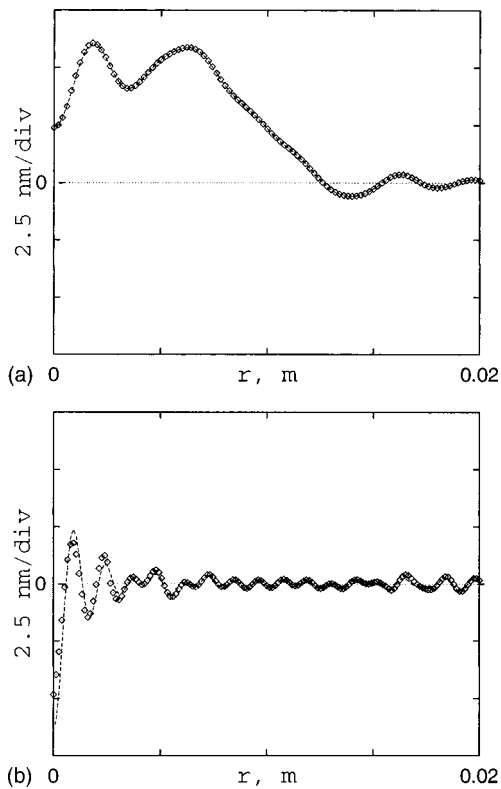


FIG. 4. Comparison between the asymptotic (boxes) and exact (dashed line) displacements at $z=10$ mm. (a) z -component of the total P field; (b) z -component of the total S field.

In the far field,

$$z > 8l^2/\lambda; \quad (30)$$

the above asymptotics may be replaced by standard far-field formulas for a circular source involving the Bessel function of the first order (e.g., Tang *et al.*, 1994). Note that the far-field results obtained by Miller and Pursey (1954) are for point-like sources and thus are not applicable to large transducers.

All the above formulas have been validated in all geometrical regions and boundary layers against the exact solution evaluated by numerical integration of the inverse Hankel transform. Some of the validation results are presented in Fig. 4, where we compare the z components of the total P [Fig. 4(a)] and total S [Fig. 4(b)] displacements at depth $z=10$ mm and various distances from the axis. The model parameters are as follows: $a=6400$ m/s, $b=3150$ m/s, $\rho=2700$ kg/m³, $Q=500$ N, $l=10$ mm, and $f=3$ MHz.

The z -component of the P wave [Fig. 4(a)] makes the most significant contribution to the field of a normal transducer. The first two terms of the penumbral uniform asymptotics, (13) and (26), give a very good quantitative agreement with the exact solution. For the S field, the agreement is slightly worse due to the fact that the uniform asymptotics for the total S field and nonuniform asymptotics (11) and (19) have been derived without taking into account the influence of the complex poles of the Rayleigh function (Gridin, 1998a). At higher frequencies this effect is less pronounced. The z component of the S field [Fig. 4(b)] inside the axial

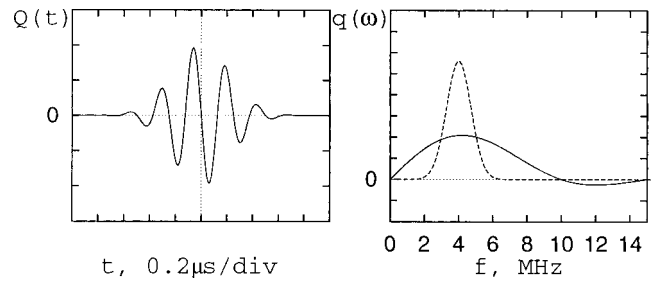


FIG. 5. Left: a realistic narrow-band pulse; right: spectra of one cycle of sine (solid line) and narrow-band pulse (dashed line).

region may be comparable with this component of the P field.

II. PROPAGATION OF PULSES

The asymptotic expressions for the radiating near- and intermediate field of a time-harmonic circular transducer which have been described in the previous section may be used to model the propagation of pulses by means of harmonic synthesis; that is, the inverse Fourier transform with respect to time. The particle velocity $\mathbf{V}(r, z, t)$ at the moment t is given by

$$\mathbf{V}(r, z, t) = \text{Re} \frac{1}{\pi} \int_0^\infty \mathbf{v}(r, z, \omega) q(\omega) e^{i\omega t} d\omega, \quad (31)$$

where $v_r(r, z, \omega)$ and $v_z(r, z, \omega)$ are the time-harmonic particle velocities considered above, and $q(\omega)$ is the Fourier transform of the load-time variation function $Q(t)$.

In computations, the same parameters have been used as described in the previous section. Two types of pulses have been considered: The first is one cycle of $\sin(2\pi ft)$ with frequency $f=5$ MHz and second, a narrow-band pulse $\sin(2\pi ft)$ with frequency $f=4$ MHz modulated by a Gaussian function (see Fig. 5). The duration of the first pulse is $0.2 \mu\text{s}$ and the second, about $1 \mu\text{s}$. Their Fourier transforms are shown in Fig. 5. The cycle of a sine contains frequencies lying between 0 and 15 MHz. The narrow-band pulse contains mostly high-frequency harmonics in the 2–6 MHz range. It reproduces features of the pulse used in Georgiou *et al.* (1989) and also realistic pulses (*ibid.* Figs. 10 and 11).

Similar to the previous section, we compare the asymptotic results with those obtained by exact numerical method combined with the fast Fourier transform. The same exact numerical scheme has been used by Baboux and Kažys (1992). In the asymptotic method, the bandwidth is taken to be 0.5–10 MHz, and in the exact, it is extended down to 0 MHz.

A. The radiating near-velocity field inside the axial region

First, let us choose the observation point to lie on the axis of the transducer and assume the load to be the wide-band pulse. At depth $z=5$ mm, the corresponding waveforms of the z component of the particle velocity are presented in Fig. 6(a). The first pulse in the train is due to the direct P wave (DP). The second and fourth pulses are due to the edge P (EP) and S (ES) arrivals, respectively. The am-

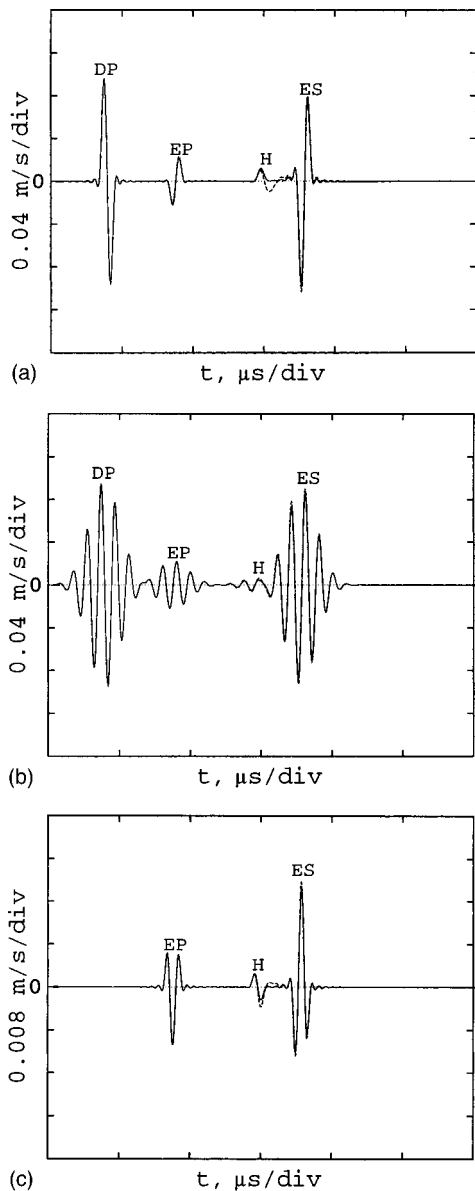


FIG. 6. The z component of the near-velocity field on the axis of the transducer at $z=5$ mm for (a) one cycle of sine and (b) narrow-band pulse; (c) the waveforms of the r component of the particle velocity near the axis ($r=0.1$ mm). Solid and dashed lines are asymptotic and exact solutions, respectively. The direct P , edge P , head, and edge S pulse are marked DP, EP, H, and ES, respectively.

plitudes of these pulses are comparable with the direct pulse due to the focusing of the edge waves along the axis. The third pulse is that of the edge head wave. There is a good agreement between the asymptotic and exact solutions for all the pulses except the head one. In this case, the amplitude and the time of arrival agree but in the asymptotic solution some part of the pulse is missing. As already mentioned above, this effect is due to the fact that the influence of the additional complex poles of Rayleigh's function is not taken into account (Gridin, 1998a). The effect is noticeable at intermediate frequencies but weaker at high frequencies. Indeed, similar results are presented in Fig. 6(b) for the realistic narrow-band pulse. The head pulses are in good agreement there. Due to the cylindrical symmetry, the r -component of the particle velocity vanishes on the axis of the

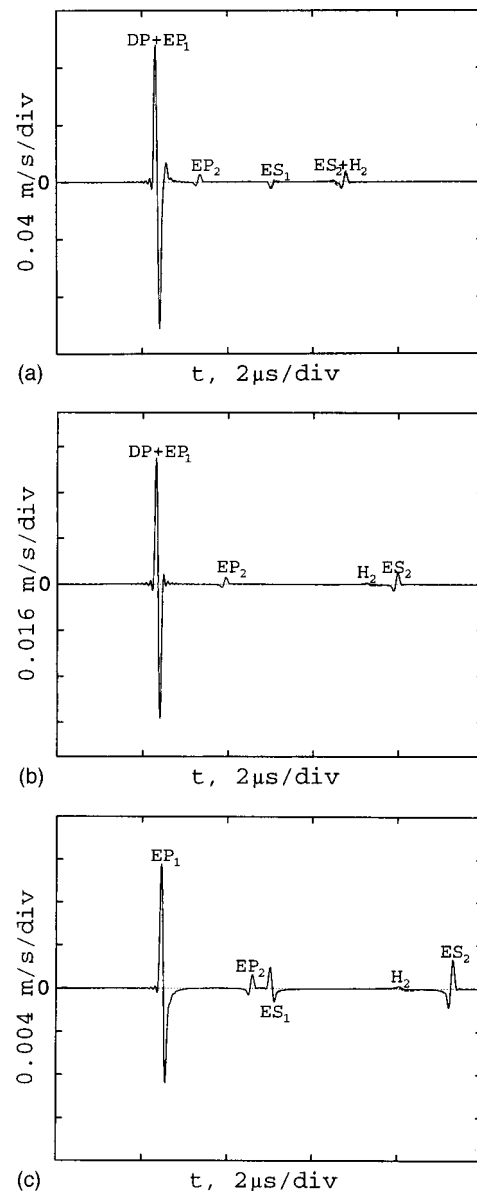


FIG. 7. The z component of the near-velocity field off the axis of the transducer for one cycle of sine at $z=15$ mm and (a) $r=5$ mm, (b) $r=10$ mm, and (c) $r=15$ mm. The key is the same as in Fig. 6. Subscripts "1" and "2" relate to edge pulses arriving from the nearest and farthest edge points, respectively.

transducer. Therefore, in Fig. 6(c) the waveforms of this component are shown at the observation point very close to the axis ($r=0.1$ mm). In this case, there is no pulse due to the direct P wave. All other pulses are present.

B. The radiating near-velocity field outside the axial region

The waveforms of the V_z for the wideband pulse at depth $z=15$ mm and various distances from the axis are presented in Fig. 7. At the observation points lying outside the axial region but still inside the main beam of the transducer, e.g., at $r=5$ mm, the direct P pulse (DP) dominates [Fig. 7(a)]. It partially overlaps with the edge P pulse arriving from the nearest edge point (EP_1). The second pulse is the edge P arriving from the farthest edge point (EP_2), and the

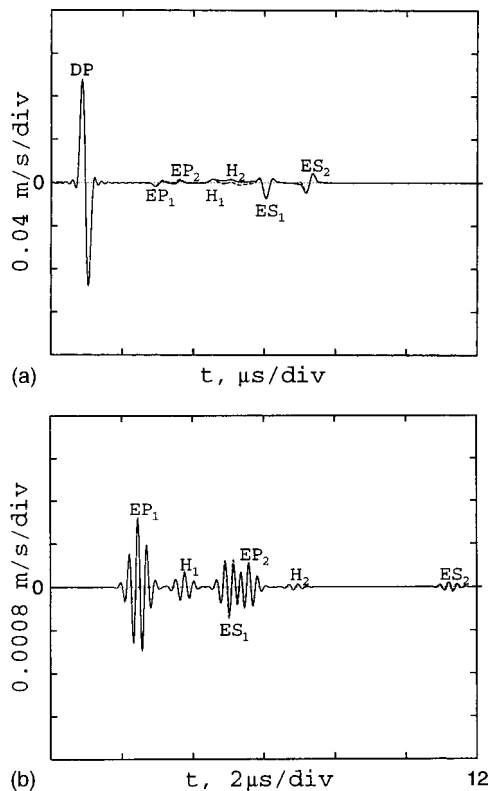


FIG. 8. The near-velocity field. (a) The z -component at $r=1$ mm and $z=3$ mm; (b) the r component at $r=25$ mm and $z=5$ mm. The key is the same as in Fig. 7.

third, the edge S arriving from the nearest edge point (ES_1). The overlapping edge S and head pulses both arriving from the farthest edge point give rise to the fourth pulse (ES_2+H_2). At this observation point there is no head wave from the nearest edge point. Straight underneath the rim of the transducer, the first pulse is due to the P wave from the nearest edge point [DP+EP₁, Fig. 7(b)]. The amplitude of this pulse is approximately equal to one-half of the direct P pulse. This may be easily seen from (13), which implies

$$v_z^{P(\text{penumbra})}|_{r=l} \approx F(0)v^{P(\text{direct})} = v^{P(\text{direct})}/2. \quad (32)$$

The other pulses are the edge P (EP₂), edge head (H_2 , very small), and edge S (ES₂), all arriving from the farthest edge point. Neither head pulse nor the z component of the S pulse arriving from the nearest edge point is present. Outside the main beam of the transducer, e.g., at the distance $r=15$ mm from the axis, there is no direct P wave [Fig. 7(c)]. The discernible pulses are the edge P arriving from the nearest and farthest edge points (EP₁ and EP₂) respectively, S arriving from the nearest edge point (ES₁), and head and S arriving from the farthest edge point (ES₂ and H_2), respectively.

The maximum number of pulses produced by a circular normal transducer inside a solid is equal to seven: The first one is due to the direct P wave (DP) and six others, to the edge P (EP₁ and EP₂), head (H_1 and H_2) and S (ES₁ and ES₂) arriving from the nearest and farthest edge points, respectively [Fig. 8(a)]. The zone where all seven pulses may be detected is very limited. Outside this zone, pulses overlap or vanish (e.g., the head wave vanishes for $\theta < \theta_{cr}$). Outside

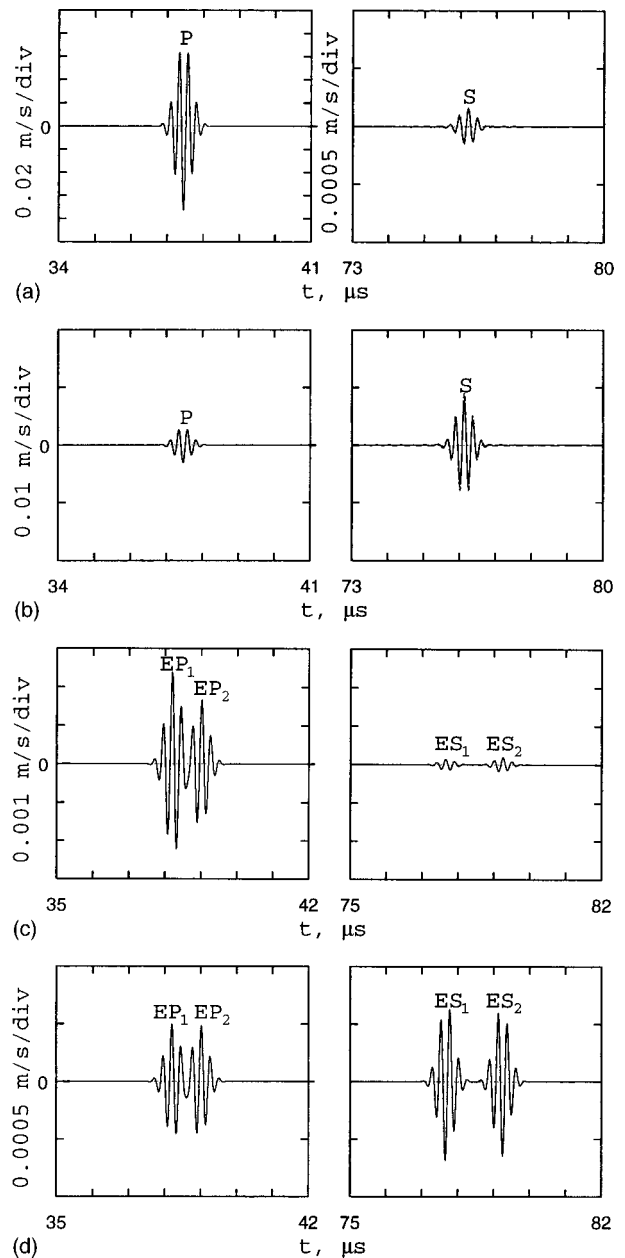


FIG. 9. The intermediate velocity field at $z=240$ mm: (a) the z component at $r=5$ mm; (b) the r component at $r=5$ mm; (c) the z component at $r=60$ mm; and (d) the r component at $r=60$ mm. The key is the same as in Fig. 7.

the main beam, the maximum number of pulses reduces by one and thus, equals six [Fig. 8(b)]. Note that here, the contribution of the head wave (H_1 and H_2) is not entirely negligible, despite the fact that the observation point is relatively far from the transducer.

C. The intermediate velocity field

The train of pulses produced by the narrow-band load in the intermediate zone as calculated by the asymptotic and exact numerical method is presented in Fig. 9. The chosen depth of $z=240$ mm is about three times larger than the size of the near zone l^2/λ , but the agreement is still good. The separation between the P and S pulses is more pronounced than in the near zone. Underneath the transducer (at $r=5$ mm), two pulses are present: the P and S [Fig. 9(a) and

(b)]. Note that the z component of the P field is much larger than that of the S field and r components of both fields. Far off the axis ($r=60$ mm) there are four pulses, the edge P (EP_1 and EP_2) and S (ES_1 and ES_2) arriving from the nearest and farthest edge points [Fig. 9(c) and (d)]. There is no discernible pulse due to the head wave.

III. CONCLUSIONS

A new method for simulating the propagation of pulses radiated by a circular normal transducer which is directly coupled to a homogeneous and isotropic elastic half-space has been proposed. The method is based on the high-frequency asymptotics and the fast Fourier transform. The results are applicable in both the radiating near- and intermediate zone, elucidate the physics, and give explicit dependence on the model parameters. The output of the new code has been fully validated against our own exact numerical results and against approximate and exact numerical solutions reported in the literature. For realistic narrow-band pulses, the asymptotic method is 100 to 1000 times faster, but practically as accurate as the exact. It has also been demonstrated that when the pulses contain low frequencies of small amplitudes, the accuracy is not significantly compromised. In comparison with other approximate models, the new model is more accurate and allows an approximate description of the head wave as well.

The approach of the paper can be extended to other types of load, e.g., to rectangular (Gridin, 1998b) and shear transducers. The asymptotic model can be easily interfaced with other partial models of ultrasonic NDE.

ACKNOWLEDGMENT

The first author gratefully acknowledges a South Bank Research Scholarship.

Achenbach, J. D. (1973). *Wave Propagation in Elastic Solids* (North-Holland, New York).

Babič, V. M., and Buldyrev, V. S. (1991). *Short-wavelength Diffraction Theory: Asymptotic Methods* (Springer-Verlag, Heidelberg).

Babič, V. M., and Kirpichnikova, N. Ya. (1975). *The Boundary-Layer Method in Diffraction Problems* (Springer-Verlag, Berlin).

Baboux, J. C., and Kažys, R. (1992). "Analysis of the transient ultrasonic fields radiated in solids by circular and annular sources," *J. Acoust. Soc. Am.* **92**, 2942–2951.

Bleistein, N., and Handelsman, R. A. (1986). *Asymptotic Expansions of Integrals* (Dover, New York).

Borovikov, V. A. (1994). *Uniform Stationary Phase Method*, IEE Electromagnetic Series, Vol. 40 (IEE, Stevenage).

Borovikov, V. A., and Kinber, B. Ye. (1994). *Geometrical Theory of Diffraction*, IEE Electromagnetic Series, Vol. 37 (IEE, Stevenage).

Bresse, L. F., and Hutchins, D. A. (1989). "Transient generation of elastic waves in solids by a disk-shaped normal force source," *J. Acoust. Soc. Am.* **86**, 810–817.

Buchal, R. N., and Keller, J. B. (1960). "Boundary layer problems in diffraction theory," *Commun. Pure Appl. Math.* **13**, 85–114.

Djelouah, H., and Baboux, J. C. (1992). "Transient ultrasonic field radiated by a circular transducer in a solid medium," *J. Acoust. Soc. Am.* **92**, 2932–2941.

Fedoryuk, M. V. (1977). *The Saddle-Point Method* (Nauka, Moscow).

Fellinger, F., and Langenberg, K. J. (1990). "Numerical techniques for elastic wave propagation and scattering," in *Elastic Waves and Ultrasonic Nondestructive Evaluation*, edited by S. K. Datta, J. D. Achenbach, and Y. S. Rajapakse (Elsevier North-Holland, Amsterdam), pp. 81–86.

Fradkin, L. J., Kiselev, A. P., and Krylova, E. (1998). "The radiating near-field asymptotics of a time-harmonic circular normal ultrasonic transducer in an elastic half-space," *J. Acoust. Soc. Am.* **104**, 1178–1187.

Georgiou, G. A., Blakemore, M., Chapman, R. K., Firth, D. (1989). "The application of the geometrical theory of diffraction to modelling pulsed ultrasonic inspection: a system model," *Br. J. Non-Destr. Test.* **31**(10), 551–561.

Gridin, D. (1998a). "High-frequency asymptotic description of head waves and boundary layers surrounding critical rays in an elastic half-space," *J. Acoust. Soc. Am.* **104**, 1188–1197.

Gridin, D. (1998b). "A fast method for simulating the propagation of pulses radiated by a rectangular normal transducer into an elastic half-space," *J. Acoust. Soc. Am.* **104**, 3199–3211.

Ilan, A., and Weight, J. P. (1990). "The propagation of short pulses of ultrasound from a circular source coupled to an isotropic solid," *J. Acoust. Soc. Am.* **88**, 1142–1151.

Kawashima, K. (1984). "Quantitative calculation and measurement of longitudinal and transverse ultrasonic wave pulses in solid," *IEEE Trans. Sonics Ultrason.* **SU-31**(2), 83–94.

Keller, J. B. (1958). "Geometrical theory of diffraction," in *Proceedings of the Symposium on Applied Mathematics* (McGraw-Hill, New York), Vol. 8, pp. 27–52.

Lamb, H. (1904). "On the propagation of tremors over the surface of an elastic solid," *Philos. Trans. R. Soc. London, Ser. A* **203**, 1–42.

Laturrelle, F. G. (1990). "The stresses produced in an elastic half-space by a normal step loading over a circular area: analytical and numerical results," *Wave Motion* **12**, 107–127.

Lhémery, A. (1994). "A model for the transient ultrasonic field radiated by an arbitrary loading in a solid," *J. Acoust. Soc. Am.* **96**, 3776–3786.

Ludwig, R., and Lord, W. (1988). "A finite-element formulation for the study of ultrasonic NDT system," *IEEE Trans. Ultrason. Ferroelectr. Freq. Control* **35**, 809–820.

Miklowitz, J. (1978). *The Theory of Elastic Waves and Waveguides* (North-Holland, Amsterdam).

Miller, G. F., and Pursey, H. (1954). "The field and radiation impedance of mechanical radiators on the free surface of a semi-infinite isotropic solid," *Proc. R. Soc. London, Ser. A* **223**, 521–541.

McNab, A., Cochran, A., and Campbell, M. A. (1989). "The calculation of acoustic fields in solids for transient normal surface force sources of arbitrary geometry and apodization," *J. Acoust. Soc. Am.* **87**, 1455–1465.

Mitra, M. (1964). "Disturbance produced in an elastic half-space by impulsive normal pressure," *Proc. Cambridge Philos. Soc.* **60**, 683–696.

Schmerr, L. W., and Sedov, A. (1989). "An elastodynamic model for compressional and shear wave transducers," *J. Acoust. Soc. Am.* **86**, 1988–1999.

Silk, M. G. (1984). *Ultrasonic Transducers for Non-destructive Testing* (Adam Hilger, Bristol).

Stepanishen, P. R. (1971). "Transient radiation from pistons in an infinite planar baffle," *J. Acoust. Soc. Am.* **49**, 1629–1638.

Tang, X. M., Zhenya, Z., and Toksöz, M. N. (1994). "Radiation patterns of compressional and shear transducers at the surface of an elastic half-space," *J. Acoust. Soc. Am.* **95**, 71–76.

Weight, J. P. (1987). "A model for the propagation of short pulses of ultrasound in a solid," *J. Acoust. Soc. Am.* **81**, 815–826.

Wong, R. (1989). *Asymptotic Approximations of Integrals* (Academic, New York).

A fast method for simulating the propagation of pulses radiated by a rectangular normal transducer into an elastic half-space

Dmitri Gridin

School of Electrical, Electronic and Information Engineering, South Bank University, 103 Borough Road, London SE1 0AA, United Kingdom

(Received 30 December 1997; accepted for publication 26 August 1998)

A new fast method for simulating the propagation of pulses radiated by a rectangular normal ultrasonic transducer which is directly coupled to an isotropic and homogeneous elastic half-space is proposed. First, the so-called two-tier approach introduced in Fradkin *et al.* [“The radiating near-field asymptotics of a time-harmonic circular normal ultrasonic transducer in an elastic half-space,” *J. Acoust. Soc. Am.* **104**, 1178–1187 (1998)] and the uniform stationary phase method are used to obtain both nonuniform and uniform high-frequency asymptotics of the time-harmonic field. Then, the transient field is described by means of harmonic synthesis. The nonuniform asymptotics elucidate the physics and all the asymptotics give explicit dependence of the radiated waves on model parameters. The formulas are applicable in the radiating near field that is the near field with the evanescent wave zone excluded. The asymptotics involve in geometrical regions elementary and inside boundary layers, well-known special functions (Fresnel integral and generalized Fresnel integral). The code based on the uniform asymptotics has been tested in all regions against an exact numerical solution. It is at least 10^4 times faster but in many realistic cases the accuracy does not suffer. The trains of pulses generated by rectangular and circular transducers are compared. © 1998 Acoustical Society of America. [S0001-4966(98)01612-9]

PACS numbers: 43.20.Bi, 43.20.Dk, 43.35.Zc [DEC]

INTRODUCTION

Simulating the propagation of pulses radiated by ultrasonic transducers into elastic solids is the first step toward mathematical modeling of ultrasonic nondestructive evaluation (NDE) of industrial materials. It precedes modeling reflection from boundaries, scatter by defects, and inclusions and reception of scattered and reflected pulses. Pioneering work in the area of propagation of elastic waves in an isotropic and homogeneous half-space was carried out by Lamb (1904). He studied *point* and *line* loads and was particularly interested in the surface waves. The classical work on *extended* sources acting on the surface of an elastic half-space has been done by Miller and Pursey (1954). They have considered several types of time-harmonic loads: an infinitely long strip of finite width vibrating normally or tangentially and a circular disk vibrating normally or performing rotational oscillations about its center. Their solutions were obtained in the integral form using Fourier and Hankel transforms for a strip and a disk, respectively. The method of steepest descent was applied to evaluate these integrals, giving the far-field asymptotics of the compressional and shear waves for the cases of a line- and pointlike source.

In the past decade the propagation of ultrasonic pulses radiated by large *circular* transducers into elastic solids has been intensively studied by various full numerical schemes (e.g., Ilan and Weight, 1990; Djelouah and Baboux, 1992) and approximate methods (e.g., Weight, 1987; Schmerr and Sedov, 1989; Lhémy, 1994). The full numerical schemes are extremely time consuming and do not produce any explicit dependence of the radiated waves upon the model parameters. The approximate models elucidate the physics of

the problem in terms of the direct compressional and edge compressional and shear waves. However, the Weight's model is phenomenological since he introduces the so-called mode-conversion factors which are estimated from the outputs of finite-difference code. The assumptions made by Lhémy (1994) lead to an overshoot for the edge shear waves for certain observation angles. The model of Schmerr and Sedov (1989) does not give the description of the field inside the penumbra.

Recently, a new method has been developed for simulating the transient field of a circular normal ultrasonic transducer. Fradkin *et al.* (1998) have proposed a two-tier approach to description of the radiating near field of a time-harmonic transducer based on the modern diffraction theory and asymptotic approximations of integrals: First, they obtain the far-field asymptotics of a point source acting on the surface of an elastic half-space (that is, of Green's function); then they integrate these asymptotics over the transducer surface and find the radiating near-field asymptotics of the transducer. Gridin (1998) has complemented their solution by applying the uniform stationary phase method (Borovikov, 1994) to the integral representation of the displacement to obtain both nonuniform and uniform high-frequency asymptotics of the head wave and the field in the vicinity of the critical rays separating regions where the head wave is present from where it is not. It has been shown that the high-frequency asymptotic method combined with the fast Fourier transform is orders of magnitude faster than an exact numerical solution but gives sufficient accuracy (Gridin and Fradkin, 1998). Below it is proposed to use a similar approach for the case of a large *rectangular* normal transducer.

Many researchers have studied the impulse response of a

rectangular transducer radiating into fluids, because such transducers have a wide medical application (e.g., Lockwood and Willette, 1973; Scarano *et al.*, 1985; Emeterio and Ullate, 1992). Less attention has been paid to the fields radiated into elastic solids by rectangular ultrasonic transducers used in industrial NDE. The application of a finite-difference/finite-element scheme to this, three-dimensional, problem results in very long run times, since even the two-dimensional problems are computationally intensive (e.g., Ludwig and Lord, 1988). Thomson and Kobori (1963) have derived the double-integral representation for the displacements caused by a rectangular normal load in an elastic half-space using the Fourier transform technique. They have computed the dynamic compliance at the center of the load. Jones and Petyt (1993) have used the same integral representation and computed the surface displacements along one of the axes of symmetry of the load. Note that in the general case of the observation point inside a solid, the integrand of the double Fourier integral includes a factor rapidly oscillating in both directions of integration. Again, the numerical evaluation of this integral is extremely time consuming. McNab *et al.* (1989) have proposed a numerical approach based on summation of the point load solutions and thus suitable for dealing with sources of any geometry or apodization.

The exact impulse response of an elastic half-space loaded over a rectangular region of its surface has been obtained by Norwood (1969), who has used the Cagniard–de Hoop method. The solutions have been found to be a superposition of plane waves directly under the load and waves emanating from the edges and corners of the loaded region. The expressions for the corner waves have been given in terms of single integrals. Therefore, the evaluation of the transient response for an arbitrary time-dependent load requires double integration.

In this paper a new fast method is proposed for simulating the propagation of pulses radiated by a rectangular normal ultrasonic transducer which is directly coupled to an isotropic and homogeneous elastic half-space. We obtain the high-frequency asymptotics of the radiating near field, and then perform the fast Fourier transform. The paper is organized as follows: First, both nonuniform and uniform high-frequency asymptotics of the field radiated by a time-harmonic rectangular transducer acting normally on the surface of an elastic half-space are derived. Then the outputs of the asymptotic code are compared with the exact numerical results. The propagation of pulses using both the asymptotic and exact methods is studied next. At the end of the paper the comparison between a rectangular and circular transducer is carried out.

I. TIME-HARMONIC RECTANGULAR NORMAL LOAD

A. Formulation of the problem

Let us consider the forced time-harmonic motion of an isotropic and homogeneous elastic half-space caused by a rectangular normal transducer. The displacement field \mathbf{u} inside the medium is described by the reduced elastodynamic equation

$$b^2 \nabla \times (\nabla \times \mathbf{u}) - a^2 \nabla (\nabla \cdot \mathbf{u}) - \omega^2 \mathbf{u} = \mathbf{0}, \quad (1)$$

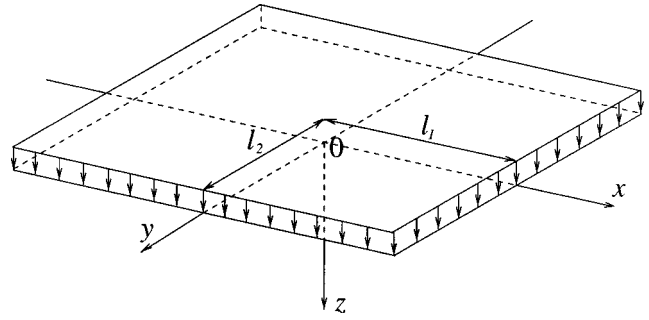


FIG. 1. The geometry of the problem.

where a is a speed of P (also known as longitudinal, compressional, or primary), b , of S (also known as transverse, shear, or secondary) wave; $a > b$; and ω is a circular frequency. The corresponding wave numbers are $k = \omega/a$ and $\kappa = \omega/b$, respectively. The Cartesian coordinates (x, y, z) are used below. The geometry of the problem is depicted in Fig. 1. The boundary conditions specify the pressure applied uniformly over a rectangle with sides $2l_1$ and $2l_2$ in the x and y directions, respectively, and may be written as follows:

$$\begin{aligned} \sigma_{xz}|_{z=0} = \sigma_{yz}|_{z=0} = 0, \\ \sigma_{zz}|_{z=0} = \begin{cases} -Q/4l_1l_2, & |x| \leq l_1, |y| \leq l_2 \\ 0, & \text{elsewhere,} \end{cases} \end{aligned} \quad (2)$$

where Q has dimension of force. There is no necessity to assume Q constant, but we do so for simplicity of presentation. We also assume that the transducer is large, i.e., we have

$$kl_1 \gg 1, \quad kl_2 \gg 1. \quad (3)$$

This means that the half-sides of the transducer are larger than the P wavelength $\lambda = 2\pi/k$.

B. The two-tier approach

It is well-known that the field radiated by a transducer into a solid can be represented as an integral of the corresponding Green's function over the transducer surface. This is the basis of the two-tier approach introduced in Fradkin *et al.* (1998) and used below.

The first tier involves finding the far-field asymptotics of the Green's function of Lamb's problem (i.e., of a point source acting normally on the surface of an isotropic and homogeneous half-space). It is well-known that the Green's function can be decomposed into P and S waves,

$$\mathbf{u}^{(\text{point})} = \mathbf{u}^{P(\text{point})} + \mathbf{u}^{S(\text{point})}. \quad (4)$$

The leading terms of the corresponding far-field asymptotics are given by

$$\mathbf{u}_0^{P(\text{point})} = -\frac{Qk}{2\pi\rho b^2} \frac{A^P(\theta)}{ks} e^{iks} \mathbf{n}^P(\theta), \quad (5)$$

and

$$\mathbf{u}_0^{S(\text{point})} = -\frac{Q\kappa}{2\pi\rho b^2} \frac{A^S(\theta)}{\kappa s} e^{i\kappa s} \mathbf{n}^S(\theta) \quad (6)$$

(e.g., Miller and Pursey, 1954; Fradkin *et al.*, 1998) with

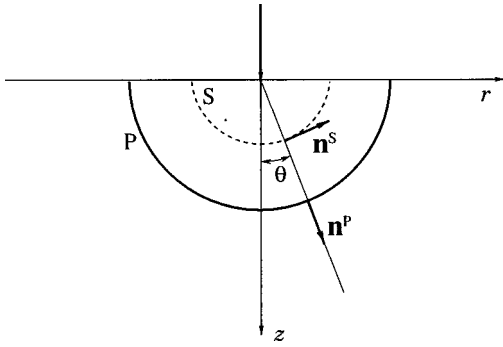


FIG. 2. Point source acting normally on an elastic half-space (head waves neglected).

$$s = \sqrt{r^2 + z^2}, \quad \sin \theta = r/s, \quad (7)$$

(see Fig. 2). Here ϱ is the density of the solid and the respective directivity functions $A^P(\theta)$ and $A^S(\theta)$ are as follows:

$$A^P(\theta) = \frac{2 \sin^2 \theta - \gamma^{-2}}{R^P(\sin \theta)} \cos \theta, \quad (8)$$

and

$$A^S(\theta) = \frac{2 \sin \theta \sqrt{\gamma^2 - \sin^2 \theta}}{R^S(\sin \theta)} \cos \theta, \quad (9)$$

with the Rayleigh functions

$$R^P(\xi) = (2\xi^2 - \gamma^{-2})^2 + 4\xi^2 \sqrt{1 - \xi^2} \sqrt{\gamma^{-2} - \xi^2}, \quad (10)$$

and

$$R^S(\xi) = (2\xi^2 - 1)^2 - 4\xi^2 \sqrt{\xi^2 - 1} \sqrt{\xi^2 - \gamma^2}, \quad (11)$$

and $\gamma = b/a$. The unit displacement vectors are given by

$$\mathbf{n}^P(\theta) = \sin \theta \mathbf{e}_r + \cos \theta \mathbf{e}_z, \quad (12)$$

and

$$\mathbf{n}^S(\theta) = \cos \theta \mathbf{e}_r - \sin \theta \mathbf{e}_z \quad (13)$$

(see Fig. 2).

The second tier involves integrating the above asymptotics over the transducer surface, so that the field can be represented as an integral of the far-field asymptotics of the Green's function over the transducer surface:

$$\mathbf{u} = \frac{1}{4l_1 l_2} \int_{-l_1}^{l_1} \int_{-l_2}^{l_2} \mathbf{u}^{(\text{point})} dx' dy'. \quad (14)$$

Then the radiating near-field asymptotics of this integral are evaluated. The form of $\mathbf{u}^{(\text{point})}$ allows us to carry out this evaluation for the P and S fields separately.

C. The high-frequency asymptotics of the P field

The P field is described by the integral

$$\mathbf{u}^P = -\frac{p_0}{2\pi\varrho b^2} \int_{-l_1}^{l_1} \int_{-l_2}^{l_2} \frac{A^P(\theta')}{s'} \mathbf{n}^P(\theta') e^{iks'} dx' dy', \quad (15)$$

where $(x', y', 0)$ and (x, y, z) are the coordinates of the point source and the observation point, respectively, and the dis-

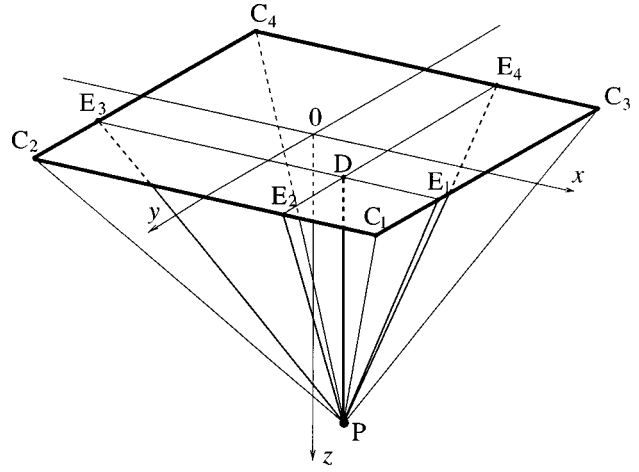


FIG. 3. Points of the transducer surface where different waves originate: D—the direct P , E_1 , E_2 , E_3 , and E_4 —edge and C_1 , C_2 , C_3 , and C_4 —corner waves. P is the observation point.

tance s' between them and the corresponding angle θ' are given by

$$s' = \sqrt{(x' - x)^2 + (y' - y)^2 + z^2}, \quad \cos \theta' = z/s'. \quad (16)$$

The pressure acting on the surface is $p_0 = Q/4l_1 l_2$.

The integrand in (15) contains a slowly varying amplitude and a rapidly oscillating exponential factor. It is well known that the main contributions to integrals of this type come from stationary points of phase functions, various types of critical boundary points, and singular points of amplitude functions (Blestein and Handelsman, 1986; Borovikov, 1994). The critical boundary points are: critical points on smooth parts of boundary where the derivative of the phase function along the boundary vanishes, and points of the boundary where its analyticity is violated, for instance, corner points.

The amplitude function in the integrand in (15) contains no singular points. Its phase function s' has one stationary point,

$$(x', y') = (x, y), \quad |x| \leq l_1, \quad |y| \leq l_2, \quad (17)$$

where it is at a minimum (point D in Fig. 3). There are four edge critical points (E_1 , E_2 , E_3 , and E_4 in Fig. 3), and four corner points (C_1 , C_2 , C_3 , and C_4 in Fig. 3). Each type of critical point gives rise to a different type of wave.

Below, we assume $x \geq 0$ and $y \geq 0$ because the other cases can be obtained from this using the considerations of symmetry. Thus some final expressions are presented only for the contribution of the edge point E_1 and corner point C_1 .

1. Geometrical regions

The geometrical regions are regions which may be efficiently modeled by using the concept of a ray. The field inside such regions may be represented in the form of a finite number of waves each described by *ray series*, that is, the asymptotic series in inverse powers of dimensionless wave number k :

$$\mathbf{u}(k, \mathbf{s}) = e^{ik\varphi(\mathbf{s})} \sum_{n=0}^{\infty} \frac{A_n(\mathbf{s})}{(ik)^{n+\nu}} \quad (18)$$

(e.g., Babich and Buldyrev, 1991) where the eikonal (or phase function) $\varphi(\mathbf{s})$ and amplitude functions $A_n(\mathbf{s})$ all depend on the coordinates of the observation point only, and ν is a different constant for different waves.

The contribution of the isolated stationary point to integral (15) gives the *direct P* wave, and for the leading term of the corresponding ray series we obtain

$$\begin{aligned} \mathbf{u}^{P(D)} &= \frac{P_0}{\rho a^2 k} e^{i(kz + \pi/2)} H(l_1 - x) H(l_2 - y) \mathbf{e}_z \\ &= H(l_1 - x) H(l_2 - y) \mathbf{u}_0^{P(D)}, \end{aligned} \quad (19)$$

where H is the Heaviside step function. In the above equation and everywhere below the superscript in brackets denotes the critical points which give rise to the corresponding wave. The direct *P* wave is plane, exists only straight underneath the transducer, and propagates without decay. It is easy to show that for a transducer of infinite extent which exerts the same pressure as our transducer the above solution is exact.

The contribution of each of the edge critical points gives rise to the *edge P* wave and for the leading term of the corresponding ray series for the edge point E_1 we obtain

$$\begin{aligned} \mathbf{u}^{P(E_1)} &= \frac{P_0}{\sqrt{2\pi\rho b^2 k}} A^P(\theta_1) \sqrt{\frac{d_1}{k(l_1 - x)^2}} e^{i(kd_1 + 3\pi/4)} \\ &\quad \times H(l_2 - y) \mathbf{n}^{P(E_1)} = H(l_2 - y) \mathbf{u}_0^{P(E_1)}, \end{aligned} \quad (20)$$

where the unit displacement vector $\mathbf{n}^{P(E_1)}$, the distance d_1 (E_1P in Fig. 3) between the point E_1 , and the observation point P and the corresponding angle are given by

$$\begin{aligned} \mathbf{n}^{P(E_1)} &= -\sin \theta_1 \mathbf{e}_x + \text{sgn}(l_1 - x) \cos \theta_1 \mathbf{e}_z, \\ d_1 &= \sqrt{(l_1 - x)^2 + z^2}, \quad \sin \theta_1 = \frac{|l_1 - x|}{d_1}. \end{aligned} \quad (21)$$

The edge *P* waves from points E_1 and E_3 exist only for $|y| \leq l_2$ and have no y components, and those from points E_2 and E_4 exist only for $|x| \leq l_1$ and have no x components. The edge *P* waves are cylindrical with the corresponding edges acting as the line sources.

The contribution of each of the corner points gives rise to the *corner P* wave, and for the leading term of the corresponding ray series for the corner point C_1 we obtain

$$\mathbf{u}^{P(C_1)} = \frac{P_0}{2\pi\rho b^2 k} A^P(\varphi_1) \frac{s_1}{k(l_1 - x)(l_2 - y)} e^{iks_1} \mathbf{n}^{P(C_1)}, \quad (22)$$

where the unit displacement vector $\mathbf{n}^{P(C_1)}$, the distance s_1 (C_1P in Fig. 3) between the point C_1 and the observation point P , and the corresponding angle are given by

$$\begin{aligned} \mathbf{n}^{P(C_1)} &= -\frac{l_1 - x}{s_1} \mathbf{e}_x - \frac{l_2 - y}{s_1} \mathbf{e}_y + \frac{z}{s_1} \mathbf{e}_z, \\ s_1 &= \sqrt{(l_1 - x)^2 + (l_2 - y)^2 + z^2}, \quad \cos \varphi_1 = z/s_1. \end{aligned} \quad (23)$$

The corner *P* waves are spherical with the corresponding corner points acting as the point sources. We have utilized formulas (4.5), (4.10), and (4.12) from Borovikov (1994)

when deriving Eqs. (19), (20), and (22), respectively.

Note that there are three distinct zones for the *P* field of a rectangular normal transducer:

$$\text{Zone I: } |x| < l_1, \quad |y| < l_2;$$

$$\text{Zone II: } |x| > l_1, \quad |y| < l_2, \quad \text{and } |x| < l_1, \quad |y| > l_2;$$

$$\text{Zone III: } |x| > l_1, \quad |y| > l_2. \quad (24)$$

In zone I the direct, four edge, and four corner *P* waves exist. In zone II there are two edge and four corner waves. Finally, in zone III only four corner *P* waves are present.

2. Boundary layers

The representation of the total *P* field as a sum of the direct, edge, and corner waves is not applicable inside the so-called *boundary layers* (e.g., Buchal and Keller, 1960; Babich and Kirpichnikova, 1975). These are transition regions surrounding lines or surfaces of irregularity along which rays of different nature meet. The fields inside boundary layers are described in terms of asymptotic series involving special functions rather than just inverse powers of dimensionless frequency. The size and shape of a boundary layer are determined by the condition that the phase difference between different rays is small (usually smaller than π). For a rectangular transducer these regions occur as $x \rightarrow l_1$ or $y \rightarrow l_2$. Below, we consider the boundary layers for the edge and corner *P* waves from the points E_1 and C_1 , respectively.

The first type of a penumbral boundary layer occurs as $x \rightarrow l_1$, i.e., when the phase difference between the direct and edge *P* wave tends to zero. Under this condition expression (19) has a discontinuity and expression (20) tends to infinity. Mathematically, this situation corresponds to the case of coalescing stationary and edge critical points (Borovikov, 1994, Sec. 4.2.4). The leading term of the asymptotics which are applicable in this, *edge*, penumbral region involves the Fresnel integral

$$F(\xi) = \frac{e^{-i\pi/4}}{\sqrt{\pi}} \int_{-\infty}^{\xi} e^{is^2} ds \quad (25)$$

[*ibid.*, Eq. (6.1a)] and therefore we obtain

$$\mathbf{u}_0^{P(DE_1)} = F[\text{sgn}(l_1 - x) \sqrt{k(d_1 - z)}] H(l_2 - y) \mathbf{u}_0^{P(D)}, \quad (26)$$

which differs from (19) only by substituting the Fresnel integral F for $H(l_1 - x)$. The shape of the edge penumbral layer is determined by the condition that the phase difference between the direct and edge waves is π , that is,

$$k(d_1 - z) = \pi. \quad (27)$$

Therefore, it is a parabolic cylinder [Fig. 4(a)].

Another type of a penumbral boundary layer occurs as $y \rightarrow l_2$, i.e., when the phase difference between the edge wave from the point E_1 and the corner wave from the point C_1 tends to zero. Under this condition expression (20) has a discontinuity and expression (22) tends to infinity. Mathematically, this situation corresponds to the case of coalescing edge critical and corner points (Borovikov, 1994, Sec.

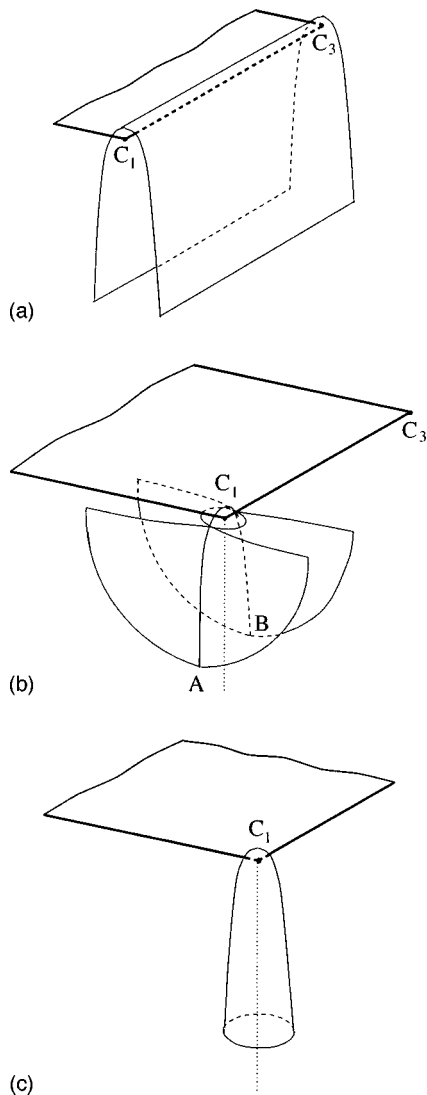


FIG. 4. Boundary layers underneath a rectangular transducer: (a) edge penumbra; (b) corner penumbra; and (c) edge-corner penumbra.

4.2.2). The leading term of the asymptotics which are applicable in this, *corner*, penumbral region also involves the Fresnel integral:

$$\mathbf{u}_0^{P(E_1C_1)} = F[\operatorname{sgn}(l_2 - y)\sqrt{k(s_1 - d_1)}]\mathbf{u}_0^{P(E_1)}, \quad (28)$$

which differs from (20) only by substituting the Fresnel integral F for $H(l_2 - y)$. The shape of the corner penumbral layer is determined by the condition that the phase difference between the edge and corner waves is π , that is,

$$k(s_1 - d_1) = \pi. \quad (29)$$

Therefore, it is a surface obtained by revolving parabola AC_1B around the edge C_1C_3 [Fig. 4(b)].

The most interesting situation occurs when $x \rightarrow l_1$ and $y \rightarrow l_2$ simultaneously, i.e., when the phase difference between the direct P and corner P wave from the point C_1 tends to zero. Under this condition expression (26) has a discontinuity and expression (28) tends to infinity. Mathematically, this situation corresponds to the case of coalescing stationary and corner points (Borovikov, 1994, Sec. 4.4). The leading

term of the asymptotics which are applicable in this, *edge-corner*, penumbral region is expressed in terms of the generalized Fresnel integral

$$G(\eta, \nu) = \frac{\nu}{2\pi} \int_{\eta}^{\infty} \frac{e^{i(\xi^2 + \nu^2)}}{\xi^2 + \nu^2} d\xi \quad (30)$$

[*ibid.*, Eq. (6.35); see also Clemmow and Senior, 1953] and therefore we obtain

$$\begin{aligned} \mathbf{u}_0^{P(DE_1E_2C_1)} = \mathbf{u}_0^{P(D)} \{ & H(l_1 - x)H(l_2 - y) \\ & - G[-\operatorname{sgn}(l_2 - y)\sqrt{k(s_1 - d_1)}, \\ & \operatorname{sgn}(l_1 - x)\sqrt{k(d_1 - z)}] \\ & - G[-\operatorname{sgn}(l_1 - x)\sqrt{k(s_1 - d_2)}, \\ & \operatorname{sgn}(l_2 - y)\sqrt{k(d_2 - z)}] \}. \end{aligned} \quad (31)$$

Note that although each term in the right-hand side of (31) is discontinuous, the left-hand side is regular since the discontinuities of $H(l_1 - x)H(l_2 - y)$ are compensated by the discontinuities of the generalized Fresnel integrals. The shape of the edge-corner penumbral layer is determined by the condition that the phase difference between the direct and corner waves is π , that is,

$$k(s_1 - z) = \pi. \quad (32)$$

Therefore, it is a paraboloid of revolution [Fig. 4(c)]. All boundary layers are the narrower the higher the frequency.

3. Uniform asymptotics

The nonuniform asymptotics elucidate the physics of the problem by producing the description of the field structure in terms of geometrical regions and boundary layers inbetween. To avoid transition from a boundary layer to a geometrical region it is often advisable to use *uniform* asymptotics, that is, asymptotics which are applicable both inside and outside the layer (Bleistein and Handelsman, 1986; Borovikov, 1994).

The leading term of the uniform asymptotics which are applicable both inside and outside the edge penumbral layer is

$$\begin{aligned} \mathbf{u}^{P(DE_1)} = \mathbf{u}_0^{P(DE_1)} + u_x^{P(E_1)} \mathbf{e}_x \\ + \frac{A_1}{k^{3/2}} H(l_2 - y) e^{ikd_1} \mathbf{e}_z. \end{aligned} \quad (33)$$

The leading term of the uniform asymptotics which are applicable both inside and outside the corner penumbral layer turns out to be

$$\begin{aligned} \mathbf{u}^{P(E_1C_1)} = \mathbf{u}_0^{P(E_1C_1)} + \frac{B_1}{k^2} e^{iks_1} \left\{ -\frac{l_1 - x}{s_1} \mathbf{e}_x + \frac{z}{s_1} \mathbf{e}_z \right\} \\ + u_y^{P(C_1)} \mathbf{e}_y. \end{aligned} \quad (34)$$

Note that it is more correct to call the asymptotics (33) and (34) *locally uniform* because Eq. (33) is not applicable as $y \rightarrow l_2$ and Eq. (34), as $x \rightarrow l_1$. In both cases the uniform asymptotics which are applicable both inside and outside the

edge-corner penumbral layer can be used and for their leading term we have

$$\begin{aligned} \mathbf{u}^{P(DE_1E_2C_1)} = & \mathbf{u}_0^{P(DE_1E_2C_1)} + u_x^{P(E_1C_1)} \mathbf{e}_x + u_y^{P(E_2C_1)} \mathbf{e}_y \\ & + \left\{ \frac{A_1}{k^{3/2}} e^{ikd_1} F[\operatorname{sgn}(l_2 - y) \sqrt{k(s_1 - d_1)}] \right. \\ & + \frac{A_2}{k^{3/2}} e^{ikd_2} F[\operatorname{sgn}(l_1 - x) \sqrt{k(s_1 - d_2)}] \\ & \left. + \frac{D_1}{k^2} e^{iks_1} \right\} \mathbf{e}_z. \end{aligned} \quad (35)$$

The coefficients A_1 , A_2 , B_1 , and D_1 are obtained by matching the uniform asymptotics to the nonuniform: (33) to (19) and (20), (34) to (20) and (22), and (35) to (19), (20) and (22). They are given in Appendix A.

Finally, the leading term of the uniform asymptotics of the total P field in the region $x \geq 0$ and $y \geq 0$ may be written as follows:

$$\mathbf{u}^{P(\text{total})} = \mathbf{u}^{P(DE_1E_2C_1)} + \mathbf{u}^{P(E_3C_2)} + \mathbf{u}^{P(E_4C_3)} + \mathbf{u}^{P(C_4)}. \quad (36)$$

The first term in the last expression includes the contributions of the stationary point of the phase function, edge points E_1 and E_2 , and corner point C_1 . The second includes the contributions of the edge point E_3 and corner point C_2 . The third is similar to the second with the edge point E_4 and corner point C_3 . The contribution of the corner point C_4 is given by the last term. Thus Eq. (36) describes all the P waves radiated by a rectangular transducer.

D. The high-frequency asymptotics of the S field

The S field is described by the integral

$$\mathbf{u}^S = -\frac{p_0}{2\pi Q b^2} \int_{-l_1}^{l_1} \int_{-l_2}^{l_2} \frac{A^S(\theta')}{s'} \mathbf{n}^S(\theta') e^{iks'} dx' dy', \quad (37)$$

which possesses the same critical points as the integral in (15). However, due to the directivity A^S of a point source [Eq. (9)] the leading term of the contribution of the stationary point is zero:

$$\mathbf{u}^{S(D)} = 0. \quad (38)$$

As with the direct P wave, it is easy to show that for a transducer of infinite extent the above solution is exact.

The leading terms of the asymptotics of the edge and corner S wave are similar to the P wave. They are

$$\begin{aligned} \mathbf{u}^{S(E_1)} &= \frac{p_0}{\sqrt{2\pi Q b^2 \kappa}} A^S(\theta_1) \sqrt{\frac{d_1}{\kappa(l_1 - x)^2}} \\ &\quad \times e^{i(\kappa d_1 + 3\pi/4)} H(l_2 - y) \mathbf{n}^{S(E_1)} \\ &= \mathbf{u}_0^{S(E_1)} H(l_2 - y), \end{aligned} \quad (39)$$

and

$$\mathbf{u}^{S(C_1)} = \frac{p_0}{2\pi Q b^2 \kappa} A^S(\varphi_1) \frac{s_1}{\kappa(l_1 - x)(l_2 - y)} e^{iks_1} \mathbf{n}^{S(C_1)}, \quad (40)$$

respectively, with the unit displacement vectors given by

$$\mathbf{n}^{S(E_1)} = -\cos \theta_1 \mathbf{e}_x - \operatorname{sgn}(l_1 - x) \sin \theta_1 \mathbf{e}_z, \quad (41)$$

and

$$\begin{aligned} \mathbf{n}^{S(C_1)} &= -\frac{z}{s_1} \frac{l_1 - x}{\sqrt{s_1^2 - z^2}} \mathbf{e}_x - \frac{z}{s_1} \frac{l_2 - y}{\sqrt{s_1^2 - z^2}} \mathbf{e}_y \\ &\quad - \frac{\sqrt{s_1^2 - z^2}}{s_1} \mathbf{e}_z. \end{aligned} \quad (42)$$

There is no edge penumbral layer for the S field, since there is no direct S wave. The corner penumbral layer for the S field is described by the expressions similar to those for the P field. For the leading term of the corresponding uniform asymptotics we obtain

$$\begin{aligned} \mathbf{u}^{S(E_1C_1)} &= \mathbf{u}_0^{S(E_1)} F[\operatorname{sgn}(l_2 - y) \sqrt{\kappa(s_1 - d_1)}] \\ &\quad + \frac{1}{\kappa^2} e^{iks_1} \{ \tilde{B}_{1x} \mathbf{e}_x + \tilde{B}_{1z} \mathbf{e}_z \} + u_y^{S(C_1)} \mathbf{e}_y. \end{aligned} \quad (43)$$

Since there is no direct S wave the leading term of the edge-corner penumbral asymptotics of the S field is simpler than that of the P : It contains no term with the generalized Fresnel integral and therefore we have

$$\begin{aligned} \mathbf{u}^{S(E_1E_2C_1)} &= u_x^{S(E_1C_1)} \mathbf{e}_x + u_y^{S(E_2C_1)} \mathbf{e}_y \\ &\quad + \left\{ F[\operatorname{sgn}(l_2 - y) \sqrt{\kappa(s_1 - d_1)}] u_z^{S(\text{edge})_1} \right. \\ &\quad + F[\operatorname{sgn}(l_1 - x) \sqrt{\kappa(s_1 - d_2)}] u_z^{S(\text{edge})_2} \\ &\quad \left. + \frac{\tilde{D}_1}{\kappa^2} e^{iks_1} \right\} \mathbf{e}_z. \end{aligned} \quad (44)$$

The coefficients \tilde{B}_{1x} , \tilde{B}_{1z} , and \tilde{D}_1 are obtained by matching the uniform asymptotics (43) and (44) to the nonuniform asymptotics (39) and (40) and are given in Appendix A. The leading term of the uniform asymptotics of the total S field in the region $x \geq 0$ and $y \geq 0$ can be constructed similarly to the total P field [Eq. (36)].

The above solution for the S field is not complete: It does not include the head wave or description of the field in the vicinity of the critical rays. It may be expected that there are four edge and four corner head waves. For a circular normal transducer the high-frequency asymptotics of the head waves and the total S field in the vicinity of the critical rays have been obtained by Gridin (1998). A similar technique can be applied to a rectangular transducer but the corresponding derivation for the corner waves is more cumbersome. However, the numerical calculations described below have shown that the contribution of head waves is small if discernible at all. Therefore, these waves have been neglected.

E. The exact numerical solution

The asymptotic formulas obtained in the previous subsection have been tested against an exact numerical solution. The latter is obtained by computing the displacements represented in the following integral form:

$$\begin{aligned} (u_x, u_y, u_z) = & \frac{P_0}{\pi^2 Q b^2} \int_{-\infty}^{+\infty} \int_{-\infty}^{+\infty} (-i\xi, -i\eta, \alpha) \\ & \times \{ [2(\xi^2 + \eta^2) - \kappa^2] e^{-\alpha z} \\ & - 2(\alpha\beta, \alpha\beta, \xi^2 + \eta^2) e^{-\beta z} \} \\ & \times \frac{\sin \xi l_1 \sin \eta l_2}{\xi \eta R} e^{i(\xi x + \eta y)} d\xi d\eta. \quad (45) \end{aligned}$$

This representation, based on the double Fourier transform, has been reported previously by Thomson and Kobori (1963), but because the relative signs of the x , y , and z components in their solution [*ibid.*, Eq. (16)] differ from ours, and for completeness, Eq. (45) is rederived in Appendix B. Note that the derivation has been carried out by Jones and Petyt (1993) as well, but their final expression [*ibid.*, Eq. (51)] contains a misprint.

The integrands in (45) include factors rapidly oscillating in both the ξ and η direction. Therefore, the numerical evaluation of the double integrals in (45) is extremely time consuming, even when special algorithms for computing such integrals are employed. The exact numerical code utilized below is based on one such algorithm in the form of the NAG subroutine D01AKF.

F. The limits of applicability and numerical results

All of the above asymptotics are applicable in the radiating near field of a rectangular transducer, i.e., for

$$kz \gg 1, \quad \frac{z}{kl^2} \ll 1, \quad (46)$$

where $l = \min(l_1, l_2)$. Numerical experiments have confirmed more precise limits as

$$\lambda \leq z \leq \frac{l^2}{\lambda}, \quad (47)$$

where λ is the wavelength of the P wave. For a typical frequency 5 MHz and the transducer half-sides 10 mm, this region extends in steels from about 1 mm to about 80 mm. Analogously to the case of a circular transducer (Gridin and Fradkin, 1998) it is expected that the asymptotic formulae give reasonable agreement with an exact numerical solution at distances several times larger than the size of the radiating near zone. This is sufficient for most applications of interest. In the far field the above asymptotics may be replaced by standard far-field formulas for a rectangular source which involve expressions of the type $\{\sin(kl_1x)/kl_1x\} \times \{\sin(kl_2y)/kl_2y\}$ (e.g., Skudrzyk, 1971, Sec. 26.9).

The asymptotic formulas have been validated in all geometrical regions and boundary layers against the exact numerical solution described above. Some of the validation results are presented below. The model parameters are as

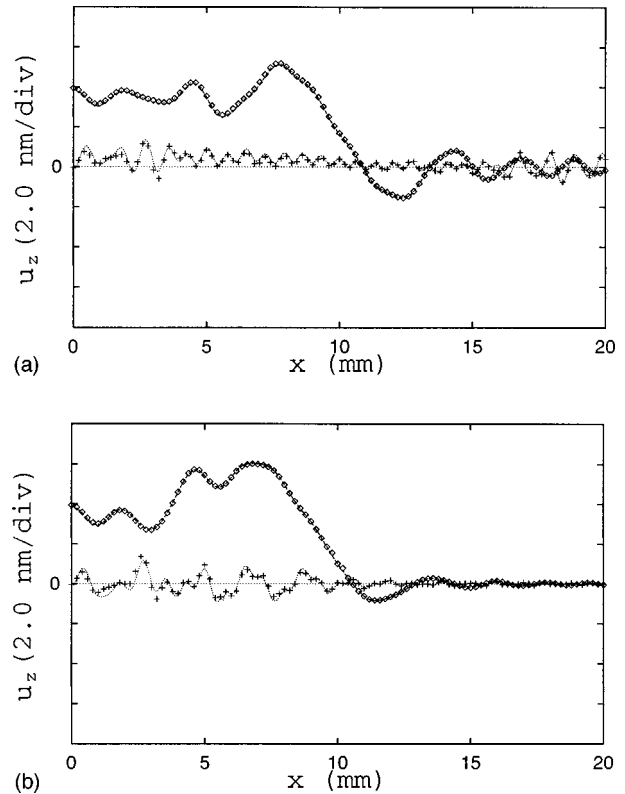


FIG. 5. The displacement field at depth $z=10$ mm and various x : (a) z component in the plane $y=0$; (b) z component in the plane $y=x/2$. Dashed line and boxes represent the exact and asymptotic P field, respectively; dotted line and crosses represent the exact and asymptotic S field, respectively.

follows: $a=6400$ m/s, $b=3150$ m/s, $\rho=2700$ kg/m³, $Q=500$ N, $l_1=10$ mm, $l_2=5$ mm, and $f=5$ MHz.

Figure 5(a) depicts the x dependence of the z components of the displacements, respectively, at depth $z=10$ mm in the plane $y=0$. It can be seen that the z component of the P field is dominant inside the main beam of the transducer, i.e., inside zone I. This component in zone II and the z component of the S field are much smaller. For the P field the agreement between the asymptotic and exact solution is very good. For the S field this agreement is slightly worse due to the fact that the contribution of the head waves has been neglected.

Figure 5(b) depicts the x dependence of the z components of the displacements, respectively, at depth $z=10$ mm in the plane $y=x/2$. This is the plane passing through the z -axis and corner C_1 . Again, inside the main beam the z component of the P field is dominant. Outside the main beam all components of the field are smaller than inside. This is so because in the plane $y=x/2$ all the points for which $x>10$ mm lie inside zone III where only the corner waves are present.

II. PROPAGATION OF PULSES

The asymptotic expressions for the radiating near field of a time-harmonic rectangular normal transducer which have been derived in the previous section can be used to model the propagation of pulses by means of harmonic syn-

thesis, that is, the inverse Fourier transform with respect to time. The displacement $U(t)$ at the moment t is given by

$$U(t) = \text{Re} \frac{1}{\pi} \int_0^\infty \mathbf{u}(\omega) q(\omega) e^{-i\omega t} d\omega, \quad (48)$$

where $\mathbf{u}(\omega)$ is the time-harmonic displacement considered above, and $q(\omega)$ is the Fourier transform of the load $Q(t)$. Below, we consider the particle velocity $\mathbf{V}(t)$, that is, the first derivative of the displacement with respect to time, since this is the quantity which is measured by the receiving probes (e.g., Weight, 1987).

In computations described below the same parameters have been used as in the previous section. The wide-band pulse containing not only high but some intermediate and low frequencies has been considered. It has been chosen to be one cycle of $\sin(2\pi ft)$ of frequency $f=5$ MHz, and consequently, the duration of $0.2 \mu\text{s}$. Similarly to the previous section, we compare the asymptotic solution with the exact numerical solution both combined with the fast Fourier transform. In the asymptotic method the bandwidth is taken to be 0.5–10 MHz, and in the exact, it is extended down to 0 MHz.

A. The velocity field inside the main beam

First, let us consider the case of the observation point lying inside the main beam of the transducer (zone I). The waveform of the z component of the particle velocity at the z -axis point $(0, 0, 10)$ mm is shown in Fig. 6(a). The first pulse is due to the direct P wave (DP). This pulse is dominant. The next pulse is due to the edge P waves arriving from the edge points E_2 and E_4 (EP_{24}). The third pulse is due to the edge P waves arriving from the edge points E_1 and E_3 (EP_{13}) partially overlapped with the corner waves from all four corner points (CP_{1234}). The edge S waves arriving from the edge points E_2 and E_4 give rise to the fourth pulse (ES_{24}). The fifth pulse is due to the combined contribution of the edge S and head waves from the edge points E_1 and E_3 ($ES_{13}+EH_{13}$). The corner S waves from all four corner points give rise to the last, quite small, pulse in the train (CS_{1234}). It can be seen that the pulses of S waves travel twice as long as the corresponding pulses of P waves since the S speed is about half the P speed. Figure 6(a) shows that the agreement between the asymptotic and exact method is very good. The small discrepancy in the fifth pulse is due to the head waves being neglected in the asymptotic method. Due to symmetry the x - and y -components of the field are equal to zero at the observation point $(0, 0, 10)$ mm.

The waveform of the z component of the particle velocity at the point $(5, 0, 10)$ mm is shown in Fig. 6(b). The amplitude of the first, direct P , pulse is the same as in Fig. 6(a), since the pressure is assumed to be uniform over the transducer surface. The distances from the observation point to the edge points E_1 , E_2 , and E_4 are equal, and therefore, the edge waves arriving from these points overlap giving rise to the second, P , and fourth, S , pulses (EP_{124} and ES_{124}). The corner P waves arriving from the points C_1 and C_3 also contribute to the second pulse (CP_{13}). The third pulse is due to the edge P wave from the point E_3 and corner P waves from the points C_2 and C_4 (EP_3+CP_{24}). The corner S and head

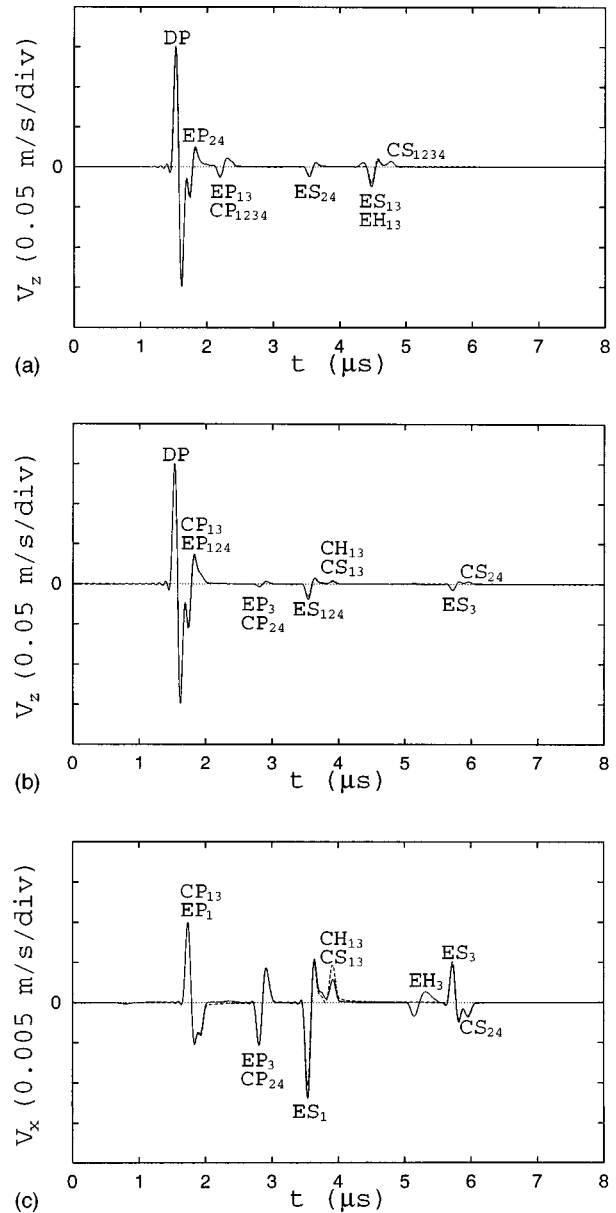


FIG. 6. The waveform of the particle velocity inside the main beam: (a) z component at point $(0, 0, 10)$ mm; (b) z component at point $(5, 0, 10)$ mm; (c) x component at point $(5, 0, 10)$ mm. Solid and dashed lines are the exact and asymptotic solutions, respectively. DP —the direct P wave, EP_i , ES_i , or EH_i —the edge P , S , or head wave from the point E_i , and CP_i , CS_i , or CH_i —the corner P , S , or head wave from the point C_i .

waves from the points C_1 and C_3 give rise to the fifth pulse. Finally, the sixth and seventh pulses are due to the edge S wave from the point E_3 and corner S waves from the points C_2 and C_4 respectively (ES_3 and CS_{24}). The waveform of the x component of the particle velocity at the same observation point is presented in Fig. 6(c). There is no direct P pulse. All other pulses are similar to the z component. The edge head pulse arriving from the point E_3 (EH_3) is more pronounced since a finer scaling is used in Fig. 6(c).

B. The velocity field straight underneath the transducer rim

First, let us consider the case of the observation point lying straight underneath the center of the transducer rim.

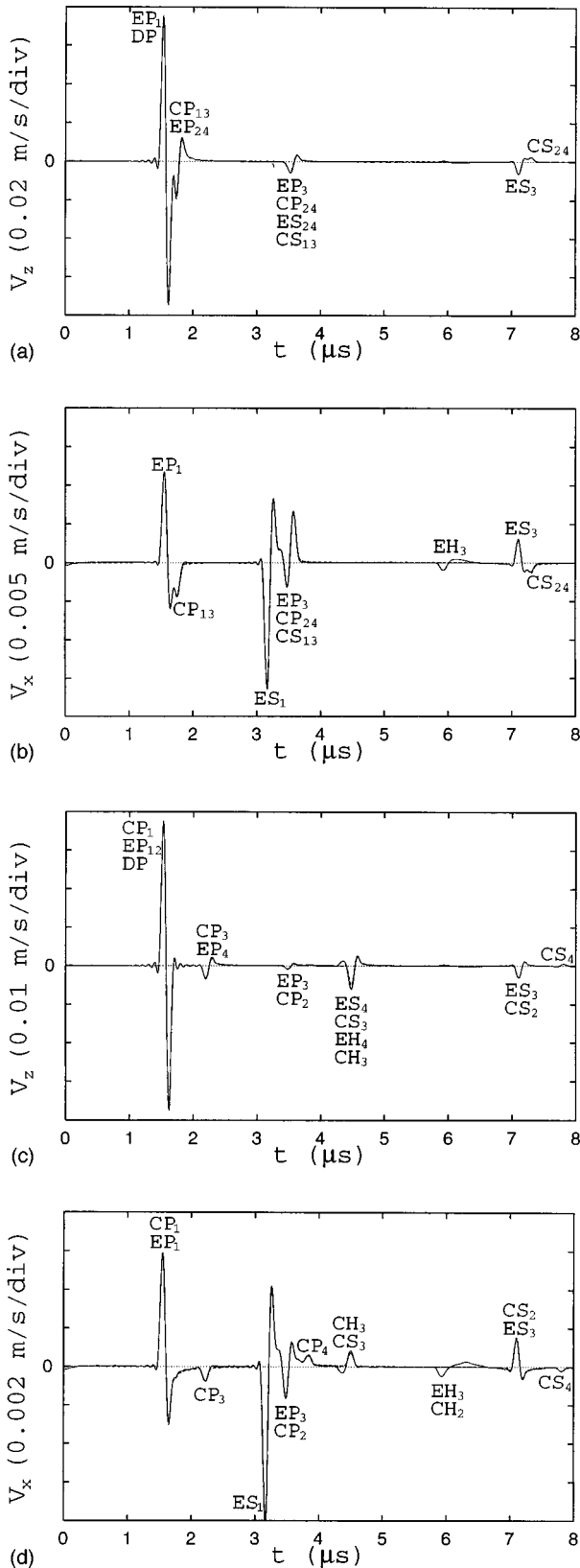


FIG. 7. The waveform of the particle velocity straight underneath the transducer rim: (a) z component at point (10, 0, 10) mm; (b) x component at point (10, 0, 10) mm; (c) z -component at point (10, 5, 10) mm; (d) x component at point (10, 5, 10) mm. The key as in Fig. 6.

The waveform of the z component of the particle velocity at the point (10, 0, 10) mm is shown in Fig. 7(a). The first pulse is due to the combined contribution of the direct P and edge P wave from the point E_1 ($DP+EP_1$). The amplitude of this

pulse is half the amplitude of the direct P pulse. This can be easily seen from (26), which implies

$$u_z^{P(DE_1)}|_{(x=l_1)} = u_0^{P(D)}F(0) = u_0^{P(D)}/2. \quad (49)$$

The waveform of the x component of the particle velocity at the same point is shown in Fig. 7(b). The first pulse in the train is due only to the edge P wave from the point E_1 . It follows that the P wave from the point E_1 has a transverse component (which is significantly smaller than the longitudinal component). This justifies our calling this wave P rather than longitudinal (see also Fradkin and Kiselev, 1997). The second pulse is due to the corner P wave from the points C_1 and C_3 and confirms that these waves have the transverse components as well (CP_{13}). There is no pulse due to the edge wave from the point E_2 or E_4 , since these waves have no x component. The third pulse is due to the edge S wave from the point E_1 which has x but no z component. All other pulses are similar to those in Fig. 7(a).

Another interesting situation occurs when the observation point lies straight underneath the transducer corner. The waveform of the z component of the particle velocity at the point (10, 5, 10) mm is shown in Fig. 7(c). In this case the first pulse is due to the combined contribution of the direct P wave, edge and corner P wave from the point C_1 ($DP+EP_{12}+CP_1$). The amplitude of this pulse is one-fourth the amplitude of the direct P pulse. This can be seen from (31) which implies

$$u_z^{P(DE_1E_2C_1)}|_{(x=l_1, y=l_2)} = u_0^{P(D)}/4. \quad (50)$$

The waveform of the x component of the particle velocity at the same point is shown in Fig. 7(d). The first pulse in the train is due only to the edge and corner P wave from the point C_1 . As above, it follows that this wave has a transverse component. The second pulse is due to the transverse component of the corner P wave from the point C_3 (CP_3). As in the previous case there is no pulse due to the edge wave from E_2 or E_4 but that due to the edge S wave from E_1 is present. Note that the head waves in Fig. 7(b) and (d) are more pronounced because of a finer scale.

C. The velocity field outside the main beam

There are two distinct regions outside the main beam of the transducer: Zone II where two edge P , two edge S , and four corner waves of each type are present, and zone III where only the corner waves exist. The representative pulse trains are shown in Fig. 8.

Figure 8(a) depicts the waveform of the z component of the particle velocity at the zone II point (15, 0, 10) mm. It contains pulses due to the edge P and S waves from the point E_1 and E_3 and due to the corner waves from all corner points. The amplitude of the largest, EP_1 , pulse is about ten times smaller than the amplitude of the direct P pulse.

Figure 8(b) depicts the waveform of the z -component of the particle velocity at the zone III point (15, 10, 10) mm. Eight pulses due to the corner P and S waves are discernible. Some pulses due to the corner head waves are also present.

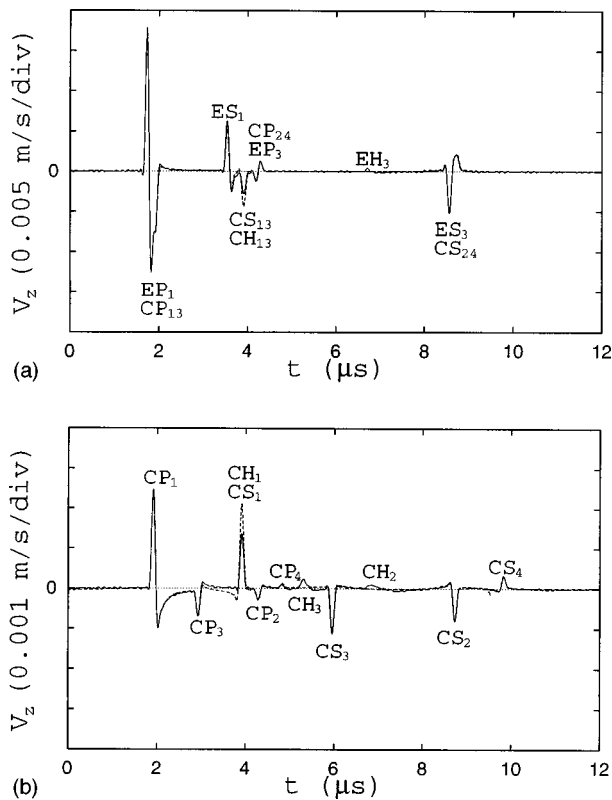


FIG. 8. The waveform of the particle velocity outside the main beam: (a) z component at point (15, 0, 10) mm (zone II); (b) z component at point (15, 10, 10) mm (zone III). The key as in Fig. 6.

The amplitude of the largest, CP_1 , pulse is about 60 times smaller than the amplitude of the direct P pulse.

Figures 6–8 confirm that the agreement between the asymptotic and exact method is very good even for realistic wide-band pulses containing some low and intermediate frequencies. The small differences are due to the head waves being neglected in our analysis. The asymptotic method is at least 10^4 times faster than the exact. Moreover, the high-frequency asymptotics elucidate the physics of the problem describing the field in terms of the direct P , edge and corner P and S waves, and produce an explicit dependence of these waves upon the problem parameters. It has been found that the edge waves are several times smaller than the direct P wave and the corner waves are smaller still. This fact is reflected in the nonuniform asymptotics of the previous section: The asymptotics of the edge waves [Eqs. (20) and (39)] are of a higher order than those of the direct P wave [Eq. (19)], and the asymptotics of the corner waves [Eqs. (22) and (40)] are of higher order still.

III. COMPARISON BETWEEN A RECTANGULAR AND CIRCULAR TRANSDUCER

The structure of the elastic field radiated by a rectangular transducer is quite different to that of a circular one. As shown in the previous section, the field inside the main beam of a rectangular transducer consists of the direct P , four edge P , four corner P , four edge S , and four corner S waves. The edge waves are much smaller than the direct P wave, and corner waves are even smaller. The field inside the main

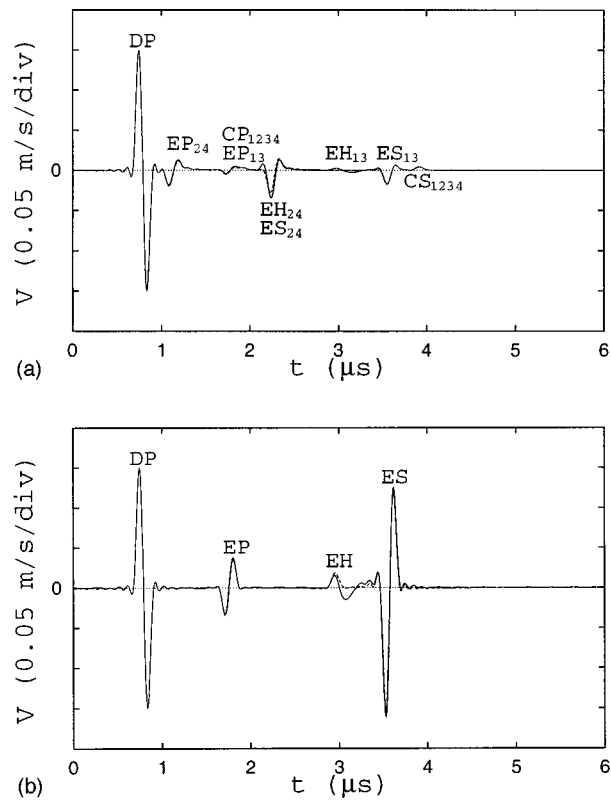


FIG. 9. The waveform of the particle velocity at the z axis of a rectangular (a) and circular (b) transducer. The key as in Fig. 6.

beam of a circular transducer consists of the direct P , toroidal edge P , and S waves (e.g., Weight, 1987). For every observation point lying inside the geometrical regions there are two arrivals of the edge wave of each type, one from the nearest and the other from the farthest edge point. The edge waves are much smaller than the direct P wave but along the transducer axis the focusing of these waves takes place. This leads to a significant increase of their amplitude. The amplitude of the edge S wave on the axis can be even larger than that of the direct P wave [e.g., McNab *et al.*, 1989, Fig. 5(c); also Fig. 9(b) below]. A rectangular transducer has no axial symmetry and therefore no such focusing takes place.

The situation is illustrated in Fig. 9 where we compare the elastic fields of rectangular and circular transducers at the axial point $z = 5$ mm. The parameters for a rectangular transducer have been specified above. The radius of a circular transducer is 10 mm, but the amplitude of the applied load Q has been chosen in such a way that the amplitudes of the direct P waves in both cases are the same. The rectangular transducer radiates a maximum number of pulses [Fig. 9(a)]. In the case of a circular transducer there are no corner pulses, but all edge pulses are comparable with that of the direct P wave due to the focusing of the edge waves along the axis [Fig. 9(b)].

Outside the main beam of a rectangular transducer there is no direct P wave and the structure of the field is different inside zones II and III: Inside zone II there are two edge P , four corner P , two edge S , and four corner S waves, while inside zone III only four corner P and four corner S waves are present. The structure of the field outside the main beam of a circular transducer is simpler: Only the edge P and S

waves exist. Thus the field of a rectangular transducer exhibits an angular dependence which is absent in a circular one.

On the whole the waveforms produced by a rectangular load are rather complex because they may contain up to seventeen pulses (not counting the head waves) many of which overlap. However, the direct P pulse when present always dominates. Therefore, the rectangular transducer is practically a plane wave only (PWO) transducer. With a circular load the maximum pulse number is five but the edge waves near the axis may be of the order of the direct P wave. For this reason, this type of transducer can be used to provide additional information.

IV. CONCLUSIONS

A new fast method for simulating the propagation of pulses radiated by a rectangular normal transducer, which is directly coupled to an isotropic and homogeneous solid, has been proposed. The method is based on the high-frequency asymptotics and the fast Fourier transform. It has been shown that in the geometrical regions the total field consists of the direct P and edge and corner P and S waves. The edge waves are several times smaller than the direct P wave. The corner waves are smaller still, but only they are present inside certain zones. The solution has been extended into the penumbral boundary layers, and the uniform asymptotics of the total field have been obtained. The formulas are applicable in the radiating near field, elucidate the physics, and give explicit dependence on the model parameters. The new code based on the uniform asymptotics has been validated in all regions against the exact numerical solution. It is at least 10^4 times faster than the exact numerical code but gives high accuracy even for the commonly used wide-band pulses when those contain low frequencies of only small amplitudes.

The asymptotic model can be easily interfaced with other partial models of ultrasonic nondestructive evaluation. It can be extended to deal with other types of transducers, e.g., shear or apodized.

ACKNOWLEDGMENTS

The author gratefully acknowledges a South Bank Research Scholarship. He would like to thank Dr. L. J. Fradkin for the careful reading of the manuscript and useful discussions.

APPENDIX A: THE COEFFICIENTS IN THE UNIFORM ASYMPTOTICS

Coefficients A_1 , A_2 , B_1 , \tilde{B}_{1x} , \tilde{B}_{1z} , D_1 , and \tilde{D}_1 of the uniform asymptotics (33), (34), (35), (43), and (44) are as follows:

$$A_1 = \frac{P_0}{\sqrt{2\pi\varrho a^2}} e^{i3\pi/4} \times \left\{ \gamma^{-2} \frac{A^P(\theta_1)z}{(l_1-x)\sqrt{d_1}} + \operatorname{sgn}(l_1-x) \frac{1}{\sqrt{2(d_1-z)}} \right\}, \quad (\text{A1})$$

$$A_2 = \frac{P_0}{\sqrt{2\pi\varrho a^2}} e^{i3\pi/4} \times \left\{ \gamma^{-2} \frac{A^P(\theta_2)z}{(l_2-y)\sqrt{d_2}} + \operatorname{sgn}(l_2-y) \frac{1}{\sqrt{2(d_2-z)}} \right\}, \quad (\text{A2})$$

$$B_1 = \frac{p_0}{2\pi\varrho b^2} \frac{s_1}{l_1-x} \left\{ \frac{A^P(\varphi_1)}{l_2-y} - \operatorname{sgn}(l_2-y) \frac{A^P(\theta_1)}{\sqrt{2d_1(s_1-d_1)}} \right\}, \quad (\text{A3})$$

$$\tilde{B}_{1x} = -\frac{p_0}{2\pi\varrho b^2} \left\{ \frac{A^S(\varphi_1)z}{\sqrt{s_1^2-z^2}(l_2-y)} - \operatorname{sgn}(l_2-y) \times \frac{A^S(\theta_1)z}{|l_1-x|\sqrt{2d_1(s_1-d_1)}} \right\}, \quad (\text{A4})$$

$$\tilde{B}_{1z} = -\frac{p_0}{2\pi\varrho b^2} \times \left\{ \frac{A^S(\varphi_1)\sqrt{s_1^2-z^2}}{(l_1-x)(l_2-y)} - \operatorname{sgn}(l_2-y) \frac{A^S(\theta_1)}{\sqrt{2d_1(s_1-d_1)}} \right\}, \quad (\text{A5})$$

$$D_1 = \frac{p_0}{2\pi\varrho b^2} \left\{ \frac{A^P(\varphi_1)z}{(l_1-x)(l_2-y)} + \operatorname{sgn}[(l_1-x)(l_2-y)] \times \frac{\gamma^2}{2(s_1-z)} \left(\sqrt{\frac{d_1-z}{s_1-d_1}} + \sqrt{\frac{d_2-z}{s_1-d_2}} \right) + \frac{e^{i\pi/4}}{2\sqrt{\pi}} \left(\operatorname{sgn}(l_2-y) \frac{A_1}{\sqrt{s_1-d_1}} + \operatorname{sgn}(l_1-x) \frac{A_2}{\sqrt{s_1-d_2}} \right) \right\}, \quad (\text{A6})$$

$$\tilde{D}_1 = -\frac{p_0}{2\pi\varrho b^2} \left\{ \frac{A^S(\varphi_1)\sqrt{s_1^2-z^2}}{(l_1-x)(l_2-y)} - \operatorname{sgn}[(l_1-x)(l_2-y)] \times \left(\frac{A^S(\theta_1)}{\sqrt{2d_1(s_1-d_1)}} + \frac{A^S(\theta_2)}{\sqrt{2d_2(s_1-d_2)}} \right) \right\}. \quad (\text{A7})$$

APPENDIX B: THE INTEGRAL REPRESENTATION OF THE DISPLACEMENTS CAUSED BY A RECTANGULAR NORMAL TRANSDUCER IN A SOLID

Let us consider the forced time-harmonic motion of an elastic homogeneous and isotropic half-space caused by a rectangular normal transducer. We seek a solution of Eq. (1) which satisfies the usual radiation condition and the boundary conditions (2).

Introducing the elastic potentials ϕ and ψ the displacement can be decomposed in the usual manner,

$$\mathbf{u} = \nabla\phi + \nabla \times \psi, \quad (\text{B1})$$

where we assume

$$\nabla\psi = 0. \quad (\text{B2})$$

In view of Eq. (1) both potentials satisfy the Helmholtz equations:

$$\frac{\partial^2 \phi}{\partial x^2} + \frac{\partial^2 \phi}{\partial y^2} + \frac{\partial^2 \phi}{\partial z^2} + k^2 \phi = 0, \quad (\text{B3})$$

and

$$\frac{\partial^2 \psi_i}{\partial x^2} + \frac{\partial^2 \psi_i}{\partial y^2} + \frac{\partial^2 \psi_i}{\partial z^2} + \kappa^2 \psi_i = 0. \quad (\text{B4})$$

In terms of the potentials the stress tensor components are

$$\begin{aligned} \sigma_{xz} &= \mu \left(2 \frac{\partial^2 \phi}{\partial z \partial x} + \frac{\partial^2 \psi_y}{\partial x^2} - \frac{\partial^2 \psi_x}{\partial x \partial y} + \frac{\partial^2 \psi_z}{\partial z \partial y} - \frac{\partial^2 \psi_y}{\partial z^2} \right), \\ \sigma_{yz} &= \mu \left(2 \frac{\partial^2 \phi}{\partial z \partial y} - \frac{\partial^2 \psi_x}{\partial y^2} + \frac{\partial^2 \psi_y}{\partial x \partial y} - \frac{\partial^2 \psi_z}{\partial z \partial x} + \frac{\partial^2 \psi_x}{\partial z^2} \right), \\ \sigma_{zz} &= \lambda \left(\frac{\partial^2 \phi}{\partial x^2} + \frac{\partial^2 \phi}{\partial y^2} + \frac{\partial^2 \phi}{\partial z^2} \right) \\ &\quad + 2\mu \left(\frac{\partial^2 \phi}{\partial z^2} + \frac{\partial^2 \psi_y}{\partial x \partial z} - \frac{\partial^2 \psi_x}{\partial y \partial z} \right). \end{aligned} \quad (\text{B5})$$

We define the direct and inverse double Fourier transform such that we have, respectively,

$$\begin{aligned} \bar{\phi} &= \int_{-\infty}^{+\infty} \int_{-\infty}^{+\infty} \phi e^{-i(\xi x + \eta y)} dx dy, \\ \phi &= \frac{1}{4\pi^2} \int_{-\infty}^{+\infty} \int_{-\infty}^{+\infty} \bar{\phi} e^{i(\xi x + \eta y)} d\xi d\eta. \end{aligned} \quad (\text{B6})$$

We apply the double Fourier transform to (B3) and (B4) and obtain for the transformed potentials $\bar{\phi}$ and $\bar{\psi}_i$ the following ordinary differential equations:

$$\begin{aligned} \frac{d^2 \bar{\phi}}{dz^2} - (\xi^2 + \eta^2 - k^2) \bar{\phi} &= 0, \\ \frac{d^2 \bar{\psi}_i}{dz^2} - (\xi^2 + \eta^2 - \kappa^2) \bar{\psi}_i &= 0. \end{aligned} \quad (\text{B7})$$

The solutions which satisfy the radiation condition are

$$\bar{\phi} = A(\xi, \eta) e^{-\alpha z}, \quad \bar{\psi}_i = B_i(\xi, \eta) e^{-\beta z}, \quad (\text{B8})$$

where

$$\alpha = (\xi^2 + \eta^2 - k^2)^{1/2}, \quad \beta = (\xi^2 + \eta^2 - \kappa^2)^{1/2}. \quad (\text{B9})$$

Applying the double Fourier transform to (B2) we obtain the condition

$$i\xi \bar{\psi}_x + i\eta \bar{\psi}_y + \frac{d\bar{\psi}_z}{dz} = 0. \quad (\text{B10})$$

The relevant transformed displacement components can be expressed as

$$\begin{aligned} \bar{u}_x &= i\xi \bar{\phi} + i\eta \bar{\psi}_z - \frac{d\bar{\psi}_y}{dz}, \\ \bar{u}_y &= i\eta \bar{\phi} - i\xi \bar{\psi}_z + \frac{d\bar{\psi}_x}{dz}, \\ \bar{u}_z &= \frac{d\bar{\phi}}{dz} + i\xi \bar{\psi}_y - i\eta \bar{\psi}_x. \end{aligned} \quad (\text{B11})$$

The transformed stress components are

$$\begin{aligned} \bar{\sigma}_{xz} &= \mu \left(2i\xi \frac{d\bar{\phi}}{dz} - \xi^2 \bar{\psi}_y + \xi\eta \bar{\psi}_x + i\eta \frac{d\bar{\psi}_z}{dz} - \frac{d^2 \bar{\psi}_y}{dz^2} \right), \\ \bar{\sigma}_{yz} &= \mu \left(2i\eta \frac{d\bar{\phi}}{dz} + \eta^2 \bar{\psi}_x - \xi\eta \bar{\psi}_y - i\xi \frac{d\bar{\psi}_z}{dz} + \frac{d^2 \bar{\psi}_x}{dz^2} \right), \\ \bar{\sigma}_{zz} &= \lambda \left(-\xi^2 \bar{\phi} - \eta^2 \bar{\phi} + \frac{d^2 \bar{\phi}}{dz^2} \right) \\ &\quad + 2\mu \left(\frac{d^2 \bar{\phi}}{dz^2} + i\xi \frac{d\bar{\psi}_y}{dz} - i\eta \frac{d\bar{\psi}_x}{dz} \right). \end{aligned} \quad (\text{B12})$$

The transformed boundary conditions take the form

$$\begin{aligned} \bar{\sigma}_{xz} = \bar{\sigma}_{yz} &= 0, \\ \bar{\sigma}_{zz} &= -\frac{Q}{4l_1 l_2} \int_{-\infty}^{+\infty} H(l_2 - |y|) e^{-i\eta y} dy \\ &\quad \times \int_{-\infty}^{+\infty} H(l_1 - |x|) e^{-i\xi x} dx, \\ &= -\frac{Q}{l_1 l_2} \frac{\sin \xi l_1}{\xi} \frac{\sin \eta l_2}{\eta}. \end{aligned} \quad (\text{B13})$$

Substituting (B8) and (B13) into (B12), and using (B10), we obtain the following system of simultaneous equations:

$$\begin{aligned} (2(\xi^2 + \eta^2) - \kappa^2)A + 2i\eta\beta B_1 - 2i\xi\beta B_2 \\ = -\frac{Q}{\rho b^2 l_1 l_2} \frac{\sin \xi l_1}{\xi} \frac{\sin \eta l_2}{\eta}, \\ -2i\xi\alpha A + \xi\eta B_1 - (\xi^2 + \beta^2)B_2 - i\eta\beta B_3 = 0, \\ -2i\eta\alpha A + (\xi^2 + \beta^2)B_1 - \xi\eta B_2 + i\xi\beta B_3 = 0, \\ i\xi B_1 + i\eta B_2 - \beta B_3 = 0. \end{aligned} \quad (\text{B14})$$

Solving it, the transformed potentials are

$$\begin{aligned} \bar{\phi} &= -\frac{Q}{\rho b^2 l_1 l_2} \frac{\sin \xi l_1}{\xi} \frac{\sin \eta l_2}{\eta} \frac{2(\xi^2 + \eta^2) - \kappa^2}{R(\xi, \eta)} e^{-\alpha z}, \\ \bar{\psi}_x &= -\frac{Q}{\rho b^2 l_1 l_2} \frac{\sin \xi l_1}{\xi} \frac{\sin \eta l_2}{\eta} \frac{2i\eta\alpha}{R(\xi, \eta)} e^{-\beta z}, \\ \bar{\psi}_y &= -\frac{Q}{\rho b^2 l_1 l_2} \frac{\sin \xi l_1}{\xi} \frac{\sin \eta l_2}{\eta} \frac{(-2i)\xi\alpha}{R(\xi, \eta)} e^{-\beta z}, \\ \bar{\psi}_z &= 0, \end{aligned} \quad (\text{B15})$$

where Rayleigh's function R is

$$R(\xi, \eta) = (2(\xi^2 + \eta^2) - \kappa^2)^2 - 4(\xi^2 + \eta^2)\alpha\beta. \quad (\text{B16})$$

Note that the geometry of the problem makes the last equation in (B15) obvious. Substituting (B15) into (B11) and taking the inverse double Fourier transform, we obtain the integral representation of displacements (45).

- Babič V. M., and Buldyrev, V. S. (1991). *Short-Wavelength Diffraction Theory: Asymptotic Methods* (Springer-Verlag, Heidelberg).
- Babič, V. M., and Kirpichnikova N. Ya. (1975). *The Boundary-Layer Method in Diffraction Problems* (Springer-Verlag, Berlin).
- Bleistein, N., and Handelman, R. A. (1986). *Asymptotic Expansions of Integrals* (Dover, New York).
- Borovikov, V. A. (1994). *Uniform Stationary Phase Method* (IEE Electromagnetic Series, Vol. 40, London).
- Buchal, R. N., and Keller, J. B. (1960). "Boundary layer problems in diffraction theory," *Commun. Pure Appl. Math.* **13**, 85–114.
- Clemmow, P. C., and Senior, T. B. A. (1953). "A note on a generalized Fresnel integral," *Proc. Cambridge Philos. Soc.* **49**, 570–572.
- Djelouah, H., and Baboux, J. C. (1992). "Transient ultrasonic field radiated by a circular transducer in a solid medium," *J. Acoust. Soc. Am.* **92**, 2932–2941.
- Emeterio, J. L. S., and Ullate, L. G. (1992). "Diffraction impulse response of rectangular transducers," *J. Acoust. Soc. Am.* **92**, 651–662.
- Fradkin, L. J., and Kiselev, A. P. (1997). "The two-component representation of time-harmonic elastic body waves in the high and intermediate frequency regime," *J. Acoust. Soc. Am.* **101**, 52–65.
- Fradkin, L. J., Kiselev, A. P., and Krylova, E. (1998). "The radiating near-field asymptotics of a time-harmonic circular normal ultrasonic transducer in an elastic half-space," *J. Acoust. Soc. Am.* **104**, 1178–1187.
- Gridin, D. (1998). "High-frequency asymptotic description of head waves and boundary layers surrounding the critical rays in an elastic half-space," *J. Acoust. Soc. Am.* **104**, 1188–1197.
- Gridin, D., and Fradkin, L. J. (1998). "High-frequency asymptotic description of pulses radiated by a circular normal transducer into an elastic half-space," *J. Acoust. Soc. Am.* **104**, 3190–3198.
- Ilan, A., and Weight, J. P. (1990). "The propagation of short pulses of ultrasound from a circular source coupled to an isotropic solid," *J. Acoust. Soc. Am.* **88**, 1142–1151.
- Jones, D. V., and Petyt, M. (1993). "Ground vibration in the vicinity of a rectangular load on a half-space," *J. Sound Vib.* **166**, 141–159.
- Lamb, H. (1904). "On the propagation of tremors over the surface of an elastic solid," *Philos. Trans. R. Soc. London, Ser. A* **203**, 1–42.
- Lhémery, A. (1994). "A model for the transient ultrasonic field radiated by an arbitrary loading in a solid," *J. Acoust. Soc. Am.* **96**, 735–741.
- Lockwood, J. C., and Willete, J. G. (1973). "High-speed method for computing the exact solution for the pressure variations in the nearfield of a baffled piston," *J. Acoust. Soc. Am.* **53**, 3776–3786.
- Ludwig, R., and Lord, W. (1988). "A finite-element formulation for the study of ultrasonic NDT system," *IEEE Trans. Ultrason. Ferroelectr. Freq. Control* **35**, 809–820.
- McNab, A., Cochran, A., and Campbell, M. A. (1989). "The calculation of acoustic fields in solids for transient normal surface force sources of arbitrary geometry and apodization," *J. Acoust. Soc. Am.* **87**, 1455–1465.
- Miller, G. F., and Pursey, H. (1954). "The field and radiation impedance of mechanical radiators on the free surface of a semi-infinite isotropic solid," *Proc. R. Soc. London, Ser. A* **223**, 521–541.
- Norwood, F. R. (1969). "Exact transient response of an elastic half space loaded over a rectangular region of its surface," *J. Appl. Mech.* **36**, 516–522.
- Scarano, G., Denisenko, N., Matteucci, M., and Pappalardo, M. (1985). "A new approach to the derivation of the impulse response of a rectangular piston," *J. Acoust. Soc. Am.* **78**, 1109–1113.
- Schmerr, L. W., and Sedov, A. (1989). "An elastodynamic model for compressional and shear wave transducers," *J. Acoust. Soc. Am.* **86**, 1988–1999.
- Skudrzyk, E. (1971). *The Foundations of Acoustics* (Springer-Verlag, Wien).
- Thomson, W. T., and Kobori, T. (1963). "Dynamic compliance of rectangular foundations on an elastic half-space," *J. Appl. Mech.* **30**, 579–584.
- Weight, J. P. (1987). "A model for the propagation of short pulses of ultrasound in a solid," *J. Acoust. Soc. Am.* **81**, 815–826.

The method of fundamental solutions for axisymmetric acoustic scattering and radiation problems

Andreas Karageorghis

Department of Mathematics and Statistics, University of Cyprus, P.O. Box 537, 1678 Nicosia, Cyprus

Graeme Fairweather^{a)}

Department of Mathematical and Computer Sciences, Colorado School of Mines, Golden, Colorado 80401

(Received 16 February 1998; accepted for publication 19 August 1998)

The method of fundamental solutions (MFS) is applied to acoustic scattering and radiation for axisymmetric bodies and boundary conditions. The fundamental solution of the governing equation and its normal derivative, which are required in the formulation of the MFS, can be expressed in terms of complete elliptic integrals, which are evaluated using library software. The method is tested on several problems from the literature and the results compared with existing solutions. Numerical experiments demonstrate that the fictitious eigenfrequency problem which is encountered with the boundary element method is not present in the MFS. © 1998 Acoustical Society of America. [S0001-4966(98)00212-4]

PACS numbers: 43.20.Bi, 43.20.Fn, 43.20.Rz, 43.20.Tb [DEC]

INTRODUCTION

The method of fundamental solutions (MFS) is a boundary method applicable to elliptic boundary value problems in which a fundamental solution of the governing differential equation is known. It shares many of the features of the boundary element method (BEM) and its advantages over domain discretization methods for certain problems. Further, it has certain advantages over the BEM, the most important of which is its adaptivity.

In the MFS, the idea is to approximate the solution of the problem by a linear combination of fundamental solutions expressed in terms of sources located outside the domain of the problem. The coefficients of the fundamental solutions and the coordinates of the sources are determined by satisfying the boundary conditions in a least squares sense. The basic principles of the MFS were introduced by Kupradze and Aleksidze¹ and the method has since been applied to a variety of problems in potential theory,² fluid dynamics,³ and elasticity.⁴ A comprehensive survey of the MFS and related methods is given in Ref. 5.

The BEM has been used successfully for the solution of acoustic scattering and radiation for axisymmetric bodies and boundary conditions.⁶ Like the BEM, the MFS is well suited for the solution of exterior problems such as problems in acoustics. In Refs. 7–10, non-axisymmetric acoustic problems were solved using the MFS. Recently, the MFS was used for the solution of axisymmetric potential problems.¹¹ In the present paper, we investigate the application of the MFS to acoustic scattering and radiation for axisymmetric bodies and boundary conditions. These problems are governed by the Helmholtz equation. The fundamental solution of the axisymmetric form of this equation and its first derivative, which are required in the formulation of the MFS, can be expressed in terms of complete elliptic integrals. These integrals can be evaluated using library software.¹²

In Sec. I, we describe the formulation of the MFS for the solution of the axisymmetric version of the Helmholtz equation. In Sec. II, we apply the MFS to several problems in acoustic scattering and radiation. The application of the MFS to acoustic scattering and radiation problems in a half-space is discussed in Sec. III. Finally, conclusions of this study are given in Sec. IV.

I. AXISYMMETRIC MFS FORMULATION FOR THE HELMHOLTZ EQUATION

Consider the Helmholtz equation

$$\Delta \phi(P) + k^2 \phi(P) = 0, \quad P \in \Omega', \quad (1)$$

subject to the boundary conditions

$$Bu(P) = f(P), \quad P \in \partial\Omega', \quad (2)$$

where k is the wave number and Ω' is an unbounded domain in R^3 with boundary $\partial\Omega'$, which we assume to be piecewise smooth, and the operator B specifies the boundary conditions.

Suppose that the region $\Omega' \in R^3$ is axisymmetric, that is, formed as the exterior of a figure of revolution by rotating a plane region Ω with boundary $\partial\Omega$ about the z axis. If $P = (r_P, z_P)$ and $Q = (r_Q, z_Q)$ are two points in Ω a distance $R(P, Q)$ apart, then

$$R^2(P, Q) = r_Q^2 + r_P^2 - 2r_Q r_P \cos \theta + (z_Q - z_P)^2, \quad (3)$$

and the fundamental solution of the axisymmetric version of the Helmholtz equation is given by

$$G(P, Q) = \int_0^{2\pi} \frac{e^{-ikR(P, Q)}}{R(P, Q)} d\theta(Q). \quad (4)$$

Now

$$G(P, Q) = G_1(P, Q) + G_2(P, Q), \quad (5)$$

where

^{a)}Electronic mail: gfairwea@mines.edu

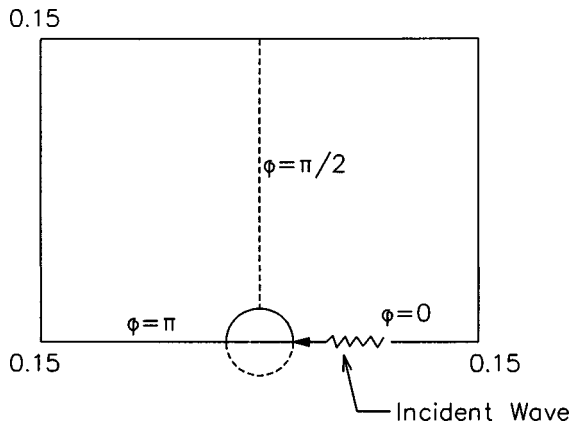


FIG. 1. Geometry of example 1.

$$G_1(P,Q) = \int_0^{2\pi} \frac{e^{-ikR(P,Q)} - 1}{R(P,Q)} d\theta(Q) \quad (6)$$

and

$$G_2(P,Q) = \int_0^{2\pi} \frac{1}{R(P,Q)} d\theta(Q). \quad (7)$$

For a given P , the integral $G_1(P,Q)$ can be evaluated numerically using a standard quadrature rule since its integrand is nonsingular. It can be shown^{13,14} that

$$G_2(P,Q) = \frac{4K(\kappa)}{\mathcal{R}}, \quad (8)$$

where $K(\kappa)$ is the complete elliptic integral of the first kind defined by

$$K(\kappa) = \int_0^{\pi/2} [1 - \kappa^2 \sin^2 \theta(Q)]^{-1/2} d\theta(Q), \quad (9)$$

with

$$\kappa^2 = \frac{4r_Q r_P^2}{\mathcal{R}} \quad (10)$$

and

$$\mathcal{R}^2 = (r_Q + r_P)^2 + (z_Q - z_P)^2. \quad (11)$$

The normal derivative of the fundamental solution is

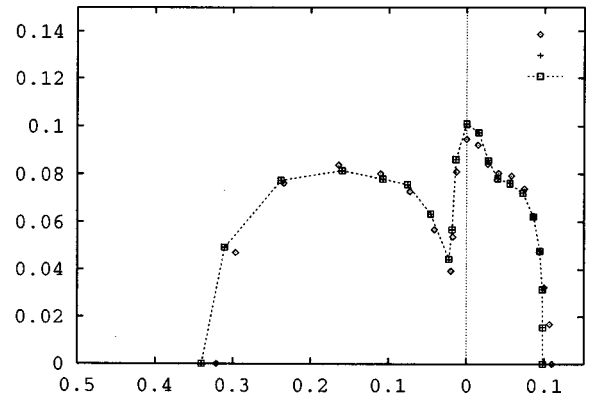


FIG. 3. Example 1, $ka=4$, NFEV=2000, \diamond : $M=35, N=5$; $+$: $M=55, N=7$; \square : $M=65, N=9$.

$$\begin{aligned} \frac{\partial G(P,Q)}{\partial n_Q} &= \int_0^{2\pi} \frac{\partial}{\partial n_Q} \left(\frac{e^{-ikR(P,Q)}}{R(P,Q)} \right) d\theta(Q) \\ &\equiv L_1(P,Q) + L_2(P,Q), \end{aligned} \quad (12)$$

where

$$L_1(P,Q) = \int_0^{2\pi} \frac{\partial}{\partial n_Q} \left(\frac{e^{-ikR(P,Q)} - 1}{R(P,Q)} \right) d\theta(Q), \quad (13)$$

which, for a given P , can be evaluated using standard quadrature, and

$$L_2(P,Q) = \int_0^{2\pi} \frac{\partial}{\partial n_Q} \left(\frac{1}{R(P,Q)} \right) d\theta(Q). \quad (14)$$

From (8), it follows that

$$\begin{aligned} L_2(P,Q) &= \frac{\partial}{\partial n_Q} \left(\frac{4K(\kappa)}{\mathcal{R}} \right) \\ &= \frac{2\{\mathcal{R}^2[E(\kappa) - K(\kappa)(1 - \kappa^2)] - 2r_Q(r_Q + r_P)E(\kappa)\}}{r_Q \mathcal{R}^3(1 - \kappa^2)} \\ &\quad \times n_r - \frac{4(z_Q - z_P)E(\kappa)}{\mathcal{R}^3(1 - \kappa^2)} n_z, \end{aligned} \quad (15)$$

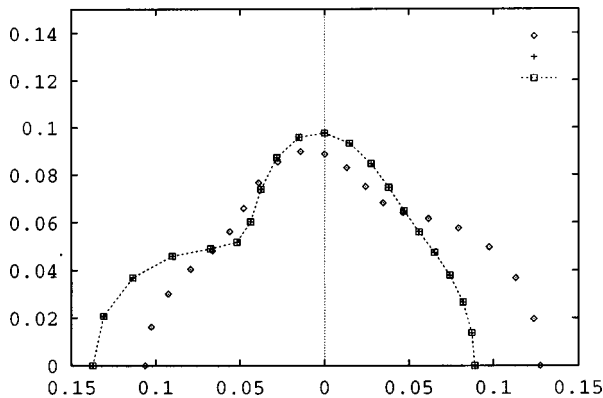


FIG. 2. Example 1, $ka=2$, NFEV=2000, \diamond : $M=20, N=3$; $+$: $M=40, N=5$; \square : $M=50, N=7$.

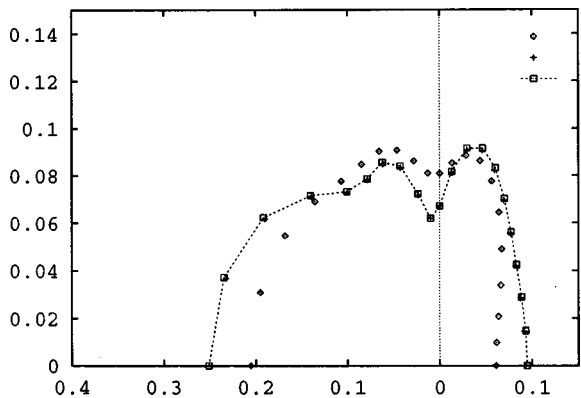


FIG. 4. Example 1, $ka=\pi$, NFEV=2000, \diamond : $M=25, N=3$; $+$: $M=35, N=5$; \square : $M=55, N=7$.

TABLE I. CPU times (in seconds) for example 1.

NFEV	$M=40, N=5$	$M=50, N=7$	$M=60, N=9$
1000	94	166	264
2000	186	326	503
3000	280	492	754
4000	372	652	1007

where $E(\kappa)$ is the complete elliptic integral of the second kind defined by

$$E(\kappa) = \int_0^{\pi/2} [1 - \kappa^2 \sin^2 \theta(Q)]^{1/2} d\theta(Q), \quad (16)$$

and n_r and n_z are the components of the outward normal vector n to the boundary in the r and z directions, respectively.

Having obtained expressions for the fundamental solution of the axisymmetric version of the Helmholtz equation and the normal derivative of the fundamental solution, we now approximate the solution of the problem by

$$u_N(\mathbf{c}, \mathbf{P}; Q) = \sum_{j=1}^N c_j G(P_j, Q), \quad Q \in \bar{\Omega}, \quad (17)$$

where $\mathbf{c} = (c_1, c_2, \dots, c_N) \in \mathbb{C}^N$, and \mathbf{P} is a $2N$ vector containing the coordinates of the singularities P_j , which lie outside $\bar{\Omega}$. A set of points $\{Q_i\}_{i=1}^M$ is selected on $\partial\Omega$, and the coefficients \mathbf{c} and the locations of the singularities \mathbf{P} are determined by minimizing the functional

$$F(\mathbf{c}, \mathbf{P}) = \sum_{i=1}^M |Bu_N(\mathbf{c}, \mathbf{P}; Q_i) - f(Q_i)|^2, \quad (18)$$

using the nonlinear least squares package LMDIF from MINPACK.¹⁵ This routine, which implements a modified version of the Levenberg–Marquard algorithm, terminates when either a user-specified tolerance is achieved or a user-specified number of function evaluations is reached. A function evaluation occurs each time there is a call from the routine LMDIF to the subroutine calculating the function $Bu_N(\mathbf{c}, \mathbf{P}; Q_i)$. Internal checks in the driver program ensure that the singularities do not move beyond the axis of rotation of the solid nor into the interior of the region. Moreover, for

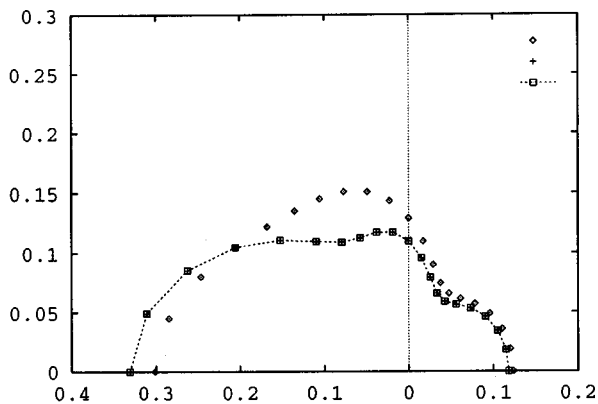


FIG. 5. Example 2, $kR_1 = kR_2 = 1$, $d = 5R_1$, NFEV=2000; \diamond : $M=40, N=4$; $+$: $M=50, N=6$; \square : $M=60, N=8$.

TABLE II. Cases considered in example 2.

Case	kR_1	kR_2	d	D
(i)	1	1	$5R_1$	$3R_1$
(ii)	2	2	$5R_1$	$3R_1$
(iii)	π	π	$5R_1$	$3R_1$
(iv)	1	$\frac{1}{2}$	$5R_1$	$3R_1$
(v)	1	2	$10R_1$	$3R_1$
(vi)	1	2	$5R_1$	$2R_1$

problems in simply connected domains, no boundary points are placed on the axis of rotation.

It should be noted that, in the present formulation of the MFS, the coefficients $\{c_j\}_{j=1}^N$ and the boundary conditions are complex. Thus, there are $4N$ unknowns to be determined, namely, the coordinates of the singularities and the real and imaginary parts of the coefficients. In the subsequent examples, N denotes the total number of singularities used, M the total number of boundary points, and NFEV the total number of function evaluations performed. The number of boundary points is usually chosen to be approximately three times the number of unknowns of the problem,⁵ that is, $M \approx 12N$. The complete elliptic integrals $K(\kappa)$ and $E(\kappa)$ are evaluated using the NAG functions S21BBF and S21BCF,¹² respectively, which implement Carlson’s algorithm.¹⁶ The integrals G_1 and L_1 are evaluated numerically using the trapezoidal rule.

In the development of the MFS in this paper, the derivation and evaluation of the fundamental solutions and their normal derivatives are those presented in Ref. 6 in the context of the classical direct BEM. In Ref. 6, no mention is made of the fictitious eigenfrequency problem present in the BEM.¹⁷ In examples 1 and 2 of Sec. II of the present paper, it is demonstrated that this problem is not encountered in the MFS.

II. ACOUSTIC SCATTERING AND RADIATION PROBLEMS

In this section, we consider a rigid obstacle immersed in a homogeneous fluid medium and impinged upon by a plane acoustic wave of the form

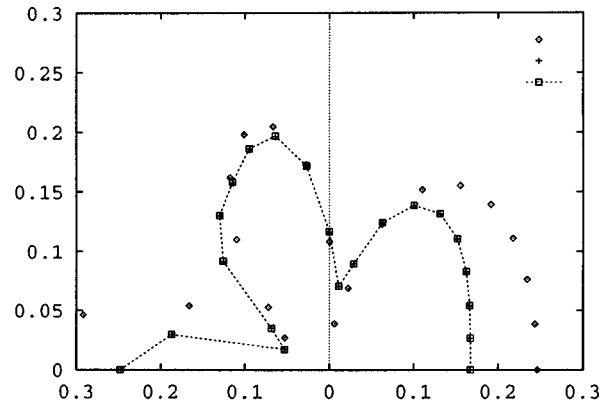


FIG. 6. Example 2, $kR_1 = kR_2 = 2$, $d = 5R_1$, NFEV=2000; \diamond : $M=48, N=6$; $+$: $M=60, N=8$; \square : $M=72, N=10$.

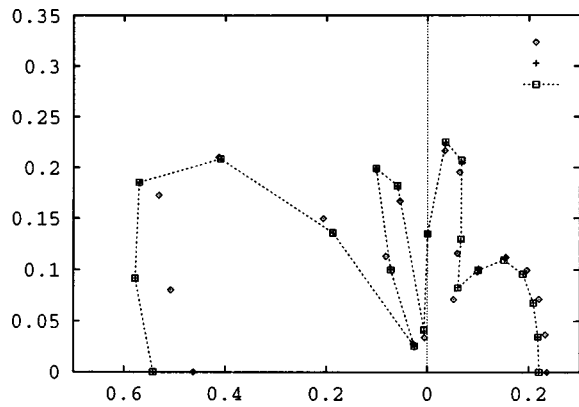


FIG. 7. Example 2, $kR_1=kR_2=\pi$, $d=5R_1$, NFEV=2000; \diamond : $M=60$, $N=8$; $+$: $M=72$, $N=10$; \square : $M=84$, $N=12$.

$$\phi'(z) = \phi_0 e^{ikz}, \quad (19)$$

where ϕ_0 is a constant. The boundary condition for scattering problems is

$$\frac{\partial \phi^I}{\partial n} + \frac{\partial \phi^S}{\partial n} = 0, \quad (20)$$

where ϕ^S is the scattered wave, which also satisfies the Helmholtz equation. For radiation problems, we neglect the incident wave and prescribe the pressure or the normal velocity distribution on the boundary.

A. Example 1

The first example involves scattering of a plane acoustic wave from a rigid sphere.⁶ The direction of the incident wave coincides with the z axis. Figure 1 illustrates the geometry of this example; the situation is similar in all subsequent examples. In Figs. 2 and 3, we plot ϕ^S/ϕ_0 versus the polar angle, φ , which is called the directivity pattern, at a distance $5a$ from the center of a sphere of radius a , for the cases $ka=2$ and $ka=4$, respectively, for various values of M and N , and NFEV=2000. The solutions clearly converge as M and N increase, and the results obtained are in excellent agreement with those of Ref. 6. In Fig. 4, we demonstrate the

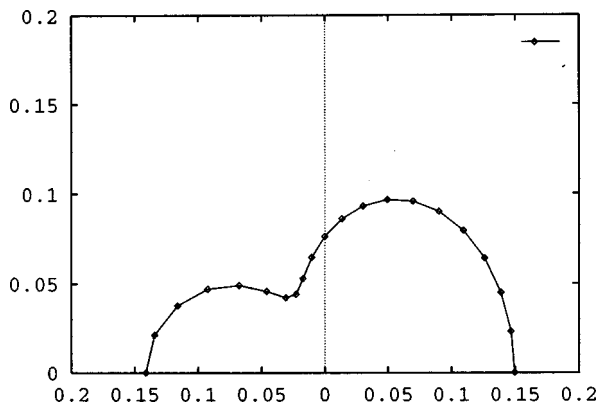


FIG. 8. Example 2, $kR_1=1$, $R_2/R_1=\frac{1}{2}$, $d=5R_1$, NFEV=2000; \diamond : $M=64$, $N=8$.

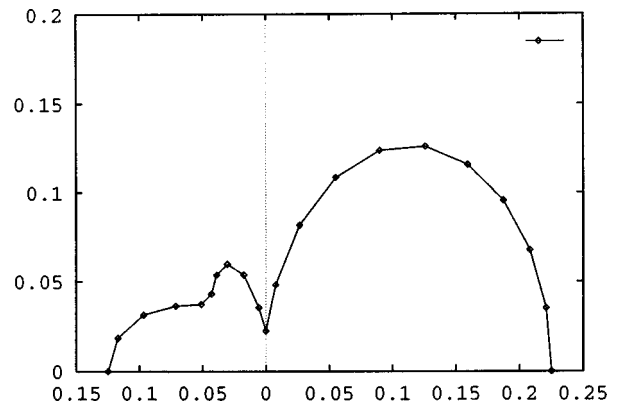


FIG. 9. Example 2, $kR_1=1$, $R_2/R_1=2$, $d=10R_1$, NFEV=2000; \diamond : $M=64$, $N=8$.

convergence of the method when $ka=\pi$, which is a frequency for which the BEM breaks down because of the fictitious eigenfrequency problem.¹⁷

In order to give an indication of the computing time required, we present in Table I the CPU times for the solution of example 1. These times were recorded on an IBM RS6000 (Processor type: Power PC 604/ 100 MHz), for which the LINPACK TPP benchmark in MFLOPS is 56.4.

B. Example 2

Here we consider scattering of a plane acoustic wave from two rigid spheres where the spheres lie on the z axis.⁶ The radii of the spheres are R_1 and R_2 and their centers are a distance d apart. The direction of the incident wave coincides with the z axis. We place half of the boundary points uniformly distributed on each sphere (semi-circle) and half of the singularities inside each sphere (semi-circle). In each test, NFEV=2000.

The six cases given in Table II are considered, and the directivity patterns for these at a distance D from the center of the first sphere are plotted in Figs. 5–10. In each of the first three cases, various values of M and N are considered, as shown in Figs. 5–7. In each case, the solution clearly converges as M and N increase. The values $M=64$ and $N=8$ were used in the solution of the remaining cases. In cases (i), (ii) and (iv)–(vi), the solutions are in excellent agreement

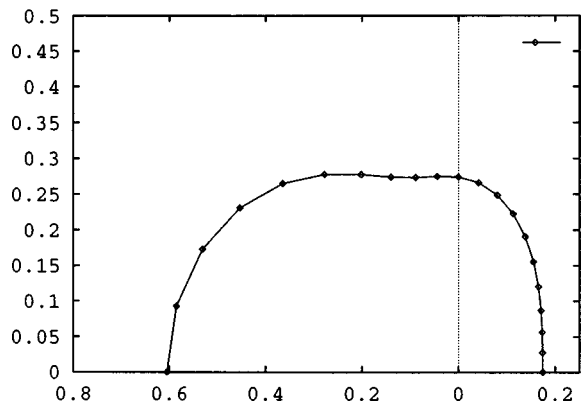


FIG. 10. Example 2, $kR_1=1$, $R_2/R_1=2$, $d=5R_1$, NFEV=2000; \diamond : $M=64$, $N=8$.

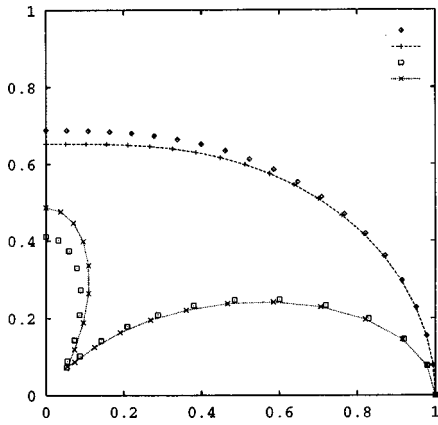


FIG. 11. Example 3, normalized far-field pressure, NFEV=4000, $N=6$; \diamond : $ka=1, M=36$; $+$: $ka=1, M=48$; \square : $ka=2, M=36$; \times : $ka=2, M=48$.

with the results of Ref. 6; in case (iii), the frequency is such that the BEM breaks down because of the fictitious eigenfrequency problem.¹⁷

C. Example 3

The final example in this section involves radiation from a finite cylinder of radius a and length $4a$ in which a uniform radial velocity ($\partial\phi/\partial n=1$) is prescribed on the curved surface of the cylinder, and the top and bottom ends of the cylinder are motionless ($\phi=0$). This example was considered in Refs. 6 and 18–21 using various integral equation formulations. In Fig. 11, we present the normalized far-field pressure (at a distance $10a$ from the origin) for $ka=1$ and $ka=2$. Our results are in good qualitative agreement with the results of Refs. 18–20.

III. ACOUSTIC SCATTERING AND RADIATION PROBLEMS IN A HALF-SPACE

We next consider the problem of acoustic radiation and scattering from bodies in the half-space $z>0$. The BEM has been used for the solution of such problems in Refs. 22 and 23. We examine the case in which the bodies under consideration are axisymmetric. By using an appropriate fundamental solution, the problem of discretizing the plane $z=0$ is

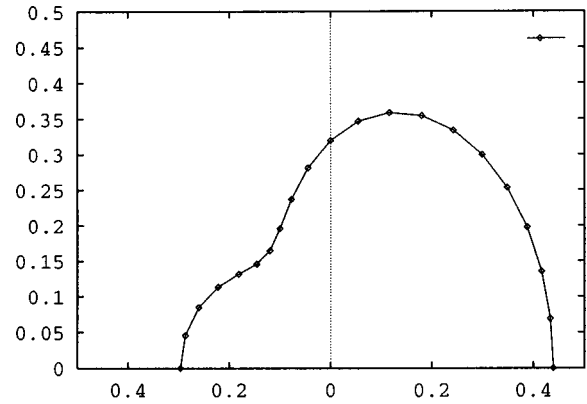


FIG. 13. Example 4, normalized pressure at a distance of $2a$, NFEV=1000; \diamond : $M=40, N=4$.

avoided. In particular, when this plane is rigid, we use the fundamental solution [see Chap. 7 of Ref. 24 and cf. (4)]

$$G^H(P, Q) = \int_0^{2\pi} \frac{e^{-ikR(P, Q)}}{R(P, Q)} d\theta(Q) + \int_0^{2\pi} \frac{e^{-ikR(P', Q)}}{R(P', Q)} d\theta(Q), \quad (21)$$

where the point P' is the image point of P in the plane. This fundamental solution satisfies the axisymmetric version of the Helmholtz equation and the boundary condition $\partial\phi/\partial z=0$ on $z=0$. In the following examples, we use this (modified) fundamental solution in the MFS formulation and thus avoid the problem of handling the boundary condition on a rigid plane.

A. Example 4

This example involves radiation from a sphere of radius a whose center is at a distance $b=3a$ from a rigid plane. The boundary condition on the sphere is a uniform velocity $\partial\phi/\partial n=1$. The normalized frequency of vibration of the sphere is $ka=1$. In Fig. 12, we present the normalized acoustic pressure at a distance $3a$ from the center of the sphere, for various values of M and N . In Fig. 13, we present the directivity pattern at a distance $2a$ from the center of the

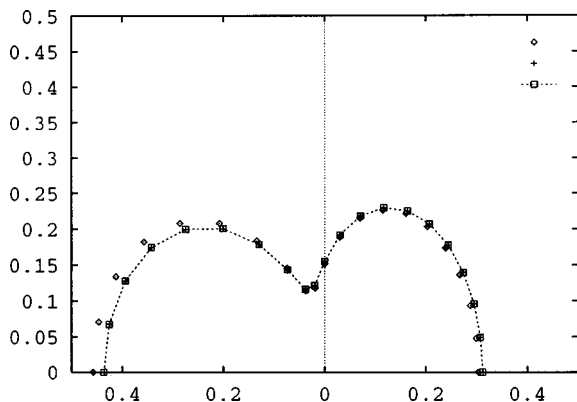


FIG. 12. Example 4, normalized pressure at a distance of $3a$, NFEV=1000; \diamond : $M=10, N=1$; $+$: $M=20, N=2$; \square : $M=40, N=4$.

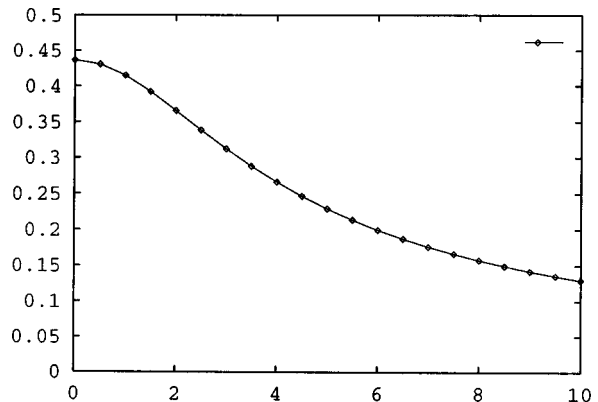


FIG. 14. Example 4, normalized pressure along infinite plane, NFEV=1000; \diamond : $M=40, N=4$.

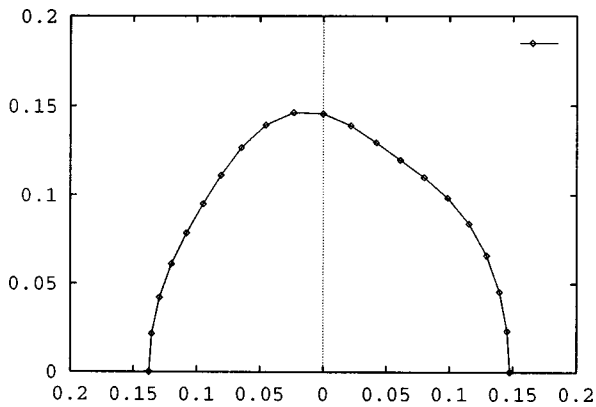


FIG. 15. Example 4, normalized pressure at a distance of $5a$, when $b = 50a$, NFEV=1000; \diamond : $M=40, N=4$.

sphere and, in Fig. 14, the normalized pressure along the surface of the plane, starting from the level of the center of the sphere. For the same problem but with the sphere at a distance $50a$ from the plane, we show, in Fig. 15, the directivity pattern at a distance $5a$ from the center of the sphere. In all cases, the results are in excellent agreement with those of Ref. 22.

B. Example 5

In this example, we consider acoustic scattering of a plane acoustic wave from a rigid sphere in a half space. As in example 1, the direction of the incident wave coincides with the z axis and we consider the case $ka=2$. We first place the sphere at a distance $b=5a$ from the plane. In Fig. 16, we present the directivity pattern at a distance $5a$ from the center of the sphere, for various values of M and N . The solution clearly converges as we increase the numbers of degrees of freedom. We then moved the sphere to a distance $50a$ from the plane. In Fig. 17, we show the directivity pattern at a distance $5a$ from the center of the sphere for various numbers of singularities and boundary points. The pattern of the solution is similar to the corresponding pattern of example 1 shown in Fig. 2.

C. Example 6

In the final example, we examine the case in which an axisymmetric body is in contact with an infinite plane. In

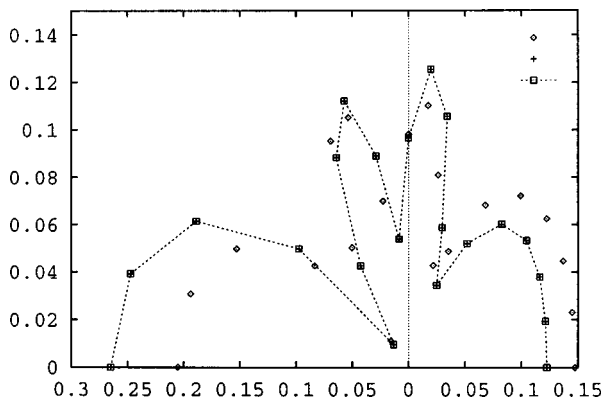


FIG. 16. Example 5, $b=5a$, $ka=2$, NFEV=2000; \diamond : $M=20, N=3$; $+$: $M=40, N=5$; \square : $M=50, N=7$.

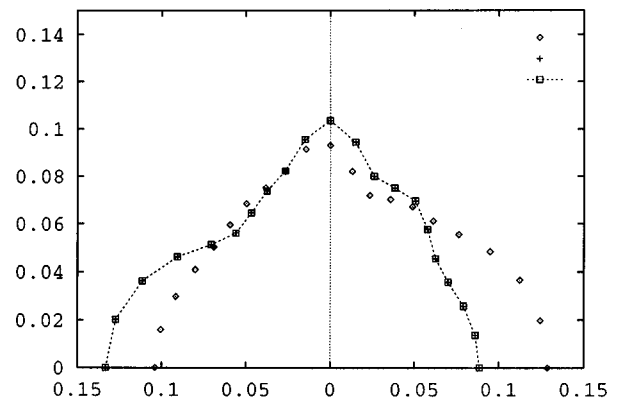


FIG. 17. Example 5, $b=50a$, $ka=2$, NFEV=2000; \diamond : $M=20, N=3$; $+$: $M=40, N=5$; \square : $M=50, N=7$.

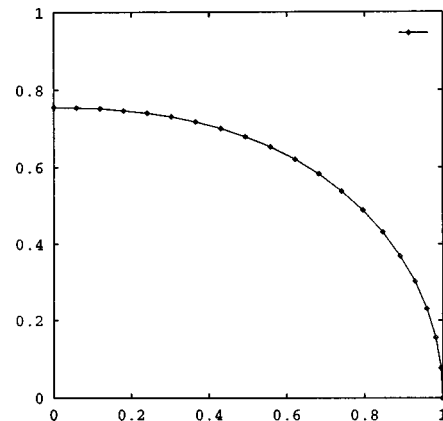


FIG. 18. Example 6, $ka=1$, NFEV=2000; \diamond : $M=40, N=12$.

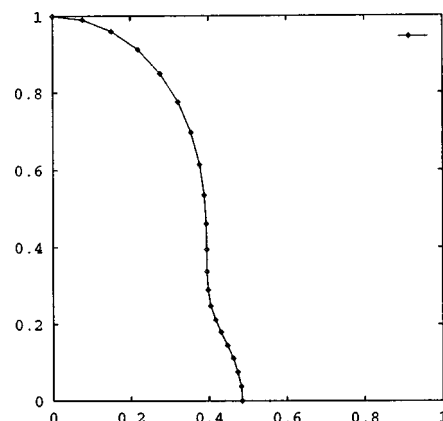


FIG. 19. Example 6, $ka=3$, NFEV=2000; \diamond : $M=40, N=12$.

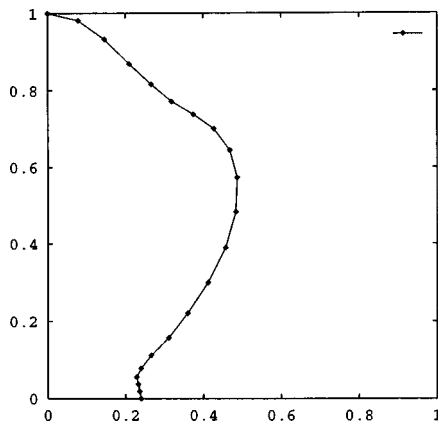


FIG. 20. Example 6, $ka = 10$, NFEV=2000; \diamond : $M = 40$, $N = 12$.

particular, we consider the problem of acoustic radiation from a hemispherical body of radius a in an infinite baffle studied in Ref. 25 using a semi-analytical method and in Ref. 26 with the BEM. Since the body is vibrating uniformly in the z direction, the boundary condition on the surface of the sphere is taken to be $\partial\phi/\partial z = 1$. The baffle is assumed to be rigid, so that the boundary condition there is $\partial\phi/\partial z = 0$. In Figs. 18–20, we present the directivity patterns of the normalized acoustic pressure at a distance $40a$ from the center of the hemisphere, for $ka = 1, 3$ and 10 , respectively. The results presented were obtained with $M = 40$, $N = 12$ and NFEV=2000 and are in excellent agreement with the corresponding results of Ref. 25.

IV. CONCLUSIONS

In this work, we demonstrate the applicability of the MFS to axisymmetric acoustic scattering and radiation problems. The fundamental solutions of the governing equations involved and their normal derivatives which are required in the formulation of the MFS are calculated using existing library software and numerical integration. The method is applied to a number of problems from the literature giving very good results. Further, we show that the fictitious eigenfrequency difficulties encountered when using the BEM are not present in the MFS.

ACKNOWLEDGMENTS

The authors wish to thank B. Soenarko of ITB, Bandung, Indonesia, and A. F. Seybert of the University of Kentucky for their helpful comments during the preparation of this work. Parts of this work were undertaken while the first author was a visiting associate professor in the Department of Mathematical and Computer Sciences at Colorado School of Mines.

¹V. D. Kupradze and M. A. Aleksidze, "The method of functional equations for the approximate solution of certain boundary value problems," *USSR Comput. Math. Math. Phys.* **4**, 82–126 (1964).

²G. Fairweather and R. L. Johnston, "The method of fundamental solutions for problems in potential theory," in *Treatment of Integral Equations by Numerical Methods*, edited by C. T. H. Baker and G. F. Miller (Academic, London, 1982), pp. 349–359.

- ³A. Karageorghis and G. Fairweather, "The method of fundamental solutions for the numerical solution of the biharmonic equation," *J. Comput. Phys.* **69**, 434–459 (1987).
- ⁴A. Karageorghis and G. Fairweather, "The Almansi method of fundamental solutions for solving biharmonic problems," *Int. J. Numer. Methods Eng.* **26**, 1668–1682 (1988).
- ⁵G. Fairweather and A. Karageorghis, "The method of fundamental solutions for elliptic boundary value problems," *Adv. Comput. Math.* **9**, 69–95 (1998).
- ⁶A. F. Seybert, B. Soenarko, F. J. Rizzo, and D. J. Shippy, "A special integral equation formulation for acoustic radiation and scattering for axisymmetric bodies and boundary conditions," *J. Acoust. Soc. Am.* **80**, 1241–1247 (1986).
- ⁷P. S. Kondapalli, "Time-harmonic solutions in acoustics and elastodynamics by the method of fundamental solutions," Ph.D. thesis, Department of Engineering Mechanics, University of Kentucky, 1991.
- ⁸P. S. Kondapalli, D. J. Shippy, and G. Fairweather, "Analysis of acoustic scattering in fluids and solids by the method of fundamental solutions," *J. Acoust. Soc. Am.* **91**, 1844–1854 (1992).
- ⁹P. S. Kondapalli, D. J. Shippy, and G. Fairweather, "The method of fundamental solutions for transmission and scattering of elastic waves," *Comput. Methods Appl. Mech. Eng.* **96**, 255–269 (1992).
- ¹⁰D. J. Shippy, P. S. Kondapalli, and G. Fairweather, "Analysis of acoustic scattering in fluids and solids by the method of fundamental solutions," *Mathl. Comput. Modelling* **14**, 74–79 (1990).
- ¹¹A. Karageorghis and G. Fairweather, "The method of fundamental solutions for axisymmetric potential problems," *Int. J. Numer. Methods Eng.* (to appear).
- ¹²"Numerical Algorithms Group Library," NAG(UK) Ltd., Wilkinson House, Jordan Hill Road, Oxford, UK.
- ¹³A. K. Gupta, "The boundary integral equation method for potential problems involving axisymmetric geometry and arbitrary boundary conditions," M. S. thesis, Department of Engineering Mechanics, University of Kentucky, 1979.
- ¹⁴F. J. Rizzo and D. J. Shippy, "A boundary integral approach to potential and elasticity problems for axisymmetric bodies with arbitrary boundary conditions," *Mech. Res. Commun.* **6**, 99–103 (1979).
- ¹⁵B. S. Garbow, K. E. Hillstom, and J. J. Moré, "MINPACK Project," Argonne National Laboratory, 1980.
- ¹⁶B. C. Carlson, "A table of elliptic integrals of the third kind," *Math. Comput.* **51**, 267–280 (1988).
- ¹⁷B. Soenarko, "An Advanced Boundary Element Formulation for Acoustic Radiation and Scattering in Three Dimensions," Ph.D. thesis, Department of Engineering Mechanics, University of Kentucky, 1983.
- ¹⁸J. J. Engblom and R. B. Nelson, "Consistent formulation of sound radiation from arbitrary structure," *J. Appl. Mech.* **97**, 295–300 (1975).
- ¹⁹A. F. Seybert, B. Soenarko, F. J. Rizzo, and D. J. Shippy, "An advanced computational method for radiation and scattering of acoustic waves in three dimensions," *J. Acoust. Soc. Am.* **77**, 362–368 (1985).
- ²⁰H. A. Schenk, "Improved integral formulation for acoustic radiation problems," *J. Acoust. Soc. Am.* **44**, 41–58 (1968).
- ²¹W. Williams, N. G. Parke, D. A. Moran, and C. H. Sherman, "Acoustic radiation from a finite cylinder," *J. Acoust. Soc. Am.* **36**, 2316–2322 (1964).
- ²²A. F. Seybert and B. Soenarko, "Radiation and scattering of acoustic waves from bodies of arbitrary shape in a three-dimensional half space," *ASME Journal of Vibration, Acoustics, Stress, and Reliability in Design* **110**, 112–117 (1988).
- ²³B. Soenarko and A. F. Seybert, "Application of the boundary element method to acoustic barrier analysis," in *Proceedings of the Third International Congress on Air- and Structure-Borne Sound and Vibration*, Montreal, Canada, 1994, pp. 831–838.
- ²⁴P. M. Morse and K. U. Ingard, *Theoretical Acoustics* (McGraw-Hill, New York, 1968).
- ²⁵H. Suzuki and J. Tichy, "Sound radiation from convex and concave domes in an infinite baffle," *J. Acoust. Soc. Am.* **69**, 41–49 (1981).
- ²⁶B. Soenarko, "Radiation and scattering of acoustic waves from axisymmetric bodies in a half space using boundary element method," in *Boundary Element Technology XII*, edited by J. I. Frankel, C. A. Brebbia, and M. A. H. Aliabadi (Computational Mechanics, Southampton, 1997), pp. 165–174.

Simple conformal methods for finite-difference time-domain modeling of pressure-release surfaces

John B. Schneider^{a)} and Christopher L. Wagner^{b)}

School of Electrical Engineering and Computer Science, Washington State University, P.O. Box 642752, Pullman, Washington 99164-2752

Robert J. Kruhlak^{c)}

Nonlinear Optics Laboratory, Department of Physics, Washington State University, P.O. Box 642814, Pullman, Washington 99164-2814

(Received 14 April 1998; revised 8 September 1998; accepted 9 September 1998)

The finite-difference time-domain (FDTD) method provides a simple and accurate means of simulating a wide range of acoustic wave propagation problems. Unfortunately, the method has a voracious appetite for computational resources. For example, to accurately model scattering from a continuously varying pressure-release boundary, an FDTD grid is typically required that has a much finer discretization than is necessary to model propagation in a homogeneous space. Such a fine discretization can become prohibitive when considering large-scale problems. Two simple conformal techniques are presented for acoustic FDTD simulations of problems involving pressure-release boundaries. These techniques, which rely upon splitting velocity cells adjacent to the pressure-release boundary, significantly improve the accuracy of the results over those of the standard “staircase” representation of the boundary. These methods permit the use of a coarser FDTD grid than would otherwise be practical and yet add negligible computational cost. The improved accuracy of these split-cell techniques is shown for both a spherical scatterer and a spherical resonator. © 1998 Acoustical Society of America. [S0001-4966(98)03912-5]

PACS numbers: 43.20.Fn, 43.30.Hw, 43.30.Gv, 43.20.Px [ANN]

INTRODUCTION

The finite-difference time-domain (FDTD) method was introduced by Yee in 1966 to study electromagnetic wave propagation.¹ The method employs a discretization of time and space to express the coupled first-order Maxwell’s equations as difference equations. From these difference equations, the future fields are expressed in terms of known past fields which yields a leap-frog technique for the advancement of the fields. A similar method was later presented by Madariaga² and Virieux^{3,4} for elastic wave propagation where the relevant fields are stress and velocity. A three-dimensional version of the stress-velocity FDTD method was presented by, among others, Randall.⁵

The FDTD simulation of acoustic propagation can be considered a special case of the elastic stress-velocity method and subsequent references to the FDTD method imply the acoustic version where the fields being modeled are pressure and velocity. The FDTD method has been used to solve a wide range of problems including the analysis of room acoustics^{6,7} and the determination of acoustic scattering from a rough ocean surface (i.e., a pressure-release surface).^{8,9} The implementation details for the method can be found in several papers (e.g., Refs. 7, 10–12).

Because the FDTD method is a full-wave solution that directly employs the governing differential equations, the solution of three-dimensional problems is often computation-

ally costly. The accuracy of the FDTD method is, in large part, tied to the fineness of the computational grid. When a fine grid must be used and the computation space is large, the computational resources needed to obtain the solution may be prohibitive. Some problems, such as those with planar boundaries which are aligned with the grid, can be solved with a relatively coarse grid. However, the simulation of more general problems, such as those with continuously varying surfaces, may suffer intolerable numerical errors when modeled with a coarse grid. The goal of the conformal methods presented here is to provide an accurate representation of pressure-release surfaces even when the grid is relatively coarse and the surface is not aligned with the grid. Thus, these methods serve to reduce the error introduced by the “staircase” representation of material boundaries.

The methods introduced here are designed to improve the geometric fidelity of simulations involving pressure-release surfaces. These methods do not address the numerical dispersion errors which are inherent in the FDTD grid and which increase as the grid becomes more coarse. However, we note that there are ways to mitigate dispersion errors and, consequently, in many simulations the staircasing errors (and not the dispersion errors) dictate the acceptable coarseness of the grid. For example, in Ref. 13 the FDTD dispersion relation was used to correct for dispersion errors. Another example is provided by the work of Hastings *et al.*⁹ where the incident field was introduced, and the scattered field was recorded, near the scatterer. In this way, the fields do not propagate far within the grid and, therefore, do not accumulate significant dispersion error.

In the standard FDTD method, the velocity and pressure

^{a)}Electronic mail: schneidj@eecs.wsu.edu

^{b)}Electronic mail: clwagner@eecs.wsu.edu

^{c)}Electronic mail: rkruhlak@wsu.edu

nodes are at fixed locations in a Cartesian grid so that a continuously varying boundary is approximated by one that is staircased. Furthermore, even flat planar surfaces must be approximated as a staircased surface when the plane is not aligned with the grid. With a sufficiently fine grid, the errors associated with the staircase approximation are small. However, to keep the computational cost as low as possible, the grid should be made as coarse as possible.

In an attempt to satisfy these competing factors, different approaches have been proposed. For example, Botteldooren presented a quasi-Cartesian scheme that can be used to distort the grid so that it conforms to a boundary.¹⁴ Unfortunately, such a scheme removes much of the simplicity and elegance of the Cartesian-grid FDTD method and the generation of quasi-Cartesian grids for arbitrary scatterers is a significant computational task. An alternative approach to reducing the errors associated with the staircase representation is to maintain the Cartesian grid away from material boundaries and to distort the grid only in the vicinity of the boundaries. Such an approach was put forward in the electromagnetics literature by, among others, Jurgens *et al.*¹⁵ and it has been used to model scattering from two-dimensional pressure-release surfaces.⁹ Unfortunately, for three-dimensional problems, there is no clear translation of this method to the acoustic case.

We present two simple methods that alleviate most of the errors associated with the staircase representation of pressure-release surfaces. The techniques, which have their antecedents in the work of Mezzanotte *et al.*¹⁶ and Dey and Mitra,¹⁷ are realized by splitting cells associated with velocity nodes. In the simplest version, the mass of a cell is reduced by a factor of 2 if the pressure-release boundary is within one quarter of the spatial step distance to either side of a velocity node. This simple modification significantly improves the accuracy as compared to the standard staircase solution and, furthermore, has associated with it virtually no additional computational cost. The simulation can still be run at the Courant limit (i.e., using the greatest possible time step as dictated by the size of the Cartesian grid away from the boundary).

The simplicity of these techniques is, in part, a consequence of only considering pressure-release surfaces and not boundaries between arbitrary materials. Nevertheless, it is envisioned that these techniques will make possible, for example, the investigation of scattering from realistic ocean surfaces (i.e., a three-dimensional problem with a two-dimensional ocean surface) via the FDTD method. Additionally, a similar sort of cell-splitting (or mass averaging) technique is possible for more general problems as was shown in Ref. 18 where the scattering from fluid–fluid interfaces was investigated. However, the more general case is not considered here.

The following section presents the details of the conformal methods for acoustic pressure-release boundaries. Results are then presented in Sec. II for a spherical pressure-release scatterer and for a spherical resonator.

I. CONFORMAL TECHNIQUES

The governing acoustic equations in three dimensions are

$$\frac{\partial p}{\partial t} = -\rho c^2 \left(\frac{\partial v_x}{\partial x} + \frac{\partial v_y}{\partial y} + \frac{\partial v_z}{\partial z} \right), \quad (1)$$

$$\frac{\partial v_x}{\partial t} = -\frac{1}{\rho} \frac{\partial p}{\partial x}, \quad (2)$$

$$\frac{\partial v_y}{\partial t} = -\frac{1}{\rho} \frac{\partial p}{\partial y}, \quad (3)$$

$$\frac{\partial v_z}{\partial t} = -\frac{1}{\rho} \frac{\partial p}{\partial z}, \quad (4)$$

where p is pressure, $\mathbf{v} = v_x \hat{\mathbf{a}}_x + v_y \hat{\mathbf{a}}_y + v_z \hat{\mathbf{a}}_z$ is velocity, ρ is density, and c is the speed of propagation. The update equations for the FDTD method are obtained by replacing the derivatives in Eqs. (1)–(4) by finite differences and solving for unknown future fields in terms of known past fields. To obtain a fully explicit scheme, the points at which the fields are evaluated must be offset spatially and temporally. Second-order accurate central differences can be used to approximate all the derivatives if the fields are discretized so that they are defined at the following evaluation points:

$$p(x, y, z, t) = p(i\Delta x, j\Delta y, k\Delta z, n\Delta t) = p^n(i, j, k), \quad (5)$$

$$\begin{aligned} v_x(x, y, z, t) &= v_x([i + 1/2]\Delta x, j\Delta y, k\Delta z, [n + 1/2]\Delta t) \\ &= v_x^{n+1/2}(i, j, k), \end{aligned} \quad (6)$$

$$\begin{aligned} v_y(x, y, z, t) &= v_y(i\Delta x, [j + 1/2]\Delta y, k\Delta z, [n + 1/2]\Delta t) \\ &= v_y^{n+1/2}(i, j, k), \end{aligned} \quad (7)$$

$$\begin{aligned} v_z(x, y, z, t) &= v_z(i\Delta x, j\Delta y, [k + 1/2]\Delta z, [n + 1/2]\Delta t) \\ &= v_z^{n+1/2}(i, j, k), \end{aligned} \quad (8)$$

where Δx , Δy , and Δz are the spatial step sizes in the x , y , and z directions, respectively, and Δt is the temporal step size. The precise interpretation of a field value in an FDTD grid is an interesting topic in itself (e.g., are the fields samples of a continuous function or do they represent average values over some region of space?), and the interested reader is referred to Ref. 19 for further discussions. For purposes of this paper, a field is assumed to be defined at a point (i.e., a particular node in the grid) and the value at the point represents the average value found over the cell associated with that field component. The arrangement of nodes associated with a given set of spatial indices is shown in Fig. 1. We assume a uniform grid so that $\Delta x = \Delta y = \Delta z = \delta$, but the development of the conformal methods do *not* require this assumption. On the right-hand side of Eqs. (5)–(8), the fields are specified by their spatial and temporal indices, i.e., the arguments and the superscripts, respectively. For the velocity components, the spatial offsets are implied by the field component [i.e., the x component of velocity $v_x^{n+1/2}(i, j, k)$ is not collocated with either the y component $v_y^{n+1/2}(i, j, k)$ or z component $v_z^{n+1/2}(i, j, k)$]. The temporal offset between the fields is explicitly retained in the temporal index. Replacing

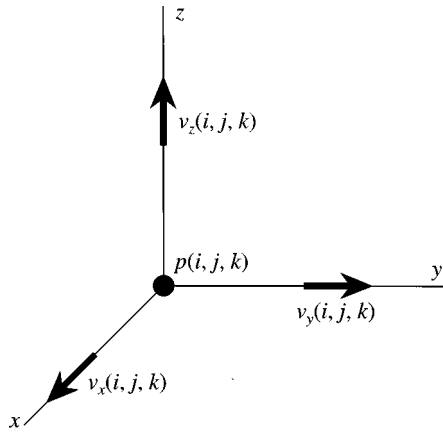


FIG. 1. The location of the velocity nodes relative to a pressure node for a given set of spatial indices. The velocity and pressure nodes are also offset in time by half of the temporal step size.

the derivatives in Eqs. (1)–(4) with finite differences and using the discretization of Eqs. (5)–(8) yields the following update equations:

$$\begin{aligned}
 p^n(i, j, k) = & p^{n-1}(i, j, k) - \rho c \frac{c\Delta t}{\delta} [v_x^{n-1/2}(i, j, k) \\
 & - v_x^{n-1/2}(i-1, j, k) + v_y^{n-1/2}(i, j, k) \\
 & - v_y^{n-1/2}(i, j-1, k) + v_z^{n-1/2}(i, j, k) \\
 & - v_z^{n-1/2}(i, j, k-1)], \quad (9)
 \end{aligned}$$

$$\begin{aligned}
 v_x^{n+1/2}(i, j, k) = & v_x^{n-1/2}(i, j, k) - \frac{1}{\rho c} \frac{c\Delta t}{\delta} \\
 & \times [p^n(i+1, j, k) - p^n(i, j, k)], \quad (10)
 \end{aligned}$$

$$\begin{aligned}
 v_y^{n+1/2}(i, j, k) = & v_y^{n-1/2}(i, j, k) - \frac{1}{\rho c} \frac{c\Delta t}{\delta} \\
 & \times [p^n(i, j+1, k) - p^n(i, j, k)], \quad (11)
 \end{aligned}$$

$$\begin{aligned}
 v_z^{n+1/2}(i, j, k) = & v_z^{n-1/2}(i, j, k) - \frac{1}{\rho c} \frac{c\Delta t}{\delta} \\
 & \times [p^n(i, j, k+1) - p^n(i, j, k)]. \quad (12)
 \end{aligned}$$

These equations are used in a leap-frog fashion to obtain the unknown future fields in terms of the known past fields. This explicit scheme is not unconditionally stable. To obtain a stable solution in three dimensions, the Courant number, i.e., $c\Delta t/\delta$, must be less than or equal to $1/\sqrt{3}$. (For more information on the Courant number and stability of the FDTD method see Ref. 10.)

The simplest staircase implementation of a pressure-release region is realized by setting all pressure nodes that lie within the pressure-release region to zero. Pressure nodes outside the pressure-release region are updated using Eq. (9) and all velocity nodes, whether they fall inside or outside the pressure-release region, are updated as dictated by Eqs. (10)–(12).

Figure 2 shows a cross-section of the cell (or cube) associated with the velocity node $v_x(i, j, k)$ (the full cell extends $\Delta y/2$ into and out of the page about the velocity node).

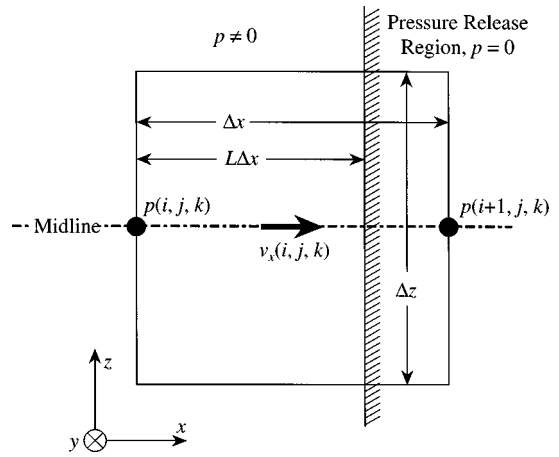


FIG. 2. Cross-section of the cell associated with a v_x node.

Assume that a pressure-release boundary is normal to the x direction at a distance $L\Delta x$ from the node $p(i, j, k)$, where $0 < L \leq 1$ and that the pressure-release region is to the right of this boundary. The simplest staircase implementation of this boundary is realized by setting $p(i+1, j, k)$ to zero while $p(i, j, k)$ and $v_x(i, j, k)$ are updated in the usual way for all values of L . However, this results in an approximation of the actual boundary that suffers unnecessarily large distortions for L 's such that $0 < L < 1/2$. Instead, the node $p(i, j, k)$, which is the closest pressure node to the boundary when $0 < L < 1/2$, should be set to zero. Thus an alternative staircase representation of the boundary can be obtained by changing the criterion used to set a pressure node to zero. Instead of setting to zero those pressure nodes that lie within the pressure-release region (i.e., beyond the pressure-release boundary), pressure nodes should be set to zero if any of their neighboring velocity nodes lie within the pressure-release region. Thus, $p(i, j, k)$ is set to zero if any of the following velocities are within the pressure-release region: $v_x(i-1, j, k)$, $v_x(i, j, k)$, $v_y(i, j-1, k)$, $v_y(i, j, k)$, $v_z(i, j, k-1)$, or $v_z(i, j, k)$. We label the staircasing technique that is based solely on the location of the pressure nodes as the Stair- p method. The staircasing technique which tests the location of the neighboring velocity nodes is labeled Stair- v .

In both staircasing methods all the velocity nodes, independent of their location, are updated in the usual way. The velocity nodes “see” the pressure-release boundary only through the pressure nodes that have been set to zero. The velocity update equations are obtained from Newton’s equation of motion. Ignoring for the moment any pressure-release boundaries, the mass of the cell associated with velocity node $v_x(i, j, k)$ is $\rho\Delta x\Delta y\Delta z$, the force on the cell in the positive x direction is $p(i, j, k)\Delta y\Delta z$, the force in the opposite direction is $p(i+1, j, k)\Delta y\Delta z$, and the acceleration in the x direction is $\partial v_x(i, j, k)/\partial t$. Setting the mass times the acceleration equal to the sum of the forces yields

$$\begin{aligned}
 \rho\Delta x\Delta y\Delta z \frac{\partial v_x(i, j, k)}{\partial t} \\
 = -\Delta y\Delta z (p(i+1, j, k) - p(i, j, k)). \quad (13)
 \end{aligned}$$

Expressing the temporal derivative as a central difference

and solving for $v_x^{n+1/2}(i,j,k)$ yields Eq. (10). When the pressure-release boundary bisects a cell, i.e., when the boundary is located at $L=1/2$, the mass of the cell is reduced by one half. Using this mass and again expressing the temporal derivative as a central difference, Eq. (13) can be solved for $v_x^{n+1/2}(i,j,k)$ to yield the following:

$$v_x^{n+1/2}(i,j,k) = v_x^{n-1/2}(i,j,k) - \frac{2}{\rho c} \frac{c \Delta t}{\delta} \times [p^n(i+1,j,k) - p^n(i,j,k)]. \quad (14)$$

Note that the pressure node $p^n(i+1,j,k)$ will be zero since it is beyond the boundary and that the only difference between Eqs. (14) and (10) is a factor of 2. This type of modification of the coefficient in some of the velocity update equations constitutes the heart of the conformal methods presented here.

In general, the true pressure-release boundary will not be perpendicular to one of the coordinates nor will it exactly bisect a cell. Thus, two obvious questions arise: (1) When should a cell be split and (2) are there other cell-splitting schemes, besides a simple halving of the mass, that will improve the fidelity of a solution? The investigation of these questions has led us to develop three cell-splitting techniques as described in the following subsections. Results obtained using two of these methods are presented in the Sec. II.

A. Quantized split-cell method

In the quantized split-cell method, the mass of a cell associated with a velocity node is either that of the complete cell or that of half the cell. For example, a v_x node would either be updated using the usual update equation of (10) or the split-cell update equation of (14). The split-cell update equation is used if the pressure-release boundary intersects the midline of the velocity cell (i.e., the imaginary line on which the velocity node is located that passes through the middle of the cell) anywhere in the range $1/4 < L < 3/4$. The curvature and tilt of the boundary within a single cell are ignored. Thus, the decision to split the cell is based solely on where the boundary intersects the midline.

Pressure nodes are set to zero if any part of the pressure-release region is closer than one quarter of a spatial step size in any direction. Thus, for the pressure node $p(i,j,k)$ the neighboring points $([i \pm 1/4] \Delta x, j \Delta y, k \Delta z)$, $(i \Delta x, [j \pm 1/4] \Delta y, k \Delta z)$, and $(i \Delta x, j \Delta y, [k \pm 1/4] \Delta z)$ are checked and if any lie within the pressure-release region the pressure node is set to zero. When a velocity node is split, one of the neighboring pressure nodes will always be set to zero.

The quantized split-cell method can be run at the Courant limit (despite the fact it appears to contain cells at the boundaries that are half the size of the cells away from the boundary). This statement is based on numerous simulations employing a wide range of resonant structures. Resonators are typically quick to show any numeric instabilities in an algorithm since, unlike in scattering problems, there is no means by which energy can exit the grid.

Depending on the implementation, there can be almost no computational cost associated with the quantized split-cell method. Some geometry preprocessing is required to deter-

mine which nodes are split and which are not. Because of the simple criterion used to determine which cells are split, the preprocessing is an insignificant portion of the total computation time (especially for three-dimensional objects). If the FDTD implementation uses an array to store the coefficients for each velocity node update equation, some coefficients will be that of the full cell and some will be that of the split cell. At this point time-stepping proceeds as usual and there is no additional cost incurred by the cell-splitting scheme. Alternatively, if coefficients arrays are not used (and they typically would not be if the bulk of the computational domain consists of a homogeneous material), the geometry preprocessing is used to construct a list of cells that are split. At each time step all nodes are updated in the usual way and then an additional subroutine (or function) is used to correct the fields at the boundary in accordance with the cell splitting. Since the list of boundary cells is associated with an object that is one dimension smaller than the total computational domain, the computational effort associated with this correction is small compared to the effort needed to advance the fields throughout the entire computational domain.

The quantized split-cell method is similar in many respects to the cell-splitting method that has been used to model perfect electrically conducting (PEC) boundaries¹⁶ (see also Ref. 20 and the citations therein). However, the electromagnetic cell-splitting method requires a global distortion of the grid to ensure that the PEC boundary is either aligned with the grid or passes through the diagonal of a cell. This distortion is necessitated by the fact that two vector fields are being advanced. In the acoustic FDTD method, where one scalar and one vector field are used, no grid distortions are required.

B. Hybrid split-cell method

The hybrid split-cell method is similar to the quantized split-cell method. The criterion used for setting pressure nodes to zero is unchanged and the simulation can still be run at the Courant limit. As before, a velocity node is split if the pressure-release boundary intersects the cell's midline anywhere in the range $1/4 < L < 3/4$. However, when a cell is split, the mass is not simply cut in half. Instead, the split incorporates more geometry information by reducing the mass in accordance with the location of the intersection. The coefficient for a velocity cell that has been split is modified by a factor of $1/L$ rather than simply a factor of 2. We identify this scheme as "hybrid" since it incorporates continuous geometry over a given range of intersections, but clips the grid to the staircase representation for intersections that fall outside the acceptable range.

C. Continuous split-cell method

The continuous split-cell method is similar in many respects to the hybrid split-cell method. However, in this method the mass associated with a velocity cell is always dictated by the intersection of the pressure-release boundary with the midline of the cell. Thus the coefficients for split velocity cells are modified by $1/L$ regardless of L . Naturally, small values of L lead to large coefficients and numerical

problems. To alleviate these problems, a threshold can be defined that L must exceed (or which $1 - L$ must not exceed) to result in splitting. When the threshold is one quarter of a cell, the hybrid method is obtained. (Pressure nodes can either be set to zero if they lie in the pressure-release region or be set to zero if any portion of some area around the node, as dictated by the threshold, falls within the pressure-release region.) For thresholds less than a quarter of cell, instabilities may occur. However, a stable solution can be obtained by reducing the Courant number.

The continuous method is similar to the conformal FDTD method recently presented by Dey and Mittra¹⁷ to solve for electromagnetic scattering from PEC surfaces. An analytic (as opposed to numeric) analysis of the accuracy of this method can be found in Ref. 21. Despite the success reported by Dey and Mittra for the electromagnetic case, it was found that there is no compelling reason to use such a method for the acoustic case. Despite the fact that the continuous method seems to include more geometry information when the thresholds are small, the results were typically no better than those obtained using the methods described above and, because of the reduced Courant number needed to obtain a stable solution, it takes longer to compute. Therefore, the results obtained using the continuous scheme will not be presented in the next section. (We have found no situation where the continuous scheme provides results consistently superior to the other cell-splitting methods.)

II. RESULTS

Before presenting the results for the scatterer and resonator, we note that the following tests were designed to establish the accuracy of the conformal methods. To this end, the tests employ simple canonical geometries for which analytic solutions are available. Thus, we do not consider more “interesting” (and physically realistic) problems such as the scattering from the ocean surface. Furthermore, the code used to solve these problems was not optimized. For example, the solutions to these problems could easily be written to exploit the inherent symmetry, but this was not done. Hence we do not discuss the computer resources needed to solve these problems (we merely note that the simulations required only modest resources and were run on typically configured personal computers running the Linux operating system).

A. Scattering from a sphere

Consider a spherical pressure-release region of radius a that is ensonified by a plane wave propagating in the z direction. A simple staircase realization of a sphere is shown in Fig. 3. The radius of the sphere is eight cells and this radius is used in all the subsequent calculations. A wire-frame box is used to indicate the size of the computational domain which was 39 by 39 by 39 cells and a heavy solid line shows the line over which scattered fields are recorded. The dashed lines indicate the plane over which the cross-sectional view of Fig. 4 is taken (both figures are drawn to scale). Ensonification is a Ricker wavelet with its peak spectral content corresponding to 20 cells per wavelength. The incident wave is introduced using a total-field/scattered-field form-

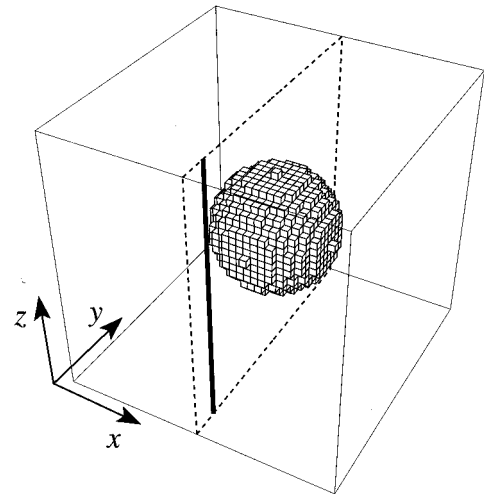


FIG. 3. Depiction of the staircase FDTD realization of a spherical scatterer. The sphere has a radius of 8 cells and the entire computational domain is 39 cells to a side. The heavy vertical line indicates the line over which the fields are recorded. The dashed lines indicate the plane over which the following figure is based.

ulation.^{22–24} The simulation is run for 512 time steps and spectral information is obtained by taking the discrete Fourier transforms at the desired frequencies²⁵ and over the evaluation points. In this way broadband information is obtained from a single simulation. The grid is terminated using a fourth-order complementary operators method (COM) absorbing boundary condition.^{26,27}

The exact solution for the pressure scattered by a sphere of radius a having a Dirichlet boundary is given by²⁸

$$p_s(r, \theta, \phi) = - \sum_m (2m + 1) i^{m+1} e^{iT_m(ka)} \sin(T(ka)) \times P_m(\cos(\theta)) h_m(kr), \quad (15)$$

where k is the wave number, $T_m(z) = \tan^{-1}(j_m(z)/n_m(z))$, P_m

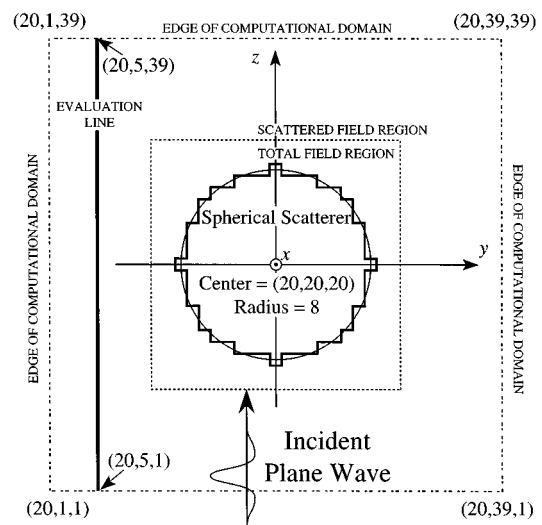


FIG. 4. Cross-sectional view of the computational domain. The drawing is to scale. The coordinates shown are grid locations (spatial indices). Subsequent results assume the origin is at the center of the grid and use physical dimensions rather than grid coordinates.

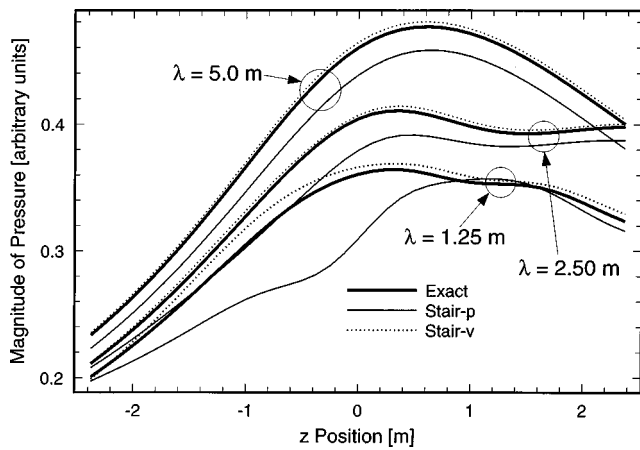


FIG. 5. Scattered pressure at evaluation line obtained using a staircase realization of the sphere.

is the Legendre polynomial, and $e^{-i\omega t}$ dependence is understood. The spherical Bessel functions are given by

$$j_m(z) = \sqrt{\pi/2z} J_{m+1/2}(z), \quad n_m(z) = \sqrt{\pi/2z} N_{m+1/2}(z)$$

and

$$h_m(z) = j_m(z) + in_m(z).$$

All simulations were done using unitless quantities such as grid coordinates, cells per wavelength, and time steps. Thus the results can be scaled to any size and material (the only constraint is the size of the scatterer relative to a wavelength). However, to make the results more tangible, it is helpful to assign convenient physical dimensions to the results. Thus, we assume the sphere has a radius a of 1.0 m and the background material is water with a sound speed of 1500 m/s and a density of 1000 kg/m³. Since the radius of the sphere spans eight cells, the corresponding spatial step size is 1/8 m and the length of one side of the computational domain is 39/8 m. The simulations are run at 98 percent of the Courant limit which corresponds to a temporal step size of 47.3 μ s. Thus, the total duration of the simulations is 24.2 ms (512 time steps). (The simulations were not run exactly at the Courant limit in order to ensure the stability of the absorbing boundary condition. As mentioned previously, the cell-splitting method can be run at the limit.)

Figure 5 shows the scattered pressure measured over the evaluation line when the sphere is realized using a staircase approximation. Results are shown for a nominal discretizations of 10, 20, and 40 points per wavelength (PPW) corresponding to wavelengths of 1.25, 2.50, and 5.0 m. However, because of the duration of the simulation, the temporal step size, and the inherent resolution of the discrete Fourier transform, the discretizations that could be recorded directly from the FDTD simulation and that were closest to the nominal values had PPW's of 10.027, 19.386, and 41.542. Rather than interpolating the FDTD results to the nominal values, the true values were used in the exact solution. Nevertheless, the nominal values will be used to identify the results. Figure 5 shows the exact solution as well the solutions obtained using either the Stair- v or Stair- p realizations of the pressure-release surface. Clearly the Stair- p results are inferior to the Stair- v results.

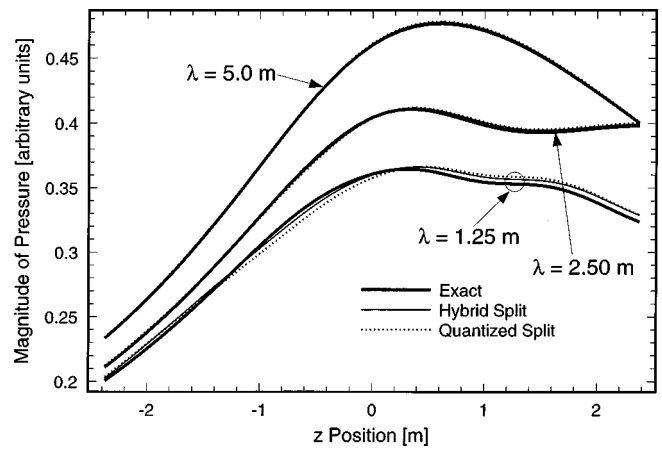


FIG. 6. Scattered pressure at evaluation line obtained using a split-cell realization of the sphere.

Figure 6 shows the scattered pressure measured over the evaluation line when the pressure-release sphere is realized using either the quantized or the hybrid techniques. At discretization of 20 and 40 PPW, the split-cell results are difficult to distinguish from the exact solution. We observe that the hybrid method typically performs slightly better (but only slightly better) than the simpler quantized method.

Figure 7 shows the relative error, given by $|FDTD - exact|/exact$, for discretizations of 10 and 40 PPW for the Stair- v and hybrid methods. At 10 PPW, there are points where the Stair- v method has lower error than the hybrid method. However, the integrated error is obviously much lower for the hybrid method than for the staircased one. At 40 PPW, the hybrid results are superior to the Stair- v results for all points along the evaluation line.

B. Resonances of a sphere

The resonant modes of a sphere of radius a that satisfies a Dirichlet (pressure-release) boundary condition are determined using the FDTD method. The realization of the sphere is similar to that shown in Figs. 3 and 4 except that the region of interest is interior to the sphere. The radius of the sphere is eight cells and will again, for the sake of concreteness, be assigned a physical dimension of 1.0 m.

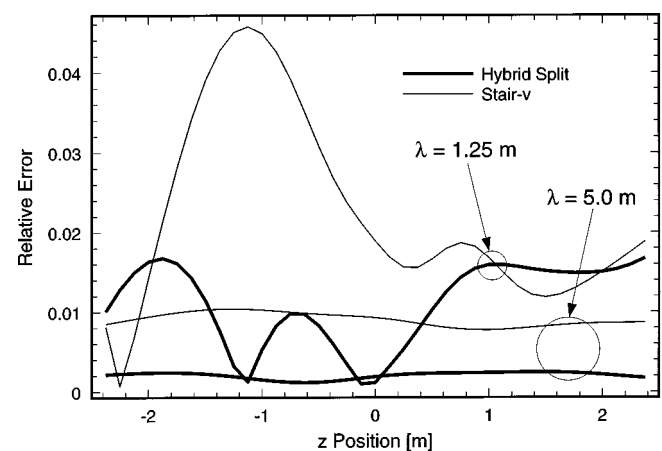


FIG. 7. Relative error in the scattered field obtained using the Stair- v or hybrid split-cell method.

TABLE I. The four lowest resonant frequencies, in Hertz, of a sphere with a radius of 1.0 m bounded by a pressure-release region. The exact frequencies are given in the top row. The data in the other rows were obtained using the FDTD method and the percent error is given in parentheses.

	Resonant mode			
	1	2	3	4
Exact	750.0	1072	1375	1500
Stair- <i>p</i>	724.0 (3.45)	1033 (3.65)	1318 (4.17)	1439 (4.01)
Stair- <i>v</i>	760.2 (1.36)	1085 (1.16)	1384 (0.61)	1510 (0.71)
Quantized	755.6 (0.76)	1078 (0.49)	1374 (0.09)	1502 (0.16)
Hybrid	752.4 (0.33)	1074 (0.14)	1367 (0.61)	1496 (0.23)

The resonant modes are determined by introducing energy into the sphere, running the FDTD simulation while recording the temporal signal at an observation point, and then taking the (fast) Fourier transform (FFT) of the temporal signal and noting the resonances (the way in which energy is introduced “transparently” into the sphere can be found in Ref. 29). The subsequent results were obtained by an automated process, i.e., a computer script was used to coordinate the tasks handled by separate programs and the resonances were found by the computer using a simple set of search rules. Simulations were run for 32 768 time steps at 98 percent of the Courant limit. The spectral resolution for this number of time steps, i.e., the difference between neighboring frequencies “bins” after taking the FFT, was 0.67 Hz. For consistency, the results presented here use the same Courant number as was used for the scattering problem. However, since the resonator does not require absorbing boundary conditions, simulations were also performed at the Courant limit and no unstable behavior was observed.

For a sphere of radius a the frequencies of the resonant modes are given by

$$f = \frac{c}{2\pi a} \zeta_{mp}, \quad (16)$$

where ζ_{mp} represents the p th zero of the spherical Bessel function of order m . The modes with the four lowest resonant frequencies correspond to values of m and p of (0,1), (1,1), (1,2), and (0,2). Table I lists these frequencies, in Hertz, for a sphere with a radius of 1.0 m. Also shown in this table are the resonant frequencies as determined from the FDTD simulations. The percent error, as given by $100 \times |\text{FDTD} - \text{exact}| / \text{exact}$ is given in parentheses. As was the case for the exterior problem, the Stair-*v* realization of the pressure-release surface is clearly better than the Stair-*p* realization. Furthermore, the split-cell methods yield results that are superior to those obtained using either of the staircase schemes. The hybrid method performs better than the quantized method at the lower frequencies, but does not provide a significant improvement at the higher frequencies.

III. CONCLUSIONS

The simplest FDTD implementation of a continuously varying pressure-release surface uses a staircase approximation of the surface. If the staircase approximation is constructed based solely on the locations of the pressure nodes themselves, significant errors may be introduced. An im-

proved staircase representation is obtained by setting to zero those pressure nodes that have any of their neighboring velocities nodes beyond the pressure release boundary. This improvement yields results that are substantially better than those obtained from the method which is based solely on pressure-node locations. This improvement is realized despite the fact that this velocity-based method still ultimately produces a staircase representation of the surface and despite there being essentially no additional computational cost.

Further improvements can be realized by splitting velocity nodes adjacent to the pressure-release boundary. The splitting can be either a simple bisection (quantized split) or one that incorporates more information about where the boundary passes through the cell (hybrid split). The computational cost of these improvements are insignificant compared to the overall computational cost of the simulation. The results obtained using either of these splitting techniques are, in general, superior to those of either of the staircase methods. These methods permit the accurate solution of problems using a coarser grid than would otherwise be possible. For example, we envision that the split-cell methods will make possible the accurate determination in the time domain of scattering from large randomly rough surfaces such as the air-sea interface.

ACKNOWLEDGMENTS

This work was supported by the Office of Naval Research, Code 3210A. We thank Todd Hefner of the Washington State University Physics Department for thought provoking discussions.

- ¹K. S. Yee, “Numerical solution of initial boundary value problems involving Maxwell’s equations in isotropic media,” *IEEE Trans. Antennas Propag.* **14**, 302–307 (1966).
- ²R. Madariaga, “Dynamics of an expanding circular fault,” *Bull. Seismol. Soc. Am.* **66**, 639–666 (1976).
- ³J. Virieux, “*SH*-wave propagation in heterogeneous media: Velocity-stress finite difference method,” *Geophysics* **49**, 1933–1942 (1984).
- ⁴J. Virieux, “*P-SV* wave propagation in heterogeneous media: Velocity-stress finite difference method,” *Geophysics* **51**, 889–901 (1986).
- ⁵C. J. Randall, “Absorbing boundary condition for the elastic wave equation: Velocity-stress formulation,” *Geophysics* **54**, 1141–1152 (1989).
- ⁶D. Botteldooren, “Finite-difference time-domain simulation of low-frequency room acoustic problems,” *J. Acoust. Soc. Am.* **98**, 3302–3308 (1995).
- ⁷J. LoVetri, D. Mardare, and G. Souloff, “Modeling of the seat dip effect using the finite-difference time-domain method,” *J. Acoust. Soc. Am.* **100**, 2204–2212 (1996).
- ⁸R. A. Stephen, “Modeling sea surface scattering by the time-domain finite-difference method,” *J. Acoust. Soc. Am.* **100**, 2070–2078 (1996).
- ⁹F. D. Hastings, J. B. Schneider, and S. L. Broschat, “A finite-difference time-domain solution to scattering from a rough pressure-release surface,” *J. Acoust. Soc. Am.* **102**, 3394–3400 (1997).
- ¹⁰J. G. Maloney and K. E. Cummings, “Adaptation of FDTD techniques to acoustic modeling,” in *11th Annual Review of Progress in Applied Computational Electromagnetics*, Vol. 2, pp. 724–731, Monterey, CA, March 1995.
- ¹¹X. Yuan, D. Borup, J. W. Wiskin, M. Berggren, R. Eidsens, and S. A. Johnson, “Formulation and validation of Berenger’s PML absorbing boundary for the FDTD simulation of acoustic scattering,” *IEEE Trans. Ultrason. Ferroelectr. Freq. Control* **44**, 816–822 (1997).
- ¹²Q. H. Liu and J. Tao, “The perfectly matched layer for acoustic waves in absorptive media,” *J. Acoust. Soc. Am.* **102**, 2072–2082 (1997).
- ¹³J. G. Maloney, K. L. Shlager, and G. S. Smith, “A simple FDTD model

- for transient excitation of antennas by transmission lines," IEEE Trans. Antennas Propag. **42**, 289–292 (1994).
- ¹⁴D. Botteldooren, "Acoustical finite-difference time-domain simulation in a quasi-Cartesian grid," J. Acoust. Soc. Am. **95**, 2313–2319 (1994).
- ¹⁵T. G. Jurgens, A. Taflove, K. Umashankar, and T. G. Moore, "Finite-difference time-domain modeling of curved surfaces," IEEE Trans. Antennas Propag. **40**, 357–366 (1992).
- ¹⁶P. Mezzanotte, L. Roselli, and R. Sorrentino, "A simple way to model curved metal boundaries in FDTD algorithm avoiding staircase approximation," IEEE Microwave Guid. Wave Lett. **5**, 267–269 (1995).
- ¹⁷S. Dey and R. Mittra, "A locally conformal finite-difference time-domain (FDTD) algorithm for modeling three-dimensional perfectly conducting objects," IEEE Microwave Guid. Wave Lett. **7**, 273–275 (1997).
- ¹⁸F. D. Hastings, J. B. Schneider, S. L. Broschat, and E. I. Thorsos, "Scattering from rough fluid-fluid interfaces using the finite-difference time-domain method," J. Acoust. Soc. Am. **101**, 3065(A) (1997).
- ¹⁹W. C. Chew, "Electromagnetic theory on a lattice," J. Appl. Phys. **75**, 4843–4850 (1994).
- ²⁰T. Weiland, "Comment on 'A simple way to model curved metal boundaries in FDTD algorithm avoiding staircase approximation'," IEEE Microwave Guid. Wave Lett. **6**, 183–184 (1996).
- ²¹J. B. Schneider and C. L. Wagner, "Analytic analysis of the CP-FDTD and C-FDTD methods for offset planar boundaries," in IEEE Antennas and Propagat. Soc. Int. Symposium, Vol. 4, pp. 1816–1819, Atlanta, GA, June 1998.
- ²²D. E. Merewether, R. Fisher, and F. W. Smith, "On implementing a numeric Huygen's source scheme in a finite difference program to illuminate scattering bodies," IEEE Trans. Nucl. Sci. **27**, 1829–1833 (1980).
- ²³A. Taflove and K. Umashankar, "Radar cross section of general three-dimensional scatterers," IEEE Trans. Electromagn. Compat. **EMC-25**, 433–440 (1983).
- ²⁴J. Fang, "Time domain finite difference computation for Maxwell's equations," Ph.D. thesis, University of California at Berkeley, Berkeley, CA, 1989.
- ²⁵C. M. Furse, S. P. Mathur, and O. P. Gandhi, "Improvements to the finite-difference time-domain method for calculating the radar cross section of a perfectly conducting target," IEEE Trans. Microwave Theory Tech. **38**, 919–927 (1990).
- ²⁶O. M. Ramahi, "Complementary boundary operators for wave propagation problems," J. Comput. Phys. **133**, 113–128 (1997).
- ²⁷J. B. Schneider and O. M. Ramahi, "The complementary operators method applied to acoustic finite-difference time-domain simulations," J. Acoust. Soc. Am. **104**, 686–693 (1998).
- ²⁸P. M. Morse and H. Feshbach, *Methods of Theoretical Physics* (McGraw-Hill, New York, 1953).
- ²⁹J. B. Schneider, C. L. Wagner, and S. L. Broschat, "Implementation of transparent sources embedded in acoustic finite-difference time-domain grids," J. Acoust. Soc. Am. **103**, 136–142 (1998).

Wave propagation in fluids contained in finite-length anisotropic viscoelastic pipes

Jinghong Yu

Nichirin, Inc., 139 Copernicus Boulevard, Brantford, Ontario N3P 1N4, Canada

Eiichi Kojima

Kanagawa University, 3-27-1, Rokkakubashi, Kanagawa-ku, Yokohama 221, Japan

(Received 21 January 1998; accepted for publication 20 August 1998)

Wave propagation characteristics are studied of a fluid-filled, finite-length anisotropic viscoelastic pipe—a flexible hydraulic hose. An analytical model in transfer matrix form is developed for relating the pressure and flow ripples at hose upstream and downstream. The anisotropic viscoelasticity of the hose wall, the coupled vibration of the hose and the fluid, and the effect of possible longitudinal resonances of the finite-length hose are considered. The static mechanical properties and frequency-dependent mechanical properties of the hose wall are determined by means of specially designed static expansion method and optimal searching method separately. Experimental confirmation is made over a wide frequency range by using an experimental procedure for measuring the transfer matrix parameters. By comparing the predicted and measured results of the hoses with different lengths, it is shown that the model yields fairly good results in a frequency range of around 0–3 kHz and even may predict the influence of longitudinal resonances of the hose wall on the wave propagation of fluid in the hose. The effectiveness of the experimental methods and procedure proposed here are also verified. © 1998 Acoustical Society of America. [S0001-4966(98)00112-X]

PACS numbers: 43.20.Mv, 43.20.Bi, 43.35.Mr, 43.25.Gf [DEC]

LIST OF SYMBOLS

a, b, h	inside, average radii, and thickness of hose wall	u, U	axial displacement of hose wall and its Laplace transform
A_0	inside cross-sectional area of auxiliary cylinder	v, V	fluid velocity and its Laplace transform
Br	Bessel function ratio, $Br(z) = 2J_1(z)/[zJ_0(z)]$	w, W	real radial displacement of hose wall and its Laplace transform
c	sonic velocity in fluid contained in rigid pipe	W'	Laplace transform of apparent radial displacement of hose wall
E_0	average Young's modulus of hose fittings	ϵ	hose strain
E, E^*	normal and complex Young's moduli of hose wall	ϵ_1	strain of the hose with closed, free end
J_0, J_1	zeroth- and first-order Bessel functions of the first kind	ϵ_2	strain of the hose with closed end pulled by a cylinder
Kl	bulk modulus of fluid	λ_i	i th-order wave propagation coefficient ($i = 1, 2$)
l	hose length	μ, μ^*	normal and complex Poisson's ratios of hose wall
p, P	pressure ripple in hose and its Laplace transform	ρ, ρ_p	fluid and hose wall densities
p_0	average pressure in hose	σ	hose stress
p_{C0}	average pressure in auxiliary cylinder	τ	time constant
r_0	inner radius of reference pipe (=9.8 mm)	ν	fluid kinematic viscosity
s	Laplace operator	Subscripts	
t	time	e	of Young's modulus
$T_{11}, T_{12}, T_{21}, T_{22}$	transfer matrix parameters of hose	$l, 1$	of the first-order, relaxation
T_{12}^*, T_{21}^*	values of T_{12} and T_{21} normalized by dividing or multiplying by $\rho c / (\pi r_0^2)$	r	radial coordinate
		$t, 1$	of the first-order, retardation
		$t, 2$	of the second-order, retardation
		x	longitudinal coordinate
		θ	circumferential coordinate
		μ	of Poisson's ratio

INTRODUCTION

With the wide use of flexible hoses for misalignment accommodation purposes and/or for pulsation reduction purposes in fluid power control systems of aerospace equipment, construction machinery, and automotive power steering systems, there is an increasing requirement to develop an accurate model for the pressure ripple transmission, or so-called wave propagation, in fluids contained in the hoses.

During such model development, special attention should be paid to the following facts: (1) since the compliance of the hose wall is near to that of the fluid, the wave propagation in the fluid is greatly affected by the mechanical properties of the hose wall besides the fluid compressibility, (2) the hose wall may exhibit viscoelasticity which is anisotropic in the longitudinal and circumferential directions owing to its special composition of inner rubber, outer rubber, and wire braid, (3) longitudinal resonance of the hose wall may have a significant influence on the coupled motion of the hose and the fluid, and (4) for a finite-length hose, the hose end support conditions exert direct effects on longitudinal vibrations of the hose wall and subsequently the wave propagation in the fluid.

Since 1950, some efforts have been contributed to wave propagation characteristics in viscoelastic fluid pipes. However, in view of the four facts mentioned above, they are not suitable to be applied to actual hoses with finite length, owing to some theoretical imperfection and lack of sufficient experimental verification. For instance, in the theoretical analyses presented by Morgan and Kiely,¹ Klip *et al.*,² and Cox,³ both longitudinal and circumferential motions of the pipe wall were considered, but the fluid was assumed to be incompressible. In the studies on wave propagation in compressible fluid through viscoelastic pipes shown by Nakano *et al.*,⁴ Gally *et al.*,⁵ Rieutord,⁶ and Suo and Wylie,⁷ stiff longitudinal constraint of the pipe wall was assumed. Longmore and Schlesinger⁸ and Nakano and Abo-Ismaïl^{9,10} have tried to include the fluid compressibility and both the longitudinal and circumferential motions of the pipe wall in their theories, but their experimental investigation was limited to a low frequency of about 0–400 Hz. Moreover, in almost all these studies, the pipe wall was assumed to be infinite length and therefore the effect of pipe end support conditions on the wave propagation characteristics of the pipe was not included. With regard to the coupled vibrations of a pipe and the fluid in the pipe, in recent years, Wiggert *et al.*¹¹ considered the effect of pipe elbow restraint on the pressure transients in the elbow; Lesmez *et al.*¹² presented a study on the Poisson-coupled vibrations in an elastic pipe and the fluid in the pipe, and obtained transfer matrix equations relating the amplitude quantities of motion transmitted through a length of pipe. The amplitude relationship is good enough for modal analysis and useful for deriving the transmission loss matrix of pipe systems,¹³ but not enough for studying the complete transmission of pressure wave (both amplitude and phase) through a viscoelastic pipe.

Recently a research for a relatively long hose considering the anisotropic viscoelasticity of the hose wall and in-

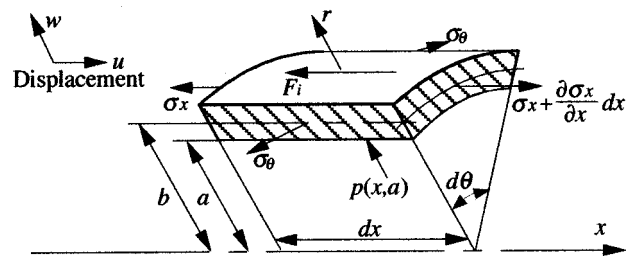


FIG. 1. Forces acting on a hose wall element.

cluding both the radial and longitudinal motions of the hose wall has been carried out by the authors.^{14,15} A mathematical model has been proposed that was found to be able to provide an approximate coincidence between the theoretical results and measured data but failed to predict the effect of longitudinal vibrations of the hose wall. In this paper, the research is extended to the practical situation of a finite-length hose under anchored end conditions, trying to develop a more accurate model which even may predict the effect of longitudinal resonances of the hose. Methods for determining mechanical properties of the hose wall and experimental procedure for determining transfer matrix parameters of the hose over a wide frequency range of 0–30 kHz are also proposed.

I. THEORETICAL DEVELOPMENT

A. Assumptions

- (1) The hose is straight, linear, and cylindrical, and of finite length while the upstream and downstream ends are fixed through the hose fittings bolted to steel blocks.
- (2) The hose wall exhibits anisotropic viscoelasticity in the longitudinal and circumferential directions. Both the longitudinal and radial motions of the hose wall are involved in the coupling hydrodynamics of the hose and fluid.
- (3) The compliance of the hose wall may be so great that it is near to or the same order as that of the fluid.
- (4) The fluid is isotropic, viscous and compressible, and its motion is laminar and axially symmetric.
- (5) The temperature variations are small enough so that the fluid viscosity and the hose wall viscoelasticity may be considered to be constant.
- (6) Only small disturbances in the fluid pressure and flow, that is, pressure and flow ripples, are considered.

B. Equations of motion of the hose and the fluid

While considering long wavelengths, the elementary membrane shell theory¹⁶ may be applied in formulating the motion of the hose wall. By neglecting the flexural stiffness, transverse-shear stiffness, and the rotatory-inertia term according to the shell membrane theory, omitting the radial inertia and the fluid viscous friction on the inner surface of the hose, and including the fluid pressure force, the forces acting on a hose wall element may be shown in Fig. 1. From

the figure, the stress equations of motion of the hose wall may be given as

$$h\sigma_\theta - ap(x,a) = 0, \quad (1)$$

$$\frac{\partial(h\sigma_x)}{\partial x} - Fi = 0, \quad (2)$$

where

$$Fi = h\rho_p \frac{\partial^2 u}{\partial t^2}.$$

Eliminating the component of normal strain and stress in the radial direction, the stress-strain relations for the other two normal stress components of the hose wall are assumed to be the following form which consists of the complex Young's moduli and complex Poisson's ratios:

$$\sigma_x = \frac{E_x^*}{1 - \mu_\theta^* \mu_x^*} (\epsilon_x + \mu_\theta^* \epsilon_\theta), \quad (3)$$

$$\sigma_\theta = \frac{E_\theta^*}{1 - \mu_\theta^* \mu_x^*} (\epsilon_\theta + \mu_x^* \epsilon_x), \quad (4)$$

where the strains ϵ_x and ϵ_θ may be assumed to be

$$\epsilon_x = \partial u / \partial x, \quad (5)$$

$$\epsilon_\theta = w / b. \quad (6)$$

Substituting σ_θ and σ_x in Eqs. (1) and (2) by Eqs. (3)–(6) gives the displacement equations of motion of the hose wall:

$$\begin{aligned} \frac{\partial^2 W'}{\partial x^2} - \lambda_0^2 W' = & - \frac{(1 - \mu_\theta^* \mu_x^*) ab \rho_p s^2}{hE_{\theta 1}^* E_x^*} P(x,a,s) \\ & + \frac{abE_{x 2}^*}{hE_{\theta 1}^* E_x^*} \frac{\partial^2 P(x,a,s)}{\partial x^2}, \end{aligned} \quad (7)$$

$$\frac{\partial^2 U}{\partial x^2} - \lambda_0^2 U = - \frac{a\mu_\theta^*}{hE_\theta^*} \frac{\partial P(x,a,s)}{\partial x}, \quad (8)$$

where

$$W' = W + aP(x,a,s)/(2K_l),$$

$$\lambda_0 = \sqrt{\rho_p s^2 / E_x^*},$$

$$E_{\theta 1}^* = E_\theta^* K_l^* / (E_\theta^* + K_l^*),$$

$$E_{x 1}^* = E_x^* K_l^* / (E_\theta^* + K_l^*),$$

$$E_{x 2}^* = E_x^* [1 - \mu_\theta^* \mu_x^* E_\theta^* / (E_\theta^* + K_l^*)],$$

$$K_l^* = 2(1 - \mu_\theta^* \mu_x^*) b K_l / h.$$

In the derivation of Eqs. (7) and (8), the fluid compressibility is included, through the relationship between the real and apparent displacements of the hose wall in the radial direction, in the compliance of the hose wall due to the assumption of large compliance.

Now that the effect of the fluid compressibility is turned into the compliance of the hose wall, the simplified Navier–Stokes equations (9) and (10) and continuity equation (11)

for a viscous, incompressible fluid may be applied, where the motion contains negligible convective inertia due to the assumption of small disturbances and the velocity component and all derivatives with respect to θ vanish due to the assumption of axial symmetry:

$$\frac{\partial v_r}{\partial t} = - \frac{1}{\rho} \frac{\partial p}{\partial r} + \nu \left(\frac{\partial^2}{\partial r^2} + \frac{\partial}{r \partial r} + \frac{\partial^2}{\partial x^2} \right) v_r - \nu \frac{v_r}{r^2}, \quad (9)$$

$$\frac{\partial v_x}{\partial t} = - \frac{1}{\rho} \frac{\partial p}{\partial x} + \nu \left(\frac{\partial^2}{\partial r^2} + \frac{\partial}{r \partial r} + \frac{\partial^2}{\partial x^2} \right) v_x, \quad (10)$$

$$\frac{\partial v_r}{\partial r} + \frac{v_r}{r} + \frac{\partial v_x}{\partial x} = 0. \quad (11)$$

The general solutions of Eqs. (9)–(11) are obtained as follows in terms of calculus of variations while only the first- and second-order solutions are considered,⁴

$$\begin{aligned} V_r(x,r,s) = & \sum_{i=1}^2 (C_i e^{\lambda_i x} + D_i e^{-\lambda_i x}) J_1(r\lambda_i) + \sum_{i=1}^2 \frac{\nu \lambda_i}{s} \\ & \times (A_i e^{\lambda_i x} - B_i e^{-\lambda_i x}) J_1(r\sqrt{\lambda_i^2 - s/\nu}), \end{aligned} \quad (12)$$

$$\begin{aligned} V_x(x,r,s) = & \sum_{i=1}^2 (-C_i e^{\lambda_i x} + D_i e^{-\lambda_i x}) J_0(r\lambda_i) \\ & - \sum_{i=1}^n \frac{\nu \sqrt{\lambda_i^2 - s/\nu}}{s} (A_i e^{\lambda_i x} + B_i e^{-\lambda_i x}) \\ & \times J_0(r\sqrt{\lambda_i^2 - s/\nu}), \end{aligned} \quad (13)$$

$$P(x,r,s) = \sum_{i=1}^2 \frac{s\rho}{\lambda_i} (C_i e^{\lambda_i x} + D_i e^{-\lambda_i x}) J_0(r\lambda_i), \quad (14)$$

where A_i , B_i , C_i , D_i , and λ_i are the constants of integration to be determined (λ_i is also called the wave propagation coefficient).

C. Boundary conditions at the hose ends and interface between the hose wall and fluid

Boundary conditions at the upstream and downstream ends of the hose wall may be specified by Eqs. (15) and (16) while treating the hose fittings as elastic pipes.

At the upstream end ($x=0$):

$$W'(0,s) = \frac{ab}{hE_0^*} P(0,a,s), \quad U(0,s) = 0. \quad (15)$$

At the downstream end ($x=l$):

$$W'(l,s) = \frac{ab}{hE_0^*} P(l,a,s), \quad U(l,s) = 0, \quad (16)$$

where $E_0^* = 2bK_l E_0 / (hE_0 + 2bK_l)$.

The boundary condition coupling the motions of the hose wall and fluid may be specified as that the radial velocity components of the hose wall and fluid are continuous at the interface ($r=a$) for any x position within the length limit of the hose, that is,

$$V_r(x,a,s) = sW'(x,s), \quad 0 \leq x \leq l. \quad (17)$$

In order to derive the wave propagation coefficient, a boundary condition coupling the motions of the hose wall and fluid in the longitudinal direction is also needed. This condition may be assumed to be the following approximate equation:

$$\begin{aligned} V_x(0,a,s) &= sU(0,s) = 0, \\ V_x(l,a,s) &= sU(l,s) = 0. \end{aligned} \quad (18)$$

D. Solution of basic equations

From Eqs. (7), (12), and (14)–(17), relationships among A_i , B_i , C_i , D_i , λ_i ($i=1,2$) may be given by the following equations:

$$\text{one of } \lambda_1 \text{ and } \lambda_2 \text{ (say, } \lambda_1) = \lambda_0, \quad (19)$$

$$C_1 = D_1 = 0, \quad (20)$$

$$\frac{C_2}{A_2} = -\frac{D_2}{B_2} = \frac{2\nu J_1(ja\sqrt{s/\nu})}{asJ_0(a\lambda_2)} \frac{1}{\xi - 1}, \quad (21)$$

$$A_1 = -g\{A_2e^{\lambda_2 l} - B_2e^{-\lambda_2 l} - (A_2 - B_2)e^{-\lambda_0 l}\}, \quad (22)$$

$$B_1 = -g\{A_2e^{\lambda_2 l} - B_2e^{-\lambda_2 l} - (A_2 - B_2)e^{\lambda_0 l}\}, \quad (23)$$

where

$$\xi = \frac{2b\rho s^2}{(\lambda_2^2 - \lambda_0^2)hE_{\theta 1}^*} \left\{ \frac{E_{x2}^*}{E_x^*} - (1 - \mu_{\theta}^* \mu_x^*) \frac{\lambda_0^2}{\lambda_2^2} \right\},$$

$$g = \frac{\lambda_2}{2 \sinh(\lambda_0 l) \lambda_0} \frac{\xi - \lambda_b^2/\lambda_2^2}{\xi - 1},$$

$$\lambda_b = \sqrt{2b\rho s^2/(hE_0^*)}.$$

The following approximation was used in the derivation:

$$\text{Br}(a\lambda_2) \approx 1, \quad \lambda_0^2 - s/\nu \approx -s/\nu, \quad \lambda_2^2 - s/\nu \approx -s/\nu. \quad (24)$$

From Eqs. (8), (13), (14), and (18), the relationships (19)–(23), and the foregoing approximation, the following characteristic equation concerning the second-order wave propagation coefficient λ_2 may be derived:

$$\begin{aligned} \sinh(\lambda_2 l) [\eta^2 + (\xi\beta_0)^2] + 2\eta\xi\beta_0 [\text{cosech}(\lambda_0 l) \\ - \cosh(\lambda_2 l)\coth(\lambda_0 l)] = 0, \end{aligned} \quad (25)$$

where

$$\eta = \xi - 1 + B_r(ja\sqrt{s/\nu}),$$

$$\beta_0 = \lambda_2/\lambda_0 - \lambda_b^2/(\lambda_2\lambda_0\xi).$$

By using Eq. (25), it is possible to determine the values of λ_2 numerically.

Now, consider two boundary conditions of the fluid on x , $x=0$ and $x=l$, and define $P_1(s)$, $Q_1(s)$ and $P_2(s)$, $Q_2(s)$ as the cross-sectionally averaged pressure ripples and flow ripples at the hose upstream and downstream, respectively. By substituting Eqs. (19)–(24) in Eqs. (13) and (14), an analytical model relating the fluidborne pressure and flow ripples at the hose upstream and downstream may be obtained in the following transfer matrix form:

$$\begin{bmatrix} P_1(s) \\ Q_1(s) \end{bmatrix} = \begin{bmatrix} T_{11} & T_{12} \\ T_{21} & T_{22} \end{bmatrix} \begin{bmatrix} P_2(s) \\ Q_2(s) \end{bmatrix}, \quad (26)$$

where

$$T_{11} = T_{22} = \cosh(\lambda_2 l) + \frac{(\beta_2 - 1)\beta_0\beta_1}{1 - \beta_0\beta_1} \cosh(\lambda_0 l),$$

$$T_{12} = Z_c(s) \sinh(\lambda_2 l) + \frac{\beta_0\beta_1^2}{1 - \beta_0\beta_1} Z_c(s) \sinh(\lambda_0 l),$$

$$T_{21} = \frac{\sinh(\lambda_2 l)}{Z_c(s)} + \frac{(\beta_0\beta_1 - \beta_1^2 + 2\beta_3)\beta_0}{1 - \beta_0\beta_1} \frac{\sinh(\lambda_0 l)}{Z_c(s)},$$

$$\beta_1 = \sinh(\lambda_2 l)/\sinh(\lambda_0 l),$$

$$\beta_2 = \cosh(\lambda_2 l)/\cosh(\lambda_0 l),$$

$$\beta_3 = \cosh(\lambda_2 l)[\cosh(\lambda_2 l) - \cosh(\lambda_0 l)]/\sinh^2(\lambda_0 l),$$

$$Z_c(s) = \rho s/(\pi a^2 \lambda_2 \xi).$$

It is obvious that all of the transfer matrix parameters, T_{11} , T_{12} , T_{21} , and T_{22} , are composed of two items, the first of which has the same form as existing models (named the “fluid mode”), and the second of which represents the direct influence of the support condition at the hose ends (named the “pipe mode”). Moreover, the new model may be easily simplified to some existing simple models (such as those in Refs. 4, 7, and 17). For instance, just by specifying zero μ_{θ}^* , μ_x^* and the same values for E_0 as E_{θ}^* , the model turns out to be the circumferentially viscoelastic and longitudinally rigid model in Ref. 4.

II. PROCEDURE FOR DETERMINING TRANSFER MATRIX PARAMETERS OF HOSES

To verify the validity of the new model, Eq. (26), it is required to measure the transfer matrix parameters of the hose over wide frequency range. The measurement is made by means of a kind of experimental procedure which was originally developed by To and Doige^{18,19} and Chung and Blaser^{20,21} for the assessment of the properties of acoustic systems. The basic principle of the procedure is that if the unknown unit under test is connected in series with two theoretically known reference pipes, such as uniform rigid pipes, at the upstream and downstream, respectively, the transfer matrix parameters of the unknown unit can be expressed in terms of those of the reference pipes and the pulsating pressures at four different locations on the reference pipes. The detailed equations are given in the Appendix.

The hydraulic circuit for measuring the transfer matrix parameters is shown in Fig. 2. An axial piston pump driven by a variable speed electric motor was used to generate wide-band pulsation source. The test hose was connected in series with two uniform rigid pipes, that is, the reference pipes, on which four piezoelectric pressure transducers were so mounted that their diaphragms were flush with the inside walls of the pipes. The two reference pipes formed the measuring sections where the standing waves were analyzed, and the standing waves could be varied by the alternative use of the two loading valves which were separated by an extension pipe. Signals taken from pressure transducers 1 and 2, 2 and

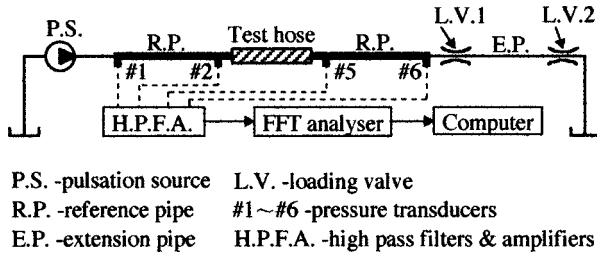


FIG. 2. Schematic diagram of test circuit for measuring the transfer matrix of hoses.

5, and 5 and 6 were simultaneously fed into the A/D converter of a two-channel FFT analyzer through high-pass filters and amplifiers, respectively. After Fourier transform the data were transferred to a computer where an averaging operation was performed and transfer matrix parameters were calculated. The results were then modified to represent the transfer matrix parameters of only the hose part of the hose assembly by excluding the effect of the hose fittings which could be considered as rigid pipes.

A result of the application of the procedure to a rigid pipe is shown in Fig. 3. The theoretical results given by the existing rigid pipe model are also shown in this figure. It is evident that the procedure can provide results with sufficient accuracy over a wide frequency range of 0–3 kHz.

III. METHODS FOR DETERMINING MECHANICAL PROPERTIES OF THE HOSE WALL

A. Representation for the hose wall

The viscoelasticity of the hose wall is assumed to be represented by two Kelvin–Voigt elements connected in series, as shown in Fig. 4. According to this representation, the complex Young’s moduli and complex Poisson’s ratios in Eq. (26) may be given by the following equations. It is obvious that the viscoelastic properties of the hose wall are governed by the normal Young’s moduli and normal Poisson’s ratios representing the static mechanical properties and the retardation and relaxation time constants representing the frequency-dependent mechanical properties:

$$\begin{aligned}
 E_{\theta}^* &= E_{\theta}(1 + \tau_{e\theta,t,1} \cdot s + \tau_{e\theta,t,2} \cdot s^2) / (1 + \tau_{e\theta,l,1} \cdot s) \\
 E_x^* &= E_x(1 + \tau_{ex,t,1} \cdot s + \tau_{ex,t,2} \cdot s^2) / (1 + \tau_{ex,l,1} \cdot s) \\
 \mu_{\theta}^* &= \mu_{\theta}(1 + \tau_{\mu\theta,t,1} \cdot s + \tau_{\mu\theta,t,2} \cdot s^2) / (1 + \tau_{\mu\theta,l,1} \cdot s) \\
 \mu_x^* &= \mu_x(1 + \tau_{\mu x,t,1} \cdot s + \tau_{\mu x,t,2} \cdot s^2) / (1 + \tau_{\mu x,l,1} \cdot s).
 \end{aligned} \tag{27}$$

B. Normal Young’s moduli and Poisson’s ratios

The values of the normal Young’s moduli and normal Poisson’s ratios may be determined by a specially designed static expansion experiment on the hose. In the experiment, the components of normal strain in the circumferential and longitudinal directions are measured by strain gauges, on two boundary conditions of the axially free downstream end and the downstream end pulled by an auxiliary hydraulic cylinder, respectively, as shown in Fig. 5. The components of normal stress in the circumferential and longitudinal directions may be assumed as

(a) the case of closed and free end,

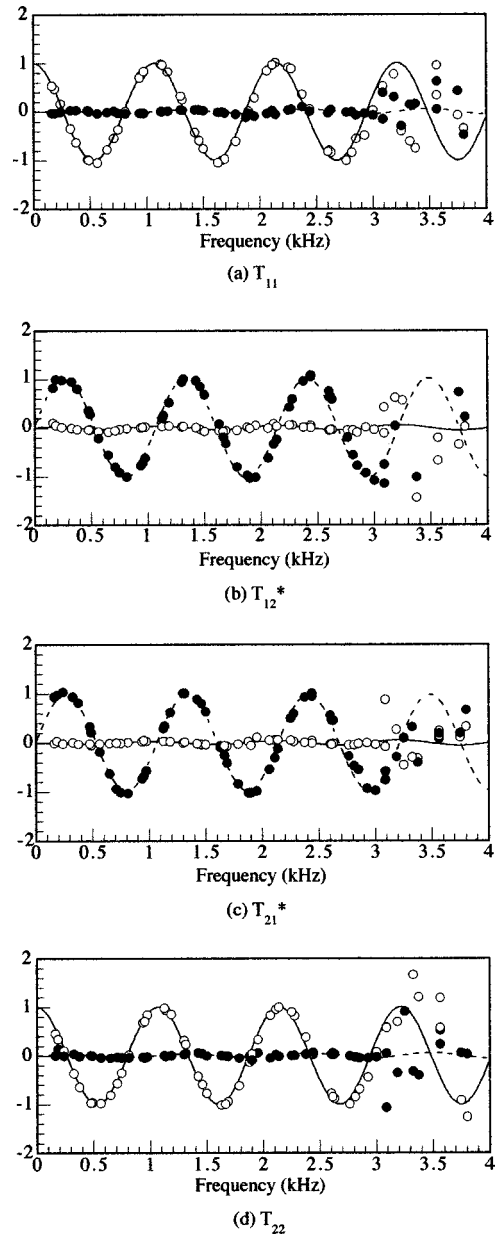


FIG. 3. Transfer matrix parameters of a rigid pipe (length=1.27 m, inside radius=0.0098 m) (○: measured real part; ●: measured imaginary part; —: calculated real part; ----: calculated imaginary part).

$$\sigma_{\theta 1} = \frac{a}{h} p_0, \quad \sigma_{x 1} = \frac{a^2}{2bh} p_0; \tag{28}$$

(b) the case of closed end pulled by the cylinder,

$$\sigma_{\theta 2} = \frac{a}{h} p_0, \quad \sigma_{x 2} = \frac{a^2}{2bh} p_0 + \frac{A_0}{2\pi bh} p_{c0}. \tag{29}$$

Using the stress–strain relations (3) and (4) and setting zero the retardation and relaxation time constants, from the measured strain and calculated stress, the values for the nor-

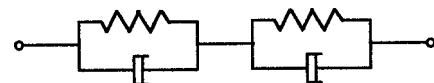


FIG. 4. Representation for the hose wall.

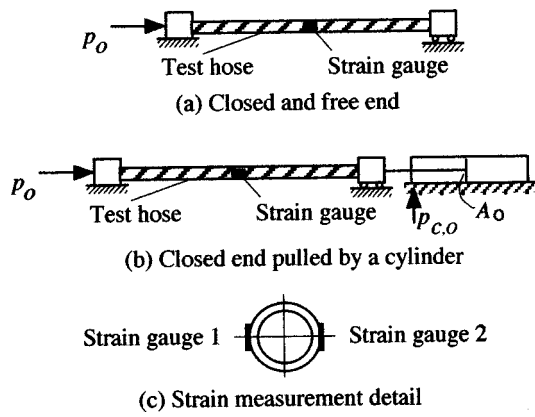


FIG. 5. Hose boundary conditions and strain gauge installation in the static expansion test.

mal Young's moduli and normal Poisson's ratios can be determined by the following equations:

$$\begin{aligned}
 E_{\theta} &= (\sigma_{\theta 1} \sigma_{x 2} - \sigma_{\theta 2} \sigma_{x 1}) / (\sigma_{x 2} \epsilon_{\theta 1} - \sigma_{x 1} \epsilon_{\theta 2}), \\
 E_x &= (\sigma_{x 1} \sigma_{\theta 2} - \sigma_{x 2} \sigma_{\theta 1}) / (\sigma_{\theta 2} \epsilon_{x 1} - \sigma_{\theta 1} \epsilon_{x 2}), \\
 \mu_{\theta} &= (\sigma_{x 1} \epsilon_{x 2} - \sigma_{x 2} \epsilon_{x 1}) / (\sigma_{x 2} \epsilon_{\theta 1} - \sigma_{x 1} \epsilon_{\theta 2}), \\
 \mu_x &= (\sigma_{\theta 1} \epsilon_{\theta 2} - \sigma_{\theta 2} \epsilon_{\theta 1}) / (\sigma_{\theta 2} \epsilon_{x 1} - \sigma_{\theta 1} \epsilon_{x 2}).
 \end{aligned} \tag{30}$$

C. Time constants

It is difficult to determine the retardation and relaxation time constants directly from the actual deformation of the hose wall. For this reason, an indirect method is proposed. In this method, values for the transfer matrix parameters T_{11} , T_{12} , T_{21} , and T_{22} are experimentally measured for a relatively long hose first. Then, the appropriate values of the time constants are so searched that their substitution in the approximate anisotropic viscoelastic model in Ref. 14 results in the best possible coincidence between the measured and calculated values of the transfer matrix parameters. For such a search, an optimization method, the complex method of constrained optimization proposed by Box,²² is applied, where the vector consisting of the time constants is the variable to be optimized and the sum of the square of the error between the experimental transfer matrix parameters and those calculated is the objective function to be minimized.

IV. EXPERIMENTAL CONFIRMATION AND DISCUSSIONS

A. The test hose and its constants

A type of thick wire-reinforced hydraulic rubber hose was used as the hose under test. The hoses have an internal radius of 9.5 mm, average wall radius of 12.1 mm, density of 2557 kg/m³. Using the foregoing determination methods, the normal Young's moduli, normal Poisson's ratios, and retardation and relaxation time constants were obtained, and they were found to be dependent on pressure and temperature. Herein are only the conditions of 14-MPa average pressure and 40 °C fluid temperature considered. For such conditions, the constants of the mechanical behavior of the hose wall are

$$E_{\theta} = 10.14 \text{ GPa}, \quad E_x = 2.60 \text{ GPa},$$

$$\mu_{\theta} = 1.58, \quad \mu_x = 0.60,$$

$$\tau_{e\theta,t,1} = 2.00 \text{ ms}, \quad \tau_{e\theta,t,2} = 0.02 \text{ ms}^2,$$

$$\tau_{e\theta,l,1} = 0.38 \text{ ms},$$

$$\tau_{ex,t,1} = 36.6 \text{ ms}, \quad \tau_{ex,t,2} = 0.13 \text{ ms}^2,$$

$$\tau_{ex,l,1} = 23.2 \text{ ms},$$

$$\tau_{\mu\theta,t,1} = 4.70 \text{ ms}, \quad \tau_{\mu\theta,t,2} \approx 0, \quad \tau_{\mu\theta,l,1} = 5.06 \text{ ms},$$

$$\tau_{\mu x,t,1} = 1.80 \text{ ms}, \quad \tau_{\mu x,t,2} \approx 0, \quad \tau_{\mu x,l,1} = 6.95 \text{ ms}.$$

During the test, the density, kinematic viscosity, and bulk modulus of the hydraulic oil were 875 kg/m³, 30 mm²/s, and 1.65 GPa, respectively.

B. Predicted and measured results of the transfer matrix parameters of the hose

Figure 6 illustrates the predicted and measured results of the transfer matrix parameters of the test hose with 1.27-m length, where the former was obtained by using the new model and the constants given previously and the latter by using the experimental procedure in Sec. II. The figure apparently shows a satisfying agreement between the calculated and measured results within the full frequency range. The agreement displays not only in the general coincidence but also in the coincidence at special frequencies at which the longitudinal resonances of the hose under anchored end conditions possibly occurred. The same model and model constants were also applied to predict the transfer matrix parameters of the hoses with different lengths. Figure 7 shows the predicted and measured results for the test hose of 0.83-m length. Good agreement is observed between the predicted and measured data. It is clear that the new model can give results with sufficient accuracy and the methods for determining the mechanical properties of the hose wall are effective.

To clarify the underlying mechanism of the transfer matrix of the hose, each term of T_{11} , T_{12} , T_{21} , and T_{22} is calculated and compared. Figure 8 indicates such a result for T_{12}^* (normalized T_{12}) of the 1.27-m-long hose, where $T_{12}^*(1)$ denotes the first term of T_{12}^* (that is, the "fluid mode") and $T_{12}^*(2)$ the second term of T_{12}^* (that is, the "pipe mode"). It is shown that the resonant vibration of the hose wall exerts great influence on both the "fluid mode" and "pipe mode." Since the longitudinal resonances of the hose wall under anchored end conditions occur while $\sinh(\lambda_0 l)$ reaches minimum, it is easy to get the calculation equation (31) for the natural frequencies f_c of longitudinal vibrations of the hose wall. Using Eq. (31), the natural frequencies for the 1.27-m-long hose were obtained approximately as 498, 996, 1494, 1992 Hz, and so on. By comparing these results with resonant frequencies of the "pipe mode" shown in Fig. 8, it is found that the resonant frequencies of the "pipe mode" agree with the natural frequencies f_c of longitudinal vibrations of the hose wall. This also indirectly proves the validity of the new model developed and the experimental methods proposed here:

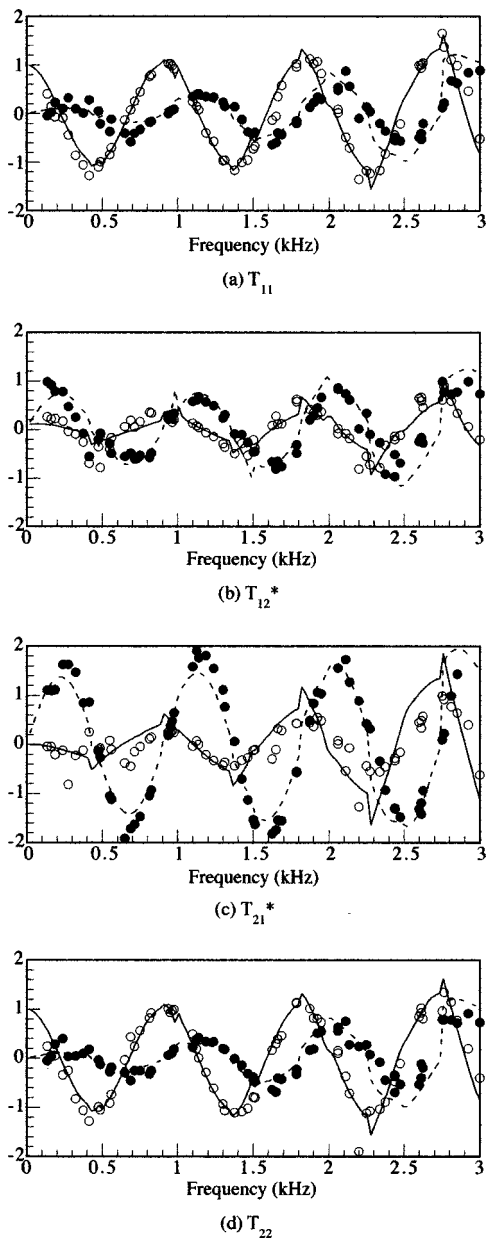


FIG. 6. Transfer matrix parameters of the test hose (length=1.27 m, inside radius=0.0095 m) (○: measured real part; ●: measured imaginary part; —: calculated real part; ---: calculated imaginary part).

$$f_c = \frac{i}{2l} \sqrt{\frac{E_x^*}{\rho_p}}, \quad i = 1, 2, 3, \dots \quad (31)$$

It is also revealed in Fig. 8 that the resonant frequencies of the “fluid mode” are smaller than those of the “pipe mode” for the same harmonics. This phenomenon results from the fact that the wave lengths of radial vibrations of the hose wall are larger, due to the radial elasticity and longitudinal rigidity of the hose fittings, than those of the longitudinal vibrations while the “fluid mode” is directly related to the radial motion of the hose wall.

The new model is compared with several existing models by theoretical computations in which necessary constants of the hose wall and fluid are from those given in the preceding section. Figure 9 shows a comparison of the calculated results of the real parts of T_{11} and T_{12}^* , where the solid

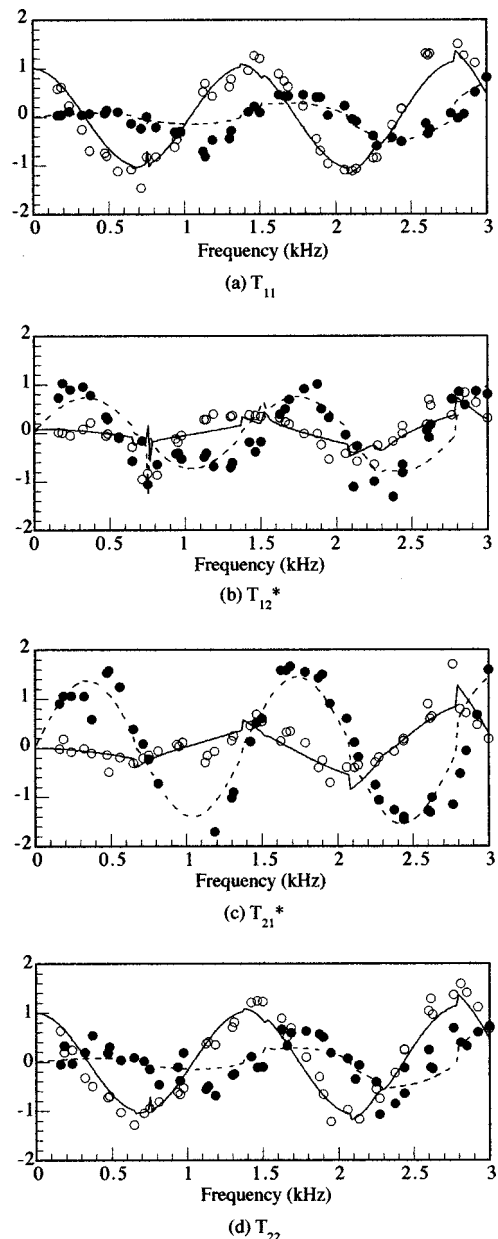


FIG. 7. Transfer matrix parameters of the test hose (length=0.83 m, inside radius=0.0095 m) (○: measured real part; ●: measured imaginary part; —: calculated real part; ---: calculated imaginary part).

line denotes the new model, the dashed line shows the approximate anisotropic viscoelastic model proposed by the authors,¹⁵ the dashed shows the circumferentially viscoelastic and longitudinally rigid model⁴ and the dotted line the anisotropic elastic model (just as one special case of the new model by specifying zero retardation and relaxation time constants). It is found that (1) only the new model may predict the influence of the longitudinal vibrations of the hose wall, (2) the approximate anisotropic viscoelastic model may give general prediction with accuracy except at resonant frequencies, (3) the circumferentially viscoelastic and longitudinally rigid model can only be used as an approximation in the low range of frequencies below 1 kHz, and (4) the elastic model cannot be employed for the hose owing to its great deviation from the actual data.

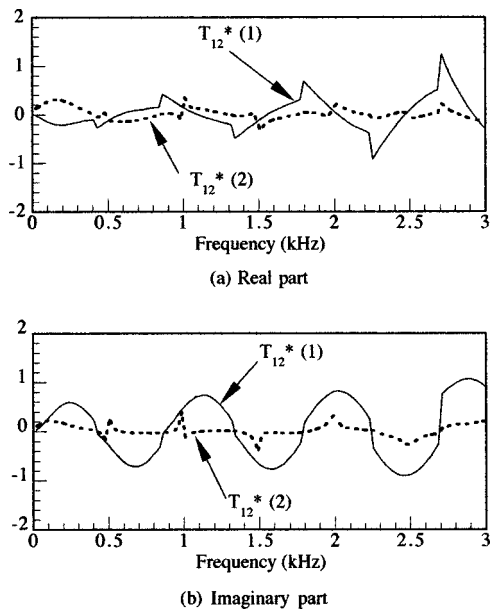


FIG. 8. Components of transfer matrix parameter T_{12}^* of the 1.27-m-long hose.

V. CONCLUSIONS

An analytical model for the wave propagation in the fluid contained within a special anisotropic viscoelastic pipe, a hydraulic flexible hose with finite length under anchored end conditions, has been developed in transfer matrix representation relating the pressure and flow ripples at the pipe upstream and downstream. The validity of the model has been investigated by the comparison of its predicted results and those obtained from measurement, for the hoses with different lengths. It has been shown that the model may yield fairly good results in a wide frequency range of up to around 3 kHz and even may achieve what existing models failed to

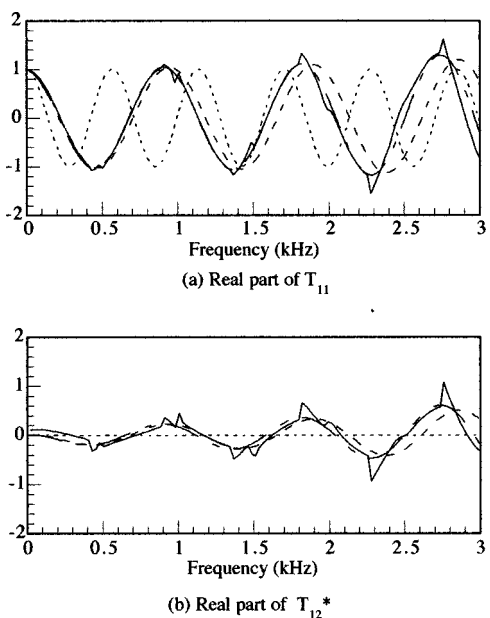


FIG. 9. Theoretical comparison of the new model and some existing models for the 1.27-m-long hose.

do, that is, predicting the influence of longitudinal resonances of the hose wall on the wave propagation of the fluid in the hose.

The methods proposed here for determining the normal Young's modulus and Poisson's ratio and the relaxation and retardation time constants of the hose wall have been found to be a useful solution to the difficult problem in finding mechanical properties of the pipewall of anisotropic viscoelastic pipes. The experimental procedure for determining the transfer matrix parameters of the hose has been proved to be able to provide results with sufficient accuracy over a wide frequency region.

It was also shown that for flexible hydraulic hoses, the approximate anisotropic viscoelastic model¹⁵ may give general prediction with accuracy except at resonant frequencies, the circumferentially viscoelastic and longitudinally rigid model may only give acceptable prediction in low frequency range, and the elastic model may not be applied.

ACKNOWLEDGMENTS

The study was one part of the first author's work at Kanagawa University as a researcher. Thanks are given to Dr. Shinada and former students T. Kitsugawa and S. Sudo, Kanagawa University, for their assistance during the testing. The first author would also like to thank his colleagues in Nichirin Inc. for their encouragement during the preparation and submission of the paper.

APPENDIX: BASIC EQUATIONS FOR TRANSFER MATRIX MEASUREMENT

Consider the test hose (unknown system) connected in series with two theoretically known reference systems, such as the two uniform steel (rigid) pipes, in a fluid power circuit as shown in Fig. A1. Let $[\gamma]$, $[\epsilon]$, $[\xi]$, $[\delta]$, $[\eta]$, and $[\kappa]$ denote the transfer matrices for the individual elements comprising the reference pipes. All these transfer matrices can be calculated by using the existing theory for two-dimensional and unsteady laminar flow in pipes^{23,24} as well as the lengths and diameters of the pipes and the physical constants of the fluid.

The pressure ripples and flow ripples at the upstream ③ and downstream ④ of the hose may be related by a four-pole model as follows:

$$\begin{bmatrix} P_3 \\ Q_3 \end{bmatrix} = \begin{bmatrix} T_{11} & T_{12} \\ T_{21} & T_{22} \end{bmatrix} \begin{bmatrix} P_4 \\ Q_4 \end{bmatrix}. \quad (\text{A1})$$

An examination of Eq. (A1) clearly indicates that two independent sets of data are necessary for the extraction of four unknown matrix parameters T_{11} to T_{22} . This can be

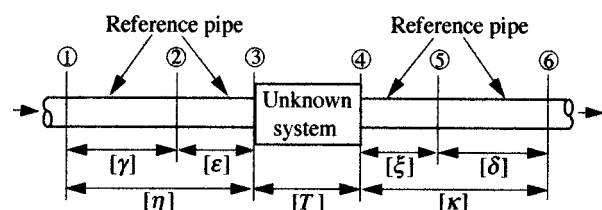


FIG. A1. Illustration of the basic principle for transfer matrix measurement.

achieved by employing two different loading conditions at the downstream of location ⑥.

By manipulating the matrix equations for the hose and reference pipes algebraically, the matrix parameters of the hose can be expressed as

$$T_{11} = \frac{H_{34}Z_4 - H'_{34}Z'_4}{Z_4 - Z'_4}, \quad (\text{A2})$$

$$T_{12} = -\frac{(H_{34} - H'_{34})Z_4Z'_4}{Z_4 - Z'_4}, \quad (\text{A3})$$

$$T_{21} = \frac{(Z_4/Z_3)H_{34} - (Z'_4/Z'_3)H'_{34}}{Z_4 - Z'_4}, \quad (\text{A4})$$

$$T_{22} = -\frac{(H_{34}/Z_3 - H'_{34}/Z'_3)Z_4Z'_4}{Z_4 - Z'_4}, \quad (\text{A5})$$

where

$$H_{34} = \frac{(\gamma_{12}\eta_{11} - \gamma_{11}\eta_{12})(P_1/P_2) + \eta_{12}}{(\delta_{12}\kappa_{11} - \delta_{11}\kappa_{12})(P_6/P_5) + \kappa_{12}} \cdot \frac{\delta_{12}(P_2/P_5)}{\gamma_{12}},$$

$$H'_{34} = \frac{(\gamma_{12}\eta_{11} - \gamma_{11}\eta_{12})(P'_1/P'_2) + \eta_{12}}{(\delta_{12}\kappa_{11} - \delta_{11}\kappa_{12})(P'_6/P'_5) + \kappa_{12}} \cdot \frac{\delta_{12}(P'_2/P'_5)}{\gamma_{12}},$$

$$Z_3 = \frac{-\epsilon_{12}(P_1/P_2) + (\epsilon_{12}\gamma_{11} + \epsilon_{22}\gamma_{12})}{\epsilon_{11}(P_1/P_2) - (\epsilon_{21}\gamma_{12} + \epsilon_{11}\gamma_{11})},$$

$$Z'_3 = \frac{-\epsilon_{12}(P'_1/P'_2) + (\epsilon_{12}\gamma_{11} + \epsilon_{22}\gamma_{12})}{\epsilon_{11}(P'_1/P'_2) - (\epsilon_{21}\gamma_{12} + \epsilon_{11}\gamma_{11})},$$

$$Z_4 = \frac{(\delta_{12}\kappa_{11} - \delta_{11}\kappa_{12})(P_6/P_5) + \kappa_{12}}{(\delta_{12}\kappa_{21} - \delta_{11}\kappa_{22})(P_6/P_5) + \kappa_{22}},$$

$$Z'_4 = \frac{(\delta_{12}\kappa_{11} - \delta_{11}\kappa_{12})(P'_6/P'_5) + \kappa_{12}}{(\delta_{12}\kappa_{21} - \delta_{11}\kappa_{22})(P'_6/P'_5) + \kappa_{22}}.$$

Note that the prime is used to denote the pulsating pressure response under a second arbitrary loading condition. It

can be seen that the transfer matrix parameters of the hose are determined from a total of six pressure transfer functions, P_1/P_2 , P_2/P_5 , P_6/P_5 , P'_1/P'_2 , P'_2/P'_5 , and P'_6/P'_5 , between locations ① and ②, ② and ⑤, and ⑥ and ⑤.

¹G. W. Morgan and J. P. Kiely, *J. Acoust. Soc. Am.* **26**, 323–328 (1954).

²W. Klip, P. Van Loon, and D. A. Klip, *J. Appl. Phys.* **38**, (9), 3745–3755 (1967).

³R. H. Cox, *Biophys. J.* **8**, 691–709 (1968).

⁴K. Nakano, M. Yoshimoto, and N. Okazaki, *Bulletin of the Tokyo Institute of Technology* **99**, 123–142 (1970).

⁵M. Gally, M. Guney, and E. Rieutord, *J. Fluids Eng.* **101**(4), 495–499 (1979).

⁶E. Rieutord, *J. Fluids Eng.* **104**, 335–341 (1982).

⁷L. Suo and E. B. Wylie, *J. Fluids Eng.* **112**, 496–500 (1990).

⁸D. K. Longmore and A. Schlesinger, *Journal of Systems and Control Engineering, Proc. Inst. Mech. Eng. Part 1* **205**, 97–104 (1991).

⁹K. Nakano and A. Abo-Ismael, *Hydraulics & Pneumatics* **7**(3), 155–162 (1976) (in Japanese).

¹⁰A. Abo-Ismael and K. Nakano, *Hydraulics & Pneumatics* **10**(7), 420–427 (1979) (in Japanese).

¹¹D. C. Wiggert, R. S. Otwell, and F. J. Hatfield, *J. Fluids Eng.* **107**, 402–406 (1995).

¹²M. W. Lesmez, D. C. Wiggert, and F. J. Hatfield, *J. Fluids Eng.* **112**, 311–318 (1990).

¹³M. L. Munjal and P. T. Thawani, *J. Acoust. Soc. Am.* **101**, 2524–2535 (1997).

¹⁴J. Yu and E. Kojima, “Dynamic Response of Unhomogeneously Viscoelastic Fluid Lines,” in *Proceedings of the 1995 American Control Conference*, Seattle, Washington, 1995, pp. 1821–1825.

¹⁵J. Yu and E. Kojima, “Transmission of Fluidborne Pressure Ripples in Fluid Power Flexible Hoses with Relatively Long Length,” in *Proceedings of the 2nd International Symposium on FPTC*, edited by Z. Chen *et al.* (Shanghai STLP, Shanghai, 1995), pp. 596–601.

¹⁶G. Herrmann and I. Mirsky, *J. Appl. Mech.* **23**, 563–568 (1956).

¹⁷E. B. Wylie and V. L. Streeter, *Fluid Transients* (McGraw-Hill, New York, 1978), p. 22.

¹⁸C. W. S. To and A. G. Doige, *J. Sound Vib.* **62**(2), 207–222 (1979).

¹⁹C. W. S. To and A. G. Doige, *J. Sound Vib.* **62**(2), 223–233 (1979).

²⁰J. Y. Chung and D. A. Blaser, *J. Acoust. Soc. Am.* **68**, 907–913 (1980).

²¹J. Y. Chung and D. A. Blaser, *J. Acoust. Soc. Am.* **68**, 914–921 (1980).

²²M. J. Box, *Comput. J. (UK)* **8**, 42–52 (1965).

²³F. T. Brown, *J. Basic Eng.* **84**, 547–553 (1962).

²⁴A. F. D’Souza and R. Oldenburger, *J. Basic Eng.* **86**, 589–598 (1964).

Transient diffraction of a plane step pressure pulse by a hard sphere: Neoclassical solution

H. Huang

13 200 Overbrook Lane, Bowie, Maryland 20715

G. C. Gaunaurd^{a)}

Naval Surface Warfare Center, Carderock Division—Code 684, West Bethesda, Maryland 20817-5700

(Received 30 March 1998; accepted for publication 20 August 1998)

The transient diffraction of a plane step pressure pulse by a hard sphere is studied via the modal series solution in a neoclassical fashion. With the advent and availability of more powerful computers and increased sophistication of computational algorithms, it is now possible to (1) accurately compute the time histories of a sufficiently large number of terms of the modal series, and (2) use the Cesàro summation to completely eradicate the Gibbs' phenomenon effects. This approach can be utilized to obtain the diffracted field in the entire space–time region. In particular, a complete treatment is developed for the diffracted field at the shadow boundary and in its neighborhood where heretofore no satisfactory analytical solution exists. © 1998 Acoustical Society of America. [S0001-4966(98)06311-5]

PACS numbers: 43.20.Px, 43.20.Fn [DEC]

INTRODUCTION

The transient diffraction of pulses by a sphere is a venerable problem which has been extensively studied in acoustics and electromagnetics throughout almost the entire twentieth century. Nevertheless, a satisfactory treatment of the field in the neighborhood of the shadow boundary has not yet been developed and is one of the unsolved problems of diffraction theory (Friedlander, 1958)! To the authors' knowledge, heretofore such a treatment still does not exist. The present paper presents a solution to this problem using the classical Laplace transform and modal series expansion techniques in a neoclassical sense. By utilizing modern algorithms and exploiting recent advances in computer capacities and floating point mathematics, sufficient terms of the inverse Laplace transform series solution can now be accurately computed. Together with the application of the Cesàro summation using up to 1000 terms of the series, uniform convergence around the discontinuous step wavefront is now obtained, completely eradicating spurious oscillations due to the Gibbs' phenomenon. Thus a uniformly convergent solution of the field in the neighborhood of the shadow boundary can now be calculated.

I. DESCRIPTION OF THE PROBLEM

Figure 1 sketches the geometry of the problem. The center of the sphere coincides with the origin O of the spherical coordinate systems (r, θ, ϕ) . The azimuthal coordinate need not be shown in the figure since by symmetry the problem is independent of it. The propagation vector of the incident plane wave is parallel to the plane of the paper and the incident wavefront is perpendicular to the polar axis of the sphere. The radius of the acoustically hard sphere is denoted by a . The surrounding acoustic medium is characterized by

its unperturbed sound speed c and mass density ρ . For clarity, the following dimensionless quantities are used:

$$T = \frac{ct}{a}, \quad R = \frac{r}{a}, \quad \Pi = \frac{p}{\rho c^2}, \quad (1)$$

where t and p denote time and pressure, respectively.

As the incident pressure wave impinges upon the sphere, it is reflected and diffracted by the sphere. The total pressure field consists of two components, namely, the incident pressure and the pressure scattered by the rigid immovable sphere, i.e.,

$$\Pi(R, \theta, T) = \Pi^{\text{inc}}(R, \theta, T) + \Pi^{\text{sra}}(R, \theta, T). \quad (2)$$

Π (and each of its components separately) satisfy the wave equation

$$\nabla^2 \Pi = \frac{\partial^2 \Pi}{\partial T^2}. \quad (3)$$

Adjusting the origin of the time coordinate such that the incident wavefront impinges upon the vertex of the sphere ($R=1, \theta=0$) at $T=0$, an incident step plane wave can be expressed as

$$\Pi^{\text{inc}}(R, \theta, T) = H(R \cos \theta - 1 + T), \quad (4)$$

where H is the Heaviside unit step function. The component Π^{sra} and its first time derivative have quiescent initial conditions at $T=0$. The boundary condition of the total pressure field at the fluid–sphere interface is

$$\frac{\partial \Pi}{\partial R} = 0 \quad \text{at } R = 1, \quad (5)$$

and Π^{sra} also satisfies the radiation condition at the far field.

^{a)}Electronic mail: gaunaurd@oasys.dt.navy.mil

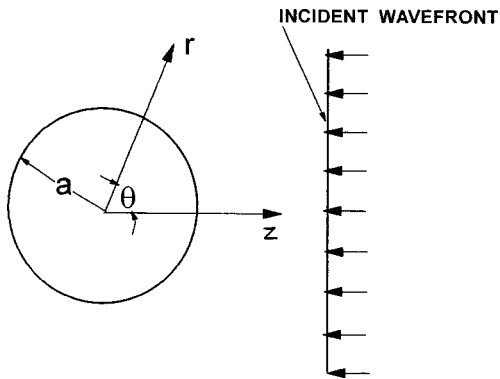


FIG. 1. Geometry of the problem.

II. CLASSICAL LAPLACE TRANSFORM MODAL SERIES SOLUTION

Applying the Laplace transform with respect to T with s as the transform parameter, the classical modal series solution to this well known initial-boundary value problem can be written as

$$\bar{\Pi}(R, \theta, s) = \sum_{m=0}^{\infty} \bar{\Pi}_m(R, s) P_m(\cos \theta), \quad (6)$$

where $P_m(\cos \theta)$ is a Legendre function, an overhead bar denotes Laplace transformed quantities, and

$$\bar{\Pi}_m(R, s) = (2m+1) \frac{e^{-s}}{s} \left[i_m(sR) - \frac{i'_m(s)}{k'_m(s)} k_m(sR) \right], \quad (7)$$

where $i_m(s)$ and $k_m(s)$ are modified spherical Bessel functions of the first and third kind, respectively, and a prime denotes differentiation with respect to the argument of the function. At the right hand side of Eq. (7), the first and the second term represent the m th mode of the Laplace transform of the incident and scattered pressure, respectively. On the surface of the sphere, $R=1$, and we have

$$\bar{\Pi}_m(1, s) = -(2m+1) \frac{e^{-s}}{2s^3} \frac{\pi}{k'_m(s)}. \quad (8)$$

Since the modified spherical Bessel function $k_m(s)$ is a finite series (Abramowitz and Stegun, 1964), Eq. (8) can be recast in the following form:

$$\bar{\Pi}_0(1, s) = \frac{1}{s(s+1)}, \quad (9)$$

and for $m > 0$

$$\bar{\Pi}_m(1, s) = \frac{(2m+1)s^{m-1}}{D_m(s)}, \quad (10)$$

where $D_m(s)$ is an $(m+1)$ th order real polynomial given by $D_m(s) = s^{m+1}$

$$+ \sum_{l=2}^{m+2} \frac{[m(m+1) + l(l+1)](m+l-2)! s^{m-l+2}}{2^{l-1}(l-1)!(m-l+2)!}, \quad (11)$$

where we have used the known finite series for $k_m(s)$:

$$k_m(s) = \frac{\pi e^{-s}}{2s} \sum_{k=0}^m \frac{(m+k)!}{k!(m-k)!(2s)^k}. \quad (12)$$

Equations (9) and (10) are rational functions of s , hence, their inverse Laplace transform can be readily found by Heaviside's inversion formula. Indeed, for low m 's, they are quite simple, e.g.,

$$\Pi_0(1, T) = 1 - e^{-T}, \quad (13)$$

and

$$\Pi_1(1, T) = 3e^{-T} \sin T. \quad (14)$$

The complexity of the inverse Laplace transform increases as m increases. The crux for the inverse Laplace transform of Eq. (10) is the accurate computation of the complex roots of the polynomial $D_m(s)$. Some plots of these roots were obtained earlier (Gaunard and Strifors, 1993). The nature of $D_m(s)$ is such that the magnitudes of its coefficients increase rapidly and its roots clutter closely together as m increases; correspondingly, numerical difficulties in floating-point mathematics are encountered. By utilizing modern algorithms and exploiting recent advances in computer capacities and floating-point mathematics, a large number of terms of the inverse Laplace transform series solution can now be accurately computed. Nevertheless, an alternate representation of $\Pi_m(1, T)$ for very large m is still needed.

III. ASYMPTOTIC SOLUTION FOR THE VERY HIGH MODES

Utilizing the uniform asymptotic expansion of the modified Bessel function for large m and large s (Erdélyi *et al.*, 1953),

$$K_\nu(s) \approx (\pi/2)^{0.5} (\nu^2 + s^2)^{-0.25} e^{[-(\nu^2 + s^2)^{0.5} + \nu \sinh^{-1} \nu/s]}, \quad (15)$$

and

$$K'_\nu(s) \approx -(\pi/2)^{0.5} s^{-1} (\nu^2 + s^2)^{0.25} \times e^{[-(\nu^2 + s^2)^{0.5} + \nu \sinh^{-1} \nu/s]}, \quad (16)$$

here $\nu = m + 1/2$, Eq. (7) at $R=1$ can be approximated as

$$\bar{\Pi}_m(1, s) = (2m+1) \frac{e^{-s}}{s} \times \left\{ i_m(s) + i'_m(s) \left[\frac{s}{\sqrt{s^2 + (m+1/2)^2}} \right] \right\}. \quad (17)$$

The inverse Laplace transform of the above equation is

$$\Pi_m(1, T) = g_m(T) + G_m(T) - (m + \frac{1}{2}) \times \int_0^T G_m(T-\tau) J_1[(m + \frac{1}{2})\tau] d\tau, \quad (18)$$

where $J_1(z)$ is the Bessel function of the first order, the inverse Laplace transform of $(2m+1)e^{-s}s^{-1}i_m(s)$ is

$$g_m(T) = \begin{cases} 0.5[P_{m-1}(1-T) - P_{m+1}(1-T)], & \text{for } 0 \leq T \leq 2, \\ 0, & \text{for } T \geq 2, \end{cases} \quad (19)$$

and the Laplace inversion of $(2m+1)e^{-s}s^{-1}i'_m(s)$ is

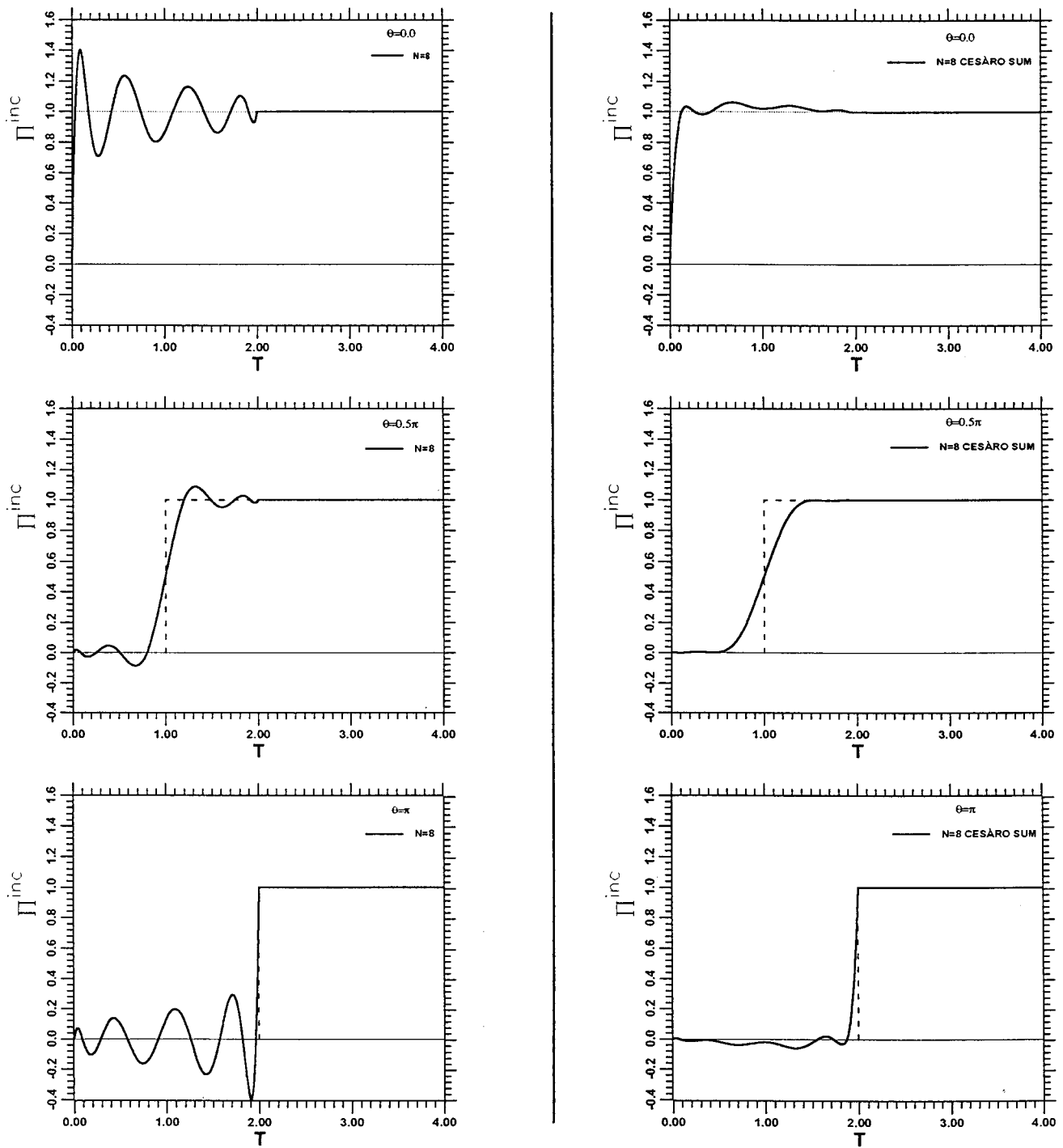


FIG. 2. A nine-term series representation of the incident waveform at the sphere's surface. At three angular locations (i.e., 0, 90, and 180 degrees), corresponding to the front apex, the shadow boundary, and the back apex of the sphere, respectively.

$$G_m(T) = \begin{cases} \frac{m}{2(2m-1)} [P_{m-2}(1-T) - P_m(1-T)] + \frac{(m+1)}{2(2m+3)} [P_m(1-T) - P_{m+2}(1-T)], & \text{for } 0 \leq T \leq 2, \\ 0, & \text{for } T \geq 2. \end{cases} \quad (20)$$

Thus $\Pi_m(1, T)$ for very large m can be calculated by evaluating the Legendre functions and the convolution integral in Eq. (18). The effectiveness of Eq. (18) will be shown later. Before calculating the total pressure field, the Gibbs' phenomenon and the convergence of the modal series solution is first discussed.

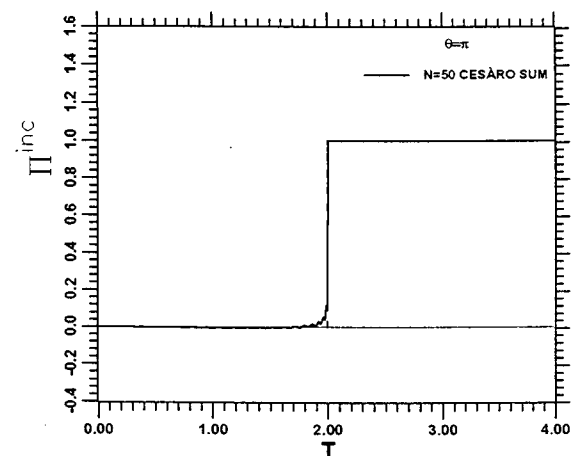
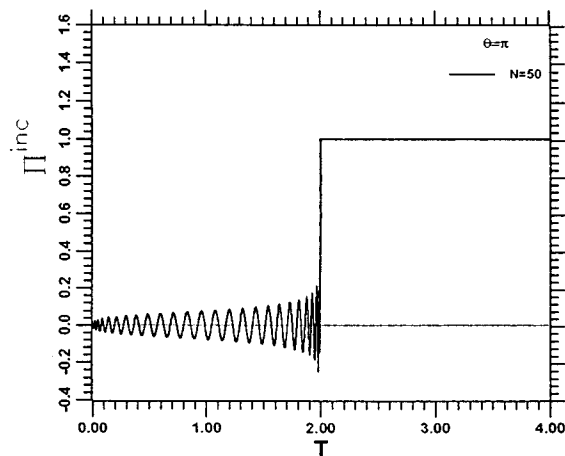
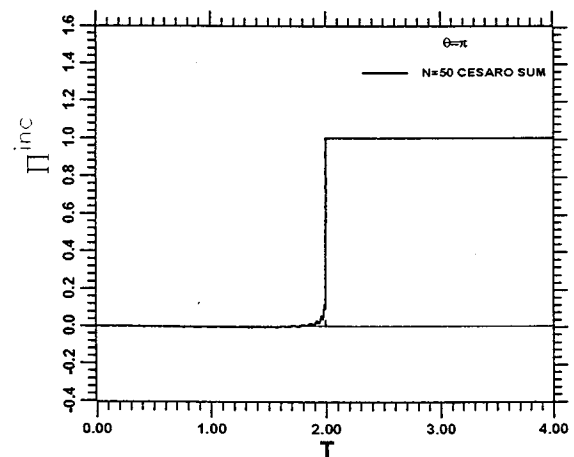
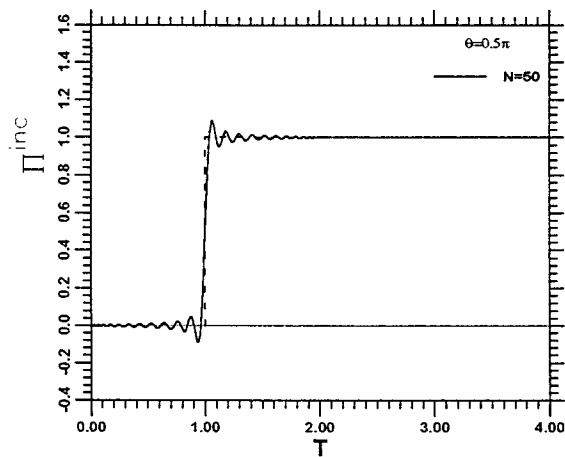
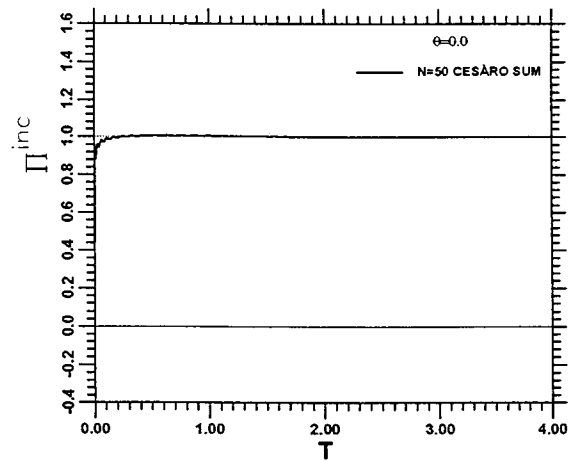
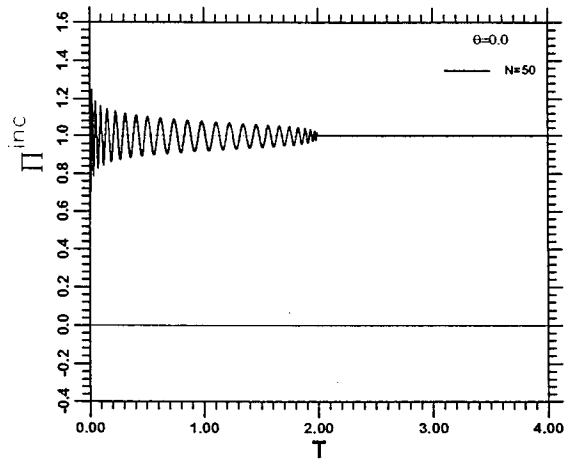


FIG. 3. A 51-term series representation of the same incident waveform in Fig. 2.

IV. GIBBS' PHENOMENON AND CESÀRO'S SUMMATION

The Laplace transform of the expression for the step incident wave, Eq. (4), is

$$\bar{\Pi}^{\text{inc}}(R, \theta, s) = \frac{1}{s} \exp[-(1 - R \cos \theta)s], \quad (21)$$

and its series expansion in terms of Legendre functions is (Huang and Mair, 1996)

$$\bar{\Pi}^{\text{inc}}(R, \theta, s) = \frac{e^{-s}}{s} \sum_{m=0}^{\infty} (2m+1) i_m(Rs) P_m(\cos \theta). \quad (22)$$

It can be shown that the inverse Laplace transform of the series in Eq. (22) for $R=1$ is

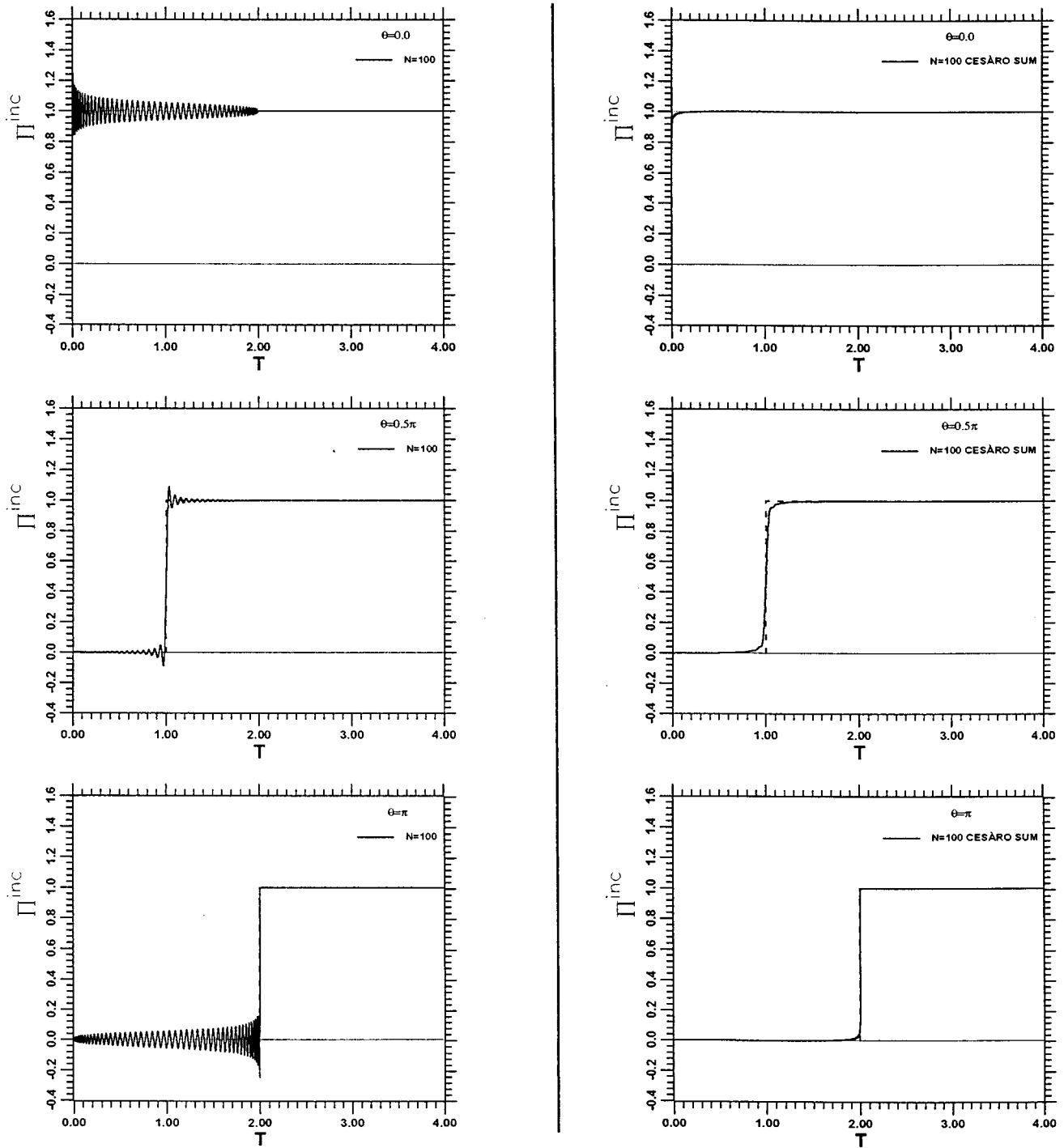


FIG. 4. Same as Fig. 2, but with 101 terms in the series representation.

$$\Pi^{inc}(1, \theta, T) = \begin{cases} 0.5T + 0.5 \sum_{m=1}^{\infty} (P_{m-1}(1-T) - P_{m+1}(1-T)) P_m(\cos \theta), & \text{for } 0 \leq T \leq 2, \\ 1.0 & \text{for } T \geq 2. \end{cases} \quad (23)$$

Since the wavefront of this step wave is a discontinuity, Gibbs' phenomenon appears in the interval $0 \leq T \leq 2$, when Eq. (23) is used to compute the time histories of Π^{inc} , such that the series in Eq. (23) never converges to the true wave

form of the unit step wave. Since Π^{inc} is the excitation pressure of the problem, it is obvious that Gibbs' phenomenon also appears in the scattered pressure time histories; predominantly the interval $0 \leq T \leq 2$ and will propagate beyond

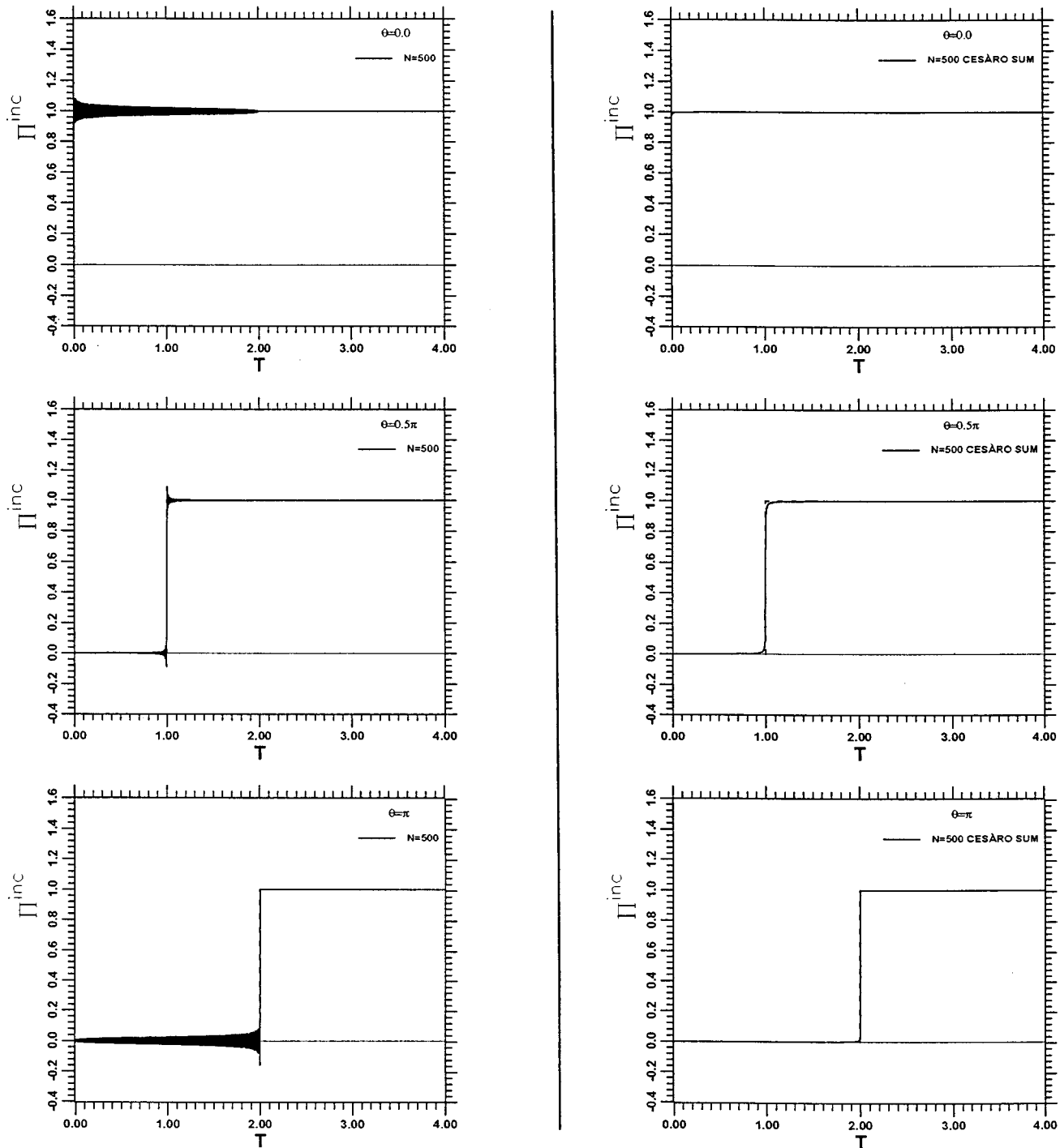


FIG. 5. Same as Fig. 2, but with 501 terms in the series representation. The right column showing the Cesàro sum already shows the complete eradication of the Gibbs' phenomenon effect, even at this relatively early stage.

this time interval. It is known that the use of the Cesàro type of summation of the series could eradicate the Gibbs' phenomenon effects. Previous applications of Cesàro summations to this type of problem (Berger, 1972; Geers and Ju, 1994), and using only the first nine terms of the series, did not sufficiently show the effectiveness of the remedy. It will be demonstrated here that a sufficiently large number of terms is required in the Cesàro sum of the series in Eq. (23) to approach the true sum. Using the first N terms of the series, the (C1) Cesàro sum can be written as (Whittaker and Watson, 1958)

$$\begin{aligned} \Pi^{\text{inc}}(1, \theta, T) = & 0.5T + 0.5 \sum_{m=1}^N [P_{m-1}(1-T) - P_{m+1}(1-T)] \\ & \times \left(1 - \frac{m-1}{N}\right) P_m(\cos \theta), \quad \text{for } 0 \leq T \leq 2. \end{aligned} \quad (24)$$

The above Cesàro sum has been mathematically proven to converge to the true sum (Whittaker and Watson, 1958). This formula is also referred to as Fejér's Arithmetic Means (Carslaw, 1930). The essence of this summation is to gradually reduce the contribution of each term as m increases. It is

readily seen from Eq. (24) that if N is small, the early m -terms could be prematurely and wrongly overreduced. Numerical computations of $\Pi^{\text{inc}}(1, \theta, T)$ at $\theta=0, 0.5\pi$, and π computed using regular summation, Eq. (23), and Cesàro summation, Eq. (24), are juxtaposed in left and right columns and compared to the respective true wave forms in Figs. 2, 3, 4, and 5. The true wave forms of this unit step incident wave at these three locations are unit step functions beginning at $T=0, 1.0$, and 2.0 , respectively. Figure 2 plots the results of using the first nine terms ($N=8$) of the series. The spurious Gibbs' phenomenon oscillations can be seen in the left column; the amplitude of the oscillations are largest near the wavefronts, and deviate as much as 40% from the true sum. It can also be seen from the right column that the use of the (C1) Cesàro summation significantly reduces these spurious oscillations but also decreases the steepness of the wavefronts due to the premature reduction of each term of the series as discussed earlier. The use of the first nine terms of the series is far from sufficient to converge to the true wave forms. Figure 3 plots the corresponding results of using the first 51 terms ($N=50$) of the series. From the left column, it can be seen that the frequency of the Gibbs' phenomenon oscillation increases significantly and the amplitude decreases slightly. From the right column, it can be seen that the Cesàro summation has basically eradicated all Gibbs' phenomenon oscillation effects and has converged to the true sum except in small neighborhoods of the wavefronts. The wave forms thus computed could already be acceptable for many applications. Figures 4 and 5 present the results of using 101 ($N=100$) and 501 ($N=500$) terms of the series, respectively. Again, It is seen from the left columns that with increasing N the amplitudes of the Gibbs' phenomenon oscillations decrease but remain significant near the wavefronts, and that the frequencies of oscillation increase greatly such that the oscillations appear as black bands for the case of $N=500$. From the right columns, it is seen that with increasing N , the Cesàro summations further narrow the imperfect neighborhoods of the wavefronts, and for $N=500$ the series representations approach very closely to the true wave forms. It is now adequately demonstrated that the series solution to this problem using the (C1) Cesàro summation of a sufficiently large number of terms will converge uniformly to the true solution. Except in neighborhoods of the wavefronts, the series converges quickly.

V. NEOCLASSICAL SOLUTION

The computations were carried out on personal computers and workstations using a code written in the FORTRAN language. Care was exercised in programming to avoid floating-point pitfalls. Many algorithms for finding the complex roots of a real polynomial were investigated; both the Jenkins' method (Jenkins, 1975) and the eigenvalue method (Press *et al.*, 1992) were employed for cross-checking. Using double precision arithmetic (REAL*8), the complex roots of $D_m(s)$ can be accurately computed up to $m=74$. Therefore, the inverse Laplace transform of the first 75 terms in the series of Eq. (6) at $R=1$ were accurately computed by the Heaviside inversion formula. The resulting total pressure time histories there by Cesàro summations for $\theta=0, 0.5\pi$,

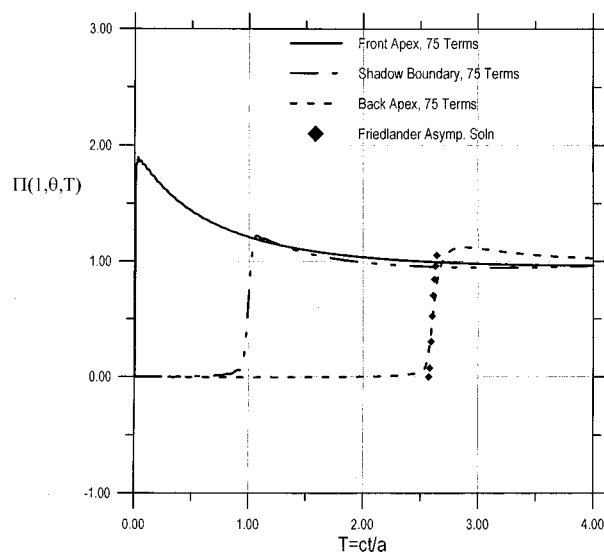


FIG. 6. Time plot of the total pressure field as given by the Cesàro summation described in the text, at three angular locations (i.e., 0, 90, and 180 degrees) on the sphere's surface. Here, $m=75$. Friedlander's asymptotic solution at the back apex of the sphere is also shown in dark diamonds for comparison.

and π are plotted in Fig. 6. It is well known that the true wavefront of $\Pi(1, 0, T)$ has a jump (discontinuity) of 2 at $T=0$. The present 75 term Cesàro sum rises monotonically from 0 at $T=0$ to 1.7964 at $T=0.0029$, then decreases monotonically to slightly below 1, and then increases slowly and approaches 1 at large times as already indicated by Eq. (13). The incident pulse arrives at the shadow boundary ($R=1, \theta=0.5\pi$) at $T=1.0$, and the total pressure also has a jump there at $T=1.0$. The results of the studies of Wait (1969) and Wait and Conda (1959) inferred that the magnitude of this jump is 1.4. It can be seen from Fig. 2 that the present result for $\Pi(1, 0.5\pi, T)$ is approaching the correct wavefront with a maximum value of 1.4 at $T=1.0$. Thence $\Pi(1, 0.5\pi, T)$ also decreases to slightly below 1 and then increases slowly and approaches 1 at larger time. Friedlander's wavefront solution (Friedlander, 1958) at the back apex ($R=1, \theta=\pi$) is also plotted in Fig. 6 for comparison. The diffracted wavefront arrives there at $T=1+\pi$ and does not have a jump. The incident wavefront does not reach the shadow region. It can be seen from Fig. 6 that the diffracted wavefront computed by the 75 term modal series is also approaching the correct wavefront. $\Pi(1, \pi, T)$ rises from 0 and overshoots 1 by about 13% and then slowly approaches 1 from above. As discussed earlier, except in the neighborhoods of the wavefronts, the modal series Cesàro summations have converged to the true time histories.

To further improve the quality of the wavefronts, many more terms of the modal series are needed. These are provided by Eq. (18). The effectiveness of Eq. (18) is shown in Figs. 7 and 8 by comparing its results to exact time histories of $\Pi_m(T)$ for m equal to 60 and 70, respectively. There it can be seen that Eq. (18) agrees completely with the exact $\Pi_m(T)$ at early time, matching both the amplitudes and periods of the time histories, and provides an excellent approximation of $\Pi_m(T)$ up to about $T=1.4$. Thereafter, the ap-

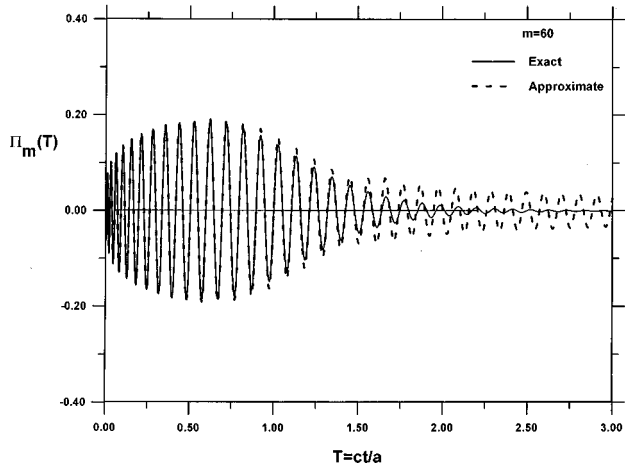


FIG. 7. Time plot of Eq. (18) for $m=60$. Comparison of exact (solid line) and approximate solution (dashed line).

proximated $\Pi_m(T)$'s are much less damped than the exact $\Pi_m(T)$'s and therefore are no longer valid approximations. Consequently, Eq. (18) is useful for the reflection region and the neighborhood of the shadow boundary, but not for the deep shadow region. For the deep shadow region, another approximation scheme is required. This is outside the scope of the present paper.

Equation (18), for $m > 74$ and $T = 0.0 - 1.4$, is applied to improve the wavefronts of $\Pi(1,0,T)$ and $\Pi(1,0.5\pi,T)$. The results of the Cesàro summations of a total of 1000 terms of the modal series are plotted in Fig. 9. Now the imperfect neighborhoods of the wavefronts have greatly shrunk and are almost invisible in the present plot. The "microscopic" structures of the computed wavefronts are the following: $\Pi(1,0,T)$ rises up from 0 at $T=0$ to 1.8966 at $T=0.0002$, increases at a slower pace to 1.9802 at $T=0.0078$, then decreases steadily and after $T=0.1$ the 1000 term result coincides with that of the 75 term sum. $\Pi(1,0.5\pi,T)$ rises up from 0.00265 at $T=0.983$ to its maximum value of 1.368 at $T=1.0052$, then decreases steadily, and after $T=1.2$ coincides with that of the 75 term sum. The curves in Fig. 9, therefore, have approached very closely the respective true time histories.

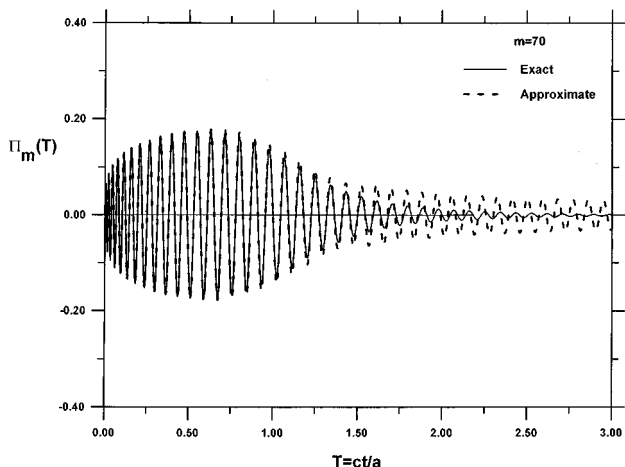


FIG. 8. Same as Fig. 7 but for $m=70$.

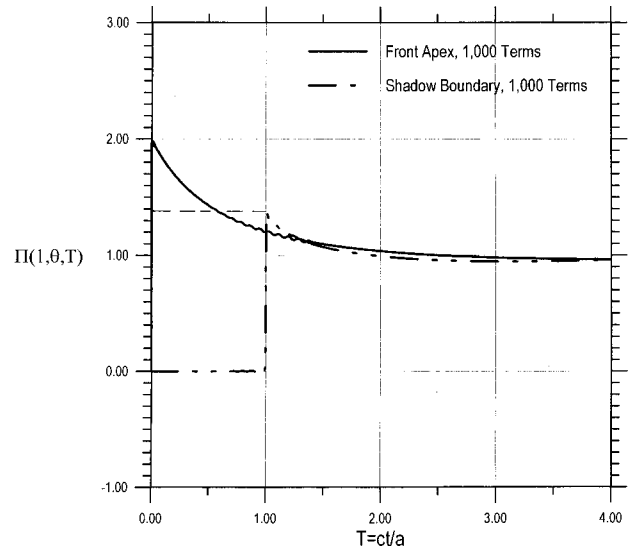


FIG. 9. Time plot of the surface pressure on the sphere using 1000 terms in the Cesàro summation procedure. The obtained results are shown at the front apex of the sphere (solid line) and exactly at the shadow boundary (dashed-dotted line) where the magnitude of the wavefront pressure is seen to be very close to 1.4.

VI. SUMMARY

This paper has presented a neoclassical solution to the problem of transient diffraction of a plane step pressure pulse by a hard sphere. A satisfactory treatment of the diffracted field at the shadow boundary and in its neighborhood has been developed. The pressure field on the sphere's surface, at the shadow boundary is 1.4 (cf. Fig. 9). This approach is capable of computing accurately the transient diffracted field for the entire space-time region. The crux lies in (1) the ability to obtain time histories for a sufficiently large number of terms in the modal series solution, and (2) the use of Cesàro summation to completely eradicate the Gibbs' phenomenon. These two elements are being fulfilled with the advent and availability of more powerful computers and increased sophistication of computational algorithms. The utility of the classical modal series for this type of problem in particular, and for transient dynamic problems in general, is now greatly enhanced, since a similarly convergent solution is still difficult to obtain with other techniques.

ACKNOWLEDGMENT

Author G.C.G. acknowledges the partial support of the Independent Research Program of the NSWC Carderock Division.

- Abramowitz, M., and Stegun, I. (1964). *Handbook of Mathematical Functions* (Dover, New York), Chap. 10.
- Berger, B. (1972). "Application of Cesàro mean to the transient interaction of a spherical acoustic wave and a spherical elastic shell," *J. Appl. Mech.* **39**, 623-626.
- Carlsaw, H. S. (1930). *Introduction to the Theory of Fourier's Series, and Integrals* (Dover, New York), Chap. IX, pp. 289-308.
- Erdélyi, A., Magnus, W., Oberhettinger, F., and Tricomi, G. (1953). *Higher Transcendental Functions* (McGraw-Hill, New York), Vol. 2, Chap. 7.
- Friedlander, F. G. (1958). *Sound Pulses* (Cambridge U.P., London), Chap. 6, pp. 147-184.

- Gaunaud, G. C., and Strifors, H. C. (1993). "Frequency and time-domain analysis of the transient resonance scattering from the interaction of a sound pulse with submerged elastic shells," *IEEE Trans. Ultrason. Ferroelectr. Freq. Control* **40**, 313–324.
- Geers, T. L., and Ju, T. H. (1994). "A computer program for a canonical problem in underwater shock," *Shock And Vibration* **1**, 331–337.
- Huang, H., and Mair, H. U. (1996). "Neoclassical solution of interaction of plane acoustic waves with a spherical elastic shell," *Shock and Vibration* **2**, 85–98.
- Jenkins, M. A. (1975). "Zeros of a real polynomial," *ACM Trans. Math. Softw.* **1**, 178–189.
- Press, W. H., Flannery, B. P., Teukosky, S. A., and Vetterling, W. T. (1992). *Numerical Recipes* (Cambridge U.P., New York), 2nd ed., pp. 362–371.
- Wait, J. E. (1969). "Transient response of penumbral currents for plane wave diffraction by a cylinder," *Can. J. Phys.* **47**, 1307–1312.
- Wait, J. E., and Conda, A. M. (1959). "On the diffraction of electromagnetic pulses by curved conducting surfaces," *Can. J. Phys.* **37**, 1384–1396.
- Whittaker, E. T., and Watson, G. N. (1958). *A Course of Modern Analysis*, 4th ed. (Cambridge U.P., New York), pp. 155.

Efficiency of a monopole sound source in the vicinity of an elastically suspended, baffled disk

Christiaan Kauffmann

Delft University of Technology, Faculty of Technical Mathematics and Informatics, P.O. Box 5031, 2600 GA Delft, The Netherlands

(Received 25 February 1997; accepted for publication 24 August 1998)

The acoustic power emitted by a point monopole sound source in the vicinity of an elastically suspended, baffled, circular piston is investigated. The sound source is located on the axis of symmetry at distance d above the piston. A closed-form analytic expression is derived for the power flow emitted by the source in terms of the radiation impedance of a baffled piston. The dependency of the result on the various parameters of interest is investigated numerically, while simple, analytical approximations are given in a parameter region that defines the near field. These parameters include: ka , kd , $\Omega = \omega/\omega_r$, $\mu' = \mu h/a$, and γ , where $k = \omega/c$ is the acoustic wave number, ω is the circular frequency of the source, a is the piston radius, ω_r is the natural frequency of the spring mounted piston, $\mu = \rho_p/\rho$ is the ratio of the volume densities of mass of the piston and the fluid, while h is the thickness of the piston disk and γ is the damping coefficient of the dashpot. © 1998 Acoustical Society of America. [S0001-4966(98)01212-0]

PACS numbers: 43.20.Rz, 43.20.Fn, 43.20.Tb, 43.50.Cb [DEC]

INTRODUCTION

The radiation of sound by compact sources can be strongly affected by the impedance of the surrounding space. This includes the acoustic properties of the ambient medium, the geometry of the space occupied by this medium, and the type of boundary conditions that are to be imposed at the boundaries of the surrounding space. A simple example may serve to illustrate the effect of the boundary conditions. The radiated far field of a point monopole source at short distance (i.e., within a fraction of a wavelength) from a large, rigid baffle is omnidirectional, but the source radiates twice as much acoustic energy as would be produced under free-field conditions. On the other hand, if the same source were placed closely (much closer than a wavelength) below a perfectly compliant surface covering a half-space, its far field directivity resembles that of a transverse dipole, while the free surface condition practically extinguishes all radiated energy. A slightly more complicated situation arises if the source is located at some distance from a thin elastic plate that supports flexural waves. This problem was treated by several authors.¹⁻⁸ Kauffmann,⁸ in a parametric study, found that a water-loaded plate in the near field of the source can be considerably excited, i.e., acoustic energy is efficiently converted to nonradiating flexural waves, which travel down the plate to infinity. This occurs if $0.1 > h/d > \frac{1}{10}kd$, where h is the plate thickness, d is the distance from the source to the plate, and k is the acoustic wave number. As a result, the efficiency of the source increases more than one order of magnitude over the free field value. On the other hand, but still under near field conditions, i.e., $kd < 1$, the effect of the plate was shown to be the same as that of a perfectly compliant surface, i.e., all energy emanating from the source is cancelled. This applies if $h/d < \frac{1}{20}kd$.

The study of sound radiation by compact sources operating in the vicinity of flexible structures, i.e., under near-field conditions, is important with respect to the problem of

propeller cavitation noise on board of ships. For ships sailing at moderate or high speed, propeller cavitation inevitably shows up as a result of the hydrodynamic pressure distribution around the propeller blades. The periodically triggered growth and collapse of large vaporous cavities on the suction sides of the blades (sheet cavitation) can be characterized acoustically as a monopole sound source of constant volume velocity, located in the upper part of the propeller disk and radiating sound at the blade passage frequency and higher order harmonics; see Ref. 9. Sound waves, after being generated, immediately reach the hull structure, excite the hull plates and, subsequently, structural acoustic energy is transmitted into the ship. Although passive noise control measures, e.g., application of absorbing material, floating floors, and resilient mounting systems have been proven to perform well at high frequencies, they usually fail at low frequencies. Therefore, propeller cavitation can be the dominating source of noise and vibration on board of ships, especially at low frequencies.

The aim of this paper is to show how a simple, one-degree-of-freedom structure of the mass-spring-dashpot-type placed in the near field of a sound source affects the acoustic energy radiated by the source. The structure is chosen to be an elastically suspended, circular piston embedded in an infinitely large, rigid baffle. The source is located on the axis of symmetry at finite distance above the piston. The piston is proposed as a simple, lumped parameter model for a hull plate. Clearly, this may appear unrealistic compared to the studies found in Refs. 1-8. However, an infinite plate does not account for resonances that occur due to the finiteness of hull plates of ships. This is why the piston model is introduced, although a finite plate is more realistic. Nevertheless, for the purpose of analyzing the effect of structural resonances on the sound production by a nearby source, the piston model makes sense, because the analysis is simpler than that for a plate. As a matter of fact, the results of such

analysis are applicable to platelike structures qualitatively, not quantitatively, and only if we consider the effect of a single, i.e., well-isolated, hull plate resonance, which is not a severe restriction, since low-frequency resonances are well-separated.

This paper is organized as follows. In the next section the problem is formulated. Subsequently, the analytical solution of the governing equations is developed and, finally, based on a formula due to Schmidt,³ an expression is derived for the power output of the source. Section II contains a parametric study of the power emitted by the source. Numerical values for the power flow are presented for various parameter ranges of interest. Qualitative features observed from the results are discussed and related to known results whenever appropriate. The paper ends with some conclusions.

I. THEORY

A. Description of the model

A perfect acoustic fluid occupies the half-space $z > 0$. The fluid is characterized by its volume density of mass ρ and speed of sound c . At the boundary $z=0$, a rigid circular disk of mass M and radius a is elastically mounted in a coplanar, rigid baffle of infinite extent. Due to the fluctuating acoustic pressure at the piston's wet surface, small amplitude, transverse vibrations are induced around its equilibrium position, $z=0$. A point monopole source of strength q_s radiates sound into the fluid at constant circular frequency ω . The source is located at distance d above the center of the disk on the axis of symmetry, which is the z axis (see Fig. 1). Noting the rotational symmetry of the configuration with respect to the z axis, a cylindrical coordinate system r, ϕ, z is used to describe and analyze the problem. The acoustic pressure p satisfies the Helmholtz equation, i.e.,

$$\{\Delta + k^2\}p(\mathbf{x}) = -q_s \delta(\mathbf{x} - \mathbf{x}_s), \quad z > 0, \quad (1)$$

where $k = \omega/c$ is the acoustic wave number and $\mathbf{x}_s = (0, 0, d)$ denotes the position of the source. The time-harmonic dependence $\exp(-i\omega t)$ is suppressed throughout. Sound radiation by the vibrating piston is described by the Neumann condition

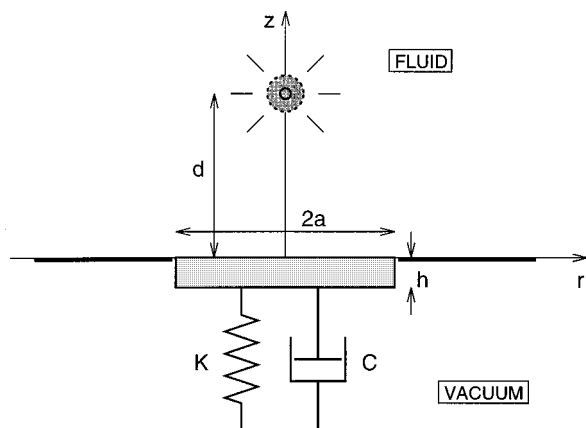


FIG. 1. Cross-sectional view of problem configuration.

$$\frac{\partial p}{\partial z} = \begin{cases} \rho i \omega v, & 0 \leq r < a, \\ 0, & r > a, \end{cases} \quad z=0, \quad (2)$$

expressing the continuity of normal fluid velocity and piston velocity, which is denoted by v , and, at the baffle, prescribing zero normal fluid velocity. The Sommerfeld condition ensures uniqueness of the solution for p . The motion of the piston can be modeled by the simple, one-degree-of-freedom system

$$M \cdot -i\omega v + 2(KM)^{1/2} \gamma v + K \frac{v}{-i\omega} = F_{\text{fluid}}, \quad (3)$$

where K is the spring stiffness, $\omega_r = (K/M)^{1/2}$ is the natural frequency of the system and γ is the damping coefficient of the dashpot. The piston is excited by the integrated surface pressure given by

$$F_{\text{fluid}} = - \int_0^{2\pi} d\phi \int_0^a r dr p(r, \phi, 0), \quad (4)$$

where the minus sign indicates that the net surface pressure drives the piston downwards, i.e., in the negative z direction.

B. Analytical solution

Green's theorem can be used to derive an expression for the pressure p in terms of the piston velocity v . The pressure can be decomposed as follows:

$$p(\mathbf{x}) = p_{\text{inc}}(\mathbf{x}) + p_{\text{scat}}(\mathbf{x}), \quad (5)$$

$$p_{\text{scat}}(\mathbf{x}) = p_{\text{spec}}(\mathbf{x}) + p_{\text{diff}}(\mathbf{x}), \quad (6)$$

where p_{inc} is the pressure radiated by the source in free space, p_{spec} is the specular reflection of the incident wave from a homogeneous baffle, and p_{diff} represents the pressure radiated by the vibrating piston. The solution reads

$$p_{\text{inc}}(\mathbf{x}) = q_s \frac{\exp(ikR_+)}{4\pi R_+}, \quad (7)$$

$$R_+ = \sqrt{r^2 + (z-d)^2} = |\mathbf{x} - \mathbf{x}_s|,$$

$$p_{\text{spec}}(\mathbf{x}) = q_s \frac{\exp(ikR_-)}{4\pi R_-}, \quad R_- = \sqrt{r^2 + (z+d)^2}, \quad (8)$$

$$p_{\text{diff}}(\mathbf{x}) = -\frac{\rho i \omega v}{2\pi} \int_0^{2\pi} d\phi \int_0^a \sigma d\sigma \frac{\exp(ikR_0)}{R_0}, \quad (9)$$

where

$$R_0 = \sqrt{r^2 + \sigma^2 - 2r\sigma \cos \phi + z^2}.$$

Next, these expressions are used to evaluate the integral in expression (4). It is straightforward to show that

$$\begin{aligned} & \int_0^{2\pi} d\phi \int_0^a r dr [p_{\text{inc}}(r, 0) + p_{\text{spec}}(r, 0)] \\ &= q_s \int_0^a r dr \frac{\exp(ik\sqrt{r^2 + d^2})}{\sqrt{r^2 + d^2}} \\ &= q_s \frac{\exp(ik\sqrt{a^2 + d^2}) - \exp(ikd)}{ik}, \end{aligned}$$

while, using a classical result for the piston impedance,

$$\int_0^{2\pi} d\phi \int_0^a r dr p_{\text{diff}}(r,0) = v \rho c \pi a^2 [R_1(2ka) - iX_1(2ka)],$$

where the functions R_1 and X_1 are given by, cf. Ref. 10

$$X_1(2ka) = \frac{2\mathbf{H}_1(2ka)}{2ka}, \quad R_1(2ka) = 1 - \frac{2J_1(2ka)}{2ka}. \quad (10)$$

In these expressions, \mathbf{H}_1 denotes the Struve function of order one, while J_1 is the Bessel function of the first kind and order one. Low- and high-frequency asymptotic expressions for R_1 and X_1 are also given in Ref. 10.

Adding these expressions gives the fluid force F_{fluid} that drives the piston. Inserting the result in the right-hand side of Eq. (4) yields a relation between the piston velocity v and the source strength q_s . This relation reads

$$\left[\left(M \cdot -i\omega + 2(KM)^{1/2} \gamma + \frac{K}{-i\omega} \right) + \rho c \pi a^2 \{R_1(2ka) - iX_1(2ka)\} \right] v = -q_s \frac{\exp(ik\sqrt{a^2+d^2}) - \exp(ikd)}{ik}. \quad (11)$$

$$\Pi' \equiv \frac{\Pi}{\Pi_\infty} = \left\{ 1 + \frac{\sin(2kd)}{2kd} \right\} + 4 \operatorname{Im} \left[\frac{\{\exp(ik\sqrt{a^2+d^2}) - \exp(ikd)\}^2 / (ka)^2}{\mu' (1 + 2i\gamma\Omega^{-1} - \Omega^{-2})ka + X_1(2ka) + iR_1(2ka)} \right], \quad (15)$$

where μ' and Ω are nondimensional parameters given by

$$\mu' = \frac{\rho_p h}{\rho a}, \quad \Omega = \frac{\omega}{\omega_r}.$$

Here ρ_p is the volume density of mass of the piston, which is a homogeneous disk of constant thickness h . Therefore the mass of the disk is $M = \rho_p \pi a^2 h$. It is noted that the first part of formula (15), i.e., the expression enclosed by curly brackets represents the power output of the source in the case that no vibrating piston were mounted in the perfectly rigid wall, cf. Ref. 8.

D. Far-field pressure, directivity, and radiated power

The power delivered by the source is partly radiated to infinity and partly absorbed by the structure's dashpot. Integration of the time-averaged acoustic intensity over a hemisphere at infinity gives the radiated power:

$$\Pi_{\text{rad}} = \frac{\pi}{\rho c} \int_0^{\pi/2} D(\theta) D(\theta)^* \sin \theta d\theta, \quad (16)$$

where $D(\theta)$ is the directivity function corresponding to the far-field pressure defined by

This relation completes the solution and all relevant quantities of interest can be expressed in terms of the source strength q_s only.

C. Power produced by the source

The net acoustic power delivered by the source can be found using the following formula due to Schmidt:³

$$\Pi = \Pi_\infty + \frac{q_s}{2\rho\omega} \operatorname{Im}[p_{\text{scat}}(\mathbf{x}_s)], \quad \Pi_\infty = \frac{1}{8\pi} \frac{|q_s|^2}{\rho c}. \quad (12)$$

In this formula Π_∞ is the power produced by the source under free-field conditions. For convenience it was assumed that q_s is real. The scattered pressure $p_{\text{scat}}(\mathbf{x}_s)$ can be evaluated easily using (6). Noting that

$$p_{\text{spec}}(\mathbf{x}_s) = q_s \frac{\exp(2ikd)}{8\pi d}, \quad (13)$$

$$p_{\text{diff}}(\mathbf{x}_s) = -\frac{\rho i \omega v}{2\pi} \int_0^{2\pi} d\varphi \int_0^a \sigma d\sigma \frac{\exp(ik\sqrt{\sigma^2+d^2})}{\sqrt{\sigma^2+d^2}} = -\rho i \omega v \frac{\exp(ik\sqrt{a^2+d^2}) - \exp(ikd)}{ik}, \quad (14)$$

and using (11) to eliminate v , it follows from formula (12) that

$$p(s, \theta) \sim \frac{\exp(iks)}{s} D(\theta), \quad 0 \leq \theta \leq \pi/2, \quad ks \gg 1, \quad d \ll s. \quad (17)$$

Here, spherical coordinates s, θ are introduced by $r = s \sin \theta$ and $z = s \cos \theta$. The directivity function is derived in a standard way for $p_{\text{inc}} + p_{\text{spec}}$ and for p_{diff} separately. The result reads, cf. Ref. 10,

$$D(\theta) = \frac{q_s}{4\pi} 2 \cos(kd \cos \theta) - \frac{i}{2} \omega \rho v a^2 \frac{2J_1(ka \sin \theta)}{ka \sin \theta}. \quad (18)$$

Inserting (18) into formula (16) yields

$$\begin{aligned} \Pi_{\text{rad}} = & \frac{1}{4\pi} \frac{|q_s|^2}{\rho c} \int_0^{\pi/2} \cos^2(kd \cos \theta) \sin \theta d\theta \\ & + \frac{\pi}{2} \rho c a^2 |v|^2 \frac{(ka)^2}{2} \int_0^{\pi/2} \left(\frac{2J_1(ka \sin \theta)}{ka \sin \theta} \right)^2 \sin \theta d\theta \\ & + q_s a \operatorname{Im}[v] \int_0^{\pi/2} J_1(ka \sin \theta) \cos(kd \cos \theta) d\theta. \end{aligned} \quad (19)$$

Evaluation of the first integral is straightforward and gives the power radiated by a source at distance d from a rigid baffle. The second integral corresponds to the power radiated by a baffled piston and is given by (cf. Refs. 10 and 11):

$$\begin{aligned} & \frac{(ka)^2}{2} \int_0^{\pi/2} \left(\frac{2J_1(ka \sin \theta)}{ka \sin \theta} \right)^2 \sin \theta d\theta \\ &= 1 - \frac{2J_1(2ka)}{2ka} \equiv R_1(2ka). \end{aligned}$$

The third integral is a special case of a tabulated integral, cf. Refs. 12 and 13, which reduces to

$$\begin{aligned} & \int_0^{\pi/2} J_1(ka \sin \theta) \cos(kd \cos \theta) d\theta \\ &= \frac{-1}{ka} \{ \cos(k\sqrt{a^2+d^2}) - \cos(kd) \}. \end{aligned}$$

Collecting terms and normalizing Π_{rad} with respect to Π_∞ yields

$$\begin{aligned} \Pi'_{\text{rad}} &= \left\{ 1 + \frac{\sin(2kd)}{2kd} \right\} + 4\pi^2 \rho^2 c^2 a^2 \frac{|v|^2}{|q_s|^2} R_1(2ka) \\ &\quad - \frac{8\pi\rho c}{k} \text{Im} \left[\frac{v}{q_s} \right] \{ \cos(k\sqrt{a^2+d^2}) - \cos(kd) \}. \end{aligned} \quad (20)$$

Finally, relation (11) is used to eliminate v . The result reads

$$\begin{aligned} \Pi'_{\text{rad}} &= \left\{ 1 + \frac{\sin(2kd)}{2kd} \right\} + 4 \frac{|\tau|^2}{|\zeta|^2} R_1(2ka) \\ &\quad + 8 \text{Re}[\tau] \text{Im} \left[\frac{\tau}{\zeta} \right], \end{aligned} \quad (21)$$

where ζ and τ are defined by

$$\zeta = \mu' (1 + 2i\gamma\Omega^{-1} - \Omega^{-2})ka + X_1(2ka) + iR_1(2ka), \quad (22)$$

$$\tau = \{ \exp(ik\sqrt{a^2+d^2}) - \exp(ikd) \} / (ka). \quad (23)$$

E. Dissipated power and power balance

The energy absorbed by the structure's dashpot is calculated by multiplying the damping force by the piston's velocity. Taking the time average yields:

$$\begin{aligned} \Pi_{\text{diss}} &= \frac{1}{2} \text{Re}[Cv v^*] = \gamma\Omega^{-1} \omega M |v|^2, \\ C &= 2(KM)^{1/2} \gamma. \end{aligned} \quad (24)$$

Eliminating v in favor of q_s using (11) and normalizing Π_{diss} with respect to Π_∞ gives the result

$$\Pi'_{\text{diss}} = 4\mu' (2\gamma\Omega^{-1})ka \frac{|\tau|^2}{|\zeta|^2}, \quad (25)$$

where ζ and τ are given by (22) and (23).

An interesting check on these results is provided by the power balance

$$\Pi' = \Pi'_{\text{rad}} + \Pi'_{\text{diss}}. \quad (26)$$

This equation states that the energy produced by the source is taken away by two physical mechanisms: (i) radiation of acoustic energy to infinity; and (ii) dissipation of vibrational energy by the structure's dashpot. It is easy to show that Eq. (26) holds. First, it is noted that

$$\Pi' = \left\{ 1 + \frac{\sin(2kd)}{2kd} \right\} + 4 \text{Im} \left[\frac{\tau^2}{\zeta} \right] \quad (27)$$

and

$$\mu' (2\gamma\Omega^{-1})ka + R_1(2ka) = \text{Im}[\zeta]. \quad (28)$$

Inserting expressions (27), (21), and (25) into the power balance (26), subtracting $\{1 + \sin(2kd)/(2kd)\}$ from both sides, collecting terms using (28), and dividing both sides by 4 the power balance reduces to

$$\text{Im} \left[\frac{\tau^2}{\zeta} \right] = \text{Im}[\zeta] \frac{|\tau|^2}{|\zeta|^2} + 2 \text{Re}[\tau] \text{Im} \left[\frac{\tau}{\zeta} \right],$$

which is an identity.

II. NUMERICAL RESULTS AND DISCUSSION

The analytic expression (15) derived in Sec. I contains five independent parameters, i.e., ka , kd , Ω , μ' , and γ . In order to investigate how the power flow from the source varies with some of these parameters, this section presents numerical data in graphical form. The results presented here are restricted to the case of a water-loaded piston, whose disk is made of steel. Thus $\mu \equiv \rho_p / \rho = 7.84$. In addition, the ratio of the disk's thickness h to the radius a will take values typically encountered for hull plates on real ships, i.e., $h/a = \mathcal{O}(10^{-2})$. Furthermore, it is assumed that the aspect ratio $\phi \equiv d/a$ of the problem geometry is neither small nor large. Finally, because radiation losses are usually much larger than structural dissipation, the value of γ is set equal to zero. It is noted, however, that the dashpot may be used to simulate the nonreversible power flow into the ship's structure. For this purpose the value of γ must be estimated from experiments or derived from statistical energy analysis considerations.

First, the efficiency of a source with a structure in its near field is investigated as a special case. Using the low-frequency expansions, cf. Ref. 10

$$X_1(2ka) = \frac{8ka}{3\pi} + \mathcal{O}((ka)^3)$$

and

$$R_1(2ka) = \frac{(ka)^2}{2} + \mathcal{O}((ka)^4),$$

it is easy to show that for $kd \rightarrow 0$, $ka \rightarrow 0$, and $\phi = \mathcal{O}(1)$

$$\Pi' = 2 + 4 \frac{\psi^2/2 - \psi\chi}{\chi^2} + \mathcal{O}((kd)^2), \quad (29)$$

where ψ and χ are given by

$$\psi = \sqrt{1 + \phi^2} - \phi \quad \text{and} \quad \chi = \mu' (1 - \Omega^{-2}) + \frac{8}{3\pi}.$$

Straightforward analysis of expression (29) reveals that the power output becomes infinitely large, i.e., $\Pi' \rightarrow \infty$, if Ω

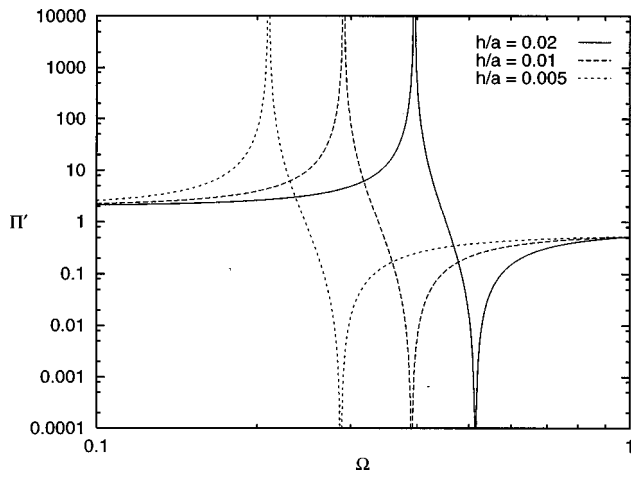


FIG. 2. Normalized power output Π' vs normalized frequency Ω under near field conditions, i.e., $kd \rightarrow 0$ for various values of h/a . $\mu = 7.84$, $\phi = 1.0$, and $\gamma = 0$.

$= \Omega_{\text{res}}$, while the source produces actually no power at all, i.e., $\Pi' = 0$, if $\Omega = \Omega_{\text{antires}}$, where

$$\Omega_{\text{res}} = \left\{ 1 + \frac{1}{\mu'} \frac{8}{3\pi} \right\}^{-1/2}$$

and

$$\Omega_{\text{antires}} = \left\{ 1 + \frac{1}{\mu'} \left(\frac{8}{3\pi} - \psi \right) \right\}^{-1/2}.$$

It is noted that $\Omega_{\text{res}} < \Omega_{\text{antires}}$ if $\psi < 8/3\pi$. The latter condition is equivalent to $\phi > (3\pi/8 - 8/3\pi)/2 = 0.165$, which is satisfied since $\phi = \mathcal{O}(1)$. In Fig. 2 the power output of the source under near-field conditions, i.e., for $kd \rightarrow 0$, is plotted as a function of frequency for various values of h/a . The results in Figure 2 show how the efficiency of the source varies with the frequency ratio Ω . In particular, it is observed that the source is very effective, if its frequency is close to the resonance frequency of the piston modified for the effect of fluid loading. On the other hand, the power output falls off down to zero, if the frequency of the source approaches the antiresonance frequency. These features clearly demonstrate the influence of a resonating structure in the near field of a source on the total power produced by that source. In addition, the results also clearly show how the resonance frequency shifts downwards if the slenderness ratio h/a of the disk decreases. Changing the volume density of mass of the disk gives rise to the same effect, since expression (29) varies with h/a through the parameter μ' only.

In addition to the near field results in Fig. 2, it is expected that the power flow from the source attains its free-field value Π_∞ for $kd \rightarrow \infty$, i.e., under far field conditions. For moderate values of kd the power flow is governed by a transition regime. This is illustrated in Fig. 3, which represents the power output as a function of both Ω and kd .

In Fig. 3 both near-field and far-field limits can be easily identified. For $kd = 0.1$ the results resemble those from Fig. 2, except that the power flow remains finite at resonance, while, at antiresonance, it does not vanish completely, but becomes very small. If the piston is more remote from the source the resonance peak falls off rapidly with distance and

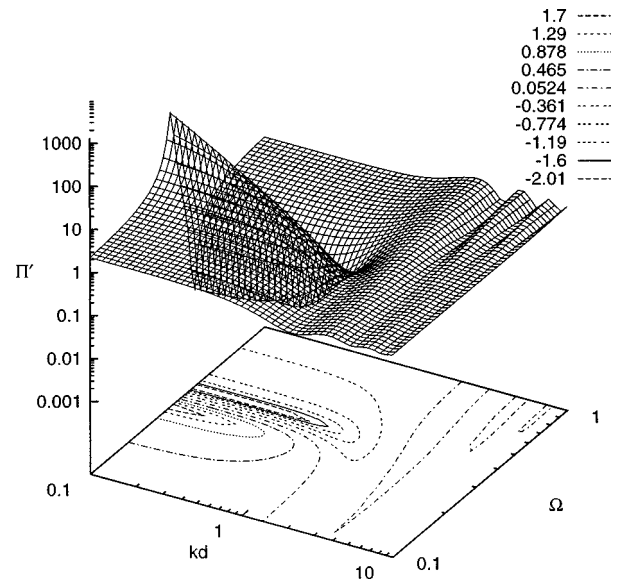


FIG. 3. Normalized power flow Π' vs normalized frequency Ω and modulation number kd for $h/a = 0.01$, $\mu = 7.84$, $\phi = 1.0$, and $\gamma = 0$. The key gives values of $\log_{10} \Pi'$ and corresponds to the equal level contour lines.

the power output approaches the free field value if kd is sufficiently large, typically $kd > 1$. Similarly, the antiresonance dip disappears if kd is large enough. Another feature shown in Fig. 3 is the modulation of the power flow with kd in the region $kd > 3$ and $\Omega > 0.5$. This is the well-known result for the source in front of an infinite baffle without a piston and is given by $1 + \sin(2kd)/2kd$.

A physical explanation for the large increase of acoustic power delivered by the source—relative to the free-field case—has been given by Heckl.² Following remarks by Rayleigh, he argued that the energy associated with the reciprocating flow of the hydrodynamic near field of the source can be converted partly into radiated energy by excitation of a resonator or a wave-bearing object.

III. CONCLUSION

The presence of an elastic structure in the near field of a source can enlarge the radiated power significantly, even up to several orders of magnitude over the free field value. This occurs if the source radiates at frequencies close enough to the resonance frequencies of the structure, including the effect of fluid loading. As a result, very high levels of structural vibration are excited, which increases subsequent acoustic radiation and gives rise to increased dissipation of structure-borne sound power within the structure. Alternatively, under antiresonance conditions, the response of the structure to the incident pressure wave resembles that of a perfectly compliant surface. The effect on the efficiency of the source can be considerable and may even lead to almost complete suppression of energy produced by the source. These features have been shown quantitatively for the case of a point source in the vicinity of a baffled piston, but should hold qualitatively if the piston were replaced by a resonating structure like a plate.

Concerning the problem of propeller cavitation noise, which is particularly dominating for kd -values in the range

$0.37 \leq kd \leq 0.45$ (see also Ref. 8), it is observed from Fig. 3 that the power output from the source is critically dependent on the value of Ω . Therefore, it is recommended to modify the design parameters that determine the structural resonances (plate thickness, rib spacing) in such a way that, under normal operating conditions, the frequency ratio Ω is close to the antiresonance, but in any case far from the resonance frequency of that structure.

¹V. N. Krasil'nikov, "Effect of a thin elastic layer on the propagation of sound in a liquid halfspace," *Sov. Phys. Acoust.* **6**, 216–224 (1960).

²M. Heckl, "Körperschallanregung von elastischen Strukturen durch benachbarte Schallquellen," *Acustica* **21**, 149–161 (1969).

³G. H. Schmidt, "Influence of an unbounded elastic plate on the radiation of sound by a point source," *J. Sound Vib.* **53**, 289–300 (1977).

⁴H. Saadat and P. Filippi, "Diffraction of a spherical wave by a thin, infinite plate," *J. Acoust. Soc. Am.* **69**, 397–403 (1981).

⁵W. van Gent, G. A. Q. Salvati, and H. C. J. van Wijngaarden, "Response of elastic flat plate to cavitation," in *Proc. ASME International Symposium on Cavitation, Noise and Erosion in Fluid Systems*, San Francisco, 1989, edited by R. E. A. Arndt, M. L. Billet, and W. K. Blake (ASME, New York, 1989), FED-Vol. 88, pp. 19–27.

⁶A. de Bruijn, "Akoestisch gedrag van onderwatergeluidbronnen in de

nabijheid van elastische structuren," *Nederlands Akoestisch Genootschap Journaal* **110**, 53–63 (1991) (in Dutch).

⁷A. de Bruijn, "Acoustical behavior of underwater sound sources near compliant layers," in *Proc. Underwater Defense Technology 1992*, edited by B. R. Longworth (Microwave Exhibitions and Publishers, London, 1992), pp. 134–140.

⁸C. Kauffmann, "Efficiency of a monopole sound source in the vicinity of a water-loaded plate," Reports of the Faculty of Technical Mathematics and Informatics no. 96–16 (Delft University of Technology, Delft, The Netherlands, 1996).

⁹J. van der Kooij, "Experimental and analytical aspects of propeller induced pressure fluctuations," in *Proc. 2nd Int. Symp. on Shipboard Acoustics, ISSA '86*, edited by J. Buiten (Martinus Nijhoff, Dordrecht, 1986), pp. 43–62.

¹⁰A. D. Pierce, *Acoustics: An Introduction to its Physical Principles and Applications* (Acoustical Society of America, Woodbury, NY, 1989), Chap. 5, §§4–5, pp. 220–227.

¹¹N. W. McLachlan, *Bessel Functions for Engineers*, 2nd ed. (Clarendon, Oxford, 1955), pp. 64–65.

¹²W. Magnus, F. Oberhettinger, and R. P. Soni, *Formulas and Theorems for the Special Functions of Mathematical Physics* (Springer-Verlag, Berlin, 1966), §3.8.2, p. 89.

¹³I. S. Gradshteyn and I. M. Ryzhik, *Table of Integrals, Series and Products* (Academic, New York, 1980), p. 742, Eq. 6.688.1.

An explicit integral formulation for transient acoustic radiation

Qiang Hu^{a)} and Sean F. Wu

Department of Mechanical Engineering, Wayne State University, Detroit, Michigan 48202

(Received 2 February 1998; revised 3 September 1998; accepted 9 September 1998)

An explicit integral formulation is derived for predicting transient acoustic radiation. The radiated acoustic pressure is shown to be expressible as a sum of integrals over simple and doublet sources and their couplings induced by the normal and tangential components of the particle velocity, which can be measured by a nonintrusive laser velocimeter. Such an integral formulation is computationally advantageous in that solutions thus obtained are unique, and the efficiency of numerical computations is high. This is because the radiated acoustic pressure is expressed as an explicit integral of known quantities, which can be readily implemented numerically by using the Gaussian quadratures. For arbitrary time-dependent excitations, the radiated acoustic pressure can be written as a sum of convolution integrals of impulse response functions over the time history of the particle velocity specified on the control surface. Validations of this integral formulation are demonstrated both analytically and numerically for acoustic radiation from an explosively expanding sphere, sudden accelerating spheres, disks, and right circular cylinders. © 1998 Acoustical Society of America. [S0001-4966(98)04012-0]

PACS numbers: 43.20.Tb, 43.20.Rz, 43.20.Px [ANN]

INTRODUCTION

Prediction of transient acoustic radiation has always been a major topic of interest, because in engineering applications most acoustic pressure signals are of transient nature. Theoretically speaking, transient acoustic pressures can be determined by the Kirchhoff integral formulation. However, unlike a steady-state case, there is no effective way of implementing this Kirchhoff integral formulation numerically for transient acoustic radiation. This is because one must first solve an integral equation for the surface acoustic pressure, given the normal component of the surface velocity. Since each element on the surface has a different emission time for an observer fixed in space, the surface integrals must be discretized in both temporal and spatial domains simultaneously. A direct numerical implementation of this integral equation can be time consuming, even for the simplest geometry such as a sphere.¹ Moreover, selection of the step size for time can be critical in obtaining an accurate numerical result, and for a chosen time step the accuracy deteriorates considerably as the time variable increases.²

Over the past few decades, considerable effort has been devoted to transient acoustic scattering, mostly from two-dimensional cylindrical shells^{3,4} or spherical shells⁵⁻⁷ which render the wave equation separable in terms of cylindrical or spherical coordinate systems. Accordingly, one can derive exact solutions by taking Laplace transformation. For a nonseparable geometry, analytic solutions cannot be found and other methods must be sought. Geers^{8,9} developed the method of doubly asymptotic approximations to calculate the transient acoustic radiation and scattering from an object in free space. This method is shown to be effective for simple geometries subject to very high frequency excitations for which plane wave relations can be used, or very low fre-

quency excitations for which virtual mass approximations are applicable. Ebenezer and Stepanishen used time-dependent eigenfunction expansions to calculate transient vibratory responses of fluid-loaded elastic planar structures^{10,11} and shells¹²⁻¹⁴ subject to mechanic and/or acoustic excitations. In this method, the axisymmetric velocity field of a fluid-loaded structure is written as an *in vacuo* eigenvector expansion with time-dependent coefficients. The effect of fluid loading is described by convolution integrals involving the modal velocity coefficients and mode-dependent acoustic radiation impulse responses.

The present paper is concerned with transient acoustic radiation from an object immersed in an unbounded fluid medium. In particular, it considers the cases in which the surface vibration responses cannot be measured by conventional miniature accelerometers. Such circumstances are encountered in flexible, lightweight, or structures with adverse environment which do not allow the attachment of transducers. Under this condition, a nonintrusive laser velocimeter must be employed.

The use of a laser velocimeter to measure the normal component of the particle velocity, which is equal to that of the surface velocity at the interface, has been known for decades. Once the normal component of the surface velocity is specified, the surface acoustic pressure can be determined by solving the Kirchhoff integral equation, which in turn allows one to calculate the radiated acoustic pressure in the field. The major disadvantage of this approach is that there is no simple way of implementing numerically the Kirchhoff integral equation in temporal and spatial domains simultaneously. A brute force numerical implementation can be very costly and time consuming. Hence an alternative approach must be sought.

Actually, the laser technique can be used to measure the velocity vector of a suspended microparticle in an insonified medium. The methodology that has been developed for mea-

^{a)}On leave from Department of Mechanical Engineering, Zhejiang University, People's Republic of China.

suring the particle velocity vectors in liquids and in air is known as laser Doppler velocimeter.¹⁵⁻²³ The work in this area, however, has not received as much attention as measurements of the normal component of surface vibration.

In this paper, we assume that the particle velocity vector is specified over a control surface that completely encloses the vibrating object under consideration. Then, it can be shown²⁴ that the field acoustic pressure is expressible in terms of integrations over the normal and tangential components of the particle velocity. This integral formulation is extended to predicting transient acoustic radiation.

Here we use an adjective *explicit* to distinguish the present formulation from the classical Kirchhoff integral formulation. This is because the latter expresses the field acoustic pressure in terms of two variables: the surface acoustic pressure and the normal component of the surface velocity. Both of them must be specified before the field pressure can be determined. The Kirchhoff integral theory is valid for any control surface that completely encloses a vibrating object. In any event, the radiated acoustic pressure is obtained in two steps. The only way to determine the field acoustic pressure directly is to specify both the surface acoustic pressure and the normal component of the particle velocity. However, this is not an easy task because one cannot accurately measure these variables simultaneously. An intensity probe may be used to produce an averaged acoustic pressure and an approximate particle velocity. The quantities thus obtained are inaccurate because the probe is designed to measure the acoustic intensity. If inaccurate surface acoustic pressure and normal component of the particle velocity are used in the Kirchhoff integral formulation, the resulting field acoustic pressure will be bound to err from the true value.²⁵ While it is possible to accurately measure the surface acoustic pressure and the normal component of the particle velocity separately, it nonetheless defeats the purpose of the Kirchhoff integral theory. Because this theory enables one to calculate the surface acoustic pressure given the normal component of the particle velocity, which is much easier than taking measurements.

On the other hand, the present integral formulation expresses the field acoustic pressure in terms of a single variable, namely, the particle velocity, which can be measured by a nonintrusive laser velocimeter. This velocity vector can be resolved into the normal and tangential components on a control surface that completely encloses a vibrating object. Hence, the field acoustic pressure can be determined directly once the particle velocity is specified. The word *explicit* is merely used to imply that the field acoustic pressure is given as an explicit function of the particle velocity. Such an integral formulation is advantageous in that the solutions thus obtained are unique, and the efficiency of numerical computations is high.²⁴

Section I presents an integral formulation for the radiated acoustic pressure as an explicit function of the particle velocity. In particular, it expresses the field acoustic pressure as a sum of surface integrals of simple and doublet sources and their couplings induced by the normal and tangential components of the particle velocity, respectively. For arbitrarily time-dependent excitations, the radiated acoustic pres-

sure can be written as a sum of Duhamel integrals. The transient acoustic pressure at any field point can be expressed as convolution integrals of the impulse response functions to the time history of the particle velocity (see Sec. II). Analytical and numerical validations of these formulations are given in Sec. III. Concluding remarks are drawn in Sec. IV.

I. EXPLICIT INTEGRAL FORMULATION

Consider an object immersed in an unbounded fluid medium with density ρ_0 and sound speed c . To facilitate the derivations of an explicit integral formulation for predicting transient sound radiation into the medium, let us first define the following Fourier transformation pairs:

$$F(\omega) = \int_{-\infty}^{+\infty} f(t) e^{i\omega t} dt, \quad (1a)$$

$$f(t) = \frac{1}{2\pi} \int_{-\infty}^{+\infty} F(\omega) e^{-i\omega t} d\omega, \quad (1b)$$

for any function $f(t)$ which is continuous and bounded as $t \rightarrow \infty$.

Assume that the medium is quiescent before the source is turned on at $t=0$. Then at any later time t the acoustic pressure at any field point can be expressed in terms of the Kirchhoff integral theory in the frequency domain as²⁶

$$P(\mathbf{x}, \omega) = \frac{1}{4\pi} \int_{S(\mathbf{x}_S)} \left[\frac{\partial R}{\partial n} \frac{(ikR-1)e^{ikR}}{R^2} P(\mathbf{x}_S, \omega) - \frac{e^{ikR}}{R} \frac{\partial P(\mathbf{x}_S, \omega)}{\partial n} \right] dS(\mathbf{x}_S), \quad (2)$$

where S represents a control surface that encloses completely the vibrating object, $R = |\mathbf{x} - \mathbf{x}_S|$ is the distance between the field point \mathbf{x} and a surface point \mathbf{x}_S , and $k = \omega/c$ is the wave number of the fluid.

Equation (2) is the starting point for most acoustic radiation and scattering problems. In a previous paper,²⁴ the authors have derived an alternate integral formulation from Eq. (2) for predicting the radiated acoustic pressure at any point external to an arbitrary object subject to constant frequency excitations

$$P(\mathbf{x}, \omega) = \mathcal{L}_1(\mathbf{x}, V_t, \omega) + \mathcal{L}_2(\mathbf{x}, V_n, \omega), \quad (3)$$

where $\mathcal{L}_{1,2}$ represent integral operators operating on the tangential and normal components of the particle velocity in the frequency domain, respectively,

$$\begin{aligned} \mathcal{L}_1(\mathbf{x}, V_t, \omega) &= \frac{i\omega\rho_0}{4\pi} \int_S \left\{ \frac{\partial \mathcal{F}}{\partial n} \left[\int_{S'} \frac{\partial \mathcal{F}}{\partial n_{S'}} \right. \right. \\ &\quad \times \left. \left. \left(\int_{(\mathbf{x}'_{S'} \rightarrow \mathbf{x}_{S'})} V_t(\mathbf{x}_{S'}, \omega) dl \right) dS' \right] \right. \\ &\quad \times \left. \left[2\pi - \int_{S'} \frac{\partial \mathcal{F}}{\partial n_{S'}} dS' \right]^{-1} \right\} dS \\ &\quad + \frac{i\omega\rho_0}{4\pi} \int_S \frac{\partial \mathcal{F}}{\partial n} \left(\int_{(\mathbf{x}'_S \rightarrow \mathbf{x}_S)} V_t(\mathbf{x}_S, \omega) dl \right) dS, \quad (4a) \end{aligned}$$

$$\begin{aligned} \mathcal{L}_2(\mathbf{x}, V_n, \omega) = & -\frac{i\omega\rho_0}{4\pi} \int_S \left\{ \frac{\partial \mathcal{G}}{\partial n} \left[\int_{S'} V_n(\mathbf{x}_{S'}, \omega) \mathcal{G} dS' \right] \right. \\ & \times \left. \left[2\pi - \int_{S'} \frac{\partial \mathcal{G}}{\partial n_{S'}} dS' \right]^{-1} \right\} dS \\ & - \frac{i\omega\rho_0}{4\pi} \int_S V_n(\mathbf{x}_S) \mathcal{G} dS, \end{aligned} \quad (4b)$$

where V_n and V_t represent the normal and tangential components of the particle velocity on a control surface S in the frequency domain. \mathcal{G} and $\partial\mathcal{G}/\partial n$ are the free-space Green's function and its normal derivative, respectively,

$$\mathcal{G} = \frac{e^{ikR}}{R} \quad \text{and} \quad \frac{\partial \mathcal{G}}{\partial n} = \frac{(ikR-1)\mathcal{G}}{R} \frac{\partial R}{\partial n}, \quad (5)$$

where n indicates the outward unit normal on S . Detailed derivations of Eqs. (3) and (4) are demonstrated in a previous paper²⁴ and therefore are omitted here for brevity.

Equation (3) shows that the radiated acoustic pressure can be expressed as an explicit function of the particle velocity distribution over a control surface that encloses completely the vibrating object under consideration. There is no need to solve an integral equation for the surface acoustic pressure, given the normal component of the surface velocity. Instead, the radiated acoustic pressure can be calculated directly once the particle velocity vector on a control surface is specified by a nonintrusive laser velocimeter. Since the surface integrals in Eq. (3) can be readily implemented by the standard Gaussian quadratures, the efficiency of numerical computations may be significantly enhanced. Moreover, the solutions thus obtained for an arbitrary object are unique. This is because the resulting integral equation for the exterior region subject to the homogeneous Neumann boundary condition does not share the same eigenvalues as those of the integral equation for the interior region.²⁴

Another advantage of Eq. (3) is that it enables one to calculate the time-domain acoustic pressure signals by taking a direct inverse Fourier transformation. Using the Fourier transformation pair defined in Eq. (1), we can write

$$\begin{aligned} p(\mathbf{x}, t) = & \int_{-\infty}^{+\infty} \mathcal{V}_n(\mathbf{x}, t-\tau) d\tau + \int_{-\infty}^{+\infty} \mathcal{V}_t(\mathbf{x}, t-\tau) d\tau \\ & + \int_{-\infty}^{+\infty} \mathcal{U}_n(\mathbf{x}, t-\tau) d\tau + \int_{-\infty}^{+\infty} \mathcal{U}_t(\mathbf{x}, t-\tau) d\tau, \end{aligned} \quad (6)$$

where \mathcal{V}_n represents the response of a simple source distribution induced by the normal component of the particle velocity, \mathcal{V}_t stands for the response of a doublet source distribution²⁷ caused by the tangential component of the particle velocity, \mathcal{U}_n depicts the response of a coupled simple/doublet source distribution generated by the normal component of the particle velocity, and \mathcal{U}_t describes the response of a coupled doublet/doublet source distribution produced by the tangential component of the particle velocity:

$$\mathcal{V}_n(\mathbf{x}, t-\tau) = \int_S v_n(\mathbf{x}_S, \tau) \epsilon(\mathbf{x}, \mathbf{x}_S, t-\tau) dS, \quad (7a)$$

$$\mathcal{V}_t(\mathbf{x}, t-\tau) = \int_S \int_{(x'_S \rightarrow x_S)} v_t(\mathbf{x}_S, \tau) \zeta(\mathbf{x}, \mathbf{x}_S, t-\tau) dl dS, \quad (7b)$$

$$\mathcal{U}_n(\mathbf{x}, t-\tau) = \int_S \int_{S'} v_n(\mathbf{x}_{S'}, \tau) \sigma(\mathbf{x}, \mathbf{x}_S, t-\tau) dS' dS, \quad (7c)$$

$$\begin{aligned} \mathcal{U}_t(\mathbf{x}, t-\tau) = & \int_S \int_{S'} \int_{(x'_S \rightarrow x_S')} v_t(\mathbf{x}_{S'}, \tau) \xi(\mathbf{x}, \mathbf{x}_S, t-\tau) \\ & \times dl dS' dS, \end{aligned} \quad (7d)$$

where $v_n(\mathbf{x}_S, \tau)$ and $v_t(\mathbf{x}_S, \tau)$ are the normal and tangential components of the particle velocity on the control surface S , ϵ and ζ are the unit impulse response functions due to simple and doublet source distributions generated by v_n and v_t , respectively, and σ and ξ are the unit impulse response functions due to coupled simple/doublet and doublet/doublet source distributions produced by v_n and v_t , respectively:

$$\epsilon(\mathbf{x}, \mathbf{x}_S, t-\tau) = - \int_{-\infty}^{+\infty} \frac{i\omega\rho_0}{8\pi^2} \frac{e^{-i\omega(t-\tau-R/c)}}{R} d\omega, \quad (8a)$$

$$\begin{aligned} \zeta(\mathbf{x}, \mathbf{x}_S, t-\tau) = & \int_{-\infty}^{+\infty} \frac{i\omega\rho_0}{8\pi^2} \left(\frac{i\omega}{c} - \frac{1}{R} \right) \\ & \times \frac{\partial R}{\partial n} \frac{e^{-i\omega(t-\tau-R/c)}}{R} d\omega, \end{aligned} \quad (8b)$$

$$\begin{aligned} \sigma(\mathbf{x}, \mathbf{x}_S, t-\tau) = & - \int_{-\infty}^{+\infty} \frac{i\omega\rho_0}{8\pi^2} \left(\frac{i\omega}{c} - \frac{1}{R} \right) \\ & \times \frac{\partial R}{\partial n} \frac{e^{-i\omega(t-\tau-R/c-R_S/c)}}{RR_S} A(\omega, \mathbf{x}_S) d\omega, \end{aligned} \quad (8c)$$

$$\begin{aligned} \xi(\mathbf{x}, \mathbf{x}_S, t-\tau) = & \int_{-\infty}^{+\infty} \frac{i\omega\rho_0}{8\pi^2} \left(\frac{i\omega}{c} - \frac{1}{R} \right) \left(\frac{i\omega}{c} - \frac{1}{R_S} \right) \frac{\partial R}{\partial n} \frac{\partial R_S}{\partial n_S} \\ & \times \frac{e^{-i\omega(t-\tau-R/c-R_S/c)}}{RR_S} A(\omega, \mathbf{x}_S) d\omega, \end{aligned} \quad (8d)$$

where $R_S = |\mathbf{x}_S - \mathbf{x}_{S'}|$ is the distance between two surface points, and $A(\omega, \mathbf{x}_S)$ is defined as

$$A(\omega, \mathbf{x}_S) = \left[2\pi - \int_{S'} \left(\frac{i\omega}{c} - \frac{1}{R_S} \right) \frac{\partial R_S}{\partial n_S} \frac{e^{-ikR_S}}{R_S} dS' \right]^{-1}. \quad (9)$$

II. TRANSIENT RADIATION DUE TO ARBITRARY TIME-DEPENDENT EXCITATIONS

The infinite integrals in Eq. (6) can be rewritten as contour integrals and evaluated by using the residue theorem.²⁸ This integral formulation can be readily extended to transient radiation from an object subject to an arbitrarily time-dependent excitation. To this end, let us examine the case in

which the normal and tangential components of the particle velocity is expressible in terms of short pulses of constant amplitudes

$$v_n(\mathbf{x}_S, t) = V_n(\mathbf{x}_S)[H(t) - H(t - \Delta t)], \quad (10a)$$

$$v_t(\mathbf{x}_S, t) = V_t(\mathbf{x}_S)[H(t) - H(t - \Delta t)], \quad (10b)$$

where $V_n(\mathbf{x}_S)$ and $V_t(\mathbf{x}_S)$ are the amplitudes of the particle velocity pulses in the normal and tangential directions, respectively, Δt is the duration of the velocity pulse, and $H(t)$ represents the Heaviside step function which is unity for $t \geq 0$ and zero for $t < 0$.

Accordingly, the time-domain acoustic pressure at any field point resulting from this velocity pulse can be written as

$$\begin{aligned} \Delta p(\mathbf{x}, t) = & [h_{\epsilon,1}(\mathbf{x}, t) - h_{\epsilon,2}(\mathbf{x}, t, \Delta t)] + [h_{\zeta,1}(\mathbf{x}, t) \\ & - h_{\zeta,2}(\mathbf{x}, t, \Delta t)] + [h_{\sigma,1}(\mathbf{x}, t) - h_{\sigma,2}(\mathbf{x}, t, \Delta t)] \\ & + [h_{\xi,1}(\mathbf{x}, t) - h_{\xi,2}(\mathbf{x}, t, \Delta t)], \end{aligned} \quad (11)$$

where $h(\mathbf{x}, t)$ is the so-called step response function corresponding to the Heaviside step function used in Eq. (10). The first subscript of h indicates the type of source distributions consistent with those defined in Eq. (7), whereas the second subscript implies the beginning and ending of a velocity pulse.

Following the procedures outlined in Ref. 26, we can derive these step response functions as

$$\begin{aligned} h_{\epsilon,1}(\mathbf{x}, t) = & -i2\pi \int_S \sum_q \frac{\eta_\epsilon(\mathbf{x}, \mathbf{x}_S, \omega_q)}{g'_\epsilon(\mathbf{x}, \mathbf{x}_S, \omega)} \\ & \times V_n(\mathbf{x}_S) e^{-i\omega_q t} H(t - R/c) dS, \end{aligned} \quad (12a)$$

$$\begin{aligned} h_{\epsilon,2}(\mathbf{x}, t) = & -i2\pi \int_S \sum_q \frac{\eta_\epsilon(\mathbf{x}, \mathbf{x}_S, \omega_q)}{g'_\epsilon(\mathbf{x}, \mathbf{x}_S, \omega)} \\ & \times V_n(\mathbf{x}_S) e^{-i\omega_q(t - \Delta t)} H(t - \Delta t - R/c) dS, \end{aligned} \quad (12b)$$

$$\begin{aligned} h_{\zeta,1}(\mathbf{x}, t) = & -i2\pi \int_S \sum_q \frac{\eta_\zeta(\mathbf{x}, \mathbf{x}_S, \omega_q)}{g'_\zeta(\mathbf{x}, \mathbf{x}_S, \omega)} \\ & \times V_t(\mathbf{x}_S) e^{-i\omega_q t} H(t - R/c) dS, \end{aligned} \quad (12c)$$

$$\begin{aligned} h_{\zeta,2}(\mathbf{x}, t) = & -i2\pi \int_S \sum_q \frac{\eta_\zeta(\mathbf{x}, \mathbf{x}_S, \omega_q)}{g'_\zeta(\mathbf{x}, \mathbf{x}_S, \omega)} \\ & \times V_t(\mathbf{x}_S) e^{-i\omega_q(t - \Delta t)} H(t - \Delta t - R/c) dS, \end{aligned} \quad (12d)$$

$$\begin{aligned} h_{\sigma,1}(\mathbf{x}, t) = & -i2\pi \int_S \sum_q \frac{\eta_\sigma(\mathbf{x}, \mathbf{x}_S, \omega_q)}{g'_\sigma(\mathbf{x}, \mathbf{x}_S, \omega)} \\ & \times V_n(\mathbf{x}_S) e^{-i\omega_q t} H(t - R/c) dS, \end{aligned} \quad (12e)$$

$$\begin{aligned} h_{\sigma,2}(\mathbf{x}, t) = & -i2\pi \int_S \sum_q \frac{\eta_\sigma(\mathbf{x}, \mathbf{x}_S, \omega_q)}{g'_\sigma(\mathbf{x}, \mathbf{x}_S, \omega)} \\ & \times V_n(\mathbf{x}_S) e^{-i\omega_q(t - \Delta t)} H(t - \Delta t - R/c) dS, \end{aligned} \quad (12f)$$

$$\begin{aligned} h_{\xi,1}(\mathbf{x}, t) = & -i2\pi \int_S \sum_q \frac{\eta_\xi(\mathbf{x}, \mathbf{x}_S, \omega_q)}{g'_\xi(\mathbf{x}, \mathbf{x}_S, \omega)} \\ & \times V_t(\mathbf{x}_S) e^{-i\omega_q t} H(t - R/c) dS, \end{aligned} \quad (12g)$$

$$\begin{aligned} h_{\xi,2}(\mathbf{x}, t) = & -i2\pi \int_S \sum_q \frac{\eta_\xi(\mathbf{x}, \mathbf{x}_S, \omega_q)}{g'_\xi(\mathbf{x}, \mathbf{x}_S, \omega)} \\ & \times V_t(\mathbf{x}_S) e^{-i\omega_q(t - \Delta t)} H(t - \Delta t - R/c) dS. \end{aligned} \quad (12h)$$

Note that in Eq. (12), we have replaced the integrands of the inverse Fourier transformations by ratios $\eta(\mathbf{x}, \mathbf{x}_S, \omega)/g(\mathbf{x}, \mathbf{x}_S, \omega)$, where the subscripts ϵ, ζ, σ , and ξ in η and g indicate simple, doublet, coupled simple/doublet, and coupled doublet/doublet source distributions, respectively. The symbols η and g represent two frequency-dependent functions, which are devised to facilitate the evaluations the infinite integrals in Eq. (6) by using the residue theorem.²⁸ In particular, the function η is analytic in ω , and a prime on g represents a derivative with respect to ω .²⁸ The symbol ω_q stands for the q th root of g

$$g(\mathbf{x}, \omega_q) = 0, \quad \text{Im}(\omega_q) \leq 0. \quad (13)$$

Equation (11) demonstrates that the transient acoustic pressure resulting from a velocity pulse can be written as a superposition of two step response functions that are of the same amplitudes, but opposite in signs, and are separated in time by Δt . These step response functions (12) consist of sums of residues at the complex roots of the homogeneous Eq. (13). The real and imaginary parts of these complex roots correspond, respectively, to the phase and amplitude of a transient acoustic wave that decays exponentially in time. A minus sign on the right side of Eq. (12) implies that the contour integration is carried out in the clockwise direction in the complex plane. This is in compliance with the requirement that the amplitude of the acoustic wave remains finite as it propagates in space and time.

Since any arbitrary time-dependent function can be represented by a sum of many short pulses of constant amplitudes, the resulting acoustic pressure can be written as a superposition of contributions from each individual pulses in the form of Eq. (11)

$$\begin{aligned} p(\mathbf{x}, t) = & \sum_j \left[\frac{h_{\epsilon,1}(\mathbf{x}, t_j) - h_{\epsilon,2}(\mathbf{x}, t_j, \Delta t)}{\Delta t} \right] \Delta t \\ & + \sum_j \left[\frac{h_{\zeta,1}(\mathbf{x}, t_j) - h_{\zeta,2}(\mathbf{x}, t_j, \Delta t)}{\Delta t} \right] \Delta t \\ & + \sum_j \left[\frac{h_{\sigma,1}(\mathbf{x}, t_j) - h_{\sigma,2}(\mathbf{x}, t_j, \Delta t)}{\Delta t} \right] \Delta t \\ & + \sum_j \left[\frac{h_{\xi,1}(\mathbf{x}, t_j) - h_{\xi,2}(\mathbf{x}, t_j, \Delta t)}{\Delta t} \right] \Delta t. \end{aligned} \quad (14)$$

As the duration of the pulse $\Delta t \rightarrow 0$, the square bracket terms on the right side of Eq. (14) become impulse response functions. The total transient acoustic pressure $p(\mathbf{x}, t)$ due to all the incremental velocity pulses prior to time t can then be written as a Duhamel integral,²⁹

$$p(\mathbf{x}, t) = \int_0^t [\hat{h}_\epsilon(\mathbf{x}, t - \tau) + \hat{h}_\zeta(\mathbf{x}, t - \tau) + \hat{h}_\sigma(\mathbf{x}, t - \tau) + \hat{h}_\xi(\mathbf{x}, t - \tau)] d\tau, \quad (15)$$

where \hat{h} is known as the impulse response function due to a velocity pulse at time τ ,

$$\begin{aligned} \hat{h}_\epsilon(\mathbf{x}, t - \tau) &= -i2\pi \int_S \sum_q \frac{\eta_\epsilon(\mathbf{x}, \mathbf{x}_S, \omega_q)}{g'_\epsilon(\mathbf{x}, \mathbf{x}_S, \omega_q)} V_n(\mathbf{x}_S) e^{-i\omega_q \tau} dS, \\ \hat{h}_\zeta(\mathbf{x}, t - \tau) &= -i2\pi \int_S \sum_q \frac{\eta_\zeta(\mathbf{x}, \mathbf{x}_S, \omega_q)}{g'_\zeta(\mathbf{x}, \mathbf{x}_S, \omega_q)} V_t(\mathbf{x}_S) e^{-i\omega_q \tau} dS, \\ \hat{h}_\sigma(\mathbf{x}, t - \tau) &= -i2\pi \int_S \sum_q \frac{\eta_\sigma(\mathbf{x}, \mathbf{x}_S, \omega_q)}{g'_\sigma(\mathbf{x}, \mathbf{x}_S, \omega_q)} V_n(\mathbf{x}_S) e^{-i\omega_q \tau} dS, \\ \hat{h}_\xi(\mathbf{x}, t - \tau) &= -i2\pi \int_S \sum_q \frac{\eta_\xi(\mathbf{x}, \mathbf{x}_S, \omega_q)}{g'_\xi(\mathbf{x}, \mathbf{x}_S, \omega_q)} V_t(\mathbf{x}_S) e^{-i\omega_q \tau} dS. \end{aligned} \quad (16)$$

Equation (15) shows that the transient acoustic pressure at any point \mathbf{x} and time t can be expressed as a convolution integral of the impulse response functions over the time history of the particle velocity specified on the control surface S .

III. VALIDATIONS

In this section, we demonstrate both analytically and numerically the validations of the explicit integral formulation (6) on transient sound radiation from various sources.

A. An explosively expanding sphere

As a first example, we consider the transient acoustic pressure signal generated by an explosively expanding sphere in an unbounded fluid medium. Assume that the particle velocity measured on a control surface of radius a is

$$\mathbf{v}(t) = V_n H(t - a/c) \mathbf{n}, \quad (17)$$

where V_n is the magnitude of the particle velocity. Since the sphere expands uniformly in all directions, the tangential component of the particle velocity is identically zero, and the normal component of the particle velocity is constant.

Substituting Eq. (17) into (6), interchanging the order of integrations, and carrying out those with respect to τ , dS' , and dS first, we obtain

$$p(\mathbf{x}, t) = \frac{\rho_0 V_n a^2}{2\pi r} \int_{-\infty}^{+\infty} \frac{e^{-i\omega(t-r/c)}}{(1-ika)} d\omega, \quad (18)$$

where r is the distance from the center of the sphere to the observation point in the field.

Evaluation of the integral in Eq. (18) can be facilitated by using the residue theorem.²⁸ Setting the denominator of the integrand in Eq. (18) to zero yields one root at $\omega_0 = -ic/a$. The residue at ω_0 multiplied by $-i2\pi$ and the Heaviside step function leads to a transient acoustic pressure signal

$$p(\mathbf{x}, t) = \frac{\rho_0 c V_n a}{r} e^{-(ct-r)/a} H(t-r/c), \quad (19)$$

which agrees perfectly with the analytic solution.²⁸

B. An impulsively accelerated sphere

As a second example we consider the transient acoustic pressure signal produced by an impulsively accelerated sphere in the positive z -axis direction in an unbounded fluid medium. Assume that the particle velocity measured on a control surface of radius a is

$$\mathbf{v}(\mathbf{x}_S, t) = V_c H(t - a/c) \mathbf{e}_z, \quad (20a)$$

whose Fourier transformation is given by

$$\mathbf{V}(\mathbf{x}_S, \omega) = \frac{iV_c e^{ika}}{\omega} \mathbf{e}_z, \quad (20b)$$

where V_c is the magnitude of the velocity at the center of a control surface.

For convenience, we assume that the normal and tangential components of the particle velocity on the control surface are specified by a nonintrusive laser velocimeter, whose Fourier transformation are given by

$$V_n(\mathbf{x}_S, \omega) = \frac{iV_c \cos \theta}{\omega} e^{ika}, \quad (21a)$$

$$V_\theta(\mathbf{x}_S, \omega) = \frac{V_c (ka + i) \sin \theta}{\omega(2 - k^2 a^2 - i2ka)} e^{ika}, \quad (21b)$$

$$V_\phi(\mathbf{x}_S, \omega) = 0, \quad (21c)$$

where θ is the angle between \mathbf{e}_z and \mathbf{e}_R , which points in the direction of wave propagation from the source to the receiver.

Substituting Eq. (21) into (6) then yields the transient acoustic pressure signal. To simplify the calculations, we assume that $a \ll r$. Hence, we can approximate $R \approx r$, $e^{ikR} \approx e^{ikr + ika \cos \theta}$, and $\partial R / \partial n \approx \cos \theta$.²⁶ With these simplifications, we can interchange the order of integrations and carry out those with respect to $d\tau$, dS' , and dS first, and obtain the following results (the details are omitted for brevity),

$$\begin{aligned} p(\mathbf{x}, t) &= \frac{\rho_0 V_c a^3}{2\pi r^2} \int_{-\infty}^{+\infty} \frac{(1-ikr)}{(2 - k^2 a^2 - i2ka)} \\ &\quad \times \cos \theta e^{-i\omega(t-r/c)} d\omega. \end{aligned} \quad (22)$$

The integral in Eq. (22) can be evaluated by using the residue theorem. Setting the denominator of the integrand on the right side of Eq. (22) to zero yields two roots, $\omega_1 = (1 - i)c/a$ and $\omega_2 = -(1 + i)c/a$. Summing the residues at these two roots and multiplying by $-i2\pi$ and the Heaviside step function, we obtain

$$\begin{aligned} p(\mathbf{x}, t) &= \frac{\rho_0 c V_c a \cos \theta}{r} e^{-(ct-r)/a} H\left(t - \frac{r}{c}\right) \left[\cos\left(\frac{ct-r}{a}\right) \right. \\ &\quad \left. - \left(1 - \frac{a}{r}\right) \sin\left(\frac{ct-r}{a}\right) \right], \end{aligned} \quad (23)$$

which agrees with the analytic result.²⁸

C. An impulsively accelerated baffled circular disk

This example involves a circular disk of radius a mounted on an infinite rigid baffle. The disk is impulsively accelerated in the positive z -axis direction at $t=0$ and the surface velocity can be depicted by

$$\mathbf{v}(\mathbf{x}_S, t) = VH(a - r_S)H(t)\mathbf{e}_z, \quad (24)$$

where V is the magnitude of the velocity and r_S is the radial distance measured from the central axis of the disk on $z=0$ plane.

Alternatively, one can replace the baffled circular disk by a thin disk centered at the $z=0$ plane in a free field. The two sides of this thin disk are impulsively accelerated simultaneously in opposite directions. The acoustic pressure resulting from this impulsively accelerated circular disk can be described by Eq. (6), and the corresponding impulse response functions are given by Eq. (8). In evaluating these impulse response functions, we make use of the antisymmetric property of $\partial R/\partial n = z/R$ and $\partial R_S/\partial n_S = z/R_S$, and obtain

$$\begin{aligned} \mathcal{F}_n(\mathbf{x}, t - \tau) &= \int_{S^+} \cdots + \int_{S^-} \cdots \\ &= 2 \int_{S^+} v_n(\mathbf{x}_S, \tau) \epsilon(\mathbf{x}, \mathbf{x}_S, t - \tau) dS, \end{aligned} \quad (25a)$$

$$\mathcal{F}_t(\mathbf{x}, t - \tau) = \int_{S^+} \int_{(\mathbf{x}'_S \rightarrow \mathbf{x}_S)} \cdots + \int_{S^-} \int_{(\mathbf{x}'_S \rightarrow \mathbf{x}_S)} \cdots \equiv 0, \quad (25b)$$

$$\begin{aligned} \mathcal{U}_n(\mathbf{x}, t - \tau) &= \int_{S^+} \int_{S^{+'}} \cdots + \int_{S^-} \int_{S^{-'}} \cdots + \int_{S^+} \int_{S^{-'}} \cdots \\ &\quad + \int_{S^-} \int_{S^{+'}} \cdots \equiv 0, \end{aligned} \quad (25c)$$

$$\begin{aligned} \mathcal{U}_t(\mathbf{x}, t - \tau) &= \int_{S^+} \int_{S^{+'}} \int_{(\mathbf{x}'_S \rightarrow \mathbf{x}_S)} \cdots + \int_{S^-} \int_{S^{-'}} \int_{(\mathbf{x}'_S \rightarrow \mathbf{x}_S)} \cdots \\ &\quad + \int_{S^+} \int_{S^{-'}} \int_{(\mathbf{x}'_S \rightarrow \mathbf{x}_S)} \cdots \\ &\quad + \int_{S^-} \int_{S^{+'}} \int_{(\mathbf{x}'_S \rightarrow \mathbf{x}_S)} \cdots \equiv 0, \end{aligned} \quad (25d)$$

where S^+ and S^- represent the $z > 0$ and $z < 0$ sides of the disk, respectively. Consequently, the acoustic pressure at any field point and time $p(\mathbf{x}, t)$ can be written as

$$p(\mathbf{x}, t) = \int_{-\infty}^{+\infty} \mathcal{F}_n(\mathbf{x}, t - \tau) d\tau. \quad (26)$$

Substituting Eqs. (8), (24), and (25) into (26), interchanging the order of integrations, and carrying out that with respect to τ first, we obtain

$$\begin{aligned} p(\mathbf{x}, t) &= -2 \int_{-\infty}^{\infty} \int_{S^+} \int_{-\infty}^{\infty} v_n(\mathbf{x}_S, \tau) \frac{i\omega\rho_0}{8\pi^2} \frac{e^{-i\omega(t-\tau-R/c)}}{R} \\ &\quad \times d\tau d\omega dS \\ &= -\frac{\rho_0 V}{4\pi^2} \int_{-\infty}^{\infty} \int_{S^+} \int_{-\infty}^{\infty} i\omega H(\tau) \frac{e^{-i\omega(t-\tau-R/c)}}{R} \\ &\quad \times d\tau d\omega dS \\ &= \frac{\rho_0 V}{4\pi^2} \int_{-\infty}^{\infty} \int_{S^+} \frac{e^{-i\omega(t-R/c)}}{R} dS d\omega. \end{aligned} \quad (27)$$

The double integrations in Eq. (27) can be evaluated by following the standard procedures that are outlined in many text books,^{28,30} and the result is

$$p(\mathbf{x}, t) = \begin{cases} 0 & ct < z \\ 0 & w > a, \quad z < ct < \sqrt{(a-w)^2 + z^2} \\ \rho_0 c V & w < a, \quad z < ct < \sqrt{(a-w)^2 + z^2} \\ \frac{\rho_0 c V}{\pi} \cos^{-1} \left(\frac{c^2 t^2 - z^2 + w^2 - a^2}{2w\sqrt{c^2 t^2 - z^2}} \right) & \sqrt{(a-w)^2 + z^2} < ct < \sqrt{(a+w)^2 + z^2} \\ 0 & ct > \sqrt{(a+w)^2 + z^2}. \end{cases} \quad (28)$$

D. Right circular cylinders

In the previous examples, the geometry of the control surface is separable so that the analytic solutions can be obtained. In what follows, we consider cases whose analytic solutions cannot be found. Suppose that the particle velocities are specified over a slender cylindrical surface with two flat ends. The aspect ratio is $b/a = 10$, where a and b are the radius and half length of the cylinder, respectively.

Since analytical solutions are not available, the transient acoustic pressures are solved numerically. As a comparison, we assume that the particle velocity distribution over the cylindrical surface is generated by an explosively expanding sphere located at the center of the cylinder:

$$\mathbf{v}(\mathbf{r}, t) = VH(t - r/c)\mathbf{e}_r. \quad (29)$$

The normal and tangential components of the particle velocity on the cylindrical surface are calculated numerically based on Eq. (29), and taken as the input data to Eq. (6). The transient acoustic pressure signal thus obtained is then compared with that of an impulsively expanding sphere.

In carrying out the surface integrations involved Eq. (6), we uniformly divide the two flat ends along the radial direction into N rings, and the side wall into L rings. Each of these rings is further divided into M equal segments along the circumference. These integrations are calculated from $ka = 0.1$ to 204.7 at an interval of $\Delta ka = 0.2$, thus generating a spectrum of 1024 discrete lines. Note that the accuracy of numerical computations can be enhanced by further widening the sampling frequency range and increasing the sampling rate. The present frequency range is selected to illustrate the usage of Eq. (6) in determining transient acoustic

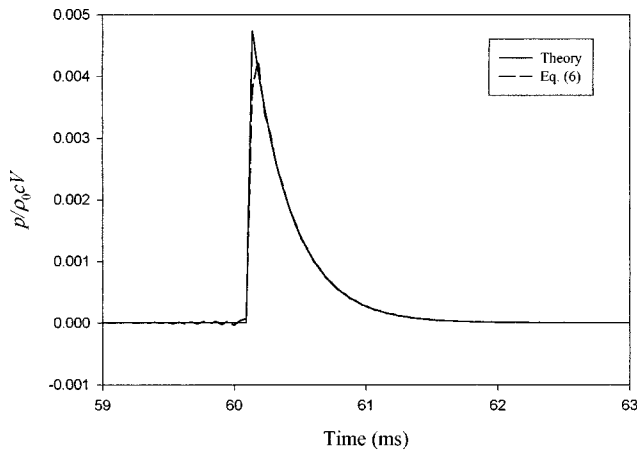


FIG. 1. Comparison of the dimensionless transient acoustic pressure signals from an explosively expanding cylinder at $r/a=20$.

pressure signals. Because of a relatively narrow frequency range and low sampling rate, some distortions in the numerical results may appear.

In this example, we use a fixed discretization scheme, namely, $N=96$, $L=1920$, and $M=192$ for all ka values. Numerical integrations over each element are carried out by using Gaussian quadratures with nine interior points.³¹ The time-domain acoustic pressure is obtained by taking a direct discrete inverse Fourier transformation.

Figure 1 shows the comparisons of nondimensionalized acoustic pressure signal p/ρ_0cV in time domain obtained by using Eq. (6) and the exact solution at a dimensionless radial distance $r/a=20$. Results show that before the arrival of the acoustic pressure pulse the field is quiescent. At $t=60.16$ ms, however, the amplitude of the dimensionless acoustic pressure rises instantly from zero to 0.00473, and then decays exponentially to zero with time. Since the acoustic pressure pulse is generated by an explosively expanding cylinder, there is a net injection of fluid into the medium, which leads to a compression wave only.

On the other hand, the numerical solutions indicate oscillations, known as Gibbs phenomenon, prior to the arrival of the acoustic pressure pulse. Moreover, the peak amplitude is 0.00425 (about 10% lower than the exact value) at 60.18 ms (0.02 ms later than the exact time). These discrepancies are caused by the discretizations in the numerical computations. The Gibbs phenomenon can be effectively reduced by increasing the sampling rate, and the rise of the acoustic pressure pulse can be enhanced by raising the cutoff frequency in the frequency domain. This is because the early portion of a transient event corresponds to the limit $\omega \rightarrow \infty$ in taking an inverse Fourier transformation. Similarly, by lowering the starting frequency to zero, we can eliminate fluctuations around the falling of the pressure pulse. This is because the late portion of a transient event is governed by the limit $\omega \rightarrow 0$ in taking an inverse Fourier transformation.

Next, we consider the case in which the particle velocity vector is generated by an impulsively accelerated sphere located at the center of the cylinder. Assume that the sphere is impulsively accelerated in the positive z -axis direction,

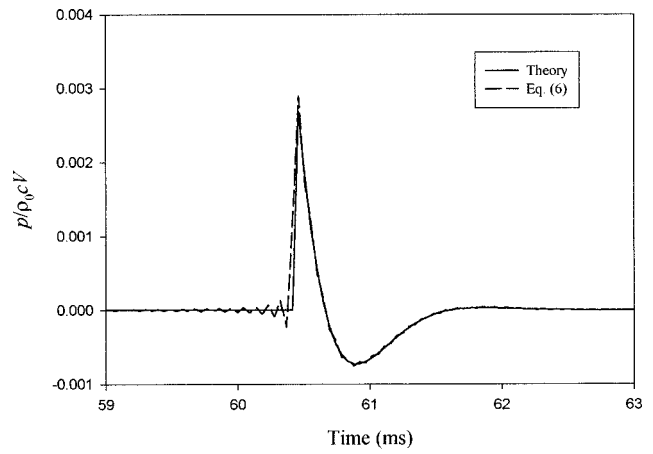


FIG. 2. Comparison of the dimensionless transient acoustic pressure signals from an impulsively accelerating cylinder at $r/a=20$.

$$\mathbf{v}(\mathbf{r}, t) = VH(t - r/c)\mathbf{e}_z. \quad (30)$$

As in the previous case, the normal and tangential components of the particle velocity over a slender cylindrical surface are calculated numerically based on Eq. (30). The results thus obtained are substituted into Eq. (6) to compute the transient acoustic pressure signal directly, and then compared with the exact solution.

The same procedures in the numerical computations as described above are repeated from $ka=0.1$ to 204.7 at an interval of $\Delta ka=0.2$, yielding a spectrum of 1024 discrete lines. Once again, a fixed discretization scheme is used with $N=96$, $L=1920$, and $M=192$, respectively.

Figure 2 depicts the comparisons of the dimensionless acoustic pressure signal thus obtained and the exact solution at a dimensionless radial distance $r/a=20$. In this case, the field is quiescent until $t=60.46$ ms when the acoustic pressure pulse arrives. At this time the amplitude of the dimensionless acoustic pressure rises instantly from zero to 0.00269, then decays exponentially. Since the acoustic pressure pulse is generated by an impulsively accelerating cylinder, the fluid is excited by a momentum, which produces a compression wave followed by a rarefaction wave in the medium.

Once again, there appear to be some oscillations (Gibbs phenomenon) in the numerical results prior to the arrival of the acoustic pressure pulse. However, the peak occurs at exactly the same time as the true value with a dimensionless acoustic pressure amplitude of 0.00289 (about 7.4% higher than the exact value). As in all numerical computations, the Gibbs phenomenon can be suppressed by further increasing the sampling rate inside the selected frequency range.

IV. CONCLUDING REMARKS

An explicit integral formulation is derived for predicting transient acoustic pressure signals. The radiated acoustic pressure is shown to be expressible as a sum of integrations of simple and doublet source distributions and their couplings induced by the normal and tangential components of the particle velocity, which can be measured by a nonintrusive laser velocimeter. For arbitrary time-dependent excita-

tions, the radiated acoustic pressure can be written as a sum of Duhamel integrals. The transient acoustic pressure at any field point and time can be expressed as convolution integrals of the impulse response functions to the time history of the particle velocity distribution over the control surface.

ACKNOWLEDGMENT

This work was supported by a grant from National Science Foundation, No. CMS-9414424.

- ¹K. M. Mitzner, "Numerical solution for transient scattering from a hard surface of arbitrary shape—Retarded potential technique," *J. Acoust. Soc. Am.* **42**, 391–397 (1967).
- ²C. L. S. Farn and H. Huang, "Transient acoustic fields generated by a body of arbitrary shape," *J. Acoust. Soc. Am.* **43**, 252–257 (1968).
- ³T. L. Geers, "Excitation of an elastic cylindrical shell by a transient acoustic wave," *ASME Journal of Applied Mechanics* **36**, 459–469 (1969).
- ⁴H. Huang, "An exact analysis of the transient interaction of acoustic plane waves with a cylindrical shell," *ASME Journal of Applied Mechanics* **37**, 1091–1099 (1970).
- ⁵H. Huang, "Transient interaction of plane acoustic waves with a spherical elastic shell," *J. Acoust. Soc. Am.* **45**, 661–668 (1969).
- ⁶H. Huang, "Transient response of two fluid-coupled spherical elastic shells to an incident pressure pulse," *J. Acoust. Soc. Am.* **65**, 881–887 (1979).
- ⁷R. T. Menton and E. B. Magrab, "Far field radiation of internally generated transient acoustic pulses transmitted through a spherical shell," *J. Acoust. Soc. Am.* **55**, 237–246 (1974).
- ⁸T. L. Geers, "Residual potential and approximate methods for three dimensional fluid-structure interaction problems," *J. Acoust. Soc. Am.* **49**, 1505–1510 (1971).
- ⁹T. L. Geers, "Doubly asymptotic approximations for transient motions of submerged structures," *J. Acoust. Soc. Am.* **64**, 1500–1508 (1978).
- ¹⁰D. D. Ebenezer and P. R. Stepanishen, "Transient response of fluid-loaded plates via an impulse response method," *J. Acoust. Soc. Am.* **82**, 659–666 (1987).
- ¹¹P. R. Stepanishen and D. D. Ebenezer, "An *in vacuo* modal expansion to determine the transient response of fluid loaded planar vibrators," *J. Acoust. Soc. Am.* **91**, 453–472 (1992).
- ¹²D. D. Ebenezer and P. R. Stepanishen, "Wave-vector-time domain and Kirchhoff integral equation methods to determine the transient acoustic radiation loading on circular cylinders," *J. Acoust. Soc. Am.* **89**, 2532–2544 (1991).
- ¹³P. R. Stepanishen and H. W. Chen, "Acoustic time-dependent loading on elastic shells of revolution using the internal source density and svd method," *J. Acoust. Soc. Am.* **99**, 1913–1923 (1996).
- ¹⁴P. R. Stepanishen, "Transient vibratory response of fluid-loaded shells using the convolution integral equations," *J. Acoust. Soc. Am.* **101**, 1877–1884 (1997).
- ¹⁵H. Yeh and H. Z. Cummins, "Localized fluid flow measurements with a He-Ne laser spectrometer," *Appl. Phys. Lett.* **4**, 176–178 (1964).
- ¹⁶L. E. Drain, *The Laser Doppler Technique* (Wiley, Chichester, 1980).
- ¹⁷J. Jarzynski, D. Lee, J. Vignola, Y. H. Berthelot, and A. D. Pierce, "Fiber-optic Doppler systems for remote sensing of fluid flow," *Proc. SPIE* **925**, 250–254 (1988).
- ¹⁸K. J. Taylor, "Absolute measurement of acoustic particle velocity," *J. Acoust. Soc. Am.* **59**, 691–694 (1976).
- ¹⁹K. J. Taylor, "Absolute calibration of microphones by a laser-Doppler technique," *J. Acoust. Soc. Am.* **70**, 939–945 (1981).
- ²⁰P. S. Dobbelday and H. C. Schau, "Laser Doppler anemometry detection of hydroacoustic particle velocity," *J. Acoust. Soc. Am.* **86**, 891–894 (1989).
- ²¹J. Vignola, Y. H. Berthelot, and J. Jarzynski, "Nonintrusive absolute measurements of acoustic particle velocity in fluids," in *Proceedings of the 13th International Congress on Acoustics*, edited by P. Pravica (Dragan Srnic, Sabac, Yugoslavia, 1989), Vol. 4, pp. 45–48.
- ²²J. Vignola, Y. H. Berthelot, and J. Jarzynski, "Laser detection of sound," *J. Acoust. Soc. Am.* **90**, 1275–1286 (1991).
- ²³J. Vignola, Y. H. Berthelot, S. Jones, and J. Jarzynski, "Equation of motion of microparticles in suspension in an insonified medium," *J. Acoust. Soc. Am.* **92**, 332–334 (1992).
- ²⁴S. F. Wu and Q. Hu, "An alternative formulation for predicting sound radiation from a vibrating object," *J. Acoust. Soc. Am.* **103**, 1763–1774 (1998).
- ²⁵T. Brooks, "An experimental evaluation of the application of the Kirchhoff formulation for sound radiation from an oscillating airfoil," NASA-TP-1048, December 1977.
- ²⁶S. F. Wu, "Transient sound radiation from impulsively accelerated bodies," *J. Acoust. Soc. Am.* **94**, 542–553 (1993).
- ²⁷L. G. Copley, "Fundamental results concerning integral representations in acoustic radiation," *J. Acoust. Soc. Am.* **44**, 28–32 (1968).
- ²⁸M. C. Junger and D. Feit, *Sound, Structures, and Their Interactions* (MIT, Cambridge, MA, 1972), Chap. 14, pp. 403–430.
- ²⁹R. R. Craig, Jr., *Structural Dynamics: An Introduction to Computer Methods* (Wiley, New York, 1981), Chap. 6, pp. 123–127.
- ³⁰A. D. Pierce, *Acoustics: An Introduction to Its Physical Principles and Applications* (McGraw-Hill, New York, 1981), Chap. 5, pp. 220–234.
- ³¹G. A. Korn and T. M. Korn, *Mathematical Handbook for Scientists and Engineers* (McGraw-Hill, New York, 1968), pp. 773–777.

Caustic diffraction fields in a downward refracting atmosphere

Erik M. Salomons

TNO Institute of Applied Physics, P.O. Box 155, 2600 AD Delft, The Netherlands

(Received 13 September 1997; revised 20 July 1998; accepted 25 August 1998)

A fast and accurate ray model is developed for sound propagation in a downward refracting atmosphere. The model employs a new approach to the classification and computation of ray paths and caustic curves. The approach is valid for a large set of smooth sound-speed profiles, including realistic, nonlinear profiles such as the logarithmic profile. An ordered series of rays and caustics is found in this case, including caustics with a cusp. The sound-pressure field is computed by combining geometrical acoustics and the theory of caustics. The field on the illuminated side of a caustic is computed by modifying the geometrical-acoustics solution. The field on the shadow side of a caustic, i.e., the caustic diffraction field, is computed by extrapolation of various quantities into the shadow region. Different approaches to this extrapolation are considered. It is found that horizontal extrapolation gives the best results. The accuracy of the ray model is demonstrated by comparison with numerical solutions of the one-way wave equation. If caustic diffraction fields are ignored, discontinuities of more than 10 dB occur in the sound-pressure field. © 1998 Acoustical Society of America. [S0001-4966(98)01012-1]

PACS numbers: 43.28.Fp, 43.20.Dk, 43.50.Vt [LCS]

INTRODUCTION

The ray model for sound propagation in a refracting medium has been widely used, in particular in ocean acoustics. The principles of ray acoustics, or geometrical acoustics, have been described by Keller.¹ Geometrical acoustics fails at caustic surfaces. At a caustic surface, focusing of sound rays occurs and infinite amplitudes are predicted by geometrical acoustics. Various theories have been developed for the field in the vicinity of a caustic.²⁻¹¹ These theories can be combined with the ray model. This yields finite amplitudes at caustics and diffraction fields in caustic shadow regions.

The ray model has also been applied to sound propagation in the atmosphere. Recent work¹²⁻¹⁷ has been concerned primarily with the effects of wind and turbulence in the atmosphere. It is of great interest to develop a practical ray model that can be used for outdoor noise control. A practical ray model should be sufficiently fast and accurate, and should be applicable to systems with realistic atmospheres (with nonlinear sound-speed profiles) and realistic ground surfaces (with complex ground impedances). It is the objective of this work to develop such a model. The model is restricted to downward refracting atmospheres. In noise control, one commonly measures noise by long-term-average sound levels, which are dominated by the high levels that are produced by downward refraction. Wind and temperature gradients in the atmosphere are represented by a smooth vertical profile of the effective sound speed.¹¹ It should be emphasized that profiles of the effective sound speed usually are highly nonlinear, with large gradients near the ground surface.¹⁸ The ray model presented in this work can be used for various smooth, nonlinear profiles, such as logarithmic or power profiles. Although efficient ray-tracing algorithms exist,^{19,20} ray-tracing computations usually require considerable computing times. The approach presented here, however, makes use of the ordering of rays for smooth profiles, and this results in relatively small computing times.

The ray representation of the sound field of a monopole source in a refracting medium is a high-frequency asymptotic limit. For a system with a reflecting (i.e., rigid) ground surface, the ray representation can be derived from wave theory, by starting from a plane-wave expansion of the field of a monopole source and using the WKB approximation and the stationary phase method.^{5,21} For a system with a finite-impedance ground surface, the ray representation can be used in combination with the spherical wave reflection coefficient as an approximation of the effect of multiple ground reflections.¹⁵ The justification of this approximation has been studied extensively.²²⁻²⁴ The effect of absorption of sound by a finite-impedance ground surface on the accuracy of the ray model has also been studied.²⁵

On the other hand, the effects of caustics have been ignored in many ray model studies of atmospheric sound propagation. This is unacceptable for a practical model. An accurate, continuous sound-pressure field is obtained only if the effects of caustics are taken into account, including diffraction fields in caustic shadow regions. If the caustic diffraction fields are ignored, discontinuities of more than 10 dB may occur in the sound-pressure field (see Fig. 9 in Ref. 15, or Fig. 11 in this work). Examples of caustic structures can be found in Refs. 5-9 and 26-31. For the smooth sound-speed profiles studied here, an infinite series of caustic curves is found, including caustics with a cusp. The series of caustic curves for the special case of a linear profile is shown in Fig. 43.8 of Ref. 5.

The work of Ludwig³ and Kravtsov⁴ gives a complete description of the field in the vicinity of caustics, including cusped caustics. Approximate expressions for smooth caustics have been obtained by Buchal and Keller,² Pierce,¹¹ Brekhovskikh,⁵ and Sachs and Silbiger.⁶ Weinberg^{7,8} and Brown^{9,10} followed different approaches to the computation of the field in the vicinity of caustics. Both Weinberg and Brown claimed that their approaches are more efficient than

the Ludwig–Kravtsov approach, for complex caustics. In this paper, however, we will use the Ludwig–Kravtsov approach, which is found to work well for the caustics studied here.

An important point of this paper is the problem of extrapolation into the shadow region of a caustic. On the illuminated side of a caustic, the field is computed directly from the geometrical-acoustics solution, following the approach proposed by Kravtsov.⁴ On the shadow side, however, this does not work since there are no rays here. The field on the shadow side can be computed by extrapolation of various quantities into the shadow region. Only in cases with an analytical geometrical-acoustics solution, extrapolation into the shadow region is not necessary. In these cases, complex rays¹ and complex saddle points may be used for the computation of the exponentially decaying field in the shadow region. In this way, the field near caustics has been computed analytically^{29,30} for a well-known analytical case.²⁷ In other cases, extrapolation into the shadow region appears the best practical approach.²⁹

I. SETUP OF THE MODEL

A. System

We consider sound propagation from a monopole source to a distant receiver, in a system with a homogeneous, finite-impedance ground surface and a downward refracting atmosphere. A layered atmosphere is assumed, with an effective sound speed that increases monotonically with height (the effective sound speed includes wind and temperature effects¹¹).

The system has axial symmetry around the vertical axis through the source. We use a rectangular rz coordinate system, with r the horizontal range measured from the source and z the height above the ground. The source position is $(0, z_1)$, the receiver position is (r, z_2) . The vertical profile of the effective sound speed is denoted as $c(z)$. The approach developed in the following is valid for a large set of smooth sound-speed profiles $c(z)$. This set is defined indirectly by the fact that all profiles have the same caustic structure. Examples of this caustic structure are shown in Fig. 5. From various other examples we concluded that a necessary condition for the smooth profiles is that there is no change of sign of the second derivative $c''(z)$.

B. Sound-pressure field

We use the symbol p for the normalized sound pressure, i.e., the sound pressure divided by the amplitude of the free-field sound pressure. We write

$$p = p_r + p_d \quad (1)$$

with p_r the geometrical-acoustics contribution and p_d the contribution of diffraction fields of caustics. By definition, the diffraction field of a caustic is nonzero only in the shadow region of the caustic. At the caustic, the diffraction field changes discontinuously between a finite value on the shadow side to zero on the illuminated side. The total field p is continuous, as the geometrical-acoustics field has an opposite discontinuity at the caustic, due to the appearance of two new rays in the illuminated region. In the standard

geometrical-acoustics approximation, the two rays have infinite amplitudes at the caustic. From the theory of caustics the correct finite amplitudes and correct phases are obtained. In Secs. III and IV of this paper, the caustic corrections in the illuminated region and the diffraction fields in the shadow regions are described. In Sec. II, the geometrical-acoustics contribution without corrections is described, as well as caustic parameters that are used in Sec. IV. It should be noted that in the acoustic literature usually all deviations from standard geometrical acoustics are referred to as diffraction phenomena.^{11,19} This would imply that p_r and p_d in Eq. (1) have opposite *infinite* discontinuities at a caustic, with nonzero p_d on the illuminated side. In this work, however, it is more convenient to include the deviations in the illuminated region in the geometrical-acoustics contribution, so that p_r and p_d have opposite *finite* discontinuities at a caustic, and $p_d = 0$ and p_r is finite on the illuminated side.

II. GEOMETRICAL-ACOUSTICS CONTRIBUTION TO THE FIELD

The term p_r in Eq. (1) is written as

$$p_r = \sum_m A_m e^{i\phi_m}, \quad (2a)$$

where the sum is over all rays m ,

$$A_m = f_m R_m^{N_m} \quad (2b)$$

is the amplitude of ray m , where f_m is the focusing factor ($f_m = 1$ in free field), R_m the ground reflection coefficient, and N_m the number of ground reflections, and

$$\phi_m = \omega t_m \quad (2c)$$

is the phase of ray m , with ω the angular frequency and t_m the travel time along the ray. A rigorous derivation of Eq. (2) for a system with a reflecting ground has been given by Brekhovskikh,⁵ who developed ray theory as a high-frequency limit of wave theory, for a monopole source in a surface waveguide (i.e., a downward refracting atmosphere). For a system with a finite-impedance ground, Eq. (2) was proposed by L'Espérance *et al.*¹⁵ These authors also describe a method to include the effect of atmospheric turbulence (turbulence causes a reduction of the coherence between sound rays). For simplicity, turbulence is ignored here.

In the following sections, first the computation of ray paths and caustic curves is described. Next the computation is described of the various quantities in Eq. (2).

A. Computation of ray paths

For a fixed source position and sound-speed profile, a ray is completely determined by the maximum height h of the ray, i.e., the height of the turning point⁵ [see Fig. 1(a)]. The horizontal distance covered by a ray can be written as follows:

$$r_{nj}(h) = 2(n + m_{0j})\delta_0(h) + m_{1j}\delta_1(h) + m_{2j}\delta_2(h) \quad (3)$$

with index $n = 0, 1, \dots$, the number of turning points along the ray, index $j = 1, 2, 3, 4$ distinguishing four rays with equal n

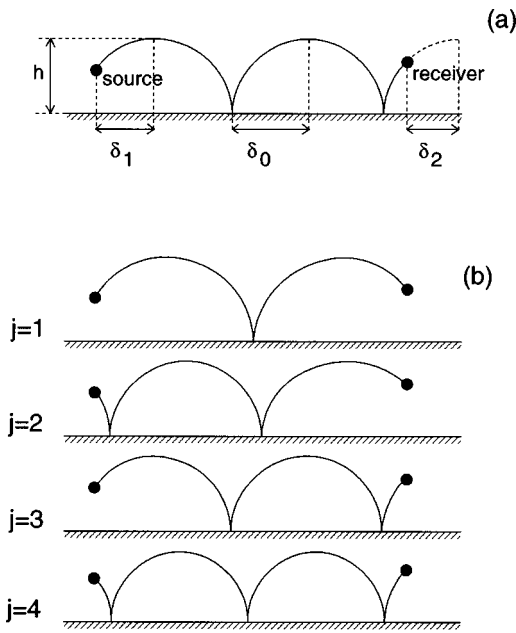


FIG. 1. A ray with maximum height h and horizontal range segments δ_1 , δ_0 , and δ_2 (a), and the four rays with index $n=2$ (b).

[see Fig. 1(b)], the coefficients m_{kj} given in Table I, and the function $\delta_k(h)$ defined as (index $k=0,1,2$):

$$\delta_k(h) = \int_{z_k}^h \frac{dz}{\tan \gamma(z)}, \quad (4)$$

where $\gamma(z)$ is the elevation angle of the ray at height z , so that $\tan \gamma(z) = dz/dx$. In Eq. (3) we use two indices n and j to identify a ray, whereas in Eq. (2) we used for brevity only one index m . Ray tracing is now reduced to solving the height h from the following equation:

$$r_{nj}(h) = r, \quad (5)$$

where r is the fixed horizontal distance between the source and the receiver. Figure 2 shows a typical example of the functions $r_{nj}(h)$, for a source height of 1.8 m and a range of receiver heights. From the figure we see that, for each $n > 0$, the number of solutions of Eq. (5) is zero or one for $j = 1$, and zero, one, or two for $j = 2, 3, 4$. For $n = 0$, the number of solutions is zero or one for all j . The solutions are denoted as h_{nj} . To distinguish the two solutions for $j = 2, 3, 4$, we extend the range of j to $j = 1, \dots, 8$. For a possible second solution we use $j+4$ instead of j : $j = 6$ for $j = 2$, $j = 7$ for $j = 3$, and $j = 8$ for $j = 4$. We choose $h_{nj} > h_{n(j+4)}$. The points with $dr_{nj}/dh = 0$ are called caustic points. Figure 3 shows an example of all rays to a receiver, for a linear sound-speed profile.

The computational approach is as follows. For $n = 1, 2, \dots$, we successively determine all solutions for j

TABLE I. The coefficients m_{kj} .

	$j=1$	$j=2$	$j=3$	$j=4$
m_{0j}	-1	0	0	1
m_{1j}	1	-1	1	-1
m_{2j}	1	1	-1	-1

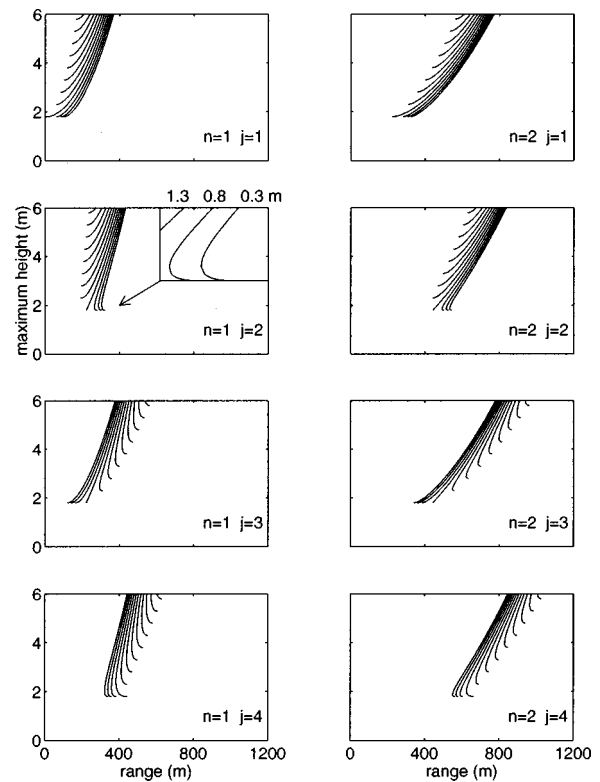


FIG. 2. The functions $r_{nj}(h)$ for $n=1$ and 2 and $j=1, 2, 3, 4$, a linear sound-speed profile with a gradient of 0.1 s^{-1} , a source height of 1.8 m, and a range of receiver heights (0.3, 0.8, 1.3, ..., 5.8 m). The receiver heights 0.3, 0.8, and 1.3 m are labeled in the enlarged section in the graph for $n=1$, $j=2$.

$= 1, \dots, 8$. At a certain value of n , no solutions are found for all j , and all rays have been found. For computational efficiency, we prepare in advance a matrix of values of the function $\delta_k(h)$ for a set of maximum heights h (e.g., $h = 0, 0.1, 0.2, \dots, 100 \text{ m}$) and a set of heights z_k (e.g., $z_k = 0, 0.1, 0.2, \dots, 9.9, 10, 11, 12, \dots, 100 \text{ m}$). This matrix is denoted as $\delta_k^*(h)$ and is used here for ray tracing but will also be used in the next section for the computation of the caustic curves. With the matrix $\delta_k^*(h)$, a first estimate of the solution of Eq. (5) is obtained. Next, an accurate solution is

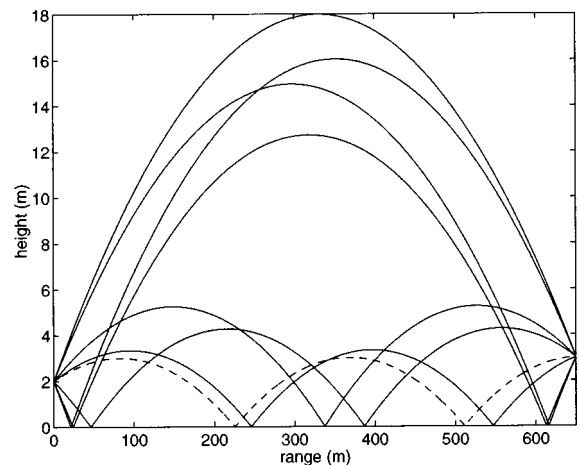


FIG. 3. Example of rays to a receiver at 650 m from the source, for a linear sound-speed profile with a gradient of 0.1 s^{-1} . The dashed line represents a solution with $j=7$, the full lines represent solutions with $j \leq 4$.

obtained by iteratively approaching the zero of the function $r_{nj}(h) - r$.

The case $n=0$ is treated separately. This case corresponds with two rays without turning points: the direct ray and the ray with a ground reflection. For the direct ray we have $j=2$ if $z_1 > z_2$, and $j=3$ if $z_1 < z_2$. Beyond a certain value of r , the direct ray has a turning point, so the ray with $n=0$ does not exist, but is replaced by a ray with $n=1$. For the ray with a ground reflection we have $j=4$. Again, this ray exists only up to a limiting value of r .

Another computational aspect of interest is the numerical evaluation of the integral in Eq. (4). From Snell's law we have $\cos \chi(z)/c(z) = 1/c(h)$, so that

$$\delta_k(h) = \int_{z_k}^h \frac{c(z)/c(h)}{\sqrt{1 - c^2(z)/c^2(h)}} dz. \quad (6)$$

The divergence of the integrand is eliminated with the substitution $y(z) = [1 - c^2(z)/c^2(h)]^{1/2}$, or equivalently $y(z) = \sin \chi(z)$:

$$\delta_k(h) = c(h) \int_0^{y(z_k)} \frac{1}{c'(z)} dy, \quad (7)$$

where the derivative $c'(z)$ is considered as a function of y . The integrand is bounded, as we assume that the sound speed increases monotonically with height, so that $c'(z) > 0$. For the evaluation of the integral we use the trapezoidal rule, with an integration step of typically $dy = 0.0001$.

B. Caustic curves

In the preceding section, caustic points were identified as points where $dr_{nj}/dh = 0$. In three dimensions, the complete set of caustic points forms a set of surfaces, which are called caustic surfaces. The intersection of the caustic surfaces and the propagation plane (i.e., the vertical plane through the source and the receiver) is a set of curves, which are called caustic curves. The caustic curves play an important role in the ray model.

The caustic curve for indices n and j is computed as follows. The caustic curve is represented by a discrete set of caustic points (r, z) . For each height z , the caustic range r is determined by solving the equation $dr_{nj}/dh = 0$ (see Fig. 2). A first estimate is obtained from the limited set $r_{nj}(h)$ computed with the matrix $\delta_k^*(h)$ described in the preceding section. Next the caustic point is approached iteratively until the variation is negligible. For each value of n we obtain caustic curves for $j=2, 3$, and 4 . Figure 4 shows caustic curves for $n=1, 2$, and 3 , with the branches for $j=2, 3$, and 4 labeled for $n=1$. The branches for $j=2$ and $j=3$ and the branches for $j=2$ and $j=4$ touch each other at their end points. The two points of contact are cusps of the complete caustic curve for a value of n . The cusp at the point of contact between the branches for $j=2$ and $j=3$ is always at the source height. The cusp at the point of contact between the branches for $j=2$ and $j=4$ is always at height zero. The latter cusp is not a real cusp, but is a consequence of the ground reflection. The cusp disappears if the $j=4$ branch is replaced by its image below the ground surface.

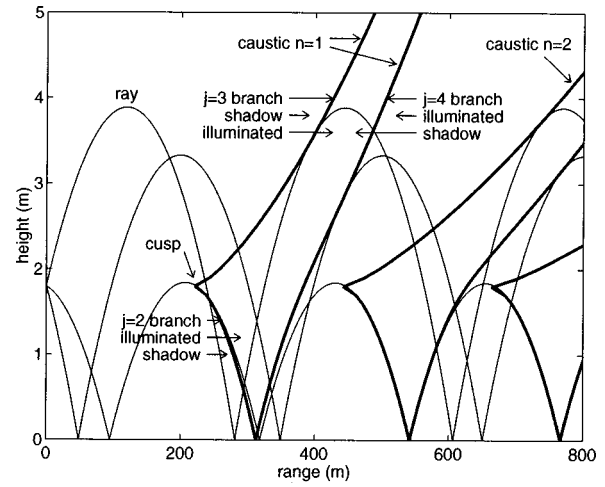


FIG. 4. Caustic branches (thick curves) and rays (thin curves) for a system with a source height of 1.8 m and a linear sound-speed profile with gradient 0.1 s^{-1} .

Also plotted in Fig. 4 are three sound rays, with different elevation angles at the source. One ray touches the caustic branches with $j=3$, one ray touches the branches with $j=2$, and one ray touches the branches with $j=4$. The branches with $j=3$ and $j=4$ are touched by rays from below, the branch with $j=2$ is touched by rays from above. This means that there are shadow regions above the branches with $j=3$ and $j=4$ and below the branch with $j=2$.

In the way described above, the caustic curves are represented by a set of points. The (r, z) coordinates of these points will be used in Sec. IV for the computation of caustic diffraction fields in the shadow regions. Figure 5 shows caustic curves for a linear profile and for a logarithmic profile, for source heights 1 and 3 m.

C. Indices of caustic rays

A ray touches each caustic curve ($n=1, 2, \dots$) at one point. These points will be referred to as the caustic contact points. Let γ_1 denote the elevation angle of the ray at the source. If $\gamma_1 = 0$, the caustic contact point is exactly at the caustic cusp, for all n . With increasing $\gamma_1 > 0$, the caustic contact point moves along the branch $j=3$. With decreasing $\gamma_1 < 0$, the caustic contact point moves along the branches $j=2$ and $j=4$.

We consider a receiver with variable range and constant height. With increasing range, the receiver crosses caustic branches from the shadow side to the illuminated side. If $z_2 > z_1$, branches $j=3$ and $j=4$ are crossed alternately. If $z_2 < z_1$, branches $j=2$ and $j=4$ are crossed alternately. Each time a branch is crossed, two new rays appear. These rays will be referred to as the "caustic rays" of the caustic branch. Table II gives the indices (n, j) of the caustic rays of the branches $j=2, 3, 4$. The indices of caustic rays will be used in Sec. IV for the computation of caustic diffraction fields in the shadow regions.

Figure 6 shows an example of the caustic rays of $j=3$ branches. The caustic rays of the first branch near $r = 350 \text{ m}$ have indices $(n, j) = (1, 3)$ and $(1, 7)$ at the point of intersection near the branch. At the second branch near r

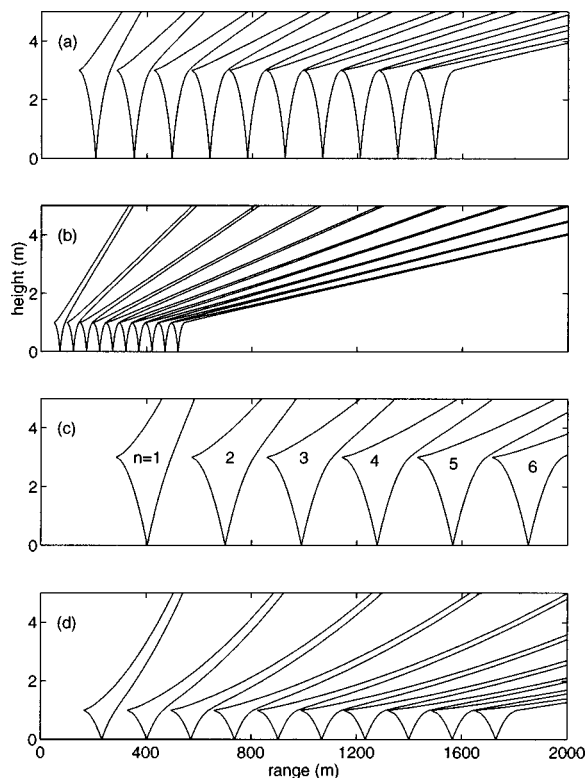


FIG. 5. Caustic curves for a logarithmic sound-speed profile $c(z) = c_0 + b \ln(z/z_0 + 1)$, with $c_0 = 340$ m/s, $b = 1$ m/s, and $z_0 = 0.1$ m, for source height 3 m (a) and 1 m (b), and for a linear sound-speed profile $c(z) = c_0 + c_1 z$, with $c_1 = 0.1 \text{ s}^{-1}$, for source height 3 m (c) and 1 m (d).

= 700 m the indices are (2,3) and (3,1). This illustrates the fact that, with increasing distance from the caustic, the ray ($n,7$) develops a turning point in front of the receiver so that its indices change to ($n+1,1$).

For the $j=2$ branch, the indices of the second caustic ray change from ($n,6$) to ($n+1,1$) with increasing range (see Table II). This change corresponds with the caustic contact point moving from the $j=2$ branch through the cusp to the $j=3$ branch.

For the $j=4$ branch, the indices of the second caustic ray are different for $z_2 > z_1$ and $z_2 < z_1$. For $z_2 > z_1$, the indices change from ($n,8$) to ($n+1,2$) with increasing range, corresponding with the development of a turning point in front of the receiver. For $z_2 < z_1$, the indices change from ($n,8$) to ($n+1,3$) with increasing range, corresponding with the caustic contact point moving from the $j=2$ branch through the cusp to the $j=3$ branch.

In the theory of caustics with a cusp, triples of caustic rays are considered instead of pairs. The illuminated region of a cusped caustic is the region between the two branches emanating from the cusp (the $j=2$ branch and the $j=3$

TABLE II. Indices of the two caustic rays of the branches $j=2,3,4$.

Caustic branch	(n,j) of ray 1	(n,j) of ray 2
$j=2$	($n,2$)	($n,6$) or ($n+1,1$)
$j=3$	($n,3$)	($n,7$) or ($n+1,1$)
$j=4$	($n,4$)	($n,8$) or ($n+1,2$) if $z_2 > z_1$ ($n,8$) or ($n+1,3$) if $z_2 < z_1$

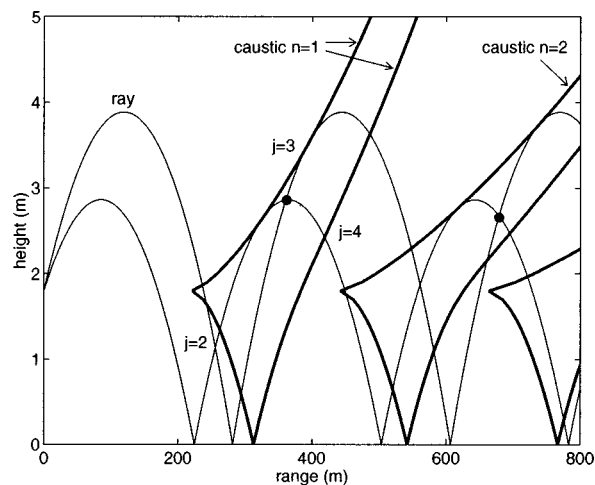


FIG. 6. Same as Fig. 4 with two caustic rays crossing each other at receiver positions (dots) in the illuminated regions of the $j=3$ caustic branches.

branch in Fig. 6). In this region, three rays that touch the caustic pass through each point. These three rays will be referred to as the caustic rays of the cusped caustic. In the shadow region of the cusped caustic, only one of the three caustic rays is present. Table III gives the indices (n,j) of the three caustic rays of the cusped caustic.

We now have a complete description of the ordered set of rays. The number of rays increases with increasing range. Figure 7 shows the set of rays as a function of range for receiver heights 1 and 3 m for a system with source height 1.8 m and a linear profile. Single rays with index $j=1, 2, 3$, or 4 are represented by open circles. Ray pairs $j=(2,6)$, (3,7), or (4,8) are represented by filled circles.

The graph in Fig. 7 for receiver height 3 m illustrates the case $z_2 > z_1$. In this case, new rays appear each time a caustic branch $j=3$ or $j=4$ is crossed. Up to range $r=350$ m, there are only two rays. At range $r=360$ m, the first caustic branch $j=3$ has been crossed (cf. Fig. 6) and two new rays have appeared, with indices (n,j) = (1,3) and (1,7). At range $r=380$ m, the indices of the latter ray have changed to (2,1). At range $r=460$ m, the first caustic branch $j=4$ has been crossed and again two new rays have appeared, with indices (n,j) = (1,4) and (1,8). At range $r=490$ m, the indices of the latter ray have changed to (2,2). Starting at range $r=650$ m, this process is repeated for $n=2$.

The graph in Fig. 7 for receiver height 1 m illustrates the case $z_2 < z_1$. In this case, only caustic branches $j=2$ and $j=4$ are crossed. New rays appear in a different order than in the case $z_2 > z_1$.

D. Ground reflections

In a downward refracting atmosphere, sound rays with multiple ground reflections occur. The number of ground reflections of a ray with indices n and j is given by

TABLE III. Indices of the three caustic rays of the cusped caustic.

(n,j) of ray 1	(n,j) of ray 2	(n,j) of ray 3
($n,3$)	($n,2$)	($n,7$) or ($n+1,1$) if $z_2 > z_1$ ($n,6$) or ($n+1,1$) if $z_2 < z_1$

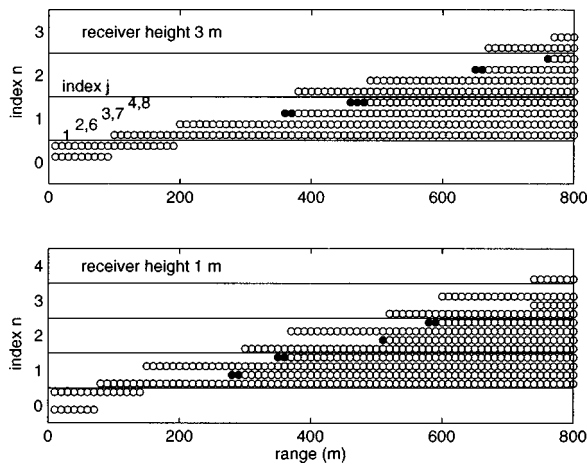


FIG. 7. Sets of rays for receiver heights 1 and 3 m as a function of range, for source height 1.8 m and a linear profile with gradient 0.1 s^{-1} . Single rays with index $j=1, 2, 3$, or 4 are represented by open circles. Ray pairs $j=(2,6), (3,7)$, or $(4,8)$ are represented by filled circles.

$$N_{nj} = n + m_{0j}. \quad (8)$$

For the ground reflection coefficient R_{nj} in a refracting atmosphere, an exact expression is not available. As an approximation, we use the spherical wave reflection coefficient,^{32,33} which represents an analytical solution for a nonrefracting atmosphere. The spherical wave reflection coefficient is a function of the ground impedance, the reflection angle, and also the distance $[r^2 + (z_1 + z_2)^2]^{1/2}$, the length of the reflected ray in a nonrefracting atmosphere. The use of the spherical wave reflection coefficient in Eq. (2b) was also proposed by L'Espérance *et al.*¹⁵ Li²²⁻²⁴ has studied the theoretical justification of this approach. In Section V we will present numerical examples for a reflecting (i.e., rigid) ground surface and for an absorbing ground surface. For the absorbing ground surface, we use a model developed by Attenborough³⁴ for the ground impedance as a function of frequency.

E. Phase angles of the rays

From Eq. (2c) we see that the phase of a ray is determined by the travel time t_{nj} along the ray (we use indices n and j instead of the index m). The travel time is given by

$$t_{nj}(h) = 2(n + m_{0j})\tau_0(h) + m_{1j}\tau_1(h) + m_{2j}\tau_2(h), \quad (9)$$

where τ_k is the travel time along the ray segment between height z_k and the turning point (see Fig. 1; $k=0,1,2$):

$$\tau_k(h) = \int_{z_k}^h \frac{dz}{c \sin \gamma}. \quad (10)$$

With the substitution of y for z [see Eqs. (6) and (7)] we obtain:

$$\tau_k(h) = \int_0^{y(z_k)} \frac{1}{c'(z)(1-y^2)} dy. \quad (11)$$

In Sec. III we will see that the phase along a ray changes discontinuously by $-\pi/2$ each time a caustic is touched. Therefore the number of touched caustics between the source

and the receiver will be required. We denote this number by K_{nj} . It is given by:

$$K_{nj} = n - 1 \quad \text{for } j=1,2,3,4, \\ K_{nj} = n \quad \text{for } j=6,7,8. \quad (12)$$

F. Focusing factors

The focusing factor f_m in Eq. (2b) is computed from the spatial divergence of two rays, relative to the divergence in free field. For each ray m to the receiver at position (r, z_2) , a second ray is traced to a receiver at position $(r + r\rho, z_2)$, with $\rho \ll 1$ (we use typically $\rho = 0.00001$). The elevation angle at the source is denoted as γ_1 for the original ray and as γ'_1 for the second ray. The focusing factor f_m follows from the difference $\delta\gamma_1 = \gamma_1 - \gamma'_1$:

$$f_m = \left(\frac{|\delta\gamma_1|}{\rho \sin \gamma_1} \right)^{1/2}. \quad (13)$$

This is the (standard) geometrical-acoustics approximation of the focusing factor.⁵ Geometrical acoustics fails near caustic points. At caustic points, the geometrical-acoustics approximation of the focusing factor diverges. From the theory of caustics, an improved approximation of the field near caustic points is obtained, as will be described in Secs. III and IV. From this solution one can deduce that the focusing factor remains approximately constant within a limited range near a caustic point.¹⁴

III. REVIEW OF THE THEORY OF CAUSTICS

A. The theory of Ludwig

Ludwig³ presents asymptotic expansions in k^{-1} of the solution of the reduced wave equation:

$$\Delta p + k^2 p = 0, \quad (14)$$

where k is the wave number. In general, the solution can be written as a superposition of plane waves:⁵

$$p(x) = \int e^{ik\phi(x,\beta)} z(x,\beta) d\beta, \quad (15)$$

where $k\phi$ is a phase function, z an amplitude function, β is a parameter, and x denotes position. At most points x , the method of stationary phase can be applied to obtain the asymptotic expansion of the solution as a sum of terms of the form:

$$p_m(x) = e^{ik\phi_m z_m} \quad (16)$$

with $\phi_m(x) = \phi(x, \beta_m(x))$ where β_m is a point of stationary phase: $\partial\phi(x, \beta_m(x))/\partial\beta \equiv \phi_{\beta}(x, \beta_m(x)) = 0$, and

$$z_m(x) = e^{\pm i\pi/4} \sqrt{\frac{2\pi}{k}} \frac{z(x, \beta_m(x))}{\sqrt{|\phi_{\beta\beta}(x, \beta_m)|}}, \quad (17)$$

where the sign of the exponent is equal to the sign of $\phi_{\beta\beta}(x, \beta_m)$. This expansion breaks down near points where $\phi_{\beta\beta}(x, \beta_m) = 0$, that is, points where two stationary points coincide. These points are the caustic points introduced in Sec. II. To obtain an expansion that is valid near caustics,

Ludwig follows Chester *et al.*³⁵ by introducing the functions $\xi(x, \beta)$, $\theta(x)$, and $\rho(x)$ such that:

$$\phi(x, \beta) = \theta + \rho \xi - \frac{1}{3} \xi^3. \quad (18)$$

This expression is substituted in Eq. (15), and the integration variable is changed from β to ξ . From the resulting expression only the terms most significant for large k are retained:

$$\begin{aligned} p(x) &= e^{ik\theta} \left\{ g_0 \int e^{ik(\rho\xi - \xi^3/3)} d\xi \right. \\ &\quad \left. + g_1 \int \xi e^{ik(\rho\xi - \xi^3/3)} d\xi \right\} \\ &= 2\pi e^{ik\theta(x)} \{ g_0(x) k^{-1/3} \text{Ai}(-k^{2/3}\rho(x)) \\ &\quad + g_1(x) ik^{-2/3} \text{Ai}'(-k^{2/3}\rho(x)) \} \end{aligned} \quad (19)$$

with $\text{Ai}(t)$ the Airy function of t , and $\text{Ai}'(t)$ its derivative. The Airy function is defined as

$$\text{Ai}(t) = \frac{1}{2\pi} \int_{-\infty}^{\infty} e^{i(t\tau + \tau^3/3)} d\tau. \quad (20)$$

Note that the integration limits must be deformed near infinity into the complex plane in order to obtain a convergent integral.³⁶⁻³⁸

Ludwig substitutes the solution (19) back into the reduced wave equation (14), and deduces differential equations which are equivalent to the eikonal equation and the transport equation. From these equations, the functions $\theta(x)$, $\rho(x)$, $g_0(x)$, and $g_1(x)$ can be constructed. It turns out that, to first order, θ measures arclength along the caustic curve and $\rho = (2/a)^{1/3}y$ with a the local radius of curvature of the caustic curve and y the normal distance to the caustic curve (this agrees with the solutions of Buchal and Keller² and Pierce¹¹).

The caustic curve is identified as the locus where we have simultaneously $\phi_\xi = 0$ and $\phi_{\xi\xi} = 0$. From Eq. (18) we obtain, after elimination of ξ , that the caustic is the locus where $\rho = 0$. In the illuminated region we have $\rho > 0$, in the shadow region we have $\rho < 0$. In the illuminated region, Eq. (19) reduces to the geometrical-acoustics approximation if the method of stationary phase is applied. The field in the shadow region can formally be described in terms of complex rays, i.e., rays with a complex phase. These complex rays represent a field that decreases exponentially with increasing distance to the caustic.

The foregoing is valid only for smooth caustics. To describe the field near caustics with a cusp, Ludwig introduces a generalized solution of the wave equation:

$$p(x) = \sum_{\alpha=0}^{\infty} (ik)^{-\alpha} \int e^{ik\phi(x, \xi)} g^\alpha(x, \xi) d\xi \quad (21)$$

with

$$\phi(x, \xi) = \theta - \sum_{l=1}^{M-1} \rho_l \frac{(-\xi)^l}{l} + \frac{(-\xi)^{M+1}}{M+1} \quad (22)$$

and

$$g^\alpha(x, \xi) = \sum_{l=0}^{M-1} g_l^\alpha(x) \xi^l, \quad (23)$$

where θ , ρ_l ($l=1, 2, \dots, M-1$), and g_l^α ($l=0, 1, \dots, M-1$; $\alpha=0, 1, \dots$) are functions of x . The solution (21) can be expressed in terms of a generalized Airy function:

$$\begin{aligned} V(t, r) &= \frac{1}{2\pi} \int_{-\infty}^{\infty} \exp \left\{ i \left[t - \sum_{l=1}^{M-1} r_l \frac{(-\eta)^l}{l} \right. \right. \\ &\quad \left. \left. + \frac{(-\eta)^{M+1}}{M+1} \right] \right\} d\eta \end{aligned} \quad (24)$$

and its derivative. We have $\text{Ai}(r) = V(0, -r)$ for $M=2$.

By substituting the generalized solution (21) in the wave equation, Ludwig derives a sequence of conditions for (21) to be an asymptotic solution of the wave equation. Only the first two conditions are used, corresponding with the first two orders in k^{-1} . The corresponding solution has only the term with $\alpha=0$ in Eq. (21).

The case $M=2$ corresponds with a smooth caustic. This case was treated in the foregoing. The conditions derived from substitution of Eq. (21) in the wave equation are the differential equations mentioned before, from which the functions θ , ρ , g_0 , and g_1 can be constructed ($\rho \equiv \rho_1$, $g_l \equiv g_l^0$).

The case $M=3$ corresponds with a caustic with a cusp. At the caustic we have simultaneously $\phi_\xi = 0$ and $\phi_{\xi\xi} = 0$. From Eq. (22) we obtain, after elimination of ξ , that the caustic in $\rho_1 - \rho_2$ space is given by the equation $(\rho_1/2)^2 = (\rho_2/3)^3$, which has a cusp at the origin.³ In x space, the caustic has a similar cusped shape, since ρ_1 and ρ_2 are regular functions of x . Between the two caustic branches emanating from the cusp, three rays pass through each point (apart from rays that are not related to the caustic). On the other sides of the branches, only a single ray passes through each point. The cusp has only local effects. Away from the cusp, the analysis for a smooth caustic can be applied.

B. The theory of Kravtsov

Kravtsov⁴ develops an alternate method for the construction of the functions θ , ρ_l , and g_l . This construction appears more practical than the construction from differential equations as proposed by Ludwig.

Kravtsov includes a factor $(ik/2\pi)^{1/2}$ in the generalized solution (21) of Ludwig, with $\alpha=0$:

$$p(x) = \sqrt{\frac{ik}{2\pi}} \int e^{ik\phi(x, \xi)} g^0(x, \xi) d\xi. \quad (25)$$

In the following, the superscript 0 of g^0 is omitted. A point x far from the caustic, on the illuminated side, is considered. At this point, the solution (25) is computed by the stationary phase method. The stationary points $\xi_m(x)$ ($m=1, 2, \dots, M$) are the roots of the M th degree algebraic equation:

$$\frac{\partial \phi(x, \xi_m)}{\partial \xi} = 0, \quad m=1, 2, \dots, M \quad (26)$$

and Eq. (25) becomes:

$$p(x) = \sum_{m=1}^M p_m(x),$$

$$p_m(x) = (\phi_{\xi\xi}(x, \xi_m(x)))^{-1/2} i \sum_{l=0}^{M-1} g_l(x) \xi_m^l e^{ik\phi(x, \xi_m)}. \quad (27)$$

Comparing with the geometrical-acoustics field

$$p(x) = \sum_{m=1}^M A_m(x) e^{ik\phi_m(x)} \quad (28)$$

we obtain

$$\phi(x, \xi_m(x)) = \phi_m(x), \quad (29)$$

$$\sum_{l=0}^{M-1} g_l(x) \xi_m^l(x) = -i (\phi_{\xi\xi}(x, \xi_m))^{1/2} A_m(x). \quad (30)$$

First the roots ξ_m of Eq. (26) are computed. Substitution in Eq. (29) yields M equations for determining the M unknown functions $\theta(x)$, $\rho_l(x)$ ($l=1,2,\dots,M-1$). Next, Eq. (30) yields M linear equations for the determination of the M amplitude coefficients $g_l(x)$ ($l=0,2,\dots,M-1$). Kravtsov shows that the solution constructed in this way is valid even for points x close to a caustic.

For $M=2$, $\phi(x, \xi)$ is given by Eq. (18). Equation (26) yields $\xi_m = \pm \rho^{1/2}$, with $m=1,2$. We use $m=1$ for the negative sign and $m=2$ for the positive sign. Substitution in Eq. (29) gives $\phi_m = \theta \pm \frac{2}{3}\rho^{3/2}$. Therefore

$$\theta(x) = \frac{1}{2}(\phi_1 + \phi_2),$$

$$\frac{2}{3}\rho^{3/2}(x) = \frac{1}{2}(\phi_2 - \phi_1). \quad (31)$$

Next we obtain from Eq. (30):

$$g_0(x) = \frac{\rho^{1/4}}{\sqrt{2}} (A_2 - iA_1),$$

$$g_1(x) = \frac{\rho^{-1/4}}{\sqrt{2}} (A_2 + iA_1). \quad (32)$$

From the values at point x of the geometrical-acoustical parameters ϕ_1 , ϕ_2 , A_1 , and A_2 , the values at point x of the functions θ , ρ , g_0 , and g_1 are computed with Eqs. (31) and (32). The field at point x is then

$$p(x) = \sqrt{2\pi} k^{1/6} e^{i\pi/4} e^{ik\theta} [g_0 \text{Ai}(-k^{2/3}\rho) + ik^{-1/3} g_1 \text{Ai}'(-k^{2/3}\rho)] \quad (33)$$

as follows from Eq. (25) for $M=2$ [cf. Eq. (19)].

The two stationary points $m=1,2$ represent two rays touching the caustic in the vicinity of the receiver (see Fig. 6). The ray with $m=1$ has yet to touch the caustic, the ray with $m=2$ has already touched it. Close to the caustic, the sound-pressure contributions of the two rays differ only by a phase shift of $\pi/2$, as can be seen from Eqs. (16) and (17). This is usually interpreted as a phase drop of $\pi/2$ after a wave has touched a caustic. This implies that near the caustic $A_2 \approx \exp(-i\pi/2)A_1 = -iA_1$, so that g_1 is small here. Therefore the term with the derivative of the Airy function in Eq. (33) is small near the caustic.

Next we consider the approach of Kravtsov for the case $M=3$, i.e., for a caustic with a cusp. In this case we have $\phi = \theta + \rho_1 \xi - \rho_2 \xi^2/2 + \xi^4/4$. For given phases ϕ_m ($m=1,2,3$) we obtain from Eqs. (26) and (29) six equations: $\rho_1 - \rho_2 \xi_m + \xi_m^3 = 0$ and $\phi_m = \theta + \rho_1 \xi_m - \rho_2 \xi_m^2/2 + \xi_m^4/4$. These six equations are easily solved iteratively for the six unknowns θ , ρ_1 , ρ_2 , ξ_1 , ξ_2 , and ξ_3 . Finally the amplitude coefficients g_m are computed from Eq. (30).

C. Extrapolation into the shadow region

With the approach of Kravtsov, the field on the illuminated side of a caustic can be computed. First the geometrical-acoustics solution is determined, including the phases ϕ_m and amplitudes A_m of the rays touching the caustic. Next the quantities θ , ρ_l , and g_l are determined, and Eq. (25) is used for the sound-pressure contribution of the rays touching the caustic, making use of (generalized) Airy functions [for example, Eq. (33) is used for $M=2$]. This approach works only for receivers in the illuminated region. To compute the caustic diffraction field at a receiver in the shadow region, we have to extrapolate the quantities θ , ρ_l , and g_l from the illuminated region into the shadow region. Since the quantities θ , ρ_l , and g_l are regular functions of the position x , linear extrapolation should work for receivers close to the caustic. With increasing distance to the caustic, linear extrapolation is expected to become inaccurate. This is not necessarily a problem, since the diffraction field goes to zero with increasing distance to the caustic. It is sufficient if the extrapolation method is accurate only in the region where the diffraction field is significant. It is remarkable that the problem of extrapolation into the shadow region has not been addressed in detail in the work of Ludwig and Kravtsov. Ludwig only mentions the possibility of extrapolation by power series expansion. In the numerical examples presented below, however, we find that quadratic extrapolation produces inaccurate results. It should be emphasized that the diffraction field in the shadow is very important in the vicinity of the caustic.

D. Comparison with solution of Pierce

The solution of Ludwig and Kravtsov for $M=2$ can be compared with the solution of Pierce.¹¹ Pierce uses a local xy coordinate system, with the x axis tangent to the caustic and the y axis normal to it. From the eikonal equation, Pierce derives an expression for the phases ϕ_m of the two rays $m=1,2$. We substitute this expression in Eq. (31) to obtain $\theta = x - yx/a$ and $\rho = (2/a)^{1/3}y$, where $\rho \equiv \rho_1$ and a is the local radius of curvature of the caustic curve. For the amplitude A_1 Pierce uses $A_1 = P(a/16y)^{1/4}$, where the constant P is the amplitude at $y = a/16$. If we use the approximate relation $A_2 \approx -iA_1$ as an identity, we have from Eq. (32) $g_1 = 0$, and we obtain from Eq. (33) the solution of Pierce:

$$p = P \pi^{1/2} 2^{1/12} e^{-i\pi/4} (ka)^{1/6} e^{ik(x-yx/a)} \text{Ai}(-k^{2/3}\rho). \quad (34)$$

A similar solution was obtained by Buchal and Keller.²

The approach of Pierce appears simpler than the approach of Kravtsov, but this is not really the case. The approach of Pierce also requires extrapolation into the shadow

region, since the amplitude P can be computed only from the geometrical-acoustics solution on the illuminated side. Moreover, some approximations are made in the derivation of Pierce, which are absent in the approach of Ludwig and Kravtsov. The solution of Pierce is not more accurate than the solution of Ludwig and Kravtsov using linear extrapolation (and probably even less accurate, in view of the approximations in the derivation of Pierce).

E. Comparison with solution of Brekhovskikh

The solution of Ludwig and Kravtsov for $M=2$ can also be compared with the solution of Brekhovskikh⁵ for the field in the vicinity of a smooth caustic (see Sec. 45.1 of Ref. 5; a similar solution was obtained by Sachs and Silbiger,⁶ based on the work of Seckler and Keller^{39,40}). Brekhovskikh starts from a plane-wave expansion $p = \int \exp(ik\phi)\Phi d\xi$, with phase $k\phi$ and amplitude Φ that are functions of the parameter ξ , the “horizontal” wave number. Using a global, rectangular (r, z) coordinate system, the phase function for a layered atmosphere is written as $k\phi = f(z_1, z_2, \xi) + \xi r$, with r the receiver range, a constant, and f a function of source height z_1 , receiver height z_2 , and ξ . A range function $r(z_1, z_2, \xi) = -\partial f / \partial \xi$ is introduced, so that the saddle point $\xi = \xi_0$ follows from the equation $r(z_1, z_2, \xi_0) = r$. At a caustic, two saddle points coincide, so that $r'_0 \equiv (\partial r(z_1, z_2, \xi) / \partial \xi)_{\xi_0} = 0$. Therefore the range function in the vicinity of a caustic is approximated by the expansion $r(z_1, z_2, \xi) = r_0 + \frac{1}{2}r''_0(\xi - \xi_0)^2$, with $r_0 = r(z_1, z_2, \xi_0)$ the range of the caustic point at the receiver height and $r''_0 = (\partial^2 r(z_1, z_2, \xi) / \partial \xi^2)_{\xi_0}$. The corresponding expansion of the phase is $k\phi = k\phi_0 + (r - r_0)(\xi - \xi_0) - (1/6)r''_0(\xi - \xi_0)^3$, with $k\phi_0 = f(z_1, z_2, \xi_0) + \xi_0 r$. This leads to a field that is proportional to an Airy function, $p \propto (r''_0)^{-1/3} \Phi(\xi_0) e^{ik\phi_0} \text{Ai}(t)$, with $t = -(r''_0/2)^{-1/3}(r - r_0)$, a parameter that is proportional to the horizontal distance to the caustic. Brekhovskikh’s solution follows from Ludwig’s solution with the substitution $\xi \rightarrow (r''_0/2k)^{1/3}(\xi - \xi_0)$. Brekhovskikh’s expansion agrees with Ludwig’s phase function $\phi = \theta + \rho\xi - \frac{1}{3}\xi^3$ if we set $\theta = \phi_0$ and $\rho = k^{-2/3}(r''_0/2)^{-1/3}(r - r_0)$. As a consequence, the Airy function $\text{Ai}(-k^{2/3}\rho)$ in Ludwig’s solution is identical with the Airy function $\text{Ai}(t)$ in Brekhovskikh’s solution. The term with the derivative of the Airy function is absent in Brekhovskikh’s solution. Brekhovskikh’s approach requires no extrapolation into the shadow region. The quantities ϕ_0 , r_0 , r''_0 in the solution follow from the phase function ϕ and derivatives evaluated at the caustic value $\xi = \xi_0$. The receiver range r enters only linearly, in the argument t of the Airy function and in the phase $k\phi_0$. This originates from the assumed approximate form of the phase function. The solution is valid only in the vicinity of the caustic, as the phase is expanded around $\xi = \xi_0$.

IV. APPLICATION OF CAUSTIC THEORY IN A RAY MODEL

A. Application of smooth caustic theory

We first neglect the effect of cusps in the caustics, so that we have only smooth caustic branches, and we can use

caustic theory for $M=2$. We distinguish two types of rays contributing to the sum in Eq. (2a), caustic rays and noncaustic rays (see Sec. II). There are at most four noncaustic rays, two with index $n=0$ and two with $n=1$. Caustic rays are the new rays that appear when a receiver crosses a caustic branch from the shadow side to the illuminated side. These rays appear as pairs. Each caustic branch is touched by a single ray pair.

Caustics affect the contribution of a caustic ray pair in two ways:

- (1) the phase along a ray shifts by $-\pi/2$ each time a caustic is touched,
- (2) the field of the ray pair is modified in the vicinity of a caustic.

This is explained in the following.

As explained in Sec. III [see the text following Eq. (33)], the construction of Kravtsov requires that the phase shifts of $-\pi/2$ be included in the amplitudes. Therefore Eq. (2b) is replaced by:

$$A_m = f_m R_m^{N_m} e^{-iK_m\pi/2}, \quad (35)$$

where K_m is the number of touched caustics. The inclusion of the phase shifts in the amplitude of a ray is straightforward if the ray-tracing algorithm described in Sec. II is used. In this algorithm, rays and caustics are ordered, and for each ray the number of touched caustics between source and receiver follows directly from the order indices of the ray (see Sec. II E). It is thus not necessary to count the number of touched rays numerically.

With the phases ϕ_m given by Eq. (2c) and the modified amplitudes A_m given by Eq. (35), the quantities θ , ρ , g_0 , and g_1 are determined, and next the modified contributions of the caustic ray pairs are computed. Each such contribution replaces two terms in the sum in Eq. (2a).

Next we consider the computation of the field p_d in Eq. (1). This field is the sum of all caustic diffraction fields. The computation of a caustic diffraction field requires the extrapolation of the quantities θ , ρ , g_0 , and g_1 into the caustic shadow region. We assume $z_2 \geq z_1$. For systems with $z_2 < z_1$, we apply the principle of reciprocity. Figure 8 illustrates two different extrapolation methods: horizontal extrapolation at the receiver height and vertical extrapolation at the receiver range. We have tried both linear and quadratic extrapolation. We obtained the best results (that is, best agreement with parabolic equation (PE) results; see Sec. V) with linear horizontal extrapolation. In this case, two positions are chosen on the illuminated side of the caustic branch, at distances of typically 10 and 20 m from the caustic, respectively. At both positions the quantities θ , ρ , g_0 , and g_1 are determined, and then extrapolated linearly to the receiver position. Quadratic extrapolation requires three receiver positions on the illuminated side. In particular for logarithmic sound-speed profiles we found inaccurate results with quadratic extrapolation (reminiscent of the well-known fact in curve-fitting that extrapolation with a polynomial of order 2 or more can lead to large errors).

A problem with vertical extrapolation arises for receivers that are at smaller ranges than the end point of the caustic

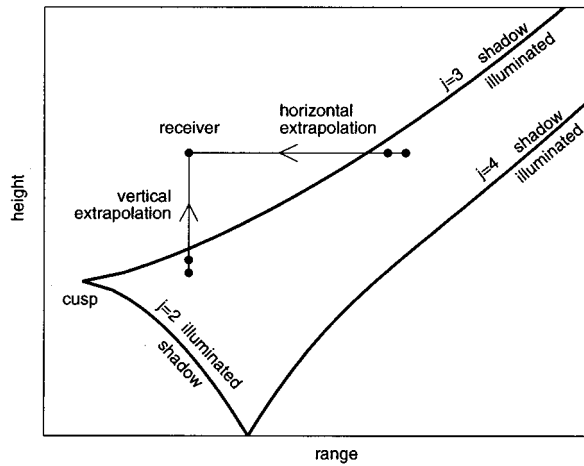


FIG. 8. Schematic representation of horizontal and vertical extrapolation into the shadow region of a caustic branch.

branch (that is, the cusp for $j=3$ branches and the end point at the ground for $j=4$ branches). In this case, additional positions on the illuminated side must be used to determine the horizontal variation of the quantities θ , ρ , g_0 , and g_1 . As we found more accurate results with horizontal extrapolation, linear horizontal extrapolation was used for the numerical examples presented below.

Figure 9 shows an example of the horizontal variation of the quantities θ , ρ , g_0 , and g_1 on the illuminated side of the first $j=3$ caustic branch, at height 5 m, for a system with source height 1 m, a linear sound-speed profile $c(z)=c_0+c_1z$ with $c_0=340$ m/s and $c_1=0.1$ s⁻¹, and a reflecting ground surface. The caustic point at height 5 m is at range $r_{\text{caustic}}=503.5$ m [see Fig. 5(d)]. At this point, we have $\rho=0$. The line in Fig. 9(b) represents the first-order approximation $\rho=(2/a)^{1/3}y$, where $a=1/|1/a_{\text{ray}}+1/a_{\text{caustic}}|$ is the effective radius of curvature of the caustic,¹¹ with a_{ray} the

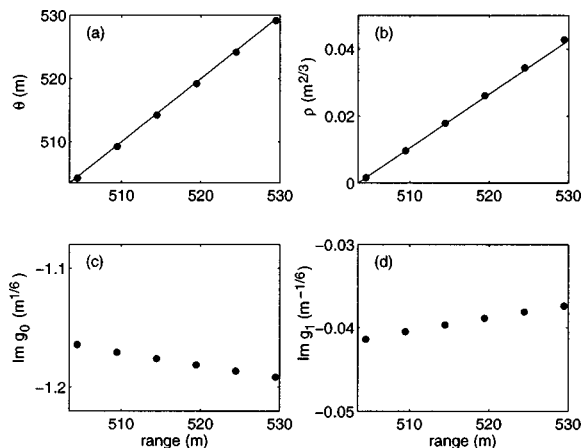


FIG. 9. Example of the horizontal variation of the quantities θ , ρ , g_0 , and g_1 , shown in graphs (a), (b), (c), and (d), respectively, on the illuminated side of the first $j=3$ caustic branch, at height 5 m, for a system with source height 1 m, a linear sound-speed profile $c(z)=c_0+c_1z$ with $c_0=340$ m/s and $c_1=0.1$ s⁻¹, and a reflecting (i.e., rigid) ground surface. The dots in the graphs represent the model. The lines in graphs (a) and (b) represent first-order approximations $\theta=r$ and $\rho=(2/a)^{1/3}y$, respectively. Graphs (c) and (d) show the imaginary parts of g_0 and g_1 , respectively, the real parts vanish identically in this case.

radius of curvature of the caustic rays at the caustic point and a_{caustic} the local radius of curvature of the caustic, and $y \approx (r-r_{\text{caustic}})\sin \gamma$ the normal distance to the caustic curve, with γ the local elevation angle of the caustic curve. The line in Fig. 9(a) represents the first-order approximation $\theta=r$. Figure 9(c) and (d) show the imaginary parts of g_0 and g_1 , respectively (the real parts vanish identically in this case). The horizontal variation of g_0 and g_1 is seen to be quite small.

Finally, a few practical points should be mentioned about the algorithm that was used for the numerical examples presented in Sec. V below. First, the horizontal extrapolation range into caustic shadows is limited to 400 m (to avoid small discontinuities here, the field is linearly tapered to zero within a range of 50 m). Second, only the diffraction fields of the two nearest $j=3$ branches and the two nearest $j=4$ branches are taken into account. These two limitations are applied in order to keep the model as efficient as possible, and have an effect on the field only at low frequency. At high frequency, the caustic diffraction field decays rapidly with increasing distance to the caustic, and the two limitations have no effect. Third, the ground reflection of the caustic diffraction field of the $j=2$ branch is neglected. The corresponding error is minimized by the choice $z_2 \geq z_1$ mentioned before. The fourth point concerns the caustic cusps. Although the effect of caustic cusps is neglected in smooth caustic theory, we found that we could improve the accuracy (that is, the agreement with PE; see Sec. V) in the region close to a cusp, by the following (empirical) approach. The diffraction field above the cusp is linearly tapered to zero, within the range interval between $r_{\text{cusp}}-\delta r$ and $r_{\text{cusp}}+\delta r$, where r_{cusp} is the range of the cusp and we use $\delta r=50$ m. We apply the same approach to the end point at the ground of the $j=4$ branch.

B. Application of cusped caustic theory

Next a brief description is given of the application of cusped caustic theory, that is, caustic theory with $M=3$ (it should be noted that in the numerical examples presented in Sec. V only the smooth caustic theory is used). There are three rays that touch the caustic branches emanating from the cusp: two rays touching the upper branch $j=3$ and one ray touching the lower branch $j=2$ (for $z_2 > z_1$). Near the cusp, the caustic theory for $M=3$ can be applied as follows: the contribution from the three cusp rays in the sum in Eq. (2a) is replaced by a modified contribution involving a generalized Airy function and its derivative (see Sec. III). Near the caustic branch $j=4$ the smooth caustic theory ($M=2$) is applied to the contribution from the two rays touching this branch. The three cusp rays and the two $j=4$ branch rays have one ray in common: a ray with $j=2$. Since this ray can be used only once, one has to choose between two possibilities. Near the cusp one should apply the cusped caustic theory, near the $j=4$ branch one should apply the smooth caustic theory. In the first case, the contribution from the ray with $j=4$ in the sum in Eq. (2a) is not modified (except for the caustic phase shifts, of course). In the second case, we are back at the case described in Sec. IV A. This holds also for the extrapolation into the shadow region: the common ray

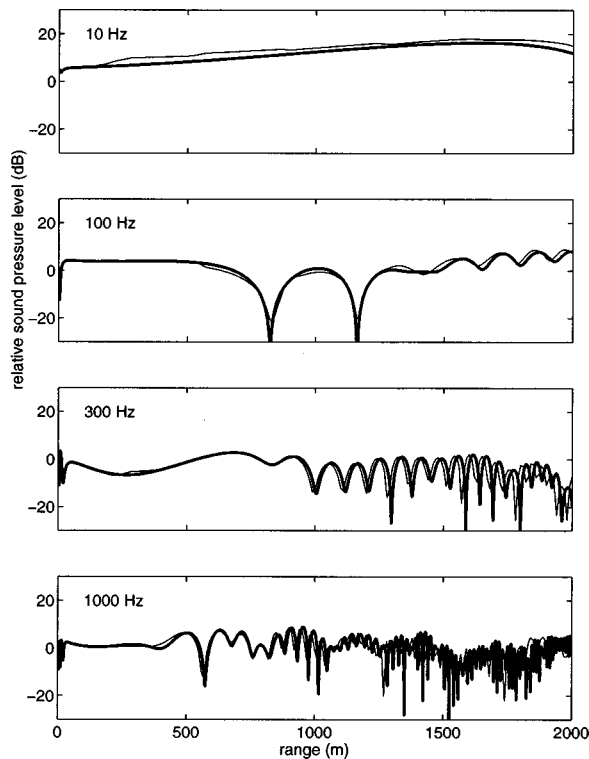


FIG. 10. Relative sound-pressure level at four frequencies, for a system with source height 1 m, receiver height 5 m, a linear sound-speed profile $c(z) = c_0 + c_1 z$ with $c_0 = 340$ m/s and $c_1 = 0.1$ s⁻¹, and an absorbing ground surface (see the text). Thin curves represent the ray model, thick curves represent PE results.

with $j=2$ should be taken into account only once, either in the cusp diffraction field or in the $j=4$ branch diffraction field. It should also be noted that when the cusp diffraction field is used, the contribution from the $j=2$ ray in Eq. (2a) should be omitted, since this contribution is included in the cusp diffraction field. To avoid discontinuities, one can introduce a gradual transition between the two solutions (the cusp solution and the $j=4$ branch solution), using a weighted average of the two solutions with gradually changing weights.

V. NUMERICAL EXAMPLES

In this section, the accuracy of the ray model is studied by comparison with finite-difference solutions of the wave equation. The effects of caustics are included in the ray model by using the theory of smooth caustics, as described in Sec. IV A. For the finite-difference solutions, the parabolic equation (PE) method was used. Both the Crank–Nicholson PE (CNPE) method⁴¹ and the Green’s function PE (GFPE) method^{42,43} were used. From the agreement between CNPE results and GFPE results (differences were indistinguishable on the scale of the figures presented below) it was concluded that the PE results can be considered as an accurate reference. Results are presented in terms of the relative sound-pressure level L , defined as the sound-pressure level relative to free field ($L = 20 \lg |p|$).

Figure 10 shows values of $L(r)$ at four frequencies, for a system with source height 1 m, receiver height 5 m, a linear sound-speed profile $c(z) = c_0 + c_1 z$ with $c_0 = 340$ m/s

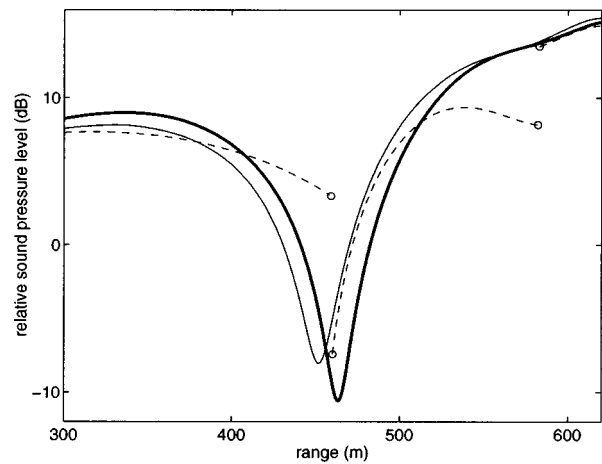


FIG. 11. Relative sound-pressure level at frequency 1000 Hz for a system with source height 3 m, receiver height 5 m, a reflecting ground surface, and the same linear sound-speed profile as for Fig. 10. Shown are results of the ray model with caustic diffraction fields neglected (dashed curve) or included (full thin curve), and PE results (thick curve).

and $c_1 = 0.1$ s⁻¹, and a finite-impedance ground surface with a flow resistivity of 300 kPa s m⁻², representative of grassland. Normalized ground impedances were $51.9 + 51.7i$, $16.7 + 16.1i$, $10.07 + 8.89i$, and $6.34 + 4.23i$ at $f = 10, 100, 300,$ and 1000 Hz, respectively. These values were computed from the assumed flow resistivity using Attenborough’s four parameter impedance model³⁴ [we use Eqs. (11) and (12) of Ref. 34, with a pore shape factor ratio of 0.75, a grain shape factor of 0.5, and a porosity of 0.3]. The agreement between the ray model (thin curves) and PE results (thick curves) is excellent.

Comparisons as shown in Fig. 10 were performed for various systems, with source heights 1 and 3 m, receiver height 5 m, absorbing ground (see above) and reflecting (i.e., rigid) ground, and a linear profile (see above) and a logarithmic profile $c(z) = c_0 + b \ln(z/z_0 + 1)$ with $b = 1$ m/s and $z_0 = 0.1$ m. For all systems with the linear profile, the agreement is similar to the good agreement shown in Fig. 10. For the systems with the logarithmic profile, the ray model deviates from PE at low frequencies. For absorbing ground, the deviations occur at 10 and 100 Hz, while good agreement is obtained at 300 and 1000 Hz. For reflecting ground, deviations occur also at 300 Hz. These results indicate that the ray model is accurate down to a lower frequency for absorbing ground than for reflecting ground. This is a consequence of the relatively strong ground attenuation of the lowest sound rays, which are most crucial for the accuracy of the ray model.²⁵

Figure 11 demonstrates the effect of caustic diffraction fields for a system with source height 3 m, receiver height 5 m, a reflecting ground surface, frequency 1000 Hz, and the same linear sound-speed profile as for Fig. 10. The dashed curve represents the ray model with caustic diffraction fields neglected, the full thin curve represents the ray model with diffraction fields included, and the thick curve represents PE results. We see that discontinuities occur of about 10 and 5 dB if the caustic diffraction fields are neglected. The discontinuities occur at the caustics [see Fig. 5(c)]. With the diffraction fields included, the solution of the ray model is con-

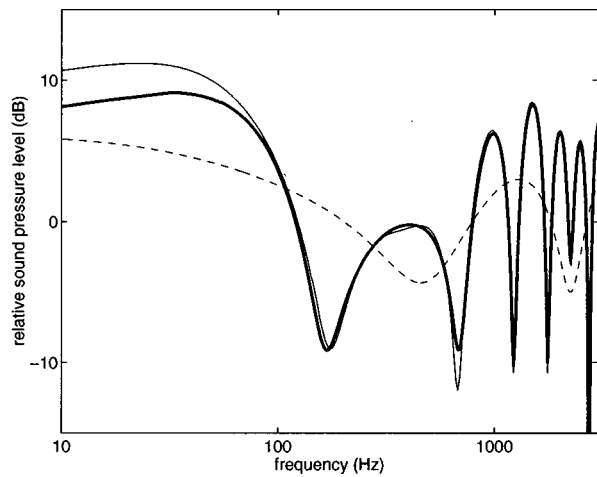


FIG. 12. Spectrum of the relative sound-pressure level at range $r=500$ m, for a system with source height 1 m, receiver height 5 m, and the same absorbing ground surface and linear sound-speed profile as for Fig. 10. Line types are as in Fig. 11.

tinuous and the agreement with the PE results is sufficiently good for practical applications.

Figure 12 demonstrates the effect of caustic diffraction fields on the spectrum of the relative sound-pressure level at range $r=500$ m, for a system with source height 1 m, receiver height 5 m, and the same absorbing ground surface and linear sound-speed profile as for Fig. 10. The receiver is located close to the caustic branch $n=1, j=3$ [see Fig. 5(d)].

Figure 13 shows values of $L(r)$ at five receiver heights

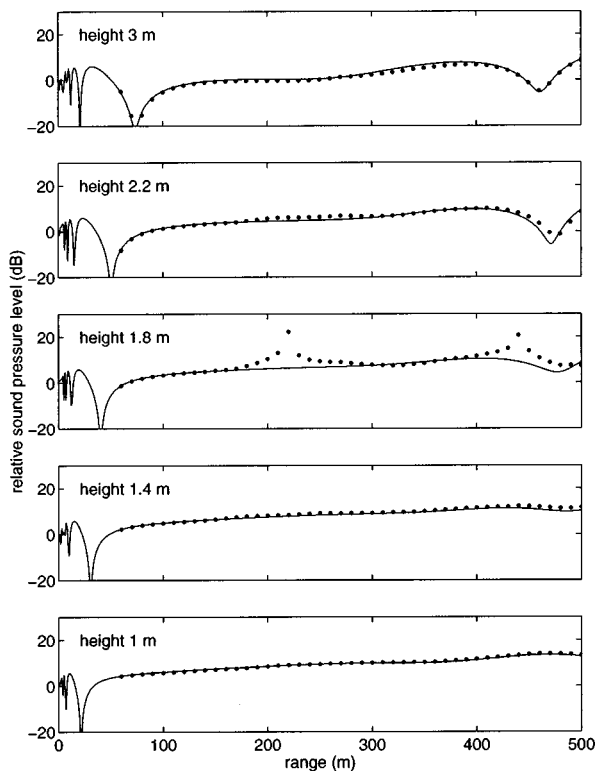


FIG. 13. Relative sound-pressure level at five receiver heights z_2 and frequency 1000 Hz, for a system with source height 1.8 m, a reflecting ground surface, and the same linear sound-speed profile as for Fig. 10. Curves represent PE results, dots represent the ray model.

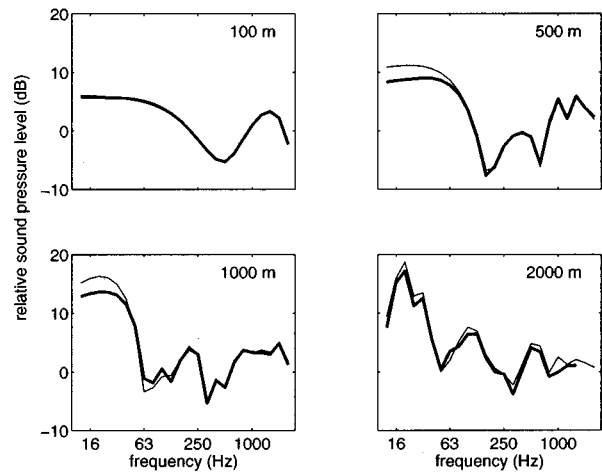


FIG. 14. Third-octave band spectra of the relative sound-pressure level at four ranges, $r=100, 500, 1000,$ and 2000 m, for a system with source height 1 m, receiver height 5 m, and the same absorbing ground surface and linear sound-speed profile as for Fig. 10. Thin curves represent the ray model, thick curves represent PE results.

z_2 and frequency 1000 Hz, for a system with source height 1.8 m, a reflecting ground surface, and the same linear sound-speed profile as for Fig. 10. For $z_2 < z_1$ the reciprocal system with $z_2 > z_1$ was used for the ray model computations. For $z_2 = z_1$ the ray model is inaccurate near the caustic cusps at $r=220$ m and $r=440$ m (see Fig. 4). For $z_2 = 2.2$ m and $z_2 = 1.4$ m, the results of the ray model are accurate. This suggests the following approach for practical applications of the ray model, for $z_2 = z_1$: use the average of the two solutions for $z_2 = z_1 + \Delta z$ and $z_2 = z_1 - \Delta z$, with, e.g., $\Delta z = 0.5$ m.

Figures 14 and 15 show third-octave band spectra of the relative sound-pressure level. Third-octave band spectra al-

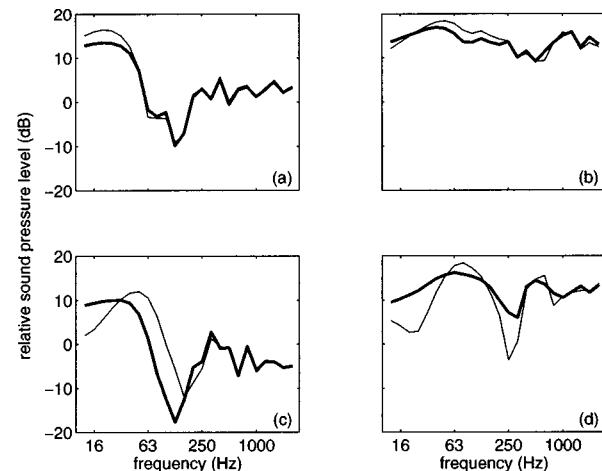


FIG. 15. Third-octave band spectra of the relative sound-pressure level at range $r=1000$ m, for a system with source height 3 m, receiver height 5 m, and
—a linear profile $c(z)=c_0+c_1z$ and an absorbing (a) or reflecting (b) ground surface,
—a logarithmic profile $c(z)=c_0+b \ln(z/z_0+1)$ and an absorbing (c) or reflecting (d) ground surface,
with $c_0=340$ m/s, $c_1=0.1$ s $^{-1}$, $b=1$ m/s, and $z_0=0.1$ m. Thin curves represent the ray model, thick curves represent PE results.

low a better comparison between the ray model and PE results than narrow-band spectra with rapid oscillations at high frequency do. Figure 14 shows spectra at four ranges, $r = 100, 500, 1000,$ and 2000 m, for a system with source height 1 m, receiver height 5 m, and the same absorbing ground surface and linear sound-speed profile as for Fig. 10. The agreement between the ray model and PE results is sufficient for practical applications, except for frequencies below 63 Hz. Figure 15 shows spectra at range $r = 1000$ m, for a system with source height 3 m, receiver height 5 m, and:

- a linear profile $c(z) = c_0 + c_1 z$ and an absorbing (a) or reflecting (b) ground surface,
- a logarithmic profile $c(z) = c_0 + b \ln(z/z_0 + 1)$ and an absorbing (c) or reflecting (d) ground surface,

with $c_0 = 340$ m/s, $c_1 = 0.1$ s⁻¹, $b = 1$ m/s, and $z_0 = 0.1$ m. For the absorbing ground the same impedance parameters were used as for Fig. 10. For the logarithmic profile, the ray model deviates from the PE results for frequencies below about 300 Hz. Similar deviations were observed in other comparisons (not shown here) for the logarithmic profile.

VI. CONCLUDING REMARKS

Computing times of the ray model presented here are small. The computation of a complete spectrum for propagation over a range of typically 1 km requires typically a few seconds on current computers. This does not include the preparation of the matrix $\delta_k^*(h)$ (see Sec. II A), which requires typically a few minutes. This preparation, however, has to be done only once for each new sound-speed profile. The prepared matrix can be used for all source–receiver configurations and ground impedances. As a practical approach for application of the ray model in outdoor noise control, one may choose a set of smooth profiles that covers the range of profiles that occur in practice, and prepare and store the matrices $\delta_k^*(h)$ for these profiles. This approach results in a fast model for computing noise levels.

The accuracy of the model has been demonstrated by comparison with numerical solutions of the one-way wave equation, computed with the PE method. For a linear sound-speed profile, good agreement was obtained between PE and the ray model down to frequencies below 100 Hz. For a realistic logarithmic profile with large gradients near the ground, however, deviations occur below about 300 Hz. These deviations must be attributed to a violation of the high-frequency assumption inherent in the ray model. To avoid the errors in the ray model at low frequency, there are two possible practical approaches:

- (i) use only profiles with small gradients,
- (ii) use a hybrid PE-ray model, with the PE method for low frequency and the ray model for high frequency.

Although the second approach appears rather complex for applications in outdoor noise control, this approach may turn out to be the best compromise between accuracy, computational speed, and the ability to model systems with realistic sound-speed profiles. It should be noted that a relatively high

computational speed can be obtained with the PE method at low frequency by using the recently developed Green's function PE method.^{42,43}

- ¹J. B. Keller, "A geometrical theory of diffraction. Calculus of Variations and its Applications," *Proceeding of Symposia Applied Mathematics* (McGraw-Hill, New York, 1958), Vol. 8, pp. 27–52.
- ²R. N. Buchal and J. B. Keller, "Boundary layer problems in diffraction theory," *Commun. Pure Appl. Math.* **13**, 85–114 (1960).
- ³D. Ludwig, "Uniform asymptotic expansions at a caustic," *Commun. Pure Appl. Math.* **19**, 215–250 (1966).
- ⁴Yu. A. Kravtsov, "Two new asymptotic methods in the theory of wave propagation in inhomogeneous media (review)," *Sov. Phys. Acoust.* **14**, 1–17 (1968).
- ⁵L. M. Brekhovskikh, *Waves in Layered Media*, 2nd ed. (Academic, New York, 1980), Secs. 20–28, 36, 43–45.
- ⁶D. A. Sachs and A. Silbiger, "Focusing and refraction of harmonic sound and transient pulses in stratified media," *J. Acoust. Soc. Am.* **49**, 824–840 (1971).
- ⁷H. Weinberg, "Application of ray theory to acoustic propagation in horizontally stratified oceans," *J. Acoust. Soc. Am.* **58**, 97–109 (1975).
- ⁸H. Weinberg, "Effective range derivative for acoustic propagation loss in a horizontally stratified ocean," *J. Acoust. Soc. Am.* **70**, 1736–1742 (1981).
- ⁹M. G. Brown, "The transient wave fields in the vicinity of the cuspid caustics," *J. Acoust. Soc. Am.* **79**, 1367–1384 (1986).
- ¹⁰M. D. Brown and F. D. Tappert, "Causality, caustics, and the structure of transient wave fields," *J. Acoust. Soc. Am.* **80**, 251–255 (1986).
- ¹¹A. D. Pierce, *An Introduction to its Physical Principles and Applications* (AIP, New York, 1991), Chaps. 8 and 9.
- ¹²B. Hallberg, C. Larsson, and S. Israelsson, "Numerical ray tracing in the atmospheric surface layer," *J. Acoust. Soc. Am.* **83**, 2059–2068 (1988).
- ¹³F. Walkden and M. West, "Prediction of enhancement factor for small explosive sources in a stratified moving atmosphere," *J. Acoust. Soc. Am.* **84**, 321–326 (1988).
- ¹⁴M. M. Boone and E. A. Vermaas, "A new ray-tracing algorithm for arbitrary inhomogeneous and moving media, including caustics," *J. Acoust. Soc. Am.* **90**, 2109–2117 (1991).
- ¹⁵A. L'Espérance, P. Herzog, G. A. Daigle, and J. R. Nicolas, "Heuristic model for outdoor sound propagation based on an extension of the geometrical ray theory in the case of a linear sound speed profile," *Appl. Acoust.* **37**, 111–139 (1992).
- ¹⁶J. S. Lamancusa and P. A. Daroux, "Ray tracing in a moving medium with two-dimensional sound-speed variations and application to sound propagation over terrain discontinuities," *J. Acoust. Soc. Am.* **93**, 1716–1726 (1993).
- ¹⁷E. M. Salomons, "Downwind propagation of sound in an atmosphere with a realistic sound-speed profile: A semianalytical ray model," *J. Acoust. Soc. Am.* **95**, 2425–2436 (1994).
- ¹⁸R. B. Stull, *An Introduction to Boundary Layer Meteorology* (Kluwer, Dordrecht, 1991), pp. 376–378.
- ¹⁹A. H. Anderson and A. C. Kak, "Digital ray tracing in two-dimensional refractive fields," *J. Acoust. Soc. Am.* **72**, 1593–1606 (1982).
- ²⁰G. E. Bold and T. G. Birdsall, "A top-down philosophy for accurate numerical ray tracing," *J. Acoust. Soc. Am.* **80**, 656–660 (1986).
- ²¹D. S. Ahluwalia and J. B. Keller, "Exact and asymptotic representations of the sound field in a stratified ocean," in *Wave Propagation in Underwater Acoustics*, edited by J. B. Keller and J. S. Papadakis, Lecture Notes in Physics Vol. 70 (Springer-Verlag, Berlin, 1977).
- ²²K. M. Li, "On the validity of the heuristic ray-trace-based modification to the Weyl-Van der Pol formula," *J. Acoust. Soc. Am.* **93**, 1727–1735 (1993).
- ²³K. M. Li, "A high-frequency approximation of sound propagation in a stratified moving atmosphere above a porous ground surface," *J. Acoust. Soc. Am.* **95**, 1840–1852 (1994).
- ²⁴K. M. Li, "Propagation of sound above an impedance plane in a downward refracting atmosphere," *J. Acoust. Soc. Am.* **99**, 746–754 (1996).
- ²⁵R. Raspet, A. L'Espérance, and G. A. Daigle, "The effect of realistic ground impedance on the accuracy of ray tracing," *J. Acoust. Soc. Am.* **97**, 154–158 (1995).
- ²⁶M. A. Pedersen and D. F. Gordon, "Comparison of curvilinear and linear profile approximation in the calculation of underwater sound intensities by ray theory," *J. Acoust. Soc. Am.* **41**, 419–438 (1967).

- ²⁷M. A. Pedersen and D. F. Gordon, "Normal-mode and ray theory applied to underwater acoustic conditions of extreme downward refraction," *J. Acoust. Soc. Am.* **51**, 323–368 (1972).
- ²⁸D. T. Raphael, "Closed-form solutions for SOFAR ray caustics in media with bilinear sound-speed profiles," *J. Acoust. Soc. Am.* **56**, 416–426 (1974).
- ²⁹J. A. Davis, "Extended modified ray theory field in bounded and unbounded inhomogeneous media," *J. Acoust. Soc. Am.* **57**, 276–286 (1975).
- ³⁰D. C. Stickler, D. S. Ahluwalia, and L. Ting, "Application of Ludwig's uniform progressing wave ansatz to a smooth caustic," *J. Acoust. Soc. Am.* **69**, 1673–1681 (1981).
- ³¹E. R. Floyd, "The existence of caustics and cusps in a rigorous ray tracing representation," *J. Acoust. Soc. Am.* **79**, 1741–1747 (1986).
- ³²K. Attenborough, S. I. Hayek, and J. M. Lawther, "Propagation of sound above a porous half-space," *J. Acoust. Soc. Am.* **68**, 1493–1501 (1980).
- ³³X. Di and K. E. Gilbert, "An exact Laplace transform formulation for a point source above a ground surface," *J. Acoust. Soc. Am.* **93**, 714–719 (1993).
- ³⁴K. Attenborough, "Acoustic impedance models for outdoor ground surfaces," *J. Sound Vib.* **99**, 521–544 (1985).
- ³⁵C. Chester, B. Friedman, and F. Ursell, "An extension of the method of steepest descent," *Proc. Cambridge Philos. Soc.* **54**, 599–611 (1957).
- ³⁶G. N. Watson, *A Treatise on the Theory of Bessel Functions* (Cambridge U.P., Cambridge, England, 1952), pp. 188–190.
- ³⁷D. Zwillinger, *Handbook of Differential Equations* (Academic, Boston, 1992), pp. 284–289.
- ³⁸*Handbook of Mathematical Functions*, edited by M. Abramowitz and I. A. Stegun (Dover, New York, 1972), pp. 446–452.
- ³⁹B. D. Seckler and J. B. Keller, "Geometrical theory of diffraction in inhomogeneous media," *J. Acoust. Soc. Am.* **31**, 192–205 (1959).
- ⁴⁰B. D. Seckler and J. B. Keller, "Asymptotic theory of diffraction in inhomogeneous media," *J. Acoust. Soc. Am.* **31**, 206–216 (1959).
- ⁴¹K. E. Gilbert and M. J. White, "Application of the parabolic equation to sound propagation in a refracting atmosphere," *J. Acoust. Soc. Am.* **85**, 630–637 (1989).
- ⁴²K. E. Gilbert and X. Di, "A fast Green's function method for one-way sound propagation in the atmosphere," *J. Acoust. Soc. Am.* **94**, 2343–2352 (1993).
- ⁴³E. M. Salomons, "Improved Green's function parabolic equation method for atmospheric sound propagation," *J. Acoust. Soc. Am.* **104**, 100–111 (1998).

Effects of a background axisymmetric potential flow on vortex ring pairing sound

S. K. Tang

Department of Building Services Engineering, The Hong Kong Polytechnic University, Hong Kong, People's Republic of China

N. W. M. Ko

Department of Mechanical Engineering, The University of Hong Kong, Hong Kong, People's Republic of China

(Received 3 November 1997; revised 14 August 1998; accepted 19 August 1998)

Sound generated by the pairing of two coaxial vortex rings in the presence of a background axisymmetric potential flow was studied numerically. Results show that the background flow substantially affects the sound generation process in the beginning of the vortex ring interaction. They also suggest that the axial jerk and radial acceleration/deceleration of vortex rings are the major mechanisms through which pairing sound is produced. The effect of background flow mean shear rate on sound generation is also discussed and the results suggest that higher sound levels will be generated when the vortex rings are interacting within the region of high mean shear in a low speed laminar jet. © 1998 Acoustical Society of America. [S0001-4966(98)06411-X]

PACS numbers: 43.28.Ra, 43.28.Py [LCS]

INTRODUCTION

Powell¹ suggested that unsteady motion of vorticity is the major source of sound in an unbound low Mach number flow. Although Howe² and Doak³ showed that the acoustic variable is the total stagnation enthalpy rather than pressure when vorticity is regarded as the source, the vortex sound theory of Powell¹ remains valid for low Mach number flow sound generation.

The common vortical structures found within the first four exit diameters of a circular jet are coaxial vortex rings and their pairing is found to be responsible for the growth of the jet mixing layer.⁴ Möhring⁵ solved analytically the sound field generated by two closely packed thin core vortex rings, while Kambe and Minota⁶ extended the investigation numerically to cover vortex rings having the initial core separation comparable to the ring diameter. Results of the latter show that a pulse is generated when the trailing vortex ring shrinks in diameter and slips through the leading ring. The importance of vortex pairing in the development of jet mixing layer and its sound generating characteristics tend to support that vortex ring pairing is a source of noise from the initially laminar low Mach number jets.⁷

Although it is well known that sound is generated by the unsteady motion of vorticity at low Mach number, it remains to be determined at which conditions the loudest noise is likely to be radiated. Investigation into the mechanism of pairing noise generation has been carried out by many researchers (for instance, Ref. 8) and there are experimental results which show that the acceleration and deceleration of vortical structures within the pairing region of a circular jet mixing layer are highly related to the far field jet noise.^{8,9} Leung *et al.*¹⁰ modified the vortex ring pairing model of Kambe and Minota⁶ by incorporating the vortex ring formation theory of Saffman¹¹ and related explicitly the vortex ring

pairing noise with jet noise parameters. There is adequate evidence to conclude that the pairing of vortical ring structures in axisymmetric jets plays a vital role in the noise generation process.

Results of the investigation on the mechanism of thick core vortex ring pairing noise generation of Tang and Ko¹² illustrate the importance of the axial jerk and radial acceleration of vortical structures in the generation of sound. However, vortex ring motions in real mixing layers are affected by the background jet mean velocity gradient. This mean velocity gradient, which is also called mean shear rate, may introduce additional jerk and acceleration of vortical structures during the pairing process, making the vortex motions more unsteady, and thus directly change the radiated noise level. The closer the vortex ring to the nozzle lip, the stronger the effect of the mean velocity gradient on pairing noise generation. Therefore, the vortex ring pairing model of Möhring,⁵ Kambe and Minota,⁶ and Leung *et al.*,¹⁰ while providing a reasonable prediction of jet noise radiation characteristics, may be inadequate in the study of jet noise generation.

In the present study, the effect of a background flow field on pairing noise is studied numerically using a model developed from the results of Leung *et al.*¹⁰ and Saffman.¹¹ The vortical structure motions, which result in different noise radiation in the presence of the background flow field, are discussed. The causes of the unsteady structure motions are also investigated. The model used in the present study is a simplified one, which may be different from the real shear layer, making comparison between the present results and existing experimental data difficult. However, it is intended here to first investigate the extent the background flow field has on the vortex sound generation and to provide information for future experimental investigations.

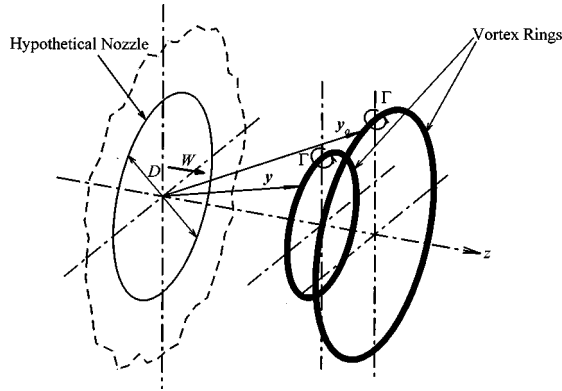


FIG. 1. Schematic diagram of vortex ring system.

I. THEORETICAL FORMULATION AND COMPUTATIONAL PROCEDURE

In the present study, the term vortex pairing refers to the mutual threading motion of two coaxial inviscid vortex rings as visualized by Yamada and Matsui.¹³ Noise from vortex coalescence, where the vortex rings merge into a single vortex ring during their mutual threading process,¹³ is not studied. It is assumed in the present investigation that the cores of the vortex rings remain circular throughout the pairing process and the vorticity is uniform within the vortex cores.

The velocity, \mathbf{V}_ω , of a vortex ring having circulation Γ and radius σ_c in the presence of another identical vortex ring and a background flow field is made up of three components:

$$\mathbf{V}_\omega = \mathbf{V}_{\text{self}} + \mathbf{V}_{\text{ind}} + \bar{\mathbf{V}}(z_c, \sigma_c), \quad (1)$$

where \mathbf{V}_{self} and \mathbf{V}_{ind} are the self-induced velocity and the velocity resulting from mutual induction, respectively. z and σ denote, respectively, the axial and radial coordinates in the near field. The subscript c denotes a quantity associated with the vortex core centre. The background flow velocity $\bar{\mathbf{V}}(z, \sigma)$ varies from point to point in the flow field. This extra term, which has been ignored by researchers (for instance, Refs. 6 and 10) in the study of vortex pairing noise, gives a higher relative velocity between the vortex rings than those of $\bar{\mathbf{V}} = 0$. Thus it introduces the effect of background mean flow on vortex ring dynamics and their pairing noise. Denoting the core radius as r_c , the results of Kelvin and Stokes on velocity induction¹⁴ gives

$$\mathbf{V}_{\text{self}} = \frac{\Gamma}{4\pi\sigma_c} \left[\ln\left(\frac{8\sigma_c}{r_c}\right) - \frac{1}{4} \right] \hat{z} \quad (2a)$$

and

$$\mathbf{V}_{\text{ind}} = -\frac{\Gamma}{4\pi} \oint \frac{\mathbf{y} - \mathbf{y}_0}{|\mathbf{y} - \mathbf{y}_0|^3} \times \frac{d\mathbf{y}_0}{ds} ds, \quad (2b)$$

respectively, where \hat{z} denotes an unit vector in the axial direction, and ds an infinitesimal arc length on the second identical vortex ring. \mathbf{y} and \mathbf{y}_0 are position vectors on the first and second vortex ring, respectively (Fig. 1). The integral in Eq. (2b) is taken over the whole periphery of the second vortex ring. Using the theory of Saffman,¹¹ Leung *et al.*¹⁰ related Γ , σ_c , r_c , and the initial vortex ring core separation with jet velocity W , nozzle diameter D , and the Strouhal number

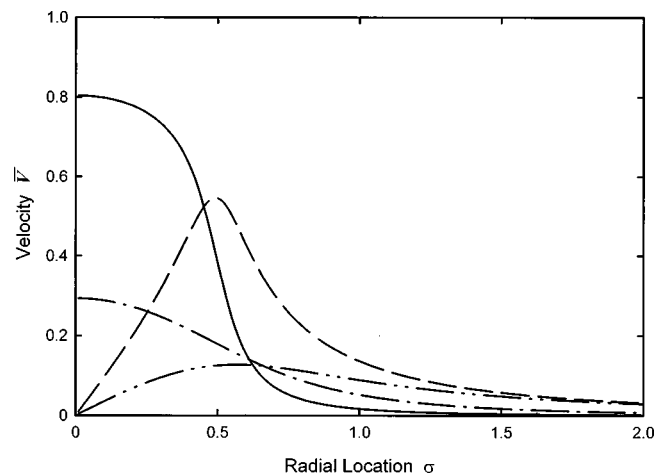


FIG. 2. Velocity profiles of present adopted background mean flow. —: Mean axial velocity at $z/D=0.1$; - - -: mean axial velocity at $z/D=0.5$; - · - : mean radial velocity at $z/D=0.1$; · · · : mean radial velocity at $z/D=0.5$.

St_D . Details of the formulation have been given in Leung *et al.*¹⁰ and are not repeated here.

In the present study, unlike the case of Leung *et al.*,¹⁰ the initial axial position, z_f , relative to the nozzle exit where a vortex ring is formed, is important because of the presence of a background mean flow velocity which varies from point to point in the flow field. The formation position of the vortex ring thus affects at least the initial separation of the vortex ring cores. Following the results of Saffman,¹¹ it can be deduced that

$$z_f = 0.09\pi^{-1/3} St_D^{-2/3} D. \quad (3)$$

The jet mean velocity profile given in Townsend¹⁵ cannot be used here to model the background mean flow $\bar{\mathbf{V}}(z, \sigma)$, as both the velocity induction laws of Stokes and Kelvin [Eq. (2)] and the vortex sound theory require divergence-free potential flow¹⁶⁻¹⁸ while that given by Townsend,¹⁵ although it resembles the velocity profile of a practical jet, does not fulfill this criterion. The potential flow adopted in the present investigation is obtained using the method shown in Morse and Feshbach¹⁹ and the mean flow $\bar{\mathbf{V}}(z, \sigma)$ is given by

$$\begin{aligned} \bar{\mathbf{V}}(z, \sigma) = \hat{z} \int_0^\infty W e^{-\alpha z} J_1(0.5\alpha D) J_0(\alpha\sigma) d\alpha \\ + \hat{\sigma} \int_0^\infty W e^{-\alpha z} J_1(0.5\alpha D) J_1(\alpha\sigma) d\alpha, \end{aligned} \quad (4)$$

where J_0 and J_1 are the Bessel function of the first kind of the zero and first order, respectively. Equation (4) gives the axial velocity W for $z=0$, $\sigma \leq 0.5D$ and 0 for $z=0$, $\sigma > 0.5D$. Details of the derivation are given in the Appendix. Some profiles of the mean flow $\bar{\mathbf{V}}(z, \sigma)$ are shown in Fig. 2. It can be observed that higher radial and axial velocity gradients appear close to the nozzle exit. Also, the initial growth rate of $\bar{\mathbf{V}}(z, \sigma)$ and the mean radial velocity are higher than those of low speed laminar or turbulent jets.^{20,21}

The initial vortex ring core separation in the present study, unlike that in Leung *et al.*,¹⁰ is found by solving the

motion of the first vortex ring through integration of Eq. (1) with $\mathbf{V}_{\text{ind}}=0$ with respect to time, using the classical fourth order Runge–Kutta procedure. The length of the time integration, t_ω , depends on the frequency or Strouhal number of vortex ring formation:

$$t_\omega = \frac{D}{St_D W}. \quad (5)$$

The motions of the vortex rings during their interactions are also obtained by integrating Eq. (1) with respect to time, using the same numerical method. Since the present model allows an infinite number of slip-through processes which are hardly visualized in a real axisymmetric mixing layer, only the computed results within the first few slip-through processes will be discussed in detail.

Far field pressure fluctuations $p(\mathbf{x}, \tau)$, where \mathbf{x} denotes a far field coordinate and τ the far field observer time, are calculated using the formula of Möhring:⁵

$$p(\mathbf{x}, \tau) = \frac{\rho_0}{4a_0^2|\mathbf{x}|^3} \sum \frac{d^3}{dt^3} \Gamma \sigma_c^2 z_c \mathbf{x} \cdot \left(\hat{z} \hat{z} - \frac{1}{3} \right) \cdot \mathbf{x}. \quad (6)$$

The sound field has the characteristics of a quadrupole. The involved time differentiations are carried out at the retarded time t , where $t = \tau - |\mathbf{x}|/a_0$. Since ρ_0 and a_0 are constants and \mathbf{x} and \hat{z} do not relate to sound generation mechanism, they are ignored in the foregoing discussions. The time steps for the differentiation and Runge–Kutta integration are so chosen such that a further halving of them does not give noticeable change in the computed results.

Investigations relating the mechanism of vortex pairing sound generation with the vortex ring motions have been carried out by the authors recently.^{9,12} Noting that the impulse, I , of a vortex ring is proportional to the product of circulation and the square of the vortex ring radius, $\Gamma \sigma_c^2$, Tang and Ko¹² investigated the mechanism of thick core vortex ring pairing sound generation by decomposing the far field pressure fluctuations into four terms, each of which represents the sound generation by the coupling of a dynamic parameter, such as velocity or acceleration, with the time derivatives of I :

$$p \propto \sum I \frac{d^3 z_c}{dt^3} + 3 \sum \frac{dI}{dt} \frac{d^2 z_c}{dt^2} + 3 \sum \frac{d^2 I}{dt^2} \frac{dz_c}{dt} + \sum z_c \frac{d^3 I}{dt^3}. \quad (7)$$

It should be noted that the right hand side of Eq. (7) is evaluated at retarded time. Equation (7) is obtained by a straightforward decomposition of Eq. (6), and thus is valid for both a thick core vortex ring and vortex filament pairing noise. The physical meanings of each of them can be found in Tang and Ko¹² and are not repeated here. The changes of these four terms during pairing in the presence of a background potential flow of Eq. (4) are calculated. For simplicity, deformation of the vortex core is ignored. The method for changing the core sizes during vortex ring interaction follows that of Yamada and Matsui.¹³ For easy reference, the time derivatives on the right hand side of Eq. (7), namely the axial jerk $d^3 z_c/dt^3$, the axial acceleration $d^2 z_c/dt^2$, and the

axial velocity dz_c/dt are represented, respectively, by J_z , A_z , and V_z in the foregoing discussion.

All computations were done using Microsoft FORTRAN PowerStation 1.0a on a 586 personal computer. Double precision calculation was adopted.

II. RESULTS AND DISCUSSIONS

In the foregoing discussion, all quantities, unless otherwise stated, are nondimensionalized. All lengths and time scales are normalized by the nozzle diameter D and D/W , respectively. W is the nozzle exit velocity. The present investigation aims at showing the trend rather than the exact values, and thus D and W are arbitrarily chosen to be unity and without unit, for simplicity. In the rest of the paper, the conditions of $\bar{\mathbf{V}} \neq 0$ and $\bar{\mathbf{V}} = 0$ denote the cases with and without background mean velocity gradient, respectively. Also, the foregoing discussion is focused on the first three slip-through processes and $0.25 \leq St_D \leq 4$, as $St_D = 0.25$ and 4 correspond roughly to the jet column mode and shear layer mode instabilities of a circular jet, respectively.^{7,20}

A. Vortex ring motions

Without background mean velocity gradient, the motions of the inviscid vortex rings and the resulting far field pressure fluctuations are periodic.⁶ In the presence of the background potential flow, the vortex rings increase in diameter during their interaction, except for a short period just after their interaction commences. However, the patterns of their interactions depend significantly on St_D . Figure 3(a) and (b) illustrates the locations of vortex ring core centers for $St_D = 0.25$ ($\Delta t = 0.4$) and 4 ($\Delta t = 0.02$), respectively. The vortex ring core center locations for $\bar{\mathbf{V}} = 0$ are included for reference. The numbers in these figures describe the sequence of the vortex ring core center motions. For all the St_D studied, the initially leading vortex ring has a larger diameter than the trailing one in the beginning of their interaction, owing to the radial velocity of the background flow field. The initial spacing between vortex rings is thus larger than that for $\bar{\mathbf{V}} = 0$ for the same St_D . It can be observed in Fig. 3(a) that the trailing vortex ring first expands in diameter (at $z/D \approx 0.5$). The decrease in the ring diameter that follows is probably due to the effect of the leading vortex ring which is then strong enough to counterbalance that of the background radial flow velocity. The major effect of the background mean flow is to increase the diameter of the initially leading vortex ring so that its diameter is larger than that of the initially trailing one at the beginning of the interaction. This is the result of the radial velocity component of the mean flow. The axial positions of the vortex cores are not affected by the mean flow as the latter is small at $z/D = 0.5$, as shown in Fig. 2, and is even smaller for $z/D > 1$. After the first slip-through process, which takes place at $z/D \approx 2.4$, the pattern of vortex ring interaction resembles that for $\bar{\mathbf{V}} = 0$, except there is a slight increase in the radius of the vortex ring system centroid due to the background flow field. As shown in Fig. 3(b), for high St_D , the much shorter vortex ring separation results in a more intense slip-through process, while the relatively weak vortex ring velocity induction cannot

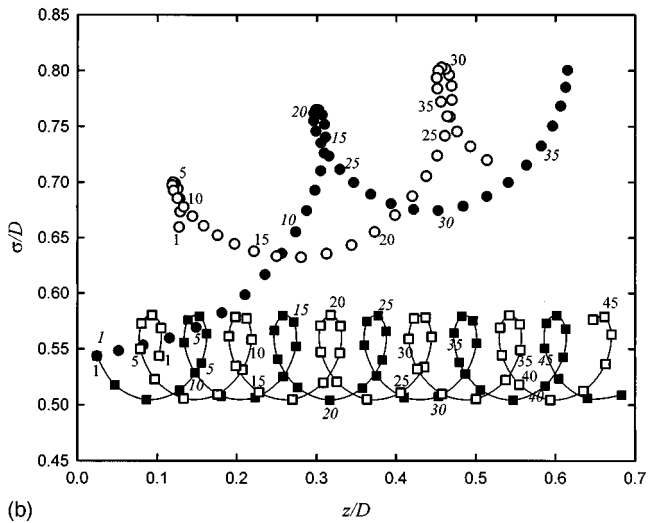
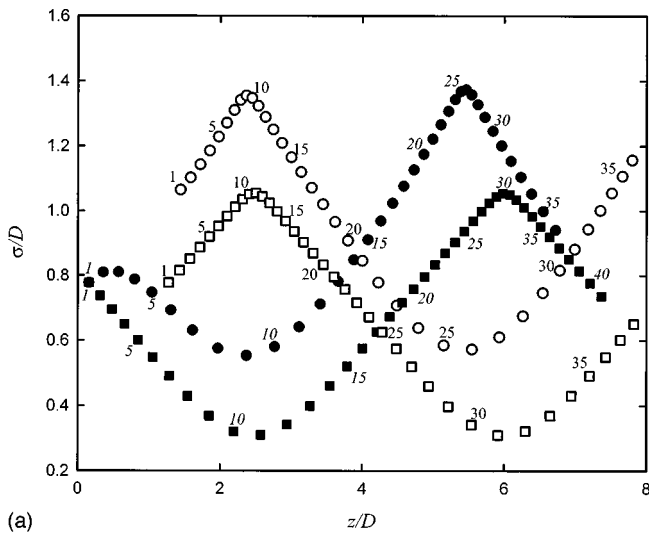


FIG. 3. Vortex ring interaction paths. (a) $St_D=0.25$; (b) $St_D=4$. \circ : Initially leading vortex ring ($\bar{V} \neq 0$); \bullet : initially trailing vortex ring ($\bar{V} \neq 0$). \square : Initially leading vortex ring ($\bar{V} = 0$); \blacksquare : initially trailing vortex ring ($\bar{V} = 0$). Numbers describe vortex core center motion sequence: italic for initially trailing vortex ring; regular for initially leading vortex ring.

overcome the strong background radial velocity close to $\sigma/D=0.5$, so that no obvious shrinkage in the trailing vortex ring diameter can be observed for $z/D < 0.2$. The backward axial motions of the vortex rings can also be observed for $\bar{V}=0$ at this St_D [Fig. 3(b)]. However, the vortex ring motions become less unsteady in the presence of the background flow field [Eq. (4)]. This is a result of the increase in the initial spatial separation between the vortex ring cores. For other values of St_D studied the corresponding patterns lie between Fig. 3(a) and (b), and thus are not presented.

Figure 4 shows the time variation of the spatial separation of the vortex ring cores at $St_D=1$ for both $\bar{V} \neq 0$ and $\bar{V}=0$. Actually, the higher the St_D , the greater the initial rate of the decrease in this spatial separation. The presence of the background flow thus facilitates vortex ring coalescence. However, this spatial separation for $\bar{V} \neq 0$ does not keep on decreasing. Its time variation pattern resembles that for $\bar{V} = 0$, when the vortex rings are interacting in a region far

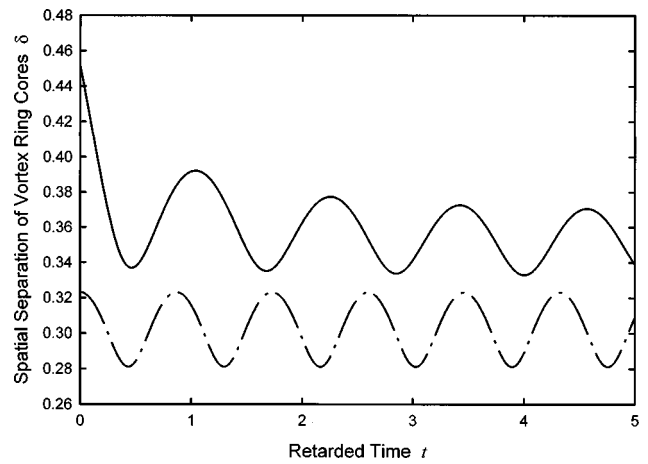


FIG. 4. Time variations of vortex ring spatial separation. $St_D=1$. —: $\bar{V} \neq 0$; - - -: $\bar{V} = 0$.

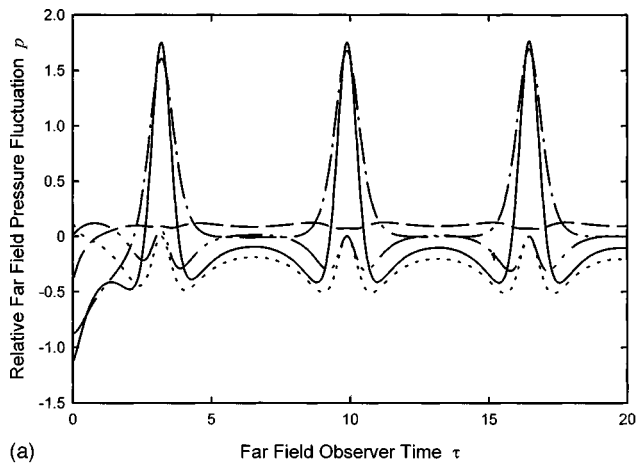
enough away from the nozzle where the background mean flow field becomes negligible when compared with that produced by the vortex rings.

It can be concluded that the background flow field does have significant effect on the details of the vortex ring interaction. The motion of the initially trailing vortex ring at small z/D is especially affected by its presence.

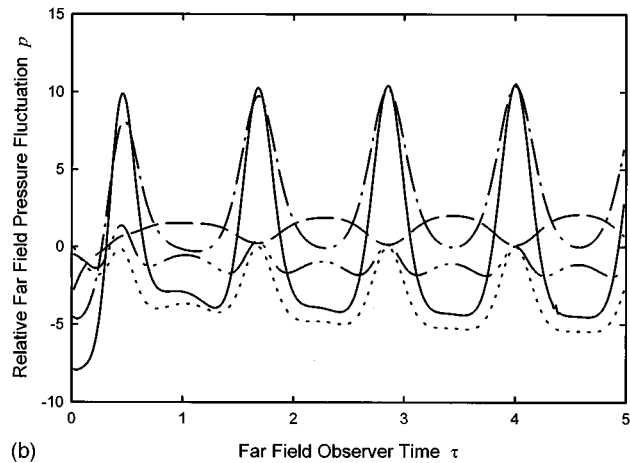
B. Pairing sound

It is well known that the far field sound pressure fluctuations resulted from the vortex ring mutual slip-through process are periodic and their time variation patterns^{6,9} are similar for all St_D . However, the latter depends on St_D in the presence of the background potential flow as defined by Eq. (4) and the far field pressure fluctuations are shown in Fig. 5. In Fig. 5, the solid lines represent the far field sound pressure fluctuations, while the other curves represent the four sound generation terms on the right hand side of Eq. (7). The major difference in the far field sound pressure fluctuations between the cases $\bar{V} \neq 0$ and $\bar{V} = 0$ (see Fig. 6) is that there is a strong negative trough P_{1-} in the beginning of the vortex ring interaction at different St_D . This implies that in the presence of the background flow field the pressure fluctuations at this instant are also significant.

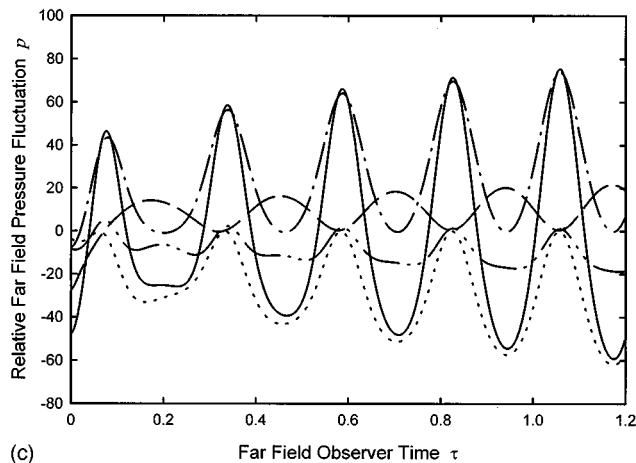
The variations of P_{1-} and the first, second, and third pressure peaks (P_{1+} , P_{2+} , and P_{3+}) with St_D are illustrated in Fig. 7. In the presence of the background flow there is a slight amplification of the sound radiated for $St_D < 0.6$, probably due to the effect of the additional vortex ring accelerations which compensate for the increased vortex ring core separation in the presence of the background flow field (Fig. 8). This will be discussed later. For $St_D > 0.6$, however, there is a significant reduction in the sound radiated due to the initial separation of the vortex ring cores is increased by the background flow field. The increase in vortex ring separation and the reduction of sound magnitude for $St_D > 0.6$ are similar to those of an uniform parallel external flow discussed by Leung *et al.*¹⁰ The amplitudes of all the far field pressure fluctuations obtained in the present study vary with the fourth power of W . This is the expected behavior of a quadrupole.



(a)



(b)



(c)

FIG. 5. Far field pressure fluctuations. (a) $St_D=0.25$; (b) $St_D=1$; (c) $St_D=4$. —: Far field pressure fluctuations; —: ΣIJ_z ; - - - : $3\Sigma A_z dI/dt$; — — — : $3\Sigma V_z d^2I/dt^2$; ·····: $\Sigma z_c d^3I/dt^3$.

Similar to the analysis of Tang and Ko,¹² the far field pressure fluctuations are decomposed into four terms, as shown in Eq. (7). Their relative contributions at $St_D=0.25$, 1, and 4 are also shown in Fig. 5(a)–(c), respectively. The corresponding sound generation terms at $St_D=0.25$ and $\bar{V}=0$ has been given in Fig. 6. The foregoing discussions will be focused on the sound generation before the second slip-through process as the subsequent far field pressure fluctuation pattern resembles those for $\bar{V}=0$, which has been dis-

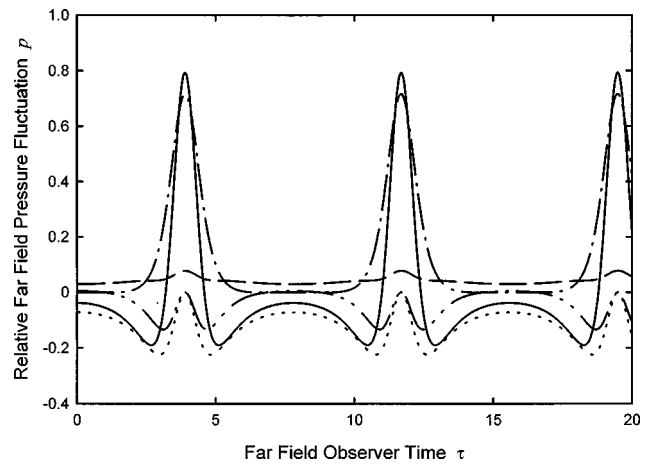


FIG. 6. Far field pressure fluctuations for $\bar{V}=0$, $St_D=0.25$. Legends: same as those in Fig. 5.

cussed elsewhere.^{9,12} In the presence of the background flow, which is diverging at small z/D , P_{1-} is mainly due to the terms ΣIJ_z and $\Sigma V_z d^2I/dt^2$, except at high St_D when the magnitudes of the other two terms become comparable to the latter. The term ΣIJ_z , which corresponds to the sound generation through the vortex ring axial jerking motions,¹² becomes more important in P_{1-} as St_D increases. Similar for the case of $\bar{V}=0$, the second term $\Sigma A_z dI/dt$ is of prime importance in the sound generation mechanism not at, or close to, the slip-through instants when the term $\Sigma V_z d^2I/dt^2$ dominates the sound radiation due to the high radial accelerations of vortex rings.¹² It is also observed from Fig. 5 that the initial period of the negative ΣIJ_z increases with St_D .

Thus the effect of the present background flow field on the sound generation is important, mainly in the beginning of the vortex ring interaction. The far field pressure time fluctuations after the first slip-through process, although of dif-

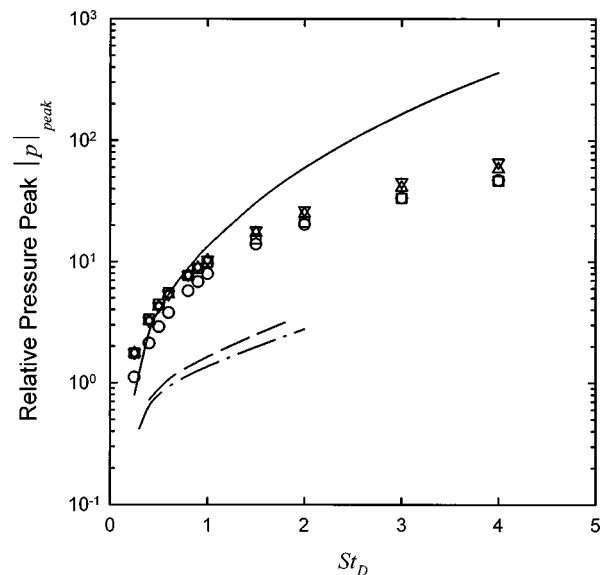


FIG. 7. Variations of pressure peaks with St_D . \circ : $|P_{1-}|$; \square : P_{1+} ; \triangle : P_{2+} ; ∇ : P_{3+} ; —: $\bar{V}=0$; — — — : $\bar{V}=0$ and $W_0/W=0.4$ (Ref. 10); - - - : $\bar{V}=0$ and $W_0/W=0.5$ (Ref. 10).

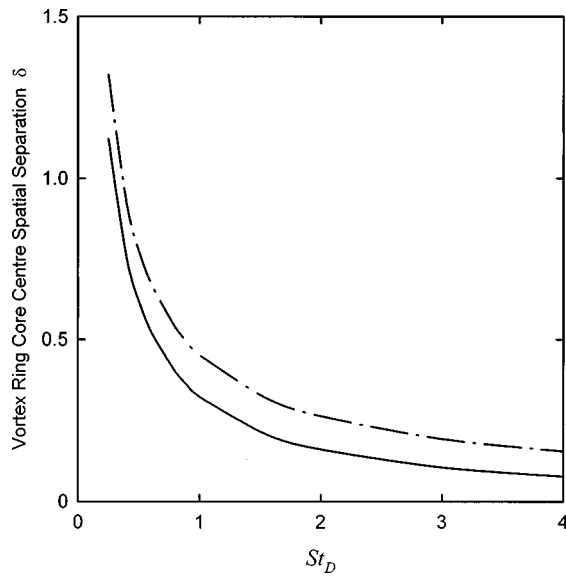


FIG. 8. Variations of initial vortex ring core separation with St_D . —: $\bar{\mathbf{V}}=0$; —·—: $\bar{\mathbf{V}}\neq 0$.

ferent magnitudes, have time variation patterns similar to that for the $\bar{\mathbf{V}}=0$ (Fig. 6), implying similar sound generation mechanism in the two cases. The following discussions thus focus mainly on the initial sound generation process in which the vortex ring axial jerking motion and the second time derivative of vortex impulse are expected to be the major sources of sound.

It is noted from Fig. 5(a) that the term $\Sigma V_z d^2I/dt^2$ dominates the initial sound field at $St_D=0.25$, but its dominance decreases as St_D increases, as shown in Fig. 5(b) and (c). As discussed in Tang and Ko,¹² this term represents the generation of sound through the second time derivative of the vortex ring impulse as a vortex ring moving in constant velocity does not radiate sound.⁵ Since the vortex ring circulation is constant,

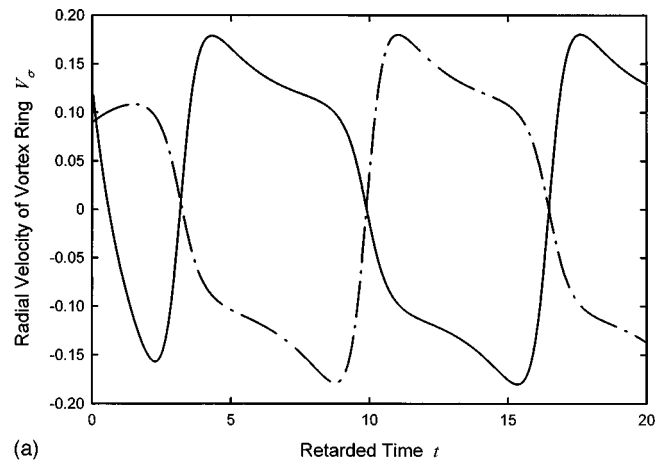
$$\frac{d^2I}{dt^2} = \frac{d^2}{dt^2} (\Gamma \sigma_c^2) = 2\Gamma (V_\sigma^2 + \sigma_c A_\sigma), \quad (8)$$

but V_σ^2 is approximately one order lower than $\sigma_c A_\sigma$ in the beginning of the vortex ring interaction at low St_D , as shown in Fig. 9(a) and (b). The dominance of the term $\Sigma V_z d^2I/dt^2$ in the sound generation process is then due to the radial accelerations of the vortex rings [Fig. 9(b)].

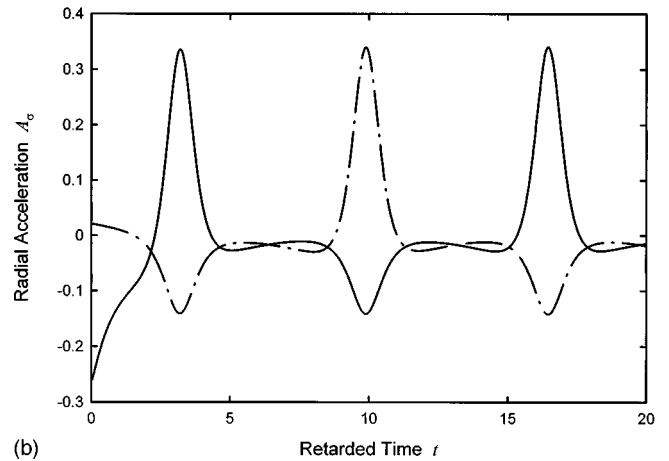
In the presence of a background flow field, the acceleration of a vortex ring depends on its velocity as well as the background flow velocity gradients in both the axial and radial directions:

$$\frac{d^2\mathbf{y}_c}{dt^2} = A_z \hat{\mathbf{z}} + A_\sigma \hat{\boldsymbol{\sigma}} = \frac{\partial}{\partial t} \mathbf{V}_{\text{ind}} + \frac{\partial}{\partial t} \mathbf{V}_{\text{self}} + \frac{d\mathbf{y}_c}{dt} \cdot \nabla \bar{\mathbf{V}}. \quad (9)$$

However, using this decomposition of acceleration, it is difficult to extract one single term from the above equation to represent the total effect of the background flow on the vortex ring motions, as both \mathbf{V}_{self} and \mathbf{V}_{ind} depend on the locations of the vortex rings which are obviously functions of the background flow field. However, it is possible to study the contributions of each terms on the right hand side of Eq. (9)



(a)



(b)

FIG. 9. (a) Time variations of vortex ring radial velocities. (b) Time variations of vortex ring radial accelerations. $St_D=0.25$. —: Initially trailing vortex ring; —·—: initially leading vortex ring.

in the overall radial acceleration of a vortex ring. The first term describes the acceleration due to mutual induction, the second term that due to self-induction, and the final one to the change in velocity directly due to the local background velocity field. The second term is not directly relevant to the vortex ring radial acceleration [Eq. (2b)]. From Fig. 10 the exceptionally high initial radial deceleration of the initially trailing vortex ring at $t=0$ mainly results from both the mutual induction and the radial background velocity field. The effect of mutual induction becomes dominant for $t>2$, when the vortex ring is moving in the region where the background flow velocity is small such that its effect on vortex ring motion is insignificant. Within this period of $t>2$, the major sound generation mechanism is due to the radial acceleration and is the same as that for $\bar{\mathbf{V}}=0$, although some contributions from the vortex ring axial jerking motions can be observed at the slip-through instants [Figs. 5(a), 6, and 9(b)]. It is also noted from Fig. 10 that the pattern of the time variation of the radial acceleration due to mutual induction resembles that for $\bar{\mathbf{V}}=0$ of Tang and Ko,⁹ but the magnitude of this acceleration for $\bar{\mathbf{V}}\neq 0$ in the beginning of the interaction is significant because of unequal vortex ring diameters [Fig. 3(a)].

The initial radial deceleration of the initially trailing vortex ring becomes less dominant as a source of sound as St_D

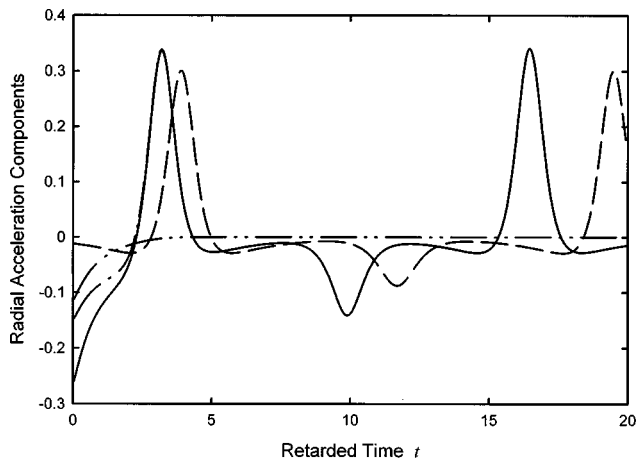


FIG. 10. Contributions of radial acceleration components for initially trailing vortex ring. $St_D=0.25$. —: Total radial acceleration; - - -: mutual induction component; - · - · -: direct contribution from background flow field; — —: $\bar{\mathbf{V}}=0$.

increases. At high St_D , the major sound generation mechanism at the initial stage of the interaction relates to the term ΣIJ_z [Fig. 5(c)]. Using the decomposition method of Eq. (1), the contribution of each of the velocity components in ΣIJ_z is summarized in Fig. 11. Again, the axial jerking motion due to the change in the local background flow velocity dominates the initial sound generation. This axial jerking motion is associated with the initially trailing vortex ring as shown in Fig. 12. The radial deceleration and the axial jerk J_z of the initially trailing vortex ring remain the major sound generation mechanisms for the intermediate St_D , and thus they are not discussed further. For all the St_D investigated, the initially leading vortex ring does not contribute much in the initial sound generation process as it is moving in a region where the background flow velocity and its gradient are small.

C. Implication for low speed laminar jet noise generation

The background flow field [Eq. (4)] adopted in the present study, while agreeing with the boundary condition of an inviscid circular jet, cannot really represent the jet because of the high initial growth rate and high radial mean velocity of the present adopted background flow field (Fig. 2). In a low speed laminar jet, the potential core extends to about four to five diameters downstream of the jet nozzle exit.²⁰ Therefore, the duration of the background flow effect on vortex ring interaction, and thus the sound generation process, is prolonged. The results at high St_D in the present study are more relevant to a low speed laminar jet, where the vortex rings are interacting in a region with significant mean shear rate.²² The prominent peak in the far field pressure spectrum, close to that of the shear layer instability mode for a low speed laminar jet,⁷ is thus believed to be generated by the axial jerking and radial accelerating/decelerating motions of the vortex rings.

It is noted from Eq. (9) that the radial acceleration of a

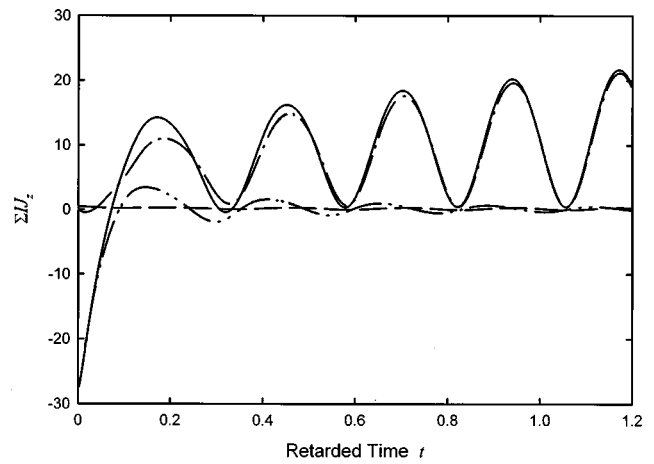


FIG. 11. Contributions of different axial jerk components in ΣIJ_z . $St_D=4$. —: Total ΣIJ_z ; - - -: mutual induction component; - · - · -: direct contribution from background flow field; — —: self-induction component.

vortex ring in the presence of the background flow is related to the background flow velocity gradient:

$$\begin{aligned} A_\sigma &= \hat{\sigma} \cdot \frac{d}{dt} (\mathbf{V}_{\text{ind}} + \bar{\mathbf{V}}) \\ &= \hat{\sigma} \cdot \left(\frac{d}{dt} \mathbf{V}_{\text{ind}} + V_z \frac{\partial U_\sigma}{\partial z} + V_\sigma \frac{\partial U_\sigma}{\partial \sigma} \right) \\ &= \hat{\sigma} \cdot \left(\frac{d}{dt} \mathbf{V}_{\text{ind}} + V_z \frac{\partial U_z}{\partial \sigma} + V_\sigma \frac{\partial U_\sigma}{\partial \sigma} \right), \end{aligned} \quad (10)$$

because $\bar{\mathbf{V}}$ is irrotational such that $\partial U_\sigma / \partial z = \partial U_z / \partial \sigma$. In the initial region of a shear layer, the mean shear rate is high due to the thin shear layer, while the radial mean velocity and its radial gradient are very small. Since the initial trailing vortex ring is propagating in the high speed side of the layer, its radial velocity depends significantly on the term $V_z \partial U_z / \partial \sigma$. The closer the vortex ring to the nozzle lip, that is the higher the Strouhal number, the more important this term becomes. Since $\partial U_z / \partial \sigma < 0$ and the vortex rings are usually moving downstream, the mean shear rate tends to produce deceleration

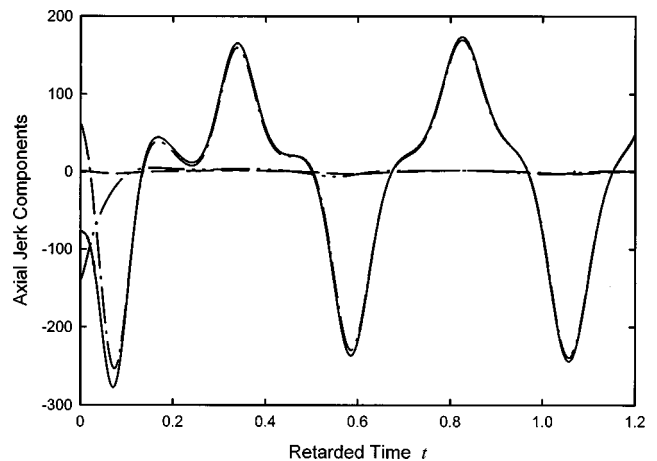


FIG. 12. Contributions of different velocity components in axial jerk of initially trailing vortex ring. $St_D=4$. —: Total jerk; - - -: mutual induction component; - · - · -: direct contribution from background flow field; — —: self-induction component.

tion. This appears consistent with the relatively high average deceleration of vortical structures measured by Tang and Ko⁹ for $z/D < 0.5$. The mean shear rate is expected to play an important role in the sound radiation before and at the first slip-through instant of the high St_D initial vortex rings in a laminar shear layer.

Likewise, the axial jerk of a vortex ring in the presence of a background flow field can be decomposed as follow:

$$J_z = (V_z^2 - V_\sigma^2) \frac{\partial^2 U_z}{\partial z^2} + A_z \frac{\partial U_z}{\partial z} + \left(A_\sigma - \frac{V_\sigma^2}{\sigma_c} \right) \frac{\partial U_z}{\partial \sigma} + \hat{z} \cdot \left(\frac{\partial^2}{\partial t^2} \mathbf{V}_{\text{self}} + \frac{\partial^2}{\partial t^2} \mathbf{V}_{\text{ind}} \right). \quad (11)$$

In a real jet, both $\partial^2 U_z / \partial z^2$ and $\partial U_z / \partial z$ are small. The radius of the initial vortex rings is more or less the same due to the small shear layer thickness so that the radial acceleration of the trailing vortex ring is small. The corresponding velocity component is large,¹² resulting in large initial negative axial jerk, as the fourth term on the right hand side of Eq. (11) is small when the coaxial vortex rings are of equal diameter. The effect of velocity induction due to vorticity has been shown to be of secondary importance in the total axial jerk of the vortex ring and in $\Sigma I J_z$ (Figs. 11 and 12). Since the growth rate of a low speed laminar jet is essentially lower than that of the background flow field adopted in the present study, it is expected that the axial jerking motion of the trailing vortex ring due to the mean shear rate is also important in the sound generation process at the slip-through instant in a low speed laminar jet. Therefore, the axial jerking motions and the radial accelerating/decelerating motions of vortex rings are believed to be the major sound generation mechanisms in a low speed laminar circular jet where a high mean shear rate exists. Also, the higher the mean shear rate, the higher is the sound level radiated. The present results therefore tend to suggest that the higher sound power of a conic nozzle than that of a large flanged one²³ is due to the higher mean shear rate in the conic nozzle shear layer.

Finally, it should be noted that the present vortex ring interaction model does not take into account the rolling-up process through which the vortex rings are formed. The reason is that in a low speed laminar jet, the shear layer instability near to the nozzle lip, from which the vortex rings are formed, is believed to be the source of the "excess" jet noise whose intensity varies approximately with the sixth power of the nozzle exit velocity.^{7,24} The corresponding sound field is not really a quadrupole, making Eq. (6) inapplicable.

III. CONCLUSIONS

In the present study, the aeroacoustics of vortex ring pairing in the presence of a background axisymmetric potential flow was investigated numerically using the velocity induction laws of Stokes and Kelvin. The background flow was obtained by solving the Laplace equation in cylindrical coordinates with the boundary condition of an inviscid circular jet. The dynamics of the vortex rings were also discussed.

Results suggest that the background flow field adopted for this paper substantially affects the initial sound generation process during the pairing of two vortex rings. Radial decelerating and axial jerking motions of the initially trailing vortex ring are the major sources of sound in the beginning of the interaction. The higher the Strouhal number, the more important the axial jerking motion in the sound generation process. At the slip-through instant, the radial acceleration of the trailing vortex ring becomes the major mechanism for sound generation.

The present results also show that the radial gradient of the background flow axial velocity, that is the mean shear rate, affects both the axial jerk and the radial acceleration/deceleration of the vortex rings. High mean shear rate gives large radial deceleration and negative axial jerk. Since the shear rate in a low speed laminar jet is considerably higher than that of the present background flow, it is expected that higher sound levels are generated when the vortex rings are interacting within the region of high mean shear.

APPENDIX: BACKGROUND POTENTIAL FLOW FIELD

Let ϕ be the potential of the incompressible axisymmetric background flow field, thus

$$\nabla^2 \phi = \frac{\partial^2 \phi}{\partial \sigma^2} + \frac{1}{\sigma} \frac{\partial \phi}{\partial \sigma} + \frac{\partial^2 \phi}{\partial z^2} = 0. \quad (A1)$$

The simplest boundary condition for an inviscid circular jet being that for $z=0$,

$$\left. \frac{\partial \phi}{\partial z} \right|_{z=0} = \begin{cases} W + W_0, & \text{for } \sigma \leq 0.5D \\ W_0, & \text{for } \sigma > 0.5D, \end{cases} \quad (A2)$$

where W_0 represents the velocity of a uniform flow external to the jet. Since W_0 has no effect on the vortex ring pairing noise as far as low Mach number flow is concerned, it is set to zero. It can be observed from Eq. (A1) that

$$\nabla^2 \left(\frac{\partial \phi}{\partial z} \right) = 0. \quad (A3)$$

The solution of Eq. (A3) with boundary condition (A2) can be obtained using the method shown in Morse and Feshbach¹⁹ which gives

$$\frac{\partial \phi}{\partial z} = W \int_0^\infty e^{-\alpha z} J_1(0.5\alpha D) J_0(\alpha \sigma) d\alpha. \quad (A4)$$

It is straightforward to show that the corresponding radial velocity is

$$\frac{\partial \phi}{\partial \sigma} = W \int_0^\infty e^{-\alpha z} J_1(0.5\alpha D) J_1(\alpha \sigma) d\alpha. \quad (A5)$$

Equations (A4) and (A5) also satisfy Eq. (A1). The flow field defined by Eqs. (A4) and (A5) is also irrotational.

¹A. Powell, "Theory of vortex sound," J. Acoust. Soc. Am. **36**, 177–195 (1964).

²M. S. Howe, "Contributions to the theory of aerodynamic sound, with application to excess jet noise and the theory of the flute," J. Fluid Mech. **71**, 625–673 (1975).

³P. E. Doak, "Fluctuating total enthalpy as the basic generalized acoustic field," Theor. Comput. Fluid Dyn. **10**, 115–133 (1998).

- ⁴C. D. Winant and F. K. Brownand, "Vortex pairing, the mechanism of turbulent mixing layer growth at moderate Reynolds number," *J. Fluid Mech.* **63**, 237–255 (1974).
- ⁵W. Möhring, "On the vortex sound at low Mach number," *J. Fluid Mech.* **85**, 685–691 (1978).
- ⁶T. Kambe and T. Minota, "Sound radiation from vortex systems," *J. Sound Vib.* **74**, 61–72 (1981).
- ⁷J. E. Bridges and A. K. M. F. Hussain, "Roles of initial conditions and vortex pairing in jet noise," *J. Sound Vib.* **117**, 289–311 (1987).
- ⁸J. Laufer and T. Yen, "Noise generation by a low-Mach-number jet," *J. Fluid Mech.* **134**, 1–31 (1983).
- ⁹S. K. Tang and N. W. M. Ko, "A Study on the noise generation mechanism in a circular jet," *ASME Trans.: J. Fluids Eng.* **115**, 425–435 (1993).
- ¹⁰R. C. K. Leung, S. K. Tang, I. C. K. Ho, and N. W. M. Ko, "Vortex pairing as a model for jet noise generation," *AIAA J.* **34**, 669–675 (1996).
- ¹¹P. G. Saffman, "The number of waves on unstable vortex rings," *J. Fluid Mech.* **84**, 625–639 (1978).
- ¹²S. K. Tang and N. W. M. Ko, "On sound generated from the interaction of two inviscid coaxial vortex rings moving in the same direction," *J. Sound Vib.* **187**, 287–310 (1995).
- ¹³H. Yamada and T. Matsui, "Mutual slip-through of a pair of vortex rings," *Phys. Fluids* **22**, 1245–1249 (1979).
- ¹⁴H. Lamb, *Hydrodynamics* (Cambridge U.P., Cambridge, MA, 1993).
- ¹⁵A. A. Townsend, *The Structure of Turbulent Shear Flow* (Cambridge U.P., Cambridge, MA, 1976).
- ¹⁶P. G. Saffman, *Vortex Dynamics* (Cambridge U.P., Cambridge, MA, 1993).
- ¹⁷T. Kambe, "Acoustic emission by vortex motion," *J. Fluid Mech.* **173**, 643–666 (1986).
- ¹⁸A. Powell, "Three-sound-pressure theorem, and its application, in aerodynamically generated sound," *J. Acoust. Soc. Am.* **34**, 902–906 (1962).
- ¹⁹P. M. Morse and H. Feshbach, *Methods of Theoretical Physics* (McGraw-Hill, New York, 1953).
- ²⁰S. C. Crow and F. H. Champagne, "Orderly structures in jet turbulence," *J. Fluid Mech.* **48**, 547–591 (1971).
- ²¹G. N. Abramovich, *The Theory of Turbulent Jets* (MIT, Cambridge, MA, 1963).
- ²²K. B. M. Q. Zaman and A. K. M. F. Hussain, "Natural large-scale structures in the axisymmetric mixing layer," *J. Fluid Mech.* **138**, 325–351 (1984).
- ²³J. Bridges and F. Hussain, "Effects of nozzle body on jet noise," *J. Sound Vib.* **188**, 407–418 (1995).
- ²⁴D. G. Crighton, "The excess noise field of subsonic jets," *J. Fluid Mech.* **56**, 683–694 (1972).

Propagation in random stratified waveguides—A modal-spectral treatment

Shimshon Frankenthal^{a)}

ComSERC, Howard University, Washington, DC

Mark J. Beran

Faculty of Engineering, Tel Aviv University, Ramat Aviv, Israel

(Received 15 September 1997; accepted for publication 28 April 1998)

The statistics of a forward-propagating wave is considered in a random, anisotropic, stratified three-dimensional waveguide, where modal analysis offers unique advantages. After extracting the vertical dependence in the usual way, the equations are formulated which govern the range evolution of the transverse horizontal spectra of the modal field coefficients (MTWS). A short-range perturbation solution is used to derive the difference equations governing the long-range behavior of the two lowest moments of the field spectra. The conditions under which these difference equations can be approximated as differential equations are given. These equations are not limited by the parabolic approximation, and are amenable to numerical treatment by marching techniques. They are used here to study the effect of scattering on the spectral redistribution of the modal power, and the related problem of the coherence of plane and cylindrical waves. It is shown that, as a result of scattering in the transverse horizontal direction, the total beam power is redistributed among the modes in proportion to the modal eigenvalues, rather than uniformly, as two-dimensional propagation models suggest. © 1998 Acoustical Society of America. [S0001-4966(98)03508-5]

PACS numbers: 43.30.Bp, 43.30.Hw, 43.30.Dr [JHM]

INTRODUCTION

The stochastic properties of random stratified waveguides are often characterized by a marked anisotropy, which is manifested in a strong disparity between the correlation lengths in the planes of stratification and in the direction perpendicular to them.¹ Beyond any other advantages it might offer, the modal approach²⁻⁷ is uniquely suitable for the treatment of propagation in such anisotropic waveguides, because it circumvents some of the theoretical complications which are associated with other formulations of the propagation problem.^{8,9} In previous publications^{10,11} we have shown how to deal with the effects of volume scattering, as well as scattering by rough surfaces, using the modal formulation. In particular, we employed the parabolic version^{12,13} of the *spatial* field equations to treat the horizontal (i.e., plane-of-stratification) propagation problem, which remains after the vertical aspects have been extracted by the modal decomposition. However, as we pointed out, the parabolic approximation breaks down for the higher modes of propagation (near the modal cutoff). Indeed, in the treatment of surface scattering,¹³ we had to use a modified version of the parabolic formulation, based on a field decomposition into right- and left-propagating components suggested in Ref. 14, in order to produce a power-conserving model even for the lower modes.

On the other hand, in the treatment of propagation in random *unbounded* media, considerable progress can be made by studying the range evolution of transverse spectra of the wave field (TWS), without recourse to the parabolic

approximation and to the assumption of narrow angular spread which is intimately associated with it.¹⁵ As we have recently shown,¹⁶ one can obtain equations for the spectral moments that share many of the advantages of the parabolic formulation, and, in particular, can be “marched” in the range direction. Although these equations are limited in that they cannot account for scattering to and from the evanescent components of the spectrum, they do offer a framework for improving on the results obtained through the use of the parabolic approximation.

The present paper combines the modal and the spectral approaches in the study of volume scattering. After decoupling the vertical (*y*) dependence in the usual way, we formulate the equations that govern the evolution in the range (*z*) direction of the transverse wave-number-spectra of the modal coefficients (MTWS). Following the procedure originally proposed by Beran and Ho,¹⁷ we then use a local (range) perturbation solution of the field equation to derive difference equations for the long-range evolution of the ensemble-averaged spectral field moments, and approximate these equations by differential equations. These equations are applied here to the propagation of plane (or cylindrical) waves, and to the related problem of the propagation of the modal power in a beam.

The plan of the paper is as follows: Sec. I contains a complete formulation of the propagation equation for the MTWS of the field components which propagate forward and backward in the range direction. In Sec. II, the one-way version of these equations is used to derive difference equations which govern the propagation of the ensemble-averaged MTWS and its ensemble-averaged coherence, and their approximate differential version is introduced. The conditions under which the differential approximation is viable

^{a)}Permanent address: Faculty of Engineering, Tel Aviv University, Ramat Aviv, Israel.

are considered in Sec. III. In Sec. IV, we apply the coherence equation to study the modal redistribution of the power which crosses any range surface, noting that the same equation also governs the coherence associated with plane and cylindrical waves. In that context, we examine the parabolic approximation, as well as an asymptotic solution of the general equation. A summary discussion is presented in Sec. V.

I. FORMULATION

A. Geometry

We consider the propagation of a monochromatic signal of frequency ω in a channel bounded by a flat rigid bottom $y=0$ and a smooth pressure-release top $y=H$. The average sound speed c depends only on y , but its random fluctuations, which are responsible for volume scattering, also depend on the horizontal vector $\mathbf{r}(x,z)$, where z is the range and x is the transverse variable. We ultimately separate the signal into components propagating in the $+z$ (right) and $-z$ (left) directions.

B. The modal field equations

The complex amplitude $\tilde{p}(\mathbf{r},y)$ of the field satisfies the equation

$$\left\{ \frac{\partial^2}{\partial \mathbf{r}^2} + \frac{\partial^2}{\partial y^2} + k^2(y)[1 + \tilde{\mu}(\mathbf{r},y)] \right\} \tilde{p}(\mathbf{r},y) = 0, \quad (1)$$

where $k(y) = \omega/c(y)$ measures the depth-dependent average sound speed, and $\tilde{\mu}(\mathbf{r},y)$ are the refractivity fluctuations which produce volume scattering. These fluctuations are assumed to constitute a real, statistically homogeneous random process with which we associate a variance $\langle \mu^2 \rangle$ and a correlation function

$$\begin{aligned} \tilde{\sigma}(s_x, s_z, s_y) &= \langle \tilde{\mu}(x_1, z_1, y_1) \tilde{\mu}(x_2, z_2, y_2) \rangle \\ &\text{with } s_x = x_1 - x_2, \text{ etc.}, \end{aligned} \quad (2a)$$

where the symbol $\langle \rangle$ denotes an ensemble average. The correlation lengths $L_{x,y,z}$ are associated with the dependence of the correlation on the separation variables $s_{x,y,z}$. The ‘‘transform’’ $\mu(\kappa, y, z)$ of the x dependence of $\tilde{\mu}$, which we shall need later, therefore satisfies

$$\mu(\kappa, z, y) = \mu^*(-\kappa, z, y) \quad (2b)$$

and has a correlation function

$$\begin{aligned} \langle \mu(\kappa_1, z_1, y_1) \mu(\kappa_2, z_2, y_2) \rangle \\ = 2\pi \delta(\kappa_1 + \kappa_2) \sigma(\kappa_1, y_1, y_2, s_z) \end{aligned} \quad (2c)$$

where

$$\sigma(\kappa, y_1, y_2, s_z) = \int_{-\infty}^{\infty} ds_x e^{-i\kappa s_x} \tilde{\sigma}(s_x, y_1, y_2, s_z). \quad (2d)$$

The modal decomposition of the solution of Eq. (1) is

$$\tilde{p}(\mathbf{r},y) = \sum_k \tilde{p}_k(\mathbf{r}) Y_k(y), \quad (3)$$

where the modal functions Y_k satisfy the following eigenvalue equation and the boundary conditions at the top ($y=H$) and bottom ($y=0$) surfaces, augmented by the usual normalization condition:

$$\begin{aligned} \left\{ \frac{\partial^2}{\partial y^2} + [k^2(y) - \beta_k^2] \right\} Y_k(y) &= 0, \\ \frac{\partial}{\partial y} Y_k(y) \Big|_{y=0} &= Y_k(H) = 0, \quad \int_0^H dy Y_m Y_k = \delta_{mk}. \end{aligned} \quad (4)$$

An equation for the modal amplitudes \tilde{p}_m is obtained by substituting the modal decomposition defined by Eqs. (3) and (4) in Eq. (1), multiplying the result by Y_m , integrating over y , and using the orthonormal property of the modal functions. The result is

$$\left[\frac{\partial^2}{\partial \mathbf{r}^2} + \beta_m^2 \right] \tilde{p}_m(\mathbf{r}) + \sum_k \tilde{\mu}_{mk}(\mathbf{r}) \tilde{p}_k(\mathbf{r}) = 0, \quad (5)$$

where

$$\tilde{\mu}_{mk}(\mathbf{r}) = \int_0^H dy k^2(y) Y_m(y) Y_k(y) \tilde{\mu}(\mathbf{r},y). \quad (6)$$

The properties of the function $\tilde{\mu}(\mathbf{r},y)$, discussed in connection with Eq. (2), carry over directly to the coefficients $\tilde{\mu}_{mk}(x,z)$ defined in Eq. (6), and to their transforms $\mu_{mk}(\kappa, z)$, which we shall need in the ensuing discussion. These transforms satisfy

$$\mu_{mk}(\kappa, z) = \mu_{mk}^*(-\kappa, z), \quad (7a)$$

and their correlation functions assume the form

$$\langle \mu_{mk}(\kappa_1, z_1) \mu_{jl}(\kappa_2, z_2) \rangle = \delta(\kappa_1 + \kappa_2) \sigma_{mklj}(\kappa_1, s_z), \quad (7b)$$

where

$$\sigma_{mklj}(\kappa, s_z) = \int_{-\infty}^{\infty} ds_x e^{-i\kappa s_x} \tilde{\sigma}_{mklj}(s_x, s_z), \quad (7c)$$

and

$$\begin{aligned} \tilde{\sigma}_{mklj}(s_x, s_z) &= \int_0^H dy \int_0^H dy' k^2(y) k^2(y') Y_m(y) \\ &\quad \times Y_k(y) Y_j(y') Y_l(y') \tilde{\sigma}(s_x, s_z, y, y'). \end{aligned} \quad (7d)$$

C. Spectra of right- and left-propagating fields

Our ultimate objective is to attain a formulation which distinguishes the right- and left-propagating components of the transverse (x) spectra of the modal pressures \tilde{p}_m . This is attained in three successive steps, as follows:

(1) The replacement of the second-order modal-pressure, Eq. (5), by two coupled first-order equations: this is accomplished by defining the particle-velocity vector

$$\tilde{\mathbf{v}} \equiv -i \frac{\partial}{\partial \mathbf{r}} \tilde{p} = \sum_k \tilde{\mathbf{v}}_k(\mathbf{r}) Y_k(y). \quad (8)$$

The expression for the modal velocity coefficients $\tilde{\mathbf{v}}_m$ is readily obtained by the procedure that led to Eq. (5). This produces the vector (gradient) equation for the evolution of the modal pressures in \mathbf{r} :

$$\frac{\partial}{\partial \mathbf{r}} \tilde{p}_m = i \tilde{\mathbf{v}}_m. \quad (9a)$$

This equation is next differentiated with respect to \mathbf{r} , and combined with Eqs. (4) and (5) to produce the scalar (divergence) equation

$$\frac{\partial}{\partial \mathbf{r}} \cdot \tilde{\mathbf{v}}_m = i \beta_m^2 \tilde{p}_m + i \sum_k \tilde{\mu}_{mk} \tilde{p}_k, \quad (9b)$$

which governs the evolution of the modal velocities in \mathbf{r} .

(2) The Fourier transform ($x \rightarrow \kappa$) of Eq. (9) produces a pair of equations that govern the z evolution of the transverse spectra (denoted by carets) of \tilde{p}_m and \tilde{v}_{zm} , the z component of $\tilde{\mathbf{v}}_m$. The transform of the x component of the vector equation (9a) produces

$$\hat{v}_{xm}(\kappa, z) = \kappa \hat{p}_m(\kappa, z), \quad (10)$$

and this is used to eliminate the transform of \tilde{v}_{xk} in Eq. (9b). The result is best written in terms of the complex quantity $g_m(\kappa)$, defined by $g_m^2(\kappa) \equiv \beta_m^2 - \kappa^2$, so that

$$\begin{aligned} g_m &= \sqrt{\beta_m^2 - \kappa^2} \quad \text{when } \kappa < \beta_m, \\ g_m &= i \sqrt{\kappa^2 - \beta_m^2} \quad \text{when } \beta_m < \kappa, \end{aligned} \quad (11)$$

and thus

$$\frac{\partial}{\partial z} \hat{p}_m(\kappa, z) = i \hat{v}_{zm}(\kappa, z), \quad (12a)$$

$$\begin{aligned} \frac{\partial}{\partial z} \hat{v}_{zm}(\kappa, z) &= i g_m^2(\kappa) \hat{p}_m(\kappa, z) + i \sum_k \int_{-\infty}^{\infty} \frac{d\kappa'}{2\pi} \\ &\quad \times \mu_{km}(\kappa - \kappa', z) \hat{p}_k(\kappa', z). \end{aligned} \quad (12b)$$

The second term on the right-hand side of Eq. (12b), which accounts for scattering, assumes the form of a convolution of the field spectrum $\hat{p}_k(\kappa, z)$ and the ‘‘transform’’ $\mu_{km}(\kappa, z)$ [see Eqs. (6) and (7)].

(3) Finally, we separate Eq. (12) into equations which govern the evolution in z of the transverse spectra p_m^\pm of the right- and left-propagating components of \tilde{p}_m . These component spectra are *defined* by the following relations:

$$\hat{p}_m(\kappa, z) = \hat{p}_m^+(\kappa, z) + \hat{p}_m^-(\kappa, z), \quad (13a)$$

$$\hat{v}_{zm}(\kappa, z) = g_m(\kappa) [\hat{p}_m^+(\kappa, z) - \hat{p}_m^-(\kappa, z)], \quad (13b)$$

so that

$$\frac{\partial}{\partial z} \hat{p}_m^\pm = \frac{\partial}{\partial z} \hat{p}_m^\pm \mp \frac{1}{g_m(\kappa)} \frac{\partial}{\partial z} \hat{v}_{zm}. \quad (13c)$$

The linear combinations in the right-hand member of (13c) may be evaluated directly from Eq. (12). In the absence of scattering, the result would simply state that

$$\frac{\partial}{\partial z} \hat{p}_m^\pm + i g_m(\kappa) \hat{p}_m^\pm = 0, \quad (14a)$$

implying that

$$\hat{p}_m^\pm = p_m^\pm \exp[\pm i g_m(\kappa) z]. \quad (14b)$$

Here, the complex exponentials reflect the diffractive variation of the field in the z direction, and their coefficients p_m^\pm are range independent. In the presence of scattering, the right-hand members of Eq. (14a) must be replaced by the scattering term in Eq. (12b), multiplied by $\pm 1/2g_m(\kappa)$. Nonetheless, it is still convenient to extract the diffractive behavior of the pressure transforms, as in Eq. (14b), and track the range dependence of the coefficients p_m^\pm . The end result can be written succinctly for both components, using the notation $\alpha = \pm$ and $\gamma = \pm$, as follows:

$$\begin{aligned} \frac{\partial}{\partial z} p_m^\alpha(\kappa, z) &= \alpha \sum_k \sum_{\gamma=\pm} \int_{-\infty}^{\infty} \frac{d\kappa'}{2\pi} R_{mk}^{\alpha\gamma}(\kappa, \kappa', z) \\ &\quad \times p_k^\gamma(\kappa', z), \end{aligned} \quad (15a)$$

where

$$\begin{aligned} R_{mk}^{\alpha\gamma}(\kappa, \kappa', z) &= \frac{i}{2g_m(\kappa)} e^{-i[\alpha g_m(\kappa) - \gamma g_k(\kappa')]z} \\ &\quad \times \mu_{mk}(\kappa - \kappa', z). \end{aligned} \quad (15b)$$

The integral version of Eq. (15a), which will be needed later, is just

$$\begin{aligned} p_m^\alpha(\kappa, z) &= p_m^{\alpha 0}(\kappa, z) + \sum_k \sum_{\gamma=\pm} \int_{z_s}^{\infty} dz' \delta_{-1}[\alpha(z-z')] \\ &\quad \times \int_{-\infty}^{\infty} \frac{d\kappa'}{2\pi} R_{mk}^{\alpha\gamma}(\kappa, \kappa', z') p_k^\gamma(\kappa', z'), \end{aligned} \quad (15c)$$

where $p_m^{\alpha 0}(\kappa, z)$ is the field that would prevail in the absence of scattering. The z' integration formally extends over the entire scattering region, but the argument of the Heaviside function δ_{-1} limits this to the z range that is appropriate for each (right- or left-propagating) component.

Equation (15) provides a starting point for the treatment of the ensemble-averaged modal spectral field and coherence. In principle, this equation allows the simultaneous treatment of both forward and backward propagation in the presence of volume scattering. It must nonetheless be pointed out that, although the equation is rigorously correct, the procedure that was employed makes sense only when the source conditions, which were not explicitly stated, indeed identify the z direction as the main direction of propagation.

II. THE ENSEMBLE-AVERAGED MODAL TRANSVERSE SPECTRA OF THE FIELD AND THE COHERENCE

The modal spectral coherence is the ensemble average of the quantity

$$\Gamma_{mn}^{\alpha\beta}(\kappa_1, \kappa_2, z) \equiv p_m^\alpha(\kappa_1, z) p_n^{\beta*}(\kappa_2, z), \quad (16)$$

which provides the joint wave number statistics of two different modal pressures, measured at the same z plane. Both α and β may be assigned the \pm signs, and thus enable us to address the correlations between all possible pairs of right- and left-propagating modal components. However, in the following discussion, we shall address the situation where p_m^- is a relatively weak backscattered field, which may be ignored relative to p_m^+ . We shall therefore consider only the one-way propagation of p_m^+ . This is accomplished by assigning α , β , and γ the $+$ sign, and eliminating the summation over γ in the right-hand member of Eqs. (15a) and (15c). The $+$ superscript is unnecessary, and will be omitted in the subsequent discussion.

We observe, in passing, that the spatial version of the parabolic (or paraxial) approximation for the one-way field equation can be derived from the one-way version of Eq. (15a) as follows: replace g_m by β_m in the scattering term on the right-hand side of the equation, but by the two-term expansion $\beta_m - \kappa^2/2\beta_m$ in the diffraction term on the left-hand side of the equation; then, retransform the result to the spatial coordinate x . The inconsistent manner in which g_m must be approximated in order to produce the spatial version of the parabolic equation has further implications, some of which will be discussed in the sequel. In any event, the ensuing discussion does not adopt either approximation at the outset, and may therefore be expected to apply to wide-angle one-way propagation.

The development follows the approach originally proposed by Beran and Ho,¹⁷ which is based on the second-order iterative solution of the integral equation (15c) in an incremental slab bounded by the planes z_0 and $z_0 + \Delta z$. This range-localized perturbation solution is used to compute the increments of the ensemble-averaged field and coherence across the slab. The result constitutes a difference equation, which may be approximated by a differential equation under appropriate conditions.

A. Iterative perturbation solution

The iterative perturbation solution of Eq. (15c) has the form

$$p_m(\kappa, z) = p_m^0(\kappa, z) + \Delta_1 p_m(\kappa, z) + \Delta_2 p_m(\kappa, z) + \dots \quad (17)$$

Here, $p_m^0(\kappa, z)$ is the homogeneous solution of Eq. (15a), that is, a z -independent function of κ , defined by the known value of $p_m(\kappa, z_0)$ at the left edge of the slab:

$$p_m^0(\kappa, z) = p_m(\kappa, z_0). \quad (18a)$$

The first two iterative corrections are

$$\begin{aligned} \Delta_1 p_m(\kappa, z) = & \sum_k \int_{z_0}^z dz' \int_{-\infty}^{\infty} \frac{d\kappa'}{2\pi} \delta_{-1}(z-z') \\ & \times R_{mk}(\kappa, \kappa', z') p_k(\kappa', z_0), \end{aligned} \quad (18b)$$

$$\begin{aligned} \Delta_2 p_m(\kappa, z) = & \sum_k \sum_p \int_{z_0}^z dz' \int_{z_0}^z dz'' \int_{-\infty}^{\infty} \frac{d\kappa'}{2\pi} \\ & \times \int_{-\infty}^{\infty} \frac{d\kappa''}{2\pi} \delta_{-1}(z-z') \delta_{-1}(z'-z'') \\ & \times R_{mk}(\kappa, \kappa', z') R_{kl}(\kappa', \kappa'', z'') p_l(\kappa'', z_0), \end{aligned} \quad (18c)$$

where R_{mk} is given by Eq. (15b) with α and γ assigned the $+$ sign, and omitted here for convenience. We have also used Eq. (18a) to replace the pressures $p_j^0(\kappa, z)$ in the integrands by their values at the left edge of the slab.

B. Ensemble averaging

Using the above, we can obtain expressions for both the field $p_m(\kappa, z_0 + \Delta z)$ and the coherence $p_m(\kappa_1, z_0 + \Delta z) \times p_n^*(\kappa_2, z_0 + \Delta z)$, and ensemble average them. The quantities that are subjected to the ensemble-averaging process are invariably products of the R_{mk} and $p_m(\kappa, z_0)$. It is crucial to observe that the coefficients R_{mk} contain the random refractivities $\mu_{mk}(\kappa, z')$ within the slab, where $z' \geq z_0$, whereas the fields $p_m(\kappa, z_0)$ are defined at the left edge of the slab, and therefore reflect only the statistics of μ in the region $z \leq z_0$. One can therefore assert that the aforementioned random quantities are statistically independent wherever $z' - z_0 \gg L_z$, the longitudinal correlation length. Thus, in a slab whose thickness far exceeds L_z ,

$$L_z \ll \Delta z, \quad (19a)$$

products of p_m 's and of μ_{mk} 's can in effect be averaged independently.

The leading terms which survive the ensemble-averaging process are of order $\langle \mu^2 \rangle$. It suffices to retain these terms provided that Δz does not exceed a certain value L_p , which varies inversely with $\langle \mu^2 \rangle$, beyond which the perturbation solution outlined above is no longer adequate. Anticipating a later result [see the discussion following Eq. (25)], we require

$$\Delta z \ll L_p, \quad \text{where } L_p = (k^2 L_z \langle \mu^2 \rangle)^{-1}. \quad (19b)$$

The resulting expressions for the ensemble-averaged field and coherence at $z_0 + \Delta z$ are

$$\langle p_m(\kappa, z_0 + \Delta z) \rangle = \langle p_m(\kappa, z_0) \rangle + \langle \Delta_2 p_m(\kappa, z_0 + \Delta z) \rangle, \quad (20a)$$

$$\begin{aligned} \langle p_m(\kappa_1, z_0 + \Delta z) p_n^*(\kappa_2, z_0 + \Delta z) \rangle \\ = \langle p_m(\kappa_1, z_0) p_n^*(\kappa_2, z_0) \rangle + \langle \Delta_2 p_m(\kappa_1, z_0 + \Delta z) \\ \times p_n^*(\kappa_2, z_0) \rangle + \langle p_m(\kappa_1, z_0) \Delta_2 p_n^*(\kappa_2, z_0 + \Delta z) \rangle \\ + \langle \Delta_1 p_m(\kappa_1, z_0 + \Delta z) \Delta_1 p_n^*(\kappa_2, z_0 + \Delta z) \rangle. \end{aligned} \quad (20b)$$

The second term on the right-hand side of Eq. (20a) is the average-field increment and will be labelled I_0 below. The first term on the right-hand side of Eq. (20b) is the averaged coherence $\langle \Gamma_{mn} \rangle$ at the left edge of the slab. The remaining

terms on the right-hand side of Eq. (20b), which constitute the increment of the averaged coherence, will be labelled I_1 , I_2 , and I_3 for brevity. Expressions for all these quantities are obtained using the definitions of the increments $\Delta_{1,2}p_m$, Eqs. (18b) and (18c), and the definition of R_{mk} , Eq. (15b):

$$I_0 = - \sum_k \sum_l \int_{\Delta} dz' \int_{\Delta} dz'' \int_{-\infty}^{\infty} \frac{d\kappa'}{2\pi} \times \int_{-\infty}^{\infty} \frac{d\kappa''}{2\pi} \delta_{-1}(z' - z'') \frac{1}{4g_m(\kappa)g_k(\kappa')} \times \langle \mu_{mk}(\kappa - \kappa', z') \mu_{kl}(\kappa' - \kappa'', z'') \rangle \times e^{-i\{[g_m(\kappa) - g_k(\kappa')]z' + [g_k(\kappa') - g_l(\kappa'')]z''\}} \langle p_l(\kappa'', z_0) \rangle, \quad (21a)$$

$$I_1 = - \sum_k \sum_l \int_{\Delta} dz' \int_{\Delta} dz'' \int_{-\infty}^{\infty} \frac{d\kappa'}{2\pi} \times \int_{-\infty}^{\infty} \frac{d\kappa''}{2\pi} \delta_{-1}(z' - z'') \frac{1}{4g_m(\kappa_1)g_k(\kappa')} \times \langle \mu_{mk}(\kappa_1 - \kappa', z') \mu_{kl}(\kappa' - \kappa'', z'') \rangle \times e^{-i\{[g_m(\kappa_1) - g_k(\kappa')]z' + [g_k(\kappa') - g_l(\kappa'')]z''\}} \times \langle p_l(\kappa'', z_0) p_n^*(\kappa_2, z_0) \rangle, \quad (21b)$$

$I_2 =$ conjugate of I_1 with interchanges of κ_1 and κ_2 and of m and n , (21c)

$$I_3 = \sum_k \sum_l \int_{\Delta} dz' \int_{\Delta} dz'' \int_{-\infty}^{\infty} \frac{d\kappa'}{2\pi} \times \int_{-\infty}^{\infty} \frac{d\kappa''}{2\pi} \frac{1}{4g_m(\kappa_1)g_n^*(\kappa_2)} \times \langle \mu_{mk}(\kappa_1 - \kappa', z') \mu_{nl}^*(\kappa_2 - \kappa'', z'') \rangle \times e^{-i\{[g_m(\kappa_1) - g_k(\kappa')]z' - [g_n^*(\kappa_2) - g_l^*(\kappa'')]z''\}} \times \langle p_k(\kappa', z_0) p_l^*(\kappa'', z_0) \rangle, \quad (21d)$$

where

$$\int_{\Delta} dz' = \int_{z_0}^{z_0 + \Delta z} dz'. \quad (21e)$$

C. Difference and differential equations

The evaluation of the integrals in Eqs. (21) produces *difference* equations for the ensemble-averaged field and coherence

$$\Delta \langle p_m(k, z) \rangle = I_0, \quad (22a)$$

$$\Delta \langle \Gamma_{mn}(\kappa_1, \kappa_2, z) \rangle = I_1 + I_2 + I_3. \quad (22b)$$

These equations are of the first order when the integrals in Eqs. (21) are proportional to Δz . Even then, however, Δz cannot be allowed to approach zero arbitrarily, because of

the condition (19a). Thus, we can formally approximate the difference equations (22) by differential equations, but this must be done with the understanding that *it is not possible to resolve features of the z evolution whose scale is finer than L_z* . In principle, the solution of the differential equations must be smoothed, or filtered, so as to eliminate such features. This can be accomplished, for example, using a sliding average over a window whose width Δz_w satisfies Eq. (19a).

The evaluation of the integrals in Eqs. (21) is simplified by the presence of δ functions in the spectral correlations of pairs of random variables μ_{km} [see Eq. (7b)]. As we shall see, further simplifications occur when we use a smoothing window Δz_w such that the product $\Delta z_w(g_m - g_k)$ is large even for the closest modes. This implies that

$$\Delta z_w \gg L_g \quad \text{with} \quad L_g \sim \frac{\bar{k}H^2}{\pi^2}, \quad (23)$$

where $1/L_g$ is the separation between the eigenvalues of the lowest propagating modes. The explicit expression for L_g in Eq. (23) uses the form which is appropriate for a uniform sound speed, where the eigenvalues of the lowest propagating modes are of the order of \bar{k} —a characteristic value of the depth-dependent wave number $k(y)$. For the higher modes, near cutoff, the eigenvalue separations are larger—of the order of $(2\pi\bar{k}/H)^{1/2}$.

D. The average-field increment

The integral I_0 is evaluated using the property of μ_{mk} in Eq. (7b) to replace

$$\langle \mu_{mk}(\kappa - \kappa', z') \mu_{kl}(\kappa' - \kappa'', z'') \rangle = 2\pi \delta(\kappa - \kappa'') \sigma_{mkk l}(\kappa - \kappa', z' - z''). \quad (24a)$$

The κ'' integration replaces κ'' by κ . We now replace z'' by $z' - s_z$, and rewrite the integral thus

$$I_0 = - \sum_l \langle p_l(\kappa, z_0) \rangle \sum_k \int_{\Delta} dz' e^{-i[g_m(\kappa) - g_l(\kappa)]z'} \times \int_{-\infty}^{\infty} \frac{d\kappa'}{2\pi} \frac{1}{4g_m(\kappa)g_k(\kappa')} \int ds_z \delta_{-1}(s_z) \times e^{-i[g_l(\kappa) - g_k(\kappa')]s_z} \sigma_{mkk l}(\kappa - \kappa', s_z). \quad (24b)$$

Recalling that $\sigma_{mkk l}(\kappa - \kappa', s_z)$ contributes significantly when s_z is of the order of L_z , we use the arguments cited above, $z' - z_0 \gg L_z$, to extend the limits of the s_z integration (which formally depend on z') to infinity. With this simplification, the z' integration can be performed, and produces

$$I_0 = - \Delta z \sum_l \langle p_l(\kappa, z) \rangle F_{ml}(\Delta z) e^{-i\Delta z g_{ml} z_0} C_{ml}(\kappa) \quad (25a)$$

where

$$C_{ml}(\kappa) = \sum_k \int_{-\infty}^{\infty} \frac{d\kappa'}{2\pi} \frac{1}{4g_m(\kappa)g_k(\kappa')} \times \int_0^{\infty} ds_z e^{-i[g_l(\kappa) - g_k(\kappa')]s_z} \sigma_{mkk'l}(\kappa - \kappa', s_z), \quad (25b)$$

and

$$F_{ml}(\Delta z) = \frac{1 - e^{-i\Delta g_{ml}\Delta z}}{i\Delta g_{ml}\Delta z}, \quad \Delta g_{ml} \equiv g_m(\kappa) - g_l(\kappa). \quad (25c)$$

If we now formally let Δz approach zero and combine Eqs. (25) and (22a), we obtain the differential equation

$$\frac{\partial}{\partial z} \langle p_m(\kappa, z) \rangle = - \sum_l \langle p_l(\kappa, z) \rangle e^{-i\Delta g_{ml}(\kappa)z} C_{ml}(\kappa), \quad (\bar{k}L_z)^2 \langle \mu^2 \rangle \ll 1. \quad (25d)$$

The significance of this equation and the limitation on its applicability are discussed below.

We first observe that, with $\sigma_{mkk'l}$ and g_m as defined in Eqs. (7d) and (11), the coefficients C_{ml} are of the order of $\bar{k}^2 L_z \langle \mu^2 \rangle$. This quantity affects the scale of the range evolution of $\langle p_m \rangle$, and determines the upper bound L_p introduced in Eq. (19b).

We next note that the nonlinear dependence of I_0 on Δz is contained in the coefficients $F_{ml}(\Delta z)$ in Eqs. (25a) and (25c). These coefficients, which arise from the z' integration in Eq. (24b), “window average” the exponentials $\exp[-i\Delta g_{ml}z']$ over Δz . This suggests that, if the $\langle p_l \rangle$'s vary sufficiently slowly over Δz , the difference Eq. (22a) is the “window-averaged” version of the differential equation (25d). In the formal limit $\Delta z \rightarrow 0$, all $F_{ml} \rightarrow 1$. Strictly speaking, this limit is meaningful only if L_z is vanishingly small. However, even when L_z is finite, we may expect that the solution of Eq. (25d), subject to the caveat stated following Eq. (22), constitutes a good approximation to the solution of the difference Eq. (22a).

Alternatively, we observe that the differential Eq. (25d) may also be obtained by the following procedure: differentiate the exact expression $\langle p_m(\kappa, z_0 + \Delta z) \rangle = \langle p_m(\kappa, z_0) \rangle + I_0$ with respect to Δz , use the argument $L_z \ll \Delta z$ to extend the s_z integration to infinity, and replace z_0 by $z = z_0 + \Delta z$ in the right-hand member of the result. The last replacement, which produces Eq. (25d), is legitimate as long as $\langle p_m \rangle$ varies weakly over the range increment Δz , that is, if $\Delta z \ll L_p$.

These observations suggest that the solution of the differential equation (25d), smoothed so as to filter out variations on scales of order L_z or less, does indeed approximate the solution of the difference equation $\Delta \langle p_m(\kappa, z) \rangle = I_0$ —provided that there exists a range of values $L_z \ll \Delta z \ll L_p$ such that both the requirements in Eqs. (19a) and (19b) are satisfied. This requires $L_z \ll L_p$, and thus restricts the applicability of Eq. (25d) to the regime $(\bar{k}L_z)^2 \langle \mu^2 \rangle \ll 1$.

The scattering term in Eq. (25d) still contains contributions of all the modal amplitudes $\langle p_l \rangle$, weighted by the fac-

tors $\exp[-i\Delta g_{ml}(\kappa)z]$. Confining our attention to the radiative part of the spectrum of the m th mode, where $g_m(\kappa)$ is real, we may argue that only the term $l=m$ contributes significantly over sufficiently long ranges, and the terms $l \neq m$ may be ignored. This simplification is legitimate when the range-evolution scales defined by the constants $C_{mm}(\kappa)$ of Eq. (25b) are longer than the scales associated with the modal separation $\Delta g_{ml}(\kappa)$, i.e., when $L_p \gg L_g$. A formal way to accomplish and assess this simplification is to replace Δz in Eqs. (25a)–(25c) by Δz_w , which satisfies Eq. (23). The “window-averaging” coefficients $F_{ml}(\Delta z_w)$ are indeed small for all values of l , except

$$l=m \quad (26)$$

for which $F_{mm} = 1$ for all values of Δz_w . This produces the simplified equation

$$\Delta p_m(\kappa, z) = -\Delta z_w \langle p_m(\kappa, z_0) \rangle C_m(\kappa) \quad \text{for } \kappa < \beta_m, \quad (27a)$$

where

$$C_m(\kappa) = \sum_k \int_{-\infty}^{\infty} \frac{d\kappa'}{2\pi} \frac{1}{4g_m(\kappa)g_k(\kappa - \kappa')} \times \int_0^{\infty} ds_z e^{-ih_{mk}(\kappa, \kappa')s_z} \sigma_{mkkm}(\kappa', s_z), \quad (27b)$$

and

$$h_{mk}(\kappa, \kappa') \equiv g_m(\kappa) - g_k(\kappa - \kappa'). \quad (27c)$$

This equation can be replaced by the simplified differential equation

$$\frac{\partial}{\partial z} \langle p_m(\kappa, z) \rangle = -C_m(\kappa) \langle p_m(\kappa, z) \rangle \quad \text{for } \kappa < \beta_m \quad \text{and} \quad \bar{k}^3 H^2 L_z \langle \mu^2 \rangle / \pi^2 \ll 1, \quad (27d)$$

subject to the understanding that, if $L_z < L_g$, the solution must be smoothed so as to eliminate any features which evolve on a scale of the order of L_g or finer [when $L_g < L_z$, this is subsumed by the caveat following Eq. (22)]. The dominant long-range features of the solution will “survive” smoothing provided that $L_g < L_p$, that is, if $\bar{k}^3 H^2 L_z \langle \mu^2 \rangle / \pi^2 \ll 1$.

Once the solution $\langle p_m(\kappa, z) \rangle$ is obtained, using either Eq. (25d) or (27d), one can compute the ensemble-averaged field $\langle \hat{p}_m^*(\kappa, z) \rangle$ [see Eq. (14)] which contains the diffractive behavior.

E. The coherence increment

The exact same treatment can be accorded the integrals I_1 and I_2 , the first two contributions to the coherence increment across the slab in Eq. (22b). Comparing Eqs. (21a) and (21b), we see that the integral I_1 differs from I_0 only in that κ_1 replaces κ , and the added factor $p_n^*(\kappa_2, z_0)$ appears in the integrand. Thus [see also Eqs. (21c) and (25)]

$$I_1 = -\Delta z \sum_l \langle \Gamma_{ln}(\kappa_1, \kappa_2, z_0) \rangle e^{-\Delta g_{ml} z_0} \times F_{ml}(\Delta z) C_{ml}(\kappa_1), \quad (28a)$$

$$I_2 = -\Delta z \sum_l \langle \Gamma_{ml}(\kappa_1, \kappa_2, z_0) \rangle e^{i\Delta g_{nl} z_0} \times F_{nl}^*(\Delta z) C_{nl}^*(\kappa_2), \quad (28b)$$

where F_{ml} is defined in Eq. (25c). The contributions to both I_1 and I_2 are proportional to the average coherences at the left edge of the slab, but do not reflect any spectral interactions.

In dealing with the third contribution I_3 , we employ Eq. (7) to replace

$$\begin{aligned} & \langle \mu_{mk}(\kappa_1 - \kappa', z') \mu_{nl}^*(\kappa_2 - \kappa'', z'') \rangle \\ &= 2\pi \delta[(\kappa_1 - \kappa') - (\kappa_2 - \kappa'')] \\ & \quad \times \sigma_{mknl}(\kappa_1 - \kappa', z' - z''). \end{aligned} \quad (29a)$$

We then perform the κ'' integration, and replace

$$\kappa''' = \kappa_1 - \kappa' = \kappa_2 - \kappa'', \quad u = \frac{z' + z''}{2} - z_0, \quad (29b)$$

$$s_z = z' - z''.$$

with the result (in which κ''' is replaced by κ' for notational convenience)

$$\begin{aligned} I_3 &= \Delta z \sum_k \sum_l \frac{d\kappa'}{2\pi} \langle \Gamma_{kl}(\kappa_1 - \kappa', \kappa_2 - \kappa', z_0) \rangle \\ & \quad \times e^{-iH_{mknl}(\kappa_1, \kappa_2, \kappa') z_0} F_{mknl}(\kappa_1, \kappa_2, \kappa', \Delta z) \\ & \quad \times C_{mknl}(\kappa_1, \kappa_2, \kappa'), \end{aligned} \quad (30a)$$

where

$$\begin{aligned} C_{mknl}(\kappa_1, \kappa_2, \kappa') &= \frac{1}{4g_m(\kappa_1)g_n^*(\kappa_2)} \int_{-\infty}^{\infty} ds_z \\ & \quad \times e^{-i[h_{mk}(\kappa_1, \kappa') + h_{nl}^*(\kappa_2, \kappa')](s_z/2)} \sigma_{mknl}(\kappa', s_z), \end{aligned} \quad (30b)$$

$$\begin{aligned} F_{mknl}(\kappa_1, \kappa_2, \kappa', \Delta z) &= \frac{1}{\Delta z} \int_0^{\Delta z} du e^{-iH_{mknl}(\kappa_1, \kappa_2, \kappa') u} \\ &= \frac{1 - e^{-iH_{mknl}(\kappa_1, \kappa_2, \kappa') \Delta z}}{iH_{mknl}(\kappa_1, \kappa_2, \kappa') \Delta z}, \end{aligned} \quad (30c)$$

$$\begin{aligned} H_{mknl}(\kappa_1, \kappa_2, \kappa') &\equiv h_{mk}(\kappa_1, \kappa') - h_{nl}^*(\kappa_2, \kappa') \\ &= g_m(\kappa_1) - g_k(\kappa_1 - \kappa') \\ & \quad - g_n^*(\kappa_2) + g_l^*(\kappa_2 - \kappa'). \end{aligned} \quad (30d)$$

Combining Eqs. (22b), (28), and (30), and proceeding again to the formal limit $\Delta z \rightarrow 0$, we now obtain the differential equation, subject to the caveat following Eq. (22):

$$\begin{aligned} & \frac{\partial}{\partial z} \Gamma_{mn}(\kappa_1, \kappa_2, z) \\ &= - \sum_l [\langle \Gamma_{ln}(\kappa_1, \kappa_2, z) \rangle e^{-i\Delta g_{ml} z} C_{ml}(\kappa_1) \\ & \quad + \langle \Gamma_{ml}(\kappa_1, \kappa_2, z) \rangle e^{i\Delta g_{nl} z_0} C_{nl}^*(\kappa_2)] \\ & \quad + \sum_k \sum_l \int \frac{d\kappa'}{2\pi} \langle \Gamma_{kl}(\kappa_1 - \kappa', \kappa_2 - \kappa', z) \rangle \\ & \quad \times e^{-iH_{mknl}(\kappa_1, \kappa_2, \kappa') z} C_{mknl}(\kappa_1, \kappa_2, \kappa'). \end{aligned} \quad (30e)$$

All the coherences $\langle \Gamma_{kl} \rangle$ contribute to the scattering term. To simplify this in the manner of the discussion following Eq. (25), we consider the use of a sliding average over a window Δz_w which satisfies Eq. (23). Replacing Δz by Δz_w fixes $l = m$ in Eq. (28a) and $l = n$ in Eq. (28b). To examine the coefficients F_{mknl} in Eqs. (30c), we temporarily set κ_1 , κ_2 , and κ' to zero. In this case, H_{mknl} vanishes only if one of the following sets of conditions is met:

$$m = n \quad \text{and} \quad k = l, \quad (31a)$$

$$k = m \quad \text{and} \quad l = n. \quad (31b)$$

The corresponding coefficients F_{mkmk} and F_{mnmn} are then 1, and all others are negligible when Δz_w satisfies Eq. (23). We may now append to the conditions (31a) and (31b) the respective requirements

$$H_{mkmk}(\kappa_1, \kappa_2, \kappa') \Delta z_w \ll 1, \quad (32a)$$

$$H_{mnmn}(\kappa_1, \kappa_2, \kappa') \Delta z_w \ll 1 \quad (32b)$$

to assure that $F_{mkmk} \sim 1$ and $F_{mnmn} \sim 1$ for all values of κ_1 , κ_2 and κ' in the range of interest.

The conditions in Eq. (31a) refer only to modal self-coherences $\langle \Gamma_{mm} \rangle$, and eliminate the l summation in Eq. (30a). The conditions in Eq. (31b) refer only to modal cross-coherences $\langle \Gamma_{mn} \rangle$ with $m \neq n$, and eliminate both the k and l summations in Eq. (30a).

The implications of the conditions (32) will be examined in the next section. However, the considerations above suffice to introduce, at this point, the eventual simplified version of the differential equation for the coherence. This equation is obtained by substituting, in Eq. (22b), the simplified version of Eq. (28), along with Eqs. (30a)–(30d) and (31) (with F_{mknl} accordingly replaced by 1). The resulting first-order difference equation may then be replaced by the differential equation

$$\begin{aligned} \frac{\partial}{\partial z} \langle \Gamma_{mn}(\kappa_1, \kappa_2, z) \rangle &= -[C_m(\kappa_1) + C_n^*(\kappa_2)] \langle \Gamma_{mn}(\kappa_1, \kappa_2, z) \rangle \\ &+ \delta_{mn} \sum_k \int_{-\infty}^{\infty} \frac{d\kappa'}{2\pi} e^{-iH_{mkmk}(\kappa_1, \kappa_2, \kappa')z} \langle \Gamma_{kk}(\kappa_1 - \kappa', \kappa_2 - \kappa', z) \rangle \bar{C}_{mk}(\kappa_1, \kappa_2, \kappa') \\ &+ (1 - \delta_{mn}) \int_{-\infty}^{\infty} \frac{d\kappa'}{2\pi} e^{-iH_{mnmn}(\kappa_1, \kappa_2, \kappa')z} \langle \Gamma_{mn}(\kappa_1 - \kappa', \kappa_2 - \kappa', z) \rangle \tilde{C}_{mn}(\kappa_1, \kappa_2, \kappa'), \end{aligned} \quad (33a)$$

where

$$\begin{aligned} C_m(\kappa) &= \sum_k \int_{-\infty}^{\infty} \frac{d\kappa'}{2\pi} \frac{1}{4g_m(\kappa)g_k(\kappa - \kappa')} \\ &\times \int_0^{\infty} ds_z e^{-ih_{mk}(\kappa, \kappa')s_z} \sigma_{mkkm}(\kappa', s_z), \end{aligned} \quad (33b)$$

$$\begin{aligned} \bar{C}_{mk}(\kappa_1, \kappa_2, \kappa') &= \int_{-\infty}^{\infty} ds_z \frac{\sigma_{mkmk}(\kappa', s_z)}{4g_m(\kappa_1)g_m^*(\kappa_2)} \\ &\times e^{-i[h_{mk}(\kappa_1, \kappa') + h_{mk}^*(\kappa_2, \kappa')](s_z/2)}, \end{aligned} \quad (33c)$$

$$\begin{aligned} \tilde{C}_{mn}(\kappa_1, \kappa_2, \kappa') &= \int_{-\infty}^{\infty} ds_z \frac{\sigma_{mnmn}(\kappa', s_z)}{4g_m(\kappa_1)g_m^*(\kappa_2)} \\ &\times e^{-i[h_{mm}(\kappa_1, \kappa') + h_{nn}^*(\kappa_2, \kappa')](s_z/2)}, \end{aligned} \quad (33d)$$

$$h_{mk}(\kappa, \kappa') = g_m(\kappa) - g_k(\kappa - \kappa')$$

and

$$H_{mknl}(\kappa_1, \kappa_2, \kappa') = h_{mk}(\kappa_1, \kappa') - h_{nl}^*(\kappa_2, \kappa'). \quad (33e)$$

The applicability of these equations is subject to the caveat stated following Eq. (27), and to additional considerations which arise from Eq. (32) and the dependence of H_{mknl} in Eq. (30d) on the wave number variables, to be discussed in the next section. We note, at this point, the effect of the ‘‘selection rules’’ in Eq. (31) on the form of the scattering term in Eqs. (33). There is no coupling between modal cross coherences $m \neq n$: the last term on the rhs of Eq. (33a) reflects only a coupling between the various spectral components. However, there is coupling between the modal self-coherences Γ_{mm} [the second term on the rhs of Eq. (33a)]. As will be shown later, the modal self-coherences at identical wave numbers $\kappa_1 = \kappa_2$ are all that is needed to compute the spectral density of the total power flux across any z plane, or the transversely integrated coherence, and in particular the coherence of a planar (transversely homogeneous) wave. In those cases, the modal coupling is of prime interest.

As indicated at the beginning of this section, the parabolic approximation to the scattering term is obtained by replacing the functions g_m by β_m , which implies the assumption $\kappa \ll \beta_m$, and retransforming the result to the spatial

coordinates x_1, x_2 and their separation s_x . When this is done in Eq. (33b), the scattering term reduces precisely to the result obtained in Ref. 10, Eq. (37).

III. THE LIMITATIONS OF THE SIMPLIFIED DIFFERENTIAL EQUATION FOR THE COHERENCE

The preceding analysis revealed that (a) a simplified first-order difference equation for the coherence is available when $H_{mknl} = 0$, and is also approximately valid if the condition $H_{mknl} \Delta z_w \ll 1$ is satisfied; and (b) a necessary condition for this is that either of the respective requirements in Eqs. (31a), (31b), (32a) and (32b) be satisfied. Thus, in order that Δz_w satisfy the upper and lower bounds imposed by Eqs. (32) and (23) or (19a), either of the following conditions must be met:

$$\begin{aligned} H_{mkmk} L_M &\ll 1 \quad (\text{a}) \quad \text{or} \\ H_{mnmn} L_M &\ll 1 \quad (\text{b}), \quad \text{where } L_M = \max(L_z, L_g). \end{aligned} \quad (34)$$

Here, the first requirement applies to the modal self-coherences, and the second to the modal cross coherences. In this section, we consider the dependence of H_{mknl} on the wave number variables κ_1 , and κ_2 , and κ' , and interpret the implications of Eq. (34) in terms of the length and wave number parameters which characterize the beam and the medium. After introducing these parameters, we identify the regimes in which $H_{mknl} = 0$ exactly, and then proceed to characterize the ‘‘neighborhood’’ of each of these regimes, where the simplified equation is approximately valid.

A. Medium and beam parameters

The dominant contribution of $\sigma_{mkjl}(\kappa', s_z)$ to the integral in Eq. (30b) arises from the region where $1/\kappa' \gg L_x$, the transverse correlation length of the medium. It therefore suffices to replace κ' in Eq. (34) by its bandwidth $1/L_x$.

To introduce the beam parameters, we use the sum-and-difference wave number variables κ_s and κ_d , and their spatial counterparts, the (average) position and separation variables x_s and s_x , defined by

$$\kappa_{1,2} = \kappa_s \pm \frac{\kappa_d}{2}, \quad x_{1,2} = x_s \pm \frac{s_x}{2}. \quad (35a)$$

The relevant transform relations between the spatial and spectral coherences can be expressed in either of the two forms:

$$\begin{aligned}
\langle \tilde{\Gamma}_{mn}(x_1, x_2, z) \rangle &= \int_{-\infty}^{\infty} \int_{-\infty}^{\infty} \frac{d\kappa_1}{2\pi} \frac{d\kappa_2}{2\pi} e^{i[\kappa_1 x_1 + \kappa_2 x_2]} \\
&\quad \times \langle \Gamma_{mn}(\kappa_1, \kappa_2, z) \rangle, \\
\langle \tilde{\bar{\Gamma}}_{mn}(x_s, s_x, z) \rangle &= \int_{-\infty}^{\infty} \int_{-\infty}^{\infty} \frac{d\kappa_s}{2\pi} \frac{d\kappa_d}{2\pi} e^{i[\kappa_d x_s + \kappa_s s_x]} \\
&\quad \times \langle \bar{\Gamma}_{mn}(\kappa_s, \kappa_d, z) \rangle.
\end{aligned} \tag{35b}$$

We therefore identify κ_d and κ_s , respectively, as the conjugate variables of the transverse position and separation variables x_s and s_x in the spatial coherence functions $\langle \tilde{\bar{\Gamma}}_{mn}(x_s, s_x, z) \rangle$. In this notation, the wave number κ_d becomes a parameter of Eq. (33b)—even the cross-spectral coupling that is described by that equation occurs between wave numbers which are separated by a constant κ_d .

The integral in Eq. (31a) is of interest (as is the entire computation) for values of κ_d and κ_s such that $\kappa_d \leq 1/L_B$, where the ‘‘beam scale’’ L_B characterizes the x_s dependence of the field; and $\kappa_s \leq 1/L_\Gamma$, where the transverse coherence length L_Γ characterizes the s_x dependence of the field. Both L_B and L_Γ are affected by scattering, and therefore depend on the range: L_B grows, whereas L_Γ decreases, with increasing range.

B. The limit $H_{mknl}=0$

Returning to Eqs. (34) and (30d), we find that H_{mkmk} vanishes identically when the conditions in Eq. (31a) are supplemented by the requirement that

$$\kappa_1 = \kappa_2 = \kappa_s < \beta_m \quad \text{and} \quad |\kappa_s - \kappa'| < \beta_k. \tag{36a}$$

Likewise, H_{mnmn} vanishes when the conditions in Eq. (31b) are supplemented by the requirement

$$\kappa' = 0. \tag{36b}$$

We next consider, in turn, each of these conditions, and the regimes surrounding them, in which Eq. (34) may be satisfied. Since the first condition has a broader range of applicability, it will occupy most of the discussion.

The transverse-homogeneity (TH) limit $\kappa_1 = \kappa_2 = \kappa_s$ (or $\kappa_d = 0$), indicated in Eq. (36a), applies to the *self-modal coherences* in situations where the spatial coherence is independent of the transverse position x_s , and the spectral coherence correspondingly contains the factor $\delta(\kappa_d)$. This occurs, for example, when we consider the scattering of an initially plane wave. With other excitations, the spectral coherence functions $\langle \Gamma_{mm}(\kappa_s, \kappa_s, z) \rangle$ or $\langle \bar{\Gamma}_{mm}(\kappa_s, 0, z) \rangle$ are relevant to computations of the transversely integrated coherence, or of the total energy-flow across a given z plane.

However, Eq. (36a) pertains only to the radiative components of the TH spectrum, where $\kappa_s < \beta_m$ and g_m is real, and only to contributions to the integral in Eq. (30a) which arise from these components, for which $|\kappa_s - \kappa'| < \beta_k$ and g_k is real. Note that H_{mkmk} , which now assumes the simple form

$$\begin{aligned}
H_{mkmk} &= i2 \operatorname{Im}[g_m(\kappa_s) - g_k^*(\kappa'')], \\
&\quad \text{where } \kappa'' = |\kappa_s - \kappa'|,
\end{aligned} \tag{37}$$

vanishes only when κ_s and κ'' do not exceed β_m and β_k , respectively. Nonetheless, for $\kappa_s < \beta_m$, the magnitude of H_{mkmk} increases rapidly as κ'' exceeds β_k . Accordingly, F_{mkmk} in Eq. (30c) decreases rapidly, and attenuates contributions to the integral in Eq. (30a) from the evanescent domain of the spectrum. This suggests that Eq. (33b), with the κ' integrations restricted to the range $|\kappa_s - \kappa'| \leq \beta_k$, remains approximately applicable to the radiative spectral components $\kappa_s < \beta_m$ of a TH wave. The approximation entails the neglect of cross-spectral coupling, within each mode, due to scattering between spectral components with wave numbers near β_k . For narrow-angle scattering, where $\beta_k L_x \gg 1$ for all the modes, these wave numbers lie in the band $\beta_k \pm \Delta\kappa$, where $\Delta\kappa$ varies inversely with L_x and is therefore much smaller than β_k . The argument above holds as long as the spectral content of each wavemode in this band is small. However, this does *not* imply that the spectral spread of the scattered radiation (which is measured by L_Γ^{-1}) must be very small.

C. Finite beams

In order to extend the preceding argument to a finite beam, where $\kappa_d \neq 0$, we express the function H_{mkmk} , as defined by Eq. (30d), in terms of the variables κ_s and κ_d and expand the product $H_{mkmk} L_M$ to lowest order in κ_d . In the regime $k_s < \beta_m$ and $|\kappa_s - \kappa'| < \beta_k$, we obtain

$$\left[\frac{\kappa_s}{g_m(\kappa_s)} - \frac{\kappa_s - \kappa'}{g_k(\kappa_s)} \right] \kappa_d L_M. \tag{38}$$

In order to satisfy Eq. (34a), we require that each term in this expression be much smaller than 1. We ignore κ' , replace κ_s and κ_d by their respective bandwidths, and replace g_m (or g_k) by the smallest possible value of β_m , i.e., $\sqrt{2\pi(k/H)}$, in order to encompass all propagating modes. The result is

$$1 \ll \frac{L_B L_\Gamma}{L_M} \sqrt{\frac{2\pi k}{H}} \left[1 - \left(\frac{k L_\Gamma^2}{H} \right) - 1 \right]^{1/2}. \tag{39a}$$

For the contribution corresponding to $k = m$, a further expansion of Eq. (38) about $\kappa' = 0$ produces

$$1 \ll \sqrt{\frac{2\pi k}{H}} L_B \frac{L_x}{L_M} \left[1 - \left(\frac{k L_\Gamma^2}{H} \right) - 1 \right]^{3/2}. \tag{39b}$$

Thus, Eq. (33a) may be used to track the range evolution of the modal self-coherence of the radiative components $\kappa_s < \beta_m$ of the spectrum of a finite beam, provided that (a) we neglect scattering to and from the slowly evanescent spectral components, and accordingly restrict the domain of integration to $|\kappa_s - \kappa'| < \beta_k$; and (b) the propagation-regime satisfies the conditions (39). It may be possible to devise an improvement of Eq. (33b) which will account for the evanescent components, e.g., by appending an artificial cut-off factor in Eqs. (33c) and (33d), whose form resembles $F_{mkmk}(L_M)$ in Eq. (30c), except that L_M replaces Δz . However, this is beyond the scope of the present paper. With narrow-angle scattering, such a correction is probably unwarranted as long as the magnitude of the spectrum is small in the range $\beta_m \pm \Delta\kappa$ discussed above.

Equation (39), which pertains to the propagation of modal self-coherences at different wave numbers, imposes interrelated lower bounds on both coherence length of the beam and the beam width. The factors involving $[1 - (\bar{k}L_\Gamma^2/H)^{-1}]$ imply that the dominant part of the spectrum must remain within the radiative domain. Since scattering broadens the spectrum, and thus reduces L_Γ , this may imply a limitation on the range where Eq. (33b) remains applicable. The remaining factors imply a lower bound on the beam dimension L_B , that is, on the scale of the transverse dependence on x_s that can be resolved by the simplified coherence equation. Alternatively, we may interpret this as an upper bound on the wave number κ_d that can be resolved by that equation. Since scattering increases the scale L_B , the severity of this restriction decreases with range. Indeed, this restriction is entirely irrelevant in scenarios where L_B is effectively infinite (or $\kappa_d=0$), such as the scattering of an initially plane wave, or the computation of the total power flow. However, it implies that the simplified differential formulation cannot resolve the rapid x_s dependence associated with very narrow or highly structured beams. This is a direct consequence of the smoothing operation, which produces the simplified coherence equation, and parallels the reduced longitudinal resolution which is associated with smoothing.

D. The forward-scattering limit

The requirement of Eq. (36b), which pertains to the third scattering term of Eq. (33a), applies only to the calculation of the cross-modal coherences. This condition is relevant only in the idealized limit of narrow-angle scattering, where $\sigma_{mmnn}(\kappa', s_z)$, or, equivalently, $L_x \rightarrow \infty$. This ideal limit is of no interest. However, we may attempt to employ it in Eq. (30a) in the narrow-angle scattering regime where $(\bar{k}/H)^{1/2}L_x \gg 1$, which guarantees narrow-angle scattering for all modes, provided that Eq. (34b) is satisfied. Applying the above approach, we find that this cannot be done for the evanescent components. For the radiative components, this produces the condition

$$1 \ll \frac{L_x L_\Gamma}{L_m} \sqrt{\frac{\bar{k}}{H}} \quad (40)$$

IV. MODAL POWER SPECTRUM AND PROPAGATION OF TRANSVERSELY HOMOGENEOUS WAVES

This section is concerned with the modal self-coherences Γ_{mm} in the limit $\kappa_1 = \kappa_2 = \kappa_s$ (for notational simplicity, we use the transverse wave number argument κ , omitting the subscript s , in the ensuing discussion). Moreover, we consider only the regime where the dominant spectral components are confined to the range $\kappa < \beta_k$ for each mode, and the components in the “evanescent” range $\beta_k < \kappa$ may be ignored. In this regime, the functions $g_k(\kappa)$ are real, and Eq. (33b) is “exact” in the sense that $H_{mkmk} = 0$ in Eq. (30). As indicated earlier, the limit in question is relevant to the propagation of a TH waves, whose initial coherence is independent of the transverse position, and to the study of the spectral distribution of the total average modal power which crosses any z plane.

A. Transverse modal power spectrum

To see the intimate relation between the two problems, note that the power-flux density is given by

$$J(z) = \text{Re} \int_0^H dy \int_{-\infty}^{\infty} dx \tilde{p} \tilde{v}_z^*, \quad (41)$$

where \tilde{v}_z is the z component of the particle velocity defined in Eq. (8). Using the various definitions leading up to the modal spectral coherence Γ_{mn} [Eq. (16)] as well as the transform relation between \tilde{p}_m and \hat{p}_m , this expression is readily recast in the form

$$J(z) = \text{Re} \sum_m \int_{-\infty}^{\infty} d\kappa J_m(\kappa, z),$$

where $J_m(\kappa, z) \equiv g_m^*(\kappa) \Gamma_{mm}(\kappa, \kappa, z)$. (42)

This expression suggests that $J_m(\kappa, z)$ is the transverse spectral density of the power in the m th mode, and shows that it differs from the modal self-coherences of a TH wave by the factor $g_m^*(\kappa)$.

Using Eqs. (33), we may readily construct a differential equation for the evolution in z of $J_m(\kappa, z)$. In this case, the s_z integrals in the definitions of $C_m(\kappa) + C_m^*(\kappa)$ [Eq. (33b)] combine to a single integral which is identical to the s_z integral in the definition of $\bar{C}_{mk}(\kappa, \kappa, \kappa')$ in Eq. (33c). Therefore, when we introduce the definition of $J_m(\kappa, z)$ in Eq. (33a), the result assumes the simple form

$$\frac{\partial}{\partial z} J_m(\kappa, z) = \sum_k \int_{-\beta_k}^{\beta_k} \frac{d\kappa'}{2\pi} [J_k(\kappa', z) - J_m(\kappa, z)] \times \frac{1}{4g_m(\kappa)g_k(\kappa')} S_{mk}(\kappa, \kappa'), \quad (43a)$$

where the κ' integration is confined to the propagating range, and

$$S_{mk}(\kappa, \kappa') = \int_{-\infty}^{\infty} ds_z e^{-i[g_m(\kappa) - g_k(\kappa')]s_z} \sigma_{mkkm}(\kappa - \kappa', s_z) = \int_{-\infty}^{\infty} ds_x \int_{-\infty}^{\infty} ds_z e^{i\{(\kappa - \kappa')s_x + [g_m(\kappa) - g_k(\kappa')]s_z\}} \times \tilde{\sigma}_{mkkm}(s_x, s_z) \quad (43b)$$

with $\tilde{\sigma}_{mkkm}$ as defined in Eq. (7). To account for the spectral redistribution of the average power by scattering in a beam, Eq. (43a) must be solved subject to the source condition $J(\kappa, 0)$ computed from the known fields at the beam aperture. The source condition is $J(\kappa, 0) = (2\pi)^2 \delta(\kappa)$ for an initial plane wave.

B. Energy considerations

It is easy to verify that Eq. (43a), and therefore Eq. (33b), conserves energy, in the sense that the total average power associated with the radiative spectral components across any plane z is constant. To ascertain this, note that the rate of change of the total power is obtained by applying, to the right-hand member of Eq. (43a), the operator $\sum_m \int d\kappa$, with $|\kappa| < \beta_m$. The resulting integral vanishes. To verify

this, interchange m and k as well as κ and κ' , and note that $S_{mk}(\kappa, \kappa')$ is insensitive to this interchange by virtue of the symmetry properties of the function σ_{mkkm} [see Eqs. (2) and (7)]. However, the right-hand member of Eq. (43a) contains only the dominant power-exchange terms. The absent subdominant terms account for the exchange of power with the evanescent spectral domain, and their κ integral probably does not vanish. Thus, the total energy is conserved only as long as the scattering process is confined to the radiative part of the modal spectra.

An equation for the modal power $\int d\kappa J_m(\kappa, z)$ cannot be derived readily from Eq. (43a). Such an equation is nonetheless available for the parabolic approximation. It can be obtained directly from Eq. (43a) when we replace g_m by β_m . We shall obtain it here by first retransforming Eq. (43a) to the spatial-separation domain, $\kappa \rightarrow s_x$.

C. Retransformation to spatial coordinates

Considerable effort has been devoted in the past to the treatment of the modal problem in spatial coordinates, and in the context of the parabolic approximation. To establish the connection of the present work with these efforts, we next obtain an equation for

$$\tilde{J}_m(s_x, z) = \int_{-\infty}^{\infty} \frac{d\kappa}{2\pi} e^{i\kappa s_x} J_m(\kappa, z). \quad (44a)$$

We apply the above transformation to Eq. (43a), taking note of Eq. (43b). This produces the equation

$$\begin{aligned} \frac{\partial}{\partial z} \tilde{J}_m(s_x, z) = & \sum_k \int_{-\infty}^{\infty} ds'_x [G_{mk}(s_x, s'_x) \tilde{J}_k(s'_x, z) \\ & - G_{mk}(s_x - s'_x, 0) \tilde{J}_m(s'_x, z)], \end{aligned} \quad (44b)$$

where the functions G_{mk} are given by

$$\begin{aligned} G_{mk}(s_x, s'_x) = & \frac{1}{4} \int_{-\infty}^{\infty} d\rho_x \int_{-\infty}^{\infty} ds_z \sigma_{mkkm}(\rho_x, s_z) \\ & \times \int_{-\beta_m}^{\beta_m} \frac{d\kappa}{2\pi} \int_{-\beta_k}^{\beta_k} \frac{d\kappa'}{2\pi} \frac{1}{g_m(\kappa)g_k(\kappa')} \\ & \times e^{i\{\kappa(s_x - \rho_x) - \kappa'(s'_x - \rho_x) + [g_m(\kappa) - g_k(\kappa')]s_z\}}. \end{aligned} \quad (44c)$$

The parabolic approximation is attained by replacing g_m by β_m in Eqs. (44b) and (44c) and extending the κ' integrations to infinity (this is consistent with this small- κ approximation). This produces

$$G_{mk}(s_x, s'_x) \sim \delta(s_x - s'_x) \frac{1}{4\beta_m\beta_k} A_{mk}(s_x), \quad (45a)$$

where

$$A_{mk}(s_x) = \int_{-\infty}^{\infty} ds_z e^{i(\beta_m - \beta_k)s_z} \sigma_{mkkm}(s_x, s_z), \quad (45b)$$

and the differential equation for \tilde{J} then assumes the approximate form

$$\begin{aligned} \frac{\partial}{\partial z} \tilde{J}_m(s_x, z) = & - \sum_k \frac{1}{4\beta_m\beta_k} [A_{mk}(0) \tilde{J}_m(s_x, z) \\ & - A_{mk}(s_x) \tilde{J}_k(s_x, z)], \end{aligned} \quad (46)$$

which readily reduces to the parabolic equation system of ordinary linear differential equations for the range evolution of the modal power

$$I_m(z) = \int_{-\infty}^{\infty} d\kappa J_m(\kappa, z) = 2\pi \tilde{J}_m(0, z), \quad (47a)$$

$$\frac{\partial}{\partial z} I_m(z) = - \sum_k \frac{1}{4\beta_m\beta_k} A_{mk}(0) [I_m(z) - I_k(z)]. \quad (47b)$$

By summing this system of equations over m , we readily verify power conservation. The equation indicates that steady state will be reached when the total power is equipartitioned among all the propagating modes.

The result in Eq. (47) is implicit in past treatments of the propagation problem in spatial coordinates, where the parabolic approximation has been adopted from the outset. The difficulty with this result can most easily be appreciated by considering propagation in a horizontally isotropic medium (such as the ocean). In this case, the correlation functions $\tilde{\sigma}$ and $\tilde{\sigma}_{mkl}$ depend on the argument $(s_x^2 + s_z^2)^{1/2}$. Correspondingly, the two-dimensional transform S_{mk} defined by Eq. (43b) is a function of the dimensionless argument

$$(\kappa - \kappa')^2 + [g_m(\kappa) - g_k(\kappa')]^2 \quad \text{where } g_m^2(\kappa) = \beta_m^2 - \kappa^2. \quad (48)$$

The approximation made in deriving Eq. (46a) replaces g_m by β_m , in which case the argument above assumes the approximate form

$$(\beta_m - \beta_k)^2 + (\kappa - \kappa')^2. \quad (49)$$

However, if we employ the two-term expansion of $g_m(\kappa)$,

$$g_m(\kappa) = \beta_m \left[1 - \frac{\kappa^2}{2\beta_m^2} \right], \quad (50)$$

the argument assumes the approximate form

$$(\beta_m - \beta_k)^2 + \beta_m\beta_k \left[\frac{\kappa}{\beta_m} - \frac{\kappa'}{\beta_k} \right], \quad (51)$$

which differs radically from the approximate form in Eq. (49), and produces an entirely different equation for the propagation of the modal power.

To derive the propagation equation for the modal power, we rewrite Eq. (43a) in terms of the variables

$$\bar{\kappa} = \frac{\kappa}{\beta_m}, \quad \bar{\kappa}' = \frac{\kappa'}{\beta_k}, \quad (52)$$

using the approximate argument of S_{mk} shown in Eq. (51):

$$\begin{aligned} \frac{\partial}{\partial z} J_m(\beta_m \bar{\kappa}, z) &= \sum_k \frac{1}{2\pi} \int_{-\infty}^{\infty} d\bar{\kappa}' [J_k(\beta_k \bar{\kappa}', z) \\ &\quad - J_m(\beta_m \bar{\kappa}, z)] \\ &\quad \times \frac{S_{mk}[(\beta_m - \beta_k)^2 + \beta_m \beta_k (\bar{\kappa} - \bar{\kappa}')^2]}{4\beta_m}. \end{aligned} \quad (53)$$

We now retransform this equation to the spatial coordinate \bar{s} , using the definitions

$$\frac{1}{2\pi} \int_{-\infty}^{\infty} d\bar{\kappa} e^{i\bar{\kappa}\bar{s}} J_m(\beta_m \bar{\kappa}, z) = \frac{1}{\beta_m} \tilde{J}_m(\bar{s}/\beta_m, z), \quad (54a)$$

$$\bar{A}_{mk}(\bar{s}) = \frac{1}{2\pi} \int_{-\infty}^{\infty} d\bar{\kappa} e^{i\bar{\kappa}\bar{s}} S_{mk}[(\beta_m - \beta_k)^2 + \beta_m \beta_k \bar{\kappa}^2], \quad (54b)$$

where \tilde{J}_m is defined in Eq. (44a). The result is

$$\begin{aligned} \frac{\partial}{\partial z} \tilde{J}_m(\bar{s}/\beta_m, z) &= \frac{1}{4} \sum_k \left[\bar{A}_{mk}(\bar{s}) \frac{1}{\beta_k} \tilde{J}_k(\bar{s}/\beta_k, z) \right. \\ &\quad \left. - \bar{A}_{mk}(0) \frac{1}{\beta_m} \tilde{J}_m(\bar{s}/\beta_m, z) \right] \end{aligned} \quad (55a)$$

and, upon setting $\bar{s}=0$, the modal power equation

$$\frac{\partial}{\partial z} I_m(z) = \frac{1}{4} \sum_k \bar{A}_{mk}(0) \left[\frac{1}{\beta_k} I_k(z) - \frac{1}{\beta_m} I_m(z) \right]. \quad (55b)$$

Total power is conserved. To verify, sum Eq. (55b) over all modes, and interchange k and m in the right-hand member, noting that $\bar{A}_{mk}(0) = \bar{A}_{km}(0)$. However, steady state is reached when I_m/β_m is constant for all modes. Thus, modal coherence, rather than modal power, is equipartitioned among the modes in the steady state. Moreover, the modal power is distributed as

$$I_m = \frac{\beta_m}{\beta_T} (\text{total beam power}), \quad \text{where} \quad \beta_T = \sum_M \beta_M, \quad (55c)$$

where M is the total number of propagating modes. This implies that the modes with lower β retain more power than the near-cutoff modes.

We note that, like Eq. (47), Eq. (55b) applies also to a cylindrically symmetric wave—in which case z is the radial coordinate and $I_m(z)$ is the total power crossing a cylindrical surface.

We observe immediately that the result in Eq. (55) is a reflection of the three-dimensional character of the medium, as manifested in this case in the horizontal isotropy. It would not be obtained if we were to consider a two-dimensional (y, z) medium with x -independent properties, excited by an x -independent source. In the context of the present theory, this would be a horizontally anisotropic regime in which the correlation-length in the transverse (x) direction is infinite. For such a regime, the functions S_{mk} in Eq. (43a) must assume the form $2\pi \delta(\kappa - \kappa') S'_{mk}$ because $\tilde{\sigma}$ is independent of s_x . Moreover, the spectral power density $J_m(\kappa, z)$ associ-

ated with an x -independent source must assume the form $\delta(\kappa) I_m(z)$. When this is incorporated in Eq. (43a), and the result integrated over all κ , one finds

$$\frac{\partial}{\partial z} I_m(z) = \sum_k [I_k(\kappa, z) - I_m(z)] \frac{S'_{mk}[\beta_m - \beta_k]}{\beta_m \beta_k}, \quad (56)$$

which has the form of Eq. (47) and therefore predicts a steady-state equipartition of modal power. This amply demonstrates the care with which two-dimensional models must be treated.

We are not aware of any experimental results which bear on the distinctly different predictions of Eqs. (47) and (55). Theoretical calculations and numerical simulations by Dozier and Tappert² (and earlier theory by Kohler and Papanicolau¹⁸) indicate an equipartition of modal power at large range distances. However, they address *azimuthally symmetric* cylindrical spreading, which is analogous to the (y, z) domain discussed in the preceding paragraph. The results are entirely consistent with Eq. (56), but have no bearing on the issue at hand. Three-dimensional cylindrical spreading is addressed by Penland,¹⁹ but the computation of the asymptotic power flux neglects the terms which are analogous to the second term in Eq. (50).

D. The asymptotic limit $\bar{k}L^2/H \equiv \Lambda \gg 1$

In order to shed further light on the results discussed in the preceding subsection, we next consider an asymptotic analysis of Eq. (53) in the limit indicated above. The relevance of the parameter Λ to Eq. (53) can be seen in the following discussion:

Since L is the characteristic length associated with the coherence functions σ_{mkjl} , the dimensionless arguments [Eq. (51)] of the scattering functions S_{mk} defined in Eq. (43b) assumes the form

$$L^2[(\beta_m - \beta_k)^2 + 4\beta_m \beta_k w^2], \quad \text{where} \quad w = \frac{1}{2}(\bar{\kappa} - \bar{\kappa}'). \quad (57a)$$

For later use, we also define at this point the normalized versions of the functions

$$S_{mk} = \langle \mu^2 \rangle k_0^4 L^2 \bar{S}_{mk}. \quad (57b)$$

The normalization takes into account the following: (1) The correlation $\tilde{\sigma}$, Eq. (2a), can be normalized by extracting from it the quantity $\langle \mu^2 \rangle$. (2) The quantities $\tilde{\sigma}_{mkjl}$ can further be normalized by extracting a characteristic value k_0^4 from the integrand in Eq. (7d). (3) A factor of L^2 must be extracted from the definition of S_{mk} , Eq. (43b), when the integral is rewritten in terms of the dimensionless separation arguments $s_{x,z}/L$.

Now consider that the dominant contribution of the functions S_{mk} to the integrals in Eq. (53) arises from the region where their (dimensionless) arguments, defined in Eq. (57a), are of order 1. The smallest modal eigenvalues occur near cutoff, and are of the order of $\sqrt{(k/H)}$. If this quantity were used to construct dimensionless versions of all β 's, the dimensionless counterpart of the term in $[\]$ in Eq. (57a) would be multiplied by Λ . Thus, the dominant contributions of the functions S_{mk} arise from the regions where w is of

order $\Lambda^{-1/2}$. When $\Lambda \gg 1$, an asymptotic series representation of the integral in Eq. (53) is possible. We convert the $\bar{\kappa}'$ integral in Eq. (53) to a w integral, extend the limits of the w integration to $\pm\infty$ (since the dominant contribution will arise near $w=0$ in any case), express the coefficient of S_{mk} in the integrand as a w power series, and integrate term by term.

For $k=m$, the integrand of Eq. (53) vanishes if $\bar{\kappa}=\bar{\kappa}'$. The leading terms of the power series are

$$w\beta_m\left(\frac{\partial}{\partial\bar{\kappa}}\right)J_m(\beta_m,\bar{\kappa},z)+w^2\frac{1}{\beta_m}\left(\frac{\partial^2}{\partial\bar{\kappa}^2}\right)J_m(\beta_m,\bar{\kappa},z), \quad (58a)$$

and only the second term will survive the w integration. When $k \neq m$, the leading term is simply

$$\frac{1}{2\beta_m}[J_k(\beta_k\bar{\kappa},z)-J_m(\beta_m\bar{\kappa},z)]. \quad (58b)$$

After performing the relevant w integrations, we find that the leading terms of the asymptotic evaluation of the integral in Eq. (53) near $\bar{\kappa}=\bar{\kappa}'$ produce the approximate equation

$$\begin{aligned} \frac{\partial}{\partial z}J_m(\beta_m\bar{\kappa},z) &= D_m\left(\frac{\partial^2}{\partial\bar{\kappa}^2}\right)J_m(\beta_m\bar{\kappa},z) \\ &+ \sum_k D_{mk}[J_k(\beta_k\bar{\kappa},z)-J_m(\beta_m\bar{\kappa},z)]. \end{aligned} \quad (59a)$$

The coefficients D_m and D_{mk} are best evaluated in terms of the normalized scattering functions \bar{S}_{mk} , defined in Eq. (58b), in order to display their dependence on the parameters of the problem

$$D_m = \frac{\langle\mu^2\rangle k_0^4}{16\pi L\beta_m^4} \int_{-\infty}^{\infty} d\bar{w} \bar{w}^2 \bar{S}_{mk}(\bar{w}^2), \quad (59b)$$

$$D_{mk} = \frac{\langle\mu^2\rangle k_0^4 L}{8\pi\beta_m\sqrt{\beta_k\beta_m}} \int_{-\infty}^{\infty} d\bar{w} \bar{S}_{mk}[L^2(\beta_m-\beta_k)^2+\bar{w}^2]. \quad (59c)$$

Equation (59a) suggests that power is scattered between the m th modes and other modes $k \neq m$, and diffuses spectrally within the m th mode. When this expression is integrated over all wave numbers, it produces the right-hand side of modal power equation (55b), which of course does not reflect the spectral diffusion within a mode. However, this diffusion process (or its spatial counterpart in the x direction) is indeed responsible for the difference between the x -independent model discussed in connection with Eq. (56) and the three-dimensional model in Eq. (55).

It should be emphasized that Eq. (59a) is probably valid only for very large values of the range, although the manner in which that equation was derived does not indicate this. Recall that this expression is but the first term of an asymptotic series in $1/\Lambda$, whose coefficients contain $\bar{\kappa}$ -derivatives of J_m of increasing order. Thus, if J_m is highly concentrated in wave-number-space, as would be the case near a perfectly coherent plane-wave source, these neglected terms will be important. Such concentrations would nonetheless be moderated at sufficiently large ranges.

To complete the discussion, we indicate that an identical treatment can be applied to Eq. (43a), except that the definition of the function w must be modified to read

$$w^2 = \frac{1}{2}[1 - \bar{\kappa}\bar{\kappa}' - \sqrt{(1-\bar{\kappa}^2)(1-\bar{\kappa}'^2)}]. \quad (60a)$$

This produces the following expression for the leading terms in the asymptotic evaluation of the right-hand member of Eq. (43a):

$$\begin{aligned} R &= D_m\left(\frac{\partial}{\partial\bar{\kappa}}\right)(1-\bar{\kappa}^2)^{1/2}\left(\frac{\partial}{\partial\bar{\kappa}}\right)J_m(\beta_m\bar{\kappa},z) + \sum_k D_{mk}(1 \\ &- \bar{\kappa}^2)^{-1/2}[J_k(\beta_k\bar{\kappa},z)-J_m(\beta_m\bar{\kappa},z)]. \end{aligned} \quad (60b)$$

This expression reduces to Eq. (59a) when $\bar{\kappa} \ll 1$. The difference between the two expressions indicates the leading corrections that arise in the departure from the parabolic limit.

V. SUMMARY AND DISCUSSION

The central general results of this paper are the differential equations (25d) and (30e), and more so their simplified versions, Eqs. (27d) and (33). These equations govern the range evolution of the ensemble-averaged spectral fields and coherences of one-way propagating modes in a stratified volume-scattering channel.

The fully coupled equations (25d) and (30e) are subject only to the condition $(\bar{k}L_z)^2\langle\mu^2\rangle \ll 1$, which guarantees that the requirements in Eq. (19) can be met simultaneously. The requirement of Eq. (19b) justifies retaining only two terms in the perturbation solution. The requirement of Eq. (19a), which warrants the independent averaging of the stochastic fields and the stochastic medium properties, results in the ‘‘resolution’’ caveat stated following Eq. (22): The equations will not predict features whose range scale is finer than the range correlation length L_z , because our treatment of the stochastic problem is intrinsically incapable of making predictions on these scales. This limitation is ‘‘enforced’’ by smoothing of the solution of these equations by a sliding average over a window $\Delta z \gg L_z$.

The much-simplified version given in Eqs. (33) eliminates many of the modal interactions whose long-scale average is zero because they take place on scales shorter than the length L_g —Eq. (23)—dictated by the smallest separation between the modal eigenvalues. This simplification is not mandated by statistical considerations but by a restricted interest in the long-term features of the solution. Indeed, it can be undertaken meaningfully only when the smoothing which it entails does not affect the long-term behavior of the solutions of interest, which takes place on the scale L_p , Eq. (19b). This imposes the much more severe restriction $\bar{k}^3 H^2 L_z \langle\mu^2\rangle / \pi^2 \ll 1$ on the propagation regime.

The above limitations on range resolution are also manifest in the transverse resolution: the solutions of the equations can only resolve transverse variations (or the corresponding wave-number-spectra) on scales which satisfy Eqs. (39) and (40). However, the simplified equations can always be used to treat transversely homogeneous beams, or to compute transversely integrated beam features (such as the total modal power).

Modal theory has largely been concerned with the analysis of the coupled-power equations. The use of the differential equation (33b) to study this feature is restricted only by the neglect of the evanescent components of the spectrum. For this reason, considerable emphasis has been placed in Sec. IV on the behavior of the transverse spectral density $\langle J_m(\kappa, z) \rangle$ of the modal power, which is governed by Eq. (43a), and the related problem of the modal coherence of an erstwhile-coherent plane wave, whose spatial coherence is governed by Eq. (44b). However, the more important implications of this discussion concern the viability of the commonly used approximate parabolic version of the equations which govern modal propagation in spatial coordinates. These equations can be obtained from the present formulation by an inconsistent limiting process, in which the quantity $g_m \equiv \sqrt{(\beta_m^2 - \kappa^2)}$ is replaced by a two-term expansion in the refractive term, and by the one-term expansion in the scattering term. This eventually produces an approximate equation for the modal power, Eq. (47a), which indicates that the total power is conserved and equipartitioned among the propagating modes. Although Eq. (43a) conserves the total power, we are not able to derive from it an exact equation for the modal power. However, we show here that a consistent use of the two-term expansion in both the diffraction terms and the scattering terms produces approximately Eq. (55) for the total power: this equation also conserves the total power, but predicts that its asymptotic distribution is proportional to the modal eigenvalues, rather than uniform.

In future publications we plan to extend the spectral analysis to surface scattering, and also to situations where the vertical spectrum consists of both discrete and continuous components.

ACKNOWLEDGMENTS

One of us (SF) wishes to acknowledge the support of AFOSR under Contract No. F49620-94-1-03039. MJB wishes to acknowledge partial support by ONR under Contract No. N000014-94-1-0201.

- ¹S. M. Flatte, R. Dashen, W. H. Munk, and F. Zachariasen, *Sound Transmission through a Fluctuating Ocean* (Cambridge U.P., New York, 1979).
- ²L. B. Dozier and F. B. Tappert, "Statistics of normal-mode amplitudes in a random ocean. I. Theory and II. Computations," *J. Acoust. Soc. Am.* **63**, 353–365 (1978); **64**, 533–547 (1978).
- ³A. D. Pierce, "Extension of the method of normal modes in an almost-stratified medium," *J. Acoust. Soc. Am.* **37**, 19–27 (1965).
- ⁴S. T. McDaniel, "Coupled Power equations for cylindrically spreading waves," *J. Acoust. Soc. Am.* **60**, 1285–1289 (1976).
- ⁵S. T. McDaniel and D. F. McCammon, "Mode coupling and the environmental sensitivity of shallow-water loss predictions," *J. Acoust. Soc. Am.* **82**, 217–223 (1987).
- ⁶G. R. Sutton and J. J. McCoy, "Scattering of acoustic signals by inhomogeneities in a waveguide—single scatter treatment," *J. Acoust. Soc. Am.* **60**, 833–839 (1976).
- ⁷G. R. Sutton and J. J. McCoy, "Spatial coherence of acoustic signals in randomly inhomogeneous waveguides—A multiple scatter theory," *J. Math. Phys.* **18**, 1052–1077 (1977).
- ⁸M. J. Beran and J. J. McCoy, "Propagation through an anisotropic medium," *J. Math. Phys.* **15**, 1901–1912 (1974).
- ⁹M. J. Beran and J. J. McCoy, "Propagation through an anisotropic medium. An integrodifferential formulation," *J. Math. Phys.* **17**, 1186–1189 (1976).
- ¹⁰M. J. Beran and S. Frankenthal, "Volume scattering in a shallow channel," *J. Acoust. Soc. Am.* **91**, 3203–3211 (1992).
- ¹¹M. J. Beran and S. Frankenthal, "Combined volume and surface scattering in a channel using the modal formulation," *J. Acoust. Soc. Am.* **100**, 1463–1472 (1996).
- ¹²A. Ishimaru, *Wave Propagation and Scattering in Random Media* (Academic, New York, 1978).
- ¹³V. I. Tatarskii, *The Effect of the Turbulent Atmosphere on Wave Propagation* (National Technical Information Service, Springfield, 1971).
- ¹⁴C. A. Boyles, *Acoustic Waveguides* (Wiley, New York, 1984), Chap. 7.
- ¹⁵C. Rino, "On propagation in continuous random media," *Waves Random Media* **1**(1), 59–72 (1991).
- ¹⁶S. Frankenthal and M. J. Beran, "Transverse spectra of waves in random media," submitted to the *Journal of Waves in Random Media* (1995).
- ¹⁷M. J. Beran and T. L. Ho, "Propagation of the fourth-order coherence function in a random medium," *J. Opt. Soc. Am.* **59**(9), 1138–1143 (1969).
- ¹⁸W. Kohler and G. Papanicolau, "Wave propagation in a randomly inhomogeneous ocean," in *Lecture Notes in Physics, Vol. 70, Wave Propagation and Underwater Acoustics*, edited by J. Keller and J. Papadakis (Springer-Verlag, Berlin, 1977).
- ¹⁹C. Penland, "Acoustic normal mode propagation through a three-dimensional internal wave field," *J. Acoust. Soc. Am.* **78**, 1356–1365 (1985).

Modeling of scattering by objects on the seabed

J. A. Fawcett, W. L. J. Fox, and A. Maguer

Saclant Undersea Research Centre, Viale San Bartolomeo 400, 19138 San Bartolomeo, La Spezia, Italy

(Received 6 November 1997; accepted for publication 3 September 1998)

This paper describes some of the theory and implementation issues of modeling the backscattered energy from cylindrical or spherical objects lying on the seabed. The model utilizes a single-scatter approximation; this approximation is compared to full multiple scattering solutions to verify its accuracy. The effects of various parameters such as grazing angle of the incident energy, receiver/scatterer geometry, and the bottom half-space geoacoustic parameters are investigated numerically. The paper is concluded with a comparison of modeled time series with experimental scattering data obtained for a steel-shelled cylinder and a solid aluminum sphere lying on a sandy seabed. [S0001-4966(98)04612-8]

PACS numbers: 43.30.Gv, 43.30.Dr [DLB]

INTRODUCTION

When a scattering object is near an interface, the interface will modify the field incident upon the object and will also modify the field scattered by the object. There are, in fact, an infinite sequence of interactions between the object and the interface. The ‘‘single-scatter’’ approximation (SSA) is achieved by modeling the scattering from the object as a free-space scattering process and including the effects of the interface on modeling the incident field and the propagation of the scattered field; only single scatterings from the object are modeled. This type of approximation has been used by other authors (e.g., Refs. 1, 2) for object/waveguide scattering problems. For the case of an object lying on the seabed we expect this approximation to be accurate for the specular reflection. However, it is not clear that this approximation will properly describe the effect of the seabed on the propagation of energy which propagates circumferentially about the object. One would expect that the character of the circumferential waves could be changed along the portion of the object on or very close to the seabed. There are methods which model all the interactions between the scattering object and the interface for proud, buried, or partially buried objects.³⁻⁸ In this paper we follow the approach of Refs. 3 and 4 in deriving full multiple scattering solutions for an infinite cylinder and sphere on the seabed. We will use these solutions to show that the single-scatter approximation, which is faster computationally, is very accurate for all portions of the backscattered time series. We will show in the temporal domain how the interface changes the nature of the signal backscattered by the object. Finally, we compare our model results (both in the spectral and temporal domains) with experimental data obtained from a water-filled cylindrical shell and for an aluminum sphere lying on the sea bottom.

I. THEORY

Solutions for scattering from cylinders and spheres in free space are most readily constructed in terms of the appropriate special functions; radial Bessel or Hankel functions with azimuthal trigonometric functions in the case of the cylinder and spherical Bessel or Hankel functions with

spherical harmonic functions in the case of scattering from a sphere. However, the modeling of propagation in a two half-space environment is most easily described in terms of wave functions with vertical and radial dependencies. Thus the functions which most easily describe the propagation process are not the same as those which most easily describe the scattering process. In order to compute the scattering solutions for an object near an interface, it will be necessary to be able to express the functions of the one representation in terms of the other. Below, we outline the necessary transformations for the two-dimensional infinite cylinder case and for the three-dimensional spherical case.

A. Incident field

We take the source to be sufficiently distant from the cylinder or sphere that the incident field can be approximated as direct and interface-reflected plane waves (see Fig. 1 below). Thus we can consider the incident field to have the form

$$p^{\text{inc}} = \exp\left(i \frac{\omega}{c} [z \cos \phi_{\text{inc}} + x \sin \phi_{\text{inc}}]\right) + \Gamma^{\text{inc}}(\omega, \phi_{\text{inc}}) \exp\left(-2ia \frac{\omega}{c} \cos \phi_{\text{inc}}\right) \times \exp\left(i \frac{\omega}{c} [-z \cos \phi_{\text{inc}} + x \sin \phi_{\text{inc}}]\right), \quad (1)$$

where $\Gamma^{\text{inc}}(\omega, \phi_{\text{inc}})$ is the plane-wave reflection coefficient for the angle of incidence ϕ_{inc} , a is the radius of the cylinder or sphere, and $\exp[-2ia\omega/c \cos(\phi_{\text{inc}})]$ accounts for the phase difference between the direct and reflected wavefronts (note that with our definition of ϕ_{inc} , $\cos \phi_{\text{inc}}$ is negative). It is straightforward, by using a distribution of generalized plane waves of the form of Eq. (1), to generate more general incident fields.

B. Scattered field

We will concentrate on the derivation of the full multiple scattering solution for the sphere above or on the seabed. The derivation of the solution for the infinite cylinder is

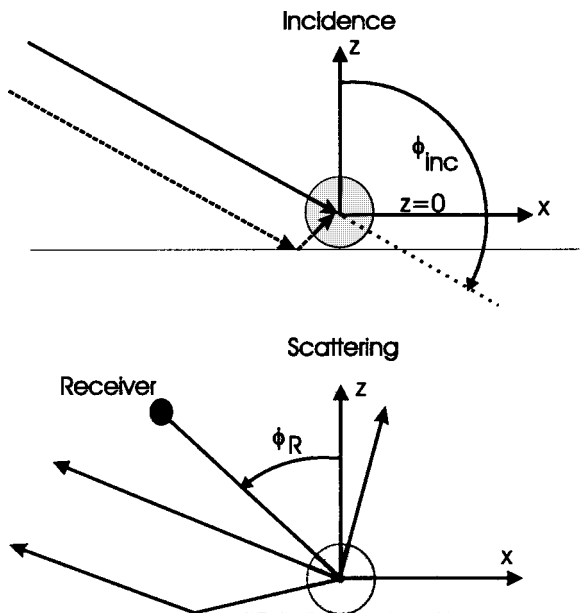


FIG. 1. Schematic of incident and scattering geometry.

similar in approach, with only a difference in some of the details. Some of the results will be merely stated for this case.

For the sphere we can write

$$p^{sc} = \sum_{n=0}^{\infty} \sum_{m=0}^n t_n h_n(kR) q_{nm} P_n^m(\cos \phi) \cos(m\beta), \quad (2)$$

where q_{nm} are the coefficients for the incident field

$$p^{in} = \sum_{n=0}^{\infty} \sum_{m=0}^n q_{nm} P_n^m(\cos \phi) j_n(kR) \cos(m\beta), \quad (3)$$

and $k \equiv \omega/c$. The scattering coefficients, t_n , are determined from the solution of the continuity equations at the spherical shell's interfaces.⁹ We have used the simplification in Eq. (3) that the incident plane wave is propagating along the direction $\beta_{inc} = 0$.

We now follow Refs. 3 and 4 in deriving a multiple scattering solution for a sphere on a seabed. Let us consider a single azimuthal order, m , for the sphere (the sphere/seabed scattering problem is azimuthally symmetric). We can write the outgoing scattered field from the sphere, above the interface, in the form

$$p_m^{sc} = \sum_{n_1=m}^N a_{n_1,m} h_{n_1}(kR) P_{n_1}^m(\cos \phi), \quad (4)$$

where we have truncated the infinite sum. The spherical coordinates (R, ϕ) are based with respect to the center of the sphere. The vertical plane-wave decomposition of the terms in Eq. (4) is for $z > 0$,

$$h_n(kr) P_n^m(\cos \theta) = i^{n-m} \int_0^{\infty} \frac{p J_m(p\xi) e^{+i\gamma z}}{k\gamma} P_n^m\left(\frac{-\gamma}{k}\right) dp, \quad (5)$$

and for $z < 0$

$$h_n(kr) P_n^m(\cos \theta) = i^{n-m} \int_0^{\infty} \frac{p J_m(p\xi) e^{-i\gamma z}}{k\gamma} P_n^m\left(\frac{+\gamma}{k}\right) dp \quad (6)$$

with $\gamma \equiv \sqrt{k^2 - p^2}$. The upgoing wave field resulting from the reflection off the seabed of the term of Eq. (6) is

$$U_{n_1}^m = i^{n_1-m} \int_0^{\infty} J_m(pr) e^{2i\gamma a} \Gamma(p) P_{n_1}^m\left(\frac{+\gamma}{k}\right) \frac{e^{i\gamma z}}{k\gamma} p dp, \quad (7)$$

where $\Gamma(p)$ is the plane-wave reflection coefficient. Now using the expansion¹⁰ that

$$J_m(pr) e^{i\gamma z} = \sum_{n_2=m}^{\infty} i^{n_2-m} (2n_2+1) \frac{(n_2-m)!}{(n_2+m)!} \times P_{n_2}^m(\cos \phi) P_{n_2}^m\left(\frac{+\gamma}{k}\right) j_{n_2}(kR), \quad (8)$$

we can write

$$U_{n_1}^m = i^{n_1-m} \sum_{n_2=m}^N i^{n_2-m} (2n_2+1) \frac{(n_2-m)!}{(n_2+m)!} P_{n_2}^m(\cos \phi) \times j_{n_2}(kR) \int_0^{\infty} P_{n_2}^m\left(\frac{\gamma}{k}\right) P_{n_1}^m\left(\frac{\gamma}{k}\right) \frac{\Gamma(p) e^{2i\gamma a}}{k\gamma} p dp, \quad (9)$$

where (R, ϕ) are the spherical coordinates corresponding to the cylindrical coordinates (r, z) . Thus the conversion matrix from the v outgoing coefficient into the u incoming coefficient, for the m azimuthal order, is given by

$$C_{uv}^m \equiv i^{v-m} i^{u-m} (2u+1) \frac{(u-m)!}{(u+m)!} P_u^m(\cos \phi) j_u(kR) \times \int_0^{\infty} P_u^m\left(\frac{\gamma}{k}\right) P_v^m\left(\frac{\gamma}{k}\right) \frac{\Gamma(p) e^{2i\gamma a}}{k\gamma} p dp. \quad (10)$$

If we systematically write down the multiple interactions between the interface and the sphere and let \mathbf{p}^{inc} denote the vector of incident coefficients, then

$$\mathbf{p}^{out,m} = (T + TCT + TCTCT + \dots) \mathbf{p}^{inc,m} = (T^{-1} - C^m)^{-1} \mathbf{p}^{inc,m}, \quad (11)$$

where T denotes the diagonal T -matrix for free space scattering with the last $N-m+1$ entries. Its diagonal elements are the t_n of Eq. (2). The incident field includes the seabed reflected component as well as the direct component. The vector of coefficients $\mathbf{p}^{out,m}$ expresses the scattered field in the neighborhood of the sphere in terms of the spherical basis set. In order to propagate this field to a receiver location the vertical plane-wave decomposition, Eq. (6) is used and the seabed reflection incorporated as was done in Eq. (7), yielding the pressure field, $p^m(r, z)$ for the m th angular order. Finally the azimuthal sum of these fields yields the field in the water column.

$$p(r, z, \beta) = \sum_{m=0}^N \epsilon_m p^m(r, z) \cos(m\beta), \quad (12)$$

where $\epsilon=1$ for $m=0$ and is equal to two otherwise. For the backscattering geometry $\beta=\pi$.

For an infinite cylinder the derivation is similar, just the details of the special functions are different; the incident field is written in the form

$$p^{\text{inc}} = \sum_{n=-N}^N a_n J_n(kr) e^{in\theta}, \quad (13)$$

and the scattered field in the form

$$p^{\text{sc}} = \sum_{n=-N}^N b_n H_n(kr) e^{in\theta}. \quad (14)$$

The scattered field components are then rewritten in terms of a plane-wave decomposition,

$$H_n(kr) e^{in\theta} = \frac{e^{-in\pi/2}}{\pi} \int_{-\infty}^{\infty} \frac{e^{i(k_x x_R + \gamma z_R)}}{\gamma} e^{in\psi} dk_x, \quad (15)$$

and $z < 0$,

$$H_n(kr) e^{in\theta} = \frac{e^{-in\pi/2}}{\pi} \int_{-\infty}^{\infty} \frac{e^{i(k_x x_R - \gamma z_R)}}{\gamma} e^{in(\pi-\psi)} dk_x, \quad (16)$$

where $\psi \equiv \cos^{-1}(\gamma/k)$.

The effect of the seabed reflection is incorporated into the expansion of Eq. (16) and the plane waves of the integral representation are expanded in terms of Bessel functions. This allows for the determination of the conversion matrix C which is given by

$$C_{uv} = i^{(u+v)} \int_{-\infty}^{\infty} \Gamma(k_x) \frac{e^{2i\gamma a} e^{-(u+v)\psi}}{\gamma\pi} dk_x. \quad (17)$$

As for the spherical case we can write an expression for the overall field scattered by the cylinder in the form,

$$\mathbf{p}^{\text{out}} = (T^{-1} - C)^{-1} \mathbf{p}^{\text{inc}}, \quad (18)$$

where the incident field includes the reflection off the seabed. The seabed is also accounted for in the propagation of the scattered field to the receiver.

The single-scatter approximation results from setting C or C^m equal to zero in Eq. (18) or Eq. (11). Thus the scattered fields from the cylinder or sphere are simply modeled by the free-space T -matrix. However, the effect of the seabed is included in the propagation of both the incident and scattered fields. The incident field is taken to be the coherent sum of the direct and seabed reflected plane waves; these plane waves are then expanded in terms of the incoming Bessel functions (spherical or cylindrical). The resultant scattered fields are then decomposed into plane waves and the downgoing portion (i.e., the decomposition for $z < 0$) is appropriately reflected off the seabed interface.

II. NUMERICAL SIMULATIONS

We will consider two basic cases; a generalized plane wave (i.e., the direct and reflected plane waves coherently combined) incident upon an infinite cylindrical shell resting on the oceanic bottom and a generalized plane wave incident upon a sphere resting on the bottom. For the infinite cylinder,

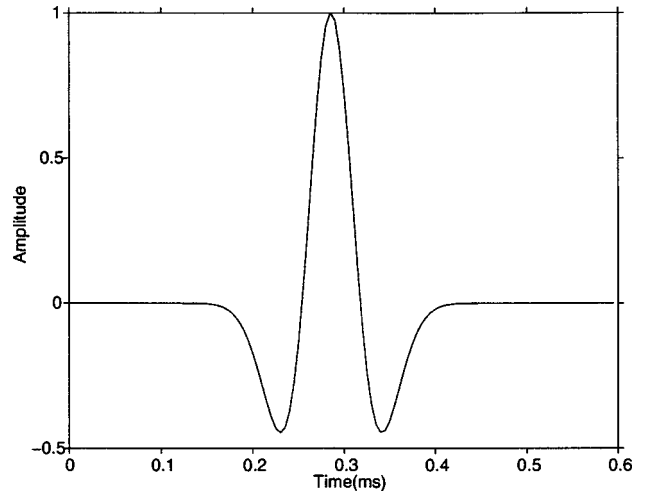


FIG. 2. Source wavelet used in computations.

the broadside geometry is considered. The numerical approach is basically the same in the two cases; the incident field and the scattered field incorporate the effect of the seabed reflection as discussed above. For the full multiple scattering solution, the free-space scattering matrix is augmented with the computed conversion matrices C_{uv}^m or C_{uv} in the manner of Eq. (11) or Eq. (18); for the single-scatter solution these matrices are not computed and are simply set to zero. In order to compute time domain signals, we compute the scattered signal at a receiver as a function of frequency and then Fourier synthesize the time domain signal. The Ricker wavelet (center frequency equals 7 kHz) which is used as the incident pulse in the simulations is shown in Fig. 2.

A. Water-filled cylindrical shell

In this first example we consider a 6-mm-thick steel-shelled cylinder of radius 0.25 m. The steel is taken to have the parameters: $C_p = 5950$ m/s, $C_s = 3240$ m/s, and $\rho = 7700$ kg/m³. The interior of the cylinder is taken to be filled with water. The cylinder lies on a sandy bottom for which we use the parameters: $C_p = 1710$ m/s, $\rho = 1800$ kg/m³, and we take the shear speed to be zero. The sound speed in the water was taken to be 1510 m/s.

For the curves of Fig. 3 we vary the angle of the receiver with respect to the cylinder center from 3° to 12° in steps of 1.5° (in Fig. 1 we showed an angle of incidence, ϕ_{inc} measured off the vertical axis; for the remainder of this paper, angles will be measured off the horizontal axis) and compute the received time series at a range of 7.5 m using the single-scatter approximation. The curves have been normalized by the maximum amplitude of the first curve. As can be seen, the specular reflection portion of the time series shows the most variation. For the range of angles considered in the computations there is a widening of the specular pulse until about 10.5° at which point the specular reflections propagating along the direct and interface reflected paths begin to become distinguishable. There is a slight increase in amplitude going from the first to second curve, and then the amplitude of the specular portion of the signal steadily decreases. In order to show the accuracy of the single-scatter

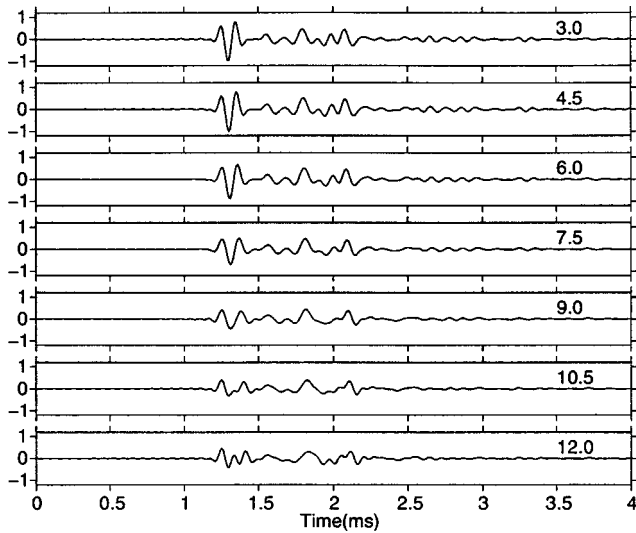


FIG. 3. Variation of backscattered time series as a function of receiver angle for an angle of incidence of 3° ; receiver angles indicated on plots.

approximation, we repeat the computations for the first and last curves of Fig. 3 using both the single-scattering and the full multiple scattering solution. For both receiver angles, the curves of Fig. 4 have been normalized by the maximum amplitude of the single-scatter solution. As can be seen, the single-scatter time series (dashed line) are very close to those of the full multiple scattering solution (solid line) for both the specular and circumferential arrivals.

We now fix the angle of incidence and the receiver angle to be 4.5° and consider variations of the bottom sediment. The sediment properties are varied in the following fashion: $c_{\text{sed}} = 1510 + (j - 1) \times 10$ m/s and the density is fixed at $\rho = 1.0$ g/cm³. The resulting normalized time series (normalized by the peak amplitude of the first curve) are shown in Fig. 5 (it should be noted that the amplitude of the first curve of Fig. 3 is very close to that of the last curve of Fig. 5, but because of the different normalizations across the sets of curves this is not apparent). There is a doubling of amplitude

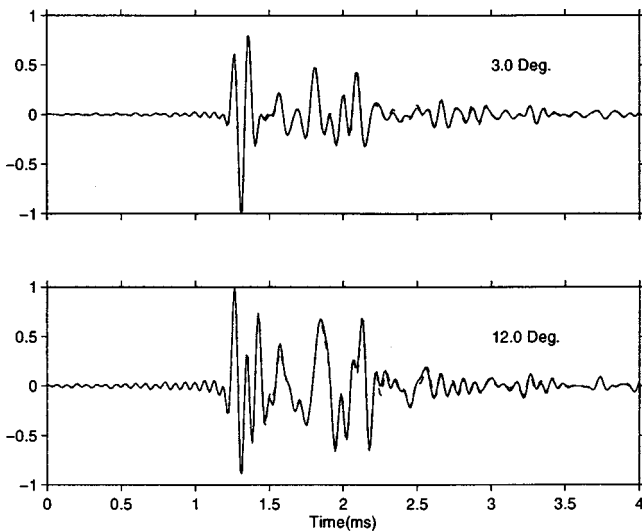


FIG. 4. Comparison of time series computed using the full multiple scattering solution (solid line) and the single-scattering solution (dashed line) for a cylinder for receiver angles of (a) 3° and (b) 12° .

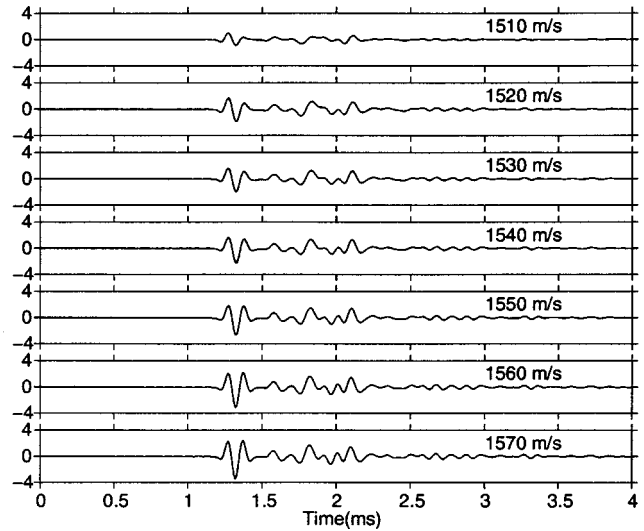


FIG. 5. Variation of backscattered time series from cylinder as a function of bottom sound speed.

in going from the first curve (free-space result) to the second curve with only a 10 m/s sound speed jump at the bottom. Over the subsequent curves there is a slower increase in amplitude and an increase in the amplitude of the second positive peak in the specularly reflected pulse (i.e., the shape of the specular reflection changes). Time series computed with higher sound speeds in the bottom showed very little change from the latter curves of Fig. 5.

We have shown in these numerical simulations that for low grazing angles (both for the incident energy and the angle of the receiver with respect to the scatterer) the scattering of energy off the bottom interface can increase the backscattered levels significantly from the free-space results. Also the shape of the specular reflection is changed as a consequence of the coherent interference between direct and bottom reflected energy. For low grazing angles, the backscattered signal is almost invariant to the sediment parameters except for sound speeds very close to the water value. This is because a small grazing angle becomes subcritical for only a small sound speed contrast at the bottom. After the angles of incidence and the receiver angle are subcritical, the bottom characteristics have a very small effect on the reflection processes in the water column. The above results are for a particular incident pulse and a particular cylinder radius. These effects will probably be different for significantly higher centre frequencies or for larger scattering objects for which the direct and bottom paths will start to become resolvable in the time domain.

B. Solid aluminum sphere

We now repeat the numerical simulations of the previous subsection but for a 0.3-m radius, solid aluminum sphere. For the sphere we use the values $c_p = 6380$ m/s, $c_s = 3100$ m/s, and $\rho = 2790$ kg/m³. The bottom sediment has the parameters of the previous subsection. In Fig. 6 we show the backscattered time series for a fixed angle of incidence of 3° and for the angle of the receiver varied. The trend of this figure is the same as in the cylinder case—there is a widening of the specularly reflected pulse with increasing angles—

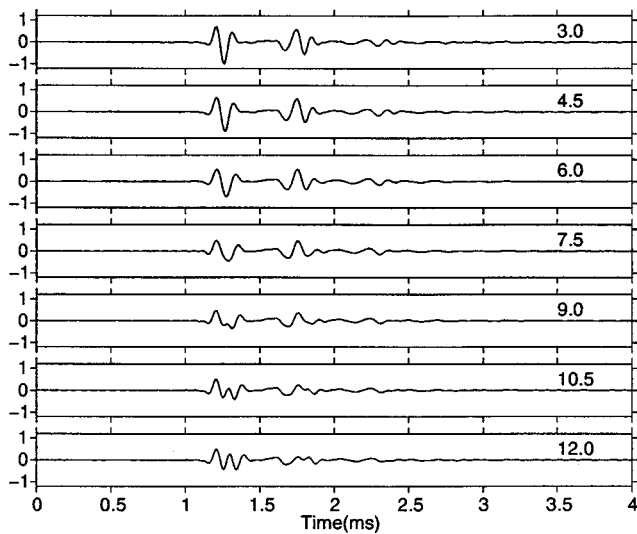


FIG. 6. Variation of backscattered time series from sphere as a function of receiver angle for an angle of incidence of 3° ; receiver angles indicated on plots.

for the case of varying the receiver angle, the direct and reflected portions of the specularly reflected pulses start to be distinct in the time domain. There is also a variation in amplitude of the backscattered signal with respect to angle. An interesting feature of the backscattered signal from the aluminum sphere is that for these low incidence and receiver angles, the reflected pulse “appears” to be the negative of the source pulse. This is the opposite of what one would expect in free space. Thus in this case, the presence of the bottom interface has dramatically changed the character of the specularly reflected pulse. The second pulse which is evident in the time series is a wave which has traveled circumferentially around the sphere; this particular wave is referred to as the Rayleigh wave in the scattering literature.⁹

In order to investigate the accuracy of the single-scattering approximation for scattering from a sphere on the seabed, we repeat the computations for the first and last curves of Fig. 6 using both the single-scatter and full-multiple scattering solutions. The curves for both receiver angles have been normalized by the maximum amplitude of the single-scatter time series. As can be seen from Fig. 7, the two computed curves, for both receiver angles, are very similar.

We now examine the variation of the backscattered time series as a function of the bottom sediment. We use the same sets of sediments as in the study of the water-filled cylinder. The resulting sets of time series are shown below in Fig. 8. As with the cylinder, the presence of the seabed significantly increases the backscattered amplitude from the free-space results (the first curve in Fig. 8). In Fig. 8 a gradual transition of the specular pulse shape due to the increasing sediment sound speed can be seen. There is a gradual change in the features of this pulse, such that the resulting pulse of the last curves seems to be the negative of the free-space pulse when shifted by a fraction of a millisecond.

III. REAL DATA EXAMPLES

During October/November 1996 the SACLANTCEN Mine Countermeasures Group performed sonar/object scat-

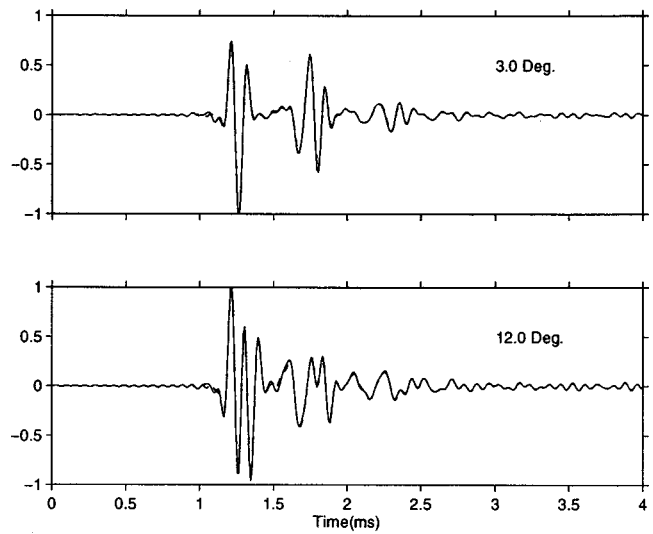


FIG. 7. Comparison of time series computed using the full multiple scattering solution (solid line) and the single-scattering solution (dashed line) for a sphere for receiver angles of (a) 3° and (b) 12° .

tering measurements near the island of Elba. We will consider data obtained for a water-filled cylinder and a solid aluminum sphere lying on a sandy bottom. A parametric source was mounted on a 3.7-m high tower and was typically 40–50 m away from the scattering object. This resulted in an effective grazing angle of approximately 4° . A receiving hydrophone was positioned 6–7.5 m in front of the object by a diver; this hydrophone is very approximately along an imaginary line from the object to the top of the tower. The same type of experiment setup was used for free-field measurements described in Ref. 11.

For the modeling, we use the single-scatter approximation; as was shown in the numerical examples, this approximation agrees very well with the full multiple scattering solution, but is significantly computationally faster.

A. Water-filled cylinder

The cylindrical shell used in these experiments is the same as that used in previous scattering experiments.¹¹ It is 2

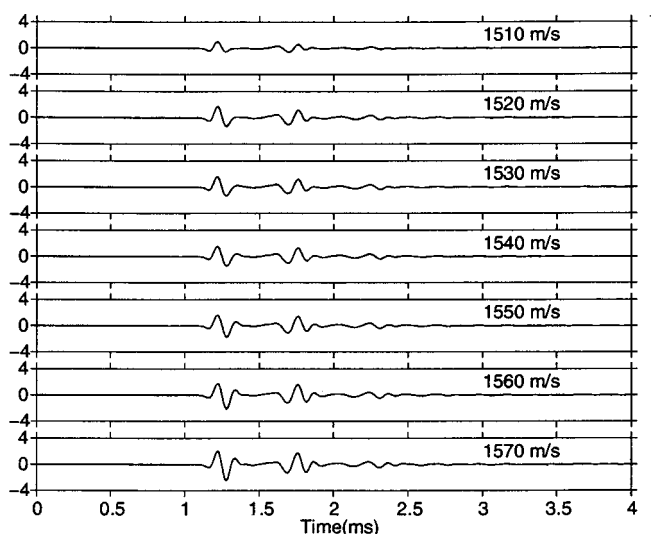


FIG. 8. Variation of backscattered time series from sphere as a function of bottom sound speed.

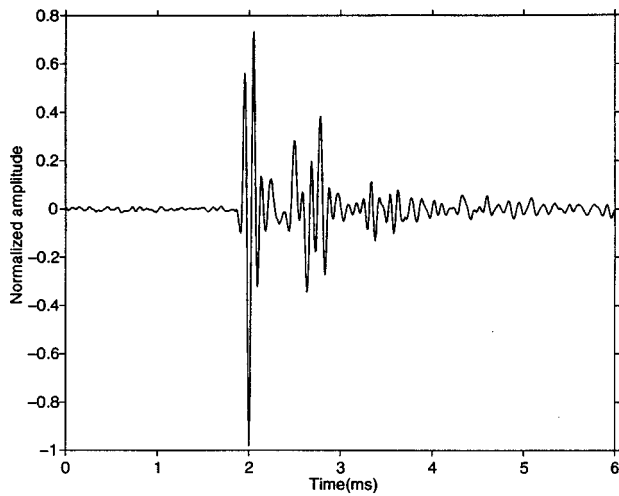


FIG. 9. Time series for backscatter from cylinder.

m long and has a radius of 0.25 m. The shell is steel and is 6 mm thick. The cylinder is filled with water. We consider the cylinder when it is in the broadside position with respect to the receiver and incident beam. The finite cylinder is modeled as an infinitely long cylinder; this is a good approximation for the frequencies and receiver range of this experiment.¹¹ The source pulse was approximately that of Fig. 2; however, instead of explicitly modeling the source, a recorded direct arrival pulse shape from the experiment of Ref. 11 was used. We did not use the recorded incident pulses from the present experiment because these pulses often included some bottom-reflected energy. For the data shown below, the source was located 44.5 m away from the cylinder.

In general, there is uncertainty with respect to some of the details of the experimental geometry. The receiver (reference) hydrophone was aligned between the source and target by having divers run a line from the tower to the target and suspending the hydrophone from this line. Even with this system, there may not have been perfect alignment between the source, hydrophone, and target due to slack in the line and currents in the water. The incident beam (which has a beamwidth of approximately $\pm 2.5^\circ$) may have not been perfectly aligned with the imaginary line between the hydrophone and object center. Because of these geometrical uncertainties, it was decided to compare normalized data and model time series (i.e., the absolute amplitude of the backscattered signal is not modeled).

We assume that the hydrophone was located at an angle of 4° with respect to the cylinder center and at a range of 7.5 m. We will take the bottom to have a compressional velocity of 1710 m/s and a density of 1800 kg/m^3 . In Fig. 9 we plot the recorded time series for the incident beam oriented at 3.5° . The amplitude of the time series has been normalized by the peak amplitude. There were other time series from this site and, although they are all fairly similar, there was some experimental variation in the details of the specular reflection.

In Fig. 10 we show the spectrum of the energy for the angle of incidence equal to 3.5° (solid line) and the resulting model spectra using: (1) a homogeneous free-space model

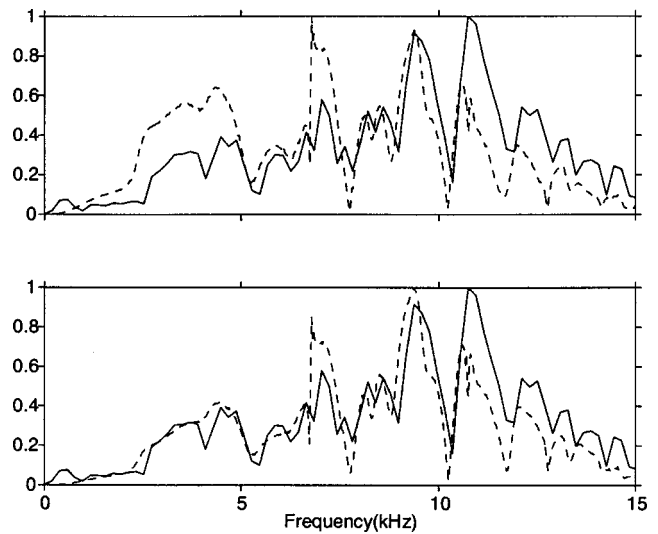


FIG. 10. Comparison of experimental (solid) and modeled (dashed) spectra for scattering from water-filled cylinder: (top) free-space model (bottom) single-scatter model.

(in fact, we use the SSA with zero impedance jump at the bottom); (2) the SSA model for the seabed. The free-space model correctly predicts the features of the spectrum but does not exhibit the correct amplitude trend. The SSA model is in better agreement, although there is still a difference in levels for the higher frequencies.

In Fig. 11 we show a similar comparison in the time domain. The modeled and experimental time series are positioned with respect to each other by aligning the positions of their maximum peak amplitudes (the maximum absolute values). As can be seen, the agreement between the data and the SSA model is very good and the SSA model has done a better job than the free-space model in predicting the backscattered signal.

B. Aluminum sphere

The aluminum sphere used in the experiments had a radius of 0.3 m. We use the following parameters for alumi-

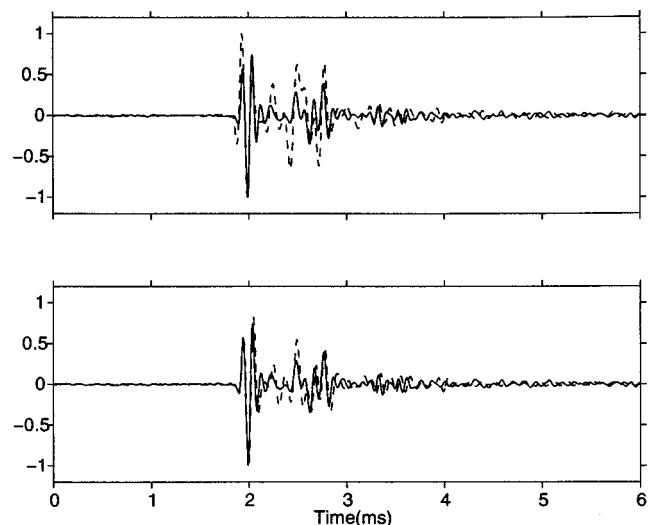


FIG. 11. Comparison of experimental (solid) and modeled time series (dashed) for (top) free-space model (bottom) single-scatter model.

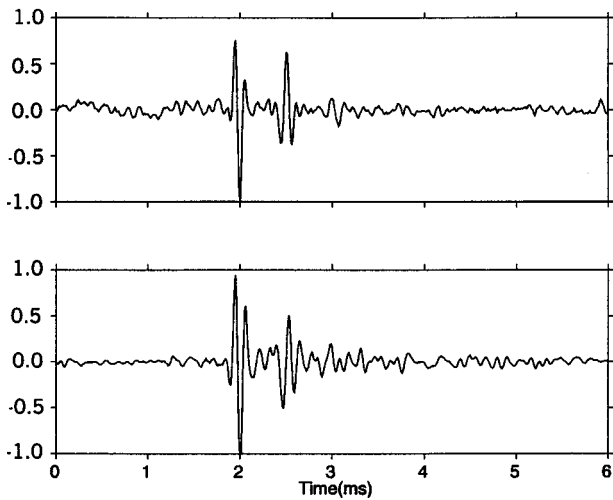


FIG. 12. Time series for scattering from aluminum sphere—different geometries and sites: (top) site 1; (bottom) site 2—Posidonia.

num: $c_p = 6380$ m/s, $c_s = 3100$ m/s, and $\rho = 2790$ kg/m³. In Fig. 12 we show two experimental time series (normalized to have unity peak amplitude). These time series are from two different days, sites, and experimental geometries. The first series was from a sandy bottom and the case the bottom was covered with a Mediterranean seagrass called Posidonia. The receiver was located approximately 6 m from the sphere in this case. Despite the different locations and somewhat different geometries, the experimental time series are very similar.

In Fig. 13 we show the experimental power spectrum of the backscattered signal (solid line) and the modeled spectra using a free-space model in Fig. 13(a) and using the SSA in Fig. 13(b). There is a slight improvement in the spectral amplitudes using the SSA. One noticeable feature in both Figs. 13(a) and 13(b) is the fact that the nulls predicted by the models are displaced from the experimental nulls. We have used an angle of incidence of 5° and a receiver angle of 3° in our numerical computations. We note that for frequen-

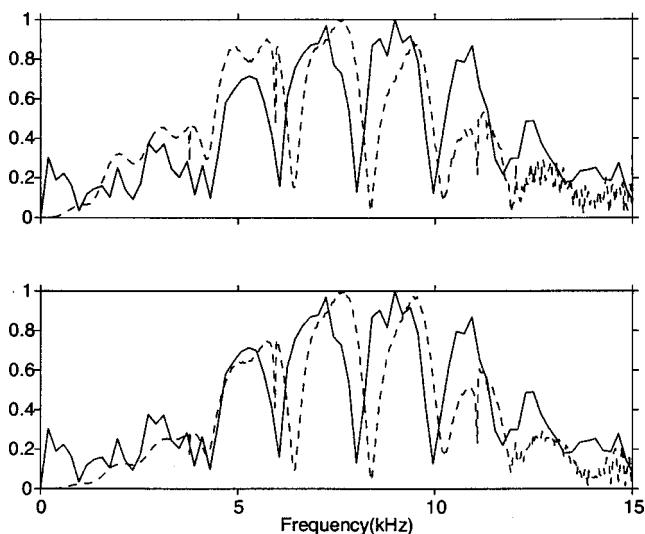


FIG. 13. Experimental (solid) and modeled (dashed) spectra for aluminum sphere at site 1: (top) free-space model; (bottom) single-scatter model.

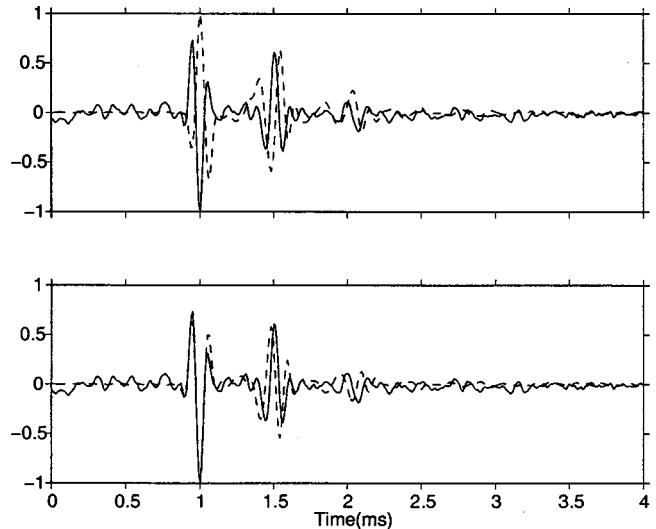


FIG. 14. Experimental (solid) and modeled (dashed) time series for site 1: (top) free-space model; (bottom) single-scatter model.

cies above about 13.0 kHz there is evidence of numerical oscillations in the model curves.

In Fig. 14 a comparison between the experimental and modeled time series is shown using first a free-space scattering model and then using the single-scatter model. The experimental and modeled time series have been positioned in time by aligning the peak amplitude of the specular reflections. In the case of the free-space model the modeled time series seems to be almost 180° out of phase with the experimental series which is consistent with the results and discussion of the simulations of Sec. II. From those simulation results (particularly, Fig. 8) it can also be seen that the peak amplitude of the free-space series should probably be aligned with the the first positive peak of the experimental data. The modeled time series using the single-scatter approximation is in very good agreement with the experimental data; however, it can be seen that the predicted Rayleigh wave arrival is slightly too fast. This is probably related to the null mismatch in the spectral domain.

We now repeat the analysis for the second site which is an area of the sea plant Posidonia. In Fig. 15 we show a comparison between the modeled and the experimental spectra. In this case, the nulls predicted by the models are even more displaced from the experimental nulls than for the previous site. Since the sphere is the same in both experiments, it would seem that either the geometry or the environment is affecting the spacing of these nulls, although changing the geometrical inputs to the model did not significantly improve the agreement. In Fig. 16 we show the comparison between the experimental and modeled time series, first using a free-space model and in the lower graph the SSA. Once again, the SSA correctly predicts the specular reflected pulse, while the free-space prediction appears to be almost 180° out of phase. It also predicts the Rayleigh pulse well in terms of shape but the arrival time is somewhat fast. The reason for this is not known; perhaps, it is some environmental effect (e.g., a slight settling of the sphere into the sediment, the presence of Posidonia, etc.), which is not correctly modeled. We can also improve the model results of the SSA by using a lower shear

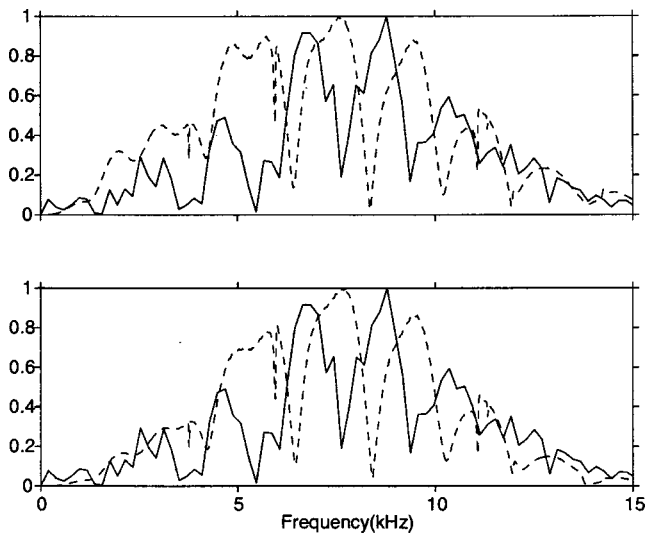


FIG. 15. Experimental (solid) and modeled (dashed) spectra for aluminum sphere at site 2 (Posidonia): (top) free-space model; (bottom) single-scatter model.

speed for aluminum (say 2900 or 3000 m/s) which effectively decreases the speed of the Rayleigh pulse.

In these figures we have aligned the modeled and experimental time series by aligning the absolute peak values. However, since the free-space results and SSA results are computed identically (the free-space result simply has no velocity or density jump at the interface) we can compare these series directly, which we do in Fig. 17. This emphasizes the previously discussed fact that the presence of the interface enlarges or diminishes certain features of the free-space specularly reflected pulse. The resulting pulse is not the negative version of the free-space pulse but only appears to be if one shifts the peak values in time by a small amount. The Rayleigh arrival looks quite similar for the two models and the relative arrival time of this pulse is the same in both cases.

Thus for the sphere we have seen that the model does a very good job in predicting the shape of the specular reflec-

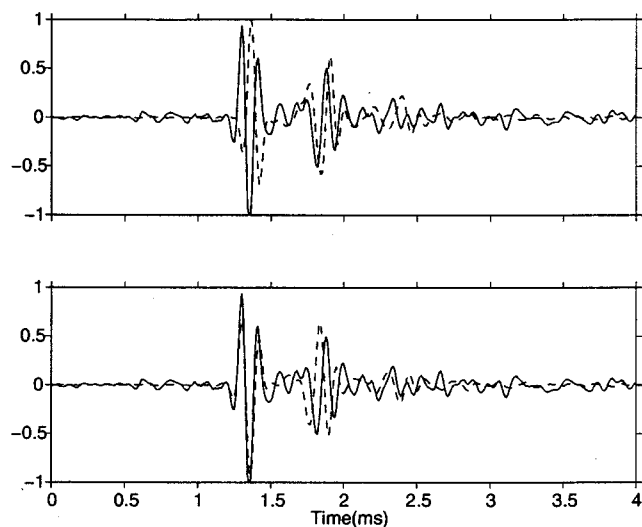


FIG. 16. Experimental (solid) and modeled (dashed) time series for site 2: (top) free-space model; (bottom) single-scatter model.

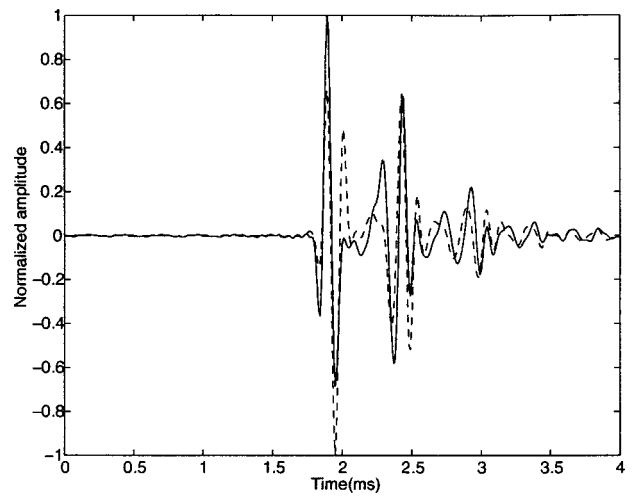


FIG. 17. Comparison of backscattered signal as computed by free-space model (solid) and single-scatter model (dashed) with same time scale.

tion. The Rayleigh arrival is also correctly predicted in terms of shape, but the model predicts a slightly earlier arrival time than is seen in the experimental data. This discrepancy was more significant for the second site (Posidonia site) than for the first.

IV. SUMMARY

In this paper a single-scattering method has been used to model scattering from cylinders and spheres lying on a seabed. This approximation was compared to the full multiple scattering solution and was found to be very accurate (for the geometries, frequencies, etc. considered in this paper). It was found that for shallow incidence and receiver angles, the amplitude and shape of the backscattered signal were significantly affected by the seabed. For these small angles, only a small velocity jump at the seabed is required to produce significant differences in the backscattered signal from the free space case. For larger impedance jumps, the backscattered signal is almost invariant to the sediment parameters.

We then modeled experimental data and had very good agreement. In the case of a water-filled cylindrical shell we showed good agreement with the entire signal. For a solid sphere we also had very good agreement in the time domain, although there was significant mismatch in the null structure in the spectral domain. In particular, the shape of the specularly reflected pulse which appears to be the negative of the incident pulse (not a positive reflection as one would expect) is correctly predicted by the model. However, the modeled arrival time for the Rayleigh pulse was a little too fast; this mismatch was larger for the second (Posidonia) site. The reasons for these mismatches are not known.

¹F. Ingenito, "Scattering from an object in a stratified medium," *J. Acoust. Soc. Am.* **82**, 2051–2059 (1986).

²M. D. Collins and M. F. Werby, "A parabolic equation model for scattering in the ocean," *J. Acoust. Soc. Am.* **85**, 1895–1902 (1989).

³R. H. Hackman and G. S. Sammelmann, "Multiple-scattering analysis for a target in an oceanic waveguide," *J. Acoust. Soc. Am.* **84**, 1813–1825 (1988).

⁴R. Lim, J. L. Lopes, R. H. Hackman, and D. G. Todoroff, "Scattering by objects buried in underwater sediments: Theory and experiment," *J. Acoust. Soc. Am.* **93**, 1762–1783 (1993).

- ⁵P. Gerstoft and H. Schmidt, "A boundary element approach to ocean seismoacoustic facet reverberation," *J. Acoust. Soc. Am.* **89**, 1629–1642 (1991).
- ⁶J. A. Fawcett, "A plane-wave decomposition method for modeling scattering from objects and bathymetry in a waveguide," *J. Acoust. Soc. Am.* **100**, 183–192 (1996).
- ⁷J. A. Fawcett, "Acoustic scattering from cylindrical objects embedded between two half-spaces," *J. Acoust. Soc. Am.* **100**, 3053–3060 (1996).
- ⁸R. Lim, "Acoustic scattering by a partially buried three-dimensional elastic object," *J. Acoust. Soc. Am.* **99**, 2498 (1996).
- ⁹N. D. Veksler, *Resonance Acoustic Spectroscopy* (Springer-Verlag, New York, 1993).
- ¹⁰J. Stratton, *Electromagnetic Theory* (McGraw-Hill, New York, 1941).
- ¹¹W. L. J. Fox, J. A. Fawcett, D. Jourdain-Albonico, and A. Tesei, "Measurements of free-field acoustic scattering from cylindrical shells," SACLANTCEN Memorandum SM-331, 1997.

Benchmark solutions of plane wave bottom reflection loss

Michael A. Ainslie and Alvin J. Robins

BAeSEMA Ltd., Apex Tower, 7 High Street, New Malden, Surrey KT3 4LH, England

Mark K. Prior

DERA, Building A22, Winfrith Technology Centre, Winfrith Newburgh, Dorset DT2 8XJ, England

(Received 25 July 1997; accepted for publication 25 August 1998)

Benchmarks of plane wave bottom reflection loss versus grazing angle are presented at three frequencies (1.5, 15, and 150 Hz) for four different bottom types. Each bottom type comprises a layered fluid sediment representing either sand or mud, overlying a uniform solid substrate (mudstone or basalt). The benchmarks are calculated using exact analytical solutions where available (primary benchmarks) or the numerical model SAFARI-FIPR (secondary benchmarks). The accuracy of the secondary benchmarks is demonstrated by comparison with alternative solution methods (diagnostics). The sensitivity to the assumed density profile is examined for one of the bottom types. © 1998 Acoustical Society of America. [S0001-4966(98)02212-7]

PACS numbers: 43.30.Ma, 43.30.Dr [DLB]

INTRODUCTION

Accurate prediction of bottom reflection loss is an essential ingredient to underwater sound propagation modeling because of the cumulative effect of repeated bottom interactions, especially in shallow water. Here we consider a layered fluid sediment overlying a uniform solid substrate using two different sediment profiles: a straightforward linear k^2 profile and a more realistic BLUG (bottom loss up-grade) profile often used to represent measured geoacoustic data.^{1,2}

For the linear k^2 profile an exact analytical solution is known³ which we evaluate. Following the convention of Buckingham and Tolstoy,⁴ we refer to evaluations of this exact solution as *primary* benchmarks because no approximations are made other than computer rounding errors. For the BLUG profile no such solutions are available and instead we use the numerical model SAFARI-FIPR⁵ (hereafter referred to as FIPR) to predict bottom loss as a function of angle and frequency for various bottom types. The FIPR predictions are referred to as *secondary* benchmarks because, although the computational method is exact, it requires the sediment to be discretized on a finite depth grid and must be checked for convergence. In addition to these convergence checks, secondary benchmarks are also checked for accuracy by comparison with approximate analytical solutions or “diagnostics.” Although approximate, these diagnostics provide asymptotic precision checks in high and low frequency limits. The purpose of the benchmarks is to provide a set of ground truth reference solutions against which the accuracy of other models can be assessed.

We acknowledge the limitation imposed by neglecting

sediment rigidity.⁶ It is hoped to extend the results in the future using methods developed for a solid sediment.^{7,8}

Section I describes four geoacoustic environments and this is followed by benchmark results for each environment in Sec. II. In Sec. III we examine sensitivity to the density profile for one of these environments. The Appendix contains a description of the analytical solutions.

I. ENVIRONMENTS

A. BLUG profile

1. Tabulated results

We consider plane waves incident from the ocean on a fluid sediment layer overlying a solid substrate. The ocean is modeled as a uniform lossless fluid of sound speed 1500 m/s (c_1) and density 1 g/cm³ (ρ_1). The sediment layer has a BLUG sound speed profile (also known as “Low Frequency Bottom Loss” or LFBL and frequently used to represent measured data^{1,2,9}) given by

$$c_2(z) = [(1 + \beta)^2 c_0^2 + 2(1 + \beta)c_0 g_0 z]^{1/2} - \beta c_0, \quad (1)$$

and a linear absorption profile so that the attenuation coefficient α (in dB per wavelength) is

$$\alpha_2(z) = (K_0 + K'z)c_2(z), \quad (2)$$

where K_0 and K' are constants determining the surface value of the sediment attenuation coefficient (in dB per meter per hertz) and its gradient. The parameters c_0 and g_0 in Eq. (1) are the sound speed and its derivative at the surface (the top of the sediment, i.e., $z=0$). The second derivative, determined by the constant dimensionless parameter β , decreases

TABLE I. Sediment parameters.

Sediment	Thickness h (m)	c_0/c_1	g_0 (/s)	β	K_0 (dB/m Hz)	K' (dB/m ² Hz)	Density ρ_2 (g/cm ³)
A (mud)	200	0.996	1.7	+0.86	3.0×10^{-5}	$+1.5 \times 10^{-7}$	1.92
B (sand)	20	1.091	20.0	-0.97	3.0×10^{-4}	-6.0×10^{-7}	1.80

TABLE II. Substrate parameters.

Substrate	Compressional wave		Shear wave		Density $\rho_3(\text{g/cm}^3)$
	Speed $c_3(\text{m/s})$	Attenuation $\alpha_3(\text{dB}/\lambda)$	Speed $v_3(\text{m/s})$	Attenuation $\delta_3(\text{dB}/\lambda)$	
1 (soft)	3000	0.3	1400	0.5	2.1
2 (hard)	4500	0.2	2400	0.5	2.6

monotonically in magnitude with increasing depth from its surface value $-g_0^2/c_0(1+\beta)$. The acoustic properties of the BLUG profile are described by Ainslie and Robins.¹⁰

Two different sediment types are considered (sediments ‘‘A’’ and ‘‘B’’ in Table I), representing layers of mud (silt-clay) and sand, respectively.¹¹ A uniform density is assumed initially for both sediment types. The rather high value for the density of mud used here is an artefact of the BLUG database, thought to result from a curve fitting exercise to match reflection loss data at steep angles; a more realistic value is considered in Sec. III. Similarly there are two substrate types (1 and 2, see Table II), based on data from Hamilton.¹² One has a high shear speed, representing basalt (substrate 2). Substrate 1 is a softer material with a significantly lower shear speed more characteristic of mudstone. Both substrates satisfy the inequality⁵

$$\frac{\delta_3}{\alpha_3} < \frac{3}{4} \left(\frac{c_3}{v_3} \right)^2. \quad (3)$$

The complete environment is made up of the sediment layer sandwiched between the substrate layer below and water above, as shown in Table III. Subscripts 1, 2, and 3 in Tables I–III refer, respectively, to properties in the water, sediment, and substrate.

B. Linear k^2 profile

By ‘‘linear k^2 ’’ we mean a profile whose wave number squared varies linearly with depth:

$$k_2(z) = k_0(1 - 2qz)^{1/2}, \quad (4)$$

where k_0 and q are complex constants which we determine by matching sound speed and attenuation at top and bottom of the sediment layer (of thickness h). Defining the terms

$$\alpha_0 = \alpha_2(0), \quad (5)$$

$$\alpha_h = \alpha_2(h), \quad (6)$$

and

$$c_h = c_2(h), \quad (7)$$

it follows that

$$k_0 = \frac{\omega}{c_0} \left(1 + i \frac{\alpha_0}{40\pi \log e} \right) \quad (8)$$

and

$$2qh = 1 - \frac{c_0^2(40\pi \log e + i\alpha_h)^2}{c_h^2(40\pi \log e + i\alpha_0)^2}. \quad (9)$$

II. RESULTS FOR UNIFORM DENSITY

A. Primary benchmarks (linear k^2)

1. Tabulated results

Ainslie³ presents an exact analytical solution for the amplitude plane wave reflection coefficient (r) due to a linear k^2 profile, the formula for which is summarized here in the Appendix. We evaluate this formula for all four combinations of sediments A and B and substrates 1 and 2. The power reflection coefficient $|r|^2$ is evaluated at 5° intervals for three frequencies (1.5, 15, and 150 Hz) and presented in Table IV. The notation A1, A2, and so on refers to the sediment and substrate types from Tables I and II in an obvious fashion. These and all subsequent numerical results are calculated using single precision arithmetic on a microVAX 3100-80. Airy functions required for the implementation of Eq. (A12) are evaluated using the NAG¹³ library routines S17DGF and S17DHF. These results are referred to as primary benchmarks and have been checked against two alternative solution methods: the PARIS program^{7,14} which inverts a small (7×7) matrix equation to obtain the reflection coefficient, and calls the same two NAG routines; and the FIPR program⁵ which implements a numerical method requiring a fine computational grid and evaluates Airy functions using the method of Schulten *et al.*¹⁵ FIPR requires that the sediment layer be represented by a number of sublayers. In each sublayer the attenuation coefficient (in dB per wavelength) and the density are fixed and the squared wave number varies linearly with depth. Successive FIPR runs were carried out with increasingly fine layering until the results had converged to three decimal places in $|r|^2$.

2. Accuracy of primary benchmarks

The accuracy of primary benchmarks is assessed by comparing them with the predictions of PARIS and FIPR. The maximum discrepancy in $|r|^2$ compared with PARIS is 0.001. The maximum discrepancy with FIPR is 0.002, but this occurs only once (A2, 150 Hz, 40°); in all other cases the discrepancy is 0.001 or less. We believe the primary benchmarks are accurate to within a tolerance of ± 0.001 .

TABLE III. Construction of three-layer environment.

Layer i	Compressional wave		Shear wave		Density ρ_i
	Speed c_i	Attenuation α_i	Speed v_i	Attenuation δ_i	
1 (water)	1500 m/s	0	0	0	1.0 g/cm ³
2 (sediment)	See Eq. (2.1) and Table I	See Eq. (2.2) and Table I	0	0	See Table I
3 (substrate)	See Table II	See Table II	See Table II	See Table II	See Table II

TABLE IV. Primary benchmarks for a linear k^2 profile: power reflection coefficient $|r|^2$ vs frequency and angle.

Angle (deg.)	Sea bed type											
	A1			A2			B1			B2		
	1.5 Hz	15 Hz	150 Hz	1.5 Hz	15 Hz	150 Hz	1.5 Hz	15 Hz	150 Hz	1.5 Hz	15 Hz	150 Hz
5	0.597	0.963	0.780	0.835	0.963	0.780	0.451	0.671	0.943	0.942	0.478	0.943
10	0.399	0.959	0.518	0.866	0.959	0.518	0.190	0.474	0.907	0.934	0.677	0.907
15	0.308	0.956	0.278	0.887	0.955	0.278	0.073	0.362	0.886	0.940	0.755	0.885
20	0.263	0.931	0.246	0.894	0.896	0.246	0.032	0.297	0.863	0.944	0.791	0.860
25	0.235	0.713	0.183	0.888	0.742	0.183	0.032	0.254	0.805	0.945	0.803	0.796
30	0.214	0.626	0.016	0.867	0.797	0.016	0.048	0.223	0.439	0.941	0.796	0.604
35	0.196	0.425	0.004	0.820	0.908	0.102	0.068	0.199	0.296	0.927	0.765	0.303
40	0.185	0.006	0.013	0.745	0.765	0.224	0.083	0.183	0.220	0.884	0.713	0.682
45	0.192	0.237	0.148	0.743	0.818	0.342	0.089	0.186	0.073	0.698	0.728	0.150
50	0.244	0.201	0.095	0.818	0.687	0.398	0.103	0.233	0.229	0.646	0.793	0.614
55	0.401	0.009	0.112	0.391	0.235	0.008	0.239	0.384	0.085	0.476	0.379	0.030
60	0.654	0.689	0.309	0.286	0.360	0.163	0.772	0.629	0.538	0.478	0.280	0.316
65	0.181	0.173	0.031	0.222	0.216	0.024	0.392	0.178	0.283	0.449	0.220	0.327
70	0.149	0.039	0.220	0.558	0.376	0.461	0.370	0.147	0.181	0.688	0.537	0.478
75	0.133	0.004	0.153	0.292	0.059	0.269	0.368	0.131	0.076	0.587	0.290	0.152
80	0.124	0.039	0.232	0.276	0.136	0.386	0.371	0.122	0.019	0.586	0.276	0.048
85	0.118	0.080	0.020	0.272	0.216	0.027	0.374	0.117	0.005	0.590	0.272	0.026
90	0.117	0.096	0.121	0.271	0.245	0.218	0.375	0.115	0.005	0.592	0.271	0.028

B. Secondary benchmarks (BLUG)

Table V presents secondary benchmarks of $|r|^2$ for the same four combinations as in Sec. II A but for a BLUG sediment profile. They are calculated using FIPR and have been checked for convergence to three decimal places. The same data (actually reflection loss $-20 \log|r|$, and on a finer angle grid) are plotted as solid lines in Figs. 1–4. The dashed and dotted lines, collectively referred to as “diagnostics,” are approximate analytical solutions used for checking purposes explained in more detail below. The figure in brackets following the absolute frequency in Hz is the dimensionless frequency $\omega h/c_1$.

1. Sediment A (mud)

The mud parameters are representative of a deep water calcareous (silt-clay) sediment with a small sound speed ratio (less than unity) at the water–sediment interface and a monotonically increasing sound speed thereafter to 1815 m/s at a depth of 200 m. Secondary benchmarks are shown in Fig. 1 (for substrate 1) and Fig. 2 (for substrate 2).

At high frequencies the appropriate diagnostic is the Langer approximation described in the Appendix, which is shown as a dashed line in Figs. 1–4. At 150 Hz, the highest frequency considered [Figs. 1(a), 2(a)] there is excellent

TABLE V. Secondary benchmarks for a BLUG profile: power reflection coefficient $|r|^2$ vs frequency and angle.

Angle (deg.)	Sea bed type											
	A1			A2			B1			B2		
	1.5 Hz	15 Hz	150 Hz	1.5 Hz	15 Hz	150 Hz	1.5 Hz	15 Hz	150 Hz	1.5 Hz	15 Hz	150 Hz
5	0.615	0.970	0.829	0.811	0.970	0.829	0.452	0.685	0.949	0.941	0.468	0.949
10	0.419	0.966	0.743	0.859	0.966	0.743	0.191	0.492	0.916	0.934	0.675	0.916
15	0.325	0.964	0.722	0.884	0.964	0.722	0.073	0.379	0.897	0.940	0.755	0.897
20	0.277	0.951	0.228	0.892	0.941	0.228	0.033	0.311	0.879	0.944	0.790	0.878
25	0.248	0.855	0.467	0.886	0.814	0.467	0.032	0.267	0.842	0.945	0.802	0.827
30	0.225	0.533	0.382	0.864	0.729	0.382	0.049	0.234	0.658	0.941	0.794	0.726
35	0.206	0.512	0.009	0.816	0.906	0.096	0.069	0.208	0.122	0.927	0.761	0.040
40	0.194	0.020	0.106	0.739	0.824	0.109	0.083	0.192	0.283	0.884	0.707	0.692
45	0.200	0.189	0.176	0.743	0.767	0.541	0.090	0.194	0.057	0.698	0.728	0.221
50	0.252	0.235	0.180	0.821	0.730	0.431	0.103	0.240	0.219	0.647	0.796	0.617
55	0.409	0.002	0.165	0.399	0.174	0.267	0.240	0.391	0.136	0.476	0.386	0.005
60	0.659	0.688	0.359	0.293	0.365	0.155	0.773	0.633	0.494	0.478	0.286	0.282
65	0.187	0.211	0.211	0.229	0.260	0.247	0.392	0.184	0.294	0.449	0.225	0.338
70	0.155	0.072	0.053	0.563	0.441	0.041	0.370	0.151	0.215	0.688	0.542	0.507
75	0.139	0.006	0.166	0.297	0.061	0.290	0.368	0.136	0.114	0.587	0.294	0.216
80	0.129	0.015	0.061	0.281	0.087	0.105	0.371	0.126	0.042	0.586	0.279	0.093
85	0.124	0.046	0.207	0.276	0.153	0.349	0.374	0.121	0.014	0.590	0.275	0.042
90	0.122	0.059	0.099	0.275	0.180	0.177	0.375	0.119	0.008	0.592	0.274	0.033

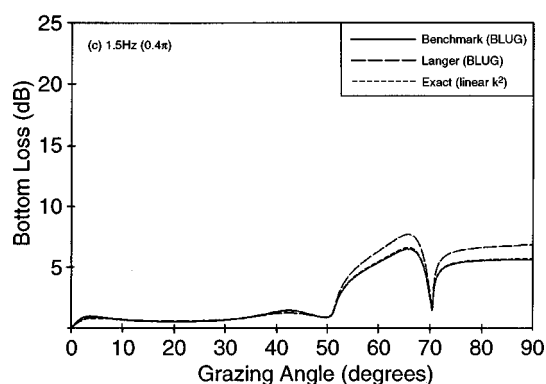
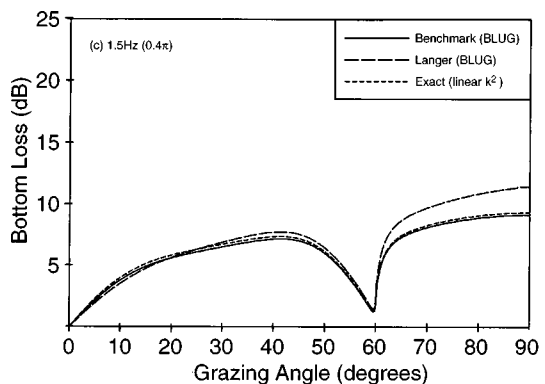
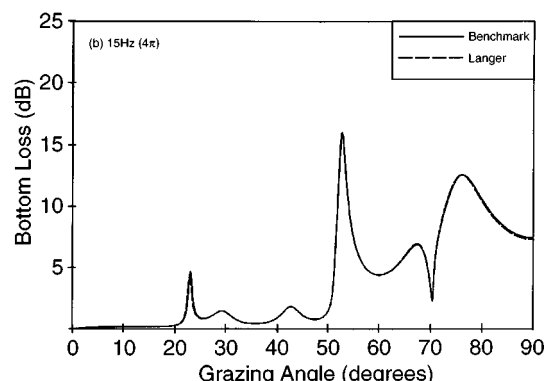
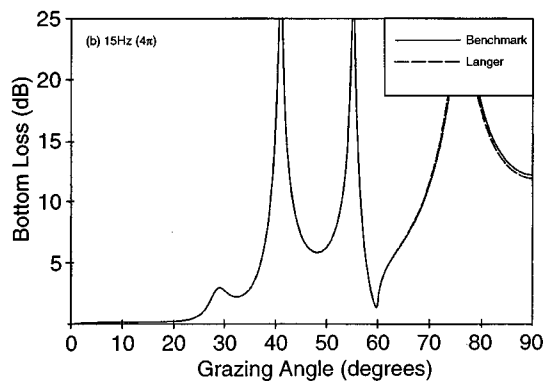
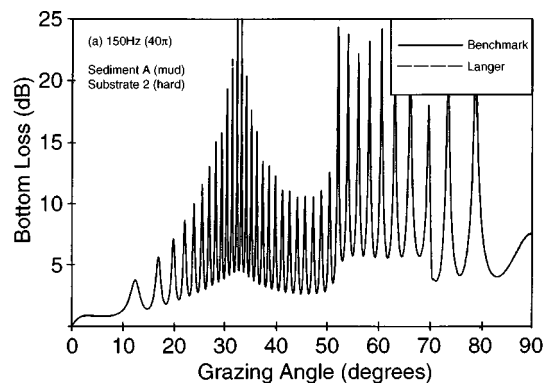
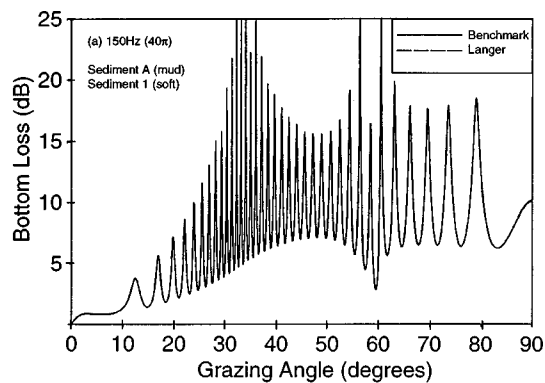


FIG. 1. Bottom loss versus angle for a mud sediment overlying a soft substrate (A1). The solid lines are benchmarks.

FIG. 2. Bottom loss versus angle for a mud sediment overlying a hard substrate (A2). The solid lines are benchmarks.

agreement between the solid and dashed lines, confirming the accuracy of the FIPR benchmarks at high frequency. At 15 Hz small differences appear near normal incidence [Figs. 1(b) and 2(b)].

At lower frequencies, agreement with the approximate Langer formula deteriorates as expected, although errors do not exceed 1 dB even at 1.5 Hz except at steep angles. At this frequency the sediment thickness is a fraction of a wavelength and we do not expect the reflection loss to be sensitive to the detailed sediment profile; we therefore present the primary benchmark (for a linear k^2 profile) as an alternative low frequency diagnostic for the BLUG profile. This calculation is shown as a “dotted” line (short dashes) at low frequencies in Figs. 1–4. Agreement with this second diagnostic is to within a fraction of a dB [Figs. 1(c), 2(c)] over the whole range of angles, providing confirmation of the accuracy of the FIPR solutions at low frequency.

Notice the very high losses for substrate 1 at 1.5 Hz

[Fig. 1(c)]. At this frequency the sediment is virtually transparent, allowing conversion to shear waves in the substrate for all angles of incidence due to the low substrate shear speed (less than 1500 m/s). The blip seen at 23° for substrate 2 at 15 Hz [Fig. 2(b)] results from the excitation of a Scholte wave at the sediment–substrate boundary,¹⁶ and is accurately reproduced by the Langer formula.

2. Sediment B (sand)

The parameters for sediment B are typical of a sandy continental terrace with a high sound-speed ratio and very high gradient. The sand sediment thickness is ten times smaller than that of the mud sediment previously considered.

In Figs. 3 and 4 we observe the deteriorating Langer accuracy at low frequencies as before, although most qualitative features are correctly predicted even at 1.5 Hz, corresponding to a dimensionless frequency of just 0.04π . Conversely, the accuracy of the linear k^2 diagnostic (dotted lines)

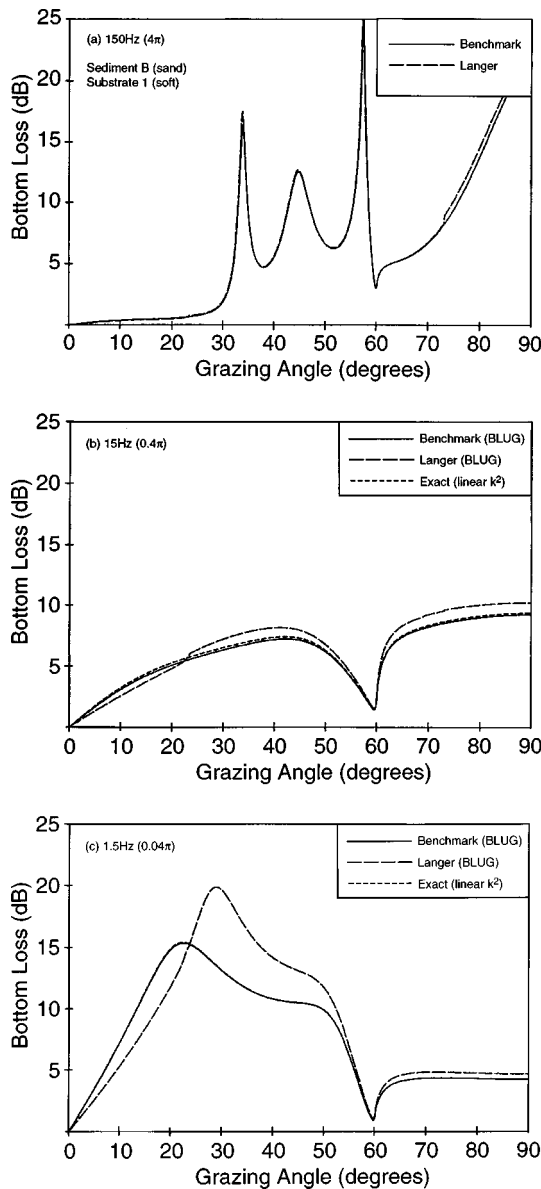


FIG. 3. Bottom loss versus angle for a sand sediment overlying a soft substrate (B1). The solid lines are benchmarks.

increases as expected with decreasing frequency because of the decreasing sensitivity to the sediment parameters. Notice the resemblance between Figs. 1 and 3 at the same dimensionless frequency [especially Figs. 1(c) and 3(b)]. One might expect a similar resemblance between Figs. 2 and 4 but it is less obvious because of the special features associated with reflection from the hard substrate, such as the Scholte wave referred to above [Fig. 2(b)] and the strong evanescent resonance¹⁷ near grazing incidence in Fig. 4(b).

3. Accuracy of secondary benchmarks

The accuracy of secondary benchmarks is assessed by comparing them with the Langer approximation at the highest dimensionless frequency considered (sediment A, 150 Hz; $\omega h/c_1 = 40\pi$). The maximum discrepancy found is 0.003. We believe the secondary benchmarks are accurate to within a tolerance of ± 0.003 .

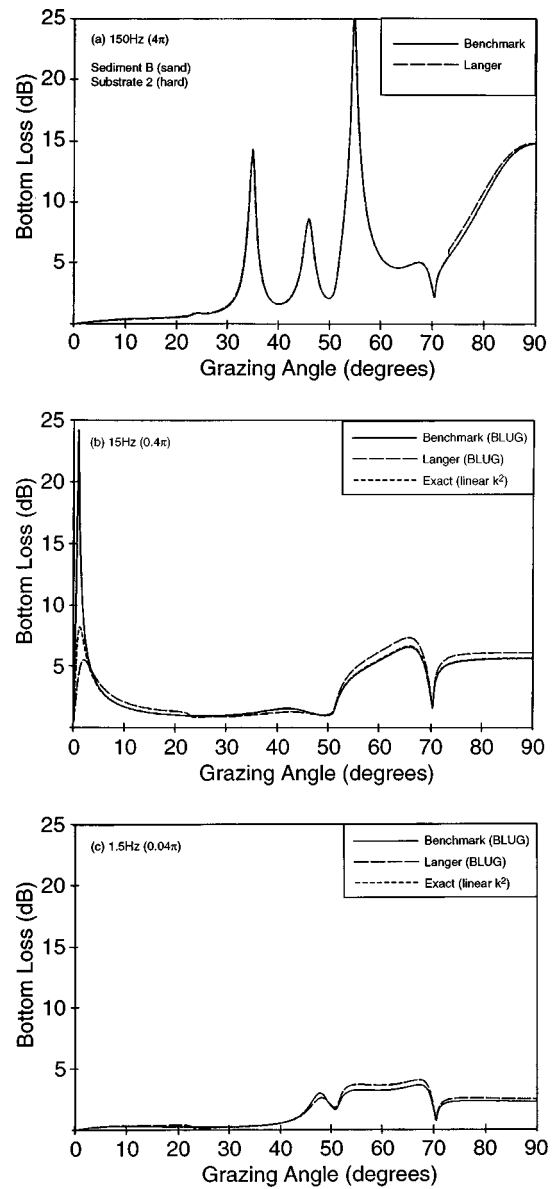


FIG. 4. Bottom loss versus angle for a sand sediment overlying a hard substrate (B2). The solid lines are benchmarks.

III. SENSITIVITY TO DENSITY PROFILE (MUD SEDIMENT)

It is commonly assumed that the sea bed can be modeled using a uniform sediment density, but it is known that effects due to a density profile are significant when the sediment thickness (in wavelengths) is of order unity.¹⁸ The benchmarks of Sec. II are for dimensionless frequencies between $O(0.1)$ and $O(100)$, so significant effects are expected at intermediate frequencies. To examine the magnitude of these effects we consider a depth dependence of the form^{3,18}

$$\rho_2(z) = \rho_0 \operatorname{sech}^2(\eta z/2) [1 - (\rho'/\eta\rho_0) \tanh(\eta z/2)]^{-2}, \quad (10)$$

where ρ_0 and ρ' are the density and its gradient at the top of the sediment ($z=0$). The constant η determines the curvature.

The method of the Appendix allows for a density profile, although we do not present primary benchmarks for this

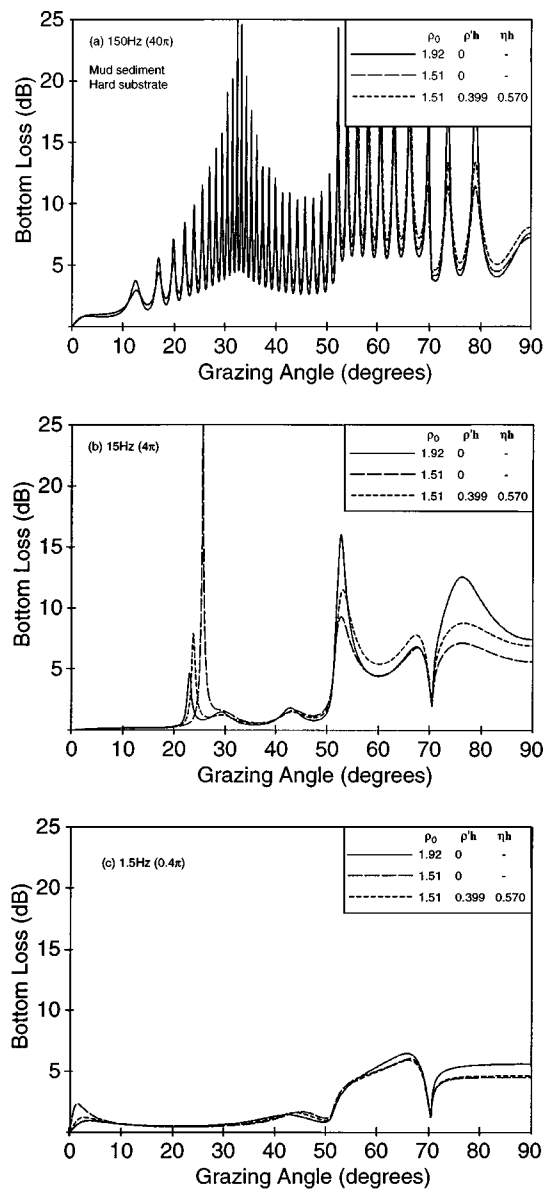


FIG. 5. Bottom loss versus angle benchmarks for a mud sediment overlying a hard substrate for three density profiles. The solid lines are from Fig. 2.

case. Additional secondary benchmarks for a mud sediment and basalt substrate are shown in Fig. 5 (graphs only) for two different uniform densities (1.92 and 1.51 g/cm³) and one layered density profile. In order to obtain a realistic profile, data from Hamilton¹¹ were used to provide a correlation between density and compressional speed for thick terrigenous sediments. The solid and dashed lines are for the two uniform densities; the dotted lines are for the density profile described by Eq. (10), with density increasing from 1.510 g/cm³ at the top of the sediment to 1.836 g/cm³ at 200 m depth. The solid curves are from Fig. 2. Large effects are observed as expected for the intermediate case [Fig. 5(b), $\omega h/c_1 = 4\pi$], with smaller effects at higher and lower frequencies [Fig. 5(a) and (c)].

IV. SUMMARY

We present primary and secondary benchmarks of bottom reflection loss versus angle at three frequencies (1.5, 15,

and 150 Hz) for four different bottom types, each comprising a layered fluid sediment representing sand or mud overlying a uniform solid substrate (limestone or basalt). The influence of a density profile is considered for one of the bottom types (mud sediment with basalt substrate).

The primary benchmarks are exact analytical solutions (Appendix) and are checked by comparison with results from the independent programs PARIS⁷ and FIPR.⁵ The secondary benchmarks are numerical solutions calculated by FIPR, checked for convergence and compared with asymptotic analytical solutions (diagnostics) at high and low frequencies.

ACKNOWLEDGMENTS

The authors acknowledge comments and advice received from Dr. S. Marks concerning the choice of geoaoustic parameters. The work has been carried out with the support of DERA (Winfrith, U.K.) and BAeSEMA Limited.

APPENDIX: REFLECTION COEFFICIENT

In this Appendix we consider a sound field of the form [omitting common factors of the form $\exp i(\kappa x - \omega t)$]

$$p(z) = \begin{cases} e^{i\gamma_1 z} + r e^{-i\gamma_1 z}, & z \leq 0 \quad (\text{ocean}) \\ p_2^+(z) + p_2^-(z), & 0 \leq z \leq h \quad (\text{sediment layer}), \\ t e^{i\gamma_3(z-h)} & z \geq h \quad (\text{substrate}) \end{cases} \quad (\text{A1})$$

where h is the sediment thickness, and γ_1 and γ_3 are the vertical wave numbers in the water and substrate, respectively. Equations for the reflection and transmission coefficients r and t are derived in Ref. 3 for arbitrary sediment profiles. The purpose of this Appendix is to present an exact formula for the reflection coefficient r associated with a linear k^2 sound speed profile and to derive new (approximate) results for a BLUG profile.

1. Reflection coefficient

For a layered fluid sediment overlying a uniform solid substrate the plane wave reflection coefficient can be written³

$$r = \frac{r_{12}(1+r_{23}) + r_{23}(1+r_{21})}{1 - r_{21}r_{23}}, \quad (\text{A2})$$

where r_{ij} is the reflection coefficient at the ij boundary, given by

$$r_{12} = \frac{\zeta_{12} - f^+(0)}{\zeta_{12} + f^+(0)}, \quad r_{21} = \frac{f^-(0) - \zeta_{12}}{f^+(0) + \zeta_{12}}, \quad (\text{A3})$$

and

$$r_{23} = \frac{p_2^+(h) \zeta_{23} f^+(h) - 1}{p_2^-(h) \zeta_{23} f^-(h) + 1}. \quad (\text{A4})$$

Here $p_2^\pm(z)$ denotes the upward or downward traveling sediment pressure wave and the function $f^\pm(z)$ is a ratio typically of order unity, given by

$$f^\pm(z) = \frac{dp_2^\pm/dz}{[\pm i \gamma_2(z) p_2^\pm(z)]}, \quad (\text{A5})$$

where

$$\gamma_2(z)^2 = \omega^2/\bar{c}_2(z)^2 - \kappa^2. \quad (\text{A6})$$

The impedance ratios ζ_{ij} are

$$\zeta_{12} = \rho_2(0) \gamma_1 / \rho_1 \gamma_2(h) \quad (\text{A7})$$

and

$$\zeta_{23} = \frac{\rho_3 \gamma_2(h)}{\omega \rho_2(h)} \left[\frac{\bar{c}_3}{\sin \theta_p} \cos^2 2\theta_s + \frac{\bar{v}_3}{\sin \theta_s} \sin^2 2\theta_s \right], \quad (\text{A8})$$

where θ_p and θ_s are the substrate compressional and shear grazing angles, respectively. These are related to the horizontal wave number κ through Snell's law

$$\frac{\bar{c}_3}{\cos \theta_p} = \frac{\bar{v}_3}{\cos \theta_s} = \frac{\omega}{\kappa}. \quad (\text{A9})$$

The tildes denote complex wave speeds \bar{c} and \bar{v} , including effects of attenuation, which are related to their real counterparts c and v according to

$$\bar{c} = \frac{c}{1 + i\alpha/(40\pi \log e)} \quad (\text{A10})$$

and

$$\bar{v} = \frac{v}{1 + i\delta/(40\pi \log e)}. \quad (\text{A11})$$

The above equations provide an explicit solution for the reflection coefficient in terms of the pressure functions $p_2^\pm(z)$. With the exception of a few special cases,^{3,19,20} in general it is necessary to make approximations in order to evaluate these wave functions.

2. Linear k^2 profile: exact solution

For the linear k^2 profile we have, without approximation and generalizing the result from Ref. 1 to allow for the density profile of Eq. (10)

$$p_2^\pm(z) = \frac{\text{Ai}[-\chi(z)] \pm i \text{Bi}[-\chi(z)]}{\text{Ai}[-\chi(0)] \pm i \text{Bi}[-\chi(0)]}, \quad (\text{A12})$$

where

$$\chi(z) = \left[\frac{\bar{c}_0 \Gamma_2(z)}{(2q\bar{c}_0\omega^2)^{1/3}} \right]^2 \quad (\text{A13})$$

and

$$\Gamma_2(z)^2 = \gamma_2(z)^2 - \eta^2/4. \quad (\text{A14})$$

3. BLUG profile: approximate solution

For the BLUG profile we invoke the approximation due to Langer^{3,21,22} in terms of $\frac{1}{3}$ order Hankel functions of the first and second kind (p. 447 of Ref. 23)

$$p_2^+(z) \sim [\phi(z)\rho_2(z)/\Gamma_2(z)]^{1/2} H_{1/3}^{(2)}[\phi(z)], \quad (\text{A15a})$$

$$p_2^-(z) \sim [\phi(z)\rho_2(z)/\Gamma_2(z)]^{1/2} H_{1/3}^{(1)}[\phi(z)]. \quad (\text{A15b})$$

The phase term ϕ is given by

$$\phi(z) = \int_z^{z_T} \Gamma_2(z) dz, \quad (\text{A16})$$

where $\Gamma_2(z)$ is the modified vertical wave number given by Eq. (A14). Defining the angle $\theta_2(z)$ by

$$\sin \theta_2(z) = \Gamma_2(z) \bar{c}_2(z) / \omega \quad (\text{A17})$$

and changing the integration variable from z to θ_2 we find that for the BLUG profile [Eq. (1)] the phase is (for $0 < z_T < h$)

$$\begin{aligned} \phi(z) = & \frac{\omega \sec \theta_2(0)}{\bar{g}_0(1+\beta)} \\ & \times \left(\frac{1}{4} [2\theta_2(z) - \sin 2\theta_2(z)] + \beta \cos \theta_2(0) \right. \\ & \left. \times \left\{ \ln \tan \left[\frac{\pi}{4} + \frac{\theta_2(z)}{2} \right] - \sin \theta_2(z) \right\} \right), \quad (\text{A18}) \end{aligned}$$

where

$$\bar{g}_0 = \frac{[\bar{c}_2(h) - \bar{c}_2(0)][\bar{c}_2(h) + \bar{c}_2(0) + 2\beta\bar{c}_2(0)]}{2(1+\beta)\bar{c}_2(0)h}. \quad (\text{A19})$$

In the high frequency limit θ_2 is just the usual (albeit complex) grazing angle determined by Snell's law because Γ_2 and γ_2 are then equal. However, at low frequency the ratio $\cos \theta_2/\bar{c}_2$, although independent of depth, is not equal to κ/ω as might be expected. Instead we see from Eqs. (A6), (A14), and (A17) that

$$\frac{\cos \theta_2(z)}{\bar{c}_2(z)} = \frac{\kappa}{\omega} \left(1 + \frac{\eta^2}{4\kappa^2} \right)^{1/2}. \quad (\text{A20})$$

The above prescription employs the BLUG sound-speed profile of Eq. (1) precisely. The absorption profile matches the BLUG values at $z=0$ and h but the depth dependence implied by Eq. (A10)

$$\alpha_2(z) = 40\pi \log e \text{Im} \left[\frac{c_2(z)}{\bar{c}_2(z)} \right] \quad (\text{A21})$$

is different from that of Eq. (2). The detailed shape of this absorption profile can be tuned by allowing complex values of β without altering the sound-speed profile. For example, the absorption gradient can be matched at $z=0$ by using

$$\bar{g}_0 = \frac{g_0 - ic_0^2 K' / (40\pi \log e)}{[1 + ic_0 K_0 / (40\pi \log e)]^2} \quad (\text{A22})$$

and rearranging Eq. (A19) for β

$$\tilde{\beta} = \frac{\bar{c}_2(h)^2 - \bar{c}_2(0)^2 - 2\bar{g}_0\bar{c}_2(0)h}{2\bar{c}_2(0)[\bar{c}_2(0) + \bar{g}_0h - \bar{c}_2(h)]}. \quad (\text{A23})$$

Values of $\tilde{\beta}$ used in the construction of Figs. 1–4 are $+0.857 - 0.087i$ for mud and -0.97 for sand.

¹E. K. Westwood and P. J. Vidmar, "Eigenray finding and time-series simulation in a layered-bottom ocean," J. Acoust. Soc. Am. **81**, 912–924 (1987).

²D. F. McCammon, "Fundamental relationships between geoacoustic parameters and predicted bottom loss using a thin layer model," J. Geophys. Res. **93**, 2363–2369 (1988).

³M. A. Ainslie, "Reflection and transmission coefficients for a layered

- fluid sediment overlying a uniform solid substrate," J. Acoust. Soc. Am. **99**, 893–902 (1996).
- ⁴M. J. Buckingham and A. Tolstoy, "An analytical solution for benchmark problem 1: The "ideal" wedge," J. Acoust. Soc. Am. **87**, 1511–1513 (1990).
- ⁵H. Schmidt, "SAFARI User's Guide," SACLANTCEN Report SR-113 (1988).
- ⁶J. M. Hovem, M. D. Richardson, and R. D. Stoll, Eds., *Shear Waves in Marine Sediments* (Kluwer, Dordrecht, 1991).
- ⁷A. J. Robins, "Plane-wave reflection from a solid layer with nonuniform density, sound speed, and shear speed," J. Acoust. Soc. Am. **103**, 1337–1345 (1998).
- ⁸M. A. Ainslie, "Plane-wave reflection and transmission coefficients for a three-layered elastic medium," J. Acoust. Soc. Am. **97**, 954–961 (1995).
- ⁹P. C. Etter, *Underwater Acoustic Modeling: Principles, Techniques and Applications* (Chapman & Hall, London, 1996), 2nd ed., p. 66.
- ¹⁰M. A. Ainslie and A. J. Robins, "Acoustic properties of two generic sediment profiles," in preparation.
- ¹¹E. L. Hamilton, "Geoacoustic modeling of the sea floor," J. Acoust. Soc. Am. **68**, 1313–1340 (1980).
- ¹²E. L. Hamilton, " V_p/V_s and Poisson's ratios in marine sediments and rocks," J. Acoust. Soc. Am. **66**, 1093–1101 (1979).
- ¹³The NAG Fortran Library Manual—Mark 13—Volume 7, NP1490/13 (NAG Ltd., Oxford, U.K., 1988).
- ¹⁴A. J. Robins, "Generation of shear and compression waves in an inhomogeneous elastic medium," J. Acoust. Soc. Am. **96**, 1669–1676 (1994).
- ¹⁵Z. Schulten, D. G. M. Anderson, and R. G. Gordon, "An algorithm for the evaluation of the complex Airy functions," J. Comput. Phys. **31**, 60–75 (1979).
- ¹⁶D. Rauch, "Experimental and theoretical studies of seismic interface waves in coastal waters," in *Bottom-Interacting Ocean Acoustics*, edited by W. A. Kuperman and F. B. Jensen (Plenum, New York, 1980), pp. 307–327.
- ¹⁷M. A. Ainslie and A. J. Robins, Bottom Loss Final Report: FFS Benchmarks and FSS Feasibility, BAeSEMA Report C4712/TR-2, May 1996.
- ¹⁸A. J. Robins, "Reflection of plane acoustic waves from a layer of varying density," J. Acoust. Soc. Am. **87**, 1546–1552 (1990).
- ¹⁹A. J. Robins, "Reflection of a plane wave from a fluid layer with continuously varying density and sound speed," J. Acoust. Soc. Am. **89**, 1686–1696 (1991).
- ²⁰A. J. Robins, "Exact solutions of the Helmholtz equation for plane wave propagation in a medium with variable density and sound speed," J. Acoust. Soc. Am. **93**, 1347–1352 (1993).
- ²¹I. C. Goyal, R. L. Gallawa, and A. K. Ghatak, "An approximate solution to the wave equation-revisited," J. Electromagn. Waves Appl. **5**, 623–636 (1991).
- ²²R. E. Langer, "On the connection formulas and the solutions of the wave equation," Phys. Rev. **51**, 669–676 (1937).
- ²³*Handbook of Mathematical Functions*, edited by M. Abramovitz and I. Stegun (Dover, New York, 1965).

Second-order perturbations of peak-arrival times due to sound-speed variations

E. K. Skarsoulis

*Institute of Applied and Computational Mathematics, Foundation for Research and Technology Hellas,
P.O. Box 1527, 711 10 Heraklion, Crete, Greece*

G. A. Athanassoulis

*Department of Naval Architecture and Marine Engineering, National Technical University of Athens,
P.O. Box 64033, 157 10 Zografos, Athens, Greece*

(Received 12 December 1997; accepted for publication 14 September 1998)

The concept of peak arrivals is used to study the second-order arrival-time behavior of broadband tomographic signals due to sound-speed variations. Peak arrivals, defined as the local maxima of the pressure amplitude at the receiver in the time domain, are the exact theoretical counterparts of the experimental observables in ocean acoustic tomography, and they offer a uniform description of all the peaks in the arrival pattern, independent of whether they can be resolved as ray/modal arrivals or not. Closed-form expressions for the first and second sound-speed derivatives of peak-arrival times are derived in terms of sound-speed derivatives of the Green's function. Using normal-mode theory the sound-speed derivatives of the Green's function are analytically expressed for the case of a range-independent medium in terms of eigenvalues and eigenfunctions at the reference state. Numerical examples are given for range-independent environments motivated from the Thetis-2 experiment, showing different kinds of nonlinear behavior of the arrival times in the large and the fine scale and demonstrating the performance of the second-order approach. © 1998 Acoustical Society of America. [S0001-4966(98)05012-7]

PACS numbers: 43.30.Pc, 43.30.Bp, 43.20.Bi [DLB]

INTRODUCTION

Ocean acoustic tomography introduced by Munk and Wunsch¹ has been commonly used in a linear framework, by assuming small perturbations of the ocean environment about a given background state and linear dependence of arrival times on the sound-speed anomaly.^{2,3} There are cases, however, e.g., due to large sound-speed variations,^{4,5} in which the nonlinear dependencies of arrival times on the sound speed become significant and have to be accounted for in the inversion procedure.

Such is the case in the Thetis-2 experiment,⁶ conducted from January to October 1994 in the western Mediterranean sea. Figure 1(a) shows the measured travel times along a Thetis-2 path (W3-H), which was systematically XBT sampled during the experiment. Figure 1(b) shows the cutoff times^{7,8} measured during the 14 XBT sampling periods, versus the EOF-1 amplitude ϑ_1 extracted from the corresponding range-averaged XBT data; EOF-1, described in Sec. III, accounts for the gross seasonal variability in the area. While for positive ϑ_1 values the data exhibit a nearly linear behavior, for negative ϑ_1 values there is a significant deviation from linearity and the data are better represented by a second-order curve, shown in Fig. 1(b) as a dashed line. The observed fluctuations are due to higher-order EOF components of the XBT data, unresolved in Fig. 1(b), and range-dependent features of the particular path. The nonlinearity of the Thetis-2 data has its origin in the large (seasonal) sound-speed variations encountered over the nine-month duration of the experiment, and the significant change in the propaga-

tion conditions, from surface reflected propagation in winter to refracted propagation in summer.

The dependence of arrival times on sound-speed changes has been studied in the literature using the concepts of ray arrivals^{1-5,9-13} and modal arrivals.^{10,14-17} Ray theory offers an efficient tool for the analysis of tomographic receptions in the case where the arrivals of distinct ray groups^{9,10} are sufficiently separated in time such that they can be resolved in the reception; these are usually the early arrivals, cf. Fig. 1(a), corresponding to steep rays. In the intermediate and late part of the reception ray group arrivals overlap with each other and cannot be easily resolved.^{3,10} Furthermore, ray arrivals occasionally face limitations due to the insufficiency of the ray approximation, e.g., in the low-frequency case.^{18,19}

Mode theory gives an exact representation of the acoustic field, and in this sense it offers a remedy to possible deficiencies of the ray approximation. Moreover, the final part of the arrival pattern corresponding to a large number of unresolved shallow rays can be represented by a small number of low-order modes. In this connection, the ray and modal approach are complementary. Nevertheless, the identification of individual modal arrivals in realistic arrival patterns, generated by finite-bandwidth transmissions in deep-water environments, is not, in general, possible.^{10,17} In order to extract the first six propagating modes from acoustic receptions in the Greenland sea tomography experiment, Sutton *et al.* used 90-m-long vertical receiving arrays and performed spatial mode filtering.²⁰⁻²² With the receivers available in Thetis-2 (arrays of 5.6 m length) no mode filter-

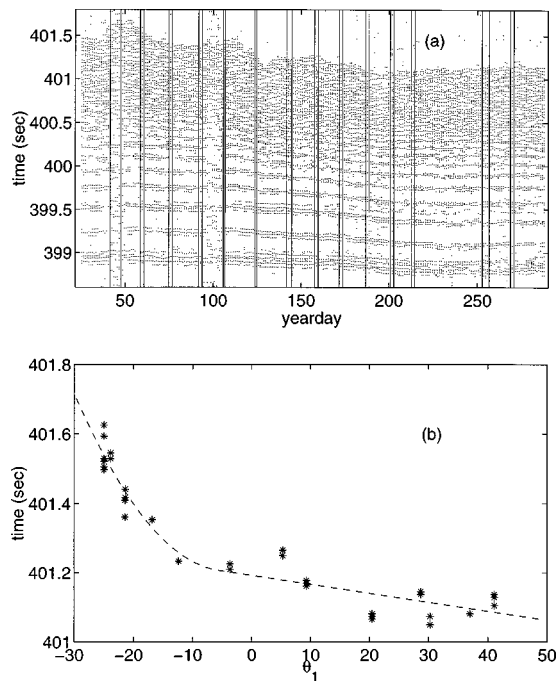


FIG. 1. (a) Measured travel times (\cdot) along Thetis-2 path W3-H. The vertical lines denote the 14 XBT sampling periods. (b) Cutoff times ($*$) measured during the XBT periods versus EOF-1 amplitude ϑ_1 of the range-averaged XBT data. The dashed line denotes a second-order/linear fit to the data.

ing could be performed and low-order modes could not be resolved.⁶

Peak arrivals,^{23,24} introduced as a generalization of ray and modal arrivals, are defined as the local maxima of the pressure amplitude at the receiver in the time domain (arrival pattern), independent of the modeling approach used. The peak-arrival approach is in full correspondence with the experimental practice in ocean acoustic tomography, peak arrivals being the exact theoretical counterparts of the experimental observables. Furthermore, it does not require the interpretation of actual (observed) peaks as ray or modal arrivals, whereas peak arrivals reduce to ray/modal ones in case of ray/mode resolvability.^{23,25} The concept of peak arrivals has been successfully used for the analysis of Thetis-1²⁴ and Thetis-2^{26,27} data. In Thetis-1, due to small sound-speed variability and stable propagation conditions (surface refracted propagation) in the north-western Mediterranean sea in winter 1991–92, the relation between travel times and sound-speed changes was close to linear such that linear perturbative inversions could be performed about a single background state. In Thetis-2, however, the large (seasonal) sound-speed variability and the induced change in the propagation conditions caused significant nonlinearities in the sound-speed/traveltime relation, cf. Fig. 1(b), with a strong impact on the inversions.^{6,26–28}

In the present work the second-order behavior of peak-arrival times with respect to sound-speed changes is studied. Expressions for the first and second sound-speed derivatives of peak-arrival times are derived in terms of sound-speed derivatives of the Green's function. The resulting expressions are general and thus free from restrictive assumptions concerning the ocean environment, the emitted signal, or the

propagation modeling used. For the case of a range-independent environment the sound-speed derivatives of the Green's function are further elaborated by using normal modes and applying perturbation theory to the vertical eigenvalue problem. Finally, closed-form expressions are derived for the first two derivatives of the Green's function with respect to the sound speed, in terms of the eigenvalues and eigenfunctions at the reference state.

The second sound-speed derivatives of peak-arrival times describe the local curvature of the relation between travel times and sound-speed parameters. Thus they can be used as a measure of smoothness, helping to reveal cases of anomalous travel time behavior. Furthermore, the second derivatives can provide model error estimates for the linearization about a particular background state, which in turn can be used as *a priori* information in connection with linear inversions. Finally, in the case of smooth evolution, the second-order description can be used as a vehicle for performing nonlinear inversions.

To demonstrate the performance of the second-order peak arrival approach, numerical results are presented for a series of range-independent ocean environments resembling winter-to-spring Mediterranean conditions, motivated from the Thetis-2 experiment. The simulations reproduce a gross nonlinear behavior of peak arrival times with respect to the EOF-1 amplitude similar to that of Fig. 1(b) for negative ϑ_1 values. Furthermore, these simulations bring into light a fine-scale nonlinear behavior of the peak arrival times with respect to the EOF-1 amplitude, predicted by full-wave theory in particular cases.

Apart from the effects of range-independent sound-speed variations studied here, arrival times are also subject to range-dependent effects due to internal waves,^{29–32} meso-scale, and large-scale activity.^{4,11–13} In Thetis-2, the effect of internal waves is expected to be small, due to the relatively limited range (600 km) and the particular propagation conditions (upward refracting sound-speed profiles in winter and very shallow acoustic channel axes in summer).^{3,29,32} Meso-scale and large-scale oceanographic features are anticipated to have a strong effect, particularly on the late arrivals; simulations based on measured Thetis-2 sections revealed significant range-dependence effects on the cutoff times, exceeding 100 ms in some cases, with respect to predictions based on the range-averaged conditions.²⁷ The present second-order analysis is currently being extended to the range-dependent case using a coupled-mode representation^{33,34} of the Green's function; the second order is particularly important in that case since, on the basis of existing results,^{11,12} the effect of range dependence on the arrival times is expected to be primarily a second-order effect.

The contents of the present work are organized as follows: In Sec. I, after the introduction of basic notions, the expressions for the first and second sound-speed derivatives of arrival times are derived. In Sec. II the sound-speed derivatives of the Green's function are elaborated for the range-independent case using normal-mode and eigenvalue perturbation theory. The numerical performance of the second-order peak arrival approach is demonstrated in Sec. III for synthetic range-independent environments representing

winter-to-spring Mediterranean conditions, motivated from the Thetis-2 experiment, and giving rise to significant nonlinear features in the large and the fine scale. An interpretation to the generating mechanisms of the observed nonlinearities is given by studying the behavior of individual modes. In Sec. IV the nonlinear behavior of the peak-arrival times and also the possibilities and limitations of the second-order approach are discussed and conclusions are drawn.

I. SOUND-SPEED DERIVATIVES OF PEAK-ARRIVAL TIMES

A standard tomographic setting is assumed with a broadband source and receiver at fixed locations in space. The acoustic pressure at the receiver in the time domain can be expressed through the inverse Fourier transform in terms of the source signal $P_s(\omega)$ in the frequency domain and the Green's function $H_{sr}(\omega; c)$:

$$p_r(t; c) = \frac{1}{2\pi} \int_{-\infty}^{\infty} H_{sr}(\omega; c) P_s(\omega) e^{j\omega t} d\omega$$

$$= \mathcal{F}^{-1}\{H_{sr}(\omega; c) P_s(\omega); \omega \rightarrow t\}. \quad (1)$$

The Green's function depends on the source/receiver locations, the circular frequency ω , and the sound-speed distribution $c(\mathbf{x})$, where \mathbf{x} represents the space vector. Due to multipath propagation, the pressure amplitude at the receiver in the time domain $a(t; c) = |p_r(t; c)|$ consists in general of a number of peaks, the acoustic arrivals, corresponding to different propagation paths. In this connection, $a(t; c)$ is called arrival pattern. The peak arrivals are defined as the local maxima of the arrival pattern, with respect to time

$$\frac{\partial a}{\partial t}(\tau_i; c) = 0, \quad i = 1, \dots, I. \quad (2)$$

This definition is in full correspondence with the experimental practice in ocean acoustic tomography, peak arrivals being the exact theoretical counterparts of the experimental observables. Furthermore, the above definition is generic and thus independent of the particular modeling approach used for the calculation of $H_{sr}(\omega; c)$, either ray or wave theoretic. Accordingly, peak arrivals provide a vehicle for the treatment of experimental observables independently of whether they can be interpreted as individual ray/modal arrivals or not.

Since the Green's function and the arrival pattern depend on the sound speed $c(\mathbf{x})$, so do the peak arrivals and peak-arrival times as well, i.e., $\tau_i = \tau_i(c)$. In the following, the actual sound-speed distribution in the water is expressed in terms of a reference distribution $c_0(\mathbf{x})$ and a set of appropriate sound-speed modes $\phi_l(\mathbf{x})$, e.g., oceanographic modes or EOFs,

$$c(\mathbf{x}) = c_0(\mathbf{x}) + \sum_l \vartheta_l \phi_l(\mathbf{x}). \quad (3)$$

Thus the Green's function, the arrival pattern, and the peak-arrival times become functions of the parameter vector $\boldsymbol{\vartheta} = \{\vartheta_l\}$: $H_{sr} = H_{sr}(\omega; \boldsymbol{\vartheta})$, $a = a(t; \boldsymbol{\vartheta})$, $\tau_i = \tau_i(\boldsymbol{\vartheta})$.

A perturbation $\delta\boldsymbol{\vartheta}$ about the reference state will cause a displacement of the i -th peak arrival by $\delta\tau_i$. Both at the reference and the perturbed state the peak arrival satisfies the local maximum condition, i.e.,

$$\frac{\partial a}{\partial t}(\tau_i^{(0)}; 0) = 0, \quad \frac{\partial a}{\partial t}(\tau_i^{(0)} + \delta\tau_i; \delta\boldsymbol{\vartheta}) = 0, \quad (4)$$

where $\tau_i^{(0)} = \tau_i(\boldsymbol{\vartheta} = 0)$. Taking the Taylor expansion of the second relation about the reference state ($\boldsymbol{\vartheta} = 0$), the following expressions can be obtained for the first and second derivatives of τ_i with respect to $\boldsymbol{\vartheta}$:

$$\left. \frac{\partial \tau_i}{\partial \vartheta_l} \right|_{\boldsymbol{\vartheta}=0} = - \frac{\partial^2 a(\tau_i^{(0)}; 0) / \partial t \partial \vartheta_l}{\partial^2 a(\tau_i^{(0)}; 0) / \partial t^2} = - \frac{\dot{a}_{i,l}}{\ddot{a}_i}, \quad (5)$$

and

$$\left. \frac{\partial^2 \tau_i}{\partial \vartheta_l \partial \vartheta_m} \right|_{\boldsymbol{\vartheta}=0} = - \frac{\ddot{a}_i \dot{a}_{i,l} \dot{a}_{i,m}}{\ddot{a}_i^3} + \frac{\dot{a}_{i,l} \dot{a}_{i,m} + \dot{a}_{i,l} \ddot{a}_{i,m}}{\ddot{a}_i^2} - \frac{\dot{a}_{i,lm}}{\ddot{a}_i}, \quad (6)$$

where the partial time derivatives are denoted through dots, the subscripts l and m denote partial derivatives with respect to ϑ_l and ϑ_m at the reference state, and the subscript i denotes the particular peak, e.g., $\dot{a}_{i,lm} = \partial^3 a(\tau_i^{(0)}; 0) / \partial t \partial \vartheta_l \partial \vartheta_m$. In the following the case $l = m$, i.e., the diagonal of the Hessian matrix, is considered in detail. Equation (6) becomes in this case

$$\left. \frac{\partial^2 \tau_i}{\partial \vartheta_l^2} \right|_{\boldsymbol{\vartheta}=0} = - \frac{\ddot{a}_i \dot{a}_{i,l}^2}{\ddot{a}_i^3} + \frac{2\dot{a}_{i,l} \ddot{a}_{i,l}}{\ddot{a}_i^2} - \frac{\dot{a}_{i,ll}}{\ddot{a}_i}. \quad (7)$$

Expressions (5) and (7) are general in the sense that they rely on definition (2) of peak arrivals and thus apply independently of the ocean environment, either range independent or range dependent, the emitted signal and the propagation modeling approach, either ray or wave theoretic. The derivatives $\partial \tau_i / \partial \vartheta_l$ and $\partial^2 \tau_i / \partial \vartheta_l^2$ represent the effect of particular sound-speed modes on the peak-arrival times and in the following they will be also referred to as first- and second-order influence coefficients, respectively.

Expressing the pressure p_r at the receiver in terms of its real and imaginary part $p_r(t, \boldsymbol{\vartheta}) = v(t, \boldsymbol{\vartheta}) + jw(t, \boldsymbol{\vartheta})$, the arrival pattern is written as $a(t, \boldsymbol{\vartheta}) = \sqrt{v^2(t, \boldsymbol{\vartheta}) + w^2(t, \boldsymbol{\vartheta})}$. Differentiating the latter expression with respect to t and ϑ_l and taking into account the definition of peak arrivals: $\dot{a}_i = 0$, i.e., $v_i \dot{v}_i + w_i \dot{w}_i = 0$, the derivatives appearing on the right-hand sides of Eqs. (5) and (7) can be expressed in terms of corresponding derivatives of v and w :

$$\dot{a}_{i,l} = \frac{1}{a_i} (\dot{v}_i v_{i,l} + v_i \dot{v}_{i,l} + \dot{w}_i w_{i,l} + w_i \dot{w}_{i,l}), \quad (8)$$

$$\ddot{a}_i = \frac{1}{a_i} (\ddot{v}_i^2 + v_i \ddot{v}_i + \dot{w}_i^2 + w_i \dot{w}_i), \quad (9)$$

$$\ddot{a}_i = \frac{1}{a_i} (3\ddot{v}_i \dot{v}_i + v_i \ddot{v}_i + 3\dot{w}_i \dot{w}_i + w_i \ddot{w}_i), \quad (10)$$

$$\begin{aligned} \dot{a}_{i,l} = & \frac{1}{a_i} (2v_{i,l}\dot{v}_{i,l} + \dot{v}_i v_{i,l} + v_i \dot{v}_{i,l} + 2w_{i,l}\dot{w}_{i,l} + \dot{w}_i w_{i,l} \\ & + w_i \dot{w}_{i,l}) - \frac{2}{a_i^2} (v_i v_{i,l} + w_i w_{i,l}) \dot{a}_{i,l}, \end{aligned} \quad (11)$$

$$\begin{aligned} \ddot{a}_{i,l} = & \frac{1}{a_i} (\ddot{v}_i v_{i,l} + 2\dot{v}_i \dot{v}_{i,l} + v_i \ddot{v}_{i,l} + \dot{w}_i w_{i,l} + 2\dot{w}_i \dot{w}_{i,l} \\ & + w_i \ddot{w}_{i,l}) - \frac{1}{a_i^2} (v_i v_{i,l} + w_i w_{i,l}) \ddot{a}_i, \end{aligned} \quad (12)$$

where the dots and the subscripts l denote partial derivatives with respect to t and ϑ_l , respectively, at the reference state, and the subscript i denotes the particular peak. The second lines in the last two expressions (11) and (12) cancel each other in (7), and this simplifies the computation. Using elementary properties of the Fourier transform,³⁵ the time and ϑ_l -derivatives of v and w can be expressed in terms of ϑ_l derivatives of the Green's function

$$\begin{aligned} & \frac{\partial^{(m+n)}[v(t, \boldsymbol{\vartheta}) + jw(t, \boldsymbol{\vartheta})]}{\partial t^m \partial \vartheta_l^n} \\ & = \mathcal{F}^{-1} \left\{ (j\omega)^m \frac{\partial^n H_{sr}}{\partial \vartheta_l^n}(\omega; \boldsymbol{\vartheta}) P_s(\omega); \omega \rightarrow t \right\}. \end{aligned} \quad (13)$$

Thus the calculation of the influence coefficients $\partial \tau_i / \partial \vartheta_l$ and $\partial^2 \tau_i / \partial \vartheta_l^2$ reduces to calculating the first and second derivatives of the Green's function with respect to ϑ_l . These derivatives are studied in the following for the case of a range-independent ocean environment.

II. GREEN'S FUNCTION DERIVATIVES USING NORMAL MODES

In this section analytic expressions are derived for the second ϑ_l -derivatives of the Green's function for a range-independent ocean environment using normal modes, whereas first-order results obtained in previous works^{23,24} are repeated for completeness. A cylindrical coordinate system (z, r) is adopted with the z -axis, measuring depth from the sea surface and positive downward. The acoustic field at (R, z_r) , far from a harmonic point source of unit strength, circular frequency ω , and time dependence $e^{j\omega t}$, located at $(0, z_s)$, can be written in terms of normal modes as follows.^{18,19,36}

$$\begin{aligned} H_{sr}(\omega; \boldsymbol{\vartheta}) = & \frac{e^{-j\pi/4}}{\rho \sqrt{8\pi}} \sum_{n=1}^M \frac{u_n(z_s; \omega; \boldsymbol{\vartheta}) u_n(z_r; \omega; \boldsymbol{\vartheta})}{\sqrt{k_n(\omega; \boldsymbol{\vartheta}) R}} \\ & \times e^{-jk_n(\omega; \boldsymbol{\vartheta}) R}, \end{aligned} \quad (14)$$

where ρ is the water density, while k_n and u_n , $n=1, \dots, M$, are the real eigenvalues and the corresponding eigenfunctions (propagating modes) of the vertical Sturm–Liouville problem:

$$\frac{d^2 u_n(z)}{dz^2} + \frac{\omega^2}{c^2(z)} u_n(z) = k_n^2 u_n(z), \quad (15)$$

supplemented by the conditions that $u_n=0$ at the sea surface ($z=0$), u_n and $\rho^{-1} du_n/dz$ are continuous across the interfaces, and u_n and du_n/dz are vanishing as $z \rightarrow \infty$. Since the circular frequency ω and the sound-speed profile $c(z)$ appear in Eq. (15), the resulting eigenvalues and eigenfunctions are dependent on ω and $c(z)$, i.e., on $\boldsymbol{\vartheta}$: $u_n(z) = u_n(z; \omega; \boldsymbol{\vartheta})$, $k_n = k_n(\omega; \boldsymbol{\vartheta})$. Applying perturbation theory^{37,38} to the above eigenvalue problem and retaining terms up to the second order, analytic relations can be derived for the first and second derivatives of the eigenvalues and eigenfunctions with respect to ϑ_l . The final expressions for the eigenvalues read

$$\frac{\partial k_n}{\partial \vartheta_l} = \frac{Q_{nn}^{l,1}}{2k_n}, \quad (16)$$

$$\frac{\partial^2 k_n}{\partial \vartheta_l^2} = \frac{1}{k_n} \left[Q_{nn}^{l,2} + \sum_{\substack{m=1 \\ m \neq n}}^M \frac{|Q_{nm}^{l,1}|^2}{\Lambda_{nm}} - \frac{|Q_{nn}^{l,1}|^2}{4k_n^2} \right], \quad (17)$$

and for the eigenfunctions

$$\frac{\partial u_n(z)}{\partial \vartheta_l} = \sum_{\substack{m=1 \\ m \neq n}}^M \frac{Q_{nm}^{l,1} u_m(z)}{\Lambda_{nm}}, \quad (18)$$

$$\begin{aligned} \frac{\partial^2 u_n(z)}{\partial \vartheta_l^2} = & 2 \sum_{\substack{m=1 \\ m \neq n}}^M \sum_{\substack{i=1 \\ i \neq n}}^M \frac{Q_{ni}^{l,1} Q_{im}^{l,1} u_m(z)}{\Lambda_{nm} \Lambda_{ni}} - u_n(z) \sum_{\substack{m=1 \\ m \neq n}}^M \frac{|Q_{nm}^{l,1}|^2}{\Lambda_{nm}^2} \\ & + 2 \sum_{\substack{m=1 \\ m \neq n}}^M \left[\frac{Q_{nm}^{l,2} u_m(z)}{\Lambda_{nm}} - \frac{Q_{nn}^{l,1} Q_{nm}^{l,1} u_m(z)}{\Lambda_{nm}^2} \right], \end{aligned} \quad (19)$$

where $\Lambda_{nm} = k_n^2 - k_m^2$. The quantities $Q_{nm}^{l,1}$ and $Q_{nm}^{l,2}$ appearing in the above expressions are weighted inner products between eigenfunctions

$$Q_{nm}^{l,1} = -\frac{2\omega^2}{\rho} \int_0^h \frac{\phi_l(z)}{c_0^3(z)} u_n(z) u_m(z) dz, \quad (20)$$

$$Q_{nm}^{l,2} = \frac{3\omega^2}{\rho} \int_0^h \frac{\phi_l^2(z)}{c_0^4(z)} u_n(z) u_m(z) dz, \quad (21)$$

where h is the water depth; note that the sound-speed modes $\phi_l(z)$ vanish for $z > h$. Differentiating Eq. (14) with respect to ϑ_l and substituting expressions (16) and (18), the first ϑ_l derivative of the Green's function is obtained

$$\begin{aligned} \frac{\partial H_{sr}}{\partial \vartheta_l} = & \frac{e^{-j\pi/4}}{\rho \sqrt{8\pi}} \sum_{n=1}^M \left\{ \sum_{\substack{m=1 \\ m \neq n}}^M \frac{Q_{nm}^{l,1} U_{nm}}{\Lambda_{nm}} \right. \\ & \left. + \frac{1}{2k_n} \frac{Q_{nn}^{l,1} U_{nn}}{k_n} + jR \frac{Q_{nn}^{l,1} U_{nn}}{k_n} \right\} \frac{e^{-jk_n R}}{\sqrt{k_n R}}, \end{aligned} \quad (22)$$

where

$$U_{nm} = \begin{cases} u_n(z_s) u_m(z_r) + u_n(z_r) u_m(z_s), & \text{for } n \neq m \\ -u_n(z_s) u_n(z_r)/2, & \text{for } n = m. \end{cases} \quad (23)$$

The terms within the curly braces in (22) correspond to the first-order variations of the eigenfunctions [$u_n(z_s)u_n(z_r)$], the geometric attenuation [$1/\sqrt{k_n R}$], and the phase term [$-jk_n R$], respectively. For long ranges the phase variation term is expected to dominate in Eq. (22),

$$\begin{aligned} \frac{\partial^2 H_{sr}}{\partial \vartheta_l^2} = & \frac{e^{-j\pi/4}}{\rho\sqrt{8\pi}} \sum_{n=1}^M \left\{ 2 \sum_{\substack{m=1 \\ m \neq n}}^M \sum_{\substack{\kappa=1 \\ \kappa \neq n}}^M \frac{Q_{n\kappa}^{l,1}(U_{nm}Q_{m\kappa}^{l,1} + Q_{nm}^{l,1}U_{m\kappa})}{\Lambda_{nm}\Lambda_{n\kappa}} + 2 \sum_{\substack{m=1 \\ m \neq n}}^M \frac{U_{nm}}{\Lambda_{nm}} \left(Q_{nm}^{l,2} - \frac{Q_{nn}^{l,1}Q_{nm}^{l,1}}{\Lambda_{nm}} \right) \right. \\ & + 2U_{nn} \sum_{\substack{m=1 \\ m \neq n}}^M \left[\frac{|Q_{nm}^{l,1}|^2}{\Lambda_{nm}^2} - \left(\frac{3}{4k_n^2} + j \frac{R}{k_n} - R^2 \right) U_{nn} \frac{|Q_{nn}^{l,1}|^2}{2k_n^2} - \left(jR + \frac{1}{2k_n} \right) \left[\frac{Q_{nn}^{l,1}}{2k_n} \sum_{\substack{m=1 \\ m \neq n}}^M \frac{Q_{nm}^{l,1}U_{nm}}{\Lambda_{nm}} \right. \right. \\ & \left. \left. - \frac{2U_{nn}}{k_n} \left(Q_{nn}^{l,2} - \frac{|Q_{nn}^{l,1}|^2}{4k_n^2} + \sum_{\substack{m=1 \\ m \neq n}}^M \frac{|Q_{nm}^{l,1}|^2}{\Lambda_{nm}} \right) \right] \right\} \frac{e^{-jk_n R}}{\sqrt{k_n R}}. \end{aligned} \quad (24)$$

The first two lines within the braces in (24) correspond to the second eigenfunction variations with respect to ϑ_l while the remaining three lines represent the second variations of phase and geometric attenuation as well as second variations of the cross terms. Again, for long ranges the second phase variations, containing the factors R^2 and jR , are expected to be dominant in (24). Substituting expressions (22) and (24) into (13) and then expressions (8)–(12) into (5) and (7) the first and second ϑ_l derivative of the peak-arrival times can be calculated in terms of eigenvalues and eigenfunctions at the reference state.

Concerning the numerical implementation of expressions (22) and (24), the main computational burden is associated with the computation of the double and triple sums. Nevertheless, due to the appearance of the quantities Λ_{nm} and Λ_{nk} in the denominators, the more important terms in these sums are the near-diagonal ones, i.e., the ones close to $n=m=k$.²³ Representing the kernel of the double sums by a $(M \times M)$ square matrix A the following identity can be used

$$\sum_{n=1}^M \sum_{\substack{m=1 \\ m \neq n}}^M A_{nm} \equiv \sum_{s=1}^{M-1} \sum_{\mu=1}^{M-s} (A_{\mu, \mu+s} + A_{\mu+s, \mu}). \quad (25)$$

This is equivalent to performing the double summation along lines parallel to the diagonal, s denoting the distance from the diagonal, $s=|m-n|$. Since low s -values correspond to adjacent modes, i.e., small Λ_{nm} values, and large s -values correspond to distant modes, i.e., large Λ_{nm} values, the outer sum $\sum_{s=1}^{M-1}$ on the right-hand side in Eq. (25) can be efficiently approximated by $\sum_{s=1}^S$, where $S \ll M-1$, i.e., keeping only the significant near-diagonal terms.

In the case of the triple sum the kernel can be represented by a $(M \times M \times M)$ cubic matrix B and the following equivalence can be used

whereas the variation of the geometric attenuation term is expected to be negligible.²³ Differentiating Eq. (14) twice with respect to ϑ_l and using Eqs. (16)–(19), the following expression results for the second ϑ_l derivative of the Green's function

$$\begin{aligned} & \sum_{n=1}^M \sum_{\substack{m=1 \\ m \neq n}}^M \sum_{\substack{\kappa=1 \\ \kappa \neq n}}^M B_{nm\kappa} \\ & \equiv \sum_{s'=1}^{2M-3} \left[\sum_{\mu=1}^{2M-s'-1} \sum_{\nu=\max\{1, \mu-M+s'+1\}}^{\min\{s', M-\mu\}} B_{\mu, \mu+\nu, \mu+s'+1-\nu} \right. \\ & + \sum_{\mu=s'+1-M}^M \sum_{\nu=\max\{1, s'+2-\mu\}}^{\min\{s', \mu-1\}} B_{\mu, \mu-\nu, \mu-s'-1+\nu} \\ & + \sum_{\mu=2}^{M-1} \sum_{\nu=\max\{1, \mu-M+s'+1\}}^{\min\{s', \mu-1\}} (B_{\mu, \mu-\nu, \mu+s'+1-\nu} \\ & \left. + B_{\mu, \mu+s'+1-\nu, \mu-\nu}) \right], \end{aligned} \quad (26)$$

where s' now represents a three-dimensional measure of the distance from the diagonal, $s' = |m-n| + |\kappa-n| - 1$. Restricting the summation to the significant near-diagonal terms, with Λ_{nm} and Λ_{nk} small, the outer sum $\sum_{s'=1}^{2M-3}$ on the right-hand side of Eq. (26) can be truncated to $\sum_{s'=1}^{S'}$, where $S' \ll 2M-3$. The above simplifications and truncations can substantially reduce the computational burden.

III. NUMERICAL RESULTS

In this section second-order calculations are presented for a series of range-independent ocean environments simulating western Mediterranean conditions, motivated from the Thetis-2 experiment. Figure 2 shows the annual reference profile in the upper 1000 m along with the first two empirical orthogonal functions (EOFs) obtained from historical data, with rms amplitudes $\vartheta_{1,\text{rms}} = 18.48$ and $\vartheta_{2,\text{rms}} = 2.88$, respectively. The first EOF counts for the bulk of the seasonal variability in the basin, taking place close to the surface. The first two EOFs explain 99.3% of the annual variance.

Figure 3 shows the arrival pattern predicted from the KRAKEN normal-mode code³⁹ for the reference profile of Fig.

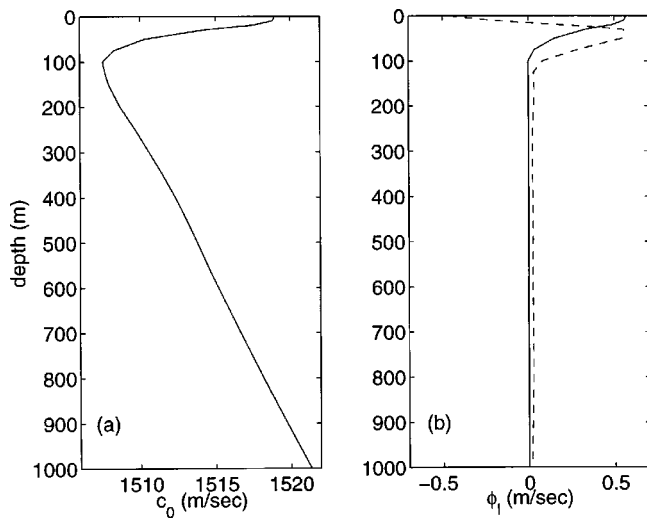


FIG. 2. (a) Annual reference profile for the western Mediterranean sea. (b) First (—) and second (---) sound-speed mode obtained from EOF analysis of historical data.

2(a) and corresponding to a source/receiver depth of 150 m and a range of 604.7 km; this range corresponds to a particular section (W3-H) of the Thetis-2 experiment. The water depth is taken 2800 m. The emitted signal is approximated by a Gaussian pulse

$$P_s(f) = \exp\left\{-2 \ln 2 \left(\frac{f-f_0}{\beta}\right)^2\right\}, \quad (27)$$

where $f = \omega/2\pi$ is the frequency and β represents the half-power (3 dB) bandwidth.⁴⁰ The central source frequency f_0 is taken 250 Hz and the bandwidth $\beta = 60$ Hz ($\approx f_0/4$).

Figure 3(a) shows the normal-mode prediction of the arrival pattern after 400.2 s using all propagating modes. On the left of the figure ray-group arrivals in the form of triplets can be distinguished, corresponding to steep rays sampling the deep water layers. The resolution of later ray-group arrivals, sampling gradually shallower layers, becomes more

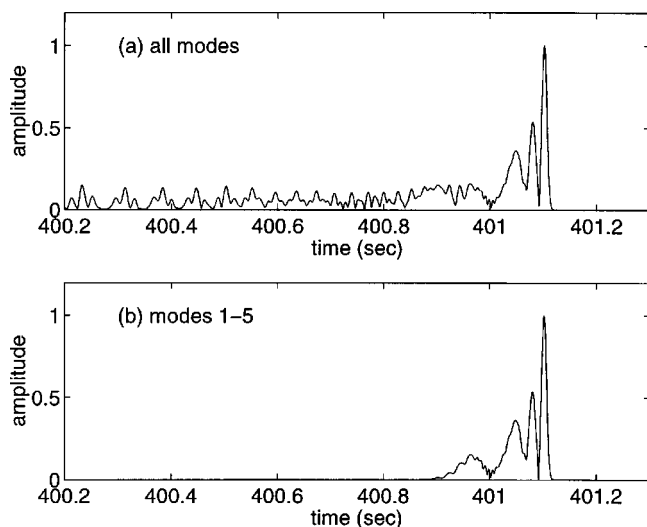


FIG. 3. Normal-mode prediction of the arrival pattern using the annual reference profile of Fig. 2(a), for a source/receiver depth 150 m, range 604.7 km, central source frequency $f_0 = 250$ Hz and bandwidth $\beta = 60$ Hz. (a) Prediction based on all propagating modes. (b) Prediction using modes 1–5.

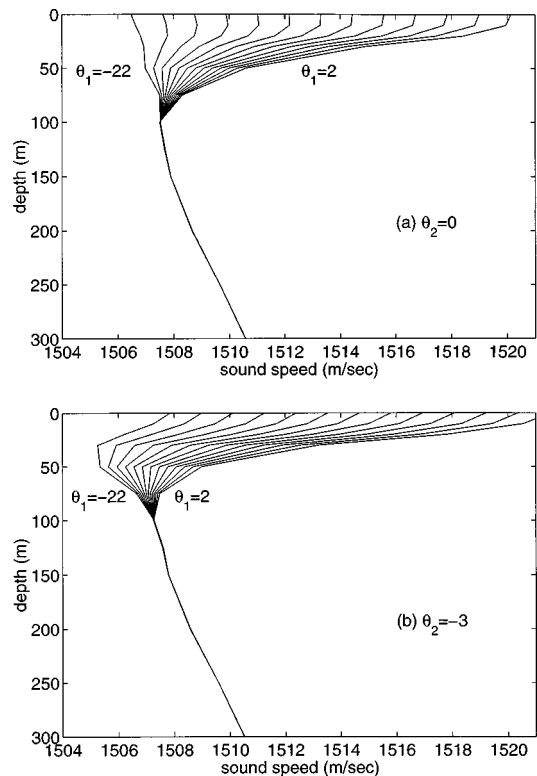


FIG. 4. Sound-speed variations of (a) the annual reference profile ($\vartheta_2 = 0$), and (b) the EOF-2 distorted annual reference profile with $\vartheta_2 = -3$, for $\vartheta_1 = 2, 0, -2, \dots, -22$.

difficult due to decreasing separation between triplets. Finally, the late part of the reception corresponds to a large number of unresolved shallow rays. Late arrivals sampling the shallow water layers are sensitive to EOF-1 (seasonal) sound-speed variations, taking place in the upper 100 m. This part of the reception can be sufficiently represented by retaining a small number of low-order modes in the normal-mode representation (14). Figure 3(b) shows the prediction using the first five propagating modes.

In the following, the behavior of the late arrival pattern to EOF-1 sound-speed variations is studied. Systematic calculations are performed over the ϑ_1 -interval $[-22, 2]$, where the stronger nonlinearity is expected on the basis of Fig. 1(b). This interval represents the transition from winter to spring conditions in the western Mediterranean sea. Two cases are considered with respect to the EOF-2 amplitude: (a) $\vartheta_2 = 0$ and (b) $\vartheta_2 = -3$. Figure 4 shows the variable sound-speed profiles with respect to ϑ_1 in the upper 300 m, ranging from near-linear profiles for $\vartheta_1 = -22$ (winter) to strongly channeled profiles for $\vartheta_1 = 2$ (spring). It is shown below that the induced changes in the propagation conditions cause a gross nonlinear arrival time behavior similar to that observed in Fig. 1(b).

The following arrival-pattern calculations are performed using propagating modes 1–5. For the calculation of influence coefficients all modes are taken into account, unless otherwise stated.

A. Nonlinear behavior

The case $\vartheta_2 = -3$, with $f_0 = 250$ Hz and $\beta = 60$ Hz, is examined first. The variation of the late arrival pattern, with

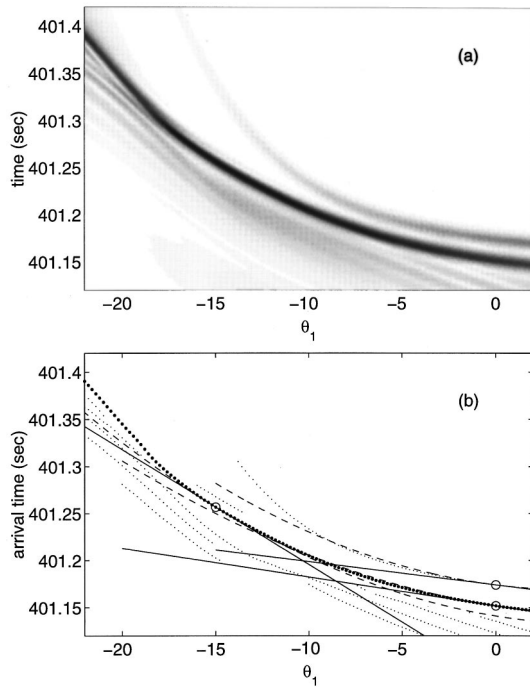


FIG. 5. Dependence of the late arrivals on ϑ_1 for the case $\vartheta_2 = -3$, $f_0 = 250$ Hz, $\beta = 60$ Hz. (a) Prediction of the late arrival pattern using modes 1–5. The gray scale represents pressure amplitude, increasing from white to black. (b) Linear (—) and second-order (---) approximations of the main and cutoff peak arrival times about reference states $\vartheta_1 = 0, -15$ (○). The exact peak locations are denoted by dots; heavy dots denote the main peak arrival.

respect to ϑ_1 , is shown in Fig. 5(a); the horizontal and vertical axes measure ϑ_1 and time, respectively, whereas the gray scale represents the pressure amplitude, increasing from white to black. A clear main (highest) peak is seen in Fig. 5(a) (darker area) exhibiting a smooth nonlinear evolution with respect to ϑ_1 . A weaker cutoff peak follows the main arrival. With decreasing ϑ_1 , the cutoff peak is fading out and its separation from the main peak grows.

The peak-arrival times corresponding to the main and the cutoff peak are regular and monotonous, nonlinear functions of ϑ_1 , as shown in Fig. 5(b). The exact peak locations, corresponding to the local maxima in Fig. 5(a), are marked with light dots in this figure, whereas heavier dots denote the main peak. The first- and second-order approximations of the main and the cutoff peak arrival times about $\vartheta_1 = 0$ and -15 are marked through solid and dashed lines, respectively, whereas the reference points, at which the first and second ϑ_1 derivatives of arrival times have been calculated, are denoted by circles. It is seen that the second-order approximation provides a significant improvement, compared to the linear approximation, in the description of the exact peak locations. The curvature of the main peak arrival times is nearly constant for $\vartheta_1 > -15$ and the errors associated with the second-order approximation are less than 10 ms throughout this interval, while the linear-approximation errors exceed 60 ms away from the reference points. For $\vartheta_1 < -15$ there is a changing curvature in the exact peak locations degrading the performance of both approximations, with the second-order description still providing better results. In that case a higher-order approximation or more closely spaced

TABLE I. ϑ_1 derivatives of the main peak-arrival time for $\vartheta_1 = 0$, $\vartheta_2 = -3$, $f_0 = 250$ Hz.

	$\partial\tau/\partial\vartheta_1$	$\partial^2\tau/\partial\vartheta_1^2$
$\beta=60$ Hz		
full expression	$-3.058\ 105\ 8 \times 10^{-3}$	$4.840\ 262\ 7 \times 10^{-4}$
single/double sum	$-3.058\ 105\ 8 \times 10^{-3}$	$4.851\ 266\ 5 \times 10^{-4}$
single sum	$-3.064\ 939\ 5 \times 10^{-3}$	$-5.161\ 537\ 2 \times 10^{-5}$
$S = S' = 20$	$-3.057\ 992\ 6 \times 10^{-3}$	$4.843\ 720\ 4 \times 10^{-4}$
10	$-3.058\ 859\ 9 \times 10^{-3}$	$4.820\ 412\ 2 \times 10^{-4}$
5	$-3.057\ 578\ 9 \times 10^{-3}$	$5.017\ 765\ 2 \times 10^{-4}$
$\beta=20$ Hz		
full expression	$1.595\ 860\ 4 \times 10^{-3}$	$9.185\ 297\ 3 \times 10^{-3}$
single/double sum	$1.595\ 860\ 4 \times 10^{-3}$	$9.189\ 244\ 1 \times 10^{-3}$
single sum	$1.705\ 464\ 9 \times 10^{-3}$	$4.896\ 562\ 2 \times 10^{-3}$
$S = S' = 20$	$1.595\ 585\ 3 \times 10^{-3}$	$9.182\ 215\ 5 \times 10^{-3}$
10	$1.599\ 280\ 3 \times 10^{-3}$	$9.191\ 056\ 1 \times 10^{-3}$
5	$1.584\ 535\ 6 \times 10^{-3}$	$9.042\ 615\ 3 \times 10^{-3}$

reference points would improve the situation. Similar remarks apply to the cutoff peak-arrival times, with nearly constant curvature for $\vartheta_1 > -10$, in which case the second-order approximation about $\vartheta_1 = 0$ provides a very satisfactory description, while the linear-approximation error reaches 30 ms at $\vartheta_1 = -10$.

Table I gives the ϑ_1 derivatives of the main peak-arrival time at $\vartheta_1 = 0$. Two different values of the bandwidth β are considered, 60 Hz and 20 Hz. Furthermore, the following alternatives in expressions (22) and (24) are considered for the calculations: full expressions, expressions without the triple sum, expressions without triple and double sums, and, finally, double/triple summation along lines parallel to the diagonals, cf. Eqs. (25) and (26), with different values of S , S' (20, 10, 5). Concerning the first-order influence coefficients, the single-sum expressions give a sufficient approximation for $\beta = 60$ Hz, with a 0.2% error; this means that the double sum in Eq. (24), associated with the eigenfunction derivatives, is of minor importance in this case. The corresponding error for $\beta = 20$ Hz is 7%; a sufficient approximation in this case can be obtained by retaining the double sum and performing the summation parallel to the diagonal with $S = 5$, reducing the error to 0.7%. For the second-order influence coefficients both the single- and the double-sum expressions must be taken into account in (24), whereas the triple-sum expressions have a very small contribution in both cases. Furthermore, the double-sum expressions can be truncated, keeping the near-diagonal ($S = 5$) terms only. With these simplifications/truncations in expressions (22) and (24) the computational burden can be significantly reduced.

From Table I it is seen that the first- and second-order influence coefficients strongly depend on the bandwidth of the emitted signal. To clarify this effect Fig. 6 shows the evolution of the late arrival pattern in the neighborhood of the main peak about $\vartheta_1 = 0$ for the two cases, $\beta = 60$ Hz and $\beta = 20$ Hz. The main peak arrival is marked through heavy dots in this figure. It is seen that the local behavior of the main peak-arrival time with respect to ϑ_1 is different in the two cases: it is close to linear for $\beta = 60$ Hz, while it is nonlinear and nonmonotonous for $\beta = 20$ Hz. It is seen also that the first- and second-order Taylor approximations about

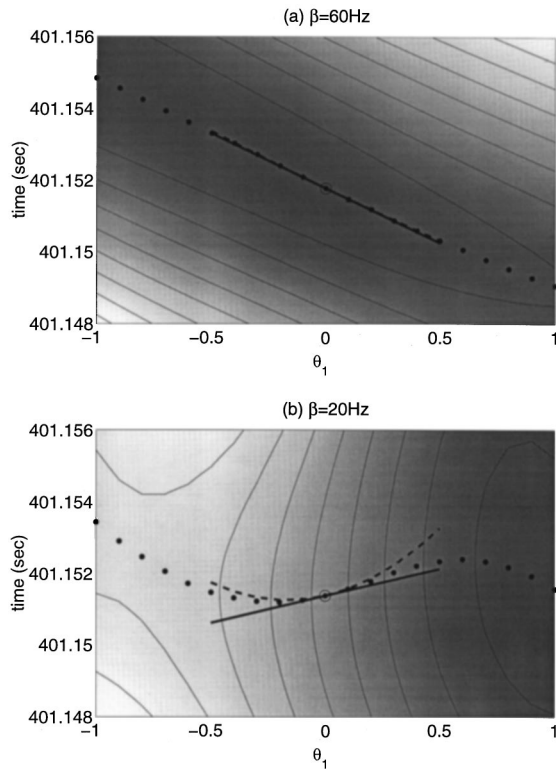


FIG. 6. Behavior of the main peak-arrival time (dots) in the neighborhood of $\vartheta_1=0$, for the case $\vartheta_2=-3$, $f_0=250$ Hz using different bandwidths: (a) $\beta=60$ Hz; (b) $\beta=20$ Hz. The gray scale, increasing from white to black, and the solid contours represent the pressure amplitude. The heavy solid and dashed lines denote the first- and second-order approximations, respectively, about reference state $\vartheta_1=0$ (O).

$\vartheta_1=0$, corresponding to the influence coefficients of Table I (solid and dashed lines, respectively), sufficiently describe the local behavior in both cases.

Case $\vartheta_2=0$, with $f_0=250$ Hz and $\beta=60$ Hz, is considered next. Figure 7 shows the evolution of the late arrival pattern, with respect to ϑ_1 . In this case, for $\vartheta_1 > -10$ the main peak coincides with the cutoff peak and is in nearly insensitive to ϑ_1 changes. For $\vartheta_1 < -10$ the smooth evolution picture with respect to ϑ_1 is replaced by a sequence of peaks fading in and out. Consequently, the peak-arrival times are no longer continuous functions of ϑ_1 but jump each time a different peak takes over. The underlying reason for this anomalous behavior, and also for the previously observed bandwidth effect, is the interference between modes in the time domain. Detailed modal considerations are presented in the following subsection.

The exact peak locations and the first/second-order Taylor approximations of the main peak-arrival times are shown in Fig. 8. The arrival times exhibit a strongly nonlinear behavior between jumps, even though the ϑ_1 variations are small. The rapidly changing nonlinear character is sufficiently described by the first and second ϑ_1 derivatives of the peak-arrival times, the first-order approximations always being the tangent lines and the second-order ones sufficiently describing the local curvature. Nevertheless, over the ϑ_1 interval $[-20, -10]$ the local (fine-scale) trend is quite different from the global (large-scale) trend. For example, for $\vartheta_1 = -16$ the local curvature is even opposite to the large-scale

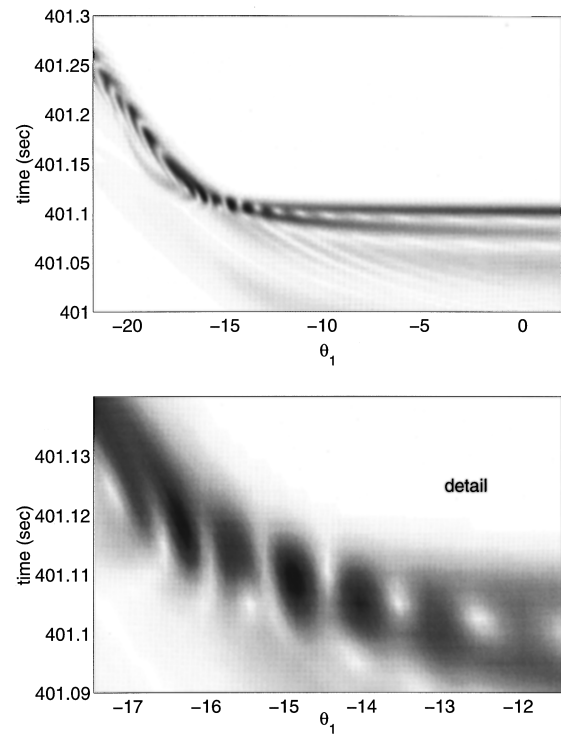


FIG. 7. Dependence of the late arrival pattern on ϑ_1 , for the case $\vartheta_2=0$, $f_0=250$ Hz, $\beta=60$ Hz. The prediction is based on modes 1–5. The bottom panel focuses on the interval $[-17, -12]$. The gray scale represents pressure amplitude, increasing from white to black.

curvature. The anomalous behavior of the second-order influence coefficients is an indication of the strong fine-scale nonlinearity in this case.

The effect of the source frequency on the arrival-time behavior is studied in the following by considering a lower central frequency $f_0=75$ Hz and bandwidth $\beta=20$ Hz, resembling the source used in the ATOC experiment.⁴¹ Figure 9(a) shows, for $\vartheta_2=0$, the evolution of the late arrival pattern with respect to ϑ_1 . In this case, the main peak coincides with the cutoff peak, and the corresponding peak-arrival time is a smooth function of ϑ_1 , in contrast to the strong fine-scale nonlinearities observed in Fig. 7. Comparing the large-scale behavior in Figs. 7 and 9(a), it is seen that while the cutoff times for $\vartheta_1 = -22$ and $\vartheta_1 = 2$ are about the same in the two figures, the large-scale behavior from $\vartheta_1 = -22$ to 2 is much closer to linear for $f_0=75$ Hz than for $f_0=250$ Hz. This is attributed to the larger acoustic wavelength (20 m) in the 75-Hz case compared to the 250-Hz case (6 m), smoothing out the effects of sound-speed changes of limited spatial scales, such as the EOF-1 variations.

The exact peak-arrival times along with their first- and second-order Taylor approximations about $\vartheta_1=0$ and -15 are shown in Fig. 9(b). The second-order approximation about $\vartheta_1=0$ provides a good description up to $\vartheta_1 = -15$, where the error in the arrival time reaches 10 ms, while the linear-approximation error is 30 ms. Due to increasing curvature with decreasing ϑ_1 the approximation about $\vartheta_1 = -15$ leads to large deviations for $\vartheta_1 > -10$; at $\vartheta_1=0$ the error in the arrival time exceeds 50 ms for both the linear and the second-order approximation. On the other hand, for $\vartheta_1 < -15$ the curvature of the exact peak-arrival times remains

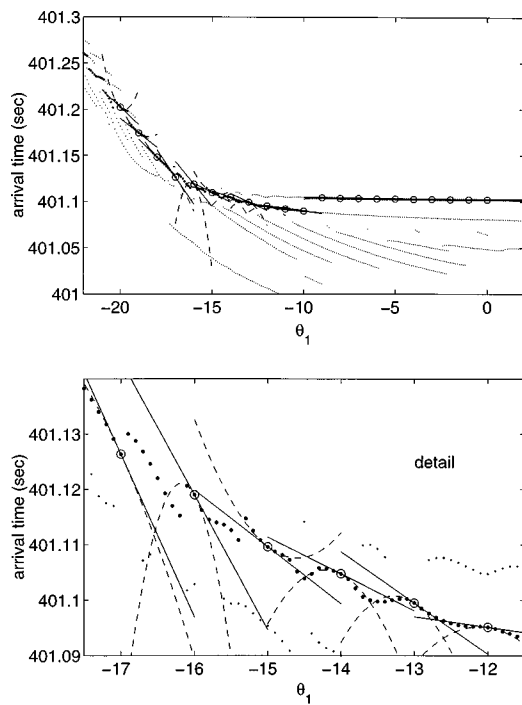


FIG. 8. Linear (—) and second-order (---) approximations of the main peak-arrival times about reference state $\vartheta_1=0, -1, \dots, -20$ (\circ) for case $\vartheta_2=0, f_0=250$ Hz, $\beta=60$ Hz. The bottom panel focuses on the interval $[-17, -12]$. The exact peak locations are denoted by dots; heavy dots denote the main peak arrival.

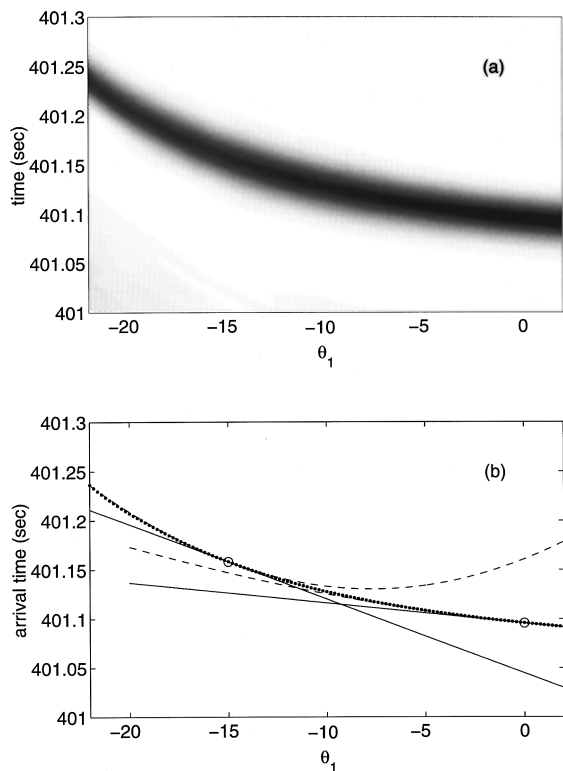


FIG. 9. Dependence of the late arrivals on ϑ_1 for case $\vartheta_2=0, f_0=75$ Hz, $\beta=20$ Hz. (a) Prediction of the late arrival pattern using modes 1–5. The gray scale represents pressure amplitude, increasing from white to black. (b) Linear (—) and second-order (---) approximations of the main/cutoff peak arrival times (dots) about reference states $\vartheta_1=0, -15$ (\circ).

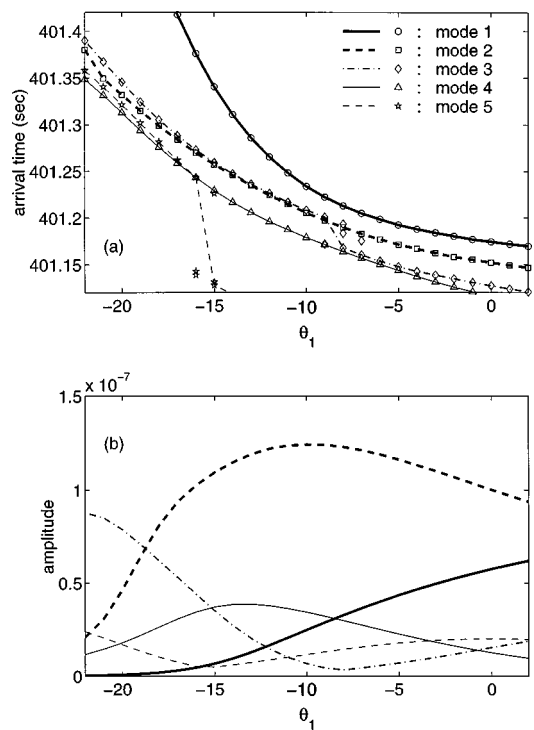


FIG. 10. Single-mode calculations for modes 1–5, for the case $\vartheta_2=-3, f_0=250$ Hz, $\beta=60$ Hz. Dependence of (a) modal peak arrival times and (b) maximum peak amplitudes on ϑ_1 ; maximum peaks are line connected in the upper figure.

nearly constant and the exact peak locations can hardly be distinguished from the second-order approximation.

B. Modal interpretation

The observed nonlinear behavior of the late peak-arrival times with respect to ϑ_1 , in both the large and the fine scale, is explained in the following in terms of the behavior of individual modes.

Figure 10 shows calculations for the case $\vartheta_2=-3$, with $f_0=250$ Hz and $\beta=60$ Hz. In particular, Fig. 10(a) shows the predicted peak-arrival times for modes 1–5, based on systematic (with respect to ϑ_1) broadband calculations of arrival patterns for each individual mode. Due to broadband propagation, a single mode results in multiple peak arrivals in general; the maximum peaks for each mode are line connected in this figure. The corresponding maximum peak amplitudes for each mode are shown in Fig. 10(b). It is seen that mode 2 dominates in this case, except for $\vartheta_1 < -18$ where mode 3 takes over; also, mode 1 has a considerable amplitude for $\vartheta_1 > -5$. The arrivals observed in Fig. 5(a) can be associated with individual modes in Fig. 10. The cutoff peak corresponds to mode 1 whereas the main peak is due to modes 2 and 3. Modes 4 and 5 correspond to the earlier arrivals in Fig. 5(a) with a significantly larger time spread than the main and the cutoff peaks.

The dependence of the modal group traveltimes on ϑ_1 at 3-dB frequencies of two different bandwidths, $\beta=60$ Hz and $\beta=20$ Hz, about the central source frequency 250 Hz is shown in Fig. 11. A dispersion effect, i.e., a dependence of group travel times on frequency, is seen in this figure, which increases with increasing mode order. Depending on the in-

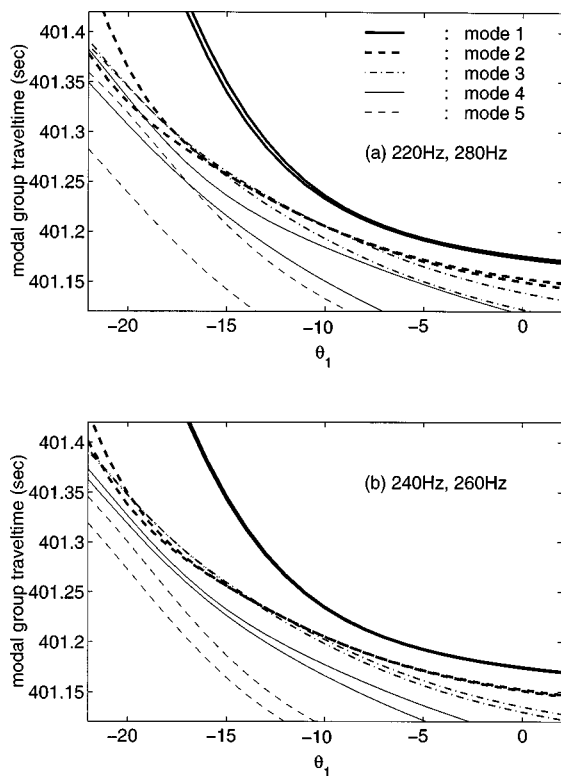


FIG. 11. Dependence of modal group travel times on ϑ_1 for the case $\vartheta_2 = -3$ at the frequencies (a) 220 Hz and 280 Hz (3-dB frequencies for $\beta = 60$ Hz), (b) 240 Hz and 260 Hz (3-dB frequencies for $\beta = 20$ Hz). The earlier travel times correspond to the lower frequency in each case (220 Hz and 240 Hz, respectively).

tensity of dispersion for each propagating mode, the corresponding signal at the receiver has a larger time spread than the emitted pulse. Modes 1, 2, and 3 are subject to small dispersion over the ϑ_1 intervals where they are dominant; in the intervals where they are less energetic, the dispersion increases. Mode 4 and, particularly, mode 5 undergo large dispersion in Fig. 11(a) and this explains the longer duration of the corresponding arrivals in Fig. 5(a). By comparing Fig. 11(a) and (b) it is seen that the dispersion effect becomes weaker with decreasing bandwidth. This can be explained by the fact that individual modes exhibit a smaller spread in group velocities over the narrower frequency interval, and, thus, the spread in associated group travel times decreases.

The bandwidth effect, observed in Table I and Fig. 6, can be explained in terms of modal arrivals 1 and 2 shown in Figs. 10 and 11. These modal arrivals are separated by about 25 ms in Fig. 10(a) for $\vartheta_1 = 0$. Furthermore, modes 1 and 2 are subject to small dispersion in Fig. 11 and, thus the duration of the corresponding arrivals is mainly defined by the source bandwidth. A bandwidth $\beta = 60$ Hz corresponds to a duration of about 16 ms; in this case modal arrivals 1 and 2 are well separated in time, as can be seen in Fig. 5(a). For $\beta = 20$ Hz, however, the duration rises to 50 ms. In this case, modal arrivals 1 and 2 overlap with each other in the time domain. Their interference gives rise to the pattern of Fig. 6(b). The corresponding peak-arrival times exhibit a nonlinear fine-scale behavior, even though the underlying modes 1 and 2 behave regularly and almost linearly in the ϑ_1 -interval $[-1, 1]$.

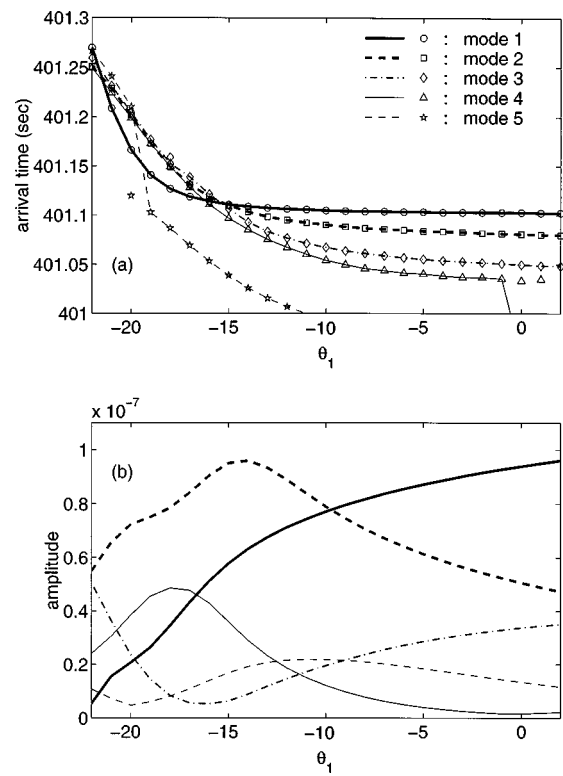


FIG. 12. Single-mode calculations for modes 1–5, for the case $\vartheta_2 = 0$, $f_0 = 250$ Hz, $\beta = 60$ Hz. Dependence of (a) modal peak-arrival times and (b) maximum peak amplitudes on ϑ_1 ; maximum peaks are line connected in the upper figure.

Mode interference is the origin of the fine-scale nonlinear behavior shown in Fig. 7 as well. Figure 12 shows the peak arrival times for modes 1–5 and the corresponding maximum amplitudes for the case $\vartheta_2 = 0$, with $f_0 = 250$ Hz and $\beta = 60$ Hz. The dominating modes in this case are modes 1 and 2, and partially modes 3 and 4. Peak-arrival times for modes 1 and 2 are well separated in the ϑ_1 interval $[-10, 0]$ in Fig. 12(a), corresponding to the last two arrivals in Fig. 7. Beyond $\vartheta_1 = -10$, however, modes 1 and 2 get closer and finally intersect each other at $\vartheta_1 \approx -15$, and the same happens for other mode combinations as well. The interference of different modes close to the intersection gives rise to the complex pattern shown in Fig. 7. Thus it becomes clear that the interference between overlapping modes may give rise to a complex nonlinear behavior of arrival times with respect to ϑ_1 in the fine scale.

Modal peak-arrival times for the lower-frequency case $f_0 = 75$ Hz, $\beta = 20$ Hz, for $\vartheta_2 = 0$ are shown in Fig. 13(a). Compared to the previous Fig. 12(a), modes 1–5 are now well separated and span a much larger time duration (600 ms) than previously; note that the vertical scale is different in Figs. 12(a) and 13(a). From the modal peak amplitudes shown in Fig. 13(b) it is seen that mode 1 dominates throughout the ϑ_1 variability interval, whereas higher-order mode amplitudes are an order of magnitude smaller, an entirely different behavior than shown in Fig. 12(b) for $f_0 = 250$ Hz. Thus the main peak shown in Fig. 9(a) is the clear arrival of mode 1 which can be resolved throughout the ϑ_1 variability interval.

Figure 14 shows the evolution with ϑ_1 of the eigenfunc-

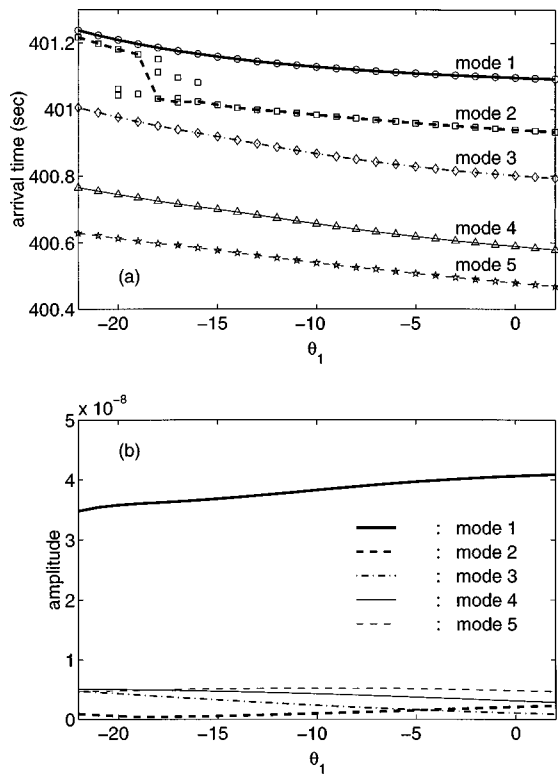


FIG. 13. Single-mode calculations for modes 1–5, for the case $\vartheta_2=0$, $f_0=75$ Hz, $\beta=20$ Hz. Dependence of (a) modal peak-arrival times and (b) maximum peak amplitudes on ϑ_1 ; maximum peaks are line connected in the upper figure.

tions (mode shapes) corresponding to modes 1 and 2 in the upper 500 m for the cases: (a) $\vartheta_2 = -3$, $f_0 = 250$ Hz; (b) $\vartheta_2 = 0$, $f_0 = 250$ Hz; and (c) $\vartheta_2 = 0$, $f_0 = 75$ Hz. The corresponding upper and lower turning depths are also shown in this figure as functions of ϑ_1 . The upper 100-m layer, where the EOF-1 variability takes place, is denoted by a dotted line.

It is seen from Fig. 14 that changes in ϑ_1 cause in general a vertical mode displacement. Thus individual modes sense the sound-speed variability area (upper 100 m) more or less intensively, depending on whether they are displaced upward or downward. This mode displacement is the underlying reason for the nonlinear dependence of modal peak-arrival times on ϑ_1 . Decreasing ϑ_1 values lead from channelled to surface reflected propagation conditions, cf. Fig. 4, which in turn are associated with an upward displacement of modes, as observed in Fig. 14. Accordingly, the sensitivity of modal arrival times to ϑ_1 , described by the absolute value of the gradient $\partial\tau_i/\partial\vartheta_1$ (first-order influence coefficient), is expected to increase as ϑ_1 decreases. In deed, this gross arrival-time behavior was observed in all cases considered so far. Furthermore, comparing Fig. 14(a) with 10(a) and Fig. 14(b) with 12(a), it is seen that the arrival-time sensitivity on ϑ_1 becomes significant in the case that the maximum of the mode function lies above 100 m, the EOF-1 variability limit. If it lies below that depth, the nonlinear behavior and the overall influence on ϑ_1 is very weak since the mode hardly senses the EOF-1 variations.

In Fig. 14(a) ($\vartheta_2 = -3$, $f_0 = 250$ Hz) a continuous displacement of modes 1 and 2 is seen throughout the ϑ_1 variability interval. Furthermore, the maxima of both modes 1

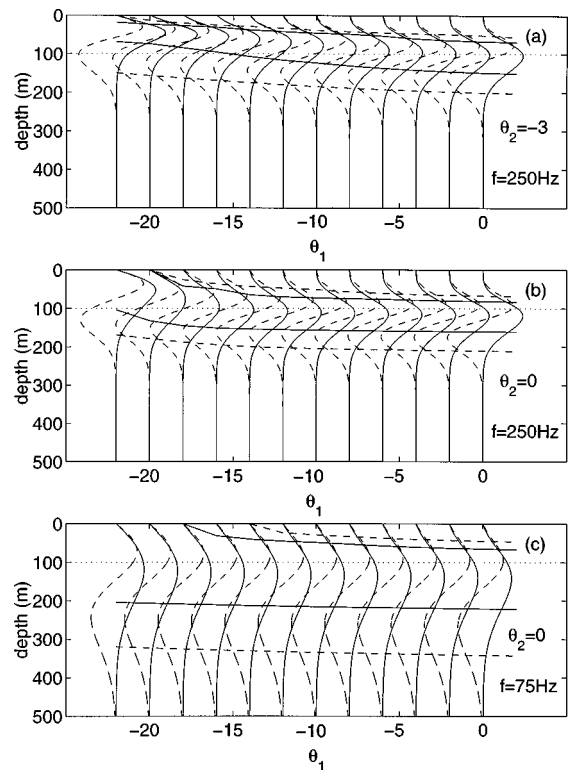


FIG. 14. Dependence of vertical eigenfunctions, upper and lower turning depths for mode 1 (—) and mode 2 (---) on ϑ_1 , for cases (a) $\vartheta_2 = -3$, $f_0 = 250$ Hz, (b) $\vartheta_2 = 0$, $f_0 = 250$ Hz, (c) $\vartheta_2 = 0$, $f_0 = 75$ Hz.

and 2 lie within the EOF-1 variability layer for all ϑ_1 values. This physically explains the significant sensitivity of modal peak-arrival times for modes 1 and 2 on ϑ_1 in Fig. 10(a) and also their nonlinearity, stronger for mode 1, in agreement with the different displacement rates in Fig. 14(a). In Fig. 14(b) ($\vartheta_2 = 0$, $f_0 = 250$ Hz) the maximum of mode 1 enters the upper 100-m layer for ϑ_1 less than -15 . This explains the very low sensitivity of mode 1 to ϑ_1 variations for $\vartheta_1 > -15$ in Fig. 12(a). For $\vartheta_1 < -15$ mode 1 undergoes significant displacement with ϑ_1 and this reflects in the rapid sensitivity increase and the associated nonlinear behavior in Fig. 12(a). Mode 2 is subject to milder changes in Fig. 14(b) and this can be also seen in Fig. 12(a). In the low-frequency case ($\vartheta_2 = 0$, $f_0 = 75$ Hz) modes 1 and 2 shown in Fig. 14(c) extend to larger depths, and ϑ_1 has a much weaker displacement effect than previously. Accordingly, the portion of mode 1 sensing the upper 100-m layer is small and only slightly changing with ϑ_1 ; this explains the weaker nonlinear behavior observed in this case.

IV. DISCUSSION AND CONCLUSIONS

A second-order description of the nonlinear dependence of the peak-arrival times on the sound speed was presented. Exploiting the generic nature of peak arrivals, expressions for the first and second sound-speed derivatives of peak-arrival times were obtained in terms of corresponding sound-speed derivatives of the Green's function. These expressions are free from any restrictive assumptions concerning the ocean environment, the emitted signal, or the particular propagation modeling. Using normal-mode and eigenvalue

perturbation theory closed-form expressions were derived for the first and second sound-speed derivatives of the Green's function for the case of a range-independent medium, in terms of the eigenvalues and eigenfunctions at the reference state. Although the resulting expressions are lengthy, especially the ones for the second derivatives, they can be simplified in practice since the involved coefficient matrices are diagonally dominant. Exploiting this fact, the multiple summations can be restricted along a small number of near-diagonal lines. This reduces the computational burden without significantly affecting the computation accuracy.

Using simulations for range-independent ocean environments describing winter-to-spring conditions in the western Mediterranean sea, motivated from the Thetis-2 experiment, the behavior of the late peak-arrival times with respect to sound-speed changes was studied and the performance of the second-order approach was assessed. The simulations reproduced a large-scale nonlinear behavior similar to that observed in the Thetis-2 data. Modal considerations revealed that this nonlinearity is due to the vertical displacement of the low-order propagating modes caused by the winter-to-spring changes in the sound-speed profile. In particular, the change from upward refracting profiles in winter to channeled profiles in spring causes a lowering of the upper turning depths of the low-order modes which no longer penetrate the shallow layers where the seasonal variability takes place. This results in an decreasing sensitivity, from winter to spring, of the corresponding arrival times to sound-speed changes.

Apart from the large-scale behavior of arrival-time variations with respect to sound-speed changes, normal-mode theory predicts that a fine-scale behavior of the late arrivals may eventually be present, in the case of mode interference. The fine-scale behavior is characterized by peaks fading in and out and also by a strongly nonlinear behavior of the corresponding peak-arrival times, even for small sound-speed perturbations. Mode interference takes place when significant (energetic) modes overlap with each other in the time domain.

The signal bandwidth determines the duration of individual modal arrivals and thus it affects overlapping and mode interference, depending on the dispersion characteristics of the individual modes as well. In the case of small dispersion, a bandwidth increase will reduce the duration of modal arrivals, weaken the overlapping and interference between modes and smoothen out the fine-scale behavior. On the other hand, if strong dispersion is present, a bandwidth increase will lead to a larger time spread of individual modal arrivals, which in turn will intensify overlapping.

The propagation range is expected to have an effect on the fine-scale behavior, depending on the strength of dispersion. If the dispersion is small, a range increase will lead to larger separation between individual modal arrivals. If the modes overlap with each other due to dispersion a range increase will merely lead to a stretching of the arrival pattern, without affecting mode overlapping.

The central source frequency plays an important role affecting both the fine- and the large-scale behavior. In the cases considered, a decrease of the source frequency led to

an increase in the separation between modes in the time domain, i.e., to better mode resolution and disappearance of fine-scale anomalies. Concerning the large-scale behavior, the decrease of the central source frequency led to a weakening of the nonlinearity. In general, on the basis of wave theory, it is expected that for lower frequencies (larger acoustic wavelengths) vertical mode eigenfunctions become less sensitive to sound-speed changes of limited spatial scales, such as the EOF-1 variations considered. Accordingly, for lower frequencies the dependence of modal peak-arrival times on sound-speed variations is expected to become closer to linear.

In all cases considered the first- and second-order approximation of peak-arrival times gives a good description of the nonlinearity locally, the first-order approximations being always the tangent lines to the exact nonlinear dependence and the second-order ones sufficiently describing the local curvature. Exploiting this fact, the second sound-speed derivatives of the peak-arrival times can be used as an indicator of the complexity of arrival pattern variations in the neighborhood of a reference state.

Furthermore, the second derivatives of the peak-arrival times can be used as a criterion for the validity of the linear approximation, commonly used for inversions. Nevertheless, care is needed in applying this criterion since a small value of the second derivative may point either to a near-linear behavior or to a turning point, whereas a large value (large curvature) definitely points to strong nonlinear behavior, i.e., insufficiency of the first-order description. Without paying attention to these issues the local first- and second-order description may be misleading for the large-scale behavior.

A currently considered extension of the present work is the use of the peak-arrival concept in combination with coupled-mode theory for predicting the influence of range-dependent sound-speed variations on arrival times. The second order is particularly important in that case, since the effect of range dependence on the arrival times is expected to be primarily a second-order effect.^{11,12}

ACKNOWLEDGMENTS

This work was supported by the European Union under Contract No. CT91-0006 (Thetis-2) in the framework of the EU MAST-2 programme. The authors would like to thank the anonymous reviewers for helpful comments.

¹W. H. Munk and C. Wunsch, "Ocean acoustic tomography: A scheme for large scale monitoring," *Deep-Sea Res.* **26A**, 123–161 (1979).

²Y. Desaubies, "Ocean acoustic tomography," in *Oceanographic and Geophysical Tomography*, edited by Y. Desaubies, A. Tarantola, and J. Zinn-Justin (Elsevier, Amsterdam, 1990), pp. 159–202.

³W. H. Munk, P. F. Worcester, and C. Wunsch, *Ocean Acoustic Tomography* (Cambridge U.P., New York, 1995).

⁴J. A. Mercer and J. R. Booker, "Long-range propagation of sound through oceanic mesoscale structures," *J. Geophys. Res.* **88**, 689–699 (1983).

⁵J. L. Spiesberger and P. F. Worcester, "Perturbations in travel time and ray geometry due to mesoscale disturbances: A comparison of exact and approximate calculations," *J. Acoust. Soc. Am.* **74**, 219–225 (1983).

⁶Thetis-2, A pilot tomography system for monitoring the western Mediterranean basin, Final Report, edited by U. Send, EU MAST-2 project CT91-0006, March 1996.

⁷The cutoff time of an acoustic reception is taken as the maximum time of the five higher peaks, and it designates the end of the arrival of nonbottom

- interacting energy. In actual measurements, the cutoff times exhibit a more stable behavior than the locations of the highest peak.
- ⁸ P. F. Worcester, B. D. Cornuelle, J. A. Hildebrand, W. S. Hodgkiss, T. F. Duda, J. Boyd, B. M. Howe, J. A. Mercer, and R. C. Spindel, "A comparison of measured and predicted broadband acoustic arrival patterns in travel time-depth coordinates at 1000-km range," *J. Acoust. Soc. Am.* **95**, 3118–3128 (1994).
 - ⁹ W. H. Munk, "Sound channel in an exponentially stratified ocean, with application to sofar," *J. Acoust. Soc. Am.* **55**, 220–226 (1974).
 - ¹⁰ W. H. Munk and C. Wunsch, "Ocean acoustic tomography: Rays and modes," *Rev. Geophys. Space Phys.* **21**, 777–793 (1983).
 - ¹¹ J. L. Spiesberger, "Ocean acoustic tomography: Travel time biases," *J. Acoust. Soc. Am.* **77**, 83–100 (1985).
 - ¹² W. H. Munk and C. Wunsch, "Biases and caustics in long-range acoustic tomography," *Deep-Sea Res.* **32**, 1317–1346 (1985).
 - ¹³ W. H. Munk and C. Wunsch, "Bias in acoustic travel time through an ocean with adiabatic range dependence," *Geophys. Astrophys. Fluid Dyn.* **39**, 1–24 (1987).
 - ¹⁴ E. C. Shang and Y. Y. Wang, "On the calculation of modal travel time perturbation," *Sov. Phys. Acoust.* **37**, 411–413 (1991).
 - ¹⁵ E. C. Shang and Y. Y. Wang, "Acoustic travel time computation based on PE solution," *J. Comput. Acoust.* **1**, 91–100 (1993).
 - ¹⁶ M. I. Taroudakis and J. S. Papadakis, "Modal inversion schemes for ocean acoustic tomography," *J. Comput. Acoust.* **1**, 395–421 (1993).
 - ¹⁷ P. J. Sutton, P. F. Worcester, G. Masters, B. D. Cornuelle, and J. F. Lynch, "Ocean mixed layers and acoustic pulse propagation in the Greenland sea," *J. Acoust. Soc. Am.* **94**, 1517–1526 (1993).
 - ¹⁸ L. Brekhovskikh and Y. Lysanov, *Fundamentals of Ocean Acoustics* (Springer-Verlag, New York, 1982).
 - ¹⁹ G. V. Frisk, *Ocean and Seabed Acoustics. A Theory of Wave Propagation* (Prentice-Hall, Englewood Cliffs, NJ, 1994).
 - ²⁰ P. J. Sutton, W. M. L. Morawitz, B. D. Cornuelle, G. Masters, and P. F. Worcester, "Incorporation of acoustic normal mode data into tomographic inversions in the greenland sea," *J. Geophys. Res.* **99**, 12487–12502 (1994).
 - ²¹ R. Pawlowicz, J. F. Lynch, W. B. Owens, P. F. Worcester, W. M. L. Morawitz, and P. J. Sutton, "Thermal evolution in the greenland sea gyre in 1988–1989," *J. Geophys. Res.* **100**, 4727–4751 (1995).
 - ²² P. J. Sutton, W. M. L. Morawitz, P. F. Worcester, and B. D. Cornuelle, "Temperature evolution in the upper ocean in the greenland sea january to march 1989," *J. Geophys. Res.* **102**, 27861–27874 (1997).
 - ²³ G. A. Athanassoulis and E. K. Skarsoulis, "Arrival-time perturbations of broadband tomographic signals due to sound-speed disturbances. A wave-theoretic approach," *J. Acoust. Soc. Am.* **97**, 3575–3588 (1995).
 - ²⁴ E. K. Skarsoulis, G. A. Athanassoulis, and U. Send, "Ocean acoustic tomography based on peak arrivals," *J. Acoust. Soc. Am.* **100**, 797–813 (1996).
 - ²⁵ G. A. Athanassoulis, J. P. Papadakis, E. K. Skarsoulis, and M. I. Taroudakis, "A comparative study of two wave-theoretic inversion schemes in ocean acoustic tomography," in *Full Field Inversion Methods in Ocean and Seismo-Acoustics*, edited by O. Diachok, A. Caiti, P. Gerstoft, and H. Schmidt (Kluwer, Dordrecht, 1995), pp. 127–132.
 - ²⁶ E. K. Skarsoulis, "An adaptive scheme for ocean acoustic tomography of large soundspeed variations," in *Proceedings of the 3rd European Conference on Underwater Acoustics*, edited by J. S. Papadakis (Crete U.P., Heraklion, 1996), pp. 803–808.
 - ²⁷ E. K. Skarsoulis and U. Send, "One-step analysis of nonlinear traveltime data in ocean acoustic tomography," submitted to *J. Atmos. Ocean. Technol.* (1998).
 - ²⁸ U. Send, G. Krahmhann, D. Mauuary, Y. Desaubies, F. Gaillard, T. Terre, J. Papadakis, M. Taroudakis, E. Skarsoulis, and C. Millot, "Acoustic observations of heat content across the Mediterranean Sea," *Nature (London)* **385**, 615–617 (1997).
 - ²⁹ S. M. Flatte (Ed.), R. Dashen, W. H. Munk, K. M. Watson, and F. Zachariassen, *Sound Transmission Through a Fluctuating Ocean* (Cambridge U.P., New York, 1979).
 - ³⁰ S. M. Flatte and R. Stoughton, "Predictions of internal-wave effect on the ocean acoustic coherence, travel-time variance, and intensity moments for very long-range propagation," *J. Acoust. Soc. Am.* **84**, 1414–1424 (1988).
 - ³¹ T. F. Duda, S. M. Flatte, J. A. Colosi, B. D. Cornuelle, J. A. Hildebrand, W. S. Hodgkiss, P. F. Worcester, B. M. Howe, J. A. Mercer, and R. C. Spindel, "Measured wavefront fluctuations in 1000-km pulse propagation in the Pacific Ocean," *J. Acoust. Soc. Am.* **92**, 939–955 (1992).
 - ³² J. A. Colosi, S. M. Flatte, and S. Bracher, "Internal-wave effects on 1000-km oceanic acoustic pulse propagation: Simulation and comparison with experiment," *J. Acoust. Soc. Am.* **96**, 452–468 (1994).
 - ³³ R. B. Evans, "A coupled mode solution for acoustic propagation in a waveguide with stepwise depth variations of a penetrable bottom," *J. Acoust. Soc. Am.* **74**, 188–1954 (1983).
 - ³⁴ G. A. Athanassoulis, K. A. Belibassakis, and E. L. Livaditi, "An enhanced coupled-mode theory for sound propagation over an arbitrary bottom topography," 4th European Conf. Underwater Acoust., Rome, Sept. 1998.
 - ³⁵ R. N. Bracewell, *The Fourier Transform and its Applications* (McGraw-Hill, Singapore, 1986).
 - ³⁶ C. A. Boyles, *Acoustic Waveguides. Applications to Oceanic Science* (Wiley, New York, 1984).
 - ³⁷ J. Mathews J. and R. L. Walker, *Mathematical Methods of Physics* (Benjamin, New York, 1964).
 - ³⁸ L. D. Landau and E. M. Lifshitz, *Quantum Mechanics: Nonrelativistic Theory* (Pergamon, Oxford, 1977).
 - ³⁹ M. B. Porter and E. L. Reiss, "A numerical method for ocean acoustic normal modes," *J. Acoust. Soc. Am.* **76**, 244–252 (1984).
 - ⁴⁰ S. Benedetto, E. Biglieri, and V. Castellani, *Digital Transmission Theory* (Prentice-Hall, Englewood Cliffs, NJ, 1987).
 - ⁴¹ B. M. Howe, S. G. Anderson, A. B. Baggeroer, J. A. Colosi, K. R. Hardy, D. Horwitt, F. W. Karig, S. Leach, J. A. Mercer, K. Metzger, Jr., L. O. Olson, D. A. Peckham, D. A. Reddaway, R. R. Ryan, R. P. Stein, K. von der Heydt, J. D. Watson, S. L. Weslander, and P. Worcester, "Instrumentation for the Acoustic Thermometry of Ocean Climate (ATOC) Prototype Pacific Ocean Network," *OCEANS '95*, San Diego, pp. 1483–1500 (1995).

Improved vertical array performance in shallow water with a directional noise field

Kwang Yoo and T. C. Yang

Naval Research Laboratory, Washington, DC 20375

(Received 13 June 1997; accepted for publication 25 August 1998)

The detection and localization performance of a vertical array against a submerged target in shallow water can be significantly improved if the noise field is directional and the signal arrives in the null (notch) of the noise field. This often happens in a summer environment with a downward refractive sound speed profile in which the surface generated noise field exhibits a notch in the noise vertical directionality distribution at mid (e.g., 500 Hz) frequencies. Using conventional beamforming, by steering the beams to the shallow arrival angle of the target signal, the (undesired) noise which arrives at steep angles can be suppressed. However, conventional beamforming often suffers from significant signal gain degradation due to multipaths in the shallow water environment. Matched-field processing yields a theoretical signal gain by coherently processing the signal, but its ability to reject the directional noise is limited. Matched-beam processing, which is matched-field processing in the beam domain, incorporates the advantages of matched-field processing for coherent signal integration, and conventional beamforming for noise rejection. For the summer environment studied, matched-beam processing yields the highest array gain, almost a twice longer detection range, and a superior capability in detecting a deep target compared with the other two processors. This is demonstrated using simulated signal and noise fields with a full water column vertical array. [S0001-4966(98)02312-1]

PACS numbers: 43.30.Re, 43.30.Wi [DLB]

INTRODUCTION

Signal processing is used in underwater acoustics to enhance the detection of a signal among unwanted signals (noise) originating from various sources. When signal and noise exhibit different directionality^{1,2} in elevation angles, the detection and localization of a submerged source can be improved by adaptive array processing which exploits this difference in signal and noise arrival angles. A well known example is adaptive nulling of strong interferences for a horizontal array using adaptive beamforming.³ In this paper, we investigate adaptive processing of vertical array in shallow water with a directional noise field.

Highly directional noise field can be found in shallow water in summer with a downward refractive sound speed profile. For this type of environments, theoretical computations of the surface generated noise field exhibit a notch in the noise vertical directionality distribution at mid (e.g., 500 Hz) frequencies.^{1,2} The existence of the noise notch has been confirmed experimentally.⁴⁻⁶ The noise notch can be weakened or disappear when sound propagation is associated with strong mode coupling.⁷

We study how directional noise is handled by various signal processing algorithms. Specifically, we investigate the performance of conventional beamforming processing (CBP), matched-field processing (MFP),⁸ and matched-beam processing (MBP)⁹ against a submerged target in a directional noise environment. For detection, array performance is measured by array gain (AG) and nominal detection range of a vertical array. [Array gain measures the improvement of the output signal-to-noise ratio (SNR) over the input SNR.] For source localization, array performance is measured by the peak-to-sidelobe levels in the range-depth ambiguity sur-

face with the peak identified as the target. Array performance is simulated in this paper using a stationary signal and noise field, the latter corresponding to a long-term averaged noise field. Detection statistics and detection performance (e.g., receiver operation curves) for fluctuating signal and noise fields are beyond the scope of this paper.

In a directional noise field when the signal arrives in directions near the noise notch, conventional beamforming can be used to improve array gain by steering beams to the direction of the signal where the noise level is weak. Signal gain is maximum when the signal arrives in one beam (as in deep water). In a multipath shallow water environment, the signal is often split into several beams for a vertical array. Signal gain (SG) is degraded due to beam splitting, resulting in a less than ideal AG for conventional beamforming.

Matched-field processing overcomes SG degradation by coherently processing the multipath signal arrivals. We note that while matched-field processing may be adaptive to the signal, it is not necessarily adaptive to the noise. We note also that the treatment of (directional) noise by matched-field processing from the aspect of signal detection (e.g., array gain) is limited in the literature. We find in this paper that matched-field processing has a limited capability in rejecting the directional noise. This is demonstrated by the MFP noise gain (measured at the target location) which is generally higher than the CBP noise gain. As a result, despite the improved signal gain, MFP yields a less than theoretical array gain. (The MFP array gain turns out to be only slightly higher than the CBP array gain.) The limited ability of the MFP in rejecting the surface generated noise can be traced to the high noise background at the target range-depth cell

which results from the accumulation of sidelobes associated with individual noise sources near the surface.

Matched-beam processing is matched-field processing in the beam domain. It overcomes the signal gain degradation of conventional beamforming as MFP does. It incorporates the beam filter of conventional beamforming by excluding the beams of high noise from the matched-beam correlation. As a result, it produces the highest array gain among the three processors for the summer environment with a directional noise field.

Matched-beam processing is based on conventional beamforming but it extends conventional beamforming to include full field (matched field) processing. Matched-beam processing correlates the data field and replica field in the beam domain (the wave number domain). Various extensive algorithms applied to conventional beamforming, such as adaptive beamforming, can be directly incorporated into matched-beam processing. The beam filter (to be illustrated below) is the simplest way to implement adaptive processing.

Both MFP and MBP localize a source in range and depth, but not CBP. MBP yields the same range and depth ambiguity surface as MFP if all beams are used in the MBP. But if only a small number of beams are used in MBP, the resulting ambiguity surface is different from the MFP surface. For a shallow water environment, both MFP and MBP produce high sidelobe levels using the Bartlett processor. Using the minimum variance (MV)¹⁰ processor, the sidelobes are much suppressed, but the MV processor is sensitive to environmental mismatch. This paper studies the Bartlett and MV processors as were most papers on MFP in the literature.

[An alternative approach to directional noise uses the method of noise pre-whitening. It is a variation of the Bartlett processor in which the data covariance matrix is divided by the noise covariance matrix before it is multiplied by (correlated with) the replica field.¹¹ This processor yields a theoretical $10 \log N$ (N is the number of sensors) for noise gain as noise has been whitened. However, because of this extra noise covariance matrix, the replica field does not match the data field at the source location; the data field is the signal field divided by the square root of the noise covariance matrix. In other words, the modified MFP may be adapted to the noise, it is not adapted to the signal. Another consequence of the normalization of the signal covariance matrix by the noise covariance matrix is the existence of many high level sidelobes in the signal ambiguity surface.¹¹ The noise pre-whitening approach will not be considered in this paper.]

To illustrate the performance difference of MFP and MBP in a directional noise field, we shall investigate the ambiguity surfaces of MFP and MBP under the assumption of low signal-to-noise (SNR) ratio. In a directional noise field, it is how noise is processed that makes the difference for detection of a weak signal.

This paper is organized as follows. The acoustic environment and the noise model used for the analysis are described in Sec. I. It is followed by the array gain comparisons of the three processors in Sec. II. The comparisons were

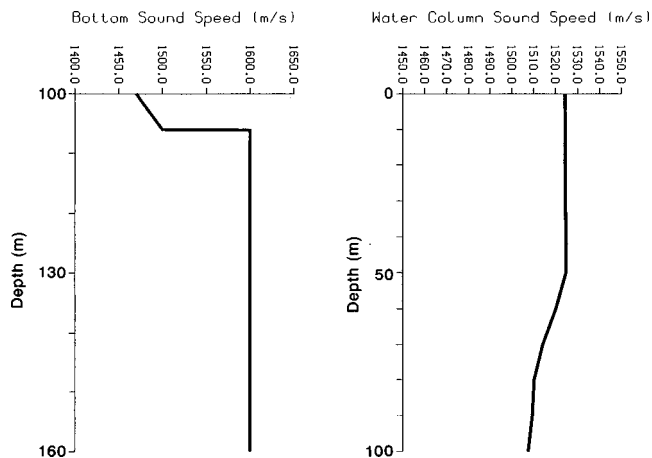


FIG. 1. Water sound-speed profile (right) and bottom sound-speed profile (left).

made by varying the source range from 100 m to 20 km. In Sec. III, the ambiguity surfaces of MFP and MBP are compared under low (input) signal-to-noise ratio conditions. System implications are discussed and detection ranges for the three processors are compared in Sec. IV. A summary is given in Sec. V.

I. THE ACOUSTIC ENVIRONMENT AND NOISE MODELING

The environment used for the present analysis is a typical summer water sound speed profile as shown in Fig. 1. The sound speed is almost constant up to 50 m depth and slowly decreases thereafter. The water column is 100 m deep with a sediment layer of 6 m thickness overlaying the basement. The sediment has a sound speed increasing linearly with the depth; the initial sound speed is slower than the water sound speed at the interface. It has a density of 1.5 g/cm^3 and an attenuation of $0.06 \text{ dB/wavelength}$. The basement has a constant sound speed of 1600 m/s , a density of 1.8 g/cm^3 , and an attenuation of $0.15 \text{ dB/wavelength}$. Because of the decreasing water sound speed near the interface we expect a lot of bottom interaction in this environment.

The receivers are on a vertical array spanning the whole water column from 5 m to 95 m. There are a total of 61 phones with uniform spacing of 1.5 m. We consider a narrow-band signal of 500 Hz. The source-to-receiver range is varied from 100 m to 20 km in the array performance study. The source is initially deployed at 90 m depth. The analysis is later extended to other source depths.

For the surface generated noise, the noise source is assumed¹ at 0.1 m below the surface so that the field generated by the source is effectively a dipole field due to reflections from the surface. We assume a uniform distribution of the noise sources on an (imaginary) plane located at 0.1 m depth. The covariance matrix elements can then be obtained by incoherently integrating the fields due to sources in thin annular rings centered around the vertical array. The details of this computation are given in Ref. 2. The noise integration is done up to 20 km which is a reasonable range for shallow water environment; noise from long range sources are significantly attenuated.

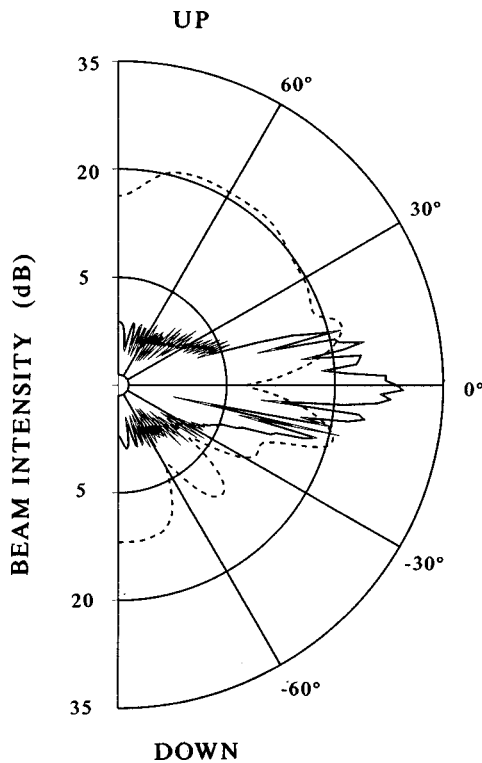


FIG. 2. Signal (solid curve) and noise (dotted curve) vertical directivity for a signal source at 10 km and 90 m depth.

In the downward refractive environment, one expects the vertical directivity of the noise field (noise vertical beam power distribution) to have a notch at the near horizontal direction.⁴⁻⁶ An intuitive explanation is given by normal modes. Note that in this environment, the low order mode depth functions peak at the lower half of the water column. Consequently, surface noise sources couple weakly with low order modes and strongly with higher modes. Since the low and high order modes arrive at shallow and steep grazing angles, respectively, the weak coupling of the noise sources to the low order modes results in low beam levels at shallow angles. Hence, the vertical directivity of the noise is expected to exhibit a noise notch. One notes that, on the other hand, a submerged source, e.g., at a depth of 90 m, would couple strongly with the low order modes. The signal from this source is expected at the direction of the noise notch. An example is shown in Fig. 2. The difference of the signal and noise arrival angles can be exploited to achieve a high AG.

II. ARRAY GAIN

Array gain (the ratio of signal and noise gain) depends on how the signal and noise are processed. We shall compare the signal gain (SG), noise gain (NG), and array gain (AG) for CBP, MFP, and MBP below with some discussions on how each processor processes the signal and noise.

A. Conventional beamforming

The SG of a vertical array is obtained by

$$SG(\theta) = N^2 \frac{s^\dagger R s}{s^\dagger s \langle p^\dagger p \rangle}, \quad (1)$$

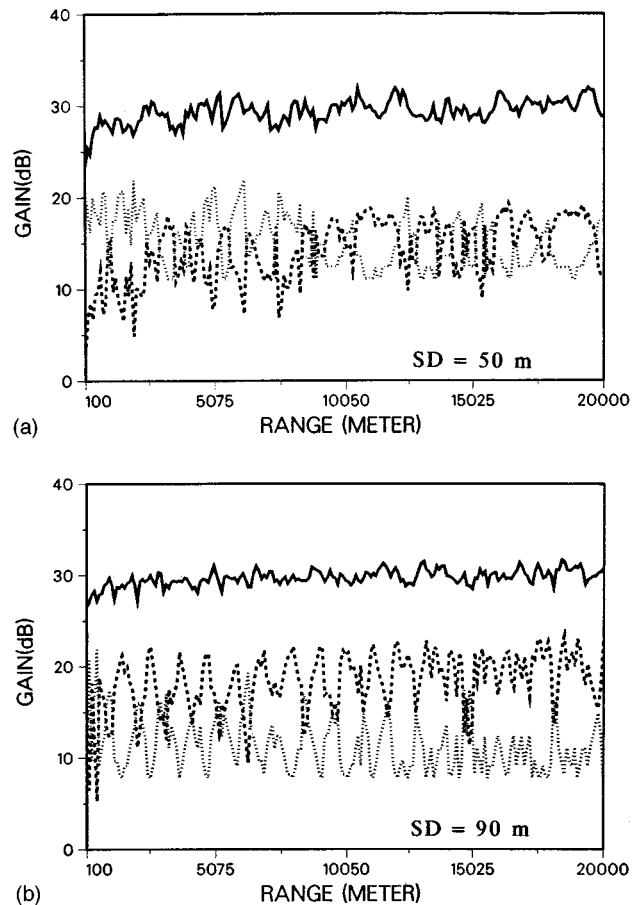


FIG. 3. Signal gain (solid curve), noise gain (dotted curve), and array gain (dash curve) as a function of source range using conventional beamforming. The source is at a depth of 50 m and 90 m for (a) and (b), respectively.

where R is the covariance matrix of the signal averaged over many data samples, s is a steering vector with elements of $e^{-ikz_j \sin \theta}$, and p is the data field. The angle bracket denotes an average of data fields. k is the wave number of the propagating sound wave, z_j is the depth of j th phone, and N is the total number of phones in the array. The angle θ is measured from the broad side of the array. As is clear from the above equation, SG will be maximized when θ is chosen to match the strongest signal power direction. The NG is similarly defined with a replacement of signal power with a noise power in the above expression. In the array gain calculation below, NG is evaluated at the direction of the signal where it yields the highest array gain.

Figure 3(a) and (b) shows the SG, NG, and AG for the source depths at 50 m and 90 m, respectively, in the case of CBP. The SGs are more or less the same in both cases, but their values are much lower than the theoretical maximum, which is 35.7 dB for 61 phones. This is due to the nature of the wave propagation in the water column. As shown in Fig. 2, the signal energy is split into several beams resulting in the signal gain degradation seen in Fig. 3. The NG in Fig. 3 is obtained by evaluating the noise at the beam direction where the signal power is maximum for each source range. The NG in Fig. 3 tends to decrease with the source range because of this selection criterion. (By convention, NG is evaluated at the target look direction.) Since the SG is almost

constant throughout the range, this results in a slight increase of AG with respect to range.

One finds from Fig. 3 that the average AG is greater when the source depth is 90 m than it is 50 m by more than 3 dB. This is because the deep source couples stronger with the lowest order modes and has a higher intensity in the direction of the noise notch. When the source is at short ranges (≤ 1 km) to the array, there will be many bottom bounced multipaths, and the signal gain (hence also the array gain) is less than when the source is at long ranges.

B. Matched-field processing

Matched-field processing correlates the data and replica fields on each phone. Matched-field signal gain is given by

$$SG(r, z) = N^2 \frac{s^\dagger \mathbf{R} s}{s^\dagger s \langle p^\dagger p \rangle}, \quad (2)$$

where \mathbf{R} is the covariance matrix as defined before, s is now the replica field vector

$$s_j = p^{\text{rplc}}(z_j, r, z),$$

which is the simulated signal field received at depth z_j on the vertical array from a source at range r and depth z ; and p is the data field vector. MFP yields the theoretical SG, $20 \log N$ when the replica field matches the data field; the maximum of Eq. (2) is obtained when r, z is at the true source position. Noise ambiguity is obtained by replacing the signal covariance matrix and average signal power in Eq. (2) by those of the noise. For the purpose of AG calculation, NG is to be evaluated at the source position.

The SG, NG, and AG of MFP are plotted in Fig. 4 as a function of the source range for two source depths. The SG is constant ($20 \log N$) as expected. The noise gain is relatively smooth as a function of the source range (compared with that of CBP). This indicates that the noise background in the range–depth ambiguity surface is relatively smooth. Again the AG is better when the source depth is at 90 m than at 50 m. The increasing trend of the AG with range is clearly visible in both plots.

We find that the NG using MFP is a few dB higher than the average NG of CBP for the deep source. Consequently, despite the higher SG, MFP does not yield a higher AG than CBP. For the mid-depth source, the NG of MFP is comparable with the average NG of CBP at ranges ≤ 10 km and is a few dB higher than the average NG of CBP at longer ranges.

It is noted that CBP uses beam steering to suppress the noise in the nonsignal directions. A different concept is used in MFP which attempts to isolate the signal from the noise using a three-dimensional ambiguity volume (i.e., bearing–range–depth). Ideally, the target should reside in a different volume cell than the noise sources. For surface generated noises, for example, one expects that the noise sources should be localized at a surface layer in the bearing–range–depth plot. But in practice, the noise sources have sidelobes which accumulatively contribute to the noise background at the target bearing–range–depth cell. In the case of strong interferences (surface ships), CBP used adaptive nulling to

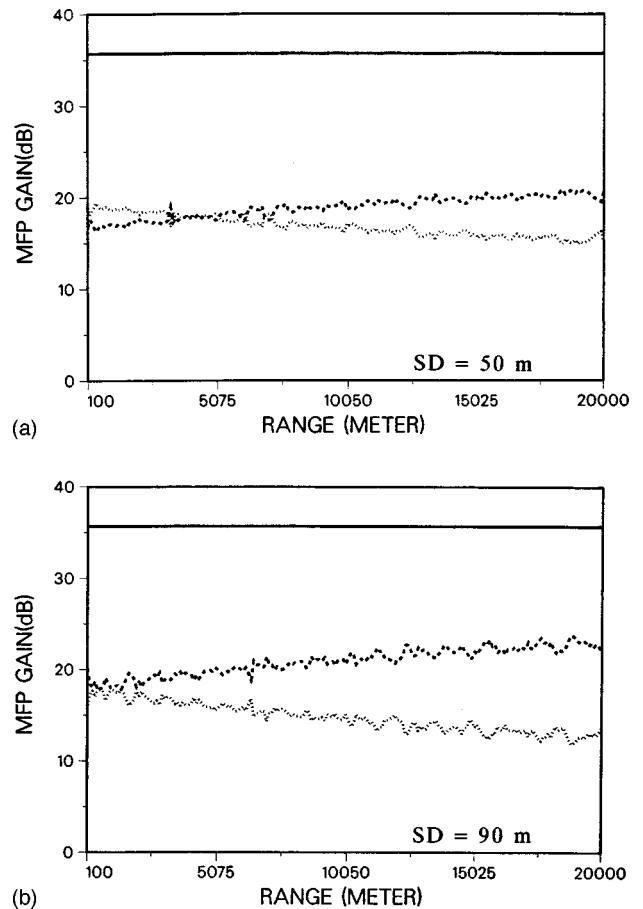


FIG. 4. Signal gain (solid curve), noise gain (dotted curve), and array gain (dashed curve) as a function of source range using matched-field processing. The source is at a depth of 50 m and 90 m for (a) and (b), respectively.

reject the interference (i.e., adaptive beamforming). MFP will attempt to look through the ships (via the bearing–range–depth distribution) to reject the interference.

We note that in various sonar applications both conventional beam steering and adaptive beam nulling have proved to be an effective way in rejection of directional noise. This feature can be incorporated into matched-field processing using matched-beam processing. We shall demonstrate this concept next. We shall find that the array gain using matched-beam processing (with a beam filter) greatly improves over that of MFP in a directional noise field.

C. Matched-beam processing

Matched-beam processing correlates the replica and data in the beam domain. The SG is given by

$$SG(r, z) = N^2 \frac{b^\dagger \mathbf{R}_B b}{b^\dagger b \langle d^\dagger d \rangle}, \quad (3)$$

where d is the data beam vector, and b is the replica beam vector obtained by conventional beamforming of the data and replica field, respectively,

$$d_i = \sum_j e^{-ikz_j \sin \theta_i} p_j^{\text{data}}(z_j) \equiv \sum_j G_{ij} p_j^{\text{data}}, \quad (4)$$

$$b_i(r, z) = \sum_j e^{-ikz_j \sin \theta_i} p_j^{\text{rplc}}(z_j, r, z) \equiv \sum_j G_{ij} p_j^{\text{rplc}}, \quad (5)$$

where the beam number i is designated by the beam angle θ_i . The G matrix represents a Fourier transform from the phone domain to the wave number ($\kappa = k \sin \theta$) domain and is hence unitary. The beam covariance matrix R_B is given by

$$\mathbf{R}_B = \mathbf{G} \mathbf{R} \mathbf{G}^\dagger = \langle d d^\dagger \rangle, \quad (6)$$

where G^\dagger represents the inverse Fourier transform. Noting that since $G^\dagger G = \mathbf{I}$, Eq. (3) reduces to the matched-field SG.

We note that adaptive beamforming can be incorporated into matched-beam processing by replacing Eqs. (4) and (5) with the adaptive beamforming formula. For excluding beams containing excess noise, the weighting will be done directly in the beam domain using

$$\tilde{b}_i(r, z) = b_i \beta_i = \sum_j e^{-ikz_j \sin \theta_i} p_j^{\text{rplc}}(z_j, r, z) \beta_i. \quad (7)$$

As an example, to exclude the high angle ($|\theta_i| > \theta_0$) beams, we shall use a beam filter,

$$\beta_i = \begin{cases} 0, & \text{for } |\theta_i| > \theta_0, \\ 1, & \text{for } |\theta_i| \leq \theta_0. \end{cases} \quad (8)$$

In this case, the matched-beam SG will be different from the matched-field SG. We note that the matched-beam SG will depend on the choice of θ_0 .

With the beam filter β , the concept of noise rejection using beam steering (as used in CBP) can now be incorporated into matched-field processing using MBP. We shall show that a higher AG is obtained using less than full beams. Two values of θ_0 will be used below. For consistency check, we have verified numerically that using all beams (i.e., from -90° to 90°) the matched-beam SG is identical to that of MFP.

Numerical values are shown for $\theta_0 = 5^\circ$ and 10° measured from the broad side direction of the vertical array. Figure 5(a) and (b) shows the results for the case of $|\theta| \leq 5^\circ$ with two different source depths. We find that for the mid-depth source (50-m depth), the AG is not much different from the AG of MFP [see Fig. 4(a)]. However, for the deep source (90 m depth), the AG is 5–10 dB higher than the AG of MFP [compare Fig. 5(b) with Fig. 4(b)]. For that matter, it is 5–10 dB higher than the AG of CBP.

For both cases, the NG using MBP (evaluated at the source location) has been drastically reduced with the beam filter. (The beam filter has removed the noise arriving at angles $> 5^\circ$. See also Fig. 8 below.) The SG suffers a small loss with the use of the 5° beam filter for the deep source. The loss in SG is greater for the mid-depth source and cancels the gain obtained in NG. This is due to the fact that the signals from the mid-depth source arrive at higher angles than the deep source and are affected by the beam filter.

The next two plots, Fig. 6(a) and (b), show the MBP results for $\theta_0 = 10^\circ$. We find a small improvement in AG over that of MFP for the deep source and almost none for the mid-water source. This result can be understood by balancing the SG with the NG shown in Fig. 6 with that of Fig. 4. What value of θ_0 should one use? The choice of θ_0 should

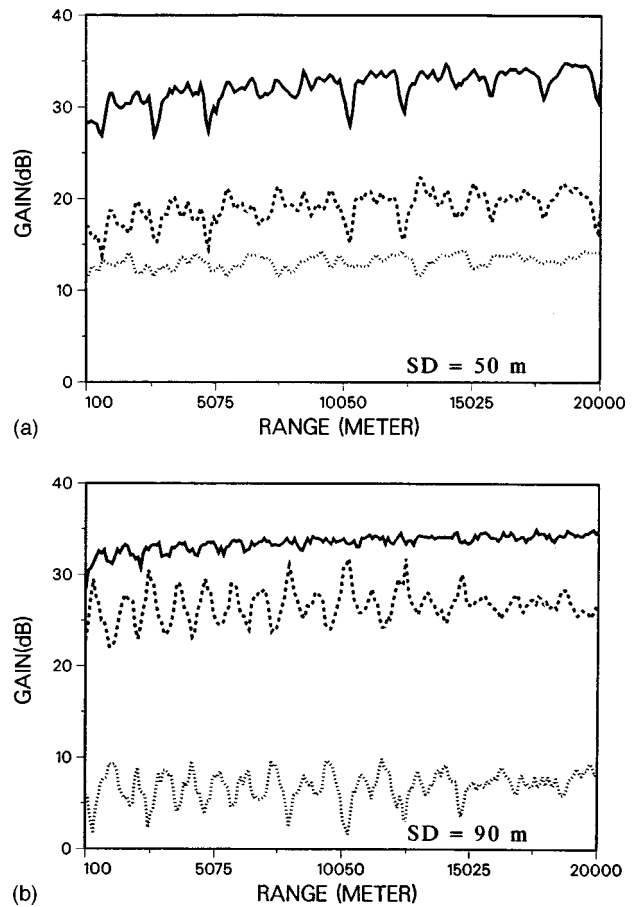


FIG. 5. Signal gain (solid curve), noise gain (dotted curve), and array gain (dashed curve) as a function of source range using matched-beam processing. Only beams with grazing angles $|\theta| \leq 5^\circ$ are used. The source is at a depth of 50 m and 90 m for (a) and (b), respectively.

be such to maximize the AG. An approximate value of the filter angle can be obtained by estimating the arrival angles of the signal and noise.

The above analysis indicates that MBP yields a significantly higher (5–10 dB) AG over MFP for a deep source. The improvement in AG is next calculated for all source depths and ranges up to 20 km. The AG difference between MBP and MFP is plotted in Fig. 7 for $\theta_0 = 5^\circ$ and 10° . Note that Fig. 7 is not the normal range-depth ambiguity surface plot. It represents the improvement in AG of MBP over MFP when the target is at the range-depth location as shown. One finds in general that the improvement in AG increases with the source depth (for this environment) and is greater at shorter ranges than at longer ranges (for a fixed source depth). Based on Fig. 7 we conclude that MBP offers an advantage for the detection of a deep source compared with MFP. The same conclusion applies to CBP as well.

We remarked earlier that the improvement in AG is primarily due to the reduction in NG. How the noise is reduced in the noise ambiguity surface is shown in Fig. 8. Figure 8(a) shows the matched-field noise gain ambiguity surface with noise only. It is normalized via Eq. (2) as such it corresponds to the matched-field noise gain at the corresponding range-depth cell. It is the same as matched-beam noise gain using all beams. Figure 8(b) shows the matched-beam noise gain with a 5° beam filter. Comparing Fig. 8(b) with Fig. 8(a), one

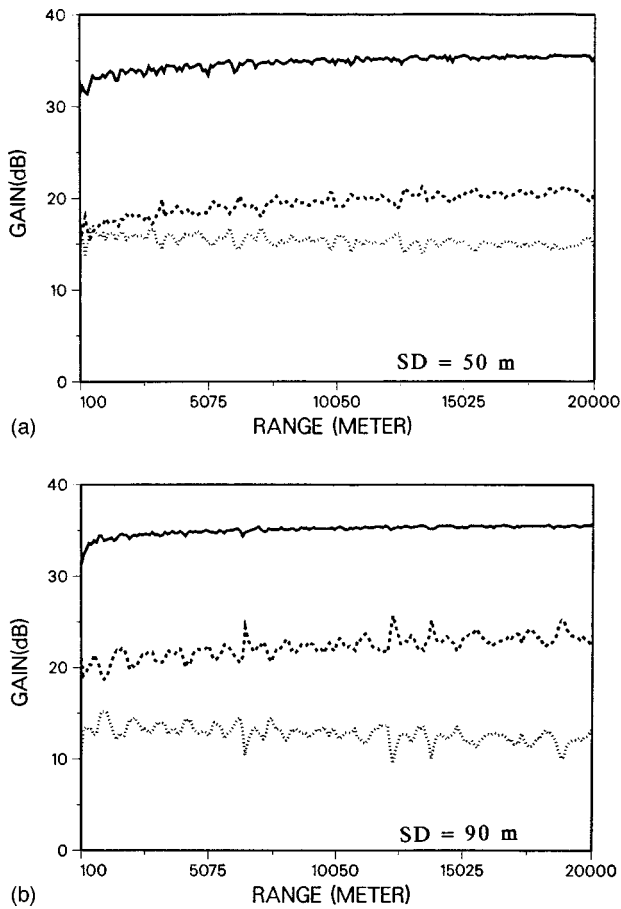


FIG. 6. Signal gain (solid curve), noise gain (dotted curve), and array gain (dashed curve) as a function of source range using matched-beam processing. Only beams with grazing angles $|\theta| \leq 10^\circ$ are used. The source is at a depth of 50 m and 90 m for (a) and (b), respectively.

sees that the noise level in the MBP ambiguity surface has been substantially (5–10 dB) reduced using the beam filter, especially in the deep water column. Figure 8(a) shows for many range–depth coordinates, the matched-field NG is ≥ 18 dB, the NG for white noise (i.e., $10 \log N$). We thus find that MFP has a limited capability in rejecting directional noise. With the beam filter incorporated in full field (matched-field) processing, the NG is substantially (6–8 dB) lower than $10 \log N$ for the lower water column [depth > 50 m in Fig. 8(b)]. This shows that MBP has certain advantages in detection of deep submerged sources in shallow water.

III. RANGE-DEPTH AMBIGUITY SURFACES

In this section we investigate source localization using MFP and MBP. Source localization is usually plotted via an ambiguity surface as a function of the source range and depth. We shall study the ambiguity surfaces using both the Bartlett (conventional) and Capon (minimum variance) processors. The Capon processor yields a high peak at the source location and low sidelobe levels elsewhere and is excellent for source localization. However, it is known to be sensitive to environmental mismatch and can consequently produce false peaks. The Bartlett processor is relatively less sensitive to mismatch but has higher sidelobes. It is an energy detector (as used above for the SG, NG, and AG calculation). As such, both processors need to be studied. In this regard, the Capon processor for matched beam processing corresponds to the so-called reduced minimum variance processor which in previous studies is shown to be more stable than the regular minimum variance processor.^{12–14}

The advantage of matched-field processing as opposed to conventional beamforming is that it can discriminate (in

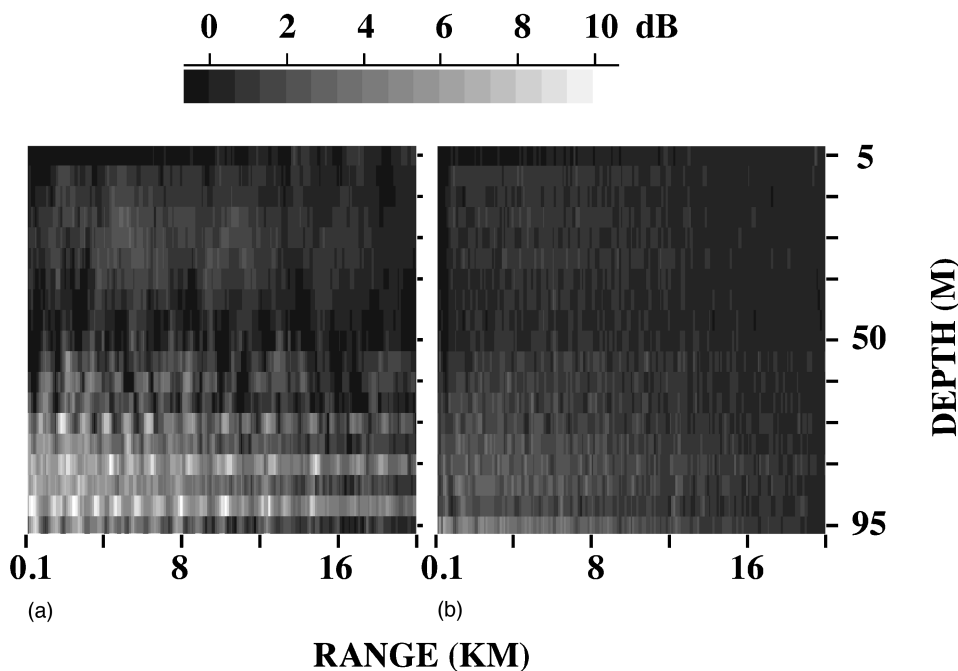


FIG. 7. The improvement in AG of matched-beam processing over matched-field processing as a function of source location. A beam filter of 5° and 10° is used in (a) and (b), respectively.

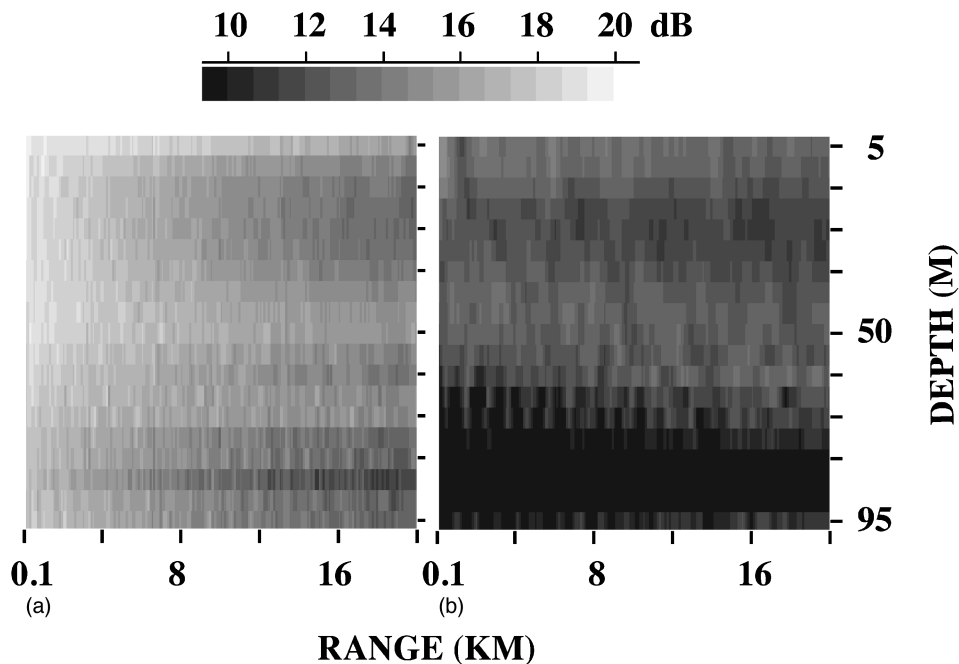


FIG. 8. The range-depth ambiguity surface of ambient noise using matched-beam processing: (a) full beams, (b) beams with grazing angles $\leq 5^\circ$.

principle) a submerged target from a surface ship. While range can be estimated by matched-field processing, range can also be estimated by other means, such as tri-angulation from two arrays using conventional beamforming. We shall explore the ability of MFP and MBP in terms of “detecting” a submerged target. This is to be done using the depth ambiguity function. An example of that will be the ambiguity function, locked at the source range, plotted as a function of depth.

A. Bartlett processor

We shall plot the range–depth ambiguity surface for an assumed input SNR, i.e., the averaged SNR on a phone. The ambiguity surfaces for MFP and MBP as conventionally defined are given by Eqs. (2) and (3) without the N^2 factor. The covariance matrix \mathbf{R} used in the above equations is now the sum of the signal and noise covariance with an assumed input SNR

$$\mathbf{R} = \mathbf{R}_n + \langle pp^\dagger \rangle, \quad (9)$$

where \mathbf{R}_n is the noise covariance matrix. The intensity of the data field includes both the signal and noise.

We shall be interested in low SNR cases since at high SNR the ambiguity surface is dominated by the signal. Noise makes a difference in terms of either localizing or detecting a target only at low SNR.

Figure 9(a) shows the MFP ambiguity surface for an input SNR of -15 dB. The range of the ambiguity surface covers from 100 m to 20 km in 100-m intervals and the depth runs from 5 m to 95 m in 5-m intervals. The source is located at a range of 10 km and a depth of 90 m. The ambiguity surface is an average over three different frequencies (450, 500, and 550 Hz). Normally, incoherent average of ambiguity surfaces over a broadband frequencies will suppress the sidelobes.¹⁵ We find only a slight improvement; the sidelobe levels change by about 1–2 dB.

Figure 9(b) shows the MBP ambiguity surface under the same SNR condition with a beam filter $\theta_0 = 5^\circ$. When all beams are included, we obtained the same results as in Fig. 9(a).

Comparing Fig. 9(a) with Fig. 8(a), we note that the two ambiguity surfaces are very similar (except for a gray scale change). The target is localized at the range of 10 km and depth of 90 m, but it has to compete with the strong noise background. Practically speaking, the ambiguity is the sum of the noise ambiguity surface with the signal ambiguity surface, the latter has been boosted (relative to the noise) by the array gain (18–20 dB). The peak-to-sidelobe ratio (PTSL) is about 1.5 dB. The low PTSL is an inherent property of the Bartlett processor.

Comparing Fig. 9(b) with Fig. 8(b), we also note that the two ambiguity surfaces are very similar for reasons given above. Comparing Fig. 9(b) with Fig. 9(a), the noise background has a much lower level (at depth ≤ 60 m) as noted before. But one observes many high level peaks at depth > 60 m. These are the sidelobes of the signal which is located at the range of 10 km and depth of 90 m. The high sidelobes can be independently verified by plotting the signal ambiguity surface separately. The reason for the high sidelobes is that part of the signal arriving at angles $> 5^\circ$ has been cut off by the beam filter (equivalently speaking, the high order modes were not used in source localization). These sidelobes are deterministic (i.e., associated with signal propagation). These sidelobes makes range estimation difficult. But the range estimation using the Bartlett processor is marginal at best [see Fig. 9(a)]. For range estimation one needs to use the Capon processor, as discussed below.

Figure 10(a) and (b) plots the range–depth ambiguity surfaces for the MFP and MBP, respectively, for an input SNR of -20 dB. The 5° beam filter is used for MBP. We reach similar conclusions as in the -15 dB SNR case. We

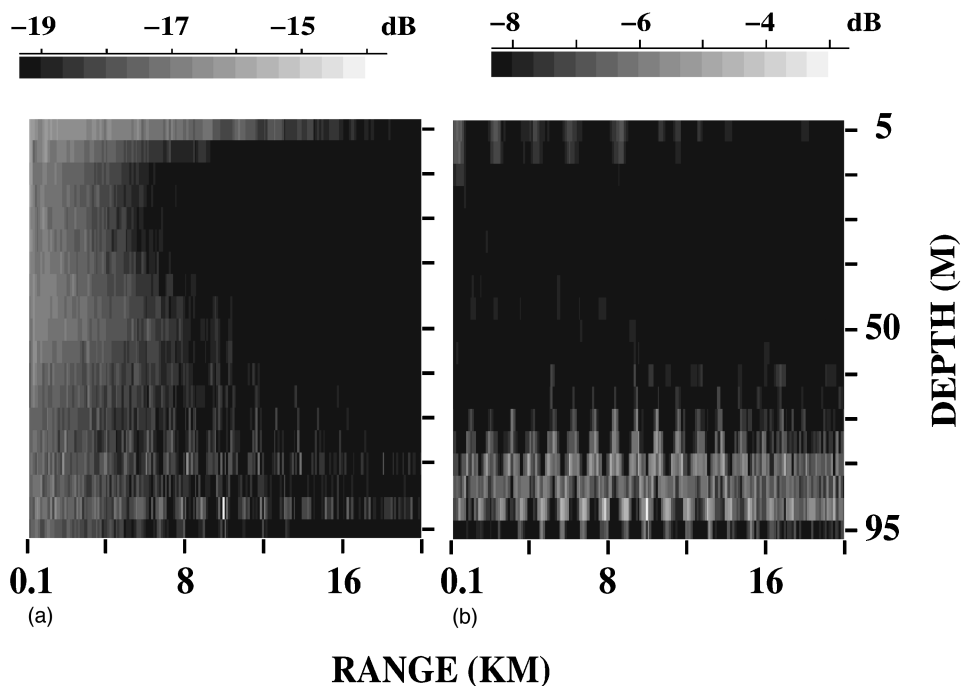


FIG. 9. The ambiguity surfaces of matched-field processing (a) and 5° matched-beam processing (b) with an input signal-to-noise ratio of -15 dB. The ambiguity surfaces are averaged over three frequency (450, 500, 550 Hz). The source is located at a range of 10 km, a depth of 90 m.

note that in Fig. 10(a), as the noise level decreases with increasing range in the ambiguity surface, a deep target has less clutter around it at 20 km than at 10 km with the same input SNR. However, due to the higher transmission loss the source needs to be ~ 10 dB louder at 20 km in order to achieve the same SNR as the source at 10 km. (See Fig. 14 below.)

Next we discuss the possibility of target detection without precise estimation of target range. For this purpose, we shall examine the depth ambiguity function.^{16,17} We shall assume three scenarios: first we know the source range, sec-

ond we know approximately the source range, and third we do not know the source range.

The depth ambiguity function is obtained from the range–depth ambiguity function. We shall illustrate the depth ambiguity function using the -15 dB SNR case shown in Fig. 9. The first depth ambiguity function will be the range–depth ambiguity function evaluated at the target range. This depth ambiguity function is plotted in Fig. 11(a) and (b) using MFP and MBP, respectively. The noise level without the target is shown by the dotted line in each figure. Next we assume that the target is somewhere in the 8–12 km

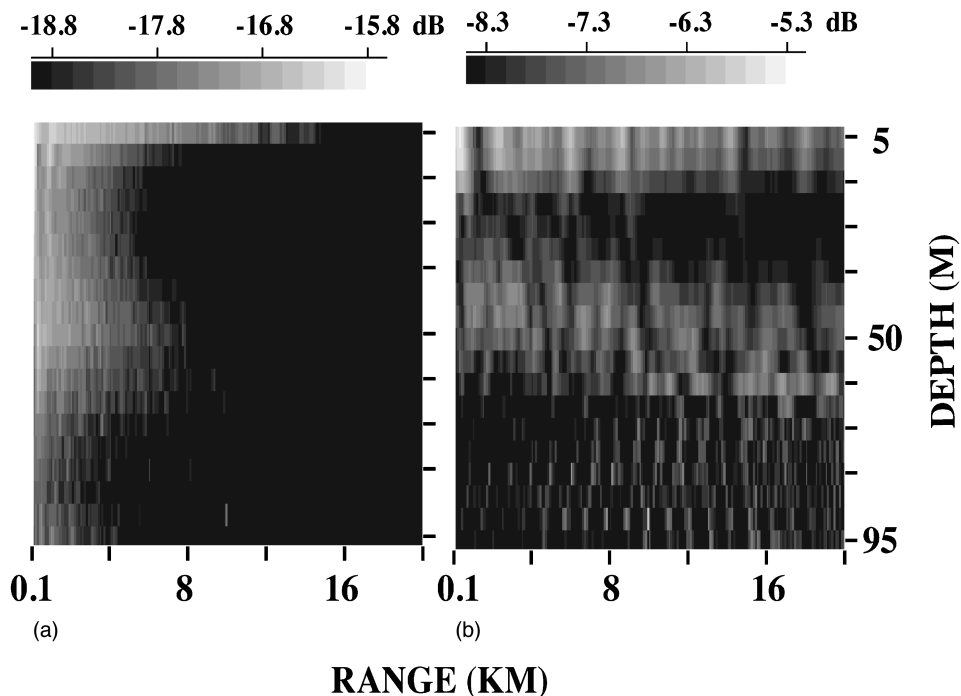


FIG. 10. The ambiguity surfaces of matched-field processing (a) and 5° matched-beam processing (b) with an input signal-to-noise ratio of -20 dB. The ambiguity surfaces are averaged over three frequency (450, 500, 550 Hz). The source is located at a range of 10 km, a depth of 90 m.

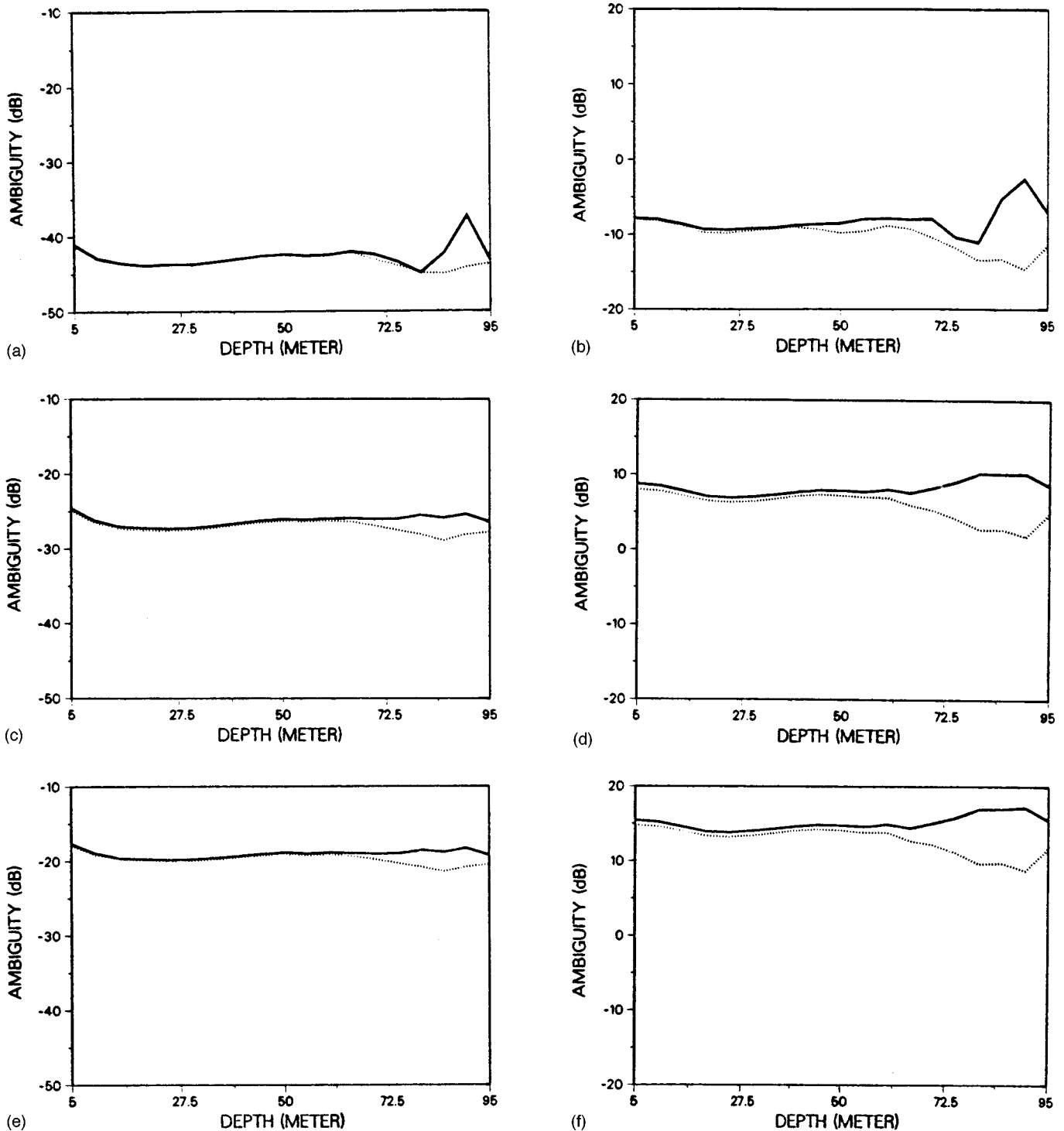


FIG. 11. The depth ambiguity function deduced from Fig. 9. (a) Matched-field processing at the source range of 10 km. (b) Matched-beam processing at the source range of 10 km. (c) Matched-field processing with range integrated over 8–12 km. (d) Matched-beam processing with range integrated over 8–12 km. (e) Matched-field processing over all ranges. (f) Matched-beam processing over all ranges. Dotted lines refer to noise only.

range. We define a second depth ambiguity function by integrating the range–depth ambiguity function (surface) over a range from 8 to 12 km. The results are shown in Fig. 11(c) and (d) for MFP and MBP, respectively. For the third case, the target range is not known, thus we integrate the ambiguity surface of Fig. 9 over all ranges (up to 20 km). The depth ambiguity function is now shown in Fig. 11(e) and (f) for MFP and MBP, respectively. Again, the dotted lines refer to the noise only ambiguity functions.

Comparing the SNR in the depth ambiguity functions between the MFP and MBP processors, we note that MBP yields a (~7 dB) higher SNR than MFP case by case. Although the input SNR is only –15 dB, the output SNR in the MBP depth ambiguity function (at the target depth) was found to exceed 10 dB. This amount of output SNR significantly enhances the detectability of a deep target. Figure 11(f) suggests that a deep target may be detected without knowing the source range. We note that the various sidelobes

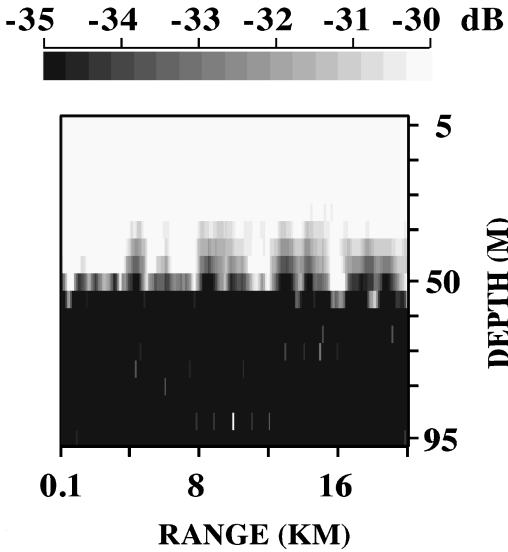


FIG. 12. The ambiguity surface of matched-beam processing (10°) using reduced minimum variance processor. The input signal-to-noise ratio is -30 dB.

in range using the 5° beam filter [Fig. 9(b)] confuses the estimation of target range. But when the target range is not required (when the question is “Is there a target?”), these signal generated sidelobes can be used to enhance the output SNR in the depth function by integrating over range.

B. Minimum variance (Capon) processor

In this section, we investigate the minimum variance (Capon) processor which is known to produce low level sidelobes. In this formalism the ambiguity function for MFP becomes the following:

$$B_{MV}(r, d) = \frac{s^\dagger s}{s^\dagger \mathbf{R}^{-1} s}, \quad (10)$$

where \mathbf{R} is the covariance matrix of the signal plus noise as defined in Eq. (9).

Equation (10) can be transformed into the beam domain using Eqs. (4) and (5)

$$B_{MV}(r, d) = \frac{b^\dagger b}{b^\dagger \mathbf{R}_B^{-1} b}, \quad (11)$$

where $\mathbf{R}_B^{-1} = \mathbf{G} \mathbf{R}^{-1} \mathbf{G}^\dagger$ and $b = \mathbf{G} s$. Equation (11) is the minimum variance (MV) matched-beam processing using all beams. A reduced minimum variance (RMV) matched-beam processor is obtained by using a subspace of the covariance matrix \mathbf{R}_B^{-1} which will be chosen to be the beam space with cutoff angle θ_0 . The reduced covariance matrix is denoted by $\tilde{\mathbf{R}}_B^{-1}$ which replaces \mathbf{R}_B^{-1} in Eq. (11).

Figure 12 plots the range–depth ambiguity using the RMV MBP with $\theta_0 = 10^\circ$. The input SNR is -30 dB. Despite the weak signal level, the target stands out clearly in the ambiguity plot at the range of 10 km and depth of 90 m. One observes that the high noise is confined primarily to depth above 60 m in Fig. 12.

Using the MV MFP, Eq. (10), we obtained practically the same ambiguity surface as in Fig. 12. On the other hand

if we reduce θ_0 to 5° the ambiguity surface (not shown) is filled with more sidelobes. Thus for the submerged target both the MV MFP (or MV MBP) and RMV MBP with $\theta_0 = 10^\circ$ can be used. The MV processor shows a better result with a lower SNR (-30 dB) than the Bartlett processor (-15 to -20 dB).

The merit of the RMV processor versus the MV processor has been discussed before.^{11–13} (They are sometimes called reduced maximum likelihood and maximum likelihood processor, respectively.) The MV processor is known to be sensitive to phase and amplitude errors⁸ (due to, for example, environmental mismatch problems). Simulation results have shown that the RMV processor is more robust in comparison. The robustness comes from a reduction of the degrees of freedom in the signal space. Note that the covariance matrix can sometimes be ill-conditioned. The MV processor uses the inverse of the covariance matrix. It is thus sensitive to the small eigenvalues of the covariance matrix which are usually not stable. A reduced minimum variance processor uses a submatrix of the covariance matrix excluding the small eigenvalues. The matrix inversion (the pseudo-inverse) is more stable. In previous RMV MFP works,^{11–13} the dominant normal modes of the signal were chosen for the RMV processor. Effectively, a mode filter was used to exclude the (higher order) modes which are either noise dominated or susceptible to environmental mismatch. In matched-beam processing, the low grazing angle arrivals are dominated by the signal and chosen for the RMV processor. Low grazing angle arrivals correspond to low order normal mode arrivals.

For the above reasons, RMV MBP may be preferred over MV MFP in practice. In the above simulations, RMV MBP and MV MFP yielded the same result—this is because we used a stationary noise model (for the purpose of mean AG calculation) which did not include noise fluctuations. The objective of the simulations was to determine the cutoff angle without sacrificing the performance of RMV MBP (compared with MV MFP). Based on the above study, we shall use $\theta = 10^\circ$ rather than 5° .

Next we show the depth ambiguity function using the RMV MBP. Since the target is precisely localized, we shall use (only) the depth ambiguity function evaluated at the target range. Figure 13(a) shows the depth ambiguity function for an input SNR of -30 dB (see Fig. 12). We observe that in the depth ambiguity function, the output signal level at the target depth is lower than the noise level at near the surface. This means that without depth discrimination, the target signal will not be detected. But since the noise level decreases significantly with depth, a deep target will be detected by depth discrimination (with a 15 dB SNR); the noise level without the target present is shown as the dotted line in Fig. 13(a). We conclude that for the directional noise environment, the RMV processor has an excellent performance in noise rejection for target in the lower water column.

Figure 13(b) shows the depth ambiguity function for an input SNR of -15 dB, the output SNR is >25 dB compared with the noise level in the lower water column.

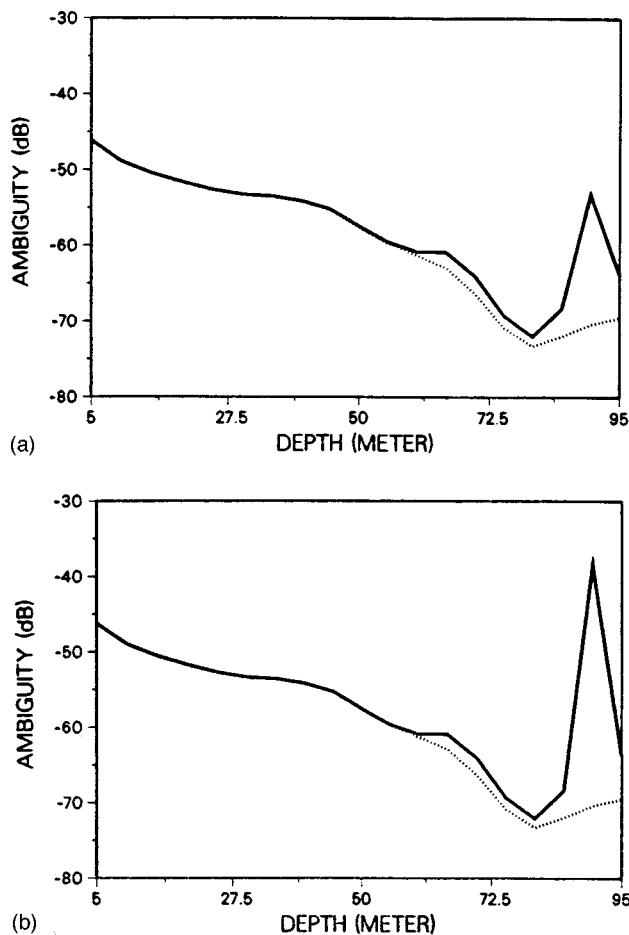


FIG. 13. The depth ambiguity function at the source range (10 km) using minimum variance matched beam processing with 10° beam filter. (a) Input signal-to-noise ratio of -30 dB as in Fig. 12. (b) Input signal-to-noise ratio of -15 dB. Dotted lines refer to noise only.

IV. SYSTEM IMPLICATIONS

The above results in AG can be used to estimate the detection range for the various processors in the shallow water environment. Maximum detection range will be estimated for a given source level, noise level, and an assumed detection threshold. Conversely, one could ask what is the minimum source level required for a given detection range assuming a certain detection threshold. As seen below, the higher AG of MBP compared with MFP and CBP implies a much extended (nearly twice) detection range for MBP.

Using the passive sonar equation, detection is determined by the following condition:

$$DT \leq SL - TL + AG - NL, \quad (12)$$

where DT on the left-hand side represents the detection threshold, SL is the source level, TL is the transmission loss, NL is the noise level per Hertz, and AG is the array gain studied before. To study detection performance, statistical distributions for NL , TL , and AG will be required. For the discussion in this section, a mean value for TL and AG would suffice; AG was calculated in Sec. II and TL will be estimated below. A nominal value of NL which falls within the range of previous experimental measurements will be used. Under this nominal condition, a maximum detection

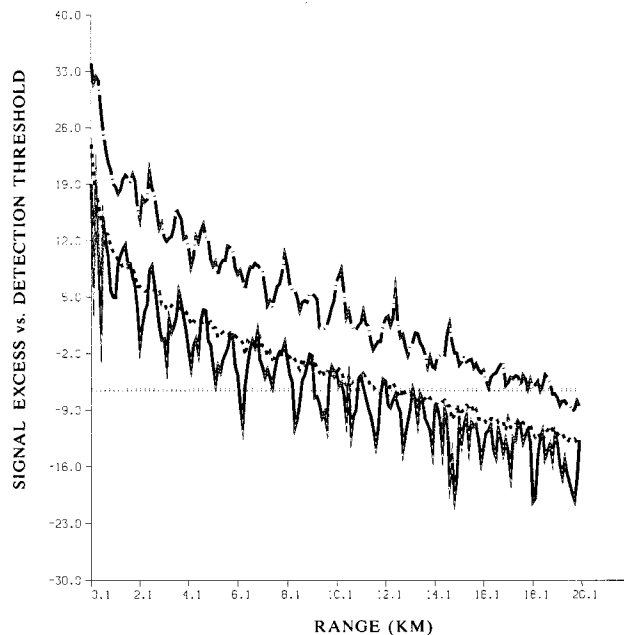


FIG. 14. Signal excess as a function of target range. Target depth is fixed at 90 m. The solid curve is for conventional beamforming, the dashed curve for matched field processing, and the dot-dash curve for matched-beam processing with $|\theta| \leq 5^\circ$. The dotted line represents a detection threshold of -6.5 dB.

range can be estimated from Eq. (12) when the right hand side (which will be called the signal excess) equals the left hand side.

Detection threshold, DT , is a system parameter. Detection threshold is discussed in Ref. 18. For example,

$$DT = 5 \log d - 5 \log \frac{T}{\beta}, \quad (13)$$

where d is the detection index, T is the integration time (s), and β is the bandwidth. For $d=10$ and $T/\beta=200$, $DT=-6.5$ dB. For the discussion below, how DT is calculated is not important. $DT=-6.5$ dB is a reasonable value that we will use. Other values can be used by the readers.

To determine detection range from Eq. (12) we need TL as a function of range. TL will be calculated for the waveguide displayed in Fig. 1 at the signal frequency of 500 Hz using a normal mode program.¹⁹ The source is assumed at a depth of 90 m. The TL is averaged over all phones on the vertical array (for a given range).

For numerical calculations, we assume a nominal value $NL=75-85$ dB// $\mu\text{Pa}/\text{Hz}$ at 500 Hz. The source level can cover a wide range from 100 to 200 dB// μPa @ 1 m. For the example below, we use $SL=120-130$ dB// μPa @ 1 m resulting in $SL-NL=45$ dB. This value is chosen by the criterion that the target can be detected by CBP at 10 km using the TL and AG given above.

With all the parameters given above, we study the difference in the detection range using all three different processors. The AG of CBP, MFP, and MBP which were previously calculated in Sec. II will now influence the detection range via Eq. (12). Figure 14 plots the right side of Eq. (12), the signal excess, as a function of source range using the three processors. In general, one finds that CBP shows the

lowest signal access level and MBP with $|\theta| \leq 5^\circ$ the highest signal access level. The MFP signal access level lies in between these two. The dotted line in Fig. 14 shows a level of DT at -6.5 dB. The (maximum) detection range of a processor can be read off the plot by the crossing point between the dotted line and the corresponding signal excess curve. The CBP detection range is a little bit hard to determine because the curve fluctuates considerably depending on the range. A fair estimate of the detection range is between 6 and 8 km. The MFP detection range is 11.5 km and the MBP detection range is 19 km. Thus based on Fig. 14, the MBP detection range is about 2.7 times of the CBP detection range and 1.65 times of the MFP detection range. Both the MFP and MBP detection ranges are far greater than CBP detection range. The MBP detection range with $|\theta| \leq 10^\circ$ (not shown in Fig. 14) is about 13 km, which is slightly longer than MFP detection range.

V. SUMMARY

Detection of a signal in a directional ambient noise field depends not only on how the signal is processed but also on how the noise is processed. The signal processing becomes more critical when the input SNR gets lower, as in this case the signal detection can be greatly improved by a clever algorithm which rejects the noise. Conventional beamforming and adaptive interference nulling are examples where the noise can be rejected by beam steering in the former case and beam nulling in the latter case.

We investigate in this paper array gain and source localization for a vertical array in a summer environment. In this environment, the noise field is highly directional at mid-frequencies and arrives at different elevation angles than the signal. This property is exploited by various signal processing methods. Specifically, we note that in a downward refracting sound speed environment in shallow water, the surface generated noise field has a notch in the near horizontal direction at mid-frequencies. On the other hand the signal from a submerged target has peaks at very shallow grazing angles. A spatial filter can be used to block out the noise beams as was done previously for conventional beamforming. This idea is generalized to a full field processing algorithm in this paper.

The reasons that full field (matched-field) processing is used in this paper are twofold. In shallow water, one encounters a problem with conventional beamforming in that the signal energy can be split over several beams. The beam splitting applies to both the signal and noise. As a consequence, the array gain will be less than theoretical and beam nulling is less than ideal. To recover the signal gain degradation, one needs coherent processing such as matched-field processing. Second, matched-field processing for a vertical array not only improves the signal gain but also yields source localization. The ability to discriminate a submerged target from a surface ship is an important feature of the matched-field processor.

We found that the matched-field (Bartlett) processor has a limited ability to reject noise (MFP noise gain can be higher than $10 \log N$ using the Bartlett processor). A much

better performance is achieved by the minimum variance processor, but the minimum variance processor may not be robust.

Noise rejection by beam steering (as used in conventional beamforming) is incorporated into matched-field processing via matched-beam processing. Matched-beam processing is matched-field processing in the beam domain. The hydrophone data and replica fields are transformed into the wave number domain; this transformation is also known as conventional beamforming. In the wave number (beam) domain, the beam filter can be incorporated naturally. Without imposing the beam filter, matched-beam processing yields identical results as matched-field processing.

The performance of three array signal processing methods, CBP, MFP, and MBP, were investigated in this paper in terms of array gain, detection ranges, source localization, and target depth discrimination against surface noise. The results can be summarized as follows. Using the Bartlett processor, the CBP generally produces a lower AG compared to MFP and MBP processors due to the multipath nature of the sound wave propagation in shallow water. The MFP performance is better than the CBP's, but it has limited means to discriminate the surface generated noise. The MBP processes the signal coherently as the MFP. It uses a spatial filter to discriminate the noise by integrating only beam angles where the signal power is strong and noise power is weak. It is found that MBP yields 5–10 dB improvement in AG and doubles the detection range compared with the other processors.

Source localization using the Bartlett processor becomes marginal for both MFP and MBP when input SNR is as low as -15 to -20 dB. The MV (Capon) processor localizes a source at an input SNR of -30 dB without difficulty. The RMV MBP has an equal performance as the MV MFP. It is expected to be more robust against environmental mismatch as indicated by previously studies; the reason is due to the reduction of the degrees of freedom in the signal space.

We compared the output SNR between the MFP and MBP processors for the detection of a (deep) submerged target. The MBP depth ambiguity function can be used to detect a submerged target without a precise knowledge of the target range for a low input SNR. This could be a useful feature in practice. Range can be further searched by iteration, or by source localization using the MV processor. The MFP depth function yields a lower output SNR.

To conclude, this paper demonstrated that for a summer environment with surface generated noise, the detection of a deep submerged target can be significantly improved by adaptive noise processing. Matched-beaming processing is a full field processor which exploits the difference in the signal and noise arrival angles in the beam domain. As noted in the Introduction, noise pre-whitening can be used to remove the noise directionality but it is not necessarily adaptive to the signal: the correlation of the modified data field with the replica field is no longer unity. In contrast, MBP keeps the signal gain as MFP.

ACKNOWLEDGMENT

This work is supported by the Office of Naval Research.

- ¹R. M. Hamson, "The theoretical responses of vertical and horizontal arrays to wind-induced noise in shallow water," *J. Acoust. Soc. Am.* **78**, 1702–1712 (1985).
- ²T. C. Yang and K. Yoo, "Modeling the environmental influence on the vertical directionality of ambient noise in shallow water," *J. Acoust. Soc. Am.* **101**, 2541–2554 (1997), and references therein.
- ³For example, B. Widrow and S. D. Stearns, *Adaptive Signal Processing* (Prentice Hall, Englewood Cliffs, NJ, 1985), Chap. 14.
- ⁴R. M. Hamson, "The modelling of vertical array response to shipping-dominated ambient noise in range-dependent environments, including comparison with measurements at two sites in the Mediterranean," Saclantcen Report SR-175.
- ⁵D. Wilson and R. Kneipfer, "Preliminary results of experiment to measure vertical directionality of ambient noise in shallow water," NUWC Tech. report, 1995 (unpublished).
- ⁶R. Heitmeyer (private communication).
- ⁷T. C. Yang and A. Al-Kurd, "The internal waves effect on the noise vertical directionality in shallow water," *Proceeding of OCEANS'96*, Vol. 1, pp. 9–16 (1996).
- ⁸See reviews by A. B. Baggeroer and W. A. Kuperman, "Matched field processing in ocean acoustics," in *Acoustic Signal Processing for Ocean Exploration*, edited by J. M. F. Moura and I. M. G. Lourtie (Kluwer, Dordrecht, The Netherlands, 1993); A. Tolstoy, *Matched Field Processing for Underwater Acoustics* (World Scientific, Singapore, 1992).
- ⁹T. C. Yang, K. Yoo, and T. Yates, "Matched-beam processing: Range tracking with vertical arrays in mismatched environments," *J. Acoust. Soc. Am.* **104**, 2174–2188 (1998).
- ¹⁰J. Capon, "High-Resolution Frequency-Wavenumber Spectrum Analysis," *Proc. IEEE* **57**, 1408–1418 (1969).
- ¹¹C. A. Zala, J. M. Ozard, and M. J. Wilmut, "Prewhitening for improved detection by matched-field processing in ice-ridging correlated noise," *J. Acoust. Soc. Am.* **98**, 2726–2734 (1995).
- ¹²C. L. Byrne, R. T. Brent, C. Feuillade, and D. R. DelBalzo, "A stable data-adaptive method for matched-field array processing in acoustic waveguides," *J. Acoust. Soc. Am.* **87**, 2493–2505 (1990).
- ¹³J. M. Ozard, G. H. Brooke, and P. Brouwer, "Improving performance for matched field processing with a minimum variance beamformer," *J. Acoust. Soc. Am.* **91**, 141–150 (1992).
- ¹⁴J. Tabrikian, J. L. Krolik, and H. Messer, "Robust maximum-likelihood source localization in an uncertain shallow-water waveguide," *J. Acoust. Soc. Am.* **101**, 241–249 (1997).
- ¹⁵For example, N. O. Booth *et al.*, "Source localization with broadband matched-field processing in shallow water," *IEEE J. Oceanic Eng.* **21**, 402–412 (1996).
- ¹⁶T. C. Yang, "A method of range and depth estimation by modal decomposition," *J. Acoust. Soc. Am.* **82**, 1736–1745 (1987).
- ¹⁷T. C. Yang, "Modal shading coefficients for high resolution source depth localization," *J. Acoust. Soc. Am.* **87**, 668–672 (1990).
- ¹⁸W. S. Burdic, *Underwater Acoustic System Analysis* (Prentice-Hall Signal Processing Series, Englewood Cliffs, NJ, 1991), 2nd ed., Chaps. 13 and 15.
- ¹⁹M. Porter, "The KRAKEN normal mode program," SAACLANTCEN Mem. SM-245 (1991).

Time-reversing array retrofocusing in simple dynamic underwater environments

Sunny R. Khosla and David R. Dowling

Department of Mechanical Engineering and Applied Mechanics, University of Michigan, Ann Arbor, Michigan 48109-2121

(Received 5 December 1997; accepted for publication 3 September 1998)

A time-reversing array (TRA) has the ability to retrofocus acoustic energy, in both time and space, to the original sound-source location without any information about the acoustic environment in which it is deployed. This unique capability may be limited or lost when the acoustic medium or its boundaries are time dependent, or propagation losses are prevalent. In this paper, predictions are made for the size, field-amplitude decay rate (or time), and location of the retrofocus for a TRA deployed in the presence of three dynamic acoustic propagation complexities commonly present in shallow ocean waters: (i) volume scattering from a random superposition of linear internal waves convecting a gradient in the sound speed profile; (ii) reflection and volume scattering from a deterministic soliton internal wave traveling on the thermocline between two water masses with differing sound speed; and (iii) surface scattering from a wind-driven dynamic random rough ocean surface. Analytical propagation models for narrow-band signals are used to highlight separately the influence of each propagation complexity on TRA retrofocusing. As expected, internal wave time scales are long enough so that TRA retrofocusing should persist for several minutes for source-array ranges of several kilometers at frequencies approaching 1 kHz. However, the comparatively rapid motion of ocean surface waves should prevent TRA exploitation of acoustic scattering from a wind-driven ocean surface at ranges greater than a few hundred meters, independent of acoustic frequency. Interestingly, multiple time-invariant propagation paths are not found to consistently enhance retrofocusing unless the TRA has sufficient angular resolution to distinguish them. © 1998 Acoustical Society of America. [S0001-4966(98)04712-2]

PACS numbers: 43.30.Vh, 43.30.Yj, 43.30.Ft, 43.30.Hw [DLB]

INTRODUCTION

The properties of time-reversed (or phase-conjugated) sound waves, and the devices to produce them, are being explored for a variety of applications in underwater sound (Jackson and Dowling, 1991; Dowling and Jackson, 1992; Dowling, 1994; Parvulescu, 1995; Kuperman *et al.*, 1998; Song *et al.*, 1998), medical ultrasound (Ikeda, 1989; Niconahad and Pusateri, 1989; Fink *et al.*, 1989; Prada *et al.*, 1991; Prada and Fink, 1994; Dorme and Fink, 1995; Parada *et al.*, 1995, 1996; Thomas and Fink, 1996; Tanter *et al.*, 1998), and nondestructive evaluation (Thomas *et al.*, 1994; Chakroun *et al.*, 1995; Draeger *et al.*, 1998). Investigations into related passive and active techniques for real-time reverberation compensation have also been undertaken (Neely and Allen, 1979; Clarkson *et al.*, 1985; Nelson *et al.*, 1992). Recent review articles on time reversal in acoustics (Fink, 1993, 1996, 1997) illustrate its elegance and allure.

Unlike ordinary acoustic radiation, time-reversed acoustic waves travel *toward* the source that produced them, instead of away from it. When the characteristics of the acoustic environment and the time-reversing device (typically an array of transducers) are appropriately matched, the time-reversed acoustic waves will spatially and temporally retrofocus at their source location. Time-reversing array (TRA) retrofocusing is possible when the TRA has sufficient aperture and the acoustic environment is reciprocal (i.e., one that is temporally invariant), but is degraded or altered when the acoustic medium or its boundaries are time dependent

(Dowling and Jackson, 1992; Dowling, 1994), moving (Dowling, 1993; Roux and Fink, 1995), or the array does not possess the requisite aperture to resolve individual propagation paths in a multipath environment (as discussed herein). This paper explores the extent to which acoustic-environment time variations typical of ocean surface and internal waves alter the underwater retrofocusing properties of a TRA composed of monopole transducers. Here, simple propagation models are exploited to clearly expose the influence of environmental dynamics when one or two dominant acoustic paths link the source and the TRA. Although waveguide effects are not addressed, the results presented in the following sections display the type of phenomena possible in more complex multipath environments, and provide new predictions of TRA retrofocusing limitations.

Time-reversing arrays attempt to exploit all time-invariant propagation complexities, except absorption, to enhance retrofocusing beyond the free-space diffraction limit without any information about the acoustic environment (Saichev, 1982; Dowling and Jackson, 1992; Derode *et al.*, 1995; Kuperman *et al.*, 1998). While amplitude compensation schemes for acoustic absorption have been found effective (Thomas and Fink, 1996; Tanter *et al.*, 1998), TRA retrofocus degradation resulting from time varying propagation complexities cannot be alleviated, in general, without detailed knowledge of the acoustic environment and its *future* variations. Given that such information is unlikely to be available, TRA retrofocusing performance in a dynamic en-

environment will typically be limited by the extent of temporal changes in the acoustic medium.

The purpose of this paper is to predict these limitations and their dependence on source-array range (z_s), acoustic frequency (f), array size (σ_x, σ_y), and round-trip time delay ($\Delta t = t_2 - t_1$) between the time of the original source transmission (t_1) and the time of the acoustic retrofocus (t_2) for individual dynamic propagation complexities. The three complexities addressed in this paper are: a random superposition of evolving linear internal waves as deduced from a simplified Garrett–Munk model compressed into a shallow water (Sec. I); a deterministic soliton internal wave traveling on a thermocline (Sec. II); and a dynamic rough wind-driven ocean surface (Sec. III). The present findings indicate that dynamic phenomena that evolve slowly compared to the round-trip time delay can be compensated by a TRA.

For simplicity and consistency with previous investigations, a narrow-band weighted-monopole formulation of the time-reversing array is chosen:

$$G_{\text{TRA}}(\mathbf{r}, \mathbf{r}_s, \omega, t_2 - t_1) = \int_{r'} G_2(\mathbf{r}, \mathbf{r}', \omega) S(\mathbf{r}') G_1^*(\mathbf{r}', \mathbf{r}_s, \omega) d^3 r', \quad (1)$$

where bold type indicates a vector quantity, $G_{\text{TRA}}(\mathbf{r}, \mathbf{r}_s, \omega, t_2 - t_1)$ is the acoustic field produced by the TRA at \mathbf{r} in response to a harmonic point source of radian frequency $\omega = 2\pi f$ at \mathbf{r}_s , $G_i(\mathbf{r}_f, \mathbf{r}_0, \omega)$ is the Helmholtz-equation Green's function for the acoustic environment at time t_i with source location \mathbf{r}_0 and field point \mathbf{r}_f , $S(\mathbf{r}')$ is the array shading or weighting function, \mathbf{r}' is the integration variable for the array coordinates, and the asterisk denotes mathematical complex conjugation. Complex conjugation implies time reversal for zero-bandwidth signals (Jackson and Dowling, 1991). Here, the acoustic environment may evolve between t_1 and t_2 , but it is assumed frozen while the signal propagates from the source to the array at t_1 , and from the array to the source at t_2 ; hence G_1 and G_2 are taken to be reciprocal but unequal when $t_2 - t_1 \equiv \Delta t > 0$ because of environmental dynamics. The exact functional form of G_1 and G_2 is determined from the acoustic environment. For a discrete array, $S(\mathbf{r}')$ is merely a sum of spatial Dirac delta functions. While other more complicated formulations of TRAs incorporating dipole sources and broadband signals are possible (Cassereau and Fink, 1993, 1994), the ansatz or definition embodied in Eq. (1) provides a simple gage for TRA performance. Broadband signals may be treated by an appropriate time domain version of (1) that properly accounts for causality (Jackson and Dowling, 1991; Cassereau and Fink, 1993, 1994).

The response of the time reversing array described by (1) has two parts. First, the received field which originated at the source at time t_1 , $G_1(\mathbf{r}', \mathbf{r}_s, \omega)$, is complex conjugated (i.e., time reversed) and weighted according to the shading function, $S(\mathbf{r}')$. After a listening and signal processing delay, this conjugated and weighted field is then retransmitted from each array location \mathbf{r}' and arrives at the field point \mathbf{r} at time t_2 . In general, the shading function has units and its

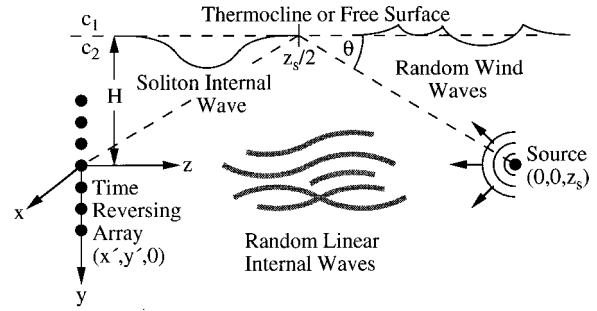


FIG. 1. Time-reversing array (TRA) geometry. The omni-directional source on the right broadcasts at $t = t_1$. The TRA receives the signal and retransmits to form the retrofocus at $t = t_2$. If the acoustic environment changes during the period $t_2 - t_1$, retrofocus properties may be degraded. Dynamic shallow-water acoustic environments typically include internal and surface waves.

magnitude is set by the transducer gain. Here, $S(\mathbf{r}')$ is normalized to have a volume integral of unity, and \mathbf{r} is chosen to lie near \mathbf{r}_s .

The next three sections present the detailed propagation formulation, and retrofocusing results for each of the three dynamic propagation complexities. In all cases the generic situation is the same and is depicted in Fig. 1 with x - y - z axes as shown. A planar or linear array centered on the origin of coordinates responds to a point source located at $\mathbf{r}_s = (0, 0, z_s)$. The final section presents the conclusions drawn from this work.

I. DYNAMIC RANDOM VOLUME SCATTERING

The results in this section are based on previous work (Dowling and Jackson, 1992; Dowling, 1994), so the formal mathematical development is minimal. The new results in this section pertain to the use of shallow-water parameters in the random medium formulation, and the utility of approximate forms for predictions of TRA retrofocus size and lifetime.

In a dynamic random medium, the mean field of the array can be computed from the expectation value of (1):

$$\langle G_{\text{TRA}}(\mathbf{r}, \mathbf{r}_s, \omega, \Delta t) \rangle = \int_{r'} S(\mathbf{r}') \langle G_2(\mathbf{r}, \mathbf{r}', \omega) G_1^*(\mathbf{r}', \mathbf{r}_s, \omega) \rangle d^3 r'. \quad (2)$$

Here, $\langle \cdot \rangle$ braces denote an ensemble expectation value computed by averaging over many realizations of the random media. The integrand in (2) is a product of the shading function and the mutual coherence function. For nearly horizontal paths in a simple environment lacking surface and bottom reflections, $\langle G_{\text{TRA}} \rangle$ can be factored into a deterministic free-space contribution, $G_{0c}(\mathbf{r}, \mathbf{r}_s, \omega)$, and a random medium correction factor obtained from the moment theory for the parabolic approximation to the wave equation (Ishimaru, 1978);

$$\langle G_{\text{TRA}}(\mathbf{r}, \mathbf{r}_s, \omega, \Delta t) \rangle = G_{0c}(\mathbf{r}, \mathbf{r}_s, \omega) \exp \left\{ -\frac{k^2 z_s}{4} \int_0^1 [A(0, 0, 0) - A(\zeta x, \zeta y, \Delta t)] d\zeta \right\}, \quad (3)$$

where $\mathbf{r}=(x,y,z_s+\Delta z)$, $\mathbf{r}_s=(0,0,z_s)$, k is ω/c_0 , c_0 is the average sound speed, and A is the projected autocorrelation function of the refractive index fluctuations of the random medium. Following Uscinski and Reeve (1990), when $k^2 z_s A(0,0,0)/4 > 2$ or 3, the exponentiated integral in (3) may be simplified by making a Taylor series expansion of $A(\xi_x, \xi_y, \Delta t)$ and keeping only quadratic terms in x , y , and Δt . For a planar Gaussian-shaded array lying in the x - y plane at $z=0$ with the field point lying near the source at $z=z_s$ (i.e., $\Delta z=0$, and x and y both much less than z_s), the Uscinski-Reeve approximation in (3) produces

$$\langle G_{\text{TRA}}(\mathbf{r}, \mathbf{r}_s, \omega, \Delta t) \rangle = \frac{1}{16\pi^2 z_s^2} \exp \left\{ -\frac{(kx\sigma_x)^2 + (ky\sigma_y)^2}{2z_s^2} - \frac{k^2 z_s}{4} \left[\frac{|A_{xx}|x^2}{6} + \frac{|A_{yy}|y^2}{6} + \frac{|A_{tt}|(\Delta t)^2}{2} \right] \right\}, \quad (4)$$

where σ_x and σ_y are the $1/\sqrt{e}$ of the array in the x and y directions, respectively, and A_{xx} , A_{yy} , and A_{tt} are the second derivatives of A with respect to x , y , and t . The absolute value signs in (4) arise because A_{xx} , A_{yy} , and A_{tt} are all negative. At any time delay Δt , the standard-deviation widths of the focal spot, w_x and w_y , in the x and y directions are

$$w_x = \frac{z_s/k\sigma_x}{\sqrt{1 + |A_{xx}|z_s^3/12\sigma_x^2}}, \quad (5a)$$

and

$$w_y = \frac{z_s/k\sigma_y}{\sqrt{1 + |A_{yy}|z_s^3/12\sigma_y^2}}. \quad (5b)$$

At this level of approximation, the spot size of the mean retrofocus field is time independent.

The effect of the random medium is felt in these results through the projected autocorrelation function A . Here, A is obtained by compressing a simplified deep-water Garrett-Munk internal wave model into a 100-m-deep ocean by adjusting the width of the vertical wave number spectrum and setting the internal wave energy level and speed of sound gradient via conservative choices from oceanographic measurements (see Appendix A). The primary intent of this exercise is to bound the influence of actual shallow-water random internal-wave phenomena on TRA retrofocusing through conservative parameter selection. The next section treats a single soliton internal wave as a deterministic limit of shallow-water internal-wave phenomena.

Results for the vertical size of the focus, w_y , based on (5b) (smooth curves) and direct numerical evaluations of (3) to find the $1/\sqrt{e}$ points (plotted symbols) are shown in Fig. 2 for: $1 \text{ m} < \sigma_y < 30 \text{ m}$, and $z_s < 10 \text{ km}$. The near alignment of the plotted symbols with the appropriate curves suggests the Uscinski-Reeve approximation is valid for spatial TRA retrofocusing beyond its normal range of applicability [$k_0^2 z_s A(0,0,0)/4 > 2$ or 3]. The scaling of the vertical axis on this plot incorporates all acoustic wavelength dependence for these Fresnel predictions. At short ranges, large arrays pro-

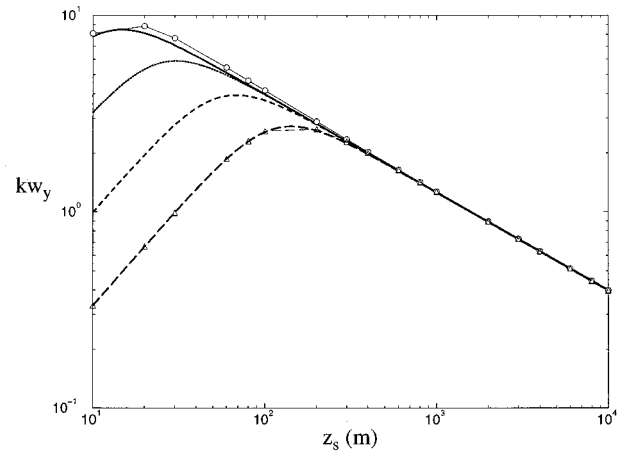


FIG. 2. Acoustic wave number scaled vertical focus size versus range for a variety of array sizes with the Uscinski-Reeve approximation (5b): — $\sigma_y=1$ m, - - - $\sigma_y=3$ m, - - - $\sigma_y=10$ m, - - - $\sigma_y=30$ m, and without it [a direct numerical evaluation of (3)]: \circ — \circ $\sigma_y=1$ m, and \triangle — \triangle $\sigma_y=30$ m. Here, $|A_{yy}|=7.6 \times 10^{-3} \text{ m}^{-1}$ and the Uscinski-Reeve approximation is found accurate throughout the range of investigation.

duce smaller focal spots and increasing range increases the focal spot size, as expected. However, at long ranges, all arrays are predicted to produce the same size focus which decreases with increasing range. The break points where the various curves join the array-size independent curve are determined by the magnitude of $|A_{yy}|$ and the size of the array. While these parametric results, including medium-aided focusing, have been noted before (Saichev, 1982; Dowling and Jackson, 1992), the vertical spot sizes in Fig. 2, based on shallow-water parameters, are generally smaller than their deep-water counter parts because the relative strength of stratification fluctuations are larger in shallow water.

Figure 3 shows the horizontal size of the focus, w_x , based on (5a). The results here are very similar to Fig. 2 except the much smaller value of $|A_{xx}|$ compared to $|A_{yy}|$

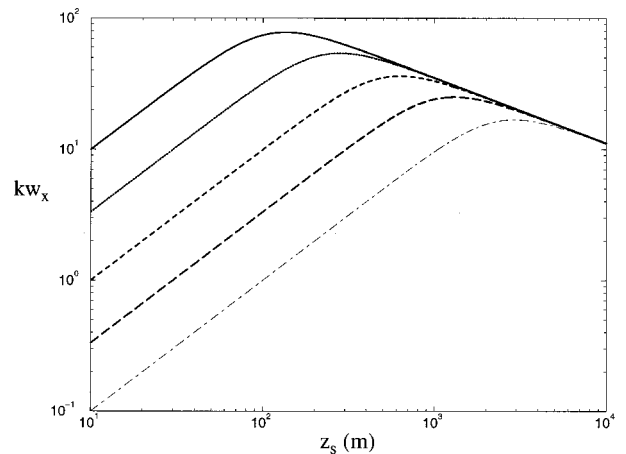


FIG. 3. Acoustic wave number scaled horizontal focus size versus range for a variety of array sizes with the Uscinski-Reeve approximation (5a): — $\sigma_x=1$ m, - - - $\sigma_x=3$ m, - - - $\sigma_x=10$ m, - - - $\sigma_x=30$ m, - - - $\sigma_x=100$ m. Here $|A_{xx}|=9.7 \times 10^{-6} \text{ m}^{-1}$ and the horizontal retrofocus size depends on the array size to larger ranges when compared to the vertical focus size (Fig. 2) because $|A_{yy}| \gg |A_{xx}|$.

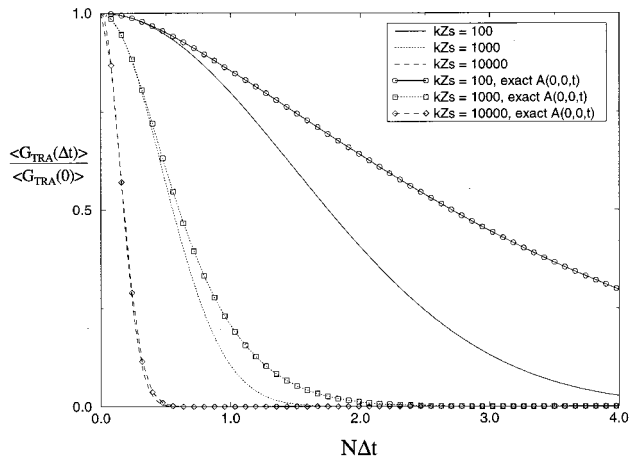


FIG. 4. Amplitude of the TRA retrofocus field divided by its value for $t_2 - t_1 = 0$ vs $N(t_2 - t_1)$ where N is the buoyancy frequency with (lines) and without (lines with symbols) the temporal extension of the Uscinski-Reeve approximation for various wave number range combinations. The temporal extension of the Uscinski-Reeve approximation (4) predicts a faster amplitude decay than the full theory (3).

shifts the medium-aided focusing regime to larger source-array ranges.

The predicted decay of the mean-field amplitude at the retrofocus location, $\mathbf{r} = \mathbf{r}_s$, is shown in Fig. 4 as a function of $N\Delta t$, where N is the internal-wave buoyancy frequency. As previously shown, these results are independent of the size of the array (Dowling, 1994). Since N sets the oscillation rate of the most dynamic internal waves, it is the natural factor for scaling the time delay axis. The three pairs of curves correspond to three different ranges with and without the temporal extension of the Uscinski-Reeve approximation at a frequency of 1 kHz. For all three ranges the approximate form does a reasonable job for $N\Delta t \leq 1/2$ or so, but underpredicts the field amplitude for $N\Delta t \geq 1/2$. The general trend in Fig. 4 shows the retrofocus decays more quickly at longer ranges and higher frequencies.

Figure 5, a diagram of the operating envelope of a TRA, combines the retrofocus field decay results for $100 \text{ Hz} \leq f \leq 10 \text{ kHz}$ by employing the focus half-life: the time delay necessary for the field amplitude to fall to half of its value at $\Delta t = 0$. The upward sloping solid line in the lower right portion of Fig. 5 represents the causality boundary. In its simplest form (ignoring geometrical corrections), causality requires the overall time delay to be greater than twice the one-way straight-ray propagation time:

$$t_2 - t_1 \geq \frac{2z_s}{c}. \quad (6)$$

Causal TRA systems cannot operate below or to the right of the causality boundary. The downward sloping curves that meet the causality boundary are the locus of the retrofocus half-life at the specified frequency. Below and to the left of these lines the retrofocus field amplitude is predicted to exceed half its value at $\Delta t = 0$. The main result in Fig. 5 is the notable expansion of the operating envelope of a TRA as the acoustic frequency or the source-array range is lowered. Although conservative parameter choices make Fig. 5 more

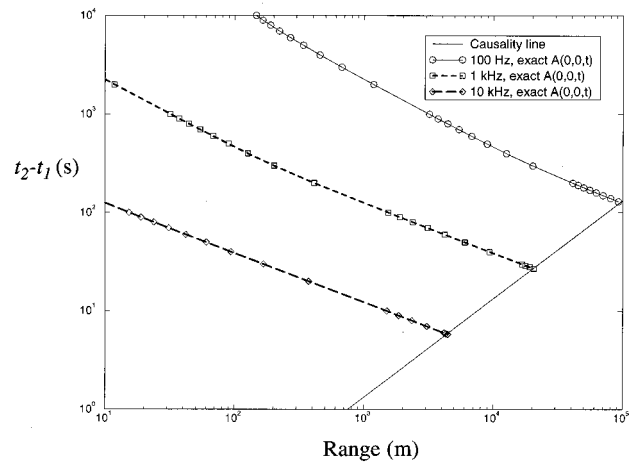


FIG. 5. Diagram of the operating envelope of a TRA. The solid line with positive slope is the causality boundary. Causal TRA systems must operate above this line. The curves with symbols having negative slopes are the time delay range locus of points where the TRA retrofocus has fallen to half of its value at $t_2 - t_1 = 0$ at the specified frequency. Below and to the left of these lines the retrofocus field amplitude is larger. This figure shows that TRA retrofocusing persists for longer periods of time at shorter ranges and lower frequencies. The region below the frequency curve of interest but above the causality line is the predicted operating envelope for a TRA.

restrictive than similar deep ocean results (Dowling and Jackson, 1992), there should still be ample opportunity to exploit TRAs in shallow ocean waters. For example, at 1 kHz and a range of 10 km, the focal half-life is predicted to be approximately 40 s, enough time for three round-trips between the source and array.

II. DYNAMIC DETERMINISTIC VOLUME SCATTERING

In this section, the impact on TRA retrofocusing from a soliton internal wave moving on a thermocline is addressed. The development here includes use of the high-frequency two-path Green's function, G_{tp} (Brekhovskikh, 1980), to treat propagation in the presence of a flat thermocline, and the Born approximation (Pierce, 1989) to address scattering from the soliton internal wave. Thus the present results include deterministic two-path propagation, and volume scattering from a moving inhomogeneity. The purpose of this study was to determine how the two deterministic paths interact to form the TRA retrofocus in the absence of medium dynamics, and to indicate the type of TRA retrofocus changes that are likely to occur when time-dependent scattering from soliton-induced thermocline motion is included. Cassereau and Fink (1994) have studied TRA retrofocusing through a plane interface separating two fluids, but their work primarily involved propagation paths nearly perpendicular to the interface while the present study addresses paths nearly parallel to it.

The basic geometry is given in Fig. 1. The array was assumed to be linear, vertical, Gaussian shaded, and deployed entirely below the thermocline so the acoustic wave number k is equal to ω/c_2 . With the chosen Cartesian coordinate system and arrangement of fluid masses: the thermocline lies on $y = -H$, so

$$\begin{aligned}
G_{tp}(\mathbf{r}_f, \mathbf{r}_0, \omega) &= D(\mathbf{r}_f, \mathbf{r}_0, \omega) + R(\mathbf{r}_f, \mathbf{r}_0, \omega, H) \\
&= \frac{\exp\{ik\sqrt{(x_f-x_0)^2+(y_f-y_0)^2+(z_f-z_0)^2}\}}{\sqrt{(x_f-x_0)^2+(y_f-y_0)^2+(z_f-z_0)^2}} \\
&\quad + \frac{\exp\{ik\sqrt{(x_f-x_0)^2+(y_f+y_0+2H)^2+(z_f-z_0)^2}\}}{\sqrt{(x_f-x_0)^2+(y_f+y_0+2H)^2+(z_f-z_0)^2}} \\
&\quad \times \left\{ \frac{\sin\theta - (\rho_2/\rho_1)\sqrt{(c_2/c_1)^2 - \cos^2\theta}}{\sin\theta + (\rho_2/\rho_1)\sqrt{(c_2/c_1)^2 - \cos^2\theta}} \right\}, \quad (7a)
\end{aligned}$$

where:

$$\sin\theta = \frac{y_f + y_0 + 2H}{\sqrt{(x_f - x_0)^2 + (y_f + y_0 + 2H)^2 + (z_f - z_0)^2}}. \quad (7b)$$

Here, ρ_1 , c_1 and ρ_2 , c_2 denote the densities and sound speeds above and below the thermocline, respectively. For the results presented below: $c_1 > c_2$, and $\rho_1 \approx \rho_2$. The first term in (7a), $D(\mathbf{r}_f, \mathbf{r}_0, \omega)$, represents the direct path between the source and the TRA. The second term, $R(\mathbf{r}_f, \mathbf{r}_0, \omega, H)$, is the interface reflected path. [D and R have been defined here to clarify the discussion of (9) below.] The lateral wave and curvature corrections for the reflected path (Brekhovskikh, 1980) were not included in this study.

Upon treating the soliton with the single scattering approximation, the Green's function, G_i , is the sum of G_{tp} and the acoustic scattering from the soliton γ_i , where γ_i is given by the familiar integral over the scattering volume

$$\begin{aligned}
\gamma_i(\mathbf{r}_f, \mathbf{r}_0, \omega, t_i) &= \frac{k^2}{4\pi} \int_{z_b=0}^{+z_b} \int_{y_b=-H}^{-H+\eta(z_b, t_i)} \int_{x_b=-\infty}^{+\infty} G_{tp}(\mathbf{r}_f, \mathbf{r}_b, \omega) \\
&\quad \times \delta n^2 G_{tp}(\mathbf{r}_b, \mathbf{r}_0, \omega) dx_b dy_b dz_b, \quad (8)
\end{aligned}$$

where $\mathbf{r}_b = (x_b, y_b, z_b)$ is the integration variable, $\delta n^2 = (c_2/c_1)^2 - 1$ is a constant in this situation, and $\eta(z_b, t_i)$ is a KdV profile for the soliton internal wave (Osborne and Burch, 1980) at time t_i . The evaluation of (8) is accomplished via the stationary-phase approximation in the x -direction, and numerical integration in the y and z directions. Appendix B provides parameter selection and implementation details.

With $G_i = G_{tp} + \gamma_i$, the TRA response defined by (1) becomes

$$G_{\text{TRA}}(\mathbf{r}, \mathbf{r}_s, \omega, t_2 - t_1) = \int_{r'} [G_{tp} + \gamma_2] S [G_{tp} + \gamma_1]^* d^3 r', \quad (9a)$$

$$\approx \int_{r'} S [G_{tp} G_{tp}^* + G_{tp} \gamma_1^* + \gamma_2 G_{tp}^*] d^3 r', \quad (9b)$$

where all arguments of the various functions have been suppressed for clarity, and the second-order term has been dropped from (9b) in this first-order perturbation scheme. The first term of (9b), $\int S G_{tp} G_{tp}^* d^3 r'$, represents TRA retrofocusing with the thermocline present but the soli-

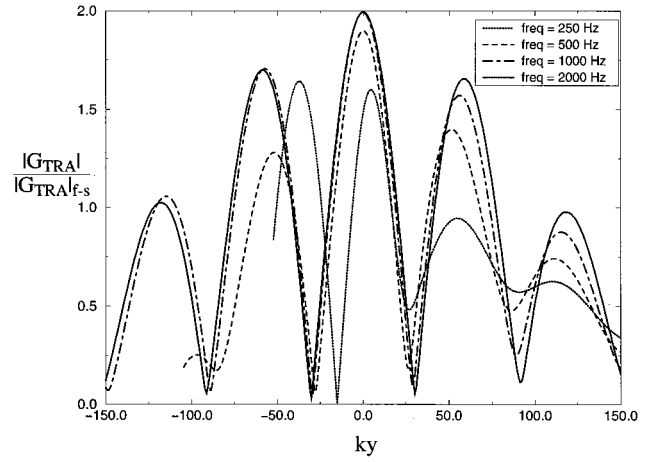


FIG. 6. TRA spatial retrofocus field amplitude with a flat thermocline for several frequencies at a range of 1 km. The size parameter for the Gaussian shaded array is $\sigma_y = 10$ m, and the array is centered at $H = 50$ m below the thermocline. The vertical axis is the TRA field amplitude divided by the field amplitude at the source location for an equivalent TRA operating in free space. When this ratio is two the TRA is properly exploiting total internal reflection from the thermocline. The horizontal axis is the product of the vertical coordinate y (at the source range z_s) and the acoustic wave number k . The retrofocus size is basically proportional to the wavelength. The loss of retrofocusing performance at 250 Hz is due to the array's inability to distinguish between direct and reflected paths at this frequency. The 250- and 500-Hz curves are truncated at the thermocline interface.

ton absent. It is time independent and contains four possible round-trip paths [direct-direct = $D(\mathbf{r}, \mathbf{r}', \omega) D^*(\mathbf{r}', \mathbf{r}_s, \omega)$, reflected-direct = $R(\mathbf{r}, \mathbf{r}', \omega, H) D^*(\mathbf{r}', \mathbf{r}_s, \omega)$, direct-reflected = $D(\mathbf{r}, \mathbf{r}', \omega) R^*(\mathbf{r}', \mathbf{r}_s, \omega, H)$, and reflected-reflected = $R(\mathbf{r}, \mathbf{r}', \omega, H) R^*(\mathbf{r}', \mathbf{r}_s, \omega, H)$]. The second two terms of (9b), $\int S G_{tp} \gamma_1^* d^3 r'$ and $\int S \gamma_2 G_{tp}^* d^3 r'$, represent unintentional coupling between direct, reflected, and soliton-scattered paths. These terms are complex conjugates of each other at $\mathbf{r} = \mathbf{r}_s$ and $\Delta t = 0$, and may either enhance or degrade retrofocusing. The neglected second-order term, $\int S \gamma_2 \gamma_1^* d^3 r'$, represents the twice soliton-scattered round-trip path. If included, it would aid retrofocusing. Results from numerical integration of (9b) using (7) and (8) are presented in Figs. 6–11 for three scenarios with increasing complexity: (i) the soliton is absent (Figs. 6, 7); (ii) the soliton is present but stationary (Figs. 8, 9); (iii) the soliton is present and moves between t_1 and t_2 (Figs. 10, 11).

Spatial TRA retrofocusing results with a flat thermocline are shown in Fig. 6 for $250 \text{ Hz} \leq f \leq 2 \text{ kHz}$ at a source-array range of 1 km with $S(y') = (\sigma_y \sqrt{2\pi})^{-1} \exp(-y'^2/2\sigma_y^2)$, $\sigma_y = 10$ m, $c_1 = 1505$ m/s, $c_2 = 1495$ m/s, and $H = 50$ m. The horizontal axis is the acoustic wave number times the vertical coordinate that passes through the source location. The desired retrofocus location is $y = 0$. The vertical axis is $|G_{\text{TRA}}|$ divided by $|G_{\text{TRA}}|$ at the retrofocus for an identical free-space geometry. At this range, the average grazing angle, θ , of the reflected path is 5.7° which is less than the critical grazing angle: $90^\circ - \sin^{-1}(c_2/c_1) = 6.6^\circ$, so both direct and thermocline reflected paths are of nearly equal strength. This leads to a smaller retrofocus, side lobes, and a near doubling the focal amplitude at the three higher frequencies when compared to free-space retrofocusing. The

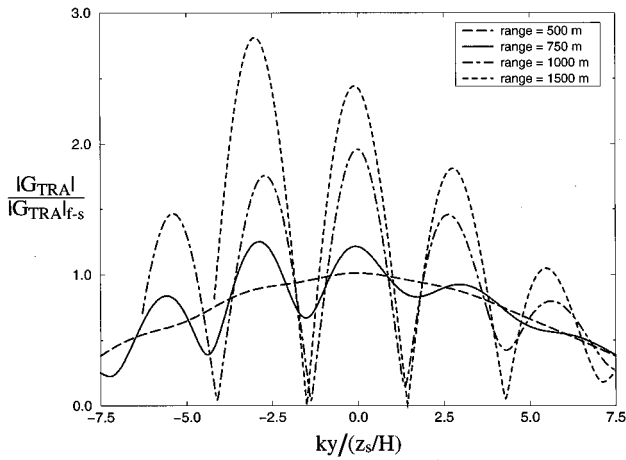


FIG. 7. TRA spatial retrofocus fields with a flat thermocline for several source array ranges at a frequency of 600 Hz. Other parameters and the vertical axis scaling are the same as in Fig. 6. The horizontal axis is the vertical coordinate y (at the source range z_s) scaled with the acoustic wave number k , and the aspect ratio z_s/H . The main retrofocus peak should appear at the source location: $y=0$. At $z_s=500$ m, the retrofocus field is nearly the same as in free space because thermocline reflection is weak. At the longer ranges, the retrofocus size is found proportional to z_s/kH . The side lobe closest to the thermocline achieves a larger amplitude than the intended retrofocus at ranges of 750 m and 1.5 km, and is caused by spatially varying reflection from the thermocline and inadequate array resolution, respectively.

vertical retrofocus sizes (based on Δy = the full width at half-maximum) shown in Fig. 6 for the three higher frequencies are consistently smaller ($k\Delta y \approx 40$) than that expected for the same array in free space ($k\Delta y \approx 250$) because the reflected path effectively increases the size of the array. The side lobes arise from interference between the direct and reflected paths. The amplitude at the source location can be predicted from a Fresnel expansion of (7) and (9) when $\gamma_1 = \gamma_2 = 0$, $H \ll z_s$, and the thermocline produces total internal reflection with constant phase shift ϕ :

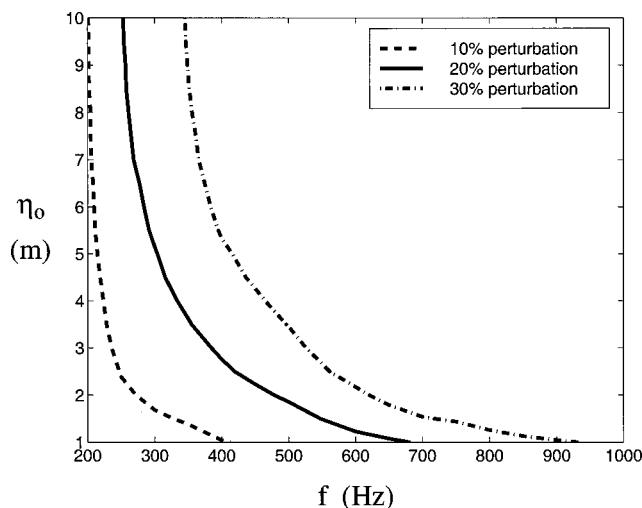


FIG. 8. A summary of the sensitivity of the TRA retrofocus amplitude to changes in acoustic frequency, f , and soliton amplitude η_0 . The curves of the constant perturbation level are approximately proportional to $f^{3/2}\eta_0^{1/2}$.

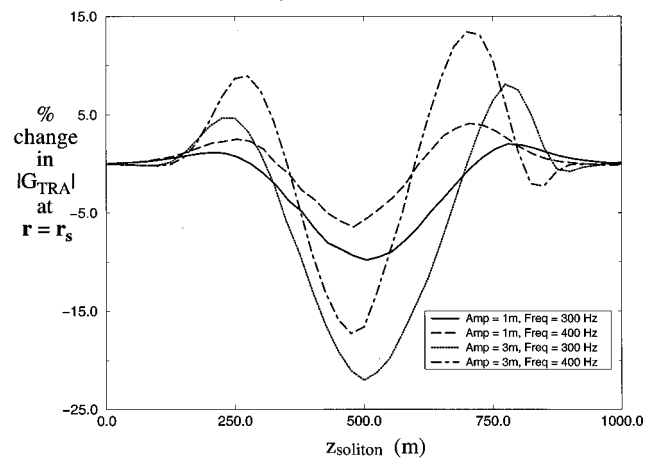


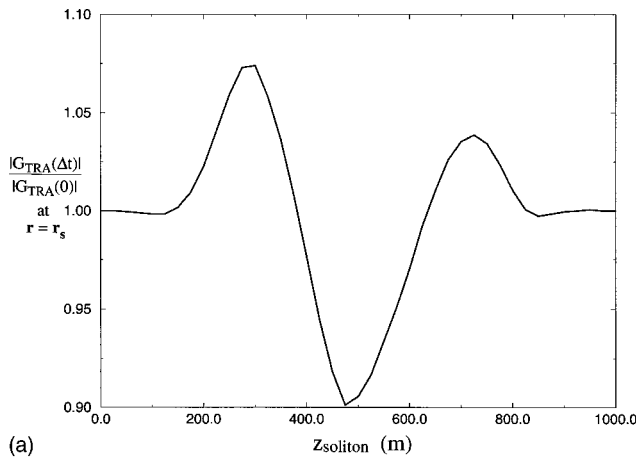
FIG. 9. TRA retrofocus amplitude changes relative to soliton-absent results at the source location (in percent) versus the location of a stationary soliton, z_{soliton} , at two acoustic frequencies (300 and 400 Hz) and two soliton amplitudes (1 and 3 m) for $z_s = 1$ km, $H = 50$ m, $\sigma_y = 10$ m. Solitons can cause retrofocus field enhancement ($z_{\text{soliton}} \approx 250$ and 750 m) or degradation ($z_{\text{soliton}} \approx 500$ m = specular reflection point on the thermocline).

$$\frac{|G_{\text{TRA}}(\mathbf{r}_s, \mathbf{r}_s, \omega, 0)|}{|G_{\text{TRA}}(\mathbf{r}_s, \mathbf{r}_s, \omega, 0)|_{f-s}} \approx 2 \left\{ 1 + \exp \left[\frac{-(2kH\sigma_y)^2}{2z_s^2} \right] \cos \left(\frac{2kH^2}{z_s} + \phi \right) \right\}, \quad (10)$$

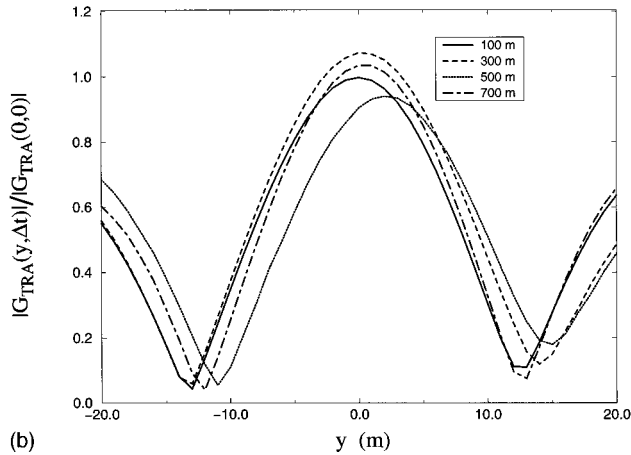
where the subscript “f-s” denotes “in free space.” The leading “1” inside the $\{\}$ braces corresponds to intended retrofocusing. The second term in (10) is oscillatory and represents unintentional cross-talk between the direct and reflected paths. Its contribution is small when the angular resolution of the array (which improves with increasing $k\sigma_y$) exceeds the angular separation between the direct and thermocline reflected paths ($\approx 2H/z_s$), i.e., when $(k\sigma_y)2H/z_s$ is above two or so. However, when $(k\sigma_y)2H/z_s \rightarrow 0$, the oscillatory crosstalk term has equal importance with the intended retrofocusing term so the retrofocus amplitude may exceed twice the free-space result (see Fig. 7) or fall to near zero. The relative amplitude of second term in (10) is less than 12% for the three higher frequencies in Fig. 6, but is 58% at 250 Hz.

The retrofocus results for 250 Hz in Fig. 6 do not follow the trends found at the higher frequencies. The intended retrofocus is slightly shifted and the side lobe at $ky \approx -35$ has the largest amplitude. Although this may be partially caused by information loss through the thermocline, the main reason for these retrofocusing problems is the failure of the array, with a nominal free-space beam resolution $[= \tan^{-1}(1/k\sigma_y)]$, of 5.5° at 250 Hz, to distinguish between the direct and reflected paths which differ in direction by 5.7° . Here, $(k\sigma_y)2H/z_s \approx 1$ and crosstalk between paths is significant. A larger array or a greater angular difference between the two paths would push the onset of crosstalk to a lower frequency.

Spatial TRA retrofocusing results with a flat thermocline are shown in Fig. 7 for $0.5 \text{ km} \leq z_s \leq 1.5 \text{ km}$ at $f = 600$ Hz. All other parameters are the same as for Fig. 6. Here, the nominal free-space angular resolution of the array is 2.3° .



(a)



(b)

FIG. 10. Evolution of the TRA retrofocus field amplitude at 500 Hz as a dynamic 3-m soliton moves from directly above the array ($z_{\text{soliton}}=0$, time $=t_1$) to directly above the source ($z_{\text{soliton}}=1$ km). Other parameters are the same as for Fig. 9. (a) Shows the normalized retrofocus field amplitude as a function of soliton location at time t_2 . (b) Shows the normalized retrofocus field amplitude on a vertical line through the source location when the moving soliton is located at $z_{\text{soliton}}=100$ m ($\Delta t=156$ s), 300 m ($\Delta t=469$ s), 500 m ($\Delta t=781$ s), and 700 m ($\Delta t=1094$ s). The retrofocus fields in (b) show that a moving soliton can alter the retrofocus amplitude, location, size, and side lobes.

The horizontal axis in Fig. 7 is the wave number scaled vertical coordinate on a path through the focal region at the range of the original source transmission divided by z_s/H . The vertical axis is the same as Fig. 6. At ranges greater than 1 km or so, the thermocline provides total internal reflection so the size of the retrofocus is found to be proportional to z_s/kH instead of $z_s/k\sigma_y$ (the free-space factor). This result is consistent with the use of acoustic images to represent reflecting surfaces since H is significantly greater than σ_y . The nontrivial range dependence of the retrofocus field shown in Fig. 7 is caused by acoustic energy losses through the thermocline and unintentional crosstalk between paths. At the shortest range ($z_s=500$ m), the retrofocus peak is essentially the same in amplitude and width as an equivalent free-space TRA retrofocus. Here, the average grazing angle of the reflected path ($\theta=11.3^\circ$) is almost twice the critical grazing angle (6.6°) so most of the acoustic energy traveling on the reflected path is lost into the upper half-space and retrofocusing is accomplished via the direct path alone. To improve retrofocusing in this situation, the TRA would have

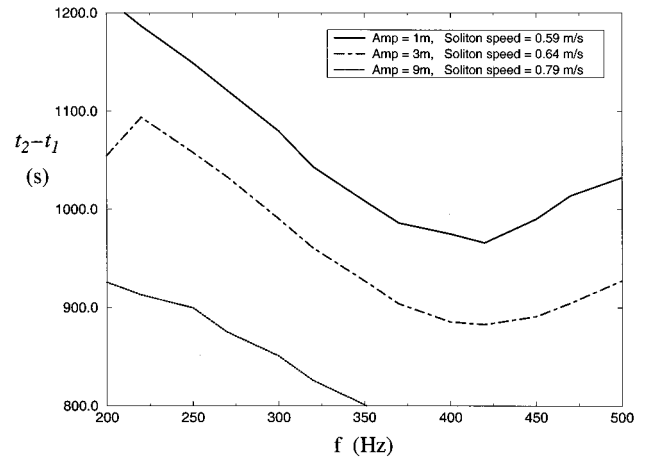


FIG. 11. Time delay, $t_2 - t_1$, for the soliton-induced retrofocus field perturbation at the source location to decrease to half its value at time t_1 for solitons placed at $z_s/2$ at t_1 versus acoustic frequency for three soliton amplitudes. Other parameters are the same as for Fig. 9. The larger (faster moving) solitons lead to more rapid changes in the retrofocus field.

to be extended above the thermocline so it could utilize the acoustic waves that penetrate into the upper half-space. At $z_s=750$ m, the reflected path regains some importance but spatially varying transmission losses through the thermocline cause the reflected path to act as a grazing-angle-dependent filter which only allows low-angle contributions and strengthens the side lobes closest to the thermocline. At $z_s=1$ km, the average grazing angle is below the critical grazing angle and the array is able to distinguish the direct and reflected paths [$(k\sigma_y)2H/z_s=2.5$], so the retrofocusing is good with twice the free-space amplitude. However, at $z_s=1.5$ km, the crosstalk parameter $(k\sigma_y)2H/z_s$ falls to 1.7, so the retrofocus amplitude changes and side lobe peaking reoccurs. Spurious side lobe peaking has also been observed in TRA experiments conducted in a shallow ocean sound channel (Hodgkiss *et al.*, 1997).

A summary of the sensitivity of TRA retrofocusing to the presence of a soliton located midway between the source and the TRA is presented in Fig. 8 for a source-array range of 1 km, $200 \text{ Hz} \leq f \leq 1 \text{ kHz}$, and soliton amplitude η_0 between 1 and 10 m. The contours in Fig. 8 represent the locus of constant soliton-produced perturbation level when $\mathbf{r}=\mathbf{r}_s$. As expected, higher frequencies and higher soliton amplitudes have the potential to produce the greatest retrofocus changes. The computed perturbation levels are approximately proportional to $f^{3/2}\eta_0^{1/2}$. Here, the perturbation level was determined from the average amplitude of the second and third terms in (9b) divided by the magnitude of the first term in (9b). A coherent sum of the second and third terms in (9b) was not used because interference between them leads to nonmonotonic behavior with increasing f or η_0 which impedes a generic interpretation of the results.

The dependence of the retrofocus field amplitude on the soliton location is shown in Fig. 9 for a source-array range of 1 km, $f=300$ and 400 Hz, and $\eta_0=1$ and 3 m. The horizontal axis is the location of a motionless soliton, z_{soliton} . The vertical axis is the percentage change in the field amplitude at the source location compared to equivalent soliton-absent

results. The peak perturbation occurs when the soliton is near the specular point for the thermocline reflected path and corresponds to a decrease in field amplitude. This change is consistent with the thermocline curvature induced by the soliton. The larger soliton causes larger field amplitude changes. Interestingly, the soliton increases the retrofocus field amplitude when it resides near 1/4 or 3/4 of the source-array range. These findings suggest that solitons will influence TRA retrofocusing in multipath sound channels most strongly when they reside near ray-path turning points.

Figure 10 shows the effects of a moving soliton with $\eta_0 = 3$ m that starts above the array at time t_1 and travels toward the source for a time period Δt , for an acoustic frequency of 500 Hz. All other parameters are the same in Fig. 9. The horizontal axis of Fig. 10(a) is the soliton location at t_2 . The vertical axis of Fig. 10(a) is the ratio of $|G_{\text{TRA}}|$ at the source location at time delay Δt to $|G_{\text{TRA}}|$ at the source location at $\Delta t = 0$. As with the stationary soliton results, the soliton increases and decreases the focal amplitude as it passes between the source and the array. Figure 10(b) shows the results for $|G_{\text{TRA}}|$ along a vertical line that passes through the source location when the soliton has traveled 100, 300, 500, and 700 m, or $\Delta t = 2.6, 7.8, 13.0,$ and 18.2 min, respectively. The retrofocus field is essentially time independent when the soliton lies outside the source-array range because backscattering from it is weak. Figure 10(b) shows that a soliton can change the TRA's retrofocus amplitude, location, size, and side lobes. Similar temporal retrofocus variations, with the appropriate time scales, have been observed in TRA experiments conducted in a shallow ocean sound channel (Song, 1998), and are exactly analogous to that found in medical-ultrasound aberration-correction studies (Wang *et al.*, 1994) where patient breathing causes motion of tissue layers.

Figure 11 summarizes the TRA soliton-interaction time-scale results for solitons with $\eta_0 = 1, 3$ and 9 m that were midway between the source and the array at t_1 . The horizontal axis is the acoustic frequency. The vertical axis is the time delay, $t_2 - t_1$, for the initial perturbation of G_{TRA} at the source location to have fallen halfway to its value when the soliton is far from the source and the array ($t_2 \rightarrow \infty$). While the precise shape of the curves in Fig. 11 depends on the chosen geometry and soliton model, the larger solitons which move faster clearly create the shortest lived perturbations. However, the fluctuation time scales are on the order of 10–20 min, more than enough time for TRA operation at source-array ranges of tens of km.

III. DYNAMIC RANDOM ROUGH OCEAN SURFACE

In this short section, scaling arguments are used to show that acoustic scattering from a wind-driven ocean surface either evolves too quickly for effective exploitation in TRA retrofocusing, or is of insufficient strength compared to time-independent coherent specular reflection to necessitate consideration. In Sec. I, slowly evolving random volume scattering was shown to cause retrofocus size reduction and retrofocus field-amplitude decay. In Sec. II, thermocline reflections were found to alter the retrofocus amplitude, size,

location, and side lobe structure while internal soliton motion dynamically altered the retrofocus amplitude and location.

Depending on the acoustic wave number k , root-mean-square wave height h , and specular scattering angle $\theta = \tan^{-1}(2H/z_s)$ (see Fig. 1), acoustic radiation that impacts a random wind-driven ocean surface may: encounter surface-wave motion, reflect coherently, and/or scatter incoherently. All three processes have been found to influence TRA retrofocusing. However, the temporal-evolution scales of ocean surface waves are approximately two orders of magnitude faster than the internal wave cases previously discussed, so the rate of TRA retrofocus degradation is expected to increase here since the operational ranges of the other parameters (k, z_s, σ_y) remain essentially the same. For clarity and simplicity, only the most important dynamic-environment effect, decay of the TRA retrofocus field at the original source location $\mathbf{r} = \mathbf{r}_s$ is used to assess TRA performance in the presence of dynamic rough surface scattering.

The starting point for this scaling analysis of TRA focal-field amplitude decay is (2) with $\mathbf{r} = \mathbf{r}_s$ and G_i assumed to include one rough surface encounter. When $\mathbf{r} = \mathbf{r}_s$, the term in the integrand of (2) remaining inside the expectation brackets is the temporal coherence function of the acoustic field reflected and scattered from the dynamic random rough surface. Since the integration over array coordinates does not involve the time delay, Δt , temporal loss of field coherence will proportionally influence the expected TRA retrofocus amplitude. Therefore it is sufficient to consider the time shift necessary for the acoustic-field temporal coherence to fall to half its zero time-shift value as a means of assessing TRA retrofocusing capability.

A previous study of temporal coherence in the field scattered from a wind-driven ocean surface with a Pierson–Moskowitz height fluctuation spectrum (Dowling and Jackson, 1993) found that about half the scattered field coherence in the specular direction is lost when $khg\Delta t/U \approx 1.5$, where $h = 0.0523U^2/g$, U is the wind speed 19.5 m above the ocean surface, and g is the acceleration of gravity. Although Dowling and Jackson's computations only involved two spatial dimensions, the temporal content should be accurate. While Dowling and Jackson did not extensively address scattering geometry or propagation ranges, their results should be sufficiently generic to indicate whether or not TRAs can operate quickly enough to retrofocus dynamic random rough ocean-surface scattering. Here, their result has been extended to arbitrary specular-reflection grazing angle, θ , by new computations using their formulation, in order to determine an upper bound on Δt for effective TRA retrofocusing:

$$(gk)^{1/2}\Delta t(kh)^{1/2} \sin \theta \approx 2.24. \quad (11)$$

Figure 12 shows the computed temporal coherence of the scattered field at the time delay Δt determined by equality in (11) to be almost independent of θ and kh . Hence, (11) is a suitable scaling relation for time delays, grazing angles, wave heights, and acoustic wave numbers. The factors and exponents in (11) result from the combined effects of the dispersion relationship for gravity waves, the Pierson–Moskowitz spectrum normalization, and the extension to grazing angles other than Dowling and Jackson's original

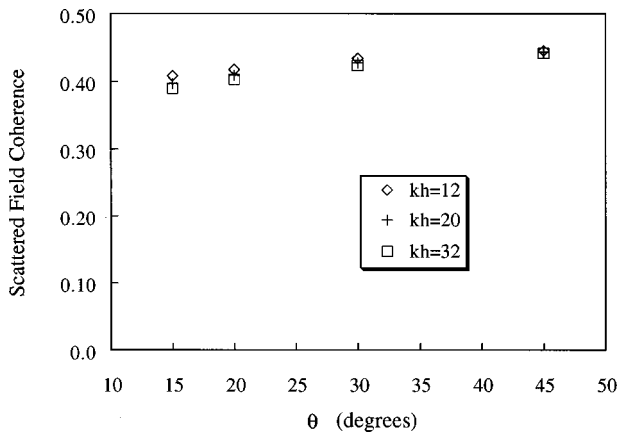


FIG. 12. Computed temporal coherence of the field scattered by a dynamic rough surface in the specular direction at the time delay determined by the equality in (11) versus the incident surface grazing angle θ . These results show that the temporal coherence at this time delay is slightly below 50% and nearly independent of θ and kh .

20°. For small time delays, or whenever (11) is abundantly satisfied, a TRA should successfully exploit dynamic random rough surface scattering. When equality holds in (11), a TRA should be somewhat less than 50% effective, i.e., the predicted field amplitude at the original source location will be a little smaller than half its value at $\Delta t = 0$. When (11) is not satisfied, TRA exploitation of scattering from a dynamic rough ocean surface should be weak or nonexistent.

As before, the causality boundary defined by (6) provides a lower bound on Δt for any z_s , so with (6) and (11), the operating envelop of a TRA subjected to a wind-driven ocean surface can be predicted. Figure 13 diagrams this envelop in dimensionless form. The horizontal axis is the

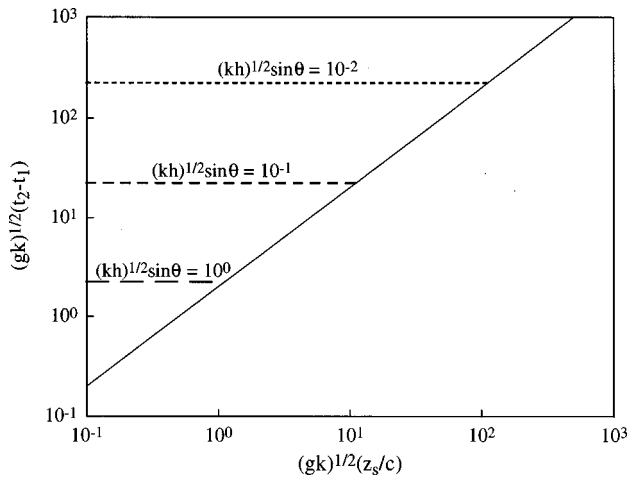


FIG. 13. Operating envelope for a time-reversing array using acoustic scattering from a wind-driven dynamic random rough ocean surface in scaled coordinates (g is the acceleration of gravity, and c is the speed of sound). The lower right half of the figure is excluded for causal arrays. The horizontal lines mark the approximate locus of the half-life of the TRA retrofocus for constant values of $(kh)^{1/2} \sin \theta$, where k is the acoustic wave number, h is the root-mean-square surface fluctuation, and θ is the specular direction grazing angle between the source and the array (see Fig. 1). Retrofocusing performance is better at small ordinate values. Retrofocus half-life increases when the effective roughness of the surface decreases. The unusual scaling of the axes results from the properties of wind-driven gravity waves.

scaled source-array range and vertical axis is the scaled time delay. On the horizontal lines in Fig. 13, $(kh)^{1/2} \sin \theta$ is constant. The diagonal line with the positive slope represents the causality limit. As before, all realizable TRA systems must operate above this line. For any set of parameters, TRA retrofocusing performance decreases as one progresses upward in Fig. 13. For example, when $(kh)^{1/2} \sin \theta = 1$, TRA retrofocusing will exploit the ocean surface in the triangular region below the bottom horizontal line and above the diagonal line.

Although partially masked by the axis scaling of Fig. 13, the possibilities for obtaining TRA retrofocusing from ocean surface scattering are restricted to short ranges. In specific dimensional terms, consider $f = 1$ kHz ($k = 4.2 \text{ m}^{-1}$), $\theta = 30^\circ$, and $h = 0.95$ m, so that $(kh)^{1/2} \sin \theta \approx 1$. These conditions imply a maximum time delay of $\Delta t = 2.24(gk)^{-1/2} = 0.35$ s for a maximum source-array range of approximately one quarter of a kilometer. Longer time delays and operation ranges are possible when $(kh)^{1/2} \sin \theta$ is smaller, but the random scattered field strength decreases in comparison to the amplitude of the coherent specular surface reflection as this parameter is reduced. If the TRA is to retrofocus using the surface-scattered field when surface scattering is significant, an additional roughness constraint is necessary. Based on simple scattering physics (Ishimaru, 1978), a reasonable dividing line between rough and smooth surfaces is

$$kh \sin \theta \approx 1, \quad (12)$$

with rough (smooth) surfaces satisfying $kh \sin \theta \geq 1$ ($kh \sin \theta \leq 1$). When (11) and (12) are combined to determine the maximum time delay, the following relationship is found:

$$(\Delta t)_{\text{maximum}} = 2.24 \sqrt{h/g} = 0.512 U/g, \quad (13)$$

where the second equality follows from the definition of h for a Pierson–Moskowitz surface spectrum. Interestingly, this result is independent of the acoustic frequency, but also shows that for ordinary windy conditions ($h = 1$ m, $U = 13.7$ m/s = 27 knots), the maximum time delay is only 0.7 s for a maximum range of just over half a kilometer.

Since listening and signal processing delays at the TRA of several tenths of seconds are likely and practical systems are never designed for regions of marginal performance, the scaling arguments presented here suggest that TRAs can only exploit dynamic random rough ocean surface scattering for retrofocusing when the overall time delay is less than half a second and the source-array range is less than a half a kilometer. However, TRAs may still retrofocus well with longer time delays and at longer ranges by exploiting time-independent coherent specular reflections from the ocean surface, as would occur in oceanic sound channels when low-order modes having small effective surface grazing angles dominate the propagation between the source and the array. The temporal stability of the retrofocus found in the shallow water experiments of Kuperman *et al.* (1998) supports this contention.

IV. CONCLUSIONS

Three common dynamic underwater propagation complexities have been individually examined for their impact on TRA retrofocusing using a variety of simple analytical and numerical models. Although idealized, the findings address the basic limitations of TRAs in dynamic multipath environments typical of the shallow ocean. Four major conclusions can be drawn from this effort. First, random linear internal waves convecting a sound speed gradient should not prevent TRA operations in the shallow ocean. Even though vertical-direction TRA superfocusing produced by random volume scattering will be altered by waveguide effects in the shallow ocean, the dynamic random-media amplitude decay results given here for a single path may be relevant, on a path by path basis, for multipath propagation. The predicted horizontal-direction TRA superfocusing from random volume scattering is likely to persist in a shallow-water waveguide. Hence, the present results provide quantitative estimates for the duration of the retrofocus in a dynamic shallow ocean. Second, soliton internal waves traveling on a thermocline may alter TRA retrofocusing but thermocline reflections provide significant retrofocusing enhancement when the array has sufficient aperture to resolve direct and reflected paths. This conclusion can be extended to multimode propagation in an underwater sound channel when the array has sufficient aperture to reliably resolve the propagating modes (as discussed in Kuperman *et al.*, 1998). In addition, oceanic solitons move slowly enough so that their influence may be minimal at ranges up to a few km and at acoustic frequencies up to 1 kHz or so for overall time delays of several minutes. Third, acoustic scattering from a dynamic rough ocean surface cannot be exploited by a TRA at technically relevant source-array ranges. Dynamic rough ocean surface scattering will either vary too rapidly for exploitation during retrofocusing, or it will not be significant enough compared to coherent specular reflection to warrant attempted exploitation.

And finally, this research suggests that the ultimate limitation on TRA performance may be best stated in terms of wavefront information collection. In a dynamic acoustic environment, time reversing arrays can only obtain current information. Future information (typically unavailable) would be required for proper retrofocusing at arbitrarily long time delays. As illustrated in this paper, the extent of this future knowledge limitation is set by the rate at which the current wavefront information becomes obsolete. This line of thinking can be applied to static environments as well. The present results for a finite array in a static two-path acoustic environment, when taken together with the recent oceanic experiments (Kuperman *et al.*, 1998) and the efforts to compensate acoustic absorption (Thomas and Fink, 1996; Tanter *et al.*, 1998) show that TRA retrofocusing in a static medium is also limited by the array's ability to gather wavefront information. Hence, insufficient array aperture and absorption losses within the medium can be interpreted as two manifestations of the same limitation.

ACKNOWLEDGMENTS

The research was supported by the Ocean Acoustics Program of the Office of Naval Research under Award No. N00014-96-1-0040. In addition, the authors would like to thank the careful and thoughtful efforts of the reviewers whose comments and suggestions greatly improved this paper.

APPENDIX A

The shallow-water random media predictions require $A(\Delta x, \Delta y, \Delta t)$, the projected autocorrelation function of refractive index fluctuations (Ishimaru, 1978). Here, A is drawn from the simplified continuous-spectra Garrett–Munk model in Dowling and Jackson (1992):

$$A(\Delta x, \Delta y, \Delta t) = 32 \left(\frac{\sigma}{c_0} \frac{\partial c}{\partial y} \right)^2 \int_0^\infty \int_0^\infty \frac{\Lambda(k_y)}{k_y} \cos \left[\left(\frac{\omega^2 - f_0^2}{N^2 - \omega^2} \right)^{1/2} k_y \Delta x \right] \times \frac{\cos(k_y \Delta y) \Omega(\omega) \cos(\omega \Delta t)}{[(\omega^2 - f_0^2)/(N^2 - \omega^2)]^{1/2}} dk_y d\omega, \quad (\text{A1})$$

where σ is the root-mean-square vertical fluctuation induced by the internal wave motion, c_0 is the average sound speed, $\Lambda(k_y)$ is the vertical direction internal wave spectrum:

$$\Lambda(k_y) = C(k_{y0}, k_{y1}) \frac{k_y^4}{(k_y^2 + k_{y0}^2)^3 (k_y^2 + k_{y1}^2)^2}, \quad (\text{A2a})$$

$$\frac{1}{C(k_{y0}, k_{y1})} = \int_{-\infty}^{+\infty} \frac{k_y^4 dk_y}{(k_y^2 + k_{y0}^2)^3 (k_y^2 + k_{y1}^2)^2}, \quad (\text{A2b})$$

f_0 is the inertial frequency associated with the rotation of the earth [$= 4\pi \sin(\text{latitude})/24h$], N is the buoyancy frequency, and $\Omega(\omega)$ is the temporal internal wave frequency spectrum

$$\Omega(\omega) = \frac{\sqrt{Nf_0}}{4(\sqrt{N} - \sqrt{f_0})} |\omega|^{-3/2} \text{ for } f_0 < |\omega| < N, \quad (\text{A3})$$

$$\Omega(\omega) = 0 \text{ for } |\omega| < f_0 \text{ or } N < |\omega|.$$

The parameters to evaluate A for shallow ocean waters were chosen to either be generic or conservative, so that the overall internal wave model was more likely to over predict than under predict the influence of dynamic random medium on TRA performance. In particular, the value of $\partial c/\partial y$ was chosen to be typical of values at the thermocline. A water-column averaged value of $\partial c/\partial y$ would be about an order of magnitude smaller. The oceanographic data in Ali *et al.* (1986), Ali (1993), Carey *et al.* (1995), and Lynch *et al.* (1996) lead to the following values:

$$\begin{aligned} \sigma &= 3 \text{ m}, \\ c_0 &= 1500 \text{ m/s}, \\ \partial c/\partial y &= 1.8 \text{ s}^{-1}, \\ k_{y0} &= 2\pi/(\text{water depth}) = 0.0628 \text{ m}^{-1}, \quad k_{y1} = 6.28 \text{ m}^{-1}, \end{aligned}$$

$$N = 8 \text{ cph,}$$

$$f_0 = 0.059 \text{ cph (a latitude of } 45^\circ\text{).}$$

APPENDIX B

The soliton profile used in this study is the classic hyperbolic-secant-squared solution:

$$y = -H + \eta(z, t) = -H + \eta_0 \operatorname{sech}^2 \left[\frac{z - ct}{L} \right] \quad (\text{B1})$$

of the Korteweg–de Vries (KdV) equation (see Osborne and Burch, 1980),

$$\frac{\partial \eta}{\partial t} + c_0 \frac{\partial \eta}{\partial z} + \alpha \eta \frac{\partial \eta}{\partial z} + \gamma \frac{\partial^3 \eta}{\partial z^3} = 0, \quad (\text{B2})$$

for a nonlinear dispersive wave traveling on the interface between two stably stratified fluid layers of density ρ_1 (upper layer) and ρ_2 (lower layer) in a gravitational field. The independent coordinates in these equations are shown in Fig. 1. Environmental parameters determine all the coefficients in (B1) and (B2) except the soliton amplitude η_0 which was varied from 1 to 10 m. The remaining parameters were selected to be representative of the shallow ocean.

$$\begin{aligned} \rho &= \text{reference fluid density} = 1025 \text{ kg/m}^3, \\ \Delta \rho &= \text{density difference between the fluid layers} \\ &= \rho_2 - \rho_1 = 3.7 \text{ kg/m}^3, \\ h_1 &= \text{depth of the upper fluid layer} = 10 \text{ m,} \\ h_2 &= \text{depth of the lower fluid layer} = 90 \text{ m,} \\ c_0 &= \text{phase speed of the associated linear wave} \\ &= \sqrt{g \Delta \rho h_1 h_2 / \rho (h_1 + h_2)} = 0.56 \text{ m/s,} \\ \alpha &= \text{nonlinearity parameter} = -3c_0/2h_1(1 - h_1/h_2) \\ &= -0.075 \text{ s}^{-1}, \\ c &= \text{soliton wave speed} = c_0(1 - \eta_0 \alpha / 3c_0) \\ &= 0.64 \text{ and } 0.78 \text{ m/s,} \\ \gamma &= \text{dispersion parameter} = c_0 h_1 h_2 / 6 = 84 \text{ m}^3/\text{s,} \\ L &= \text{soliton length scale} = \sqrt{-12\gamma / \eta_0 \alpha} = 67 \text{ and } 39 \text{ m.} \end{aligned}$$

The KdV soliton model has been used in other underwater acoustic studies (Tielburger *et al.*, 1997), and is sufficiently realistic for the goals of the present study.

The soliton profile enters the time-reversing array formalism in Sec. II in the integration limits in (8). Scaling the integration variables in (8) by the source-array range produces an integrand that allows the x_b integration to be performed using the stationary phase approximation when $kz_s \geq 1$. For path lengths of more than a km and frequencies above 100 Hz, kz_s will minimally be of order 10^3 or larger so the stationary phase approximation should be accurate. The remaining double integral over $\Psi = y_b/z_s$ and $\zeta = z_b/z_s$ has four terms corresponding to the various combinations of direct and reflected paths:

$$\begin{aligned} \gamma_i(\mathbf{r}_f, \mathbf{r}_0, \omega, t_i) &= \frac{k^2 \delta n^2}{4\pi} \sqrt{2\pi z_s/k} \int_0^1 \int_{y_b = -H/z_s}^{(-H + \eta(z_b, t_i))/z_s} \\ &\quad \times \{T_1 + T_2 + T_3 + T_4\} d\psi d\zeta, \end{aligned} \quad (\text{B3})$$

where

$$T_1 = \frac{\exp\{ikz_s(a+b) + i\pi/4\}}{\sqrt{ab(a+b)}},$$

$$T_2 = \frac{\exp\{ikz_s(a+c) + i\pi/4\}}{\sqrt{ac(a+c)}} R_1,$$

$$T_3 = \frac{\exp\{ikz_s(d+b) + i\pi/4\}}{\sqrt{db(d+b)}} R_2,$$

$$T_4 = \frac{\exp\{ikz_s(d+c) + i\pi/4\}}{\sqrt{dc(d+c)}} R_1 R_2,$$

$$R_1 = \frac{\{y'/z_s + \psi + 2H/z_s\} - (\rho_2/\rho_1) \sqrt{(c_2/c_1)^2 c^2 - \zeta^2}}{\{y'/z_s + \psi + 2H/z_s\} + (\rho_2/\rho_1) \sqrt{(c_2/c_1)^2 c^2 - \zeta^2}},$$

$$R_2 = \frac{\{y_s/z_s + \psi + 2H/z_s\} - (\rho_2/\rho_1) \sqrt{(c_2/c_1)^2 d^2 - (1-\zeta)^2}}{\{y_s/z_s + \psi + 2H/z_s\} + (\rho_2/\rho_1) \sqrt{(c_2/c_1)^2 d^2 - (1-\zeta)^2}},$$

$$a = \sqrt{(\psi - y_s/z_s)^2 + (1-\zeta)^2}, \quad b = \sqrt{(y'/z_s - \psi)^2 + \zeta^2},$$

$$c = \sqrt{\{y'/z_s + \psi + 2H/z_s\}^2 + \zeta^2},$$

and

$$d = \sqrt{\{y_s/z_s + \psi + 2H/z_s\}^2 + (1-\zeta)^2}.$$

In this formulation, the field and source points in (B3) have been chosen for the source-to-array propagation step: i.e., $\mathbf{r}_f = (0, y', 0)$ and $\mathbf{r}_0 = (0, y_s, z_s)$. The array-to-source propagation is handled similarly.

- Ali, H. B. (1993). "Oceanic variability in shallow-water acoustics and the dual role of the sea bottom," *IEEE J. Ocean Eng.* **18**, 31–41.
- Ali, H. B., Akal, T., and Hastrup, O. F. (1986). "Temporal variability in shallow water acoustic transmission and its correlation with the environment," in *Aero- and Hydro-Acoustics*, edited by G. Comte-Bellot and J. E. Ffowcs Williams (Springer-Verlag, Berlin), pp. 323–331.
- Brekhovskikh, L. M. (1980). *Waves in Layer Media* (Academic, New York), Chap. 4.
- Carey, W. M., Douth, J., Evans, R. B., and Dillman, L. M. (1995). "Shallow-water sound transmission measurements on the New Jersey Continental shelf," *IEEE J. Ocean Eng.* **20**, 321–336.
- Cassereau, D., and Fink, M. (1993). "Focusing with plane time-reversal mirrors: An efficient alternative to closed cavities," *J. Acoust. Soc. Am.* **94**, 2373–2386.
- Cassereau, D., and Fink, M. (1994). "Time-reversal focusing through a plane interface separating two fluids," *J. Acoust. Soc. Am.* **96**, 3145–3154.
- Chakroun, N., Fink, M., and Wu, F. (1995). "Time reversal processing in ultrasonic nondestructive testing," *IEEE Trans. Ultrason. Ferroelectr. Freq. Control* **42**, 1087–1098.
- Clarkson, P. M., Mourjopoulos, J., and Hammond, J. K. (1985). "Spectral, phase, and transient equalization for audio systems," *J. Audio Eng. Soc.* **33**, 127–132.
- Derode, A., Roux, P., and Fink, M. (1995). "Robust acoustic time reversal with high-order multiple scattering," *Phys. Rev. Lett.* **75**, 4206–4209.
- Dorme, C., and Fink, M. (1995). "Focusing in transmit-receive mode through inhomogeneous media: The time-reversal matched filter approach," *J. Acoust. Soc. Am.* **98**, 1155–1162.

- Dowling, D. R. (1993). "Phase-conjugate array focusing in a moving medium," *J. Acoust. Soc. Am.* **94**, 1716–1718.
- Dowling, D. R. (1994). "Acoustic pulse compression using passive phase-conjugate processing," *J. Acoust. Soc. Am.* **95**, 1450–1458.
- Dowling, D. R., and Jackson, D. R. (1992). "Narrow-band performance of acoustic phase-conjugate arrays in dynamic random media," *J. Acoust. Soc. Am.* **91**, 3257–3277.
- Dowling, D. R., and Jackson, D. R. (1993). "Coherence of acoustic scattering from a dynamic rough surface," *J. Acoust. Soc. Am.* **93**, 3149–3157.
- Draeger, C., Cassereau, D., and Fink, M. (1998). "Theory of the time-reversal process in solids," *J. Acoust. Soc. Am.* **102**, 1289–1295.
- Fink, M. (1993). "Time-reversal mirrors," *J. Phys. D* **26**, 1333–1350.
- Fink, M. (1996). "Time-reversal in acoustics," *Contemp. Phys.* **37**, 95–109.
- Fink, M. (1997). "Time reversed acoustic," *Phys. Today* **50**(3), 34–40.
- Fink, M., Prada, C., Wu, F., and Cassereau, D. (1989). "Self focusing with time reversal mirror in inhomogeneous media," *Proc. IEEE Ultrasonics Symp. (Montréal)*, Vol. 2, pp. 681–686.
- Hodgkiss, W. S., Kuperman, W. A., and Song H. C. (1997). private communication.
- Ikeda, O. (1989). "An image reconstruction algorithm using phase conjugation for diffraction-limited imaging in an inhomogeneous medium," *J. Acoust. Soc. Am.* **85**, 1602–1606.
- Ishimaru, A. (1978). *Wave Propagation and Scattering in Random Media* (Academic, San Diego), Vol. 2.
- Jackson, D. R., and Dowling, D. R. (1991). "Phase-conjugation in underwater acoustics," *J. Acoust. Soc. Am.* **89**, 171–181.
- Kuperman, W. A., Hodgkiss, W. S., Song, H. C., Akal, T., Ferla, C., and Jackson, D. R. (1998). "Phase-conjugation in the ocean: Experimental demonstration of an acoustic time reversal mirror," *J. Acoust. Soc. Am.* **103**, 25–40.
- Lynch, J. F., Guoliang, J., Pawlowicz, R., Ray, D., Plueddemann, A. J., Chiu, C.-S., Miller, J. H., Bourke, R. H., Parsons, A. R., and Muench, R. (1996). "Acoustic travel time perturbations due to shallow-water internal waves and internal tides in the Barents Sea Front: Theory and experiment," *J. Acoust. Soc. Am.* **99**, 803–821.
- Neely, S. T., and Allen, J. B. (1979). "Invertability of a room impulse response," *J. Acoust. Soc. Am.* **66**, 165–169.
- Nelson, P. A., Hamada, H., and Elliot, S. J. (1992). "Adaptive inverse filters for stereophonic sound reproduction," *IEEE Trans. Signal Process.* **40**, 1621–1632.
- Nikoonahad, M., and Pusateri, T. L. (1989). "Ultrasonic phase conjugation," *J. Appl. Phys.* **66**, 4512–4513.
- Osborne, A. R., and Burch, T. L. (1980). "Internal solitons in the Andaman Sea," *Science* **208**, 451–460.
- Parvulescu, A. (1995). "Matched-signal (MESS) processing by the ocean," *J. Acoust. Soc. Am.* **98**, 943–960.
- Pierce, A. D. (1989). *Acoustics* (Acoustical Society of America, New York), pp. 441–443.
- Prada, C., and Fink, M. (1994). "Eigenmodes of the time-reversal operator: A solution to selective focusing in multiple-target media," *Wave Motion* **20**, 151–163.
- Prada, C., Thomas, J.-L., and Fink, M. (1995). "The interactive time reversal process: Analysis of the convergence," *J. Acoust. Soc. Am.* **97**, 62–71.
- Prada, C., Wu, F., and Fink, M. (1991). "The interactive time reversal mirror: A solution to self-focusing in the pulse echo mode," *J. Acoust. Soc. Am.* **90**, 1119–1129.
- Prada, C., Manneville, S., Spoliansky, D., and Fink, M. (1996). "Decomposition of the time reversal operator: Detection and selective focusing on two scatterers," *J. Acoust. Soc. Am.* **99**, 2067–2076.
- Roux, P., and Fink, M. (1995). "Experimental evidence in acoustics of the violation of time-reversal invariance induced by vorticity," *Europhys. Lett.* **32**, 25–29.
- Saichev, A. I. (1982). "Effect of compensating distortions due to scattering in an inhomogeneous medium by the use of a reflector turning the front," *Radio Eng. Electron. Phys.* **27**, 23–30.
- Song, H. C. (1998). Private communication.
- Song, H. C., Kuperman, W. A., and Hodgkiss, W. S. (1998). "A time-reversal mirror with variable range focusing," *J. Acoust. Soc. Am.* **103**, 3234–3240.
- Tanter, M., Thomas, J.-L., and Fink, M. (1998). "Focusing and steering through absorbing and aberrating layers: Application to ultrasonic propagation through the skull," *J. Acoust. Soc. Am.* **103**, 2403–2410.
- Thomas, J.-L., and Fink, M. (1996). "Ultrasonic beam focusing through tissue inhomogeneities with a time reversal mirror: Application to trans-skull therapy," *IEEE Trans. Ultrason. Ferroelectr. Freq. Control* **43**, 1122–1129.
- Thomas, J.-L., Roux, P., and Fink, M. (1994). "Inverse scattering analysis with an acoustic time-reversal mirror," *Phys. Rev. Lett.* **72**, 637–640.
- Tielbürger, D., Finette, S., and Wolf, S. (1997). "Acoustic propagation through an internal wave field in a shallow water waveguide," *J. Acoust. Soc. Am.* **101**, 789–808.
- Uscinski, B. J., and Reeve, D. E. (1990). "The effect of ocean inhomogeneities on array output," *J. Acoust. Soc. Am.* **87**, 2527–2534.
- Wang, H., Ebbni, E. S., O'Donnell, M., and Cain, C. A. (1994). "Phase aberration correction and motion compensation for ultrasonic hyperthermia phased arrays: Experimental results," *IEEE Trans. Ultrason. Ferroelectr. Freq. Control* **40**, 34–43.

Detection performance of two efficient source tracking algorithms for matched-field processing

Michael J. Wilmut

School of Earth and Ocean Sciences, University of Victoria, Victoria, British Columbia V8W 2Y2, Canada

John M. Ozard

Defence Research Establishment Ottawa, Building 29, 3701 Carling Avenue, Ottawa, Ontario K1A 0Z4, Canada

(Received 6 March 1996; revised 20 April 1998; accepted 23 July 1998)

Detection performance is evaluated for two efficient algorithms that track sources moving linearly at constant speed and depth. One of the algorithms uniformly weights the contributions from each ambiguity surface along the tracks examined, and the other weights the contributions in proportion to the expected signal level. It is shown that these essentially "detect after track" algorithms are applicable to the situation where the signal-to-noise ratio is low and the apparent position of a moving acoustic source on a single matched-field ambiguity surface is highly ambiguous. They may be employed to reduce the ambiguity of the source position and to provide an improved detection probability at a given probability of false alarm. Algorithms that examine all possible tracks in multidimensional tracking are computationally prohibitive. However, the linear tracking algorithms described in this paper are based on only those tracks through the strongest peaks in the ambiguity surfaces. If the source track is likely to be detected after tracking, it is shown that the loss in detection performance after tracking, due to the possibility of not examining a track, is small since the probability of examining the source track is high. At high signal-to-noise ratios the performance loss vanishes. [S0001-4966(98)00611-0]

PACS numbers: 43.30.Wi, 43.60.Gk [JCB]

INTRODUCTION

If an acoustic source has been detected in a search region, knowledge of the environment may be employed for determining the position of the acoustic source. In particular, the technique known as matched-field processing (MFP)¹⁻⁵ correlates the measured acoustic field against a prediction of the acoustic field for all possible positions of the source over a search region. This correlation can be used to estimate the location of a source assuming one is known to be present *a priori*. Such localization techniques including tracking have been successfully applied to experimental data.⁶

Detection employing MFP may be used to determine whether a source is present anywhere in the search region. In this study it is required that the source be detected and its position determined. At sufficiently low signal-to-noise ratios (SNRs) the probability of detecting a source for a short duration of data becomes so small that detection cannot be made with any certainty (i.e., any detection would require an unacceptably high false alarm probability). To improve detection performance for low SNR sources, algorithms have been developed to track sources present on a series of ambiguity surfaces. Two such efficient source tracking algorithms have been described^{7,8} and applied to the detection of low SNR sources moving linearly at constant speed and depth. Thus detection occurs after tracking. These algorithms differ from previously described algorithms⁹ in that they only examine tracks through the largest peaks on successive ambiguity surfaces. This is necessary to keep the computational load within practical limits. While the detection performance for the general MFP detection problem is very difficult to

predict,^{10,11} some analytic results can be obtained for these efficient tracking algorithms.

In the next section the algorithms will be described and in the following section their theoretical performance found. The performance cost of restricting tracking to the largest peaks is also discussed.

I. TRACKING ALGORITHMS

In this paper trackers are described for detecting and locating sources that move along linear tracks at constant speed and depth. Maneuvering sources, of sufficiently high SNR, will probably show up as a series of linear segments that approximate the source path.¹² The inputs to the tracking algorithms are the Bartlett processor statistics $B(\mathbf{r})$ on a set of contiguous constant depth ambiguity surfaces. More precisely,

$$B(\mathbf{r}) = \frac{1}{N_A} \sum_{l=1}^{N_A} |\mathbf{r}^* \mathbf{d}_l|^2, \quad (1)$$

where the replica vectors \mathbf{r} are unit norm and cover the search region, and the statistic is averaged over N_A data vectors. The Bartlett processor was chosen for its robustness, although statistics from other processors could have been chosen. Here

$$\mathbf{d}_l = a \mathbf{r}' e^{j\theta_l} + \mathbf{n}_l, \quad (2)$$

where a is the signal amplitude and \mathbf{n}_l is a vector of N complex Gaussian distributed variables with mean 0 and standard deviation σ that represent the acoustic noise received on the N element array. The noise is assumed to be independent

across the array and in time, and $a\mathbf{r}'$ is approximated as being constant for the N_A averages. This means that, in practice, it is best to keep N_A small enough that this approximation holds. The N -dimensional complex vector $a\mathbf{r}'e^{j\theta_i}$ represents the noiseless acoustic signal received on the array where \mathbf{r}' is the normalized replica vector for the source position and θ_i is randomly distributed on $(-\pi, \pi)$. The single snapshot array SNR is thus a^2/σ^2 .

There are five steps in the computations for the linear tracking algorithms (LTAs), the first three of which are the same for both the unweighted algorithm and the weighted algorithm. These are: (1) for each of the N_S surfaces, the positions of the largest N_{PK} peaks are determined; (2) all possible tracks joining these largest peaks on all surfaces, the combinatoric tracks, are found; and (3) a constraint to realistic maximum speeds for the source is imposed to reduce the combinatoric tracks to the physically possible tracks.

For uniform weighting, which hereafter is called unweighted, the last two calculations are: (4a) the unweighted track statistic, is calculated for each physically possible track,

$$T_u = \frac{1}{N_S} \sum_{i=1}^{N_S} B(\mathbf{r}_i), \quad (3)$$

where $B(\mathbf{r}_i)$ is the Bartlett output for the replica vector \mathbf{r}_i on the i th surface at the position determined from a physically possible track whose statistic is being calculated; (5a) the estimated unweighted track SNR outputs, $\widehat{\text{SNR}}_u$, are calculated:

$$\widehat{\text{SNR}}_u = \frac{T_u - \bar{x}}{s} \sqrt{N_S}, \quad (4)$$

where \bar{x} is the average value and s is the standard deviation of the Bartlett statistic, $B(\mathbf{r}_i)$, for all points on all ambiguity surfaces in noise alone. Thus \bar{x} represents the average value of T_u and $s/\sqrt{N_S}$ represents the standard deviation of T_u in noise alone. The quantity $\widehat{\text{SNR}}_u$ represents the difference between the track statistic under consideration and the mean noise track statistic measured in noise track standard deviations.

One can improve the trackers performance by weighting the statistics in the sum of Eq. (3) in proportion to the expected source strength from the propagation model. For this propagation weighting, which hereafter is called weighted, the last two calculations are (4b) the weighted track statistic, T_w , is calculated for each physically possible track:

$$T_w = \sum_{i=1}^{N_S} c_i B(\mathbf{r}_i), \quad (5)$$

where c_i is the normalized received signal power at the i th point at range R_i and bearing ϕ_i along the track:

$$c_i = c_i(R_i, \phi) = \frac{\lambda_i(R_i, \phi)}{\sum_{i=1}^{N_S} \lambda_i(R_i, \phi)}, \quad (6)$$

where λ_i is the modeled signal power for the i th surface. (Note that for uniform weighting, $c_i = 1/N_S$.) It is important from a practical point of view to recognize that the modeled

received signal powers may be scaled as a group without affecting the values of c_i in the algorithm or the algorithm output.

(5b) The estimated weighted track SNR outputs, $\widehat{\text{SNR}}_w$, are calculated

$$\widehat{\text{SNR}}_w = \frac{T_w - \bar{x}}{s \sqrt{\sum_{i=1}^{N_S} c_i^2}}, \quad (7)$$

for a noise track T_w would have mean \bar{x} and standard deviation $s \sqrt{\sum_{i=1}^{N_S} c_i^2}$. If $c_i = 1/N_S$, then $\sqrt{\sum_{i=1}^{N_S} c_i^2} = 1/\sqrt{N_S}$ and Eq. (7) reduces to Eq. (4).

These algorithms are run for each depth at which the source may transit. The nonduplicate tracks with the largest values of $\widehat{\text{SNR}}_u$ and $\widehat{\text{SNR}}_w$ are reported. Five to ten tracks are usually reported in our studies.⁶⁻⁸ Two tracks are determined to be nonduplicate if either of the end points of the tracks differ by more than 10 m from one another. The expected value of $\widehat{\text{SNR}}_u$ is SNR_u and of $\widehat{\text{SNR}}_w$ is SNR_w where

$$\text{SNR}_u = \sqrt{\frac{N_A}{N_S}} \sum_{i=1}^{N_S} \frac{a_i^2}{\sigma^2} \quad (8)$$

and

$$\text{SNR}_w = \sqrt{N_A \sum_{i=1}^{N_S} \left(\frac{a_i^2}{\sigma^2} \right)^2}. \quad (9)$$

These are the unweighted and weighted track SNR outputs, respectively. This follows as the expected value of SNR_u is by definition the expected value of T_u for signal plus noise minus the expected value of T_u for noise only divided by the standard deviation of T_u for noise only. From the assumptions of Eqs. (1)–(3), $B(\mathbf{r}_i)$, for noise alone, is the sum of N_A chi-squared random variables with two degrees of freedom.¹³ Hence the mean and standard deviation of T_u for noise only are σ^2 and $\sigma^2/\sqrt{N_A}\sqrt{N_S}$, respectively. When a source is present, $B(\mathbf{r}_i)$ is a noncentral chi-squared random variable with two degrees of freedom and mean $a_i^2 + \sigma^2$; thus the expected value of T_u is $\sum_{i=1}^{N_S} a_i^2/N_S + \sigma^2$ and the value of SNR_u is $\sqrt{N_A}/N_S \sum_{i=1}^{N_S} a_i^2/\sigma^2$. Similarly SNR_w can be shown to be given by Eq. (9).

The quantity SNR_u is equivalent to the square root of Urlick's¹⁴ detection index parameter, and is the parameter required to calculate detection performance for the simple hypothesis problem. It can be shown that $\text{SNR}_w \geq \text{SNR}_u$ with equality when all a_i^2/σ^2 are equal. SNR_w can be larger than SNR_u as it incorporates *a priori* knowledge of the received source levels along the track.

These algorithms successfully detect the source track if the source track is one of those examined and if its track SNR value is the maximum. The probabilities of these events are determined in the next section.

II. PERFORMANCE

A. Probability that the source track is examined

The source track is examined if the Bartlett statistic at the source location is in the top N_{PK} peaks at least twice in

TABLE I. The probability that the source track is examined as a function of the number of surfaces N_S and the constant probability p_i that the source peak is one of the top peaks on any one surface.

p_i	N_S		
	10	15	20
0.1	0.26	0.740	0.84 000
0.2	0.62	0.940	0.98 000
0.3	0.85	0.960	0.99 800
0.4	0.95	0.995	0.99 990
0.5	0.99	0.995	0.99 998

the N_S ambiguity surfaces. The complement of this event is the event of exactly 0 or 1 detects, thus the probability the source track is examined (PTE) is

$$\text{PTE} = 1 - [P(0 \text{ detects}) + P(1 \text{ detect})]. \quad (10)$$

The Bartlett statistics on different surfaces are independent, since the noise is assumed independent; hence the above may be written as

$$\text{PTE} = 1 - \left[\prod_{i=1}^{N_S} (1 - p_i) + \sum_{i=1}^{N_S} (p_i) \prod_{j=1, j \neq i}^{N_S} (1 - p_j) \right], \quad (11)$$

where p_i is the probability that the source is one of the top N_{PK} peaks on the i th surface. The quantity p_i depends on many factors¹⁵ including the number and location of the sensors, the array length, SNR, and noise type. While the distributions of the individual $B(\mathbf{r}_i)$ are known analytically, on any surface, they are correlated, so that it is difficult to determine the p_i theoretically. This is the subject of ongoing research.¹⁶ The limitation on the size of N_S depends on whether it is reasonable to assume the source stays on a linear track for the time necessary to collect the N_S surfaces. PTE is listed in Table I for constant values of p_i for the N_S surfaces.

B. Probability that the source track is detected if examined

The source track is detected if its unweighted statistic T_u , or weighted statistic T_w , is greater than the noise and sidelobe track statistics, and greater than a threshold for a preassigned false alarm probability. The probability the source track is detected is calculated below after discussing noise and sidelobe tracks.

A noise track is one where the array SNRs along the track are all zero. For noise tracks the quantity $|\mathbf{r}^* \mathbf{d}_i|^2$ of Eq. (1) is a chi-squared random variable with two degrees of freedom and parameter σ^2 . Using the central limit theorem when $N_A N_S$ is sufficiently large, as it is in this application, the T_u noise statistics are identically and approximately Gaussian distributed with mean σ^2 and standard deviation $\sigma^2 / \sqrt{N_A N_S}$. The maximum of the transformed noise statistics, X_{MAX} , is the maximum of a set of K identically distributed Gaussian variables with mean zero and standard deviation 1. Here K represents the number of possible noise

tracks. From Ref. 17 the distribution of X_{MAX} for identically distributed independent Gaussian random variables and large K is

$$G(X_{MAX}) = \exp(-\exp(-X_{ON}(X_{MAX} - X_{ON}))), \quad (12)$$

where

$$X_{ON} = (2 \ln(K))^{0.5} \left[1 - \frac{\ln(4\pi) + \ln(\ln(K))}{4 \ln(K)} \right]. \quad (13)$$

The propagation environment, noise source distribution, the sampling of the acoustic field by the hydrophone array, and the replica sampling grid determine whether the noise tracks can be considered independent. If the field has not been oversampled by the sampling grid, then the number of independent tracks will be the number of possible tracks through the sampling grid points. Assuming the array SNRs are small, the T_u source statistics are also Gaussian distributed with mean $\sigma^2 + \sum_{i=1}^{N_S} a_i^2$ and standard deviation $\sigma^2 / \sqrt{N_A N_S}$. If the T_u variables are transformed by $(T_u - \sigma^2) / \sqrt{N_A N_S} / \sigma^2$, then the transformed source statistic, say X_T , is a Gaussian random variable with mean SNR_u and standard deviation 1. The noise track statistics and source track statistics are uncorrelated and Gaussian and hence independent. Thus the probability the source track statistic is greater than the noise track statistic (PSGN) is the sum of the probabilities that X_T lies between x and $x + \delta x$ and that X_{MAX} is less than x , that is,

$$\begin{aligned} \text{PSGN} &= \sum_x P(x \leq X_T \leq x + \delta x) P(X_{MAX} < x) \quad (14) \\ &= \frac{1}{\sqrt{2\pi}} \int_{-\infty}^{\infty} \exp\left(-\frac{(x - \text{SNR}_u)^2}{2}\right) G(x) dx. \quad (15) \end{aligned}$$

A sidelobe track is one where the array SNRs along the track are not all zero. For a sidelobe track statistic to be larger than the source track statistic, the sidelobe track's SNR would need to be close to the source track's SNR. Except for the case where sidelobe tracks are almost physically coincident with the source track—giving rise to very little uncertainty, sidelobe tracks did not exceed the source track in any of our many simulations^{7,8} or data analysis⁶ for a moving source. Subject to the above provisos, the probability that an examined source track is detected at a preassigned false alarm probability, PDET, is

$$\text{PDET} = \frac{1}{\sqrt{2\pi}} \int_{T_H}^{\infty} \exp\left(-\frac{(x - \text{SNR}_u)^2}{2}\right) G(x) dx. \quad (16)$$

The threshold is chosen so that the false alarm probability is α , that is $G(T_H) = 1 - \alpha$. PDET is given in Fig. 1 as a function of K , SNR_u and two values of α . This curve as a function of SNR is quite steep when PDET is near 0.5. For $\alpha = 10^{-3}$ and K between 10^4 and 10^{12} , a factor of 2 (3 dB) in SNR changes PDET from a few percent to over 99%. That is, for any K the minimum SNR for which the tracker will be successful is sharply defined by the steep part of the curve. For larger search areas, and hence a higher number of noise tracks, a higher track SNR, and therefore a longer track and hence a larger number of ambiguity surfaces, will be re-

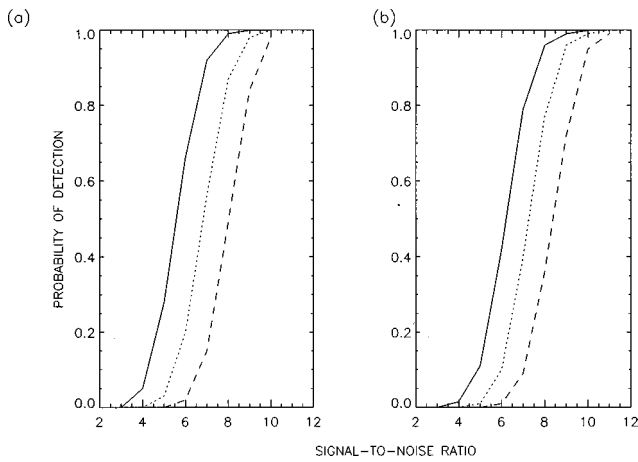


FIG. 1. The probability that the source track is detected, if examined, as a function of the track SNRs (K the number of noise tracks and the false alarm probability α). Solid lines $K=10^4$; dotted line, $K=10^8$; dashed line, $K=10^{12}$; (a) $\alpha=10^{-3}$ and (b) $\alpha=10^{-4}$.

quired to maintain a constant probability of detection. Thus the search area must be matched to the linear track length. The mean, standard deviation and percentile values for the maximum noise statistic derived from Eq. (12) are given in Table II. The mean and 99.9 and 99.99 percentile values slowly increase and the standard deviation slowly decreases as K increases by several orders of magnitude. As noted in Table II, the percentile values are the threshold values for associated false alarm probabilities. The mean and standard deviation are used below to compare theory and simulation.

III. APPLICATION

Application of the tracking algorithms and analysis of the results will be illustrated for an Arctic environment with a 25-element 720-m-long bottom-mounted horizontal array. The sound speed profile in the 650-m-deep water was upward refracting and the bottom consisted of two layers. The top layer was modeled as a fluid with a sound speed of 2000 m/s overlaying a basement modeled as a fluid with a sound speed of 2600 m/s.⁷ Simulations of the Fourier transformed signal were made for this environment. These simulations modeled the propagation of a 25-Hz signal at a 300-m depth, with 19 waterborne normal modes. The noise was modeled as spatially white noise with Gaussian amplitudes as outlined in Eq. (2). This represents a first approximation to the noise field produced by surface noise received by a horizontal ar-

TABLE II. The mean and standard deviation of the maximum of K independent normal random variables with mean 0 and standard deviation 1. The 99.90 and 99.99 percentile values of the distribution or equivalently the 10^{-3} and 10^{-4} false alarm probability threshold values are tabulated in the last two columns.

No. of random variables (K)	Mean	Standard deviation	Percentile	
			99.90	99.99
10^4	4.43	0.30	5.90	6.43
10^8	6.16	0.21	7.24	7.58
10^{10}	6.86	0.19	7.85	8.17
10^{12}	7.43	0.17	8.36	8.67

ray at half-wavelength spacing. Matching was carried out at 100-m increments over a Cartesian grid extending from 5000 to 25 000 m in both coordinates with the array at the origin. Matching was repeated at each 30-m depth increment from 30 to 630 m with 3.64×10^4 search grid points at each depth. One hundred data vectors were averaged and then matched to the replicas to form the Bartlett statistics on each of ten ambiguity surfaces. An exhaustive search would have had 1.32×10^9 tracks at each depth. By using 15 peaks per surface in the tracking algorithm only 10 125 combinatoric tracks were found. These were then examined by the tracking algorithm.

To verify the above theory, simulations and tracking were performed for noise only and for signal plus noise. Three noise-only simulations were done at the 300-m search depth yielding maximum SNR_u 's of 6.5, 6.61, and 6.73. The maximum noise SNR_u 's are consistent with the value of the maximum of 1.3×10^9 independent Gaussian random variables with mean 0 and standard deviation 1. This can be seen from Table II where we note that the SNR_u 's all lie within a few standard deviations of the mean of such random variables.

The results reported in Ref. 7 for when a signal is present were also consistent with the above theory. From Fig. 1 it can be seen that when $K=10^9$, a signal with track SNR of about 10 dB or larger, if examined, will almost certainly be the largest and detected, with a false alarm probability of 10^{-3} , while those with lower SNRs will not always be both largest and detected. Sources with a track SNR_u 's of 11.98 and 9.98 dB were detected. A track with a SNR_u of 8.99 dB was at the threshold for detection and sources with SNR_u 's of less than 8 dB were not detected.

Finally, we note that for this scenario a source track SNR of at least 10 dB was sufficient to guarantee the p_i 's of Eq. (11) were large enough to ensure the source track was one of those examined—when reasonably small values of N_{PK} were employed. That is, for the above conditions a track SNR of 10 dB, assuming an array that samples the acoustic field well, ensures with high probability that the source track is detected with the linear tracking algorithm.

IV. DISCUSSION

The examples illustrate empirical results for the distributions of noise-only track SNRs and source track SNRs when noise is present. Conditions under which the source track is examined and under which the source track is detected, if examined, were shown to agree with theory.

In this paper we examined a case where the noise was Gaussian and spatially white. This is sometimes the situation encountered in practice. However, one often encounters directional or spatially colored noise such as that from shipping or that from ice ridging in ice-covered oceans. Whether the theory described here is applicable under these circumstances depends on, among other things, the proportion of the noise that is colored. In the presence of stationary colored noise prewhitening has been used¹⁸ in a simulation study to improve detection. Assuming such processing, the performance evaluation results given here would apply.

V. CONCLUSIONS

Analytic results have been obtained for determining the performance of two efficient source tracking algorithms. These analytic results include an expression for the probability that a source track is examined as a function of the probability that the source track statistic is one of the top peaks on a number of ambiguity surfaces. An expression for the probability the source track is detected, if examined, is also derived. These findings agreed with the simulation studies that were previously employed to demonstrate the tracking algorithms.

The performance of the algorithms was evaluated for practical search regions as well as practical source and tracking algorithm parameters. The evaluation assumes a benign environment and an array well designed to sample the acoustic field. Based on theory and extensive simulation it was established for the realistic case studied that for a track SNR of 10 dB a moving source will be detected with a high probability.

¹A. Tolstoy, *Matched Field Processing for Underwater Acoustics* (World Scientific, Singapore, 1993).

²R. Fizell, "Application of high-resolution processing to range and depth estimation using ambiguity function methods," *J. Acoust. Soc. Am.* **82**, 606–613 (1987).

³G. B. Smith, C. Feuillade, D. R. Del Balzo, and C. L. Byrne, "A nonlinear matched-field processor for detection and localization of a quiet source in a noisy shallow-water environment," *J. Acoust. Soc. Am.* **85**, 1158–1166 (1989).

⁴A. B. Baggeroer, W. A. Kuperman, and H. Schmidt, "Matched field processing: source localization in correlated noise as an optimum parameter estimation problem," *J. Acoust. Soc. Am.* **83**, 571–587 (1988).

⁵J. M. Ozard, "Matched field processing in shallow water for range, depth and bearing determination: Results of experiment and simulation," *J. Acoust. Soc. Am.* **86**, 744–753 (1989).

⁶J. M. Ozard, M. L. Jeremy, N. R. Chapman, and M. J. Wilmut, "Matched-field processing in a range-dependent shallow water environment in the Northeast Pacific Ocean," *IEEE J. Ocean Eng.* **21**, 1–7 (1996).

⁷M. J. Wilmut, J. M. Ozard, and P. Brouwer, "Evaluation of Two Efficient Target Tracking Algorithms For Matched Field Processing with Horizontal Arrays," *J. Comput. Acoust.* **3**, 311–326 (1995).

⁸M. J. Wilmut, J. M. Ozard, and B. Woods, "An Efficient Target Tracking Algorithm For Matched Field Processing," *IEEE Oceans 93*, 19–22 October 1993, Victoria, BC, Canada, pp. 81–85.

⁹J. A. Fawcett and B. H. Miranda, "Localization by maximizing long-time integrated spectral power," *IEEE Trans. Signal Process.* **40**, 460–462 (1992).

¹⁰E. J. Sullivan and D. Middleton, "Estimation and Detection Issues in Matched Field Processing," *IEEE J. Ocean Eng.* **18**, 156–166 (1993).

¹¹E. J. Sullivan and D. Middleton, "Estimation and Detection in Matched Field Processing," *IEEE Oceans 93*, 19–22 October 1993, Victoria, BC, Canada pp. 70–74.

¹²H. Bucker, "Matched-field tracking in shallow water," *J. Acoust. Soc. Am.* **96**, 3809–3811 (1994).

¹³H. O. Lancaster, *The Chi-Squared Distribution* (Wiley, New York, 1969).

¹⁴R. J. Urick, *Principles of Underwater Sound for Engineers* (McGraw-Hill, New York, 1967).

¹⁵C. S. Clay and M. J. Hirsch, "Use of a two-dimensional array to receive an unknown signal in a dispersive waveguide," *J. Acoust. Soc. Am.* **47**, 435–440 (1969).

¹⁶C. A. Zala, J. M. Ozard, and M. J. Wilmut, "Efficient estimation of the probability that a source track is examined in a matched field processing algorithm," *J. Acoust. Soc. Am.* **103**, 374–379 (1998).

¹⁷M. Kendall and A. Stuart, *The Advanced Theory of Statistics* (MacMillan, New York, 1977).

¹⁸C. A. Zala, J. M. Ozard, and M. J. Wilmut, "Prewhitening for improved detection by matched-field processing in ice-ridging correlated noise," *J. Acoust. Soc. Am.* **98**, 2726–2734 (1995).

Elastic constants of the lithium tantalate crystal in the hypersonic range

Tomasz Błachowicz and Zygmunt Kleszczewski

Institute of Physics, Silesian Technical University, Krzywoustego 2, 44-100 Gliwice, Poland

(Received 21 October 1997; revised 14 April 1998; accepted 20 August 1998)

Elastic constants of the lithium tantalate LiTaO_3 crystal were determined in the hypersonic range by the use of the Brillouin laser light scattering method. Obtained values show variation with respect to ultrasonic measurements. Results are interesting because the same effects are qualitatively different in isomorphous lithium niobate LiNbO_3 crystal. © 1998 Acoustical Society of America. [S0001-4966(98)00512-8]

PACS numbers: 43.35.Dh [HEB]

INTRODUCTION

Ferroelectric lithium tantalate crystal is isomorphous to lithium niobate crystal, which is well known from wide applications. Despite the great crystallographic symmetry of both materials, surprising differences can be found in the values of basic physical constants, for example, in the melting and Curie temperatures. The melting temperature is equal to 1923 K for LiTaO_3 and 1526 K for LiNbO_3 . The Curie temperature for LiNbO_3 (1483 K) is comparable to its melting temperature; however, the Curie temperature for LiTaO_3 (883 K) is much smaller than its melting temperature. This curious fact was explained by Abrahams *et al.*^{1,2} who pointed to the subtle differences in space atom distribution in an elementary cell of both crystals. The consequences of these differences are seen in acoustic wave propagation parameters, especially in changes of values of the elastic constants in different frequency ranges. The elastic constants of both materials measured ultrasonically are well known,³ but there has been little research for the hypersonic range.

The main purpose of this work was to determine the elastic constants of the LiTaO_3 crystal in the hypersonic range from 20.9 to 38.5 GHz. From these data it can be determined if there are divergences from the values previously measured in the ultrasonic range.

I. EXPERIMENT

All measurements were made by the Brillouin laser light scattering method. This consists in measuring changes of photon frequency nonelastically scattered on acoustical phonons lying at the beginning of the first Brillouin zone. At the quantum level annihilation and creation processes are responsible for the typical picture of the Brillouin spectrum where lines of lowered and increased frequency can be observed. The equipment used in these measurements included: a single-mode ion argon laser working at 514.5 nm with 100-mW power, a single-pass pressure-scanned Fabry-Perot interferometer designed in our laboratory and a PMT 614 unit (from PTI Inc.) for single photon counting with a Hamamatsu R4220P photomultiplier tube. The PMT 614 unit was coupled with a digital counter sensitive to a TTL standard signal and then connected with a parallel port of a PC computer by an interface designed in our laboratory. The

systematic error in phonon frequency measurement caused by the choice of the interferometer's full spectral range and numerical treatment of data was equal to 0.15 GHz. Statistical error derived from individual measurements fell in the range from 0.04 to 0.27 GHz, but in most cases was equal to 0.08 GHz. All measurements were performed on three cubic samples cut in known crystallographic directions with an accuracy equal to 20'. In all cases the angle between the direction of incident and scattered light was equal to 90 degrees. Polarization of light was also controlled, which is a standard treatment in such experiments. Before measurements, the frequency and kind of acoustic wave polarization, were calculated in the ultrasonic range. There are two main principles for performing the calculations. The first one is the second Newton's law describing the propagation of an acoustic wave in any direction of the crystal. The second one is the momentum conservation law which connects the momentum wave vector of the incident light with the wave vector of the scattered light and with the wave vector of the acoustic wave. The piezoelectricity of the LiTaO_3 crystal was taken into account in values of the stress tensor connected by the Hook's law with strains represented by the strain tensor and with the stress-induced electric field in which the piezoelectric tensor appears. Solving the equation of motion we obtain eigenvectors and eigenvalues of a so-called "characteristic matrix," which is a function of the propagation direction of the acoustic wave and the elastic constants of the medium. The eigenvectors describe states of the wave polarization and the eigenvalues, divided by a density of the medium, inform

TABLE I. Comparison of hypersonic and ultrasonic values of elastic constants for the LiTaO_3 crystal.

	Frequency of an acoustic wave or range of frequencies (GHz)	Measured elastic constants (10^{10} Pa)	Ultrasonic data ³ (10^{10} Pa)	Relative difference (%)
c_{11}	33.74 ± 0.16	22.98 ± 0.21	23.3	1.4
c_{33}	36.43 ± 0.19	25.84 ± 0.26	27.5	6.0
c_{44}	20.94 ± 0.16	8.85 ± 0.14	9.4	5.9
c_{66}	21.45 ± 0.19	9.28 ± 0.16	9.3	0.2
c_{12}	(21.45–33.74)	4.42 ± 0.53	4.7	6.0
c_{14}	(20.94–21.70)	0.45 ± 0.29	-1.1	59.1 ^a
c_{13}	(20.94–36.43)	5.12 ± 0.45	8.0	36.0

^aA change of an algebraical sign.

TABLE II. Comparison of hypersonic and ultrasonic values of elastic constants for the LiNbO₃ crystal.

	Hypersonic data (Ref. 5) (10 ¹⁰ Pa)	Ultrasonic data (Ref. 3) (10 ¹⁰ Pa)	Relative difference (%)
c_{11}	20.125	20.3	0.9
c_{33}	24.01	24.5	2.0
c_{44}	5.963	6.0	0.6
c_{66}	7.167	7.5	4.4
c_{12}	5.791	5.3	8.5
c_{14}	0.943	0.9	4.6
c_{13}	7.108	7.5	5.2

us about velocities of the wave.⁴ Table I provides the experimental results, as well as a comparison with ultrasonic data. Table II provides a similar comparison for the LiNbO₃ crystal.^{3,5}

In our experiments, elastic constants c_{11} , c_{33} , c_{44} and c_{66} were measured directly. Remainder values were achieved indirectly as a combination of measured frequencies of acoustic waves and the above constants, so their experimental uncertainties are greater. We can see from Table II that there exists a change of c_{12} , c_{13} , c_{14} and c_{33} elastic constants for the LiNbO₃ crystal, while the variation is quite different for the LiTaO₃ crystal. For example the c_{12} constant increased and the relative difference of this change is equal to 8.5%. As was mentioned earlier, the strong similarity in crystallographic symmetry is not reflected in the physical behavior of both materials. In other published research^{3,5} experimental error was not reported, so our comparison of results in Table I is more accurate.

II. CONCLUSION

The values of elastic constants obtained are not in full agreement with ultrasonic data, so a significant difference can be observed, especially for the c_{13} elastic constant. One of the reasons for the magnitude of this difference is that this value was obtained from the remaining data which belonged to the 20.94–36.43-GHz range of frequencies. It seems that there is a more subtle relation for this constant in the hypersonic range. On the other hand, a similar procedure for the c_{12} constant was used, and, in the range of experimental error, there is no variation for this constant. There is also no variation for c_{66} . Generally, all the elastic constants stayed weaker. It seems that these results were the consequence of subtle differences of atom distribution in the crystallographic elementary cell. The situation is similar to that for the above-mentioned values of melting and Curie temperatures. More theoretical and experimental investigation is required to confirm this interpretation.

¹S. C. Abrahams and J. L. Bernstein, *J. Phys. Chem. Solids* **28**, 1685 (1967).

²S. C. Abrahams, W. C. Hamilton, and J. M. Reddy, *J. Phys. Chem. Solids* **28**, 1693 (1967).

³J. Xu and R. Stroud, *Acousto-optic Devices: Principles, Design and Applications* (Wiley, New York, 1992).

⁴T. Błachowicz and Z. Kleszczewski, *Arch. Acoust.* **22**, 351 (1997).

⁵R. J. O'Brien, G. J. Rosasco, and A. Weber, in *Light Scattering Spectra of Solids—Proceedings of the International Conference on Light Scattering Spectra of Solids*, New York, September 1968, edited by G. B. Wright (Springer-Verlag, New York, 1969), p. 623.

Surface-wave modes on soft gels

Y. Onodera and P.-K. Choi

Department of Physics, Meiji University, 1-1-1 Higashimita, Tama-ku, Kawasaki 214, Japan

(Received 29 April 1998; revised 1 September 1998; accepted 4 September 1998)

To understand behavior of surface waves on sols and gels, the dispersion relation of surface modes on isotropic materials with both surface tension and elasticity is studied. The dispersion relation consists of two separate branches: one corresponds to the truly localized Rayleigh-type modes which can exist only at low frequencies, while the other, which is connected continuously to the capillary modes, gives pseudo-surface waves that are damped, radiating elastic transverse waves into the bulk of the medium just like the ones known in surface waves on elastically anisotropic materials. The result is compared with recent experiments on sols and gels. © 1998 Acoustical Society of America. [S0001-4966(98)04312-4]

PACS numbers: 43.35.Pt [HEB]

INTRODUCTION

In relation to sol-gel transitions, the behavior of surface waves on elastic media with surface tension is receiving attention.¹⁻⁶ In sols or liquids, the surface tension gives the restoring force for dispersive capillary waves, while in gels the elasticity inherent of solids supports elastic surface waves called Rayleigh waves. Then, a problem of immediate physical interest is how the surface waves behave in the presence of both types of restoring forces. In case one of the two kinds of restoring forces is overwhelmingly large, the other one is expected to play a secondary role of strengthening the restoring force, thus increasing the phase velocity of surface waves. Actually, recent experiments on sol-gel systems have confirmed that the phase velocity increases as gelation proceeds.²⁻⁶ Furthermore, these experiments commonly suggest that the crossover from the capillary wave to elastic Rayleigh wave occurs continuously, rather than abruptly. This would mean that the two modes do not persist but unite to form a single branch in the dispersion relation.

Theoretically, the presence of dispersive modes on solid surfaces was noted by Murdoch,^{7,8} who studied effects of the residual surface tension on solid-surface waves. However, much of the above experimental works have been motivated by the theory of Harden, Pleiner, and Pincus,¹ who solved the hydrodynamic equation for surface waves on viscoelastic materials and evaluated the light-scattering spectra for several typical cases. Their spectra certainly show that the two modes may persist in some cases. More recently, Jäckle and Kawasaki⁹ developed a similar, but more transparent, theory from their interest in the surface response of supercooled glassy melts.

Although the theoretical background has already been established by those theoretical works, it appears to us that the dispersion relation and behavior of the surface modes have not yet been fully studied. In this paper, we wish to clarify the entire physical picture contained in the dispersion-relation equation. We will show that the dispersion relation consists of two disconnected branches. One of them describes surface waves truly localized on the surface, and approaches the Rayleigh wave in the limit of vanishing surface tension. The other, which corresponds to capillary modes, is

no longer localized in the presence of finite elasticity. It couples with the transverse sound wave that diverges into the bulk of the body with canted wave vector. It has much the same character as the pseudo-surface waves¹⁰⁻¹² known in the theory of surface waves on anisotropic materials. These results will be discussed in light of recent related experiments on sols and gels.

I. SURFACE RESPONSE FUNCTIONS

Dynamics of surface waves on an elastic medium with surface tension may be studied by means of two different approaches. In one of them,¹ the medium is essentially regarded as a viscous liquid, and the shear elasticity is taken into account as the imaginary part of the viscosity. The dispersion relation for the surface waves is then determined by solving the equation of motion within the framework of hydrodynamics.¹³ This approach was recently extended to allow a surface adsorption layer.¹⁴ In the other approach,^{7,9} the medium is regarded as an elastic solid, whose viscosity may be incorporated into the imaginary part of the elastic constants. Then, the theory of Rayleigh waves known in the elasticity theory¹⁵ will give the required dispersion relation after an appropriate generalization to allow nonvanishing surface tension.

Both of the above two approaches are known to lead to the same result in the limit of incompressible media. Since the latter approach based on the elasticity theory⁹ is more straightforward and is valid for compressible media in general, we will recapitulate it below, together with a slight extension on the surface-response functions.

Suppose that a homogeneous medium with density ρ occupies the half-infinite space $z \leq 0$. Its isotropic elasticity is characterized by two elastic constants: the shear modulus $G(\omega)$ and the longitudinal modulus $C_l(\omega)$, which correspond respectively to c_{44} and c_{11} in cubic crystals. We understand them to depend on the angular frequency ω of oscillation.

Sound waves in the bulk of an isotropic medium are necessarily either transverse ($\text{div } \mathbf{u}_t = 0$) or longitudinal ($\text{rot } \mathbf{u}_l = 0$), and the displacement \mathbf{u} is, in general, given by their superposition,

$$\mathbf{u}(x, z, t) = a\mathbf{u}_t(x, z, t) + b\mathbf{u}_l(x, z, t), \quad (1)$$

with use of the constants a and b to be determined by the boundary condition on the surface. When we consider waves that run along the x direction with wave number k and frequency ω , then we have

$$\mathbf{u}_t(x, z, t) = (i\kappa_t \mathbf{e}_x + k\mathbf{e}_z) \exp[i(kx - \omega t) + \kappa_t z], \quad (2)$$

$$\mathbf{u}_l(x, z, t) = (ik\mathbf{e}_x + \kappa_l \mathbf{e}_z) \exp[i(kx - \omega t) + \kappa_l z], \quad (3)$$

in terms of the unit vectors \mathbf{e}_x and \mathbf{e}_z in the respective directions. The decay constants κ_t and κ_l are defined by

$$\kappa_t = \sqrt{k^2 - \rho\omega^2/G(\omega)}, \quad (4)$$

$$\kappa_l = \sqrt{k^2 - \rho\omega^2/C_l(\omega)}. \quad (5)$$

They have positive real parts, since the displacement should vanish toward the depth of the medium ($z = -\infty$).

Now, the boundary condition on the surface requires the stress components on the surface to be

$$\sigma_{zz,0} = P_z + \gamma \frac{\partial^2 u_{z,0}}{\partial x^2}, \quad (6)$$

$$\sigma_{xz,0} = X_z, \quad (7)$$

where the suffix 0 refers to the surface plane, $z=0$, and P_z and X_z stand for the pressure and the tangential stress applied onto the surface, respectively. The second term in Eq. (6) arises from the restoring force due to the surface tension γ . Since the stress components are related to strain by

$$\sigma_{zz} = C_l(\omega) \frac{\partial u_z}{\partial z} + [C_l(\omega) - 2G(\omega)] \frac{\partial u_x}{\partial x}, \quad (8)$$

$$\sigma_{xz} = G(\omega) \left(\frac{\partial u_x}{\partial z} + \frac{\partial u_z}{\partial x} \right), \quad (9)$$

we obtain linear equations for the coefficients a and b , which may be solved to yield the displacement on the surface in the form

$$u_{z,0} = \chi_{zz}(k, \omega) P_z + \chi_{zx}(k, \omega) X_z, \quad (10)$$

$$u_{x,0} = \chi_{xz}(k, \omega) P_z + \chi_{xx}(k, \omega) X_z. \quad (11)$$

The response functions $\chi_{ij}(k, \omega)$ on the right-hand side describe what surface displacements are induced by applied external stress. Explicit expressions for them are found to be

$$\chi_{zz}(k, \omega) = \frac{\kappa_l}{D(k, \omega)}, \quad (12)$$

$$\chi_{zx}(k, \omega) = -\chi_{xz}(k, \omega) = \frac{ik(k^2 + \kappa_t^2 - 2\kappa_t \kappa_l)}{(k^2 - \kappa_t^2)D(k, \omega)}, \quad (13)$$

$$\chi_{xx}(k, \omega) = \frac{\kappa_t + \gamma k^2(k^2 - \kappa_t \kappa_l)/\rho\omega^2}{D(k, \omega)}, \quad (14)$$

where the common denominator $D(k, \omega)$ is given by

$$D(k, \omega) = \gamma k^2 \kappa_l + \frac{4G^2(\omega)k^2 \kappa_t \kappa_l - [2G(\omega)k^2 - \rho\omega^2]^2}{\rho\omega^2}. \quad (15)$$

As regards the relevance of these response functions to experiment, the so-called dynamic structure factor defined by

$$S(k, \omega) = (2k_B T/\omega) \text{Im} \chi_{zz}(k, \omega) \quad (16)$$

gives the spectra of light scattered by thermally excited surface waves.^{1,9} Although the light-scattering technique is indeed powerful in that it provides us with direct information on the $S(k, \omega)$ spectra, it is restricted to sound waves of relatively high frequencies, say above 10 kHz.

To investigate surface waves of lower frequencies, it is conventional to generate them by means of direct mechanical excitation. In that case, the driving force will induce both normal and tangential stress components on the surface. It is then the functions $\chi_{ij}(k, \omega)$ themselves that describe the response of the resulting surface waves. When the induced surface waves are detected by measuring deflection of a light beam normally incident on the surface, it is only $u_{z,0}$ that matters, and hence surface waves with large χ_{zz} and χ_{zx} are susceptible to such excitations.

II. DISPERSION RELATION OF SURFACE WAVES

Normal modes of vibration are determined by the vanishing denominator,

$$D(k, \omega) = 0. \quad (17)$$

Actually, surface waves with k and ω satisfying Eq. (17) can stand by themselves even in the absence of applied stress P_z and X_z . We are going to consider below the dispersion relation between k and ω resulting from Eq. (17). Even though the expression for $D(k, \omega)$ has already been known in literature,^{1,7,9} the dispersion relation resulting from it has not been fully worked out. By solving explicitly Eq. (17), we will clarify that the dispersion relation in soft materials consists of two separate branches of different character.

In soft materials of our interest, like sols and gels, which are almost incompressible except at very high frequencies, the longitudinal elastic modulus is much greater than the shear modulus. We can therefore put $\kappa_l = k$ in Eq. (5), which gives the denominator

$$D(k, \omega) = \gamma k^3 + \frac{4G(\omega)}{k + \kappa_t} k^2 \kappa_t - \rho\omega^2. \quad (18)$$

This expression for $D(k, \omega)$ is equivalent to Eq. (10) of Ref. 1, despite the different appearance. Note that their kinetic viscosity $\nu(\omega)$ corresponds to $G(\omega)/i\omega\rho$ in our notation.

As usually done in consideration of dispersion relations in general, we disregard dissipation and understand $G(\omega)$ to consist of only the shear-elastic constant G_0 :

$$G(\omega) = G_0. \quad (19)$$

The neglected viscosity, which should appear as the imaginary part in $G(\omega)$, will be restored later when we compare our result with experiment in the following section.

Though the dispersion relation is usually determined by seeking ω for given k , we take the opposite approach here; we seek wave number k that satisfies Eqs. (17) and (18) with Eq. (19) for given real values of frequency ω . For this purpose, it is convenient to introduce the nondimensional frequency

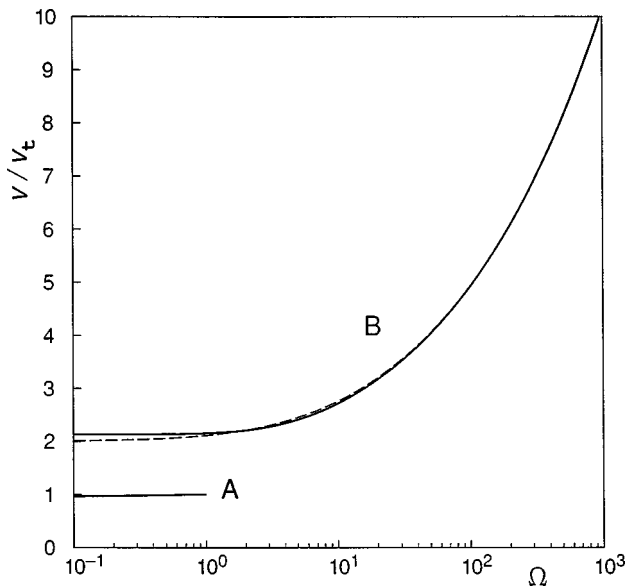


FIG. 1. Reduced phase velocity v/v_t plotted against the reduced frequency $\Omega = \gamma\omega/\rho v_t^3$. The dispersion relation determined by Eq. (17) with Eqs. (18) and (19) consists of two branches: the lower branch A gives surface waves localized on the surface, while the upper branch B is quasilocalized. The dashed line shows Eq. (26), which approximates the B branch considerably well.

$$\Omega = \frac{\gamma\omega}{\rho v_t^3}, \quad (20)$$

where

$$v_t = \sqrt{G_0/\rho} \quad (21)$$

denotes the velocity of transverse elastic waves in the bulk of the medium. Briefly, Ω measures the relative importance of the surface tension as compared with the elastic restoring force. At high frequencies, the surface tension excels the elasticity, and vice versa at low frequencies. We have $\Omega=1$ when the two restoring forces are equal in strength.

The dispersion relation obtained from Eqs. (17) and (18) with Eq. (19) is shown in solid lines in Fig. 1. Here, the phase velocity

$$v = \omega/k \quad (22)$$

is plotted in units of v_t against the reduced frequency Ω . As the figure shows, the dispersion relation consists of two separate branches referred to as A and B for convenience. These two branches have entirely different characters as explained below.

We will begin with the case of real k . When the wave number k is restricted to be real, then Eq. (17) admits a solution only for frequencies in the limited range $0 \leq \Omega \leq 1$, providing the branch A of Fig. 1. Toward the limit $\Omega \rightarrow 0$, where the surface tension tends to vanish, the velocity approaches $v/v_t \rightarrow 0.9553$, a value which is well known for Rayleigh waves in soft materials with the Poisson ratio $\sigma=1/2$.

As Ω departs from 0, the surface tension gradually enhances the restoring force, giving higher phase velocity (though the curve A in Fig. 1 looks almost flat). As a result of this increased velocity, the constant κ_t given by Eq. (4)

now decreases, and the localized Rayleigh wave begins to extend deep into the bulk of the material. When Ω is further increased up to 1, then the wave runs with the velocity v_t , the constant κ_t vanishes, and it extends over the entire body. Such a mode can no longer be called a surface mode; it is rather a transverse wave extended throughout the bulk. Thus, the branch A terminates at $\Omega=1$. It has no continuation even when k is relaxed to be complex, since this terminal point is mathematically a branch point.

It is important to note that Eq. (17) has no solution at any other than the branch A, so long as k is confined on the real axis; even capillary modes cannot exist as localized modes in the presence of elasticity.¹⁶ We will explain shortly its physical implications, but at any rate, we relax k to possess an imaginary part. Then a mathematical problem arises as to which sign to choose in evaluating κ_t , using Eq. (4).

According to ordinary physical considerations, we would choose one with a positive real part, inasmuch as the displacement must vanish at $z = -\infty$. We should certainly do so, if we consider truly localized modes. However, Eq. (17) loses even a capillary-mode solution with such a sign convention. This can be seen most clearly in the limit of high frequencies. For sufficiently large ω , where the surface tension prevails, we may put

$$k = (\rho\omega^2/\gamma)^{1/3} + ik'', \quad (23)$$

with a positive imaginary part k'' which ensures the surface wave to decay as it runs. Using Eq. (23) in Eq. (18), we find

$$\text{Im } \kappa_t < 0, \quad (24)$$

in order for the imaginary parts to cancel out, or for Eq. (17) to have a solution. This choice in sign inevitably leads to

$$\text{Re } \kappa_t < 0, \quad (25)$$

since the argument of the square root in Eq. (4) now resides on the second quadrant of the complex plane at large ω . We have thus found that normal modes in the B branch or self-supporting capillary waves should be accompanied by a complex κ_t with the above-mentioned sign in the presence of elasticity.

This result may be interpreted as follows. The signs in Eqs. (24) and (25) indicate that the wave is no longer localized on the surface. Equation (24) means that the capillary mode radiates a transverse wave with a canted-wave vector into the negative z -direction. In general, surface waves that run with a velocity higher than the transverse velocity v_t will always emit a transverse wave into the bulk of the material. This may be seen from the following argument: Suppose that a capillary wave runs on the surface with a phase velocity ω/k which is much greater than v_t . Obviously, elasticity cannot support such a wave, since an elastic wave is unable to run so quickly. However, with an added wave-vector component in the z -direction, it can fulfill the relation $\omega = v_t k$, because it now gains a larger magnitude of k . Since the energy of the transverse wave is supplied by the capillary wave, the latter is necessarily damped. An overall picture emerging from the above argument is that the capillary wave itself decays, emitting a diverging transverse-bulk wave. Since this solution no longer satisfies the conventional

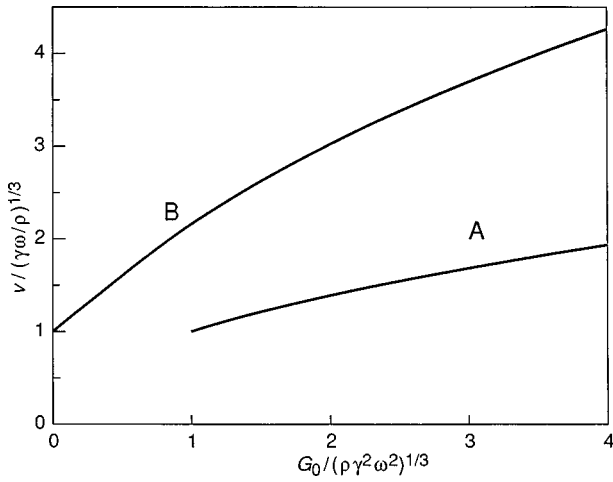


FIG. 2. Phase velocity v plotted as a function of shear modulus G_0 .

boundary condition that the displacement should vanish at infinite depth, it cannot truly be called a surface wave. A quite similar situation is known to occur in surface waves on anisotropic materials.¹⁰⁻¹² Accordingly, surface modes on the B branch in Fig. 1 may be called pseudo-surface waves or leaky-surface waves, though “pseudo-capillary waves” may also be appropriate. Although these pseudo-capillary waves are not localized on the surface, they may be detected in experiments as surface waves insofar as their damping is not strong.

To summarize, we have found that the dispersion relation consists of two separate branches, A and B, in the absence of dissipation. The former corresponds to the Rayleigh waves truly localized on the surface, while the latter, which are connected to capillary waves at high frequencies, are pseudo-surface waves that decay, emitting transverse elastic waves into the bulk of the medium.

Before closing this section, we would like to add a comment on the B branch. The dispersion curve drawn in Fig. 1 requires numerical work involving complex numbers. However, a fairly good approximation is available to the B branch. If we note that $|\kappa_t| \gg k$ holds for large ω , then Eq. (18) will give the approximate dispersion relation

$$\omega^2 = (\gamma/\rho)k^3 + 4(G_0/\rho)k^2. \quad (26)$$

Although Eq. (26) has been derived analytically on the assumption $\Omega \gg 1$, the dashed line in Fig. 1 tells us that it is remarkably useful in a wider region of Ω . This approximate relation seems to allow a simple interpretation, as though the two restoring forces simply add in the B branch, except that the latter is intensified by a factor four. It also means that misidentification of the flat dispersion of the B branch with the truly localized Rayleigh modes will lead to overestimation of the shear modulus by a factor four.

Finally, in order to facilitate comparison with experiments done for fixed frequencies and varying degrees of gelation, we replot Fig. 1 as Fig. 2, drawing the phase velocity v as a function of the shear modulus G_0 . Roughly speaking, the left and right ends of Fig. 1 are reversed here because the quantity on the abscissa is equal to $\Omega^{-2/3}$. Note that the ordinate is no longer scaled by v_t . The figure shows how the

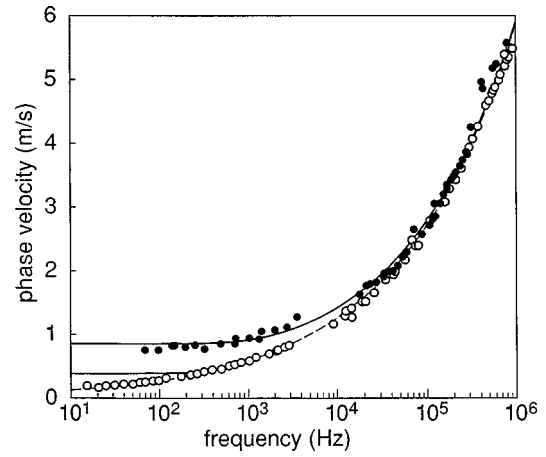


FIG. 3. Velocity dispersion of surface waves in 5.0 wt % gelatin sol at 50 °C (open circles) and gel at 20 °C (solid circles) observed by Kikuchi *et al.*⁴ The dashed curve represents the dispersion of capillary waves, whereas the solid curves represent theoretical fit to the gel dispersion with $G_0 = 160$ Pa.

velocity varies as gelation proceeds. At $G_0 = 0$, the B branch starts with the pure-capillary mode, and increases its velocity with G_0 . When the shear elasticity develops and reaches the critical value $(\rho\gamma^2\omega^2)^{1/3}$, another branch A emerges. Velocity of both branches increases in proportion to $G_0^{1/2}$ at large G_0 .

III. COMPARISON WITH EXPERIMENT

To compare the theoretical dispersion curve with experiment, dispersion has to be observed in a sufficiently wide range of frequency. In this regard, many of the available experimental data are insufficient, since they are done only for several selected frequencies. However, the desired dispersion data were recently obtained by Kikuchi, Sakai, and Takagi for gelatin gels.⁴ They succeeded in elaborate determination of the dispersion relation using the light-scattering technique at high frequencies (20 to 800 kHz) and the mechanical induced-oscillation technique at low frequencies (20 Hz to 10 kHz). Figure 3 shows their data for sol (50 °C) and gel (20 °C) of 5.0 weight-percent gelatin dissolved into water. The phase velocity of sol (open circles) is seen to obey the $\omega^{1/3}$ law of capillary waves, drawn in dashed lines with density $\rho = 1.0 \times 10^3$ kg/m³ and surface tension $\gamma = 3.20 \times 10^{-2}$ N/m.

The data for gel (solid circles) may now be compared with the theoretical dispersion relation. If we choose $G_0 = 160$ Pa, the theoretical curve drawn in solid lines in Fig. 3 gives a satisfactory overall agreement with experiment. From this fit, we find that the observed dispersion data correspond entirely to the B branch, or to pseudo-capillary waves. Even though the observed velocity is almost dispersionless around $10^2 \sim 10^3$ Hz, the theory shows that such a behavior alone cannot guarantee that they are true Rayleigh waves or A modes, because the B branch is also flat at low frequencies. The overall good agreement in Fig. 3 suggests that true surface modes would appear below 10^2 Hz because of weak shear-restoring force. In fact, it is possible that the data points for gel in Fig. 3 for the lowest frequencies correspond

to two concurrent modes, considering that the critical frequency evaluated from the above material parameters is 320 Hz.

To see the possibility of concurrence of the two modes, it is useful to consider the response functions in detail. In addition, inclusion of viscosity, which has so far been neglected, is necessary in realistic comparison with experiment. In experiments using mechanical excitation of surface waves, the surface is driven mechanically at a given frequency, and the phase velocity of the resulting wave train is observed by detecting it at a distance. In this type of experiment, mechanical excitation generates waves of various wave numbers, as opposed to the light-scattering where k may be specified by the scattering geometry.

To consider the above problem for the particular experimental data of Fig. 3, we will begin with estimation of the viscosity. In their light-scattering experiment, Kikuchi *et al.*⁴ analyzed the observed scattering spectra with an asymmetric Lorentzian to determine the frequency ω and the width Γ . Since the width Γ determined in this way for the gel is almost proportional to ω in the frequency range $\omega = 10^7 \sim 4 \times 10^8$ rad/s, we assume that the viscosity η_0 may be included in $G(\omega)$ as

$$G(\omega) = G_0 - i\omega\eta_0. \quad (27)$$

With this choice for $G(\omega)$, we calculated numerically the scattering spectra $S(k, \omega)$ for the gel, and found that $\eta_0 = 0.01$ Pa·s reproduces the observed width. In evaluation of the corresponding spectra, it is convenient to introduce the reduced nondimensional viscosity

$$\eta^* = \eta_0 v_t / \gamma \quad (28)$$

which turns out to be $\eta^* = 1/8$ in the present case.

Figure 4 shows the spectra of absolute values of $\chi_{zz}(k, \omega)$ and $\chi_{zx}(k, \omega)$ for the above choice of η^* . Note that the abscissa is not the wave number k , but the phase velocity v . These spectra show surface waves with what phase velocity are likely to be generated by a mechanical excitation at given frequencies. As seen from the figure, both $|\chi_{zz}|$ and $|\chi_{zx}|$ have a broad peak corresponding to the B branch in the dispersion relation. In addition to this, for frequency $\Omega \leq 1$, they have also a peak at $v \approx v_t$ corresponding to the A branch. This means that mechanical excitations can concurrently induce surface waves of both modes when $\Omega \leq 1$. On the other hand, such a concurrence is not remarkable when $\Omega \geq 1$, in support of our overall identification in Fig. 3 of the gel data points with the B branch modes.

Apart from Ref. 4, most experiments²⁻⁶ have been done at fixed frequencies, to which Fig. 2 will be pertinent. They commonly show continuous increases in velocity as seen for the B branch of Fig. 2.

We have, thus far, no experimental evidence for the two A and B branches. Mechanical excitations, which work at low frequencies, have an inherent drawback of simultaneously exciting both. However, a possibly good clue to this is given by the marked difference of their velocities, which amounts to a factor two. If the excitation is done by only a few shots of pulses, then their responses in the A and B branches will be resolved by their different traveling times.

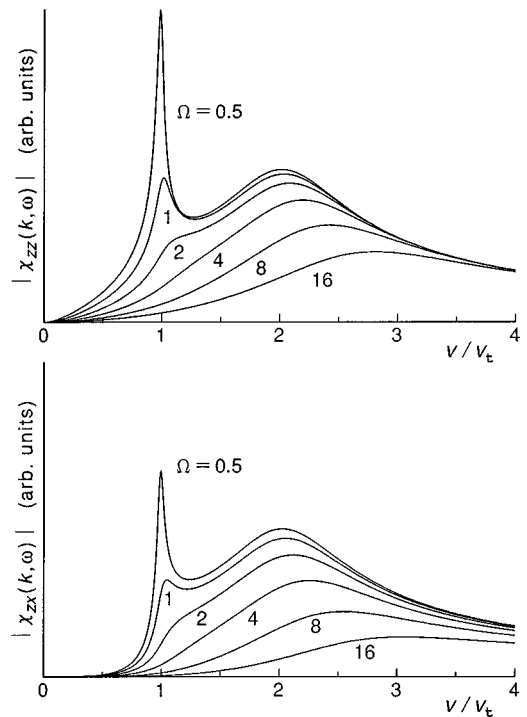


FIG. 4. Absolute values of the response functions $\chi_{zz}(k, \omega)$ and $\chi_{zx}(k, \omega)$ plotted against phase velocity v for the reduced viscosity $\eta^* = 1/8$ and the reduced frequency $\Omega = 0.5, 1, 2, 4, 8, \text{ and } 16$.

IV. CONCLUSION

Because of their coexisting liquid- and solid-like character, gels possess both surface tension and shear elasticity. Dispersion relation of surface waves on such materials consists of two disconnected branches. One of them corresponds to the elastic Rayleigh waves well-known in solids, which are truly localized on the surface. The other corresponds to the capillary waves arising from the surface tension. In the presence of nonvanishing elasticity, the latter waves are no longer localized on the surface. They decay, emitting transverse elastic waves into the bulk of the medium. The theoretical dispersion relation reproduces the experiment on gelatin considerably well, but no direct experimental evidence has yet been found on the existence of the two branches of different character. Experiments using pulse excitation are considered to be promising.

¹J. L. Harden, H. Pleiner, and P. A. Pincus, "Hydrodynamic surface modes on concentrated polymer solutions and gels," *J. Chem. Phys.* **94**, 5208–5221 (1991)

²R. B. Dorshow and L. A. Turkevich, "First observation of capillary to Rayleigh mode crossover on the surface of polymer solutions," *Phys. Rev. Lett.* **70**, 2439–2442 (1993).

³K. Motonaga, H. Okabe, K. Hara, and K. Matsushige, "Surface wave measurements during gelation process of tungstic acid," *Jpn. J. Appl. Phys., Part 1* **33**, 3514–3517 (1994).

⁴H. Kikuchi, K. Sakai, and K. Takagi, "Complex propagation of surface waves on soft gels," *Phys. Rev. B* **49**, 3061–3065 (1994).

⁵B. H. Cao, M. W. Kim, and H. Z. Cummins, "Surface waves on polymer solutions: Complete capillary wave–elastic wave crossover," *J. Chem. Phys.* **102**, 9375–9379 (1995).

⁶H. Takahashi and P.-K. Choi, "Sol–gel transition in gelatin observed with surface waves," *Jpn. J. Appl. Phys., Part 1* **35**, 2939–2943 (1996).

- ⁷A. I. Murdoch, "The propagation of surface waves in bodies with material boundaries," *J. Mech. Phys. Solids* **24**, 137–146 (1976).
- ⁸M. E. Gurtin and A. I. Murdoch, "Surface stress in solids," *Int. J. Solids Struct.* **14**, 431–440 (1978).
- ⁹J. Jäckle and K. Kawasaki, "Intrinsic roughness of glass surfaces," *J. Phys.: Condens. Matter* **7**, 4351–4355 (1995).
- ¹⁰T. C. Lim and G. W. Farnell, "Surface elastic waves in cubic crystals," *J. Appl. Phys.* **39**, 4319–4325 (1968).
- ¹¹T. C. Lim and G. W. Farnell, "Character of pseudo surface waves on anisotropic crystals," *J. Acoust. Soc. Am.* **45**, 845–851 (1969).
- ¹²G. W. Farnell, "Properties of Elastic Surface Waves," in *Physical Acoustics, Vol. VI*, edited by W. P. Mason and R. N. Thurston (Academic, New York, 1970), pp. 109–166.
- ¹³V. G. Levich, *Physicochemical Hydrodynamics* (Prentice-Hall, Englewood Cliffs, NJ, 1962), Chap. XI, Sec. 117.
- ¹⁴C. H. Wang and Q. R. Huang, "Hydrodynamic surface waves in concentrated polymer solutions in the presence of surface adsorption," *J. Chem. Phys.* **107**, 5898–5906 (1997).
- ¹⁵L. D. Landau and E. M. Lifshitz, *Theory of Elasticity* (Nauka, Moscow, 1965), 2nd ed., Secs. 22, 24.
- ¹⁶S. Kubota and H. Nakanishi, "Surface wave of viscoelastic material," *Prog. Theor. Phys. Suppl.* **126**, 359–362 (1997).

Perception of microphone noise in hearing instruments

Lidia W. Lee^{a)}

Department of Communicative Disorders, Northern Illinois University, DeKalb, Illinois 60115

Earl R. Geddes^{b)}

GedLee Associates, 43516 Scenic Lane, Northville, Michigan 48167

(Received 23 December 1997; accepted for publication 6 August 1998)

In a well-designed instrument the noise level is reduced until it is dominated by the front end noise. In a hearing instrument this is the microphone noise. This paper examines the perception of noise in a hearing instrument by both normal-hearing and hearing-impaired listeners. The noise levels are specified as input-referred values in one-third octave bands. Two sets of measurements, the just-objectionable level (JOL) and the just-audible level (JAL), were assessed in third octave bands from 250 to 5000 Hz. The data indicated that the use of a subjectively described acceptability of noise, JOL, is an unreliable measure due to a very large variability across listeners. It is recommended that mean values for the noise threshold level, the JAL, be used as a guide in the optimization of microphone noise design. © 1998 Acoustical Society of America.

[S0001-4966(98)05011-5]

PACS numbers: 43.38.Kb, 43.50.Ba [SLE]

INTRODUCTION

A major concern in hearing instruments is the issue of noise floor. Noise design, however, is a tradeoff among several variables, such as noise level, miniaturization, and cost. A design goal beyond the point of perceivable benefits to the user is unwarranted. In order to optimize any given design, it is important to understand the perception of noise among hearing-instrument users and its relevance to the design; hence the focus of this research. This research does not have direct clinical application and is intended to provide data that may facilitate an optimum noise design in microphones for hearing instruments.

I. BACKGROUND

Input-referred noise is a hypothetical noise which would be present at the input of a noiseless system to yield the noise level observed at the output. Input-referred noise is the preferred measure used in engineering design to describe total system noise, which consists primarily of the microphone and its associated preamplifier (Armstrong, 1995). It is common to measure microphone input-referred noise as a single, frequency-nonspecific A-weighted level in decibels. This number is acoustic in nature because the input to the microphone is an acoustic pressure. Using an acoustic value to represent noise which is in fact electrically generated may seem unusual but is quite convenient since these numbers can then be compared with common environmental noise found in the field. The A-weighted level was originally derived from a 40-phon equal loudness curve (Fletcher and Munson, 1933) measured on normal-hearing listeners and may be misleading when applied to hearing-impaired listeners for several reasons. First, hearing-impaired listeners do not have the same loudness perception as normal-hearing listeners. Second, the perception of noise at levels below the

40-phon level, as typically found in a hearing instrument, does not approximate the contour of an A-weighting scale (Geddes, 1995) for any listener. It has been shown in numerous other industries, where noise perception is an issue, that the A-weighted level value can be deceptive in terms of perception (Hellman and Zwicker, 1987). Therefore, two A-weighted measures should not be compared unless they have very similar spectral shapes, and this prerequisite is often violated. Consequently, the A-weighting curve may not be valid particularly when referenced to hearing-impaired listeners, and its basis for comparing different instruments is highly suspect when different spectrums are present.

In general, a single number indicator is not very useful to the microphone designer. The noise in a microphone is typically a complex function of frequency (Geddes, 1995). The purpose of this study is to estimate the tolerable noise level of hearing-instrument users as a function of frequency that are of interest to microphone design. These frequency values can then be used by a microphone designer to determine the expected subjective response of a user to a change in the spectrum of the microphone noise.

One-third octave bands of equivalent input noise have often been used in noise perception studies in the past (Dillion and Macrae, 1984; Macrae and Dillion, 1986, 1996). In a recent study, Macrae and Dillion (1996) reported the EINL (equivalent input noise level) recommended in one-third octave bands from 250–4000 Hz for high-gain instruments. Preves (1996) suggested that the use of one-third octave bands could be an alternative method of equivalent input noise (EIN) measures, which were subsequently recommended in ANSI S3.22 (1996).

These studies stress the importance of representing the distribution of noise across frequencies if an accurate assessment of noise levels is to be made. The use of a one-third octave band analysis is preferred for the following reasons. First, it is the standard method used in industrial and environmental noise measurements. Second, one-third octave

^{a)}Electronic mail: LLEE@niu.edu

^{b)}Electronic mail: GedLee@ibm.net

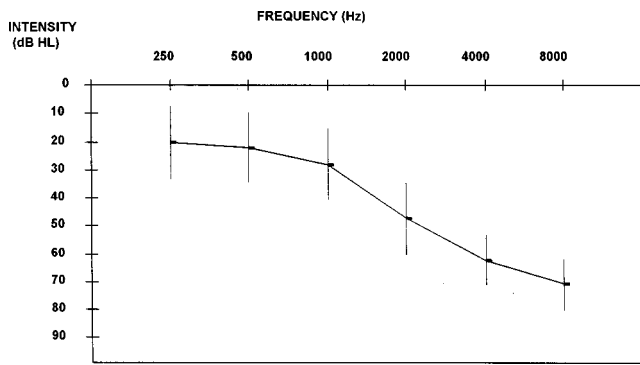


FIG. 1. Mean pure-tone air-conduction threshold and standard deviation for the hearing-impaired group ($N=15$).

bands approximate the critical bands in the frequency range under consideration; and critical band is the bandwidth where the loudness perception of a stimulus is independent of its frequency range. Therefore, it suggests that narrower analysis is not warranted. Given that loudness summation does not occur at low sensation levels (Scharf, 1959), the use of one-third octave bands will provide the detailed information crucial to the optimum design of microphone noise at the component level.

The current research investigated the perception of input-referred noise among normal-hearing and hearing-impaired listeners in one-third octave bands. Two noise-perception measures were evaluated, the just-audible level (JAL) and the just-objectionable level (JOL). The JAL and the JOL were assessed under quiet listening conditions among normal-hearing and hearing-impaired listeners.

II. EXPERIMENTAL METHODS

A. Subjects

Two groups of listeners were included in this study: 5 normal-hearing and 15 hearing-impaired adults. All normal-hearing listeners had pure-tone air-conduction thresholds <20 dB hearing level (HL) (ANSI, 1989) at octave frequencies from 250 to 8000 Hz. All hearing-impaired listeners had symmetric hearing loss, and were tested monaurally. Figure 1 displays the mean air-conduction threshold and standard deviation data of the test ear of the hearing-impaired group. All listeners underwent a 1 h session and were paid for their participation.

B. Instrumentation

A Grason-Stadler model 16 audiometer, coupled with the TDH-49p headphones, was used for the pure-tone air-conduction test. A Knowles Electronics Processor for Acoustic Research (KEPAR) was used in this experiment. All stimuli were generated and presented via KEPAR software and routed to the test ear. A pair of ER-3A insert earphones were used; one to deliver the stimuli to the test ear, and the other to occlude the non-test ear. KEPAR is a real-time simulator which includes operators such as waveform generators, filters, attenuators, amplifiers, etc. The use of KEPAR is preferred over the use of actual hearing instruments in this research because of its simplicity and flexibility

TABLE I. List of 14 one-third octave band stimuli.

Center frequency (Hz)	One-third octave band (Hz)
250	225–280
315	280–355
400	355–450
500	450–560
630	560–710
800	710–900
1000	900–1120
1250	1120–1400
1600	1400–1800
2000	1800–2240
2500	2240–2800
3150	2800–3550
4000	3550–4500
5000	4500–5600

in frequency shaping of the stimuli. Furthermore, it provided a direct measure of the objectives of this study. The internal noise of the KEPAR system is a relatively flat spectrum of 18 dB sound pressure level (SPL). This small but not insignificant system noise will be discussed later in Sec. III. A user interface box, with paddle-type level controls, was used by the listener to control the level of the stimuli.

C. Stimuli

Fourteen one-third octave narrow-band noise components (Table I), ranging from 250 to 5000 Hz, were used as stimuli. All stimuli were derived by band-pass filtering (fifth-order Butterworth) white noise. All stimuli were real-time, digitally generated from KEPAR at a sampling rate of 20 000 Hz. The stimuli were subsequently routed from KEPAR to an ER-3A earphone.

D. Procedure

Pure-tone air-conduction audiometric data were obtained at the beginning of the session. Each listener was tested in a sound-treated booth, and a paddle was used to adjust the intensity level. When seated in front of the user-interface box, each listener was instructed to adjust the paddle when a green signal light came on. The intensity of the signal would increase when the paddle was pushed forward, and vice versa. The initial starting level of each noise band was at the system's lowest permissible level, which was at 18 dB SPL. The listener was asked to adjust the level of the stimulus to the JAL, pause, and then proceed to obtain the JOL. The definition of JAL was given to the listener as "the level at which one could just hear the stimulus." The definition of JOL was given as "the level at which one would no longer consider evaluating the hearing instrument if that noise was to be continuously present in the instrument." This definition of JOL is similar to that used by Dillion and Macrae (1984) at National Acoustic Laboratories in Australia (NAL). Each listener was encouraged to use a bracketing approach, that is, to move the paddle up and down around each of these points to find the most representative setting. Two practice trials were given to each listener.

Each set consisted of 14 stimuli, and two measures (JAL and JOL) were made for each stimulus. Randomization was used within each set of stimuli. Each set was presented three times. A fourth repetition was given whenever there was a difference of 10 dB or greater between any of the two repetitions. Each listener underwent a total of 84 trials (14 stimuli \times 2 measures \times 3 repetitions).

Based on the audiometric data, the insertion gain values were prescribed using the National Acoustic Laboratories new procedure (NAL-R; Byrne and Dillion, 1986) and the POGO (prescription of gain/output; McCandless and Lyregaard, 1983) methods. These two prescriptive methods were the most popular methods used in hearing aid industry today. The gain values were interpolated into one-third octave bands. These values were used as the gain for calculating the input-referred level (input-referred; IR) values for the JAL (JAL-IR) and the JOL (JOL-IR). The JOL-IR for each listener was calculated by subtracting the prescribed gain value from the measured JOL value. Similarly, the JAL-IR for each listener was obtained by subtracting the prescribed gain value from the measured JAL value.

III. RESULTS

A. Reliability

1. Individual data

Test-retest reliability was examined within each listener. The raw data were scanned for inconsistent responses within repetitions for each listener. It was evident that a couple of the hearing-impaired listeners found the task difficult. This was indicated by their variable results across repetitions and across stimuli. Two listeners' data sets were removed from further analysis because of poor reliability. Most of the listeners could repeat their responses within a few decibels. Dillion and Macrae (1984) reported that six of the seven subjects had an average test-retest difference of 2.4 dB across trials and stimuli, while the seventh subject had a test-retest standard deviation of 11.5 dB. The next step was to scan and remove any listener's sets of trials if it had a standard deviation greater than 10 dB. About 20 sets were removed in this fashion.

It was noted that one normal-hearing listener rated JOL, on the average, about 25 dB above the other four listeners. When asked about this, this listener had interpreted "objectionable" as "annoying" or "uncomfortable." The authors decided that this interpretation was not consistent with the instructions, and this data set was subsequently removed from group analysis.

2. Group data

The experimental design also encompassed an internal validity check. The mean audiometric threshold data were compared to the mean JALs. The only difference between the two measures is that the octave band audiometric data were measured using pure-tone stimuli, and the JAL data were obtained using one-third octave noise bands. The third octave band estimates were interpolated from the octave band audiometric data. The HL values in dB under TDH headphones were converted to one-third octave band SPL

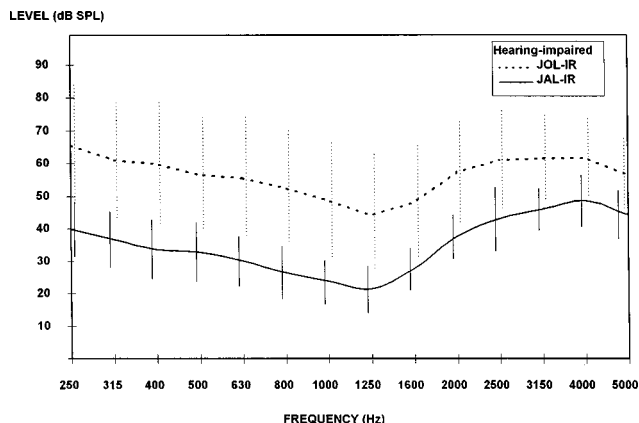


FIG. 2. Mean JAL-IR (solid line) and JOL-IR (dotted line) for the hearing-impaired group. The error bar represents one standard deviation about the mean.

values in dB under 6-cm^{-3} coupler (Bentler and Pavlovic, 1986). This comparison confirmed the validity of the JAL-IR among the hearing-impaired listeners. The 18 dB SPL noise floor in the KEPAR system prevented this same confirmation for the normal-hearing group.

B. Analysis

The data was imported into an Excel spreadsheet for reduction and analysis. For each individual, the repetitions across each stimulus for the JAL and the JOL were averaged and the standard deviation was taken. The prescribed gain values were then subtracted from averaged values to yield the input-referred values. As expected, both prescriptive methods yield very similar results. Consequently, only the NAL-R analyses will be discussed.

Analysis was performed separately for the hearing-impaired and the normal-hearing group. The prescription gains were not applied for the latter group. The mean JAL-IR and JOL-IR were obtained across listeners for each stimulus.

1. Hearing-impaired group

Figure 2 displays the mean and standard deviations for the JAL-IR (solid line) and the JOL-IR (dotted line) of the hearing-impaired group. The error bars signify one standard deviation about the mean. The mean standard deviation across the frequencies for the JAL-IR was ± 8 dB. Note that the upper limits here represent the level below which 83% of the listeners could not perceive the noise. Unlike the JAL-IR data, the JOL-IR data revealed a very large standard deviation (± 16 dB) across frequencies. Even though both measures required subjective judgement, the JOL measures reflected an unexpectedly high variability.

The response of one particular listener resulted in a large variance. The patient commented that it was unacceptable to have any noise in an instrument. Consequently, any audible noise becomes objectionable noise.

Figure 3 compares the JAL-IR among the hearing-impaired group with the JOL-IR values of the normal-hearing group. The results of Student's *t*-test indicates that

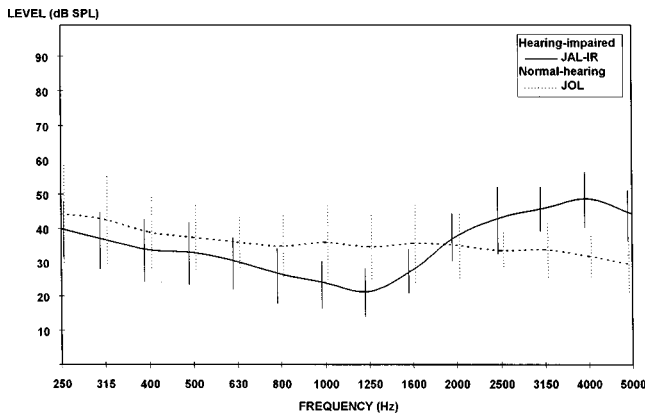


FIG. 3. Mean JAL-IR of the hearing-impaired group (solid line) and the JOL of the normal-hearing group (dotted line). The error bar represents one standard deviation about the mean.

none of the one-third octave bands revealed a significant separation of the two distributions at 95% confidence interval.

2. Normal-hearing group

Figure 4 displays the mean JAL and the mean JOL as a function of one-third octave band frequency for the normal-hearing listeners. The mean JAL is represented by the dotted line at 18 dB SPL which is the noise floor of the test system. The mean JOL is represented by the solid line, the error bars indicate one standard deviation about the mean. The mean standard deviation across all bands for the JOL is 10 dB. This is substantially less than the variability in the hearing-impaired group. The JOL for normal-hearing listeners may be reliable.

IV. DISCUSSION

The large variance in the hearing-impaired JOL data is notable. Either the task that these subjects were asked to perform was ambiguous or the subjects had different interpretations of the task. Clearly, our data and experiences lead to the conclusion that it was the latter. Thus, the JOL-IR is not likely to be a good indicator of what a hearing-instrument user is likely to object to. On the other hand, one could hardly argue with the use of the JAL-IR curve as the objectionable criteria, since the listener could hardly object to a noise level which they could not even perceive.

Figure 3 indicates that there is an expectation that a normal-hearing listener will object to a level of noise which may not be audible to a hearing-impaired listener. This is because there is no statistical difference between an objectionable level to a normal-hearing listener and a just-audible level to a hearing-impaired listener. This indicates that the designer must consider who is the target customer: the end user or the dispensing audiologist. Designing for the end user will clearly yield an objectionable level of noise for the normal-hearing dispenser while a design aimed at satisfying the dispenser will be over-designed (and thus not optimum) for the hearing-impaired customer. A clear set definition of the target market is thus required before the microphone de-

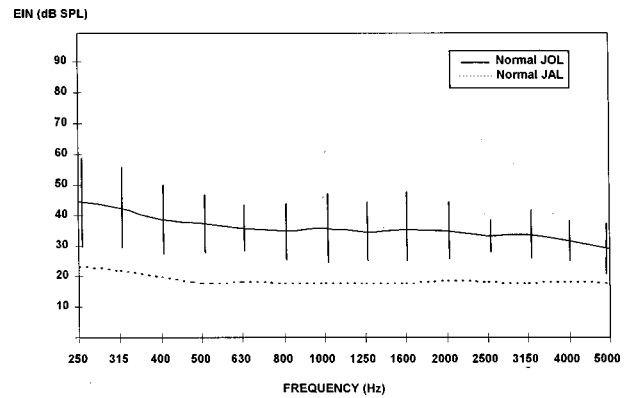


FIG. 4. Mean JAL (dotted line) and mean JOL (solid line) for the normal-hearing group. The error bar represents one standard deviation about the mean.

signer can effectively achieve an optimized design and it must be realized that optimizing for one set of customers will be suboptimal for the other.

V. SUMMARY

These analyses lead to the following general conclusions regarding noise perception among hearing-impaired listeners. First, the JAL-IR can be a reliable measure among hearing-impaired listeners. Second, the JOL-IR is probably an unreliable measure of noise perception among the hearing-impaired listeners because of its large variability across listeners. Finally, since the JOL-IR of the normal-hearing group is not significantly different from the JAL-IR of the hearing-impaired group, complaints in regards to the noise level of a hearing instrument by normal-hearing listeners should be taken with caution.

This investigation examined only listeners with high-frequency hearing loss and more data is needed to provide a better representation of the JAL-IR in reference to a particular hearing configuration.

- American National Standards Institute. (1989). Specification for Audiometers (ANSI S3.6-1989) (ANSI, New York).
- ANSI (1996). ANSI S3.22-1996, "Specification of Hearing Aid Characteristics" (American National Standards Institute, New York).
- Armstrong, S. (1995). "Finding and reducing the causes of circuit noise," *Hearing Res.* **2**(2), 9-11.
- Bentler, R., and Pavlovic, C. (1986). "Transfer functions and correction factors used in hearing aid evaluation and research," *Ear and Hearing* **10**(1), 58-63.
- Byrne, D., and Dillon, H. (1986). "The National Acoustic Laboratories' (NAL) new procedure for selecting the gain and frequency response of a hearing aid," *Ear and Hearing* **7**, 257-265.
- Dillon, H., and Macrae, J. (1984). *Derivation of Design Specifications for Hearing Aids*, National Acoustics Laboratories Report Number 102 (Australian Government Publishing Service, Canberra, Australia).
- Fletcher, H., and Munson, W. (1933). "Loudness: Its derivation, measurement, and calculation," *J. Acoust. Soc. Am.* **5**, 82-108.
- Geddes, E. (1995). *Noise Notes: the Noise Spectrum and the Customer's Perspective*. Knowles Electronics Bulletin Report (Knowles Electronics, Itasca, IL).

- Hellman, R., and Zwicker, E. (1987). "Why can a decrease in dB(A) produce an increase in loudness?" *J. Acoust. Soc. Am.* **82**(5), 1700–1705.
- Macrae, J., and Dillon, H. (1986). *Updated Performance Requirements for Hearing Aids*, National Acoustics Laboratories Report Number 109 (Australian Government Publishing Service, Canberra, Australia).
- Macrae, J., and Dillon, H. (1996). "An equivalent input noise level criterion for hearing aids," *Journal of Rehabilitation Research and Development* **33**(4), 355–362.
- McCandless, G., and Lyregaard, P. (1983). "Prescription of gain/output (POGO) for hearing aids," *Hearing Instruments* **1**, 12–16.
- Preves, D. (1996). "Standardizing Hearing Aid Measurement Parameters and Electroacoustic Performance Tests." in: *Hearing Aids: Standards, Options, and Limitations*, edited by McValente (Thieme Medical, New York), pp. 1–71.
- Scharf, B. (1959). "Critical bands and the loudness of complex sounds near threshold," *J. Acoust. Soc. Am.* **31**, 365–370.

Simplified models of transient elastic waves in finite axisymmetric layered media

Michael El-Raheb

The Dow Chemical Company, Midland, Michigan 48674

(Received 12 December 1997; accepted for publication 14 August 1998)

A simplified model, termed the flexure model, is used to analyze elastic waves in a weakly coupled periodic stack of disks bonded by thin layers of a weak polymer. Comparison with results of a more complete two-dimensional (2-D) axisymmetric model reveals the importance of axial stress and nonlinear distribution of radial displacement across the thickness. Also, in the 2-D model, it is possible to eliminate extensional modes through the thickness and inertia of the bond without compromising accuracy. In the 2-D model and for low radial wave numbers for a defined mode, its phase and group velocities can be approximated by the 1-D mass-spring model. They undergo discontinuities at the boundaries of extensional propagation zones. The flexure model reproduces the 2-D characteristic speeds but with slightly wider propagation zones and faster wavefronts. © 1998 Acoustical Society of America. [S0001-4966(98)04811-5]

PACS numbers: 43.40.Dx, 43.20.Jr [CBB]

INTRODUCTION

Wave propagation in layered media finds a wide variety of applications. Examples include geological oil exploration, shock isolation and crash management in automotive components, delamination in composites, and ballistic protection by passive stacked armor. Elastic waves in layered media have been studied extensively. Propagation of harmonic waves in one-dimensional (1-D) layered media by monochromatic sources can be found in Refs. 1–5. Extension of the theory to 3-D periodic media is treated in Refs. 6–10. Analysis of simple periodic structures adopting Floquet theory to propagation and attenuation zones is treated in Refs. 11–21. The methods used to analyze this problem ranged from purely numerical, like discretization and geometric optics, to purely analytical, like modal and transform techniques. In contrast with the extensive work reported on harmonic waves, relatively less attention was devoted to transient waves despite their importance in many practical applications. Reference 22 treats transient uniaxial waves in finite ordered and disordered bi-periodic stacks. The method relies on deriving transfer matrices in harmonic space relating state vectors at the interface between layers. Equilibrium of stress and continuity of displacement at each interface produces a system of tri-diagonal block matrices yielding modal characteristics of the stack. Transient response is found from an expansion of these modes. Simplified analytical models of the exact analysis in Ref. 22 are constructed in Ref. 23 yielding insights into the mechanics of uniaxial waves by reducing the parameters to those essential in controlling propagation.

Reference 24 extends the analysis in Ref. 22 to 2-D axisymmetric waves in a finite periodic stack of disks bonded by weak layers. In this work, radial dependence satisfies approximately the condition of “simple supports”, i.e., axial displacement and radial derivative of radial displacement vanish at the lateral boundary. This approximation yields a dispersion relation in radial wave number enabling the separation of axial and radial dependencies. Transfer ma-

trices relating displacement and surface traction at the two faces of a disk in the stack are then determined. The solution then proceeds along steps similar to the 1-D analysis. From Ref. 24, important results of analyzing 2-D propagation in a stack of N periodic sets are:

(1) Fixing the radial wave number m_r , there exists an infinite number of system resonant frequencies of the stack $\Omega_j(m_r)$, $j=1,2,3,\dots$, which appear as an ascending series of points in an Ω vs m_r plot. A line drawn through the lowest Ω_j ($j=1$) for each m_r forms the first “frequency line.” Similarly, a line drawn through the next higher Ω_j ($j=2$) forms the second frequency line, etc. In a plot of resonant frequency Ω versus radial wave number m_r satisfying the dispersion relation, Ω follows lines belonging to one of four groups:

- (a) a flexural group of N lines with dominant flexural motion of the disk;
- (b) an extensional group of N lines with dominant radial and axial motions of the disk;
- (c) a shear group of $N-1$ lines with dominant shear motion of the bond;
- (d) a second shear group of N lines with dominant shear motion of the disk.

Lines of one group may change type to another near coalescence although frequency lines never cross. Groups (c) and (d) above may be neglected without changing the response appreciably.

(2) For the excited disk, radial and circumferential stress ($\sigma_{rr}, \sigma_{\theta\theta}$) is the sum of an equivoluminal part from flexure, antisymmetric about the disk’s neutral plane, and a volumetric part from axial stress over the footprint of the excitation. The volumetric part is large close to the footprint and diminishes steeply elsewhere.

(3) For other disks in the stack, ($\sigma_{rr}, \sigma_{\theta\theta}$) mostly depend on flexure with an anti-symmetric distribution about the disk’s neutral plane. Unlike the linear distribution characteristic to plate flexure theory, termed the Kirchhoff assump-

tion, the 2-D distribution is not linear and deviation from linearity rises with disk thickness.

The purpose of this study is to understand the roles of axial stress, the Kirchhoff assumption in the Mindlin plate equations,²⁵ inertia of the bond producing motions in 1(c) above, and extensional motions of the disk producing motions in 1(b) above. Neglecting these motions yields a simpler and more efficient algorithm with prescribed error bounds, useful in preliminary parametric analysis of wave propagation in periodic stacks. Characteristic of wave propagation in periodic media is the existence of propagation and attenuation zones, PZ's and AZ's. Within each zone, propagation constants, and phase and group velocities control transmission and speeds of wavefront and energy. These will be called propagation quantities. They reveal in a more direct way the effects of various assumptions and approximations than can be seen from frequency spectra and histories of transient response.

A number of simplified models will be constructed, some based on the flexure model which allows only flexure of the disks, and others based on a more complete 2-D axisymmetric analysis. Comparing results from these models reveals the importance of their underlying approximations and the effects which they ignore.

Section I develops the analysis of a periodic stack adopting Mindlin's plate flexure theory. It treats the bond as an elastic spring resisting relative axial and shear motions from flexure of the adhering disks. Section II revises the analysis of the periodic stack adopting the 2-D Navier equations of elasto-dynamics. It differs from Ref. 24 in that displacements rather than potentials are chosen for dependent variables. In contrast to the flexure model which uses a body force, the 2-D model for the external excitation uses the static-dynamic superposition method which reduces substantially the number of eigenfunctions needed for convergence of transient response by modal analysis (see Ref. 26). Section III compares transient histories computed by the various models and explains how differences in response amplitude relate to the approximations in flexure analysis. Section IV compares propagation quantities (μ, c_p, c_g) by the various models and explains how they change with radial wave number where μ is propagation constant and c_p, c_g are phase and group velocities.

I. ANALYSIS BY PLATE FLEXURE THEORY

Assume that the stack is made of disks of radius a , bonded by thin elastic layers modeled as linear springs resisting relative axial motion along z and radial motion along r of the adhering disks. In cylindrical coordinates and axisymmetric motions, Mindlin's plate equations for axial displacement w and cross sectional rotation ψ are

$$\begin{aligned} \frac{D}{2} \left[(1-\nu)\nabla_1^2\psi + (1+\nu)\frac{\partial\varphi}{\partial r} \right] - \kappa Gh \left(\psi + \frac{\partial w}{\partial r} \right) \\ = \rho \frac{h^3}{12} \frac{\partial^2\psi}{\partial t^2} + \bar{M}_r, \end{aligned} \quad (1a)$$

$$\kappa Gh(\nabla_0^2 w + \varphi) + q_z = \rho h \frac{\partial^2 w}{\partial t^2}, \quad (1b)$$

$$\varphi = \nabla \cdot \boldsymbol{\psi} = \frac{\partial\psi}{\partial r} + \frac{\psi}{r},$$

$$\nabla_n^2 = \frac{\partial^2}{\partial r^2} + \frac{1}{r} \frac{\partial}{\partial r}, \quad (1c)$$

where r is radial coordinate, $D = Eh^3/12(1-\nu^2)$, κ is shear constant, ν is Poisson's ratio, (E, G) are moduli of elasticity and shear, h is thickness, ρ is density, t is time; q_z is transverse loading from external pressure or bond extension, and \bar{M}_r is moment from bond shear. Operating (1a) by $(\partial/\partial r + 1/r)$ converts ψ to φ , then eliminating φ from (1b) reduces (1a,b) to a single fourth order equation in w :

$$\begin{aligned} \left\{ \left[\nabla_0^2 - \frac{1}{c_0^2} \frac{\partial^2}{\partial t^2} \right] \left[\nabla_0^2 - \frac{1}{c_s^2} \frac{\partial^2}{\partial t^2} \right] + \frac{12}{c_s^2 h^2} \frac{\partial^2}{\partial t^2} \right\} w \\ = \frac{1}{D} \left[1 - \frac{Eh^2}{12\kappa G(1-\nu^2)} \nabla_0^2 + \frac{h^2}{12c_s^2} \frac{\partial^2}{\partial t^2} \right] q_z \\ + \frac{1}{D} \left(\frac{\partial \bar{M}_r}{\partial r} + \frac{\bar{M}_r}{r} \right), \\ c_0^2 = \frac{E}{\rho(1-\nu^2)}, \quad c_s^2 = \frac{\kappa G}{\rho}. \end{aligned} \quad (2)$$

Let “ i ” denote the order of a disk in the stack. For disks bonded by thin elastic layers, q_z applied to disk “ i ” is proportional to the bond axial stiffness and relative axial displacement of disks “ i ”, “ $i+1$,” and “ $i-1$ ”:

$$\begin{aligned} q_z = \frac{E_{b\epsilon}}{h_b} (2w_i - w_{i-1} - w_{i+1}), \\ E_{b\epsilon} = E_b \frac{(1-\nu_b)}{(1+\nu_b)(1-2\nu_b)}. \end{aligned} \quad (3)$$

$E_{b\epsilon}$ is the modulus of the bond in uniaxial strain, (E_b, ν_b) are bond modulus in uniaxial stress and Poisson ratio, and h_b is bond thickness. From Appendix A, \bar{M}_r is proportional to bond shear stiffness and relative radial motion of disks “ i ”, “ $i+1$,” and “ $i-1$ ”:

$$\bar{M}_r = \frac{G_b h^2}{h_b} (2\psi_i + \psi_{i-1} + \psi_{i+1}), \quad (4)$$

where G_b is bond shear modulus. Invoking (4) in (2) yields

$$\frac{\partial \bar{M}_r}{\partial r} + \frac{\bar{M}_r}{r} = \frac{G_b h^2}{h_b} (2\varphi_i + \varphi_{i+1} + \varphi_{i-1}); \quad (5a)$$

eliminating φ_i in (5a) using (1b) yields

$$\begin{aligned} \frac{\partial \bar{M}_r}{\partial r} + \frac{\bar{M}_r}{r} = - \frac{G_b h^2}{h_b} \left(\nabla_0^2 - \frac{1}{c_s^2} \frac{\partial^2}{\partial t^2} \right) \\ \times (2w_i + w_{i-1} + w_{i+1}). \end{aligned} \quad (5b)$$

Substituting (3) and (5b) in (2) produces the coupled flexural equation of the i th disk

$$\begin{aligned}
& \left\{ \left[\nabla_0^2 - \frac{1}{c_0^2} \frac{\partial^2}{\partial t^2} \right] \left[\nabla_0^2 - \frac{1}{c_s^2} \frac{\partial^2}{\partial t^2} \right] + \frac{12}{c_s^2 h^2} \frac{\partial^2}{\partial t^2} \right\} w_i \\
&= \frac{12E_b \epsilon (1 - \nu^2)}{E h_b h^3} \left[1 - \frac{E h^2}{12kG(1 - \nu^2)} \nabla_0^2 + \frac{h^2}{12c_s^2} \frac{\partial^2}{\partial t^2} \right] \\
& \quad \times (\hat{\delta}_i w_i - w_{i-1} - w_{i+1}) - \frac{3G_b(1 - \nu^2)}{E h_b h} \left[\nabla_0^2 - \frac{1}{c_s^2} \frac{\partial^2}{\partial t^2} \right] \\
& \quad \times (\hat{\delta}_i w_i + w_{i-1} + w_{i+1}), \tag{6} \\
\hat{\delta}_i &= 3 - \text{integer} \left(\frac{i+1}{i} + \frac{i}{N} \right).
\end{aligned}$$

The left-hand side of (6) accounts for flexural stiffness and inertia of the disk. On the right hand side, the first part accounts for axial coupling along z of neighboring disks by the bond, and the second part accounts for shear coupling along r by the bond.

It was shown in Ref. 24 that simple supports at the lateral boundary of the disk can be approximated by $\partial u(a)/\partial r \equiv 0$, which in plate theory reduces to $\partial \psi(a)/\partial r \equiv 0$. This boundary condition allows separation of variables and yields the dispersion relation

$$J_0''(\gamma_r) = 0, \quad \gamma_r = k_r a, \tag{7}$$

where k_r is the radial wave number. Assuming harmonic motions in time with frequency ω , a solution to (6) satisfying (7) has the form:

$$\begin{aligned}
w_i(r, t) &= w_{0i} J_0(k_r r) e^{i\omega t}, \\
\psi_i(r, t) &= \left(-\gamma_r^2 + \frac{\omega^2 a^2}{c_s^2} \right) \frac{w_{0i}}{\gamma_r a} J_1(k_r r) e^{i\omega t}. \tag{8}
\end{aligned}$$

Substituting (8) in (1) for all disks in the stack determines a banded system of simultaneous equations with width 3:

$$\begin{aligned}
\mathbf{A} \mathbf{w}_0 &= \mathbf{0}, \\
A_{ii} &= (-\gamma_r^2 + \gamma_0^2)(-\gamma_r^2 + \gamma_s^2) - \gamma_0^2 \frac{a^2}{h_1^2} + \hat{\delta}_i B_a + \hat{\delta}_i B_s, \\
A_{i, i+1} &= A_{i, i-1} = -B_a + B_s, \\
B_a &= \frac{12E_b \epsilon (1 - \nu^2) a^4}{E h_b h_3} \left[1 + \gamma_r^2 \frac{h_2^2}{a^2} - \gamma_s^2 \frac{h_1^2}{a^2} \right], \tag{9} \\
B_s &= \frac{3G_b(1 - \nu^2) a^2}{E h_b h} (-\gamma_r^2 + \gamma_s^2), \\
h_1^2 &= \frac{h^2}{12}, \quad h_2^2 = \frac{h^2}{6(1 - \nu)\kappa}, \quad \gamma_0 = \frac{\omega a}{c_0}, \\
\gamma_s &= \frac{\omega a}{c_s}.
\end{aligned}$$

Solution of the implicit eigenproblem (9) yields eigenfrequencies ω_{fm} and eigenfunctions Φ_{fm} of the stack for flexural and shear motions. Since dispersion relation (7) does not satisfy natural boundary conditions, the set $\{\Phi_{fm}\}$ is not orthogonal.

TABLE I. Properties of basic stack.

	E (lb/in. ²)	ρ (lb s ² /in. ⁴)	ν	h (in.)
Disk	4.64×10^7	3.04×10^{-4}	0.24	0.5
Bond	2×10^4	10^{-4}	0.48	0.01

Consider a stack of five disks with radius $a = 3$ in. bonded by four weak layers with the properties given in Table I. This will be termed the ‘‘basic stack.’’ Let N be the number of disks in the periodic stack. Fixing the number of radial half-waves, $m_r = \gamma_r / \pi$, there exists a group of N low resonant frequency lines corresponding to flexural modes and a group of N high resonant frequency lines corresponding to disk shear modes. In the flexural group, the first mode is anti-symmetric about the stack’s plane of bilateral symmetry, i.e., all deformed disks are identical in shape and magnitude [see Fig. 1(a) and (f)]. Its frequency is slightly higher than that of the lone disk because of shear stiffness from the bond. The second mode is symmetric about the plane of bilateral symmetry, i.e., deformed disks on one side of this plane are mirror images to those on the other side [see Fig. 1(b) and (j)]. More complex coupled modes follow with shapes alternating between symmetric and anti-symmetric [see Fig. 1(c), (d), (e), and 1(h), (i), (j)]. For each m_r , the set of N flexural modes resembles the set of $(N - 1)$ modes in the first propagation zone PZ1 of a 1-D free stack.²² In 2-D, N distinct coupled motions are possible. In 1-D, only $(N - 1)$ possible motions have nonzero frequency, the N th being a rigid body translation of the 1-D stack.

At this point it is possible to create another approximate model by neglecting bond inertia in the flexure model above. Comparing the resulting frequency spectra will reveal its effect. Figure 2(a) plots eigenfrequency Ω (Hz) of the flexural group versus m_r for the stack with massless bond and properties in Table I. The gap between Ω lines narrows smoothly with m_r . Figure 2(b) plots Ω of the disk’s flexural and shear groups versus m_r including bond inertia. Close to the shear frequency of the bond, the lowest $(N - 1)$ lines of the disk shear group change type and follow the bond shear line until coalescence with the flexural group. These lines change type again near coalescence with the flexural group, while $(N - 1)$ lines of the flexural group change type to become the bond shear group. This coalescence without crossing of frequency lines manifests uniqueness of the solution imposed by linearity of the problem. The gap between frequency lines of the flexural group widens after coalescence with the shear group because of the drop in bond mobility caused by a change in phase after crossing the bond shear resonance.

Transient response to external excitation is found by modal decomposition of the axial displacement vector \mathbf{w}

$$\mathbf{w}(r, z, t) = \sum_{m=1}^M a_m(t) \Phi_{fm}(r, z). \tag{10}$$

Substituting (10) in (6), multiplying each side by $\Phi_{fm}(r, z)$, and integrating over the stack’s volume yields

$$\mathbf{M}(\ddot{\mathbf{a}} + \omega^2 \mathbf{a}) = \mathbf{F} f_0(t), \tag{11a}$$

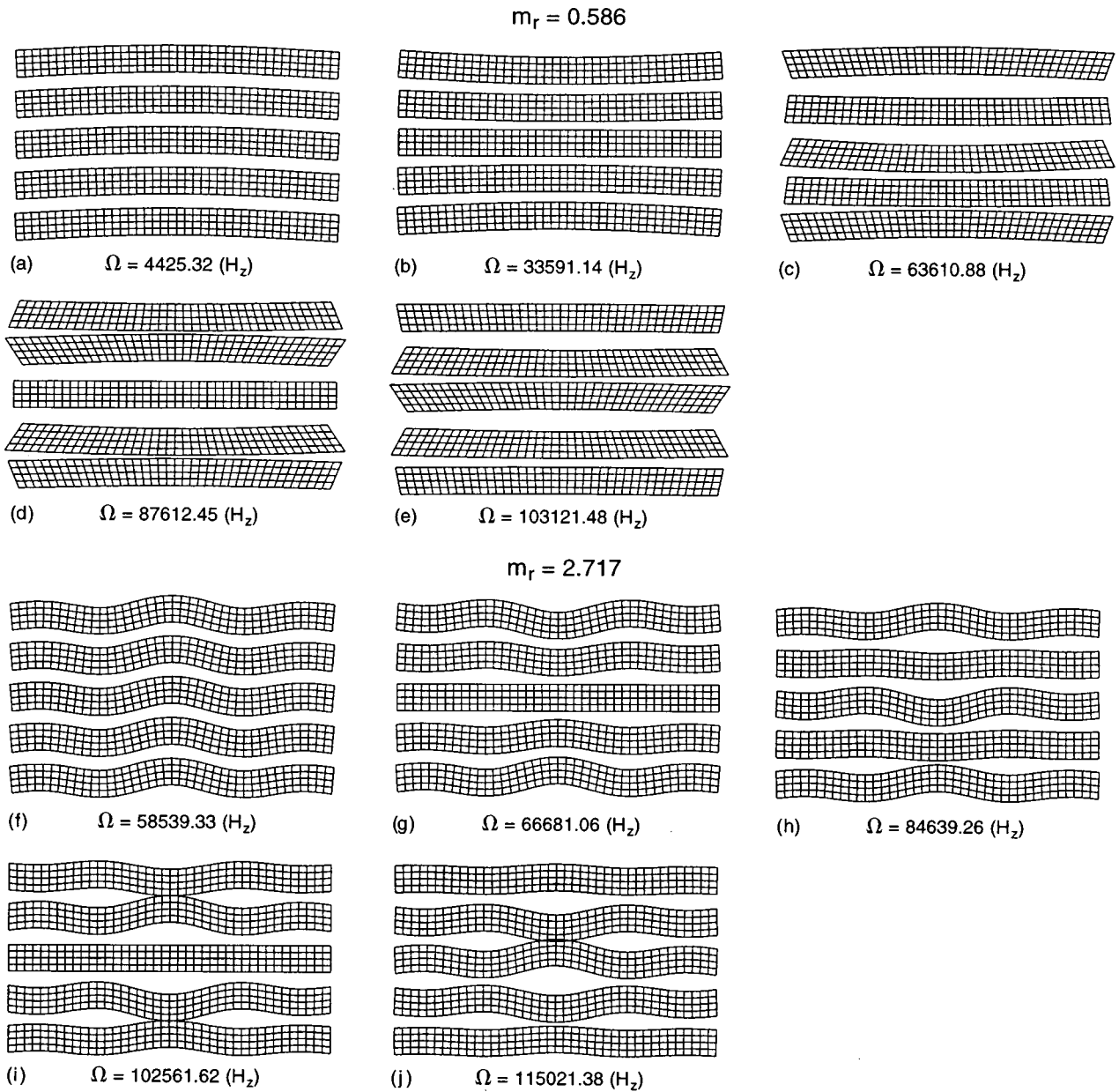


FIG. 1. Eigenmodes of the stack of five periodic sets (flexure model): (a)–(e) $m_r=0.586$; (f)–(j) $m_r=2.717$.

where $(\dot{})$ is time derivative, \mathbf{M} is the full matrix of generalized mass, and \mathbf{F} is the vector of generalized force:

$$M_{mn} = \langle m | \rho | n \rangle, \quad F_n = \langle n | p_0 \rangle, \quad (11b)$$

where $p(r, t) = p_0(r) f_0(t)$ is the external pressure excitation acting on the stack. Inverting \mathbf{M} in (11a) yields uncoupled equations in the generalized coordinates $\mathbf{a}(t)$:

$$\ddot{a}_m(t) + \omega_m^2 a(t) = P_m f_0(t), \quad \mathbf{P} = \mathbf{M}^{-1} \mathbf{F}. \quad (12)$$

A solution to (12) follows in terms of Duhamel's integral:

$$a_m(t) = -\frac{P_m}{\omega_m} \int_0^t f_0(\tau) \sin \omega_m(t - \tau) d\tau. \quad (13)$$

II. ANALYSIS BY 2-D AXISYMMETRIC THEORY

For axisymmetric motions of a disk, the Navier equations of elasto-dynamics in cylindrical coordinates are:

$$(\lambda + 2\mu) \nabla_1^2 u + \mu \frac{\partial^2 u}{\partial z^2} + (\lambda + \mu) \frac{\partial^2 w}{\partial r \partial z} = \rho \frac{\partial^2 u}{\partial t^2}, \quad (14)$$

$$(\lambda + \mu) \frac{\partial}{\partial z} \left(\frac{\partial u}{\partial r} + \frac{u}{r} \right) + \mu \nabla_0^2 w + (\lambda + 2\mu) \frac{\partial^2 w}{\partial z^2} = \rho \frac{\partial^2 w}{\partial t^2},$$

$$\nabla_n^2 \equiv \frac{\partial^2}{\partial r^2} + \frac{1}{r} \frac{\partial}{\partial r} - \frac{n^2}{r^2}, \quad (15)$$

where (u, w) are radial and axial displacements, and (λ, μ) are Lamé's constants. Assuming harmonic motions in time with frequency ω , separation of variables yields:

$$\begin{aligned} u(r, z, t) &= J_1(k, r) \bar{u}(z) e^{i\omega t}, \\ w(r, z, t) &= J_0(k, r) \bar{w}(z) e^{i\omega t}. \end{aligned} \quad (16)$$

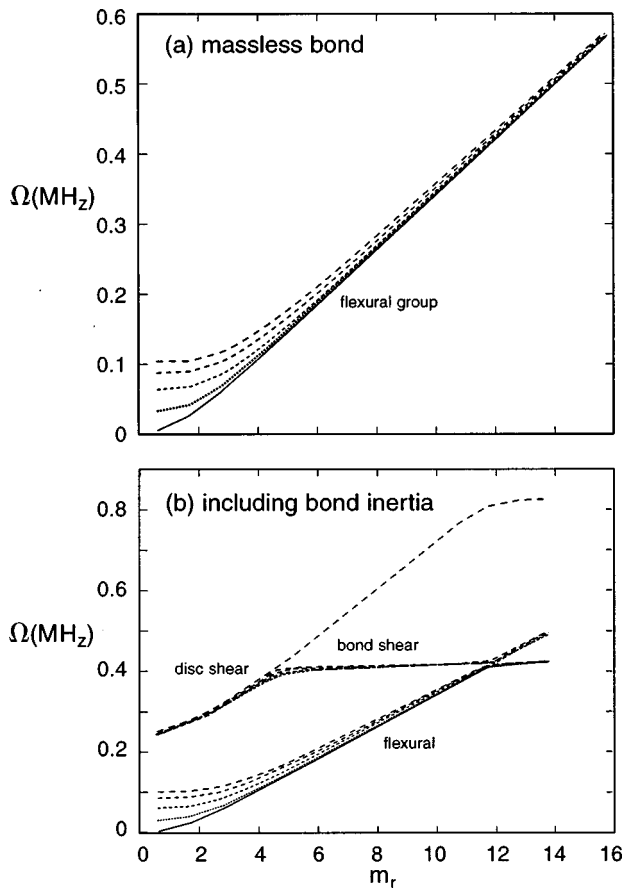


FIG. 2. Spectra of stack resonant frequency Ω vs m_r (flexure model): (a) massless bond; (b) including bond inertia.

The radial function approximates simple supports at $r=a$ [see Eq. (7)]:

$$\frac{\partial u(a, z, t)}{\partial r} = 0 \quad (17a)$$

which defines the radial wave number k_r as

$$J_0''(k_r a) = 0. \quad (17b)$$

Substituting (16) in (14) and (15) yields

$$\begin{aligned} \frac{\mu}{\lambda + 2\mu} \frac{\partial^2 \bar{u}}{\partial z^2} + \left(\frac{\rho \omega^2}{\lambda + 2\mu} - k_r^2 \right) \bar{u} - \frac{\lambda + \mu}{\lambda + 2\mu} k_r \frac{\partial \bar{w}}{\partial z} &= 0, \\ \frac{\lambda + \mu}{\mu} k_r \frac{\partial \bar{u}}{\partial z} + \frac{\lambda + 2\mu}{\mu} \frac{\partial^2 \bar{w}}{\partial z^2} + \left(\frac{\rho \omega^2}{\mu} - k_r^2 \right) \bar{w} &= 0. \end{aligned} \quad (18)$$

Equations (18) admit solutions in the form:

$$\bar{u}(z) = C e^{\alpha z}, \quad \bar{w}(z) = D e^{\alpha z}, \quad (19)$$

where C, D are constant coefficients. Substituting (19) in (18) produces the axial dispersion relation in α :

$$\begin{bmatrix} a_{11} & a_{12} \\ a_{21} & a_{22} \end{bmatrix} \begin{Bmatrix} C \\ D \end{Bmatrix} = 0, \quad (20)$$

$$C = - \left(\frac{a_{12}}{a_{11}} \right) D, \quad (20a)$$

$$a_{11} = \frac{\mu}{\lambda + 2\mu} \alpha^2 + \left(\frac{\rho \omega^2}{\lambda + 2\mu} - k_r^2 \right), \quad (20b)$$

$$a_{12} = - \frac{\lambda + \mu}{\lambda + 2\mu} k_r \alpha; \quad a_{21} = \frac{\lambda + \mu}{\mu} k_r \alpha,$$

$$a_{22} = \frac{\lambda + 2\mu}{\mu} \alpha^2 + \left(\frac{\rho \omega^2}{\mu} - k_r^2 \right).$$

Equation (20) is quadratic in α^2 yielding four complex values α_j , $j=1,4$. From (19),

$$\bar{u}(z) = \sum_{j=1}^4 C_j e^{\alpha_j z} = - \sum_{j=1}^4 \left(\frac{a_{12}}{a_{11}} \right)_j D_j e^{\alpha_j z}, \quad (21)$$

$$\bar{w}(z) = \sum_{j=1}^4 D_j e^{\alpha_j z}.$$

The constitutive equations are

$$\bar{\sigma}_{zz} = \lambda k_r \bar{u} + (\lambda + 2\mu) \frac{\partial \bar{w}}{\partial z}, \quad \bar{\tau}_{rz} = \mu \left(\frac{\partial \bar{u}}{\partial z} - k_r \bar{w} \right). \quad (22)$$

Define the state vector \mathbf{S} as

$$\mathbf{S} = \{\mathbf{f}, \mathbf{g}\}^T, \quad (23a)$$

where $\mathbf{f} = \{\bar{\sigma}_{zz}, \bar{\tau}_{rz}\}^T$ and $\mathbf{g} = \{\bar{u}, \bar{w}\}^T$ are traction and displacement vectors over a face of the disk. Substituting (21) in (22) relates the state vector $\mathbf{S} = \{\bar{\sigma}_{zz}, \bar{\tau}_{rz}, \bar{u}, \bar{w}\}^T$ to coefficients $\mathbf{D} = \{D_j\}^T$:

$$\mathbf{S}(z) = \mathbf{B}(z) \mathbf{D}, \quad (23b)$$

$$B_{1,j}(z) = \{\lambda k_r C_j + (\lambda + 2\mu) \alpha_j D_j\} e^{\alpha_j z},$$

$$B_{2,j}(z) = (\mu \alpha_j C_j - k_r) e^{\alpha_j z}, \quad (23c)$$

$$B_{3,j}(z) = C_j e^{\alpha_j z},$$

$$B_{4,j}(z) = D_j e^{\alpha_j z},$$

where in (23c) C_j is related to D_j by (20a). Evaluating (23b) at $z=0$ and $z=h$, then eliminating \mathbf{D} , produces the transfer matrix \mathbf{T} relating state vectors on the two faces of a disk:

$$\mathbf{S}(h) = \mathbf{T} \mathbf{S}(0), \quad \mathbf{T} = \mathbf{B}(h) \mathbf{B}^{-1}(0). \quad (24)$$

\mathbf{T} is expressed in terms of four submatrices t_{kl} as

$$\mathbf{T} = \begin{bmatrix} \mathbf{t}_{11} & \mathbf{t}_{12} \\ \mathbf{t}_{21} & \mathbf{t}_{22} \end{bmatrix}. \quad (25)$$

For a bi-periodic stack of N repeated sets, where each set except the last is made of two layers (one disk and one bond) continuity of \mathbf{S} at the interfaces of layers produces the global tri-diagonal block matrix \mathbf{M}_G :

$$\mathbf{M}_G \mathbf{S}_G = \mathbf{0}, \quad (26a)$$

where \mathbf{S}_G is the ensemble of the \mathbf{S}_k at all interfaces and the two boundaries of the stack:

$r=0, r_p, 2r_p,$ and $4r_p$. In contrast, shear stress is computed along the neutral plane ($z=h/2$) of each disk and at the same four radial stations. Plots of histories of displacements (u, w), and stress ($\sigma_{zz}, \sigma_{rr}, \sigma_{rz}$) are presented for each disk in columnar form. The column at left results from a flexure model, while the column at right results from a 2-D model. In both models, bond inertia is neglected and 16 radial wave numbers are considered in the radial expansion. In the flexure model, only the flexural group shown in Fig. 2(a) is included. In the 2-D model, the flexural and first extensional groups shown in Fig. 3 are included.

Figure 4 compares histories on the first disk subjected to the forcing pulse. Flexure analysis underestimates displacements and stresses by 15%. For $r \leq r_p$, σ_{rr} and u are lower by 50% and 30% respectively, while the difference drops to 15% for $r > r_p$. In 2-D analysis, σ_{rr} and $\sigma_{\theta\theta}$ are made of two parts: an equivoluminal part from flexure anti-symmetric about the disk's neutral plane and a volumetric part from axial stress. The latter is large under the footprint and diminishes rapidly remote from it. It is this part in 2-D which accounts for the larger σ_{rr} and u when $r \leq r_p$. For $r > r_p$, the difference in the two models is caused by the Kirchhoff assumption in plate theory.

Figure 5 compares histories on the second disk. In contrast to the first disk, flexure analysis overestimates displacements by 15% and stresses by 25%. This can be explained as follows. In the first disk, the volumetric part in 2-D from axial stress raises strain energy. Since total instantaneous strain energy of the stack is conserved, strain energy of succeeding disks along the stack must be reduced. Also, the shape of the τ_{rz} histories from the two analyses differ substantially before reflexion from the lateral boundary [compare Fig. 5(e₁) to (e₂)] yet the relative magnitudes are still within 25%.

Figure 6 compares histories on the third disk. As with the second disk, flexure analysis overestimates all variables by 15%. The difference in τ_{rz} histories grows even more although magnitude drops, diminishing its importance in response. The drop in τ_{rz} is caused by radial dispersion of the pulse as it propagates across the stack.

The same observations apply to histories on the fourth disk (not shown), where the difference between the two analyses drops to 10%. However, this trend is broken for the fifth disk where the difference in magnitude depends on the variable (see Fig. 7). After 60 μs , σ_{rr} traveling at the shear speed reaches the axis of the stack after reflecting from the lateral boundary. After dropping to a minimum on the second disk, σ_{rr} rises again and peaks on the last disk.

Figure 8 illustrates instantaneous snapshots of the deformed stack at intervals of 5 μs for the duration of 60 μs . At $t=5 \mu s$ [Fig. 8(a)], the pulse applied to the lower disk produces local deformation confined by the wave front. At $t=10 \mu s$ [Fig. 8(b)], the pulse spreads radially along the first disk, and propagates axially reaching the second disk. At $t=20 \mu s$ [Fig. 8(d)], the pulse reaches the back of the stack. Note that disk curvature diminishes along the stack, producing lower flexural stress, consistent with the inverted conoid of fracture observed experimentally. At $t=25 \mu s$ [Fig. 8(e)], the forcing pulse elapses, reducing local deformation of the

forced disk over the footprint. At $t=30 \mu s$ [Fig. 8(f)], flexural waves in the first two disks reach the lateral boundary. At $t=50 \mu s$ [Fig. 8(j)], dispersion has caused all disks to move in unison with almost equal amplitude and shape, which is not clearly described by specific waves propagating with defined wave fronts. At $t=60 \mu s$ [Fig. 8(l)], reflections from the lateral boundary reach the axis raising amplitude and flexural stress of the last disk, as confirmed in Fig. 7(d₂) by the negative peak of σ_{rr} at 60 μs . This is the second highest intensity of σ_{rr} next to that on the excited face of the first disk. This tensile stress on the bottom face of the stack causes "spallation."

IV. RESULTS OF PROPAGATION QUANTITIES

This section derives propagation quantities (μ, c_p, c_g) of the bi-periodic stack adopting flexure and 2-D models. Since radial wave number γ_r is prescribed by a dispersion relation that satisfies approximate simple supports at the lateral boundaries [see Eq. (7)] propagation quantities are computed for specific values of γ_r . In this way, propagation relates to frequency groups in Figs. 2 and 3.

In the flexural model, Floquet theory requires that

$$w_i = e^\mu w_{i-1}, \quad w_{i+1} = e^\mu w_i, \quad (33)$$

where w_i, w_{i-1} , and w_{i+1} are axial displacement of disks $i, i-1$, and $i+1$, respectively, and μ is propagation constant. Substituting (33) in the i th row of Eq. (9) yields

$$A_{ii} + A_{i,i+1}(e^\mu + e^{-\mu}) = 0. \quad (34a)$$

Solving the quadratic in (34a) for e^μ gives

$$e^\mu = (-A_{ii} \pm \sqrt{A_{ii}^2 - 4A_{i,i+1}}) / (2A_{i,i+1}) \equiv \lambda_{1,2},$$

$$\Rightarrow \mu = \log(\lambda). \quad (34b)$$

Since μ is related to axial wave number k_z by

$$k_z = \mu / h_s, \quad (35a)$$

where h_s is set thickness ($h_s = h + h_b$), then phase and group velocities c_p and c_g follow:

$$c_p = \frac{\omega h_s}{\mu}, \quad c_g = h_s \frac{\partial \omega}{\partial \mu}. \quad (35b)$$

In the 2-D model, the transfer matrix \mathbf{T} in Eq. (25) relates state vectors at two faces of a layer:

$$\mathbf{S}_{i+1} = \mathbf{T} \mathbf{S}_i,$$

$$\mathbf{S}_{i+2} = \mathbf{T}_b \mathbf{S}_{i+1}, \quad (36a)$$

where \mathbf{T} and \mathbf{T}_b correspond to disk and bond in the bi-periodic set. \mathbf{T}_s of a set then follows from (36a)

$$\mathbf{T}_s = \mathbf{T}_b \mathbf{T}. \quad (36b)$$

Floquet theory requires that

$$\mathbf{S}_{i+2} = e^\mu \mathbf{I} \mathbf{S}_i = \mathbf{T}_s \mathbf{S}_i, \quad (37a)$$

$$\Rightarrow |\mathbf{T}_s - \mathbf{I} e^\mu| = 0. \quad (37b)$$

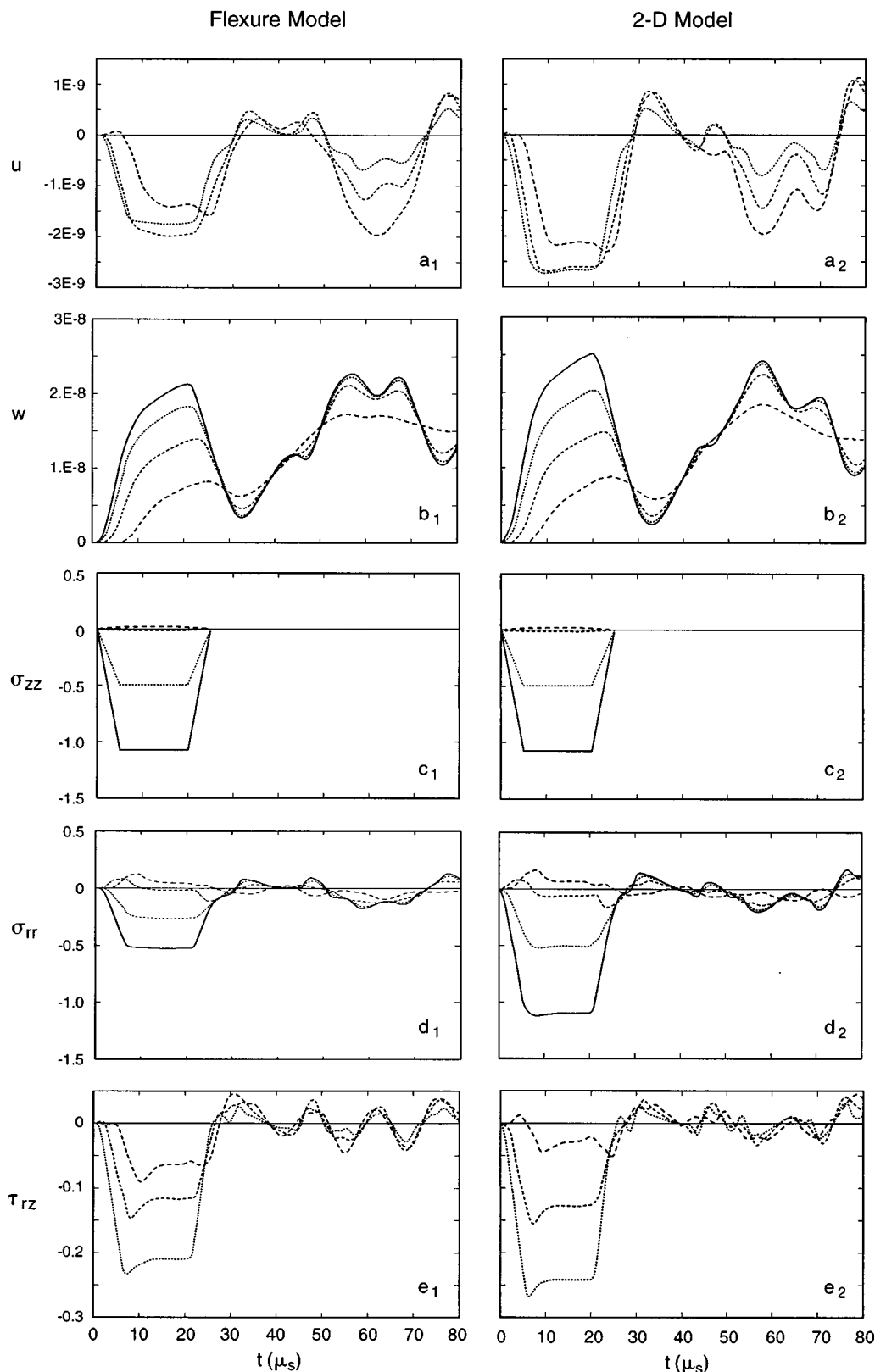


FIG. 4. Comparison of histories from the two models for disk 1: — $r=0$; \cdots $r=r_p$; $-\cdot-\cdot-$ $r=2r_p$; $-\cdot-\cdot-$ $r=4r_p$.

Propagation constants are related to the eigenvalues of \mathbf{T}_s yielding (c_p, c_g) by applying (35b).

Results from the 2-D model are presented first, while those of the flexure model are presented later because it is more approximate and the disappearance of any features can be readily observed. For direct comparison with the 1-D

results in Ref. 23, $\mu = (\mu_R, \mu_I)$ is normalized by π , and c_p and c_g are normalized by c_0 where

$$c_0 = h_s \left[\frac{E_{b\epsilon}}{\rho h h_b (1 + \tilde{\tau}/\tilde{z})(1 + 1/(\tilde{z}\tilde{\tau}))} \right]^{1/2},$$

$$\tilde{z} = \rho c / \rho_b c_{b\epsilon}, \quad \tilde{\tau} = h_b c / h c_{b\epsilon}, \quad c_{b\epsilon} = \sqrt{E_{b\epsilon} / \rho_b}. \quad (38a)$$

$(\tilde{z}, \tilde{\tau})$ are impedance and travel time ratios in the bi-periodic

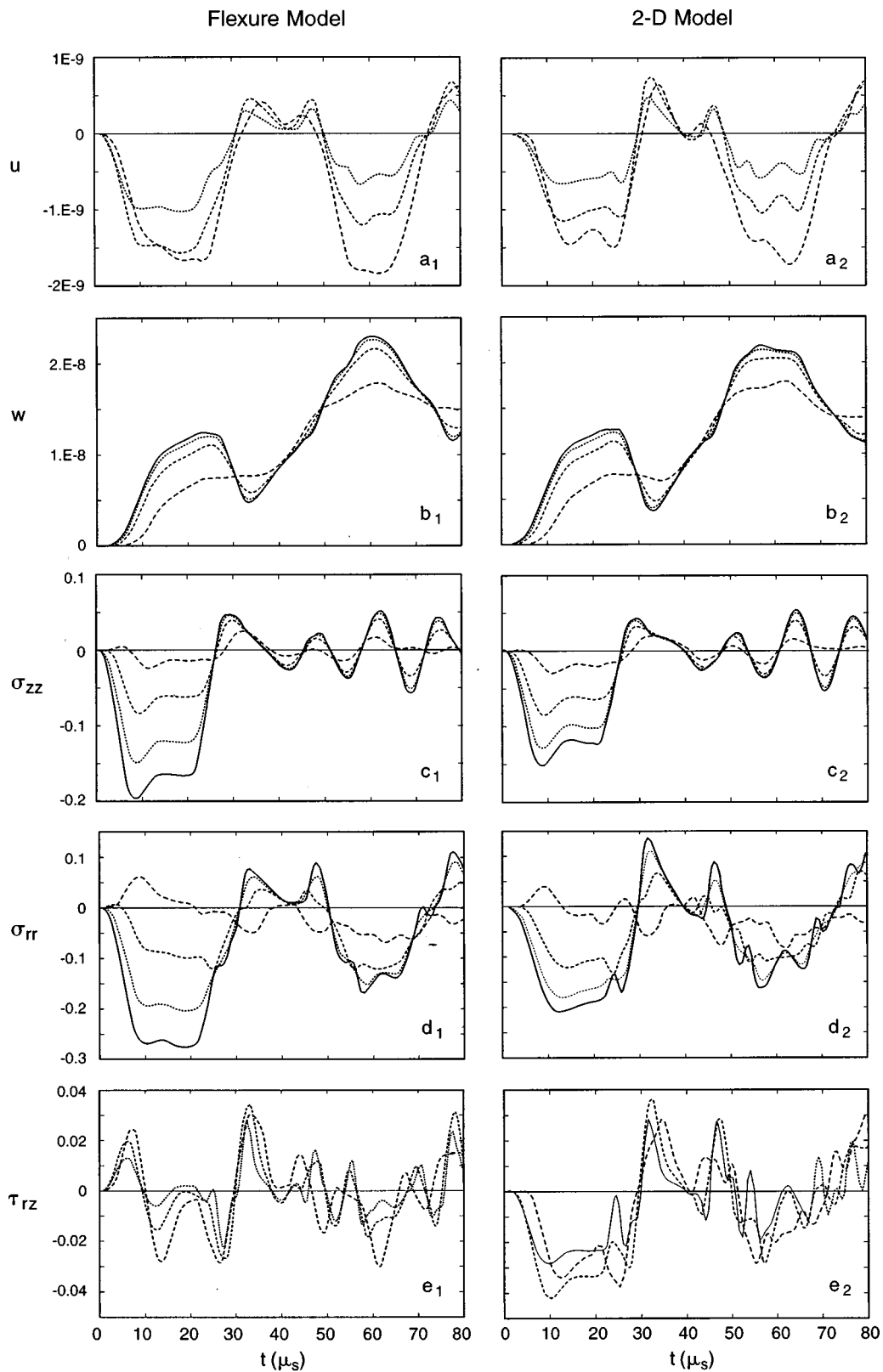


FIG. 5. Comparison of histories from the two models for disk 2: — $r=0$; \cdots $r=r_p$; $-\cdot-\cdot-$ $r=2r_p$; $-\cdot-\cdot-$ $r=4r_p$.

set. For some number of radial half-waves $m_r = \gamma_r / \pi$, propagation quantities ($\mu_R / \pi, \mu_I / \pi, c_p / c_0, c_g / c_0$) are plotted against normalized frequency $\omega h_s / c_0$, where (μ_R, μ_I) are real and imaginary parts of μ . Note that

$$\omega_e = c_0 / h_s \quad (38b)$$

is the resonant frequency of the set when the disk acts as arigid mass and the bond as an elastic spring (see Ref. 23 and Appendix A). To reproduce 1-D results in Ref. 23, propagation quantities are computed for $m_r = 0$, as shown in Fig. 9. The solid lines in c_p / c_0 and c_g / c_0 agree closely with those of 1-D shown in Fig. 5(a) of Ref. 23.

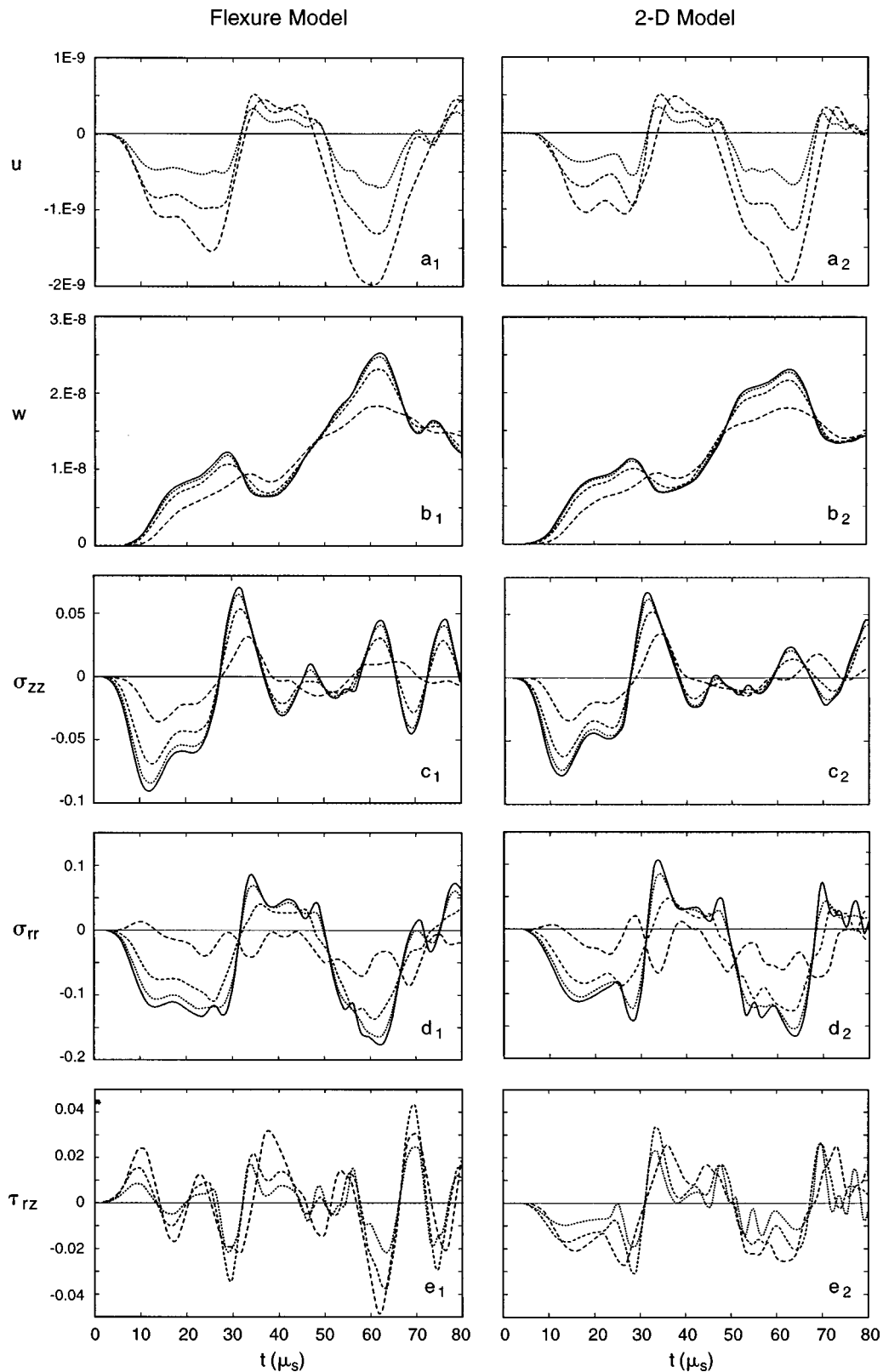


FIG. 6. Comparison of histories from the two models for disk 3: — $r=0$; \cdots $r=r_p$; - - - $r=2r_p$; - · - $r=4r_p$.

For the first radial mode with $\frac{1}{4}$ wave along r , $m_r = 0.59$, propagation quantities of the flexural group shown as solid lines in Fig. 10 are not segregated from those of the first extensional group shown as dashed lines, as also noted in Fig. 3. Lines of (c_p, c_g) undergo discontinuities marking the start of PZ2 and the end of PZ1. Ignoring the singular

behavior of c_p and the sharp drop of c_g at the boundaries of PZ1 and PZ2, their average lines follow approximately the same shape and magnitude as the $m_r=0$ lines in Fig. 9. The fact that the propagation quantities for the low m_r are similar to those for $m_r=0$ supports a valuable simplification. The $m_r=0$ case is the same as a 1-D model of periodic masses

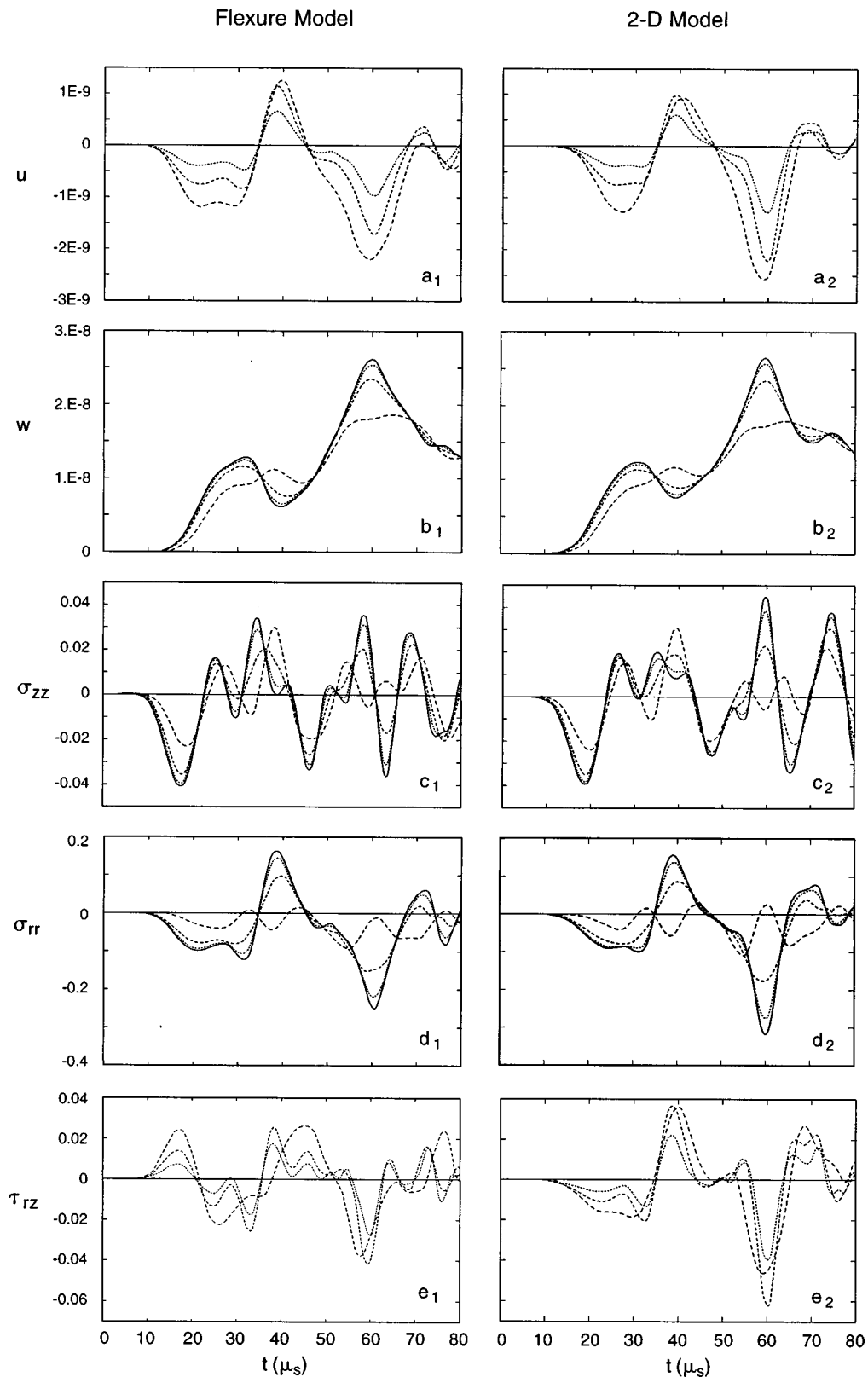


FIG. 7. Comparison of histories from the two models for disk 5: — $r=0$; \cdots $r=r_p$; $\cdots\cdots$ $r=2r_p$; $-\cdot-\cdot-$ $r=4r_p$.

and springs described in Ref. 23 where propagation quantities are extensively characterized. This implies that all conclusions drawn from the 1-D model can be carried over to a good approximation to both flexure and 2-D models.

As m_r increases, PZ1 becomes narrow, reproducing the

width of the flexural frequency group in Fig. 3 (see Figs. 11 and 12 for $m_r=1.7$ and 2.72). In fact, fixing m_r , all stack resonant frequencies within a group (see Fig. 3) fall within the boundaries of PZ's.

Propagation quantities drawn from the flexure model re-

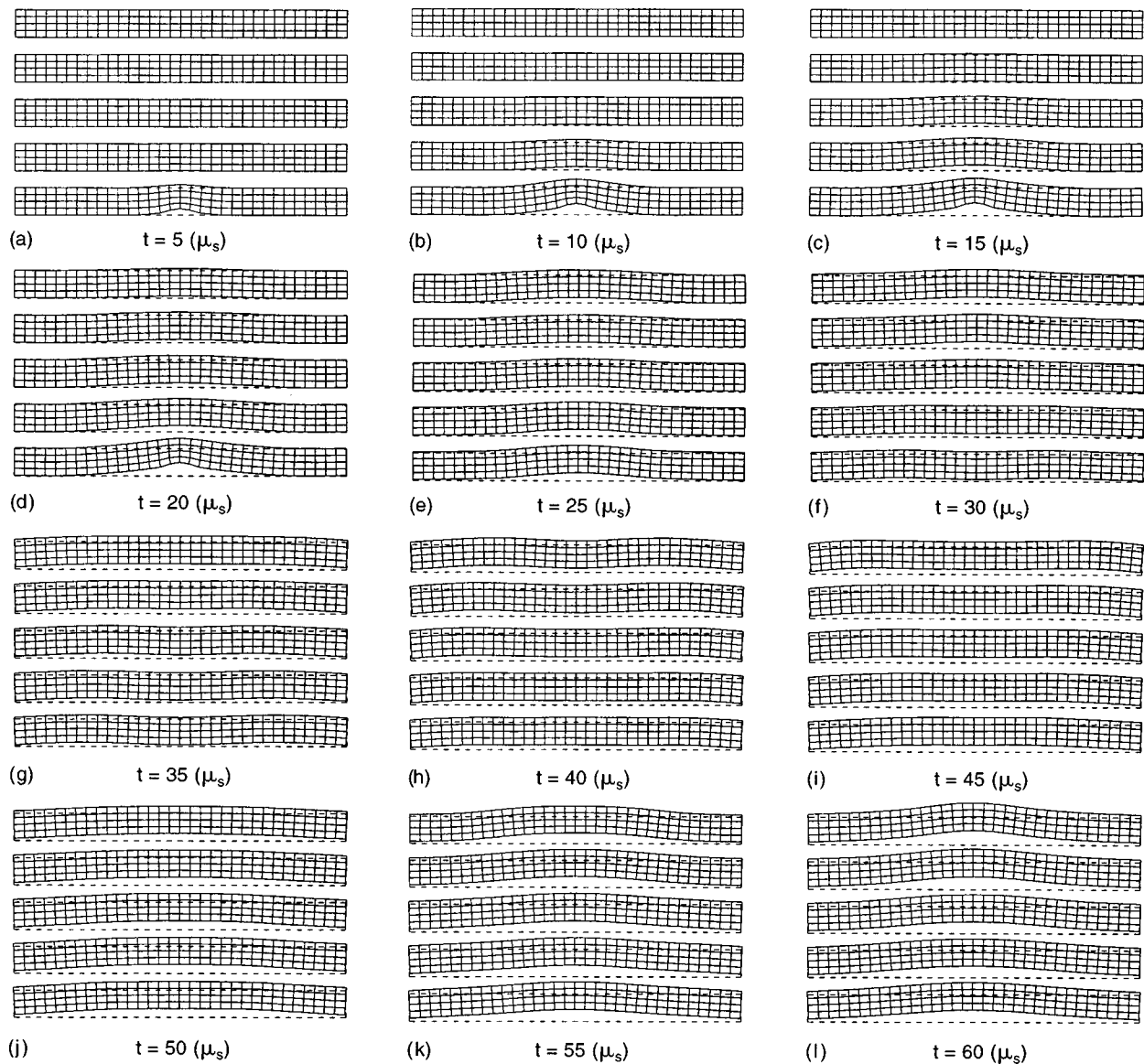


FIG. 8. Snap shots of the deformed stack.

semble those drawn from the 2-D model in the following way. For the lowest m_r , where flexure and extensional groups are not segregated, lines of propagation quantities (Fig. 13) follow the trend of the 2-D's (Fig. 10) except that they are continuous across boundaries of PZ2. For the higher m_r , when flexure and extensional groups are segregated, the lines resemble those of the 2-D's flexural group. Also, flexure analysis over-estimates (c_p, c_g) and width of PZ's by at least 5%. In turn, wavefronts predicted by the flexure model move faster than those predicted by the 2-D model, yielding shorter arrival times of waves along the stack. This is seen by comparing arrival times, which can be measured as the times when a dependent variable's history first departs from the undisturbed state, in corresponding columns of Figs. 6 and 7. The plane stress and Kirchhoff assumptions behind the flexure model are the causes of this discrepancy.

V. CONCLUSION

Results from treating wave propagation in a finite periodic stack according to the different models developed above

are compared in order to reveal the effects of their differing assumptions. Histories of a stack forced by a trapezoidal pulse were used. Important features from comparison of the two primary models are:

- (1) On the forced disk, the flexure model underestimates all variables by 15% remote from the footprint and by as much as 50% in the vicinity of the footprint. This difference is caused by the volumetric part of the stress from axial compression.
- (2) On succeeding disks, the flexure model overestimates all variables by as much as 25%, while the difference diminishes along the stack. This difference is caused by the Kirchhoff assumption behind the flexure model. The effects on response of the approximations in the 2-D models are:
- (3) Neglecting inertia of the bond suppresses frequencies of the bond shear group leaving response histories unchanged.
- (4) Omitting the extensional frequency groups in the modal

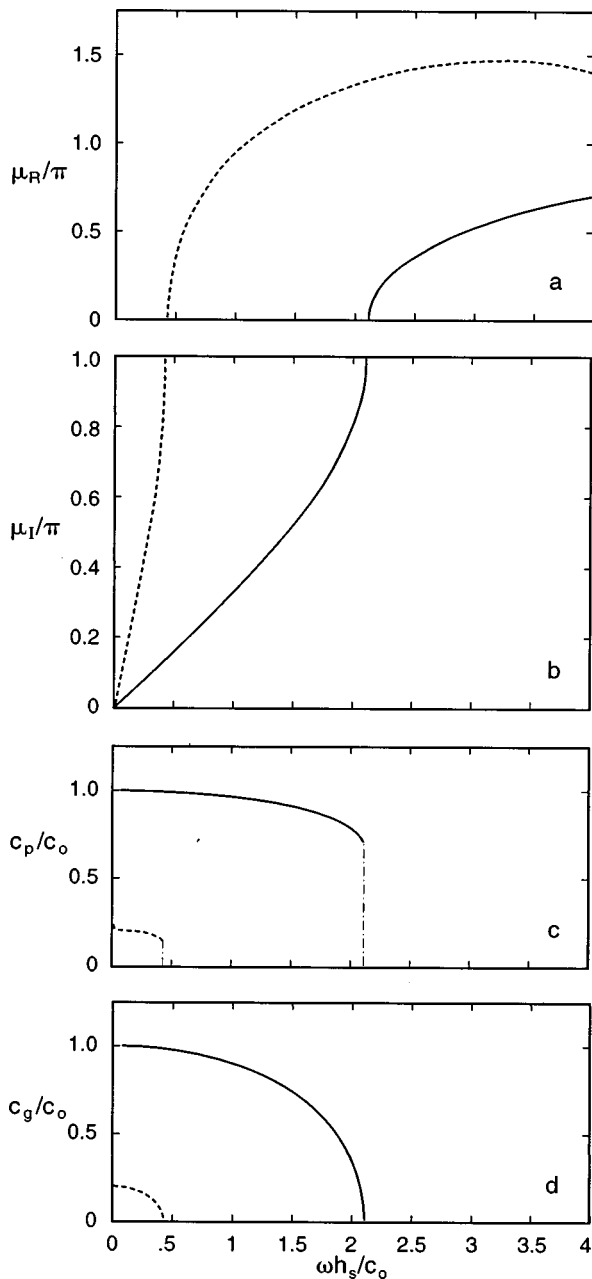


FIG. 9. Propagation quantities for $m_r=0$ (2-D model).

expansion does not alter response histories.

The reason behind conclusion (4) is that extensional motions are already included in the analysis by the static part of the solution in $\mathbf{u}_s f_0(t)$ in (28). This fact emphasizes the importance of using static-dynamic superposition which produces an accurate solution with the smallest set of eigenfunctions. Indeed, the body force method was unsuccessful in modeling the forcing function. Trading computational efficiency for degree of approximation, the plate flexure model may be used with caution for initial screening of parameters in the design of shock isolation devices involving stacks. The 2-D model is preferred when accurate prediction of wave propagation is essential.

Some further conclusions are drawn from consideration of propagation quantities:

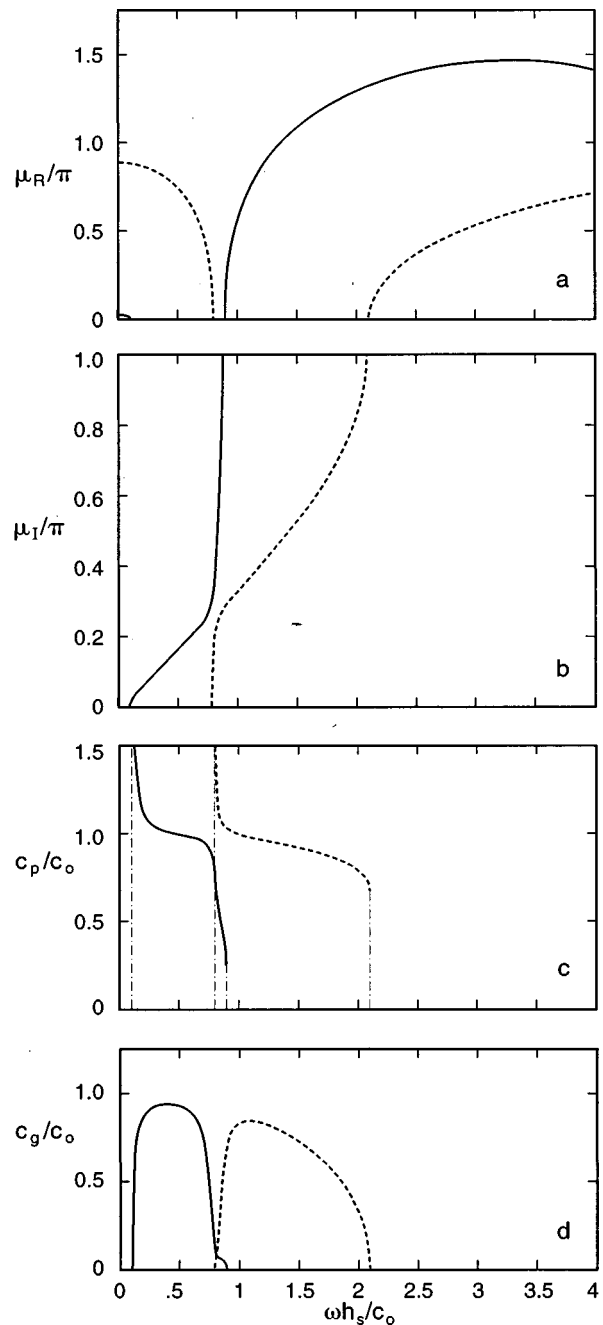


FIG. 10. Propagation quantities for $m_r=0.59$ (2-D model).

- (5) To a good approximation, all the conclusions drawn from the 1-D model of periodic masses and springs can be carried over to the flexure and 2-D models (see Ref. 23).
- (6) Waves with higher m_r are more dispersed and every transient model becomes dominated eventually by waves with low m_r .
- (7) Predictions with the flexure model are close to those of 2-D when limited to the flexure groups.

APPENDIX A: RADIAL MOMENT FROM BOND SHEAR

Flexure of the disks induces shear of the bond. Inertia of the bond introduces shear resonances that raise or lower mobility of the bond depending on their proximity to flexural

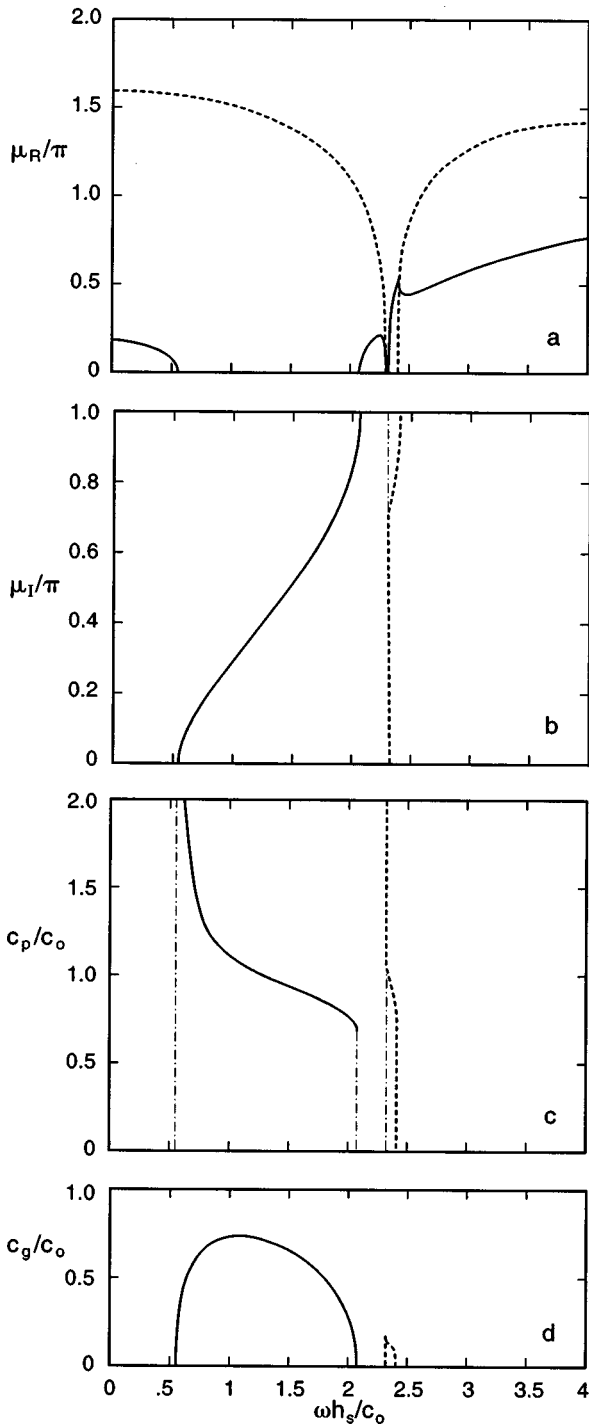


FIG. 11. Propagation quantities for $\gamma_r=1.70$ (2-D model).

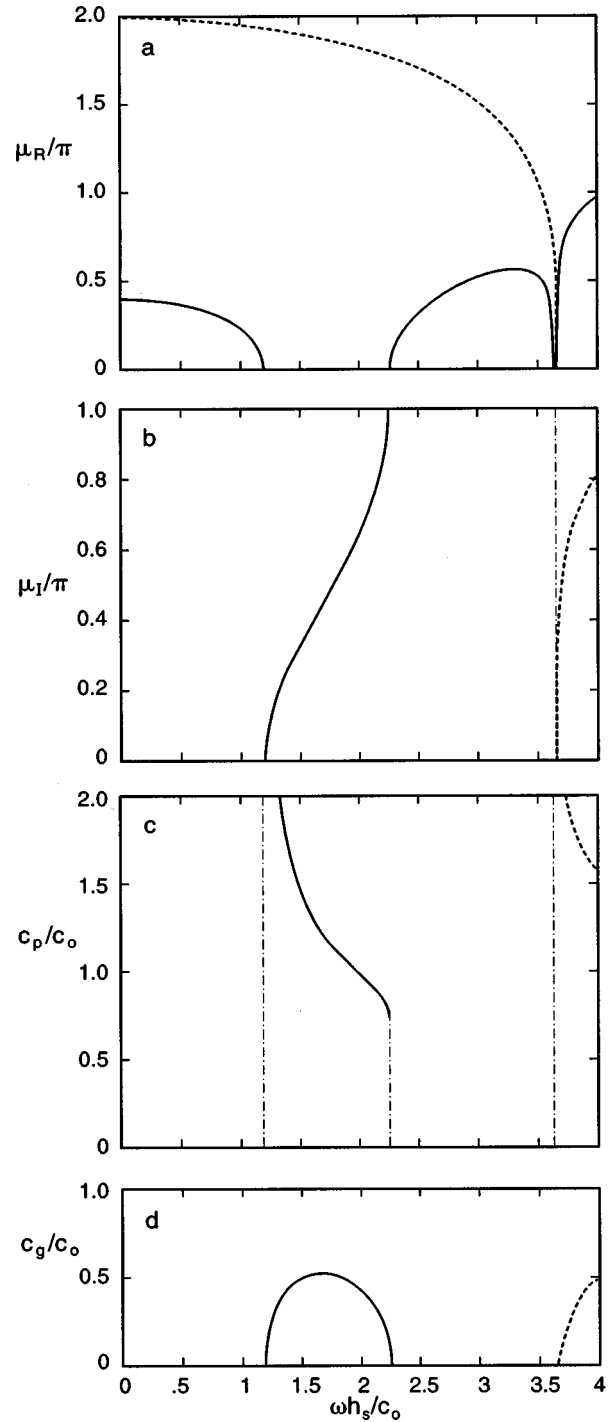


FIG. 12. Propagation quantities for $m_r=2.72$ (2-D model).

resonances. The effects of bond shear and inertia are considered invoking motions with vanishing axial displacement in the 2-D axisymmetric equations of elasto-dynamics:

$$\alpha^2 \nabla_1^2 u + \frac{\partial^2 u}{\partial z^2} = \frac{1}{c_{sb}^2} \frac{\partial^2 u}{\partial t^2}; \quad c_{sb}^2 = \frac{G_b}{\rho_b},$$

$$\nabla_1^2 \equiv \frac{\partial^2}{\partial r^2} + \frac{1}{r} \frac{\partial}{\partial r} - \frac{1}{r^2}, \quad (\text{A1})$$

where u is radial displacement, and (G_b, ρ_b) are shear modulus and density of the bond. For uniaxial strain α^2

$= 2(1-\nu_b)/(1-2\nu_b)$. For approximate simple supports and harmonic motions in time

$$u(r, z, t) = J_1(k_r r) u_0(z) e^{i\omega t}, \quad (\text{A2})$$

where $J_0''(k_r a) = 0$ [see Eq. (7)]. Substituting (A2) in (A1) produces an equation in $u_0(z)$

$$\frac{d^2 u_0}{dz^2} + k_z^2 u_0 = 0, \quad k_z = \sqrt{\left(\frac{\omega}{c_{sb}}\right)^2 - (k_r \alpha)^2}. \quad (\text{A3})$$

To find the shear stresses on disk “ i ” from bonds “1” and “2” connecting it to disks “ $i-1$ ” and “ $i+1$,” respec-

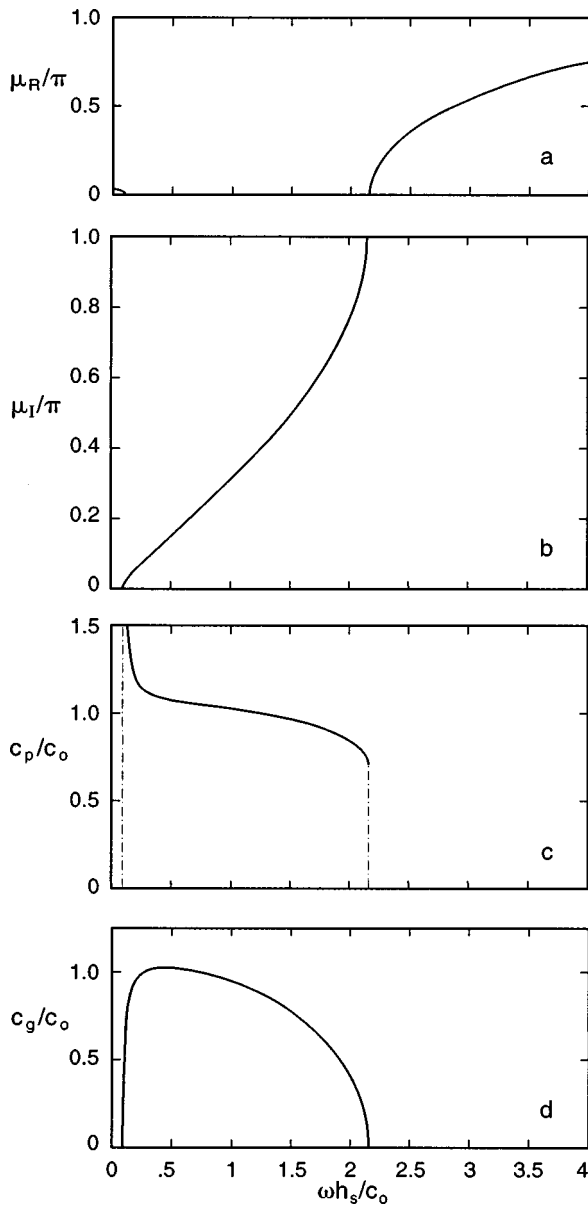


FIG. 13. Propagation quantities for $m_r=0.59$ (flexure model).

tively, solve bond equation (A3) and apply continuity of axial displacement at the interfaces of disks “ i ,” “ $i+1$,” and “ $i-1$.” For bond “1” connecting disks “ $i-1$ ” to “ i ”:

$$u_{01}(0) = \frac{h}{2} \psi_{i-1}, \quad u_{01}(h_b) = -\frac{h}{2} \psi_i, \quad (\text{A4})$$

where h_b and h are bond and disk thicknesses, and ψ is rotation angle of the disk cross section. Also for bond “2” connecting disks “ i ” to “ $i+1$ ”:

$$u_{02}(0) = \frac{h}{2} \psi_i, \quad u_{02}(h_b) = -\frac{h}{2} \psi_{i+1}. \quad (\text{A5})$$

The two solutions of (A3) with boundary conditions (A4) and (A5) yield $u_{ok}(z)$ in the form:

(a) bond “1”: connecting “ $i-1$ ” to “ i ”:

$$u_{01}(z) = \frac{h}{2} \psi_{i-1} \cos k_z z - \frac{h}{2} (\psi_i + \psi_{i-1} \cos k_z h_b) \frac{\sin k_z z}{\sin k_z h_b}; \quad (\text{A6a})$$

(b) bond “2”: connecting “ i ” to “ $i+1$ ”:

$$u_{02}(z) = \frac{h}{2} \psi_i \cos k_z z - \frac{h}{2} (\psi_{i+1} + \psi_i \cos k_z h_b) \frac{\sin k_z z}{\sin k_z h_b}. \quad (\text{A6b})$$

Shear stress of the k th bond follows from the relation

$$\tau_k(z) = \frac{\partial u_{0k}}{\partial z} G_b; \quad k=1,2. \quad (\text{A7})$$

Substituting (A6a,b) in (A7) produces

$$\tau_k(z) = -\frac{h}{2} k_z G_b \left[\psi_{i+k-2} \cos k_z z + (\psi_{i+k-1} + \psi_{i+k-2} \cos k_z h_b) \frac{\sin k_z z}{\sin k_z h_b} \right]. \quad (\text{A8})$$

Shear stresses $\tau_1(h_b)$ and $\tau_2(0)$ acting on top and bottom faces of disk “ i ” from bonds “1” and “2” produce a radial moment \bar{M}_r on disk “ i ”:

$$\begin{aligned} \bar{M}_r &= -(\tau_1(h_b) + \tau_2(0)) \frac{h}{2}, \\ &= \left(\frac{h}{2}\right)^2 \frac{k_z h_b}{\sin k_z h_b} G_b [2\psi_i \cos k_z h_b + \psi_{i+1} + \psi_{i-1}]. \end{aligned} \quad (\text{A9})$$

In the limit as $(k_z h_b) \rightarrow 0$, the quasi-static moment is recovered

$$\bar{M}_r = \left(\frac{h}{2}\right)^2 G_b [2\psi_i + \psi_{i+1} + \psi_{i-1}]. \quad (\text{A10})$$

In (A9) as $(k_z h_b) \rightarrow \pi$, the fundamental shear resonance of the bond is crossed. As this resonance is approached from below, the bond mobility rises, reducing coupling between disks which narrows the gap between resonances. As shear resonance is crossed, bond mobility falls abruptly because of a change in phase, raising coupling between disks which widens the gap between resonances.

APPENDIX B: INNER PRODUCTS IN 2-D AXYSYMMETRIC ANALYSIS

Consider the n th eigenfunction and l th layer in the stack

$$N_{aln} = \langle u_s | \rho | u_{dn} \rangle_l + \langle w_s | \rho | w_{dn} \rangle_l. \quad (\text{B1})$$

From Ref. 24

$$u_s(r,z) = \sum_{m=1}^{\infty} \left\{ \sum_{j=1}^2 C_{smj} e^{\beta_{mj} z} + \sum_{j=3}^4 C_{smj} |\beta_{mj}| z e^{\beta_{mj} z} \right\} J_1(k_{rm} r),$$

$$w_s(r, z) = \sum_{m=1}^{\infty} \left\{ \sum_{j=1}^2 D_{smj} e^{\beta_{mj}z} + \sum_{j=3}^4 D_{smj} |\beta_{mj}| z e^{\beta_{mj}z} \right\} J_0(k_{rm}r),$$

$$\beta_{mj} = (-1)^{j+1} k_{rm}. \quad (\text{B2})$$

Also from (21a,b)

$$u_{dn}(r, z) = \sum_{i=1}^4 C_{dni} e^{\alpha_{ni}z} J_1(k_{rn}r),$$

$$w_{dn}(r, z) = \sum_{i=1}^4 D_{dni} e^{\alpha_{ni}z} J_0(k_{rn}r). \quad (\text{B3})$$

Substituting (B2) and (B3) in (B1) and performing the inner product yields

$$N_{an}^{(l)} = \rho_l \sum_{m=1}^{\infty} \sum_{i=1}^4 \left\{ \sum_{j=1}^2 C_{dni} C_{smj} \frac{e^{\delta_{mnij}z}}{\delta_{mnij}} \Big|_0^{h_l} + \sum_{j=3}^4 C_{dni} C_{smj} \frac{e^{\delta_{mnij}z}}{\delta_{mnij}^2} (\delta_{mnij}z - 1) \Big|_0^{h_l} \right\} \bar{N}_{1mn}$$

$$+ \rho_l \sum_{m=1}^{\infty} \sum_{i=1}^4 \left\{ \sum_{j=1}^2 D_{dni} D_{smj} \frac{e^{\delta_{mnij}z}}{\delta_{mnij}} \Big|_0^{h_l} + \sum_{j=3}^4 D_{dni} D_{smj} \frac{e^{\delta_{mnij}z}}{\delta_{mnij}^2} (\delta_{mnij}z = 1) \Big|_0^{h_l} \right\} \bar{N}_{omn},$$

$$\delta_{mnij} = \beta_{mj} + \alpha_{ni}, \quad (\text{B4})$$

$$\bar{N}_{jmn} = \frac{1}{\alpha^2} \int_0^{\alpha} J_j(k_{rm}r) J_j(k_{rn}r) r dr, \quad j = 1, 2.$$

Expressions for $N_{mn} = \langle m | \rho | n \rangle$ follow

$$N_{mn}^{(l)} = \rho_l \sum_{i=1}^4 \sum_{j=1}^4 C_{dmi} C_{dnj} \frac{e^{\delta_{mnij}z}}{\delta_{mnij}} \Big|_0^{h_l} \bar{N}_{1mn}$$

$$+ \rho_l \sum_{i=1}^4 \sum_{j=1}^4 D_{dmi} D_{dnj} \frac{e^{\delta_{mnij}z}}{\delta_{mnij}} \Big|_0^{h_l} \bar{N}_{omn},$$

$$\delta_{mnij} = \alpha_{mi} + \alpha_{nj}. \quad (\text{B5})$$

In (B4) and (B5), h_l is thickness of the l th layer. To find N_{an} and N_{mn} for the stack, sum over all layers

$$N_{an} = \sum_{l=1}^N N_{an}^{(l)}, \quad N_{mn} = \sum_{l=1}^N N_{mn}^{(l)}. \quad (\text{B6})$$

¹W. Thomson, "Transmission of elastic waves through a stratified medium," J. Appl. Phys. **21**, 89–93 (1950).

- ²N. A. Haskell, "The dispersion of surfaced waves in multi-layered media," Bull. Seismol. Soc. Am. **43**, 17–34 (1953).
- ³S. M. Rytov, "Acoustical properties of a thinly laminated medium," Sov. Phys. Acoust. **2**, 68–70 (1956).
- ⁴D. L. Anderson, "Elastic wave propagation in layered anisotropic media," J. Geophys. Res. **66**, 2953–2963 (1961).
- ⁵R. A. Tenenbaum and M. Zindeluk, "An exact solution for the one-dimensional elastic wave equation in layered media," J. Acoust. Soc. Am. **92**, 3364–3370 (1992).
- ⁶C. T. Sun, J. D. Achenbach, and G. Herrmann, "Time harmonic waves in a stratified medium, propagating in the direction of the layering," J. Appl. Mech. **35**, 408–411 (1968).
- ⁷T. J. Delph, G. Herrmann, and R. K. Kaul, "Harmonic wave propagation in a periodically layered infinite elastic body: Antiplane strain," J. Appl. Mech. **45**, 343–349 (1978).
- ⁸T. J. Delph, G. Herrmann, and R. K. Kaul, "Harmonic wave propagation in a periodically layered infinite elastic body: Plane strain, analytical results," J. Appl. Mech. **46**, 113–119 (1979).
- ⁹T. J. Delph, G. Herrmann, and R. K. Kaul, "Harmonic wave propagation in a periodically layered infinite elastic body: Plane strain, numerical results," J. Appl. Mech. **47**, 531–537 (1980).
- ¹⁰G. Herrmann and M. Hemami, "Plane-strain surface waves in a laminated composite," J. Appl. Mech. **49**, 747–753 (1982).
- ¹¹D. J. Mead, "Vibration response and wave propagation in periodic structures," Journal of Engineering in Industry **93**, 783–792 (1971).
- ¹²D. J. Mead, "Wave propagation and natural modes in periodic systems, I: Mono-coupled systems," J. Sound Vib. **40**, 1–18 (1975).
- ¹³D. J. Mead and A. S. Bansal, "Free wave propagation and response to convected loadings," J. Sound Vib. **61**, 481–515 (1978).
- ¹⁴D. J. Mead and S. M. Lee, "Receptance methods and the dynamics of disordered one-dimensional lattices," J. Sound Vib. **92**, 427–445 (1984).
- ¹⁵D. J. Mead, "A new method of analyzing wave propagation in periodic structures: Applications to periodic Timoshenko beams and stiffened plates," J. Sound Vib. **104**, 9–27 (1986).
- ¹⁶R. C. Engels and L. Meirovitch, "Response of periodic structures by modal analysis," J. Sound Vib. **56**, 481–493 (1978).
- ¹⁷Sen G. Gupta, "Vibration of periodic structures," Shock & Vibration Digest **12**(3), 17–29 (1980).
- ¹⁸T. J. McDaniel and M. J. Carroll, "Dynamics of bi-periodic structures," J. Sound Vib. **81**, 311–335 (1982).
- ¹⁹M. G. Faulkner and D. P. Hong, "Free vibrations of a mono-coupled periodic systems," J. Sound Vib. **99**, 29–42 (1985).
- ²⁰A. J. Keane and W. G. Price, "On the vibrations of mono-coupled periodic and near-periodic structures," J. Sound Vib. **128**, 423–450 (1989).
- ²¹M. Rousseau, "Floquet wave properties in a periodically layered medium," J. Acoust. Soc. Am. **86**, 2369–2376 (1989).
- ²²M. El-Raheb, "Transient elastic waves in finite layered media: One-dimensional analysis," J. Acoust. Soc. Am. **94**, 172–184 (1993).
- ²³M. El-Raheb, "Simplified analytical models for transient uniaxial waves in a layered periodic stack," Int. J. Solids Struct. **34**(23), 2969–2990 (1997).
- ²⁴M. El-Raheb and P. Wagner, "Transient elastic waves in finite layered media: Two dimensional axisymmetric analysis," J. Acoust. Soc. Am. **99**, 3513–3527 (1996).
- ²⁵R. D. Mindlin, "Influence of rotary inertia and shear deformation on flexural motions of isotropic elastic plates," Trans. ASME, J. Appl. Mech. **73**, 31–38 (1951).
- ²⁶M. El-Raheb, "The static-dynamic superposition method applied to uniaxial waves in a bi-periodic stack," J. Acoust. Soc. Am. **101**, 610–612 (1997).

Use of genetic algorithms for the vibroacoustic optimization of a plate carrying point-masses

Alain Ratle and Alain Berry

GAUS, Université de Sherbrooke, Sherbrooke, Québec J1K 2R1, Canada

(Received 15 April 1998; accepted for publication 24 August 1998)

Optimal design of mechanical structures for vibration or noise reduction often requires finding the minima of highly nonlinear multi-dimensional functions. In this paper, genetic algorithms are introduced as a new promising tool for numerical optimization of such problems. The application presented is on the control of the vibroacoustic response of a plate carrying point-masses. Genetic algorithms have been used to determine the optimal positions of the masses on the plate. Several cases are presented, using various optimization criteria, showing the importance of selecting the most appropriate criterion. © 1998 Acoustical Society of America. [S0001-4966(98)01812-8]

PACS numbers: 43.40.Dx, 43.40.Rj, 43.50.Gf [CBB]

INTRODUCTION

Genetic algorithms have recently been recognized as a promising tool for numerical optimization of structural design problems. These algorithms, as presented by Holland,¹ make use of the principles of natural selection for dealing with complex nonlinear optimization problems. Genetic algorithms (GA) have outperformed classical optimization methods such as linear or even nonlinear programming in several cases,^{2,3} especially when considering multi-modal functions. These functions are defined as functions having a large number of local extremal points, thus requiring an optimization algorithm able to sort the globally optimal solution out of a large number of locally optimal solutions.

GA have been successfully applied in the fields of mechanics and acoustics on beams and truss structures design problems,⁴⁻⁶ as well as active control of noise and structural vibrations.⁷⁻¹⁰ These algorithms have the main advantage of being *blind* algorithms in the sense that they do not require any knowledge about the function to be optimized other than function values at selected points. There is no need for derivatives evaluations, or initial bracketing of optimal points.

More traditional optimization approaches have already been used for dealing with problems of optimal vibroacoustic design. St. Pierre and Koopmann¹¹ used an analytic sensitivity approach for optimally sizing discrete masses on a plate. As shown in this paper, the use of GA avoids such analytical developments.

In this paper, a thorough presentation of the basic principles of genetic algorithms is given first. The application of such algorithms to the optimal placement of point-masses on a vibrating plate is presented. Such a numerical application can be considered as a building block for a more general design approach of complex structures with added masses, stiffeners and damping materials. The main goal is to reduce as much as possible a certain mechanical or acoustical criteria over a given frequency band. The basic principle of shifting resonances from a frequency band using point-masses has already been proposed by McMillan and Keane.¹² These authors have devised an analytical procedure for placing point-masses in order to obtain some prescribed eigenvalues. In a second paper,¹³ McMillan and Keane also compared an

analytical approach for sequentially placing masses on a plate with the use of a genetic algorithm for simultaneously optimizing the position of all the masses. In both cases, strong assumptions were made *a priori* over the optimal positions in order to effect only the eigenvalues lying under a threshold frequency. In the present paper, the proposed approach is to make as few assumptions as possible and to explore the searching capability of genetic algorithms over very large search spaces. Another objective of this paper is to study the effect of various optimization criteria on the search results of a genetic algorithm.

Genetic algorithms, as well as all other heuristic methods, require a large number of function evaluations. Due to this constraint, a computationally simple function to be optimized is preferable. For this reason, an optimized method for solving the equations of motion is presented, in the case of a plate carrying point-masses, based on the subdivision of a complex structure into several subsystems linked by equivalent forces. The optimization method has been numerically tested on a rectangular plate carrying up to five point-masses, and excited either by mechanical point-forces or by acoustic plane waves. Considerations on the choice of an appropriate criterion are also presented, as a guideline for future works.

I. GENETIC ALGORITHMS

This section describes the fundamentals of genetic algorithms that are used in this paper for optimizing the vibroacoustic response of structures. The original idea of genetic algorithms is to mimic natural processes of evolution. The concept emerged from mathematical models of natural evolutionary processes developed in the framework of biological sciences. As an example, one can refer to Fraser,¹⁴ among many others. However, the first well known application of these models outside of the framework of biological researches is generally attributed to Holland.¹

A. General description

1. Data structure

The basic feature of genetic algorithms is a translation of the traditional concepts of function optimization into the framework of natural evolution of species. In the case of the

vibroacoustic optimization of a plate carrying a certain number R of point-masses, a good optimization method is expected to find out the best possible positions for the masses with respect to a given optimization criterion. Using genetic algorithms, a solution to this problem will be given as a character string, the *genetic code*, built by linking together all the variables of the problem. In that case the genetic code contains the $2R$ variables representing the X and Y coordinates of the R masses on the plate. A value of *fitness function*, i.e., the value of the function to be optimized, is associated with a given genetic code, and these two parts, genetic code and fitness function form what is termed an *individual*. Examples of possible fitness functions in the present case would be the mean square velocity of the plate, or the radiated sound power.

2. Fundamental process

A basic genetic algorithm is initiated by randomly creating a set of individuals forming the *first generation* individuals. These individuals are therefore an initial random search over the fitness function surface. A second generation is then created from the first one by successive application of the following three fundamental operators: selection of two parents, crossing over in order to create a new individual and natural mutation of this new individual. The fitness function of all the individuals of the new generation is then evaluated, and if the solution is judged satisfactory the algorithm is stopped. Otherwise, other generations are created until a satisfactory solution is obtained.

B. Basic operators

1. Selection

The purpose of the selection operator is to choose among the population a pair of parents to be bred together in order to create an *offspring*. The average fitness of the population from one generation to another is expected to increase, since the selection operator is designed as a biased random process, giving a higher probability of selection to the most fit individuals and a lower probability to the least fit ones.

Among the various practical implementations,^{15,16} the best known is the *biased roulette wheel* method. This method has been used for the applications presented in this paper. In this method, the selection is modeled by a casino wheel where each individual has a portion of the wheel proportional to its fitness value. Hence, the best individuals have more chances to be selected, although less fit ones still have a non-zero probability of selection. Such a nonzero probability for all individuals is necessary in order to maintain a high level of diversity into the genetic pool. Otherwise, premature convergence would prevent the algorithm from reaching the global optimum. Premature convergence is defined as the entrapment of the algorithm into a local optimum at an early stage of the search.

2. Crossover

Crossover consists in a genetic recombination of the two parents in order to create a new individual sharing characteristics of both parents. Among the various existing formula-

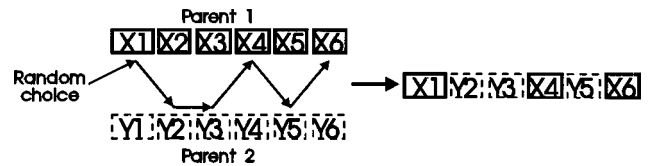


FIG. 1. Uniform crossover for a six-variables problem. The offspring is built up from variables randomly chosen between parent 1 and parent 2.

tions for this operator, *uniform* crossover is retained for this study. In uniform crossover, the genetic code of the new offspring is determined by randomly selecting for each position on the genetic code, the value pertaining to one parent or the other. This selection is performed using a Bernoulli trial,¹⁷ also known as a coin-toss operation. The mechanism of uniform crossover is illustrated in Fig. 1 for a six-variables problem.

A fundamental point that should be noted is that selection and crossover do not bring any new information into the genetic pool; these operators just perform a recombination of the already present information. Translating this into the framework of mathematical optimization, selection and crossover perform a local search around the best solutions found at a given stage of optimization, *exploiting* the available information, while the mutation operator is rather an *exploration* operator, investigating new regions of the fitness landscape. The concept of *exploitation vs exploration* is illustrated in Fig. 2, for a two-variables fitness function. Starting with any two parents, the crossover operator can place an offspring at one of the four corners of the rectangle defined by the original positions of the parents, as shown on the top part of Fig. 2. On the other hand, the mutation operator is able to place a new individual at any position, regardless of the original position, as shown on the bottom part of Fig. 2.

3. Mutation

The mutation operator is equivalent to introducing *errors* in the transmission of genetic information from one generation to another. This error is necessary since it is the only way to take a population out of a local optimum entrapment. Using optimization language, mutation is equivalent to a random search over the whole optimization space. While muta-

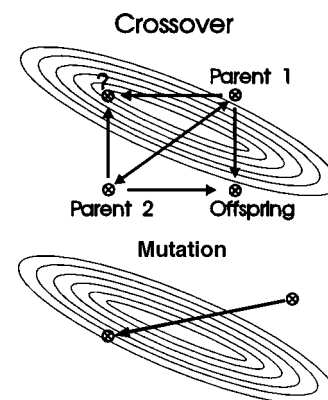


FIG. 2. Modelization of crossover and mutation operators for a two-variables fitness function. The thin lines represent isocontours of fitness function.

tion was considered in the early years of GA as nothing but a background operator,¹ recent works tends to consider mutation to be as important as the other operators.¹⁸

One of the most simple method for the implementation of the mutation operator is to randomly select a position on the genetic code of an individual, and to enforce a random value to that position. The mutation operator is applied stochastically to each individual with a probability ranging in most cases between 10^{-3} and 10^{-1} .

The same operator is also used in a deterministic way to enforce constraints on the population for several reasons. The first application is for eliminating duplicate genetic codes in the population. Whenever two duplicate individuals are detected, one of them is modified using a forced mutation. A second reason for using forced mutations is to enforce boundaries on the optimization space. Whenever an individual moves to a position out of the optimization space boundaries, it is eliminated and replaced by a randomly created one.

Forced mutations can also be used to impose problem-dependent constraints. For example, in the present case of optimization of mass positions on a vibrating plate, the non-collocation of two masses must be imposed, in order to avoid trivial solutions.

C. Algorithm refinements

The canonical GA described above contains theoretically all the elements required to ensure convergence to a globally optimal solution as demonstrated by several convergence studies.¹⁹⁻²² However, several refinements have been introduced by theoreticians as well as practitioners of GA in order to solve two main problems: (1) Increasing the rate of convergence, and (2) Avoiding premature convergence to a local optimum. For that purpose, three aspects have been considered in the present application:

1. Selective pressure

Selective pressure defines the degree of severity the selection operator is against weaker individuals. In the GA used in this paper, selective pressure is introduced as a modification of the fitness function as:

$$P_i = \frac{F_i^p}{\sum_{j=1}^N F_j^p}, \text{ for } 0 < P_i < 1, \quad (1)$$

where P_i is the probability of the individual i to be selected, F_i is the fitness value of this same individual, N is the population size and the exponent p is a constant value defining the selective pressure. Using a high selective pressure means that highly fit genetic codes are going to rapidly dominate the whole population, ensuring a fast convergence. However, such a fast convergence may be attained before a path to the global optimum has been found, leading to a nonoptimal solution. On the other hand, using a low value of the selective pressure gives better chances of selection to less fit individuals, slowing down the convergence rate, but ensuring that a thorough exploration of the optimization space is performed. Consequently, a compromise must be made between

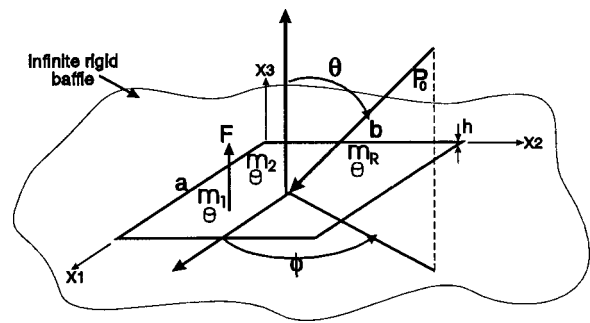


FIG. 3. Description of the plate-mass system considered in the present application.

the rate of convergence and the probability of reaching the optimal solution.

2. Rank selection

In the cases where the fitness function is highly irregular, with very sharp extrema, a common situation is when a single individual placed on the top of a sharp ‘hill’ dominates the whole population. An alternative formulation of the problem can help avoid these situations. Instead of using the fitness value as a selection factor, the population is first classified with respect to the fitness value of each individual, and a new fitness value proportional to its rank in the classification is attributed to each individual.¹⁰ Following this procedure and using a population of N individuals, the best fit is given a fitness value of N , the second best, $N-1$, and the worst, 1. This transformation has a smoothing effect over the fitness function, allowing us to deal with highly irregular functions. Rank selection is also useful for dealing with non-positive functions, since a negative fitness would result in an erroneous value of the probability of selection, P_i .

3. Elitism

Following the canonical form of GA, each new generation is composed of new individuals created by manipulations of the previous generation. However, a potential drawback of this procedure is that an excellent solution found in early generations might be disrupted by crossover at the next generation. An efficient way to deal with that situation is by using *elitist* selection. Such a selection model implies that the best solution of each generation is left untouched for the next generation, allowing the most fit individual to survive with a probability of 100%. Care must be taken however since an elitist selection scheme might lead to premature convergence in the direction of a highly fit individual, which is not necessarily on the way to the global optimum.

II. VIBROACOUSTIC RESPONSE OF A PLATE CARRYING POINT-MASSSES

In this section, the vibroacoustic behavior of a simply supported plate is considered. The plate is excited either by point-forces or by plane acoustic waves with oblique incidence, and the plate carries a number R of point-masses. The system considered is illustrated in Fig. 3. The vibratory response as well as sound radiation in the half-space $x_3 > 0$ are considered, under the hypotheses of infinite baffle and neg-

ligible fluid loading. In the following analysis, plate damping is implicitly taken into account through the use of a complex elastic modulus, e.g., $E = E_r(1 + j\eta)$, where E_r is the real part of the elastic modulus E , η is the so-called loss factor and j is the imaginary unit.

A. Rayleigh–Ritz approach

Application of the Rayleigh–Ritz approach to a flexural plate with no fluid loading leads to the following equation of motion:

$$[-\omega_0^2[M] + [K]]\{A\} = \{F\}, \quad (2)$$

where $[M]$ and $[K]$ represent the mass and stiffness matrix, while $\{A\}$ and $\{F\}$ are the displacement and load vectors projected over the Rayleigh–Ritz basis functions, and ω_0 is the excitation frequency. Using appropriate basis functions, corresponding to the natural vibration modes, the response of a simply supported plate excited by a point-force F applied at the point (x_1^0, x_2^0) , and without any added point-mass is given by a set of decoupled equations, allowing an independent calculation of each modal amplitude:

$$A_{mn} = \frac{F w_{mn}(x_1^0, x_2^0)}{(ab/4) \rho h (\omega_{mn}^2 - \omega_0^2)}, \quad (3)$$

where a , b and h are the plate length, width and thickness, ρ is the fluid density and ω_{mn} is the natural frequency of the mode (m, n) . In the case of a simply supported plate, the basis functions $w_{mn}(x_1, x_2)$ and the total displacement field $w(x_1, x_2, t)$ are given with respect to the physical coordinates (x_1, x_2) and time t by the following equations:

$$w_{mn}(x_1, x_2) = \sin\left(\frac{m\pi x_1}{a}\right) \sin\left(\frac{n\pi x_2}{b}\right), \quad (4)$$

$$w(x_1, x_2, t) = \sum_{m=1}^M \sum_{n=1}^N A_{mn} w_{mn}(x_1, x_2) e^{j\omega_0 t}. \quad (5)$$

However, for a plate connected to other structural elements, the stiffness and mass matrix become full in general. Considering R point-masses m_r , $1 \leq r \leq R$, fixed to the plate at the points (x_1^r, x_2^r) , $1 \leq r \leq R$, the mass matrix is expressed as:

$$[M] = \begin{bmatrix} \frac{ab}{4} \rho h + \sum_{r=1}^R m_r w_{11}^2(x_1^r, x_2^r) & \cdots & \cdots & \text{(symmetric)} \\ \sum_{r=1}^R m_r w_{12}(x_1^r, x_2^r) w_{11}(x_1^r, x_2^r) & \ddots & & \vdots \\ \cdots & \ddots & \ddots & \vdots \\ \sum_{r=1}^R m_r w_{mn}(x_1^r, x_2^r) w_{11}(x_1^r, x_2^r) & \cdots & \cdots & \frac{ab}{4} \rho h + \sum_{r=1}^R m_r w_{mn}^2 \end{bmatrix}. \quad (6)$$

The stiffness matrix is left unchanged in this case, being a diagonal matrix containing the terms $\frac{1}{4} ab \rho h \omega_{mn}^2$ on its diagonal. For a problem where the number of modes considered is large, the CPU time required for solving Eq. (2) can grow to an unacceptable value, especially when using an optimization method where a large number of fitness function calls are required.

B. Substructuring method for a point-loaded plate carrying point-masses

The proposed genetic algorithm optimization method makes use of a large number of *trials*, each one requiring the solution of the equation of motion, Eq. (2). It points out the need for a minimization of the required CPU time for each trial. A new approach is proposed in this section for solving the equation of motion in a more efficient way. The proposed substructuring method has the effect of diagonalizing the mass and stiffness matrix, thus allowing an easier and faster solution of the equation of motion. The mechanical substructuring method relies on the definition of adequate boundary conditions between parts of the structure. Figure 4 illustrates

the principle of equivalent forces connecting the point-masses to the base plate.

Using the notion of mechanical admittance, the plate displacement at an arbitrary point $q(x_1, x_2)$ can be expressed as a function of the excitation force, F_0 , the interface force applied on the plate by the mass, F_m , and the admittances of the plate without masses, denoted \mathcal{A} :

$$w(x_1, x_2) = \mathcal{A}_{fq} F_0 + \mathcal{A}_{mq} F_m. \quad (7)$$

In the general case, the admittance \mathcal{A}_{ij} is defined as the ratio of the displacement at point j divided by the force applied at point i . Subscripts f and m refer, respectively, to the excitation point and to the mass position. Using the same

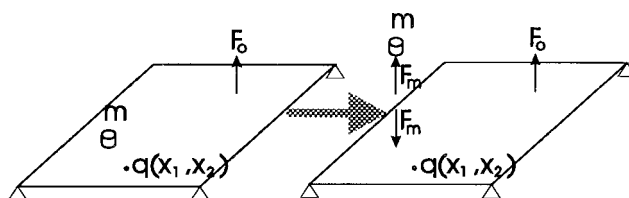


FIG. 4. Equivalent forces used for the mechanical substructuring method.

principle, the plate displacement at the application point of a discrete mass can be written as:

$$w(x_1^m, x_2^m) = \mathcal{A}_{fm} F_0 + \mathcal{A}_{mm} F_m. \quad (8)$$

On the other hand,

$$w(x_1^m, x_2^m) = -\mathcal{A}_m F_m. \quad (9)$$

In the latter equations, \mathcal{A}_m denotes the mechanical admittance of the isolated mass while $w(x_1^m, x_2^m)$ is the plate displacement at the location of the mass. For a point-mass, \mathcal{A}_m is equal to $-1/(m\omega_0^2)$. Equation (9) ensures continuity of displacements between the base plate and the isolated mass under the action of the interface force F_m . From Eqs. (8) and (9), the interface force is found to be:

$$F_m = -\left(\frac{\mathcal{A}_{fm}}{\mathcal{A}_{mm} + \mathcal{A}_m}\right) F. \quad (10)$$

For a simply supported plate excited by a point-force at the point (x_1^0, x_2^0) , the frequency-dependent mechanical admittance between the excitation point and point (x_1, x_2) , denoted $\mathcal{A}(x_1, x_2, \omega_0)$, is obtained as a function of position (x_1, x_2) , plate dimensions a and b , plate density ρ , angular frequency ω_0 and natural frequencies of the plate without masses ω_{mn} :

$$\mathcal{A}(x_1, x_2, \omega_0) = \sum_{m=1}^M \sum_{n=1}^N \frac{w_{mn}(x_1^0, x_2^0) w_{mn}(x_1, x_2)}{(ab/4) \rho h (\omega_{mn}^2 - \omega_0^2)}. \quad (11)$$

Using this expression for calculating \mathcal{A}_{fm} and \mathcal{A}_{mm} in Eq. (10), the modal amplitudes for the plate carrying a point-mass are finally obtained as:

$$A_{mn} = \frac{F_0 [w_{mn}(x_1^0, x_2^0) - [\mathcal{A}_{fm}/(\mathcal{A}_{mm} + \mathcal{A}_m)] w_{mn}(x_1^m, x_2^m)]}{(ab/4) \rho h (\omega_{mn}^2 - \omega_0^2)}. \quad (12)$$

The mechanical substructuring method can be easily extended to the multiple-masses case, by replacing each mass by an equivalent interface force. For the general case where R masses are connected to the plate, the R equivalent forces are calculated by solving an $R \times R$ matrix equation, given by:

$$(\mathcal{A}_{ii} + \mathcal{A}_i) F_i + \sum_{j=1, j \neq i}^R \mathcal{A}_{ij} F_j = -\mathcal{A}_{fi} F_0. \quad (13)$$

In this equation, F_i (F_j) is the interface force between the i th (j th) mass and the plate, \mathcal{A}_i represents the admittance of the isolated i th mass [$\mathcal{A}_i = -1/(m_i \omega_0^2)$] and \mathcal{A}_{ij} and \mathcal{A}_{ii} are the transfer and direct admittances of the plate without masses, respectively. Since the dimension of the linear system to be solved is equal to the number of added masses, the mechanical substructuring method will generally be faster than the direct resolution of the linear system of Eq. (2), whose dimension is $M \times N$, the total number of modes.

C. Substructuring method for acoustically excited plate with point-masses

This section presents the response of a plate carrying an arbitrary number of point-masses under an acoustic excita-

tion. Assuming an excitation by a plane acoustic wave with incidence angles (θ, ϕ) (Fig. 3), harmonic time dependence with pulsation ω_0 and wave amplitude P_0 and wave number $k = \omega_0/c_0$, where c_0 is the sound velocity, the incident pressure wave is described by the following expression:

$$P_i(x_1, x_2, x_3, t) = P_0 e^{-jkx_1 \sin \theta \cos \phi} e^{-jkx_2 \sin \theta \sin \phi} \times e^{+jkx_3 \cos \theta} e^{j\omega_0 t}. \quad (14)$$

Using the blocked pressure hypothesis, the surface pressure $P(x_1, x_2, 0, t)$ exciting the plate is approximately equal to $2P_i(x_1, x_2, 0, t)$. Assuming no mass on the plate in a first instance, the modal amplitudes of the plate are given as a function of the generalized modal forces F_{mn} by

$$A_{mn} = \frac{F_{mn}}{(ab/4) \rho h (\omega_{mn}^2 - \omega_0^2)}. \quad (15)$$

The generalized forces are obtained as

$$F_{mn} = \int_0^a \int_0^b 2P_i(x_1, x_2, 0) w_{mn}(x_1, x_2) dx_2 dx_1. \quad (16)$$

Using the following coordinates transform:

$$\lambda = k \sin \theta \cos \phi, \quad \mu = k \sin \theta \sin \phi, \quad (17)$$

the generalized forces are finally given by the following equation:

$$F_{mn} = \int_0^a \int_0^b 2P_0 e^{-j\lambda x_1} e^{-j\mu x_2} w_{mn}(x_1, x_2) dx_2 dx_1 = 2P_0 \tilde{w}_{mn}(\lambda, \mu), \quad (18)$$

where $\tilde{w}_{mn}(\lambda, \mu)$ is the space-wave number Fourier transform of the modal shape function $w_{mn}(x_1, x_2)$. Considering now the case of a plate excited by an acoustic plane wave and carrying a single point-mass, the plate displacement can be obtained using the substructuring approach, Eq. (8), and substituting for the excitation point a continuous distribution of infinitesimal forces, representing the surface sound pressure field on the plate:

$$w(x_1^m, x_2^m) = -\mathcal{A}_m F_m = \mathcal{A}_{mm} F_m + \int_0^a \int_0^b [2P_0 \mathcal{A}_{fm}(x_1, x_2) e^{-jkx_1 \sin \theta \cos \phi} \times e^{-jkx_2 \sin \theta \sin \phi}] dx_2 dx_1. \quad (19)$$

Introducing the expression of the mechanical admittances [Eq. (11)] into (19):

$$w(x_1^m, x_2^m) = -\mathcal{A}_m F_m = \mathcal{A}_{mm} F_m + \int_0^a \int_0^b \left[\sum_{m,n} \frac{w_{mn}(x_1^m, x_2^m) w_{mn}(x_1, x_2)}{(ab/4) \rho h (\omega_{mn}^2 - \omega_0^2)} 2P_0 \times e^{-jkx_1 \sin \theta \cos \phi} e^{-jkx_2 \sin \theta \sin \phi} \right] dx_2 dx_1. \quad (20)$$

By rearranging, and using the coordinate transformation (17):

$$w(x_1^m, x_2^m) = -\mathcal{A}_m F_m = \mathcal{A}_{mm} F_m + 2P_0 \sum_{m,n} \frac{w_{mn}(x_1^m, x_2^m) \int_0^a \int_0^b w_{mn}(x_1, x_2) e^{-j\lambda x_1} e^{-j\mu x_2} dx_2 dx_1}{(ab/4) \rho h (\omega_{mn}^2 - \omega_0^2)}. \quad (21)$$

The double integral being again equal to the space-wave number Fourier transform of the modal functions, the latter equation can be simplified as:

$$w(x_1^m, x_2^m) = -\mathcal{A}_m F_m = \mathcal{A}_{mm} F_m + 2P_0 \tilde{\mathcal{A}}_{fm}, \quad (22)$$

where the quantity $\tilde{\mathcal{A}}_{fm}$ is defined as:

$$\tilde{\mathcal{A}}_{fm} = - \sum_{m,n} \frac{w_{mn}(x_1^m, x_2^m) \tilde{w}_{mn}(\lambda, \mu)}{(ab/4) \rho h (\omega_{mn}^2 - \omega_0^2)}. \quad (23)$$

Using Eq. (22) to calculate the interface force F_m applied by the mass on the plate, the modal amplitudes of the plate-mass system can be expressed as a set of decoupled equations:

$$A_{mn} = \frac{2P_0 \tilde{w}_{mn}(\lambda, \mu) + F_m w(x_1^m, x_2^m)}{(ab/4) \rho h (\omega_{mn}^2 - \omega_0^2)}, \quad (24)$$

where F_m is given by $-2P_0 \tilde{\mathcal{A}}_{fm} / (\mathcal{A}_{mm} + \mathcal{A}_m)$. Generalizing this equation to the case of a plate carrying R point-masses applied at the points (x_1^r, x_2^r) is a straightforward task, adding to the numerator of Eq. (24) another interface force term $F_m w(x_1^m, x_2^m)$. Interface forces are obtained by solving an $R \times R$ system similar to Eq. (13):

$$(\mathcal{A}_{ii} + \mathcal{A}_i) F_i + \sum_{j=1, j \neq i}^R \mathcal{A}_{ij} F_j = -\tilde{\mathcal{A}}_{fi} F_0. \quad (25)$$

D. Vibroacoustic optimization criteria

In the present work, the mean square velocity of the plate is used as an optimization criterion, as well as the far-field sound pressure in a prescribed direction. For a simply supported rectangular plate, the mean square velocity is defined as:

$$\langle \dot{w}^2(\omega) \rangle = \frac{\omega^2}{8} \sum_{m,n} A_{mn}^2. \quad (26)$$

The far-field sound pressure radiated in the far field is given by the following equation (see for example Junger and Feit²³):

$$p(R, \theta, \phi, \omega) = -\rho_0 \omega^2 \tilde{w}(\lambda, \mu) \frac{e^{jkR}}{2\pi R} \\ = -\rho_0 \omega^2 \frac{e^{jkR}}{2\pi R} \sum_{m,n} A_{mn} \tilde{w}_{mn}(\lambda, \mu), \quad (27)$$

where $\lambda = k \sin \theta \cos \phi$ and $\mu = k \sin \theta \sin \phi$.

E. Comparison of structural analysis algorithms

An estimate of the relative performance of both methods, the substructuring approach and the direct solution, can be obtained by calculating an order of complexity, defined by the summation of all the basic operations required for each algorithm, as a function of the variable quantities: the number of modes, MN , and the number of masses, R .²⁴ Such a measure cannot be taken as a direct estimate of the actual CPU time, but rather as a comparative quantity between two competing algorithms. A reasonable estimate is to consider that a floating point addition, subtraction, multiplication, or division takes one unit of time while a sine or cosine takes six units. Experiments on a personal computer have shown that the approximation is correct. Although this parameter is partially machine-dependent, its influence on the global order of complexity is small, as it will be shown. Calculating a modal function $w(x_1, x_2)$ at one point, following Eq. (4), requires 2 sines and 7 multiplications or divisions. Therefore, 19 units of time are required.

The total number of operations required for calculating the mean square velocity of a plate carrying R masses and excited by a point-force is equal, for the Rayleigh–Ritz method, to the values given in Table I. The same analysis for the substructuring algorithm is found in Table II.

Summing up the terms of Tables I and II, the complexity of the Rayleigh–Ritz algorithm is expected to be:

$$O\left(\frac{19}{2}(MN+3) + MN[R(MN+1) + 6 + (MN)^3]\right), \quad (28)$$

TABLE I. Analysis of the Rayleigh–Ritz resolution algorithm.

Algorithm step	$w(x_1, x_2)$	+ or -	\times or \div
$[M]$	$\frac{1}{2}(MN)(MN+1)$	$\frac{1}{2}R(MN)(MN+1)$	$\frac{1}{2}R(MN)(MN+1)$
$[K]$	0	MN	MN
$\{F\}$	MN	MN	MN
A_{mn}	0	$\frac{1}{2}(MN)^3$	$\frac{1}{2}(MN)^3$
$\langle \dot{w}^2(\omega) \rangle$	0	MN	MN

TABLE II. Analysis of the substructuring algorithm.

Algorithm step	$w(x_1, x_2)$	+ or -	× or ÷
A_{ij}	$\frac{1}{2}R(R+1)MN$	$\frac{1}{2}R(R+1)MN$	$\frac{1}{2}R(R+1)MN$
F_m	0	$\frac{1}{2}R^3$	$\frac{1}{2}R^3$
A_{mn}	$1+R$	$6MN$	$2MN$
$\langle \dot{w}^2(\omega) \rangle$	0	MN	MN

while the substructuring algorithms has a complexity order given by:

$$O(MN^{\frac{19}{2}}R(R+1) + (10+R(R+1)) + R^3). \quad (29)$$

The substructuring method is therefore expected to be faster than the direct Rayleigh–Ritz method by the ratio of Eq. (28) divided by Eq. (29). Since this ratio is a machine-independent quantity, it can be compared with experimental results obtained using any computer. Both theoretical and experimental results are presented in Fig. 5, as a dimensionless ratio of the CPU time required for the substructuring method divided by that required for the direct method. A ratio smaller than one means that a shorter time is required by the substructuring approach.

For a plate carrying a single point-mass, results presented in Fig. 5 shows that the substructuring method is always faster, for any number of modes considered. For a larger number of masses, the substructuring method is still faster, but only when a larger number of modes is taken into account. The modal order given here corresponds to the number of modes considered over one direction of the plate. The total number of modes is hence the square of the modal order.

It can also be seen from Fig. 5 that the theoretical analysis is a very conservative bound over the real efficiency of the substructuring method for the five masses problems, while the theoretical curve for the one mass problem is slightly optimistic. Therefore, the theoretical curves taken together give correct upper and lower bounds over the expected performance of the substructuring algorithm. Some error is inherent to these curves since everything but floating point operations have been neglected. It is also obvious from Eqs. (28) and (29) that the sine-dependent terms, that is, the terms related to the 19/2 factor have a small influence for large M and N . Therefore, the relative CPU time required for

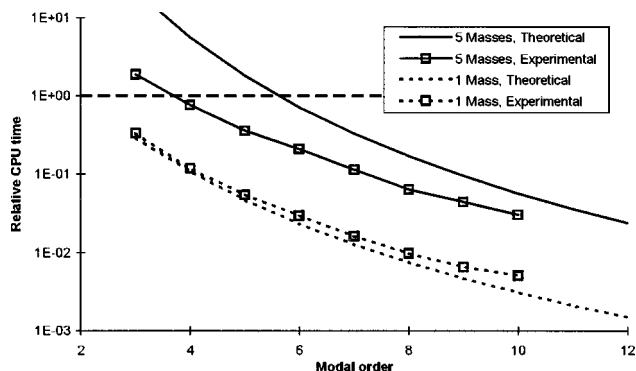


FIG. 5. Comparison of relative CPU times for the substructuring method and the direct method, for the plate carrying a single mass and five masses.

TABLE III. Structural and acoustic data of the test case.

Plate properties:		
Length	a	0.7 m
Width	b	0.5 m
Thickness	h	5 mm
Elastic modulus	E	210 GPa
Loss factor	η	10^{-3}
Poisson ratio	ν	0.3
Density	ρ	7850 kg/m ³
Fluid properties:		
Density	ρ_0	1.22 kg/m ³
Sound velocity	C_0	340 m/s

calculating a sine compared to another operation has a small influence on the global complexity. Using these results, it can also be forecast that CPU times required for solving optimization problems with a genetic algorithm will be reduced by one or two orders of magnitude with the substructuring approach, compared to a direct Rayleigh–Ritz solution.

III. SINGLE POINT-MASS OPTIMIZATION

The genetic algorithm optimization method has been tested on a rectangular plate carrying up to five point-masses. However, a simpler test case is studied first, using the GA for optimally positioning a single point-mass. The system considered here is described in Table III. The single-mass problem is useful for evaluating the performance of the optimization algorithm since in this case, an exhaustive search over all possible mass locations can be performed and the results can be plotted as a surface representing the fitness value in three-dimensional space. This plotting would not be possible for the general case of R masses because it would require plotting a function in a $(2R+1)$ -dimensional space.

Two test cases are presented here. In both cases, the plate is excited by a point-force of 1 Newton at the point $(17a/64, 23b/64)$, and the mean square velocity averaged over a given frequency band is used as the optimization criterion. The value of the point-mass is equal to 30% of the plate mass. For the first case, the frequency band, from 50 to 70 Hz is centered around the first natural frequency of the plate (60 Hz). For the second case, the 0–600 Hz band is considered, including 12 vibration modes of the plate.

Figure 6 shows the mean square velocity averaged over the 50–70 Hz band as a function of the mass location, while the same results for the 0–600 Hz band are presented in Fig. 7. In both cases, the plate was discretized into 64×64 positions and the axis scaling therefore represents the values of the discretized positions, between 0 and 64. Average values, in all cases, were calculated using a frequency increment of 1 Hz, in order to take into account sharp resonance peaks. Decibels values for the mean square velocities are always calculated using a reference velocity of $1 \text{ m}^2/\text{s}^2$.

Comparing both figures, it can be seen that the optimal mass position with respect to the selected criterion (mean square velocity) is a function of the excitation point as well as of the maximum displacement points of the excited modes. For a narrow band excitation, including only the first

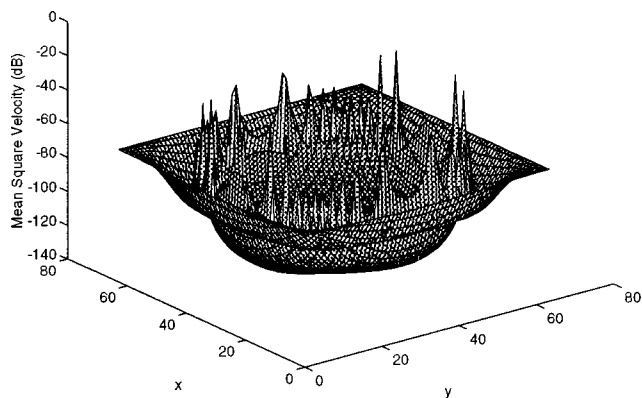


FIG. 6. Mean square velocity averaged over the 50–70 Hz band for all the possible positions of a point-mass on the plate. The frequency band includes only the first vibration mode of the plate.

vibration mode (Fig. 6), the optimal position tends to be close to the point of maximum displacement for the dominant mode (plate center). However, for a large number of modes, the maximum displacement points of the various modes tend to average out and the optimal position of the mass drifts to the excitation point, as can be seen in Fig. 7. The excitation point is indicated by an arrow in Fig. 7.

The same results are presented in Fig. 8 under the form of a frequency response function for the best solution in each case. As can be seen on this figure, optimizing the response into the 50–70 Hz band by placing the mass at the center of the plate effectively creates a “hole” in that band, while the best average reduction is achieved by placing the mass on the excitation point.

A. GA behavior for the single mass optimization

The GA have been tested on the two cases presented above. Selection of the best GA parameters for a given problem is far from a straightforward task. In some cases, when interested in exploiting the maximum of the possibilities of GA, this task might become as complicated as requiring a meta-GA for optimizing the GA parameters.²⁵ However, in the present case, only the parameters described in Sec. I are considered:

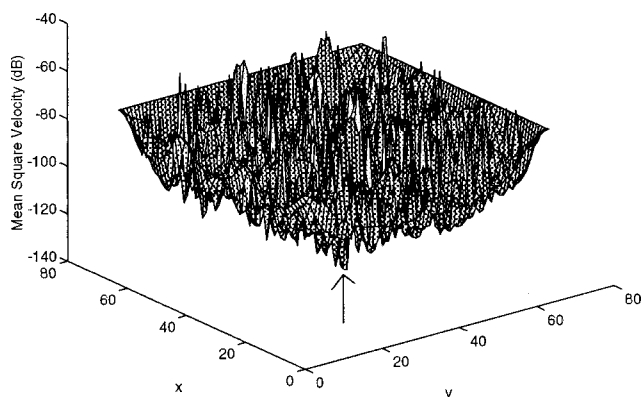


FIG. 7. Mean square velocity averaged over the 0–600 Hz band for all the possible positions of a point-mass on the plate. The frequency band includes 12 vibration modes, and the global minimum is indicated by an arrow.

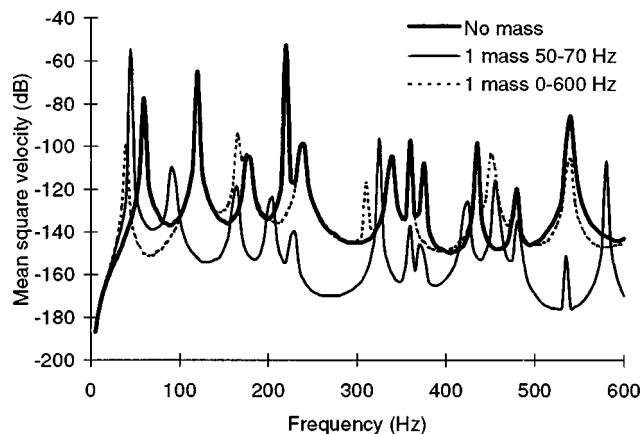


FIG. 8. Mean square velocity versus frequency for the plate alone, for the plate carrying a single mass optimized to reduce vibration level in the 50–70 Hz band, and in the 0–600 Hz band.

- Integer numbers coding;
- Uniform crossover;
- Mutation rate: 1/40;
- Rank selection, due to the irregular nature of the fitness functions;
- Elitist selection, in order to prevent the best solution found at a given generation from being lost at the next generation.

The stopping criterion for the genetic algorithm was chosen as a maximum number of generations to be performed. Since the 50–70 Hz fitness function is quite smooth while the 0–600 Hz function is highly irregular (as can be seen in Figs. 6 and 7), a larger population size and a greater number of generations must be used for the second case. These parameters were selected respectively as 25 individuals and 20 generations for the 50–70 Hz case, and 40 individuals and 50 generations for the 0–600 Hz case.

The effect of the selective pressure, Eq. (1) has been studied for the two cases. Results obtained from an average of five GA runs are shown in Fig. 9 for the 50–70 Hz case and in Fig. 10 for the 0–600 Hz case. Both curves show the fitness value (mean square velocity) of the best solution found at each generation as a function of the total number of function calls. It can be seen from Fig. 9 that a high value of

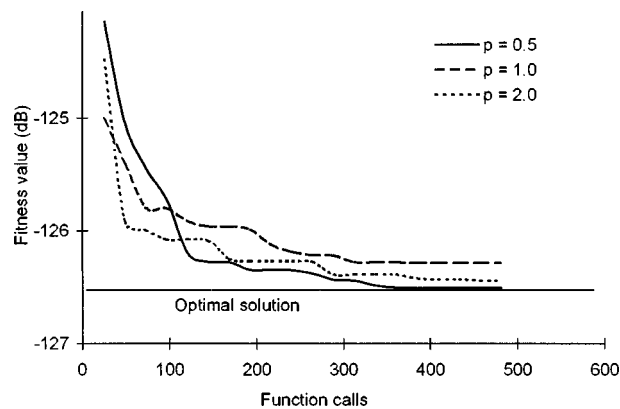


FIG. 9. Effect of selective pressure on the rate of convergence for the minimization of mean square velocity of the plate carrying a single point-mass in the 50–70 Hz band.

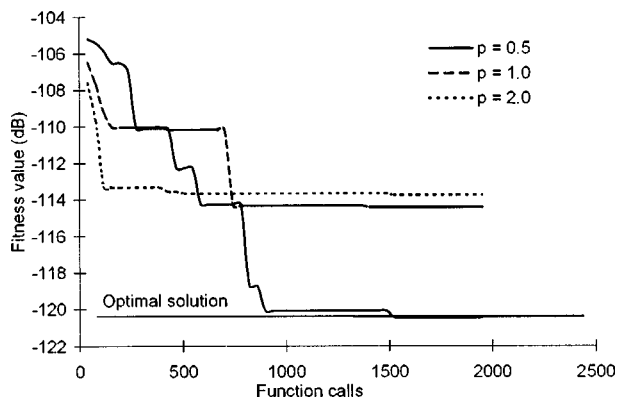


FIG. 10. Effect of selective pressure on the rate of convergence for the minimization of mean square velocity of the plate carrying a single point-mass in the 0–600 Hz band.

selective pressure (2.0) significantly increases the rate of convergence, but at the expense of a slightly suboptimal solution. Selective pressure corresponds to the exponent p in Eq. (1). However, in this case, the difference between the three curves is small enough that even the worst case gives an acceptable solution. In all of the runs, the solution found by the GA was very close to the optimal solution, in the middle of the plate, giving a variability in the resultant vibration reduction of less than 0.5 dB.

For the 0–600 Hz case, the algorithm is getting more sensitive to the correct selection of parameters. In this case, due to the highly irregular nature of the fitness function, a high value of selective pressure induces premature convergence to nonoptimal solution. Only the lowest value of selective pressure ensures convergence to the optimal solution. Optimal positions found by the GA with a higher selective pressure were somehow far from the true optimal point, e.g., close to the excitation point, due to entrapment into local minimums.

It should also be noted that the CPU times required for the 0–600 Hz case was about 120 times that of the 50–70 Hz case. This huge difference can be explained by several factors: (1) the total number of fitness function calls, (2) the larger frequency integration bandwidth of the fitness function and (3) the larger number of modes that must be taken into account for an adequate representation of the plate response, growing from 5^2 to 8^2 .

IV. MULTIPLE MASSES OPTIMIZATION

The case considered now consists of determining the optimal positions of five masses on the plate, each one representing 20% of the plate mass. Adding the five point-masses is thus equivalent to doubling the total mass. This case represents a much more difficult optimization problem compared to the single mass problem, due to the large number of possible combinations. For a plate spatially discretized into K possible positions with R nondistinct masses, it can be shown that the total number of possible combinations is given by the binomial coefficient:

$$\binom{K}{R} = \frac{K!}{R!(K-R)!} \quad (30)$$

By nondistinct masses, it is meant that the permutation of two masses is not considered as a distinct combination. This applies when all masses are identical. Otherwise, using differently sized masses, the size of the search space would be multiplied by $(R!)$, the number of permutations of R masses. In order to maximize the efficiency of the search, a redundancy-checking step should be added to the basic genetic algorithm, for rejecting duplicate solutions, in order to maintain population diversity. With this aspect in mind, solutions are considered to be duplicates if they bear the same coordinate values, even if these coordinates are not placed in the same order on the genetic code. It should also be noted that for multi-modal functions, the same position on the genetic code from two parents may be occupied by different locally optimal solutions. Crossover necessarily causes the loss of one of these two solutions. However, by the virtue of selection, if both solutions are good enough, many copies of them will be used as parents, ensuring that no relevant information is lost.

Using $K=64 \times 64$ discrete positions, the single mass problem has 4096 possible combinations, while the 5 identical masses problem yields as many as 9.6×10^{15} possibilities, making an exhaustive search impractical. For this reason, the five masses problem must be dealt with using a larger population and a greater number of generations. Values of 100 individuals and 200 generations have been chosen. Several cases were considered, using various excitations and optimization criteria. It should be noted that in all cases, repeated GA runs have given different values of the optimal positions, but these positions corresponded to very similar values of the fitness function. Since the masses coordinates were dealt with using integer numbers, there is no possible accumulation of numerical roundoff error. Therefore, variations in optimal solution from one run to another suggest either that the solution to the problem is not unique, or that slightly suboptimal solutions were attained in each case.

A. Mean square velocity minimization under point-force excitation

The case considered here is the minimization of the mean square velocity over the 200–250 Hz frequency band, an intermediate case including two vibration modes, under excitation by a point-force at the point $(17a/64, 23b/64)$. In order to reduce as much as possible the plate mobility at the excitation point, one could think about placing all of the concentrated masses right on that point. The optimal positions of the five point-masses after running the GA is shown in Fig. 11(a). This configuration does not correspond to the intuitive solution of putting all the masses at the excitation point. It should be noted that other runs gave significantly different positions, but small differences in fitness values. The effect of the optimization is shown in Fig. 12 by plotting the mean square velocity of the plate without masses, of the plate with optimally placed masses and with all masses placed on the excitation point. Since the total mass of the plate plus point-masses is twice that of the plate alone, a comparison is done with the frequency-response of a double thickness plate. It can be seen that the optimal solution actually represents a minimum in the frequency range of interest,

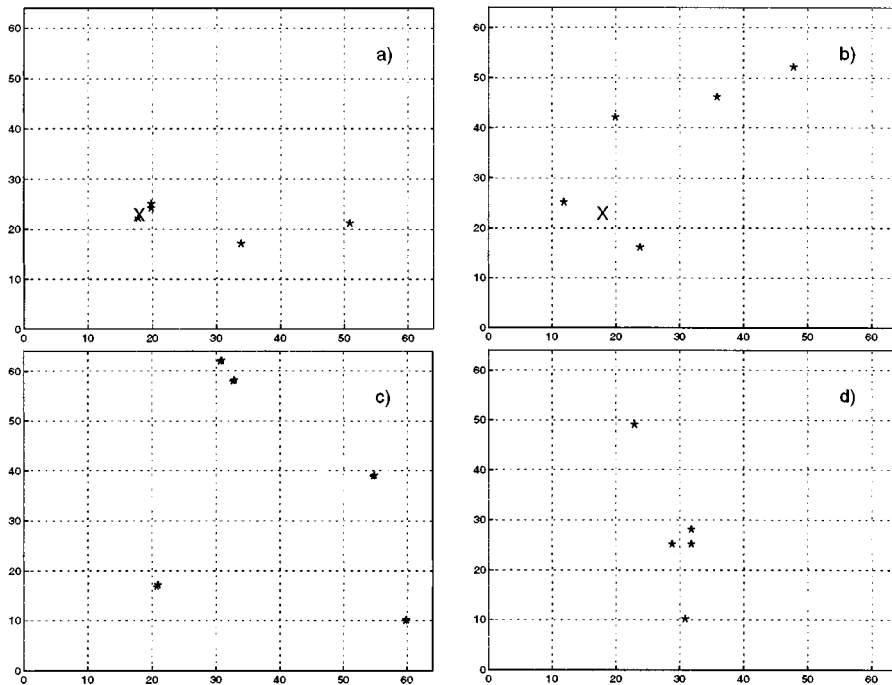


FIG. 11. Optimal positions of five point-masses in the 200–250 Hz band. Each mass represents 20% of the plate mass. X: excitation point, in case of a point-force excitation. (a) Point-force excitation on coordinates $(17a/64, 23b/64)$, minimization of the mean square velocity. (b) Point-force excitation, minimization of sound pressure radiated in the direction $(\theta, \phi) = (\pi/4, \pi/4)$. (c) Plane wave excitation at an angle $(\theta, \phi) = (\pi/4, \pi/4)$, One-point pressure reduction. (d) Plane wave excitation, minimization of the average far-field sound pressure.

compared to placing all the masses on the excitation point, although the plate response may be increased at other frequencies. The optimal solution gives an average reduction of 70 dB in the 200–250 Hz band by rejecting all the resonant frequencies out of that band, while the intuitive solution gives only 56 dB of reduction. Doubling the thickness has the effect of shifting resonances to higher frequencies, but does not yields any important reduction compared to the optimal placement of point-masses.

B. Far-field sound pressure minimization under point-force excitation

The case considered now is that of a plate excited by a point-force, using an acoustical optimization criterion: the far field sound pressure radiated in the far-field in direction $(\theta, \phi) = (\pi/4, \pi/4)$. Using the genetic algorithm, resulting optimal positions of the five masses are those shown in Fig. 11(b). It can be seen that these positions are somewhat different from those found when minimizing a vibratory criterion. The effect of mass position optimization is illustrated by plotting the far-field sound pressure in the direction $(\theta, \phi) = (\pi/4, \pi/4)$ with and without masses (Fig. 13). In this figure, the far-field sound pressure is plotted as a normalized directivity value, dividing the effective sound pressure by a factor of $\rho_0 \omega^2$. The reference value for the calculation of the normalized far-field sound pressure is thus one (dimensionless). Figure 13 shows that the optimal solution is actually better than placing all the masses on the excitation point, by rejecting the modes out of the frequency band of interest and introducing two sound pressure minima in this band.

Some physical insights into the sound radiation minimization can be gained by observing the modal redistribution of the displacement field after using the optimally placed masses. The most interesting phenomenon arises at the frequency of 212 Hz, corresponding to a minimum of sound radiation in Fig. 13. Without any added mass, plate displace-

ment at this frequency is mainly contributed by mode 3-1, a symmetric, and efficiently radiating mode. Using the optimally placed masses, contribution has been mainly transferred to modes 1-2 and 2-1, which are asymmetrical and therefore have a lower radiation efficiency than mode 3-1.

In order to reduce the cost of computing the frequency response in a relatively large frequency band, a ‘‘quick and dirty’’ fitness function has been tried out using a single frequency of 220 Hz instead of integrating the function over the whole frequency band. It can be seen that great care must be taken for the choice of the fitness function since in that case, the 200–250 Hz function gives a 58 dB reduction while the single-frequency fitness function gives an overall reduction of only 42 dB. However, this reduction is still better than the intuitive solution (all the masses on the excitation point) with a 28 dB reduction.

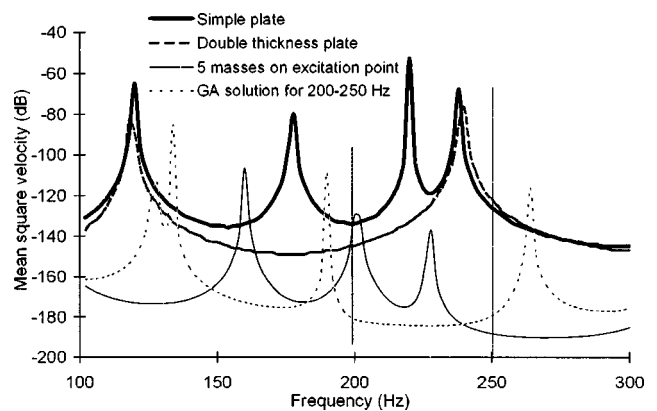


FIG. 12. Mean square velocity of the plate carrying five masses on optimal positions. Optimization with respect to the mean square velocity in the 200–250 Hz band.

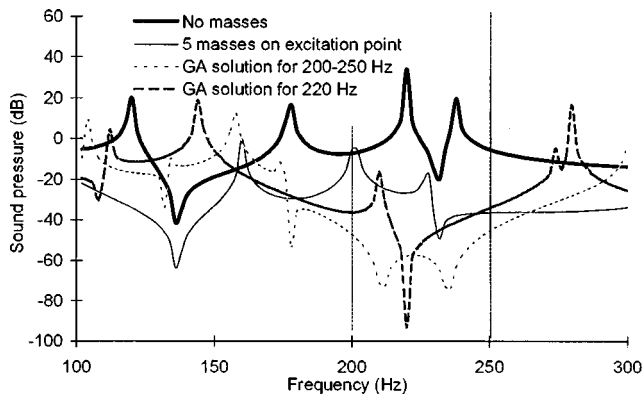


FIG. 13. Normalized far-field sound pressure (directivity) in the direction $(\theta, \phi) = (\pi/4, \pi/4)$ for the plate without masses and with five masses optimally placed for reducing the sound radiation in this direction. Point-force excitation.

C. Far-field sound pressure minimization under plane wave excitation

In the previous cases, reduction of noise radiated by a mechanically excited plate has been studied, giving insights into the control of structure-borne sound. However, another important aspect of the problem is the control of sound transmission through a plate. This latter aspect can be dealt with in the exact same framework, by considering the case of a plate excited by an acoustical plane wave in the direction $(\theta, \phi) = (\pi/4, \pi/4)$. Minimization of the sound transmitted in the same direction in the 200–250 Hz band has been considered as an optimization criterion. Optimal positions of five masses on the plate were found using the genetic algorithm, and these positions are shown in Fig. 11(c). It can be seen that the optimal positions are different from those obtained for the mechanically excited plate, indicating that the optimal solution strongly depends on the excitation as well as on the structure itself.

The sound pressure radiated by the plate without masses, and by the plate with optimally placed masses is shown in Fig. 14. The solution of placing all the masses at the center of the plate is also presented in Fig. 14. According to the results, placing all the masses at the center of the plate is actually harmful, giving an average increase of 4 dB in the

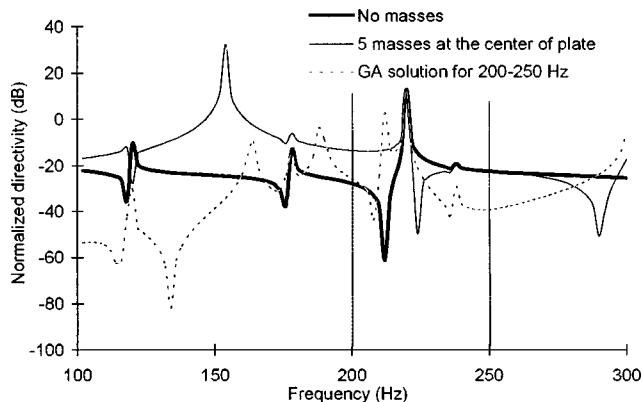


FIG. 14. Normalized far-field sound pressure (directivity) in the direction $(\theta, \phi) = (\pi/4, \pi/4)$ for the plate alone, with five masses placed at the center of the plate, and with masses optimized for reducing the sound pressure in the direction $(\theta, \phi) = (\pi/4, \pi/4)$. Plane wave excitation.

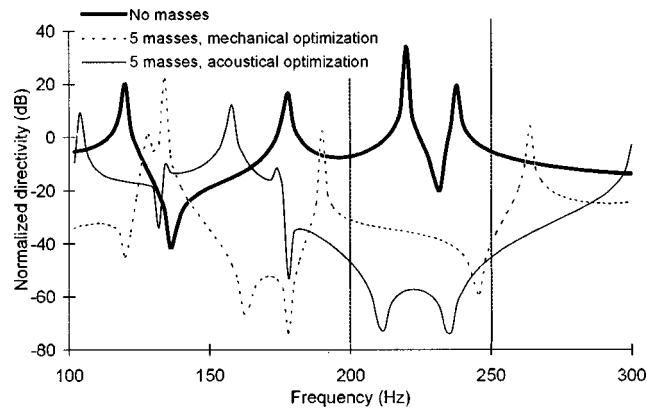


FIG. 15. Normalized far-field sound pressure (directivity) in the direction $(\theta = \pi/4, \phi = \pi/4)$ for the plate without masses and with five masses optimized for: (1) sound pressure minimization in the direction $(\theta, \phi) = (\pi/4, \pi/4)$ point and (2) mean square velocity minimization. Point-force excitation.

200–250 Hz band while the optimal solution found by the GA gives a reduction of 4 dB. These values also indicate that the control of acoustic transmission with added masses seems to be, at least for the present case, much less efficient than the control of structure-borne noise.

D. Selection of an optimization criterion

A question arising at this point is whether an optimization based on a vibratory criterion can help reduce noise radiation or not, and on the other hand, whether an acoustic optimization can contribute to the reduction of structural vibrations or not. An indication on this is provided by calculating both vibratory and acoustical responses using the optimal mass positions found for both criteria. Results shown in Fig. 15 for the sound radiated, and in Fig. 16 for the mechanical response indicate that, in both cases, some reduction is obtained using either criterion, but the maximum reduction cannot be attained unless the correct criterion is used. For the noise reduction, using the appropriate criterion gives a 58 dB reduction compared to 38 dB with the vibra-

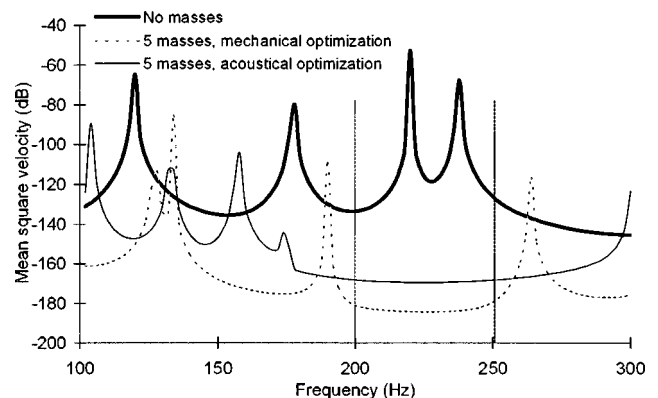


FIG. 16. Mean square velocity for the plate without masses and with five masses optimized for: (1) sound pressure minimization in the direction $(\theta = \pi/4, \phi = \pi/4)$ and (2) mean square velocity minimization. Point-force excitation.

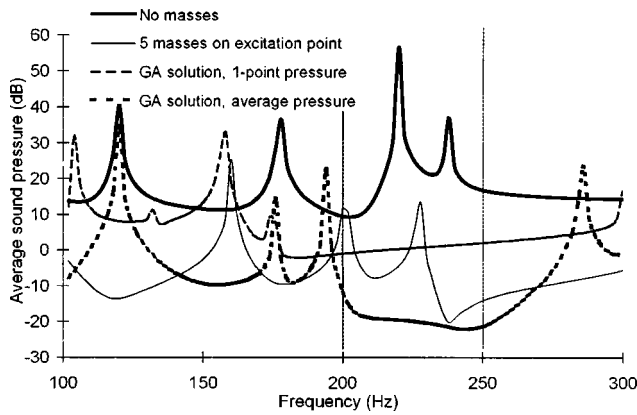


FIG. 17. Average far-field sound pressure with masses positions optimized for average sound pressure minimization and for one-point sound pressure minimization in the direction ($\theta = \pi/4, \phi = \pi/4$). Point-force excitation.

tory criterion, and for the vibration reduction, using the right criterion gives a reduction of 70 dB compared to 56 dB using the acoustic criterion.

In the case presented in this paper, the characteristic quantity ka , wave number times characteristic length of the vibrating structure, is in the range of 1 to 5. For such an intermediate range of ka , directivity effects must be taken into account, and minimizing the mean square velocity may help reducing radiated noise or not, as well as minimizing volume velocity. No conclusion may therefore be drawn *a priori*. Another aspect of the same question concerns the potential reduction of the overall sound pressure radiated when minimizing the sound pressure in a prescribed direction. The average sound pressure is in this case proportional to the integral of the sound pressure over the half-space above the plate:

$$p_{\text{ave}}(\omega) = \int_0^{\pi/2} \int_0^{2\pi} \left[\rho_0 \omega^2 \sum_{m=1}^M \sum_{n=1}^N A_{mn} \tilde{w}_{mn}(\lambda, \mu) \right] d\phi d\theta. \quad (31)$$

As can be seen in Fig. 17, average sound pressure reduction using the solution obtained for minimization of sound radiation in one direction gives a reduction of 21 dB, while the trivial solution that consists in placing all the masses on the excitation point gives 28 dB of reduction. However, when the optimization is properly done using the overall sound pressure as an optimization criterion, a maximal reduction of 41 dB is attained as shown in Fig. 17. The case presented here is for a point-force excitation. Such an increased reduction is obtained at the expense of a (numerically speaking) very expensive fitness function, since it is required to integrate the sound pressure over the frequency range and over the whole half-space above the plate.

V. CONCLUSION

Genetic algorithms have been presented in the context of structural design optimization for vibroacoustic reduction. It has been shown that the use of such an optimization procedure can help in finding original solutions that would not have been found by any intuitive means. In these cases, a serious advantage of GA is that no *a priori* bracketing of the

optimal solution is needed, allowing a completely open search over the whole optimization space. Therefore, GA are well-suited for vibroacoustics problems for their ability to deal with highly irregular functions. Performing such an open search can be done using GA at a very low cost, when compared to the cost of an exhaustive search, especially for problems having a large number of dimensions. In the five-masses problem considered in this paper, an optimal solution has been found after running the GA for 2×10^5 function calls while an exhaustive search in this case requires about 10^{16} function calls.

Numerical results also demonstrated that great care must be taken for the choice of an optimization criterion, since a compromise must always be made between the computational efficiency and the quality of the solution. This quality is influenced by several factors, including the choice of an appropriate frequency band corresponding to a given application and the choice of the most suitable vibroacoustic parameter. This vibroacoustic parameter must also be computed using an appropriate algorithm, since an improvement in computation time of two orders of magnitude have been attained in some cases by selecting the most appropriate algorithm.

ACKNOWLEDGMENT

This work was made possible thanks to the support from IRSST.

- ¹J. H. Holland, *Adaptation in Natural and Artificial Systems* (MIT, Cambridge, 1975).
- ²A. J. Keane, "Experiences with optimizers in structural design," in *Proceedings of the Conference on Adaptive Computing in Engineering Design and Control 94*, edited by I. C. Parmee (1994), pp. 14–27.
- ³A. J. Keane, "A brief comparison of some evolutionary optimization methods," in *Modern Heuristic Search Methods*, edited by V. Rayward-Smith *et al.* (Wiley, New York, 1994).
- ⁴A. J. Keane, "Passive vibration control via unusual geometries: The application of genetic algorithm optimization to structural design," *J. Sound Vib.* **185**, 441–453 (1995).
- ⁵A. J. Keane and S. M. Brown, "The design of a satellite boom with enhanced vibration performance using genetic algorithm techniques," in *Proceedings of the Conference on Adaptive Computing in Engineering Design and Control 96*, edited by I. C. Parmee (1996), pp. 107–113.
- ⁶M. O. Tokhi and M. A. Hossain, "Active vibration control of flexible beam structures using genetic algorithms," in *Proc. 4th Int. Congress on Sound and Vibration*, St-Petersburg, Russia (Int. Scientific Publications, Auburn, AL, 1996), pp. 423–430.
- ⁷J. Onada and Y. Hanawa, "Actuator placement optimization by genetic and improved simulated annealing algorithms," *AIAA J.* **31**, 1167–1169 (1992).
- ⁸B.-T. Wang, "Applications of genetic algorithms to the optimum design of active control system," in *Proc. Noise 93* (1993), pp. 231–236.
- ⁹K. H. Baek and S. J. Elliott, "Natural algorithms for choosing source locations in active control systems," *J. Sound Vib.* **186**, 245–267 (1995).
- ¹⁰M. T. Simpson and C. H. Hansen, "Use of genetic algorithms to optimize vibration actuator placement for active control of harmonic interior noise in a cylinder with floor structure," *Noise Control Eng. J.* **44**, 169–184 (1996).
- ¹¹R. L. St. Pierre, Jr. and G. H. Koopmann, "A design method for minimizing the sound power radiated from plates by adding optimally sized, discrete masses," *Trans. of the ASME, Special Design Issue* **117**, 243–251 (1995).
- ¹²A. J. McMillan and A. J. Keane, "Shifting resonances from a frequency band by applying concentrated masses to a thin rectangular plate," *J. Sound Vib.* **192**, 549–562 (1996).
- ¹³A. J. McMillan and A. J. Keane, "Vibration isolation in a thin rectangular

- plate using a large number of optimally positioned point masses,” *J. Sound Vib.* **202**, 219–234 (1997).
- ¹⁴A. S. Fraser, “Simulation of genetic systems,” *J. Theor. Biol.* **2**, 329–346 (1962).
- ¹⁵D. E. Goldberg and K. Deb, “A Comparative Analysis of Selection Schemes Used in Genetic Algorithms,” in *Foundations of Genetic Algorithms*, edited by G. J. E. Rawlins (Morgan Kaufmann, San Mateo, CA, 1991), pp. 69–93.
- ¹⁶P. J. B. Hancock, “An empirical comparison of selection methods in evolutionary algorithms,” in *Evolutionary Computing, AISB Workshop*, edited by T. C. Fogarty (Springer-Verlag, Berlin, 1994), pp. 80–94.
- ¹⁷W. W. Hines and D. C. Montgomery, *Probability and Statistics in Engineering and Management Science* (Wiley, New York, 1987).
- ¹⁸T. Bäck and H.-P. Schwefel, “An Overview of Evolutionary Algorithms for Parameter Optimization,” *Evolutionary Computation* **1**, 1–23 (1993).
- ¹⁹D. B. Fogel, “An Introduction to Simulated Evolutionary Optimization,” *IEEE Trans. Neural Netw.* **5**, 3–14 (1985).
- ²⁰G. Rudolph, “Convergence analysis of canonical genetic algorithms,” *IEEE Trans. Neural Netw.* **5**, 96–101 (1985).
- ²¹X. Qi and F. Palmieri, “Theoretical analysis of evolutionary algorithms with an infinite population size in continuous-space. Part I: Basic properties of selection and mutation,” *IEEE Trans. Neural Netw.* **5**, 102–119 (1985).
- ²²X. Qi and F. Palmieri, “Theoretical analysis of evolutionary algorithms with an infinite population size in continuous space. Part II: Analysis of the diversification role of crossover,” *IEEE Trans. Neural Netw.* **5**, 120–128 (1985).
- ²³M. C. Junger and D. Feit, *Sound, Structures and Their Interaction* (Acoustical Society of America, Woodbury, NY, 1993).
- ²⁴D. E. Knuth, *The Art of Computer Programming* (Addison-Wesley, Reading, MA, 1997), 3rd ed., Vol. 1.
- ²⁵J. J. Grefenstette, “Optimization of control parameters for genetic algorithms,” *IEEE Trans. Syst. Man Cybern.* **16**, 122–128 (1986).

Active structural acoustic control of an infinite ribbed plate under light fluid loading

Nicole J. Kessissoglou and Jie Pan

Department of Mechanical and Materials Engineering, University of Western Australia, Western Australia, 6907, Australia

(Received 21 May 1997; accepted for publication 25 August 1998)

Active control can be applied to a vibrating structure to attenuate the acoustic radiation from the structure. In this paper, active structural acoustic control (ASAC) techniques are applied to a ribbed plate in order to minimize the structurally radiating sound fields. Using feedforward control strategies, multiple control forces are applied to the reinforcing beam. Modifying the structural response results in attenuation of the radiating sound fields. Cost functions are developed for the minimization of the far-field radiating sound pressure and far-field sound power. Optimization of the control system is achieved by using information on the structural coincidence conditions, and in determining the optimal error sensor location. Results demonstrate that significant reduction in the far-field sound pressure and sound power can be achieved in a large range away from the grazing angles. The effect of the control system on the structural response is also investigated. © 1998 Acoustical Society of America. [S0001-4966(98)03412-2]

PACS numbers: 43.40.Vn [PJR]

INTRODUCTION

Many structures containing discontinuities can be found in a wide variety of applications such as ship and submarine hulls, aircraft structures, and as large panels in acoustic enclosures. These discontinuities scatter the structural vibrations that primarily exist due to mounted machinery or engines, and the scattered vibrations generate wave types that subsequently result in sound fields radiating from the structure. Although sound radiation from ribbed plates has been extensively researched in the last few decades,^{1,2} there has been very little consideration given to the attenuation of the sound radiation from such structures using active control methods.

Active structural acoustic control is the relatively new approach to actively attenuate the structurally radiated sound fields. It is achieved by the more practical approach of applying control inputs to the structure, instead of in the surrounding fluid field. Reduction of the far-field sound radiation can be achieved by modifying the structural response. Previous work concerned with the control of sound radiation from fluid-loaded structures have mainly been concerned with homogeneous structures.³ However, it is important to recognize that discontinuities in structures can result in different wave types that may subsequently lead to the far-field radiation of sound. More recently, some work has been directed toward the active control of the far-field radiated sound fields resulting from the scattering of vibrational waves due to discontinuities on fluid-loaded plates.⁴ Gu and Fuller⁴ have investigated the active control of sound radiation due to subsonic wave scattering from discontinuities represented by a line constraint or a uniform reinforcing rib positioned on a fluid-loaded plate. They consider a subsonic incident flexural wave normal to the discontinuity. The rib discontinuity is described by a lumped mass system that has both translational and rotational inertia, which is approximated as exerting a reaction force and moment on the plate.

The far-field pressure is evaluated using the stationary phase approach on the Fourier wave number transformation. Active control is achieved by adding secondary line forces applied to the plate near the discontinuity.

In this paper, the acoustic fields resulting from the scattering of a structural wave field across a beam discontinuity are attenuated using ASAC methods. The active control system consists of multiple control forces applied to the reinforcing beam in order to modify the structural response. It is shown that significant reduction of the far-field sound pressure and sound power can be achieved by directly modifying the structural waves that contribute to the far-field sound radiation. The control application is optimized by using information of the structural coincidences. The effectiveness of the control system is evaluated by comparing the control performance due to an arbitrarily located error sensor with that of an optimally located error sensor. The effect of the control system on the structural response and near-field sound pressure is also investigated.

I. PRIMARY SOUND PRESSURE RADIATING FROM A RIBBED PLATE

The ribbed plate consists of an infinite homogeneous thin plate lying in the x - y plane which is symmetrically reinforced by two identical rectangular beams lying along the y direction at $x=0$, as shown in Fig. 1. The coupled structure is loaded with an acoustic fluid of density ρ_0 and sound speed c_0 on the upper side of the plate for $z>0$, and is *in vacuo* for $z<0$. If the fluid loading acting on the structure is considered to be light, then it can be assumed that the fluid loading does not affect the structural vibrations.

Figure 1 shows a subsonic flexural plane wave of amplitude A_{in} traveling in the x - y plane at a frequency ω and wave number k_p in the direction of its propagation, impinging obliquely at an angle φ to the x axis on the beam. The subsonic traveling plane wave can be described by

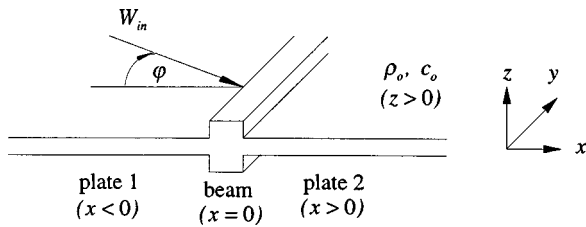


FIG. 1. Beam-plate structure separated into three subsystems: plate 1, beam, and plate 2, showing the flexural plane wave in plate 1 incident at the beam boundary.

$$W_{in}(x, y, t) = A_{in} e^{-j(k_p \cos \varphi)x} e^{j(k_p \sin \varphi)y} e^{j\omega t}, \quad x \leq 0. \quad (1)$$

The plate flexural wave number k_p is related to the plate parameters by

$$k_p = \sqrt{\omega} \left(\frac{\rho_p h}{D} \right)^{1/4}, \quad (2)$$

where $D = E_p h^3 / 12(1 - \nu^2)$ is the flexural rigidity of the plate, and ρ_p , h , D , E_p , and ν are, respectively, the density, thickness, flexural rigidity, Young's modulus, and Poisson's ratio of the plate. At frequencies well below critical, the speed of sound of the subsonic incident wave is less than the sound speed in the adjacent fluid (that is, $c_p < c_0$), and therefore no energy is radiated into the far field of the surrounding fluid. When the flexural wave motion in the plate impinges on the beam discontinuity, both flexural and torsional motions are induced in the beam, which results in transmitted and reflected subsonic propagating waves of coefficients T_p and R_p , respectively, and transmitted/reflected near-field decay waves of coefficients T_n/R_n in the plate. The scattering of the structural wave field produces supersonic structural waves, which contribute to the radiation of sound fields into the far field. To facilitate the discussion of the structural response, the ribbed plate system is separated as plate 1 for

$x < 0$ and plate 2 for $x > 0$, as shown in Fig. 1. For an infinite plate, there are no waves reflected from the infinities, and the resulting flexural displacement in plate 1 (on the same side of the beam as the incoming incident wave) consists of three wave components along the x direction: the subsonic incident wave, the subsonic reflected propagating wave, and the supersonic near-field reflection:

$$W_1(x, y, t) = [A_{in} e^{-j(k_p \cos \varphi)x} + R_p e^{j(k_p \cos \varphi)x} + R_n e^{k_n x}] e^{j(k_p \sin \varphi)y + j\omega t}, \quad x \leq 0, \quad (3)$$

where the coefficients R_p and R_n are the amplitudes of the reflected propagating and near-field waves, respectively, and $k_n = k_p(1 + \sin^2 \varphi)^{1/2}$ is the wave number of the near-field decay term in the plate.¹ Similarly, the flexural displacement in plate 2 can be described by

$$W_2(x, y, t) = [T_p e^{-j(k_p \cos \varphi)x} + T_n e^{-k_n x}] \times e^{j(k_p \sin \varphi)y + j\omega t}, \quad x \geq 0, \quad (4)$$

where T_p and T_n are the amplitudes of the transmitted propagating and near-field waves, respectively. For continuity of the plane waves in the y direction, the beam-plate system has the same periodicity of motion along the y direction. The coefficients T_p , R_p , T_n , and R_n have been determined previously,⁵ by making use of the equations of motion of the structural vibrations and the coupling conditions at the beam-plate boundaries.

An expression for the primary sound pressure field has also been determined previously,⁶ using the acoustic wave equations and the coupling conditions between the structure and the fluid at the surface of the structure. The expression consists of a constant in terms of the scattered structural waves, and an integration of the structural wave number spectrum:

$$p_p(x, y, z) = - \frac{\omega^2 \rho_0 e^{j(k_p \sin \varphi)y - (k_p^2 - k_0^2)^{1/2} z}}{2(k_p^2 - k_0^2)^{1/2}} [A_{in} e^{-j(k_p \cos \varphi)x} + R_p e^{j(k_p \cos \varphi)x} + T_p e^{-j(k_p \cos \varphi)x} + R_n e^{k_n x} + T_n e^{-k_n x}] - \frac{j\omega^2 \rho_0 e^{j(k_p \sin \varphi)y}}{2\pi} \int_{-\infty}^{\infty} \left[\frac{A_{in}(k_p \cos \varphi - \gamma_{x_p}) - R_p(k_p \cos \varphi + \gamma_{x_p}) - T_p(k_p \cos \varphi - \gamma_{x_p})}{k_p^2 \cos^2 \varphi - \gamma_{x_p}^2} - \frac{R_n(jk_n - \gamma_{x_p}) + T_n(jk_n + \gamma_{x_p})}{k_n^2 + \gamma_{x_p}^2} \right] \frac{e^{j\gamma_{x_p} x - \gamma_{z_p} z}}{\gamma_{z_p}} d\gamma_{x_p}, \quad (5)$$

where γ_{x_p} is the primary structural wave number in the x domain. γ_{z_p} represents the primary acoustic wave number of the pressure field in the z direction and is defined as $\gamma_{z_p} = \sqrt{\gamma_{x_p}^2 - (k_0^2 - k_p^2 \sin^2 \varphi)}$, where $k_0 = \omega/c_0$ is the acoustic wave number of the fluid. The sound pressure field is evaluated in a cylindrical coordinate system defined by $x = r \cos \theta$, $z = r \sin \theta$, and $y = 0$, as shown in Fig. 2.

The wave number spectrum of the sound pressure field

can be separated into supersonic and subsonic wave number spectrums. The supersonic wave number spectrum directly contributes to the far-field radiating sound pressure, whereas the subsonic wave number spectrum dominates the near-field response. The supersonic wave number spectrum is defined by: $\gamma_{x_p} \leq \sqrt{k_0^2 - k_p^2 \sin^2 \varphi}$, which results in $\gamma_{z_p} = j\sqrt{k_0^2 - k_p^2 \sin^2 \varphi - \gamma_{x_p}^2}$. The supersonic wave number spectrum is further restricted by a limiting range for the incident

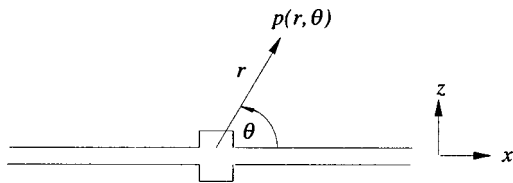


FIG. 2. Primary sound pressure field evaluated in the $x-z$ cylindrical coordinate system.

angle, where φ must be less than the critical incident angle, φ_c , which is defined by $\varphi_c = \sin^{-1}(k_0/k_p)$.

The far-field primary sound power is obtained by integrating the far-field radiated acoustic intensity over a semi-cylindrical surface centered at the beam discontinuity in the half-filled fluid space. The acoustic intensity I_π , is related to the square of the sound pressure by $I_\pi = |p|^2 / 2\rho_0 c_0$. Therefore the primary sound power radiated per unit length in the y direction is expressed as⁷

$$\Pi_p = \int_0^\pi \frac{|p_p|^2}{2\rho_0 c_0} r d\theta, \quad (6)$$

and only corresponds to far-field distances. The analysis and results of the primary sound pressure and sound power radiating from a lightly fluid-loaded ribbed plate has been previously discussed in great detail.⁶

II. ACTIVE CONTROL OF THE SOUND RADIATION

A. Secondary sound pressure field

The relatively new active control technique known as active structural acoustic control (ASAC) is employed to attenuate the radiating structure-borne sound. The control inputs are located on the surface of the structure, while the error sensing devices are represented as microphones which are located in the surrounding fluid field. The control system consists of multiple point control forces applied to the reinforcing beam. As shown in Fig. 3, the point forces are equally distributed by a distance Δ , and generate secondary flexural waves in the beam. The complexity of this control application is initially reduced by grouping the actuators together to have the same amplitudes, F_s , and a certain prefixed phase relationship with each other. This strategy is known as biologically inspired control.⁸ In order to optimize the system performance, the control system is then further modified using information on the structural coincidences. It has been previously shown that the greatest transmission of the plate flexural waves through the reinforcing beam occurs at the structural coincidences.⁹ Structural coincidences occur when the trace wave number of the incident flexural waves in the plate match either the natural flexural wave number in the beam (flexural coincidence), or the natural torsional wave number in the beam (torsional coincidence). The coincidence conditions occur at an angle of incidence corresponding to $\varphi_B = \sin^{-1}(k_B/k_p)$ for flexural coincidence, and $\varphi_T = \sin^{-1}(k_T/k_p)$ for torsional coincidence, where k_B, k_T are, respectively, the natural flexural and torsional wave numbers in the beam (see Table I). However, at the structural coincidences, the far-field primary sound pressure level is slightly decreased.⁶ This is due to the fact that at the coincidences,

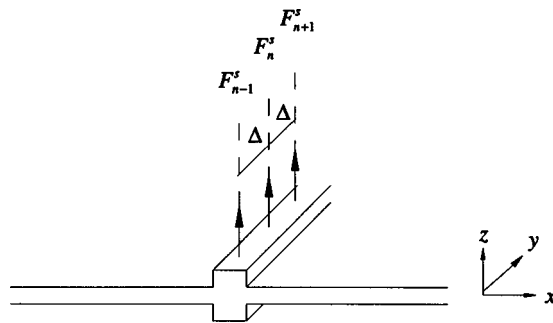


FIG. 3. Application of multiple point control forces to the reinforcing beam.

there is a large amount of flexural wave transmission through the reinforcing beam, thereby resulting in a more balanced distribution of the structural waves along the x direction (perpendicular to the beam). It has been previously shown that an imbalance in the structural response along the x -direction will generate a greater number of supersonic wave number components, which will thereby result in an increase in the far-field sound pressure level.⁶ Due to the symmetry of this control application, the secondary flexural waves generated by the forces radiate away equally in plates 1 and 2. This initially results in a uniform distribution of the secondary flexural waves in the plates. The phases of the control forces are pre-fixed such that the forces have a spatial phase variation with each other at the flexural coincidence condition. Hence, the secondary waves generated by the control forces radiate away equally from the beam into plates 1 and 2 at the flexural coincidence angle φ_B . Although the primary structural response may be either at coincidence or off-coincidence, the secondary structural response is always generated by forces with the phase delay in the beam corresponding to that of the flexural coincidence condition. Hence, at flexural coincidence, the total far-field sound pressure due to the superposition of the primary and secondary sound fields is optimized. At any off-coincidence condition, the superposition of the primary and secondary sound fields will result in the least increase in the supersonic wave number components to be attenuated.

The control approach described above has been previously applied to a ribbed plate, in order to achieve significant reduction of the flexural energy transmission in the far field of plate 2.⁹ For $2N+1$ forces, the control forces are described by

$$F_n^s = \sum_{n=-N}^N F_s e^{jk_B n \Delta} \delta(y - n \Delta), \quad (7)$$

where F_s is the complex amplitude of the control forces. Using this control approach, the total spectral response of the secondary waves in the plates is derived in the Appendix,

TABLE I. Material properties.

Material	Young's modulus (N/m ²)	Poisson's ratio	Density (kg/m ³)	Free wave speed (m/s)
Aluminum	$E = 6.9 \times 10^{10}$	$\nu = 0.33$	$\rho = 2700$	$c_p = \omega/k_p$
Air	$\rho_0 = 1.21$	$c_0 = 343$

and described in (A8). A general expression for the secondary sound pressure in wave number space can be obtained as⁶

$$P(\gamma_{x_s}, \gamma_{y_s}; z) = -\frac{\omega^2 \rho_0}{\gamma_{z_s}} \tilde{W}(\gamma_{x_s}, \gamma_{y_s}) e^{-\gamma_{z_s} z}, \quad (8)$$

where $\gamma_{z_s} = \sqrt{\gamma_{x_s}^2 + \gamma_{y_s}^2 - k_0^2}$ is the acoustic wave number of the secondary sound pressure in the z direction. The secondary sound pressure field can be obtained by taking a double inverse Fourier transform of $P(\gamma_{x_s}, \gamma_{y_s}; z)$.⁷ For an infinite number of control forces ($2N+1 \rightarrow \infty$), and using the following expressions:¹⁰

$$p_s(x, y, z) = -F_s \frac{\omega^2 \rho_0}{2E_b I} H(k_B) e^{jk_B y} \left[A_1 \cos(\sqrt{k_p^2 - k_B^2} x) \frac{e^{-(k_p^2 - k_0^2)^{1/2} z}}{\sqrt{k_p^2 - k_0^2}} + A_2 \cos(\sqrt{k_p^2 + k_B^2} x) \frac{e^{-j(k_p^2 + k_0^2)^{1/2} z}}{j\sqrt{k_p^2 + k_0^2}} \right] - F_s \frac{\omega^2 \rho_0}{2\pi E_b I} H(k_B) e^{jk_B y} \int_{-\infty}^{\infty} \left(\frac{\sqrt{k_p^2 + k_B^2} A_2}{k_p^2 + k_B^2 + \gamma_{x_s}^2} - \frac{j\sqrt{k_p^2 - k_B^2} A_1}{k_p^2 - k_B^2 - \gamma_{x_s}^2} \right) \frac{e^{j\gamma_{x_s} x - \gamma_{z_s} z}}{\gamma_{z_s}} d\gamma_{x_s}, \quad (11)$$

where A_1 and A_2 now become

$$A_1 = \frac{\sqrt{k_p^2 + k_B^2}}{\sqrt{k_p^2 + k_B^2 - j\sqrt{k_p^2 - k_B^2}}}$$

and

$$A_2 = -j \frac{\sqrt{k_p^2 - k_B^2}}{\sqrt{k_p^2 + k_B^2 - j\sqrt{k_p^2 - k_B^2}}};$$

$$H(k_B) = \frac{1}{(2jD/E_b I)(k_p^4 - k_B^4)[(k_p^2 - k_B^2)^{-1/2} + j(k_p^2 + k_B^2)^{-1/2}]},$$

and

$$\gamma_{z_s} = \sqrt{\gamma_{x_s}^2 - (k_0^2 - k_B^2)}.$$

It can be clearly observed in Eq. (12) that only the structural near-field decay waves (of coefficient A_2), and the secondary supersonic wave number spectrum (corresponding to $\gamma_{x_s} \leq \sqrt{k_0^2 - k_B^2}$) will contribute to the far field of the secondary sound pressure. There are also two pole locations in the wave number spectrum in Eq. (12), which are similar to those in the expression for the primary sound pressure field [Eq. (5)]. The first pole is located in the supersonic wave number spectrum and corresponds to the zero of γ_{z_s} . The second pole is contributed by the structural response, and corresponds to $\gamma_{x_s} = \sqrt{k_p^2 - k_B^2}$. This second pole lies in the subsonic wave number spectrum, and only contributes to the near-field sound pressure.

B. Minimization of the far-field sound pressure

The cost function chosen for the minimization of the far-field sound radiation from the ribbed plate is the square of the total sound pressure at an error sensor location

$$\lim_{K \rightarrow \infty} \frac{\sin Kx}{x} = \pi \delta(x), \quad (9)$$

$$\lim_{x \rightarrow 0} \frac{\sin x}{x} = 1, \quad (10)$$

yields the following expression for the secondary sound pressure described by a constant, and a wave number integration in the x domain:

(r_e, θ_e). The total sound pressure is the superposition of the primary and secondary sound fields, and can be expressed as:

$$p_{\text{tot}}(r, \theta) = p_p(r, \theta) + p_s(r, \theta), \quad (12)$$

where both sound fields are evaluated by the cylindrical coordinate system. By rewriting the secondary sound pressure field as $p_s = F_s G_s$, then the only variable to optimize is the complex amplitude of the control force. Hence, with this control arrangement, only a single control signal is required to drive the control actuators. Using standard methods, the cost function can be expressed as a quadratic function of the control force amplitude, F_s , by¹¹

$$|p_{\text{tot}}(r, \theta)|^2 = F_s A_p F_s^* + B_p F_s^* + F_s B_p^* + C_p, \quad (13)$$

where $A_p = G_s G_s^*$, $B_p = G_s^* P_p$, and $C_p = P_p P_p^*$. The solution for the optimal control force for the minimization of the total pressure field squared can be obtained as:¹¹

$$F_s^p|_{\text{opt}} = -\frac{B_p}{A_p}, \quad (14)$$

resulting in $|p_{\text{tot}}(r, \theta)|_{\text{min}}^2 = 0$.

C. Minimization of the radiated sound power

The total radiated sound power is obtained by the integration of the square of the total sound pressure, and can therefore also be expressed as a quadratic function of the secondary control force amplitude F_s as:

$$\Pi_{\text{tot}} = F_s A_{\Pi} F_s^* + F_s B_{\Pi}^* + F_s^* B_{\Pi} + C_{\Pi}, \quad (15)$$

where

$$A_{\Pi} = \frac{1}{2\rho_0 c_0} \int_0^{\pi} A_p r d\theta,$$

TABLE II. Beam parameters.

Flexural wave number k_B (m^{-1})	Torsional wave number k_T (m^{-1})	Mass moment of inertia (kg/m)	Flexural stiffness (Nm^2)	Polar moment of inertia (kgm)	Torsional rigidity (Nm^2)
$\sqrt{\omega} \left(\frac{\rho_b A}{E_b I} \right)^{1/4}$	$\omega \left(\frac{\rho_b J_p}{GJ} \right)^{1/2}$	$\rho_b A$	$E_b I$	$\rho_b J_p$	GJ

$$B_{\Pi} = \frac{1}{2\rho_0 c_0} \int_0^{\pi} B_p r \, d\theta,$$

and

$$C_{\Pi} = \frac{1}{2\rho_0 c_0} \int_0^{\pi} C_p r \, d\theta.$$

C_{Π} represents the primary sound power as previously described by Eq. (7). The optimal control force for the minimization of the total sound power is

$$F_s^{\Pi}|_{\text{opt}} = -\frac{B_{\Pi}}{A_{\Pi}} \quad (16)$$

and the attenuated sound power becomes

$$\Pi_{\text{tot}}|_{\text{min}} = C_{\Pi} - \frac{B_{\Pi}^* B_{\Pi}}{A_{\Pi}}. \quad (17)$$

D. Control results and discussion

Numerical simulations are performed using the material properties of aluminium for the plate of thickness 1.6 mm, and reinforcing beams of both width and height of 2 cm. Air representing the acoustic fluid results in light fluid loading on the structure for all frequencies. The material and acoustic properties are listed in Table I. The parameters of the reinforcing beams are listed in Table II, where the torsional rigidity of the rectangular beams was calculated using the analysis of Wang.¹² The internal distributed damping in the structure is included in the complex Young's modulus by $\tilde{E} = E(1 + j\eta)$, where $\eta = 0.001$ is the structural loss factor. In previous work, the authors have determined the coincidence angles using the same system properties and dimensions, an amplitude of the incident wave $A_{\text{in}} = 10^{-4}$ m, and for an excitation frequency of 500 Hz. $\varphi_B = 11.5^\circ$ and $\varphi_T = 1.5^\circ$, respectively, correspond to the flexural and torsional coincidence angles.⁹ The critical angle has also been previously determined for the same material parameters and dimensions, resulting in $\varphi_c = 15^\circ$. Since both coincidence angles are less than critical, they both contribute to the radiation of sound into the far field.

It has been previously shown that the radiation directivity of the primary sound pressure at a far-field dimensionless radius of $k_0 r = 10$ increases at the directivity angles close to the surface of the structure ($0^\circ \leq \theta < 5^\circ$ and $175^\circ < \theta \leq 180^\circ$).⁶ This is due to the fact that even at a far-field radius, directivity angles close to the surface of the plate correspond to the near field, which is dominated by the structural propagating waves. Therefore, in order to accurately represent the radiating sound power, these ‘‘grazing’’ angles

were discluded from the integration of the sound intensity. The sound power was evaluated over the hemispherical range of $5^\circ \leq \theta \leq 175^\circ$.

The far-field sound pressure and sound power are analytically evaluated for three angles of incidence less than critical: $\varphi = 5^\circ$ corresponds to an off-coincidence condition, $\varphi = 11.5^\circ$ corresponds to an incident angle at flexural coincidence, and $\varphi = 14.5^\circ$ corresponds to an incident angle close to critical. In a previous paper on the sound fields radiating from a lightly fluid-loaded ribbed plate due to an obliquely incident structural wave, the authors have shown that the far-field sound pressure level differs for different incident angles.⁶ At coincidence, the far-field sound pressure level is reduced due to a more uniform distribution of the structural waves across the rib. The critical incident angle corresponds to the pole location in the supersonic wave number spectrum of the primary sound pressure field. Hence, at an incident angle near critical, the far-field sound pressure is dramatically increased. Similarly, the primary sound power levels have been previously evaluated over the far-field directivity range of $5^\circ \leq \theta \leq 175^\circ$, and correspond to 112 dB, 105 dB, and 120 dB for the incident angles of 5° , 11.5° , and 14.5° , respectively.⁶ As expected, the radiated sound power is a minimum at the flexural coincidence angle, and a maximum at the incident angle near critical.

Figure 4(a)–(c) shows the normalized magnitudes of the optimal control forces for the minimization of the local sound pressure as defined by Eq. (14), for the incident angles of 5° , 11.5° , and 14.5° , respectively. The sound pressure was minimised at a far-field error sensor location of $k_0 r_e = 10$, and at each θ_e . At the off-coincidence angle of 5° , the non-dimensional force magnitude is around 0.85, in a large range away from the grazing angles. At the flexural coincidence angle of 11.5° , a smaller control force amplitude is required, and the nondimensional optimal control force magnitude is only around 0.33. Incident angles approaching critical result in the optimal coupling between the structural and acoustic fields, and hence a larger force amplitude is required to attenuated the primary sound pressure field. At $\varphi = 14.5^\circ$, the normalized force magnitude is dramatically increased to up to 1.95, as shown in Fig. 4(c).

It is now of interest to select the optimal error sensor location that will result in the maximum global attenuation of the acoustic fields. This can be best achieved by initially investigating the total sound power resulting from the minimization of the far-field sound pressure. Figure 5(a)–(c), respectively, displays the attenuated sound power as a function of the error sensor location θ_e for the three incident angles of 5° , 11.5° , and 14.5° . The curves in each figure compare the attenuated sound power resulting from the minimization of

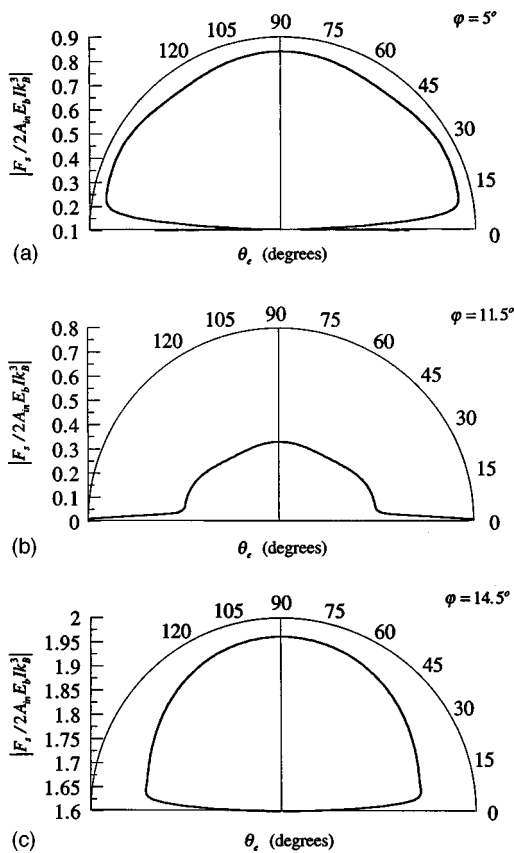


FIG. 4. (a)–(c) Normalized magnitudes of the optimal control forces for the local minimization of the far-field sound pressure at each error sensor location θ_e .

the sound power as described by Eq. (18), and the attenuated sound power resulting from the minimization of the far-field sound pressure at each local error sensor location in the range of $5^\circ \leq \theta_e \leq 175^\circ$. That is, the optimal control forces obtained in Fig. 4(a)–(c) are used to determine the total sound power for the corresponding local error sensor location, in a large range away from the grazing angles. Using the sound power as the cost function results in significant levels of attenuation of 23 dB, 16 dB, and 36 dB for the incident angles of 5° , 11.5° , and 14.5° , respectively. Similar levels of sound power attenuation can be achieved by minimizing the far-field sound pressure at the error sensors located in the range of $45^\circ \leq \theta_e \leq 55^\circ$ and $125^\circ \leq \theta_e \leq 135^\circ$, as shown in Fig. 5(a)–(c). The exact location for the optimal error sensor differs slightly for each incident angle of the incoming structural wave. In comparison, at an arbitrary error sensor location of $\theta_e = 90^\circ$ for the minimization of the local sound pressure, the attenuation levels of the sound power are 18 dB, 11 dB, and 32 dB for the incident angles of 5° , 11.5° , and 14.5° , respectively. The phenomenon shown in Fig. 5(a)–(c) also gives some initial insight into the effect of the reinforcing beam on altering the directivities of the radiating acoustic fields.

The error sensor location for the minimization of the local sound pressure can be optimized by choosing an error sensor location that results in the maximum attenuation of both the radiated sound power and local sound pressure. Figure 6(a)–(c), respectively, shows the primary and attenuated

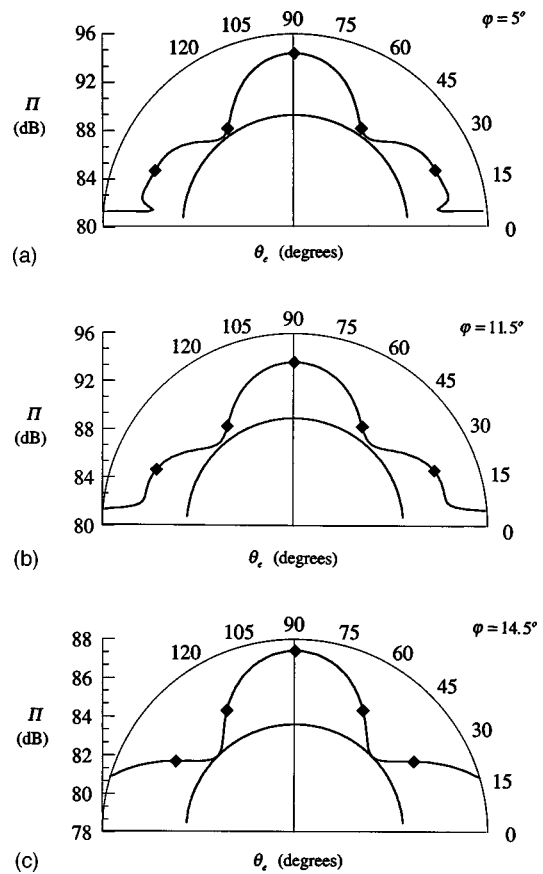


FIG. 5. (a)–(c) Attenuation of the sound power as a function of the local error sensor location θ_e , comparing the control performance using $F_s^{II}|_{\text{opt}}$ (—) and $F_s^I|_{\text{opt}}$ (—◆—).

sound pressure fields using a localized control system for the incident angles of 5° , 11.5° , and 14.5° . The attenuated sound pressure field for the optimally located error sensors is compared with the control performance of an arbitrarily located sensor at $\theta_e = 90^\circ$. The optimally located error sensors are at $\theta_e = 51^\circ$, 48° , and 45° , respectively, for the incident angles of 5° , 11.5° , and 14.5° . These error sensor locations are optimal as they result in the maximum attenuation of the sound power from the minimization of the local sound pressure. However, due to the symmetry of Figs. 4 and 5, optimally locating the error sensors at 129° , 132° , and 135° for the incident angles of 5° , 11.5° , and 14.5° , respectively, results in the same levels of attenuation achieved for both the far-field sound pressure and sound power. Also, Fig. 6(a)–(c) shows that the influence of the error sensor location on the attenuated sound fields is to alter the radiation directivity from a half-dipole (at an arbitrary location of $\theta_e = 90^\circ$) to a half-quadrupole (at the optimal error sensor location), which results in the reduction of the radiation efficiency. Hence, optimizing the control system greatly increases the control performance in two ways: (i) maximum attenuation of the radiated sound power is achieved through the minimization of the local sound pressure at an optimal sensor location; and (ii) the radiation efficiency of the controlled sound pressure is decreased.

In all Fig. 6(a)–(c), there is a large reduction in the sound pressure away from the grazing angles. At off coinci-

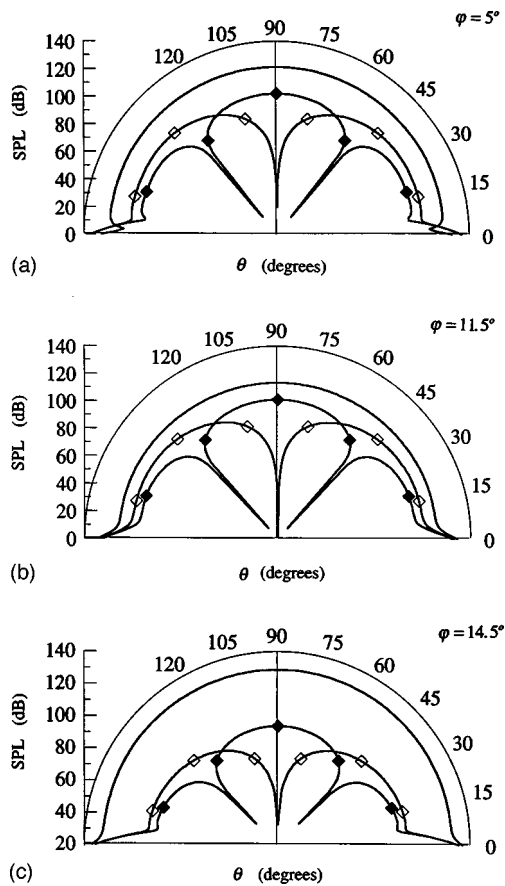


FIG. 6. (a)–(c) Primary (—) and attenuated sound pressure fields, comparing the attenuated sound pressure levels for an arbitrarily located (\diamond — \diamond) and optimally located (\blacklozenge — \blacklozenge) local error sensor.

dence ($\varphi = 5^\circ$) in Fig. 6(a), there is an increase in the total sound pressure level at the grazing angles mainly due to the imbalance in the propagating waves along the x -direction. At flexural coincidence ($\varphi = 11.5^\circ$) in Fig. 6(b), significant global attenuation also results in a large range away from the grazing angles, and with very little change in the total pressure level at the grazing angles. At $\varphi = 14.5^\circ$ [Fig. 6(c)], global attenuation of the far-field sound pressure level is achieved, although the reduction at the grazing angles is insignificant. For each case, the sound pressure level is completely minimized at the error sensor location, as well as symmetrically attenuated about the beam.

The control system can be designed with an optimal cost function and a corresponding error sensor location to achieve the best performance. Maximum attenuation of the acoustic fields can be achieved by using the far-field sound pressure as the cost function, and optimally locating the error sensor corresponding to a given angle of incidence. This reduces the complexity of the control system, since using the sound power as the cost function requires multiple error sensors located in a hemispherical range around the ribbed plate. Also, optimally locating the error sensor in the minimization of the sound pressure, results in significant attenuation of the radiated sound power.

E. Effect of the ASAC system on the structural response

It is of interest to investigate the effect of the ASAC system designed to minimize the radiating acoustic fields on the structural response. This is achieved by using the optimal control force $F_s^p|_{\text{opt}}$ obtained from the minimization of the far-field sound pressure at the optimal error sensor location, to determine the total structural response at the corresponding incident angle. The primary and total averaged flexural energy distributions along the x direction in plates 1 and 2 are evaluated, starting from a far-field location in plate 1 at $x = -10\lambda_p$ to a far-field location in plate 2 of $x = 10\lambda_p$ (where $\lambda_p = 2\pi/k_p$).

The primary flexural displacement in plate 1 is described by Eq. (3) and only corresponds to those values of x for $x \leq 0$, and similarly, the primary flexural displacement in plate 2 is described by Eq. (4) for $x \geq 0$. The energy distribution in the plates is then obtained by averaging the square of the primary plate flexural displacements, where the square of the displacement is obtained by multiplying the displacement by its complex conjugate. The squared flexural displacement is averaged over M discrete locations along the y direction in the range of $(-2\lambda_B, 2\lambda_B)$, where $\lambda_B = 2\pi/k_B$.

The total flexural displacement at a location $(\pm x, y)$ in the plates is the superposition of the primary and secondary plate displacements at that location. The secondary flexural displacement in the plates can be analytically derived using the expressions in Eqs. (10), (11), and in (A6). The secondary flexural displacement in plate 1 can be expressed as:

$$W_{1_s}(x, y) = \frac{F_s}{2E_b I} H(k_B) [A_1 e^{j(k_p^2 - k_B^2)^{1/2} x} + A_2 e^{(k_p^2 + k_B^2)^{1/2} x}] e^{jk_B y}; \quad x \leq 0, \quad (18)$$

and similarly, plate 2 can be described by:

$$W_{2_s}(x, y) = \frac{F_s}{2E_b I} H(k_B) [A_1 e^{-j(k_p^2 - k_B^2)^{1/2} x} + A_2 e^{-(k_p^2 + k_B^2)^{1/2} x}] e^{jk_B y}; \quad x \geq 0. \quad (19)$$

Due to the arrangement of the control forces, the secondary waves in the plates radiate away from the beam at an angle corresponding to that at the flexural coincidence condition. After superimposing the primary and secondary structural responses, the total energy distribution is obtained by the square of the total flexural displacement. The averaged total energy distribution is then obtained by averaging the square of the total flexural displacement over the M discrete locations along the y direction in the range $(-2\lambda_B, 2\lambda_B)$, and is described by:

$$J^F = \frac{1}{M} \sum_{i=1}^M [W_{\text{tot}}^p(x, y_i) + W_{\text{tot}}^s(x, y_i)] \times [W_{\text{tot}}^p(x, y_i) + W_{\text{tot}}^s(x, y_i)]^* \quad (20)$$

Figure 7(a)–(c) shows the primary and total flexural energy distributions in the plates corresponding to the incident angles of 5° , 11.5° , and 14.5° , respectively, and for $M = 401$ discrete locations. The energy distribution in plate 1

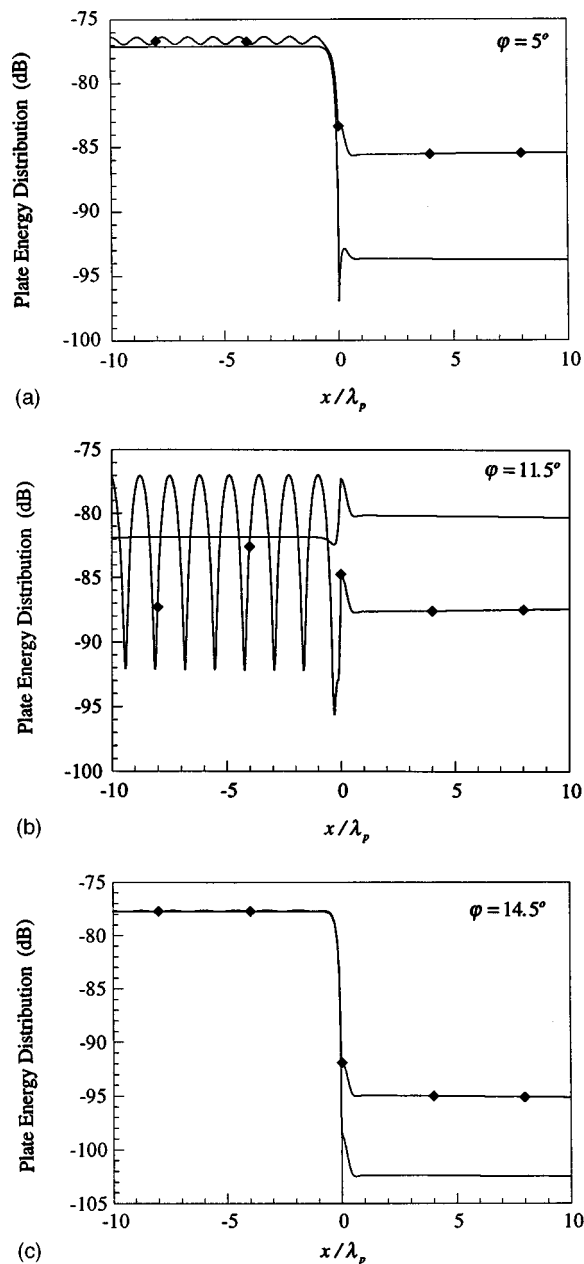


FIG. 7. (a)–(c) Primary (—) and total (◆—◆) flexural energy distributions in the plates.

can be observed for the range of $-10 \leq x/\lambda_p \leq 0$, and similarly, the energy distribution in plate 2 corresponds to the range of $0 \leq x/\lambda_p \leq 10$. At the incident angle corresponding to off coincidence ($\varphi = 5^\circ$) in Fig. 7(a), local control of the far-field sound pressure at the optimal error sensor location of $\theta_e = 51^\circ$ has the effect of increasing the total flexural energy in the plates. Previously at the off-coincidence angle, there was very little transmission of the primary waves in plate 2. Superimposing the primary and secondary waves, results in the total transmitted structural energy dramatically increasing by as much as 9 dB. The total flexural energy distribution in plate 1 exhibits strange behavior, with the energy oscillating about its slightly increased value.

Figure 7(b) corresponds to the structural flexural coincidence condition ($\varphi = 11.5^\circ$), at which there is maximum transmission of the primary plate flexural waves through the

reinforcing beam. Arrangement of the ASAC system using information on the flexural coincidence condition results in the secondary flexural waves in plate 2 having their optimal coupling with the primary transmitted flexural waves. Hence, attenuation of the local sound pressure still results in a decrease in the transmitted energy distribution in plate 2, although a even stranger phenomenon can be observed in plate 1. This phenomenon in plate 1 can be attributed to the fact that the secondary waves in plate 1 do not have the optimal phase match with the incoming incident waves, which carries most of the energy in plate 1.

At $\varphi = 14.5^\circ$ in Fig. 7(c), the total structural energy distribution due to the ASAC system shows only an increase in the transmitted energy in the positive x direction in plate 2. The increase in the transmitted energy also arises from the fact that away from the structural coincidence, there is very little transmission of the flexural waves in plate 2. Hence, $\varphi = 14.5^\circ$ also corresponds to an off-coincidence angle, and the secondary flexural waves result in an increase in the total flexural response in plate 2. The secondary waves also appear to have insignificant effect on the total energy distribution in plate 1, although close examination reveals that there is slight oscillation of the total energy slightly above its primary value, and hence parallels the phenomenon in Fig. 7(a). The decrease in the sound pressure level at $\varphi = 14.5^\circ$ at the grazing angles may possibly be attributed to the more balanced distribution of the total structural waves propagating along the x direction.

It has also been observed for each incident angle that altering the location of the local error sensor by using an arbitrary error sensor location at $\theta_e = 90^\circ$ for the minimization of the far-field sound pressure, has no significant effect on the total structural energy distribution in both plates 1 and 2.

III. CONCLUSIONS

In this paper, an analytical study to attenuate the acoustic fields radiating from a ribbed plate has been presented using active structural acoustic control techniques. Using previous work on the sound fields radiating from a ribbed plate due to a structural incident wave, it was possible to design the feedforward ASAC system to maximise the control performance. Optimization of the control system was achieved in two ways: first by pre-fixing the phases of the control forces to have a spatial phase variation with each other corresponding to the flexural coincidence condition, and also by optimally locating the local error sensor in the surrounding fluid field. From the minimization of the local far-field sound pressure, the following observations were made:

- (i) optimizing the error sensor location altered the directivity of the attenuated sound field from a dipole to a quadrupole, and hence reduces the radiation efficiency;
- (ii) significant reduction in the far-field sound pressure can be achieved for all incident angles in a large range away from the grazing angles;

- (iii) minimization of the far-field sound pressure at an optimal error sensor location results in significant attenuation of the radiated sound power;
- (iv) the effect of the ASAC system on the structural response is to slightly increase the overall energy in plate 1, and dramatically increase the transmitted energy in plate 2, except at the flexural coincidence angle;
- (v) at flexural coincidence, the primary transmitted waves have their optimal spatial phase match with the secondary waves, thereby reducing the total transmitted energy in plate 2.

APPENDIX: SPECTRAL RESPONSE OF THE SECONDARY FLEXURAL WAVES IN THE PLATES

The secondary flexural motion in the beam of a ribbed plate system generated by the multiple point control forces as described by Eq. (8), is given by the following fourth order differential equation:

$$E_b I \frac{\partial^4 u_s}{\partial y^4} + \rho_b A \frac{\partial^2 u_s}{\partial t^2} = F_{BR} + \sum_{n=-N}^N F_s e^{jk_B n \Delta} \times \delta(y - n \Delta). \quad (A1)$$

F_{BR} is a result of the backward reaction from plates 1 and 2 on either side of the beam, and is described as the net vertical shear force acting at the boundaries between the beam and the plates.¹³ There are no external forces acting on the plates, hence the equation of motion for the secondary flexural waves in the plates is simply:

$$D \nabla^4 W_s + \rho_p h \frac{\partial^2 W_s}{\partial t^2} = 0. \quad (A2)$$

Taking the Fourier transform of Eq. (A1) results in the following expression for the spectral response of the secondary flexural waves in the beam:

$$\tilde{u}_s(\gamma_{y_s}) = \frac{F_s}{E_b I} \cdot \frac{\sum_{n=-N}^N e^{-j(\gamma_{y_s} - k_B)n \Delta}}{\gamma_{y_s}^4 - k_B^4 + (2jD/E_b I)(k_p^4 - \gamma_{y_s}^4)[(k_p^2 - \gamma_{y_s}^2)^{-1/2} + j(k_p^2 + \gamma_{y_s}^2)^{-1/2}]}, \quad (A3)$$

where γ_{y_s} is the secondary structural wave number in the y domain. Using the following relationship:¹⁰

$$\sum_{n=-N}^N e^{-j\omega n \Delta} = \frac{\sin[\omega(2N+1)\Delta/2]}{\sin[\omega\Delta/2]}, \quad (A4)$$

simplifies Eq. (A3) to:

$$\tilde{u}_s(\gamma_{y_s}) = \frac{F_s}{E_b I} H(\gamma_{y_s}) \frac{\sin[(\gamma_{y_s} - k_B)(2N+1)\Delta/2]}{\sin[(\gamma_{y_s} - k_B)\Delta/2]}, \quad (A5)$$

where

$$H(\gamma_{y_s}) = \frac{1}{\gamma_{y_s}^4 - k_B^4 + (2jD/E_b I)(k_p^4 - \gamma_{y_s}^4)[(k_p^2 - \gamma_{y_s}^2)^{-1/2} + j(k_p^2 + \gamma_{y_s}^2)^{-1/2}]}.$$

The spectral response of the total secondary flexural displacement in the plates can be obtained by taking a double Fourier transform, in terms of the secondary wave number spectrums in the x - and y domains:

$$\begin{aligned} \tilde{W}_s(\gamma_{x_s}, \gamma_{y_s}) &= [\tilde{W}_{1_s}(\gamma_{x_s}) + \tilde{W}_{2_s}(\gamma_{x_s})] \tilde{W}_s(\gamma_{y_s}) \\ &= \left[\int_{-\infty}^0 (A_1 e^{j\sqrt{k_p^2 - \gamma_{y_s}^2} x} + A_2 e^{\sqrt{k_p^2 + \gamma_{y_s}^2} x}) e^{-j\gamma_{x_s} x} dx \right. \\ &\quad \left. + \int_0^{\infty} (A_1 e^{-j\sqrt{k_p^2 - \gamma_{y_s}^2} x} + A_2 e^{-\sqrt{k_p^2 + \gamma_{y_s}^2} x}) e^{-j\gamma_{x_s} x} dx \right] \\ &\quad \times \frac{F_s}{E_b I} H(\gamma_{y_s}) \frac{\sin[(\gamma_{y_s} - k_B)(2N+1)\Delta/2]}{\sin[(\gamma_{y_s} - k_B)\Delta/2]}, \quad (A6) \end{aligned}$$

where γ_{x_s} is the secondary structural wave number in the x domain.

$$A_1 = \frac{\sqrt{k_p^2 + \gamma_{y_s}^2}}{\sqrt{k_p^2 + \gamma_{y_s}^2} - j\sqrt{k_p^2 - \gamma_{y_s}^2}}$$

and

$$A_2 = -j \frac{\sqrt{k_p^2 - \gamma_{y_s}^2}}{\sqrt{k_p^2 + \gamma_{y_s}^2} - j\sqrt{k_p^2 - \gamma_{y_s}^2}},$$

respectively, represent the amplitudes of the structural propagating and near-field decay waves. Due to the symmetry of the control arrangement, A_1 and A_2 are the same for both plates 1 and 2, and are obtained from the coupling conditions between the beam and plates at the beam-plate boundaries. Using the following formula:¹⁰

$$\int_0^{\infty} e^{jkx} dx = \pi \delta(k) + \frac{j}{k}, \quad (\text{A7})$$

results in an expression for the total spectral response of the secondary flexural waves in the plates described by

$$\begin{aligned} \tilde{W}_s(\gamma_{x_s}, \gamma_{y_s}) = & \left\{ A_1 \left(\pi \delta(\sqrt{k_p^2 - \gamma_{y_s}^2} - \gamma_{x_s}) + \pi \delta(\sqrt{k_p^2 - \gamma_{y_s}^2} + \gamma_{x_s}) - \frac{j}{\sqrt{k_p^2 - \gamma_{y_s}^2} - \gamma_{x_s}} - \frac{j}{\sqrt{k_p^2 - \gamma_{y_s}^2} + \gamma_{x_s}} \right) \right. \\ & \left. + A_2 \left(\pi \delta(j\sqrt{k_p^2 + \gamma_{y_s}^2} - \gamma_{x_s}) + \pi \delta(j\sqrt{k_p^2 + \gamma_{y_s}^2} + \gamma_{x_s}) + \frac{j}{j\sqrt{k_p^2 + \gamma_{y_s}^2} - \gamma_{x_s}} + \frac{j}{j\sqrt{k_p^2 + \gamma_{y_s}^2} + \gamma_{x_s}} \right) \right\} \\ & \times \frac{F_s}{E_b I} H(\gamma_{y_s}) \frac{\sin[(\gamma_{y_s} - k_B)(2N+1)\Delta/2]}{\sin[(\gamma_{y_s} - k_B)\Delta/2]}. \end{aligned} \quad (\text{A8})$$

¹R. H. Lyon, "Sound radiation from a beam attached to a plate," J. Acoust. Soc. Am. **34**, 1265–1268 (1962).

²D. G. Crighton and G. Maidanik, "Acoustic and vibration fields generated by ribs on a fluid-loaded panel, I: Plane-wave problems for a single rib," J. Sound Vib. **75**, 437–452 (1981).

³C. R. Fuller, "Analysis of active control of sound radiation from elastic plates by force inputs," Proceedings of Inter Noise '88, Avignon, France, 1061–1064 (1988).

⁴Y. Gu and C. R. Fuller, "Active control of sound radiation due to subsonic wave scattering from discontinuities on fluid loaded plates, I: Far-field pressure," J. Acoust. Soc. Am. **90**, 2020–2026 (1991).

⁵E. E. Ungar, "Transmission of plate flexural waves through reinforcing beams; Dynamic stress concentrations," J. Acoust. Soc. Am. **33**, 633–639 (1961).

⁶N. J. Kessissoglou and J. Pan, "The effect of the structural coincidences on the acoustic fields radiating from a ribbed plate," J. Sound Vib. (submitted).

⁷M. C. Junger and D. Feit, *Sound, Structures and Their Interaction* (MIT, Cambridge, MA, 1986), pp. 52–54, 92, 95–97.

⁸C. R. Fuller and J. P. Carneal, "A biologically inspired controller," J. Acoust. Soc. Am. **98**, 386–396 (1995).

⁹N. J. Kessissoglou and J. Pan, "An analytical investigation of the active attenuation of the plate flexural wave transmission through a reinforcing beam," J. Acoust. Soc. Am. **102**, 3530–3541 (1997).

¹⁰D. G. Crighton *et al.*, *Modern Methods in Analytical Acoustics, Lecture Notes* (Springer-Verlag, New York, 1992), pp. 75, 109–110.

¹¹J. Pan and C. H. Hansen, "Active control of total vibratory power flow in a beam: I. Physical system analysis," J. Acoust. Soc. Am. **89**, 200–209 (1991).

¹²C. T. Wang, *Applied Elasticity* (McGraw-Hill, New York, 1953), pp. 85–89.

¹³M. A. Heckl, *Compendium of Impedance Formulas* [BBN Report No. 774, Contract Nonr 2322 (00), 1961].

Increasing the insertion loss of noise barriers using an active-control system

Jingnan Guo^{a)} and Jie Pan

Department of Mechanical and Materials Engineering, University of Western Australia, Nedlands, WA 6907, Australia

(Received 31 July 1997; accepted for publication 6 September 1998)

In recent studies on active noise control in open space, a multichannel active-control system was used to create the largest quiet zone with the least increase of total sound-power output when its sensors and actuators were optimally arranged. This control system was also applied to increase the insertion loss of noise barriers. The control system was arranged to create quiet zones on the top of the barrier; thus, the sound diffraction along the barrier top was reduced and the insertion loss of the barrier increased. It was found that the control system significantly increases the insertion loss of the noise barrier at low frequencies when the ground on both sides of the barrier is totally nonreflective. In practice, a nearby reflective ground may deteriorate the performance of the active noise-control system. The effects of ground reflection on the effectiveness of the active-noise barrier are considered in this paper. Both simulation and experimental results show that the reflective ground significantly reduces the effectiveness of the active noise-control system on the barrier. Reflection from the ground on the noise-source side has the greatest influence on the control efficiency. This suggests that passive reduction of the reflection from the ground on the source side should be incorporated in the design of the active-control system. Experiments were made for noise with multiple-frequency components in a low-frequency band. The results suggest that the active-control system can be effective at improving the performance of the noise barrier for noise with multiple-frequency components. © 1998 Acoustical Society of America.

[S0001-4966(98)04412-9]

PACS numbers: 43.50.Ki, 43.50.Gf [MRS]

INTRODUCTION

Noise barriers are classical and practical noise-control devices. When a noise barrier is interposed between a noise source and a receiver, the direct sound from the source is blocked. The sound field at the position of the receiver results mainly from sound diffraction at the top of the barrier. As the diffracted sound is relatively weak compared with the direct sound in the area behind the barrier, the sound attenuation occurs in this area. The area experiencing significant sound attenuation after the insertion of the barrier is called the “dark area”.

According to the theory of diffraction, the strength of the diffracted field is proportional to the wavelength of the sound.¹ In other words, while the barrier is effective at blocking high-frequency noise, it is less effective, or even useless, in the case of low-frequency noise, especially when the frequency of the noise is so low that its wavelength is comparable to the height of the barrier. Increasing the height of the barrier is an obvious way to improve the low-frequency performance of the barrier, but it is usually not practical. As a result, the improvement of the performance of a barrier, especially for low-frequency noise, has been a research topic in the field of acoustics for more than 20 years.²⁻⁵

Studies on active noise control (ANC) have demon-

strated that ANC is effective for low-frequency noise.^{6,7} It is reasonable to believe that the low-frequency performance of a barrier may be improved by this technique. Ise first applied a single-channel adaptive control system to a 1:2 scale model of a passive barrier.⁸ In Ise's system, a loudspeaker acting as a monopole control source was positioned on the top of the barrier and an error microphone was set in the desired area immediately behind the barrier. A “quieter” area around the error microphone was obtained at very low frequencies (125 Hz or lower). Omoto took a different approach.⁹ In his system, a multichannel-control system was used to cancel the noise around the barrier top, rather than the diffracted noise in the dark area. His research applied to pure-tone noise and nonreflective ground. For the specific configuration studied, Omoto concluded that when the separation of distance between the error microphones on the diffraction edge is less than half of the wavelength, the active-noise barrier works effectively. Omoto then extended his work to barriers on reflective ground, and found that the efficiency of the control system was seriously affected by the reflective ground.¹⁰

The application of the active noise-control system to the noise barrier is, in fact, the problem of active noise control in open space. The present authors studied the active-noise barrier with a different approach. They have developed an active noise-control system for open space that can create the largest quiet zone with the least total power output increase when optimally arranged (the interval of the control sources and error microphones is not necessary less than half of the wavelength),¹¹ and then applied the developed optimal local

^{a)}Present address: Occupational Hygiene Program and Department of Mechanical Engineering, University of British Columbia, 3rd Floor, 2206 East Mall, Vancouver, British Columbia V6T 1Z3, Canada.

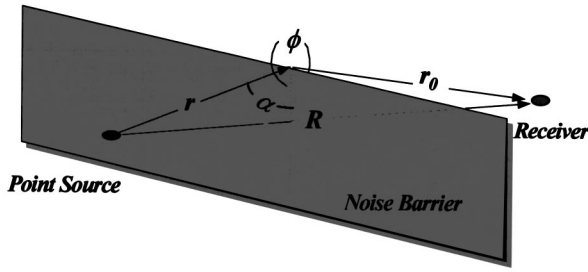


FIG. 1. Schematic of a noise barrier.

control system to noise barriers with nonreflective ground.¹² It has been found that their active local-control system significantly improves the performance of the noise barrier by creating a large (relative to the wavelength) area of noise attenuation in the dark area. The extra insertion loss of the active-noise barrier can be as high as 10 dB or more.

In this paper, the efficiency of an active noise barrier will be further investigated in two more practical aspects. First, reflection from the grounds on either side of the barrier is considered. It has been found that, for most control-system arrangements, reflection from the rigid ground near the sources reduces the size of the quiet zone created by the active noise-control system in open space.¹³ It is necessary to determine the effect of ground reflection on the performance of the active-noise barrier. Secondly, the effectiveness of the active-noise barrier at controlling noise consisting of several frequency components within some frequency range will be investigated.

I. INSERTION LOSS OF NOISE BARRIERS

Many theories can be used to predict and describe the sound-insertion loss of noise barriers. The basic ones are Huygen's principle and Kirchhoff's diffraction formulation.^{14,15} For the reflective noise barrier shown in Fig. 1, if the noise source is a point source that radiates a sound-pressure field in open space as described by,

$$P_0 = \frac{A}{kr} e^{ikr}, \quad (1)$$

the diffracted field arriving at the receiver position in the dark area can be approximately expressed as,¹⁶

$$P_d = -\sqrt{\frac{2}{\pi k R_1}} A e^{-i\pi/4} \times \left\{ \begin{aligned} &\text{sgn}(\pi + \alpha - \phi) \frac{e^{ikR}}{\sqrt{k(R_1 + R)}} F[\sqrt{k(R_1 - R)}] \\ &+ \text{sgn}(\pi - \alpha - \phi) \frac{e^{ikR}}{\sqrt{k(R_1 + R')}} F[\sqrt{k(R_1 - R')}] \end{aligned} \right\} \quad (2)$$

for $kR_1 \gg 1$, where k is the wave number of the sound, R and R' are, respectively, the distances from the receiver to the source and to the source mirror-image in the barrier. $R_1 = r + r_0$ is the shortest distance from the source to the receiver over the barrier top, $A = -iZ_0q$, where q is the strength of the source, $Z_0 = \omega^2 \rho_0 / 4\pi c_0$, and

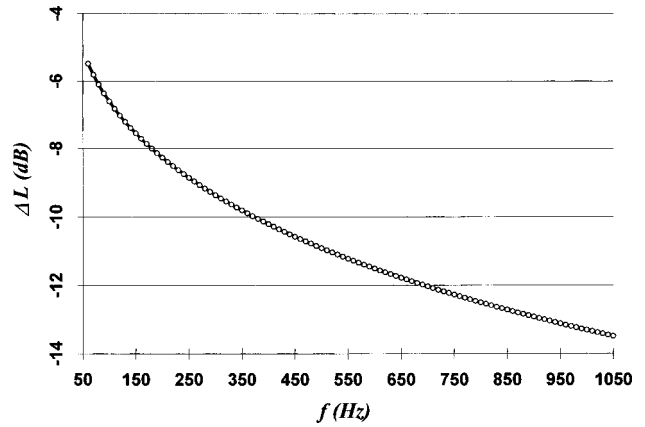


FIG. 2. Sound insertion loss of a specific barrier as a function of frequency.

$$F(\mu) = \int_{\mu}^{\infty} e^{i\chi^2} d\chi \quad (3)$$

is the Fresnel integral.

The sound-insertion loss of the barrier is then defined as,

$$\Delta L = 20 \log(|P_d|/|P_0|), \quad (4)$$

where P_0 is the sound pressure at the receiver position when the barrier is absent, as expressed by Eq. (1). The relationship between the insertion losses of the barrier and the frequency of the noise is shown in Fig. 2 for a typical case, for which the barrier is 1 m high. Located on different sides of the barrier, the noise source and receiver are both 0.5 m high, and 2 m away from the barrier.

Figure 2 shows that the insertion loss of a noise barrier decreases with increasing frequency. While the sound attenuation at a point in the dark area is only 5 dB ($\Delta L = -5$ dB) at low frequencies, it can be more than 10 dB ($\Delta L < -10$ dB) at high frequencies. This characteristic of noise barriers has stimulated much research to improve the performance of the noise barrier at low frequencies.

II. ACTIVE-NOISE BARRIER

A multichannel active noise-control system has been developed by the authors, in which N control sources and N error microphones are equally spaced in two parallel lines, with $r_{ss} = r_{ee}$, as shown in Fig. 3. The sum of the squared sound pressures at the error-microphone positions was selected as the cost function of the control system. The source

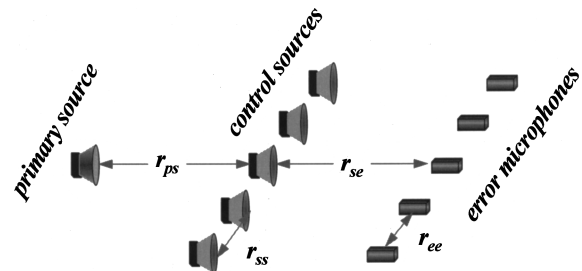


FIG. 3. A multichannel active noise-control system in open space.

strengths of the N control sources were adjusted to drive the total sound pressures at the N error microphones to a minimum (to zero, theoretically) as expected by,

$$\mathbf{q}_s = -\mathbf{Z}_{se}^{-1} \mathbf{Z}_{pe} q_p, \quad (5)$$

where \mathbf{Z}_{se} is an $N \times N$ matrix of acoustic transfer impedance from the control sources to the error microphones, \mathbf{Z}_{pe} is the vector of acoustic transfer impedance from the primary source to the error microphones, and q_p is the strength of the primary source. A quiet zone is thus created in the area around the error microphones. The quiet zone is defined as the area in which the sound pressure has been attenuated by more than 10 dB.

It has been found that there exists an optimal range of spacing of the adjacent control sources and error microphones for this control system. The upper and lower limits of this optimal range are given by:¹¹

$$r_{ss-\max} \cong \begin{cases} \frac{\lambda}{2} \sqrt{1 + \frac{4r_{se}}{N\lambda}}, & N=2,4,6,\dots, \\ \frac{\lambda}{2} \sqrt{1 + \frac{N+1}{N-1} \frac{4r_{se}}{N\lambda}}, & N=3,5,7,\dots, \end{cases} \quad (6)$$

and

$$r_{ss-\min} \cong \begin{cases} \frac{5\lambda}{2} \exp\left\{-\left[\frac{3(\lambda + 0.04r_{ps})}{2r_{se} - \lambda} + \frac{20\lambda}{15\lambda + r_{ps}}\right]\right\}, \\ \quad N=4,6,8,\dots, \\ \frac{3\lambda(N+1)}{N} \exp\left\{-\left[\frac{\lambda + 2r_{ps}}{2(2r_{se} - \lambda)} + \frac{12\lambda}{5\lambda + r_{ps}}\right]\right\}, \\ \quad N=3,5,7,\dots \end{cases} \quad (7)$$

The lower limit for $N=2$ is a special case discussed in Ref. 10. Only when the spacing of the adjacent control sources and error microphones of the control system is arranged within this range, does the control system generate the largest area of quiet zone with the least increase of total power output. If the control system is arranged outside the optimal range, the control either causes a large increase of total power output, with increase of sound pressure in some places, or it becomes ineffective at creating the quiet zone. It has been found that the quiet zone created by this control system with optimal arrangement has the shape of a wedge, with its edge at the position of the control source array; its size is proportional to the wavelength of the noise and the number of control channels.¹¹ This means that the lower the frequency of the noise and the more control channels, the larger the size of the quiet zone. The fact that the optimal spacing of control sources and error microphones is given by a range also suggests that the optimally arranged control system is effective not only for a specific frequency, but for a frequency range. It has been found that the developed optimal-control system is also applicable when the primary source is not a point source, or not placed in the central position.¹⁷

Since the sound field around the barrier top contributes a diffracted sound field in the dark area behind the barrier, it is reasonable to believe that, if the sound around the barrier top

can be canceled, the diffractive sound in the dark area behind the barrier should also be attenuated. This approach should have the equivalent effect of increasing the height of the noise barrier. Consequently, the insertion loss of the barrier can be increased.

The multichannel-control system developed for active noise control in open space was applied to a noise barrier. The control system consisted of N control sources and N error microphones, as shown in Fig. 4. The control sources and error microphones were equally spaced in two parallel lines. The array of error microphones was located immediately on top of the barrier. The control-source array was located between the primary source and the error-microphone array, and in the same plane containing both the primary source and the error-microphone array. The efficiency of active-noise barrier was investigated for two ground conditions: nonreflective and totally reflective.

A. Nonreflective ground

When reflection from the ground on both sides of the barrier is negligible, the sound field in the dark area propagates directly from the noise source by diffraction over the barrier top; the total diffracted sound pressure at the receiver is:

$$P = P_{pd} + \sum_{i=1}^N P_{sd}^{(i)}, \quad (8)$$

where P_{pd} is the diffraction caused by the primary noise source only (this also represents the diffracted sound while the active control system is off), and $P_{sd}^{(i)}$ is the diffraction caused by the i th control source. Both P_{pd} and $P_{sd}^{(i)}$ are predicted using Eq. (2). The extra sound-insertion loss created by the multichannel active noise-control system can thus be written as:

$$\Delta L = 20 \log(|P|/|P_{pd}|). \quad (9)$$

It has been found that the optimal configuration of the control system in open space also applies to the active-noise barrier, and that the control system can significantly increase the insertion loss of the noise barrier ($\Delta L < 0$ dB) when it is within the optimal range, but may decrease the insertion loss ($\Delta L > 0$ dB) when it is outside the optimal range.¹² Figure 5 shows the extra insertion loss in the dark area behind the barrier caused by an active noise-control system with 11 control sources and 11 error microphones. The ground is con-

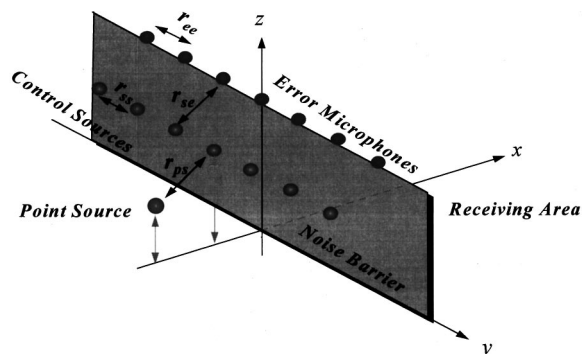


FIG. 4. Active noise-control system on a noise barrier.

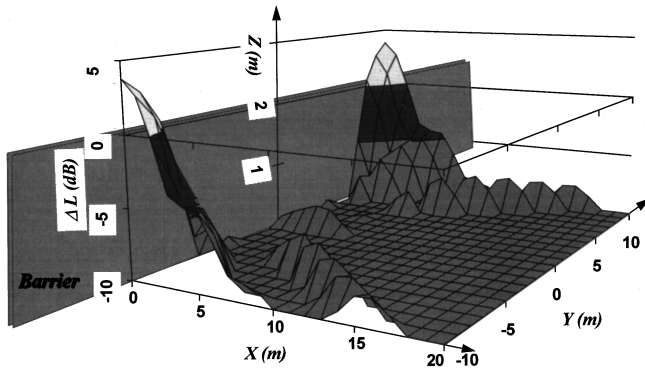


FIG. 5. Extra insertion loss caused by the active control system.

sidered to be nonreflective. For this example, the height of the barrier is 2 m, and the coordinates of the primary source, the control sources, and the error microphones are, respectively, $(-4,0,1)$, $[-2,(i-6)r_{ss},1.5]$, and $[0,(i-6)r_{ss},2]$ ($i = 1, \dots, 11$), in meters. The frequency of the noise is chosen as $f=200$ Hz, the interval r_{ss} of the control sources is optimally arranged within the range defined by Eqs. (6) and (7) as $r_{ss}=1.0$ m. The simulated results were obtained for the x - y plane, which is 1 m in height and immediately behind the receiving side of the barrier. It has been found that a large extra insertion loss ($\Delta L < -10$ dB) is obtained over a large area behind the barrier not only in the x - y plane for this particular simulation height, but in all x - y planes with heights lower than that of the noise barrier.

B. Totally reflective ground

Practically, ground always provides a certain amount of sound reflection. At low frequencies, the reflection can be very large. It has been found that the nearby reflective ground reduces the size of the quiet zone created by the active control system in open space for most configurations.¹³ The effect of reflection from the ground on the extra-insertion loss of an active-noise barrier should also be analyzed.

When the ground on both sides of the barrier is reflective, there are four pathways from each noise source to the receiver over the barrier top, as shown in Fig. 6. They are: (1) direct from the source to the receiver, (2) via the reflective ground on the source side, which is equivalent to the path from the source image to the receiver, (3) via the reflective ground on the receiving side, which is equivalent to the path from the source to the receiver image, and (4) via the reflective ground on both sides, which is equivalent to the path from the source image to the receiver image. If the ground is regarded as rigid, and total reflection is assumed (it is often the case for low-frequency noise), the total diffracted sound pressure at the receiver expressed by Eq. (8) becomes,

$$P = \sum_{j=1}^4 P_{pd}(j) + \sum_{j=1}^4 \sum_{i=1}^N P_{sd}^{(i)}(j), \quad (10)$$

where j represents the j th pathway. The extra insertion loss of the barrier can be then calculated by,

$$\Delta L = 20 \log(|P|/|P_p|), \quad (11)$$

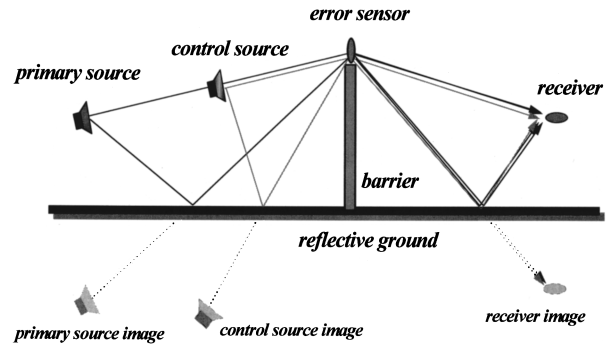
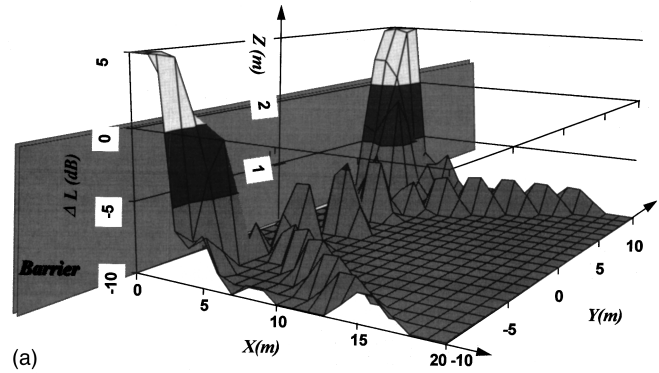
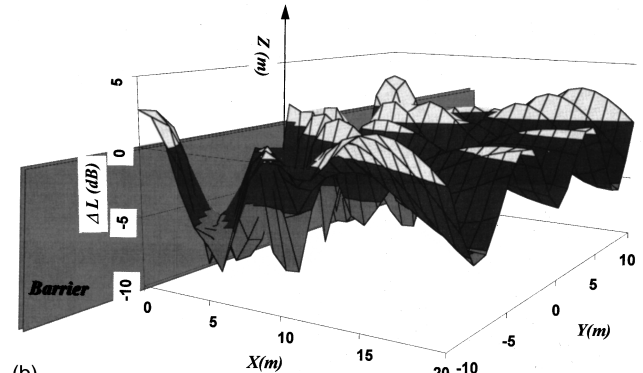


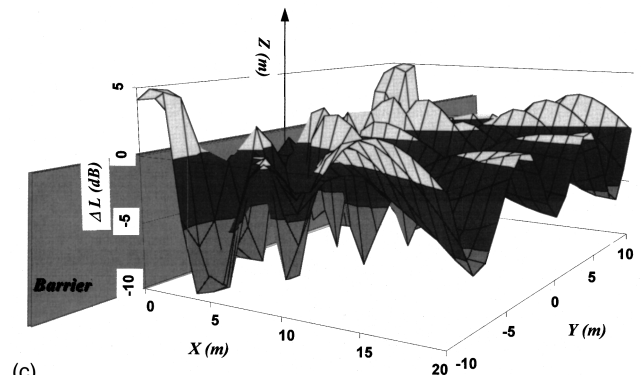
FIG. 6. Four pathways of sound diffraction over the barrier on reflective ground.



(a)



(b)



(c)

FIG. 7. Extra sound attenuation due to the active noise-control system with 11 control sources when the rigid ground is on (a) the receiving side only, (b) the side where the sources are located only, and (c) both sides of the barrier.

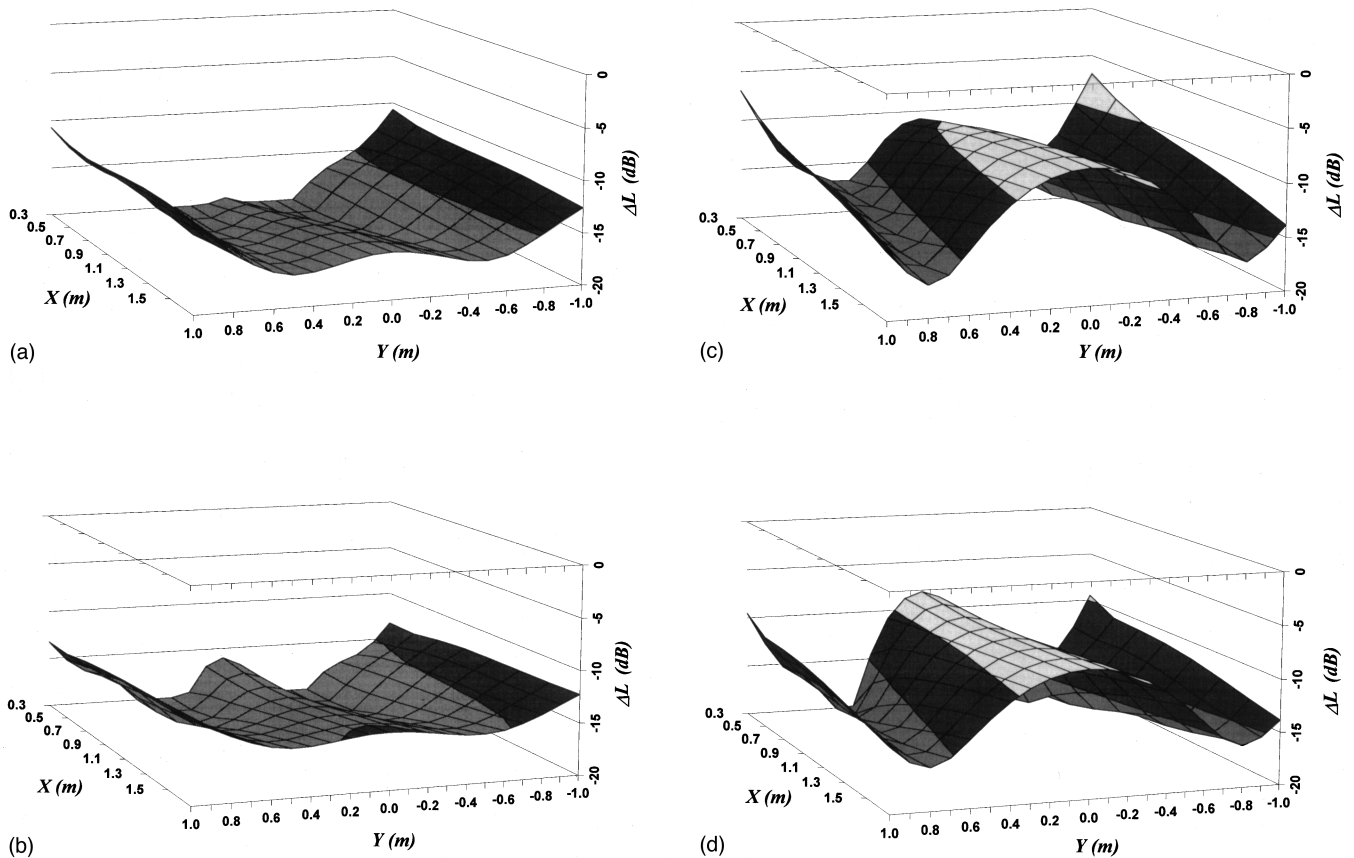


FIG. 8. Extra sound attenuation due to the active noise-control system with three control sources when (a) the ground on both sides of the barrier is nonreflective, (b) reflective ground on receiving side only, (c) reflective ground on source side only, and (d) reflective ground on both sides.

where

$$P_p = \sum_{j=1}^4 P_{pd}(j)$$

is the diffracted sound from the primary source only. Both P_{pd} and P_{sd} are expressed in the form of Eq. (2).

The effect of nearby reflective ground on the effectiveness of the control system in increasing the insertion loss of the noise barrier has been studied. The insertion losses of the noise barrier for four different circumstances, where (1) the ground is nonreflective, (2) only the ground on the receiving side is reflective, (3) only the ground on the side where the sources are located is reflective, and (4) the ground on both sides of the barrier is reflective, are calculated and compared. It has been found that reflection from the ground significantly reduces the extra insertion loss of the barrier. This effect is mainly attributed by the reflection from the ground on the source side.

The extra insertion loss of the active-noise barrier with 11 control sources is shown in Fig. 7, when (a) only the ground on the receiving side is reflective, (b) only the ground on the source side is reflective, and (c) the ground on both sides is reflective. Here, all of the simulation parameters are the same as those in the previous nonreflective ground simulation. Compared with Fig. 5, it is obvious that reflection from either side of the ground reduces the extra insertion loss of the active-noise barrier. Figure 7 also indicates that the reduction of extra insertion loss caused by the reflection from

the ground on the receiving side is relatively small; the extra sound attenuation is still more than 10 dB ($\Delta L < -10$ dB) over most of the area. However, the reflections from the ground on the source side can significantly reduce the extra sound attenuation of the active-noise barrier, as shown in Fig. 7(b). Although the extra insertion loss of the noise barrier can also be achieved over most of the area, it becomes relatively small for this case. There are some areas in which the extra insertion loss is positive ($\Delta L > 0$ dB). Comparing Fig. 7(b) to the case where the ground on both sides is rigid, shown in Fig. 7(c), it can be seen that there is not much difference in the extra insertion losses for these two cases. This indicates that reflection from the ground on the source side contributes most significantly to the reduction of the extra insertion loss of the active-noise barrier.

In order to allow comparison with the experimental results, results for another active-noise barrier are presented in Fig. 8 which demonstrate the effect of rigid ground on the control efficiency; here, the noise barrier is 1 m high and located along the y axis. The control system consists of three control sources and three error microphones. The location of the primary source is $(-1.38, 0, 0.5)$, the control sources are at $[-0.69, (i-2)r_{ss}, 0.75]$, and the error microphones are at $[0, (i-2)r_{ss}, 1]$ ($i=1,2,3$). The operating frequency is chosen as 500 Hz. It can be calculated from Eqs. (6) and (7) that the optimal range of r_{ss} is $[0.22\lambda, 0.98\lambda]$ for this control system; r_{ss} is selected within the range as $r_{ss}=0.75\lambda$. The simulated results are obtained in the x - y plane, which is 0.5

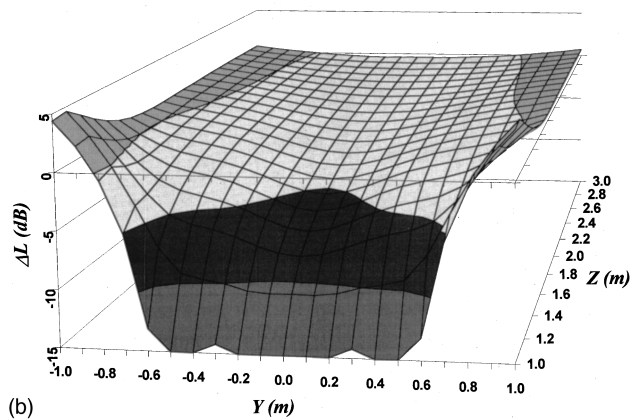
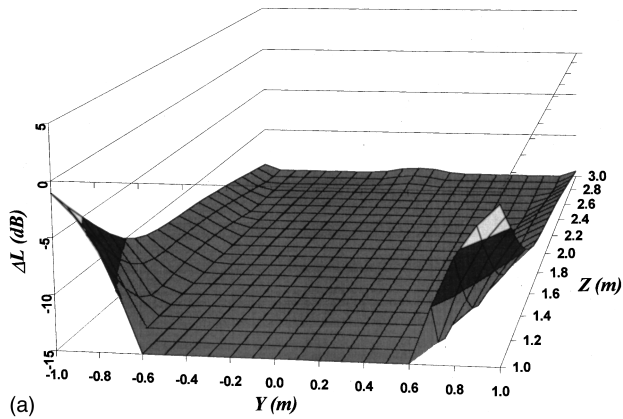


FIG. 9. Sound attenuation in the y - z plane immediately above the barrier top when (a) the ground on both sides of the barrier is nonreflective, and (b) reflective ground on source side only.

m in height and immediately behind the barrier.

It is clear that when the ground is nonreflective, the active noise-control system can effectively improve the insertion loss of the barrier; the extra sound attenuation of the barrier due to the control system is more than 10 dB in the area behind the barrier. The study of the effect of reflections from the rigid ground on the extra insertion loss leads to the same conclusion as that of the control system with 11 control sources: reflection from the ground on the side where the sources are located contributes most significantly to the reduction of the extra insertion loss of the barrier. The mechanism involved is that the extra insertion loss of the barrier is mainly determined by the size of the quiet zone created on the barrier top. According to Ref. 13, for the control system arranged as shown in Fig. 6, the reflection from the ground on the source side reduces the quiet zone created at the barrier top. This is because the presence of the reflective ground on the source side reduces the wavefront matching between the primary and control sources at the barrier top, and the size of the quiet zone is determined by the wavefront matching between the primary and control sources. As a result, the extra sound attenuation in the area behind the barrier is decreased. Figure 9 demonstrates that rigid ground does reduce the size of the quiet zone at the barrier top created by the active noise-control system. The sound-pressure attenuation is shown in the y - z plane (2.0×2.0 m) immediately above

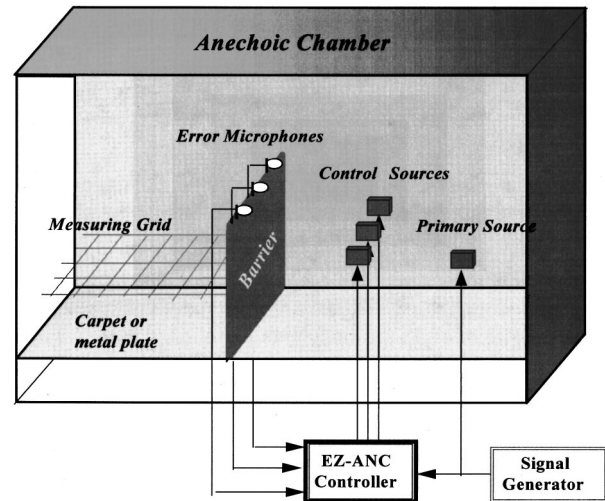


FIG. 10. Experiment setup in an anechoic chamber.

the barrier top. The ground on the source side is nonreflective in Fig. 9(a) and totally reflective in Fig. 9(b). It can be seen that the control system greatly attenuates the sound pressure at the barrier top ($\Delta L < -15$ dB over most of the area) when the ground is nonreflective. Figure 9(b) shows that, when the rigid ground is present, the size of the quiet zone at the barrier top decreases significantly. The sound pressure in some areas even increases ($\Delta L > 0$ dB).

It can thus be concluded, that for the practical application of active noise-control system to the noise barrier, the efficiency of the active control system can be significantly increased if appropriate nonreflective treatment is applied to the rigid ground on the side where the sources are located.

Although only two specific control systems (3 control sources and 11 control sources) were illustrated here to demonstrate the efficiency of active-noise barriers, the above conclusions are drawn from numerical simulations with various configurations of multichannel active control system.

III. EXPERIMENTS

Experiments were carried out in an anechoic chamber with a dimension of $4.2 \times 4.2 \times 4.2$ m. The barrier was made of two plywood plates sandwiched with a foam layer. The barrier, 0.05 m thick, 1.0 m high, and 4.2 m long, was placed on the suspended metal-grid floor of the anechoic chamber. For the “nonreflective” experiments, the metal-grid floor was fully covered with a thick carpet; for the “reflective” cases, several metal plates were used to cover the floor on either side as the rigid ground. The primary noise source was 1.38 m away from the barrier, 0.5 m above the floor and along the central axis of the chamber. The control system consists of three half-enclosed speakers as control sources, three microphones as error sensors, and a multichannel EZ-ANC as the controller. The arrangement of the control system is shown in Fig. 10.

To show that the control system is also effective for noise with multiple-frequency components, the sound signal used in the experiment was a ramp wave with the fundamental frequency of 130 Hz. A low-pass filter with a cutoff frequency of 500 Hz was used to eliminate the high-frequency

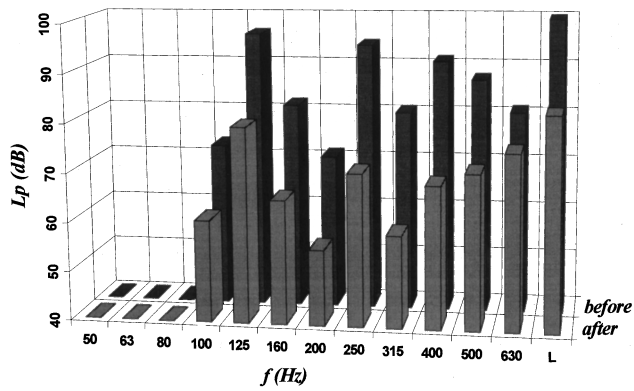


FIG. 11. 1/3-octave spectra of sound-pressure levels at an error microphone before and after control.

components. This signal from the filter was fed directly into the primary source, and was also provided to the controller as a reference signal. Three control channels of the controller were used to cancel the total sound pressure at the positions of three error microphones. The coordinates of the control sources and error microphones are the same as those used in the computer simulation discussed above: $[(-0.69, (i-2)r_{ss}, 0.75)]$ and $[0, (i-2)r_{ss}, 1]$, respectively, in meters, where $i = 1, 2, 3$. Using the upper limit of the frequency range, $f = 500$ Hz, to calculate the optimal range, the interval of the

control sources is also chosen within the optimal range as $r_{ss} = 0.75\lambda$.

The 1/3-octave spectra of the sound-pressure level of the noise at one of the microphones on the barrier top, before and after the control, are presented in Fig. 11. The figure shows that the noise consists of several components (130, 260, 390, and 520 Hz) in the frequency range from 0–630 Hz. The control system attenuated about 20-dB sound-pressure level at the error microphone. This sound-pressure reduction is achieved for all components of the spectrum.

The extra insertion losses caused by the active control system for four arrangements, (1) the ground on both sides of the barrier is nonreflective, (2) only the ground on the receiving side is reflective, (3) only the ground on the source side is reflective, and (4) the ground on both sides of the barrier is reflective, were measured in the x - y plane that is 0.5 m in height and immediately behind the receiving side of the barrier. The experimental results on the overall band are presented in Fig. 12.

Figure 12 demonstrates that reflections from the ground do reduce the efficiency of the active noise-control system used for improving the low-frequency performance of the noise barrier. The extra insertion loss caused by the control system is greatest when the ground on both sides is totally nonreflective, as shown in Fig. 12(a). Figure 12(b) indicates that, although the increased reflection from the ground on the

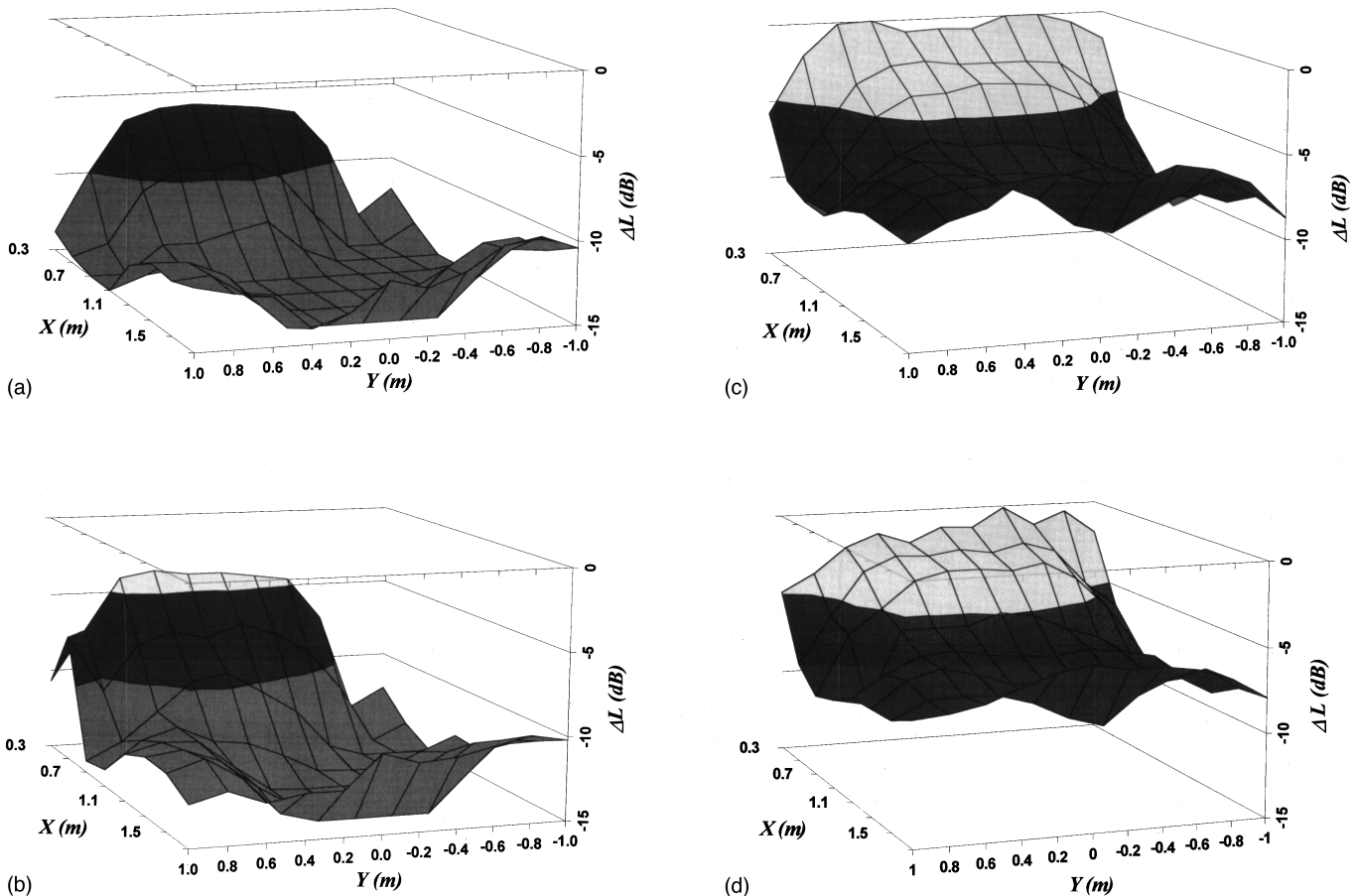
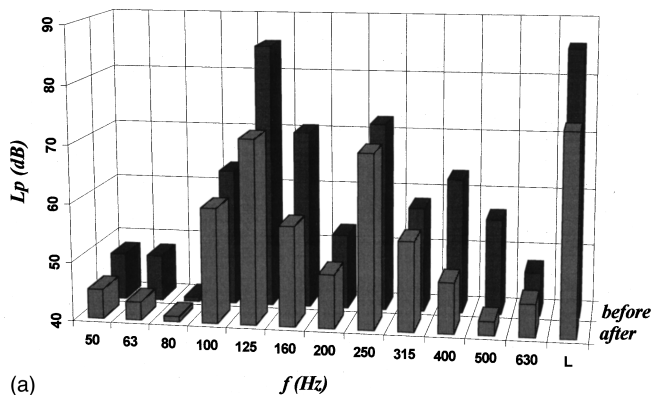
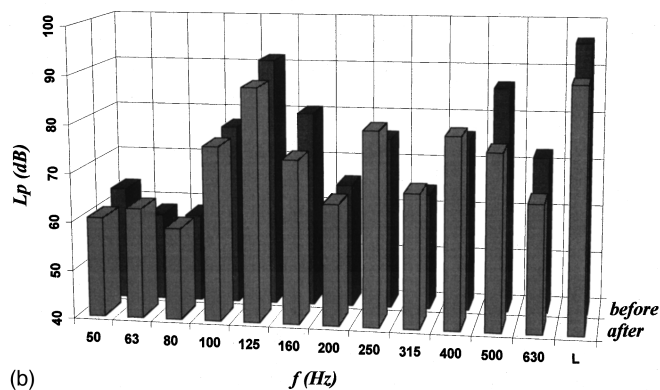


FIG. 12. Extra insertion loss of the active-noise barrier when (a) nonreflective ground on both sides, (b) reflective ground on receiving side only, (c) reflective ground on source side only, and (d) reflective ground on both sides.



(a)



(b)

FIG. 13. 1/3-octave spectra of noise at a position in dark area before and after control when (a) the ground is totally nonreflective and (b) the ground is totally reflective.

receiving side decreases the extra insertion loss, this decrease is relatively small. However, reflection from the ground on the source side significantly reduces the efficiency of the active-noise barrier, as shown in Fig. 12(c). The reduction of the extra insertion loss in this case is more than 5 dB over most of the area in the measuring plane. Figure 12(d) shows the extra insertion loss of the active-noise barrier when the ground on both sides of the barrier is totally reflective. It is obvious that the difference between the two cases, as shown in Fig. 12(c) and (d) in terms of extra insertion loss, is small. This demonstrates that the effect of the reflective ground on the efficiency of active noise control in increasing the insertion loss of the barrier comes mainly from reflection from the ground on the source side. It can be concluded that when the active noise-control system is applied to increase the insertion loss of the noise barrier, some passive treatment in reducing reflection from the ground on the source side can significantly improve the performance of the active-noise barrier.

The 1/3-octave spectra of the noise at a position located at (0.9,0,0.5) in the observation plane, before and after control, are given in Fig. 13. Figure 13(a) and (b) show the cases when the ground on both sides of the barrier is totally nonreflective and totally reflective, respectively. It can be seen that the total extra sound attenuation at that position is more than 10 dB for the case of nonreflective ground; each com-

ponent of the noise achieves some level of reduction. For the case of reflective ground, the total sound-pressure level is attenuated by only about 5 dB. While some peak components of the noise are reduced to some extent, the levels of the other components of the noise may even increase after the control.

IV. CONCLUSIONS

The insertion loss of the noise barriers can be significantly increased by introducing a multichannel active noise-control system in which the sensors and actuators of the system are optimally arranged. The optimal spacing of the control sources and error microphones is not necessarily less than 1/2 wavelength,⁹ but is given as a range expressed by Eqs. (6) and (7). For the multichannel active-control system, the more control sources are used, the larger the size of the improved dark area. As the size of the improved dark area is proportional to the wavelength of the noise, it can be concluded that the active-noise barrier is more useful in the low-frequency range where the passive-noise barrier is not effective.

Reflection from the ground significantly reduces the effectiveness of applying an active noise-control system to improve the performance of the barrier. This conclusion was also obtained previously.¹⁰ However, it has been demonstrated in this paper that this reduction is due to the reduction of sound attenuation on the barrier top by the reflective ground. It has also been demonstrated in this paper that reflection from the ground on the source side contributes most significantly to this reduction. This suggests that, in practice, the extra insertion loss of the active-noise barrier can be increased by reducing reflection from the ground on the source side.

The experiments in this research indicate that the active-noise barrier is also effective for noise with multiple-frequency components. When the system is optimally arranged with respect to a specific frequency, the system is also able to increase the insertion loss of the barrier for a range of frequency components around the specified frequency.

¹Z. Maekawa, "Noise reduction by screens," *Appl. Acoust.* **1**, 157–173 (1968).

²K. Fujiwara, Y. Ando, and Z. Maekawa, "Noise control by barriers-part 2: noise reduction by an absorptive barrier," *Appl. Acoust.* **10**, 167–179 (1977).

³D. N. May and M. M. Osman, "Highway noise barriers: new sharps," *J. Sound Vib.* **71**, 73–101 (1980).

⁴D. Lohmann, "A noise reduction by single- and double-wall barriers," *J. Acoust. Soc. Am.* **67**, 1974–1979 (1980).

⁵J. J. Hajek and C. T. Blaney, "Evaluation of T-profile Highway Noise Barriers," *Transp. Res. Rec.* **983**, 8–17 (1985).

⁶P. A. Nelson and S. J. Elliott, *Active Control of Sound* (Academic, San Diego, 1992).

⁷J. Guo and J. Pan, "Analysis of active noise control in a free field," *Proceedings of Active 95*, Newport Beach, California, 649–660 (1995).

⁸S. Ise, H. Yano, and H. Tachibana, "Basic study on active noise barrier," *J. Acoust. Soc. Jpn.* **12**, 299–306 (1991).

⁹A. Omoto and K. Fujiwara, "A study of an actively controlled noise barrier," *J. Acoust. Soc. Am.* **94**, 2173–2180 (1993).

- ¹⁰ A. Omoto, K. Takashima, and K. Fujiwara, "Active suppression of sound diffracted by barrier-cancellation of reflected sound from the ground," *J. Acoust. Soc. Jpn.* **51**, 375–383 (1995).
- ¹¹ J. Guo, J. Pan, and C. Bao, "Actively created quiet zones by multiple control sources in free space," *J. Acoust. Soc. Am.* **101**, 1492–1501 (1997).
- ¹² J. Guo and J. Pan, "Application of active noise control to noise barriers," *Acoustics Australia* **25**(1), 11–16 (1997).
- ¹³ J. Guo and J. Pan, "Effects of reflective ground on the actively created quiet zones," *J. Acoust. Soc. Am.* **103**, 944–952 (1998).
- ¹⁴ A. Sommerfeld, *Optics* (Academic, New York, 1954).
- ¹⁵ M. Born and E. Wolf, *Principles of Optics* (Pergamon, London, 1959).
- ¹⁶ J. J. Bowman, T. B. A. Senior, and P. L. E. Uslenghi, *Electromagnetic and Acoustic Scattering by Simple Shapes* (North-Holland, Amsterdam, 1969).
- ¹⁷ J. Guo, "Active noise control in open space and its application to noise barriers," Ph.D. thesis, University of Western Australia, 1997.

Combined feedback–feedforward active control of sound in a room

Wen-Kung Tseng,^{a)} B. Rafaely, and S. J. Elliott

Institute of Sound and Vibration Research, University of Southampton, Southampton, SO17 1BJ, United Kingdom

(Received 16 February 1998; accepted for publication 10 August 1998)

This paper presents an active noise control system with a combined feedback–feedforward configuration, which may be useful when the location and directivity of the primary source in a room are not known. Using the combined system, the need to choose between a feedforward or a feedback system configuration beforehand is avoided. The optimum performance of feedforward, feedback, and the combined active control systems have been calculated from measurements taken in a $7 \times 6 \times 3 \text{ m}^3$ room with various primary source positions. Internal model control (IMC) together with optimal Wiener filtering are used in the design of the optimum controllers, which was performed for each primary source position and also included robust stability to guarantee the stability of the controllers in face of plant uncertainty. The performance of the feedforward controller alone was much more dependent on the position of the primary source than that of the feedback controller alone, but the combined system always performed better than either of those systems. The results also suggested that the combined system could obtain good performance even if the response of its feedback controller was fixed, independently of the primary source location, but the response of its feedforward controller was adapted for different primary source positions. © 1998 Acoustical Society of America. [S0001-4966(98)05111-X]

PACS numbers: 43.50.Ki [MRS]

INTRODUCTION

Active techniques to control sound have recently attracted considerable attention compared to passive techniques.^{1,2} Active noise control (ANC) systems for headsets, air ducts, and aircraft cabins are now commercially available. In general, ANC systems use one of two broad control strategies: feedforward or feedback. A feedforward system uses the input from a reference sensor to produce the control signal, which then drives the secondary actuator to cancel the primary field at the position of an error sensor. A feedforward control system can give good control performance if a reference signal can be obtained which is well correlated with a single primary source, and gives time-advanced information about the primary waveform. Feedforward control has been successfully used for the active control of sound in air ducts and propeller aircraft cabins,^{2–4} for example. However, it is not always possible in practice to obtain a reference signal which is coherent with the primary noise source and is guaranteed to give time advanced information. This situation can arise when the position of the primary source is unknown, or there are multiple primary sources. In this case, a feedback control system can be employed which uses the signal from the error sensor to produce the control signal, and does not require a separate reference sensor. This method has been successfully applied to noise reducing headsets and vibrating panels,^{5–8} for example.

In some situations it is not clear whether a good reference signal can be obtained, because of uncertainties about the primary field. Consider, for example, a room with several

noise sources, e.g., open windows, open doors, machines inside the room, etc. It is not apparent whether a reference sensor placed at one position in the room will always provide a good reference for the primary disturbance, as measured in the location of an error sensor. In this case it is not clear whether to use a feedback system with error sensors only, or a feedforward system with one (or more) reference sensors. For these situations a combined feedback–feedforward system is suggested in this work, which has the ability to operate in a feedforward mode, a feedback mode, or a combined mode, thus avoiding the need to choose the system configuration beforehand. The system is designed as a single unit, and its feedback or feedforward characteristics are decided automatically.

Active noise control systems which use both the error and the reference sensor in a multi-channel configuration have previously been suggested for air ducts^{9,10} and plates.¹¹ In this paper we analyze the performance of such a system in a room, for various locations of the primary noise source. Internal model control (IMC)¹² has been used for the configuration of both the feedforward and feedback controllers,¹³ in which each controller is constructed from a control filter and a plant model. The optimal finite impulse response (FIR) control filter which minimizes the mean-squared error was calculated using Wiener filtering.^{14,15} The need for robust stability of both controllers in the face of plant uncertainty has been emphasized.

An experimental system which included a primary loudspeaker, a secondary loudspeaker, a reference microphone, and an error microphone was designed and placed in a room. The effects of different primary source positions on the performance of the combined system have been investigated

^{a)}Electronic mail: wkt@isvr.soton.ac.uk

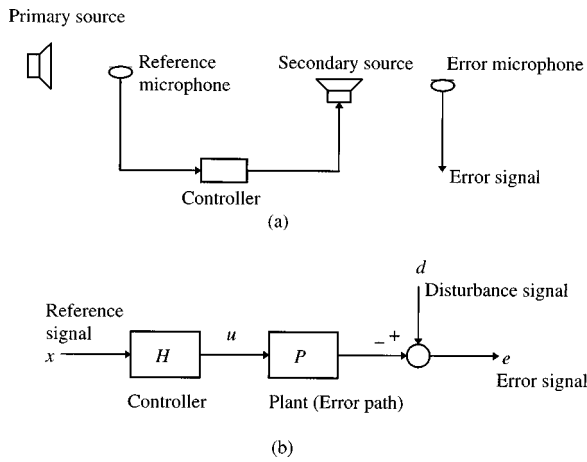


FIG. 1. The configuration of a feedforward active noise control system. (a) Experimental setup; (b) block diagram.

through computer simulations with data measured using the experimental system. The performance of the combined system was compared to that of separate feedback and feedforward control systems for a random disturbance of limited bandwidth produced by the primary loudspeaker. The results show that the performance of the combined feedback-feedforward system was better than the performance of the separate feedback and feedforward systems for all primary source positions.

The paper is presented as follows: in Sec. I we introduce the control systems and the controllers design method. The experimental setup is described in Sec. II, and the results are presented in Sec. III. The paper is then concluded in Sec. IV.

I. CONTROL METHODS

In this section we present the configuration of the feedforward, feedback, and combined feedback-feedforward controllers, and the method used to design the control filters.

A. Feedforward control

The feedforward active noise control system as used here is shown in Fig. 1(a). A reference microphone is used to detect the signal from the primary source, which is then used as the controller input. The controller output signal drives the secondary source (loudspeaker) to cancel the primary noise. An error microphone detects the residual noise, or error signal, which is used in the design of the controller. The behavior of the feedforward system can be described in terms of an equivalent electrical block diagram with discrete signals and frequency response functions as shown in Fig. 1(b). Here x is the reference signal measured from the reference microphone, u is the output of the controller, d is the disturbance signal measured by the error microphone when only the primary source is operating, e is the error signal measured by the error microphone when both the secondary and primary sources are operating, H is the frequency response of the control filter, and P is the frequency response of the plant, i.e., the response from the secondary source to the error microphone.

It is assumed that all the electrical, acoustic, and electroacoustic elements of the physical system are linear and

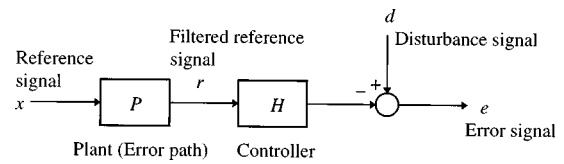


FIG. 2. A feedforward system with the controller and plant changed places.

time invariant. The controller and plant in Fig. 1(b) can then be transposed with no effect on the error signal, as shown in Fig. 2. The filtered reference signal can be written in the sampled time domain as

$$r(n) = \mathbf{p}^T \mathbf{x}(n), \quad (1)$$

where $r(n)$ is the current sample of the reference signal, \mathbf{p} is the vector of N coefficients of the plant impulse response, and the vector $\mathbf{x}(n)$ represents the current and past samples of the reference signal, which can be written as

$$\mathbf{p} = (p_0 \ p_1 \ p_2 \ \cdots \ p_{N-1})^T, \quad (2)$$

$$\mathbf{x}(n) = (x(n) \ x(n-1) \ \cdots \ x(n-N+1))^T. \quad (3)$$

The error signal can be written in terms of the filtered reference signal and the control filter impulse response as

$$e(n) = d(n) - \mathbf{h}^T \mathbf{r}(n), \quad (4)$$

where \mathbf{h} is the vector of control filter coefficients of length L :

$$\mathbf{h} = (h_0 \ h_1 \ h_2 \ \cdots \ h_{L-1})^T, \quad (5)$$

and $\mathbf{r}(n)$ represent the current and past samples of signal r .

The system in Fig. 2 can be recognized as an optimal filtering problem with r as the input signal, d the desired signal, and \mathbf{h} the filter.^{14,15} A control filter that minimizes a cost function of the form $J = E[e^2]$ can therefore be computed as follows.

The cost function can be written using Eq. (4) as

$$\begin{aligned} J &= E[e^2(n)] = E[e(n)e^T(n)] \\ &= \mathbf{h}^T E[\mathbf{r}(n)\mathbf{r}^T(n)]\mathbf{h} - 2\mathbf{h}^T E[\mathbf{r}(n)d(n)] \\ &\quad + E[d^2(n)] = \mathbf{h}^T \mathbf{A} \mathbf{h} - 2\mathbf{h}^T \mathbf{b} + c. \end{aligned} \quad (6)$$

The optimal filter \mathbf{h}_{opt} can now be found by setting the derivative of J with respect to \mathbf{h} to zero, and is given by

$$\mathbf{h}_{\text{opt}} = \mathbf{A}^{-1} \mathbf{b}, \quad (7)$$

where \mathbf{h}_{opt} is the optimal filter, \mathbf{A}^{-1} is the inverse of the autocorrelation matrix of signal r , and \mathbf{b} is the cross-correlation vector of signals d and r . Equation (7) was used in this paper in the design of the optimal feedforward controller.

The Wiener solution was used here to investigate the performance of a feedforward system through computer simulations with data measured using an experimental system. If a real-time system was to be implemented, an adaptive algorithm such as the least-mean square (LMS) could be used, which under optimal conditions will converge to the Wiener filter.¹⁵

In the feedforward active noise control system presented above, the secondary loudspeaker generates a cancelling sound which propagates also in the direction of the reference microphone as well as in the direction of the error sensor.

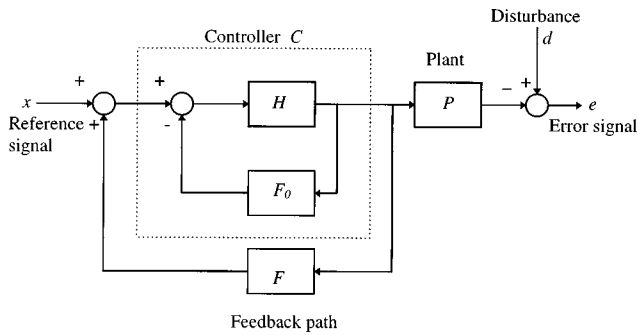


FIG. 3. A block diagram of a feedforward system which includes a model of the feedback path F_0 .

The path from the secondary source input to the reference microphone output is referred to as the feedback path. The existence of a feedback path can result in a corrupted reference signal and may cause instability to the controller if the controller is not carefully designed. This problem can be reduced by using a cancellation filter, or neutralization filter,^{16,17} which is connected in parallel to the feedback path and reduces its effect. In this paper, a cancellation filter F_0 was used within the controller to cancel the effect of the feedback path, as shown in Fig. 3. In the feedforward systems designed in this paper a fixed cancellation filter was used, even though the physical feedback path varied to some extent with conditions in the room. It was found, however, that because the feedback path in this case was relatively weak, the stability and performance of the feedforward controller were not significantly affected when a fixed cancellation filter was used. If, however, the feedback path did affect the system stability, even with the cancellation filter in place, due to a strong feedback path subject to large changes, for example, a robust control filter could still be designed, using techniques similar to the robust feedback controller design described below.

B. Feedback control

The feedback active noise control system used in this paper is shown in Fig. 4(a), in which the signal from an error microphone is fed back to a secondary source through a controller C . The behavior of the system in Fig. 4(a) can be described in terms of an equivalent electrical block diagram as shown in Fig. 4(b), where P is the frequency response of the plant which is again the response from the secondary loudspeaker to the error microphone, C is the frequency response of the feedback controller, d is the disturbance signal measured by the error microphone with only the primary source operating, e is the error signal measured by the error microphone when both the primary and secondary sources are operating, and u is the controller output.

The feedback system shown in Fig. 4(b) can be implemented using an internal model control (IMC) architecture with an internal model of the plant within the controller, which is driven by the same signal as the plant, as shown in Fig. 5. Here H is the frequency response of the control filter, P_0 is the frequency response of the plant model, and x is the input to the control filter.

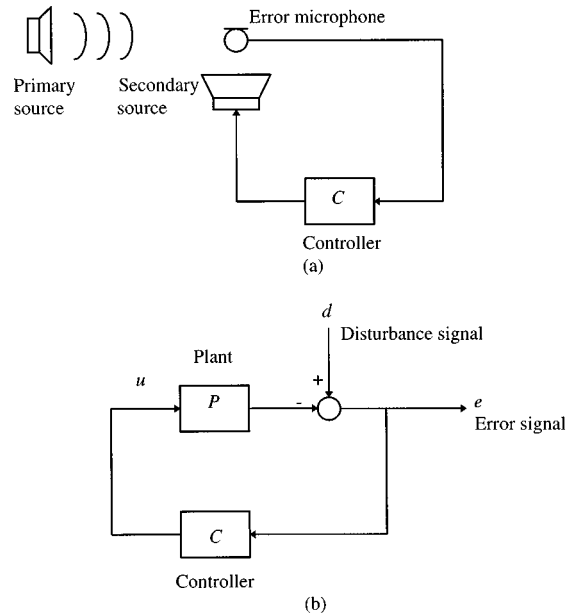


FIG. 4. The configuration of an active noise control system which uses feedback control. (a) Schematic diagram; (b) electrical block diagram.

The frequency response of the feedback controller can be written as

$$C = \frac{H}{1 - P_0 H}. \quad (8)$$

If the plant model is perfect so that $P_0 = P$, then the IMC controller (as in Fig. 5) reduces to a pure feedforward system as shown in Fig. 1(b).¹³ This is since the path from the controller output back to its input through the plant is cancelled by a similar path, but opposite in sign, through the plant model. With the feedback path cancelled, the IMC controller is equivalent to a feedforward system. In this case the signal x is equal to the disturbance signal d , and the design of the feedback controller can be reduced to a standard optimal filtering problem, similar to the feedforward case presented above. However, since in practice $P \neq P_0$, the feedback controller must be designed to be robustly stable for some given uncertainty in the plant response. This is achieved by adding an effort term to the cost function, as follows:

$$J = E[e^2(n)] + \beta \mathbf{h}^T \mathbf{h}, \quad (9)$$

where β is the effort coefficient. A similar approach to increase robustness is found in linear quadratic Gaussian (LQG) controller design methods.¹⁸ The optimal control fil-

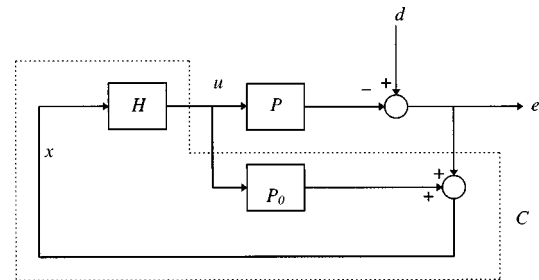


FIG. 5. Block diagram of an internal model controller in a feedback control system.

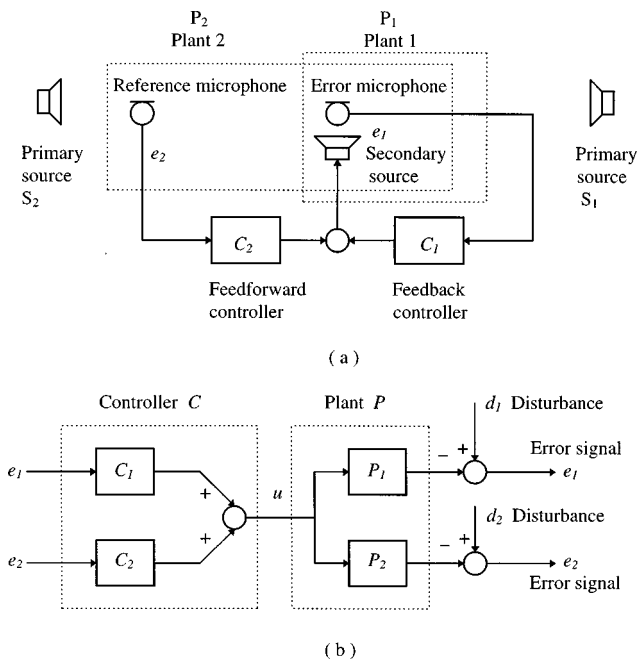


FIG. 6. The configuration of a combined feedback–feedforward system. (a) Schematic diagram; (b) electrical block diagram.

ter can now be found in a similar way to the feedforward case presented above, and is given by

$$\mathbf{h}_{\text{opt}} = (\mathbf{A} + \beta \mathbf{I})^{-1} \mathbf{b}, \quad (10)$$

where \mathbf{A} is the autocorrelation matrix of the filtered reference signal r (the signal x filtered by the plant model filter), and \mathbf{b} is the cross-correlation vector of the filtered reference signal r and disturbance signal d .

Although β is used here to increase system robustness, a measure to system robustness is still required for choosing an appropriate value for β . A multiplicative model for the plant uncertainty is used to derive the robust stability condition.^{12,19} It is assumed that the set of all possible plants, representing the system in various conditions, is described by a multiplicative uncertainty model and can be written as

$$P = P_0(1 + \Delta P), \quad (11)$$

where P_0 is the nominal plant response and ΔP is the fractional change in the plant response. The limit of the magnitude of ΔP , which can be found from measurements, for example, is given by

$$|\Delta P(j\omega)| \leq \ell(\omega), \quad (12)$$

where $\ell(\omega)$ is a real function of frequency.

The robust stability condition for the feedback controller can now be written as¹⁹

$$|HP_0\ell| < 1, \quad \text{for all } \omega, \quad (13)$$

which can be written in terms of the ∞ -norm as

$$\|HP_0\ell\|_{\infty} < 1. \quad (14)$$

Equations (10) and (14) can be used to design the feedback controller as follows:

- (a) Compute H using $\mathbf{h}_{\text{opt}} = (\mathbf{A} + \beta \mathbf{I})^{-1} \mathbf{b}$ for increasing values of β .

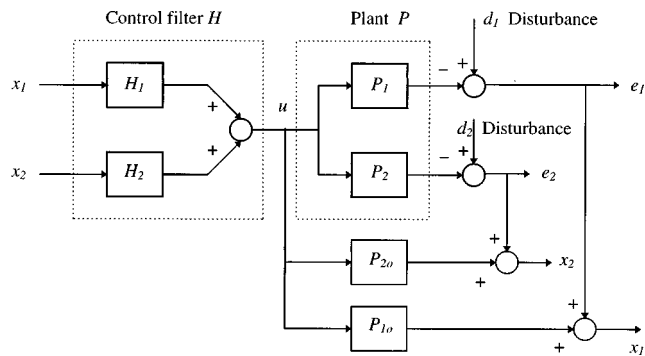


FIG. 7. Block diagram of the combined system with an internal model control configuration.

- (b) Repeat (a) until the robust stability condition, $\|HP_0\ell\|_{\infty} < 1$, is satisfied with the smallest β .

The configuration and design method for the combined feedback–feedforward system are presented in the following section.

C. Combined feedback–feedforward control

Active control system which uses a combined feedback–feedforward configuration is shown in Fig. 6(a), in which the signal e_1 from the error microphone is fed back to a secondary source through the controller C_1 , and the signal e_2 from the reference microphone is used to drive a secondary source through the controller C_2 . The behavior of the system in Fig. 6(a) can be described in terms of an equivalent electrical block diagram as shown in Fig. 6(b), where d_2 and d_1 are the disturbance signals, as detected by the reference and error microphones respectively.

The combined system shown in Fig. 6(b) can be implemented using internal model control, as shown in Fig. 7, where H_1 and H_2 are control filters, P_{1o} and P_{2o} are the plant models, and x_1 and x_2 are inputs to the control filters. If the plant models are perfect so that $P_1 = P_{1o}$ and $P_2 = P_{2o}$, then the inputs to the control filters H_1 and H_2 are equal to d_1 and d_2 , respectively, and the system can be represented as shown in Fig. 8. Since the objective here is to minimize the signal e_1 from the error sensor, only a part of the combined system need be considered. It has also been assumed that the plant and controller responses are linear and time invariant, so we can commute their order, as shown in Fig. 8. The inputs to the control filters are denoted by r_1 and r_2 , which can be written in the sampled time domain as

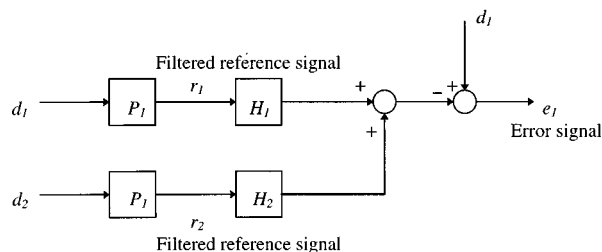


FIG. 8. A simplified configuration of the combined system with the control filters and plants changed places, assuming $P_1 = P_{1o}$ and $P_2 = P_{2o}$.

$$r_1(n) = \mathbf{p}_1^T \mathbf{d}_1(n), \quad (15)$$

$$r_2(n) = \mathbf{p}_1^T \mathbf{d}_2(n), \quad (16)$$

where $r_1(n)$ and $r_2(n)$ are the current samples of the filtered reference signals, \mathbf{p}_1 is the impulse response vector of the feedback plant, and $\mathbf{d}_1(n)$ and $\mathbf{d}_2(n)$ are the current and past samples of the disturbance signals, which can be written in the following form:

$$\mathbf{p}_1 = (p_{10} \ p_{11} \ \cdots \ p_{1N-1})^T, \quad (17)$$

$$\mathbf{d}_1(n) = (d_1(n) \ d_1(n-1) \ \cdots \ d_1(n-N+1))^T, \quad (18)$$

$$\mathbf{d}_2(n) = (d_2(n) \ d_2(n-1) \ \cdots \ d_2(n-N+1))^T. \quad (19)$$

The error signal can now be written in terms of the control filters as

$$e_1(n) = d_1(n) - \mathbf{h}_1^T \mathbf{r}_1(n) - \mathbf{h}_2^T \mathbf{r}_2(n), \quad (20)$$

where \mathbf{h}_1 and \mathbf{h}_2 are the discrete impulse responses of the control filters H_1 and H_2 respectively, written as

$$\mathbf{h}_1 = (h_{10} \ h_{11} \ \cdots \ h_{1N-1})^T, \quad (21)$$

$$\mathbf{h}_2 = (h_{20} \ h_{21} \ \cdots \ h_{2N-1})^T, \quad (22)$$

and $\mathbf{r}_1(n)$ and $\mathbf{r}_2(n)$ are vectors representing the time history of signal r_1 , r_2 , written as

$$\mathbf{r}_1(n) = (r_1(n) \ r_1(n-1) \ \cdots \ r_1(n-N+1))^T, \quad (23)$$

$$\mathbf{r}_2(n) = (r_2(n) \ r_2(n-1) \ \cdots \ r_2(n-N+1))^T. \quad (24)$$

Equation (20) can also be expressed in the more compact form as

$$e_1(n) = d_1(n) - \mathbf{h}_c^T \mathbf{r}_c(n), \quad (25)$$

where

$$\mathbf{h}_c = [\mathbf{h}_1^T \ \mathbf{h}_2^T]^T \quad \text{and} \quad \mathbf{r}_c(n) = [\mathbf{r}_1^T \ \mathbf{r}_2^T]^T. \quad (26)$$

We can now design the coefficients of both the feedback and feedforward controllers, contained in \mathbf{h}_c , to minimize a cost function of the form

$$J = E[e_1^2(n)] + \beta \mathbf{h}_c^T \mathbf{h}_c, \quad (27)$$

which is similar to the design of the feedback system presented above, where β is an effort coefficient, and the term $\beta \mathbf{h}_c^T \mathbf{h}_c$ is an effort term used to increase the robustness of the controllers. The optimal set of filter coefficients \mathbf{h}_{copt} , which minimize the quadratic cost function described above, can therefore be computed using

$$\mathbf{h}_{\text{copt}} = (\mathbf{A} + \beta \mathbf{I})^{-1} \mathbf{b}, \quad (28)$$

where \mathbf{A} is now the autocorrelation matrix of the filtered reference signal r_c , and \mathbf{b} is now the cross-correlation vector of the filtered reference signal r_c and disturbance signal d_1 as follows:

$$\mathbf{A} = E[\mathbf{r}_c(n) \mathbf{r}_c^T(n)] = \begin{bmatrix} \mathbf{A}_{11} & \mathbf{A}_{12} \\ \mathbf{A}_{21} & \mathbf{A}_{22} \end{bmatrix}, \quad (29)$$

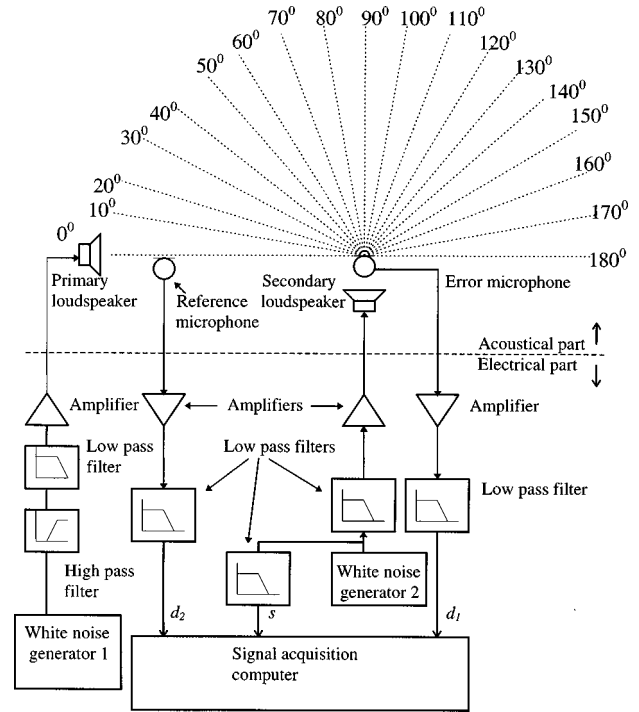


FIG. 9. The experimental setup with the primary source at different positions relative to the error microphone, i.e., 0 to 180 degrees.

where \mathbf{A}_{11} is the autocorrelation matrix of the reference signal r_1 , \mathbf{A}_{22} is the autocorrelation matrix of the reference signal r_2 , and \mathbf{A}_{12} and \mathbf{A}_{21} are the cross-correlation matrices of the reference signals r_1 and r_2 . It is important to note that the matrix \mathbf{A} now includes not only the autocorrelation matrices but also the cross-correlation matrices of the reference signals r_1 and r_2 . The vector \mathbf{b} can be written as

$$\mathbf{b} = E[\mathbf{r}_c(n) d_1(n)] = [\mathbf{b}_1 \ \mathbf{b}_2], \quad (30)$$

where \mathbf{b}_1 is the cross-correlation vector between r_1 and d_1 , and \mathbf{b}_2 is the cross-correlation vector between r_2 and d_1 . We consider here robust stability of the feedback system only (which simplifies the calculation), since, as argued above, the effect of the uncertainty in the feedback path of the feedforward system was found to be negligible. The combined system was therefore designed as follows:

- Compute the optimal filters using $\mathbf{h}_{\text{copt}} = (\mathbf{A} + \beta \mathbf{I})^{-1} \mathbf{b}$.
- Repeat (a) to find the smallest β so that H_1 satisfies $\|H_1 P_{1o}\|_{\infty} < 1$, which is the robust stability condition for the feedback part of the combined system.

II. EXPERIMENTAL SETUP

In this experiment we investigate the active noise control of a random disturbance having limited bandwidth with the feedforward, the feedback, and the combined feedback-feedforward systems described above. To simulate a situation where the position of the primary source is not known in advance, or is time varying, the performance of these systems was studied with a primary source at various angles, ranging from 0 to 180 degrees relative to the error microphone. The experimental setup as shown in Fig. 9 includes a primary loudspeaker, a secondary loudspeaker, a reference

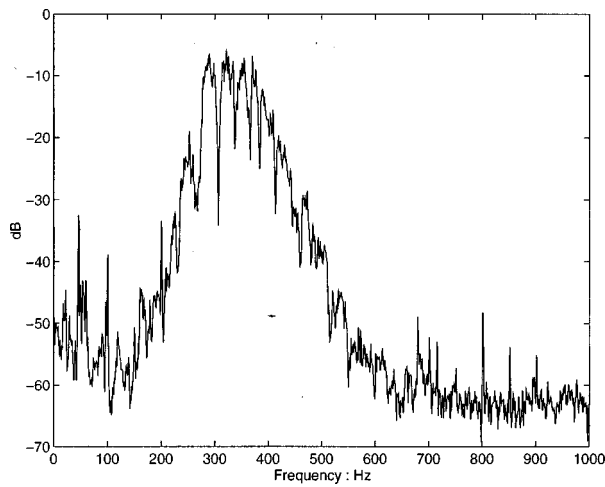


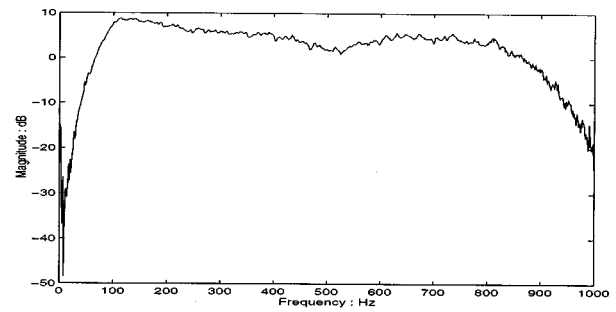
FIG. 10. The power spectral density of the disturbance signal.

microphone, and an error microphone, placed close to the center of a room of dimensions $7 \times 6 \times 3 \text{ m}^3$ with reverberation time of 450 ms at the center frequency of the disturbance. The distance between the primary loudspeaker and the error microphone was 1.3 m and the distance between the reference microphone and the error microphone was 1 m.

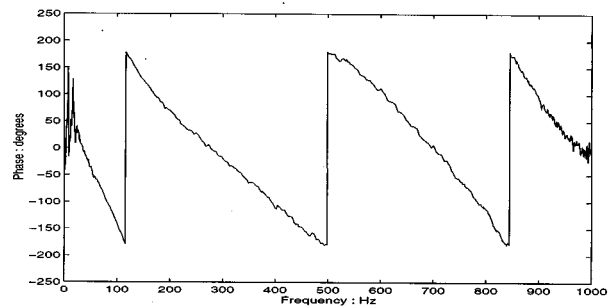
The primary loudspeaker was located in different positions, as shown in Fig. 9. A high-pass filter with a cutoff frequency of 300 Hz and a low-pass filter with a cutoff frequency of 350 Hz were connected between a white noise generator and the primary loudspeaker, to generate a random disturbance with 50-Hz bandwidth. The power spectral density of this disturbance measured at the error microphone is shown in Fig. 10. The primary disturbance was measured using both microphones, through low-pass filters with a cut-off frequency of 900 Hz, and then sampled at a frequency of 2 kHz. The sampled signals were acquired into a PC; 20 000 samples were acquired for each microphone signal in each measurement. The disturbance signals were used later in the design of the controllers.

In a separate experiment, a second white noise generator was connected to the secondary loudspeaker through a low-pass filter and an amplifier as shown in Fig. 9, and was used for the measurement of the frequency response functions between the loudspeaker and microphones. The control simulations described below used the measured frequency response and signals to investigate the performance of the various controllers. If a real-time digital system was to be implemented, then other system components such as the converters and filtering delay would have to be included in the frequency response measurements.

In the design of the feedback controllers a model of the plant response, obtained from measurements, was used rather than that of the real plant. In practice, however, there will be some variation between the response of the plant and that of the model, due to measurement errors and changes in the acoustic environment, for example. These may cause the system to become unstable when the controller designed for the plant model is used, and, therefore, must be considered in the design. To establish the plant uncertainty, the response of the plant was measured when the system was placed in different



(a)



(b)

FIG. 11. The frequency response of feedback plant. (a) Magnitude; (b) phase.

locations in the room and when a $30 \times 20 \times 15 \text{ cm}^3$ box was placed at various positions near the error microphone. These conditions simulated real situations where the system location might vary, or when listeners approach the microphones. The system located at the center of a room was used as a nominal plant response. The measured frequency response of the nominal plant for the feedback system is shown in Fig. 11(a) and (b). Then, the plant response with the system placed at ten different positions in the room was measured, after which the plant response was measured when the box (described above) was placed around the error microphone at ten different positions, at a distance varying from 10 to 150 cm from the error microphone. The maximum multiplicative plant uncertainty ℓ for all the conditions described above was calculated using

$$\ell(\omega) = \max_{P \in \tilde{P}} \left| \frac{P(\omega)}{P_0(\omega)} - 1 \right|, \quad (31)$$

where P_0 is the response of the plant model, and \tilde{P} represents the set of the plant response measurements in the various conditions. The maximum plant uncertainty ℓ is shown in Fig. 12. This uncertainty was used later in the design of robust feedback controllers. The uncertainty of the feedback path in the feedforward system was analyzed in a similar way to that of the plant of the feedback system. It was found to be relatively small, and did not affect the stability or performance of the feedforward system. It was therefore neglected in the design presented below.

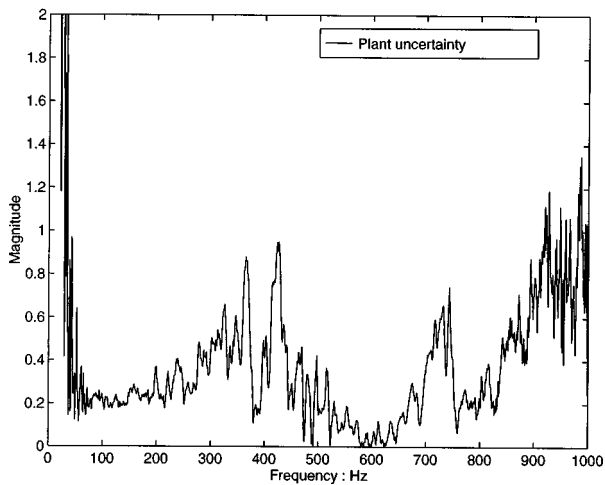


FIG. 12. The multiplicative uncertainty bound of the feedback plant calculated as $\max_p |p(\omega)/p_0(\omega) - 1|$.

III. RESULTS

The data as measured using the experimental setup was used in the design of the controllers as described in Sec. I. The performance of the various controllers was then predicted using simulations with the measured data, where the optimal controllers were calculated for each different primary source position. Figure 13 shows the overall attenuation of the resulting feedforward, feedback, and combined systems, as a function of primary source location. As can be seen, the performance of the feedback controller is similar for all primary source locations, while the feedforward system performs well only when the primary source is located in the direction of the reference microphone. The combined system, however, performs better than both the feedback and the feedforward systems, and is therefore advantageous in this case.

The optimal feedback controller, as presented in Sec. I, depends only on the disturbance power spectrum, measured at the error microphone, which was similar for the various

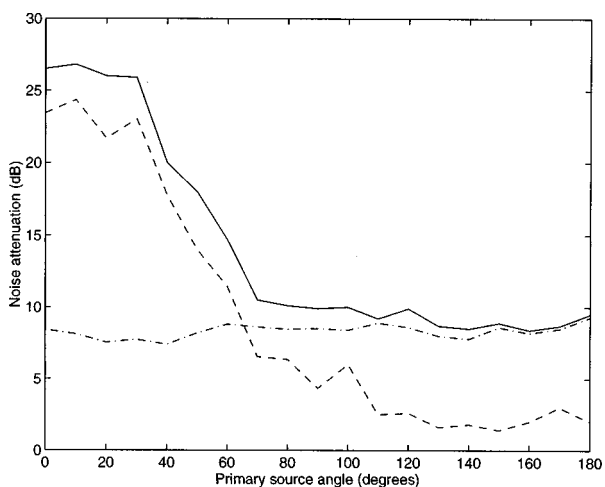


FIG. 13. The variation of noise attenuation with the angle of the primary source for the feedforward system, feedback system, and combined system. Feedforward system (---); feedback system (-.-.); combined system (—).

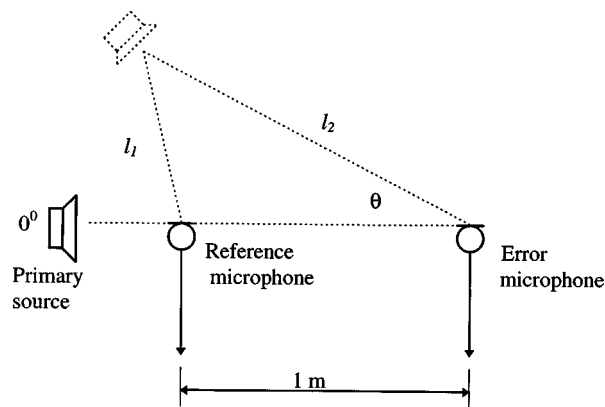


FIG. 14. The geometric arrangement of the primary source relative to the microphone positions.

primary source positions, which explains why the performance was relatively independent of the primary source position. The performance of the feedback system was, however, limited by the delay of the plant, which was about 2.4 ms in this case, since the optimal filter has to perform a prediction of the narrow band disturbance. The performance of the feedforward controller, however, depended significantly on the position of the primary source. As described in Sec. I, the computation of the feedforward controller depends not only on the power spectrum of the disturbance, but also on the cross correlation between the output of the two microphones [see Eq. (7)]. A simple interpretation of the effect of this cross-correlation term is that good performance is achieved as long as the acoustic delay of the primary disturbance, from the reference microphone to the error microphone, is longer than the electronic delay of the feedback plant, or error path, assuming the loudspeaker and error microphone are colocated.¹⁴ The acoustic delay can be calculated using the geometric scheme in Fig. 14. Here, l_1 represents the distance between the primary source and reference microphone, l_2 represents the distance between the primary source and the error microphone, and θ represents the angle between the primary source and the error microphone, as illustrated in Fig. 14. The distance between the reference microphone and the error microphone was 1 m, l_2 was 1.3 m, and l_1 increased as θ increased. It was found that at a primary source position of 21 degrees, the acoustic delay calculated by $(l_2 - l_1)/c_0$, where c_0 is the speed of sound, was equivalent to the delay of the plant, which was about 2.4 ms. Beyond this angle, the optimal controller would be noncausal and will require to perform prediction. Indeed, Fig. 13 shows that for angles above 21 degrees, the performance of the feedforward system does drop, although gradually, since some prediction of the narrow-band disturbance is still possible.

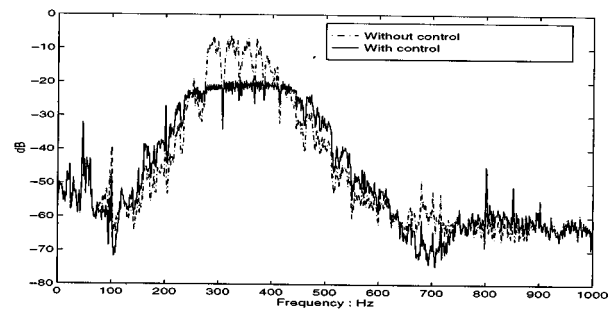
Figure 13 also shows that the performance of the feedforward controller is equal to that of the feedback controller for a primary source position of about 67 degrees. Since the feedback controller was shown to be equivalent to a feedforward controller with a reference signal equal to the disturbance signal [see Sec. I B], it is expected that both controllers will have similar performance when these two signals

are similar. This will occur when $l_1 = l_2$ in Fig. 14, in which case $\theta = 67$ degrees. This results in agreement with the attenuation values presented in Fig. 13.

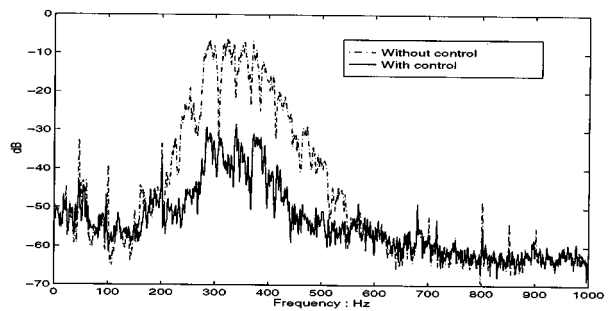
Figure 13 shows that the combined feedback–feedforward system always performed as well as either systems when operated independently. At a source position of 0 degrees, the combined system thus had a predominantly “feedforward” nature, while at source position of 180 degrees it had more “feedback” nature. Therefore, by using the combined system approach, one does not need to decide in advance whether to use feedback or feedforward control, but the design process, which takes account of the primary sound field conditions, determines the best configuration.

It is interesting to note that the combined system actually performed somewhat better than the feedforward system for primary source angle near 0 degrees. The power spectral density of the disturbance before and after control was calculated at 0 degrees for the feedback system, feedforward system, and combined system, and is presented in Fig. 15(a)–(c), respectively. The overall attenuation was 8.4 dB for the feedback system, 23.4 dB for the feedforward system, and 26.5 dB for the combined system. In this case the power spectral density of the disturbance after control with the combined system was more uniform than that with the feedforward system. The improvement of the combined system over the feedforward system in this case can be explained by the fact that the performance of the feedforward system is limited by the coherence between the disturbance signal and the filtered reference signal, which is dependent on the exact excitation frequency and source and microphone positions in the room, and can be poor for some excitation frequencies in any particular geometry. This leads to the rather peaky nature of the residual disturbance for the feedforward controller observed in Fig. 15(b). The feedback controller alone is able to suppress spectral peaks in the disturbance by predicting their waveform, even though the level of suppression is limited by the delay in the plant, as shown in Fig. 15(a). The feedback part of the combined controller is therefore able to suppress the relatively narrow spectral peaks in the residual spectrum of the feedforward controller to give the more uniform residual spectrum shown in Fig. 15(c), and hence achieve a further 3.1 dB of overall attenuation.

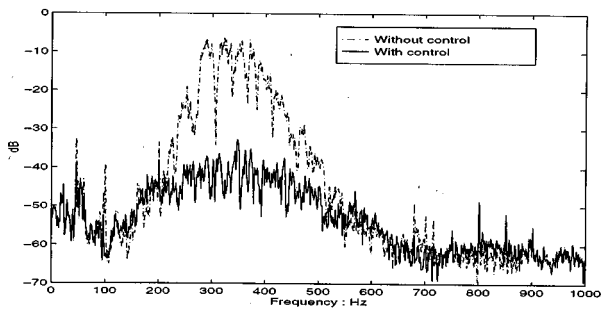
The effect of the primary source position on the performance of the combined system was also investigated for fixed feedback and feedforward control filters, i.e., control filters which did not vary as a function of source location. The feedback and feedforward control filters in the combined system were set to the average value over all source positions. Figure 16 shows the noise attenuation curves of the combined system with varying and fixed feedback and feedforward control filters. From Fig. 16 it is clear that the performance of the combined system with a fixed feedback control filter and a varying feedforward control filter is similar to that with both control filters varying. However, the performance is poor when both the feedforward and feedback control filters are fixed. This is because the optimal feedforward control filter in the combined system depends significantly on source position, whereas the optimal feedback filter does not as argued above. Therefore, a practical combined



(a)



(b)



(c)

FIG. 15. The power spectral density of the disturbance, before control (---) and after control (—). (a) The feedback system; (b) the feedforward system; and (c) the combined system with the primary source at 0 degrees.

feedback–feedforward system could be implemented using a fixed, analog, or digital feedback controller part, and an adaptive feedforward controller part, using the filtered- x LMS algorithm, for example.¹⁵

IV. CONCLUSION

In this paper a combined feedback–feedforward active noise control has been suggested for situations in which the location and directivity of the primary sources are not known. Optimal feedforward, feedback, and combined controllers have been designed for the active control of sound in a room with various primary source locations. The design of the optimal feedback controller included robust stability and thus the predictions of performance are felt to be realistic in representing a practical control system. It has been shown that in this case a combined feedback–feedforward system

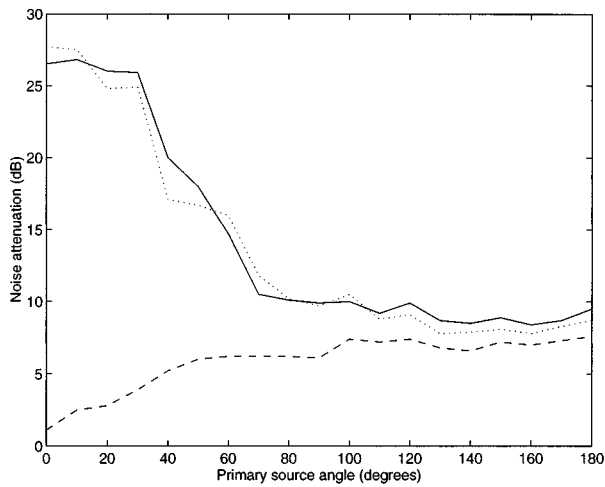


FIG. 16. The noise attenuation curves of the combined system for varying and fixed feedback and feedforward control filters. (1) Feedback control filter is fixed and feedforward control filter is varying (\cdots); (2) both control filters are fixed with the feedforward control filter set to an average value ($---$); and (3) both control filters are varying ($---$).

performs better than either a separate feedback or a separate feedforward system. The use of the combined system avoids the need to decide in advance between these two configurations. It has also been found that the optimal design of the feedforward controller is very dependent on primary source position, whereas that of the feedback controller is not.

A practical combined system could thus be designed with a fixed feedback controller part, and an adaptive feedforward controller part, which “tracks” primary source location. The real-time implementation of a combined system, and the use of other multi-input–multi-output (MIMO) design techniques to obtain robust stability in the combined system are suggested for future research.

¹S. J. Elliott and P. A. Nelson, “Active noise control,” *IEEE Signal Process. Mag.* **10**, 12–35 (1993).

²C. R. Fuller and A. H. von Flotow, “Active control of sound and vibration,” *IEEE Control Systems Magazine* **15**(6), 9–19 (1995).

³M. S. Bai and D. J. Lee, “Implementation of an active headset by using the H_∞ robust control theory,” *J. Acoust. Soc. Am.* **102**, 2184–2190 (1997).

⁴J. C. Burgess, “Active adaptive sound control in a duct: A computer simulation,” *J. Acoust. Soc. Am.* **70**, 715–726 (1981).

⁵B. Rafaely and S. J. Elliott, “Internal model controller for feedback control of sound and vibration,” Technical memorandum No. 776, ISVR, University of Southampton, England (1996).

⁶J. G. Casali and G. S. Robinson, “Narrow-band digital active noise reduction in siren-cancelling headset: real-ear and acoustical manikin loss,” *Noise Control Eng. J.* **42**(3), 101–115 (1994).

⁷B. Rafaely and S. J. Elliott, “ H_2/H_∞ active control of sound in a headset: design and implementation,” to be published in the *IEEE Transactions on Control Systems Technology* (1999).

⁸B. Rafaely, “Feedback control of sound,” Ph.D. thesis, University of Southampton, England, 1997.

⁹Y. Chait, C. V. Hollot, P. Mehta, and Y. Zheng, “Active noise control in ducts using non-adaptive feedforward/feedback control,” National Conference on Noise Control Engineering, Washington, September 1996.

¹⁰N. J. Doelman, “Design of systems for active sound control,” Ph.D. thesis, Delft University, Netherland, 1993.

¹¹R. S. William, H. R. Harry, and A. B. Ricardo, “A hybrid structural control approach for narrow-band impulsive disturbance rejection,” *Noise Control Eng. J.* **44**(1), 11–21 (1996).

¹²M. Morari and E. Zafiriou, *Robust Process Control* (Prentice–Hall, Englewood Cliffs, NJ, 1989).

¹³S. J. Elliott and T. J. Sutton, “Feedforward and feedback methods for active noise control,” *Proc. I. O. A.* **16**, 255–274 (1994).

¹⁴P. A. Nelson and S. J. Elliott, *Active Control of Sound* (Academic, New York, 1992).

¹⁵B. Widrow and S. D. Stearns, *Adaptive Signal Processing* (Prentice–Hall, New York, 1985).

¹⁶S. M. Kuo and D. R. Morgan, *Active Noise Control Systems: Algorithms and DSP Implementations* (Wiley, New York, 1995).

¹⁷M. S. Bai and T. Y. Wu, “Study of the acoustic feedback problem of active noise control by using the l_1 and l_2 vector space optimization approaches,” *J. Acoust. Soc. Am.* **102**, 1004–1012 (1997).

¹⁸B. D. O. Anderson and J. B. Moore, *Optimal Control: Linear Quadratic Methods* (Prentice Hall, Englewood Cliffs NJ, 1989).

¹⁹J. C. Doyle, B. A. Francis, and A. R. Tannenbaum, *Feedback Control Theory* (Macmillan, New York, 1992).

Sound exposure level of railway bridge noise

Rufin Makarewicz^{a)} and Jun-ichi Koga

Department of Acoustic Design, Kyushu Institute of Design, 9-1, Shiobaru 4-chome, Minami-ku, Fukuoka, 815 Japan

(Received 28 June 1997; revised 10 September 1998; accepted 12 September 1998)

A train is considered to be a homogeneous line source; therefore, the concept of the linear density of the A-weighted sound power, W_A , is used. The process of noise generation on a bridge is characterized by the product, $\alpha \cdot W_A$, and that beyond a bridge by $\beta \cdot W_A$, where $\alpha \gg \beta$. Geometrical spreading is considered to be the only wave phenomena that governs noise propagation. The theory presented here requires measurements at two locations in the vicinity of the bridge in question and makes possible the calculation of the sound exposure level, L_{AE} . The obtained experimental values are consistent with the theoretical values. © 1998 Acoustical Society of America. [S0001-4966(98)05312-0]

PACS numbers: 43.50.Lj, 43.50.Vt [MRS]

INTRODUCTION

For common rolling stock at speeds less than 250 [km/h], the main source of noise is wheel–rail interaction, i.e., rolling noise.¹ The time history of noise from a train indicates that at the perpendicular distance from the track exceeding 10 [m], the model of the line of incoherent point sources with dipole directivity can be used.^{2–4} Due to the uniformity of the line source, the concept of the linear density of the A-weighted sound power, W_A , expressed in Watts per meter, is applied. The increase in noise due to a bridge is caused principally by noise emission from the bridge structure itself.^{5–7} We assume the bridge increases the linear density of the A-weighted sound power, $W_A \rightarrow \alpha \cdot W_A$.

In an open space, noise propagation is governed by geometrical spreading, ground effect, refraction, air absorption, and turbulence.⁸ During a sunny and windy day, turbulence destroys the coherent interference between the direct and reflected waves.^{9,10} So, when the train is on an embankment or at-grade, the only result of the ground effect is the virtual change of sound power due to the noise reflection from the ballast bed beneath the train, $W_A \rightarrow \beta \cdot W_A$.

The train noise due to a single passby can be assessed in terms of the sound exposure level,

$$L_{AE} = 10 \lg \left\{ \frac{E}{p_0^2 t_0} \right\}, \quad (1)$$

where $p_0 = 20 \mu\text{Pa}$ and $t_0 = 1 \text{ s}$. The sound exposure, E , is given by an integral of the A-weighted squared sound pressure,

$$E = \int_{-\infty}^{+\infty} p_A^2(t) dt. \quad (2)$$

Within 100 [m] from the track, under the circumstances mentioned above, L_{AE} depends mostly on geometrical spreading, which is described in Sec. I. We consider two cases. The general case, with noise reaching the receiver

from the whole track, i.e., from two track segments on both sides of the bridge, and the bridge itself. In the special case, we assume one track segment passes through an urban area. Thus, the main contribution to noise at the receiver is made by the train on the bridge and on the second segment of the track. In Sec. II we study the noise increment due to the bridge, and in Sec. III we demonstrate how to assess the accuracy of noise prediction. Finally, in Sec. IV, comparison between the predicted values of the sound exposure level and the experimental results is made.

I. THEORY

When a unit length line source ($l_0 = 1 \text{ m}$) of dipole directivity is on a bridge, the A-weighted squared sound pressure is given by^{11,12}

$$p_{Ab}^2 = \frac{3}{4\pi} \frac{\alpha \cdot W_A l_0 \rho c}{r^2} \cos^2 \Theta, \quad (3)$$

where Θ denotes the angle between the source–receiver line and the y axis (Fig. 1), the product, $W_A \cdot l_0$, expresses the A-weighted sound power, ρc is the characteristic impedance of air, and r is the source–receiver distance. In the above equation $\alpha \gg 1$ accounts for the noise enhancement due to the bridge structure. For the unit length line source on an embankment or at-grade, we write,

$$p_{Ae}^2 = \frac{3}{4\pi} \frac{\beta \cdot W_A l_0 \rho c}{r^2} \cos^2 \Theta, \quad (4)$$

where β describes the noise reflection from the ballast bed. The A-weighted sound power, $W_A l_0$, is assumed to be constant when on the bridge and also constant when on the embankment. This is not always valid, e.g., when train is on jointed track. The objective of this study, however, is not the time history of noise, $L_A(t)$, but the numerical value of the sound exposure level, L_{AE} .

Assuming the train moves with a steady speed, V , along the x axis, we introduce the new variable, $\Phi = \tan^{-1}(Vt/y)$ (Fig. 2). For nearly horizontal propagation close to the

^{a)}On leave from: Institute of Acoustics, A. Mickiewicz University, 60-769 Poznan, Matejki 48, Poland.

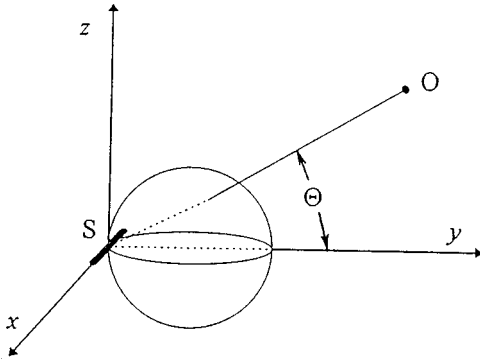


FIG. 1. Noise generation by a unit length line source ($l_0 = 1$ m) with maximum radiation along the y axis.

ground surface $x-y$, we can write $\Theta \approx \Phi$ (Figs. 1, 2). Hence, the sound exposure for the train of length, l , is given by^{11,12}

$$E = \frac{yl}{Vl_0} \int_{-\pi/2}^{+\pi/2} \frac{p_A^2(\Phi) d\Phi}{\cos^2 \Phi}, \quad (5)$$

where y is the perpendicular distance between the track and receiver, O . Figure 2 illustrates the relationship between y and the horizontal distance, $d = y/\cos \Phi$.

A. General case

The noise event related to a single passby consists of three parts: train motion on the left-hand side of the bridge from $x = -\infty$ to $x = -L$, then comes the bridge crossing from $x = -L$ to $x = 0$, and finally, the train motion along the track segment on the right-hand side of the bridge from $x = 0$ to $x = +\infty$. Thus, the sound exposure is (Fig. 3)

$$E = \frac{yl}{Vl_0} \left[\int_{-\pi/2}^{\Phi_1} \frac{p_{Ae}^2 d\Phi}{\cos^2 \Phi} + \int_{\Phi_1}^{\Phi_2} \frac{p_{Ab}^2 d\Phi}{\cos^2 \Phi} + \int_{\Phi_2}^{\pi/2} \frac{p_{Ae}^2 d\Phi}{\cos^2 \Phi} \right]. \quad (6)$$

From Eqs. (1) and (6), the formula for calculating the sound exposure level becomes

$$L_{AE} = L_\mu + 10 \lg \left\{ \frac{3l_0}{8y} [1 + (m-1) \cdot R(x,y)] \right\}, \quad (7)$$

where $m = \alpha/\beta$ is the *bridge coefficient* and

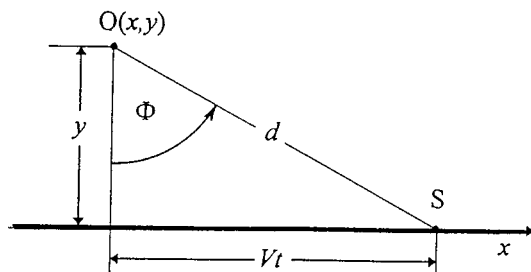


FIG. 2. Location of the unit length line source, S , is determined by the perpendicular distance, y , and the angle, Φ .

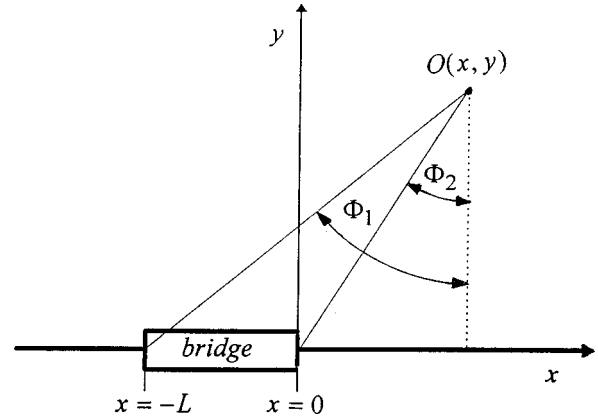


FIG. 3. Location of the bridge of length, L , is determined by the angles, Φ_1 , and Φ_2 .

$$R = \frac{1}{\pi} \left[\tan^{-1} \left(\frac{x+L}{y} \right) - \tan^{-1} \left(\frac{x}{y} \right) + \frac{(x+L)y}{(x+L)^2 + y^2} - \frac{xy}{x^2 + y^2} \right] \quad (8)$$

quantifies the influence of the bridge length, L , and its location in respect to the receiver, $O(x,y)$. For example, R tends to zero when the bridge is short as compared with the longitudinal distance ($L \ll x$), the receiver is far away from the bridge ($|x| \gg L$ and/or $|y| \gg L$) or close to the track ($|y| \ll |x|$). If $x = -L/2$ and $|y| \ll L/2$, the value of R achieves the maximal value of 1. The first term of Eq. (7),

$$L_\mu = 10 \log \left\{ \beta \frac{\mu}{\mu_0} \right\}, \quad (9)$$

expresses the *sound energy density level*, where the ratio of the train power, $W_A \cdot l$, and the train speed, V ,

$$\mu = \frac{W_A \cdot l}{V}, \quad (10)$$

has the dimensions of Joules per meter. Therefore, μ can be interpreted as the linear density of sound energy. The reference quantity is defined by $\mu_0 = W_0/V_0$, where $W_0 = 10^{-12}$ W and $V_0 = 1$ [m/s].

Both free parameters of the model, i.e., the bridge coefficient, m , and the sound energy density level, L_μ , can be estimated from two simultaneous measurements of the sound exposure level, L_{AE} , at longitudinal distances, $x = x_1$ and $x = x_2$, with the same perpendicular distance, $y = D$ (Fig. 4). Considering Eq. (7) as a theoretical prediction with two adjustable parameters, we arrive at

$$m = \frac{1-k}{k \cdot R(x_2, D) - R(x_1, D)} + 1, \quad (11)$$

where the quantity,

$$k = 10^{[L_{AE}(x_1) - L_{AE}(x_2)]/10}, \quad (12)$$

is readily measured. By substituting $x = x_1$, $y = D$, $L_{AE} = L_{AE}(x_1)$, and bridge coefficient, m , into Eq. (7), the sound energy density level, L_μ , is obtained. Both values of m and L_μ depend on the rolling stock, the method of joining the rail

(welded or bolted), the type of track system (wood ties with or without ballast, concrete slab, steel plate deck, etc.), the construction of the bridge, and the train speed.^{13,14}

B. Special case

When the left-hand side segment of the track, $x < -L$ (Fig. 3), is shielded by buildings (urban area), noise from the track segment, $(-\pi/2, \Phi_1)$, can be neglected [Eq. (6)]. Thus, the sound exposure can be calculated from,

$$E \approx \frac{yL}{Vl_0} \left[\int_{\Phi_1}^{\Phi_2} \frac{p_{Ab}^2 d\Phi}{\cos^2 \Phi} + \int_{\Phi_2}^{\pi/2} \frac{p_{Ae}^2 d\Phi}{\cos^2 \Phi} \right]. \quad (13)$$

Proceeding along the lines analogous to those in derivation of Eq. (7) we arrive at

$$L_{AE} = L_\mu + 10 \log \left\{ \frac{3l_0}{8y} [S(x,y) + m \cdot R(x,y)] \right\}, \quad (14)$$

where the function $R(x,y)$ is defined by Eq. (8) and

$$S(x,y) = \frac{1}{2} + \frac{1}{\pi} \left[\tan^{-1} \left(\frac{x}{y} \right) + \frac{xy}{x^2 + y^2} \right] \quad (15)$$

describes the noise contribution from the track segment located on the right-hand side of the bridge, $x > 0$ (Fig. 3). Close to the track, $|y| \ll |x|$, we get $S \rightarrow 1$ and $R \rightarrow 0$, which means that noise radiation from the bridge is negligible.

The bridge coefficient m can be calculated from,

$$m = \frac{S(x_1, D) - k \cdot S(x_2, D)}{k \cdot R(x_2, D) - R(x_1, D)}, \quad (16)$$

where k is determined by Eq. (12). One can find L_μ by substituting $x = x_1$, $y = D$, $L_{AE} = L_{AE}(x_1)$ and m into Eq. (14).

II. BRIDGE COMPONENT OF NOISE

A. General case

Equation (7) yields the sound exposure level, L_{AE} , for the train moving from $x = -\infty$ to $x = +\infty$, and, in the process, traversing the bridge. Let $L_{AE}^{(e)}$ be the sound exposure level of noise from the same train on a plain track, $-\infty < x < +\infty$, as if the bridge were absent. For $\alpha = \beta$ [Eqs. (3), (4)] we get the bridge coefficient, $m = 1$, and Eq. (7) simplifies to the form,

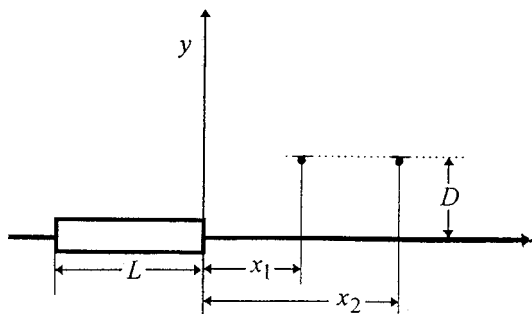


FIG. 4. Scenario of L_{AE} measurements close to the track: both microphones at the same perpendicular distance, D , and the same height, z_0 .

$$L_{AE}^{(e)} = L_\mu + 10 \lg \left\{ \frac{3l_0}{8y} \right\}. \quad (17)$$

The difference, $\Delta L = L_{AE} - L_{AE}^{(e)}$, gives the noise increase due to the bridge itself,

$$\Delta L = 10 \lg \{ 1 + (m-1) \cdot R(x,y) \}, \quad (18)$$

where $R(x,y)$ is defined by Eq. (8). It is seen that the noise increase is a function of location (x,y) . Far away from the bridge, $|x| \gg L$ and/or $|y| \gg L$, and close to the track, $|y| \ll |x|$, the bridge influence decreases, $R \rightarrow 0$, and the above equation yields, $\Delta L \rightarrow 0$. When $x = -L/2$ and $|y| \ll L/2$, the value of R tends to 1 and we obtain the maximal noise increase,

$$\Delta L_{\max} = 10 \lg \{ m \}. \quad (19)$$

B. Special case

When noise produced by the bridge and only one track segment, $x > 0$ (Fig. 3) reaches the receiver, the sound exposure level, L_{AE} , can be calculated from Eq. (14). If the process of noise generation is identical on the track and on the bridge, $m = 1$, then Eq. (14) takes the form

$$L_{AE}^{(e)} = L_\mu + 10 \lg \left\{ \frac{3l_0}{8y} [S(x,y) + R(x,y)] \right\}, \quad (20)$$

and the noise increase caused by the bridge is [Eqs. (14), (20)]

$$\Delta L = 10 \lg \left\{ \frac{S(x,y) + m \cdot R(x,y)}{S(x,y) + R(x,y)} \right\}. \quad (21)$$

Here $R(x,y)$ and $S(x,y)$ are defined by Eqs. (8) and (15), respectively. Similar to the general case considered above, far away from the bridge and close to the track ($R \rightarrow 0$), we get, $\Delta L \rightarrow 0$. When the receiver is opposite to the bridge end ($x = 0$, $|y| \ll L/2$), the noise increase due to the bridge is,

$$\Delta L_* = 10 \lg \{ m + 1 \} - 3. \quad (22)$$

The value of ΔL_* shall be calculated in Sec. IV.

III. PREDICTION ACCURACY

We consider the standard deviation of the sound exposure level, σ_L , as the measure of prediction accuracy. Owing to differences among the cars, varying number of cars, and different speeds, the bridge coefficient, m , and the sound energy density level, L_μ , are random. As a result, the sound exposure level, L_{AE} , is different for each train. Introducing the means, \bar{m} , \bar{L}_μ , and \bar{L}_{AE} , we write for the j -th train,

$$m_j = \bar{m} + \delta m_j, \quad L_{\mu j} = \bar{L}_\mu + \delta L_{\mu j},$$

and

$$L_{AEj} = \bar{L}_{AE} + \delta L_{AEj}. \quad (23)$$

If $\langle u \rangle$ denotes an averaging operation with respect to u for $j = 1, 2, \dots, N$ trains, then the variance of the sound exposure level is,

$$\sigma_L^2 = \langle [L_{AE} - \bar{L}_{AE}]^2 \rangle. \quad (24)$$

Assuming that fluctuations of the bridge coefficient, m , and the sound energy density level, L_μ , are small,

$$|\delta m| \ll \bar{m}, \quad |\delta l_\mu| \ll \bar{L}_\mu, \quad (25)$$

the relationship [Eqs. (7), (14)]

$$L_{AE} = f(L_\mu, m), \quad (26)$$

yields the average,

$$\bar{L}_{AE} = f(\bar{L}_\mu, \bar{m}), \quad (27)$$

and the variance of the sound exposure level,

$$\sigma_L^2 = \left(\frac{\partial f}{\partial L_\mu} \right)^2 \sigma_\mu^2 + 2 \frac{\partial f}{\partial L_\mu} \cdot \frac{\partial f}{\partial m} \sigma_{\mu m} + \left(\frac{\partial f}{\partial m} \right)^2 \sigma_m^2. \quad (28)$$

Here the variances and the covariance of L_μ and m are defined as follows:

$$\sigma_\mu^2 = \langle [L_\mu - \bar{L}_\mu]^2 \rangle, \quad \sigma_m^2 = \langle [m - \bar{m}]^2 \rangle, \quad (29)$$

$$\sigma_{\mu m} = \langle [L_\mu - \bar{L}_\mu] \cdot [m - \bar{m}] \rangle.$$

Now we illustrate application of the above equations.

A. General case

When noise contribution is made by the bridge and both track segments on its right- and left-hand sides, combination of Eqs. (7), (27), and (28) yields the average sound exposure,

$$\bar{L}_{AE} = \bar{L}_\mu + 10 \lg \left\{ \frac{3l_0}{8y} [1 + (\bar{m} - 1) \cdot R(x, y)] \right\}, \quad (30)$$

and its standard deviation,

$$\sigma_L = \sqrt{\sigma_\mu^2 + \frac{20}{\ln 10} \cdot \frac{R}{1 + (\bar{m} - 1)R} \sigma_{\mu m} + \left[\frac{10}{\ln 10} \cdot \frac{R}{1 + (\bar{m} - 1)R} \right]^2 \sigma_m^2}, \quad (31)$$

where $\ln 10 \approx 2.30$. The above equations hold at any longitudinal distance, $-\infty < x < +\infty$. Refraction and air attenuation must not be neglected at a distance exceeding 100 [m]. On the other hand, at the distance $y < 10$ [m], a train cannot be modeled by a line source. Therefore, the perpendicular distance of the receiver has to fulfill the condition, $10 < y < 100$ [m].

When $|x| \gg L$ and $R \rightarrow 0$ [Eq. (8)], we get $\sigma_L = \sigma_\mu$, i.e., standard deviation of the sound exposure level, L_{AE} , equal to the standard deviation of the sound energy density level, L_μ . Close to the bridge end ($x = 0$, $|y| \leq L/2$) with $R \rightarrow 1/2$, $S \rightarrow 1/2$, Eq. (31) yields the standard deviation,

$$\sigma_L \approx \sqrt{\sigma_\mu^2 + \frac{8.68}{\bar{m} + 1} \sigma_{\mu m} + \frac{18.9}{(\bar{m} + 1)^2} \sigma_m^2}. \quad (32)$$

B. Special case

When noise from the left-hand side of the bridge, $x < -L$, is suppressed by buildings or any other obstacles, the average sound exposure level and its standard deviation can be calculated from [Eqs. (14), (27), (28)],

$$\bar{L}_{AE} = \bar{L}_\mu + 10 \lg \left\{ \frac{3l_0}{8y} [S(x, y) + \bar{m} \cdot R(x, y)] \right\}, \quad (33)$$

and

$$\sigma_L = \sqrt{\sigma_\mu^2 + \frac{20}{\ln 10} \cdot \frac{R}{S + \bar{m}R} \sigma_{\mu m} + \left[\frac{10}{\ln 10} \cdot \frac{R}{S + \bar{m}R} \right]^2 \sigma_m^2}. \quad (34)$$

Because of noise reflection and scattering from buildings along the track segment, $x < -L$, the above equations can be applied when $-L < x < +\infty$ and $10 < y < 100$ [m]. Similar to the general case, with $|x| \gg L$ and $R \rightarrow 0$, $S \rightarrow 1/2$ [Eqs. (8), (15)], the above equation yields $\sigma_L = \sigma_\mu$. Close to the bridge

end ($x = 0$, $|y| \leq L/2$), with $R \rightarrow 1/2$ and $S \rightarrow 1/2$, the standard deviation, σ_L achieves the value given by Eq. (32).

IV. MEASUREMENTS AND CALCULATIONS

Close to the Nishitetsu Bridge Line, the north bank of the Nakagawa River in Fukuoka (Japan) is an urban area with relatively high buildings, so the conditions suits to the special case (B) analyzed in previous sections.

Measurements were performed over ten days in summer, 1996. The bridge of length, $L = 141$ [m], is made of four parallel girders, supported by nine concrete columns, on to which wooden sleepers are placed. To obtain the sound exposure levels, $L_{AE}(x_1)$ and $L_{AE}(x_2)$, two microphones were located at the height, $z_0 = 1.2$ [m], above the ground surface at the perpendicular distance, $D = 14$ [m], from the center of the nearest track. The height of the embankment was 1.3 [m]. In order to separate the bridge noise component from that of the train on the embankment, measurements were made close to the bridge end ($x_1 = 0$) with large value of R [Eq. (8)] and in front of the embankment ($x_2 = 50$ m) with small value of R (see Fig. 4). To verify the prediction of the model, a third measurement of \bar{L}_{AE} was made at the study point, $\bar{x} = 0$ and $\bar{y} = 64$ m.

We measured noise of 249 train passages. For each train, the value of the sound energy density level, L_μ , and the bridge coefficient, m , were estimated [Eqs. (14), (16)]. The bridge coefficient is independent of the train speed, V (Fig. 5). The variance is $\sigma_m^2 = 26.9$ and the average is $\bar{m} \approx 17.1$, so the noise increase due to the bridge does not exceed $\Delta L_* \approx 10$ dB [Eq. (22)].

The sound energy density level, L_μ , increases with the train velocity, V (Fig. 6),

$$L_\mu = 16.2 \lg\{V/V_0\} + 84.7, \quad V_0 = 1 \text{ [m/s]}. \quad (35)$$

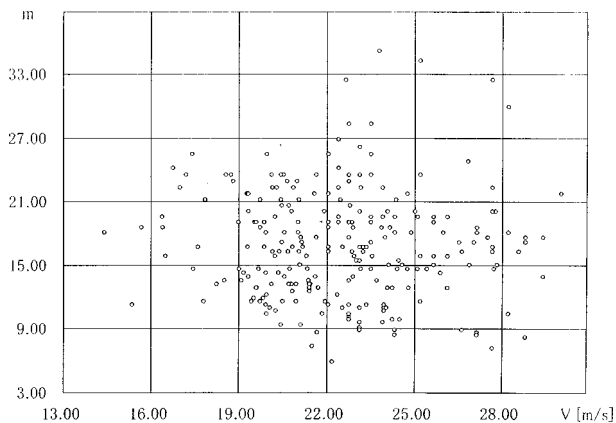


FIG. 5. The bridge coefficient, m , versus train's speed, V [m/s].

The above equation is typical of speed dependence found for train noise.² The variation and the covariance calculated from Eq. (29) are $\sigma_\mu^2 = 3.70$ and $\sigma_{\mu m} = -4.95$, respectively.

To validate the theory, we used the numerical values of L_μ and m for each train, and predicted the sound exposure, L_{AE}^* , for the study point, $\bar{x} = 0$, $\bar{y} = 64$ m [Eqs. (8), (14), (15)]. The measured, \tilde{L}_{AE} , and predicted, L_{AE}^* , sound exposure levels at the study point are shown in Fig. 7. The diagonal line indicates the ideal relationship between the two levels in which the prediction would correspond exactly to the measured value. The difference, $L_{AE}^* - \tilde{L}_{AE}$, ranges from an underprediction of -2.6 dB to an overprediction of $+2.5$ dB. The mean error for 249 measurements is -0.45 dB, and the standard deviation is $\sigma_L = 1.2$ dB. Now, making use of Eq. (32) with $\bar{m} = 17.1$, $\sigma_m^2 = 40.7$, $\sigma_\mu^2 = 3.74$, and $\sigma_{\mu m} = -4.95$, we calculated the standard deviation of the sound exposure level: $\sigma_L^* = 1.7$ dB. The theory yields a relatively good prediction model.

Finally, for the bridge under consideration, with the receiver location given by, $-L < x < +\infty$ and $10 < y < 100$ [m], the mean value of the sound exposure level can be calculated from [Eqs. (34), (35)]

$$\begin{aligned} \bar{L}_{AE} = 10 \log \left\{ \frac{3I_0}{8y} [S(x,y) + 17.4 \cdot R(x,y)] \right\} \\ + 16.2 \cdot \lg \left(\frac{V}{V_0} \right) + 84.7 \text{ dB}, \end{aligned} \quad (36)$$

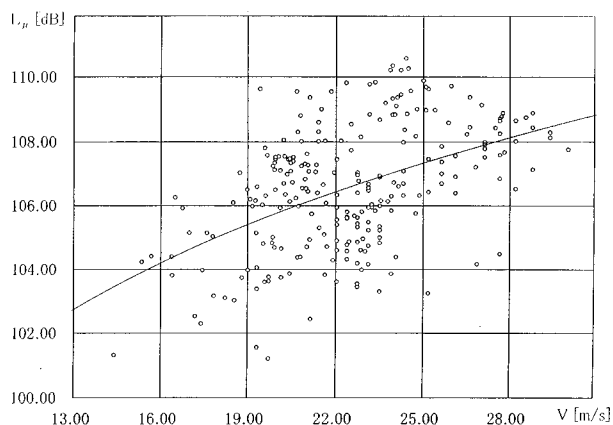


FIG. 6. The sound energy density level, L_μ , versus the train's speed, V [m/s] [Eq. (35)].

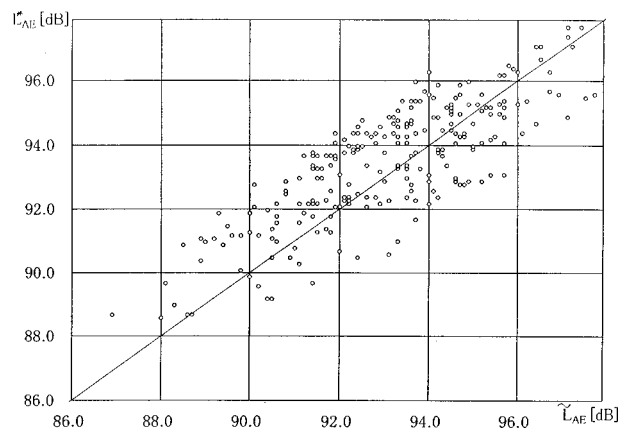


FIG. 7. Measured, \tilde{L}_{AE} , and predicted, L_{AE}^* , sound exposure levels for the study point $\bar{x} = 0$, $\bar{y} = 64$ [m].

where the functions $R(x,y)$ and $S(x,y)$ are defined by Eqs. (8), (15) and the bridge length, $L = 141$ [m]. The standard deviation of L_{AE} should be less than 2 dB.

V. CONCLUSIONS

When noise comes from the bridge and both segments of track, $x < -L$ and $x > 0$ (Fig. 3), the average sound exposure level, L_{AE} , is determined by Eq. (30). When one of the track segments is screened by buildings or any other obstacles, we can apply Eq. (33). In the general and special cases, Eq. (32) yields the standard deviation of L_{AE} prediction.

Equations (30) and (33) hold for the perpendicular distance, $10 < y < 100$ [m], while a slight wind and/or thermal radiation induce atmospheric turbulence. The above equations were derived with the following assumptions:

- turbulence destroys the coherent interference between the direct and ground reflected waves,
- a train is modeled by a uniform line source with dipole directivity and the linear density of the A-weighted sound power, W_A ,
- the products, $\alpha \cdot W_A$, and $\beta \cdot W_A$, describe the process of noise generation on a bridge and beyond the bridge, respectively, where the ratio, $m = \alpha/\beta$, defines the bridge parameter.

Relatively good agreement between theory and experiment were obtained (Sec. IV). Because the theory validation was performed at a single point, the further measurements are necessary.

ACKNOWLEDGMENTS

The authors are grateful to the reviewers for their valuable comments and to M. Imanishi for his technical assistance.

¹P. H. de Vos, "Railway noise: The physics of airborne sound generation and propagation," *J. Sound Vib.* **193**, 77–82 (1996).

²B. Hemsworth, "Prediction of train noise" in *Transportation Noise Reference Book*, edited by P. M. Nelson (Butterworths, London, 1987).

³D. Hohenwarter, "Railway noise propagation models," *J. Sound Vib.* **141**, 17–41 (1990).

⁴Y. Okumura and K. Kuno, "Multiple regression analysis of railway noise

- based on finite line source model,” *J. Acoust. Soc. Jpn. (E)* **13**, 161–169 (1992).
- ⁵T. Odebrant, “Noise from steel railway bridges: A systematic investigation on methods for sound reduction,” *J. Sound Vib.* **193**, 227–234 (1996).
- ⁶M. H. A. Janssen and D. J. Thompson, “A calculation model for the noise from steel railway bridges,” *J. Sound Vib.* **193**, 295–306 (1996).
- ⁷J. G. Walker, N. S. Ferguson, and M. G. Smith, “An investigation on noise from trains on bridges,” *J. Sound Vib.* **193**, 307–314 (1996).
- ⁸T. F. W. Embleton, “Tutorial on sound propagation outdoors,” *J. Acoust. Soc. Am.* **100**, 31–48 (1996).
- ⁹J. E. Piercy, T. F. W. Embleton, and L. C. Sutherland, “Review of noise propagation in the atmosphere,” *J. Acoust. Soc. Am.* **61**, 1403–1418 (1977), Figure 16.
- ¹⁰K. Yamamoto and M. Yamashita, “Measurements and analysis of sound propagation over lawn,” *J. Acoust. Soc. Jpn. (E)* **15**, 1–12 (1994), Figure 3.
- ¹¹R. Makarewicz, K. B. Rasmussen, and P. Kokowski, “Ground attenuation of railroad noise,” *Acust./Acta Acust.* **4**, 636–641 (1996).
- ¹²R. Makarewicz and M. Yoshida, “Railroad noise in an open space,” *Appl. Acoust.* **49**, 291–306 (1996).
- ¹³P. J. Remington, L. G. Kurzweil, and D. A. Towers, “Practical examples of train noise and vibration control,” in *Transportation Noise Reference Book*, edited by P. M. Nelson (Butterworths, London, 1987).
- ¹⁴R. E. Hanson, H. J. Saurenman, and D. A. Towers, “Rail transportation noise and vibration,” in *Handbook of Acoustical Measurements and Noise Control*, edited by C. M. Harris (McGraw-Hill, New York, 1991).

Exposure-response relationships for transportation noise

Henk M. E. Miedema^{a)} and Henk Vos

TNO Prevention and Health, P.O. Box 2215, 2301 CE Leiden, The Netherlands

(Received 17 September 1997; accepted for publication 20 August 1998)

This article presents synthesis curves for the relationship between DNL and percentage highly annoyed for three transportation noise sources. The results are based on all 21 datasets examined by Schultz [J. Acoust. Soc. Am. **64**, 377–405 (1978)] and Fidell *et al.* [J. Acoust. Soc. Am. **89**, 221–233 (1991)] for which acceptable DNL and percentage highly annoyed measure could be derived, augmented with 34 datasets. Separate, nonidentical curves were found for aircraft, road traffic, and railway noise. A difference between sources was found using data for all studies combined and for only those studies in which respondents evaluated two sources. The latter outcome strengthens the conclusion that the differences between sources cannot be explained by differences in study methodology. © 1998 Acoustical Society of America. [S0001-4966(98)02012-8]

PACS numbers: 43.50.Qp, 43.50.Sr [MRS]

INTRODUCTION

Annoyance and sleep disturbance are the most important health effects of environmental noise exposures if DNL is below 70 dB. This can be concluded from two extensive overviews prepared by an international committee of the Health Council of the Netherlands (Gezondheidsraad, 1994) and by Berglund and Lindvall (1995). The range below 70 dB is usually considered when noise limits are established. Therefore, information about the relationships between exposure on the one hand, and annoyance and sleep disturbance, on the other hand, is very relevant for the evaluation of environmental noise.

Sleep disturbance has been quantified with various parameters, such as the number of EEG awakenings, the number of sleep stage changes, but also, for example, on the basis of the self-reported sleep disturbance. Research conducted so far does not provide sufficient evidence for quantitative statements about the relationship between noise exposure during sleep and sleep disturbance parameters. An attempt (Pearsons *et al.*, 1989) to integrate results from various studies on noise-induced awakenings has shown great variability, and also a large difference between results from laboratory and from field studies. Since then several new studies have been initiated so that future overviews may reveal more definite quantitative results.

This paper concerns *annoyance* due to environmental noise. Existing data will be reanalyzed to establish functions which summarize the relationship between annoyance experienced in and around the house and the incident noise at the most exposed facade in steady state situations.

We use the term “dataset” for the data with respect to a single noise source (aircraft, road traffic, or railway) from a single survey. In datasets derived from the same survey, the exposure and effect variables related to the noise source have different values in each dataset while others variables, e.g., characterizing the respondent or his dwelling, have identical values in each dataset. Note that more datasets are only de-

rived from a single survey when more than one noise source is evaluated.

Table I gives an overview of the datasets that are used in the present synthesis. Each dataset is identified by its code from Fields’ catalogue of noise annoyance surveys (Fields, 1994b). The datasets marked with an asterisk were also included in the synthesis of Fidell *et al.* (1991). The 55 datasets in the present synthesis encompass information for a total of 63 969 respondents (counting respondents twice if they appear in two datasets). They are derived from 45 surveys with a total of 58 065 respondents. Only respondents for whom DNL and an annoyance response are available are counted.

Results from previous analyses on a part of the dataset have been reported at the ICBEN conference in Nice by Miedema (1993). Before our synthesis is discussed, some previous syntheses will be reviewed.

I. STATE OF THE ART

Several authors (e.g., Alexandre, 1973; Finke *et al.*, 1980, pp. 248–252; Fields and Walker, 1982) have attempted to integrate results from individual exposure-response studies. However, most publications used only a limited number of studies, or did not pay much attention to the comparability of the definition of variables in different studies. Alexandre (1973) included five aircraft noise studies, Finke *et al.* (1980) included nine road traffic studies, and Fields and Walker (1982) compared six studies (one on railway, two on road traffic, and three on aircraft).

A very influential attempt that included many more studies was Schultz’s synthesis (Schultz, 1978). His paper was followed by an intense discussion between Schultz and Kryter (Schultz, 1982; Kryter, 1982, 1983). In his 1978 article Schultz discussed 24 noise annoyance surveys carried out in several countries. These investigations concerned aircraft, road traffic, and railway noise. In an attempt to make the investigations comparable, Schultz used the available data to estimate a common noise measure and a common

^{a)}Electronic mail: HME.Miedema@pg.tno.nl

TABLE I. Datasets included in analyses in this paper. There are 45 surveys included with a total of 58 065 respondents. From these surveys 55 datasets are derived with a total 63 969 respondents, counting respondents twice if they appear in two datasets. Our count of surveys is based on Fields (1994b) catalogue. A study is counted as a separate survey if it is assigned there a separate code. This leads to small differences between our counts of surveys and counts based on the grouping in Schultz (1978) or Fidell *et al.* (1991).

Fields' code	Name of the survey	Number of respondents (for this source)
Aircraft		
AUL-210	Australian Five Airport Survey (1980)	3288
CAN-168	Canadian National Community Noise Survey (1979)	631
FRA-016	French Four-Airport Noise Study (1965)	2000
FRA-239	French Combined Aircraft/Road Traffic Survey (1984)	565
NET-240	Schiphol Combined Aircraft/Road Traffic Survey (1984)	573
NOR-311	Oslo Airport Survey (1989)	1548
NOR-328	Bodo Military Aircraft Exercise Study (1991–1992)	702
NOR-366	Vaernes Military Aircraft Exercise Study (1990–1991)	391
SWE-035	Scandinavian Nine-Airport Noise Study (1969, 1970, 71, 72, 74, 76)	1662
SWI-053	Swiss Three-City Noise Survey (1971)	3934
UKD-024	Heathrow Aircraft Noise Survey (1967)	4515
UKD-242	Heathrow Combined Aircraft/Road Traffic Survey (1982)	1993
UKD-238	Glasgow Combined Aircraft/Road Traffic Survey (1984)	598
USA-022	U.S.A. Four-Airport Survey (phase I of Tracor Survey) (1967)	3499
USA-032	U.S.A. Three-Airport Survey (phase II of Tracor Survey) (1969)	2828
USA-044	U.S.A. Small City Airports (small City Tracor Survey) (1970)	1954
USA-082	LAX Airport Noise Study (1973)	702
USA-203	Burbank Aircraft Noise Change Study (1979)	924
USA-204	John Wayne Airport Operation Study (1981)	1033
USA-338	U.S.A. 7-Air Force Base Study (1981)	874
	Total Aircraft (20 datasets)	34 214
Road Traffic		
CAN-120	Western Ontario University Traffic Noise Survey (1975)	1149
CAN-121	Southern Ontario Community Survey (1975/1976)	1304
CAN-168	Canadian National Community Noise Survey (1979)	568
BEL-122	Antwerp Traffic Noise Survey (1975)	896
BEL-137	Brussels Traffic Noise Survey (1976)	297
FRA-092	French Ten-City Traffic Noise Survey (1973/1975)	975
FRA-239	French Combined Aircraft/Road Traffic Survey (1984)	524
FRA-364	French 18-site Time of Day Study (1993/1994)	895
GER-192	German Road/Railway Noise Comparison Study (1978/1981)	1649
GER-372	Ratingen-Dusseldorf Road Traffic/Aircraft Survey (1985/1986)	559
GER-373	Ratingen Road Traffic/Aircraft Study (1987)	440
NET-106	Dordrecht Home Sound Insulation Study (1974)	420
NET-240	Schiphol Combined Aircraft/Road Traffic Survey (1984)	473
NET-258	Amsterdam Home Sound Insulation Study (1975)	365
NET-276	Netherlands Tram and Road Traffic Noise Survey (1993)	697
NET-361	Netherlands Environmental Pollution Annoyance Survey (1983)	880
NET-362	Amhem Road Traffic Study (1984)	293
SWE-142	Stockholm, Visby, Gothenburg Traffic Noise Study (1976)	811
SWE-165	Gothenburg Tramway Noise Survey (1976)	464
SWI-053	Swiss Three-City Noise Survey (1971)	945
SWI-173	Zurich Time-of Day Survey (1978)	1371
UKD-071	B.R.S. London Traffic Noise Survey (1972)	2903
UKD-072	English Road Traffic Survey (1972)	1043
UKD-157	London Area Panel Survey (1977/1978)	364
UKD-242	Heathrow Combined Aircraft/Road Traffic Survey (1982)	410
UKD-238	Glasgow Combined Aircraft/Road Traffic Survey (1984)	536
	Total Road Traffic (26 datasets)	21 228
Railway		
FRA-063	Paris Area Railway Noise Survey (1972)	334
GER-192	German Road/Railway Noise Comparison Study (1978/1981)	1648
NET-153	Netherlands Railway Noise Survey (1977)	671
NET-276	Netherlands Tram and Road Traffic Noise Survey (1983)	265
NET-361	Netherlands Environmental Pollution Annoyance Survey (1993)	71
SWE-165	Gothenburg Tramway Noise Survey (1976)	464
SWE-228	Swedish Railway Study (1978–1980)	856
SWE-365	Swedish 15-site Railway Study (1992–1993)	2833
UKD-116	British National Railway Noise Survey (1975/1976)	1385
	Total Railway (9 datasets)	8527

annoyance measure, namely, DNL and the percentage of respondents who could be considered to be highly annoyed.

For each of the investigations he drew a curve showing the percentage highly annoyed persons as a function of DNL (Schultz, 1978, Figs. 1 and 2). On the basis of 11 individual “clustering” surveys he synthesized a single curve as the “best currently available estimate of public annoyance due to transportation noise of all kinds.” Eight “nonclustering” surveys were not included in the synthesis. Five surveys were obtained after the analyses and discussed in an addendum. They were not included in the synthesis.

Kryter (1982) cast doubt on the adequacy of the synthesized curve. Most important are his comments with respect to the criteria used for excluding investigations when drawing up the synthesized curve, the definitions of the percentage highly annoyed persons for the different investigations, and the methods used to estimate DNL from the data.

Kryter argued that for ground traffic (i.e., road and rail traffic) and air traffic separate, nonidentical curves give a significantly better representation of the data used by Schultz (Kryter, 1982, Fig. 11). According to Kryter, for a given DNL the annoyance due to aircraft lies above the level specified by the synthesized curve, whereas the annoyance due to ground transportation noise lies below that level. The argument between Kryter and Schultz regarding the adequacy of a single curve for transportation noise did not lead to agreement between them.

Fidell *et al.* (1991) extended the original compilation of Schultz and arrived at substantially the same curve. Their curve was based on 26 datasets: the 11 datasets Schultz (1978) used as a basis for his synthesis curve, 4 of the 5 datasets which he discussed in his addendum, and 11 additional datasets. Although their additional data appear to support Kryter’s point that at the same exposure level aircraft noise is more annoying than ground transportation noise, the authors ignored the discussion with Kryter in which this point was brought forward.

Fields (1994a) reviewed the abovementioned original and updated synthesis. Although his review was not conducted with the objective of identifying errors in the data, “a few major errors and a large number of minor inaccuracies have been identified” (cf. his Sec. 2.5). Fields criticizes, among others, the selection process of studies for the synthesis (cf. his Secs. 3.4 and 3.5), weaknesses in the data included in the synthesis (cf. his Sec. 3.8), the comparability of the determination of the percentage highly annoyed for different studies (cf. his Sec. 4.1), and the assignment of equal weights to datapoints that represent different numbers of cases (cf. his Sec. 4.2). The scope of the problems will be illustrated in Sec. III. The overall conclusion that can be drawn from Fields’ review is that much can be improved in the process of establishing synthesis curves.

This article presents a synthesis based on all studies examined by Schultz (1978) and Fidell *et al.* (1991) for which DNL and percentage highly annoyed meeting certain minimal requirements could be derived, augmented with a number of additional studies. Consequently, the present synthesis is more comprehensive. Moreover, the kind of errors and

TABLE II. Boundary quantifications for different annoyance scales.

Number of effective categories	Boundary quantifications
3	0-33-67-100
4	0-25-50-75-100
5	0-20-40-60-80-100
6	0-17-33-50-67-83-100
7	0-14-28-43-57-72-86-100
10	0-10-20-...-80-90-100
11	0-9-18-...-82-91-100

inaccuracies Fields (1994a) found in the previous syntheses are avoided.

II. DNL AND PERCENTAGE HIGHLY ANNOYED (%HA)

Following Schultz (1978) and Fidell *et al.* (1991), we use DNL as a noise exposure measure and percentage highly annoyed (%HA) as a noise annoyance measure. DNL is a measure with a night-time penalty of 10 dB calculated from L_{Aeq} for the daytime and L_{Aeq} for the night-time:

$$DNL = 10 \lg(15.10^{L_{Aeq}(7-22h)/10} + 9.10^{[L_{Aeq}(22-7h)+10]/10})/24.$$

The L_{Aeq} ’s are measured, or calculated with noise propagation models. As much as possible we derived the L_{Aeq} ’s for the incident sound at the most exposed facade of a dwelling for the one year period preceding a social survey. However, it is not a common practice to report information on these aspects of the determination of L_{Aeq} , so that often they were unknown.

%HA is the percentage of annoyance responses which exceed a certain cutoff point. To assess the percentage above a cutoff point, the response alternatives have to be quantified. This quantification is simplest when the following two assumptions can be made:

- Equal intervals: each category from a set of response alternatives occupies an equal portion of the annoyance continuum;
- Equal extremes: the extreme (lower and upper) category boundaries from different sets of annoyance response alternatives coincide.

Quantification of boundaries of annoyance categories based on the above assumptions are given in Table II. They depend only on the number of effective categories. The boundary quantifications are determined as follows:

$$\text{score}_{\text{boundary}i} = 100i/m,$$

where m is the number of effective categories and $i = 0, 1, \dots, m$ is the rank of the boundary, starting with the lower boundary of the lowest annoyance category.

To arrive at a percentage responses above a cutoff point x , a score is assigned to each respondent in the following way. Let L and U be the quantifications of the lower and the upper boundary of the category selected by a respondent. Then the score assigned to the respondent for the calculation of the percentage is 0 if the respondent chose a category that

is below the cutoff point x (i.e., $U < x$) and is 1 if the respondent chose a category that is above the cutoff point x (i.e., $x \leq L$). If the category chosen by the respondent encompasses the cutoff point (i.e., $L < x \leq U$), then it is not known whether this is a response below or above the cutoff point. The score assigned to these respondents is the probability that the annoyance score for the respondent actually is above the cutoff point, assuming that the annoyance score is uniformly distributed within a category.

The following example illustrates the above procedure for the calculation of a percentage annoyed respondents. Suppose that a ten-point scale is used and that the percentage annoyed respondents is calculated for a cutoff at 72 on the scale from 0 to 100. The respondents who chose one of the seven categories corresponding to relatively low annoyance are assigned 0 because the upper boundaries of these categories (10, 20, 30, 40, 50, 60, and 70, respectively) are below the cutoff point. Respondents who chose one of the highest two annoyance categories are assigned 1 because the lower boundaries of these category (80 and 90, respectively) are above the cutoff point. The respondents who chose the two but highest category (with boundaries 70 and 80), which encompasses the cutoff at 72, are assigned $(80-72)/(80-70) = 0.8$.

Schultz (1978) used a cutoff at 72 (highest two categories of seven: see Table II) in his influential synthesis, and he called the percentage obtained with this cutoff point the percentage "highly annoyed." The interpretation of a percentage does not depend on this label, but on the value chosen as the cutoff point, i.e., 72. We also use the label "highly annoyed," if the cutoff is (sufficiently close) to 72. An advantage of using a cutoff at 72 over lower cutoff values is that percentages obtained with the cutoff at 72 are less affected by differences between studies in the usage of a filter question (see Sec. IV).

III. SURVEYS EXAMINED BY SCHULTZ (1978), AND FIDELL *et al.* (1991)

Schultz (1978) and Fidell *et al.* (1991) derived DNL and percentage highly annoyed (%HA) from a number of studies. If DNL and %HA satisfy minimal requirements, possibly after improvements, then a study examined in these publications is also included in the present synthesis. The minimal requirements concerning DNL and %HA and the evaluation of studies with respect to these requirements are discussed here with the aid of Table III.

Schultz (1978) and Fidell *et al.* (1991) gave a short description of the individual studies they examined and the way they derived DNL and %HA. The pages where the reader can find these descriptions are given in the first and second column of Table III. A description is lacking for one study (USA-082). The third column gives the page in Fields (1994a) where the reader can find a critical discussion of the study concerned. The fourth column of Table III indicates for which studies we used the original dataset in our synthesis. For these studies additional information is given in the next section.

We consider the following requirements concerning DNL and %HA to be minimal requirements:

- *Source specific:* DNL and %HA pertain to one and the same source of transportation noise (aircraft, road traffic, or railway);
- *General noise annoyance question:* %HA is directly derived from the responses to a question about the general noise annoyance from the source concerned. Thus it is not based on, e.g., an index constructed from multiple questions concerning specific disturbances or a ranking of sources by respondents;
- *Consistent cutoff:* %HA is derived with a cutoff point sufficiently close to 72 on a scale from 0 (no annoyance at all) to 100 (very high annoyance).

A. Source specific

The fifth and seventh columns of Table III indicate whether DNL and %HA were source specific or not. In one study (USA-102) neither DNL nor %HA pertained to a single transportation noise source; in two other studies DNL did not pertain to a single source (SWE-142 and USA-301); and in four more studies (AUS-093, CAN-121, DEN-075, and FRA-041) %HA did not pertain to a single transportation noise source. For this reason all but one of these studies are excluded from the present synthesis. CAN-121 was not excluded because we could derive %HA specifically for the source concerned (road traffic) on the basis of an annoyance question other than the one used by Schultz (1978). Thus six studies had to be excluded on the basis of this criterion.

B. General noise annoyance question

For nine studies in the syntheses (DEN-200, FRA-041, GER-034, SWE-021, UKD-008, UKD-024, USA-022, USA-032, and USA-044) %HA is not based on a question about general noise annoyance, but on an index constructed from multiple questions concerning among others specific disturbances, or it is based on a ranking by respondents (see Table III, eight column). There is no clear relation between such a "%HA" and %HA as defined here [or by Schultz (1978) and Fidell *et al.* (1991) themselves]. Therefore these studies had to be excluded from the present synthesis unless we were able to derive %HA from a general annoyance question. This was the case for four studies (UKD-024, USA-022, USA-032, and USA-044) for which we have the original data. Thus five studies had to be excluded on the basis of this criterion.

C. Consistent cutoff

Schultz (1978) chose, in our terminology, 72 on a scale from 0 (no annoyance) to 100 (highest annoyance) as the cutoff point above which respondents are counted as highly annoyed. Following Fidell *et al.* (1991), we adopted this convention. For the studies not already excluded on the basis of the above discussed criteria, we tried to determine %HA with a cutoff point as close to 72 as possible (see Table III). If this led to another cutoff than the cutoff used in the previous syntheses, this latter point is shown between parentheses. For five studies (AUS-014, AUS-093, FRA-019, JAP-065, and USA-250) with a cutoff point very different from 72 (60, 50, 50, 50, and between 50 and 60, respectively) we could not

TABLE III. For studies examined by Schultz (1978) and/or Fidell *et al.* (1991), represented by the code assigned to that study by Fields (1994b), the pages where they are described or discussed in three publications, an indication whether we used the original individual data, aspects of the DNL and percentage highly annoyed (%HA) that determine the quality of these measures, the cutoff above which persons were counted as highly annoyed, and the inclusion or exclusion of the studies. A point ‘.’ means that an aspect is not rated because the study is excluded (on the basis of other aspects). Ratings for DNL and %HA used by Schultz (1978) and/or Fidell *et al.* (1991) are given between parentheses if they are different.

ID Fields (1991)	Page Schultz (1978) ^a	Page Fidell <i>et al.</i> (1991) ^b	Page Fields (1994a: Appendix B) ^c	Original individual data used ^d	DNL source specific ^e	DNL without relations other studies ^f	%HA source specific ^g	%HA general ^h	%HA cutoff ⁱ	Dataset included ^j
AUL-210		222	76	+	+	+	+		72 (80)	+
AUS-014	392		–	.	+?	–	+	+	60	–
AUS-093	400		–	.	+?	–	–	+	50	–
BEL-122,137	401		76,–7	–	+	+	+	+	70	+
								[daytime]		
CAN-121	402		77	+	+	+	+(-)	+	72 (60)	+
CAN-168 road & air		222	77	+	+	+	+	+	72 (60)	+
DEN-075	400		77	.	+	.(+)	–	+	.(67)	–(+)
DEN-200		228	77	.	+	.(–)	+	–	.(?)	–(+)
FRA-016	392		78	–	+	–	+	+	72 (75)	+
FRA-019	394		80	.	+	.(–)	+	+	.(50)	–
FRA-041	395		78	.	+	.(–)	–	–	.(?)	–(+)
FRA-063	398		78	–	+	–	+	+	72	+
GER-034	396		78	.	+	.(–)	+	–	.(?)	–(+)
JAP-065	398		–	.	+	.(+)	+?	+ [worst case]	50	–
SWE-021	394		81	–	+	.(–)	+	–	.(?)	–
SWE-035	397		78	–	+	–	+	+	67–75	+
SWE-142	394		–	–	–	–	+	+	67–75	+(-)
SWE-165		225	78	–	–	.(+)	+	+	.(67–75)	+
SWE-228		226	–	–	+	–	+	+	67–75	+
SWI-053 road & air	396,–9		78,–9	–	+	–	+	+	73	+
UKD-008	391		79	.	+	.(–)	+	–	.(?)	–(+)
UKD-024	393		79	+	+	+(-)	+	+(-)	72(?)	+
UKD-071	399		–	+	+	+	+	+	72 (67)	+
UKD-116		225	–	+	+	+	+	+	72 (5)	+
USA-- 022,032,044	398		81	+	+	+(-)	+	+(-)	72 (?)	+(-)
USA-082	–	–	79	+	+	+	+	+	72 (60)	+
USA-102	399		79	.	–	+	–	+	.(60)	–(+)
USA-203		223	80	+	+	+	+	+	72 (60)	+
USA-204		224	80	–	+	+	+	+	63–70 (50–60)	+
USA-250		225	80	.	+	+	+	+	.(50–60)	–(+)
USA-301		228	80	.	–	+	+	+	.(50–60)	–(+)
USA-338		227	80	–	+	+	+	+	70	+

^aThe page where the description of the study in Schultz (1978) starts.

^bThe page where the description of the study in Fidell *et al.* (1991) starts.

^cThe page where the discussion of the study in Appendix B of Fields (1994a) starts.

^d‘+’ means that the original individual data are used, ‘–’ means we do not have the original dataset.

^e‘+’ means that DNL pertains to noise from the source concerned, ‘–’ means that also other sources contributed substantially to the noise.

^f‘+’ means that DNL was calculated from the L_{Aeq} ’s for the day and night or estimated on the basis data about L_{Aeq} ’s for other periods or data about sound events. ‘–’ means that DNL is estimated from one or more other metrics using relations established in other studies or rules of thumb to convert these metrics into DNL.

^g‘+’ means that %HA is derived from responses to an annoyance question that refers to the source concerned, ‘–’ means that the question used was not restricted to that source.

^h‘+’ means that %HA is derived from responses to a question about general annoyance from the source concerned, ‘–’ means that an index constructed from multiple questions or a ranking by respondents is used.

ⁱThe cutoff point above which respondents are counted as highly annoyed.

^j‘+’ means that a dataset is included, ‘–’ means that it is excluded.

derive percentages with a cutoff point closer to 72. Because 72 is by convention the cutoff to be used for determining %HA, we excluded these five studies.

As mentioned above, Fidell *et al.* (1991) based their synthesis curve on 26 datasets, and Schultz (1978) examined

eight additional “nonclustering” datasets and one study in his addendum which were excluded by them. After improvements we still had to exclude 8 of the 26 datasets that were included by Fidell *et al.* (1991) because they did not meet the minimal criteria discussed, but we could include four of the

TABLE IV. Derivation of DNL and %HA from the datasets available in the TNO-archive (see text).

Fields' code	DNL	%HA
AUL-210		
CAN-168		
FRA-239		
NET-240		
NOR-311	EFN	notice filter & responses for indoor and for outdoor situation
	general transformation rule	
NOR-328	EFN	notice filter
	general transformation rule	
NOR-366	EFN	notice filter
	general transformation rule	
UKD-024	average PNdB, average log duration and N for the periods 7–19h, 19–22h, and 22–7h relation between L_{Amax} and PNdB from this study and event pattern model	
UKD-238		
UKD-242	$L_{Aeq}(7-19h)$, $L_{Aeq}(19-23h)$, $L_{Aeq}(23-7h)$ L_{Aeq} pattern model	notice filter
USA-022	average PNdB and N for the periods 6–21h and 21–6h per site and N for three hour period for aggregated over sites relations between L_{Amax} and PNdB, and between duration and PNdB from this study, event pattern model and traffic intensity model	notice filter
USA-032	see USA-022	notice filter
USA-044	see USA-022	notice filter
USA-082		
USA-203	DNL based on measurements during one week only	
CAN-120		
CAN-121	$L_{Aeq}(7-19h)$, $L_{Aeq}(19-23h)$, $L_{Aeq}(23-7h)$ L_{Aeq} pattern model	bipolar scale
CAN-168		
FRA-092	$L_{Aeq}(8-20h)$, $L_{Aeq}(20-24h)$, $L_{Aeq}(24-5h)$, $L_{Aeq}(5-8h)$ staircase model	
FRA-239		
FRA-364	$L_{Aeq}(6-22h)$, $L_{Aeq}(22-6h)$, $L_{Aeq}(8-20h)$, $L_{Aeq}(20-22h)$ $L_{Aeq}(6-7h) = L_{Aeq}(6-8h)$	
GER-192	for about half of the sites: $L_{Aeq}(6-22h)$, $L_{Aeq}(22-6h)$, N per hour traffic intensity pattern model for the other sites: $L_{Aeq}(6-22h)$, $L_{Aeq}(22-6h)$ L_{Aeq} pattern model based on above sites	
GER-372	$L_{Aeq}(6-22h)$ linear regression model based on sites in same city L_{Aeq} pattern model based on GER-192	
GER-373	$L_{Aeq}(6-22h)$ linear regression model based on sites in same city	
NET-240		
NET-106		two nil annoyance labels
NET-258		two nil annoyance labels
NET-276	L_{Aeq} 's for variable periods L_{Aeq} pattern model based on one site same study	
NET-361	L_{etm} L_{Aeq} pattern model based on other studies	
NET-362	$L_{Aeq}(7-19h)$, $L_{Aeq}(19-23h)$, $L_{Aeq}(23-7h)$, N per hour traffic intensity pattern model	
SWI-173		responses for daytime and for night-time situation;
UKD-071	$L_{Aeq}(8-20h)$, $L_{Aeq}(22-6h)$, $L_{Aeq}(6-24h)$, $L_{Aeq}(24h)$ staircase model	bipolar with only endpoint labeled
UKD-072	average of hourly NPL and σ for the periods 6–24h, 22:30–7:30h, and 24h staircase model	
UKD-157	$L_{Aeq}(6-24)$ L_{Aeq} pattern model based on other study	

TABLE IV. (Continued.)

Fields' code	DNL	%HA
UKD-238		
UKD-242	$L_{Aeq}(24h)$	notice filter
GER-192	L_{Aeq} pattern model based on other study for about half of the sites: $L_{Aeq}(6-22h)$, $L_{Aeq}(22-6h)$, N per hour traffic intensity pattern model for the other sites: $L_{Aeq}(6-22h)$, $L_{Aeq}(22-6h)$ $L_{Aeq}(6-7h) = L_{Aeq}(6-22h)$	
NET-153	$L_{Aeq}(7-19h)$, $L_{Aeq}(19-23h)$, $L_{Aeq}(23-7h)$ $L_{Aeq}(22-23h) = L_{Aeq}(19-23h)$	notice filter & bipolar scale
NET-276	$L_{Aeq}(7-19h)$, $L_{Aeq}(19-23h)$, $L_{Aeq}(23-7h)$, N per hour traffic intensity pattern model	notice filter & indoor situation evaluated
NET-361	L_{etm} general transformation rule based on NET-153	
SWE-365	$L_{Aeq}(24h)$, $N(6-18h)$, $N(18-22h)$, $N(22-6h)$ traffic intensity pattern model	two nil annoyance labels
UKD-116		notice filter

nine datasets that were previously excluded. Thus we included on the basis of the above discussed criteria 22 of the 35 datasets examined by Fidell *et al.* (1991) and Schultz (1978).

IV. ORIGINAL DATASETS INCLUDED IN THE PRESENT SYNTHESIS

In the last seven years TNO in Leiden has compiled an archive of original datasets from studies about annoyance caused by environmental noise. These studies concerned different modes of transportation (aircraft, road traffic, and railway) and were carried out in Europe, North America, and Australia. As far as possible a common set of variables is derived for all studies which includes, among others, noise exposure measures and annoyance measures. Much effort has been put into the derivation of the variables from different studies. Studies are included in the archive if and only if DNL [or $L_{Aeq}(24h)$] and %HA can be derived in such a way that they satisfy the criteria presented in the section about DNL and percentage highly annoyed. This section describes some aspects of the derivation of DNL and %HA from the information in these datasets with the aid of Table IV.

The first column in Table IV pertains to the *derivation of* DNL. If DNL or $L_{Aeq}(7-22h)$ and $L_{Aeq}(22-7h)$ were available, then a cell in this column is empty. Otherwise it indicates from what data DNL was estimated (above the broken line) and how it was estimated (below the broken line). The following types of estimation have been carried out.

For four aircraft noise datasets (UKD-024, USA-022, USA-032, and USA-044) DNL has been estimated using average maximum perceived noise level (PNL), average duration, and number of overflights (N). First, average maximum PNL was converted into average maximum A-weighted sound level using relations between these quantities established in the survey concerned, or a very similar survey. Then sound exposure level (SEL) has been estimated from average maximum A-weighted sound level and average du-

ration of events, using an *event pattern model*. This assumes a linear increase and a linear decrease at the same rate of the A-weighted sound level during an event.

For three datasets (road traffic: FRA-364; railway: GER-192; NET-153) $L_{Aeq}(7-22h)$ and $L_{Aeq}(22-7h)$ were obtained by combining L_{Aeq} 's possibly after equating a L_{Aeq} to a L_{Aeq} for a slightly different period. For a number of datasets (aircraft: USA-022, USA-032, USA-044; road traffic: GER-192, NET-362; railway: GER-192, NET-276, SWE-365) $L_{Aeq}(7-22h)$ and $L_{Aeq}(22-7h)$ have been estimated from available or estimated L_{Aeq} 's and information about traffic intensity as a function of the time of the day. In most cases the *traffic intensity models* used were site specific, i.e., they were based on traffic intensity data per site. In three cases (road traffic: FRA-092, UKD-071, and UKD-72) a *staircase model* of the pattern of L_{Aeq} as a function of the time of the day was fitted to available L_{Aeq} 's. This model assumed a decrease of L_{Aeq} in the evening and night until about 3 to 5 a.m. with constant steps from hour to hour and an increase with constant steps in the morning. Depending on available L_{Aeq} 's, the magnitudes of the downward steps and upward steps were either equated or estimated independently. Also, the point in the evening where the decrease started, the time and width of the minimum, and the point in the morning where the pattern leveled off, varied somewhat depending on available information with respect to the pattern. Not all details of the assumed pattern affected the estimation of the target L_{Aeq} 's. It was, e.g., not really necessary to specify the pattern during daytime.

For a number of studies (aircraft: UKD-242; road traffic: CAN-121, GER-192, NET-276, UKD-157, UKD-242; railway: NET-361) an L_{Aeq} *pattern model* was used to derive the differences between available L_{Aeq} 's and target L_{Aeq} 's. An L_{Aeq} pattern model specifies differences between L_{Aeq} 's for different time periods. Derivation of DNL from another metric using a rule of thumb or a transformation rule established

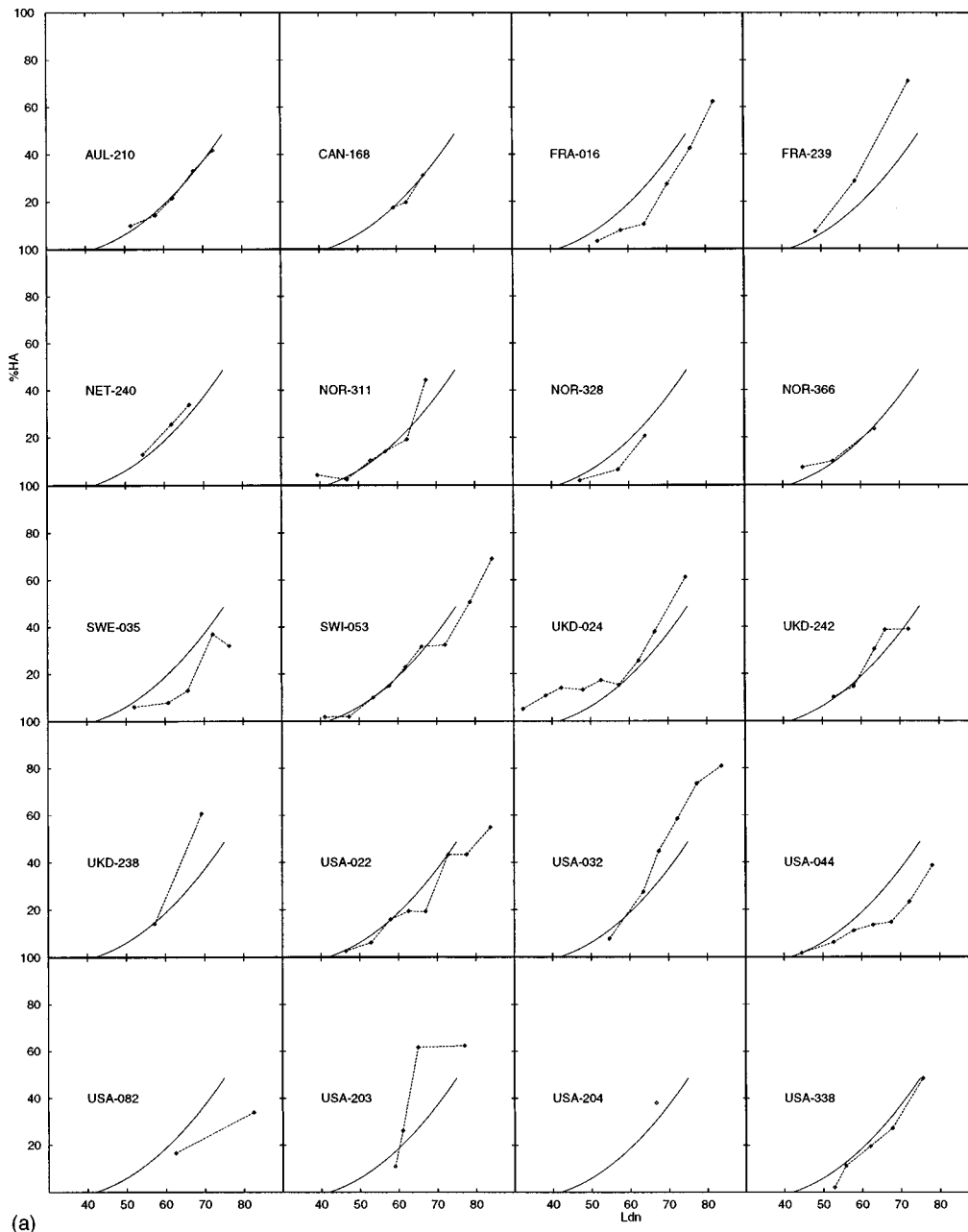


FIG. 1. Percentage highly annoyed persons (%HA) as a function of DNL for aircraft (a), road traffic (b), and railway noise (c). In addition to the curves from individual datasets, the synthesis curve for aircraft, road traffic, and railway noise, respectively, are shown.

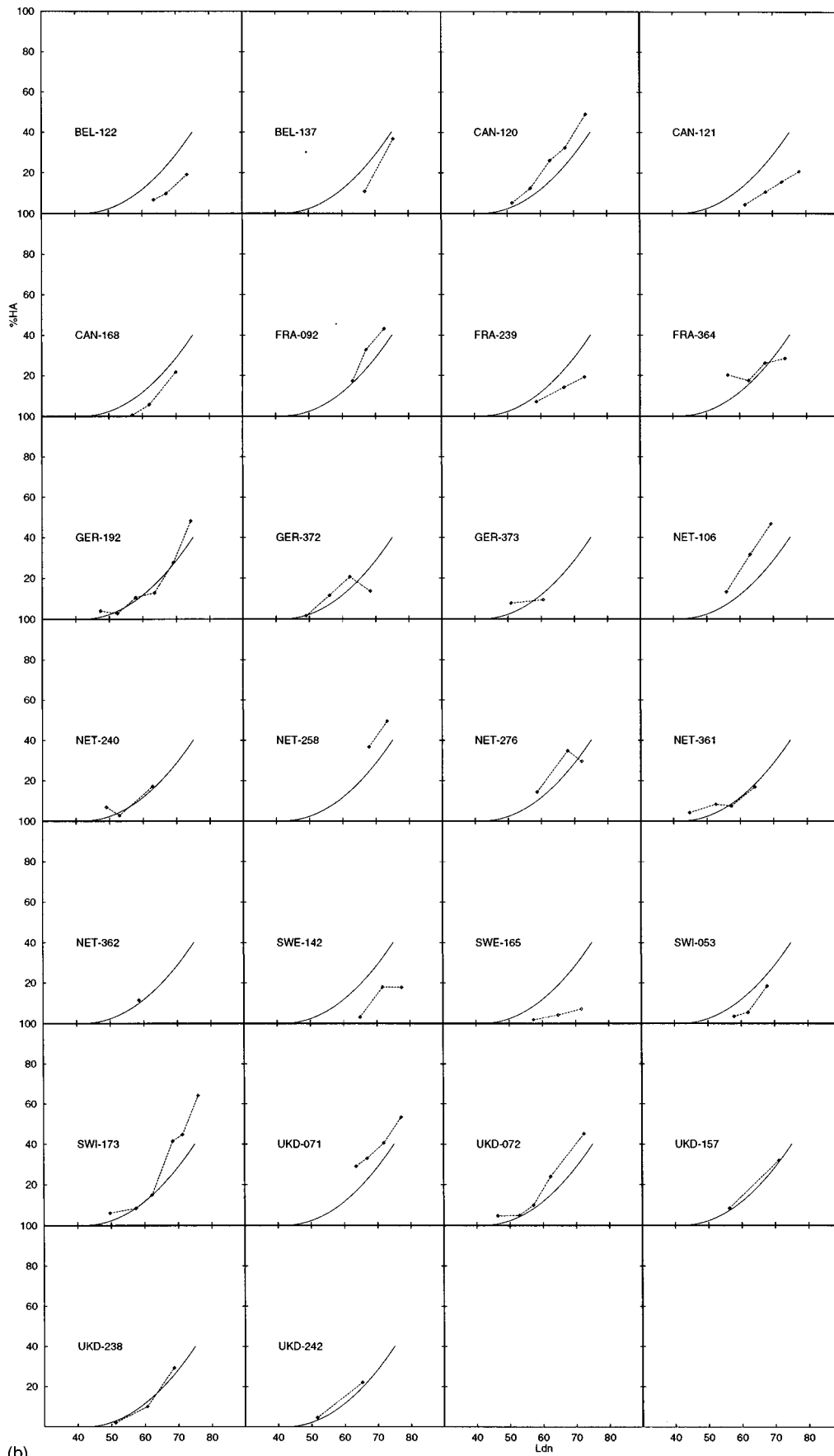
in one or more other surveys is used for the following datasets: aircraft: NOR-311, NOR-328, NOR-366; road traffic: GER-372, GER-373; railway: NET-361.

The second column in Table IV pertains to the *derivation of %HA*. If the derivation of %HA could be carried out with the procedure described in Sec. II, then a cell in this column is empty. Otherwise the complications are indicated and are discussed below.

Verbal labels used in questionnaires may lead to violations of the “equal intervals” and “equal extremes” assumptions which underlie the derivation of %HA with different scales (see Sec. II). In general, violations are expected if labels deviate from a gradual transition from no annoyance to very high annoyance. Especially bothersome are bipolar scales with a neutral label for the middle category, scales

with only the endpoints labeled and a positive label (e.g., “definitely satisfactory”) instead of a no annoyance label at one end, and scales with at one end two categories whose labels express zero annoyance (e.g., “definitely not annoyed” and “not annoyed”). In order to adjust for the effect of these labels categories are combined. The categories obtained after the necessary adjustments are referred to as the effective categories.

The general rules applied for these adjustments are as follows. For bipolar scales all categories on the favourable side of the scale up to and including the neutral category are combined. For category scales with only the extremes labeled and one extreme category labeled favourably, this latter category is combined with the adjacent category. Finally,



(b)

FIG. 1. (Continued.)

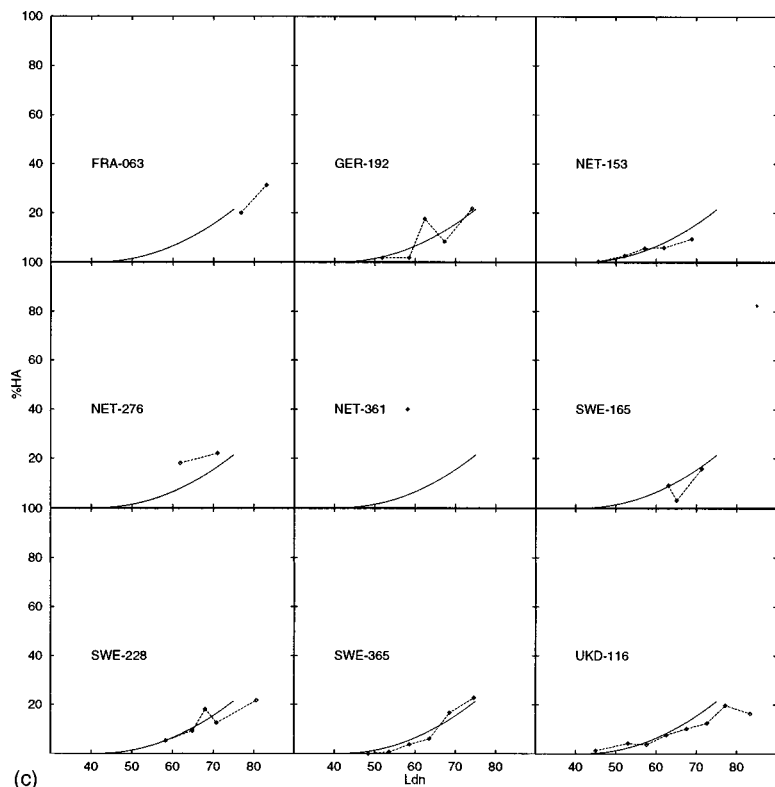


FIG. 1. (Continued.)

two categories with labels which both express no annoyance are combined.

In several surveys the noise annoyance question was preceded by a question about noticing the source or annoyance from the source, and respondents who did not (or seldom) notice the source or who were not annoyed skipped the (more detailed) annoyance question. We assigned the respondents who skipped the annoyance question on the basis of such a so-called filter question to the lowest category of the annoyance question. This procedure can be expected to affect %HA less than annoyance percentages obtained with a lower cutoff, because with a lower cutoff it becomes more likely that the respondents who skipped the main annoyance question would have chosen a response above the cutoff.

Some questionnaires do not contain a general annoyance question, but only questions regarding complementary parts of the situation in and around the house (e.g., questions with respect to the situation with the windows open and closed, or with respect to weekdays and weekends). If questions regarding "all" complementary situations were available, then they were combined. For some surveys only responses with respect to the daytime or the indoor situation were available.

V. EXPOSURE-RESPONSE RELATIONSHIPS

To establish curves for each dataset showing %HA as a function of DNL, DNL is divided into intervals of 5 dB. If for a dataset such an interval contains less than 100 cases, it is combined with the adjacent interval with the least observations. This step is repeated until every interval contains at

least 100 cases. For each resulting interval the average DNL and %HA are determined and plotted. The curves are shown for each dataset separately (Fig. 1) and combined in one figure per mode of transportation (Fig. 2). Synthesis curves for aircraft, road traffic, and railway noise are determined in two ways: with a straight forward least squares regression analysis, and with a multilevel approach. The straight forward regression analysis is the conventional, well-known procedure. The curves determined through this approach are also shown in the Figs. 1 and 2, and they will be discussed first.

To determine the curves DNL is divided per mode of transportation into intervals of 5 dB. Then for each mode of transportation a quadratic ordinary least squares regression was carried out, weighting each point according to the number of observation on which it is based. Extreme exposure levels (<45 and >75 dB) were excluded from this analysis. It turned out that the three curves reached %HA=0 at circa DNL=42 dB. Therefore a new analysis was conducted in which the curves were forced through zero at 42 dB. Above 50 dB the (absolute) %HA difference between the curves forced through zero at 42 dB and the curves with a free intercept is smaller than 0.8 for aircraft, 1.5 for road traffic, and 0.3 for railway noise. The equations of the curves with zero annoyance at 42 dB(A) are:

$$\begin{aligned} \text{Aircraft:} & \quad \%HA = 0.53(DNL - 42) + 0.0285(DNL - 42)^2; \\ \text{Road traffic:} & \quad \%HA = 0.03(DNL - 42) + 0.0353(DNL - 42)^2; \\ \text{Rail:} & \quad \%HA = 0.01(DNL - 42) + 0.0193(DNL - 42)^2. \end{aligned}$$

The relationship for aircraft noise has a substantial linear component while for road traffic and railway noise an equa-

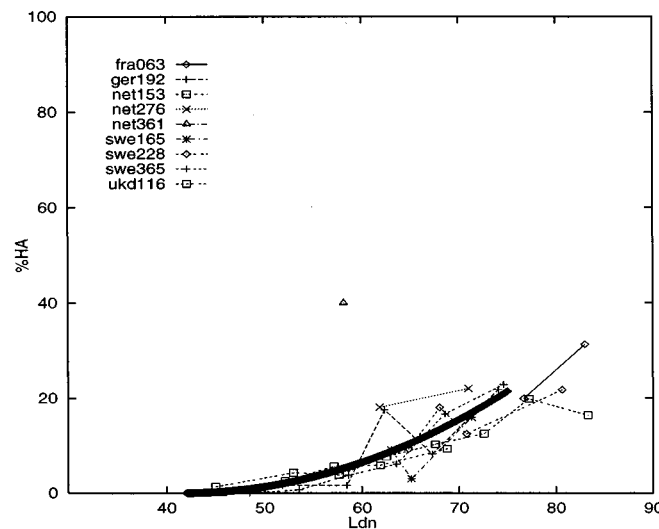
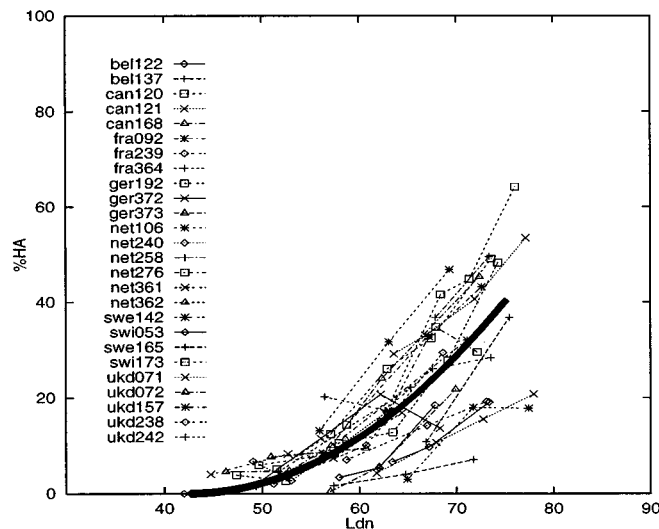
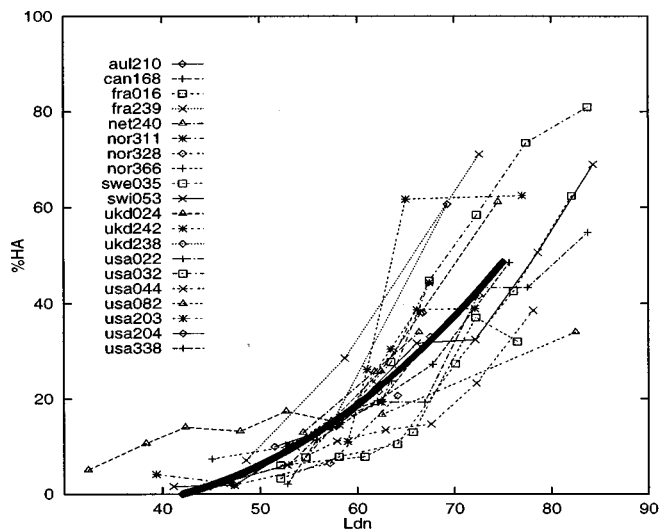


FIG. 2. The same curves as shown in Fig. 1, here combined in three subfigures for aircraft (top), road traffic (middle), and railway noise (bottom), respectively.

tion with only a quadratic term would also give an adequate description of the data.

Figure 3 shows the curves for the three modes of transportation fitted with the ordinary least squares regression

procedure together with the data points. At a given exposure level aircraft noise causes the highest %HA, followed by road traffic and rail traffic, respectively.

Standard procedures for estimating confidence intervals around regression curves are based on the assumption that the cases have been drawn at random from a population. Actually, however, the cases in these analyses are not drawn at random, but can be thought of as having been drawn in clusters defined by the studies. If this study level in the sample is ignored and simple random sampling is assumed, then the width of the true confidence intervals is underestimated.

Therefore, curves were also fitted by a multilevel procedure which takes into account that the cases are selected in two stages: first the studies and then the cases within each study. In the multilevel model (Goldstein, 1995) studies are assumed to have a normally distributed effect on the parameters of the (quadratic) curves fitted. The parameters of the curves, and the mean and standard deviation of the distributions of these parameters were estimated using the software package MLn (Rasbash and Woodhouse, 1995). The curves and the confidence intervals found by this procedure are also shown in Fig. 3. The equations of the curves are:

$$\begin{aligned} \text{Aircraft: } \%HA &= -0.02(\text{DNL}-42) + 0.0561(\text{DNL}-42)^2; \\ \text{Road traffic: } \%HA &= 0.24(\text{DNL}-42) + 0.0277(\text{DNL}-42)^2; \\ \text{Rail: } \%HA &= 0.28(\text{DNL}-42) + 0.0085(\text{DNL}-42)^2. \end{aligned}$$

The curves fitted with the two different procedures are similar except for aircraft noise at high exposure levels. The curve for aircraft obtained with the multilevel procedure has a stronger quadratic component, and predicts at high exposure levels more annoyance than the other curve. The curve obtained with the multilevel approach may be preferred because this approach takes the structure of the data better into account. An important observation is that the confidence intervals are mutually exclusive at higher levels. This is a strong indication that the curves for the three modes of transportation are different.

Figure 1(a), (b), and (c) for air traffic, road traffic, and rail traffic, respectively, show a large variation between the curves from different studies for the same mode of transportation. In order to determine whether the variation between modes of transportation can be attributed to methodological or other differences, studies in which the same respondents evaluated more than one noise source were examined. Differences between modes of transportation found with these respondents cannot be attributed to study variables. The studies used in the comparison between aircraft and road traffic noise are CAN-168, UKD-238, FRA-239, NET-240, and UKD-242, and the studies used in the comparison between road traffic and railway noise are: GER-192, NET-276, and NET-361. Figure 4 shows the results.

Overall the road traffic curve in Fig. 4 lies below the aircraft curve and above the railway curve, indicating a systematic and substantial difference between these sources. Each data point contains at least 100 responses. Aircraft noise and railway noise could not be compared directly, be-

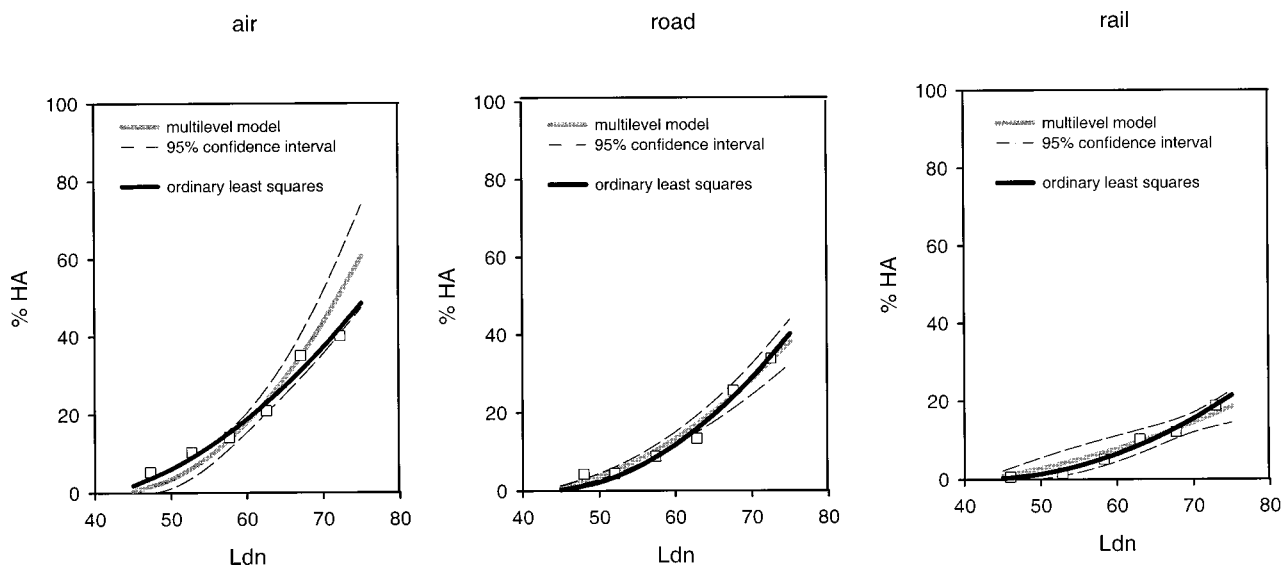


FIG. 3. Percentage highly annoyed persons (%HA) as a function of DNL. Two synthesis curves per mode of transportation, and the datapoints are shown. For the curves obtained with multilevel analysis the 95% confidence intervals are shown.

cause no studies treating both sources were available. Figure 4 supports the interpretation that the differences between modes of transportation found when analyzing all datasets are indeed related to the mode of transportation and not caused by differences between studies.

Variation between road traffic studies by type of road was also investigated. For the majority of road traffic studies we were able to distinguish three subclasses: local road traffic, expressway traffic and all other road traffic, mainly traffic on arterial and district roads. For the latter category it was determined whether the traffic was free flowing or interrupted, if possible. Sometimes this was coded as a variable in the dataset, in other cases we used maps presented in articles, reports, or readily available city maps. When there was no crossing with a same level road or regulated by traffic lights within 150 m, the traffic was assumed to be free flowing. If no specific information about the traffic type was available, the road traffic type was left "unspecified." Figure 5 shows the results for datasets with multiple road traffic types. Each data point represents at least 100 cases.

No substantial systematic difference can be found in Fig. 5, other than differences which can be explained by a differ-

ence in exposure level. Thus it is not likely that differences between road traffic studies in Fig. 1(b) are caused by a difference in road type between studies.

VI. DISCUSSION

The percentage highly annoyed persons (%HA) is zero below 40–45 dB, and increases at higher levels monotonically as a function of DNL. Different functions were found for aircraft, road traffic, and railway noise. The rate of increase is higher for aircraft noise than for road traffic noise, which in turn has a higher rate of increase than railway noise. The 95% confidence intervals around the different functions are mutually exclusive at higher exposure levels. Moreover, differences between sources were found using data for all studies combined and for only those studies in which respondents evaluated two sources. These outcomes justify the conclusion that the differences between sources cannot be explained by random factors or differences in study methodology. Consequently, above 40–45 dB the %HA at a given DNL depends on the mode of transportation that causes the noise.

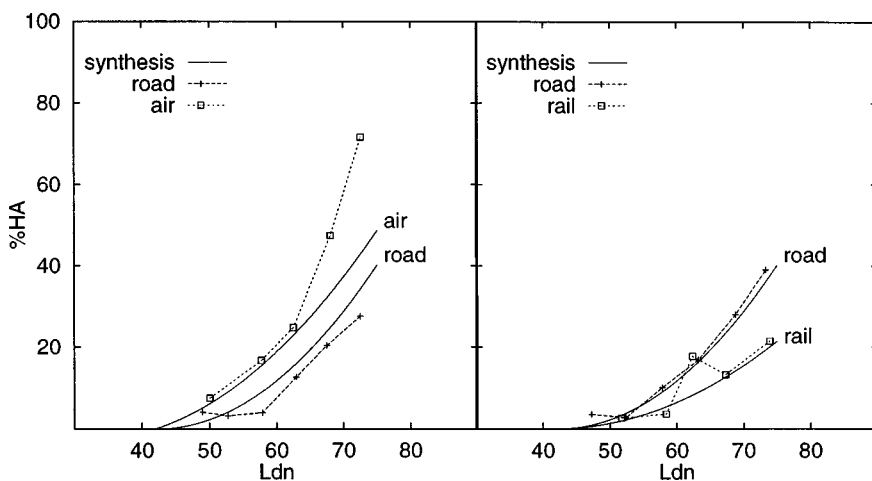


FIG. 4. Comparison of curves giving percentage highly annoyed persons (%HA) as a function of DNL. They are based on the responses of persons who evaluated both aircraft and road traffic noise (left), or both road traffic and railway noise (right).

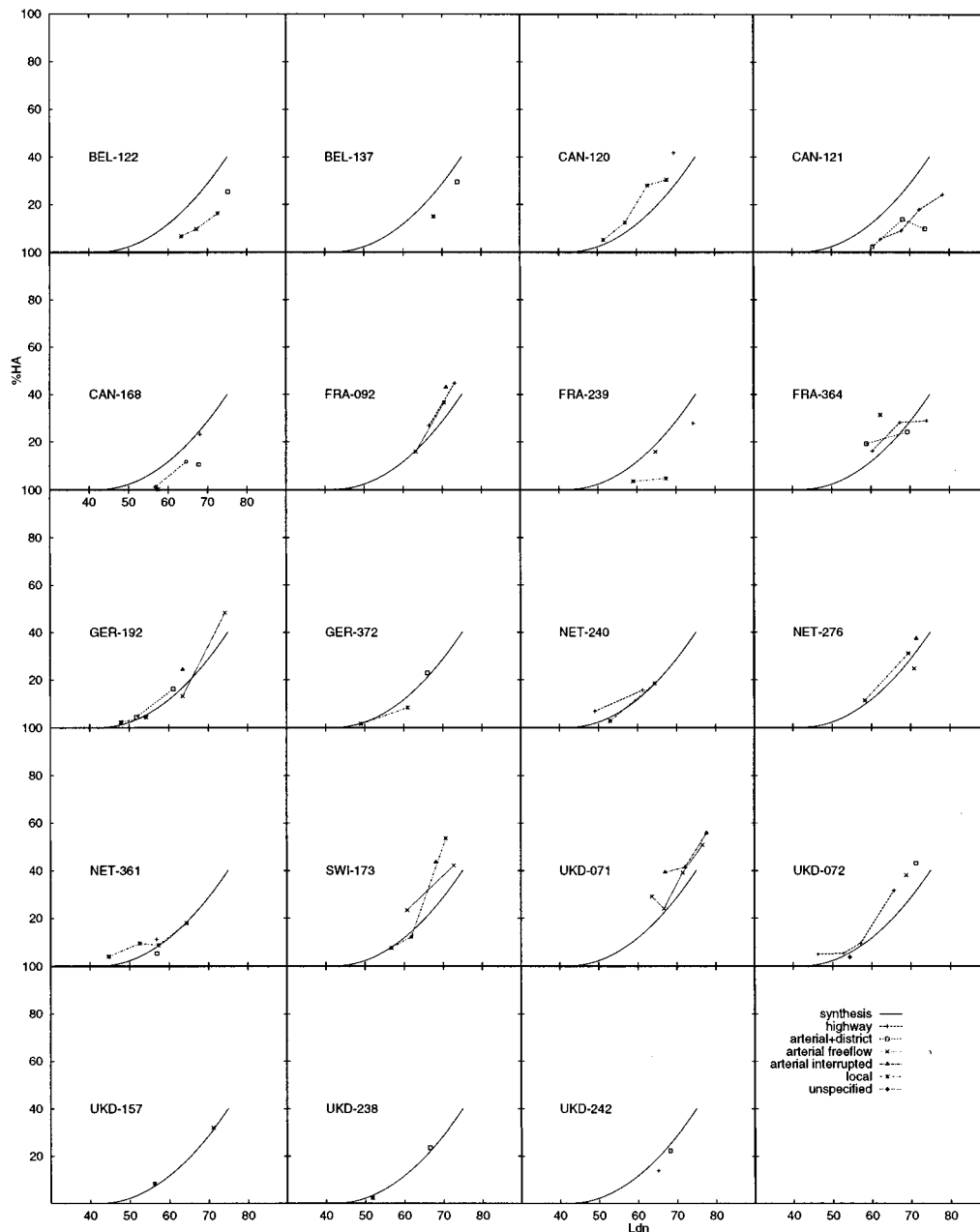


FIG. 5. Percentage of highly annoyed persons as a function of DNL. Per dataset the results for different road types are shown.

There is a considerable variation between curves for %HA as a function of DNL for different studies and for the same mode of transportation. This variation is highest for road traffic noise and appears to be lowest for railway noise. The between-study variation for road traffic noise could not be explained by a difference between the types of roads causing the exposures in different studies. Although the classification of the type of road may have not always been accurate, we believe on the basis of the results in Fig. 5 that type of road is not an important variable for predicting the noise annoyance.

The differences between the curves for the three modes of transportation may be caused by acoustical as well as nonacoustical factors. The exposure of an individual at home to noise from a single source is complex and varies over

time, and between places in and around the dwelling. A metric such as DNL summarizes this complex exposure of an individual by one number. Theoretically it is possible that no differences between sources would be found if this complex exposure was summarized in another way, by a metric which uses for example other weights for the time of day, or is more sensitive to quiet periods. It may be important that DNL is determined at the most exposed facade and therefore is not sensitive to differences between noise levels in and around the dwelling, notably indoor-outdoor differences and differences between the most and the least exposed side of a dwelling. In general, the latter differences, between sides of a dwelling, may be higher for road traffic than for aircraft noise. Consequently, a relatively quiet side for persons exposed to road traffic noise may cause annoyance to be lower

while DNL at the most exposed facade is equal. In addition nonacoustical factors may contribute to the differences between sources. For example, fear of a crash may cause people to focus more on noise from aircraft than on other noise and, as a consequence, they may be more annoyed by aircraft noise.

VII. CONCLUSIONS

The synthesis curves presented in this paper can be used to obtain estimates of noise annoyance (%HA) on the basis of noise exposure (DNL at the most exposed facade). The curves apply to steady state situations. If DNL is used as a descriptor of the noise exposure, different curves have to be used for different modes of transportation. The curves presented can be used to establish noise limits, and they can be used to compare plans with respect to the noise impact on the community.

To treat different transportation sources equally with respect to the amount of noise annoyance tolerated, a *noise limit* in terms of DNL at the most exposed facade must be lower for aircraft noise than for road traffic noise, and the limit for road traffic must be lower than for railway noise. Which DNL values correspond to an equal %HA can be read from the curves presented in this paper.

The *noise impact* of alternative traffic policies or alternative realizations of an infrastructural project (extending an airport, building a new road or railway line) can be compared by calculating the noise exposures for the dwellings in the area concerned first. Then the curves presented in this paper can be used to estimate the expected number of highly annoyed persons in the area (after the changed situation has become the new steady state). By doing this for each alternative the noise impacts of the alternatives on the community can be compared.

ACKNOWLEDGMENTS

This publication depends on the research effort of many investigators whose surveys we included in our archive. We thank especially Dr. James M. Fields for providing us the datasets he already collected at NASA together with his valuable information on those datasets. Building of the data

archive was and is still made possible through the financial support of the Netherlands Ministry of Housing, Spatial Planning, and the Environment. This ministry also supported the analyses and the present publication based on them.

- Alexandre, A. (1973). "Decision criteria based on spatio-temporal comparisons of surveys on aircraft noise," Proceedings of the International Congress on Noise as a Public Health Problem, Dubrovnik, Yugoslavia, Environmental Protection Agency, Washington, DC: U.S., pp. 619–626.
- Berglund, B., and Lindvall, L. (Eds.) (1995). "Community noise," Archives of the Center for Sensory Research, Stockholm University and Karolinska Institute. Vol. 2, No. 1.
- Fields, J. M. (1994a). "A review of an updated synthesis of noise/annoyance relationships," NASA Report 194950, Georgia Institute of Technology, Atlanta, GA.
- Fields, J. M. (1994b). "An updated catalog of 360 social surveys of residents reactions to environmental noise (1943–1993)," Georgia Institute of Technology, Atlanta, GA.
- Fields, J. M., and Walker, J. G. (1982). "Comparing the relationships between noise level and annoyance in different surveys: A railway noise vs. aircraft and road traffic comparison," J. Sound Vib. **81**, 51–80.
- Fidell, S., Barber, D. S., and Schultz, Th. J. (1991). "Updating a dosage-effect relationship for the prevalence of annoyance due to general transportation noise," J. Acoust. Soc. Am. **89**, 221–233.
- Finke, H. O., Guski, R., and Rohrmann, B. (1980). "Betroffenheit einer Stadt durch Lärm," Bericht über eine interdisziplinäre Untersuchung, Forschungsbericht 80-10501301, Physikalisch-Technische Bundesanstalt, Braunschweig.
- Gezondheidsraad (1994). "Noise and Health," Report of a committee of the Health Council of the Netherlands, Report no. 1994/15E, Gezondheidsraad, Den Haag.
- Goldstein, H. (1995). "Multilevel statistical models" Edward Arnold/Halsted, London/New York.
- Kryter, K. D. (1982). "Community annoyance from aircraft and ground vehicle noise," J. Acoust. Soc. Am. **72**, 1212–1242.
- Kryter, K. D. (1983). "Community annoyance from aircraft and ground vehicle noise," (Response of K. D. Kryter to modified comments by Th. J. Schultz on K. D. Kryter's paper), J. Acoust. Soc. Am. **73**, 1066–1068.
- Miedema, H. M. E. (1993). "Response functions for environmental noise," Proceedings of the 6th International Congress Noise and Public Health Problem, Nice, pp. 428–433.
- Pearsons, K. S., Barber, D. S., and Tabachnick, B. G. (1989). "Analyses of the predictability of noise-induced sleep disturbance," Report AD-A220 156, BBN Systems and Technologies Corporation, Canoga Park.
- Rasbash, J., and Woodhouse G. (1995). "Mln command reference, version 1.0," University of London–Institute of Education, London.
- Schultz, T. H. J. (1978). "Synthesis of social surveys on noise annoyance," J. Acoust. Soc. Am. **64**, 377–405.
- Schultz, T. H. J. (1982). "Comments on K. D. Kryter's Community annoyance from aircraft and ground vehicle noise," J. Acoust. Soc. Am. **1972**, 1243–1252.

Ultrasonic tomographic imaging of temperature and flow fields in gases using air-coupled capacitance transducers

William M. D. Wright^{a)}

Department of Engineering, University of Warwick, Coventry CV4 7AL, United Kingdom

David W. Schindel

Institute for Aerospace Research, NRC, Montreal Road, Ottawa, Ontario K1A 0R6, Canada

David A. Hutchins and Peter W. Carpenter

Department of Engineering, University of Warwick, Coventry CV4 7AL, United Kingdom

Dion P. Jansen

Ontario Hydro Technologies, Toronto, Ontario M8Z 5S4, Canada

(Received 25 July 1997; revised 5 August 1998; accepted 18 August 1998)

A pair of air-coupled ultrasonic capacitance transducers with polished metal backplates have been used to image temperature and flow fields in gases using ultrasonic tomography. Using a filtered back-projection algorithm and a difference technique, cross-sectional images of spatially variant changes in ultrasonic attenuation and slowness caused by the presence of temperature and flow fields were reconstructed. Temperature fields were produced in air by a commercial soldering iron, and the subsequent images of slowness variations used to reconstruct the air temperature at various heights above the iron. When compared to measurements made with a thermocouple, the tomographically reconstructed temperatures were found to be accurate to within 5%. The technique was also able to resolve multiple heat sources within the scan area. Attenuation and velocity images were likewise produced for flow fields created by an air-jet from a 1-mm-diam nozzle, at both 90 and 45 degrees to the scanning plane. The fact that temperature and flow fields can be measured in a gas without the need to insert any measuring devices into the image region is an advantage that may have many useful applications. © 1998 Acoustical Society of America.

[S0001-4966(98)00412-3]

PACS numbers: 43.58.Dj, 43.35.Zc, 43.38.Bs, 43.60.Rw [SLE]

INTRODUCTION

Tomographic reconstruction¹ is a well-established imaging technique that allows spatial variations of a physical variable in a material to be determined using only measurements made at the periphery of the area of interest. This may be accomplished by propagating ultrasonic waves or x-rays through the material in many different directions in the imaging plane, and using information extracted from this data to reconstruct a cross-sectional image. In the case of ultrasonic tomography, measurements of wave amplitudes and propagation delays are usually used to produce cross-sectional images of ultrasonic attenuation and slowness. These acoustic properties are in turn related to other material properties of interest, such as temperature or flow velocity, as will be demonstrated in this work.

Ultrasonic tomographic imaging has already been widely investigated, especially for the inspection of solid materials such as silicon dioxide ingots,² wood,³ and solid rocket propellants.⁴ Techniques for speeding up the collection of data have also been studied, including automated data acquisition⁵⁻⁷ and noncontact wave transduction.⁸⁻¹¹ One promising form of noncontact transduction is the air-coupled ultrasonic transducer,¹²⁻¹⁴ in which ultrasonic energy is

coupled to a material through an intervening air layer. Such transducers have been shown recently by the authors to be well suited for noncontact tomographic imaging of solids.¹⁵

Ultrasonic tomography has not yet been extended in any appreciable way to the characterization and imaging of gases themselves, which may be due in part to the lack of suitable gas-coupled transducers in the past. However, the air-coupled ultrasonic capacitance transducers used previously by the authors for noncontact tomographic inspection of solids¹⁵ are ideally suited for developing tomographic imaging applications within gases themselves. As a direct result of their ability to generate and receive ultrasonic waves in gases over a large frequency bandwidth (<100 kHz to 2.25 MHz), these devices are ideal for accurate measurements of propagation delay and frequency content. It will be shown in the work to be described here that such broadband air-coupled transducers can now be used to image temperature and flow fields in gases using ultrasonic tomographic imaging.

I. THE TOMOGRAPHIC RECONSTRUCTION THEOREM

Of the two main types of algorithm used to reconstruct cross-sectional images from boundary data, iterative techniques or series expansion methods are the most popular.¹⁶⁻¹⁹ The widespread use of these algorithms arises

^{a)}Now at Department of Electrical Engineering and Microelectronics, University College Cork, College Road, Cork, Ireland.

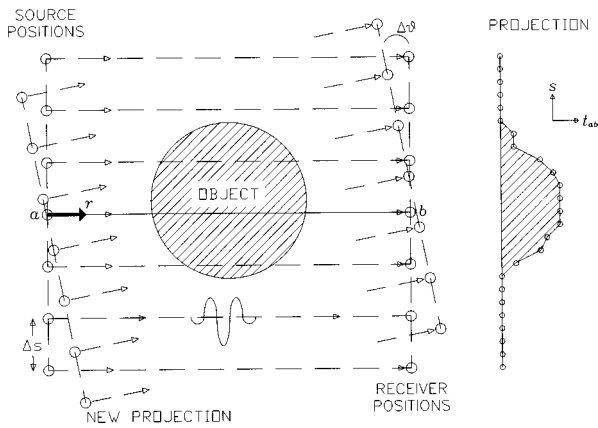


FIG. 1. The tomographic scanning geometry.

from their ability to correct for ray bending, anisotropy, and irregular sampling geometries, although such methods are computationally intensive. Transform methods²⁰⁻²³ which use Fourier analysis are quicker and more efficient, but are not as versatile and require a precise sampling geometry. For this reason, Fourier transform methods have been less popular. In the work to be presented here, a filtered back-projection algorithm using Fourier transforms was used to reconstruct tomographic images. This method has been described in detail elsewhere,²³ but for completeness a brief outline of the technique will be given.

Consider the sampling geometry shown in Fig. 1, where an ultrasonic source and receiver with a fixed separation ab are scanned together in a linear path over the object to be imaged. At regular spatial intervals Δs , a waveform or "ray" is recorded by the receiver and the source-receiver propagation time-delay t_{ab} is extracted to form one point on a "silhouette" or projection at an angle θ through the center of the object (the projection in Fig. 1 plots the result for $\theta=0$). Assuming a linear ray path along ab , the propagation delay t_{ab} is given by

$$t_{ab} = \int_{r_a}^{r_b} \frac{dr}{c_r}, \quad (1)$$

where c_r is the sound speed at any distance r along ab . The integrand is more commonly known as the slowness. When a single projection has been completed, the transducer pair (or the object of interest) is then rotated through small angular increments $\Delta\theta$, and the scanning process repeated at each angle so that a series of projections is built up, each one passing through the center of the object like the spokes of a wheel. When a full 180 degrees has been scanned, the projections may then be reconstructed into a cross-sectional image of all the slowness variations anywhere within the scan area.

The projection theorem states that the one-dimensional Fourier transform of a projection passing through the object at an angle θ is equal to a section through the two-dimensional Fourier transform of the slowness function at the same angle. By substitution and manipulation, this reduces to a filtered back-projection which is a simple convolution of each projection with a kernel function in the Fourier domain. If data is then taken in specific geometries, the result

of applying the filtered back-projection algorithm is an image showing spatial variations in slowness. Although tomographic imaging has been described in terms of propagation delays and slowness function, other acoustic wave properties such as signal amplitude and frequency content can be used to reconstruct images of other useful functions such as attenuation, as will be demonstrated.

II. TOMOGRAPHIC IMAGING IN CASES

In the specific case of ultrasonic tomographic imaging of the properties of a gas, the "object" in Fig. 1 may consist of a region with either (a) an appreciable flow velocity, (b) a variation in the local sound speed (e.g., due to a change in temperature or pressure), or (c) a combination of both (a) and (b). To consider these effects, the effective sound speed c_e at any distance r along the line ab between the source and receiver may be given approximately by

$$c_e = c_r + \mathbf{v} \cdot \hat{\mathbf{r}}, \quad (2)$$

where c_r is the local sound speed, \mathbf{v} is the local flow velocity of the gas (a vector quantity), and $\hat{\mathbf{r}}$ is a unit vector parallel with the ray path and pointing in the direction of integration. The dot-product in Eq. (2) ensures that the appropriate component of flow velocity will be added to, or subtracted from the local sound speed. Note that at high flow velocities, c_r will also vary with the gas flow speed, and so Eq. (2) is a linear approximation which is reasonably accurate provided that $|\mathbf{v}| \leq 0.3c$.

With a substitution of Eq. (2), Eq. (1) thus becomes

$$t_{ab} = \int_{r_a}^{r_b} \frac{dr}{c_r + \mathbf{v} \cdot \hat{\mathbf{r}}}, \quad (3)$$

which shows that the propagation delay t_{ab} will vary with spatial variations in both the local sound speed and gas flow velocity. Since the local sound speed c_r is known to vary with temperature according to

$$c_r = 331.31 \sqrt{\frac{T}{273.16}}, \quad (4)$$

where T is the air temperature in degrees Kelvin,²⁴ spatial variations in air temperature may also be extracted from the information contained in the measurements of propagation delay.

In most ultrasonic tomography experiments, absolute measurements of propagation delay or signal amplitude along known ray paths are usually required for the reconstruction of images. However, unknown delays and attenuation effects may be introduced by the pulser/receiver, while the exact propagation path between the source and receiver may be difficult to determine. In order to reduce the effect of such uncertainties, a form of difference tomography was employed in this work, in which the values obtained from each ray were normalized with respect to the first ray in each projection (taken in a region of ambient temperature and negligible flow velocity). In this way, a comparative image would be formed of only the *changes* in a physical variable induced by the presence of local sound speed variations or flow effects.

In the present application, comparative measurement can be included by rewriting Eq. (3) in the following form:

$$t_{ab} - t_{\text{ref}} = \int_{r_a}^{r_b} \frac{dr}{c_{\text{ref}} + \Delta c_r + (\mathbf{v}_{\text{ref}} + \Delta \mathbf{v}) \cdot \hat{\mathbf{r}}} - \int_{r_a}^{r_b} \frac{dr}{c_{\text{ref}} + \mathbf{v}_{\text{ref}} \cdot \hat{\mathbf{r}}}, \quad (5)$$

where c_{ref} and \mathbf{v}_{ref} are the values of c_r and \mathbf{v} corresponding to the first ray in each projection, and Δc_r and $\Delta \mathbf{v}$ are the deviations from those values found at r along ab . Provided that $|\Delta c_r + \Delta \mathbf{v} \cdot \hat{\mathbf{r}}| \ll |c_{\text{ref}} + \mathbf{v}_{\text{ref}} \cdot \hat{\mathbf{r}}|$, then to a good approximation Eq. (5) further reduces to

$$t_{ab} - t_{\text{ref}} \approx - \int_{r_a}^{r_b} \frac{\Delta c_r + \Delta \mathbf{v} \cdot \hat{\mathbf{r}}}{(c_{\text{ref}} + \mathbf{v}_{\text{ref}} \cdot \hat{\mathbf{r}})^2} dr, \quad (6)$$

which describes what will actually be recorded in the experiments to follow.

In many applications of practical interest, the flow effects can be considered negligible such that $|\mathbf{v}_{\text{ref}}| \ll c_{\text{ref}}$ and $|\Delta \mathbf{v}_r| \ll \Delta c_r$. In such cases, Eq. (6) may be simplified to

$$t_{ab} - t_{\text{ref}} \approx - \frac{1}{c_{\text{ref}}^2} \int_{r_a}^{r_b} \Delta c_r dr, \quad (7)$$

where it has been assumed that the reference ray is chosen well away from the region containing sound-speed variations. Equation (7) shows that a distribution in sound-speed variation can, in principle, be imaged by means of ultrasonic topography. One specific example in this case is the variation in sound speed due to the existence of a temperature field in air, where slowness variations may be converted to a reconstruction of the actual temperature field using Eqs. (7) and (4).

There are also many gas flows of practical interest where $|\Delta \mathbf{v}_r| \gg |\Delta c_r|$, i.e., where the variations in local sound speed are negligible. In such cases, Eq. (6) reduces to

$$t_{ab} - t_{\text{ref}} \approx - \int_{r_a}^{r_b} \frac{\Delta \mathbf{v} \cdot \hat{\mathbf{r}}}{(c_{\text{ref}} + \mathbf{v}_{\text{ref}} \cdot \hat{\mathbf{r}})^2} dr, \quad (8)$$

which shows how tomographic reconstruction of a flow field in a gas should also be feasible using only measurements made around the periphery of the flow. It is important to point out, however, that not all flow velocity fields can be uniquely reconstructed using equations such as Eq. (8).^{25,26} The flow field must be ‘‘divergenceless’’ (which means that the flow-velocity field must satisfy $\nabla \cdot \mathbf{v} = 0$). Such a divergenceless flow field is ensured when the fluid is incompressible and has no sources or sinks of flow within the image plane. However, as air is a compressible fluid, not all flow velocity fields in air can be uniquely reconstructed using ultrasonic tomographic methods,²⁵ although reconstruction of other flow parameters such as vorticity is still possible.²⁶⁻²⁸

In the preceding equations, only the expected effects of temperature and flow on propagation delays have been considered, yet the amplitude of the ultrasonic waves will also be affected as they traverse the temperature- or flow-affected

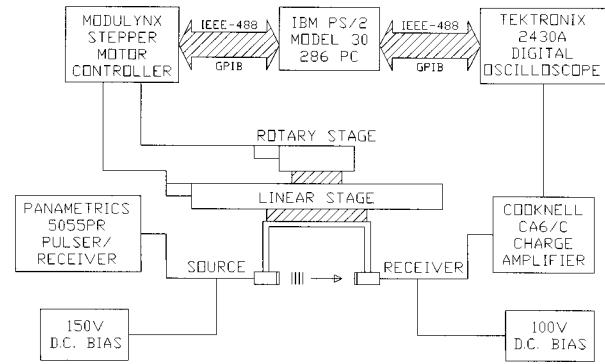


FIG. 2. Schematic diagram of the tomographic scanning equipment.

region. A sound wave traveling through a gas flow may be diverted from a direct path between the source and receiver by flow velocity components acting in directions perpendicular to the wave propagation. Similarly, temperature variations causing a local change in sound speed (and also gas density and specific acoustic impedance) will produce non-linear ray paths and divert further sound energy away from the receiver. Rather than developing mathematical relationships for each amplitude effect, their effects will simply be discussed as they become apparent in the work to be described.

III. THE SCANNING SYSTEM

The experimental apparatus used for tomographic imaging in air is shown schematically in Fig. 2. Ultrasonic waves were both generated and detected in air using a pair of capacitance-type air-coupled transducers.¹² Each transducer consisted of a thin polymer film (2.5- μm -thick Mylar) which was placed upon a brass backplate whose surface had been polished to a roughness R_a of 0.02 μm . The upper surface of the Mylar film was metallized so that a capacitive structure was formed with the conducting backplate, to which a bias voltage was applied. In order to generate ultrasound in air, a transient voltage was superimposed upon the bias voltage, causing motion of the film via electrostatic forces; similarly, when acting as an ultrasonic receiver, an incident ultrasonic wave in air caused the film to move and vary the charge upon the backplate of the capacitive structure. Both the transmitting and receiving transducers had a 10-mm-diam aperture, which will have an effect on the spatial resolution of the reconstructed images, due to averaging of the signal across the transducer aperture in both the horizontal and vertical directions.

The air-coupled capacitive source was driven by a Panametrics 5055PR pulser/receiver, which delivered -250-V transients with a rise time of <10 ns. A dc bias voltage of 150 V was superimposed upon this transient voltage using a capacitive decoupling circuit. Received signals, resulting from charge variations at the air-coupled receiver, were detected using a Cooknell CA6/C charge amplifier. This charge amplifier had a sensitivity of 250 mV/pC, and applied its own well-regulated dc bias voltage of 100 V. The resulting output waveforms were captured on a Tektronix 2430A digital oscilloscope, and then transferred via an IEEE-488/GPIB

interface to an IBM PS/2 model 30 286 computer. This computer was also used to position the transducer pair using rotary and linear Daedal stages, which were driven by a Modulynx stepper-motor controller. The positioning system had an overall precision of ± 0.01 mm per 50 mm of travel. The distance between the source and receiver was fixed at 165 mm, whereas the height of the scanning plane could be manually altered. Unless stated otherwise, the dimensions of each scan were 100 mm in 2-mm steps and 180 degrees in steps of 3 degrees, giving 61 projections of 51 rays each.

IV. EXPERIMENTAL RESULTS AND DISCUSSION

A. Imaging temperature fields in air

In order to verify that the effects of temperature in a gaseous medium could be tomographically imaged (i.e., when $|\mathbf{y}_{\text{refl}}| \ll c_{\text{ref}}$ and $|\Delta \mathbf{y}_r| \ll |\Delta c_r|$), a temperature field was created in air above a 15-W miniature soldering iron, and the ultrasonic slowness field was imaged using tomographic reconstruction. The soldering iron, whose long axis had been clamped vertically in the center of the scan area, was insulated cylindrically using flexible glass-fiber high-temperature sleeving so that only the top 1-mm length of the 3.5-mm-diam tip was protruding. The soldering iron had a constant tip temperature of 340 °C.

Typical waveforms obtained in this arrangement are shown in Fig. 3(a), with the signal traveling through the heated column of air (dashed line) being lower in amplitude than the signal traveling through the surrounding ambient atmosphere (solid line). This reduction in amplitude of the ray passing through the heated air is attributed to a combination of refraction of the waves away from the receiver, and the mismatch in specific acoustic impedance between the heated air and the ambient atmosphere. From property tables²⁹ and Eq. (4), the specific acoustic impedance of air can be shown to change from $480 \text{ kg}\cdot\text{m}^{-2}\cdot\text{s}^{-1}$ to $354 \text{ kg}\cdot\text{m}^{-2}\cdot\text{s}^{-1}$ for a change in air temperature from 300 K to 400 K, respectively. This corresponds to a reflection coefficient at the interface between the heated and ambient regions of 0.5%. Diffraction of the waves will also have occurred as the diameter of the air column above the soldering iron (approximately 3.5 mm) was only five times the wavelength in air at the frequencies of interest (at 500 kHz, $\lambda=0.7$ mm). Note that the heated wave also arrives sooner since the ultrasonic velocity is higher in the heated air as predicted by Eq. (4). The corresponding normalized frequency spectra obtained from these waveforms are shown in Fig. 3(b), where it can be seen that the frequency content of the heated wave has also reduced slightly. This was also attributed in part to refraction of the wave through the heated air which would cause the higher frequencies to arrive at an angle (i.e., incoherently) across the receiver aperture.

A full tomographic reconstruction of the soldering iron temperature field was also produced, using waveforms taken in a horizontal plane at a height of 10 mm above the vertical tip. The results may be seen in Fig. 4(a) for signal amplitude ($\text{dB}\cdot\text{mm}^{-1}$) and Fig. 4(b) for slowness ($\text{ns}\cdot\text{mm}^{-1}$). It is evident that the area immediately above the tip was most affected, as would be expected from a rising column of hot air.

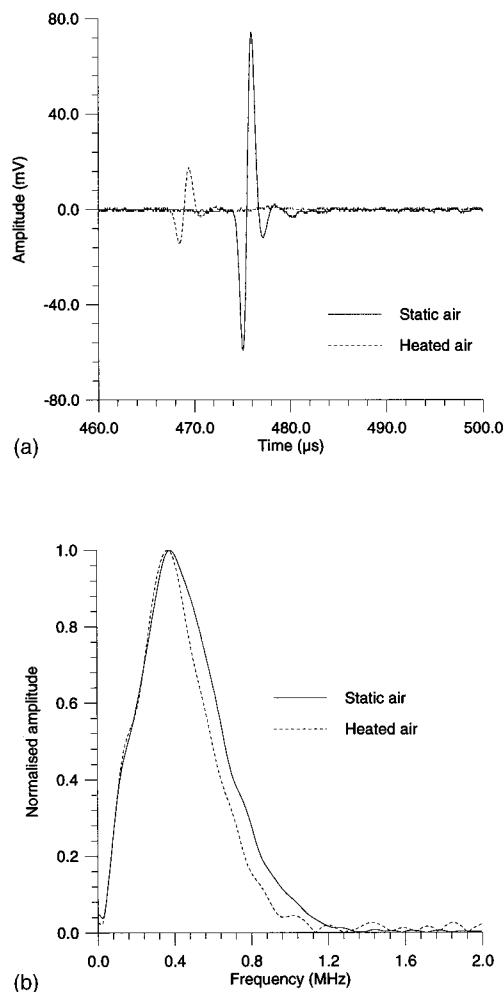


FIG. 3. (a) Typical waveforms through static air (solid line) and heated air (dashed line). (b) Normalized frequency spectra of waveforms shown in (a).

The fact that the amplitude image in Fig. 4(a) shows a larger affected area suggests that the ultrasonic amplitude is more susceptible to refraction and aperture effects than the propagation delays used to reconstruct the slowness image. The attenuation images thus complement the slowness images by indicating the presence of a temperature affected area which may not necessarily produce a measurable change in arrival time. Note that values of attenuation greater than zero are obtained in Fig. 4(a) due to noise both in the experimentally acquired acoustic data, and in the reconstruction algorithm. To minimize this effect, a Hamming window was used in conjunction with the kernel function in the filtered back-projection algorithm.

1. Effects of temperature-driven convective flow

It is important to point out that the soldering iron will produce a column of hot air that will be rising vertically due to convective (or buoyancy) forces.³⁰ This temperature-driven convective flow field may have an effect on the reconstructed tomographic images, an effect that is independent of the temperature effects already discussed. A simple theoretical calculation³⁰ was therefore used to predict the maximum vertical flow velocity due to natural convection for a cylindrical heat source of 3.5-mm diameter, with a con-

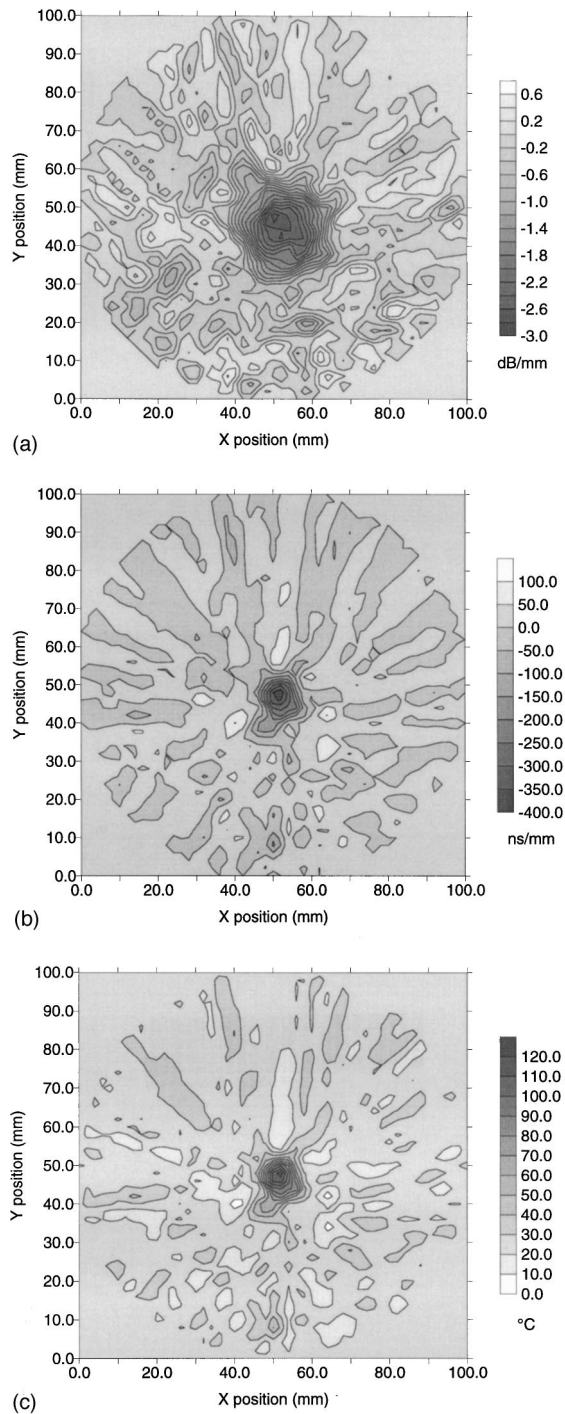


FIG. 4. (a) Attenuation image in $\text{dB}\cdot\text{mm}^{-1}$, (b) slowness image in $\text{ns}\cdot\text{mm}^{-1}$, and (c) temperature image in $^{\circ}\text{C}$, taken 10 mm above a vertical 15-W soldering iron.

stant surface temperature of 340°C in ambient air at 26°C . This calculation resulted in a maximum vertical flow velocity of approximately $0.3\text{ m}\cdot\text{s}^{-1}$, which, although small, may still affect received signal amplitudes, since the ultrasonic wave will be diverted away from the axis of the receiver. The magnitude of such a diversion effect was further calculated as follows. The diameter of the convective region in Fig. 4(b) traversed by the ultrasonic wave was approximately 5 mm. This means that the ultrasonic beam spends approximately $5\text{ mm}/350\text{ m}\cdot\text{s}^{-1}=14.3\text{ }\mu\text{s}$ in the region of convec-

tive flow, which at a maximum vertical flow velocity of $0.3\text{ m}\cdot\text{s}^{-1}$ would deflect the ultrasonic beam vertically by only $4\text{ }\mu\text{m}$; quite obviously, this is negligible compared to the 10-mm transducer aperture. As a result, the dominant effects in the attenuation image of Fig. 4(a) may therefore be attributed to a combination of impedance mismatch, ray bending, and refraction arising from temperature variations, and not convective flow. Similarly for propagation delays, the flow velocity was primarily perpendicular to the velocity of the ultrasonic waves and so such effects would only become important if there were an appreciable horizontal flow component.³⁰ Therefore, Eq. (7) should be a good approximation, since the changes in propagation delay used to produce the slowness image in Fig. 4(b) were predominantly due to the increased air temperature as described by Eq. (4), and not changes in flow speed.

2. Reconstructing temperature fields from ultrasonic slowness fields

The ultrasonic slowness data of Fig. 4(b) was further converted to a tomographic image of temperature within the image plane, by means of Eqs. (4) and (7). Using an ambient air temperature of 26°C (299.16 K) and thus an ambient air sound velocity of $347\text{ m}\cdot\text{s}^{-1}$, a temperature image in $^{\circ}\text{C}$ of the scan area was reconstructed as depicted in Fig. 4(c). Here it can be seen that the maximum reconstructed air temperature at a height of 10 mm occurred immediately over the tip center and was 126.5°C . Once again, values less than the ambient temperature were a result of noise introduced during the reconstruction.

In order to verify the reconstructed temperatures in Fig. 4(c), the air temperature was independently measured using a 1-mm-diam miniature K-type thermocouple and a Maplin ‘‘Precision Gold’’ M-1300K thermometer. As the instantaneous air temperature was found to fluctuate wildly (often by 20°C or more), an average of seven readings was taken at 20-s intervals, and a delay of 2 min was left between moving the thermocouple and taking the readings to allow the system to stabilize. Figure 5(a) shows the temperature profile measured in a line through the image plane at a distance of 10 mm above the soldering iron tip, with the tip center located at a distance of 5 mm. Figure 5(b) shows the temperature profile measured in a vertical line starting at the tip center, where the temperature can be seen to fall from 340°C at the tip to a temperature of 134.5°C at a height of 10 mm. It is apparent from these two figures that the air temperature does not vary with height to the same extent as with horizontal distance.

It can also be seen in Fig. 5(a) that the maximum temperature recorded in the image plane by the thermocouple was 165.4°C directly over the center of the tip, a value somewhat higher than that produced by the ultrasonic data. However, the measurements by the thermocouple were effectively at a single point, whereas the ultrasonic measurements were averaged over a 10-mm area (i.e., both horizontally and vertically) due to the aperture size of the transducers. Therefore, in order to make a meaningful comparison, the temperature profiles measured by the thermocouple were averaged over 10-mm distances centered about the tip of the iron.

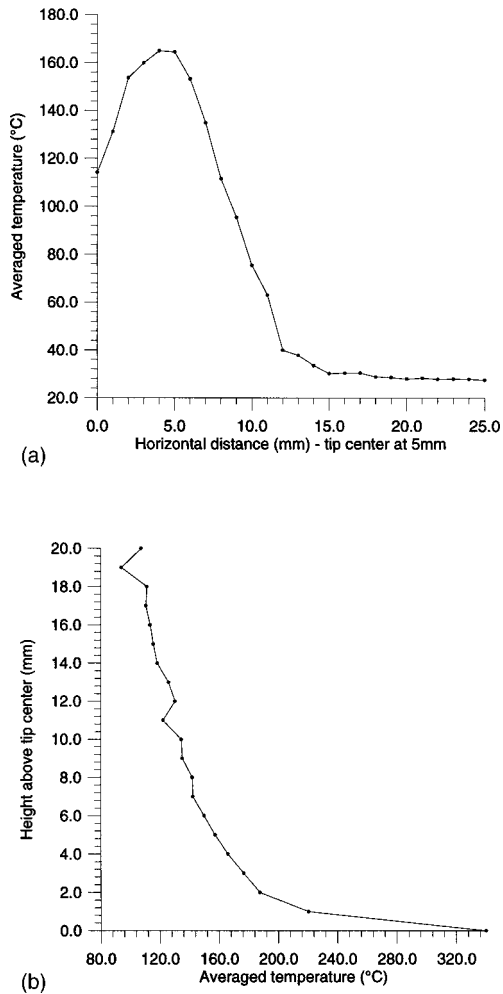


FIG. 5. (a) Horizontal and (b) vertical temperature distribution measured over the soldering iron tip with a thermocouple.

When this was done for the horizontal data of Fig. 5(a), the “measured” temperature by the thermocouple becomes 132.2 °C, while for the vertical data of Fig. 5(b) an average value of 133.9 °C results. As both of these average measured values are within 5% of the reconstructed temperature of 126.5 °C obtained through ultrasonic tomographic imaging, it can be concluded that the tomographic system can measure temperature profiles with reasonable accuracy. This ability of the air-coupled transducers to measure the temperature profile in air without the need to insert any object into the temperature field is an interesting application that merits further investigation.

3. Other experiments involving temperature fields

A second experiment undertaken with the single vertical soldering iron involved reconstructions at different heights above the tip. A series of five tomographic reconstructions was taken at 5-mm vertical intervals between 10 and 30 mm above the tip, and the results are shown in Fig. 6. Note that in this axial region from 10 to 30 mm, the reconstructed temperature above the iron tip varied between 131.3 °C and 87.1 °C, which is in good agreement with the thermocouple measurements, and indicates that there is very little horizontal spread in the temperature distribution with increasing

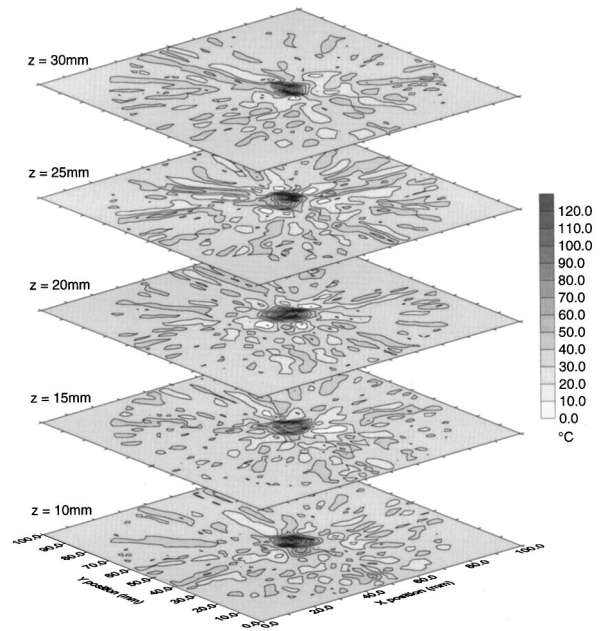


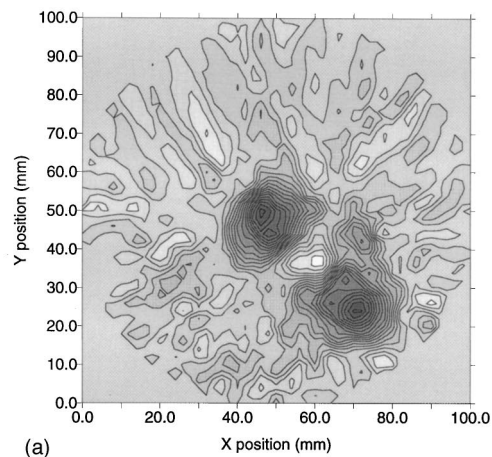
FIG. 6. Temperature images in °C at different heights z above the soldering iron.

height. This lack of horizontal temperature spread was verified by introducing a source of smoke at the tip, and observing a narrow well-defined column of heated air.

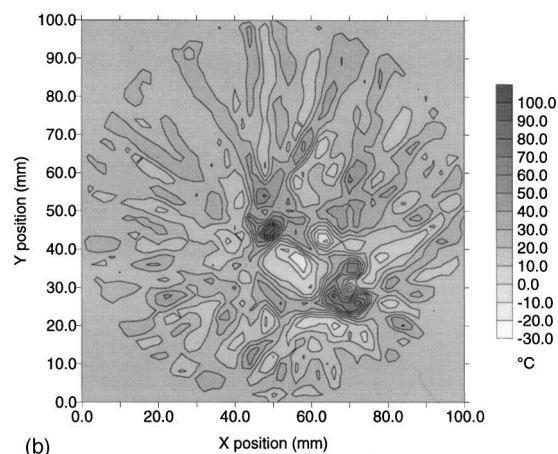
Other studies undertaken with temperature fields sought to image more complex temperature profiles. Figure 7, for example, shows the reconstructed images when two separate thermal sources were present in the scan area. A 15-W iron 3.5 mm in diameter was located in the center of the scan as before, while a 25-W iron 4.5 mm in diameter was added, offset by 20 mm in both x and y directions. The amplitude image in Fig. 7(a) in $\text{dB} \cdot \text{mm}^{-1}$ has clearly reconstructed the two sources, and the temperature image in Fig. 7(b) shows a larger affected area for the 4.5-mm (25-W) iron when compared to the 3.5-mm 15-W iron. There is considerable noise present in these images, however, possibly due to (a) horizontal velocity components in the air columns, (b) the use of an insufficient number of rays or projections, or (c) air turbulence caused by the close proximity of the two heat sources. Such additional sources of noise also appeared in a study that produced Fig. 8, where the 15-W iron was uninsulated and clamped horizontally to give a $3.5 \times 45\text{-mm}^2$ rectangular heat source. The attenuation image in $\text{dB} \cdot \text{mm}^{-1}$ in Fig. 8(a) does give an indication of the size and shape of the heat source, but the temperature profile in Fig. 8(b) has not been correctly reconstructed, perhaps due to the sources of noise just mentioned. Investigations are currently underway to determine the best technique required to image various types of temperature fields.

B. Imaging flow fields in air

Experiments were performed in order to verify the earlier prediction that flow fields could be imaged using ultrasonic tomography (i.e., when $|\mathbf{v}_{\text{ref}}| \gg c_{\text{ref}}$ and $|\Delta \mathbf{v}_r| \gg |\Delta c_r|$). To do so, the soldering iron was replaced by an air jet having a nozzle diameter of 1 mm and an air flow rate of 15 l/min



(a)



(b)

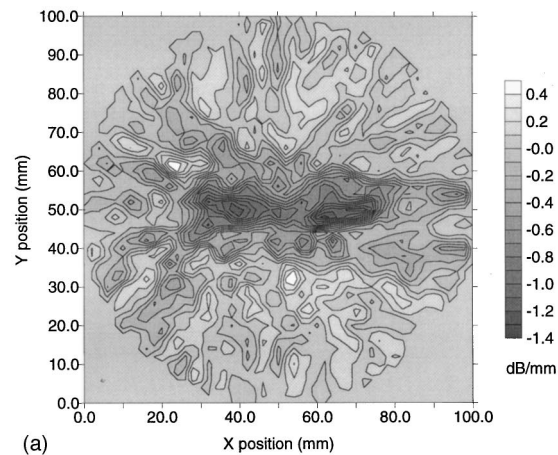
FIG. 7. (a) Attenuation image in $\text{dB}\cdot\text{mm}^{-1}$ and (b) temperature image in $^{\circ}\text{C}$, taken 20 mm above two vertical soldering irons.

(as measured using a Platon A10HS flowmeter). A tomographic scan was performed at a vertical height of 20 mm from the nozzle tip, with the scanning plane perpendicular to the direction of flow, and the results are presented in Fig. 9. Figure 9(a) shows the attenuation image in $\text{dB}\cdot\text{mm}^{-1}$ for the air jet, while Fig. 9(b) shows an image of the effective sound speed c_e , as reconstructed from the slowness data using a sound speed of $c_r = 347 \text{ m}\cdot\text{s}^{-1}$. Recall that the reconstruction of c_e in Fig. 9(b) includes only the horizontal components of the flow velocity [see Eq. (2)], which in this case will be much smaller than the vertical flow velocity of the air jet.

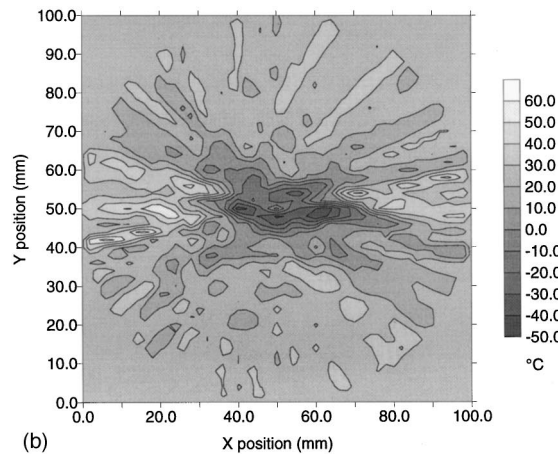
In order to interpret the results of Fig. 9, certain theoretical aspects of the flow-field produced by a vertical jet must be considered in some detail. For the nozzle dimension and flow rate described, the maximum vertical flow velocity at the nozzle exit (v_e) was calculated to be $319 \text{ m}\cdot\text{s}^{-1}$. However, the flow velocity in such a jet reduces at a rate inversely proportional to distance from the nozzle exit, and so the following semi-empirical formula³¹ was used to predict the centerline flow speed v_c for a circular jet as a function of distance z from the nozzle exit:

$$\frac{v_c}{v_e} = A \frac{d}{z+a}. \quad (9)$$

In Eq. (9), d is the nozzle exit diameter, and a and A are



(a)



(b)

FIG. 8. (a) Attenuation image in $\text{dB}\cdot\text{mm}^{-1}$ and (b) temperature image in $^{\circ}\text{C}$, taken 20 mm above a horizontal soldering iron.

semi-empirical constants³¹ (with $A = 5.9$, and a equal to either $-0.5d$ or $-3d$). For a distance $z = 20 \text{ mm}$ above the nozzle (i.e., $20d$), Eq. (9) suggests that v_c equals either 96 or $111 \text{ m}\cdot\text{s}^{-1}$, depending on which value of a is used. Thus to a reasonable approximation it can be assumed that the centerline flow speed v_c will have dropped to about $100 \text{ m}\cdot\text{s}^{-1}$ at the scanning plane, which means that the basic assumption leading to Eq. (2) is still valid (namely $|\mathbf{v}| \leq 0.3c$).

It is apparent from Fig. 9(a) and (b) that the diameter of the air jet is much larger than the 1-mm diameter of the nozzle. This was not unexpected, as such an air jet is known to spread radially outwards in an approximately linear fashion with distance z from the nozzle exit, according to the following semi-empirical formula:³¹

$$\frac{d_{1/2}}{d} = \frac{z}{z_c}. \quad (10)$$

In this equation, $d_{1/2}$ is the diameter at which the flow speed has fallen to half its centerline value v_c , and z_c is the length of the so-called potential core, typically $4d$ to $5d$. As the velocity profile of the air jet is approximately Gaussian in shape, the total diameter of the jet (d_j) is actually about $2d_{1/2}$, and thus Eq. (10) gives $d_j = 0.4z$ or $0.5z$ (depending on the value of z_c). For $z = 20 \text{ mm}$, the beam diameter d_j is therefore expected to be approximately 8–10 mm, which is in good agreement with the reconstructed images in Fig.

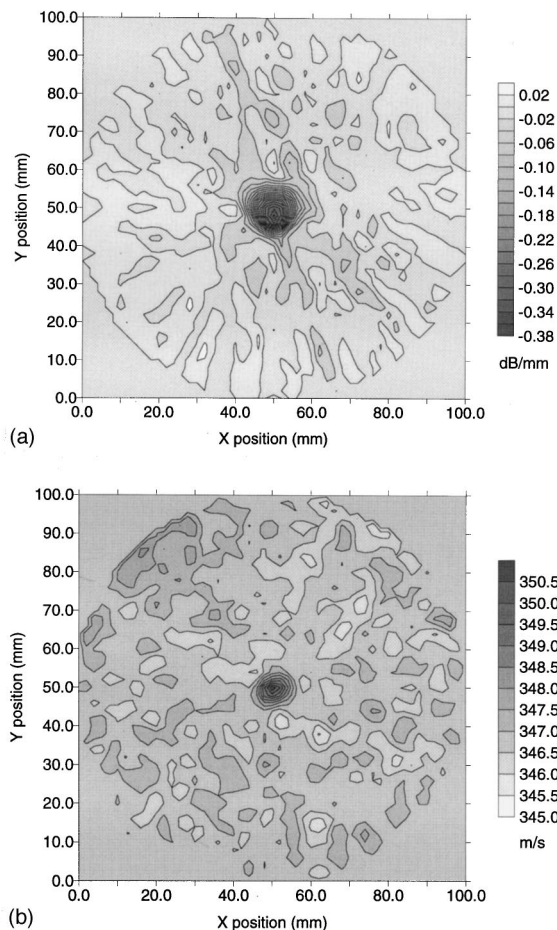


FIG. 9. (a) Attenuation image in $\text{dB}\cdot\text{mm}^{-1}$ and (b) velocity image in $\text{m}\cdot\text{s}^{-1}$ taken 20 mm above a vertical air jet.

9(a) and (b). Thus, these images clearly demonstrate that a region of high flow velocity can be successfully imaged in a gas from both ultrasonic signal amplitudes and propagation delay data.

Note that the maximum vertical flow velocity of $100 \text{ m}\cdot\text{s}^{-1}$ for the air jet is far higher than the convective flow velocity calculated earlier for the temperature field above the soldering iron. This means that over the 10-mm region affected by the air jet as seen in Fig. 9(a) and (b), the ultrasonic wave will have been diverted by approximately 3 mm, which is a significant offset distance when compared to the 10-mm aperture of the transducers. For this reason, the amplitude variations of Fig. 9(a) may be attributed primarily to the ultrasound being diverted away from the receiver by the flow.

It is also important to point out that the flow field will be turbulent in the case of the air jet, and so highly unsteady. Even though the flow is predominantly in the vertical direction, turbulent jets can still have instantaneous horizontal flow-velocity components that reach levels approaching $0.25v_c$.³¹ The maximum horizontal component of flow velocity due to turbulence is actually expected at the jet periphery,³¹ and would be of the order of $20\text{--}30 \text{ m}\cdot\text{s}^{-1}$ in the present case. Therefore, in principle, substantial propagation delays could be recorded by the tomographic system due to the instantaneous horizontal turbulent components. However,

Fig. 9(b) was obtained from *time-averaged* propagation delay data and, accordingly, should represent the time-averaged horizontal component of the velocity field, which should be small compared with v_c . Moreover, the time-averaged horizontal flow velocity should be directed radially inward towards the vertical axis of the jet, such that for any particular ray *ab* the contributions to slowness on opposite sides of the jet would tend to cancel. A perfectly symmetric jet would not be expected to exhibit any variation in slowness. The data of Fig. 9(b) is not inconsistent with these ideas, as the measured variations in horizontal flow speeds were about $4 \text{ m}\cdot\text{s}^{-1}$ (i.e., only 4% of v_c), but whether Fig. 9(b) truly provides a measure of the horizontal flow components requires a more detailed future investigation. This is particularly necessary when one recalls that the flow velocity field cannot always be uniquely reconstructed from tomographic time-of-flight data for a compressible fluid (as previously discussed), and may be complicated by the existence of invisible flow.^{25,26}

The need to investigate the effects of compressibility on tomographic reconstruction can further be seen in the following way. At the relatively high maximum flow speed (about $100 \text{ m}\cdot\text{s}^{-1}$ at the measuring plane), the variation in sound speed c_r across the jet is around $3 \text{ m}\cdot\text{s}^{-1}$, using estimates based on the isotropic flow relations. Accordingly, Eq. (2) is a less good approximation than at low flow speeds, such that the variation in slowness reflected in Fig. 9(b) could be explained by the variation in local sound speed owing to compressible flow effects. It is also possible that ray bending contributed to some of the measured variations in slowness. Whatever the explanation for the variations in slowness, it does appear from Fig. 9(b) that the expected dimensions of the jet (8–10 mm in diameter) are faithfully reproduced, which is a remarkable result considering the relatively large size of the transducers. Therefore, until further research is undertaken, it is safe to say that air flows can be reliably imaged tomographically by air-coupled ultrasonic transducers, but that quantitative information about the actual reconstructed parameters will not necessarily be accurate.

1. Other experiments involving flow fields

Other experiments with different flow field configurations were additionally carried out. To produce a definite measurable horizontal component of the flow velocity, the air jet was inclined at an angle of 45 degrees to the scanning plane. The flow rate was also reduced from 15 to 10 l/min, so that v_c reduced to $213 \text{ m}\cdot\text{s}^{-1}$. In this way elliptic, rather than circular, jet cross sections were produced. At a height of 20 mm above the nozzle exit, the jet axis cuts the scanning plane at a distance of $z = 20\sqrt{2} = 28.3 \text{ mm}$ from the nozzle. In this case Eq. (9) gives an estimated maximum flow speed v_c of approximately 45.2 to $49.7 \text{ m}\cdot\text{s}^{-1}$ (at 45 degrees to the scanning plane). The corresponding horizontal component should therefore be about $(47 \pm 2)/\sqrt{2} = 33 \pm 1.4 \text{ m}\cdot\text{s}^{-1}$, and so this should be the expected range of velocity variations.

Figure 10(a) shows the reconstructed amplitude image in $\text{dB}\cdot\text{mm}^{-1}$ for the tilted air jet. As expected, the jet cross section is elliptical. The corresponding velocity contours, based on Eq. (8), are further plotted in Fig. 10(b). Note that the range of flow velocities obtained (about $34 \text{ m}\cdot\text{s}^{-1}$) is

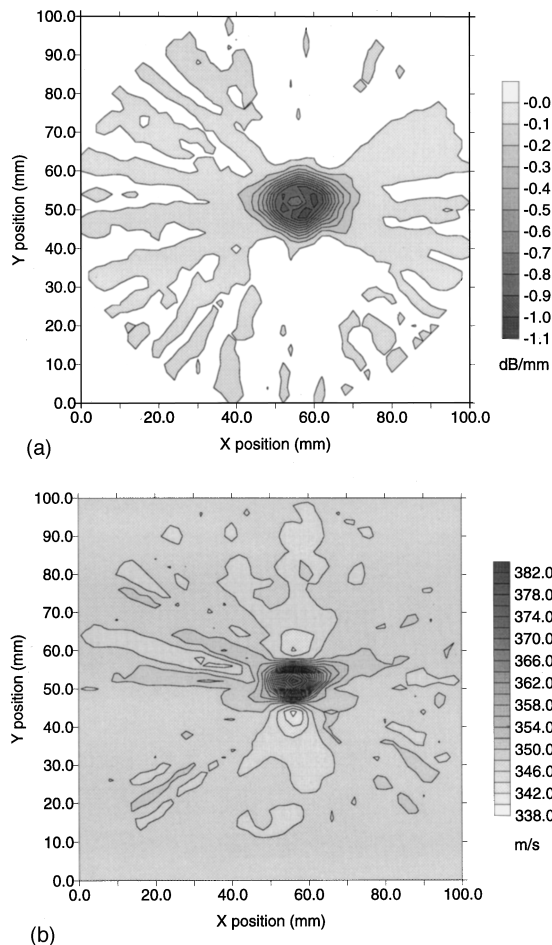


FIG. 10. (a) Attenuation image in $\text{dB}\cdot\text{mm}^{-1}$ and (b) velocity image in $\text{m}\cdot\text{s}^{-1}$ taken 20 mm above an angled air jet.

similar to the estimate given above (although compressible flow effects and ray bending may again be significant). A further selection of velocity profiles through the jet, taken at 5 mm vertical intervals between 20 and 40 mm above the nozzle tip, is included in Fig. 11. Here, the jet cross section is seen to increase in size and the velocity range reduce in amplitude as the height of the scanning plane above the nozzle is increased, as expected.

Note that a more accurate reconstruction of the flow profiles would have resulted in the above images if a full 360-degree angular range had been scanned, since this would have produced projections of slowness for ultrasound propagated both with and against the horizontal flow components. Such a method would have made it possible to either eliminate the effects of the flow or the effects of the variation in local sound speed, by adding and subtracting propagation times.²⁷ In principle, tomographic reconstruction of the vorticity field is also possible by this method.²⁸ Although this approach has not yet been employed, it will form part of future work. Nevertheless, this initial study still demonstrates the feasibility of using ultrasonic measurements in gas flows to obtain tomographic images of the flow field without the need to insert measuring devices into the flow.

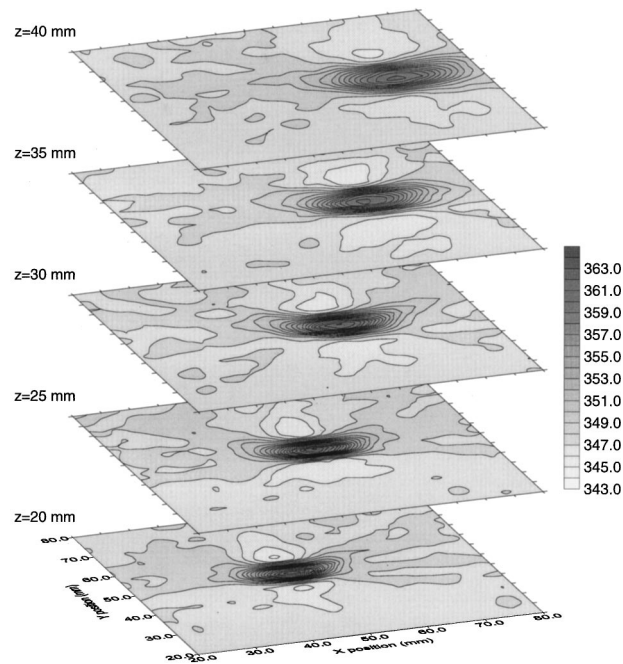


FIG. 11. Velocity images in $\text{m}\cdot\text{s}^{-1}$ at different heights z above an angled air jet.

V. CONCLUSIONS

Tomographic imaging of temperature and flow fields in air was carried out using a pair of capacitance-type ultrasonic transducers with polished metal backplates. Using a filtered back-projection algorithm and a form of difference tomography, images of both attenuation in $\text{dB}\cdot\text{mm}^{-1}$ and slowness in $\text{ns}\cdot\text{mm}^{-1}$ were obtained. The values of slowness were converted into air temperatures in $^{\circ}\text{C}$ and the temperature fields produced by commercial soldering irons were plotted at different heights above the tip. The reconstructed air temperatures were found to be in good agreement (5%) with average air temperatures measured with a miniature thermocouple. The technique was also able to resolve more than one heat source in the scan area. In terms of imaging flow fields, attenuation and velocity images were also successfully produced of cross sections through an air jet at different heights above a 1-mm-diam nozzle, and at both 90 and 45 degrees to the flow direction. In this way we have demonstrated that it is possible to use ultrasound measurements in gas flows to produce tomographic images of temperature and flow fields, without the need to insert any measuring device into the flow. Such a capability should have many interesting and useful applications.

¹A. C. Kak and M. Slaney, *Principles of Computerized Tomographic Imaging* (IEEE, New York, 1988).

²H. Yamada, Y. Tomikawa, and M. Nishida, "Application of ultrasonic computed tomography to non-destructive inspection of SiO_2 ingot material qualities," *J. Acoust. Soc. Am. Suppl.* 1 **84**, S71-S72 (1988).

³Y. Tomikawa, "Non-destructive inspection of wooden poles using ultrasonic computed tomography," *IEEE Trans. Ultrason. Ferroelectr. Freq. Control* **UFFC-33**, 354-358 (1986).

⁴A. M. H. Satti and J. Szilard, "Computerized ultrasonic tomography for testing solid propellant rocket motors," *Ultrasonics* **21**, 162-166 (1983).

⁵D. P. Jansen, D. A. Hutchins, and R. P. Young, "Ultrasonic tomography

- using scanned contact transducers," J. Acoust. Soc. Am. **93**, 3242–3249 (1993).
- ⁶T. M. Chow, D. A. Hutchins, and J. T. Mottram, "Simultaneous acoustic emission and ultrasonic tomographic imaging in anisotropic polymer composite material," J. Acoust. Soc. Am. **94**, 944–953 (1993).
- ⁷T. Chow, D. A. Hutchins, M. D. C. Moles, and R. P. Young, "Stress dependence of the acoustic properties of Zr-2.5 wt% Nb alloy," Ultrasonics **31**, 183–192 (1993).
- ⁸D. A. Hutchins, J. K. Hu, R. P. Young, R. Stoner, D. Jansen, and Q. L. Zhang, "Ultrasonic tomography of metals using non-contact transduction," J. Acoust. Soc. Am. **85**, 747–752 (1989).
- ⁹D. A. Hutchins, D. P. Jansen, and C. Edwards, "Lamb-wave tomography using non-contact transduction," Ultrasonics **31**, 97–103 (1993).
- ¹⁰J. K. Hu, D. A. Hutchins, J. Ungar, Q. L. Zang, and D. K. Mak, "Non-contact ultrasonic reflection tomography," Mater. Eval. **47**, 736–740 (1987).
- ¹¹D. P. Jansen, D. A. Hutchins, and J. T. Mottram, "Lamb wave tomography of advanced composite laminates containing damage," Ultrasonics **32**, 83–89 (1994).
- ¹²H. Carr and C. Wykes, "Diagnostic measurements in capacitive transducers," Ultrasonics **31**, 13–20 (1993).
- ¹³W. Manthey, N. Kroemer, and V. Mágóri, "Ultrasonic transducers and transducer arrays for applications in air," Meas. Sci. Technol. **3**, 249–261 (1992).
- ¹⁴D. W. Schindel, D. A. Hutchins, L. Zou, and M. Sayer, "The design and characterization of micro-machined air-coupled capacitance transducers," IEEE Trans. Ultrason. Ferroelectr. Freq. Control **UFFC-42**, 42–50 (1995).
- ¹⁵W. M. D. Wright, D. A. Hutchins, D. P. Jansen, and D. W. Schindel, "Air-coupled Lamb wave tomography," IEEE Trans. Ultrason. Ferroelectr. Freq. Control **UFFC-44**, 53–59 (1997).
- ¹⁶Y. Censor, "Finite series expansion reconstruction techniques," Proc. IEEE **71**, 409–419 (1984).
- ¹⁷R. Gordon, R. Bender, and G. T. Herman, "Algebraic reconstruction techniques for three-dimensional electron microscopy and x-ray photography," J. Theor. Biol. **29**, 471–481 (1970).
- ¹⁸P. Gilbert, "Iterative methods for the three-dimensional reconstruction of an object from projections," J. Theor. Biol. **29**, 105–117 (1972).
- ¹⁹R. A. Kline and Y. Q. Wang, "A technique for ultrasonic tomography in anisotropic media," J. Acoust. Soc. Am. **91**, 878–884 (1992).
- ²⁰R. M. Lewitt, "Reconstruction algorithms: transform methods," Proc. IEEE **71**, 390–408 (1984).
- ²¹H. H. Stark, J. W. Woods, I. Paul, and R. Hingorani, "Direct Fourier reconstruction in computer tomography," IEEE Trans. Acoust., Speech, Signal Process. **ASSP-29**, 237–245 (1981).
- ²²G. T. Herman, *Image Reconstruction from Projections: The Fundamentals of Computerized Tomography* (Academic, New York, 1980).
- ²³D. P. Jansen and D. A. Hutchins, "Immersion tomography using Rayleigh and Lamb waves," Ultrasonics **30**, 245–254 (1992).
- ²⁴R. Hickling and S. P. Marin, "The use of ultrasound for gauging and proximity sensing in air," J. Acoust. Soc. Am. **79**, 1151–1160 (1986).
- ²⁵S. J. Norton, "Tomographic reconstruction of 2-D vector fields: application to flow imaging," Geophys. J. **97**, 161–168 (1988).
- ²⁶S. A. Johnson, J. F. Greenleaf, C. R. Hansen, W. F. Samayoa, M. Tanaka, A. Lent, D. A. Christensen, and R. L. Woolley, "Reconstructing three-dimensional fluid velocity vector fields from acoustic transmission measurements," in *Acoustical Holography* (Plenum, New York, 1977), Vol. 7, pp. 307–326.
- ²⁷H. Braun and A. Hauck, "Tomographic reconstruction of vector fields," IEEE Trans. Signal Process. **SP-39**, 464–471 (1991).
- ²⁸K. B. Winters and D. Rouseff, "Tomographic reconstruction of stratified fluid flow," IEEE Trans. Ultrason. Ferroelectr. Freq. Control **UFFC-40**, 26–33 (1993).
- ²⁹G. F. C. Rogers and Y. R. Mayhew, *Thermodynamic and Transport Properties of Fluids* (Blackwell, Oxford, 1995), 5th ed.
- ³⁰J. P. Holman, *Heat Transfer* (McGraw-Hill, New York, 1986), 6th ed., pp. 323–329.
- ³¹J. O. Hinze, *Turbulence* (McGraw-Hill, New York, 1975), 2nd ed., pp. 535 *et seq.*

Maximum likelihood localization of sources propagating in a random media using intensity measurements

Bong-Gee Song and James A. Ritcey^{a)}

Department of Electrical Engineering, Box 352500, University of Washington, Seattle, Washington 98195

Terry E. Ewart

Applied Physics Laboratory, College of Ocean and Fishery Sciences, University of Washington, Seattle, Washington 98195

(Received 15 March 1996; revised 18 June 1998; accepted 30 July 1998)

A statistical signal processing solution is proposed for locating a monochromatic source propagating in a random media. The media is fully parametrized by the normalized scattering strength γ and scaled range X , which depend upon the physics of the media. M independent intensity measurements are observed, each drawn from the generalized gamma distribution. This has been shown by Ewart [J. Acoust. Soc. Am. **86**, 1490–1498 (1989)] to describe sources propagating through internal waves in ocean environments. The parameters of the distribution are related to the scattering parameters, γ and X . Maximum likelihood estimation is used to infer X , given the observations and our knowledge of γ . The estimation performance is well-characterized by the Cramer–Rao lower bound (CRLB). The results show that we can estimate range to a precision of about 20%, for ranges up to half the distance to the focus of the medium. Simulation results verify both the normality of the estimates and the validity of the CRLB as a predictor of the estimator precision at these ranges. The practical value of this method will depend on our ability to gather enough independent measurements, and on the accuracy of the statistical models we assume, including prior knowledge of γ . It can be expected to augment other methods such as matched field processing. © 1998 Acoustical Society of America. [S0001-4966(98)02011-6]

PACS numbers: 43.60.–c [JCB]

INTRODUCTION

Source localization of monochromatic sources in ocean environments using passive acoustics has now been well developed. The most recent methods are variations of the matched-field technique.^{1–3} In matched field, we presume that an accurate model of ocean propagation is available, and templates, each depending on source location in range and depth, are computed. One computes the ambiguity surface, the peaks of which are the source position estimates. Matched field depends on accurate propagation models, and these are parametrized by a variety of environmental parameters including bottom and surface properties and the sound speed profile. At low frequencies, performance is good as the mismatch with the environmental model is small. At higher frequencies, matched field performance drops, often because of the stochastic nature of ocean acoustic propagation.² We propose to use stochastic models.⁴

In our statistical approach, we model the observations as random, arising from independent samples from a known distribution, whose parameters determine the location of the source. At the present time, these models are incomplete, especially in the case of joint complex observations. For this reason, we ignore phase and utilize only the intensity of the observation. In Ewart,⁵ the generalized gamma distribution is shown to model the distribution of the intensity of a monochromatic source at a single point in space and time. Most importantly, the mapping between the parameters of the gen-

eralized gamma and the physical parameters is determined, and is provided in Appendix A. We use this mapping to infer the range to the source, based on maximum likelihood estimates of the distributional parameters, given a set of independently identically distributed observations of source intensity.

This paper proceeds through an exposition of the statistical signal model and discusses our maximum likelihood approach. A comparison with the Cramer–Rao lower bound (CRLB) is presented. Simulation results verify the efficiency of the estimation procedure and the utility of the CRLB in characterizing the precision. Asymptotic normality is evidently reached at the moderate sample size of $M=25$ independent observations. Knowledge of the scattering strength γ is assumed, so that we need only estimate the parameter of interest scaled range X . Incomplete knowledge of γ would necessitate a two-dimensional search over γ, X jointly, or the imposition of a mismatch loss due to erroneous specification of γ . This extension is left as future work.

I. SIGNAL MODEL

We model an acoustic wave propagating in a random medium (WPRM) as a monochromatic wave of the form

$$A \cos(2\pi f_0 t + \psi) = \text{Re}\{A e^{j\psi} e^{j2\pi f_0 t}\}, \quad (1)$$

where A is the amplitude, f_0 is the frequency of the monochromatic observation, and ψ is the phase of the wave due to the angle of arrival. The randomness of the wave lies in amplitude A and phase ψ , and is determined by the propaga-

^{a)}Electronic mail: ritcey@ee.washington.edu

tion parameters such as the index of refraction (sound speed variation), scattering strength, and the range between source and receiver.⁶ The probability distribution function (PDF) of the intensity (or the amplitude) for a given environment is known to vary depending on the environmental variables.^{7,8} For example, at long range in the saturated regime, the signal intensity approaches an exponential distribution. At short ranges, in the Rytov regime, intensity approaches lognormal. The distribution varies for intermediate ranges, and Ewart⁵ has found a useful model over this regime.

The generalized gamma ($G\Gamma$) distribution has been proposed and validated as a useful full range statistical model of the intensity and amplitude variations. Ewart and Percival⁷ have obtained the model of the intensity fluctuations using the $G\Gamma$ distribution as

$$p(I|[a,b,k]^T) = \frac{|b|}{a} \frac{1}{\Gamma(k)} \left(\frac{I}{a}\right)^{bk-1} \exp\left[-\left(\frac{I}{a}\right)^b\right]. \quad (2)$$

In their work, maximum likelihood estimation is used to find the parameter set $[a,b,k]^T$ for a given environment. The intensity PDF has been extended to the joint PDF of the quadrature components in Ritcey *et al.*⁹

The physical parameters are the scattering strength γ and the scaled range X

$$\gamma = k_a^3 E[\mu^2] L_p L_v^2, \quad X = \frac{X_u}{k_a L_v^2}. \quad (3)$$

These two dimensionless scattering parameters are used in Refs. 10 and 6 to characterize random media. In (3), k_a is the acoustic wave number, μ is the index of refraction fluctuations, L_p is an integral range scale of the index of refraction fluctuations, L_v is the transverse correlation scale of the index of refraction fluctuations, and X_u is the unscaled true range in units of length. The product of γ and X , $\Phi^2 = \gamma X$, is the mean-square phase deviation of the wave at X . It can be regarded as the number of scatterers of the wave and is a measure of the randomness of the medium. Larger values of Φ^2 correspond to more severe fluctuations of the medium.

To use the $G\Gamma$ distribution for range estimation, we need an explicit relation between the distributional parameter vector $[a,b,k]^T$ and the environmental variables $[\gamma,X]^T$. Ewart⁵ has obtained a graphical relationship for the mapping between the two parameter sets. Define $\Theta = [a,b,k]^T$ and $\Psi = [\gamma,X]^T$, and let $ggparam(\gamma,X)$ be the mapping between Θ and Ψ . Then

$$\Theta = \begin{bmatrix} a \\ b \\ k \end{bmatrix} = ggparam(\Psi) = \begin{bmatrix} f_a(\gamma,X) \\ f_b(\gamma,X) \\ f_k(\gamma,X) \end{bmatrix}. \quad (4)$$

The Ewart–Oakley formulas¹¹ for $ggparam(\Psi)$, the result of curve fitting the data in Ref. 5, are provided in Appendix A. Figure 1 shows curves of the mapping for several values of γ and X . Both f_a and f_b are increasing functions of the range, and f_k is a decreasing function. As $X \rightarrow 0$, $k \rightarrow \infty$, leading to the lognormal distribution. As $X \rightarrow \infty$, $b \rightarrow 1$ and $k \rightarrow 1$, resulting in the exponential distribution. Therefore, these are consistent with the previous studies. The purpose of this paper is to combine the intensity fluctuation and the

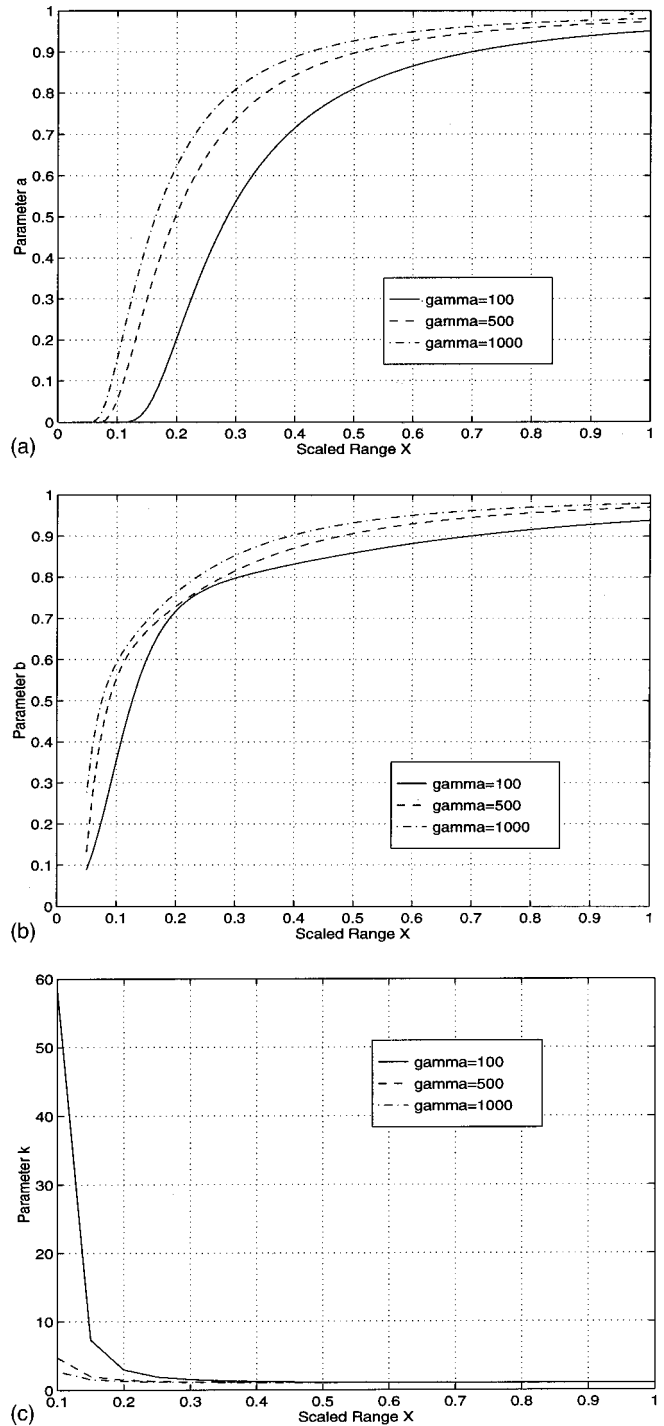


FIG. 1. $[a,b,k]^T = ggparam(\gamma,X)$: (a) Parameter a . (b) Parameter b . (c) Parameter k .

parameter mapping formulas to obtain a maximum likelihood range estimator. We assume complete knowledge of the scattering strength γ , and infer scaled range X .

II. SOURCE LOCALIZATION

A. Maximum likelihood estimation of the range

In the previous section, we have discussed the relation between the two parameter sets. All powers of $G\Gamma$ distributed random variables are $G\Gamma$ distributed with different pa-

parameter values. Hence, the signal amplitude ($A = \sqrt{I}$) is also $G\Gamma$ distributed. Throughout our simulations, we use the amplitude instead of the intensity.

We assume M independent observations of the signal amplitude $\mathbf{A} = [A_1, A_2, \dots, A_M]$. Independent samples may be obtained through spatial or temporal sampling. If the data are obtained temporally, the sampling interval may have to be on the order of minutes in order to assure independence. For spatial sampling down a vertical array, the interval is much more reasonable; samples should be taken no faster than once per vertical correlation interval, L_v . In our work, we use $L_v = 147$ m, which is appropriate for deep water oceans.

Since all the observations are assumed to be independent, the overall likelihood function for \mathbf{A} is the product of the individual likelihood functions for each A_i . We find

$$L(\mathbf{A}; \Theta) = \prod_{i=1}^M L(A_i; \Theta)$$

$$= \left\{ \frac{|b|}{a} \frac{1}{\Gamma(k)} \right\}^M \prod_{i=1}^M \left(\frac{A_i}{a} \right)^{bk-1} \exp \left[- \sum_{i=1}^M \left(\frac{A_i}{a} \right)^b \right]. \quad (5)$$

Using $ggparam(\Psi)$ in (4), we convert $L(\mathbf{A}; \Theta)$, a function of the distributional parameter vector Θ , to a function of the environmental parameter vector Ψ ,

$$L(\mathbf{A}; \Psi) = L(\mathbf{A}; \Theta) \Big|_{\Theta = ggparam(\Psi)}. \quad (6)$$

The estimates of the environmental parameters are obtained by maximizing the likelihood function (6) $[\hat{\gamma}, \hat{X}]^T = \hat{\Psi} = \arg \max_{\Psi} L(\mathbf{A}; \Psi)$. In this paper, we assume prior knowledge of γ , and estimate only the range, $X = \arg \max_X L(\mathbf{A}; X)$. The maximization of $L(\mathbf{A}; X)$ is simpler than maximizing $L(\mathbf{A}; \Psi)$, since it is a one-dimensional function. We can use a search algorithm to carry out the maximization. Next we characterize the estimation performance.

B. Cramer–Rao lower bound

The performance of an estimator is often evaluated by the mean square error (MSE) between the true value and the unbiased estimated value. According to the Cramer–Rao theorem,¹² the Cramer–Rao lower bound (CRLB) provides a theoretical lower bound on MSE, $E[(\hat{\Psi} - \Psi)^2] \geq J^{-1}(\Psi)$, where $J(\Psi)$ is the Fisher information matrix¹² for the physical parameter vector Ψ . Using the chain rule, we derive the Fisher information matrix and the CRLB. When $\gamma = \gamma_0$ is known, the CRLB(X) with M observations is given by

$$\text{CRLB}(X) = \frac{1}{M} \left\{ \left(\frac{d\Theta}{dX} \right)^T J(\Theta) \left(\frac{d\Theta}{dX} \right) \right\}^{-1}, \quad (7)$$

where

$$\frac{d\Theta}{dX} = \frac{ggparam(X)}{dX} = \left[\frac{df_a}{dX}, \frac{df_b}{dX}, \frac{df_k}{dX} \right]^T,$$

and the 3×3 matrix $J(\Theta)$ is the Fisher information matrix for the distributional parameter vector Θ .¹³ The derivation of

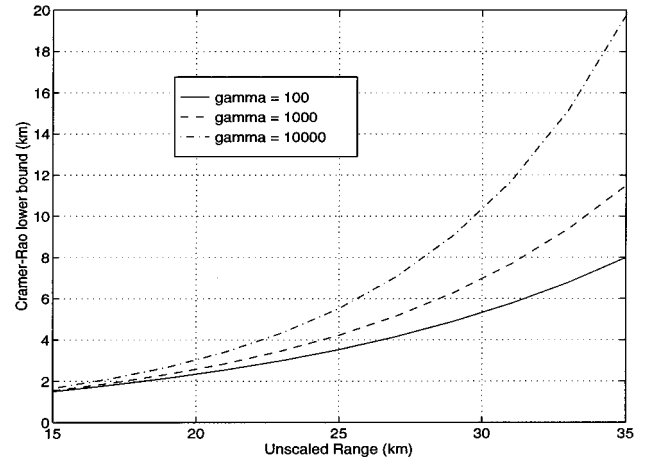


FIG. 2. Cramer–Rao lower bound with $M=25$ samples.

the Fisher information matrix is given in Appendix B. Notice that the Fisher information matrix $J(\Theta)$ enters into $J(X)$ due to $ggparam(\Psi)$, even though Θ itself is not estimated.

Figure 2 shows the CRLB curves for various γ and X . We show the CRLB curves over unscaled range X_u in (3). In the figure, the horizontal axis is the unscaled range X_u , from 15 km to 35 km, and the vertical axis is the square root of the CRLB, the standard error. It provides a confidence interval of the estimation performance. Observe from the figure that when γ is small, the CRLB is small for short range. In other words, the scattering does not have a large effect on short range estimation. However, for ranges greater than 25 km, γ has a strong influence on the performance. Strong scattering leads to a large mean square error, and the CRLB increases rapidly. For a given γ , there is a maximum range at which source localization, based on a limited number of M independent intensity measurements, is useful.

III. SIMULATION RESULTS

To evaluate the estimator performance in small samples, we simulate the observation and processor. In our simulation, we use the numerical parameter values

$$E[\mu^2]L_p = 1.7 \times 10^{-5}, \quad L_v = 147 \text{ m}.$$

Here, $C_0 = 1480$ m/s is the mean sound speed of the model ocean. We consider various (γ, X) and $M = 5, 10,$ and 25 independent samples. Figures 3 and 4 display the root-mean-square error (RMSE) of the range estimates and the square root of the CRLB. For Figs. 3 and 4, $\gamma = 100$ and 1000 are used, respectively. We have tested the method for different range values for different γ , the range values of $0.2X_{\text{focus}} \leq X \leq 0.8X_{\text{focus}}$ have been used. The focus range,⁵ the range at which the variance of intensity takes on its largest value, is estimated from $X_{\text{focus}} = 2.5\gamma^{-0.43}$, and is a monotonic decreasing function of γ . In Fig. 3, the horizontal axis is the scaled range, and the vertical axis is the RMSE. Again, the RMSE can be used to provide a confidence interval for the estimates. Each RMSE is computed with 200 estimates, and $M = 5, 10,$ and 25 samples are used, respectively. The observations are noise free. In the figures, we can see that the MLE is efficient, that is, for each M and range below X_{focus} .

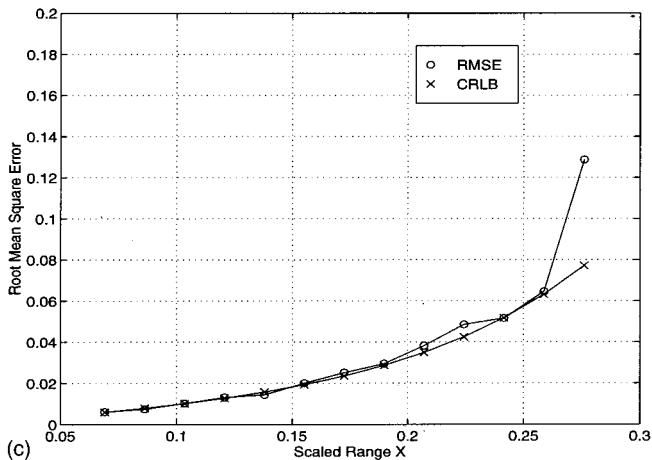
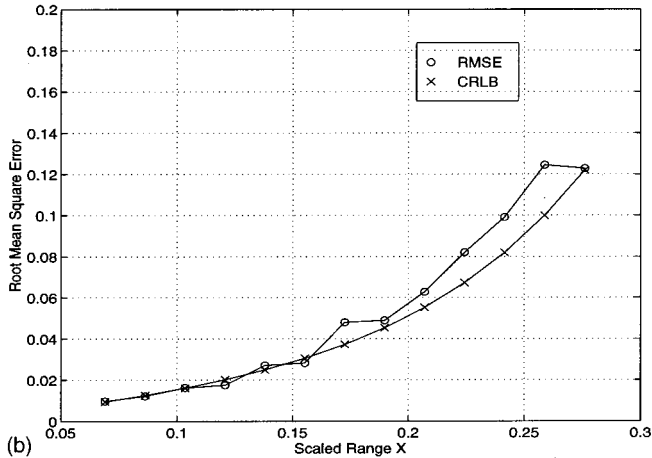
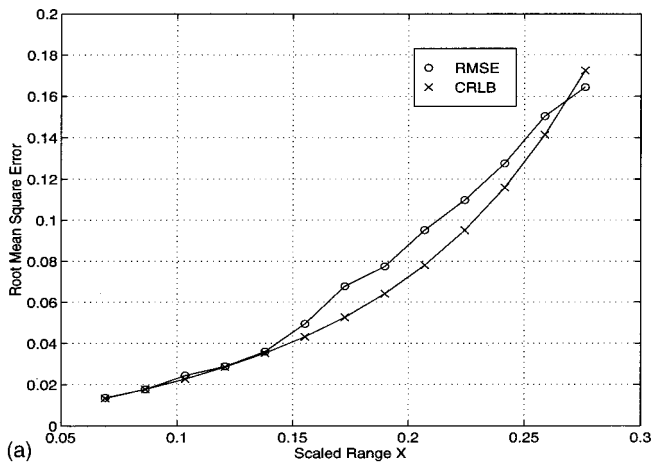


FIG. 3. Comparison of the root mean square error with the Cramer–Rao lower bound for the range estimation ($\gamma=100$, $X_{\text{focus}}=0.3451$): (a) $M=5$ samples. (b) $M=10$ samples. (c) $M=25$ samples.

However, the CRLB depends on the number of observations, and we increase precision as we add independent observations. Here, we analyze the results with $M=25$ samples in detail. In both cases ($\gamma=100$ and 1000), the MLE is efficient for most of the ranges tested here. Beyond that range, the MSE exceeds the CRLB.

For better understanding, we convert Fig. 3(c) and Fig. 4(c), and show in unscaled range X_u . The following two equations are used for the conversion from scaled range and

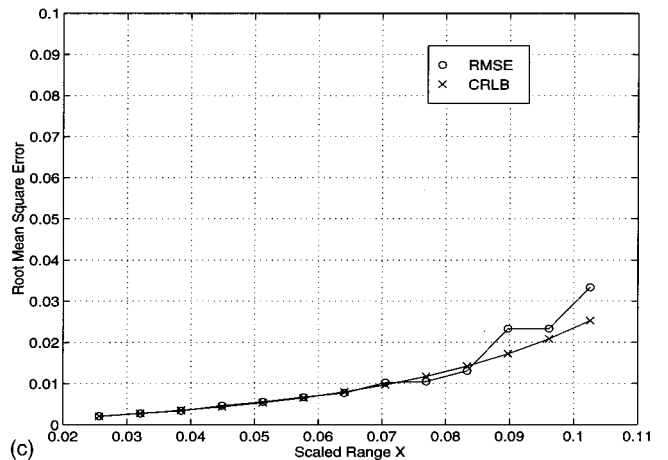
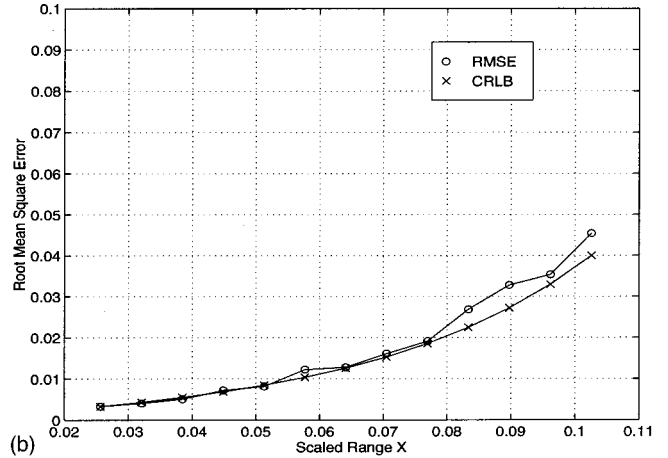
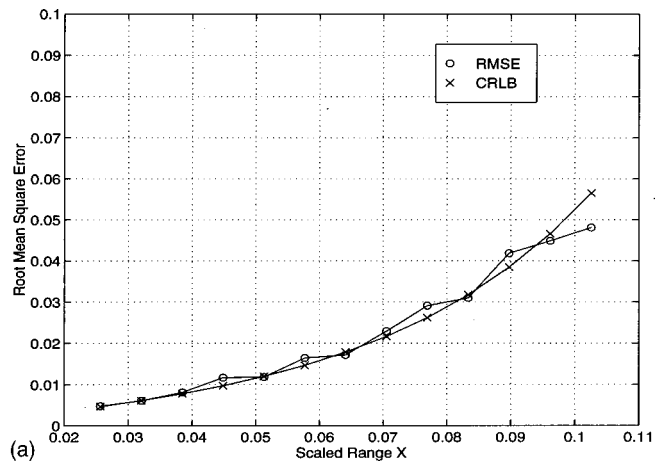


FIG. 4. Comparison of the root mean square error with the Cramer–Rao lower bound for the range estimation ($\gamma=1000$, $X_{\text{focus}}=0.1282$): (a) $M=5$ samples. (b) $M=10$ samples. (c) $M=25$ samples.

scattering strength, to unscaled range and frequency:

$$f_0 = \frac{C_0 \gamma^{1/3}}{2\pi(E[\mu^2]L_p)^{1/3}L_v^{2/3}}, \quad (8)$$

$$X_u = \frac{\gamma^{1/3}XL_v^{4/3}}{(E[\mu^2]L_p)^{1/3}}. \quad (9)$$

Figure 5 shows the results after conversion. The real distance of the tested range is from 10 to 40 km when $\gamma=100$, and

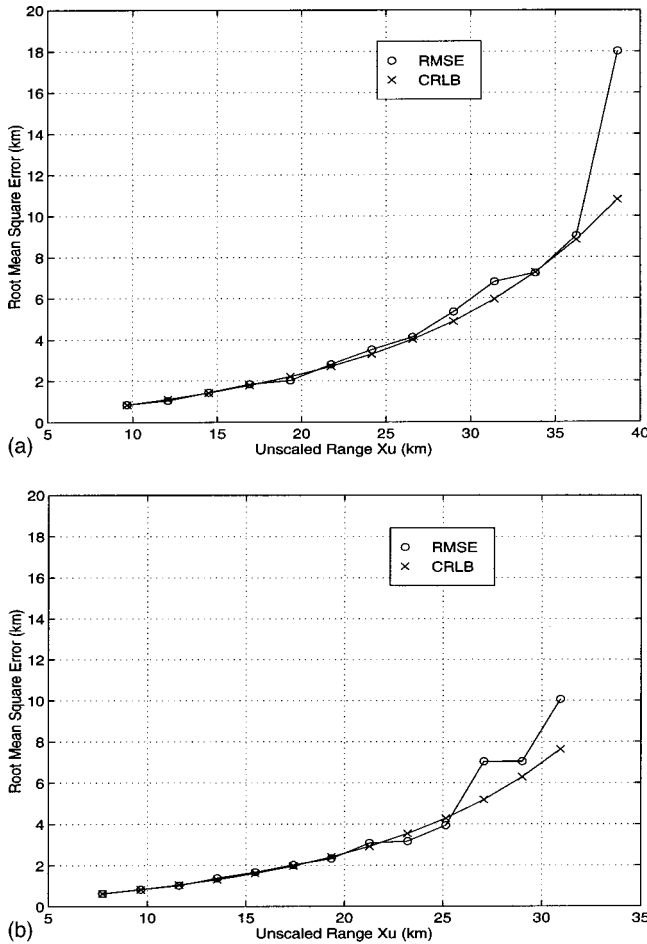


FIG. 5. Comparison of the root mean square error with the Cramer–Rao lower bound for the range estimation with $M=25$ samples (unscaled range). (a) $\gamma=100 \rightarrow f_0=1.53$ kHz, $X_{\text{focus}}=48.3$ km. (b) $\gamma=1000 \rightarrow f_0=3.29$ kHz, $X_{\text{focus}}=38.7$ km.

from 8 to 32 km when $\gamma=1000$. When $X_u=20$ km and $\gamma=100$, the RMSE is about 2 km. If we assume that this is Gaussian distributed, it implies that 95% of the estimates lie within the interval of $[X_u - 4, X_u + 4]$ km. In other words, in this particular case, we can say most estimation error is less than 20%. The confidence interval increases as the range increases. However, the results show that we can obtain a 20% error for the distances up to half of X_{focus} , about 20 km to 25 km.

In our analysis, we have used a confidence interval based on a Gaussian assumption. While this is true asymptotically for maximum likelihood, since the number of observations here is finite, we have checked the validity of this assumption through a histogram and a comparison with the Gaussian distribution. According to Ref. 14, the probability density function of the estimated range \hat{X} approaches Gaussian as more independent samples are used; in fact,

$$\hat{X} \sim \mathcal{N}(E(\hat{X}), \text{Var}(\hat{X})) = \mathcal{N}(X, J^{-1}(X)).$$

The fit is very good so the CRLB is close to the MSE of the estimates, and we can use the square root of the Cramer–Rao lower bound for the confidence interval. The importance of this is that it eliminates the need for extensive simulation to obtain confidence bounds on the estimate.

IV. CONCLUSION

We have proposed a new maximum likelihood estimation method for source localization. An empirically obtained model of the PDF of signals is incorporated into the maximum likelihood method. The simulation results show that signal processing techniques combined with physics can be used in areas where physics can provide a reliable random signal model.

We have derived the Cramer–Rao lower bound for the statistical estimation method. By computing the CRLB, we predict the confidence interval for the estimate. For up to half of the range to the focus, our method yields a relative errors less than 20%. The validity of the confidence interval has been verified by comparing the empirical distribution and the approximate Gaussian distribution. The practical value of this method will depend on our ability to gather enough independent measurements, and on the accuracy of the statistical $G\Gamma$ model.

Our statistical signal processing algorithm relies on intensity only, and ignores coherent phase information even when available. Phase is the basis for matched-field methods, which performs well under matched conditions. In random ocean environments, matched field eventually breaks down. In the intermediate regime, range estimation with intensity only measurements may prove most useful in eliminating the range ambiguities that complicate the interpretation of matched-field correlator plots. For examples of the effects of internal waves on matched field, see Jackson and Ewart.⁴

Future studies may address a lack of prior knowledge of the scattering strength γ , assumed to be completely specified in this study. Two options are fairly clear. First, one can specify γ and suffer a performance degradation in the event of a mismatch. This mismatch loss can be determined by further simulation study. The second and more complicated alternative is to jointly estimate both γ and X . This will lead to an increase in estimation variance and it is not at all clear that the increased complexity of a two-dimensional joint estimation is beneficial. Most likely, small mismatch can be tolerated, but complete uncertainty must be overcome using the joint estimation procedure.

ACKNOWLEDGMENTS

This work was supported by the Office of Naval Research under Contract No. N-00014-92-J-1253 and Contract No. J-00014-90-J-1260. We are pleased to acknowledge many pleasant discussions with the Multi-Discipline Group at APL, University of Washington, in particular Dr. Darrell R. Jackson.

APPENDIX A: $G\Gamma$ PARAMETER MAPPING FORMULA

Parameters (a, b, k) are described in (A3)–(A5) by two functions $Q(\gamma, X)$ and $S(\gamma, X)$. The first is

$$S(\gamma, X) = \frac{1}{2} \left\{ 1 - \frac{1 - \exp\{s_2(s_1 - s_0)\}}{1 + \exp\{s_2(s_1 - s_0)\}} + \frac{4s_m \exp\{s_2(s_1 - s_0)\}}{(1 + \exp\{s_2(s_1 - s_0)\})^2} \right\}, \quad (\text{A1})$$

with

$$s_m = \frac{7}{100} \log \gamma + \frac{3}{5},$$

$$s_0 = \frac{1}{2} \exp\left\{-\frac{2}{3}(\log \gamma + \frac{5}{3})\right\} + \frac{1}{2},$$

$$s_1 = \frac{2}{5} \log \gamma + \log X,$$

$$s_2 = -\exp\left\{-\frac{1}{4}(\log \gamma + 3)\right\} + 2.$$

The second is

$$Q(\gamma, X) = \frac{1}{2} \left\{ 1 - \frac{1 - \exp\{q_2(q_1 - q_0)\}}{1 + \exp\{q_2(q_1 - q_0)\}} + \frac{4q_m \exp\{q_2(q_1 - q_0)\}}{(1 + \exp\{q_2(q_1 - q_0)\})^2} \right\}, \quad (\text{A2})$$

with

$$q_m = \frac{3}{2} \exp\left\{-\frac{9}{50}(\log \gamma - \frac{5}{2})\right\} - \frac{3}{2},$$

$$q_0 = \exp\left\{-\frac{3}{20}(\log \gamma - \frac{9}{2})\right\} - \frac{3}{2},$$

$$q_1 = \frac{1}{3} \log \gamma + \log X,$$

$$q_2 = \begin{cases} 3 \exp\{\frac{1}{4}(\log \gamma - 3)\} + 1, & \text{if } \gamma \leq 10, \\ 17 \exp\{-\frac{1}{2}(\log \gamma + \frac{3}{2})\} + \frac{7}{4}, & \text{if } \gamma > 10. \end{cases}$$

Then the mapping is given by

$$b = f_b(\gamma, X) = \frac{Q(\gamma, X)}{S(\gamma, X)}, \quad (\text{A3})$$

$$k = f_k(\gamma, X) = \frac{1}{Q^2(\gamma, X)}, \quad (\text{A4})$$

$$a = f_a(\gamma, X) = \frac{\Gamma[f_k(\gamma, X)]}{\Gamma[f_k(\gamma, X) + 1/f_b(\gamma, X)]}, \quad (\text{A5})$$

where $\Gamma(x)$ is the gamma function. The mapping is shown graphically in Fig. 1.

APPENDIX B: DERIVATION OF THE CRAMER–RAO LOWER BOUND

Let $F(\Theta)$ be the log-likelihood function for $\Theta = [a \ b \ k]^T$,

$$F(\Theta) = \log L(A_i; \Theta(\gamma, X)). \quad (\text{B1})$$

By the chain rule, its derivative is

$$\begin{aligned} \frac{\partial F(\Theta)}{\partial \gamma} &= \nabla_{\Theta}[F(\Theta)]^T \left(\frac{d\Theta}{d\gamma} \right), \\ \frac{\partial F(\Theta)}{\partial X} &= \nabla_{\Theta}[F(\Theta)]^T \left(\frac{d\Theta}{dX} \right), \end{aligned} \quad (\text{B2})$$

where

$$\nabla_{\Theta}[\cdot] = \left[\frac{\partial}{\partial a}(\cdot) \quad \frac{\partial}{\partial b}(\cdot) \quad \frac{\partial}{\partial k}(\cdot) \right]^T. \quad (\text{B3})$$

Similarly, the second derivative is

$$\begin{aligned} \frac{\partial^2 F(\Theta)}{\partial \gamma^2} &= \frac{\partial}{\partial \gamma} \left\{ \nabla_{\Theta}[F(\Theta)]^T \left(\frac{d\Theta}{d\gamma} \right) \right\} \\ &= \frac{\partial}{\partial \gamma} \left\{ \nabla_{\Theta}[F(\Theta)] \right\}^T \left(\frac{d\Theta}{d\gamma} \right) + (\nabla_{\Theta}[F(\Theta)])^T \left(\frac{\partial^2 \Theta}{\partial \gamma^2} \right) \\ &= \left(\frac{\partial \Theta}{\partial \gamma} \right)^T \nabla_{\Theta}^2[F(\Theta)] \left(\frac{\partial \Theta}{\partial \gamma} \right) + (\nabla_{\Theta}[F(\Theta)])^T \left(\frac{\partial^2 \Theta}{\partial \gamma^2} \right), \end{aligned} \quad (\text{B4})$$

$$\begin{aligned} \frac{\partial^2 F(\Theta)}{\partial \gamma \partial X} &= \left(\frac{\partial \Theta}{\partial \gamma} \right)^T \nabla_{\Theta}^2[F(\Theta)] \left(\frac{\partial \Theta}{\partial X} \right) \\ &\quad + (\nabla_{\Theta}[F(\Theta)])^T \left(\frac{\partial^2 \Theta}{\partial \gamma \partial X} \right), \end{aligned} \quad (\text{B5})$$

$$\frac{\partial^2 F(\Theta)}{\partial X \partial \gamma} = \frac{\partial^2 F(\Theta)}{\partial \gamma \partial X}, \quad (\text{B6})$$

$$\begin{aligned} \frac{\partial^2 F(\Theta)}{\partial X^2} &= \left(\frac{\partial \Theta}{\partial X} \right)^T \nabla_{\Theta}^2[F(\Theta)] \left(\frac{\partial \Theta}{\partial X} \right) \\ &\quad + (\nabla_{\Theta}[F(\Theta)])^T \left(\frac{\partial^2 \Theta}{\partial X^2} \right). \end{aligned} \quad (\text{B7})$$

By the definition in (B3),

$$\nabla_{\Theta}^2[\cdot] = \begin{bmatrix} \frac{\partial^2}{\partial a^2}(\cdot) & \frac{\partial^2}{\partial a \partial b}(\cdot) & \frac{\partial^2}{\partial a \partial k}(\cdot) \\ \frac{\partial^2}{\partial b \partial a}(\cdot) & \frac{\partial^2}{\partial b^2}(\cdot) & \frac{\partial^2}{\partial b \partial k}(\cdot) \\ \frac{\partial^2}{\partial k \partial a}(\cdot) & \frac{\partial^2}{\partial k \partial b}(\cdot) & \frac{\partial^2}{\partial k^2}(\cdot) \end{bmatrix}. \quad (\text{B8})$$

The Fisher information matrix for γ and X is

$$\begin{aligned} J(\gamma, X) &= -E \begin{bmatrix} \frac{\partial^2 F(\Theta)}{\partial \gamma^2} & \frac{\partial^2 F(\Theta)}{\partial \gamma \partial X} \\ \frac{\partial^2 F(\Theta)}{\partial X \partial \gamma} & \frac{\partial^2 F(\Theta)}{\partial X^2} \end{bmatrix} = - \begin{bmatrix} \left(\frac{\partial \Theta}{\partial \gamma} \right)^T \\ \left(\frac{\partial \Theta}{\partial X} \right)^T \end{bmatrix} E \{ \nabla_{\Theta}^2[F(\Theta)] \} \begin{bmatrix} \left(\frac{\partial \Theta}{\partial \gamma} \right) \\ \left(\frac{\partial \Theta}{\partial X} \right) \end{bmatrix} \\ &\quad + \begin{bmatrix} -E \{ \nabla_{\Theta}[F(\Theta)] \} \left(\frac{\partial^2 \Theta}{\partial \gamma^2} \right) & -E \{ \nabla_{\Theta}[F(\Theta)] \} \left(\frac{\partial^2 \Theta}{\partial \gamma \partial X} \right) \\ -E \{ \nabla_{\Theta}[F(\Theta)] \} \left(\frac{\partial^2 \Theta}{\partial X \partial \gamma} \right) & -E \{ \nabla_{\Theta}[F(\Theta)] \} \left(\frac{\partial^2 \Theta}{\partial X^2} \right) \end{bmatrix}. \end{aligned} \quad (\text{B9})$$

In (B9), $-E \{ \nabla_{\Theta}^2[F(\Theta)] \}$ in the first term is the Fisher information matrix for the parameter Θ , or $-E \{ \nabla_{\Theta}^2[F(\Theta)] \} = J(\Theta)$. On the other hand, $-E \{ \nabla_{\Theta}[F(\Theta)] \}$ in the second term is the mean *score function*,¹² and it is known to be zero in

any case, $-E\{\nabla_{\theta}[F(\Theta)]\}=\mathbf{0}$. Therefore, the second term disappears, and the Fisher information matrix $J(\gamma, X)$ becomes

$$J(\gamma, X) = \begin{bmatrix} J_{11}(\gamma, X) & J_{12}(\gamma, X) \\ J_{21}(\gamma, X) & J_{22}(\gamma, X) \end{bmatrix} = \begin{bmatrix} \left(\frac{\partial \Theta}{\partial \gamma}\right)^T J(\Theta) \left(\frac{\partial \Theta}{\partial \gamma}\right) & \left(\frac{\partial \Theta}{\partial \gamma}\right)^T J(\Theta) \left(\frac{\partial \Theta}{\partial X}\right) \\ \left(\frac{\partial \Theta}{\partial X}\right)^T J(\Theta) \left(\frac{\partial \Theta}{\partial \gamma}\right) & \left(\frac{\partial \Theta}{\partial X}\right)^T J(\Theta) \left(\frac{\partial \Theta}{\partial X}\right) \end{bmatrix}, \quad (\text{B10})$$

where the 3×3 matrix $J(\Theta)$ is known to be¹³

$$J(\Theta) = \begin{bmatrix} \frac{b^2}{a^2} k & -\frac{k}{a} \frac{\Gamma'(k+1)}{\Gamma(k+1)} & \frac{b}{a} \\ -\frac{k}{a} \frac{\Gamma'(k+1)}{\Gamma(k+1)} & \frac{1}{b^2} \left[1 + \frac{\Gamma''(k+1)}{\Gamma(k+1)} \right] & -\frac{1}{b} \frac{\Gamma'(k)}{\Gamma(k)} \\ \frac{b}{a} & \frac{1}{b} \frac{\Gamma'(k)}{\Gamma(k)} & \frac{\Gamma''(k)\Gamma(k) - (\Gamma'(k))^2}{\Gamma^2(k)} \end{bmatrix}. \quad (\text{B11})$$

If both γ and X are unknown, the Cramer–Rao lower bounds with M independent samples are CRLB (γ) $= M^{-1}H_{11}(\gamma, X)$ and CRLB (X) $= M^{-1}H_{22}(\gamma, X)$ where

$$H(\gamma, X) = \begin{bmatrix} H_{11}(\gamma, X) & H_{12}(\gamma, X) \\ H_{21}(\gamma, X) & H_{22}(\gamma, X) \end{bmatrix} = \begin{bmatrix} J_{11}(\gamma, X) & J_{12}(\gamma, X) \\ J_{21}(\gamma, X) & J_{22}(\gamma, X) \end{bmatrix}^{-1}. \quad (\text{B12})$$

If $\gamma = \gamma_0$ is known, only J_{22} exists, and the Fisher information matrix for X becomes

$$J(X) = J_{22}(\gamma_0, X) = \left(\frac{\partial \Theta}{\partial X}\right)^T J(\Theta) \left(\frac{\partial \Theta}{\partial X}\right). \quad (\text{B13})$$

¹A. B. Baggeroer, W. A. Kuperman, and H. Schmidt, ‘‘Matched field processing: Source localization in correlated noise as an optimum parameter estimation problem,’’ *J. Acoust. Soc. Am.* **83**, 571–587 (1990).

²J. L. Krolik, ‘‘Matched-field minimum variance beamforming in a random ocean channel,’’ *J. Acoust. Soc. Am.* **92**, 1408–1419 (1992).

³J. C. Preisig, ‘‘Robust maximum energy adaptive matched field processing,’’ *IEEE Trans. Signal Process.* **42**(7), 1585–1593 (1994).

⁴D. R. Jackson and T. E. Ewart, ‘‘The effect of internal waves on matched-field processing,’’ *J. Acoust. Soc. Am.* **96**, 2945–2955 (1994).

⁵T. E. Ewart, ‘‘A model of the intensity probability distribution for wave propagation in random media,’’ *J. Acoust. Soc. Am.* **86**, 1490–1498 (1989).

⁶B. J. Uscinski, *The Elements of Wave Propagation in Random Media* (McGraw-Hill, New York, 1977).

⁷T. E. Ewart and D. B. Percival, ‘‘Forward scattered waves in random media—The probability distribution of intensity,’’ *J. Acoust. Soc. Am.* **80**, 1745–1753 (1986).

⁸C. Macaskill and T. E. Ewart, ‘‘The probability distribution of intensity for acoustic propagation in a randomly varying ocean,’’ *J. Acoust. Soc. Am.* **76**, 1466–1473 (1984).

⁹J. A. Ritcey, S. D. Gordon, and T. E. Ewart, ‘‘A probability distribution in the complex field of waves propagating in random media,’’ *J. Acoust. Soc. Am.* **100**, 237–244 (1996).

¹⁰Akira Ishimaru, *Wave Propagation and Scattering in Random Media* (Academic, New York, 1978), Vol. 2.

¹¹T. E. Ewart and P. Oakley (unpublished manuscript, 1994).

¹²L. L. Scharf, *Statistical Signal Processing: Detection, Estimation, and Time Series Analysis* (Addison-Wesley, Reading, MA, 1991).

¹³A. C. Cohen and B. J. Whitten, *Parameter Estimation in Reliability and Life Span Models* (Marcel Dekker, New York, 1988).

¹⁴E. L. Lehmann, *Theory of Point Estimation* (Wiley, New York, 1983).

Measurements and model of the cat middle ear: Evidence of tympanic membrane acoustic delay

Sunil Puria^{a)}

Eaton-Peabody Laboratory of Auditory Physiology, Massachusetts Eye and Ear Infirmary, 243 Charles Street, Boston, Massachusetts 02114 and Department of Otology and Laryngology, Harvard Medical School, Boston, Massachusetts 02114 and The Research Laboratory of Electronics, Massachusetts Institute of Technology, 77 Massachusetts Avenue, Cambridge, Massachusetts 02139

Jont B. Allen

AT&T Labs—Research, 180 Park Avenue, P.O. Box 971, Florham Park, New Jersey 07932-0971

(Received 16 February 1998; revised 17 August 1998; accepted 29 August 1998)

In order to better understand the mechanics of tympanic membrane (TM) transduction at frequencies above a few kHz, the middle-ear (ME) impedance measured near the tympanic membrane is studied for three anesthetized cat ears after widely opening the ME cavities (MEC). Three conditions were measured: intact ossicles, drained cochlea, and disarticulated stapes. When the cochlear load is removed from the ME by disarticulating the stapes, the impedance magnitude varies by about ± 25 dB in the 5- to 30-kHz range, with peaks and valleys at intervals of ≈ 5 kHz. These measurements suggest middle-ear standing waves. It is argued that these standing waves reside in the TM. In contrast, the magnitude of the impedance for the intact case varies by less than ± 10 dB, indicating that for this case the standing waves are damped by the cochlear load. Since the measurements were made within 2 mm of the TM, standing waves in the ear canal can be ruled out at these frequencies. Although the ME cavities were widely opened, reflections from the ME cavity walls or surrounding structures could conceivably result in standing waves. However, this possibility is ruled out by model predictions showing that such large standing waves in the ME cavity space would also be present in the intact case, in disagreement with the observation that standing waves are damped by cochlear loading. As a first-order approximation, the standing waves are modeled by representing the TM as a lossless transmission line with a frequency-independent delay of 36 μ s. The delay was estimated by converting the impedance data to reflectance and analyzing the reflectance group delay. In the model the ossicles are represented as lumped-parameter elements. In contrast to previous models, the distributed and lumped parameter model of the ME is consistent with the measured impedance for all three conditions in the 200-Hz to 30-kHz region. Also in contrast with previous models, the ear-canal impedance is not mass dominated for frequencies above a few kHz. Finally, the present model is shown to be consistent, at high frequencies, with widely accepted transfer functions between (i) the stapes displacement and ear-canal pressure, (ii) the vestibule pressure and ear-canal pressure, and (iii) the umbo velocity and ear-canal volume velocity. An improved understanding of TM mechanics is important to improve hearing aid transducer design, ear-plug design, as well as otoacoustic emissions research. © 1998 Acoustical Society of America. [S0001-4966(98)02812-4]

PACS numbers: 43.64.Bt, 43.64.Ha, 43.64.Jb [BLM]

INTRODUCTION

The tympanic membrane (TM) transduces the ear-canal sound pressure into a mechanical motion of the ossicles. The goal of the research reported in this paper is to improve our understanding of the function of the TM and other middle-ear (ME) structures. Consider the following: (1) In theory, mass inertia of the ossicles should result in an increase in ME input impedance as frequency increases (Shaw and Stinson, 1981), and (2) surface displacement patterns of the cat TM suggest that above a few kHz the TM surface has modes (i.e., standing waves) (Khanna and Tonndorf, 1972). In both of these cases the coupling of the ear-canal sound pressure to the ossicles will effectively decrease as stimulus frequency

increases above a few kHz. The basic question asked by this paper is: *How does the TM couple sound into the cochlea above a few kHz?*

Figure 1 shows the ME input impedance $Z_{ec}(\omega)$ measured close to the TM with middle-ear cavities (MECs) wide open, for three different conditions: (I) intact middle and inner ear, (II) drained cochlea, and (III) disarticulated stapes. In the disarticulated stapes and drained-cochlea cases, the impedance magnitude periodically increases and decreases by as much as ± 25 dB [Fig. 1(C) and (E)], indicative of low-loss standing waves. In the intact case these standing waves are damped by the cochlea [Fig. 1(A)]. The figure shows that the standing waves are significantly damped in all three ears measured. These results suggest that the ME supports the propagation of low-loss traveling waves, and that the damping of these waves is provided by cochlear loading.

^{a)}Electronic mail: purial@leland.Stanford.edu

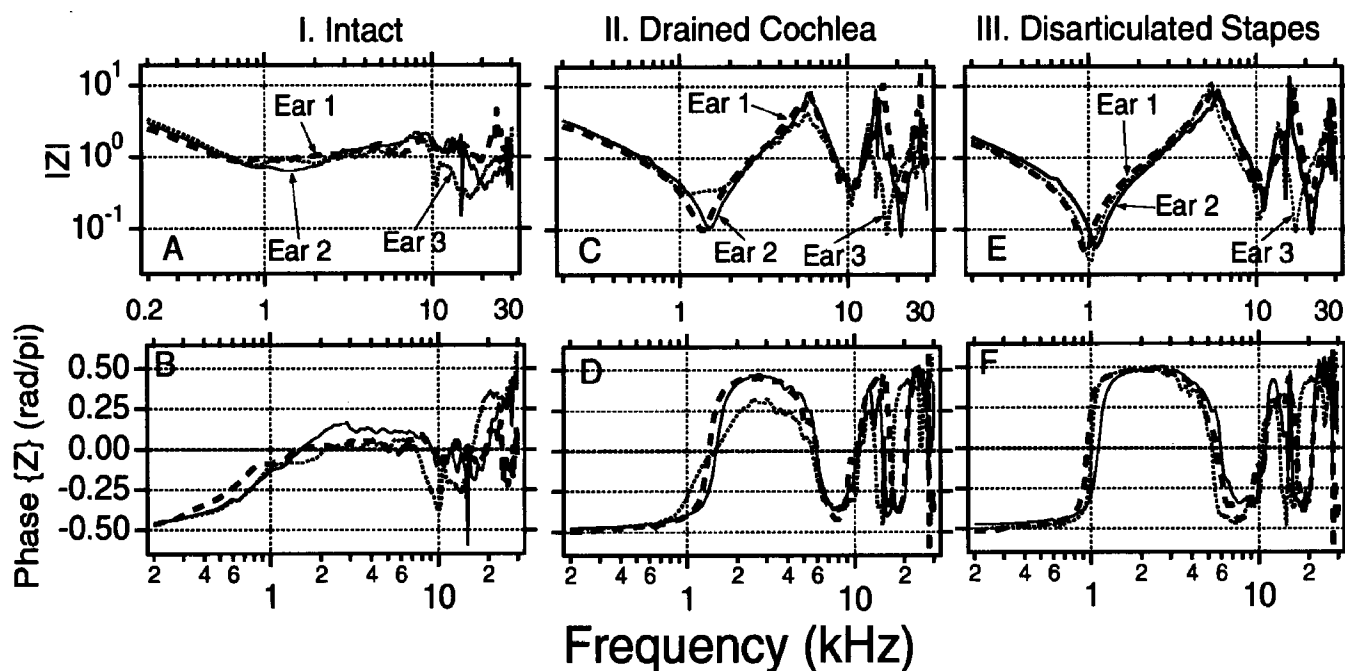


FIG. 1. The middle-ear (ME) input impedance was measured by placing a calibrated sound-delivery tube and microphone assembly within 2 mm of the TM surface with the bulla wall wide open and the bony septum removed. Measurements in three cat ears, from 0.2 to 30 kHz, are shown. Impedance measurements of Z_i , Z_{dc} , and Z_{ds} were made in the following order: (I) intact: ossicles and cochlea in their normal state (Z_i), (II) drained cochlea: scala-vestibule and scala-tympani perilymph removed (Z_{dc}), and (III) disarticulated stapes: cut stapes away from incus at the incudo-stapedial joint (Z_{ds}). The top panels (A,C,E) show impedance magnitudes, normalized by the characteristic impedance of the transducer sound-delivery tube $Z_{ot}=400$ ohms (dyne-s/cm⁵). The bottom panels (B,D,F) show phase angles of the impedance in rad/ π (e.g., ± 0.5 rad/ $\pi = \pm 90^\circ$). In all figures, the line types of the unlabeled panels are identical to the line types of the labeled panels (e.g., the solid line corresponds to ear 2 in panels B and A).

Thus a primary problem posed in this paper is how do we understand these measurements? The answer will lead to a better understanding of the TM with respect to high-frequency ME sound transmission.

To study the question of ME sound transmission, ME input impedance was transformed to reflectance magnitude and reflectance group delay. For the disarticulated stapes and drained cochlea cases, the mean group delay is approximately 100 μ s in the 3–20-kHz frequency region. A delay of 100 μ s corresponds to the round-trip delay in a 1.7-cm-long air-filled tube. Given that measurements were made within approximately 0.2 cm of the surface of the TM, standing waves in the ear canal can be ruled out for frequencies below 30 kHz. It is unlikely that there are standing waves (i.e., large delays) in the ossicles. Thus a secondary question posed in this paper is: *How can we account for the large delays measured in the middle ear?* Since the cochlea is removed by disarticulating the stapes, these 100- μ s delays cannot originate from the inner ear.

Attempts to understand the data of the type shown in Fig. 1 with standard lumped parameter model representations for the TM (Zwislocki, 1962; Møller, 1965; Matthews, 1983) have been successful for frequencies below 6–8 kHz, but fail at the higher frequencies (Puria, 1991b). Existing ME models (Flanagan, 1962; Zwislocki, 1962, 1963; Peake and Guinan, 1967; Nuttall, 1974; Shaw and Stinson, 1981; Kringelbotn, 1988; Shera and Zweig, 1991; Goode *et al.*, 1994) are also limited at frequencies above approximately 8 kHz (Rabbitt and Holmes, 1986, 1988). Finite-element models have been previously proposed to circumvent this problem

(Funnell *et al.*, 1987). In the present work we explore a more parsimonious solution by using a distributed parameter (i.e., transmission line) model.

Two likely hypotheses for the measurements shown in Fig. 1 are presently explored: (1) standing waves in the tympanic membrane, or (2) standing waves in the open MEC space. Mathematical models constrained by measurements are used to explore both hypotheses. We conclude that the MEC model is inconsistent with measurements, and thus can be ruled out.

It follows that the physical mechanism for the observed 100- μ s delay is TM transverse wave propagation. We show (i) to a first-order approximation the TM can be modeled as a transmission line with a frequency-independent delay, and (ii) the TM model, along with a lumped-parameter representation of the ossicles, is consistent with both the ME input impedance data shown in Fig. 1, as well as with numerous physiological measurements of the cat ME reported in the literature. Model calculations, valid to at least 25 kHz, are for a single set of parameters. A preliminary version of this paper was previously presented (Puria and Allen, 1996).

I. METHODS

A. Preparation

Methods of animal preparations have been previously described (Allen, 1983). Briefly, the bulla cavity was widely opened and the bony septum that separates the bulla cavity from the tympanic cavity removed (Fig. 2). The ear canal was surgically removed and a calibrated receiver and probe-

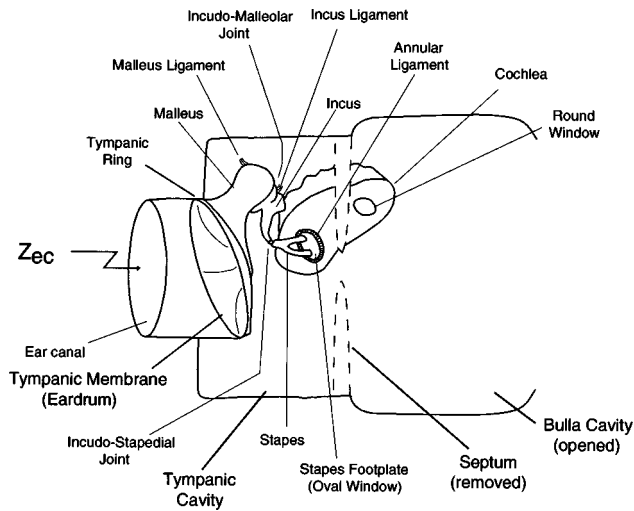


FIG. 2. Simplified cat ME anatomy. The bulla cavity was widely opened and the septum removed (dashed line). The ear-canal impedance was measured by placing a calibrated microphone and sound delivery system in the ear canal close to the TM. The impedance was measured for the intact ossicles, after draining the cochlea and after disrupting the ossicular chain by cutting the incudo-stapedial joint. The malleus and incus are attached to the walls of MEC space by the malleus and incus ligaments.

tube microphone assembly was put in place near the bony end of the ear canal (the microphone probe tube was typically less than 2 mm from the surface of TM).

Following the ear preparation, the ME input impedance and cochlear microphonic (CM) were measured. The acoustic impedance calibration of the sound delivery system has been previously described (see Sec. I B). The sound delivery system was always calibrated at the start of each impedance measurement session. If either the CM or the ME impedance showed any indication of a bulla resonance, the bulla was opened more widely and the impedance remeasured until there were no indications of a ME cavity resonance. Once the experimental series of cochlear and ME modifications was started, no further modifications to the MECs were made.

B. Measurements

The definition of impedance is based on the assumption that the ear-canal pressure, in the measurement plane, is independent of spatial location; in other words, higher-order spatial modes are assumed to be negligible. Complex wave motions on the TM result in higher-order evanescent modes near the eardrum which complicate measurements of impedance. Theoretical arguments suggest that for distances greater than 0.15 cm, and for frequencies below 25–30 kHz,

TABLE I. Constants presently assumed and shown below are valid for $27 \pm 10^\circ\text{C}$: ρ_a is the mass density of air; c_a is the speed of sound in air, A_t is the area of the sound delivery tube, and $Z_{ot} = \rho_a c_a / A_t$ is the characteristic impedance of the sound delivery tube.

ρ_a	1.177×10^{-3}	g/cm^3
c_a	3.472×10^4	cm/s
A_t	0.102	cm^2
Z_{ot}	400	dyn-s/cm^5

the effect of these evanescent modes on the ear-canal pressure is insignificant (Lynch, 1981, pp. 146–148; Stinson, 1994).

Ear-canal pressure measurements were made for frequencies up to $33\frac{1}{3}$ kHz with a frequency resolution of 65.1 Hz and 512 frequency points (the response at 0 Hz was not measured) using the SYSid™ (Puria and Allen, 1992; Puria *et al.*, 1993) measurement and analysis system (SYSid Labs, Berkeley, CA). A 1024-point buffer with a chirp stimulus sampled at a rate of $15 \mu\text{s}$ was used. As described elsewhere (Allen, 1983), cochlear microphonic measurements were also made on these ears using tones.

The four-load impedance measurement technique was used. This method was developed by Allen (1986), and has been previously described (Allen, 1986; Puria, 1991b; Keefe *et al.*, 1992; Voss and Allen, 1994). Briefly, the Thévenin source impedance $Z_0(\omega)$ and source pressure $P_0(\omega)$ of the sound delivery system are estimated by measuring the probe microphone pressure responses to four known acoustic loads.¹ The ME acoustic impedance may then be calculated directly from measured ear-canal pressure and the Thévenin source parameters $Z_0(\omega)$ and $P_0(\omega)$. Throughout this paper all Thévenin and ME input impedance measurements have been normalized by the characteristic impedance $Z_{ot} = \rho_a c_a / A_t = 400$ (cgs-ohms) of the sound delivery tube (see Table I).

C. Impedance minimum-phase test

Impedance measurement techniques require that Thévenin (or Norton) equivalent parameters for the source do not change from the time of calibration to the time of measurements. Measurement errors otherwise occur. The source characteristics will change, for example, if the temperature changes. A procedure to check for possible inconsistencies in impedance measurements, by checking the ratio of the Thévenin source pressure to the ear-canal pressure $H(\omega) \equiv P_0(\omega)/P_{ec}(\omega)$ for minimum-phase behavior, was outlined by Voss and Allen [1994, Eqs. (15)–(17)]. $H(\omega)$ for the data reported here was checked for their minimum-phase property. It was found that $H(\omega)$ had an all-pass delay of 2–4 μs , and thus was not minimum phase. This all-pass delay corresponds to less than $\frac{1}{3}$ of a Nyquist sample at the 15- μs Nyquist rate, and this delay error can be accounted for by the difference in temperature of the sound delivery system at the time of calibration (room temperature) and temperature of the sound delivery system at measurement time (animal body temperature). All the data shown here have been corrected by subtracting a delay of 2–4 μs such that the pressure ratio $H(\omega)$ is minimum phase for frequencies below about 25 kHz. This guarantees that the ear-canal impedance is minimum phase.

D. Middle-ear modifications

The ME input impedance was measured in approximately 27 animals, but the complete set of measurements,

- (I) the intact ear— $Z_i(\omega)$,
- (II) perilymph removed—“drained cochlea”
 $Z_{dc}(\omega)$, and
- (III) “disarticulated stapes”— $Z_{ds}(\omega)$ by cutting
at the incudo-stapedial joint,

was obtained on 3 ears (two animals), reported here.²

All of these measurements are with the MEC wide open, as described in Sec. I A. The cochlea was drained by removing the round-window membrane, and wicking out the scala-tympani perilymph. The basilar membrane was next removed, allowing the scala-vestibule perilymph to drain via the wick. The disarticulated stapes case was measured after cutting at the incudo-stapedial joint. Several intermediate impedance measurements were made, but are not reported here (Allen, 1986). All surgical modifications and measurements were performed by the second author, following the technique and guidance of J. Tonndorf (Tonndorf and Pastaci, 1986).

II. FROM IMPEDANCE TO REFLECTANCE

A. Impedance

Normalized impedance measurements from ears 1–3, shown in Fig. 1, have a similar pattern for any given condition. For frequencies below about 800 Hz the impedance is stiffness dominated for all three cases, and the magnitude is larger for the drained cochlea [panel (C)] than for the disarticulated stapes case [panel (E)]. This difference in stiffness represents the additional stiffness of the annular ligament. Note also that the phase for the disarticulated case is more bimodal (i.e., reactive) than that of the drained case due to the removal of annular ligament damping.

The drained cochlea [panels (C) and (D)] and disarticulated stapes [panels (E) and (F)] cases clearly show standing waves (i.e., high-Q low-loss modes). For example, panel (C) near 6 kHz shows a local maximum in the impedance magnitude while the phase data in panel (D) shows a corresponding phase shift from +0.5 to –0.5 rad/ π . Given the ± 25 dB variations in impedance magnitude (the peaks and valleys) we may conclude that the ME damping is quite small. Since the stapes, annular ligament, and cochlea are not present for the disarticulated case, it is clear that these structures are not responsible for the standing waves. What is surprising about these figures, besides the low damping of the isolated ME, is the large ME delays that must be present to produce these standing waves with such low resonant frequencies.

Panels (A) and (B) show that the cochlear load dampens the standing waves because of the energy absorbed by the cochlea (Møller, 1965; Lynch, 1981; Tonndorf and Pastaci, 1986). This is consistent with how we might imagine the ME and cochlea might function to have a reasonable efficiency.

Since the magnitudes of the ME impedances for the three ears have multiple maxima and minima that are not exactly at the same frequency, there is no simple way to shift the impedances so that all the maxima and minima are aligned. Averaging these data would smear these peaks and valleys, which would result in a loss of data features. Rather

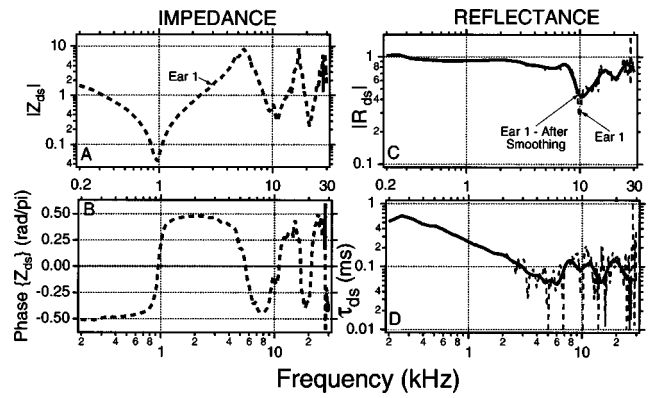


FIG. 3. Disarticulated stapes for ear 1. (A) Normalized impedance magnitude, and (B) phase in rad/ π . (C) Reflectance magnitude before and after smoothing. (D) Reflectance group delay before and after smoothing the reflectance phase and then using Eq. (4) to calculate the group delay. For both magnitude and phase, recursive-exponential smoothing filters were used (see text).

than average data, we have used ear 1 as a prototypical example for modeling purposes.³ The best middle ears, defined as having the smoothest impedance frequency responses, the widest frequency bandwidth, and the largest cochlear microphonic to drum pressure ratios over frequency, correspond to clean transparent ear drums.

B. Reflectance

The ME impedance measured near the TM, normalized by the characteristic impedance of the transducer sound-delivery tube (Z_{ot}), is defined as $Z_{me}(\omega)$. This normalized impedance may be expressed in terms of the pressure reflectance (Puria and Allen, 1989; Puria, 1991a, b; Keefe *et al.*, 1992, 1993; Voss and Allen, 1994)

$$R(\omega) = \frac{Z_{me}(\omega) - 1}{Z_{me}(\omega) + 1}, \quad (1)$$

where

$$R(\omega) \equiv \frac{P_-}{P_+} \quad (2)$$

$$= |R(\omega)| e^{j\angle R(\omega)}. \quad (3)$$

In Eq. (2) the pressure reflectance is defined as the transfer function between the retrograde $P_-(\omega)$ and incident $P_+(\omega)$ pressure waves. In Eq. (3) the reflectance is expressed in polar coordinates in terms of a magnitude $|R|$ and phase angle $\angle R$.

The group delay of the reflectance

$$\tau(\omega) \equiv - \frac{\partial \angle R(\omega)}{\partial \omega} \quad (4)$$

is a measure of the delay between the retrograde pressure wave $P_-(\omega)$ and the incident pressure wave $P_+(\omega)$ (Puria and Allen, 1989; Puria, 1991a, b; Voss and Allen, 1994). In other words, group delay is a measure of the latency of the reflected sound relative to the incident sound; this interpretation is restricted to frequency regions where the derivative

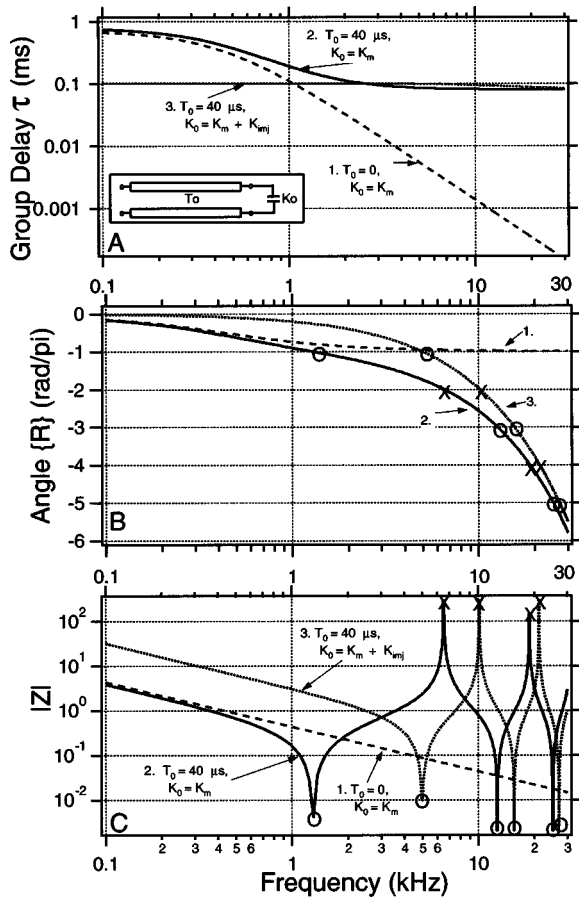


FIG. 4. Three examples of a simple middle-ear model consisting of a lossless transmission line having a frequency-independent delay T_0 , terminated by a stiffness K_0 , as defined in the insert. This model illustrates the point that the frequency location of the maxima and minima (poles and zeros) of the impedance depends mainly on the group delay of the reflectance. The three examples are: (1) $T_0 = 0$ (e.g., no transmission line), $K_0 = K_m = 1.1 \times 10^6$ (dyn/cm⁵), (2) $T_0 = 40 \mu\text{s}$, $K_0 = K_m$, and (3) $T_0 = 40 \mu\text{s}$, $K_0 = K_m + K_{mi} = 3.81 \times 10^7$ (dyn/cm⁵). (A) The group delay of the reflectance for the three cases. (B) The phase of the reflectance is computed from the integral of the group delay [Eq. (10)]. (C) The \circ 's indicate location of zeros while \times 's indicate location of poles of the impedance. The frequency of the zeros is when the reflectance phase is at odd multiples of π , while the frequency of the poles is at even multiples of π . As the amount of delay increases, the accumulated reflectance phase increases and the pole-zero frequency spacings of the impedance decrease.

of $|R(\omega)|$ with respect to frequency is small (Papoulis, 1962, p. 135). Given the above view point, reflectance is a measure that is conceptually related to transient evoked otoacoustic emissions. In the present case the reflectance is derived from measurements using chirps, rather than clicks.

In Fig. 3, panels (A) and (B) show the impedance for the disarticulated stapes case of ear 1, panel (C) shows the corresponding reflectance magnitude, while panel (D) shows the reflectance group delay (dashed lines). The reflectance magnitude $|R(\omega)|$ [Fig. 3(C)] is typically greater than 0.4 for all frequencies measured and is greater than 0.8 for frequencies below 8 kHz. The group-delay data for the disarticulated stapes case [Fig. 3(D)] decreases from about 0.5 to 0.1 ms as frequency increases from 0.2 to 3 kHz. At frequencies above 3 kHz the group delay on the average stays near 0.1 ms. Although there are trends for frequencies above 3 kHz, the

group delay shows greatly increased variability (dashed lines).

1. Smoothing of reflectance data

To better analyze the trends in the reflectance group delay, the phase of the reflectance was first smoothed using recursive-exponential filters (Shera and Zweig, 1993, Appendix). These filters avoid prolonged ringing in the frequency domain while minimizing splatter in the time domain.⁴ Equation (4) was then used to compute the group delay. The reflectance magnitude was also smoothed with the same recursive-exponential filters. It is evident from the group delay after smoothing [Fig. 3(D), solid line] that there are systematic variations in the delay. These variations are related to the variability in reflectance magnitude above 3 kHz which is likely due to radiation from the back side of the TM (see the Appendix). Below approximately 2 kHz, the delay estimates have a small variance. Group delay for the drained inner-ear and intact cases will be discussed after the full ME model is presented.

III. A SIMPLE MIDDLE-EAR MODEL: A PRELUDE

In this section we present a greatly simplified ME model, shown in the insert of Fig. 4(A). With this lossless and massless model, consisting of a TM as a transmission line with delay T_0 terminated by stiffness K_0 , we can account for much of the observed ear-canal reflectance group delay $\tau(\omega)$ for the modified ME conditions for a wide range of frequencies. We then proceed to show how the ME impedance is related to the group delay using Eqs. (1) and (4), along with the lossless assumption $|R(\omega)| = 1$.

A. Modeling the group delay $\tau(\omega)$

It is widely accepted that the ear-canal impedance is stiffness dominated below a few kHz (Onchi, 1961; Zwislocki, 1962; Møller, 1965). By substituting the stiffness-dominated TM impedance $K_{tm}/j\omega$ into Eq. (1), and using the definition of $\tau(\omega)$ given by Eq. (4), Voss and Allen (1994) found a formula for the reflectance group delay. In their formulation, a transmission line representing the ear canal is terminated by a compliance representing the TM stiffness K_{tm} . Generalizing the Voss and Allen (1994) model to include the proposed TM delay, we model the ear canal and TM as a uniform tube, having a characteristic impedance Z_{ot} and an effective acoustic delay T_0 , terminated by an effective stiffness K_0 [as shown in Fig. 4(A) insert].

The reflectance for this simplified model is

$$R(\omega) = \frac{1 - j\omega\tau_c}{1 + j\omega\tau_c} e^{-j\omega 2T_0}, \quad (5)$$

where

$$\tau_c = Z_{ot}/K_0. \quad (6)$$

The group delay $\tau(\omega)$ for the model represented by Eq. (5) is (Voss and Allen, 1994)

$$\tau(\omega) = 2T_0 + \frac{2\tau_c}{1 + (\omega\tau_c)^2}. \quad (7)$$

Equation (7) predicts a high-frequency round trip delay of $\tau(\omega \rightarrow \infty) = 2T_0$, and a low-frequency round trip delay of $\tau(\omega \rightarrow 0) = 2T_0 + 2\tau_c$. Thus the total delay consists of the sum of a low-frequency delay below f_c , and a fixed wide-band delay, where

$$f_c \equiv 1/2\pi\tau_c. \quad (8)$$

From this definition and Eq. (7) we find

$$\tau(2\pi f_c) \equiv 2T_0 + \tau_c. \quad (9)$$

From Fig. 3(D) we see a delay which is qualitatively similar to the prediction of Eq. (7). At high frequencies the terminating compliance has an impedance that is much smaller than the characteristic impedance of the transmission line, and the termination reflects all the energy above that frequency with the round trip line delay of $2T_0$. At low frequencies, defined as $f < f_c$, the transmission line has an effective acoustic length that is longer than $2T_0$ due to the terminating compliance (Voss and Allen, 1994).

Equations (7)–(9) are important because they separate the delay of the transmission line T_0 from the delay due to the terminating stiffness K_0 . If the TM operates as a delay line, then its delay appears as an extension of the canal delay line, rather than as part of the stiffness of the ossicles. Thus this model allows us to address one of the basic issues of the physical properties of the tympanic membrane: *Is the TM best modeled as a combination of a few stiffness, mass, and damping elements, or as a transmission line?*

1. An estimate of the TM delay

An approximation to the TM delay may be obtained using previously established ossicle stiffness values, the group delay shown in Fig. 3(D), and the equations for the simple ME model [Fig. 4(A) insert] outlined above.

Below about 1 kHz the ossicle impedance is dominated by the ligament stiffness, and the element impedances are approximately known. Based on an extensive series of cat middle-ear impedance measurements, Lynch (1981, pp. 226–231) estimated the malleus-ligament stiffness K_m (1.1×10^6 dyn/cm⁵) and the IM joint stiffness K_{inj} (37×10^6 dyn/cm⁵).

For the disarticulated stapes case, the stiffness of the malleus is dominated by the anchoring ligaments $K_0 = K_m$. Using $K_m = 1.1 \times 10^6$ (dyn/cm⁵), we find $\tau_c = 365 \mu\text{s}$ from Eq. (6), and $f_c = 437$ Hz from Eq. (8). Using this cutoff frequency, the delay $\tau(f_c)$ for the disarticulated stapes case [Fig. 3(D)] is 0.45 ms. From Eq. (9) we estimate the TM and ear-canal delay T_0 to be 42.5 μs .

For the measurements shown in Fig. 1, the ear-canal space is estimated to be approximately 1.5 mm, corresponding to an ear-canal propagation delay of 4.3 μs . Subtracting this delay from the combined ear-canal and TM-delay estimate requires that the TM delay is $\approx 38 \mu\text{s}$. The distance corresponding to this delay for sound propagation in air is 1.3 cm, which is significantly larger than the physical dimensions of the tympanic membrane. Thus, the above theoretical considerations, combined with previous middle-ear measurements, suggest that there is significant delay in the tympanic

membrane. It follows that the velocity of wave propagation must be slower than the speed of sound in air, by an amount that is ≈ 3.6 (radius of 0.36 cm).

B. Examples of the simple model

In this section we illustrate how the frequency spacing of the poles (maxima) and zeros (minima) of the ME impedance of the delay and stiffness model depends on the reflectance delay and terminating stiffness. Three examples are given: (1) a pure stiffness, (2) a short piece of transmission line terminated with a stiffness, and (3) same as case 2 but with increased stiffness. This last case corresponds to “blocked incus.” Finally the impedance is computed from the group delay using the reflectance formula Eq. (1) with no losses (i.e., $|R| = 1$). In these three examples the group delay $\tau(\omega)$ is the only model parameter (as dictated by T_0 and K_0). The delay and phase are calculated from model equation (7), while the loss is set to zero.

1. Group delay

The group delay of the simple model [Fig. 4(A) insert] consisting of a lossless transmission line with delay T_0 and a terminating impedance determined by stiffness K_0 is shown in Fig. 4(A), for three different conditions. In the three examples the group delay of the reflectance is given by Eq. (7). We use Lynch’s parameters for K_m and K_{inj} and TM delay estimated in the previous section.

For example 1 the stiffness is $K_0 = K_m = 1.1 \times 10^6$ (dyn/cm⁵) and $T_0 = 0$ (e.g., no transmission line). Using Eq. (6) we find that τ_c is 365 μs . Thus, as shown in Fig. 4(A), the reflectance delay asymptotically approaches 730 μs as frequency decreases. According to Eq. (8) the cutoff frequency f_c is approximately 435 Hz. Above f_c , the delay decreases by a factor of 4 for each octave increase in frequency.

For example 2, we add a transmission line with delay $T_0 = 40 \mu\text{s}$ to the stiffness $K_0 = K_m$. According to Eq. (7), when a transmission line is terminated with stiffness K_m , one simply adds the delay of the transmission line to the delay due to the stiffness alone to obtain the total delay. This is graphically illustrated in Fig. 4(A). The group delay for example 2 is always greater than for example 1.

If we assume that the malleus mass and all middle-ear losses are negligible, then example 2 approximates the disarticulated stapes case. This is apparent from the comparisons of the group delays shown in Figs. 3(D) and 4(A).

In example 3, the incudo-malleolar joint stiffness $K_{inj} = 3.7 \times 10^7$ (dyn/cm⁵) is added to the malleus stiffness (e.g., $K_0 = K_{inj} + K_m$) terminating the $T_0 = 40 \mu\text{s}$ transmission line. Example 3 is similar to example 2 except that the incudo-malleolar joint stiffness is added to the malleus stiffness. Thus stiffness K_0 is more than an order of magnitude greater for example 3 than for example 2. This example corresponds to the incus blocked at the IS joint. For this case τ_c is approximately 10.5 μs [Eq. (6)]. At low frequencies we expect the delay $\tau(0) = 2T_0 + 2\tau_c$ to be 101 μs . At high frequencies the reflectance delay τ should decrease to $2T_0 = 80 \mu\text{s}$ with a cutoff frequency f_c of 15 kHz.

2. From reflectance back to impedance

The reflectance group delay determines the reflectance phase, which in turn determines the location of the poles and zeros of the impedance. The magnitude of the reflectance, on the other hand, determines the bandwidths of the poles and zeros. This follows from two formulas: the integral of Eq. (4),

$$\angle R(\omega) = - \int_0^\omega \tau(\omega) d\omega \quad (10)$$

for $\omega > 0$, and

$$Z_{\text{me}}(\omega) = \frac{1 + |R(\omega)|e^{j\angle R(\omega)}}{1 - |R(\omega)|e^{j\angle R(\omega)}}, \quad (11)$$

which follows from Eqs. (1) and (3). The group delay may be transformed into a reflectance phase angle by using Eq. (10). As frequency increases, the phase angle increases (assuming a positive group delay), and $R(\omega)$ rotates about the origin in the complex plane. When R is close to ± 1 , the impedance Z_{me} shows poles, defined as the set of complex frequencies $s_n = \sigma_n + j\omega_n$ where $R(s_n) = 1$, and zeros, defined by $R(s_n) = -1$.

Since the magnitude of the reflectance is close to one for conditions when the cochlear load is removed from the middle ear, to a first-order approximation, we can model the impedance over a wide range of frequencies given only the group delay data.

In example 1 there is no added delay; thus the reflectance angle asymptotically approaches π as frequency increases (e.g., $\angle R(\omega)|_{\omega \rightarrow \infty} \rightarrow \pi$) and asymptotically approaches 0 as frequency decreases (e.g., $\angle R(\omega)|_{\omega \rightarrow 0} \rightarrow 0$). Thus there is a zero in the impedance as $\omega \rightarrow \infty$ and a pole in the impedance as $\omega \rightarrow 0$. Note that by simply adding delay (example 2), multiple maxima and minima are introduced in the impedance magnitude above 1 kHz. Example 1 thus demonstrates that, when there is insufficient delay, the reflectance phase angle [Eq. (10)] rotates about the origin so slowly that the poles and zeros of Eq. (11) occur with a much wider frequency spacing. When there is delay (as in the case in examples 2 and 3), the poles and zeros in the ME impedance occur due to standing waves in the transmission line. In this simple model there are no losses (e.g., $|R| = 1$) and thus the poles and zeros have infinite Q 's. More realistically $|R| < 1$, and, correspondingly, the bandwidth increases and the Q 's having finite values.

In summary, addition of group delay to the reflectance is the key to a model that works over a wide frequency range, as shown by our three simple examples.

IV. THE MIDDLE-EAR MODEL

Up to this point we have explored the possibility that there is delay in the tympanic membrane. In this section we formulate a more complex model that allows us to investigate the possibility that the measured ear-canal reflectance delay is in the residual postsurgical, widely opened ME cavity.

Middle-ear models are commonly defined in terms of lumped-parameter (parametric) models. We shall follow this

approach with three significant exceptions. We represent the measured delay [Fig. 3(D)] first as delay in the TM, and second as delay in the middle-ear cavity. Third, we define the cochlear impedance in nonparametric terms as $Z_c(\omega)$. The remaining elements are described as lumped-parameter elements.

A. Description of the models

The motions of the middle ear can be described by the general model of Fig. 5(A) consisting of three basic components: (1) the residual ear-canal space between the tip of the probe-tube microphone and the tympanic membrane, (2) the radiation impedance due to the residual ME cavity $Z_{\text{mec}}(\omega)$, and (3) the ossicular chain impedance $Z_{\text{oc}}(\omega)$ due to the TM, the ossicles and cochlea. In Fig. 5(A) the MEC and the ossicular chain impedances appear in series. This assumption has been previously shown to be valid for a wide range of frequencies [Lynch, 1981 (Chap. II); Puria, 1991b (pp. 133–135)].

Figure 5(B) shows the detailed electrical circuit representation for the tympanic membrane, ossicles, and the middle-ear cavity. In Fig. 5(B) the TM and the MEC, enclosed by the dashed box, represent delay in the TM and the radiation load impedance of the open MEC. Thus the circuit of Fig. 5(B) allows us to test the TM-delay hypothesis. To test the MEC-delay hypothesis, the components in the dashed box of Fig. 5(B) are replaced by the components in the dashed box shown of Fig. 5(C).

In Fig. 5, currents and voltages of the acousto-mechanical system correspond respectively to either volume velocities and pressures, or ‘‘particle’’ velocities and forces.

1. The ear canal

The ear canal is represented by a lossy cylindrical tube (i.e., an acoustic transmission line) of length L_{ec} and diameter D_{ec} . The ear canal and the open ME cavity are separated by the TM and thus they must have the same volume velocity U_{tm} , resulting in a series configuration for the two impedances (i.e., $Z_{\text{oc}} + Z_{\text{mec}}$) that terminate the ear-canal space.

2. Middle-ear cavity radiation impedance

For the TM-delay hypothesis the ME cavity impedance Z_{mec} is represented by a radiation load impedance

$$Z_{\text{mec}} = \frac{j\omega M_{\text{rl}} \times R_{\text{rl}}}{(R_{\text{rl}} + j\omega M_{\text{rl}})}. \quad (12)$$

In Eq. (12) M_{rl} is the mass of the radiation load and R_{rl} is the effective damping due to loss of energy through the widely opened ME cavity.⁵ Equation (12) represents the functional form for either a plane piston in an infinite baffle or of a plane piston at the end of a long tube (Beranek, 1954, pp. 124–125). Our case seems to lie somewhere between these two extremes.

3. Tympanic membrane model

The ligaments of the malleus and the attachment of the anterior process of the malleus to the tympanic bone helps to

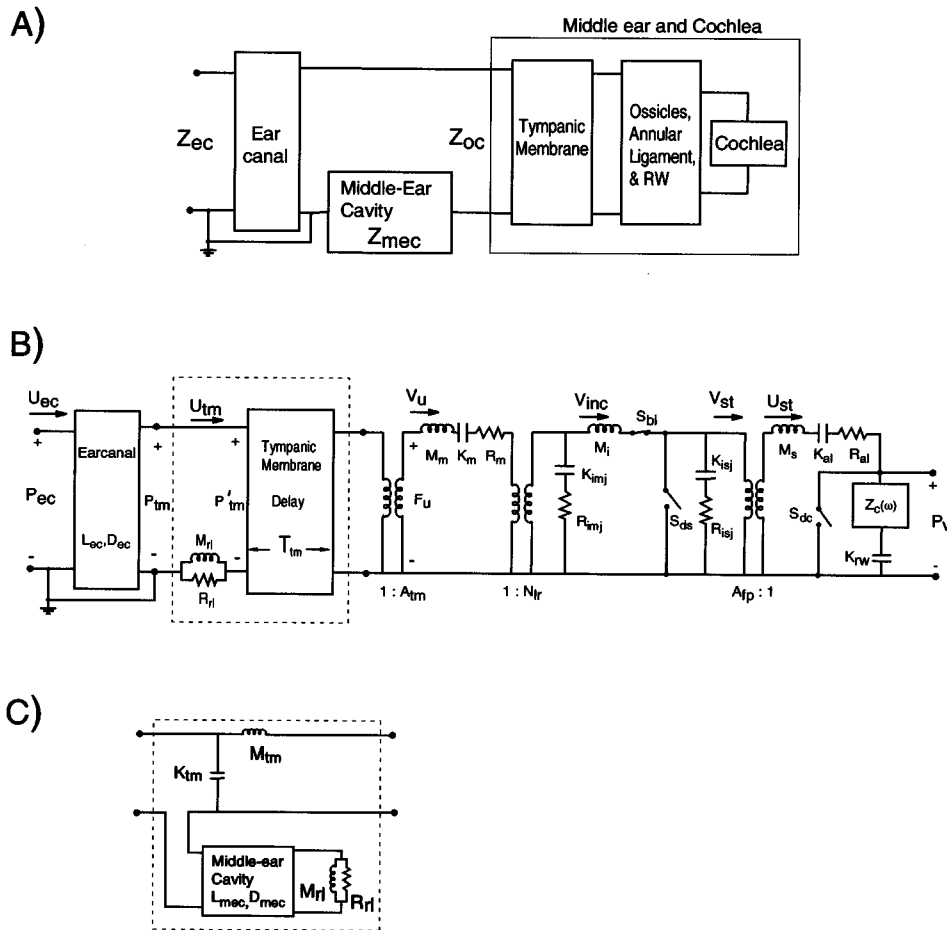


FIG. 5. Three middle-ear model circuit representations. (A) The ear-canal impedance Z_{ec} is the sum of the impedance of the middle-ear cavity Z_{mec} and the impedance of the ossicular chain Z_{oc} , which is a function of the properties of the tympanic membrane (TM), ossicles, and the cochlea. Panels B and C show two different models proposed for the TM and MEC. (B) The tympanic membrane is represented by a nondispersive lossless transmission line. This transmission line has a frequency-independent delay T_{tm} from the tympanic ring to the umbo and characteristic impedance Z_{ot} . The space between the measurement plane and the TM is represented by a cylindrical tube with diameter D_{ec} and length L_{ec} . The radiation impedance of the open middle-ear cavity is represented by the parallel combination of R_{rl} and M_{rl} . The rotational mass of the malleus is represented by M_m while malleus and incus ligaments (Fig. 2) are represented by stiffness K_m . See the text for a description of the other circuit elements. The three different measurement conditions of Fig. 1 are modeled by appropriate setting of switches S_{dc} and S_{ds} : when both switches are open, the circuit represents the intact measurement condition. With switch S_{dc} closed and S_{ds} open, the circuit represents the drained cochlea measurement condition. With switch S_{ds} closed the circuit represents the disarticulated stapes measurement condition. The third switch S_{bi} corresponds to the blocked incus case, which is discussed in the text. (C) An alternative representation for the TM and MEC is shown. The MEC-delay model is obtained by replacing the contents of the dashed box of panel B with the contents of the dashed box shown in panel C. In this model the delay is in the MEC rather than in the TM. The MEC is represented as a cylindrical tube with length L_{mec} and D_{mec} terminated by a radiation impedance. The TM is represented by a piston having stiffness K_{tm} and mass M_{tm} . The parameters for both models are listed in the Appendix.

maintain the conic shape of the TM. Békésy (1960, p. 195) has argued that the human eardrum resembles a stiffened cone rather than a stretched membrane.

The ossicular chain and TM components of the impedance is defined as Z_{oc} . In the model of Fig. 5(B) the TM is represented as a lossless transmission line having a matched characteristic impedance Z_{ot} , and a frequency-independent delay T_{tm} between the input at the tympanic ring and the output at the umbo (i.e., the tip of the manubrium). In this representation, a small segment of the TM transmission line corresponds to an annulus of the TM. The TM model shown in Fig. 5(B) can be succinctly represented in terms of a two-port matrix as follows:

$$\begin{bmatrix} P'_{tm} \\ U_{tm} \end{bmatrix} = \begin{bmatrix} A_{tm} & B_{tm} \\ C_{tm} & D_{tm} \end{bmatrix} \begin{bmatrix} F_u \\ V_u \end{bmatrix}. \quad (13)$$

The pressure in front of the TM under the condition that the MEC is short circuited ($R_{rl}=0$ or $M_{rl}=0$) is defined as P'_{tm} . The tympanic membrane matrix elements (A_{tm} , B_{tm} , C_{tm} , and D_{tm}) in Eq. (13) are due to the product of two matrices:

$$\begin{bmatrix} A_{tm}(\omega) & B_{tm}(\omega) \\ C_{tm}(\omega) & D_{tm}(\omega) \end{bmatrix} = \begin{bmatrix} \cos(\omega T_{tm}) & jZ_{ot} \sin(\omega T_{tm}) \\ jZ_{ot}^{-1} \sin(\omega T_{tm}) & \cos(\omega T_{tm}) \end{bmatrix} \times \begin{bmatrix} A_{tm}^{-1} & 0 \\ 0 & A_{tm} \end{bmatrix}. \quad (14)$$

The diagonal matrix on the right-hand side represents the TM as a transformer, with turns ratio A_{tm} . In Eq. (14) ωT_{tm} is often written as kl in transmission line terminology, where k is the wave number (ω/c) and l is the length of the line.

TABLE II. Physical dimensions assumed for the cat middle ear.

Description	Symbol	Value	Units
Length of ear canal	L_{ec}	0.15	cm
Diameter of ear canal	D_{ec}	0.36	cm
Area of TM	A_{tm}	0.41	cm ²
Area of stapes footplate	A_{fp}	0.0126	cm ²
Ossicular lever ratio	N_{lr}	2	(dimensionless)

4. Ossicular chain impedance

In Fig. 5(B), the impedance of the malleus is represented by $Z_m(\omega) = R_m + K_m/j\omega + j\omega M_m$. Stiffness K_m and damping R_m are due to the ligaments of the malleus and incus.

The transformer with turns ratio N_{lr} represents the lever ratio between the malleus and incus. The shunt impedance $Z_{imj}(\omega) = R_{imj} + K_{imj}/j\omega$ represents the slippage at the IM joint. The incus is represented by the mass M_i . The shunt impedance $Z_{isj}(\omega) = R_{isj} + K_{isj}/j\omega$ represents the slippage at the incudo-stapedial joint. The transformer with turns ratio A_{fp} converts the stapes velocity into the footplate volume velocity. The stapes is represented by mass M_s . The annular ligament which holds the stapes in the oval window is represented by a parametric viscoelastic spring, $Z_{al}(\omega) = R_{al} + K_{al}/j\omega$.

5. Cochlear load

The ‘‘load’’ on the stapes is the cochlea, consisting of the cochlear input impedance $Z_c(\omega)$ in series with the round window impedance $Z_{rw}(\omega)$. Our 1991 model results for the cochlear input impedance with tapered scalae area cochlea and viscous perilymph (Puria and Allen, 1991, Fig. 18) were used as a cochlear load, since the actual load for the animals used in this study is unknown.

6. Middle ear cavity delay model

In Fig. 5(C) the delay in the MEC is represented by a tube terminated by a radiation load impedance [Eq. (12)]. The TM is represented by a piston with stiffness K_{tm} and mass M_{tm} . The value of K_{tm} is chosen such that it has the same impedance at low frequencies as the TM-delay model ($K_{tm} = Z_{ot}/T_{tm}$). For the MEC-delay model, the widely open ME cavity is represented by a tube of length L_{mec} and diameter D_{mec} terminated in a radiation load impedance of the same form as Eq. (12) but with different parameter values.

B. Parameter selection and reduction

For the disarticulated stapes case, the TM-delay model of Fig. 5(B) requires specification of 13 parameters, while the MEC-delay model of Fig. 5(C) requires specification of 14 parameters. Since we do not know *a priori* any of the specific parameters for the ME impedance shown in Fig. 1, our approach is to draw average parameter values from the literature as a starting point and then use an optimization procedure that varies many of the parameter values, minimizing the error [Eq. (A3)] between the model and the ear-canal impedance measurements of Fig. 1.

The four parameters shown in Table II were not adjusted

by the error minimization procedure. The dimensions for L_{ec} and D_{ec} were based on the approximate location of the transducer in relation to the eardrum and ear-canal dimensions. Average values for dimensions A_{tm} and N_{lr} were taken from the literature (Wever and Lawrence, 1954).

1. The matched-impedance condition

Ossicle mass can limit the high-frequency behavior of the middle ear (Shaw and Stinson, 1981). If, however, each mass element is followed by an appropriate compliance, such that a section of ‘‘matched’’ transmission line is formed by the two elements, then ossicle mass does not limit the frequency response. Such a properly matched system will attain a wide frequency response at the price of acoustic delay. This is a necessary and favorable trade. In Fig. 5(B), two of the series masses (inductors) have corresponding shunt stiffnesses (capacitors), since the malleus mass M_m may be associated with joint stiffness K_{imj} , and the incus mass M_i may be associated with joint stiffness K_{isj} . Thus the ossicles may be viewed as a lumped-parameter transmission line [e.g., Giacoletto (1977), Chap. 8]. In addition to providing a means for achieving higher-frequency response, the number of unknown parameters may be reduced by one if we assume that the IM joint stiffness K_{imj} and the malleus mass M_m are related by their *local characteristic impedance*. In summary, the basic equation for the characteristic impedance of a lumped-parameter mechanical transmission line is

$$Z_o = \sqrt{MK}, \quad (15)$$

where M and K correspond to the elements of the series mass and shunt stiffness. Solving for K in Eq. (15) we get $K = Z_o^2/M$, which we call the *matched-impedance condition*. To calculate the IM joint stiffness, we assume that the local characteristic impedance at the malleus is $Z_{ot}A_{tm}^2N_{lr}^2$, which is the characteristic impedance of the ear canal transformed to the IM joint.

Applying the matched-impedance condition, the IM joint stiffness K_{imj} is therefore

$$K_{imj} = \alpha_{im} \frac{(Z_{ot}A_{tm}^2N_{lr}^2)^2}{M_mN_{lr}^2}, \quad (16)$$

where the quantity in the parentheses is the local characteristic impedance at the malleus. The denominator is the malleus mass transferred to the other side of the transformer, with N_{lr} representing the lever ratio. We define the constant α_{im} as an impedance mismatch parameter between $\sqrt{K_{imj}M_m}$ and the local characteristic impedance. Based on direct observations of the cat IM joint slippage (Guinan and Peake, 1967), we have set $\alpha_{im} = \frac{2}{3}$. While the total number of parameters for the IM joint is two, the number of search parameters is one because of the estimate of α_{im} .

How does the matched impedance constrain help? If the ossicles were not matched, energy would be less effectively coupled to the cochlea, and the coupling would depend on frequency. Since wideband frequency measures of the cochlea (such as the cochlear microphonic, middle-ear pressure gain, and threshold of hearing) do not vary significantly with

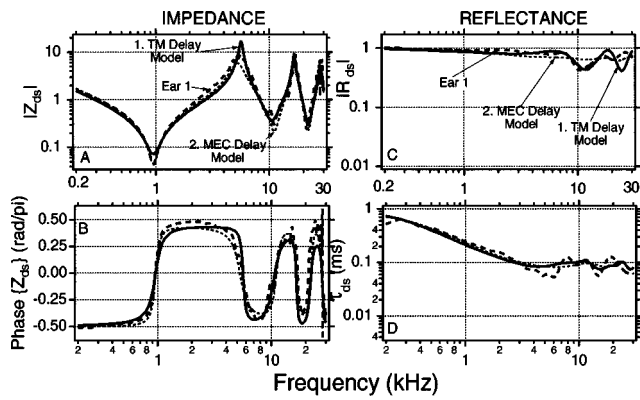


FIG. 6. Two model calculations are shown for the disarticulated stapes case, along with the measured data for ear 1: (1) The TM-delay model, and (2) the MEC-delay model. (A) Ear-canal impedance magnitude. (B) Impedance phase angle. (C) Reflectance magnitude. (D) The reflectance group delay $\tau(\omega)$.

frequency above a few kHz, we believe that the middle ear effectively couples ear-canal energy to the cochlea, justifying our assumption that $\alpha_{im} = \frac{2}{3}$.

C. Disarticulated stapes

Because the stapes and cochlea have been removed, the disarticulated stapes case has the fewest number of parameters of the three conditions shown in Fig. 1. Fitting the TM and ossicle model requires the estimation of eight unknown parameters: the radiation load (2), the TM delay T_{tm} (1), the malleus stiffness K_m , mass M_m and damping R_m (3), the IM joint damping R_{imj} (1), and the incus mass M_i (1).

An automatic search procedure was used that minimizes the error [see Eq. (A3)] between the measured impedance log magnitude and phase angle and model impedance log magnitude and phase angle. Starting from an initial estimate, the algorithm minimizes the error while searching a constrained parameter space (typically within 0.005 to 200 times the starting values) using a quasi-Newton algorithm. Several random perturbations by 25% of the initial parameters lead to the same solution.

Using this search procedure, the tympanic membrane delay model parameters were estimated for all three ears. The final parameters for ear 1 are listed in Table AI of the Appendix. Parameters for the other two ears typically differed from model parameters for ear 1 by less than a factor of 2. The TM delay in the other two ears was found to be approximately 34 μ s for ear 2 and 41 μ s for ear 3. Rather than list the parameters for the other two ears, we show the sensitivity of the TM-delay model to changes in model parameters in Fig. A1 of the Appendix.

The model and measured impedances for ear 1 for the disarticulated stapes case are shown in Fig. 6(A) and (B), while the reflectance magnitude and group delay are shown in Fig. 6(C) and (D). Both the TM-delay and MEC-delay models account for the high- Q standing waves.

Although the measured group delay at frequencies above 3 kHz has a mean value of approximately 100 μ s, there is tendency for the delay of ear 1 to “oscillate” in frequency. The TM-delay model shows a similar oscillation. These cor-

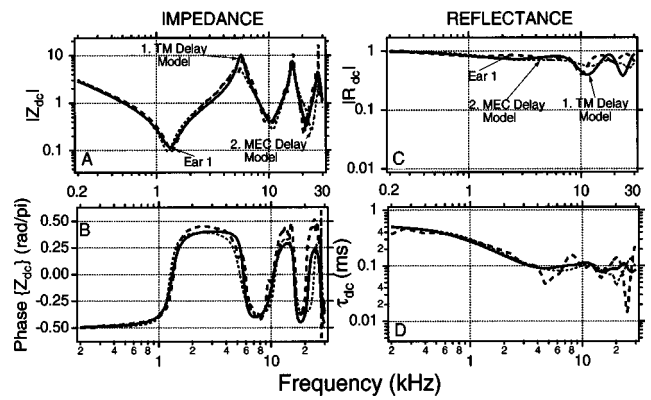


FIG. 7. Measurements (ear 1) and model calculation for the drained cochlea case. The complexity of this case increased from the disarticulated stapes case by the addition of the incudo–stapedial joint, the footplate area transformer, the annular ligament, and the stapes mass. These elements have an effect on the impedance and reflectance mostly at frequencies below 4–5 kHz. Above 4–5 kHz, the drained cochlea and the disarticulated stapes impedances and reflectances are approximately the same for both model calculations. (See Fig. 6 for a description of panels.)

related variations seem to be due to the acoustical properties of the middle ear. By removing the radiation load Z_{rl} in the model, we determined that $\tau_{ds}(\omega)$ is a monotonically decreasing smooth function, suggesting that the small oscillations above 6 kHz may be due to the radiation load impedance Z_{rl} causing a small impedance miss-match (see also Fig. A1).

Figure 6 shows that, for the entire range of frequencies tested, both models are in agreement with measurements. We conclude that on the restricted evidence of impedance or reflectance, the delay can be either in the tympanic membrane or in the middle-ear cavity.

D. Drained cochlea

In going from the disarticulated stapes case to the drained cochlea case, model complexity increases by the addition of the incudo-stapedial joint, stapes mass M_s , and annular ligament impedance. Four additional values for parameters R_{isj} , K_{al} , R_{al} , and M_s are required for this case. Theoretical considerations suggest that the input impedance of the drained cochlea Z_{c_0} is negligible⁶ in comparison with damping of the annular ligament R_{al} [Puria and Allen, 1991, Eq. (6a)].

As in the IM joint case, we apply the matched-impedance condition to the incudo-stapedial joint, treating the joint stiffness K_{isj} and the incus mass M_i as a segment of a parametric matched transmission line. The equation for the impedance-matched joint stiffness in terms of the mass and the local characteristic impedance is

$$K_{isj} = \frac{(Z_{ot} A_{tm}^2 N_{lr}^2)^2}{M_i}, \quad (17)$$

where the quantity in the parentheses is the local characteristic impedance at the incus.

The four additional parameters were obtained by manually adjusting them to obtain agreement between model and measured impedance magnitudes and phases, and are listed in Table AI. During this adjustment the parameters found for

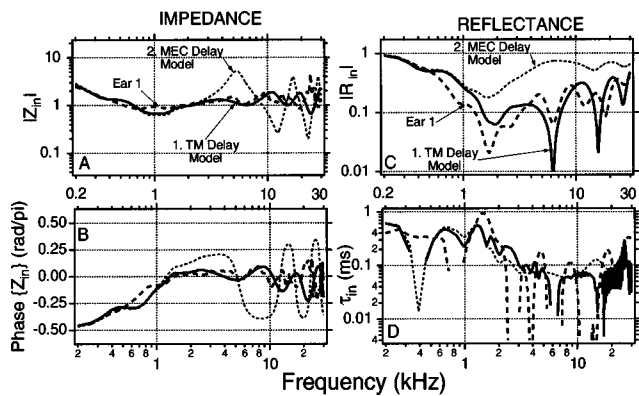


FIG. 8. Measurements (ear 1) and model calculations for the intact case. The complexity of this case is increased from that of the drained cochlea case by the addition of the cochlear load. The input impedance of a tapered cochlea with viscous perilymph was used as the cochlear load (Puria and Allen, 1991). (Note the change in scales of $|Z|$ and $|R|$ from previous figures.)

the disarticulated stapes case were held fixed. The estimated parameters for the stapes and annular ligament were found to be within a factor of 2 of those obtained experimentally by Lynch *et al.*, (1982). The average footplate area A_{fp} is known from anatomical measurements (Lynch *et al.*, 1982).

Model and measured impedances for ear 1, for the drained cochlea case, are shown in Fig. 7(A) and (B) and the reflectance magnitude and group delay are shown in Fig. 7(C) and (D). As may be seen from the measurements and model calculations, adding the stapes and the annular ligament stiffness has a significant effect below 5 kHz.

As in the disarticulated stapes case, Fig. 7 shows that both model results are consistent with measurements for a wide range of frequencies. We conclude that, if one is given only impedance (or reflectance) measurements of the disarticulated stapes case or the drained cochlea case, it is impossible to determine the source of the delay. We shall next show, however, that, once a cochlear load is attached (the ‘‘intact ear’’ case), the two hypothesis may be distinguished.

E. Intact ear

In going from the drained cochlea to the intact ear, the model complexity increases by the addition of the cochlear load impedance $Z_c(\omega)$ on the middle ear. As previously mentioned, our 1991 model of the cochlear input impedance, with tapered scalae area cochlea and viscous perilymph (Puria and Allen, 1991, Fig. 18), was used as the model cochlear load.

The parameters for both ME models were held fixed, and no new parameters were required for this calculation. The model and measured impedance magnitude and phase for the intact case of ear 1 is shown in Fig. 8(A) and (B), while the reflectance magnitude and group delay is shown in Fig. 8(C) and (D). With the cochlear load the impedance magnitude for ear 1 varies by about ± 6 dB. Consistent with previous results (Møller, 1965; Lynch, 1981; Allen, 1986), Fig. 8 shows that the cochlear load has a dramatic effect on the middle-ear impedance (and thus its reflectance).

For the TM-delay model, the standing waves in the impedance magnitude are significantly reduced, in comparison

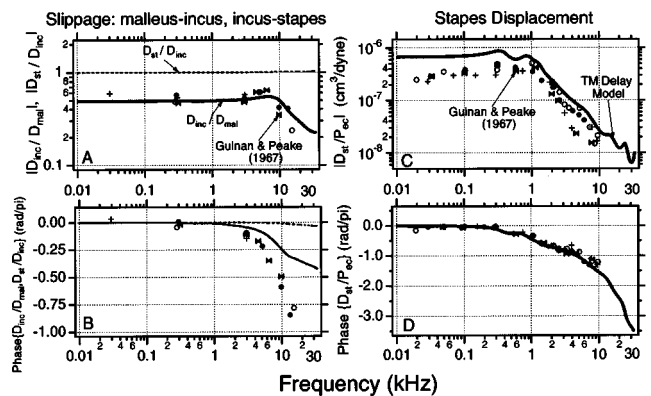


FIG. 9. Comparison of model calculations to measured data of the motions of the ossicles. Magnitude (A) and phase angle (B) of the slippage at the incudo-malleolar joint D_{inc}/D_{mal} and slippage at the incudo-stapedial joint D_{stap}/D_{inc} . Magnitude (C) and phase angle (D) of the ratio of the stapes displacement in cm per dyn/cm² (74 dB SPL). The stapes volume-velocity $U_{st}(\omega)$ of the model was divided by $j\omega$ and the footplate area A_{fp} to obtain the stapes displacement D_{st} . Measurements by Guinan and Peake (1967) in four cat ears are shown as different symbols.

to the drained cochlea and the disarticulated stapes cases (Figs. 7 and 6). However, for the MEC-delay model, the impedance magnitude varies by as much as ± 15 dB, indicating standing waves that are much larger than in the TM-delay model. We conclude that the TM-delay model is consistent with measurements, while the MEC-delay model is inconsistent. Thus, the middle-ear cavity delay hypothesis is ruled out.

V. FURTHER TESTS OF THE TM-DELAY MODEL

An important test of any good model is that it can predict measurements not explicitly used in its formulation. In this section generalizability of the middle-ear model with TM delay is verified by comparing our model calculations with known physiological measurements from the literature.

We compare model results for the following middle-ear measurements from the literature: (1) incudo-malleolar and incudo-stapedial joint slippage, (2) the stapes displacement to ear-canal pressure ratio, and (3) the middle-ear pressure gain. These measurements were not used in the model formulation, with the exception of the IM joint slippage data.

A. Ossicular motion

1. Slippage of the ossicles

The ratio of the incus to malleus displacement (D_{inc}/D_{mal} solid line) from the model is shown in Fig. 9(A) and (B) along with data points measured by Guinan and Peak (1967). Measurements and model magnitudes agree, while phase angles disagree by more than $0.5 \text{ rad}/\pi$ above 10 kHz. In Eq. (16) the IM joint stiffness, and thus the impedance of the IM joint, is directly proportional to α_{im} . Although not shown, decreasing α_{im} has the effect of increasing the joint slippage. As is apparent from Fig. 5(B), decreasing the IM joint impedance will result in an increase in the current through the IM joint shunt branch and thus a decrease in V_{inc} , corresponding to increased slippage. Changes in α_{im} by 50% have a large effect on the IM slippage.

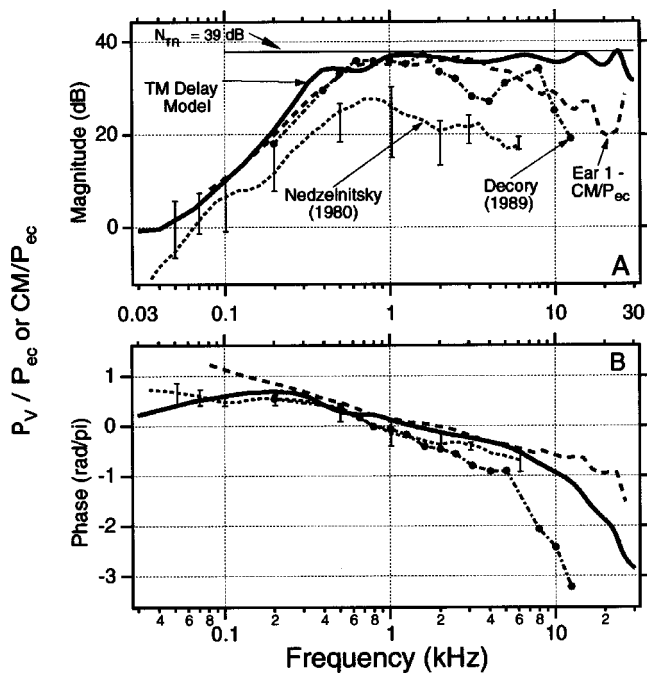


FIG. 10. Compared here are the middle-ear pressure gain of Nedzelnitsky and Décorcy, the ratio of the round window cochlear microphonic (CM) to the ear-canal pressure (P_{ec}) for ear 1, and model calculations of the middle-ear pressure gain. Two measurements of the middle-ear pressure gain with middle-ear cavities wide open are shown: (1) Nedzelnitsky's (1980) measurement is the median and range of six cats, and (2) Décorcy's (1989, Fig. 105) measurement is from one ear. Also shown is the CM data chosen from the linear regime of the CM (i.e., just before it started to saturate) and its magnitude scaled⁷ (to agree with the pressure gain at 1 kHz) to allow comparison with the calculated middle-ear pressure gain. Panel A shows the magnitude in dB [$20 \log_{10}(X/P_{ec})$], where X is either P_v or CM] of the transfer function and panel B shows the phase angle in rad/ π . The "ideal mechanical transformer model" is a zero-delay model that proposes that the product $(A_{im}/A_{fp}) \times N_{lr}$ is the pressure gain N_{TR} (Wever and Lawrence, 1950). For the cat, $N_{TR} \approx 39$ dB as shown by the straight line in panel A.

Our model calculations of the ratio of the incus to stapes displacement D_{inc}/D_{st} , as shown in Fig. 9(A) and (B), suggest that there is no significant slippage between these two ossicles even at the highest frequencies. This result is consistent with measurements of amplitude and phase between the incus and stapes displacement by Guinan and Peake (1967, pp. 1248–1249). Changes in K_{isj} by a factor of $\frac{1}{5}$ to 5 do not have a significant effect on the IS slippage because the stiffness of the IS joint is large. In order for there to be significant slippage in the IS joint, K_{isj} would need to be lower by a factor of 10 or more.

2. Stapes displacement

An important measure of middle-ear transmission is the ratio of the stapes displacement to the ear-canal pressure. The model computation of the stapes displacement (in cms) per unit of pressure at 1 dyn/cm² (74 dB SPL) is shown in Fig. 9(C) and (D). For comparison, the stapes displacement per unit ear-canal pressure data published by Guinan and Peak (1967) are also shown.

Below 500 Hz the model stapes displacement magnitude is greater than the measured values. For example, at 100 Hz the model results are greater by a factor of 2. At low frequencies, the stapes displacement is dominated by the

malleus stiffness K_m (see Fig. A1) and the stiffness of the annular ligament K_{al} . Increases in K_m or K_{al} result in a decrease in stapes displacement, and this results in an increase in ear-canal impedance for frequencies below 1 kHz.

Lynch *et al.* (1994) established a correlation between body weight and eardrum compliance. One possible reason for the higher stapes displacement is that our animals (Fig. 1) had systematically lower stiffness than the Guinan and Peak animals (Fig. 9).

At high frequencies the phase shift in the stapes displacement re the ear-canal pressure [Fig. 9(D)] is much greater than the phase shift in the IM joint [Fig. 9(B)]. Thus the model IM joint does not account for most of the stapes displacement to ear-canal pressure phase shift. In the TM-delay model a portion of this phase is due to delay in the tympanic membrane.

B. ME pressure gain and round window cochlear microphonic

The *middle-ear pressure gain* is defined as the ratio of the vestibule pressure near the footplate to the ear-canal pressure near the tympanic membrane $P_v(\omega)/P_{ec}(\omega)$. This important ratio is related to the behavioral threshold (Puria *et al.*, 1997) and the cochlear microphonic (CM) response (Dallos, 1970; Nedzelnitsky, 1980; Allen, 1983).

As shown in Fig. 10 there is mixed agreement between the calculated middle-ear pressure gain and the measured pressure gain. In 1980 Nedzelnitsky (Fig. 15) reported measurements of the ME pressure gain in six cats with open ME cavity. In Fig. 10 these calculated and measured pressure gains are shown along with the measurements of cat middle-ear pressure gain from Décorcy (1989, Figs. 104–105), also for the wide open bulla condition. (Although not shown here, Décorcy also measured the pressure gain with an open bulla cavity but intact septum, and found the pressure to be lower than the mean of the removed septum by 3–6 dB.) Décorcy's measured pressure gain is greater than Nedzelnitsky's by 3–12 dB, while the phase angles are in reasonable agreement.

The middle-ear pressure gain was not measured for the ears used in the present study. However, the ratio of the round window cochlear microphonic⁷ (CM) to ear-canal pressure was measured, and is labeled "Ear 1-CM/ P_{ec} " in Fig. 10. It has been argued (Dallos, 1970; Allen, 1983), and is now widely accepted, that the CM is proportional to the pressure drop across the cochlear partition because, (a) the CM is proportional to basilar membrane displacement, (b) basilar membrane displacement is stiffness dominated for frequencies less than the characteristic frequency corresponding to the place of measurement, and (c) characteristic frequencies near the round window are greater than 30 kHz.

There is close agreement between the model calculations and both the pressure gain and the CM data in the 0.03–8-kHz frequency range (Fig. 10). Above 8 kHz, there are systematic differences in slopes of the magnitude of the round window CM and measured pressure gain and middle-ear model pressure gain. Above about 4 kHz the model slope is less than the CM slope by about 4 dB/oct.

VI. DISCUSSION

A. Testing the two hypotheses

The goal of the present work is to understand middle-ear mechanisms for frequencies above a few kHz. A reflectance group delay of approximately $100 \mu\text{s}$ has been found in the disarticulated stapes and drained cochlea cases for frequencies above 2 kHz [Figs. 6(D) and 7(D)]. Two hypotheses for the measured delay were tested: (1) the delay is in the tympanic membrane (TM-delay model), and (2) the delay is in the middle-ear cavity space (MEC-delay model). As shown in Fig. 5, we have assumed a series model for the ossicular chain and the middle-ear cavity space (Lynch, 1981, Chap. II; Puria, 1991b, pp. 133–135). We have quantitatively analyzed the two models.

Quantitative model calculations suggest that the two models are *not* distinguishable if one includes only the impedance for the disarticulated stapes and drained cochlea cases (Figs. 6 and 7). However, the two models are easily distinguished when the intact case is included, as seen in Fig. 8(A) and (B). The cochlear load significantly reduces the magnitude of the standing waves for the TM-delay model but not for the MEC-delay model. *All of the arguments above refute the middle-ear cavity delay hypothesis.*

1. The MEC-delay model

When the delay is in the middle-ear cavities, the resonances come from the standing waves in the MEC. In the MEC-delay model, the drum impedance is typically much smaller than the MEC impedance, namely $|Z_{oc}| \ll |Z_{mec}|$. For the intact case, the experimental TM impedance is approximately matched to the ear-canal characteristic impedance. This is inconsistent with the MEC-delay model because the large MEC impedance appears in series with Z_{oc} . In all three cases the impedance of the middle-ear cavity dominates at frequencies above 4–5 kHz and consequently changes in the ossicular chain impedance (i.e., due to draining the cochlea or disarticulating the stapes) do not have a significant effect on the ear-canal impedance at those frequencies.

2. The TM-delay model

When the delay is in the tympanic membrane, standing waves in the TM surface give rise to resonant modes. In this model the relative magnitude of Z_{mec} (due to the open middle-ear cavity) is small in comparison to Z_{oc} . Thus the ear-canal impedance Z_{ec} is dominated by Z_{oc} . The TM-delay model is sensitive to changes in the load to the ossicular chain, unlike the MEC-delay model.

B. Transmission line representation of the tympanic membrane

Once sound is collected by the external ear, it propagates into the ear canal where all higher-order modes below the ear-canal cutoff frequency are exponentially damped. Thus below approximately 25 kHz acoustic signals have a plane wave mode of propagation. Ideally, when this plane wave reaches the tympanic membrane 100% of the energy

would be absorbed by the drum, and transferred to the cochlea. This could only happen if the TM had the same impedance as air, which it does not.

However, if at each point the stiffness were controlled, for example, by the TM curvature, then the annulus having the largest radius from the umbo would have the lowest stiffness, since its curvature there is smallest. If this stiffness were controlled in the proper way, the impedance of this outer annulus could have an impedance that is close to that of air. The wave speed on the TM would necessarily be lower, by the ratio of the density of air to the density of the TM. This would mean that the impinging plane wave would be absorbed in this portion of the TM with nearly zero reflection, and would be transformed into a transverse, slowly moving wave on the surface of the TM.

The resulting wave would then propagate into the umbo region along the radial axis. Due to the increasing TM curvature with radius, the local impedance of the transverse wave would increase. In this model of the TM, the main impedance transformation of the middle ear is in the TM itself, resulting from the propagation of the wave, and the gradient of the ear-drum stiffness. *This view of the acoustic surface wave on the eardrum is analogous to an acoustic horn having a radially dependent characteristic impedance.*

That portion of the ear-canal plane wave, incident on the umbo and manubrium, would be reflected, as this more central portion of the TM (unlike the annulus bounding the TM's circumference) would not match the impedance of air. Thus the reflectance, as measured in the ear canal, would depend on the percentage of the TM that is unmatched in specific acoustic impedance. This would set a low bound on the magnitude of the reflectance.

In this tympanic membrane with waves, the mass of the TM does not limit the performance of the system at high frequencies. The local TM mass is canceled by the local TM stiffness, forming a transmission line with delay. *Thus the distributed design trades mass for delay, giving the transfer function a much wider bandwidth than attainable with a lumped parameter model* (e.g., the two-piston model of the TM of Shaw or the one-piston TM model of Zwislocki).

Specifically, we represent the TM by a lossless transmission line, with a frequency independent delay of approximately $36 \mu\text{s}$ (for ear 1). This representation allows for the possibility of standing waves on the tympanic membrane.⁸ Representing the TM as a lossless frequency-independent delay, as in Eq. (13), is only a first-order approximation, and one that is shown to be reasonable to fairly high frequencies. Recent measurements between 2 and 46 kHz provide further evidence that there is frequency-independent delay in the middle-ear system. Olson (1998) has shown that the phase of the gerbil middle-ear pressure gain is approximately linear with a corresponding delay of approximately $25 \mu\text{s}$. Future measurements of the TM transmission matrix [Eq. (14)] will be the definitive tests of the model presented here.

In summary, the mechanics of the auditory periphery consists of a cascade of transmission lines. These are the concha, the ear canal, the tympanic membrane, the ossicles, and the organ of Corti.

1. Tympanic membrane wave speed

For a TM area of 0.41 cm^2 (Wever and Lawrence, 1954, p. 416) the radius is approximately 0.361 cm , and the corresponding wave speed, for a $35.7\text{-}\mu\text{s}$ delay, is approximately $10.1 \times 10^3 \text{ cm/s}$. Such a wave speed on the TM is slower, by a factor of 3.4, than the speed of sound in air.

In our formulation for the TM [Eq. (13)], a small section of the TM corresponds to an annulus on the TM which has a local wave velocity approximated to be same regardless of the radial position. A refinement to this idea could be a model where the local wave velocity depends of the radial position along the TM; however, the motivation for such a model remains unclear.

2. Standing waves on the tympanic membrane

We have analyzed the transmission line representation for the TM from an input–output point of view. Another approach is to analyze the *spatial* response of the TM transmission line.

Given a unit ear-canal pressure, the ear-canal impedance is the reciprocal of the volume velocity. Cancellations of the volume velocities across the TM surface, due to portions of the TM moving with different phases, would result in a relatively small ear-canal volume velocity, and thus a relatively large middle-ear impedance magnitude. Conversely, when the entire TM surface moves in phase, the ear-canal volume velocity is relatively large, corresponding to a small middle-ear impedance magnitude.

Time-averaged holographic methods show that for frequencies above 3 kHz and levels greater than 90 dB SPL, the surface of the “tympanic membrane vibrations break up into sections,” suggesting that the TM is not a stiff plate (Khanna and Tonndorf, 1972). These measurements are consistent with our conclusions that there are standing waves on the TM. Thus, the Khanna and Tonndorf (1972) observation is consistent with our model that acoustic waves travel on the tympanic membrane.

It would be instructive to measure the tympanic membrane surface displacement patterns before and after removing the cochlear load from the middle ears of the same animals. Our model prediction is that the magnitude of the standing waves observed on the tympanic membrane surface should increase significantly after draining the cochlea, or after cutting the incudo-stapedial joint.

C. Two-port matrix representation

The most important difference between the current model and previous models is the representation of the tympanic membrane. Comparisons among various models for the TM can be facilitated by analyzing them in terms of a two-port transmission matrix representation. Such a characterization is interesting because two of the elements of the transmission matrix have a specific physical interpretation in terms of area (Shera and Zweig, 1991). The reciprocal of the matrix element $A_{tm}(\omega)$ in Eq. (13) is the effective area $A_F(\omega)$ corresponding to the ratio of the ear-canal pressure and umbo force. Matrix element $D_{tm}(\omega)$ is the effective area $A_V(\omega)$ corresponding to the ratio of the ear-canal volume

velocity and umbo velocity. For a piston (ridged plate) model of the TM, the magnitude of the A_F to A_V ratio is by definition unity and deviations from unity indicate the degree to which a particular TM model deviates from a plate model.

In our two-port formulation for the TM model [Eqs. (13) and (14)] A_F is $A_{tm}/\cos(\omega T_{tm})$ and A_V is $A_{tm} \cos(\omega T_{tm})$. Thus the ratio of the areas is simply

$$\frac{A_F}{A_V} = \frac{1}{\cos^2(\omega T_{tm})}. \quad (18)$$

This equation states that in the present model the ratio of the areas clearly does not behave like a piston and, furthermore, the area ratio is a periodic function of frequency. The first peak in the area ratio occurs when $\omega T_{tm} = \pi/2$, or at a frequency of $(4T_{tm})^{-1}$. For a TM delay of $35.7 \mu\text{s}$ this corresponds to a frequency of 7 kHz, and thus the maxima and minima in Eq. (18) occur at multiples of 7 kHz. Further measurements of the transmission matrix elements [Eq. (14)] are needed to verify Eq. (18).

D. Previous tympanic membrane models

1. Lumped parameter representations

Matthews (1983) represented the cat TM with a one-degree of freedom model, consisting of a series resistor, mass, and stiffness. He showed that the model input impedance diverges from the measured data for frequencies above 3–4 kHz. The problem is that the model impedance is mass dominated above 4 kHz, whereas the measurements are approximately resistive. As discussed by Matthews (1983), the failure is primarily due to an inadequate representation of the tympanic membrane.

A natural extension of the one-degree of freedom TM piston model is the two-degrees of freedom model. We have previously attempted to model the data of Fig. 1 with such a model (Puria, 1991b; Puria and Allen, 1994). However, that model proved unsatisfactory because the parameters depended on the measurement condition, which is nonphysical.

Another two-degrees of freedom model is the “two-piston model” for the human TM (Shaw, 1977; Shaw and Stinson, 1981, 1983; Goode *et al.*, 1994). The two-piston model has been tested only for frequencies up to approximately 8 kHz (Shaw and Stinson, 1981). To evaluate delays in the most recent incarnation of the two-piston model we have calculated the reflectance group delay in the Goode *et al.* (1994) model. Above 5 kHz the group delay is less than $30 \mu\text{s}$ in contrast to the approximately $100 \mu\text{s}$ measured in the cat ear (Fig. 3). Thus the two-piston model with parameters for the human ear does not appear to have the required delays for high frequencies and it therefore seems inconsistent with the cat middle-ear measurements. We feel the two-piston model needs further study.

2. Finite-element models

Most finite-element models of the middle ear have only been tested at low frequencies (Funnell and Laszlo, 1978; Funnell, 1983; Wada *et al.*, 1992). Very interesting is the work of Funnell *et al.* (1987) in which the magnitude of the umbo displacement, and points anterior and posterior, were

reported for frequencies up to 20 kHz. Their model calculations suggest that not all parts of the TM move with the same amplitude. However, the overall behavior of the TM is not evident from the calculations reported. It would be instructive to recompute the input impedance for the finite-element models for the conditions of Figs. 6 and 7. Wada *et al.* (1992) have made such calculations, but only for frequencies below 2 kHz. Other important measures, such as the middle-ear pressure gain, should also be calculated by loading the finite-element model with a cochlear load. One undesirable aspect of finite-element models is the large number of parameters that need to be estimated. The present finding of TM-delay imposes important model constraints and thus incorporating TM delay can help to greatly reduce the number of parameters in the finite-element models.

E. Mass of the ossicles

We next ask: Are the parameters for the mass of the ossicles used in the model reasonable? We chose these values by a global parameter search under the constraint that the ossicles form a matched segment of discrete transmission line. Lynch (1981, p. 236) measured the malleus mass to be 11.134 ± 0.627 mg, while the incus mass was 4.313 ± 0.328 mg. The malleus mass used in TM-delay models may be estimated from

$$M_m = \frac{M_m^w \kappa^2}{L_m^2}, \quad (19)$$

where M_m^w is the measured mass of the malleus, κ is the radius of gyration, and L_m is the length of the malleus. The numerator in Eq. (19) corresponds to the moment of inertia of the malleus. If one uses Lynch's (1981, pp. 231–233) estimate of 0.15 cm for κ , 0.4 cm for L_m (Wever and Lawrence, 1954), and $M_m = 0.37$ mg (Table AI), then the model M_m^w is 2.6 mg, which is a factor of 4.2 smaller than Lynch's average malleus mass. This factor might be accounted for by the smaller size animals used in the present study in comparison to those of Lynch *et al.* (1994). Another explanation might be differences in the radius of gyration between Lynch's measurements and those in the present study.

Lumped-parameter models typically have mass element values that are significantly greater than measured values. Examples 1 and 2 in Fig. 4(C) indicate that at low frequencies the lumped-parameter model is indistinguishable from models that have added delay (since they are both stiffness dominated). The higher frequency resonances are apparent due to the added delay [Fig. 4(C), examples 2 and 3]. The resonances appear as a quasi-periodic series of mass and stiffness dominated regions. In the past, modelers have used inductors and capacitors to represent mass and stiffness regions (e.g., Matthews, 1983; Kringlebotn, 1988; Puria, 1991; Puria and Allen, 1994). For instance, in Fig. 4(C) example 2, the impedance is masslike in the 2- to 6-kHz region. To account for this masslike impedance one could add a mass term to K_m to obtain a reasonable fit for frequencies below 6 kHz. However, this would result in a model that works only for frequencies below 6 kHz. In addition, this mass term

needs to be fairly large in comparison with measured mass of the ossicles. It is perhaps for these reasons that estimates of the malleus mass in previous middle-ear models (Peake and Guinan, 1967; Matthews, 1983; Puria, 1991b) have been approximately an order of magnitude greater⁹ than the mass estimated by the model with TM delay (Table AI). Thus in the model of Fig. 5(B), *mass has been traded for delay resulting in a middle-ear input impedance which is, consistent with experiments, not mass dominated at high frequencies* [Fig. 8(A) and (B)].

F. Pressure reflectance to power

Transforming the impedance to the reflectance domain allows for a much simpler description of a distributed system; the relative power transfer from a source to a load is equal to $1 - |R|^2$ (Carlin and Giordano, 1964; Siebert, 1970; Puria, 1991b; Voss and Allen, 1994), while the poles and zeros are described by the phase of R [Eq. (11)].

For the disarticulated stapes case almost all the energy is returned; the reflectance magnitude is between 0.8 and 1.0 for frequencies below 8 kHz. This means that the drum and ossicles are largely reactive, with a relative power absorption that is on the average less than $1 - 0.9^2 \approx 0.20$, or 20%. The TM is loaded by the stiffness of the malleus ligament and the stiffness of the incudo-malleolar joint. Losses seen in these measurements are probably due to damping in the ligaments and, at higher frequencies, to losses in the radiation load impedance.

For the drained cochlea, $1 - 0.8^2$ or 36% of the power is absorbed in the mid-frequency range. This implies that, to a first-order approximation, $36\% - 20\% = 16\%$ of the energy may be absorbed by the annular ligament in this frequency range.

For the intact case, and in the 1–6-kHz region, the pressure reflectance is less than 0.2. This means that $1 - 0.2^2 = 0.96$ is the fraction of the power absorbed. We conclude that more than $96\% - 36\% \approx 60\%$ of the power is absorbed by the cochlea.

G. Middle-ear pressure gain

In Fig. 10 the middle-ear pressure gain from the model is compared to measurements of the middle-ear pressure gain and of the round-window CM to ear-canal pressure ratio (CM/P_{ec}). For frequencies below approximately 8 kHz, the middle-ear pressure gain in the model is similar to the measured pressure gain, and has similar frequency dependence to CM/P_{ec} . However, the model gain is typically higher than both measurements for frequencies above 8 kHz. Possible reasons include: (1) nonpistonlike stapes motion or (2) inadequate representation of the cochlear load.

Dallos (1974) has noted that the magnitude of the CM transfer function, recorded with differential electrodes, and the magnitude of the scala-vestibule pressure (Nedzelnsky, 1974), are in good agreement for the 20-Hz to 2-kHz range. Our observations extend in frequency Dallos' observation.

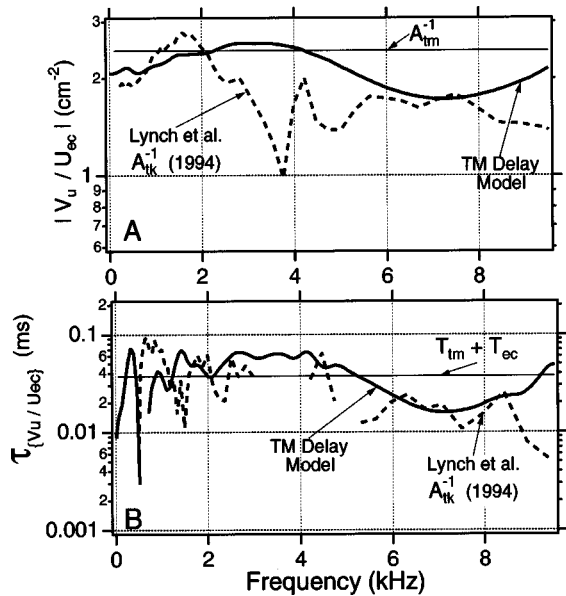


FIG. 11. Umbo-velocity to ear-canal volume-velocity ratio $V_u(\omega)/U_{ec}(\omega)$ in the “TM-delay model” is compared with A_{tk}^{-1} the reciprocal of the kinematic area reported by Lynch *et al.* (1994). (A) The magnitude of V_u/U_{ec} . The reciprocal of the area of the TM is labeled A_{tm}^{-1} . (B) The group delay calculated from the phase of V_u/U_{ec} . The sum of the delay in the TM transmission line T_{tm} and the delay in the residual ear-canal space T_{ec} is labeled $T_{tm} + T_{ec}$. For both the model calculations and the data, negative group delays have been omitted from the plot.

H. Umbo-velocity to ear-canal volume-velocity ratio

Another test of the tympanic membrane acoustic delay hypothesis is the umbo velocity V_u to the ear-canal volume-velocity U_{ec} ratio (V_u/U_{ec}), which can be expressed as the product of two measurable functions: (1) the umbo velocity to ear-canal pressure ratio, and (2) the middle-ear input impedance Z_{ec} . Namely

$$\frac{V_u}{U_{ec}} = \frac{V_u}{P_{ec}} Z_{me}, \quad (20)$$

which has dimensions of an inverse area (cm^{-2}) and is the reciprocal of the effective area of the tympanic membrane (e.g., Wever and Lawrence, 1954, Chap. 6,7; Møller, 1983, pp. 25–30).

The two measurements (V_u/P_{ec} and Z_{me}) have not been made in the same animals with the middle-ear cavities wide open. However, the product of the two measurements was reported by Lynch *et al.* (1994). In the Lynch *et al.* terminology, V_u/U_{ec} is the reciprocal of the kinematic area $1/A_{tk}$ of the tympanic membrane. For a piston model of the tympanic membrane A_{tk}^{-1} is A_{tm}^{-1} . Figure 11 shows V_u/U_{ec} for the TM-delay model and $1/A_{tk}$ from measurements. Not surprisingly, there are differences in the model and measurements in the 2–5-kHz region due to closed middle-ear cavity for the measurements. However, the measured group delay of $1/A_{tk}$ and model group delay of V_u/U_{ec} are consistent with our TM delay hypothesis. Measurements of V_u/U_{ec} from the same animals, with open MECs and at higher frequencies, are needed.

VII. SUMMARY

The present study reveals the presence of tympanic membrane acoustic delay in physiological measurements of the cat middle ear. The simplified TM-delay model presented here allows us to address one of the basic issues of the physical properties of the ear drum: *Is the tympanic membrane acting as a combination of stiffness and mass terms (lumped-element system), or does it act as a transmission line (distributed system)?* We conclude that to a first-order approximation the tympanic membrane may be represented as lossless transmission line with frequency-independent delay. Our model of a tympanic membrane delay structure, and the assumption of a matched impedance condition for the ossicles, allows effective coupling of sound to the inner ear over a much higher frequency range than would be otherwise possible.

The tympanic membrane delay model is used in a comprehensive middle-ear model [Fig. 5(B)] that describes a wide range of measurements, namely:

- middle-ear impedance and reflectance for the disarticulated stapes, drained cochlea, intact ossicles and cochlea,
- stapes displacement to ear-canal pressure ratio,
- middle-ear pressure transfer function,
- umbo velocity to ear-canal volume-velocity ratio.
- incudo-malleolar joint slippage, and
- incudo-stapedial joint slippage.

All the model calculations to 25 kHz use a single set of parameters. Above a few kHz, measurements and model calculations critically depend on our hypothesis that tympanic membrane acoustic delay is large in comparison with delay in other middle-ear structures.

ACKNOWLEDGMENTS

We thank Paul Fahey, Patricia Jeng, Douglas H. Keefe, William T. Peake, John J. Rosowski, Christopher A. Shera, M. Mohan Sondhi, Neshie Tiwari, Arnold Tubis, and Susan Voss. They have helped shape this manuscript over the past few years. We specially thank J. Tonndorf who was our

TABLE AI. Estimated parameters for the cat middle-ear model of Fig. 5(B). The form of the first seven functions (Z_m to Z_{rw}) is $Z = R + K/j\omega + j\omega M$. The units for mechanical impedances, denoted by superscript “m” in column 2, are: R (dyne-s/cm), K (dyn/cm), and M (g). The units for acoustical impedances, denoted by superscript “a” in column 2, are: R (dyne-s/cm⁵), K (dyn/cm⁵), and M (g/cm⁴). The radiation load impedance of the vented middle-ear cavity is given by Eq. (12).

Description	Symbol	R	K	M
Malleus	Z_m^m	4	1.5×10^5	3.7×10^{-4}
IM joint	Z_{imj}^m	1	3.3×10^7	0
Incus	Z_i^m	0	0	1.1×10^{-4}
IS joint	Z_{isj}^m	10	6.6×10^8	0
Annular ligament	Z_{al}^a	1×10^5	5.3×10^9	0
Stapes	Z_s^a	0	0	3.3
Round window	Z_{rw}^a	0	1.2×10^8	0
Radiation load	Z_{rl}^a	160	...	5.6×10^{-3}
Eardrum delay	$T_{tm} = 35.72 \mu\text{s}$			

teacher and colleague. Many of our experimental techniques regarding the modifications to the ear were developed under his guidance. Support for author SP came in part from Grant Nos. F32 DC00073, R03 DC02677, PO1 DC00119, and R29 DC03085 of the National Institute on Deafness & Other Communication Disorders of the National Institutes of Health.

APPENDIX: MODEL PARAMETERS AND SENSITIVITY ANALYSIS

A. Tympanic membrane delay model parameters

The middle-ear parameters for the tympanic membrane delay model of Fig. 5(B) were first estimated for the simplest case of the disarticulated stapes. An automatic search algorithm was used to estimate the parameters from the measured impedance Z_{ds} for this case. Additional parameters were then estimated for the case of the drained cochlea, while holding the established parameters fixed. Finally, calculations were

made for the intact case by loading the drained cochlea model with a cochlear load (Puria and Allen, 1991). In all cases, once each parameter was established, it was not allowed to change for the next more complex case. The parameters used in this model are shown in Table AI.

B. Sensitivity analysis of the TM-delay model

The sensitivity of the tympanic membrane delay model to parameter changes was estimated by computing the ear-canal impedance and reflectance before and again after increasing and decreasing each parameter by a factor of 3. Calculations for six of the eight parameters used in the minimization procedure, for the disarticulated stapes case, are shown in Fig. A1. The incus mass (M_i) has a sensitivity similar to that of M_m , while Z_{ds} is insensitive to changes in R_{jim} and thus are not shown.

To quantify the effect of changes in model parameters we estimate the rms error in both the log magnitude and

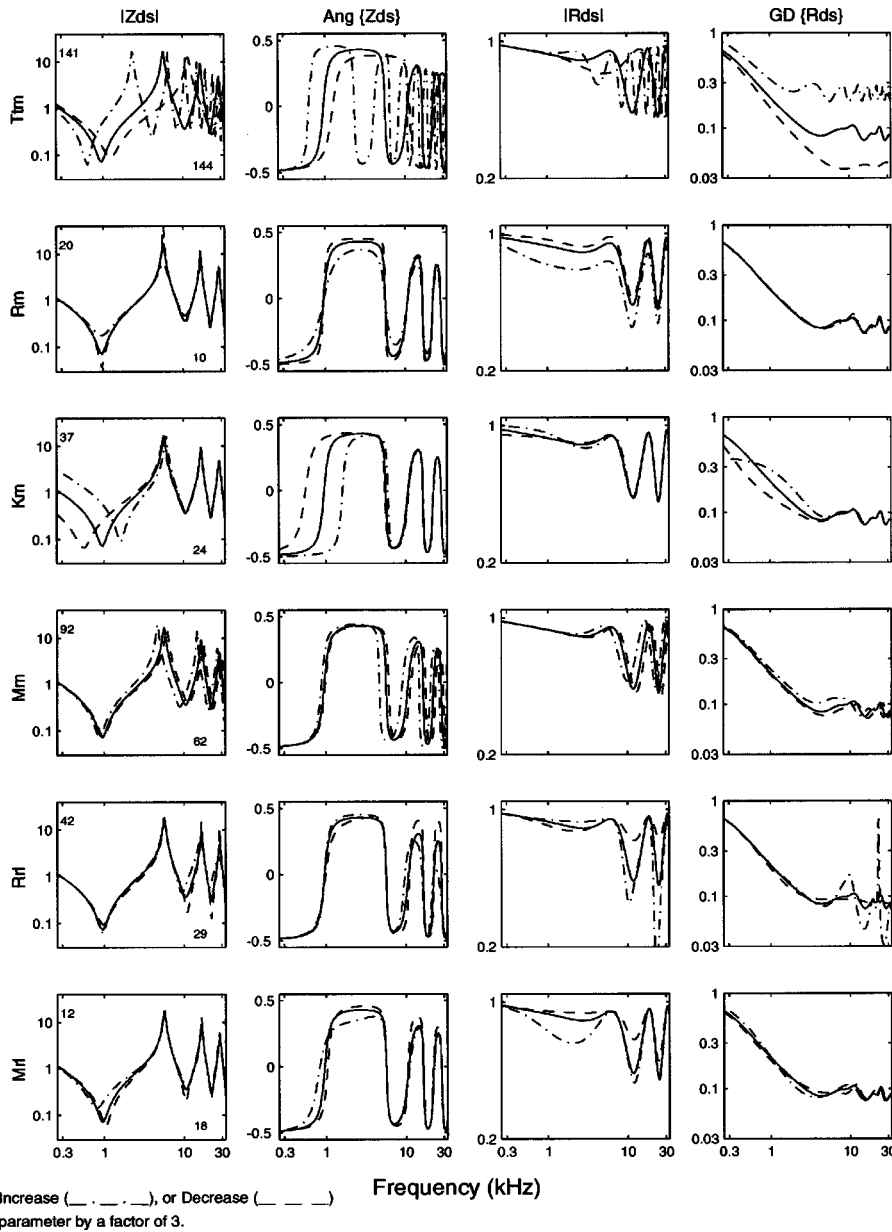


FIG. A1. Sensitivity of the tympanic membrane delay model (disarticulated stapes case) to a parameter increase and decrease by a factor of 3. In all plots, the solid line indicates the model calculated with parameters from Table AI. Model computations with the increased parameter are plotted with a dash-dot line (— · — · —), while calculations with the decreased parameter are plotted with a dashed line (— — —). The first and second columns show the normalized impedance magnitude and angle (rad/π), while the third and fourth columns show the (dimensionless) reflectance magnitude and group delay (ms). The frequency range is from 300 Hz to 30 kHz. The parameter varied for a given row is indicated on the left side of the row. For example, in row 1 the tympanic membrane delay T_{tm} is varied. The total error in the impedance magnitude and phase [Eq. (A3)], due a variation in parameter, is indicated in each plot of column one (labeled $|Z_{ds}|$). The number on the upper-left side indicates the error due to an increase in the respective parameter, while the number on the lower-right side indicates the error due to a decrease in the respective parameter.

TABLE AII. Parameters estimated for the middle-ear cavity delay model [Fig. 5(B) and (C)]. The form of the functions in Table AI.

Description	Symbol	R	K	M
Malleus	Z_m^m	5×10^{-11}	1.7×10^5	3.2×10^{-5}
IM joint	Z_{mj}^m	1	3.9×10^8	0
Incus	Z_i^m	0	0	3.1×10^{-2}
Radiation load	Z_{rl}^a	90.4	...	6.4×10^{-3}
Middle-ear cavity	$L_{mec} = 1.4$ cm $D_{mec} = 0.35$ cm			

phase of the impedance as a function of model parameters. The rms error in the log impedance magnitude domain is

$$\varepsilon_m = \sqrt{\frac{1}{N_f} \sum_{i=1}^{N_f} \{100[\log_{10}|Z_{ds}(\omega_i)| - \log_{10}|\bar{Z}_{ds}(\omega_i)|]\}^2}. \quad (\text{A1})$$

The rms error in the phase of the impedance is

$$\varepsilon_p = \sqrt{\frac{1}{N_f} \sum_{i=1}^{N_f} [\angle Z_{ds}(\omega_i) - \angle \bar{Z}_{ds}(\omega_i)]^2}, \quad (\text{A2})$$

where the impedance angle is in degrees.

The total error in the impedance domain is

$$\varepsilon_z = \varepsilon_p + \varepsilon_m. \quad (\text{A3})$$

In the above equations Z_{ds} is the model impedance with normal parameters (Table AI) and \bar{Z}_{ds} is for the model impedance with modified parameters. The factor of 100 in Eq. (A1) introduces a weighting factor that gives approximately equal weights to the magnitude and phase of the error in Eq. (A3). The error function ε_z was evaluated on a log-frequency axis. The minimization procedure used to estimate the middle-ear model parameters depended on the error function described by Eq. (A3).

In Fig. A1, ε_z due to an increase in the parameter is indicated in the upper left corner, while ε_z due to a decrease in the parameter is indicated in the lower right corner of the first column. For reference, if $|\bar{Z}_{ds}| = 1$ and $\angle \bar{Z}_{ds} = 0$, then ε_z is just a little more than 100. Figure A1 shows that the TM-delay model is most sensitive to the TM-delay T_{tm} and the malleus mass M_m . This is primarily because both T_{tm} and M_m have a broadband effect on the ear-canal impedance, whereas the other parameters have their greatest effect either at low frequencies (R_m, K_m, M_{rl}), or at high frequencies (R_{rl}).

For the drained cochlea case, the sensitivity of the model to changes in K_{al} and R_{al} is similar to changes in K_m and R_m , respectively.

C. Middle-ear cavity model parameters

As in the TM-delay model, the parameters for the middle-ear cavity model [Fig. 5(B) and (C)] were also estimated for the disarticulated stapes case using the same methods described above. The optimum parameters found for the disarticulated stapes case are listed in Table AII. A sensitivity analysis (like that shown in Fig. A1) shows that a perturbation (by a factor of 2–3) of the parameters listed in Table

AII resulted in a significant change in ear-canal impedance. Parameter R_m , required a much a significantly larger perturbation.

Another important parameter is the length of the middle-ear cavity L_{mec} because the delay in the middle-ear cavity is a function of this length. Here L_{mec} was estimated to be 1.4 cm by the search procedure. Although the dimensions of the tympanic cavity and the bulla cavity are irregular, this length estimate is consistent with reported dimensions of the cat middle ear cavities (Huang *et al.*, 1997). Based on this length, and volumetric measurements of middle-ear space of the cat (Huang *et al.*, 1997), the effective diameter the cat middle-ear cavity D_{mec} should be approximately 0.9 cm. A diameter of 0.35 cm, found by the minimization procedure, is much smaller than the expected value.

¹The four-load calibration method requires that the impedances of the four loads be different at all frequencies by carefully choosing the lengths of the four calibration cavities (Allen, 1986; Voss and Allen, 1994). The lengths of the cavities used for the measurements reported here were such that the impedances of the four cavities were very close to each other in the 15–16-kHz frequency region. As a result calibration errors are larger in that frequency region.

²Ear 1, ear 2, and ear 3 here correspond to C82-L, C88-L, and C88-R, respectively.

³Measurements on ear 1 were previously reported (Allen, 1986). We choose this ear based on several criteria, designed to select the pristine ear. The best predictor we have found of the undamaged ear is a visually transparent TM (Stinson and Khanna, 1994).

⁴The tenth-order filter coefficients were truncated to a length of 65 in the time domain.

⁵Although not shown here, a few impedance measurements made after removing the TM confirm that the functional form of Eq. (12) is approximately correct.

⁶When drained, air replaces the perilymph of the inner ear. The characteristic impedance of the cochlea at the stapes is

$$Z_{c_0} = \sqrt{\frac{4\rho_0 K'_0}{S_0}},$$

given the assumption that viscous and thermal effects are insignificant when the cochlea is air filled. Using $\rho_0 = 1.18 \times 10^{-3}$ g/cm³ for the density of air, $K'_0 = 1.7 \times 10^9$ dyn/cm⁴ for the BM stiffness at the base, and $S_0 = 0.02$ cm² for the area at the base of the cochlea, we obtain $Z_{c_0} \approx 2 \times 10^4$ dyn-s/cm⁵. Lynch *et al.*'s (1982) experimental averaged value for R_{al} is 2×10^5 ; an order of magnitude greater than Z_{c_0} . Thus the impedance of the air filled cochlea represents an insignificant load to the stapes in the drained cochlea case [Puria and Allen, 1991, Eq. (6a)].

⁷The CM sensitivity at 1 kHz is about 1 mv/Pa (Allen, 1983). The CM magnitude was multiplied by 86 and then converted to dB.

⁸Zwislocki (1962, p. 1517) postulated that at high frequencies the motion of the TM could perhaps be represented by a transmission line.

⁹The acoustic mass of the malleus in three previous models of the cat middle ear are: 0.04 g/cm⁴ (Matthews, 1983), 0.022 g/cm⁴ (Peake and Guinan, 1967), and 0.013 g/cm⁴ (Puria, 1991b). The mechanical mass of malleus transformed to the ear canal side of the TM, where it can be measured, is referred to as the acoustic mass. The relationship between acoustical mass and mechanical mass is: $M_a^m = A_{tm}^2 M_m^a$. For a TM area of 0.41 cm² (Table AI) the mechanical mass for the three models is 6.7, 3.7, and 2.2 mg, respectively.

Allen, J. B. (1983). "Magnitude and phase-frequency response to single tones in the auditory nerve," *J. Acoust. Soc. Am.* **73**(6), 2071–2092.

Allen, J. B. (1986). "Measurement of eardrum acoustic impedance," in *Peripheral Auditory Mechanisms*, edited by J. B. Allen, J. L. Hall, A. Hubbard, S. T. Neely, and A. Tubis (Springer-Verlag, New York), pp. 44–51.

Békésy, G. (1960). *Experiments in Hearing* (McGraw-Hill, New York).

Beranek, L. L. (1954). *Acoustics* (McGraw-Hill, New York).

- Carlin, H. J., and Giordano, A. B. (1964). *Network Theory—An Introduction to Reciprocal and Nonreciprocal Circuits* (Prentice-Hall, Englewood Cliffs, NJ).
- Dallos, P. (1970). “Low-frequency auditory characteristics: Species dependence,” *J. Acoust. Soc. Am.* **48**, 489–499.
- Dallos, P. (1974). “Comments,” in *Facts and Models in Hearing*, edited by E. Zwicker and E. Terhardt (Springer-Verlag, New York), p. 54.
- Décory, L. (1989). “Origins of interspecific differences in susceptibility to noise,” Ph.D. thesis, The University of Bordeaux II.
- Flanagan, J. L. (1962). “Computational model for basilar-membrane displacement,” *J. Acoust. Soc. Am.* **34**, 1370–1376.
- Funnell, W. R. J. (1983). “On the undamped natural frequencies and mode shapes of a finite-element model of the cat eardrum,” *J. Acoust. Soc. Am.* **73**, 1657–1661.
- Funnell, W. R. J., and Laszlo, C. A. (1978). “Modeling of the cat eardrum as a thin shell using the finite-element method,” *J. Acoust. Soc. Am.* **63**, 1461–1466.
- Funnell, W. R. J., Decraemer, W. F., and Khanna, S. M. (1987). “On the damped frequency response of a finite-element model of the cat eardrum,” *J. Acoust. Soc. Am.* **81**, 1851–1859.
- Giacoletto, L. J. (1977). *Electronic Designers’ Handbook* (McGraw-Hill, New York), 2nd ed.
- Goode, R., Killion, M., Nakamura, K., and Nishihara, S. (1994). “New knowledge about the function of the human middle-ear: development of an improved analog model,” *Am. J. Otolaryngol.* **15**(2), 145–154.
- Guinan, J., and Peake, W. T. (1967). “Middle-ear characteristics of anesthetized cats,” *J. Acoust. Soc. Am.* **41**, 1237–1261.
- Huang, G. T., Rosowski, J. J., Flandermeyer, D. T., Lynch, T. J., III, and Peake, W. T. (1997). “The middle ear of a lion: Comparison of structure and function to domestic cat,” *J. Acoust. Soc. Am.* **101**, 1532–1549.
- Keefe, D. H., Ling, R., and Bulen, J. C. (1992). “Method to measure acoustic impedance and reflection coefficient,” *J. Acoust. Soc. Am.* **91**, 470–485.
- Keefe, D. H., Bulen, J. C., Arenhart, K. H., and Burns, E. M. (1993). “Method to measure acoustic impedance and reflection coefficient,” *J. Acoust. Soc. Am.* **94**, 2617–2638.
- Khanna, S. M., and Tonndorf, J. (1972). “Tympanic membrane vibrations in cats studied by time-averaged holography,” *J. Acoust. Soc. Am.* **51**, 1904–1920.
- Kringlebotn, M. (1988). “Network model for the human middle ear,” *Scand. Audiol.* **17**, 75–85. Lync
- h, T. J. (1981). “Signal processing by the cat middle ear: Admittance and transmission, measurements and models,” Ph.D. thesis, MIT.
- Lynch, T. J., Nedzelnitsky, V., and Peake, W. T. (1982). “Input impedance of the cochlea in cat,” *J. Acoust. Soc. Am.* **72**, 108–130.
- Lynch, T. J., Peake, W. T., and Rosowski, J. J. (1994). “Measurements of the acoustic input impedance of cat ears: 10 Hz to 20 kHz,” *J. Acoust. Soc. Am.* **96**, 2184–2209.
- Matthews, J. W. (1983). *Modeling Reverse Middle Ear Transmission of Acoustic Distortion Signals* (Delft U.P., Delft, The Netherlands), pp. 11–18.
- Møller, A. R. (1965). “An experimental study of the acoustic impedance of the middle ear and its transmission properties,” *Acta Oto-Laryngol.* **60**, 129–149.
- Møller, A. R. (1983). *Auditory Physiology* (Academic, New York).
- Nedzelnitsky, V. (1974). “Measurements of sound pressure in the cochlea of anesthetized cats,” in *Facts and Models in Hearing*, edited by E. Zwicker and E. Terhardt (Springer Verlag, New York), pp. 45–53.
- Nedzelnitsky, V. (1980). “Sound pressures in the basal turn of the cat cochlea,” *J. Acoust. Soc. Am.* **68**, 1676–1689.
- Nuttall, A. L. (1974). “Measurements of the guinea-pig middle-ear transfer characteristic,” *J. Acoust. Soc. Am.* **56**, 1231–1238.
- Olson, E. S. (1998). “Observing middle and inner ear mechanics with novel intracochlear pressure sensors,” *J. Acoust. Soc. Am.* **103**, 3445–3463.
- Onchi, Y. (1961). “Mechanism of the middle ear,” *J. Acoust. Soc. Am.* **33**, 794–805.
- Papoulis, A. (1962). *The Fourier Integral and its Applications* (McGraw-Hill, New York).
- Peake, W., and Guinan, J. (1967). “Circuit model for the cat’s middle ear,” MIT Research Laboratory of Electronics, Quarterly Prog. Rep. No. 84, 320–326.
- Puria, S. (1991a). “A physical model for the middle-ear cavity,” *J. Acoust. Soc. Am.* **89**, 1864.
- Puria, S. (1991b). A theory of cochlear input impedance and middle ear parameter estimation, Ph.D. thesis, The City College, CUNY.
- Puria, S., and Allen, J. B. (1989). “Impedance measurements in the ear canal,” *J. Acoust. Soc. Am.* **86**, S44.
- Puria, S., and Allen, J. B. (1991). “A parametric study of cochlear input impedance,” *J. Acoust. Soc. Am.* **89**, 287–309.
- Puria, S., and Allen, J. B. (1992). “SYSid—audio-band measurement and analysis system,” *J. Acoust. Soc. Am.* **92**, 2469.
- Puria, S., and Allen, J. B. (1994). Unpublished observations.
- Puria, S., and Allen, J. B. (1996). “Cat middle-ear measurements and model: Evidence of acoustic delay in the tympanic membrane,” *Assn. for Research in Oto-Laryngology Abstracts*.
- Puria, S., Peake, W., and Rosowski, J. (1997). “Sound-pressure measurements in the cochlear vestibule of human-cadaver ears,” *J. Acoust. Soc. Am.* **101**, 1–17.
- Puria, S., Rosowski, J. J., and Peake, W. (1993). “Middle-ear pressure gain in humans: preliminary results,” in *Biophysics of Hair Cell Sensory Systems*, edited by H. Duifhuis, J. Horst, P. van Dijk, and S. van Netten (World Scientific, Singapore), pp. 345–351.
- Rabbitt, R. D., and Holmes, M. H. (1986). “A fibrous dynamic continuum model of the tympanic membrane,” *J. Acoust. Soc. Am.* **80**, 1716–1728.
- Rabbitt, R. D., and Holmes, M. H. (1988). “Three-dimensional acoustic waves in the ear canal and their interaction with the tympanic membrane,” *J. Acoust. Soc. Am.* **83**(3), 1064–1080.
- Shaw, E. A. G. (1977). “Eardrum representation in middle-ear acoustical networks,” *J. Acoust. Soc. Am.* **62**, E5.
- Shaw, E. A. G., and Stinson, M. R. (1981). “Network concepts and energy flow in the human middle ear,” *J. Acoust. Soc. Am.* **69**, S44.
- Shaw, E. A. G., and Stinson, M. R. (1983). *The Human External and Middle Ear: Models and Concepts* (Delft U.P., Delft, The Netherlands), pp. 3–10.
- Shera, C. A., and Zweig, G. (1991). “Phenomenological characterization of eardrum transduction,” *J. Acoust. Soc. Am.* **90**, 253–262.
- Shera, C. A., and Zweig, G. (1993). “Noninvasive measurement of the cochlear traveling-wave ratio,” *J. Acoust. Soc. Am.* **93**, 3333–3352.
- Siebert, W. T. (1970). “Simple model of the impedance matching properties of the external ear,” MIT Research Laboratory of Electronics, Quarterly Prog. Rep. No. 96, 236–242.
- Stinson, M. R., and Khanna, S. M. (1994). “Spatial distribution of sound pressure and energy flow in the ear canals of cats,” *J. Acoust. Soc. Am.* **96**, 170–180.
- Tonndorf, J., and Pastaci, H. (1986). “Middle ear sound transmission: A field of early interest to Merle Lawrence,” *Am. J. Otolaryngol.* **7**, 120–129.
- Voss, S. E., and Allen, J. B. (1994). “Measurement of acoustic impedance and reflectance in the human ear canal,” *J. Acoust. Soc. Am.* **95**, 372–384.
- Wada, H., Metoki, T., and Kobayashi, T. (1992). “Analysis of dynamic behavior of human middle ear using a finite-element method,” *J. Acoust. Soc. Am.* **92**, 3157–3168.
- Wever, E. G., and Lawrence, M. (1950). “The acoustic pathways to the cochlea,” *J. Acoust. Soc. Am.* **22**, 460–467.
- Wever, E. G., and Lawrence, M. (1954). *Physiological Acoustics* (Princeton U.P., Princeton, NJ).
- Zwislocki, J. (1962). “Analysis of the middle-ear function. Part I: Input impedance,” *J. Acoust. Soc. Am.* **34**, 1514–1523.
- Zwislocki, J. (1963). “Analysis of the middle-ear function. Part II: Guinea-pig ear,” *J. Acoust. Soc. Am.* **35**, 1034–1040.

Low-level steady-state auditory evoked potentials: Effects of rate and sedation on detectability

Robert A. Dobie^{a)} and Michael J. Wilson

Department of Otolaryngology—Head & Neck Surgery, The University of Texas Health Science Center, 7703 Floyd Curl Drive, San Antonio, Texas 78284-7777

(Received 4 February 1998; revised 10 September 1998; accepted 11 September 1998)

Steady-state auditory evoked potentials (SSAEPs) in alert adults are most detectable at stimulus or modulation rates of about 40 Hz. Sedation reduces the detectability of 40-Hz SSAEPs and increases it for higher rate SSAEPs. This study examined whether rates higher than 40 Hz would be preferable for detecting responses to low-intensity tones in sedated adults. Fourteen normal adults listened to 640-Hz tones at modulation rates (and toneburst rates) of 20–160 Hz, in 10-Hz steps, at levels of 38 and 58 dB peak equivalent sound-pressure level (peSPL) (20 and 40 dB normal hearing level (nHL) for amplitude-modulated (AM) tones), both alert and sedated (1–2 g chloral hydrate). Sedation reduced both signal (SSAEP) power and noise power at all rates, but noise power reduction was greater for higher rates. Detectability in the alert condition was always greatest at 40 Hz. Under sedation, a second detectability peak was present at 90 Hz for 58-dB peSPL tones, approximately equal to that seen at 40 Hz. At 38 dB peSPL (sedated), peak detectability moved from 40 to 50 Hz. These results suggest that presentation/modulation rates around 40 Hz may be optimal for SSAEP detectability at low levels in adults, whether alert or sedated. © 1998 Acoustical Society of America. [S0001-4966(98)05412-5]

PACS numbers: 43.64.Ri, 43.64.Qh [RDF]

LIST OF SYMBOLS

$\hat{}$	[superscripted] unbiased estimate made from actual measurements
Ω	ohm
μV	microvolt
ABR	auditory brainstem response
AM	amplitude-modulated
ANOVA	analysis of variance
ANSI	American National Standards Institute
dB	decibel
EEG	electroencephalogram
EFF	detection efficiency
f_m	frequency of modulation
HL	hearing level
Hz	Hertz
kHz	kilohertz
MLR	middle-latency response
MP	mean power (average power of the subaverages)

MSC	magnitude-squared coherence
ms	millisecond
nHL	normal hearing level
p	statistical measure of probability
p-p	peak-to-peak
peSPL	peak-equivalent sound pressure level
PM	power of the mean (grand average power)
P_n	noise power
P_s	signal power
q	number of subaverages
rms	root-mean-square amplitude ($\sqrt{\text{power}}$)
s.d.	standard deviation
s	second
SNR	signal-to-noise ratio
SPL	sound-pressure level
SSAEPs	steady-state auditory evoked potentials

INTRODUCTION

Steady-state auditory evoked potentials (SSAEPs) are increasingly used for threshold estimation because they can be recorded at low sensation levels using relatively frequency-specific stimuli across the speech frequency range, and can be objectively detected using statistical tests. For clinical use, it is important to know the effects of parameters such as subject state and stimulus rate.

SSAEPs can be recorded using amplitude-modulated

(AM) tones or impulsive stimuli such as clicks and tonebursts. In either case, for awake adults, the best rate (of presentation or modulation) appears to be about 40 Hz (Galambos *et al.*, 1981; Kuwada *et al.*, 1986). While some authors report that SSAEP amplitude may be greater at much lower frequencies (e.g., Rees *et al.*, 1986), such reports have not considered the markedly higher background EEG noise levels at frequencies below about 20 Hz, and there are no data suggesting that SSAEPs are more *detectable* at frequencies lower than 40 Hz.

Infants and very young children are different, both developmentally and because they are usually tested in natural

^{a)}Electronic mail: dobie@uthscsa.edu

or sedated sleep. Several reports have shown that 40-Hz SSAEPs are harder to record in young children, and that optimal rates are in the 80–100-Hz range (Levi *et al.*, 1993; Aoyagi *et al.*, 1993; Rickards *et al.*, 1994), at least for moderate levels (50–60 dB re: normal hearing level, or nHL).

State effects are apparent for adults tested asleep or sedated; 40-Hz SSAEPs are smaller than in the awake state but may not be less detectable, because background noise levels are also reduced (e.g., Linden *et al.*, 1985; Levi *et al.*, 1993). Nevertheless, using moderate levels and statistical response detection, sedated adults show better SSAEP detectability at 80 Hz than at 40 Hz (Levi *et al.*, 1993; Aoyagi *et al.*, 1993).

Since SSAEPs are used extensively for threshold estimation, it is important to know how detectability is affected by state and rate at low stimulus intensity levels (defined for the purposes of this paper as 40 dB nHL or less). Cohen, Rickards, and Clark (1991) presented AM tones binaurally at 30 dB nHL to both awake and sleeping adult subjects, and concluded that “for sleeping subjects, modulation frequencies above 70 Hz may be best when using steady-state potentials for hearing threshold estimation.” Our primary goal in this project was to test this finding using low-frequency tones (our results suggest instead that 40–50 Hz remains optimal for sedated adults).

Secondary goals included comparing SSAEPs elicited by tonebursts to those elicited by AM tones (with AM tones, rate and rise time are necessarily confounded, while tonebursts of varying rate can have constant rise times) and determining whether individual subjects had different best rates. Finally, we wished to independently assess sedation effects on signal power and noise power across a range of rates.

I. MATERIALS AND METHODS

A. Subjects

Fourteen adults (seven male, seven female) ranging in age from 22 to 30 years, all had right-ear hearing sensitivity better than 15 dB HL (ANSI, 1996) at octave frequencies from 0.25 to 8 kHz, and also at 0.75 kHz, the audiometric test frequency closest to our stimulus carrier frequency of 0.64 kHz (see below). Each participated in four to six sessions. In “alert” sessions, subjects sat in an erect armchair and either read or worked crossword puzzles. In “sedated” sessions, subjects took 1–2 g of chloral hydrate orally, the armchair was tilted back to a supine position, and the room was darkened; data collection did not begin until subjects were asleep. Identification of a “sleep” state was based on (1) contrasts between relaxed–waking ongoing EEG and markedly lower levels after sedation took effect, as monitored by both audio (EEG routed to a loudspeaker in the control booth) and visual (EEG oscilloscope trace) observations, (2) slow, rhythmic breathing pattern characteristic of true sleep, as monitored via a microphone placed next to the subject’s head. During sedation sessions, each subject exhibited occasional brief (20–90 s duration) elevations of state (abrupt, deep inhalation and slight self-repositioning in the chair, followed by resumption of the clearly diminished activity levels which had preceded); data collection was manu-

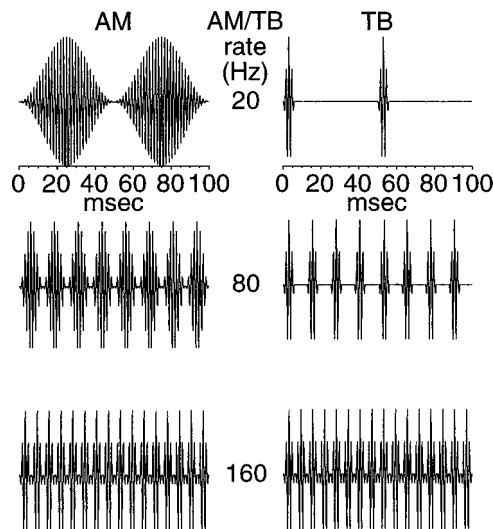


FIG. 1. Waveforms of AM tones and tonebursts (TB) delivered to transducer, for three different rates.

ally interrupted during these episodes. There were two instances of failure to achieve true sleep, one probably due to Prozac (an antidepressant drug), and the other probably due to prior excessive caffeine intake; both subjects were rescheduled at times when the drugs were not present, and subsequently underwent normal sedation sessions. There were a few instances (usually coincident with increased bladder pressure) where the brief self-repositioning described above was not followed by drifting back to true sleep levels. Afternoon sedation sessions tended to run more smoothly than morning sessions, probably due to subjects’ natural internal “nap-time” inclinations.

B. Stimuli

640-Hz tones were synthesized as the 64th harmonic in a 100-ms stimulus sequence (fundamental frequency=10 Hz). These tones were sinusoidally amplitude-modulated at rates (f_m) varying in 10-Hz steps from 20–160 Hz. A single modulation cycle at $f_m = 160$ Hz had a duration of 6.25 ms (rise time=3.125 ms) and was also used as a toneburst, presented at rates of 20–160 Hz. Thus, at each rate, there was both an AM tone, with rise time determined by f_m , and a toneburst, with a fixed rise time. At 160 Hz, of course, these were identical (Figs. 1 and 2).

Stimuli were filtered (480 to 800 Hz, 48 dB/octave) and the AM tones were presented to the right ear at levels of 38 and 58 dB peak-equivalent SPL (peSPL) (20 and 40 dB re: normal threshold). Our subjects’ thresholds for 640 Hz AM tones averaged 18 dB peSPL (s.d.=4 dB), without any effect of modulation frequency. For tonebursts, peak levels were constant (and equal to those used for AM tones); as expected, thresholds were up to 10 dB higher as the toneburst rate dropped from 160 to 20 Hz. Thus, for the tonebursts presented at 20/s, our two presentation levels (38 and 58 dB peSPL) were equivalent to 10 and 30 dB nHL, respectively (see Stapells *et al.*, 1982, for a discussion of behavioral threshold versus rate for transient stimuli).

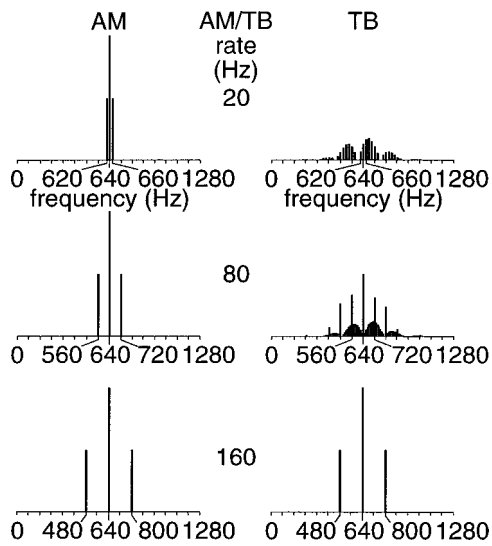


FIG. 2. Amplitude spectra of stimuli shown in Fig. 1.

C. Recording and analysis

Gold-plated cup electrodes were attached to the scalp at vertex (active), ipsilateral mastoid (reference), and contralateral mastoid (ground), and impedances were all $<3 \text{ k}\Omega$ at 30 Hz. Scalp potentials were amplified ($\times 200\,000$), filtered (10 to 1000 Hz), then digitized at 2.564 kHz. Response filter slope was 6 dB/octave. Artifact rejection was performed with a criterion value of $\pm 10 \mu\text{V}$, resulting in response rejection approximately 2% of the time. Each response sequence was 100 ms long, and data for each run were collected continuously for 204.8 s (2048 sweeps of the response sequence). These were subdivided into 16 contiguous subaverages, each containing 12.8 s of data.

For each run, magnitude-squared coherence (MSC) was calculated for the frequency of interest (the modulation or toneburst presentation rate). MSC is equal to the power of the mean or grand average (PM) divided by the mean power of the subaverages (MP), varies from 0 (no signal, all noise) to 1 (all signal, no noise), and can be used as a statistic for objective response detection (Dobie and Wilson, 1989). For example, when using 16 subaverages, MSC values above 0.266 can be accepted as significant at the 0.01 alpha level. In addition, unbiased estimates of signal and noise power (at the grand average level) were calculated at the same frequency (Dobie and Wilson, 1990):

$$\hat{P}_s = \frac{1}{15}(16\text{PM} - \text{MP}), \quad (1)$$

$$\hat{P}_n = \frac{1}{15}(\text{MP} - \text{PM}). \quad (2)$$

Figure 3 shows time-domain responses from three sedated subjects to AM tones modulated at 40, 80, and 160 Hz. Each response has been displayed in “split-halves” format to show replication; the solid and dashed curves each represent data from eight subaverages. The MSC values to the right all are highly significant at the 0.01 level. The signal power estimates are all 15–20 dB higher than the noise power estimates, and the unbiased signal-to-noise ratio estimates (SNRs) are obtained by subtraction (but are also easily

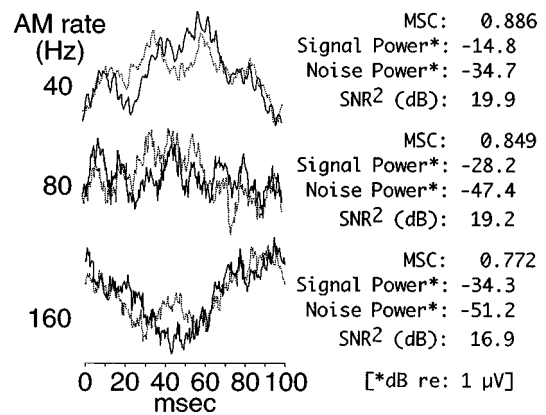


FIG. 3. Replicated time-domain responses of three sedated subjects to AM tones at 58 dB peak-equivalent SPL, at three different modulation rates. MSC, signal power, and noise power are estimated as described in the text.

calculated as a function of MSC, where q equals the number of subaverages):

$$\text{SNR}(\text{dB}) = 10 \log \left(\frac{q\text{MSC} - 1}{1 - \text{MSC}} \right). \quad (3)$$

It should be noted that the signal power estimates are unbiased, i.e., they have been calculated so that they are as likely to overestimate as to underestimate the true signal power (which could be measured directly only in the absence of noise). When there is no signal present at all, signal power estimates are as likely to be negative as positive; they are unbiased with respect to the true signal power of zero. The simplest way to obtain unbiased signal and noise power estimates is to record separately under conditions of no stimulus (noise only) and stimulus (signal and noise both may be present); noise power is estimated from the former record, signal power by the difference in power between the two records. Obviously, in the absence of any signal, or even when true signal power is low compared to random fluctuations in sampled noise power, such signal power estimates are often negative. Our technique has two advantages over the conceptually simpler technique of separate recordings: first, we save time by estimating signal and noise powers from the same data set; second, the effects of nonstationarities in noise power, such as those caused by changes in subject state, are reduced. The technique of separate recordings assumes the noise is stationary, but if the subject is alert during one recording (high EEG noise) and relaxed or asleep in the next (low EEG noise), the signal power estimate obtained by subtraction will be grossly and spuriously increased or decreased, depending on which recording included stimulus presentation.

Each subject had eight complete response sets across the range of rates from 20–160 Hz: two levels (38 and 58 dB peSPL) by two stimulus types (AM tones and tonebursts) by two states (alert and sedated). Figure 4 shows one subject’s MSC values for two of these response sets (AM tones and tonebursts, sedated, 58 dB) to illustrate our method of estimating “best rates.” Based on the frequent finding (seen also in the group average data) of bimodality in MSC-rate functions, we defined rates of 20–60 Hz as “low” and rates of 70–160 Hz as “high.” In the example shown, the best

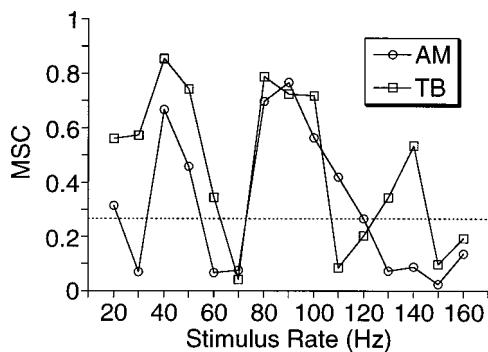


FIG. 4. MSC as a function of modulation rate for AM tones and tonebursts (TB) (58 dB peak-equivalent SPL) in the sedated state for one subject. The dotted line indicates the critical value above which an MSC value can be considered significant at the 1% level.

low rate is 40 Hz for both stimulus types. The best high rates are 80 Hz for tonebursts and 90 Hz for AM tones.

Analysis of variance (ANOVA) was used to determine whether there were significant effects of rate, sedation, gender, stimulus type (AM vs toneburst), or level on MSC, signal power, and noise power. In addition, ANOVAs were performed to determine whether there were effects of sedation, gender, stimulus type, or level on best low rate and best high rate (i.e., the rates yielding the highest MSC values for an individual subject). Because of the large number of variables and interactions under consideration, only p values less than 0.01 were considered *a priori* to be significant, with values between 0.01 and 0.05 considered suggestive. Gender effects were never significant, alone or in interaction, and will not be further discussed.

II. RESULTS

Figure 5 shows MSC averaged across subjects as a function of stimulus rate for each of the eight conditions. All MSC values were averaged, whether or not they exceeded the arbitrary critical value ($p < 0.01$) of 0.266. ANOVA showed highly significant effects ($p < 0.0001$) for level and rate: MSC is obviously higher, and SSAEPs are thus more detectable, at 58 dB than at 38 dB, and rate effects are equally obvious, with low MSC values above 100 Hz. Highly significant interaction effects were seen for state \times rate and level \times rate, and are apparent in Fig. 5. In the awake state (filled symbols), there are clear and expected maxima at 40 Hz, while in the sedated state (open symbols), a bimodal pattern is apparent at the higher intensity level (peaks at 40 and 90 Hz). At the lower intensity level, the best

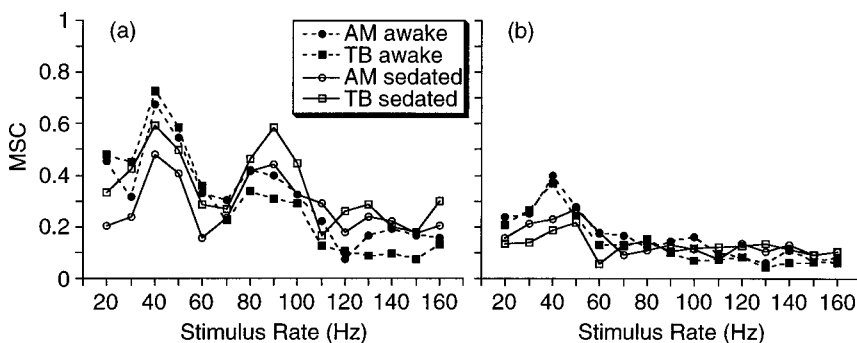


FIG. 5. MSC averaged across all 14 subjects for 58 dB (a) and 38 dB (b) peak-equivalent SPL stimuli.

rate appears to shift to 50 Hz (the state \times rate \times level effect was significant at $p = 0.0095$). There was no significant main effect of stimulus type (AM vs toneburst), but the stimulus type \times level \times rate interaction was highly significant. This appears to reflect the fact that at the higher level, tonebursts yield slightly higher MSCs at low rates; this is less clear at rates above 70 Hz (as expected, since the two stimulus types become more and more similar at higher rates). The stimulus type \times state \times level interaction effect was suggestive ($p = 0.0197$). Because stimulus type (AM vs toneburst) effects were insignificant in subsequent analyses, these data have been combined for presentation in subsequent figures.

Figure 6 shows the number of cases in each condition exceeding the MSC critical value of 0.266, for which the individual's response can be accepted as statistically significant at the $p < 0.01$ level. In general, this shows the same effects as described for the mean MSC values in Fig. 5: a strong 40 Hz peak in the awake state, and bimodality with a second peak at 90 Hz in the sedated state/higher intensity level. A smaller peak appears at 130–140 Hz for the higher-intensity stimuli. Both figures suggest that, even in the sedated state, 40 Hz is as good or better than 90-Hz. Near threshold, 50 Hz may be better than either 40 or 90 Hz. It should be noted that when $p(\text{false positive}) = 0.01$ for each trial, $p(\text{one or more false positives out of 28 trials}) = 0.2453$ (binomial distribution). However, two or more false positives will occur uncommonly ($p = 0.0291$), and three or more false positives will be rare ($p = 0.0027$). Thus, we can accept that at 58 dB peSPL, some subjects have genuine response at rates up to 160 Hz, awake or sedated. At 38 dB peSPL, genuine response is present in the awake state at least up to 100 Hz, and probably at 140 Hz.

Figure 7(a) shows average signal and noise power estimates for the higher intensity-level conditions. The reference level is a $1\text{-}\mu\text{V}$ peak-to-peak sinusoid (rms value $= 0.3536\ \mu\text{V}$). For example, the -20 dB value for signal power corresponds to a $0.1\ \mu\text{V}$ (p-p) sinusoid.

The most striking results in Fig. 7(a), confirmed by highly significant ANOVA results ($p < 0.0001$), are the separate effects of state and rate on signal power. SSAEP power declines steadily, with a slight peak at 40 Hz (note that this small peak of about 3–5 dB would correspond to a 40%–80% increase in response potential), as rate increases from 20–160 Hz. At least through 110 Hz, sedation reduces signal power. Figure 7(a) also shows highly significant effects of state and rate on noise power, as well as a highly significant state \times rate interaction. In other words, not only

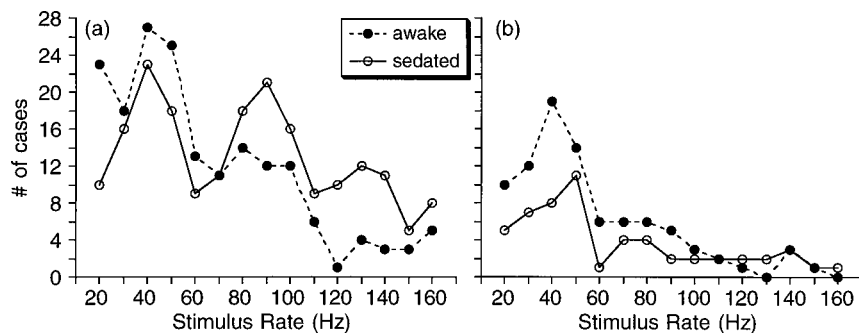


FIG. 6. Number of cases (out of 28 trials: 14 subjects \times 2 stimulus types) exceeding critical value (significant at the 1% level) for 58 dB (a) and 38 dB (b) peak-equivalent SPL stimuli.

does noise power decline (as expected) with increasing rate and with sedation, but the sedation effect is greater at higher rates.

Figure 7(b) repeats the signal power/noise power analysis for the low-intensity conditions. An overlay of Fig. 7(a) and (b) shows, as expected, that noise power is unaffected by stimulus intensity. When signal power averaged across all 28 trials (14 subjects \times 2 stimulus types) was negative, this was plotted as “undefined” and represents a condition in which either signal power was absent or the SNR was very low, even after averaging. Note that the four undefined points in Fig. 7(b) are for conditions and rates for which two or fewer subjects had individually statistically significant responses [Fig. 6(b)]. Comparing Fig. 7(a) and (b), it is apparent that SSAEP power is less at the lower stimulus level ($p = 0.0003$). The interaction between level and rate was highly significant for signal power ($p < 0.0001$); this may reflect the more precipitous decline in signal-power values with rate at the lower intensity. Suggestive interaction effects were seen for state \times level ($p = 0.0409$) and state \times level \times stimulus type ($p = 0.0483$).

Figure 8 shows scattergrams of individuals’ best low rates (≤ 60 Hz) and best high rates (≥ 70 Hz) for different conditions (see the Materials and Methods section). For example, Fig. 8 shows the expected tendency for most subjects to have a best low rate of 40 Hz for both tonebursts and AM tones in the awake state. Best low rates were more variable in the sedated condition. It is notable that best high rates were much less clustered, even in the higher intensity/sedated state, where a strong detectability peak was apparent in the group average at 90 Hz. If individuals had their own best rates that were stable, we would expect to see points clustered along the diagonal; instead, these scattergrams suggest that there is as much variation within individuals as

across individuals. ANOVA showed no significant main or interaction effects of state, stimulus type, or level on best low rate or best high rate.

III. DISCUSSION

Our primary finding was that there are two approximately equal peaks in the SSAEP detectability function for 640-Hz tonebursts and AM tones at 58 dB peak-equivalent SPI in sedated adults: one at rates of about 40 Hz, and one at about 90 Hz. A smaller peak was seen at 130–140 Hz. At 38 dB, only a 50-Hz detectability peak remains. Our results are most comparable with (but do not entirely agree with) those of Cohen *et al.* (1991), who found, for 500-Hz AM tones in sleeping subjects, maximum detectability at 90 Hz, with secondary peaks at 40, 140, and 190 Hz.

It is possible, but seems unlikely, that this discordance is related to small procedural differences between the two studies: 640 Hz vs 500 Hz tones; 20 and 40 dB nHL vs 30 dB nHL for AM tones; and monaural vs binaural presentation. Our sedated state may have differed from the natural sleep state of Cohen *et al.*, but one could argue that the sedated state is, if anything, further from the alert state than natural sleep. Thus, it might be surprising if only the intermediate state showed the remarkable detectability at high rates found by Cohen *et al.* In addition, it is possible that best rates at 30 dB nHL, as in Cohen *et al.* (1991), are different from best rates at 20 and 40 dB nHL.

A more likely explanation is found in the different methods of calculating detectability in the two papers. We have used the MSC statistic, which is directly related to the SNR (and to several other statistics used in evoked potential detection; see Dobie and Wilson, 1993). As expected, the peaks in average MSC (Fig. 5) correspond well to the peaks in the

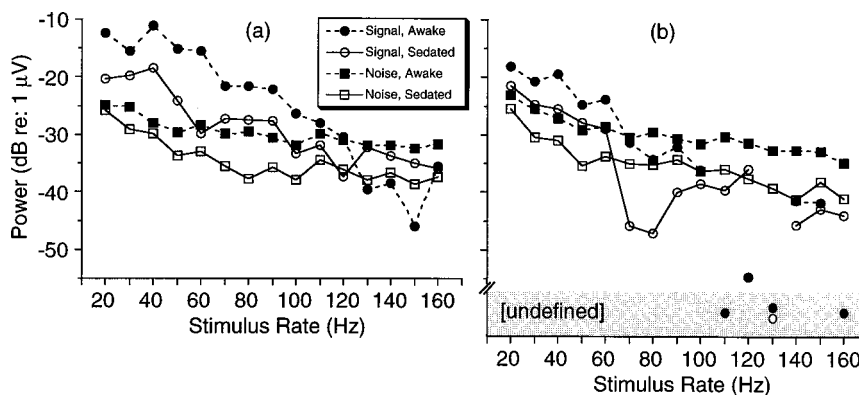


FIG. 7. Unbiased signal power and noise power estimates for responses to 58 dB (a) and 38 dB (b) peak-equivalent SPL stimuli.

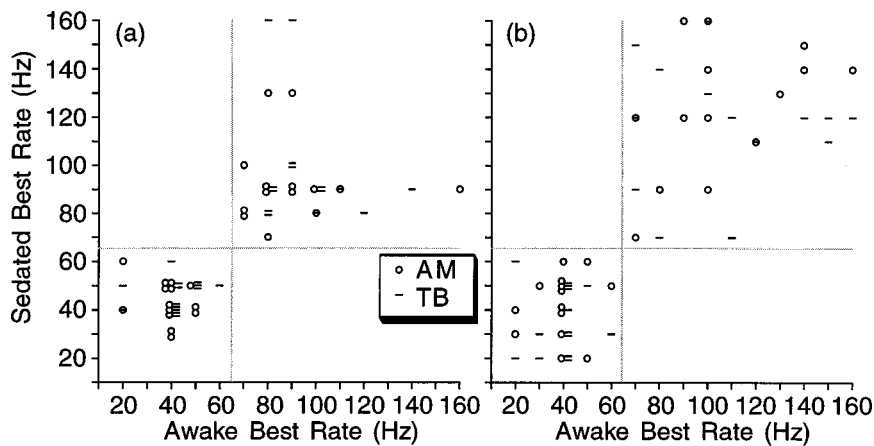


FIG. 8. Best low rates (≤ 60 Hz) and best high rates (≥ 70 Hz) for all 14 subjects for 58 dB (a) and 38 dB (b) peak-equivalent SPL stimuli.

number of subjects' responses meeting a $p < 0.01$ detection criterion. Cohen *et al.*, in contrast, did not report the number or proportions of responses actually detected for different modulation rates, but rather estimated "detection efficiency" (EFF) with this formula:

$$\text{EFF} = (\text{modulation frequency})(\text{SNR}^2). \quad (4)$$

Cohen *et al.* correctly reasoned that detectability would be related to the SNR after averaging; however, because they estimated the SNR for each modulation rate based on a fixed number of modulation cycles, their SNR estimates for low modulation rates were based on much longer data-collection times than the estimates for high modulation rates. To simulate comparisons of detectability after equal data-collection times, they (again correctly) multiplied SNR^2 estimates by modulation frequencies. The problem with this approach is that their SNR estimates were probably biased, i.e., the method of calculation ($\text{SNR} = \text{signal amplitude} \div \text{EEG noise level}$) appears to always yield a positive SNR, even when there is no signal present, i.e., when true $\text{SNR} = 0$ (no negative signal amplitudes or efficiencies are plotted in any of their figures). This would not pose a problem if the original data-collection times, rather than the number of modulation cycles, had been held constant across modulation rates, because all rates at which true $\text{SNR} = 0$ would yield biased SNR estimates of similar magnitudes, while the rates at which true $\text{SNR} > 0$ would yield higher (biased) SNR estimates reflecting genuinely better detectability. However, the multiplication of biased SNR estimates by modulation frequencies must introduce a spurious upward tilt to the final plot of detectability vs modulation rate. For example, in Cohen *et al.* (1991), Figs. 9 and 11 show rising detectability throughout the range of modulation rates tested for 4-kHz tones, leading to the (probably false) conclusion that the optimal modulation rate for SSAEP detection would be 190 Hz, or even higher.

We conclude that SSAEPs at low intensities in adults are best recorded in the alert/awake state, at modulation or presentation rates around 40 Hz. Even if adult subjects are sedated, 40–50 Hz is the preferred rate, especially very near behavioral threshold. This study sampled only a few frequencies below 60 Hz; further research would be necessary to more specifically identify best frequency for the low-level/sedated state. In an earlier paper (Levi *et al.*, 1993), we

found that sedated adults listening to 500-Hz AM tones at 60 dB nHL demonstrated better detectability at 80 Hz modulation than at 40 Hz. In this study, 40 and 90 Hz displayed equal detectability for AM tones at 40 dB nHL, while at 20 dB nHL, 40–50 Hz was preferable. Thus, best rates for sedated adults appear to vary with stimulus intensity. At moderate levels, 80–90 Hz may be best, i.e., statistically significant responses could be confirmed in a shorter test time (sedated) than at other rates.

ANOVA showed no statistically significant differences between tonebursts and AM tones with respect to SSAEP power, detectability, or best rates. Nevertheless, it is worth noting that, at 40 Hz, AM tone-presentation levels were 20 and 40 dB nHL, while toneburst levels were 12 and 32 dB nHL. Thus, at these low presentation rates, tonebursts are detectable closer to behavioral threshold than are AM tones.

While group MSC averages clearly peaked at 40–50 Hz and 90 Hz, individuals showed quite variable best rates, and these were not particularly consistent from trial to trial. We cannot conclude that individuals have their own best rates that would be worth seeking in clinical test settings. Rather, it appears reasonable to continue to use a fixed rate—around 40 Hz—for everyone. These conclusions are based on a single carrier frequency (640 Hz); at higher carrier frequencies, higher modulation rates could be optimal (Cohen *et al.*, 1991).

Reduction of EEG noise by sedation is no surprise, but the interaction of this effect with frequency is interesting. Higher-frequency noise was reduced more than lower-frequency noise, and this probably partially explains the emergence of the 90-Hz detectability peak at our higher presentation level.

Low-rate SSAEPs—below about 70 Hz—are commonly considered to be closely related to middle-latency responses (MLRs), and it is thus no surprise that sedation reduces SSAEP power in this frequency range. In contrast, higher-rate SSAEPs are often considered more analogous to auditory brainstem responses (ABRs); indeed, if MLRs are absent, one can synthesize SSAEPs using a series of repeated ABR waveforms. To the extent that high-rate SSAEPs represent repeating ABRs, it may be surprising to see sedation-induced SSAEP power reduction up to at least 110 Hz (Fig. 7), because ABRs are ordinarily thought to be quite resistant

to state effects. Nevertheless, most previous reports have focused on ABR latency and detectability rather than amplitude or power, and there are several papers showing sedative or anesthetic and even attentional effects on ABR amplitude (Stockard *et al.*, 1980; Thornton *et al.*, 1984; Lukas, 1981; Goff *et al.*, 1977; Palaskas *et al.*, 1989; Marsh *et al.*, 1984).

ACKNOWLEDGMENTS

This work was supported in part by research Grant No. 2 R01 DC 00337-11 from the National Institute on Deafness and Other Communication Disorders, National Institutes of Health. Additional support was provided by the National Organization for Hearing Research. The authors wish to express their thanks to Thomas J. Prihoda, Ph.D., and Connie S. Sakai, M.S.P.A., for assistance with statistical analysis, and to Chris Prall for National Instruments LABVIEW™ and Apple Macintosh™ programming.

American National Standards Institute (1996). (ANSI S3.6-1996), "American National Standard Specification for Audiometers" (Acoustical Society of America, New York).

Aoyagi, M., Kiren, T., Kim, Y., Suzuki, Y., Fuse, T., and Koike, Y. (1993). "Optimal modulation frequency for amplitude-modulation following response in young children during sleep," *Hearing Res.* **65**, 253–261.

Cohen, L. T., Rickards, F. W., and Clark, G. M. (1991). "A comparison of steady-state evoked potentials to modulated tones in awake and sleeping humans," *J. Acoust. Soc. Am.* **90**, 2467–2479.

Dobie, R. A., and Wilson, M. J. (1989). "Analysis of auditory evoked potentials by magnitude-squared coherence," *Ear Hear.* **10**, 2–13.

Dobie, R. A., and Wilson, M. J. (1990). "Optimal ('Wiener') digital filtering of auditory evoked potentials: use of coherence estimates," *Electroencephalogr. Clin. Neurophysiol.* **77**, 205–213.

Dobie, R. A., and Wilson, M. J. (1993). "Objective response detection in the frequency domain," *Electroencephalogr. Clin. Neurophysiol.* **88**, 516–524.

Galambos, R., Makeig, S., and Talmachoff, P. J. (1981). "A 40 Hz auditory

potential recorded from the human scalp," *Proc. Natl. Acad. Sci. USA* **78**, 2643–2647.

Goff, W. R., Allison, T., Lyons, W., Fisher, T. C., and Conte, R. (1977). "Origins of short latency auditory evoked potentials in man," in *Progress in Clinical Neurophysiology II*, edited by J. E. Desmedt (Karger, Basel), pp. 30–44.

Kuwada, S., Batra, R., and Maher, V. L. (1986). "Scalp potentials of normal and hearing-impaired subjects in response to sinusoidally amplitude-modulated tones," *Hearing Res.* **21**, 179–192.

Levi, E. C., Folsom, R. C., and Dobie, R. A. (1993). "Amplitude-modulation following response (AMFR): Effects of modulation rate, carrier frequency, age, and state," *Hearing Res.* **68**, 42–52.

Linden, R. D., Campbell, K. B., Hamel, G., and Picton, T. W. (1985). "Human auditory steady state evoked potentials during sleep," *Ear Hear.* **6**, 167–174.

Lukas, J. H. (1981). "The role of efferent inhibition in human auditory attention: An examination of the auditory brainstem potentials," *Intl. J. Neurosci.* **12**, 137–145.

Marsh, R. R., Frewen, T. C., Sutton, L. N., and Potsic, W. P. (1984). "Resistance of the auditory brain stem response to high barbiturate levels," *Otolaryngol.-Head Neck Surg.* **92**, 685–688.

Palaskas, C. W., Wilson, M. J., and Dobie, R. A. (1989). "Electrophysiologic assessment of low-frequency hearing: Sedation effects," *Otolaryngol.-Head Neck Surg.* **101**, 434–441.

Rees, A., Green, G. G. R., and Kay, R. H. (1986). "Steady-state evoked responses to sinusoidally amplitude-modulated sounds recorded in man," *Hearing Res.* **23**, 123–133.

Rickards, F. W., Tan, L. E., Cohen, L. T., Wilson, O. J., Drew, J. H., and Clark, G. M. (1994). "Auditory steady-state evoked potential in newborns," *Br. J. Audiol.* **28**, 327–337.

Stapells, D. R., Picton, T. W., and Smith, A. D. (1982). "Normal hearing thresholds for clicks," *J. Acoust. Soc. Am.* **72**, 74–79.

Stockard, J. J., Stockard, J. E., and Sharbrough, F. W. (1980). "Brainstem auditory evoked potentials in neurology: Methodology, interpretation, clinical application," in *Electrodiagnosis in Clinical Neurology*, edited by M. J. Aminoff (Churchill Livingstone, New York), pp. 370–413.

Thornton, C., Heneghan, C. P. H., James, M. F. M., and Jones, J. G. (1984). "The effects of halothane and enflurane anesthesia on the early auditory evoked potentials in humans," in *Evoked Potentials II*, edited by R. H. Nodar and C. Barber (Butterworth, Boston), pp. 483–489.

Nonmonotonicity of informational masking

Eunmi L. Oh

Waisman Center, University of Wisconsin, Madison, Wisconsin 53705

Robert A. Lutfi

Department of Communicative Disorders, University of Wisconsin, Madison, Wisconsin 53706

(Received 13 February 1998; revised 19 August 1998; accepted 20 August 1998)

Neff and Green [Percept. Psychophys. **41**, 409–415 (1987)] report that the masking of single tones by random-frequency multitone maskers varies nonmonotonically with number of masker components (peaking at 10–50 components). In this paper it is shown that such results are well predicted by a model (the component-relative-entropy model, CoRE) wherein thresholds increase linearly with the ensemble variance of masker spectra smoothed by peripheral auditory filters [R. A. Lutfi, J. Acoust. Soc. Am. **94**, 748–758 (1993)]. Three experiments were conducted. In the first, the nonmonotonic relation was replicated for 9 of 11 listeners in conditions similar to those of Neff and Green. In the second, the frequencies of masker components were fixed and the levels of components were varied randomly across presentations to simulate Gaussian noise. In this case, the nonmonotonicity and the total amount of masking for these listeners were shown to be significantly reduced. In the third experiment, masked thresholds for the signal were found to vary monotonically with the frequency spacing of masker components for a fixed number of masker components. Large individual differences among listeners were obtained in some experimental conditions. Individual as well as mean thresholds were well predicted by the CoRE model with an appropriate selection of the values of the two free parameters of the model for each listener. © 1998 Acoustical Society of America. [S0001-4966(98)01912-2]

PACS numbers: 43.66.Ba, 43.66.Dc, 43.66.Fe [JWH]

INTRODUCTION

In most everyday listening situations, listeners must attend to relevant sounds (signals) embedded in an acoustic background containing the sounds of many other irrelevant sources (maskers). It may be difficult to detect the signal if signal and masker significantly overlap in frequency and time. This type of masking called *energetic masking* is well explained by the signal-to-noise ratio within a small region of frequencies surrounding the signal frequency (Fletcher, 1940; Patterson *et al.*, 1982). Often, however, there exists acoustic variability in natural listening environments that can additionally interfere with signal detection by introducing stimulus uncertainty. Stimulus uncertainty is considered to produce another type of masking called *informational masking* (Pollack, 1975). Informational masking associated with stimulus uncertainty is thought to be related to central or attentional mechanisms, while energetic masking is believed to involve peripheral systems (Watson and Kelly, 1981).

It has been shown that masker uncertainty has a much more detrimental effect on signal detection than signal uncertainty (Watson *et al.*, 1976). Dynamic properties of maskers can produce as much as 10 dB of masking for sequential maskers (Kidd and Watson, 1992; Watson *et al.*, 1990; Watson and Kelly, 1981; Watson *et al.*, 1976, 1975), and as much as 50 dB of masking for simultaneous maskers (Neff and Callaghan, 1987, 1988; Neff and Green, 1987; Spiegel *et al.*, 1981; Spiegel and Watson, 1981). One result, however, is particularly intriguing; that is, when masker uncertainty is introduced by varying the frequencies of simultaneous masker tones on each presentation, the amount of multitone masking depends in a nonmonotonic fashion on

the number of masker components (Neff and Green, 1987; Neff and Callaghan, 1988; Oh and Lutfi, 1997). For small numbers (less than 10–20), adding more components produces more masking. Interestingly, however, further increases in the number of components produce less masking, not more.

Green (1988) suggests a *post hoc* account of why there exists a nonmonotonic relation between the amount of masking and the number of masker components. According to Green, the stability of sound quality over trials is an important factor in auditory masking experiments. When maskers are comprised of larger numbers of components, individual masker components become more difficult to resolve resulting in a rather constant sound quality, even though the actual waveforms vary from trial to trial. With 10 or 20 components, on the other hand, each masker component is individually resolved and maskers sound quite different over trials. These changes in masker sound quality make it difficult to compare the intensity levels in the two temporal intervals, leading to greater amounts of masking.

Green's qualitative analysis is similar in principle to the quantitative analysis provided by a recently developed model of informational masking. According to the component-relative-entropy (CoRE) model, the signal threshold in the context of masker uncertainty is related to the variance of masker parameters taken across the ensemble of maskers in a given experiment (Lutfi, 1993). In detecting a fixed-frequency signal in maskers whose spectra vary from one presentation to the next, signal threshold is predicted to be proportional to the degree of level variability of the individual spectral components of the maskers from one presen-

tation to the next. The CoRE model predicts less masking when maskers are comprised of large numbers of components, because multiple frequency components tend to fall in the same auditory filter and effectively serve to reduce the variability in component level. Given the bandwidths of auditory filters across frequency (Patterson *et al.*, 1982) and the conditions of past experiments, the largest spectral variation across maskers occurs effectively for maskers with 10 or 20 components. Hence, the model predicts greatest masking at this point.

Experiment 1 was conducted to replicate the nonmonotonicity of masking and test predictions of the CoRE model. In experiment 2, the CoRE model was tested in conditions where masker uncertainty was introduced by varying amplitudes with fixed frequencies. It has been reported that the Rayleigh amplitude variation, characteristic of Gaussian noise, has little effect on the amount of masking (Neff and Callaghan, 1988). The CoRE model predicts much smaller masking by amplitude randomization than by frequency randomization in this case, because the spectral variation associated with the Rayleigh distribution of amplitudes is small compared to that associated with frequency variation. Experiment 3 provided a still stronger test of the CoRE model in conditions where spectral variation across maskers was manipulated by varying masker bandwidth for a fixed number of masker components. For a fixed number of components, the CoRE model predicts less masking as masker bandwidth is reduced because the probability increases that two or more components will fall within the same auditory filter, thus effectively reducing spectral variation across maskers. Experiment 3 therefore investigates whether the amount of informational masking is determined by variation in the effective spectrum of maskers independent of the number of masker components.

I. GENERAL METHODS

A. Stimuli

The signal was a 1000-Hz tone presented simultaneously with the maskers. No masker component was allowed to fall at the signal frequency. Maskers were constructed from 50 Gaussian noise samples, bandpass filtered from 0.1 to 10 kHz. The magnitude and phase spectra of each noise sample were analyzed into individual spectral components, with 11-Hz spacing between components. The amplitude distribution of these samples is Rayleigh, and the phase distribution is rectangular. On each trial, two of the noise samples for a two-interval, forced-choice procedure were selected at random. For each sample, a fixed number of frequency components was drawn at random with equal probability of occurrence within the permissible range of frequencies. The phases and amplitudes of the selected frequency components were then used to synthesize the multitone maskers played on each trial. In different blocks of trials, the number of frequency components varied from 2 to 906. For comparison, masked threshold for a broadband noise was obtained with maskers comprised of all frequency components bandpass filtered from 0.1 to 10 kHz at 2.7-Hz interval. Masker components within a rectangular critical-band arithmetically

centered around the signal (920–1080 Hz) were excluded to reduce the contribution of energetic masking to the total masking.

Both signal and maskers were gated on and off together with 10-ms, \cos^2 onset/offset ramps for a total duration of 370 ms. The rms values of the maskers were adjusted to be the same regardless of the number of masker components. Average total power of maskers was kept constant at 60 dB SPL. The signal and maskers were computer generated and played over a 16 bit, digital-to-analog converter (Tucker Davis Technologies DD1) at a sampling rate of 44.1 kHz. All stimuli were presented monaurally through Sennheiser model HD-520 headphones. The Sennheiser headphones were calibrated using a binaural loudness balancing procedure with a TDH-49 earphone. All stimuli were presented to individual listeners who were seated in a double-walled, IAC sound attenuation chamber.

B. Procedure

An adaptive, two-interval, forced-choice procedure was used to measure signal threshold in quiet and in the presence of the multitone maskers. The decision rule estimated the 70.7% point on the psychometric function (Levitt, 1971). The level of signal was varied by a programmable attenuator (Tucker Davis Technologies PA4) with an initial step size of 4 dB reduced to 2 dB after the third reversal. A trial block consisted of a total of 12 reversals, and threshold for that block was designated as the average of the last 8 reversal levels. Within an experimental condition, the number of masker components was fixed. Threshold for each condition was the average of five thresholds obtained from five consecutive blocks of trials. Blocks were run consecutively to facilitate practice within each condition. The order in which experimental conditions were run, however, was randomized. Ten blocks of trials were collected for an experimental session lasting approximately 1 h with breaks.

On each trial, two multitone complexes were presented to listeners separated by a 500-ms silent interval. The signal occurred with equal *a priori* probability in the first or second interval. Listeners were asked to indicate by key press which one of the two intervals contained the signal on each trial. Visual feedback was presented on a CRT after each response indicating whether the response was correct or incorrect. Listeners were instructed to use the feedback to aid their performance. In a further attempt to aid listeners' performance, the signal was presented in quiet preceding each block.

C. Listeners

Eleven normal-hearing listeners, four males and seven females, were paid at an hourly rate for their participation. The ages of the listeners ranged from 20 to 37 years. The listeners' pure-tone air conduction thresholds were less than 15 dB HL (ANSI, 1989) between 150 and 8000 Hz in both ears. Four listeners (LCA, LHC, LJA, and LOE) had considerable previous experience on similar auditory discrimination tasks before this study. The rest of the listeners received

several days of training before data collection. All listeners except LKL, LTA, LHC, and LCA ran in all conditions of the three experiments.

D. Analysis

1. Effect of energetic masking

In some conditions of our experiments we expect energetic masking to be significant. Therefore, we attempt to quantify the relative contribution of energetic and informational masking to the obtained total masking in each experimental condition.

Energetic masking can be measured precisely by obtaining signal thresholds in quiet, and in the presence of maskers in a minimal uncertainty condition where the same signal and masker sample are presented on all trials (Watson and Kelly, 1981; Lutfi, 1990). Energetic masking in this case is defined as the threshold elevation in dB in the minimal uncertainty condition. The practical difficulty with this approach is that different masker samples yield different masked thresholds, so that no one sample can be taken as representative of the entire ensemble of possible samples.

An alternative approach is to make use of a well-accepted model of energetic masking, the auditory filter model of masking.¹ According to this model, the auditory filter shape can be approximated by a simple mathematical expression, a rounded exponential (roex) function with few parameters (Patterson *et al.*, 1982). In this study, a three-parameter roex filter, $\text{roex}(p, w, t)$, was applied to estimate energetic masking produced by maskers in each experimental condition. A three-parameter roex filter was chosen over a one or two-parameter roex filter, because the frequency range used in this study is quite broad, making it necessary to approximate the tail section of the filter. The expression specifying this filter is:

$$W(g) = (1 - w)(1 + pg)e^{-pg} + w(1 + tg)e^{-tg}, \quad (1)$$

where g is the distance from the center frequency of the filter f_c to the evaluation point f , normalized by the signal frequency f_0 , that is, $g = |f - f_c|/f_0$ [see Eq. (A8) in Patterson *et al.*, 1982]. The $\text{roex}(p, w, t)$ consists of two exponential functions. The first exponential defines the passband, and the second defines the tail section of the filter. The relative weight of the second exponential is determined by the parameter w . For the values of filter parameters we chose $p = 25$, $t = 6$, and $w = 0.002$. These values are close to the ones used by Patterson *et al.* to represent the average normal-hearing adult.

The power of the signal at threshold P_S is assumed to be proportional to the integral of the product of the auditory filter $W(g)$ and the long-term power spectrum of a masker $N(g)$:

$$P_S = K \int_0^\infty N(g)W(g)dg, \quad (2)$$

where K represents the efficiency of the detection process. The value of K is assumed constant across all experimental conditions, and is determined by equating the estimated signal threshold to the mean of listeners' thresholds for broad-

band noise maskers (cf. Patterson *et al.*, 1982). The thresholds for broadband noise maskers are used because the contribution of informational masking is assumed minimal for broadband noise maskers. The amount of energetic masking in each experimental condition was estimated by computing P_S for each of the 50 maskers in each condition, and then taking the average of these values. This estimate of energetic masking is used to evaluate the predictions of the CoRE model.

2. Predictions of the CoRE model

Predictions of the CoRE model are based on the premise that listeners adopt a maximum-likelihood decision rule in detection tasks, but implement this rule imperfectly because of an inability to ignore irrelevant information that varies from trial to trial. In formal terms, listeners are assumed to integrate information in the maximum-likelihood decision variable over a rectangular frequency window with bandwidth that far exceeds the bandwidth of the signal.

The predictions of the CoRE model are easily developed for the particular task used in this study. The task is to detect a fixed tone in a collection of masker tones that vary on each presentation in level and frequency. Any single masker can therefore be represented by its power spectrum:

$$X = [P_1 \ P_2 \ \cdots \ P_{921}], \quad (3)$$

where the indices correspond to individual spectral components.

In the first stage of the CoRE model, some preprocessing of the masker spectrum is necessary to take into account mechanical filtering of the cochlea. When maskers are composed of large numbers of frequency components, some components will fall in the same auditory filter thus reducing overall spectral variability. Also, because the bandwidth of auditory filter increases with frequency, variability will be less at high frequencies than at low frequencies.² To incorporate the effects of mechanical filtering of the cochlea, masker spectra are smoothed by convolution with equivalent-rectangular-bandwidth (ERB) auditory filters (Glasberg and Moore, 1990). The resulting masker spectrum is represented as a vector of tone levels:

$$L = 10 \log \text{ERB}(X), \quad (4)$$

where the function ERB represents the spectral smoothing by the equivalent rectangular bandwidths of auditory filters.

In the second stage of the model listeners are assumed to integrate information in a maximum-likelihood decision statistic over a rectangular frequency window G_W with bandwidth W ,

$$G_W = \begin{cases} 1, & f < W, \\ 0, & f > W. \end{cases} \quad (5)$$

The window G_W can be thought of as an attentional filter or weighting function of frequency. The rectangular window is chosen for simplicity, but a more realistic form could be used.³ In the present experiments the maximum-likelihood statistic is tone level, hence, the decision variable is

$$D = \sum_{i=1}^n G_W L_i, \quad (6)$$

where L_i represent the levels at the outputs of n independent auditory filters within the bandwidth W . A prediction for average sensitivity is derived based on the expectations of the decision variable D ,

$$d' \cong \frac{\mathbf{E}[D|SN] - \mathbf{E}[D|N]}{\sqrt{\text{var}[D|N]}}. \quad (7)$$

Since the outputs of the n auditory filters are assumed to be independent, $\mathbf{E}[D|SN] - \mathbf{E}[D|N]$ is equivalent to the difference between the signal-plus-noise and noise-alone output of the filter centered at the signal frequency. The numerator of Eq. (7) can therefore be rewritten as $10 \log(P_S + N) - 10 \log(N)$, where P_S is the power of the signal and N is the power of the noise at the output of this filter. In the present experiment, P_S is typically much larger than N . Hence $10 \log(P_S + N)$ is approximately equal to the level of the signal L_S at threshold. Moreover, in the auditory filter model $10 \log(N)$ is approximately equal to the amount of energetic masking E . Finally because auditory filters are assumed to be independent, the denominator of Eq. (7) is equivalent to $\sqrt{n} \sigma_L$, where $\sigma_L = \sqrt{E[\text{var}(L_i)]}$. Taking these points into consideration and rewriting Eq. (7) as a prediction for masked threshold we have

$$L_S \approx E + d' \sqrt{n} \sigma_L, \quad (8)$$

where $I = d' \sqrt{n} \sigma_L$ is the predicted amount of informational masking. In the present application, the amount of energetic masking E in each condition is estimated according to the predictions of the roex filter model from Eqs. (1) to (2). The value of σ_L is a measure of the effective spectral variation across maskers. It is estimated by computing the variance in level of each component of the 50 smoothed masker spectra within the bandwidth W , and then taking the square root of the mean of these variances. The value of d' is set to 0.78 corresponding to 70.7% correct in the adaptive, two-interval, forced-choice task. The only free parameters of the model are the number of auditory filters n assumed to be involved in the decision, and the attentional bandwidth W . The attentional bandwidth largely determines the shape of the masking function and the point at which maximum masking occurs. The number of auditory filters largely serves as a scaling factor on this function. The predictions of the CoRE model for the total masking are then given by the dB sum of the estimated energetic masking E and the estimated informational masking I . These predictions are compared to the total masking obtained from listeners to evaluate the CoRE model.

II. EXPERIMENT 1: EFFECT OF THE NUMBER OF MASKER COMPONENTS

This experiment attempted to replicate earlier results and to determine how well the nonmonotonic relation between the amount of masking and the number of masker components can be predicted by the CoRE model. Masker uncer-

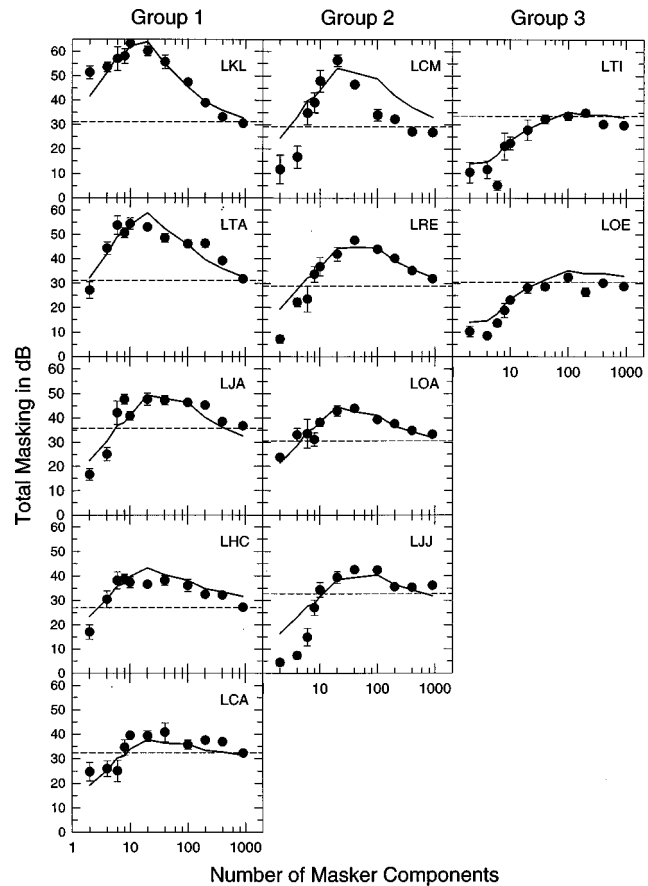


FIG. 1. Total masking for individual listeners as a function of the number of masker components. Each circle represents the total masking averaged over five blocks of trials with standard errors. Solid lines represent the predictions of the CoRE model for individual listeners. Dashed lines represent the total masking for a broadband noise of equal total power. The masking functions were categorized into three groups based on the point of maximum masking. Each group is plotted in a separate column.

tainty was introduced by randomizing both the frequencies and amplitudes of masker tones on each presentation.

A. Stimuli

Maskers were comprised of 2, 4, 6, 8, 10, 20, 40, 100, 200, 400, or 906 spectral components. Masker bandwidth, the frequency range over which components were chosen, was fixed at 0.1–10 kHz. Maskers were chosen to be similar to those used by Neff and her colleagues. They differed in that a wider frequency range and larger numbers of masker components were used.

B. Results

Total masking for individual listeners is plotted in Fig. 1. Each circle represents the total masking averaged over five blocks of trials for a fixed number of masker components. Solid lines represent the total masking predicted by the CoRE model for individual listeners. We will return to the individual fitting in the discussion. The horizontal dashed line in each graph represents the total masking for the broadband noise samples which corresponds to the maximum amount of masking the auditory filter model would predict. There exist large individual differences in masking func-

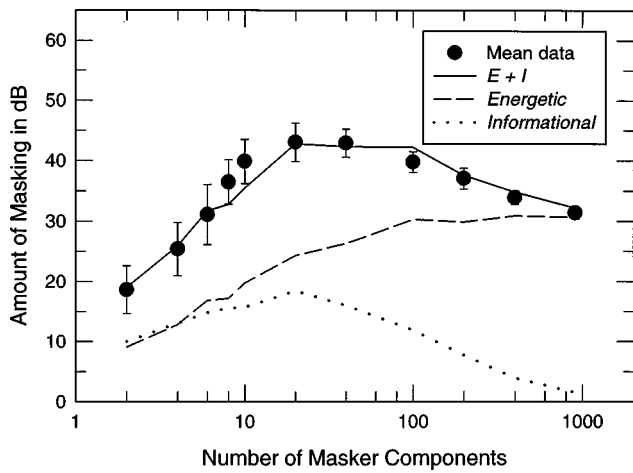


FIG. 2. The total masking averaged over 11 listeners (filled circles) with standard errors and the prediction of the CoRE model for the total masking (solid line) given by adding the estimates of energetic (dashed line) and informational masking (dotted line).

tions, as have been reported by Neff and Dethlefs (1995). The masking functions in Fig. 1 have been grouped based on the point of maximum masking. Each of these groups is plotted in a separate column of Fig. 1. The listeners in the first group have an early rise in their masking functions, peaking at 6–10 masker components. In the second group, masking functions have peaks at 20 or 40 masker components. The amount of masking obtained from the listeners in the first two groups is larger at the peak than the total masking for broadband noise samples. Finally, the masking functions in the third group do not show dominant peaks, and asymptote at the total masking for broadband noise samples. Only 2 out of 11 masking functions belong to the third group. Individuals within this group have been termed “low-threshold listeners” by Neff and Dethlefs.

Figure 2 shows the total masking averaged over 11 listeners (circles) and the total masking predicted by the CoRE model (solid line). The prediction of the CoRE model is the dB sum of the estimates of energetic (dashed line) and informational masking (dotted line). The mean data replicate results from previous studies of multitone masking. More than 40 dB of masking is observed with a broad peak in the masking function at 20 components. Maskers were, on average, expected to produce as much as 30 dB of energetic masking for larger numbers of masker components. The CoRE model predicts greatest informational masking for maskers with 20 components because after ERB filtering the largest spectral variation across maskers occurs for maskers with 10 or 20 components. Further increases in the number of components in effect reduce spectral variation by increasing the likelihood that two or more components will fall in the same auditory filter. The total masking predicted by adding the estimates of energetic and informational masking agrees well with the average data from listeners.

Recall that the free parameters of the CoRE model are the number of independent auditory filters n and the attentional bandwidth W . The value of $W=0.1-2.5$ kHz gives the best agreement between the mean of total masking and the predictions of the CoRE model. This implies that listeners

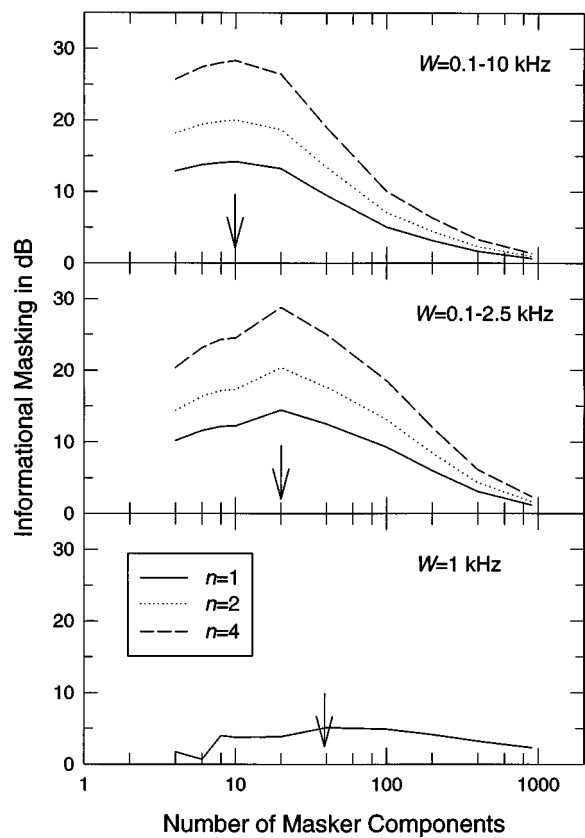


FIG. 3. Informational masking predicted by the CoRE model for different values of the number of independent auditory filters n and the attentional bandwidth W . Arrows indicate the point of maximum informational masking.

could ignore some of the irrelevant information at the highest frequencies, but their ability to detect the signal was still hindered by changes in spectral information quite remote from the signal. The value of n that best describes the estimated total masking is 1.64, implying that listeners attend to only one or two frequency channels simultaneously. These values of parameters suggest that a listener’s response is based on information in one or two separate frequency regions that may vary from trial to trial over a quite wide frequency range. The values of $W=0.1-2.5$ kHz and $n=1.64$ will be used for predictions of the mean data in all subsequent experiments.

1. Individual differences

We next examine whether thresholds for the three groups could be predicted by the CoRE model. Figure 3 shows how different values of n and W change the estimate of informational masking. The width of the attentional filter largely determines the point where maximum informational masking occurs, while the number of auditory filters serves primarily as a scaling factor. Figure 4 shows the prediction of the CoRE model (solid line) and the total masking averaged across the listeners (filled circles) in each group. The estimate of informational masking (dashed line) depends on the values of n and W in each case, while the estimate of energetic masking (dotted line) stays the same across groups. The agreement between the obtained and the predicted

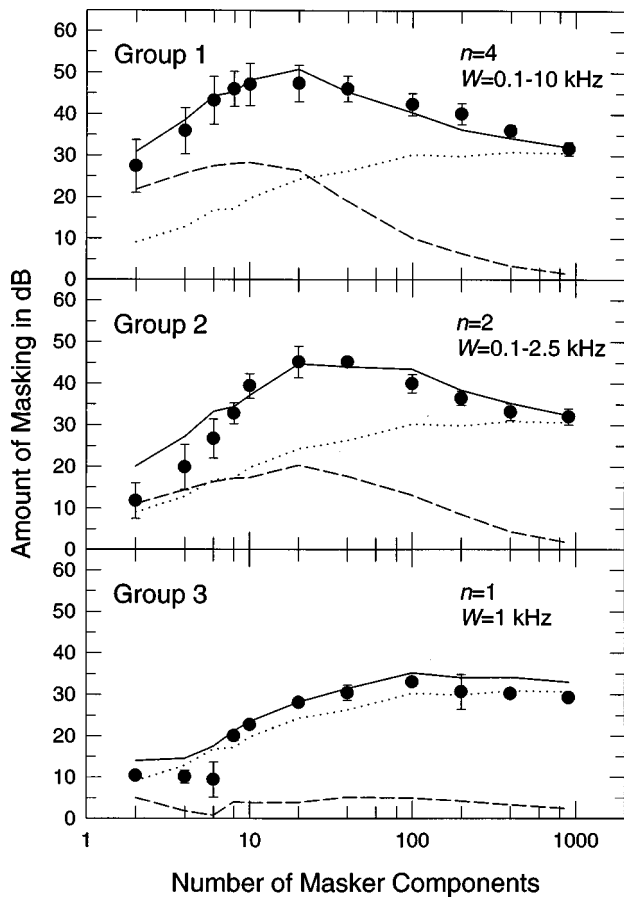


FIG. 4. The total masking averaged across the listeners in each group (filled circles) with standard errors and the prediction of the CoRE model (solid line) in each group. The estimate of informational masking (dashed line) varies depending on the values of n and W , while the estimate of energetic masking (dotted line) stays the same across groups.

amount of total masking is quite good in all three groups. This implies that individual differences are largely due to the differences in attentional factors rather than differences in the functioning of the auditory periphery (e.g., Berg and Green, 1990; Hirsh and Watson, 1996; Neff *et al.*, 1993; Viemeister and Schlauch, 1992; Wightman and Allen, 1992). The masking functions in the first group are well fitted when n is equal to 4 and W is equal to the entire frequency range over which maskers were drawn. These values suggest that the listeners in the first group integrate information over a larger number of auditory filters and that they are distracted by changes in spectral information over a wide frequency range. The masking functions in the third group agree well with the predictions of the traditional auditory filter model. According to the auditory filter model, listeners are assumed to focus on the output of a single auditory filter centered at the signal frequency. In this limiting case, n is equal to 1 corresponding to the auditory filter centered at the signal frequency. The CoRE model only slightly overpredicts the thresholds in the third group. This is likely due to the practice of forcing the maximum amount of energetic masking to be equal to the threshold for the broadband masker condition (see methods in Sec. I D 1). This procedure fails to allow for a small amount of informational masking in the broadband masker condition.

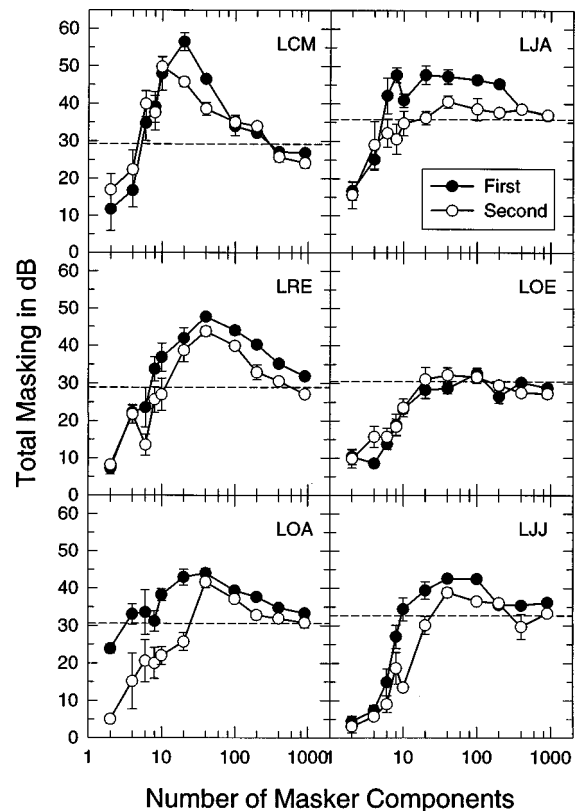


FIG. 5. Filled circles represent total masking for six listeners from experiment 1. Open circles represent total masking from a replication of experiment 1 conducted three months to more than a year later. Dashed lines represent the amount of total masking for a broadband noise.

2. Practice effects

After the listeners finished all other experiments in this study, experiment 1 was repeated by the same listeners to examine whether there exist practice effects. The interval between the initial and the replicated experiments ranged from three months to more than a year. As shown in Fig. 5, an improvement in performance was observed for all listeners except the low-threshold listener (LOE). Although there are individual differences, the point where maximum masking occurs tends to shift to the right. Within the framework provided by the CoRE model, this tendency is expected if listeners were to integrate information over the outputs of a smaller number of auditory filters within a narrower attentional bandwidth. The result from the replication suggests that some listeners were able to narrow their attentional bandwidth and attend to the outputs of auditory filters that are closer to the signal frequency.

III. EXPERIMENT 2: EFFECT OF AMPLITUDE RANDOMIZATION

Neff and Callaghan (1988) report that simulating Gaussian noise by randomizing the amplitudes of masker components within a trial has little effect on the amount of masking, while randomizing the frequencies within a trial significantly increases the amount of masking. In that study, the amplitudes of masker components were drawn at random from a Rayleigh distribution to approximate Gaussian noise, hence the degree of amplitude variation was small. In this

TABLE I. Frequencies of components used in experiment 2. The frequencies of maskers with fewer than eight components were equally spaced starting from 1800 Hz, while the frequencies of other maskers were equally spaced starting from 100 Hz.

The number of masker components	Frequency spacing in Hz	Frequency range in Hz
2	4867	1800–6667
4	2433	1800–9100
6	1623	1800–9916
8	1217	100–9832
10	975	100–9843
20	486	100–9811
40	243	100–9811
100	97	100–9908
200	49	100–9956
400	24	100–9956
906	11	100–10000

case, the CoRE model would predict much less masking because overall spectral variation (as measured by σ_L) would also be quite small. Experiment 2 was conducted to provide a quantitative test of this prediction.

A. Stimuli

Stimulus configurations were the same as in experiment 1, except masker frequencies were fixed. Maskers were comprised of 2–906 components whose amplitudes were randomized (Rayleigh) from one presentation to the next. The frequencies of masker components were equally spaced on a linear scale as in previous studies by Neff and Callaghan (1988). The frequency spacing and the starting frequency are specified in Table I.

B. Results

Figure 6 shows total masking for eight listeners when only amplitude was varied. For comparison, the results from experiment 1 where frequency and amplitude were varied simultaneously are also plotted in this figure. Varying only amplitude in experiment 2 appears to have significantly reduced the differences in masking functions observed across listeners. All listeners of experiment 2 except LKL can be categorized as the low-threshold listeners. Moreover, the amount of masking for maskers with fixed frequencies depends monotonically on the number of masker components. These results suggest that total masking in this experiment is due exclusively to energetic masking. The results further imply that individual differences in multitone masking as observed in experiment 1 largely derive from differences in central or attentional factors (e.g., Berg and Green, 1990; Hirsh and Watson, 1996; Neff *et al.*, 1993; Viemeister and Schlauch, 1992; Wightman and Allen, 1992).

The top panel of Fig. 7 displays the total masking averaged over eight listeners (open circles) when only amplitude was randomized. In this figure, the solid line represents the prediction of the CoRE model for the total masking given by adding the estimates of energetic (long dashed line) and informational (dotted line) masking. The bottom panel of Fig. 7 shows the total masking predicted (solid lines) and the total masking obtained in this experiment (open circles) and in

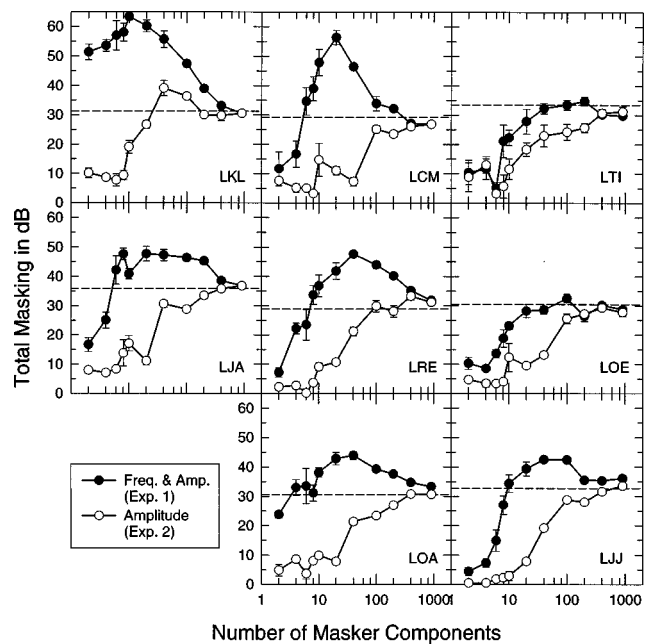


FIG. 6. Total masking with standard errors for individual listeners when only amplitude was varied (open circles) and when both frequency and amplitude were varied (filled circle). Dashed lines represent the amount of total masking for a broadband noise.

experiment 1 (filled circles). The short dashed line represents the amount of total masking for a broadband noise of equal total power. As in Fig. 4 (and for the same reasons), the CoRE model overpredicts thresholds by a small amount when the contribution of informational masking is small. As illustrated in the bottom panel of Fig. 7, however, the CoRE model predicts the large reduction in masking when only amplitude is varied. The estimates of energetic and informational masking in this experiment can be compared to those in experiment 1 plotted in Fig. 2. Even though there is a small reduction of energetic masking in the current experiment, by far the largest reduction is in informational masking.

IV. EXPERIMENT 3: EFFECT OF MASKER BANDWIDTH

The CoRE model predicts that less masking is produced by maskers with large numbers of components because the limited resolution of components spaced closely in frequency effectively reduces variation across the pool of masker spectra. In this experiment, we attempt to test this prediction directly. If spectral variation across maskers in fact determines the amount of informational masking, then we should expect a similar reduction in informational masking with decreasing frequency spacing of components, independent of the number of masker components. In experiment 3, the frequency spacing of masker components was controlled by varying masker bandwidth for a fixed number of masker components.

A. Stimuli

The number of masker components was fixed at 20 where masking was previously observed to be the greatest in

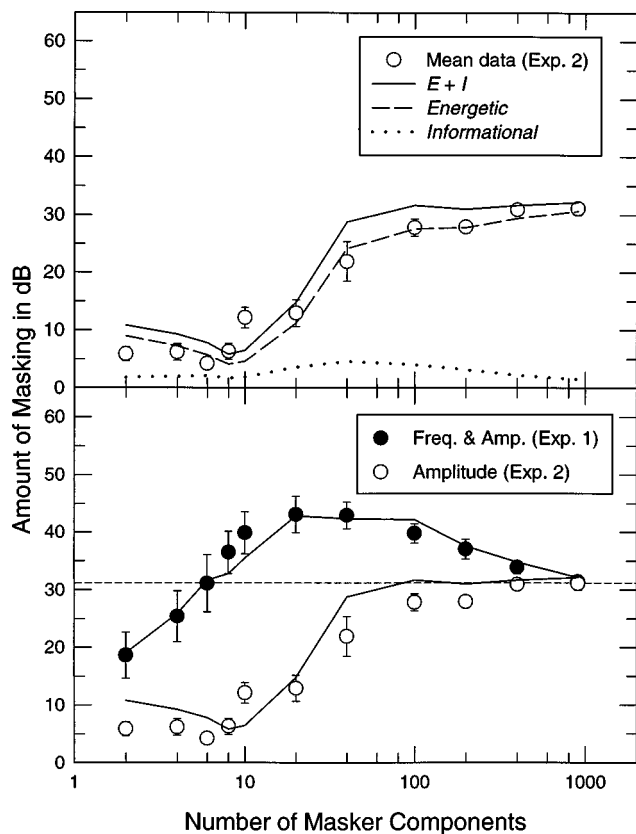


FIG. 7. Top panel: The solid line represents the prediction of the CoRE model for the total masking given by adding the estimates of energetic (long dashed line) and informational (dotted line) masking in the conditions where only amplitude was randomized. Open circles represent the total masking averaged over eight listeners with standard errors. Bottom panel: The total masking predicted by the CoRE model (solid lines) and the total masking obtained from listeners when only amplitude was varied (open circles) and when both frequency and amplitude were varied (filled circles). The short dashed line represents the amount of total masking for a broadband noise.

experiment 1. Masker bandwidth was varied to match the frequency spacing of components for each number of components used in experiment 1. The bandwidth of maskers extended an equal distance above and below the signal in log frequency. The frequency spacing and masker bandwidth in each condition of experiment 3 are specified along with those in corresponding conditions of experiment 1 in Table II.

TABLE II. The frequency spacing of masker components, the number of masker components, and masker bandwidth used in experiments 1 and 3. (a) In experiment 1, the number of components was varied. (b) In experiment 3, masker bandwidth was varied. Notice that critical band components were excluded in all experimental conditions.

Average frequency spacing (Hz)	(a) Variable number (Exp. 1)		(b) Variable bandwidth (Exp. 3)	
	Number	Bandwidth (Hz)	Number	Bandwidth (Hz)
486	20	100–10 000	20	100–10 000
243	40	100–10 000	20	509–5548
97	100	100–10 000	20	756–2877
49	200	100–10 000	20	843–1984
24	400	100–10 000	20	875–1532
11	906	100–10 000	20	896–1284

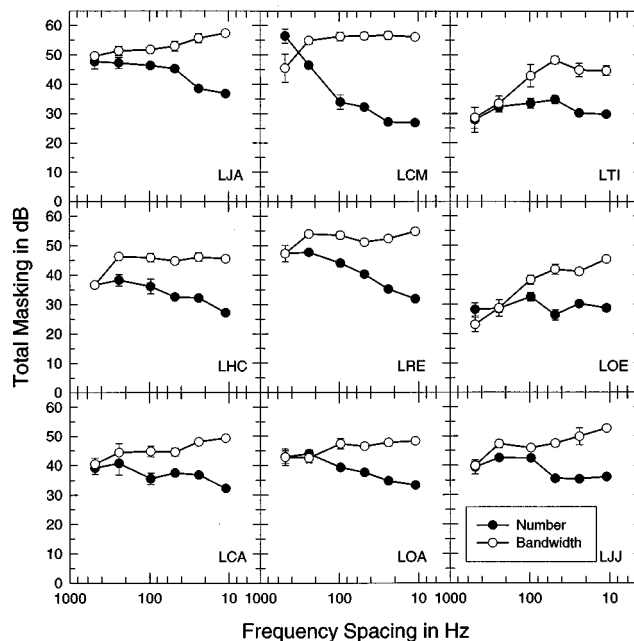


FIG. 8. Total masking with standard errors as a function of the frequency spacing of masker components. Open circles represent total masking with variable masker bandwidth, and solid circles represent total masking with variable number of masker components.

B. Results

Total masking for individual listeners in experiment 1 and this experiment is plotted in Fig. 8. When frequency spacing is reduced by increasing the number of masker components, the total masking decreases. In contrast, when frequency spacing is reduced by decreasing masker bandwidth for fixed number of components, the total masking increases. Figure 9 shows the mean data and the prediction of the CoRE model when the number of masker components was varied in experiment 1 (top panel) and when masker bandwidth was varied in the present experiment (bottom panel). In the current experiment, because masker bandwidth was varied in each condition, a listener might be able to adjust his or her attentional bandwidth accordingly. Thus in computing σ_L , a variable bandwidth that is equal to masker bandwidth was used as well as the fixed attentional bandwidth of $W = 0.1\text{--}2.5$ kHz. The values of σ_L turned out to be very simi-

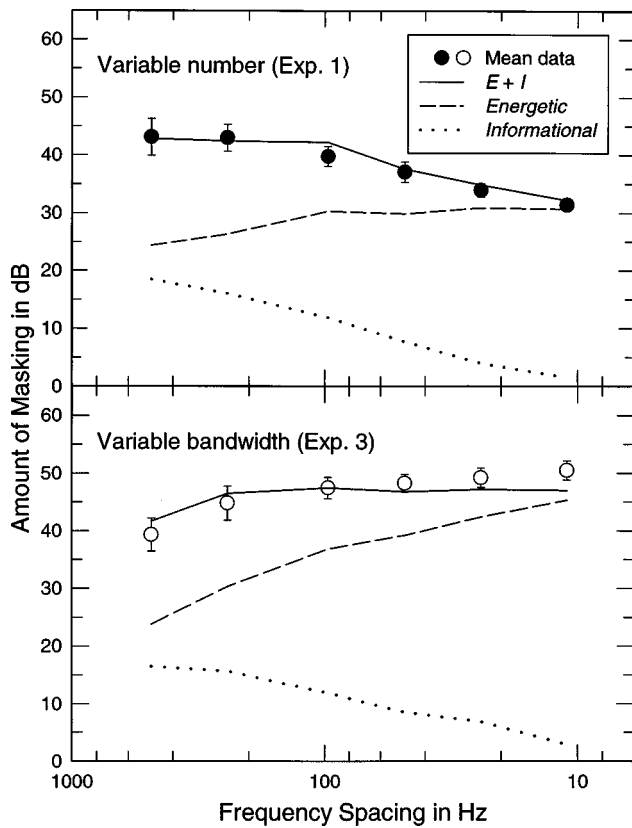


FIG. 9. Top panel: The amount of masking for the condition where the number of masker components was varied (experiment 1). Bottom panel: The amount of masking for the condition where masker bandwidth was varied (experiment 3). Circles represent the total masking averaged over nine listeners with standard errors. The solid line represents the prediction of the CoRE model given by adding the estimates of energetic (dashed line) and informational masking (dotted line). The estimates of informational masking in the two experiments are similar to each other, while the estimates of energetic masking are different.

lar in each case. In both panels of Fig. 9, the values of σ_L computed with the fixed bandwidth are plotted for the comparison. The predicted amount of total masking in this case agrees well with the total masking obtained from listeners. As shown in this figure, the difference in the total masking between the two experiments is largely due to the difference in energetic masking. The decrease in frequency spacing by adding more than 100 components does not increase energetic masking. However, energetic masking continues to increase with the decrease in frequency spacing produced by reducing masker bandwidth. The amount of informational masking shows little dependency on the number of components, but it decreases systematically with decreasing frequency spacing of components. It matters little whether the decrease in frequency spacing is caused by either reducing masker bandwidth or by adding masker components. This result supports the CoRE model prediction that the decrease in spectral variation across maskers results in reduction in informational masking.

V. DISCUSSION

A. Model parameters

Recall that there are two free parameters of the CoRE model: The attentional bandwidth W and the number of au-

ditory filters n over which the listener integrates information within this bandwidth. The mean data agree well with the predictions of the CoRE models for $n \cong 2$ and $W = 0.1 - 2.5$ kHz. Given the large amount of masking obtained from listeners, one might expect that listeners integrate irrelevant information over large numbers of auditory filters. However, the values of the free parameters suggest that the listeners' performance is based on the outputs of only one or two auditory filters over a wide frequency range. One possible explanation for this result is that the listeners are able to focus on the outputs of one or two filters as they should when detecting a single fixed-frequency tone, but that they do not have good control over the center frequency of these filters, perhaps because they are in some way "confused" by trial-by-trial variation of maskers. This confusion may, in fact, simply amount to mistaking one or another of the masker tones for the signal.

This notion of stimulus "confusion" is similar to the notion of a random or roving attentional band as has been suggested by other authors (Allen and Wightman, 1995; Lutfi *et al.*, 1996). Allen and Wightman (1995) investigated the effects of stimulus uncertainty on preschool children's and adults' detection of a pure-tone signal in Gaussian noise. The children's thresholds were consistently higher than those of adults when one of two signal frequencies was randomly selected and when the signal frequency was fixed. The adults showed only a slight reduction in performance for the random-frequency signal compared to the fixed-frequency signal case, while the children showed no reduction in performance. The reduction in performance is expected if it is assumed that listeners simultaneously attend to the outputs of filters centered at the two signal frequencies. Allen and Wightman explain this result by suggesting that the children may not focus on a specific frequency region but may instead change their attention band at random even when the signal frequency is fixed.

Lutfi *et al.* (1996) present a similar argument for adults. These authors measured the shape of the psychometric function for the discrimination of spectral variance. The stimuli were comprised of six tones whose levels varied independently on each presentation, and listeners were asked to indicate which complex had the greater variance in component level. The shape of the obtained psychometric function suggested that listeners failed to give appropriate weight to the information in individual components. The exact shape of the psychometric function could be predicted if it was assumed that listeners attended to only one or two components in the complex, not necessarily the same components on all trials. In this regard, the results of the study by Lutfi *et al.* are consistent with the results of the present study, suggesting that listeners attend to the outputs of only one or two independent auditory filters over a wide frequency range.

B. Individual differences

In this study, as in past studies (Neff and Dethlefs, 1995), large individual differences in masking functions were observed. According to the CoRE model, these individual differences derive from differences in the size of the attentional bandwidth (W) and the number of auditory filters

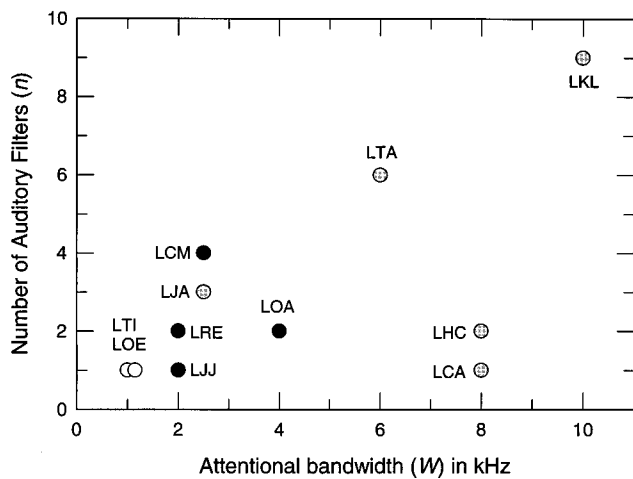


FIG. 10. The values of the attentional bandwidth (W) and the number of independent auditory filters (n) selected for each listener. The listeners in the first, second, and third group are represented by gray, black, and white circles, respectively.

used within this band (n). The predictions of the CoRE model for individual listeners are represented by solid lines in Fig. 1. The values of the two free parameters of the model selected for each listener are plotted in Fig. 10. The listeners in the first, second, and third group are represented by gray, black, and white circles, respectively. The high-threshold listeners (LKL and LTA) tend to have wider attentional bandwidth (W) and larger number of auditory filters (n). For the low-threshold listeners, the values of W and n reach their minimum. However, the relationship between n and W is not simple. In particular, listeners LHC and LCA have wide W but small n , while LTA and LKL have wide W and large n . Notwithstanding these differences, the CoRE model predicts well the individual differences in masking functions with an appropriate selection of the values of the two free parameters of the model.

The predictions of the CoRE model were based on a simplified assumption that there exist no differences in the listeners' peripheral auditory filters. Presumably, actual auditory filter measures for individual listeners would improve the predictions. Nevertheless, we were able to demonstrate that attentional mechanisms within the framework provided by the model could account for the large differences among the listeners in the amounts of masking. Previous studies are consistent with these results, since they suggest that individual differences in processing complex, dynamic sounds should derive from nonsensory central factors such as memory, learning, and selective attention (cf. Hirsch and Watson, 1996). Neff *et al.* (1993) measured peripheral and attentional filters for high- and low-threshold listeners using maskers with spectral gaps. The two groups of listeners did not differ significantly in their peripheral auditory filters. However, the low-threshold listeners had narrower attentional filters and better processing efficiency. Berg and Green (1990) estimated the relative weights listeners give to different components of complex spectra. They showed that the weighting functions of "good profile listeners" are closer to the optima, while the weighting function of a "poor profile listener" is further away from the optima. The importance of

central factors has also been suggested in developmental psychoacoustics. Higher thresholds and flattened psychometric functions among children have been simulated by assuming that some children may be inattentive or confused on some trials (Viemeister and Schlauch, 1992; Wightman and Allen, 1992).

VI. CONCLUSIONS

In the current study, we tested specific predictions of the CoRE model for the detection of a fixed-frequency signal in the context of maskers with uncertain spectra. In such conditions the CoRE model predicts that signal threshold is simply related to the ensemble variance of masker spectra smoothed by peripheral auditory filters. The two free parameters of the model are the number of auditory filters and the attentional bandwidth over which listeners are assumed to integrate information in the stimulus.

(1) The CoRE model predicts the nonmonotonic relation between the amount of total masking and the number of masker components. Individual as well as mean thresholds were well predicted by the CoRE model with appropriate values of the two free parameters of the model for each listener.

(2) The model predicts the large reduction in total masking when masker uncertainty is introduced by varying the amplitudes of masker components with fixed frequencies to simulate Gaussian noise.

(3) When the number of masker components is held constant, the amount of informational masking decreases systematically with decreasing frequency spacing of components as predicted by the model.

(4) Future studies are needed to determine how well the CoRE model can predict mean and individual data for more complex types of detection and discrimination tasks.

ACKNOWLEDGMENTS

The authors would like to thank Dr. Donna Neff and Dr. Charles Watson for their comments on an earlier draft of the paper. This research was supported by a grant from the NIDCD (Grant no. R01 CD01262-04).

¹It should be noted that this approach represents a rather strong endorsement of the auditory filter model, and that it remains an empirical question as to what extent predicted thresholds using this approach would agree with the average of thresholds for maskers presented individually.

²Note that this frequency effect is likely to be less pronounced when the frequency spacing of components is logarithmic rather than linear.

³*Ad hoc* analyses using more realistic forms for G yielded essentially identical results for these experiments. This is to be expected as the distribution of masker frequencies is uniform over a wide range. In different conditions where the distribution in frequency is nonuniform or where masker components are remote from the signal frequency, the exact form selected for G can be expected to have greater impact.

Allen, P., and Wightman, F. (1995). "Effects of signal and masker uncertainty on children's detection," *J. Speech Hear. Res.* **38**, 503–511.

ANSI (1989). ANSI S3.6-1989, "Specifications for audiometers" (ANSI, New York).

Berg, B. G., and Green, D. M. (1990). "Spectral weights in profile listening," *J. Acoust. Soc. Am.* **88**, 758–766.

Fletcher, H. (1940). "Auditory patterns," *Rev. Mod. Phys.* **12**, 47–56.

- Glasberg, B. R., and Moore, B. C. J. (1990). "Derivation of auditory filter shapes from notched noise data," *Hearing Res.* **47**, 103–138.
- Green, D. M. (1988). *Profile Analysis: Intensity Discrimination* (Oxford U.P., New York).
- Hirsh, I. J., and Watson, C. S. (1996). "Auditory psychophysics and perception," *Annu. Rev. Psychol.* **47**, 461–484.
- Kidd, G. R., and Watson, C. S. (1992). "The proportion-of-total-duration rule for the discrimination of auditory patterns," *J. Acoust. Soc. Am.* **92**, 109–3118.
- Levitt, H. (1971). "Transformed up–down methods in psychacoustics," *J. Acoust. Soc. Am.* **49**, 467–477.
- Lutfi, R. A. (1990). "How much masking is informational masking?" *J. Acoust. Soc. Am.* **88**, 2607–2610.
- Lutfi, R. A. (1993). "A model of auditory pattern analysis based on component-relative-entropy," *J. Acoust. Soc. Am.* **94**, 748–758.
- Lutfi, R. A., Doherty, K. A., and Oh, E. (1996). "Psychometric functions for the discrimination of spectral variance," *J. Acoust. Soc. Am.* **100**, 2258–2265.
- Neff, D. L., and Callaghan, B. P. (1987). "Simultaneous masking by small numbers of sinusoids under conditions of uncertainty," in *Auditory Processing of Complex Sounds*, edited by W. A. Yost and C. S. Watson (Erlbaum, Hillsdale, NJ), pp. 37–46.
- Neff, D. L., and Callaghan, B. P. (1988). "Effective properties of multicomponent simultaneous maskers under conditions of uncertainty," *J. Acoust. Soc. Am.* **83**, 1833–1838.
- Neff, D. L., and Dethlefs, T. M. (1995). "Individual differences in simultaneous masking with random-frequency, multicomponent maskers," *J. Acoust. Soc. Am.* **98**, 125–134.
- Neff, D. L., and Green, D. M. (1987). "Masking produced by spectral uncertainty with multicomponent maskers," *Percept. Psychophys.* **41**, 409–415.
- Neff, D. L., Dethlefs, T. M., and Jesteadt, W. (1993). "Informational masking for multicomponent maskers with spectral gaps," *J. Acoust. Soc. Am.* **94**, 3112–3126.
- Oh, E., and Lutfi, R. A. (1997). "Effects of masker uncertainty on masking by familiar sounds," *J. Acoust. Soc. Am.* **101**, 3148.
- Patterson, R. D., Nimmo-Smith, I., Weber, D. L., and Milroy, R. (1982). "The deterioration of hearing with age: Frequency selectivity, the critical ratio, the audiogram, and speech threshold," *J. Acoust. Soc. Am.* **72**, 1788–1803.
- Pollack, I. (1975). "Auditory informational masking," *J. Acoust. Soc. Am.* **57**, S5.
- Spiegel, M. F., and Watson, C. S. (1981). "Factors in the discrimination of tonal patterns III: Frequency discrimination with components of well-learned patterns," *J. Acoust. Soc. Am.* **69**, 223–230.
- Spiegel, M. F., Picardi, M. C., and Green, D. M. (1981). "Signal and masker uncertainty in intensity discrimination," *J. Acoust. Soc. Am.* **70**, 1015–1019.
- Viemeister, N. F., and Schlauch, R. S. (1992). "Issues in infant psychoacoustics," in *Developmental Psychoacoustics*, edited by L. A. Werner and E. W. Rubel (American Psychological Association, Washington, DC), pp. 191–209.
- Watson, C. S., and Kelly, W. J. (1981). "The role of stimulus uncertainty in the discrimination of auditory patterns," in *Auditory and Visual Pattern Recognition*, edited by D. J. Getty and J. H. Howard, Jr. (Erlbaum, Hillsdale, NJ), pp. 37–59.
- Watson, C. S., Foyle, D. C., and Kidd, G. R. (1990). "Limits of auditory pattern discrimination for patterns with various durations and numbers of components," *J. Acoust. Soc. Am.* **88**, 2631–2638.
- Watson, C. S., Kelly, W. J., and Wroton, H. W. (1976). "Factors in the discrimination of tonal patterns II: Selective attention and learning under various levels of stimulus uncertainty," *J. Acoust. Soc. Am.* **60**, 1176–1186.
- Watson, C. S., Wroton, H. W., Kelly, W. J., and Benbassat, C. A. (1975). "Factors in the discrimination of tonal patterns I: Component frequency, temporal position, and silent intervals," *J. Acoust. Soc. Am.* **57**, 1175–1185.
- Wightman, F., and Allen, P. (1992). "Individual differences in auditory capability among preschool children," in *Developmental Psychoacoustics*, edited by L. A. Werner and E. W. Rubel (American Psychological Association, Washington, DC), pp. 113–133.

Suppression and the upward spread of masking

Andrew J. Oxenham^{a)}

Communication Research Laboratory, Department of Speech-Language Pathology and Audiology (133 FR),
Northeastern University, Boston, Massachusetts 02115

Christopher J. Plack

Laboratory of Experimental Psychology, University of Sussex, Brighton, E. Sussex BN1 9QG, England

(Received 26 March 1998; revised 20 July 1998; accepted 10 September 1998)

The purpose of this study is to clarify the role of suppression in the growth of masking when a signal is well above the masker in frequency (upward spread of masking). Classical psychophysical models assume that masking is primarily due to the spread of masker excitation, and that the nonlinear upward spread of masking reflects a differential growth in excitation between the masker and the signal at the signal frequency. In contrast, recent physiological studies have indicated that upward spread of masking in the auditory nerve is due to the increasing effect of suppression with increasing masker level. This study compares thresholds for signals between 2.4 and 5.6 kHz in simultaneous and nonsimultaneous masking for conditions in which the masker is either at or well below the signal frequency. Maximum differences between simultaneous and nonsimultaneous masking were small (<6 dB) for the on-frequency conditions but larger for the off-frequency conditions (15–32 dB). The results suggest that suppression plays a major role in determining thresholds at high masker levels, when the masker is well below the signal in frequency. This is consistent with the conclusions of physiological studies. However, for signal levels higher than about 40 dB SPL, the growth of masking for signals above the masker frequency is nonlinear even in the nonsimultaneous-masking conditions, where suppression is not expected. This is consistent with an explanation based on the compressive response of the basilar membrane, and confirms that suppression is not necessary for nonlinear upward spread of masking. © 1998 Acoustical Society of America. [S0001-4966(98)03812-0]

PACS numbers: 43.66.Dc, 43.66.Ba, 43.66.Mk [RVS]

INTRODUCTION

For tonal signals presented in a band-limited masker, thresholds increase roughly linearly with increasing masker level for signal frequencies around the masker frequency region. In contrast, thresholds increase more rapidly for signal frequencies well above the masker frequency region (Wegel and Lane, 1924; Egan and Hake, 1950). This leads to the well-known “upward spread of masking.” Frequency selectivity, and hence masking as a function of frequency separation, is generally believed to be established at the level of the cochlea. This assumption has support from studies that have compared behavioral and physiological frequency selectivity in the same species (e.g., Evans *et al.*, 1992). Traditionally, it has been assumed in psychophysics that masking is excitatory. That is, the masker is assumed to produce sufficient activity to make the additional activity due to the signal inaudible. Consequently, with the additional assumption that a constant “internal” signal-to-masker ratio is required for detection, the threshold of a sinusoidal signal is thought to reflect the excitation produced by a masker at the signal frequency. This assumption is used in most psychophysical models of masking (Zwicker, 1970; Glasberg and Moore, 1990; Rosen and Baker, 1994), intensity discrimination (Florentine and Buus, 1981), and loudness perception (Zwicker, 1960; Moore *et al.*, 1997). An alternative mechanism that

could account for masking is suppression. Suppression refers to the reduction in the response to one stimulus by the introduction of a second. Masking by suppression alone implies that the neural activity due to the signal is reduced by the masker to a level indistinguishable from spontaneous activity. Suppression has been observed physiologically at the level of the auditory nerve (Sachs and Kiang, 1968) and the basilar membrane (Ruggero *et al.*, 1992a) and it is thought to be an inherent property of nonlinear cochlear mechanics.

Delgutte (1990) has pointed out that the two masking mechanisms, excitation and suppression, are not necessarily mutually exclusive; a masker may partially suppress a signal to a level at which its excitation is not distinguishable from that produced by the masker. In his extensive study at the level of the auditory nerve, Delgutte sought to differentiate between these two mechanisms over a range of masker levels and for conditions where the signal frequency was either below, at, or above the masker frequency. For signals well above the masker frequency, the amount of suppressive masking was large, and increased with masker level more rapidly than did excitatory masking. This led Delgutte to suggest that “the upward spread of masking is largely due to the growth of suppression rather than to that of excitation.” This view has been supported by other physiological studies (e.g., Pang and Guinan, 1997). If this interpretation is correct, it has important consequences for psychoacoustic models. As pointed out by Moore and Vickers (1997), if suppression plays a dominant role in some simultaneous-masking

^{a)}Electronic mail: aoxenham@lynx.neu.edu

conditions, then models that equate simultaneous-masking patterns with excitation patterns must be inaccurate.

Some psychoacoustic evidence suggests that suppression is not necessary to produce nonlinear growth of masking at frequencies above that of the masker. Oxenham and Plack (1997) found highly nonlinear growth of masking in a forward-masking condition, where suppression should presumably play no role (Arthur *et al.*, 1971). In fact, they found that the growth of masking was much steeper than previously found for any simultaneous-masking condition. The slope of the masking function at signal frequencies of 2 and 6 kHz, when the masker was an octave below the signal, was between 5 and 6 dB/dB, compared with typical values of around 2 dB/dB for simultaneous-masking conditions (Stelmachowicz *et al.*, 1987).¹ Oxenham and Plack argued that the large value is expected, based on the following known properties of basilar-membrane (BM) mechanics: the BM response to tones well below characteristic frequency (CF) is linear, while the response to tones at CF is highly compressive over a wide range of levels. Thus, for a masker well below the signal frequency, an increase in masker level by 1 dB will result in a 1-dB increase in excitation at the place on the BM corresponding to the CF of the signal. If the BM response to the signal grows at a rate of $1/x$ dB per dB increase in signal level, then, assuming a constant signal-to-masker ratio at threshold, the signal level will have to be increased by x dB to match the increase in excitation due to the masker. Rates of growth of 0.2 dB/dB and lower have been recorded from BM measurements (Ruggero, 1992; Murugasu and Russell, 1996). Thus, it is expected that the growth of masking slope could exceed 5 dB/dB in some cases. Note that this explanation of the nonlinear upward spread of masking does not rely on suppression. In fact, it has been argued that suppression may *reduce* the slope of the masking function, as the presence of a high-intensity, low-frequency stimulus can linearize the response to a tone at CF (Ruggero *et al.*, 1992b).

The psychoacoustic finding by Oxenham and Plack (1997) of strong upward spread of masking in nonsimultaneous masking seems inconsistent with the physiological results of Delgutte (1990), who found essentially linear growth of masking for his “nonsimultaneous masking” conditions. Oxenham and Plack suggested that this apparent discrepancy may be due to the different range of signal levels used in the two studies. In Delgutte’s study, in the frequency regions where most suppression was observed, signal levels in the nonsimultaneous conditions rarely exceeded 40 dB SPL; in Oxenham and Plack’s study, measurements were concentrated on signal levels between 40 and 90 dB SPL. According to physiological measurements, the BM response to CF tones is nearly linear at low levels and becomes highly compressive only at levels above about 30–40 dB SPL (Yates *et al.*, 1990; Murugasu and Russell, 1995; Ruggero *et al.*, 1997). Thus, the finding by Delgutte of linear growth in his nonsimultaneous-masking condition may be due to the fact that high signal levels were not tested.

This study has two main aims. The first is to use psychophysical methods to investigate whether the upward spread of masking is due primarily to suppression or excita-

tion, or a combination of both. This has important implications for most psychoacoustic models. As mentioned above, if it were found that suppression is dominant in producing the upward spread of masking, then models that equate simultaneous-masking patterns with excitation patterns (Florentine and Buus, 1981; Glasberg and Moore, 1990; Rosen and Baker, 1994; Moore *et al.*, 1997) may require some revision. The second aim is to test the hypothesis that the apparent discrepancy between the physiological results of Delgutte and the psychophysical results of Oxenham and Plack can be ascribed to the different ranges of signal levels tested. This is important in resolving apparent differences between physiological and psychophysical data. If the data from the two studies are found to be comparable when similar signal levels are used, this will provide further support for the idea that psychophysical suppression reflects processes already apparent at the level of the BM and auditory nerve. If not, it will be more likely that other effects, such as lateral inhibition at higher levels of the auditory pathways, play a significant role in basic masking experiments.

Experiment 1 compares thresholds for simultaneous and nonsimultaneous maskers in an on-frequency condition and in a condition where the masker is centered at a frequency well below that of the signal (off-frequency condition). In line with physiological studies, it is assumed that the effects of suppression on the signal can only be observed in the off-frequency, simultaneous-masking condition. Thus, by comparing the results from the off-frequency simultaneous- and nonsimultaneous-masking conditions, it should be possible to draw conclusions about the role of suppression in the upward spread of masking.

I. EXPERIMENT 1: GROWTH OF SIMULTANEOUS AND NONSIMULTANEOUS MASKING IN ON- AND OFF-FREQUENCY CONDITIONS

A. Stimuli

Thresholds were measured for a brief 4-kHz sinusoidal signal in the presence of a 500-Hz-wide Gaussian-noise masker that was either centered at the signal frequency (on-frequency condition) or centered at a lower frequency of 2.4 kHz (off-frequency condition). The signal had a total duration of 10 ms and was gated with 5-ms raised-cosine ramps (no steady state). The masker was gated with 2-ms ramps. In the simultaneous-masking condition, the signal was presented in the temporal center of a 400-ms (half-amplitude duration) masker. In the nonsimultaneous-masking condition, the signal was presented in a temporal gap between two 200-ms masker bursts. The silent interval between the end of the first masker (forward masker) and the beginning of the signal was 2 ms (defined as the time between the 0-voltage points in the electrical envelope); the interval between the end of the signal and beginning of the second masker (backward masker) was 5 ms. The backward masker was added to reduce the possibility of “off-time listening” at high signal levels (see Robinson and Pollack, 1973; Oxenham and Moore, 1994).² A high signal frequency was chosen to reduce the possibility that nominally nonsimultaneous stimuli overlapped in the auditory periphery, due to “ringing” in the

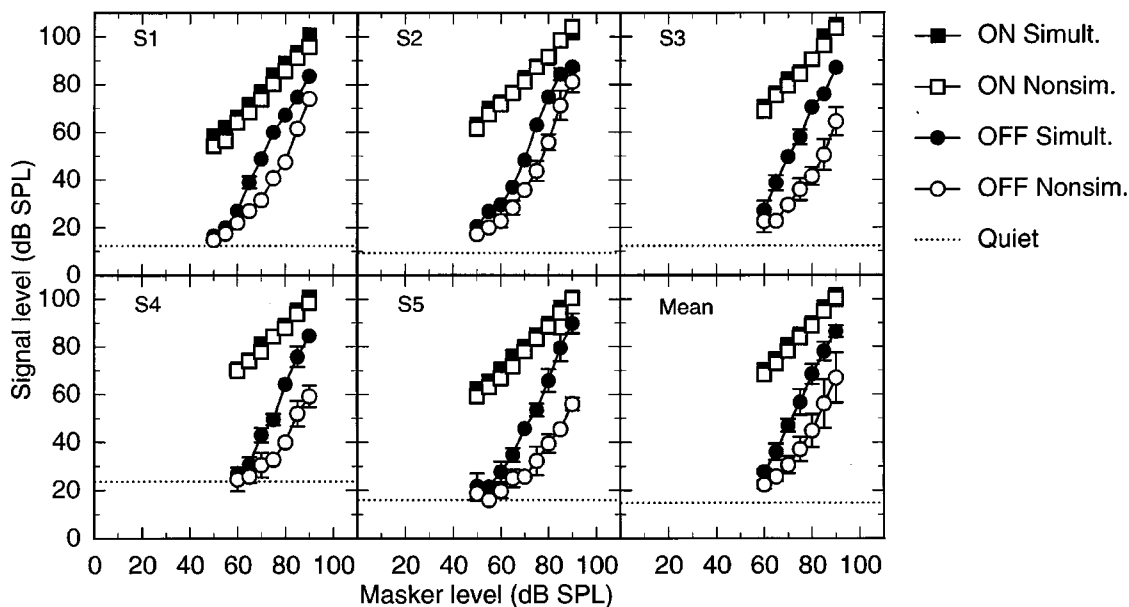


FIG. 1. Thresholds for a brief 4-kHz signal as a function of masker level. Filled and open symbols represent simultaneous- and nonsimultaneous-masking conditions, respectively. Circles represent off-frequency conditions, where the masker center frequency was 2.4 kHz; squares represent on-frequency conditions, where the masker center frequency was 4 kHz. Thresholds in quiet are shown as dotted lines. Error bars represent ± 1 s.d. of the mean and are omitted if smaller than the symbol.

auditory filters. To reduce the possibility that “confusion” effects (Moore and Glasberg, 1982; Neff, 1986) were playing a role in the on-frequency nonsimultaneous conditions, an independently generated contralateral noise with the same spectral properties and level as the masker was always gated with the masker. Contralateral noise has been shown to have little or no effect on thresholds in simultaneous noise masking (e.g., Kohlrausch and Langhans, 1992), but may lower thresholds in some forward-masking situations in which confusion could play a role (see the Appendix). Signal thresholds were measured in quiet and for masker levels between 50 and 90 dB SPL (between 60 and 90 dB SPL for two listeners), in steps of 5 dB.

Bandpass noise was created at the beginning of each run by generating a 2-s circular buffer of wideband Gaussian noise, performing a discrete Fourier transform, setting the amplitude of the components outside the desired passband to zero, and applying an inverse Fourier transform. A random starting point within the resulting noise buffers was selected on each presentation interval. Thus, only the gating of the noise produced spectral components beyond the specified passband. All stimuli were generated digitally at a 32-kHz sampling rate, and were played out using the built-in 16-bit D/A converter and reconstruction (anti-aliasing) filter of a Silicon Graphics workstation. Stimuli were passed through a programmable attenuator (TDT PA4) and a headphone buffer (TDT HB6) before being presented to listeners via a Beyer DT990 headset. The signal was always presented to the listener’s left ear.

B. Procedure

Thresholds were measured using a three-interval forced-choice method with a two-down, one-up adaptive procedure that tracks the 70.7%-correct point of the psychometric func-

tion. Each trial consisted of three intervals containing the masker and the contralateral noise. The interstimulus interval was 300 ms. The signal occurred randomly in one of the three intervals and listeners were required to select the signal interval. The signal level was initially adjusted in steps of 8 dB. After every two reversals, the step size was halved until a minimum step size of 2 dB was reached. The run terminated after a further eight reversals. Threshold was defined as the median level at the last eight reversals. For every listener, four such threshold estimates were made for each condition, and the mean and standard deviation of the four estimates were recorded. Listeners were tested in 2-h sessions, including short breaks. The four estimates for each data point were generally collected on four separate days. Responses were made via a computer keyboard, and feedback was provided via a computer monitor placed outside the listening booth. Listeners were tested in a single-walled sound-attenuating booth, which was situated in a sound-attenuating room.

C. Listeners

Five listeners were tested. Listener 1 was the author A.O.; the others were students who were paid for their participation. The listeners were between 19 and 28 years of age and had absolute thresholds of less than 15 dB HL at octave frequencies between 250 and 8000 Hz. Listeners S1 and S3 were male; listeners S2, S4, and S5 were female. None reported histories of hearing disorders or difficulties. The listeners were given at least three hours practice before data were collected. No consistent improvements in performance were noted during the course of the experiment.

D. Results

The individual and mean results for the five listeners are shown in Fig. 1. The dotted lines represent thresholds for the

signal in quiet. Filled and open symbols represent simultaneous- and nonsimultaneous-masking conditions, respectively. Squares represent on-frequency conditions, where the masker center frequency is 4 kHz (labeled ON in Fig. 1), and circles represent off-frequency conditions, where the masker center frequency is 2.4 kHz (labeled OFF in Fig. 1). Error bars represent ± 1 s.d. and are shown if they exceed the size of the symbol. Standard deviations for thresholds in quiet were less than 2 dB for all listeners.

Consider first the results from the simultaneous-masking conditions (filled symbols). In line with many previous studies, the growth of masking for the on-frequency condition (filled squares) is approximately linear. Linear regression analysis of the individual data resulted in slope estimates of between 0.94 and 1.14 (slope of mean data: 1.01; percent of variance accounted for, $R^2=99.7\%$). Again consistent with many previous studies, the growth of masking for the off-frequency condition (filled circles) is steeper than linear. Taking into account only data points that lie 5 dB or more above threshold in quiet, a linear regression analysis produced individual slope estimates between 1.80 and 2.18 (slope of mean data: 2.01; $R^2=99.8\%$). The slope of the mean data is in good agreement with a survey of previous growth-of-masking studies carried out by Stelmachowicz *et al.* (1987).

Consider next the results from the nonsimultaneous-masking conditions (open symbols). Results from the on-frequency condition (open squares) are very similar to those from the on-frequency simultaneous condition. There is a tendency for thresholds to be somewhat lower in the nonsimultaneous than in the simultaneous condition, but the difference is always less than 6 dB. The mean difference between the on-frequency simultaneous and nonsimultaneous conditions, pooled across listeners and conditions, is 2.1 dB. A small difference in thresholds between a simultaneous-masked signal and a signal presented in a brief gap has been reported before: Oxenham and Moore (1994) found that thresholds in very brief gaps were either similar to or, in some cases, even higher than thresholds in a simultaneous masker. As this was found using a broadband masker with a 6-kHz sinusoidal signal, it is unlikely that the present results are due to the confusion of the signal with the 500-Hz-wide masker. A linear regression analysis produced individual slopes of between 0.96 and 1.12 (slope of mean data: 1.06; $R^2=99.9\%$). Thus, there appears to be no difference in the slope of the growth of masking between the two on-frequency conditions. Linear growth of nonsimultaneous masking is unusual, but has also been reported for a very brief signal in forward masking alone (Oxenham and Plack, 1997). Furthermore, linear growth is expected when the masker and signal levels are nearly equal, based on a recent theory of forward masking that links the nonlinear growth of forward masking to the nonlinear response of the BM (Oxenham and Moore, 1995; Oxenham and Moore, 1997; Plack and Oxenham, 1998). In contrast to the small difference between the two on-frequency conditions, the differences between the two off-frequency conditions are considerable, especially at medium to high levels.

If the difference between the two on-frequency condi-

tions reflects the difference in effectiveness between simultaneous and nonsimultaneous masking *per se*, any further differences between the two off-frequency conditions may be due to suppression. In this way, the nonsimultaneous thresholds may reflect masker excitation at or near the signal frequency, while the simultaneous thresholds reflect masker excitation *plus* the increase in signal level required to compensate for the effects of suppression.

It can be seen that, at least at higher masker levels, the growth of masking of the nonsimultaneous off-frequency condition is steeper than linear. This suggests that suppression is not necessary for nonlinear upward spread of masking. However, at lower levels the function appears shallower for the nonsimultaneous than for the simultaneous condition. According to the hypothesis stated in the Introduction, we might expect the off-frequency growth of masking to be linear up to a certain signal level, and then to become nonlinear. The breakpoint between these two regions should reflect the level at which the on-frequency BM response becomes compressive. For the purposes of this analysis, we assume that the breakpoint occurs at 40 dB SPL.³ A linear regression performed using data from the off-frequency nonsimultaneous condition for signal levels between 5 dB SL and 40 dB SPL resulted in individual slopes ranging from 0.90 to 1.0 (slope of pooled data: 0.94; $R^2=93.6\%$).⁴ For the same condition, linear regression using only data points where thresholds were above 40 dB SPL resulted in slopes between 1.93 and 2.56 (slope of pooled data: 2.32; $R^2=97.9\%$). Thus, if only signal levels at or below 40 dB SPL are taken into account, the off-frequency growth of masking in the nonsimultaneous condition is essentially linear. This is consistent with the finding of Delgutte (1990) that, at low signal levels, there was no nonlinear upward spread of masking in the nonsimultaneous-masking condition. It is also consistent with the hypothesis that BM nonlinearity governs the upward spread of nonsimultaneous masking: at low levels, where the BM is thought to respond linearly, linear growth of masking is observed; at higher levels, where the BM response is compressive, nonlinear growth of masking is observed.

The difference between the off-frequency simultaneous and nonsimultaneous conditions may provide us with an estimate of the amount of suppression found for a given masker-signal combination. Once differences in effectiveness between on-frequency simultaneous and nonsimultaneous masking are accounted for, the difference in dB between the two off-frequency conditions can be interpreted as the gain required to restore the simultaneous-masked signal to its unsuppressed internal representation. Note that in this interpretation, also made by many others (Houtgast, 1973; Shannon, 1976; Duifhuis, 1980; Moore and Glasberg, 1981), the nonsimultaneous threshold provides a better estimate of the masker excitation at or near the signal frequency than the simultaneous threshold. In estimating the amount of suppression, the difference between the on-frequency conditions was accounted for individually by taking the mean difference for each listener between the two on-frequency conditions and subtracting it from the difference between the two off-frequency conditions at each masker level. The mean difference between the on-frequency conditions ranged from 0.4

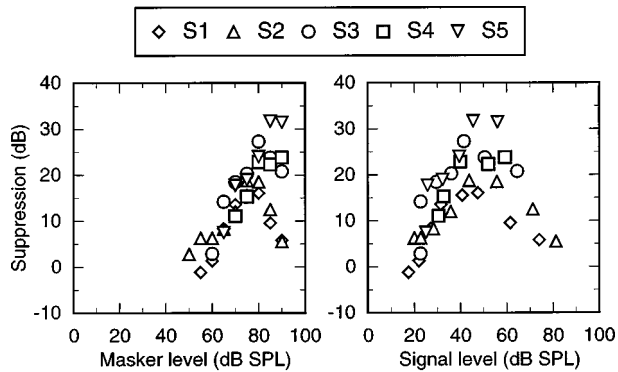


FIG. 2. Amount of suppression, estimated as described in the text, as a function of masker level (left panel) and as a function of nonsimultaneous-masked signal level (right panel). Different symbols represent results from the different listeners.

(S2) to 3.7 dB (S1). The estimated amounts of suppression for the individual listeners are shown in Fig. 2.

The amount of suppression estimated in this way is substantial for all listeners. However, there are also large differences between individual listeners, especially at the highest masker levels, as can be seen in the left panel of Fig. 2. For listeners S1, S2, and S3, suppression seems to reach a maximum at masker levels of around 80 dB SPL and then decrease somewhat at higher levels. For listeners S4 and S5, suppression remains high at the highest masker levels. An alternative way of plotting the results is shown in the right panel. Here, suppression is plotted as a function of nonsimultaneous signal level. This measure could also be thought of as reflecting the *effective* masker level at the signal CF. Generally, maximum suppression seems to occur for signal levels between about 40 and 60 dB SPL and to decline below and above that. Listeners exhibit a maximum amount of suppression of between 15 (S1) and 32 dB (S5). The amounts of suppression observed here are in line with those observed at similar masker–signal frequency ratios by previous investigators. Duifhuis (1980) showed that suppression using the pulsation-threshold method could be very large when the suppressor was well below the frequency of the suppressor. The maximum amounts of suppression measured by him with frequencies of 600 Hz and 1 kHz for the suppressor and suppressor, respectively, ranged from about 12 to 35 dB, depending on the listener. Similarly, Shannon (1986), also using the pulsation-threshold method, found that the suppression of a 1-kHz 60-dB SPL tone produced by a 400-Hz 80-dB SPL tone lay between 20 and 30 dB for all three of his listeners. Moore and Vickers (1997), using an on-frequency forward masker at 2200 Hz and a higher-level suppressor at 500 Hz, also found that the effective level of the on-frequency masker was reduced by between 12 and 20 dB for all four listeners.

Returning to Fig. 1, the growth-of-masking slope in the nonsimultaneous off-frequency condition generally does not exceed about 2.5, even when only signal levels above 40 dB SPL are taken into account. The slope of 2.3 for the data pooled across listeners is only marginally greater than the slope of 2.0 for signal levels above 40 dB SPL in the simul-

taneous off-frequency condition. A repeated-measures analysis of covariance (ANCOVA) allowing two-way interactions, with masker level, simultaneity, and listener as factors showed that this difference in slope was significant ($F_{1,146} = 13.13$; $p < 0.001$), although the difference in slopes for listeners 4 and 5 did not fit this trend. Given that suppression should reduce the apparent compression (Ruggero *et al.*, 1992a), we expected a larger difference in slope between the simultaneous and nonsimultaneous off-frequency conditions at these higher signal levels. Also, the slope of 2.3 contrasts with the growth of masking found by Oxenham and Plack (1997) using a sinusoidal forward masker and signal. In that study, a slope of about 6 was observed for signal levels between 50 and 80 dB SPL, which is more in line with the slope expected based on BM measurements. It is possible that the difference may in part be due to “off-frequency” listening at high signal levels (Johnson-Davies and Patterson, 1979; O’Loughlin and Moore, 1981). In the previous study a highpass noise was added to restrict the listening band. However, other differences in the present experiment may also play a role. These include the use of a noise, rather than a tonal, masker and the different frequency ratio between masker and signal used (1:1.67, as opposed to 1:2). Further experiments are required to clarify the difference.

In summary, experiment 1 supports the hypothesis that suppression plays a major role in the upward spread of masking. This can be seen by the amount by which the off-frequency simultaneous-masked thresholds exceed the nonsimultaneous-masked thresholds. Also, no evidence for nonlinear growth of masking is found for the nonsimultaneous condition at signal levels below 40 dB SPL. However, at higher signal levels, nonlinear growth of masking is also observed in the off-frequency nonsimultaneous condition. Thus, it seems that the apparent discrepancy between the physiological findings of Delgutte and psychophysical findings of Oxenham and Plack may be due to the different ranges of signal levels studied.

The second experiment investigates how the growth of masking and the amount of suppression changes with increasing masker–signal frequency ratio.

II. EXPERIMENT 2. EFFECT OF INCREASING MASKER–SIGNAL FREQUENCY RATIO

A. Method

In this experiment, the 500-Hz-wide masker had a fixed center frequency of 2.4 kHz. The signal frequency was either 2.4, 4, 4.8, or 5.6 kHz. In order to produce reasonably high signal thresholds, even at the largest masker–signal frequency interval, the duration of the signal was reduced to a total duration of 4 ms, gated with 2-ms raised-cosine ramps (no steady state). For the 2.4-kHz signal frequency (on-frequency condition), thresholds were measured at masker levels from 25 to 85 dB SPL in 10-dB steps. For the other three (off-frequency) conditions, thresholds were measured at masker levels of 40, 50, 55, 60, and 65 dB SP, and then at 2.5-dB steps up to 90 dB SP. The smaller steps at the higher levels were designed to trace the growth of masking in more

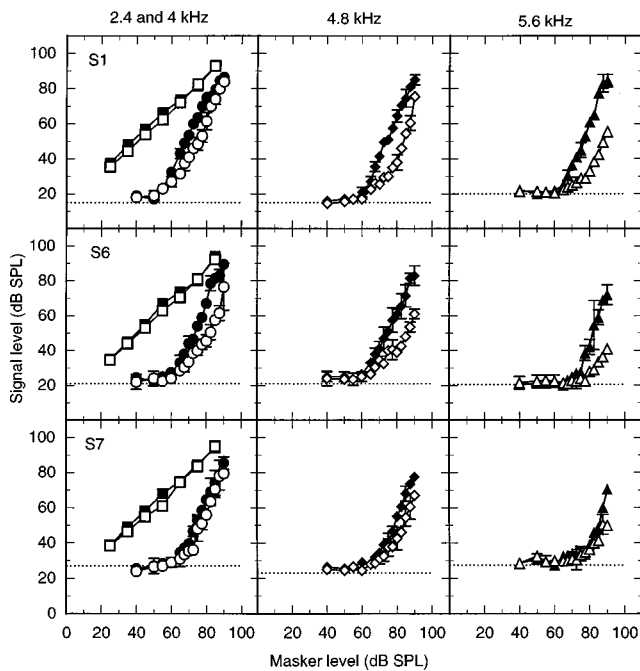


FIG. 3. Growth of masking using a noise masker with a center frequency of 2.4 kHz. Different symbols represent different signal frequencies. Data from the three listeners are shown in the three rows. See Fig. 1 for further details.

detail than was done in experiment 1. All other parameters, including masker durations and masker-signal time intervals, were the same as in experiment 1.

Thresholds were measured using a similar adaptive procedure to that used in experiment 1. Due to the larger number of conditions, and the finer level steps, the measurement procedure was shortened by terminating each run after six reversals at a step size of 2 dB and taking the median value of the last six reversals, and by measuring only two estimates for each data point. All other aspects were the same as in experiment 1.

Three listeners participated in experiment 2. Listener S1 (author A.O.) was joined by two new listeners (S6 and S7), both students 20 years old, who were given at least 4 h training on the task. Listener S6 was male; listener S7 was female. Both had absolute thresholds of less than 15 dB HL at octave frequencies between 250 and 8000 Hz and reported no history of hearing difficulties or disorders.

B. Results

The individual results from experiment 2 are shown in Fig. 3. The left panels show data for signal frequencies of 2.4 kHz (on-frequency; squares) and 4 kHz (circles). The middle and right panels show data for signal frequencies of 4.8 and 5.6 kHz, respectively. Filled symbols represent the simultaneous-masking conditions and open symbols represent the nonsimultaneous-masking conditions. Dotted lines represent signal thresholds in quiet. Error bars represent ± 1 s.d. and are shown if they exceed the size of the symbol.

The results for the on-frequency conditions (left panels; squares) are very similar to those found in experiment 1 at 4 kHz. There is very little difference between the simultaneous and the nonsimultaneous conditions for all three listeners.

Linear regression analysis resulted in individual slopes between 0.89 and 0.95 with no systematic differences between listeners or conditions. The fact that the slopes are somewhat less than unity may be due to listeners being able to detect some off-frequency “spectral splatter” at the higher levels. The use of a shorter signal and a lower center frequency than in experiment 1 may have made such a cue more salient. Again, the fact that there was very little difference between the two on-frequency conditions suggests that the large differences between the simultaneous and nonsimultaneous conditions at other frequency intervals may be primarily due to suppression.

Linear regression on the three off-frequency simultaneous conditions, taking into account data points 5 dB or more above threshold in quiet, resulted in individual slopes ranging from 1.9 to 2.8. There was a slight tendency for the simultaneous-masked slopes to become steeper with increasing frequency interval: slopes from the data pooled across listeners (see footnote 4) were 2.04 at 4 kHz ($R^2=98\%$), 2.09 at 4.8 kHz ($R^2=98.5\%$), and 2.50 at 5.6 kHz ($R^2=96\%$). This finding is consistent with some previous studies (e.g., Smits and Duifhuis, 1982; Stelmachowicz *et al.*, 1987; Murnane and Turner, 1991; Nelson and Schroder, 1997), although data from Schöne (1977), using tonal maskers, suggest little or no change with increasing masker-signal frequency interval.

Linear regression on the three off-frequency nonsimultaneous conditions, taking only signal levels between 5 dB SL and 40 dB SPL into account, again provides no evidence for nonlinear growth of masking. The slopes for the data pooled across the three listeners are 1.02 ($R^2=94.6\%$), 1.01 ($R^2=87.4\%$), and 0.91 ($R^2=91.5\%$) for the 4-, 4.8-, and 5.6-kHz conditions, respectively. Taking only signal levels above 40 dB SPL into account resulted in slopes for the pooled data of 2.4 ($R^2=95.6\%$), 2.5 ($R^2=93.7\%$), and 2.47 ($R^2=98.1$) for the 4-, 4.8-, and 5.6- kHz conditions, respectively. Thus, there seems to be no effect of signal frequency on the nonsimultaneous growth of masking for the off-frequency conditions tested. As in experiment 1, the slope of around 2.5 is less than that expected based on BM measurements and on the psychophysical data of Oxenham and Plack (1997). Kidd and Feth (1981) measured growth-of-masking functions for off-frequency forward-masked signals for masker-signal frequency ratios up to 2.0. However, because of their more typical stimulus conditions (i.e., longer signal duration and no backward masker), the amount of masking measured by them at the large frequency ratios never exceeded 25 dB, making a direct comparison with our data difficult.

The amount of suppression, estimated as in experiment 1 by subtracting the mean difference for each listener between the two on-frequency conditions from the differences between each pair of off-frequency conditions, is shown in Fig. 4. The differences are plotted as a function of the signal level in the nonsimultaneous conditions, as in the right panel of Fig. 2. Generally, suppression seems to increase with increasing masker-signal frequency interval over the range tested here. Reassuringly, S1’s pattern of suppression in experiment 2 for the 4-kHz signal is very similar to that in

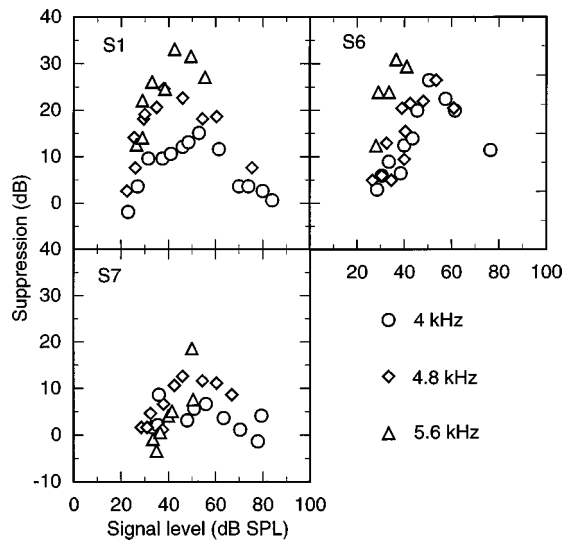


FIG. 4. Amount of suppression, estimated as described in the text, as a function of nonsimultaneous-masked signal level. Different symbols represent different signal frequencies. Data from three listeners are shown individually in the three panels.

experiment 1, despite the slightly different stimulus conditions, with suppression maxima of 16 dB and 15 dB in experiments 1 and 2, respectively. S7 generally shows less suppression at all frequency intervals. Again, for all three listeners at all three frequency intervals, suppression seems to be maximal at signal levels between about 40 and 60 dB SPL.

III. GENERAL DISCUSSION

A. The role of suppression in masking

Both experiments 1 and 2 indicate that suppression plays a major role in the psychophysical upward spread of masking. This is consistent with physiological studies of masking in the auditory nerve (Delgutte, 1990; Pang and Guinan, 1997). Experiment 2 suggests that the relative contribution of suppression continues to increase with increasing signal-masker frequency ratio at least up to the highest ratio of 2.33 measured here (signal frequency of 5.6 kHz). However, even at this ratio, excitation seems to produce some masking, as evidenced by the nonsimultaneous-masked thresholds. Therefore, for the conditions tested here, it can in some sense be argued that the masking process *per se* is entirely excitatory. In other words, the (suppressed) signal is only rendered undetectable because it is obscured by masker excitation. Except in cases where the signal is suppressed below absolute threshold, suppression *alone* will not produce any masking. It is possible that such situations are encountered at larger signal-masker frequency ratios than were measured here. However, Moore and Vickers (1997) measured the effect of a 500-Hz suppressor at a signal frequency of 2200 Hz. Even at this frequency ratio of 4.4, evidence for excitatory masking was found. Similarly, auditory-nerve rate-level functions for a pure-tone signal at CF in the presence of a lower frequency-masking noise show both a shift to the right, i.e., to higher signal levels (suppression), and an increase in the background firing rate (due to excitation from

the noise) as noise level is increased (Delgutte, 1990; Pang and Guinan, 1997). Only for very low signal levels could it be argued, on the basis of these physiological measurements, that signal threshold would be determined entirely by suppressive processes.

Both the present experiments showed that suppression seems to be maximal for signal levels between about 40 and 60 dB SPL. It is important to note, however, that this measure of suppression does not necessarily reflect the decrease in signal excitation produced by the simultaneous masker. If the signal is compressed, then a given decrease in signal level reflects a smaller decrease in signal excitation. Thus, the apparently greater suppression between 40 and 60 dB SPL may in part reflect the greater compression of the BM in that level region.

The assumption of this study has been that psychophysical suppression primarily reflects the suppression measured at the level of the BM and the auditory nerve. This assumption is supported by the similarity in the form of our data with those of Delgutte (1990). In contrast, some investigators have argued that psychophysical suppression probably also reflects mechanisms such as neural inhibition occurring at higher stages of the auditory pathways (Champlin and Wright, 1993). This claim was based on results showing a relatively slow (>10 ms) build-up for some effects ascribed to suppression. However, the main effect found by Champlin and Wright (1993) has since been shown to be compatible with an instantaneous (and hence peripheral) suppression mechanism (Bacon, 1996). Furthermore, in line with previous studies, the results from the present study indicate a very rapid release from suppression; the gap between the beginning of the masker offset and the peak of the signal in our experiment 2 is only 6 ms. Thus, the assumption that psychophysical suppression is mediated primarily by peripheral processes remains reasonable.

B. Possible implications for comodulation masking release (CMR) and thresholds in fluctuating maskers

While we have ascribed the threshold differences in our off-frequency conditions to suppression, at least one alternative explanation is possible. It may be that the off-frequency masker, by exciting many frequency channels that are not excited by the signal, allows an across-channel comparison of "internal" stimulus level within the noise gap that is not possible in the on-frequency condition. This cue may also be used in conditions eliciting comodulation masking release (CMR) (Hall *et al.*, 1984). However, we think that a CMR-like mechanism is not likely to account for our data for the following reasons. First, the contralateral masker should have provided a CMR-like cue, even in the on-frequency condition. Second, similar amounts of suppression have been found in pulsation-threshold studies (Duifhuis, 1980; Shannon, 1986) where CMR should not play a role.

Conversely, it may be that some effects previously ascribed to CMR may in part be due to suppression. For instance, Buus (1985) found a large release from masking by introducing level fluctuations in a masker well below the signal in frequency. He argued that the release may be due to

the auditory system comparing the fluctuations across different frequency channels—something not possible with an on-frequency masker. However, a release from masking would also be predicted based on the effects of suppression, as follows: suppression would generally reduce the effective level of the signal more at a masker peak than in a masker valley, due to the nonlinear growth of suppression. Thus, the release from masking introduced by brief reductions in masker level will be greater for off-frequency maskers than for on-frequency maskers, where suppression plays no role.

A similar argument can be applied to the findings reported by Zwicker (1976), Nelson and Swain (1996), and Gregan *et al.* (1998) that the peak-to-valley difference in thresholds for a brief signal in a modulated masker is greater for signal frequencies well above the masker frequency than for those at or below the masker frequency. It has been argued that this difference is due in part to the upward spread of masking found for stationary maskers; the difference is thought to reflect the internal difference in excitation between the peak and the valley of a masker at the signal frequency (Zwicker, 1976). However, at rapid modulation rates and large modulation depths, thresholds in masker valleys have been found to be determined by forward masking from the masker peak, rather than by simultaneous masking from the masker valley (Gregan *et al.*, 1998). In such cases, the explanation in terms of stationary maskers does not hold. It seems possible that the differences in such cases can be accounted for by suppression: consider a 100% amplitude-modulated sinusoidal masker and a brief sinusoidal signal well above the masker in frequency. When the signal is presented at a time corresponding to a peak in the masker envelope, thresholds will be determined by the excitation and suppression produced by the peak. When the signal is presented in a masker valley, the signal is no longer suppressed by the masker peak. Thus, the peak-to-valley difference in thresholds represents the combined decay of forward masking and release from suppression. When the signal is at the same frequency as the masker, the peak-to-valley difference reflects only the decay of forward masking. Therefore, the peak-to-valley threshold difference is expected to be smaller for on-frequency maskers than for maskers well below the signal frequency, as has been found.

For these reasons, caution should be used in interpreting CMR purely in terms of across-channel comparisons in situations where masker energy below the signal is sufficiently high to potentially produce suppression effects.

C. An alternative theory

The psychophysical effects of suppression on masking have been controversial. Although early measures of suppression found large effects, later studies showed that some of these effects may have been due to factors other than suppression, such as confusion. Lutfi (1984, 1988) proposed that it may not even be necessary to consider the effects of suppression when explaining the difference between tuning curves measured in forward and simultaneous masking. While this theory is controversial (Lutfi, 1985; Moore, 1985), it has been endorsed in a review article (Jesteadt and Norton, 1985) and seems not to have been totally disproved

even now (Sommers and Gehr, 1998). A stated, and fundamental, assumption of Lutfi's model is that masking patterns in forward masking are identical to those in simultaneous masking, but shifted down in level by a fixed dB amount. It is clear from the present data that this assumption is not tenable, at least for the frequency intervals tested here; differences between simultaneous and nonsimultaneous conditions are much greater for the off-frequency conditions than for the on-frequency conditions. Thus, Lutfi's model does not hold at least for masker-signal frequency ratios between 1.67 and 2.33. This somewhat restricts the applicability and attractiveness of the model.

IV. SUMMARY

Suppression seems to play a major role in the nonlinear upward spread of masking, especially at signal levels below 40 dB SPL. However, it seems that masking is rarely, if ever, purely suppressive. At signal levels higher than 40 dB SPL, suppression is substantial, but not necessary for the nonlinear upward spread of masking. The results suggest that the theoretical underpinnings of psychoacoustic models that equate simultaneous-masking patterns with excitation patterns may require reconsideration. In particular, the assumption that the upward spread of masking is due solely to a broadening of auditory filters at high levels (Glasberg and Moore, 1990; Rosen and Baker, 1994) seems questionable. As many stimuli in the natural environment are masked by simultaneous sounds, these assumptions may still provide a useful model of *effective* processing. Nevertheless, it should be remembered that the amount of excitation may be considerably less than that estimated in simultaneous-masking tasks. This may have some implications for the underlying theory in models of loudness or intensity discrimination, which assume a summation of excitation across frequency (Zwicker and Scharf, 1965; Florentine and Buus, 1981; Moore *et al.*, 1997).

ACKNOWLEDGMENTS

This work was carried out while the first author was a Wellcome Trust Research Fellow (Grant No. 0044215/Z/95/Z) at the Institute for Perception Research (IPO), Eindhoven, The Netherlands. The second author is supported by the Royal Society. Preparation of the manuscript was made possible by NIH/NIDCD Grant No. R01DC00187. We thank Mary Florentine, Søren Buus, Michelle Hicks, and Monita Chatterjee, for useful comments on a previous version of the manuscript.

APPENDIX: AVOIDING POSSIBLE CONFOUNDING FACTORS

1. Effects of "confusion"

Differences between simultaneous and nonsimultaneous masking have been interpreted as evidence for suppression in the past (Houtgast, 1972, 1973, 1974; Shannon, 1976; Weber and Green, 1978; Moore, 1980b). However, in certain stimulus conditions other effects have also been shown to play a role. For instance, when the signal is at the same frequency

as the masker, the signal may be confused with a continuation of the forward masker, resulting in elevated thresholds. The addition of a second stimulus, gated with the masker but at a different frequency, may provide a cue for the detection of the signal and thus reduce thresholds without actually producing any suppression. Similarly, a reduction in threshold as the signal moves away from the masker in frequency may reflect an increase in perceptual dissimilarity between the masker and signal as well as the effects of frequency selectivity. The role of confusion and its alleviation have been studied in considerable depth (Moore, 1980a; Moore and Glasberg, 1982, 1985; Neff, 1985, 1986). Briefly, “confusion” can occur if the masker and signal are in the same frequency region and (1) both masker and signal have the same bandwidth (e.g., a sinusoidal masker and signal), or (2) the masker is a narrow-band noise and the signal can be confused with the inherent fluctuations of the masker. Thresholds affected by confusion are generally less stable, are more susceptible to practice effects, and can depend strongly on the starting level of an adaptive threshold-tracking procedure (Neff, 1985, 1986). Confusion can generally be alleviated by introducing a temporal “cue” to demarcate the masker. This cue can be either ipsi- or contralateral (Moore and Glasberg, 1982).

The stimulus configuration used in the present experiment was designed to avoid confusion effects. The masker bandwidth of 500 Hz was sufficiently wide to avoid slow, audible fluctuations in the envelope, and the percept of the 10-ms sinusoidal signal was rather different from that of the noise. Furthermore, a contralateral noise was gated with the masker in all conditions to further cue the temporal boundaries of the masker. Pilot studies using a range of different starting levels in the adaptive tracking procedure showed no effect of starting level. Also, no long-term practice effects were observed for any of the listeners. Thus, we conclude that confusion probably did not play a major role in our experiment.

2. Physical overlap of nonsimultaneous stimuli in the auditory periphery

The underlying assumption of this study is that, since suppression is thought to be the result of nonlinear interactions on the BM, suppression only occurs when the stimuli physically overlap in time on the BM. Due to the filtering action of the cochlear partition, it is possible that acoustic stimuli that are separated in time may in fact overlap temporally in the cochlea. This has been termed “ringing in the auditory filters.” A number of studies have investigated the possible effects of peripheral stimulus interactions. Carlyon (1988), by measuring thresholds as a function of masker duration, found that forward-masked thresholds behaved like simultaneous-masked thresholds at a center frequency of 250 Hz when the signal was placed very close to the masker. He ascribed this effect to continued ringing in the auditory filters, effectively producing simultaneous masking, even though the acoustic signals did not physically overlap. At a signal frequency of 2 kHz, no such effects were found. His masker and signal were both gated with 2-ms ramps, the signal had a half-amplitude duration of 5 ms, and the shortest

masker–signal interval tested was 1 ms (0–V points in the envelope). Even in this situation, no evidence for interaction was found at 2 kHz, suggesting that filter ringing did not limit performance to any significant degree.

Vogten (1978) studied peripheral interactions by manipulating the phase relationship between a sinusoidal masker and signal, both at 1 kHz. Vogten used ramps of 10 ms and a signal with no steady state. He found no evidence for interaction at 1 kHz even when the masker and signal overlapped at the –6-dB points in their envelopes. In this condition, the delay between the beginning of the masker offset and the peak of the signal is 10 ms, which is comparable to the 9 ms used in experiment 1 of the present study. In a gap-detection study, Shailer and Moore (1987) found that the phase relationship between the stimulus portions preceding and following the gap could influence performance at short gap durations (up to 8 ms) for signal frequencies up to and including 1 kHz. They interpreted this in part as being due to cancellation and/or addition in the auditory filters. No such effect was found at 2 kHz.

In summary, there is no evidence suggesting that ringing in the auditory filters affects performance at frequencies of 2 kHz or higher. As the lowest center frequency tested here is 2.4 kHz, we can conclude that peripheral interactions probably play no role in our experiments.

¹Oxenham and Plack (1997) plotted masker level as a function of signal level. Thus, the slopes in their graphs are the reciprocal of the typical growth-of-masking functions discussed here.

²Off-time listening refers to the possibility that listeners can attend to the decay of an “internal representation” of the signal, after the offset of the physical stimulus, thereby enhancing detection. The addition of a backward masker should reduce the availability of this cue.

³The value of 40 dB SPL is based on the physiological findings and accompanying model of Yates *et al.* (1990) and Yates (1990). The assumption also corresponds reasonably well with the psychophysical data of Oxenham and Plack (1997), who found a breakpoint of around 45 dB SPL, and Plack and Oxenham (1998), who in a different set of tasks found a breakpoint of around 35 dB SPL. It should be noted, however, that the exact level of this breakpoint is still a matter of debate. Direct physiological measurements of BM response have resulted in estimates ranging from 20 dB (Ruggero *et al.*, 1997) to 65 dB SPL (Murugasu and Russell, 1995). These differences may result in part from differences in calibration procedures, but may also reflect real differences within and across species.

⁴Due to the partitioning of the data from the off-frequency conditions into ranges below and above 40 dB SPL, different masker levels were included for different individuals. In order to pool the data to obtain summary slopes, the individual data were first swept to eliminate differences in means on both axes.

Arthur, R. M., Pfeiffer, R. R., and Suga, N. (1971). “Properties of ‘two-tone inhibition’ in primary auditory neurones,” *J. Physiol. (London)* **212**, 593–609.

Bacon, S. P. (1996). “Comments on ‘Manipulations of the duration and relative onsets of two-tone forward maskers’ [J. Acoust. Soc. Am. **94**, 1269–1274 (1993)],” *J. Acoust. Soc. Am.* **99**, 3246–3248.

Buus, S. (1985). “Release from masking caused by envelope fluctuations,” *J. Acoust. Soc. Am.* **78**, 1958–1965.

Carlyon, R. P. (1988). “The development and decline of forward masking,” *Hearing Res.* **32**, 65–80.

Champlin, C. A., and Wright, B. A. (1993). “Manipulations of the duration and relative onset of two-tone forward maskers,” *J. Acoust. Soc. Am.* **94**, 1269–1274.

Delgutte, B. (1990). “Physiological mechanisms of psychophysical masking: Observations from auditory-nerve fibers,” *J. Acoust. Soc. Am.* **87**, 791–809.

- Duifhuis, H. (1980). "Level effects in psychophysical two-tone suppression," *J. Acoust. Soc. Am.* **67**, 914–927.
- Egan, J. P., and Hake, H. W. (1950). "On the masking pattern of a simple auditory stimulus," *J. Acoust. Soc. Am.* **22**, 622–630.
- Evans, E. F., Pratt, S. R., Spenner, H., and Cooper, N. P. (1992). "Comparisons of physiological and behavioural properties: Auditory frequency selectivity," in *Auditory Physiology and Perception*, edited by Y. Cazals, K. Horner, and L. Demany (Pergamon, Oxford).
- Florentine, M., and Buus, S. (1981). "An excitation-pattern model for intensity discrimination," *J. Acoust. Soc. Am.* **70**, 1646–1654.
- Glasberg, B. R., and Moore, B. C. J. (1990). "Derivation of auditory filter shapes from notched-noise data," *Hearing Res.* **47**, 103–138.
- Gregan, M. J., Bacon, S. P., and Lee, J. (1998). "Masking by sinusoidally amplitude-modulated tonal maskers," *J. Acoust. Soc. Am.* **103**, 1012–1021.
- Hall, J. W., Haggard, M. P., and Fernandes, M. A. (1984). "Detection in noise by spectro-temporal pattern analysis," *J. Acoust. Soc. Am.* **76**, 50–56.
- Houtgast, T. (1972). "Psychophysical evidence for lateral inhibition in hearing," *J. Acoust. Soc. Am.* **51**, 1885–1894.
- Houtgast, T. (1973). "Psychophysical experiments on 'tuning curves' and 'two-tone inhibition'," *Acustica* **29**, 168–179.
- Houtgast, T. (1974). "Lateral suppression in hearing," Ph.D. thesis, Free University of Amsterdam.
- Jesteadt, W., and Norton, S. J. (1985). "The role of suppression in psychophysical measures of frequency selectivity," *J. Acoust. Soc. Am.* **78**, 365–374.
- Johnson-Davies, D., and Patterson, R. D. (1979). "Psychophysical tuning curves: Restricting the listening band to the signal region," *J. Acoust. Soc. Am.* **65**, 765–770.
- Kidd, G., and Feth, L. L. (1981). "Patterns of residual masking," *Hearing Res.* **5**, 49–67.
- Kohrausch, A., and Langhans, A. (1992). "Differences in masked thresholds between monaural and diotic conditions: Influence of contralateral efferent stimulation?" in *Auditory Physiology and Perception*, edited by Y. Cazals, L. Demany, and K. Horner (Pergamon, Oxford).
- Lutfi, R. A. (1984). "Predicting frequency selectivity in forward masking from simultaneous masking," *J. Acoust. Soc. Am.* **76**, 1045–1050.
- Lutfi, R. A. (1985). "A reply to Moore [*J. Acoust. Soc. Am.* **78**, 253–255 (1985)]," *J. Acoust. Soc. Am.* **78**, 255–257.
- Lutfi, R. A. (1988). "Interpreting measures of frequency selectivity: Is forward masking special?" *J. Acoust. Soc. Am.* **83**, 163–177.
- Moore, B. C. J. (1980a). "Detection cues in forward masking," in *Psychophysical, Physiological and Behavioural Studies in Hearing*, edited by G. van den Brink and F. A. Bilsen (Delft U.P., Delft).
- Moore, B. C. J. (1980b). "Mechanisms and frequency distribution of two-tone suppression in forward masking," *J. Acoust. Soc. Am.* **68**, 814–824.
- Moore, B. C. J. (1985). "Comments on 'Predicting frequency selectivity in forward masking from simultaneous masking'," *J. Acoust. Soc. Am.* **78**, 253–255.
- Moore, B. C. J., and Glasberg, B. R. (1981). "Auditory filter shapes derived in simultaneous and forward masking," *J. Acoust. Soc. Am.* **70**, 1003–1014.
- Moore, B. C. J., and Glasberg, B. R. (1982). "Contralateral and ipsilateral cueing in forward masking," *J. Acoust. Soc. Am.* **71**, 942–945.
- Moore, B. C. J., and Glasberg, B. R. (1985). "The danger of using narrow-band noise maskers to measure suppression," *J. Acoust. Soc. Am.* **77**, 2137–2141.
- Moore, B. C. J., Glasberg, B. R., and Baer, T. (1997). "A model for the prediction of thresholds, loudness, and partial loudness," *Journal of the Audio Engineering Society* **45**, 224–240.
- Moore, B. C. J., and Vickers, D. A. (1997). "The role of spread of excitation and suppression in simultaneous masking," *J. Acoust. Soc. Am.* **102**, 2284–2290.
- Murmane, O., and Turner, C. W. (1991). "Growth of masking in sensorineural hearing loss," *Audiology* **30**, 275–285.
- Murugasu, E., and Russell, I. J. (1995). "Salicylate ototoxicity: The effects on basilar membrane displacement, cochlear microphonics, and neural responses in the basal turn of the guinea pig cochlea," *Aud. Neurosci.* **1**, 139–150.
- Murugasu, E., and Russell, I. J. (1996). "The effect of efferent stimulation on basilar membrane displacement in the basal turn of the guinea pig cochlea," *J. Neurosci.* **16**, 325–332.
- Neff, D. L. (1985). "Stimulus parameters governing confusion effects in forward masking," *J. Acoust. Soc. Am.* **78**, 1966–1976.
- Neff, D. L. (1986). "Confusion effects with sinusoidal and narrowband-noise forward maskers," *J. Acoust. Soc. Am.* **79**, 1519–1529.
- Nelson, D. A., and Schroder, A. C. (1997). "Linearized response growth inferred from growth-of-masking slopes in ears with cochlear hearing loss," *J. Acoust. Soc. Am.* **101**, 2186–2201.
- Nelson, D. A., and Swain, A. C. (1996). "Temporal resolution within the upper accessory excitation of a masker," *Acust. Acta Acust.* **82**, 328–334.
- O'Loughlin, B. J., and Moore, B. C. J. (1981). "Off-frequency listening: Effects on psychoacoustical tuning curves obtained in simultaneous and forward masking," *J. Acoust. Soc. Am.* **69**, 1119–1125.
- Oxenham, A. J., and Moore, B. C. J. (1994). "Modeling the additivity of nonsimultaneous masking," *Hearing Res.* **80**, 105–118.
- Oxenham, A. J., and Moore, B. C. J. (1995). "Additivity of masking in normally hearing and hearing-impaired subjects," *J. Acoust. Soc. Am.* **98**, 1921–1934.
- Oxenham, A. J., and Moore, B. C. J. (1997). "Modeling the effects of peripheral nonlinearity in normal and impaired hearing," in *Modeling Sensorineural Hearing Loss*, edited by W. Jesteadt (Erlbaum, Hillsdale, NJ).
- Oxenham, A. J., and Plack, C. J. (1997). "A behavioral measure of basilar-membrane nonlinearity in listeners with normal and impaired hearing," *J. Acoust. Soc. Am.* **101**, 3666–3675.
- Pang, X. D., and Guinan, J. J. (1997). "Growth rate of simultaneous masking in cat auditory-nerve fibers: Relationship to the growth of basilar-membrane motion and the origin of two-tone suppression," *J. Acoust. Soc. Am.* **102**, 3564–3575.
- Plack, C. J., and Oxenham, A. J. (1998). "Basilar-membrane nonlinearity and the growth of forward masking," *J. Acoust. Soc. Am.* **103**, 1598–1608.
- Robinson, C. E., and Pollack, I. (1973). "Interaction between forward and backward masking: A measure of the integrating period of the auditory system," *J. Acoust. Soc. Am.* **53**, 1313–1316.
- Rosen, S., and Baker, R. J. (1994). "Characterising auditory filter nonlinearity," *Hearing Res.* **73**, 231–243.
- Ruggero, M. A. (1992). "Responses to sound of the basilar membrane of the mammalian cochlea," *Curr. Opin. Neurobiol.* **2**, 449–456.
- Ruggero, M. A., Rich, N. C., Recio, A., Narayan, S. S., and Robles, L. (1997). "Basilar-membrane responses to tones at the base of the chinchilla cochlea," *J. Acoust. Soc. Am.* **101**, 2151–2163.
- Ruggero, M. A., Robles, L., and Rich, N. C. (1992a). "Two-tone suppression in the basilar membrane of the cochlea: Mechanical basis of auditory-nerve rate suppression," *J. Neurophysiol.* **68**, 1087–1099.
- Ruggero, M. A., Robles, L., Rich, N. C., and Recio, A. (1992b). "Basilar membrane responses to two-tone and broadband stimuli," *Philos. Trans. R. Soc. London, Ser. B* **336**, 307–315.
- Sachs, M. B., and Kiang, N. Y. S. (1968). "Two-tone inhibition in auditory nerve fibers," *J. Acoust. Soc. Am.* **43**, 1120–1128.
- Schöne, P. (1977). "Nichtlinearitäten im Mithörschwellen-Tonheitsmuster von Sinustönen," *Acustica* **37**, 37–44.
- Shailer, M. J., and Moore, B. C. J. (1987). "Gap detection and the auditory filter: Phase effects using sinusoidal stimuli," *J. Acoust. Soc. Am.* **81**, 1110–1117.
- Shannon, R. V. (1976). "Two-tone unmasking and suppression in a forward masking situation," *J. Acoust. Soc. Am.* **59**, 1460–1470.
- Shannon, R. V. (1986). "Psychophysical suppression of selective portions of pulsation threshold patterns," *Hearing Res.* **21**, 257–260.
- Smits, J. T. S., and Duifhuis, H. (1982). "Masking and partial masking in listeners with a high-frequency hearing loss," *Audiology* **21**, 310–324.
- Sommers, M. S., and Gehr, S. E. (1998). "Auditory suppression and frequency selectivity in older and younger adults," *J. Acoust. Soc. Am.* **103**, 1067–1074.
- Stelmachowicz, P. G., Lewis, D. E., Larson, L. L., and Jesteadt, W. (1987). "Growth of masking as a measure of response growth in hearing-impaired listeners," *J. Acoust. Soc. Am.* **81**, 1881–1887.
- Vogten, L. L. M. (1978). "Low-level pure-tone masking: A comparison of 'tuning curves' obtained with simultaneous and forward masking," *J. Acoust. Soc. Am.* **63**, 1520–1527.
- Weber, D. L., and Green, D. M. (1978). "Temporal factors and suppression effects in backward and forward masking," *J. Acoust. Soc. Am.* **64**, 1392–1399.
- Wegel, R. L., and Lane, C. E. (1924). "The auditory masking of one sound by another and its probable relation to the dynamics of the inner ear," *Phys. Rev.* **23**, 266–285.

- Yates, G. K. (1990). "Basilar membrane nonlinearity and its influence on auditory nerve rate-intensity functions," *Hearing Res.* **50**, 145–162.
- Yates, G. K., Winter, I. M., and Robertson, D. (1990). "Basilar membrane nonlinearity determines auditory nerve rate-intensity functions and cochlear dynamic range," *Hearing Res.* **45**, 203–220.
- Zwicker, E. (1960). "Ein Verfahren zur Berechnung der Lautstärke," *Acustica* **10**, 304–308.
- Zwicker, E. (1970). "Masking and psychological excitation as consequences of the ear's frequency analysis," in *Frequency Analysis and Periodicity Detection in Hearing*, edited by R. Plomp and G. F. Smoorenburg (Sijthoff, Leiden).
- Zwicker, E., and Scharf, B. (1965). "A model of loudness summation," *Psychol. Rev.* **72**, 3–26.
- Zwicker, E. B. (1976). "Mithörschwellen-Periodenmuster amplitudenmodulierter Töne," *Acustica* **36**, 113–120.

Profiling the perceptual suppression of partials in periodic complex tones: Further evidence for a harmonic template^{a)}

Jeffrey M. Brunstrom^{b)} and Brian Roberts

School of Psychology, University of Birmingham, Edgbaston, Birmingham B15 2TT, England

(Received 28 April 1998; revised 12 August 1998; accepted 19 September 1998)

The basis for the perceptual cohesion of periodic complex tones was investigated. In experiment 1, 2–4 consecutive components (harmonics 6 and above) were removed from a 14-harmonic complex and replaced with a sinusoidal “probe,” located at one of a set of regularly spaced positions spanning the gap. On each trial, subjects heard a complex tone followed by an adjustable pure tone in a continuous loop. Subjects were better able to match the pure tone to the probe when the probe did not coincide with a harmonic position. Minima in “hit rate” were more pronounced when harmonic probes were in positions adjacent to other harmonics than when they were not. These findings suggest that the pitch of each in-tune partial was actively suppressed by a template whose influence attenuated with distance from regions of consecutive harmonics. In experiment 2, the partials on either side of the spectral gap were harmonics of different fundamental frequencies. Hit-rate minima corresponding to both fundamentals were found, indicating an upward and downward spread of suppression, and also demonstrating the concurrent operation of two templates. The results confirm recent findings in support of template models, and are consistent with the idea that partial-pitch suppression underpins harmonic fusion. © 1998 Acoustical Society of America. [S0001-4966(98)05812-3]

PACS numbers: 43.66.Fe, 43.66.Hg, 43.66.Ba, 43.66.Lj [DWG]

INTRODUCTION

Partials in a periodic complex tone typically fuse to form a coherent perceptual entity with a single low pitch. This low pitch may be perceived without any interactions between components in the cochlea (Houtsma and Goldstein, 1972; Houtgast, 1976). These findings suggest that low pitch is derived from the spectrum of the complex by a central pattern-recognition mechanism (Goldstein, 1973; Wightman, 1973; Terhardt, 1974). The optimum processor theory developed by Goldstein and his colleagues (e.g., Goldstein, 1973; Gerson and Goldstein, 1978) first introduced the concept of a central harmonic template in pitch perception. This account has since been extended to instances where more than one sound is heard concurrently (Duijfhuis *et al.*, 1982; Scheffers, 1983a, b). These models assume that the pitch of a complex tone corresponds to the fundamental (F_0) frequency of a “harmonic sieve” that best fits the distribution of resolved components. Subsequent studies have shown that partials lying outside narrow regions around the harmonic values defined by this F_0 frequency are excluded from the pitch computation (e.g., Moore *et al.*, 1985), and are heard as separate perceptual entities (e.g., Moore *et al.*, 1986). Hartmann *et al.* (1990) devised a pitch-matching task to provide a performance measure of this perceptual segregation. Subjects were asked to match the pitch of an adjustable pure tone to the pitch of a mistuned harmonic. The probability of a correct match by chance was low, and so accurate matches were

taken as evidence of the segregation of the mistuned partial. Hartmann *et al.*'s (1990) experiments indicate that segregation increases over the range of mistunings 0.5%–4%, irrespective of sign.

Bregman (1990, pp. 243–244) has speculated that an individual harmonic may be difficult to hear out from a periodic complex tone because its pitch is actively suppressed by the auditory system. By this account, a template is used to estimate the low pitch of a complex tone, and the auditory system then inhibits partial pitches that fall near integer multiples of the template's F_0 frequency. Partial-pitch suppression based on the location of slots in a harmonic template further predicts that the perceptual fusion of a harmonic into a complex tone does not depend directly on the presence of its immediate neighbors. Lin and Hartmann (1998) have recently provided indirect evidence in support of this prediction (see Sec. III for a full discussion). A modified pitch-matching procedure, based on that devised by Hartmann *et al.* (1990), was used in the current experiments to provide a more direct test of Bregman's (1990) proposal.

I. EXPERIMENT 1

A. Method

1. Overview and conditions

A pitch-matching procedure was used to explore how the salience of a pure-tone “probe,” located within a spectral gap in a periodic tone, changes as its frequency is varied in relation to the “harmonic frame” provided by the other components. If the salience of harmonic partials is suppressed, then correct matches to probes that are harmonically related to the frame should be more difficult, and hence less frequent, than correct matches to probes that are not. Within

^{a)}A preliminary account of this research was presented at the Joint 16th International Congress on Acoustics and 135th Meeting of the Acoustical Society of America, Seattle, WA, June 1998 [J. Acoust. Soc. Am. **103**, 2768(A) (1998)].

^{b)}Electronic mail: j.m.brunstrom@bham.ac.uk

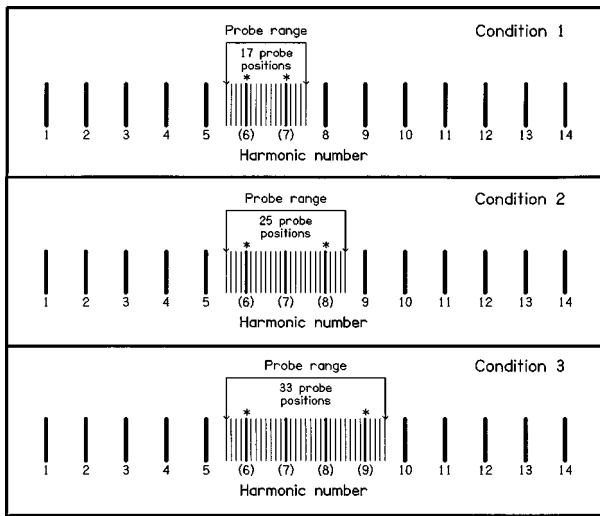


FIG. 1. Schematic of the test tones and probe ranges used for conditions 1–3 in experiment 1. Harmonics comprising the test tones are shown heavy and in bold. For each condition, in-tune probe positions are shown in bold and the corresponding harmonic numbers are given in brackets. Consecutive in-tune probe positions are indicated with an asterisk.

each trial, subjects listened to a repeating cycle of a complex “test” tone followed by an adjustable, pure, “comparison” tone. Subjects were instructed to adjust the pitch of the comparison tone to that of the probe, which was described as a pure-tone-like sound embedded in the test tone.

Figure 1 illustrates the spectra of the complex tones used in conditions 1–3. These test tones were created by removing 2, 3, or 4 consecutive harmonics (number 6 and above), respectively, from complex tones comprising harmonics 1–14. A single probe was then inserted at one of 17, 25, or 33 (conditions 1–3) possible positions across a range spanning the gap created in the spectrum of the test tone. In units of harmonic number, the probe range corresponded to 5.5–7.5, 5.5–8.5, and 5.5–9.5, for conditions 1–3, respectively. The probe positions used were equally spaced within each probe range, in units of $0.125 \times F_0$ frequency.

Probe positions shown in bold in Fig. 1 represent occasions when the probe frequency coincides with the position of a missing harmonic. These are called *in-tune probe positions*. Other positions in the range are described as out-of-tune. An in-tune probe position sometimes forms a consecutive series with either the lower or the upper set of partials in the harmonic frame, in which case it is referred to as a *consecutive in-tune probe position*. Positions of this kind are indicated with an asterisk in Fig. 1 and in subsequent figures. When both harmonics adjacent to an in-tune probe position are missing, so that the probe does not form a consecutive series with either set of partials in the harmonic frame, it is called a *nonconsecutive in-tune probe position*. Template models of harmonic fusion predict a reduction in successful matches around both consecutive and nonconsecutive in-tune probe positions. This is because the optimum alignment of a harmonic template with the partials of the test tone should lead to vacant template slots centered around all harmonic frequencies in the spectral gap, irrespective of whether or not those frequencies form a consecutive series with either set of partials in the harmonic frame. If a reduction in pitch-

matching success can be found only for consecutive in-tune probes, then this would suggest that the effect is a consequence of local rather than more global processes.

For conditions 1–3, the number of nonconsecutive in-tune probe positions tested was zero, one, and two, respectively. The nonconsecutive positions used in condition 3 differed from their counterpart in condition 2 in that neither was equidistant from the edges of the spectral gap. Therefore, condition 3 served both to extend the range of nonconsecutive harmonic frequencies tested and to provide a control for the effects of any factors unique to an equidistant probe position, especially the equal intermodulation rate evoked between the probe and the two neighboring partials in the test tone. Two consecutive in-tune probe positions were tested in all conditions.

2. Subjects

Every subject had some prior experience of listening to stimuli of the kind used in this experiment. As a strict test of general pitch-matching ability, it was decided *a priori* to reject the data of anyone who failed to match successfully (see “hit” criteria in Sec. I A 5) on at least 60% of occasions, when collapsed across probe positions and conditions. Only one subject failed to meet this criterion. Of the six subjects who passed, one was the first author and the rest were students. All of them reported normal hearing, and two were musically trained.

3. Stimuli

Pilot tests using a fixed F_0 frequency had indicated that ceiling effects on performance were a potential problem. Some subjects regularly matched the probe successfully after relatively few trials, irrespective of its position in the probe range. Therefore, the F_0 frequency of the test tones was roved to reduce across-trial learning. It was chosen randomly on each trial from a rectangular distribution with a width of $\pm 20\%$ around 200 Hz.

The durations of the test and the adjustable tones were 420 ms and 310 ms, respectively, both including linear onset and offset ramps of 20 ms each. Test tones were followed by a 200-ms silent interval and adjustable tones were followed by a 500-ms silent interval. The durations of the silent intervals were chosen to create a rhythm that clearly defined the within-cycle order of the tones. The probe and all components in the harmonic frame began in sine phase. The partials in the harmonic frame were set to 60 dB SPL, and the probe and adjustable tone were set to 54 dB SPL. Setting the probe level at 6 dB below that of the test-tone partials made it more difficult to match, which further reduced ceiling effects on performance. Each session consisted of three consecutive sets, each in a new randomized order, of all probe positions for the three conditions, giving a total of 225 trials [$3 \text{ sets} \times (17 + 25 + 33)$]. Subjects were run 4 times, providing 12 responses per subject to each probe position in the 3 conditions.

All stimuli were generated using MITSYN software (see Henke, 1990). Stimuli were synthesized at a sampling rate of 16 kHz and played back via a 16-bit digital-to-analog con-

verter (Data Translation DT2823). They were low-pass filtered (corner frequency=5.2 kHz, roll-off=100 dB/oct.) and presented binaurally over Sennheiser HD 480-13II earphones. The levels of the stimuli were set using a programmable attenuator (0.25-dB steps), and were calibrated with a sound-level meter (Brüel and Kjaer, type 2209, linear weighting) connected to the earphones by an artificial ear (type 4153). Stimuli were played to the listeners in a double-walled sound-attenuating chamber (Industrial Acoustics 1201A).

4. Procedure

The adjustable tone was controlled using a trackball mouse with two different sensitivity settings, which could be selected freely via a mouse button. The default setting was a coarse control. The fine control was ten times more sensitive. The initial frequency of the adjustable pure tone was chosen randomly from the range $(1.5-13.5) \times F_0$ frequency. The range was restricted to this region to prevent matches to either the F_0 frequency of the complex or to the prominent edge pitch (Kohlrausch and Houtsma, 1992) associated with the highest harmonic present (the 14th). At the end of each trial, subjects were given feedback on their performance via a computer screen. If the response was within $\pm 1.0 \times$ test-tone F_0 from the probe frequency, then the message “within range” was displayed. Above and below this range, the message “much too high” or “much too low” was displayed, as appropriate. Subjects were given unlimited time to complete each trial and were free to rest between trials.

5. Data analysis (definitions of hit rate and ambiguity)

The reasons for choosing the analysis described below merit discussion before the details of its implementation are explained. Were it the case that subjects' responses always clustered near the frequency of the probe, then their accuracy could be quantified in terms of their variance. However, responses tended to cluster either near the probe, or near one or more of the partials in the harmonic frame, or both. Consequently, matches to salient nontargets in the harmonic frame often contributed to the variance in our data. This meant that the variance associated with two probe positions at a similar spectral distance from the most salient nontarget could be the same even when each received a very different proportion of near-matches. Therefore, it was necessary to quantify subjects' matching ability by estimating the proportion of responses clustered around the probe frequency.

The pitch of a mistuned partial in a periodic tone differs from its pitch when heard in isolation; typically it is shifted slightly in the same direction as the mistuning (Hartmann *et al.*, 1990; Hartmann and Doty, 1996; Lin and Hartmann, 1998; Roberts and Brunstrom, 1998). Since most of the probe positions tested in our experiment were mistuned from harmonic values, this complicated the process of categorizing a response to the probe as either a “hit” or a “miss.” Following previous pitch-matching studies, a two-stage test was adopted for a response to be accepted as a hit (Hartmann *et al.*, 1990; Roberts and Brunstrom, 1998). First, a response had to fall within $\pm 1.0 \times$ test-tone F_0 frequency from the

probe. This stage ensured that all responses falling in the general vicinity of the probe were flagged as possible hits. Second, those responses that survived the initial criterion were entered into a recursive clustering procedure that rejected individual matches until the standard deviation of those remaining fell below 2.5% of the probe frequency. This criterion was based on the assumption that genuine matches would be clustered together, and that outliers should be rejected because they are likely to be chance matches. On each cycle of the recursion, the response most distant from the mean was rejected until either the clustering criterion was met or only two responses remained. Following Roberts and Brunstrom (1998), the data point further from the frequency of the probe was rejected in those cases where these two responses failed the clustering criterion. In cases where only one response passed the first criterion, it was accepted as a hit. The proportion of responses passing both criteria was expressed as a percentage hit rate.

The pattern of errors of matching observed in pilot work led to the inclusion of a check on the reliability of our response classification for some probe positions. It was found that incorrect matches tended to cluster around the components in the test tone defining the edges of the spectral gap. This observation is consistent with the finding that an edge component below about 3 kHz has a salient pitch (Kohlrausch and Houtsma, 1992), which probably reflects phase-locking in the responses of auditory filters tuned to frequencies on the unmasked skirt of the excitation pattern (Moore and Ohgushi, 1993). Since the probe was 6 dB below the level of the test-tone partials, the *gap-edge components* in our stimuli would have experienced limited masking, even in the presence of probes at the nearby extremes of the probe range. Matches to these gap-edge components did not present a problem for the classification of hits to probes in the middle of the range, as these positions were relatively distant from the edges of the spectral gap. However, this was not the case for probes near the ends of the range. The application of the clustering criterion to responses passing the initial criterion for these probes might, in some cases, lead to the unwanted acceptance as hits of a cluster of matches around a gap-edge component.

Pilot data for probe positions in the middle of the range suggested that matches to the gap-edge components almost always fell within $\pm 0.5 \times F_0$ of their frequency. Hence, the reliability of our hit criteria for probes near the ends of the range was quantified using a window of this width, centered around the nearer gap-edge component. Those responses classified as hits that also fell within this window were considered ambiguous. A low proportion indicates that the vast majority of responses classified as hits to a particular probe were genuine attempts to match its pitch, rather than spuriously classified matches to the nearby gap-edge component.

B. Results

Figure 2 shows the mean hit rates and inter-subject standard errors for all probe positions in a separate panel for each condition. Vertical dashed lines represent in-tune probe positions. The hit-rate profiles are characterized by distinct, regularly spaced, troughs in performance that are centered

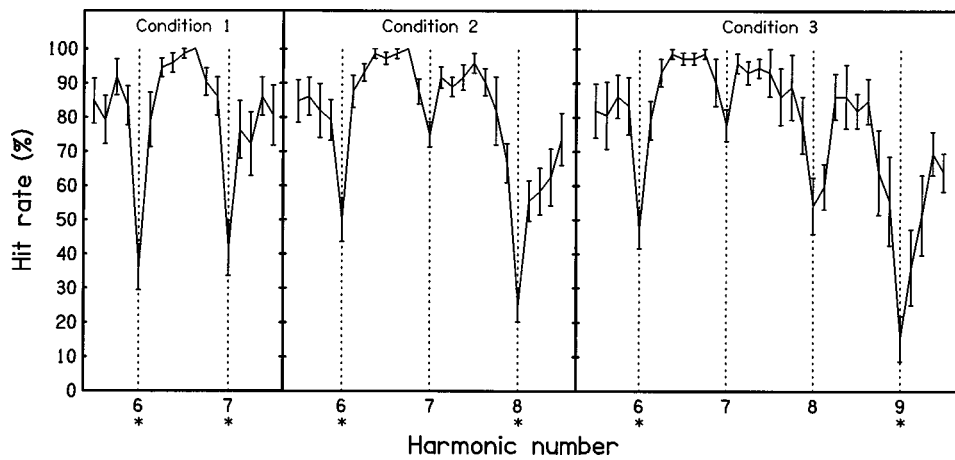


FIG. 2. Mean hit rates for six subjects, with inter-subject standard errors, for all probe positions used in conditions 1–3 of experiment 1. Each in-tune probe position is marked with a vertical dashed line, and the corresponding harmonic number is shown. Harmonic numbers corresponding to consecutive in-tune probe positions are indicated with an asterisk. The number of probe positions tested for conditions 1–3 was 17, 25, and 33, respectively. For probe positions where no error bar is given, the hit rate was identical for all subjects.

around in-tune probe positions. In condition 1, these troughs represent a reduction in performance of 40%–50% for probes corresponding to harmonic numbers 6 and 7. In condition 2, performance was reduced by about 35% and 50% at the lower and upper consecutive in-tune probe positions (harmonics 6 and 8), respectively, and by about 20% at the nonconsecutive in-tune probe position (harmonic 7). In condition 3, hit rates were reduced at the lower and upper consecutive in-tune probe positions (harmonics 6 and 9) by about 35% and 60%, and at the lower and upper nonconsecutive in-tune probes positions (harmonics 7 and 8) by about 20% and 30%, respectively.

The proximity of probes near the ends of the range to the gap-edge components made it necessary to assess the degree to which the computed hit rates for those probe positions might have been inflated by the spurious inclusion of matches to those components. Table I shows the degree of ambiguity associated with hits to probes near the ends of the ranges used for the three conditions. For a given probe position, ambiguity is expressed as the percentage of hits that also fell within $\pm 0.5 \times F_0$ of the proximal gap-edge component. For all conditions, the set of probes analyzed in this way extended inward from each end of the range to include the two consecutive in-tune probe positions, which are shown in bold in Table I. At the edges of the probe range, about 60%–75% of hits were ambiguous, making it difficult to gauge the accuracy of performance at these positions. However, the degree of potential overlap between matches to

the probe and matches to the nearby gap-edge component decreased markedly toward the consecutive in-tune probe positions. Consequently, 10% or fewer of responses classified as hits to the in-tune probes and to probes in directly adjacent positions can be considered ambiguous. Indeed, the ambiguity was often small even for probes two steps away from an in-tune position. This indicates that the sloping sides of the troughs in the hit-rate profiles around consecutive in-tune positions represent a genuine decrement in ability to match the pitch of the probe correctly.

C. Discussion

Reduced hit rates at in-tune probe positions indicate that the pitch of the probe was perceptually suppressed when it fell at a harmonic frequency, making it more difficult to match. The profiles of hits for conditions 2 and 3 show that suppression can occur at nonconsecutive in-tune probe positions, as well as consecutive ones. Furthermore, the hit-rate profile for condition 3 shows that partial-pitch suppression at nonconsecutive harmonic positions is not dependent on equidistance between neighboring in-tune partials (see Sec. I A 1). Together, these findings suggest that minima in the salience of partial pitches are induced not simply by local interactions between neighboring components, but rather by a template mechanism that responds to more global aspects of spectral pattern.

In addition to the principal findings, other features of the

TABLE I. Ambiguity associated with hits to probes near the ends of the probe range in experiment 1. Results are rounded to the nearest percentage point. Results for probe positions corresponding to consecutive harmonic frequencies are shown in bold.

Condition 1 (17 probe positions)											
Probe position	<i>1</i>	<i>2</i>	<i>3</i>	<i>4</i>	<i>5</i>	----	13	<i>14</i>	<i>15</i>	<i>16</i>	<i>17</i>
% ambiguous hits	67	26	8	0	0	----	7	0	8	42	67
Condition 2 (25 probe positions)											
Probe position	<i>1</i>	<i>2</i>	<i>3</i>	<i>4</i>	<i>5</i>	----	21	<i>22</i>	<i>23</i>	<i>24</i>	<i>25</i>
% ambiguous hits	57	26	2	0	0	----	0	0	31	64	77
Condition 3 (33 probe positions)											
Probe position	<i>1</i>	<i>2</i>	<i>3</i>	<i>4</i>	<i>5</i>	----	29	<i>30</i>	<i>31</i>	<i>32</i>	<i>33</i>
% ambiguous hits	70	29	5	10	0	----	0	0	24	54	63

hit-rate profiles merit discussion. For example, there was a progressive decline in performance across conditions 1–3 for the higher of the two consecutive in-tune probe positions tested in each case. These corresponded to harmonics 7, 8, and 9, respectively. This finding probably reflects the growing effect of resolution constraints with increasing harmonic number, leading to increased masking by the adjacent test-tone partial above. Support for this interpretation comes both from the decline in performance for out-of-tune probes at higher positions, and from the widening of the troughs in performance for higher harmonic numbers. These features were particularly evident in condition 3. Likewise, the increase in hits to the probe corresponding to harmonic 6 in conditions 2 and 3, relative to condition 1, probably resulted from a reduction in masking. Such a reduction would be expected given the increase across conditions in the spectral distance between that probe and the nearest partial above it in the harmonic frame. An alternative account based on the progressive removal of a downward spread of harmonic suppression from the upper set of partials seems less likely, because the hit rate for harmonic 6 did not improve in condition 3, relative to condition 2.

The shallower troughs in the hit-rate profile associated with nonconsecutive harmonic positions, evident in conditions 2 and 3, suggest that the partial-pitch suppression effect produced by our hypothetical harmonic template attenuates with spectral distance from the set of partials that evoke it. However, this interpretation is complicated by ceiling effects on performance. Since probes corresponding to nonconsecutive harmonic frequencies are further from the partials of the test tone than probes corresponding to consecutive harmonic frequencies, and consequently less subject to masking, one might expect higher hit rates for them. In cases where hit rates to nearby out-of-tune probes are already near-perfect, an increase in hits to an in-tune probe can only manifest itself as a shallower trough in the hit-rate profile. Consistent with this cautionary note is the observation that the deepest trough in performance for a nonconsecutive in-tune position was for the probe corresponding to harmonic 8 in condition 3, whose neighboring out-of-tune probes were not associated with near-perfect hit rates. Nonetheless, a comparison between the hit rates for probes at the in-tune position and its immediate neighbors for harmonic 8 shows a much greater difference in condition 2 than in condition 3, despite the fact that the mean hit rates for all of these probes were below 80%.

II. EXPERIMENT 2

Experiment 1 has shown that hit-rate minima can extend into the spectral gap separating a lower and higher set of partials, each of which comprised consecutive harmonics of the same F_0 frequency. These troughs in the hit-rate profile were found at both consecutive and nonconsecutive harmonic frequencies within the spectral gap. Experiment 2 sought to determine whether or not the pattern of suppression established by a set of consecutive harmonics can extend both upward and downward in frequency, as the direction of the effect was not tested explicitly in experiment 1. This was

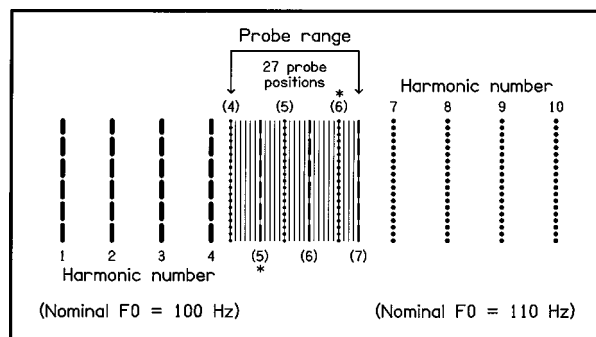


FIG. 3. Schematic of the test tone and probe range used in experiment 2. Harmonic multiples of the lower and higher nominal F_0 frequencies are depicted by dashed and dotted lines, respectively. Harmonics comprising the test tone are shown heavy and in bold. In-tune probe positions are shown in bold and the corresponding harmonic numbers are given in brackets. Consecutive in-tune probe positions are indicated with an asterisk.

ascertained by making the lower and upper sets of partials in the test tone harmonics of different F_0 frequencies.

A. Method

1. Stimuli and conditions

Figure 3 illustrates the spectra of the test tones that were used in this experiment. Each comprised harmonics 1–4 of a 100-Hz nominal F_0 frequency and harmonics 7–10 of a 110-Hz nominal F_0 frequency. The actual F_0 frequencies were roved from trial to trial, using a multiplier in the range 1.0–2.0. The same multiplier was used for the two sets of partials in order to maintain the proportional separation between in-tune positions across trials. While maintaining a wide range of F_0 's, this restricted the frequency of the highest component in the upper set to a maximum of 2.2 kHz. This upper limit was chosen because of the abrupt decline in the precision of neural synchrony at higher frequencies (Johnson, 1980), and the associated progressive decline in the ability to hear out a mistuned harmonic (Hartmann *et al.*, 1990). The intention was to ensure that each partial contributed in full to the auditory organization of the complex.

Probes were inserted at one of 27 positions in the spectral gap between the lower and the higher sets of partials. These probe positions were spaced in units of $0.1 \times F_0$ frequency of the lower set. The lowest and highest probe positions corresponded to the 4th harmonic of the higher F_0 and the 7th harmonic of the lower F_0 , respectively. In Fig. 3, probe positions shown in bold represent in-tune probe positions; i.e., occasions when the probe location corresponded exactly with an integer multiple of one or other F_0 .

The durations, levels, method of synthesis, and presentation of the stimuli were the same as in experiment 1. The frequency range for the adjustable pure tone was from $1.5 \times$ lower nominal F_0 to $9.5 \times$ higher nominal F_0 . The initial frequency of the adjustable tone was chosen randomly from within this range. Each session consisted of five consecutive sets of all probe positions, each in a new randomized order, giving a total of 135 trials (5 sets \times 27 positions). Subjects were run twice, providing ten responses to each probe position.

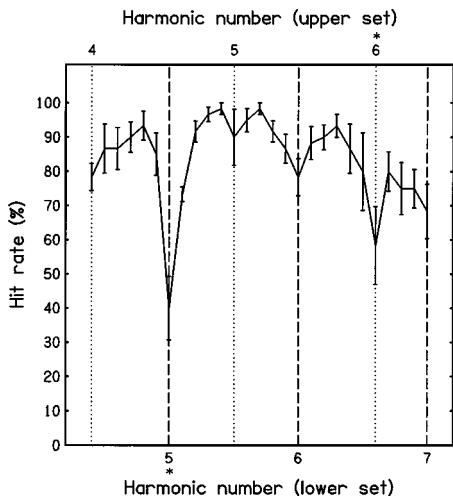


FIG. 4. Mean hit rates for six subjects, with inter-subject standard errors, for the 27 probe positions used in experiment 2. In-tune probe positions corresponding to harmonics of the lower and higher nominal F_0 frequencies (100 and 110 Hz) are depicted by vertical dashed and dotted lines, respectively. Harmonic numbers corresponding to consecutive in-tune probe positions are indicated with an asterisk.

2. Subjects

Once again, subjects had to reach an overall performance criterion of 60% or more hits for inclusion in the analysis. Six subjects satisfied this condition, three of whom had earlier taken part in experiment 1, and one failed. All subjects were students with normal hearing, four of whom were musically trained.

3. Procedure and data analysis

As in experiment 1, subjects received feedback on their performance via a computer screen. Matches were described as “within range” when they fell within $\pm 1.0 \times F_0$ of the lower set of partials from the probe frequency. This range was also used as the initial criterion for classifying responses as hits, before the application of the recursive clustering procedure. Hits to probes near the extremes of the range of positions tested were considered to be ambiguous if they fell within $\pm 0.5 \times$ lower F_0 from a gap-edge component. The percentage of ambiguous hits was calculated for positions up to and including the 5th harmonic multiple of the 100-Hz nominal F_0 series (probes 1–7), and for probes including and above the 6th harmonic multiple of the 110-Hz nominal F_0 series (probes 23–27). All other aspects of the procedure and analysis were the same as for experiment 1.

B. Results

Figure 4 shows the mean hit rates and inter-subject standard errors for all probe positions. Hit rates were lower at the in-tune positions in the spectral gap, whether consecutive or

nonconsecutive, as defined either by the lower or the upper sets of harmonics. These positions are marked in the figure as dashed and dotted lines, respectively. As in experiment 1, minima in the hit-rate profiles were lower for probes corresponding to consecutive harmonic numbers than to nonconsecutive harmonic numbers. The deepest and shallowest troughs in performance (about 50% and 10%) corresponded to harmonic 5 of the lower set of partials, and harmonic 5 of the higher set, respectively.

Table II shows the degree of ambiguity associated with hits to probes near the upper and lower ends of the probe range, extending inward to include the consecutive in-tune positions. In these regions, the edges and slopes of the troughs in performance were defined primarily by hit rates to the two nearest out-of-tune probes (positions 5 and 6 for the lower set of harmonics, and positions 24 and 25 for the upper set of harmonics). There was no ambiguity associated with matches to these probes, which again indicates that the decrement in performance observed for the consecutive in-tune probes was genuine.

It is unclear how to interpret the modest dips in performance at the very edges of the probe range (positions 1 and 27). Although these dips are consistent with the spectral spacings defined by the two sets of harmonics, the decline in performance at the extremes of the probe range may simply reflect the spread of masking from the nearby partials in the test tone. However, it is perhaps worth noting that hit rates for the end-of-range probes used in experiment 1, which were not coincident with harmonic frequencies, did not show much evidence of a decline.

C. Discussion

The results have confirmed the main finding of experiment 1, that the pitch of a probe is suppressed when it falls either at a consecutive or a nonconsecutive harmonic position in a spectral gap between two sets of harmonics. Moreover, by using two sets of harmonics that were related to different F_0 frequencies, experiment 2 has shown that the harmonic suppression effect established by a set of partials can extend both upward and downward in frequency.

Once again, the troughs in the hit-rate profiles were shallower for the nonconsecutive in-tune probes tested than for the consecutive in-tune ones. Notwithstanding the issue of ceiling effects raised in the discussion of experiment 1, this finding does support the idea that the strength of suppression declines with distance from the set of harmonics establishing it. First, the difference in hit rate between the probe positions corresponding to harmonic 5 of the lower F_0 and harmonic 5 of the higher F_0 seems too marked to be explained simply by a decline in the upward spread of masking from the lower set of test-tone partials to the probe. Second, for the lower F_0 , the difference in hit rate between probes at the in-tune

TABLE II. Ambiguity associated with hits to probes near the ends of the probe range in experiment 2. Results are rounded to the nearest percentage point. Results for probe positions corresponding to consecutive harmonic frequencies are shown in bold.

Probe position	1	2	3	4	5	6	7	----	23	24	25	26	27
% ambiguous hits	81	56	21	7	0	0	0	----	0	0	0	2	22

position and its immediate neighbors was substantial for the position corresponding to harmonic 5, but modest for that corresponding to harmonic 6. This was despite the fact that the hit rates for the immediately adjacent probes were very similar (around 85%) on the lower-frequency slopes of these troughs.

A comparison of the hit-rate minima associated with the two consecutive in-tune probes tested here and their counterparts in experiment 1 reveals an important difference. In experiment 1, the higher of the two consecutive in-tune probes had an associated hit rate roughly equal to or below that of the lower one. The finding of a progressively lower hit rate for the higher consecutive in-tune probe across conditions 1–3 has been attributed to a decline in frequency resolution. However, the shallower trough associated with the higher of the two consecutive in-tune probes tested here cannot be explained in this way. Rather, this finding is consistent with the notion that the lower set of partials was the more effective at evoking partial-pitch suppression at nearby harmonic frequencies. Furthermore, it is consistent with Hartmann's (1996) proposal that the fusion of a set of harmonics depends directly on the low pitch evoked by them, because the lower set of partials in the test tone included most of the dominant region (Ritsma, 1967; Plomp, 1967).

Despite the consistency, the relative strength of the low pitches associated with the two sets of partials suggests that this conclusion is not compelling. Informal listening tests showed that, when heard together, the low pitch associated with the lower set of partials was much stronger than that associated with the higher set, yet the difference in trough depth between the consecutive in-tune positions associated with the two sets of partials was moderate rather than overwhelming. Also, the strength of harmonic suppression associated with the upper set was still sufficient to produce a minimum in the hit-rate profile at a nonconsecutive in-tune probe position, albeit a modest one. A possible interpretation of these findings is that the perceptual suppression of individual partials in a harmonic complex is a process governed directly by their common spectral pattern, rather than a process dependent on the mechanism that estimates low pitch. The findings of Roberts and Brunstrom (1998) concerning the perceptual segregation of mistuned partials from regular but inharmonic complexes (see Sec. III C) add credence to this suggestion.

III. GENERAL DISCUSSION

A. Evidence supporting a template model of harmonic fusion

In experiment 1, probes corresponding to harmonic frequencies were less successfully matched than those at other positions. Consequently, hit-rate profiles were characterized by distinct, regularly spaced, troughs in performance (see Fig. 2). This result is consistent with Bregman's (1990) proposal that the individual pitches of in-tune partials in a harmonic complex tone are actively inhibited. Furthermore, the profiles of hits produced in conditions 2 and 3 indicate that the partial-pitch suppression established by a set of harmonics extends to nonconsecutive as well as consecutive har-

monic positions. Experiment 2 showed that the suppression of harmonics can extend both upward and downward in frequency from a spectral region containing a set of consecutive partials. These results are consistent with template models of harmonic fusion, because they show that suppression is primarily determined by spectral pattern rather than by local interactions between neighboring partials.

The principal findings of these experiments confirm those of Lin and Hartmann (1998), who exploited the phenomenon of pitch shifts to infer the operation of a template in the perception of periodic complex tones. Matches to a mistuned harmonic are typically somewhat displaced from the true frequency in the same direction as the mistuning (e.g., Hartmann *et al.*, 1990). These authors have shown that this finding cannot be explained by Terhardt's (1971, 1979) proposal that pitch shifts result from partial masking interactions between neighboring components. Furthermore, a combined place-and-time model of local interactions between partials, developed by Hartmann and Doty (1996), was unable to account for some key aspects of the pattern of pitch shifts, particularly those associated with mistuning of the fundamental component. This led Lin and Hartmann (1998) to explore how the pitch shifts associated with mistuning a given partial upward and downward in frequency changed when that partial was heard in different spectral contexts. In particular, these authors were interested in comparing the effects of removing the components immediately adjacent to a target partial (local changes) with the effects of manipulating more remote aspects of spectral structure so as to affect the harmonic status of the in-tune frequency for the target partial (global changes). In each of the spectral contexts tested, a measure called the *pitch-shift gradient* was computed for the target partial by taking the difference between the percentage pitch shifts resulting from mistuning it by $\pm 8\%$.

Two of Lin and Hartmann's (1998) results are of particular note in relation to our findings. First, the pitch-shift gradient fell to near zero when the frequency straddled by the pair of mistuned targets was changed from an odd-harmonic value (3.0) to an inharmonic value (1.5) by an octave increase in overall spectral spacing that did not change the frequencies or harmonic nature of the immediately adjacent partials. Second, positive pitch-shift gradients were found for pairs of mistuned targets straddling harmonic frequencies in a three-component spectral gap created in a consecutive-harmonic complex tone, even for the nonconsecutive harmonic position in the middle of the gap. Together, these findings suggest that a set of harmonics can activate a template that affects the perceptual processing of other partials that fall close to frequencies harmonically related to the same F_0 .

B. How global are the effects of an active template on the salience of individual partials?

What can be inferred about the properties of a template activated by a set of harmonics? It is common for implementations of templates in algorithms designed to separate concurrent harmonic series (e.g., Duifhuis *et al.*, 1982; Schefers, 1983a, b) to assume tacitly that an active template will

pass all resolved partials falling close to harmonic multiples of its F_0 frequency. However, experiments 1 and 2 have suggested that a template's range of operation is related to the set of partials that activate it. In both cases, there was evidence that the shallower troughs in the hit-rate profile associated with nonconsecutive harmonic positions reflected an attenuation of harmonic suppression with distance from the spectral region or regions containing the test-tone partials. Similarly, Lin and Hartmann (1998) found that the pitch-shift gradient associated with the F_0 component of a periodic complex tone declined progressively as harmonics 2–4 were removed successively. Therefore, it seems that the operation of a template is a medium-range process rather than a truly global one. However, it remains to be established precisely how the number and positions of contributing partials determine the strength and spread of harmonic suppression.

Whatever the details of how particular aspects of stimulus structure determine the scope of these inhibitory effects, it is clear from our results that these effects can extend to in-tune probe positions further than one equivalent rectangular bandwidth (see Moore, 1997) away from the harmonic frame. This indicates that harmonic suppression, like profile analysis, comodulation masking release, and modulation detection interference, is another example of an across-channel process in auditory perception (see Hall *et al.*, 1995, for a review).

In addition to demonstrating that partial-pitch suppression can extend both upward and downward in frequency from a set of consecutive harmonics, experiment 2 has also shown that more than one template can be applied simultaneously to the same spectral region. The evidence for this is the interleaving of minima in the hit-rate profile associated with each of the two F_0 frequencies used. Previous studies have not attempted to explore the perception of individual partials under these conditions. Therefore, it is gratifying that this result is consistent with a central assumption of models of the perceptual separation of concurrent speech—that more than one harmonic template can be active at once (e.g., Parsons, 1976; Scheffers, 1983a; Assmann and Summerfield, 1990).

C. A comparison of methods: Hit-rate profiles and pitch-shift gradients

Lin and Hartmann (1998) recorded the pitch-shift gradients associated with matches to partials mistuned from harmonic values by $\pm 8\%$. A positive gradient was taken to indicate that a template slot fell between a pair of mistuned targets, and the magnitude of the gradient was assumed to reflect the strength of the template's influence in that region. This method has certain advantages over our hit-rate profiling technique. In particular, stimuli in which the probe is widely separated from the other partials are highly susceptible to ceiling effects on performance. This is because any isolated component tends to be highly salient (e.g., Hartmann, 1997, Chapter 6), and hence easily matched. Measures of pitch shift are not subject to this limitation. Also, a measure of the hit rate for a given probe relies on the presence of other partials that can act as false targets. This set of alter-

native matches is further determined by the range of adjustment allowed for the pure tone. Measures of pitch shift are not dependent on false targets in this way. Finally, both the choice of matching range and the provision of feedback may influence listeners' responses by providing them with information about which part of the stimulus spectrum contains the probe. This kind of learning is unlikely to influence pitch-shift measures.

The pitch-shift gradient method does, however, have shortcomings when compared with our hit-rate profiling method. First, the perceptual processing of a partial falling at an in-tune position spanned by a pair of mistuned targets must be inferred from the pitch shifts associated with those targets. In contrast, our method explicitly tests the perceptual processing of in-tune partials. Second, the origin of these pitch shifts remains unclear. Lin and Hartmann (1998) have suggested that they serve to exaggerate the contrast between a mistuned harmonic and other partials present in the complex, thus enhancing the tendency of a mistuned partial to be heard as a separate entity. In contrast, de Cheveigné (1997) has interpreted these pitch shifts as a direct consequence of the perceptual suppression of in-tune partials. Specifically, he has argued that the internal representation of the frequency of any partial is subject to random variation, and that a mistuned partial is more likely to integrate into a harmonic complex (and hence be more difficult to match) on occasions when its representation is closer to the center of a template slot. Thus the mean of a set of matches is shifted relative to the mistuned frequency, because the pitch-matching procedure elicits a skewed distribution that is increasingly under-represented near the slot centers. Our findings complement this interpretation, because they provide direct evidence for partial-pitch suppression at template slot positions. However, Lin and Hartmann (1998) have argued that de Cheveigné's (1997) model cannot account for both the pitch shifts and the high hit rates observed by Hartmann and Doty (1996). Further work is needed to resolve these issues.

A third, perhaps more significant, shortcoming of the pitch-shift gradient method is that the positions of slots in a hypothetical template are assumed from the outset to be fully predictable. Clearly, this does not present a problem for studies of harmonic complexes, but this may not be the case for other kinds of complex. For example, Roberts and Brunstrom (1998) found that listeners were able to adjust a pure tone to match the pitch of a mistuned partial in a regular inharmonic complex, created by applying a frequency shift or a small degree of spectral stretch to a harmonic complex, almost as well as they could in an otherwise unmodified harmonic complex. This unexpected sensitivity to the spectral structure of these complexes could not easily be explained in terms of the operation of a harmonic template. Therefore, these authors speculated that their results indicated the operation of a template responsive to regular but inharmonic spectral patterns.

One approach to testing Roberts and Brunstrom's (1998) suggestion might be to create spectral gaps in stimuli of the kind that they used, and to establish exactly where the slots of the hypothetical template fall within these gaps. The precision required for this is achievable using our hit-rate pro-

filing method—but not using Lin and Hartmann's (1998) method, which could only establish that a slot fell somewhere between a pair of targets mistuned by $\pm 8\%$ from a pre-selected frequency. It is true that the resolving power could be improved to some extent by reducing the mistuning to $\pm 4\%$. However, any possible benefits of a further reduction in the degree of mistuning would be offset by a reduction in the magnitude of the associated pitch shifts, giving rise to smaller, and probably less stable, estimates of the pitch-shift gradient. Furthermore, these estimates would probably be very sensitive to how symmetrically the target pair was placed around a slot center. In contrast, the probe spacing used to obtain a hit-rate profile within a spectral gap can be set to measure with high resolution the position of template slots.

D. Concluding remarks

The profiling technique introduced in the current study has confirmed and extended the main findings of Lin and Hartmann (1998) regarding the operation of a template-based mechanism in the perception of periodic complex tones. The patterns of hit-rate minima found in experiments 1 and 2 are consistent with the action of a template that suppresses the pitch of any individual partial that is harmonically related to a common F_0 frequency, as hypothesized by Bregman (1990). This suppression effect can spread both upward and downward in frequency, but appears to attenuate with distance from regions of consecutive harmonics. The profiling technique also offers the frequency resolution necessary to evaluate the idea that the auditory system may be sensitive to spectral patterns that are inharmonic but predictable, as proposed by Roberts and Bailey (1996) and by Roberts and Brunstrom (1998). Although the exact nature of the relationship between partial-pitch suppression and the perceptual fusion of harmonics is not understood, it seems plausible that the experience of a unified sound requires the identities of the individual partials to be made less salient.

ACKNOWLEDGMENTS

This research was supported by Research Grant No. 6/S04782 from the Biotechnology and Biological Sciences Research Council (U.K.). We thank Al Bregman and the anonymous reviewer for their comments and suggestions on an earlier version of this manuscript. Our thanks also go to Nik Hargaden for his assistance in the testing of subjects.

Assmann, P. F., and Summerfield, Q. (1990). "Modeling the perception of concurrent vowels: Vowels with different fundamental frequencies," *J. Acoust. Soc. Am.* **88**, 680–697.

Bregman, A. S. (1990). *Auditory Scene Analysis: The Perceptual Organization of Sound* (MIT, Cambridge, MA).

de Cheveigné, A. (1997). "Harmonic fusion and pitch shifts of mistuned partials," *J. Acoust. Soc. Am.* **102**, 1083–1087.

Duifhuis, H., Willems, L. F., and Sluyter, R. J. (1982). "Measurement of pitch in speech: An implementation of Goldstein's theory of pitch perception," *J. Acoust. Soc. Am.* **71**, 1568–1580.

Gerson, A., and Goldstein, J. L. (1978). "Evidence for a general template in

central optimal processing for pitch of complex tones," *J. Acoust. Soc. Am.* **63**, 498–510.

Goldstein, J. L. (1973). "An optimum processor theory for the central formation of the pitch of complex tones," *J. Acoust. Soc. Am.* **54**, 1496–1516.

Hall, J. W., Grose, J. H., and Mendoza, L. (1995). "Across-channel processes in masking," in *Hearing: Handbook of Perception and Cognition*, edited by B. C. J. Moore (Academic, London), 2nd ed., pp. 243–266.

Hartmann, W. M. (1996). "Pitch, periodicity, and auditory organization," *J. Acoust. Soc. Am.* **100**, 3491–3502.

Hartmann, W. M. (1997). *Signals, Sound, and Sensation* (American Institute of Physics, Woodbury, NY).

Hartmann, W. M., and Doty, S. L. (1996). "On the pitches of the components of a complex tone," *J. Acoust. Soc. Am.* **99**, 567–578.

Hartmann, W. M., McAdams, S., and Smith, B. K. (1990). "Hearing a mistuned harmonic in an otherwise periodic complex tone," *J. Acoust. Soc. Am.* **88**, 1712–1724.

Henke, W. L. (1990). "MITSYN: A coherent family of high-level languages for time signal processing" [Software package] (Belmont, MA).

Houtgast, T. (1976). "Subharmonic pitches of a pure tone at low S/N ratio," *J. Acoust. Soc. Am.* **60**, 405–409.

Houtsma, A. J. M., and Goldstein, J. L. (1972). "The central origin of the pitch of complex tones: Evidence from musical interval recognition," *J. Acoust. Soc. Am.* **51**, 520–529.

Johnson, D. H. (1980). "The relationship between spike rate and synchrony in responses of auditory-nerve fibers to single tones," *J. Acoust. Soc. Am.* **68**, 1115–1122.

Kohlerausch, A., and Houtsma, A. J. M. (1992). "Pitch related to spectral edges of broadband signals," in *Processing of Complex Sounds by the Auditory System*, edited by R. P. Carlyon, C. J. Darwin, and I. J. Russell (Oxford U.P., Oxford, UK), pp. 81–88.

Lin, J.-Y., and Hartmann, W. M. (1998). "The pitch of a mistuned harmonic: Evidence for a template model," *J. Acoust. Soc. Am.* **103**, 2608–2617.

Moore, B. C. J. (1997). *An Introduction to the Psychology of Hearing*, 4th ed. (Academic, London).

Moore, B. C. J., Glasberg, B. R., and Peters, R. W. (1985). "Relative dominance of individual partials in determining the pitch of complex tones," *J. Acoust. Soc. Am.* **77**, 1853–1860.

Moore, B. C. J., Glasberg, B. R., and Peters, R. W. (1986). "Thresholds for hearing mistuned partials as separate tones in harmonic complexes," *J. Acoust. Soc. Am.* **80**, 479–483.

Moore, B. C. J., and Ohgushi, K. (1993). "Audibility of partials in inharmonic complex tones," *J. Acoust. Soc. Am.* **93**, 452–461.

Parsons, T. W. (1976). "Separation of speech from interfering speech by means of harmonic selection," *J. Acoust. Soc. Am.* **60**, 911–918.

Plomp, R. (1967). "Pitch of complex tones," *J. Acoust. Soc. Am.* **41**, 1526–1533.

Ritsma, R. J. (1967). "Frequencies dominant in the perception of the pitch of complex sounds," *J. Acoust. Soc. Am.* **42**, 191–198.

Roberts, B., and Bailey, P. J. (1996). "Spectral regularity as a factor distinct from harmonic relations in auditory grouping," *J. Exp. Psychol.* **22**, 604–614.

Roberts, B., and Brunstrom, J. M. (1998). "Perceptual segregation and pitch shifts of mistuned components in harmonic complexes and in regular inharmonic complexes," *J. Acoust. Soc. Am.* **104**, 2326–2338.

Scheffers, M. T. M. (1983a). "Sifting vowels: Auditory pitch analysis and sound segregation," Doctoral thesis, University of Groningen, The Netherlands.

Scheffers, M. T. M. (1983b). "Simulation of auditory analysis of pitch: An elaboration on the DWS pitch meter," *J. Acoust. Soc. Am.* **74**, 1716–1725.

Terhardt, E. (1971). "Pitch shifts of harmonics, an explanation of the octave enlargement phenomenon," in *Proc. 7th Int. Congr. Acoustics, Budapest*, Vol. 3, pp. 621–624.

Terhardt, E. (1974). "Pitch, consonance, and harmony," *J. Acoust. Soc. Am.* **55**, 1061–1069.

Terhardt, E. (1979). "Calculating virtual pitch," *Hearing Res.* **1**, 155–182.

Wightman, F. L. (1973). "The pattern-transformation model of pitch," *J. Acoust. Soc. Am.* **54**, 407–416.

Behavioral assessment of acoustic parameters relevant to signal recognition and preference in a vocal fish

Jessica R. McKibben^{a)}

Section of Neurobiology and Behavior, Cornell University, Ithaca, New York 14853

Andrew H. Bass

Section of Neurobiology and Behavior, Cornell University, Ithaca, New York 14853
and University of California Bodega Marine Laboratory, Bodega Bay, California 94923

(Received 19 April 1998; revised 11 June 1998; accepted 26 August 1998)

Acoustic signal recognition depends on the receiver's processing of the physical attributes of a sound. This study takes advantage of the simple communication sounds produced by plainfin midshipman fish to examine effects of signal variation on call recognition and preference. Nesting male midshipman generate both long duration (>1 min) sinusoidal-like "hums" and short duration "grunts." The hums of neighboring males often overlap, creating beat waveforms. Presentation of humlike, single tone stimuli, but not grunts or noise, elicited robust attraction (phonotaxis) by gravid females. In two-choice tests, females differentiated and chose between acoustic signals that differed in duration, frequency, amplitude, and fine temporal content. Frequency preferences were temperature dependent, in accord with the known temperature dependence of hum fundamental frequency. Concurrent hums were simulated with two-tone beat stimuli, either presented from a single speaker or produced more naturally by interference between adjacent sources. Whereas certain single-source beats reduced stimulus attractiveness, beats which resolved into unmodulated tones at their sources did not affect preference. These results demonstrate that phonotactic assessment of stimulus relevance can be applied in a teleost fish, and that multiple signal parameters can affect receiver response in a vertebrate with relatively simple communication signals. © 1998 Acoustical Society of America. [S0001-4966(98)02412-6]

PACS numbers: 43.66.Gf, 43.80.Lb [DWG]

INTRODUCTION

The function and underlying mechanisms of communication in the acoustic modality have remained largely unexplored in the largest of extant vertebrate taxa, teleost fish. Studies of teleost hearing have demonstrated fundamental similarities with auditory processing in higher vertebrates, in spite of differences in their auditory endorgans (review: Popper and Fay, 1993); thus one might expect similar acoustic dimensions to have been exploited by both fish and terrestrial vertebrates for encoding behaviorally relevant information. We used playback of synthetic signals to test which acoustic features affect call recognition and attractiveness in a sound-producing teleost, the plainfin midshipman (*Porichthys notatus*).

Acoustic signals, generated by vibration of intrinsic swimbladder muscles, are a prominent feature of social interactions in midshipman fish. Midshipman breed along the west coast of North America (Walker and Rosenblatt, 1988) where the parental, or "type I," males establish nests under rocks in the intertidal zone (see Bass, 1996). From these nests, the type I males emit long-duration, multi-harmonic signals known as "hums" (Ibara *et al.*, 1983; Brantley and Bass, 1994; Fig. 1A–C). When a female enters his nest, a male stops humming, and spawning may begin. Spawning can take several hours as the eggs are affixed to the under-surface of the rock, after which the female departs and the

male alone guards and maintains the developing embryos. Whereas, in any breeding season, a female probably spawns only once, depositing all her eggs in one nest (DeMartini, 1988; Brantley and Bass, 1994), a male may continue to hum and attract mates and may have several clutches at different stages of development in his care. Midshipman also have a smaller, "type II," male morph, which pursues sneak spawning strategies, does not hum, and lacks the type I male's secondary sexual characteristics, including its specialized vocal system (Bass, 1992, 1996).

Midshipman hums can be continuous for minutes to an hour or more, often with minimal variation in frequency or amplitude (Ibara *et al.*, 1983; Brantley and Bass, 1994; Bass *et al.*, in press). Hum fundamental frequency is linearly related to water temperature, increasing about 5 Hz/°C, and is approximately 100 Hz at 16 °C (Brantley and Bass, 1994; also see Bass and Baker, 1991). Ibara *et al.* (1983) found with simple playback experiments that recorded hums, or pure tones in the same frequency range, were sufficient to attract gravid females (phonotaxis). This finding, along with aquarium observations of midshipman nesting behavior (Brantley and Bass, 1994), suggests the hum functions as a mate call. Midshipman also produce brief (50–200 ms) "grunt" sounds (Fig. 1D–F) that probably serve an agonistic function. Both females and type II males have been recorded making infrequent, single grunts; but only type I males produce trains of grunts (Fig. 1D–F), emitted, during aquarium observations, in response to intruder males (Brantley and Bass, 1994).

^{a)}Electronic mail: jrm11@cornell.edu

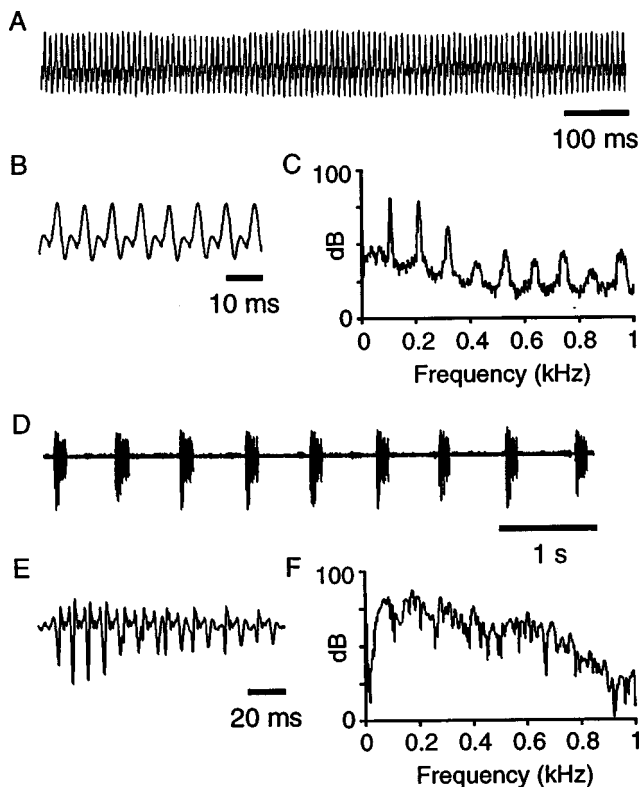


FIG. 1. Midshipman calls recorded in the field. (A) Segment (1 s) of a hum waveform showing the nearly flat envelope. (B) An expansion of the hum waveform. (C) Frequency spectrum of same hum showing peaks at the 107-Hz fundamental frequency and harmonics. Amplitude values are relative only. (D) Waveform for segment (6 s) of a grunt train. (E) Expanded waveform of single grunt. (F) Spectrum of grunt shown in (E).

This study first tests the hypothesis that the hum functions as a mate call by examining the phonotactic responses of gravid and spent females and of both male morphs. Then, one- and two-choice tests with gravid females are used to assess the importance of certain acoustic parameters to hum recognition and attractiveness. Finally, we examine the effects of signal overlap. Midshipman nests are often clustered, and males hum simultaneously; thus receivers must commonly process concurrent acoustic signals (Bodnar and Bass, 1997; Bass *et al.*, in press). We chose to present playback choices as they would be encountered in a natural situation, that is, with alternative calls originating from closely spaced sources and overlapping in time. Therefore, inherent in every choice task presented here is the problem of identifying, locating and evaluating concurrent acoustic signals. The effect of overlap on stimulus effectiveness is further investigated by presenting two-tone beat stimuli.

I. MATERIALS AND METHODS

A. Experimental animals

Midshipman, including females and type I and type II males, were collected from nests exposed at low tide along Tomales Bay and San Quentin Point in Marin County, California. Females and males (type I and II) are distinguished by the size and shape of the urogenital papilla, while the two male morphs are easily further separated on the basis of size and coloration. Gravid females typically have a very dis-

tended abdomen, which becomes flaccid and often darker in coloration in spent females (e.g., see Brantley and Bass, 1994; Bass, 1996). Females taken from nests were in various stages in the spawning process, with many having begun egg deposition, but the majority were still conspicuously gravid.

Each fish was measured, weighed, and labeled either with subcutaneous injections of poster paint, creating a unique color/location pattern, or with a numbered tag sutured just rostral to the dorsal fin. Most experiments were conducted using gravid females ($n=265$), which ranged in size from 8.9 to 20.4 cm (mean 13.5 ± 2.0 cm) standard length and 9.3 to 121.8 g (mean 33.8 ± 18.1 g). Fish were held for at least 24 h prior to testing in outdoor, running sea water tanks at the University of California Bodega Marine Laboratory, where all experiments were conducted. The temperature the fish were housed at varied with the temperature of the incoming seawater (usually between 10 and 15 °C). Live grass shrimp, brine shrimp and goldfish, and chopped anchovies were occasionally offered as food. Under these conditions, females usually would retain their eggs and remain responsive for up to several weeks.

Females and both type I and type II males were tested for responses to humlike, continuous tones; but all tests of comparative responses were done with gravid females. Due to limited numbers of subjects, individual females were used for multiple tests (median number of tests per fish: 6, median number of responses: 3), and may have encountered the same stimulus as one of the choices in different tests. Except for serial one-choice tests, fish were used for no more than one response per night; and, because some fish were used for the same test on different nights or for tests that were later grouped, only the first response of a fish to a stimulus pair is included in the analysis. Variables such as length of time in captivity and hormonal state could also have affected individual responsiveness. However, since all tests involved choices or response comparisons, loss of responsiveness was controlled for. It is not possible to rule out experiential effects on preference strengths, although it seems likely that any habituation to the artificial sound sources or stress due to time constraints on egg viability would tend to decrease rather than increase selectivity.

B. Experimental layout

Tests were done outdoors in a cylindrical concrete tank (4-m diameter, 0.75-m water depth) supplied with running seawater. Since midshipman normally call next to the substrate in water a few meters or less in depth, the boundary conditions in the experimental tank were not entirely unnatural. Underwater loudspeakers (UW-30; University Sound, Buchanan, MI) were suspended just above the bottom from water-filled PVC frames, so that no direct contact substrate conduction was possible. The speakers were placed near the center of the tank facing outward (Fig. 2), well removed from the wall to reduce both the influence of reflected sound and incidental approach by the fish, which tended to hug the tank perimeter in the absence of sound stimuli. For experiments conducted in 1995, the speakers were 137 cm apart center to center and angled toward the release site (configuration C in Fig. 2). These experiments include one of the

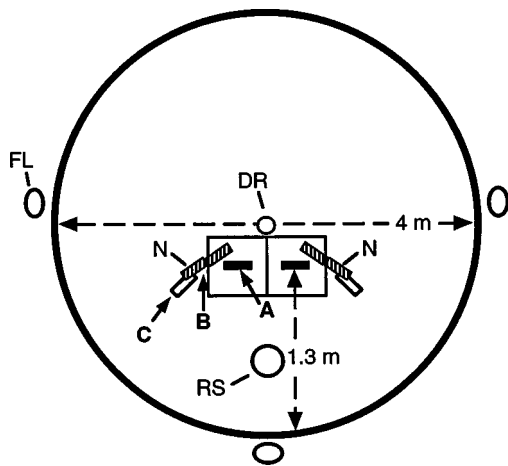


FIG. 2. Diagram of playback tank showing speaker positions for two-speaker tests (A, black bars; and C, open bars) and four-speaker tests (B, hatched bars). Squares around speakers in position A represent 50×50 cm areas marked with tape. DR = drain pipe; FL = floodlight; N = neighbor speaker; RS = release site.

response specificity experiments (Table II, experiment 1), one of the beat test stimuli (Table VI, test C), and the 90- vs 110-Hz frequency preference tests (Fig. 7A). However, for most experiments reported here (conducted in 1996–97), the speakers were side by side and 50 cm apart center to center (configuration A in Fig. 2). Fish are highly mobile subjects and tend to swim along barriers, such as that formed by the release cage, rather than simply orienting to a stimulus. Thus, their initial swimming direction may not reflect localization of a sound but it can quickly bias any response. The goal in placing the speakers side by side was to minimize such random responses by increasing the likelihood of a fish being able to perceive both stimuli upon release. Natural nests are often as close or closer together (see Fig. 1 in Bass, 1996). Around each speaker, 50 by 50 cm squares were marked with tape to allow quantification of time spent in the proximity. Two-choice tests of multi-source beat versus tone preferences utilized two pairs of speakers. One speaker in each pair played the test tone with the adjacent “neighbor” speaker either playing a second tone or silent (configuration B in Fig. 2).

C. Acoustic stimuli

This study involved both one-choice playbacks, to test for recognition and response specificity, and two-choice playbacks, to test for preferences. One-choice tests were used to compare elicitation of phonotaxis by continuous tones, grunts and noise, by tones at different frequencies, and by pulsed, short duration tones. Two-choice tests were used to assess preferences for tones with different frequencies or intensities as well as to compare the attractiveness of tones with harmonic, frequency modulated, and beat stimuli.

Stimuli were synthesized (except for the natural grunt train) and played (SoundEdit 16 software) using a portable computer (Apple Macintosh PowerBook 540c). All stimuli were looped for continuous, transient-free playback; and, for two-choice tests, individual stimuli were stored as separate audio tracks in the same file. The stereo output was con-

TABLE I. Summary of synthetic stimuli and variables presented.

Stimulus type	Frequency components	Variables	Range
Continuous tone	$F1$	Frequency Amplitude	80–140 Hz 128–136 dB
Pulsed tone	$F1$	Pulse duration Interval duration	0.5–2 s (0.1 s) ^a 0.25–0.5 s (0.4 s) ^a
Harmonic	$F1$ and $2 \cdot F1$	Harmonic phase $dF(=F2-F1)$	0° or 90° 2 or 5 Hz
Beat ^b	$F1$ and $F2$	$F2$ amplitude Total amplitude	–12 to 0 dB <i>re: F1</i> 0 to +3 dB <i>re: tone</i>
FM	100 Hz ± modulation frequency	FM range	±5 or 10 Hz
Noise	Noise band 95–130 Hz	none	

^aFor one-choice, specificity tests.

^bFor single-source beat.

nected to Nagra battery powered amplifiers, which drove the UW-30 loudspeakers. Speaker output was monitored and recorded for analysis using a hydrophone (Cornell Bioacoustics Research Program, Laboratory of Ornithology; CBRP; response flat ±1 dB, 60–500+ Hz), suspended with the sensing element approximately 7.5 cm above the bottom and 15 cm in front of a speaker, connected to a Sony Professional Walkman. Recordings were digitized at 11 kHz and spectra computed using Canary, a sound analysis program (CBRP).

Table I summarizes the types and ranges of synthetic stimuli used in this study. The basic humlike stimulus consisted of a continuous pure tone with a frequency between 80 and 140 Hz. Tone levels were set at 130–140 dB *re: 1 μPa*, 15 cm in front of each speaker and matched between speakers for any given test. These stimulus levels are comparable to what has been recorded at midshipman nests in the field (CBRP hydrophones; A. Bass and M. Marchaterre, unpublished observations) and to the reported levels for advertisement calls in the related oyster toadfish (Tavolga, 1971; Barimo and Fine, 1998). Amplitudes were equalized across frequencies by adjusting synthesis amplitudes. Harmonic distortion at the second harmonic was less than –40 dB *re: the fundamental* 15 cm in front of the speaker. For tests with amplitude as the variable parameter, both synthesis and amplification adjustments were made to achieve 3 dB (±0.5 dB) pressure differences between 90- or 100-Hz tones played from the two speakers. Levels were verified by measuring the spectral peaks of stimuli recorded in the tank.

Pulsed stimuli were synthesized by reiteration of a unit composed of a specified silent interval added to a 0.5-, 0.75-, 1-, or 2-s tone. The tone segment had approximately 45-ms rise and fall times. Both harmonic stimuli and single-source beat stimuli consisted of two digitally mixed tones. For the harmonic stimulus, these were the fundamental frequency, $F1$ (90 or 100 Hz), and its second harmonic, $2 \cdot F1$. The second harmonic is generally very prominent in midshipman calls, often containing at least as much energy as the fundamental (e.g., Fig. 1C), thus harmonic stimuli were synthe-

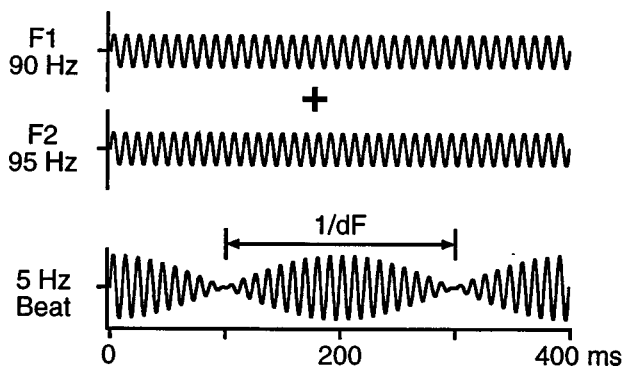


FIG. 3. Synthesis of beat stimuli. Two tones of slightly different frequency, F_1 and F_2 , are added together, resulting in amplitude and phase modulations, known as beats, at their difference frequency (dF).

sized with equal energy at F_1 and $2 \cdot F_1$. Beat stimuli were composed of F_1 (90 or 100 Hz) plus a second tone, F_2 , equal to $F_1 + 2$ Hz or $F_1 + 5$ Hz (Fig. 3).

Frequency-modulated (FM) stimuli consisted of a 100-Hz carrier modulated by ± 5 or ± 10 Hz at 10 modulations per second (i.e., frequency was continually either increasing or decreasing over a 10- or 20-Hz range). In order to compensate for the frequency response of the speakers, the computer-synthesized FM waveform was low-pass filtered, and then re-digitized and amplified for playback. The noise stimulus used for response specificity tests was generated within SoundEdit, then low-pass filtered to produce a 5 s looped stimulus with peak power, upon playback, between 95 and 130 Hz. Finally, the natural grunt train stimulus was recorded (CBRP hydrophone into Sony Professional Walkman) near a midshipman nest in Tomales Bay, CA, digitized (11 kHz sampling rate), and a 10 s segment looped for continuous playback.

Sound pressure in the tank was mapped with measurements taken at 29 points, forming a grid with 6 in. (15.2 cm) steps moving away from and perpendicular to the speaker faces and 10.5 in. (26.7 cm) steps from side to side in parallel with the speaker faces. The hydrophone was positioned 3.5 cm (transducing element approximately 7.5 cm) above the tank bottom and stimuli were recorded on a Sony Professional Walkman and then digitized (11 kHz sampling rate, 16 bit) for analysis. Sound pressure values at the stimulus frequency were computed using Canary software based on stimulus spectra (FFT size 8192 points). Over the relevant frequency range, sound pressure dropped off logarithmically (0.25 dB/cm) from the speaker to the release site with no apparent discontinuities. Thus reflections or standing waves were unlikely to have affected responses. It was not possible to eliminate all background noise, which sometimes had peaks within the frequency range of interest (i.e., 60 and 120 Hz). However, noise peaks in the 20–200-Hz band were at least 30–50 dB below the stimulus frequency peak level 15 cm in front of a speaker.

D. Experimental protocol

Testing was conducted during the midshipman breeding season, from June through September, between 18:00 and 03:00 h, when midshipman are normally most active. Three

red floodlights around the tank perimeter (FL, Fig. 2) allowed observation and videotaping of responses. Although this light was apparently visible to the fish (fish at the perimeter sometimes swam to the surface beneath the floodlights), it did not seem to affect phonotaxis. The water temperature in the test tank varied with the temperature of the incoming sea water and solar heating and could be “regulated” from night to night by adjusting the rate of water flow (off during all tests). Prior to testing, females were held, several to a bucket, in water from the test tank at the test temperature and allowed to acclimate for at least 15 min when the test temperature differed from that in their holding tanks. Tests began with one fish placed in a 30 cm diameter, plastic mesh cylinder approximately 60 cm in front of the speakers (RS, Fig. 2). Fish were released by manually raising the cylinder.

The release protocol was modified over the course of experimentation in order to reduce the occurrence of fish not leaving the release site or retreating to the tank perimeter. Thus, one of three release procedures was followed:

- (1) The fish was placed in the mesh cage, allowed to acclimate for at least 2 min, the stimuli were then turned on for 30 s, and the fish released.
- (2) The fish was placed in the mesh release cage while the stimuli were playing and then released after 30 s.
- (3) For most experiments reported here, the fish was placed in the mesh release cage while the stimuli were playing and released as soon as it swam to the front center of the cage (used with speakers in configuration A).

Releasing the fish without an acclimation period seemed to increase the likelihood of a response, especially in oft tested fish. Likewise, releasing the fish when they were at the front of the release cage appeared to increase response rates. This was presumably because of the steep drop-off in stimulus level with distance from the speakers. In all cases the stimuli played continuously after the fish was released. Trials ended either when the fish swam away from the speaker area or when the sound from one or both speakers was shut off, the latter being after at least 30 s in nearly all cases. Most tests were videotaped (Sony Handycam) to allow verification of observations and detailed response analysis.

Preliminary experiments showed that fish sometimes responded after initially bypassing the speakers and swimming around the tank. Although such free exploration would likely be the case in nature, the position of the fish when it began attending to the playback was not controlled. Thus, only fish that swam directly to a speaker without leaving the area between the release site and the speakers were counted as responding. A positive response was scored if a fish approached a speaker, and then touched or circled in front of or under the speaker.

For one-choice tests, a single stimulus was presented out of one speaker, with a second speaker serving as a silent control. In order to compare responses to different, individually presented signals while controlling for various levels of responsiveness across fish, multiple stimuli were presented serially to the same fish. Such tests with individual fish were separated by at least 30 min to avoid problems with handling

stress or short-term experience, and the active speaker was switched randomly between trials.

For two-choice tests, the alternative stimuli were presented simultaneously from the two speakers and stimulus locations were switched either pseudo-randomly to achieve equal responses in each configuration or alternated from response to response. A preference was considered significant if the distribution of responses was significantly ($p \leq 0.05$) different from the two-tailed binomial distribution expected given the null hypothesis that the proportions of fish approaching each speaker were equal. Fish that did not approach either of the stimulus options for a given test were considered "nonresponders." Since nonresponses could not be attributed to the acoustic stimuli, they were excluded from analysis. Further details of stimulus presentation for each experiment are presented in the results section.

II. RESULTS

A. Morph-specific phonotactic responses

Gravid females showed phonotactic responses to humlike continuous tone stimuli, and most of the tested females responded at some point during their captivity (81% of 74 in 1995, 64% of 101 in 1996, and 69% of 90 in 1997). When spent females were tested with the same stimuli, none approached the speaker ($n=13$). For a representative sample of consecutive trials, the videotaped behavior of gravid females was analyzed in detail. Phonotactic responses by gravid females included several typical behaviors (summarized in Fig. 4A), and usually began with a straight approach to one speaker. Most fish approached the speaker with a distinctive pause-and-glide swimming pattern. Once at the speaker, the specific movements of a responding fish reflected the structure of the speaker and stand; but circling (CI, AF), and a tendency to go under objects (UN, TU) are probably general female midshipman response characteristics. Most responses were unambiguous, incorporating both physical contact (TU, TF) and prolonged active interest in the chosen speaker (Fig. 4B). However, in a small percentage (<10%) of trials, fish swam toward a speaker but then continued immediately toward the back of the tank or stopped near the speaker and sat on the bottom. Including these approaches, which lacked speaker contact or circling, did not change data trends; however, since the fish were not clearly responding to the sound, they were not counted as responses. Figure 4B shows the time spent within a 50 by 50 cm marked square around the speaker for 79 approaches meeting the response criteria (either touching the speaker or circling or both; "Responses") and 13 that did not ("Non-responses"). Most responding fish spent at least 30 s around the speaker.

Although not tested as systematically as females, several type I males approached and showed prolonged interest in a speaker playing a 90- or 100-Hz continuous tone ($n=9$ of 24 fish; 13.1–28 cm standard length). The responses elicited from type I males were quite different from those of gravid females. Whereas females always approached the speaker head-on, type I males were sometimes observed to back up to and under the speaker and frequently performed "dig-

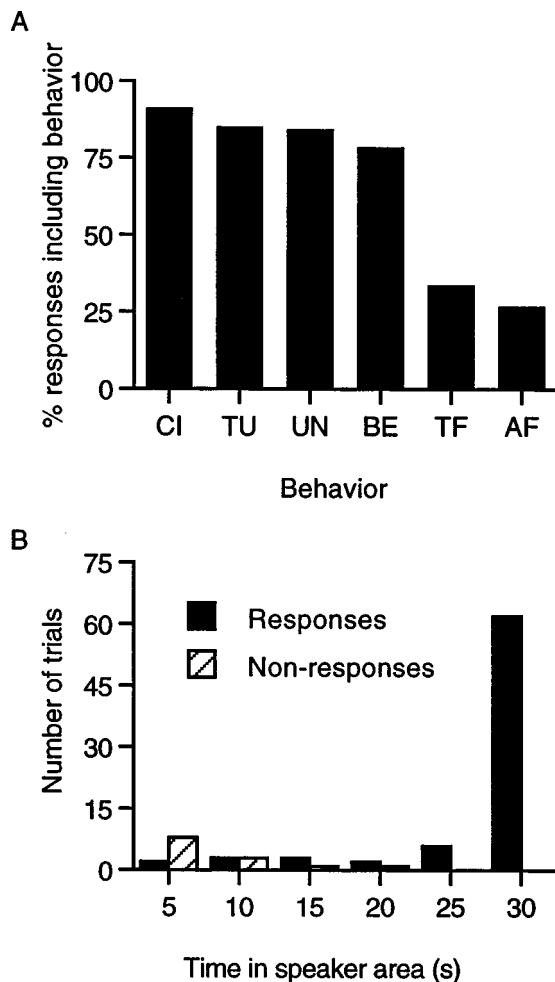


FIG. 4. (A) Histogram showing frequencies of occurrence of different behaviors in a sample of 87 videotaped phonotactic responses by gravid females. Only trials which included either circling (CI) or contact with the speaker (TU, TF) are included in this analysis. CI=circling: swimming in circles or back and forth in front of or under the speaker. TU=touching underside of speaker: approaching speaker head-on or from side and making contact with underside of projecting speaker face. UN=under: going under the speaker from front to back, back to front, or from the side. BE=behind: approaching or lingering behind the speaker within the boundaries of the speaker stand. TF=touching speaker face: contacting, often appearing to nuzzle or swim against speaker face. AF=around frame: swimming near the bottom around the square frame supporting the speaker. (B) Time spent within 50×50 cm area around speaker during first 30 s after entering area. Data are shown for 92 trials including 79 responses (the 87 in A minus 8 responses without the full 30 s of time data) and 13 instances where fish crossed into the speaker area but did not circle or touch the speaker (non-responses). Five-second bins; values are upper limits.

ging" motions with their tail and pectoral fins. These movements resemble the nest-building behavior typical of type I males (Brantley and Bass, 1994). Type II males rarely approached a speaker playing humlike, 90- or 100-Hz tones, but the few observed phonotactic responses ($n=5$ responses from 3 fish out of 22 tested; 7–11 cm) included "sneaker-like" behaviors such as sidling up to the speaker frame or working their tails underneath the frame (see Brantley and Bass, 1994). Unlike females, neither type I nor type II males touched the speaker face or circled rapidly back and forth in front of the speaker.

TABLE II. Results of one-choice playback tests showing specificity of phonotactic response by gravid female midshipman. Experiment 1: Two stimuli individually presented (in random order) to each fish (16.3–16.8 °C). Experiment 2: Three stimuli individually presented to each fish (15.7–16.2 °C). The number of fish responding to each stimulus is indicated for each position of that stimulus in the presentation order.

Experiment	Stimulus:	Presentation order:			Total responses: Total fish tested
		1	2	3	
1	Continuous tone 110 Hz	4	4	...	8:11
	Field recorded grunts (110 Hz fundamental)	0	0	...	0:11
2	Continuous tone 100 Hz	4	3	3	10:14
	Pulsed tone 100 Hz (100 ms on, 400 ms off)	0	0	0	0:14
	Filtered noise	0	0	0	0:14

B. Response specificity

Table II shows results for two one-choice experiments where gravid females responded selectively to humlike stimuli. For each experiment, stimuli were presented one at a time, in random order, so that each fish was tested once with each stimulus. The speakers were in the widely spaced configuration (configuration C in Fig. 2) for the first experiment and side by side for the second (configuration A in Fig. 2). In the first experiment, 8 of 11 fish approached a continuous tone (matched to the 110-Hz fundamental frequency of the natural grunt train) but none approached the grunts. Likewise, in the second experiment, 10 of 14 fish approached a speaker playing a continuous 100-Hz tone, but no fish approached a 100-ms pulsed tone, approximating a grunt train, or noise centered around 100 Hz. No fish approached the silent control speaker.

C. Stimulus duration

The importance of signal duration to hum recognition was further investigated with one-choice tests of phonotaxis using pulsed tone stimuli with various pulse durations and intervals (Fig. 5A). Experimentally naive gravid females were presented with one of various sets of two to four different pulsed 90-Hz stimuli. Stimuli were presented individually; and, within each set, the order of presentation was varied across subjects to reduce any experiential bias. Following a set of pulsed stimuli, each fish was tested with a continuous 90-Hz tone. This served as a control for responsiveness and was presented last to prevent expectations from influencing the attractiveness of the pulsed signals. For analysis, only data from fish that responded to the continuous control (80 of 101 fish tested) were included; and results for specific stimuli were combined across the different stimulus sets. Thus the same individual may be represented in the data for various combinations of stimuli (no fish were tested with all five stimuli), but never more than once for the same stimulus.

The results graphed in Fig. 5B show that pulsed stimuli of 2 s or less elicited phonotaxis by at least some fish. However, the percentage of fish approaching the sound tended to decrease as pulse duration was shortened from 2 to 0.5 s (stimulus a to e). Significant differences between pairs of stimuli (Fisher's exact test, $p < 0.05$) are indicated by matching symbols above the corresponding bars. The pulsed stimuli also varied in interpulse interval length and, thus, total energy. A higher percentage of fish approached a 1 s pulse when the interpulse interval was 0.25 s (stimulus b) than when it was increased to 0.5 s (stimulus c) (Chi-square = 3.107, $p = 0.078$). Over the range of stimuli tested, the percentage of fish responding correlated well with the proportion of the stimulus the sound was on (duty cycle) (Fig. 5C, $r^2 = 0.826$).

The attractiveness of a pulsed tone relative to a continuous tone was directly compared using a two-choice protocol. Given a choice between a 90-Hz stimulus consisting of 1 s pulses with 0.5 s intervals (same as stimulus c in Fig. 5) and a 90-Hz continuous tone, 10 of 13 fish approached the continuous tone ($p < 0.05$). The three fish that initially approached the pulsed signal all subsequently went to the speaker playing the continuous tone.

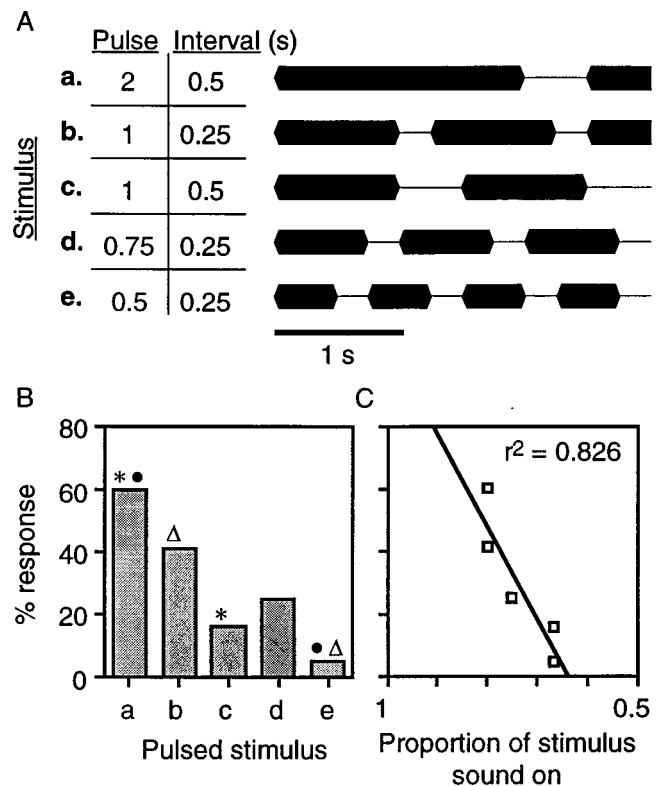
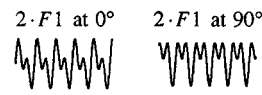


FIG. 5. (A) Pulsed stimuli (a–e) consisted of 90-Hz tones with the pulse and interval durations indicated. Envelopes are shown at right for three seconds of each stimulus. (B) Percent of fish that subsequently responded to a continuous tone (responsive fish) that approached each of the five different pulsed stimuli. Significant differences (Fisher's exact test, $p < 0.05$) between responses to pairs of stimuli are indicated with matching symbols over the corresponding bars. Total number of responsive fish tested with each stimulus: a, 10; b, 22; c, 19; d, 12; e, 22. (C) Same response data plotted in terms of duty cycle (proportion of stimulus sound was on). Testing conducted at 14.4–15.6 °C.

TABLE III. Results of two-choice tests showing approaches to stimuli with or without second harmonic ($2 \cdot F1$) (A and B), and to stimuli with phase of second harmonic at 0° or 90° relative to fundamental ($F1$) (C).

Test	$F1$ (Hz)	To	To	Total responses	p -value
		$F1 + (2 \cdot F1)$	$F1$ alone		
A	100	5	8	13	0.29
B	90	4	5	9	0.5
					
C	90	4	4	8	0.64

D. Harmonics

Although natural hums contain considerable energy at the first two or three harmonics (Fig. 1C), pure tones (second harmonic < -40 dB *re*: fundamental frequency) were sufficient to elicit phonotaxis. Two-choice experiments tested whether harmonics might affect the attractiveness of a hum. Fish were presented with a choice between a pure tone and that same tone plus its second harmonic, at the same intensity and at the same starting phase as the fundamental. Despite the greater intensity of the harmonic signal, fish showed no preference in tests with either a 90- or 100-Hz fundamental frequency (Table III, tests A and B). Because harmonic phase, which affects fine waveform structure, including peak amplitude, might have affected signal attractiveness (e.g., as shown for anurans; Bodnar, 1996), fish were also given a choice between harmonic stimuli that differed in the phase of

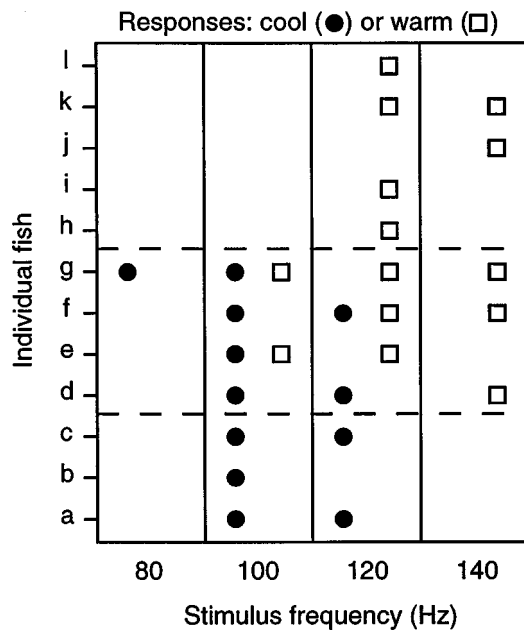


FIG. 6. Approaches to individually presented tones at two temperatures. Each fish was tested with 80, 100, 120, and 140 Hz and the results are divided (horizontal dashed lines) according to whether the fish were tested at just cool (fish a–c), just warm (fish h–l), or both temperatures (fish d–g). Responses to a given frequency at the cool temperature (14.2–14.4 °C) are indicated with filled circles, and, at the warm temperature (19.4–21.5 °C), with open squares.

the harmonic. With a 90-Hz fundamental, no preference for relative phase of the second harmonic, 0° or 90° starting phase relative to the fundamental at synthesis, was detected (Table III, test C).

E. Fundamental frequency

In order to test the frequency selectivity of hum recognition, gravid females were presented individual tones spanning a 60-Hz range. Figure 6 shows the results of one-choice tests with 80-, 100-, 120-, and 140-Hz continuous tones at two temperatures. Each fish was presented one of the four

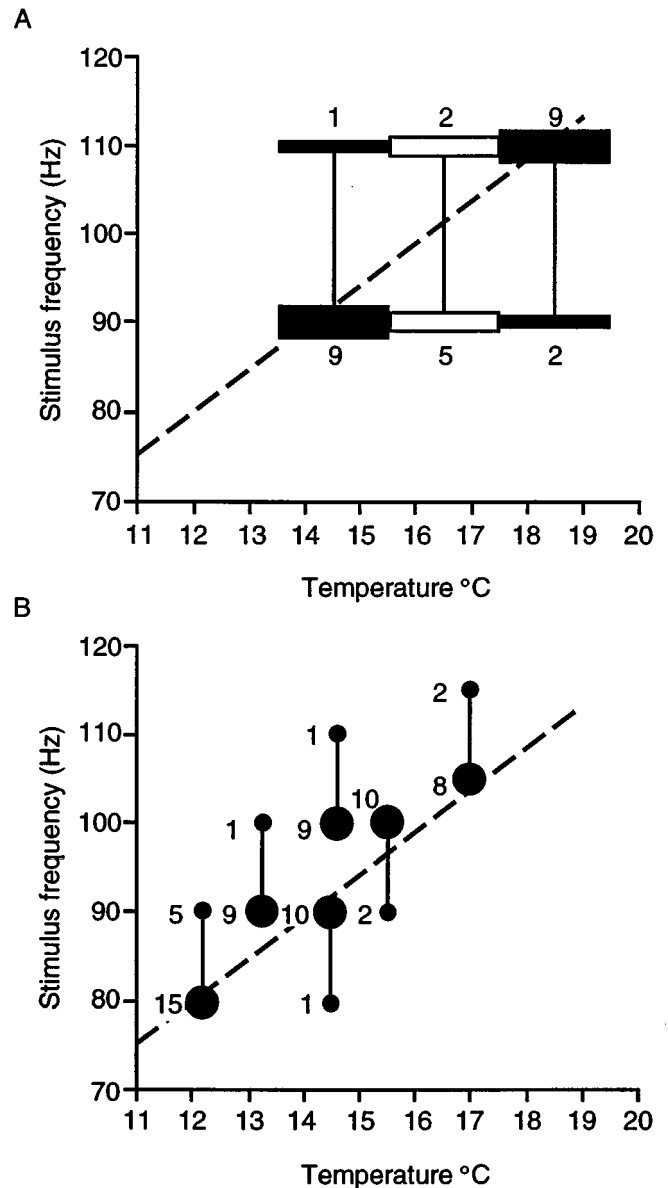


FIG. 7. Two-choice, continuous tone frequency preferences at different temperatures. (A) Choice of 90 or 110 Hz over three temperature ranges: 13.6–15.5, 15.6–17.5, and 17.6–19.5 °C. The number of fish choosing that stimulus is shown next to each bar. Dashed lines in (A) and (B) indicate expected hum frequency at each temperature (based on Brantley and Bass, 1994; and unpublished observations). (B) Frequency preferences between pairs of tones differing by 10 Hz at indicated temperatures. For each test, paired frequency choices are connected with vertical lines, and the preferred ($p \leq 0.05$; large filled circles) and nonpreferred (small filled circles) frequencies are indicated.

TABLE IV. Results of two-choice tests with tonal stimuli that differed by 3 dB. Response values are numbers of individual fish approaching each stimulus.

Test	Frequency (Hz)	Stimulus levels (dB <i>re</i> : 1 μ Pa)	To lower intensity	To higher intensity	Total responses	<i>p</i> -value
A	100	133 and 136	4	14	18	0.015
B	90	131 and 134	1	9	10	0.011
C	90	128 and 131	2	9	11	0.033

frequencies per trial, in random order, for a total of four trials per fish; only data from fish that responded to at least one frequency at the specified temperature are included. Subjects are grouped (separated by dashed lines) according to whether they were tested at either the cool (14.2–14.4 °C; fish a–c) or warm (19.4–21.5 °C; fish h–l) temperature, or at both temperatures (fish d–g). Approaches to each frequency tone are plotted with filled circles (cool temperature) or open squares (warm temperature). At a single temperature (i.e., either cool or warm), 7 of the 12 responding fish (fish a, c–g, k) approached two or more of the frequencies tested, a 20–40 Hz range. An effect of temperature on the attractiveness of different frequencies was also suggested. Fish tended to respond more to higher frequencies (120 and 140 Hz) at the higher temperature, although, due to small numbers of responding fish, the differences were not significant.

To further test the effect of temperature on frequency preference, fish were given choices between two continuous tones differing by 10 or 20 Hz at various temperatures. Prior to testing, subjects were acclimated to the test temperature for at least 15 min and up to approximately 1 h. The first experiment (Fig. 7A) tested preferences for 90- or 110-Hz tones as temperature varied. Results are grouped into 2 °C bins and plotted with bars extending over the applicable temperature range. Preferred frequencies are indicated with thick filled bars and nonpreferred frequencies with thin filled bars. At the lowest temperatures (13.6–15.5 °C), 9 of 10 responding fish chose the 90-Hz tone ($p=0.011$); and at the highest temperatures, (17.6–19.5 °C), 9 of 11 fish chose the 110-Hz tone ($p=0.033$). There was no clear preference at intermediate temperatures (open bars; 15.6–17.5 °C).

Figure 7B shows the results of two-choice tests with stimuli differing by 10 Hz at specific temperatures. Stimulus choices consisted of continuous tones at 80 and 90 Hz, 90 and 100 Hz, 100 and 110 Hz, and 105 and 115 Hz. Paired frequency choices are linked by vertical lines, and preferred frequencies ($p\leq 0.05$) are marked with large filled circles; nonpreferred frequencies, with small filled circles. The number of fish approaching each stimulus is indicated to the left of each marker. Frequency preference, significant for all tests, was neither absolute nor simply directional but depended upon temperature. For example, whereas fish chose 80 Hz over 90 Hz near 12 °C, that preference was reversed at 14.5 °C. The 80-, 90-, and 100-Hz stimuli were each, in different tests, both the preferred and nonpreferred stimulus. Also plotted in Fig. 7A and B is the expected hum frequency (dashed line; Brantley and Bass, 1994; and unpublished observations), which increases linearly over this temperature range. Frequency test pairs (Fig. 7B) were chosen to bracket expected hum frequency, and, for all six tests, fish preferred

the frequency closest to the expected hum frequency at the test temperature. In four cases this was the lower frequency, and, in two cases, the higher.

F. Stimulus amplitude

Fish were given a choice between continuous tonal stimuli that differed by 3 dB (± 0.5 dB). Table IV shows results for three tests demonstrating preferential approach to the more intense of the two signals. Although speaker output and the steep drop in sound intensity with distance limited the range of levels that could be presented, this preference was apparent over a 6 dB range at 90 Hz as well as at 100 Hz and thus was clearly based on amplitude.

G. Frequency modulation

In order to test the importance of frequency constancy (which is also an indicator of fine temporal waveform periodicity) to signal effectiveness, we compared attraction to constant frequency and frequency-modulated tones (Table V). FM signals consisted of 100 Hz modulated ± 5 or ± 10 Hz with a modulation rate of 10 Hz. In two-choice tests, fish preferred a 100-Hz tone to the 100 \pm 10-Hz FM stimulus (Table V, test A; $p=0.038$), although, in separate tests, four fish presented with just the ± 10 -Hz FM stimulus approached the speaker. When the FM stimulus was modulated only ± 5 Hz, no preference for the tone or FM was observed (Table V, test B).






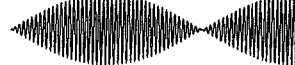

H. Beat stimuli

When two concurrent tones, or hums, of slightly different frequencies summate, constructive and destructive interference results in beats at their difference frequency (dF). Because female midshipman approaching a group of humming males will often encounter beats in the summated acoustic waveform (see Bodnar and Bass, 1997), we used

TABLE V. Results of two-choice tests between continuously frequency-modulated (FM) and constant frequency tones. Response values are numbers of individual fish approaching each stimulus. Testing conducted at 14.5–15.1 °C (test A) and 15.1–15.3 °C (test B).

Test	FM stimulus	FM	100 Hz tone	Total responses	<i>p</i> -value
A	100 Hz \pm 10 Hz at 10 Hz	4	12	16	0.038
B	100 Hz \pm 5 Hz at 10 Hz	14	8	22	0.143

TABLE VI. Results of two-choice playback tests comparing approaches to single tone and two-tone beat stimuli. Beat stimulus tones ($F1$ and $F2$) were combined and presented out of a single speaker.

Test ^a	Beat stimulus $F1 + F2$ (amplitudes <i>re</i> tone)	dF (Hz)	Beat $F2 - F1$ (dB)	Beat stimulus (750 ms segment)	# Fish to Tone	# Fish to Beat	Total	<i>p</i> -value
A	90+95 Hz (50%+50%)	5	0		11	2	13	0.011
B	90+95 Hz (75%+25%)	5	-9.5		10	1	11	0.006
C	110+105 Hz (100%+100%)	5	0		10	0	10	0.001
D	90+95 Hz (100%+50%)	5	-6		8	2	10	0.055
E	90+95 Hz (100%+25%)	5	-12		8	9	17	0.500
F	90+92 Hz (100%+100%)	2	0		5	5	10	0.620
Nonbeat stimulus: Tone at $F1$ (90 or 110 Hz) 100% amplitude								

^aTest temperatures (°C): A, 14.3–14.6; B, 13.7–13.8; C, 18.3–19; D, 14.8; E, 13.3–14.2; F, 14.4–14.8.

two-choice tests to assess what impact beats might have on hum attractiveness. First we compared the attractiveness of a beat waveform played from one speaker (single-source beat) with a single tone from a second speaker. Then we compared the attractiveness of a single tone with or without beat interference from an adjacent speaker (multi-source beat).

Single-source beat stimuli were generated by adding two tones, $F1$ and $F2$ (equal to $F1 + 2$ or $+5$ Hz), together (Fig. 3). Tests paired the beat stimulus played out of one speaker with a single tone stimulus, $F1$, played out of the second speaker. Depending on the test, beat stimuli were either equal in intensity (averaged over a complete beat cycle) to the tone alternative or equivalent to the tone intensity plus the $F2$ intensity. In the latter case, this meant beat stimuli were up to 3 dB more intense than the tone stimulus. The depth of the beat modulation was varied by changing the relative contribution of $F2$ to the beat stimulus.

Table VI summarizes the results of the two-choice beat tests. When fish were given a choice between $F1$ and an equal intensity 5-Hz beat signal composed of $F2$ equal in amplitude to $F1$ (maximum beat depth), 11 of 13 fish ($p = 0.011$) went to the nonbeat signal (Table VI, test A). When the depth of beating was reduced, by reducing the relative amplitude of the $F2$ component to one third that of $F1$, while keeping total signal energy the same (test B), 10 of 11 ($p = 0.006$) fish approached the nonbeat stimulus. In tests C–F, the beat $F1$ component was not attenuated, resulting in beat stimuli with higher average intensity than the single tone stimulus. With $F1$ equal in amplitude to $F2$ (Test C), 10

of 10 fish preferred the nonbeat, lower intensity stimulus. (This one test was conducted with speaker arrangement C in Fig. 2). When $F2$ was reduced to half the amplitude of $F1$, producing shallower envelope modulation (test D), fish still tended to approach the nonbeat stimulus (8 of 10, $p = 0.055$). However, there was no preference when $F2$ was only one quarter the amplitude of $F1$ (test E). Likewise, when $F2$ was equal to the amplitude of $F1$ but the dF was only 2 Hz (test F), there was no detectable preference.

Unlike the single-source beat stimuli presented above, naturally occurring beat waveforms result from interference between separate sources, which are themselves nonbeating. In order to separate out the attractiveness of beat stimuli at a distance from acceptability at the source, fish were tested with multi-source beat stimuli. This experiment used two pairs of speakers (Fig. 2, configuration B) with one speaker in each pair playing the test tone and the neighboring speaker either playing a second tone, creating a multi-source beat, or silent. When the test tone, 90, 95, or 100 Hz (chosen to be attractive at test temperature) was paired with a single tone “neighbor” of equal amplitude and ± 5 Hz from the test tone, there was no detectable preference among 12 fish for the tone or beat signal (Table VII, tests A–C). Likewise, with a multi-source beat consisting of a 90-Hz test tone plus a 92-Hz neighbor (test D), fish went equally to the tone and beat speakers. When fish approached the beat speakers during these tests, they responded to either or both of the tones.

TABLE VII. Results for two-choice tests with single tone versus multi-source beat stimuli. For beat stimuli, equal intensity tones with dF's of 5 or 2 Hz were projected from adjacent speakers. Response numbers indicate individual fish approaching each stimulus.

Test ^a	Tone stimulus (Hz)	Beat stimulus components (Hz)	To tone	To multi-source beat	Total responses	p-value
A	90	90 & 95	2	4	6	0.34
B	95	90 & 95	2	0	2	0.25
C	100	100 & 105	2	2	4	0.69
A-C	Totals for 5 Hz dF		6	6	12	0.61
D	90	90 & 92	4	6	10	0.38

^aTest temperatures (°C): A, 12.7–14; B, 14; C, 14.2; D, 14.4–14.8.

III. DISCUSSION

A. Playback and acoustic communication

This study has examined attraction by females and type I and type II males to synthetic type I male calls in the plainfin midshipman fish. By isolating acoustic signals from the potentially complex behavioral milieu, playback allows more direct comparison between the physical properties of a sound and the receiver's response. Whereas playback has been broadly exploited in terrestrial vertebrates (e.g., reviews by Gerhardt, 1988; Searcy, 1992; Hauser, 1996), the study of midshipman reported here is the first we are aware of in fish that uses two-choice presentations to test the relative attractiveness of signals that vary in precisely specified parameters.

This study has used one-choice tests of call recognition and two-choice tests of preferences between simultaneously presented variants to elucidate several acoustic dimensions important to female midshipman attraction to male hums. Recognition and preference are likely to be measures of the same underlying sensory and neural processing (Ryan and Rand, 1993). A call may evoke a response (recognition) over a range of values for an acoustic parameter (e.g., frequency); and, within that range, certain values may be chosen over others (preference).

B. Fish phonotaxis

Historically, much more has been known about the production of sounds by fish than about their communicatory significance (reviews by Fine *et al.*, 1977; Myrberg, 1981; Ladich, 1997). A small number of playback experiments with vocal fish have been used to test call function, species specificity of responses, and behavioral relevance of call parameters; however, only a very few experiments have tested differential phonotaxis. Experiments with sunfish (Gerald, 1971), and cyprinids (Delco, 1960) showed greater attraction to conspecific than to heterospecific calls. Likewise, in bicolor damselfish, a conspecific call was more effective than heterospecific calls in facilitating courtship by males (Myrberg and Spire, 1972) and more effective than heterospecific calls or noise in attracting females (Myrberg *et al.*, 1986). Tavalga (1958) found that female and male gobies, *Bathygobius soporator*, increased activity or approached the transducer, respectively, in response to playbacks of male courtship sounds. Tavalga then presented, one at a time, synthetic call variants and concluded that the fish were not very selec-

tive as long as stimulus fundamental frequency, pulse duration and pulse repetition rate fell within certain ranges. By playing back the calls of a large and a small male bicolor damselfish near the natural territories of several females, Myrberg *et al.* (1986) demonstrated preferential attraction to the larger male's call. The larger male's call was lower in frequency (see also Myrberg *et al.*, 1993), although it is possible that temporal differences between these two natural, amplitude-modulated signals could have influenced female preference.

An Atlantic relative of the midshipman, the oyster toadfish, *Opsanus tau*, also has nesting males that produce advertisement calls. These "boatwhistle" calls are generally less than 500 ms in duration and have fundamental frequencies similar to midshipman signals, though warmer ambient temperatures tend to make boatwhistle frequencies higher (Fine, 1978; Bass and Baker, 1991; Barimo and Fine, 1998). Most playback experiments with toadfish have been directed at calling males, which will increase or decrease their calling rates in response to certain signals (Winn, 1967, 1972; Fish, 1972). Winn (1972) showed that gravid female, and very occasionally male, toadfish approach speakers playing back pre-recorded boatwhistles. Only one signal was used, so no conclusions about call preference could be made.

Ibara *et al.* (1983) tested plainfin midshipman responses to recorded hums and pure tones. Gravid, but not spent, females were found to become more active in response to individually presented tones between 80 and 115 Hz, and five fish for which data were collected were most responsive to frequencies around 95 Hz (playback temperatures were not given). Midshipman were apparently unable to localize sound sources in the small test tanks, but in additional tests in a larger tank, fish approached the active speaker. Again, fish were not given a choice between signals; and only stimulus frequency was varied.

C. Phonotaxis and function

Aquarium observations of midshipman acoustic and spawning behavior (Brantley and Bass, 1994) and both the present and previous (Ibara *et al.*, 1983) playback studies strongly support the hypothesis that the midshipman hum functions as a mate call. Gravid females show the most robust and consistent phonotactic responses and are clearly able to localize sound sources even in a non-ideal acoustic environment, such as the shallow tank used in this study.

The observation that both type I and type II males will sometimes approach a loudspeaker playing humlike signals suggests that the hum has a general meaning of “nesting male present,” and probably plays a role in male–male interactions as well. As noted above, in the related oyster toadfish, playback of male calls influenced the calling behavior of nearby males (Winn, 1967; Fish, 1972) as well as attracting gravid females (Winn, 1972). Although all three midshipman morphs showed some degree of phonotaxis to hums, they differed in the motor patterns elicited. This implies that a neural mechanism couples auditory input to the evocation of sex- and morph-specific reproductive behaviors (as described by Brantley and Bass, 1994).

D. Spectral and temporal waveform selectivity

Female midshipman were selective with regard to the type of sound they found attractive. Pure tones or tones with harmonics evoked phonotaxis, but noise with comparable energy at relevant frequencies was never attractive. Thus, audible sound is not sufficient for mate recognition. Noise, by definition, lacks periodicity in its fine waveform structure, and the periodicity of the hum waveform is one of its most salient characters (Fig. 1B). Hums can be remarkably constant in frequency (Bass *et al.*, in press), and recordings in the midshipman peripheral auditory system have shown that inner ear afferents can precisely synchronize (i.e., phase lock) to the periodicity of tones over the range of frequencies that attract gravid females (McKibben, 1998).

To investigate the importance of fine temporal waveform periodicity to female preference, fish were given a choice between constant frequency and frequency-modulated signals. Continuous frequency modulation produced an approximately sinusoidal signal with varying intervals between successive peaks in the waveform. While a pure tone was preferred over a ± 10 -Hz modulated signal, the FM signal was attractive to at least some fish, and four fish presented with the FM stimulus alone approached the speaker. Fish went equally to the tone and FM signal when the modulation was only ± 5 Hz. Thus, hum recognition does not require strict frequency constancy, although increasing degrees of modulation are likely to make a signal less attractive. A confounding aspect of frequency modulation in this system is the relationship between temperature and frequency preference. Although frequency variation over 20 Hz does not exceed the demonstrated range of recognition at a given temperature (Fig. 6), a preference for lower or higher frequencies could affect the relative attractiveness of the FM signal depending on temperature and apart from modulation effects.

E. Duration

Hums generally last on the order of minutes (Ibara *et al.*, 1983; Brantley and Bass, 1994), but we observed females responding to trains of stimuli as short as 500–750 ms (Fig. 5). Although much shorter than most hums, 500 ms is considerably longer than a grunt (Brantley and Bass, 1994). Indeed, duration may be the critical difference between calls

perceived as hums and as grunts. [Fine *et al.* (1977) review both graded and categorical differences in duration in the call repertoires of several fish species.]

Over the range of pulsed stimuli tested with midshipman there was a positive correlation between the duty cycle (percent of time the sound was on) and the attractiveness of the stimulus (Fig. 5C). However, in the two cases where stimuli with different pulse durations had the same duty cycle (Fig. 5, stimuli a and b, c and e), the stimulus with longer pulse durations attracted a higher percentage of fish (Fig. 5B). This suggests that the duration component of hum recognition cannot be solely a matter of temporal integration (over hundreds of milliseconds) but depends on the duration of individual sound pulses. The threshold duration for hum recognition appears to be around 0.5–1 s. In two-choice tests, females preferred a continuous tone over a 1 s pulsed stimulus. This result, along with the observation that female search behavior usually ceases when a hum stops, suggests that females would be more likely to locate and approach a continuously humming male.

F. Harmonics

The hum fundamental frequency alone is sufficient to attract female midshipman, and adding the second harmonic had no effect on stimulus preference. The midshipman's peripheral auditory system can encode frequencies up to at least the third harmonic (around 300 Hz; McKibben, 1998), so harmonics could have some behavioral relevance. For example, harmonics could increase the detectability of a near-threshold hum, especially given constraints on sound transmission presented by the physical environment. Midshipman often nest in the intertidal zone where the water depth is variable but often considerably less than the 1/4 to 1/2 wavelength (15 m for a 100 Hz signal) necessary for efficient propagation of the fundamental (Forrest *et al.*, 1993). In such a constricted space the harmonics' shorter wavelengths may be able to propagate further than the fundamental (Fine and Lenhardt, 1983).

G. Frequency preference and temperature coupling

In this study, gravid female midshipman approached tones with fundamental frequencies of 80 to 140 Hz. This is greater than the 80–115-Hz range found by Ibara *et al.* (1983), and the full range of attractive frequencies, especially as temperature is varied, is presumably greater. The fundamental frequency of a male's hum is a function of muscle contraction rate, determined by the output of a pacemaker-motoneuron circuit in the hindbrain (Cohen and Winn, 1967; Bass and Baker, 1990). The frequency of this rhythmic output and, hence, of the hum, increases linearly with ambient temperature (Bass and Baker, 1991; Brantley and Bass, 1994).

The two-choice experiments reported here show that midshipman are capable of discriminating and choosing between two signals differing by 10 or 20 Hz. Although these tests used tones well within the frequency range of midshipman calls, analysis of field recordings has shown that the differences in hum fundamental frequency that a female is

likely to encounter at any one temperature are less than 10 Hz (Bodnar and Bass, 1997). Thus, the question of whether midshipman can discriminate frequency differences that could influence choice between humming males remains open. In psychophysical tests with tones around 100 Hz, goldfish are able to detect frequency differences down to approximately 5 Hz (Fay, 1970).

Female frequency preference was temperature dependent and in accord with the temperature dependence of hum frequency. In two-choice tests with tones differing by 10 or 20 Hz, fish preferred the frequency closest to the expected hum frequency at the test temperature. However, when fish were given a choice between 90 and 110 Hz at intermediate temperatures (15.6–17.5 °C) where the expected hum frequency would be around 100 Hz, they showed no preference. These results suggest that at a given temperature there will be a most attractive frequency, with attractiveness falling off as the frequency is either increased or decreased. Similar temperature coupling of male calling song and female response preferences has been described in crickets (Pires and Hoy, 1992) and frogs (e.g., Gerhardt and Doherty, 1988) and has been linked to underlying sensory processes (Brenowitz *et al.*, 1985). Temperature dependence of call characteristics is common in poikilothermic species, and temperature-dependent reception presumably can enhance the sensitivity or accuracy of recognition of conspecific calls.

H. Amplitude

Female midshipman preferentially approached the higher intensity of two tones that differed by just 3 dB. Using our experimental layout, the responding fish were presumably able to hear both signals and choose the higher amplitude. Since both sources were equi-distant from the release site, this response could reflect assessment either of source intensity or of relative intensity at the fish's location (see Forrest and Raspet, 1994). Three dB sensitivity is better than the 3.7–5.2 dB intensity discrimination thresholds obtained for 110-Hz pulsed tones in conditioning experiments with cod and haddock (Chapman and Johnstone, 1974). Like the midshipman, these species lack specialized connections between the swimbladder and inner ear. Goldfish, known as “hearing specialists” for just such an enhanced transmission pathway, are sensitive to differences in pulsed tone amplitude of only 2.1 dB at 100 Hz (Fay, 1989). We did not test the limits of midshipman discrimination, but the demonstration of a preference based on a 3 dB difference suggests that midshipman sensitivity is likely to be comparable to that of goldfish and to other vertebrates (Fay, 1989). It remains to be seen whether there are true interspecies difference in fish intensity discrimination abilities or just differences in experimental methods.

I. Concurrent hums and beat stimuli

Perhaps the most striking aspect of the hum signal is its essential lack of gross temporal structure. Whereas acoustic communication signals typically have some form of distinct envelope modulation that contributes to the signal's behavioral effectiveness (e.g., Winn, 1972; Myrberg *et al.*, 1978;

Van Tasell *et al.*, 1987; Gerhardt, 1988; Crawford *et al.*, 1997; Penna, 1997), the midshipman hum is effectively continuous and flat in amplitude. However, females commonly encounter acoustic waveforms that are more complex than those of individual hums. Neighboring males often hum simultaneously, and small differences in their fundamental frequencies (<8 Hz) produce beats in the summated acoustic waveform (Bodnar and Bass, 1997).

In both the two-choice, frequency preference tests (Fig. 7) and the beat stimulus experiments (Tables VI and VII) reported here, fish were able to discriminate and localize sounds in the presence of beat waveforms. For the frequency tests, the concurrent tones originated from separate speakers and differed by 10 or 20 Hz. Thus, their interference produced beats at 10 or 20 Hz. Just as these overlapping signals did not effectively jam each other and eliminate phonotaxis, fish were also able to localize and respond to individual sources in tests with single- or multi-source beat stimuli with dF's of 2 or 5 Hz. Thus, female preference for the hums of individual males must be based on auditory processing that can extract overlapping hums (Bodnar and Bass, 1997).

Fish preferred pure tones over certain single-source beat stimuli. Both beat frequency (dF) and depth of beating appear to be limiting factors for stimulus attractiveness. In two-choice tests, fish rejected 5-Hz dF, 100% modulated (*F*₁ and *F*₂ equal amplitude) beat stimuli in favor of *F*₁ presented alone (Table VI, tests A, C). When *F*₂ was attenuated, reducing the depth of modulation, this preference gradually disappeared (Table VI, tests D, E). Fish did not prefer tone over beat stimuli when the dF was only 2 Hz (Table VI, test F).

Beat stimuli differ from single tones in their envelope modulation and in their spectrum and fine waveform structure. Any of these differences could have reduced the attractiveness of certain beat stimuli relative to a tone. As the frequency components of rejected beat stimuli differed by only 5 Hz, and FM stimuli that varied by ± 5 Hz (a 10-Hz range) were not distinguished from tones, envelope modulation may be the critical factor.

When we presented females with a choice between a beat waveform created by the summation of single tones from adjacent speakers and a tone stimulus, no preference was apparent (Table VII). Thus, beats did not affect stimulus attractiveness as long as at their sources they resolved into individual tones. Multi-source beats more closely mimic natural beats resulting from the overlap of hums from adjacent males.

Comparing responses to single- and multi-source beats suggests strategies females may use to accomplish the real world listening task, extracting individual calls from summated waveforms. Single- and multi-source beats are likely to be perceived similarly at some distance from the speakers. If this is the case, the differences in response could reflect differential perception based on spatial sampling. The apparent depth of modulation for multi-source beats is dependent upon the relative amplitudes and distances to the two signals. Thus, not only can the effective magnitude of the beating change, and become smaller, with position for a multi-source beat, but, by attending to beats, receivers could gauge their

relative proximity to an individual source. Given the response criteria applied in this study, it is also possible that rejection of single-source beat stimuli occurs only after the fish has approached the source. Indeed, fish were sometimes observed to orient toward and begin to approach a speaker playing a strongly beating waveform and then to swim away, implying recognition of the summated waveform that operates at a distance but not at the source.

Alternatively, although the two speakers used here to create the multi-source beat were side by side, it is possible that, due to directional selectivity of sound transducing hair cells in the fish ear, the angular separation of the sources was sufficient to diminish the effective interference (review of directional masking data in Fay, 1988; Fay and Edds-Walton, 1997). In effect, each tone would be processed by a separate channel, and beating would not be a problem.

IV. SUMMARY AND CONCLUSIONS

First, this study supports the conclusion of Ibara *et al.* (1983) that the plainfin midshipman hum functions as a mate call, and extends that finding by describing the phonotactic response of both male morphs as well as of gravid females. Second, results from one and two-choice tests show that female midshipman fish respond selectively to audible sounds and are capable of differentiating and choosing between acoustic signals that differ in duration, frequency, amplitude, and spectral/temporal content. Although it is most straightforward to examine preference functions along one dimension, in reality there are probably interactions between various signal parameters such that they create a multi-dimensional preference space (Doherty, 1985; Ryan and Rand, 1993; Forrest and Raspet, 1994). This study has not directly addressed the influences of one parameter on another, but it is apparent, for example, that, although fish can discriminate small amplitude differences, they do not always prefer the more intense signal.

In the absence of any data correlating hum characteristics with male or nest quality, we do not know whether females would benefit from acoustic choosiness beyond that necessary to locate a conspecific male. However, females do make a large investment in one clutch of eggs that is apparently deposited in a single nest (DeMartini, 1988; Brantley and Bass, 1994), and search behavior could be costly. Thus, selection would likely have favored acoustic discrimination that enabled females to extract any available information about mate or nest quality from male hums.

The midshipman's simple acoustic signals and unambiguous phonotactic responses make it a promising system for understanding the receiver mechanisms of communication, both in terms of behavioral decisions and the underlying neural coding.

ACKNOWLEDGMENTS

We would like to thank Margaret Marchaterre and Deana Bodnar for logistical support and advice during this study, and Deana Bodnar, Christopher Clark, Ronald Hoy, and the reviewers for their comments on the manuscript.

This research was supported by a training grant from NIMH (5T32GM07469), a Clare Booth Luce Fellowship, and NIH Grant No. DC-00092.

- Barimo, J. F., and Fine, M. L. (1998). "Relationship of swim-bladder shape to the directionality pattern of underwater sound in the oyster toadfish," *Can. J. Zool.* **76**, 134–143.
- Bass, A. H. (1992). "Dimorphic male brains and alternative reproductive tactics in a vocalizing fish," *Trends Neurosci.* **15**, 139–145.
- Bass, A. H. (1996). "Shaping brain sexuality," *Am. Sci.* **84**, 352–363.
- Bass, A. H., and Baker, R. (1990). "Sexual dimorphisms in the vocal control system of a teleost fish: Morphology of physiologically identified neurons," *J. Neurobiol.* **21**, 1155–1168.
- Bass, A. H., and Baker, R. (1991). "Evolution of homologous vocal control traits," *Brain Behav. Evol.* **38**, 240–254.
- Bass, A. H., Bodnar, D. A., and Marchaterre, M. A. (in press). "Complementary explanations for existing phenotypes in an acoustic communication system," in *Neural Mechanisms of Communication*, edited by M. Hauser and M. Konishi (MIT, Cambridge).
- Bodnar, D. A. (1996). "The separate and combined effects of harmonic structure, phase, and FM on female preferences in the barking treefrog (*Hyla gratiosa*)," *J. Comp. Physiol. A* **178**, 173–182.
- Bodnar, D. A., and Bass, A. H. (1997). "Temporal coding of concurrent acoustic signals in auditory midbrain," *J. Neurosci.* **17**, 7553–7564.
- Brantley, R. K., and Bass, A. H. (1994). "Alternative male spawning tactics and acoustic signals in the plainfin midshipman fish, *Porichthys notatus* (Teleostei, Batrachoididae)," *Ethology* **96**, 213–232.
- Brenowitz, E. A., Rose, G., and Capranica, R. R. (1985). "Neural correlates of temperature coupling in the vocal communication system of the gray treefrog (*Hyla versicolor*)," *Brain Res.* **359**, 364–367.
- Chapman, C. J., and Johnstone, A. D. F. (1974). "Some auditory discrimination experiments on marine fish," *J. Exp. Biol.* **61**, 521–528.
- Cohen, M. J., and Winn, H. E. (1967). "Electrophysiological observations on hearing and sound production in the fish, *Poichthys notatus*," *J. Exp. Zool.* **165**, 355–370.
- Crawford, J. D., Cook, A. P., and Heberlain, A. S. (1997). "Bioacoustic behavior of African fishes (*Mormyridae*): Potential cures for species and individual recognition in *Pollimyrus*," *J. Acoust. Soc. Am.* **102**, 1200–1212.
- Delco, E. A., Jr. (1960). "Sound discrimination by males of two cyprinid fishes," *Tex. J. Sci.* **12**, 48–54.
- DeMartini, E. E. (1988). "Spawning success of the male plainfin midshipman. I. Influences of male body size and area of spawning site," *J. Exp. Mar. Biol. Ecol.* **121**, 177–192.
- Doherty, J. A. (1985). "Temperature coupling and 'trade-off' phenomena in the acoustic communication system of the cricket, *Gryllus bimaculatus* De Geer (Gryllidae)," *J. Exp. Biol.* **114**, 17–35.
- Fay, R. R. (1970). "Auditory frequency discrimination in the goldfish (*Carassius auratus*)," *J. Comp. Physiol. Psychol.* **73**, 175–180.
- Fay, R. R. (1988). *Hearing in Vertebrates: A Psychophysics Databook* (Hill-Fay Associates, Winnetka, IL).
- Fay, R. R. (1989). "Intensity discrimination of pulsed tones by the goldfish (*Carassius auratus*)," *J. Acoust. Soc. Am.* **85**, 500–502.
- Fay, R. R., and Edds-Walton, P. L. (1997). "Directional response properties of saccular afferents of the toadfish, *Opsanus tau*," *Hearing Res.* **111**, 1–21.
- Fine, M. L. (1978). "Seasonal and geographical variation of the mating call of the Oyster Toadfish, *Opsanus tau* L.," *Oecologia* **36**, 45–57.
- Fine, M. L., and Lenhardt, M. L. (1983). "Shallow-water propagation of the toadfish mating call," *Comp. Biochem. Physiol. A* **76**, 225–231.
- Fine, M. L., Winn, H. E., and Olla, B. L. (1977). "Communication in fishes," in *How Animals Communicate*, edited by T. A. Sebeok (Indiana U.P., Bloomington), pp. 472–518.
- Fish, J. F. (1972). "The effect of sound playback on the toadfish," in *Behavior of Marine Animals, Volume 2: Vertebrates*, edited by H. E. Winn and B. L. Olla (Plenum, New York), pp. 386–434.
- Forrest, T. G., Miller, G. L., and Zagar, J. R. (1993). "Sound propagation in shallow water: Implications for acoustic communication by aquatic animals," *Bioacoustics* **4**, 259–270.
- Forrest, T. G., and Raspet, R. (1994). "Models of female choice in acoustic communication," *Behav. Ecol.* **5**, 293–303.
- Gerald, J. W. (1971). "Sound production during courtship in six species of sunfish (*Centrarchidae*)," *Evolution* (Lawrence, Kans.) **25**, 75–87.

- Gerhardt, H. C. (1988). "Acoustic properties used in call recognition by frogs and toads," in *The Evolution of the Amphibian Auditory System*, edited by B. Fritsch, M. J. Ryan, W. Wilczynski, T. E. Hetherington, and W. Walkowiak (Wiley, New York), pp. 455–483.
- Gerhardt, H. C., and Doherty, J. A. (1988). "Acoustic communication in the gray treefrog, *Hyla versicolor*: Evolutionary and neurobiological implications," *J. Comp. Physiol. A* **162**, 261–278.
- Hauser, M. D. (1996). *The Evolution of Communication* (MIT, Cambridge).
- Ibara, R. M., Penny, L. T., Ebeling, A. W., Van Dykhuizen, G., and Cailliet, G. (1983). "The mating call of the plainfin midshipman fish, *Porichthys notatus*," in *Predators and Prey in Fishes*, edited by D. L. G. Noakes, D. G. Lindquist, G. S. Helfman, and J. A. Ward (Dr. W. Junk Publishers, The Hague, The Netherlands), pp. 205–212.
- Ladich, F. (1997). "Agonistic behavior and significance of sounds in vocalizing fish," *Mar. Fresh. Behav. Physiol.* **29**, 87–108.
- McKibben, J. R. (1998). "A neuroethological analysis of acoustic communication in the plainfin midshipman fish, *Porichthys notatus*," Ph.D. thesis, Cornell University, Ithaca, NY.
- Myrberg, A. A., Jr. (1981). "Sound communication and interception in fishes," in *Hearing and Sound Communication in Fishes*, edited by W. N. Tavolga, A. N. Popper, and R. R. Fay (Springer-Verlag, New York), pp. 395–425.
- Myrberg, A. A., Jr., Ha, S. J., and Shablott, M. J. (1993). "The sounds of bicolor damselfish (*Pomacentrus partitus*): Predictors of body size and a spectral basis for individual recognition and assessment," *J. Acoust. Soc. Am.* **94**, 3067–3070.
- Myrberg, A. A., Jr., Mohler, M., and Catala, J. C. (1986). "Sound production by males of a coral reef fish (*Pomacentrus partitus*): Its significance to females," *Anim. Behav.* **34**, 923–933.
- Myrberg, A. A., Jr., and Spires, J. Y. (1972). "Sound discrimination by the bicolor damselfish, *Eupomacentrus partitus*," *J. Exp. Biol.* **57**, 727–735.
- Myrberg, A., Spanier, E., and Ha, S. (1978). "Temporal patterning in acoustic communication," in *Contrasts in Behavior*, edited by E. Reese and F. Lighter (Wiley, New York), pp. 137–179.
- Penna, M. (1997). "Selectivity of evoked vocal responses in the time domain by frogs of the genus *Batrachyla*," *J. Herpetology* **31**, 202–217.
- Pires, A., and Hoy, R. R. (1992). "Temperature coupling in cricket acoustic communication: I. Field and laboratory studies of temperature effects on calling song production and recognition in *Gryllus firmus*," *J. Comp. Physiol. A* **171**, 69–78.
- Popper, A. N., and Fay, R. R. (1993). "Sound detection and processing by fish: Critical review and major research questions," *Brain Behav. Evol.* **41**, 14–38.
- Ryan, M. J., and Rand, A. S. (1993). "Species recognition and sexual selection as a unitary problem in animal communication," *Evolution* (Lawrence, Kans.) **47**, 647–657.
- Searcy, W. A. (1992). "Song repertoire and mate choice in birds," *Am. Zool.* **32**, 71–80.
- Tavolga, W. N. (1958). "The significance of underwater sounds produced by males of the gobiid fish, *Bathygobius soporator*," *Physiol. Zool.* **31**, 259–271.
- Tavolga, W. N. (1971). "Sound production and detection," in *Fish Physiology*, edited by W. S. Hoar and D. J. Randall (Academic, New York), Vol. 5, pp. 135–205.
- Van Tasell, D. J., Soli, S. D., Kirby, V. M., and Widin, G. P. (1987). "Speech waveform envelope cues for consonant recognition," *J. Acoust. Soc. Am.* **82**, 1152–1161.
- Walker, H. J., and Rosenblatt, R. H. (1988). "Pacific toadfishes of the genus *Porichthys* (Batrachoididae) with descriptions of three new species," *Copeia* **1988**, 887–904.
- Winn, H. E. (1967). "Vocal facilitation and the biological significance of fish sounds," in *Marine Bioacoustics*, edited by W. N. Tavolga (Pergamon, Oxford), Vol. 2, pp. 213–230.
- Winn, H. E. (1972). "Acoustic discrimination by the toadfish with comments on signal systems," in *Behavior of Marine Animals, Volume 2: Vertebrates*, edited by H. E. Winn and B. L. Olla (Plenum, New York), pp. 361–385.

Effects of ear of entry and perceived location of synchronous and asynchronous components on mistuning detection^{a)}

Hedwig Gockel^{b)} and Robert P. Carlyon

MRC Cognition and Brain Sciences Unit, 15 Chaucer Road, Cambridge CB2 2EF, United Kingdom

(Received 24 October 1997; revised 8 April 1998; accepted 16 September 1998)

Listeners were required to detect mistuning imposed on the center (“target”) component of a 200-ms complex consisting of the first seven harmonics of a 500-Hz fundamental. In the standard interval of each 2IFC trial, all components were frequency modulated in-phase by a 5-Hz sinusoid. In the signal interval the frequency modulation of the target component was inverted in-phase, thereby introducing a mistuning proportional to the depth of FM. In a similar experiment, using monaural presentation, Carlyon [J. Acoust. Soc. Am. **95**, 2622–2630 (1994)] reported a substantial elevation of thresholds in the presence of an unmodulated asynchronous interferer with frequency identical to the mean frequency of the target. This was attributed to the interferer, causing the target component to be perceptually segregated from the remainder of the complex, thereby impairing across-frequency comparisons. Experiment 1 of the present study showed that an interferer presented *contralaterally* for 200 ms before and 100 ms after the signal complex (no simultaneous presentation) also impaired performance, but to a lesser extent than an *ipsilaterally* presented one. Experiment 2 showed that an interferer which was presented dichotically with an interaural level difference (ILD) of 10 dB, so that it was perceived *contralaterally*, had the same (large) effect as if it were presented *ipsilaterally*. Experiment 3 showed that, in the absence of any interferer, performance was impaired when the nontarget components were presented *contralaterally* to the target component. However, performance was not impaired when the nontarget components were presented dichotically with an ILD of 20 dB, so that they were perceived *contralaterally* to the target component. It is concluded that the level of performance in the mistuning task is determined by whether the target is presented to the same ear as the rest of the complex, rather than by its perceived location. © 1998 Acoustical Society of America. [S0001-4966(98)05212-6]

PACS numbers: 43.66.Hg, 43.66.Rq, 43.66.Mk [DWG]

INTRODUCTION

In our physical world a single periodic source gives rise to components with a harmonic frequency relationship, i.e., components which have frequencies corresponding to integer multiples of a common fundamental frequency (“ F_0 ”). Such harmonically related components are usually perceptually grouped together, i.e., perceived as one sound source. However, most often there are not only one but several sound sources present at the same time. This means that many components originating from different sources reach our ears simultaneously, so that we are confronted with the problem of which components to group together, and which components to segregate from each other in order to identify the number and characteristics of the sound sources in the environment. This process, concurrent sound segregation, stresses our ability to organize *simultaneous* auditory input. There is another question, namely how to group together auditory events *spaced in time*. The effectiveness of a certain cue in sound segregation may differ, depending on whether the simultaneous or the sequential aspect of the condition is more dominant. The two processes are not independent of each other, and although the first two experiments in the present paper included sequential aspects, the focus will be

on concurrent sound segregation. A number of studies have demonstrated the importance of across-channel processes for concurrent sound segregation (for a review, see Darwin and Carlyon, 1995). Some of the paradigms used in these studies, together with relevant cues that were identified to play a role in concurrent sound segregation, will be reviewed below.

One of the most important cues for concurrent sound segregation is mistuning (Moore *et al.*, 1986; Hartmann *et al.*, 1990). Moore *et al.* (1985) showed that the detection of a mistuned component in a complex tone can be based on two different cues, depending on the number or the resolvability of the mistuned harmonic. For low harmonics, the inharmonic partial appears to stand out from the complex tone as a whole. For high harmonics (above the fifth) the mistuning is detected as a kind of beat or roughness. This beat cue arises from the interaction of the mistuned component with its neighbors in a single auditory filter, and its usefulness depends crucially on stimulus duration. For stimulus durations of 50 ms, Moore *et al.* found approximately constant thresholds for the detection of mistuning across harmonic number (thresholds expressed as percentage of the harmonic frequency), while for longer stimulus durations (410 ms and longer) thresholds decreased with increasing harmonic number.

Another important factor affecting concurrent sound segregation is onset and offset asynchrony. For example, Bregman and Pinker (1978) demonstrated that for onset

^{a)}Some of the results in this paper were presented at the 133rd meeting of the Acoustical Society of America [J. Acoust. Soc. Am. **101**, 3107(A) (1997)].

^{b)}Electronic mail: hedwig.gockel@mrc-cbu.cam.ac.uk

asynchronies of at least 30 ms, the perceived timbre of a two-tone complex changed, a consequence of the leading tone being "heard out" as an individual stream with a much reduced influence on the timbre of the complex. Similarly, Darwin and Ciocca (1992) found that the pitch shift produced by a slightly mistuned harmonic in an otherwise harmonic complex tone was reduced by turning on the mistuned harmonic more than about 80 ms before the rest of the complex. The effect of onset asynchrony could be partially eliminated by presenting an (in-tune) complex tone simultaneously with the leading part of the mistuned component (Ciocca and Darwin, 1993). Thus presenting another stimulus, with which the leading part of the mistuned component could be grouped, prevented its continuation (the simultaneous part of the mistuned component) from being segregated from the original complex tone and thereby restored its influence on the calculation of pitch.

Evidence that onset asynchronies can affect across-channel processes for concurrent sound segregation has also been found in another paradigm. In a profile analysis task, subjects typically discriminate between two complex tones, one with a flat spectrum and the other with an amplitude increment added in-phase to one of its components (the target component). Green and Dai (1992) reported that thresholds (the size of the increment) in this task increased considerably when the target started about 50 ms earlier than the remainder of the complex, compared to the case where all components started together. Again, the effect of onset asynchrony could be counteracted by presenting a complex tone simultaneously with the leading part of the incremented component (Hill and Bailey, 1997). Analogous findings to the effects of onset asynchrony and the ability of regrouping the leading part in pitch matching and profile analysis paradigms have been reported for the detection of a mistuned component in a complex tone (Carlyon, 1994a), for the influence of an individual harmonic on vowel perception (Darwin and Sutherland, 1984), and for the influence of an individual harmonic on vowel perception when there are interaural time disparities (Darwin and Hukin, 1997).

A third factor, lateralization, has been found to produce more varied results, especially in concurrent sound segregation. In *sequential* streaming, where subjects can attend to a sequence of auditory events extended over time, lateralization effects may be more substantial. For example, Deutsch (1979) found much worse performance for identification of a melodic configuration (an example of sequential streaming) when the component tones of the melody switched between ears than when they were presented to the same ear. Similarly, Hartmann and Johnson (1991) found improved melody recognition when the alternating tones of two interleaved melodies were presented with an interaural time difference of 500 μ s, leading at the left for one melody and leading at the right for the other melody. Thus perceiving the corresponding notes from different directions affected sequential segregation. For *concurrent* sound segregation, Darwin and Ciocca (1992) found pitch shifts to be only slightly larger when the mistuned harmonic was presented to the same ear as the rest of the complex as opposed to the opposite ear (see also Houtsma and Goldstein, 1972; Beerends and Houtsma,

1989). For detection of mistuning of a single, low-numbered harmonic, Lee and Green (1994) found no difference at all between thresholds obtained with ipsilateral and with contralateral presentation of the mistuned component relative to the remainder of the complex. In contrast, in profile analysis, thresholds increased considerably if the target component was presented to the opposite ear as the remainder of the complex (Green and Kidd, 1983; Bernstein and Green, 1987). Similarly, Hukin and Darwin (1995) reported a significantly reduced contribution to vowel quality of a contralaterally presented component compared to ipsilateral presentation. This did not hold for contralateral lateralization due to interaural time differences. Culling and Summerfield (1995a) found that listeners could take advantage of common interaural level differences to group together formants for vowel identification when presented with two simultaneous vowels, but could take no advantage of interaural time differences.

Another potential factor in concurrent sound segregation, that of frequency modulation (FM), has also been extensively investigated (Carlyon, 1991, 1992, 1994b; Culling and Summerfield, 1995b; McAdams, 1989). It has been found that the *existence* of frequency modulation against a steady *unmodulated* background can lead to increased segregation (McAdams, 1989; Summerfield and Culling, 1992). However, incoherent FM *per se* did not increase segregation if no concomitant inharmonicity cues were provided. For example, Summerfield and Culling (1992) showed that two vowels with a static F_0 difference between them were not segregated according to incoherent FM. Carlyon (1991) showed that incoherent FM of one component in a complex harmonic tone was detected only by virtue of the resulting mistuning. Once the complex tone was inharmonic (when steady), coherent FM could not be discriminated from incoherent FM. He also showed that the psychometric functions for the detection of a simple mistuning imposed on one component of a harmonic sound could account for the corresponding functions describing the detection of FM incoherence.

The present experiments extended Carlyon's (1994a) study on the effects of onset/offset asynchrony on the detection of mistuning (see above) from monaural to dichotic presentation. Listeners were presented with frequency-modulated harmonic complex tones where the mistuning resulted from inverting the phase of the frequency modulation of the target component. In such a task, the subjective cue is described as hearing out the mistuned component. The onset/offset timing differences between the target and the nontarget components (NTCs) were produced by presenting a sinusoidal "interferer," identical in frequency to the mean frequency of the target component, for a certain time before and after (but not simultaneously with) the complex tone. The experiments investigated how listeners' ability to detect mistuning is affected by differences in lateralization of the asynchronous part of the stimuli and by differences in lateralization between the mistuned component (the target) and the nontarget components of the complex tone. A crucial distinction is drawn between those effects driven by the perceived location of a component, and those determined by its

“ear of entry.” In experiments 1 and 2, the lateralization of the interferer was manipulated, while, in experiment 3, the lateralization of the NTCs relative to the target component was varied. The results indicated that detection of mistuning is a robust ability, which is impaired most by differences in onset and offset timing, and to a lesser extent by differences in lateralization.

I. GENERAL METHOD

In this section, the general procedure and stimuli in the absence of any interferer will be described. Variations in procedure and stimulus presentation in the different conditions will be given in the sections describing the individual experiments.

In a 2I-2AFC task, subjects were required to discriminate between two complex tones both consisting of the first seven harmonics of a 500-Hz fundamental, frequency modulated by a 5-Hz sinusoid. In the standard interval, all components were frequency-modulated (FM) in-phase, and by the same percentage of their carrier frequency. Thus at all times the component frequencies were harmonically related to each other. In the signal interval, the FM of the target component was inverted in-phase, thereby introducing a mistuning proportional to the depth of FM (Demany and Semal, 1988). The use of FM sounds should prevent subjects from basing their judgements on sequential pitch comparisons and make them rely solely on momentarily inharmonicity. As mentioned above, the difference between incoherent and coherent FM can only be detected by virtue of the resulting mistuning introduced (e.g., Carlyon, 1991, 1994b). The initial phase of the modulator was chosen randomly for each presentation, following a rectangular distribution ranging from 0 to 2π . Equation (1) specifies the basic stimuli:

$$y(t) = \sum_{n=1}^7 A \sin 2\pi \left[f_n t + 0.01 P f_n \int_{\tau=0}^t [\cos(2\pi f_m \tau + \theta_{\text{rand}} + \theta_{nm}) d\tau] \right], \quad (1)$$

where A is an amplitude constant, f_n is the (carrier) frequency of the n th component, P is the modulation depth as percentage of the carrier frequency, f_m is the modulation frequency (5 Hz), θ_{rand} specifies the initial modulator phase for all components and has a random value between 0 and 2π , and θ_{nm} is the modulator phase of component n *re*: the modulator phase of the other components. θ_{nm} was equal to π for the target component in the signal interval and was zero in the standard interval. Schematic spectrograms of the stimuli are shown in Fig. 1(a), (b), and (c). Figure 1(a) shows an example of the standard stimulus, while Fig. 1(b) and (c) shows examples of the signal stimulus for two different initial modulator phases [θ_{rand} equals 90° and 270° in Fig. 1(b) and (c), respectively].

The stimuli were presented at a level of 45 dB SPL per component in a background of pink noise (low-pass filtered at 5 kHz, with a spectrum level of 6.5 dB at 2 kHz). The low sensation level and pink noise background were chosen to minimize possible within-channel cues. The stimulus dura-

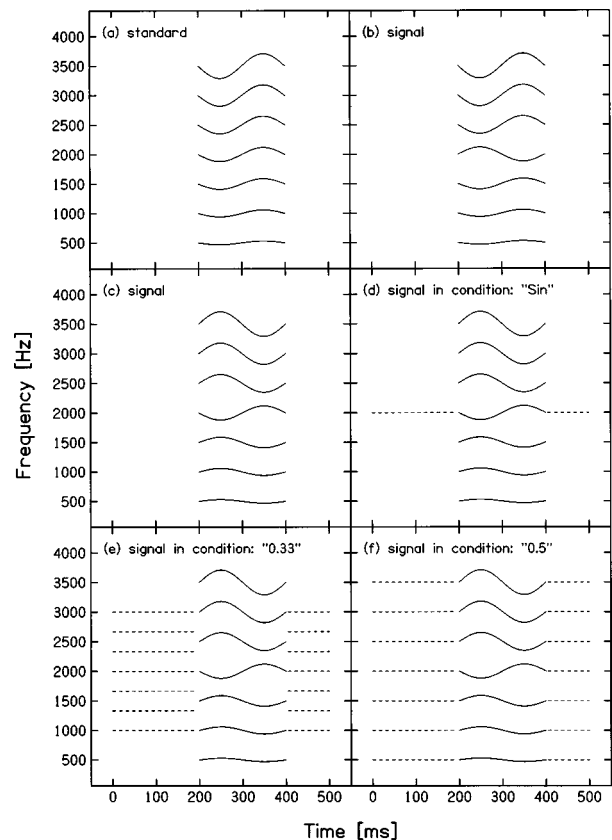


FIG. 1. Schematic spectrograms of stimuli: (a) standard interval, $\theta_{\text{rand}} = 90^\circ$; (b) signal interval, $\theta_{\text{rand}} = 90^\circ$; (c) signal interval, $\theta_{\text{rand}} = 270^\circ$; (d) signal interval with sinusoidal interferer, $\theta_{\text{rand}} = 270^\circ$; (e) signal interval with “0.33” complex interferer; (f) signal interval with “0.5” complex interferer. Note that an extreme FM depth has been chosen for illustrative purposes.

tion was 200 ms including 5-ms raised-cosine ramps. The inter-stimulus interval was 450 ms. All stimuli were generated digitally, played out by a 16-bit digital-to-analog converter (CED 1401 plus) at a sampling rate of 10 kHz, and low-pass filtered at 4.3 kHz (target component: Kemo VBF/25.01; attenuation 100 dB/oct; other components: Kemo VBF/25.03; attenuation 48 dB/oct¹). The stimuli were presented over Sennheiser HD 414 headphones. Subjects were seated individually in a sound-insulated booth. Feedback was provided following each response.

The same four subjects participated in all experiments. Subjects ranged in age from 25 to 36 years, and their quiet thresholds at octave frequencies between 250 and 8000 Hz were within 15 dB of the 1969 ANSI standard. In monaural conditions, the stimuli were delivered to the right ear for subject 01 and to the left ear for subjects 02, 03, and 04. The ear used in monaural conditions will be referred to as the “reference ear.” In binaural conditions, the “contralateral” side generally means contralateral to the reference ear. Only subject 03 had a high level of musical education, and only subject 04 was male. Subject 02 was the first author.

II. EXPERIMENT 1

A. Rationale

In a similar experiment, using *monaural* presentation, Carlyon (1994a) reported a substantial elevation of thresh-

olds in the presence of an unmodulated asynchronous sinusoidal interferer whose frequency was identical to the mean frequency of the target component. He explained this by stating that the interferer caused the target component to be perceptually segregated from the remainder of the complex (similar to the effect of asynchronously gating the onset of the target component), thereby impairing across-frequency comparisons. While Carlyon (1994a) ran some conditions where the interferer was presented simultaneously with the main signal (as well as before and after), in the present experiments the interferer was only presented before and after but never simultaneously with the main signal.

The objective of the first experiment was to investigate whether an interferer presented contralaterally to the main signal complex would also result in perceptual segregation of the target component, and thereby lead to an increase in thresholds relative to a condition without any interferer. This would provide some information concerning the possible "site" of the streaming mechanism in the processing of auditory information. If there were no effect of a contralaterally presented interferer at all, then this would argue for the streaming mechanism being driven by ear-specific information only. If, on the other hand, the effects of the contralateral and ipsilateral interferer were of the same size, then this would argue for a streaming mechanism located at a stage in auditory processing which follows the combination of information across the two ears (the superior olive or a higher level).

To control for the possibility that the contralateral interferer might reduce performance not because of streaming effects but due to pure distraction or shift in spatial attention, three different types of interferers were used: (a) a sinusoid whose frequency was identical to the mean frequency of the target component [see Fig. 1(d)]; (b) a complex tone with F_0 equal to 333 Hz, consisting of seven successive harmonics, with the frequency of the first component equal to 1 kHz [see Fig. 1(e)]; and (c) a complex tone consisting of the first seven harmonics of 500 Hz [see Fig. 1(f)]. These three types of interferers will be abbreviated as "Sin," "0.33," and "0.5," respectively. The sinusoidal interferer was expected to stream out the target component (at least for ipsilateral presentation). The complex tones were expected to produce little or no streaming effect, because the component in them corresponding in frequency to the mean frequency of the target component was assumed to be perceptually grouped with the rest of the complex, thereby preventing it from streaming out the target component (see, Darwin and Sutherland, 1984; Ciocca and Darwin, 1993; Carlyon, 1994a; Darwin and Hukin, 1997; Hill and Bailey, 1997 for similar regrouping of a leading "interferer"). Two different F_0 s were used for the complex interferers, one identical to and one different from the mean F_0 of the main complex, to assess the importance of a correspondence in F_0 of the interferer and the main complex in reducing or canceling the streaming effect.

If contralateral presentation of the complex interferers produced a similar reduction in performance to that of the contralateral sinusoidal interferer, then this would argue for an explanation in terms of "distraction" or "spatial atten-

tion" rather than in terms of auditory streaming. If, however, a reduction in performance with contralateral presentation occurred only for *sinusoidal* interferers, then this would provide evidence for an explanation based on streaming rather than on distraction or shifts of spatial attention.

Two levels of presentation for the interferer, 39 dB and 45 dB SPL per component, were used. Carlyon (1994a) reported a larger increase in thresholds for higher interferer levels than for lower. However, in his conditions (which included level variation) the simultaneous part of the interferer was presented too. Since, in his study, a synchronous/simultaneous interferer increased thresholds for higher but not for low presentation levels, the level effect observed for asynchronous interferers could have been mainly due to the increase in level of the simultaneous part. The use of two different levels in the present paradigm allows us to determine whether the level of the (nonsimultaneous) interferer affects its ability to capture the target component (cf. Warren *et al.*, 1994; Darwin, 1995; McAdams *et al.*, 1998).

B. Method

In all experiments, interferers (when present) were presented for 200 ms immediately before and 100 ms immediately after the main signal complex (including 5-ms raised-cosine ramps) with no simultaneous portion. As described above, three types of interferer were used: "Sin," "0.33," and "0.5." Note that all interferers included the 2-kHz sinusoidal component, which was presented alone in the first condition, but corresponded to the fourth of the harmonics presented in the complex tones for conditions "0.33" and "0.5." Two levels of presentation for the interferer, 39 dB and 45 dB SPL per component, were used. The interferer could be presented either ipsilaterally or contralaterally to the main signal complex. Thresholds in these 12 interferer conditions were compared to those for the baseline condition without any interferer.

In each condition, an adaptive procedure was used to estimate thresholds. The depth of FM varied according to a 1-up 2-down method, tracking the 70.7% point on the psychometric functions (Levitt, 1971). The initial factor by which the depth of FM was changed was 1.21. Following four reversals, the factor was decreased to 1.1 and 12 further reversals were obtained. The threshold was defined as the geometric mean of the FM depth at the last 12 reversals. The total duration of a single session was about 2 h, including rest times, which gave 30 threshold estimates. After at least 4 h of practice, 12 threshold estimates were obtained for each condition and subject.

C. Results

Figure 2 shows the geometric mean thresholds over the four subjects, and the corresponding standard errors of the means for the 13 conditions. The asterisk indicates the mean threshold in the baseline condition (no interferer). In the baseline condition the mean threshold was about 0.7% modulation depth. Thresholds were highest in the "Sin" conditions (triangles), with a maximum of about 4.5% modulation depth for the ipsilateral presentation at a level of 45 dB

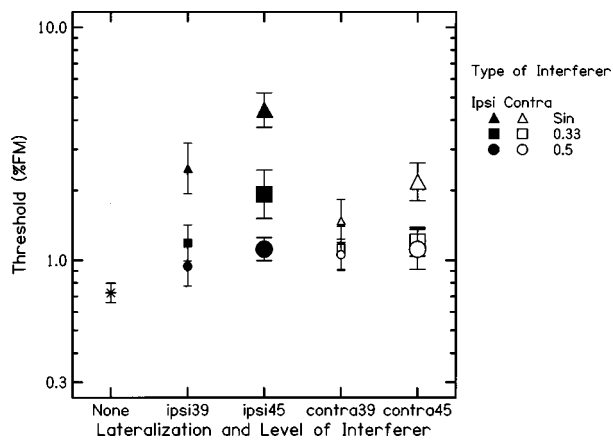


FIG. 2. Mean thresholds and corresponding standard errors for the 13 conditions (three types of interferer \times two sides of presentation \times two levels of presentation+baseline) in experiment 1.

SPL (large filled triangle). Thresholds were second highest in the “0.33” (squares) and lowest in the “0.5” (circles) conditions. In the “Sin” and the “0.33” conditions the higher level of the interferers (large symbols) led to higher thresholds than the lower presentation level (small symbols). For the ipsilateral presentation of the interferer (filled symbols), thresholds were on average higher than for the contralateral presentation (open symbols).

These results were confirmed by a three-way ANOVA² (interferer type \times side \times level) which showed that all main effects (within-subjects) were significant [type: $F(2,6) = 94.2$, $p < 0.01$; side: $F(1,3) = 10.1$, $p = 0.05$; level: $F(1,3) = 34.5$, $p < 0.05$]. Moreover, *post hoc* contrasts showed that all types of interferers were significantly different from each other. There were also significant interactions between type and side [$F(2,6) = 9.29$, $p < 0.05$], and type and level [$F(2,6) = 17.51$, $p < 0.01$]. To investigate specific effects, data were submitted to specific two-way and one-way analyses, the results of which will be mentioned where relevant to the hypotheses under investigation.

For the “0.5” interferer (circles) thresholds were not significantly different from the baseline [one-way ANOVA $F(4,12) = 3.1$, $p = 0.057$]. This indicates that a complex interferer with an F_0 equal to the mean F_0 of the main complex did not impair detection of mistuning, regardless of the ear to which it was presented. Presumably, the 2-kHz component in the interferer was grouped with the other harmonically related components of the interferer. Because they all corresponded in frequency to the mean frequencies of the components in the main complex, in the case of ipsilateral presentation, they all grouped with the main stimulus to form a single integrated percept of the interferer complex and the main stimulus. In the case of contralateral presentation, the whole interferer was probably grouped separately from the main complex. Thus neither contralateral nor ipsilateral presentation of an interferer impairs performance *per se*.

For the “0.33” interferer (squares) thresholds were significantly different from the baseline [one-way ANOVA $F(4,12) = 16.39$, $p < 0.01$]. Thus presenting a complex interferer which differed in F_0 from the main complex did impair detection of mistuning. There are at least two possible expla-

nations for this finding: (1) The change in F_0 which resulted in a marked change in the perception of the pitch of the stimulus might have distracted subjects and thereby reduced reliable perception of the more subtle mistuning cue. (2) If there is a temporal overintegration process in pitch determination (Carlyon, 1996; Micheyl and Carlyon, 1998), this could have led to a less clear perception of the main complex’s pitch at its beginning and end. This would have reduced the effective presentation time of the main complex and hence reduced the detectability of the mistuning.

For the ipsilateral presentations, the general pattern of results described above is quite clear, confirming the findings reported by Carlyon (1994a). Although the thresholds measured in the present experiment were in general a bit lower than the ones he reported, presumably due to more practice and/or interindividual differences, the overall pattern was replicated.³ Thresholds in the ipsi45 conditions were also lower than reported by Carlyon (1994a). However, this is probably partly due to the fact that in the present experiments there was no simultaneous part to the interferer, while in the earlier experiments the simultaneous part of the interferer was also presented, and was found to have an effect for higher levels but not for lower levels.

For the contralateral presentations, the pattern of results was in general the same as for the ipsilateral presentations, but threshold shifts were smaller. The sinusoidal interferer significantly impaired detection of mistuning even when it was presented contralaterally to the main complex (open triangles > asterisk at both levels). The increase in thresholds was greater for the higher than for the lower level of the sinusoidal interferer. This was supported by the outcome of a two-way ANOVA (calculated exclusively for the contralateral interferers), which showed a significant main effect of type of interferer [$F(2,6) = 102.07$, $p < 0.01$] and a significant interaction between type and level [$F(2,6) = 5.55$, $p < 0.05$]. It is important to note that the substantial effect of the contralateral sinusoidal interferer cannot be attributed to a shift of attention to the contralateral ear, since the contralateral complex interferer “0.5” produced no significant increase in thresholds. Thus the effect of the sinusoidal interferer is interpreted in terms of streaming, for both sides of presentation. The sinusoidal interferer probably led to segregation of the target component in both the signal and the standard interval, thereby making it more difficult to detect mistuning, since the mistuning itself was detected by hearing out the target component. The level dependence of the size of the effect of the sinusoidal interferer might be explained in terms of perceptual subtraction of the asynchronous interferer from the complex tone: i.e., the higher the level of the asynchronous interferer, the smaller the remainder of the target component within the complex tone (Warren *et al.*, 1994; Darwin, 1995; McAdams *et al.*, 1998).

The streaming effect of the sinusoidal interferer was significantly less strong for the contralateral presentation than for the ipsilateral presentation: a two-way ANOVA calculated exclusively for the sinusoidal interferer showed a significant main effect of side, with $F(1,3) = 15.92$, $p < 0.05$. Hence, although a contralateral interferer can increase thresholds, the elevation is smaller than with ipsilateral pre-

sentation. Experiment 2 investigated whether the smaller effect obtained with a contralateral interferer was due to a shift in its perceived location, or due to there being no interferer energy in the same ear as the complex.

III. EXPERIMENT 2

A. Rationale and method

Experiment 2 investigated whether perceived location or ear of presentation was responsible for the reduced effect of the sinusoidal contralateral interferer in experiment 1. Only one type of interferer was used, a steady sinusoid whose frequency was identical to the mean frequency of the target component (corresponding to “Sin” in experiment 1). Two new conditions were run with the same subjects: (1) the interferer was presented diotically at a level of 39 dB SPL; and (2) the interferer was presented dichotically at a level of 39 dB SPL ipsilaterally and 49 dB SPL contralaterally to the main signal complex. These two conditions will be abbreviated as “I39C39,” and “I39C49,” respectively. Again, 12 threshold estimates were obtained for each condition and subject.

If the reduced streaming effect of the contralaterally presented interferer in experiment 1 was due to the difference in perceived location of the interferer relative to the perceived location of the main complex, thresholds in condition “I39C49,” where the interferer was clearly perceived contralaterally (see, e.g., Blauert, 1983), should be lower than the observed thresholds in the ipsilateral conditions in experiment 1, and be equal to or higher⁴ than thresholds in the contralateral condition with a 45 dB SPL interferer. Following the same reasoning, one would expect thresholds in condition “I39C39,” where the interferer was lateralized in the center of the head, to be somewhere between thresholds observed in the ipsilateral 39 dB and the contralateral 39 dB conditions of experiment 1. If, on the other hand, ear of presentation was the important factor, then shifting the *perceived* location of the interferer to the contralateral side should not reduce thresholds compared to the observed thresholds in the ipsilateral 39 dB SPL condition of experiment 1.

B. Results

Figure 3 shows the geometric mean thresholds and the corresponding standard errors of the means for the two new conditions, and the four conditions with the sinusoidal interferer in experiment 1, plus the baseline condition. As expected from the results of experiment 1, a repeated measures one-way ANOVA showed a significant main effect of condition [$F(5,15) = 13.48, p < 0.01$]. However, thresholds in conditions “ipsi39,” “I39C39,” and “I39C49” (all of which had the same interferer level at the ipsilateral side) did not differ significantly from each other, as was shown by a one-way ANOVA [$F(2,6) = 2.43, p = 0.17$] calculated exclusively for these three conditions. Thus although interferers in conditions “ipsi39,” “I39C39,” and “I39C49” were heard at markedly different locations (ipsilateral, central, and contralateral, respectively), performance was about the same. On the other hand, *post hoc* calculated contrasts showed that

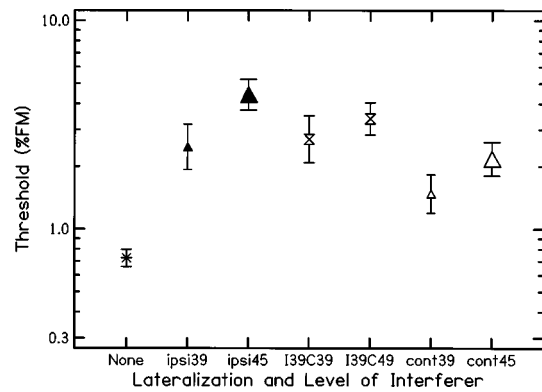


FIG. 3. Mean thresholds and corresponding standard errors for the two binaural sinusoidal interferer conditions (experiment 2) together with the four monaural sinusoidal interferer conditions (+ baseline) of experiment 1.

thresholds in condition “I39C39” were significantly higher than thresholds in condition “contra39” [$F(1,3) = 12.68, p < 0.05$] and that thresholds in condition “I39C49” were significantly higher than in condition “contra45” [$F(1,3) = 744.0, p < 0.01$] even though in the latter case both interferers were perceived in approximately the same location. The simplest explanation of these results is that it was the ear of presentation rather than the perceived lateralization of the interferer relative to the main signal complex which affected detection of mistuning via auditory streaming processes. This issue will be considered in more detail below.

C. Discussion

The results of experiments 1 and 2 were interpreted as showing that the ear of presentation rather than the perceived location of an asynchronous interferer determined performance level. This is the most parsimonious explanation. However, it could be argued that there is an effect of perceived location (similar to purely contralateral presentation) of the interferer but that this effect of perceived location is counteracted by an effect of level of presentation, so that it does not show up in the results. Specifically, performance in conditions I39C39 and I39C49 might have been similar to performance in condition ipsi39 not because the level of the ipsilateral interferer was similar, but because the increase in level of the interferer from conditions ipsi39 to I39C39 to I39C49 reduced performance, and because this deterioration was counterbalanced by the beneficial effects of the corresponding shift in perceived location. This “counterbalance” explanation for the results of experiment 2 is not parsimonious, but in the absence of a conclusive control condition we cannot rule it out. However, the third experiment—without any interferers producing level dependent effects—provided a clear cut control condition; albeit in a slightly different paradigm.

IV. EXPERIMENT 3

A. Rationale

As mentioned in the Introduction, effects of lateralization have been found more consistently in sequential than in concurrent sound segregation (Deutsch, 1979; Hartmann and

Johnson, 1991; Hukin and Darwin, 1995; Darwin and Hukin, in press). The results of experiment 1 and experiment 2 showed an effect of lateralization on concurrent sound segregation. However, even though the task itself was a concurrent sound segregation task, the stimuli in these first two experiments contained a sequential component, the interferer. Experiment 3 investigated whether the observed lateralization effect would generalize to a purely simultaneous task, without presentation of an interferer. For detection of mistuning in *steady* tones, Lee and Green (1994) concluded that in the absence of within-channel cues (for low target harmonics) there were no differences between performance obtained with ipsilateral and performance obtained with contralateral presentation of the mistuned component relative to the remainder of the complex. However, preliminary measurements with our FM stimuli—without interferer—indicated that for contralateral presentation the task seemed much harder. Being quite surprised, since we had taken care to minimize within-channel cues, we chose to run the experiment using both the original target harmonic number (four), and a target with a lower harmonic number (two). The latter was intended to reduce within-channel cues still further, and to allow us to check on the possible role of within-channel cue effects.

B. Method

Experiment 3 investigated the effects of lateralization on detection of mistuning. Unlike the first two experiments, no interferer was presented in experiment 3. The basic stimulus was similar to the one used in the baseline condition in experiment 1. However, in three conditions the ear of presentation/lateralization of the target component and the nontarget components (NTCs) were varied independently from each other. In the first condition, the NTCs were presented ipsilaterally to the target component and with the same level (45 dB SPL) per component. In the second condition, the target was monaural, and the NTCs were presented dichotically with a level of 45 dB SPL in the ear ipsilateral and 65 dB SPL in the ear contralateral to the target component, and thus were perceived contralaterally (see, e.g., Blauert, 1983). In the third condition, the NTCs were presented contralaterally to the target component with a level of 45 dB SPL. These conditions will be abbreviated as “ipsi,” “dichotic,” and “contra,” respectively. The target component was either the second or the fourth harmonic of the complex. The second harmonic was chosen as an additional target component in this experiment, as an extra control for the use of within-channel cues. One possible within-channel cue for discriminating between a harmonic and an inharmonic stimulus is the difference between the patterns of amplitude modulation produced by these two stimuli at the output of an auditory filter centered between the target component and the next-highest component. This cue is described in detail in Sec. IV D. The low presentation levels and the pink background noise used throughout the experiments should have minimized such within-channel cues anyway. However, the use of the second harmonic would reduce the usefulness of these cues even further, due to the reduction in auditory filter bandwidth with decreasing center fre-

quency (Glasberg and Moore, 1990). Another possible within-channel cue, which was discussed by Lee and Green, is an envelope cue (derived from an auditory filter centered on the target harmonic frequency). This envelope cue would be less dependent on presentation level and less affected by the pink noise background (as the signal-to-background ratio is greater at the output of an auditory filter centered on the target). But, as for the first kind of within-channel cue, this second type of cue would also be less available for the second harmonic than for the fourth. Below (Sec. IV D) it will be argued that such an envelope cue was not available for the present stimuli.

Seven-point psychometric functions were measured for all conditions, since initially it was hard to measure adaptive thresholds in the “contra” condition, as performance was very poor for some subjects. The amounts of frequency modulation were 0.47%, 0.76%, 1.23%, 1.98%, 3.19%, 5.14%, and 8.28%, respectively. Performance for these percentages of FM was measured in a blocked design, going from easy (high % FM) to harder (low % FM) trials and then from harder to easy trials in blocks of 120 trials each. The order of conditions “ipsi,” “dichotic,” “contra,” and second versus fourth harmonic was randomized over subjects. Each subject ran 480 trials in each condition, for each percentage level of FM.

If there is no segregation of the target component due to ear of presentation or perceived localization relative to the NTCs, then performance should be the same in all three conditions. If, however, ear of presentation has an influence on segregation processes when detecting a mistuned harmonic, then performance in condition “contra” should be worse than performance in conditions “ipsi” and “dichotic,” which should be about the same. If, on the other hand, the segregation processes depend on perceived location, then performance in condition “ipsi” should be superior to performance in conditions “dichotic” and “contra,” which should be about the same.

C. Results and discussion

Figure 4 shows the individual detectability indices d' , and Fig. 5 shows mean d' scores (averaged over individual d' values of the four subjects) as a function of percentage of frequency modulation. Circles correspond to condition “ipsi,” while squares and triangles correspond to conditions “dichotic” and “contra,” respectively. Filled and open symbols indicate that the target component corresponded to the second and the fourth harmonic, respectively. Performance tended to be better for the second harmonic target component (1000 Hz) than for the fourth harmonic target component (2000 Hz). This may be due to a loss of phase locking for higher frequencies (Hartmann *et al.*, 1990). However, this trend did not reach significance.⁵ Note that if within-channel cues had been used in the ipsilateral condition, then performance would have been better for the fourth than for the second target component (Moore *et al.*, 1985; Lee and Green, 1994). Also, the use of within-channel cues is not compatible with the finding that performance tended to be superior for the second target component in all conditions to the same extent; within-channel cues such as beating

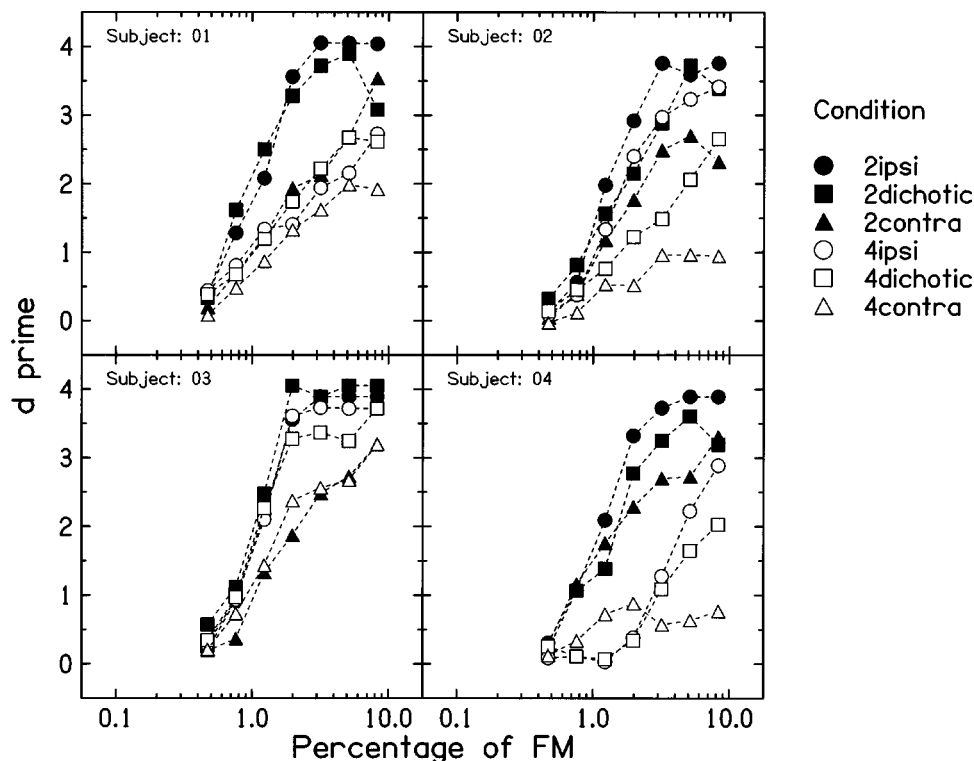


FIG. 4. Individual detectability indices d' (each data point is based on 480 trials) measured in experiment 3 as a function of percentage of frequency modulation. Circles correspond to condition “ipsi,” while squares and triangles correspond to conditions “dichotic” and “contra,” respectively. Filled and open symbols indicate that the target component corresponded to the second and the fourth harmonic, respectively.

could not be present in the contralateral condition. With respect to the main questions investigated in the present experiment, the following effects were confirmed by a repeated measures three-way ANOVA (harmonic no. \times lateralization \times percentage of FM) and *post hoc* calculated contrasts. When the NTCs were presented contralaterally (triangles) performance was markedly and significantly worse than when they were presented ipsilaterally (circles) to the target component [*post hoc* comparison: $F(1,3) = 36.72$, $p < 0.01$]. However, dichotic presentation (squares), in which the NTCs were perceived contralaterally, did not significantly impair performance relative to ipsilateral presentation [*post hoc* comparison: $F(1,3) = 2.29$, $p = 0.23$]. This was true for both target component conditions (significant main effect of lateraliza-

tion [$F(2,6) = 19.0$, $p < 0.01$], but there was *no* significant interaction between harmonic number and lateralization [$F(2,6) = 0.51$, $p = 0.63$]).

For experiment 3 the “counterbalance” explanation for the results (see Sec. III C) leads to the prediction that performance in conditions “dichotic” and “ipsi” should be similar, because the higher level of the NTCs in the ear contralateral to the target component (65 dB) would improve performance, and this would be approximately counterbalanced by a negative effect of perceived location of the NTCs, which shifted away from the target component. If that were true, then presenting the NTCs only contralaterally with a level of 65 dB per component (“contra65”) should improve performance compared to condition “contra” (45 dB SPL) and should lead to similar performance as in condition “dichotic.” To check this, two subjects (01 and 03) ran the control condition “contra65” interleaved with a replication of the “dichotic” condition for the second harmonic as the target component. The results (not shown) indicated no effect of level of the NTCs in the contralateral ear: values of d' in conditions “contra65” and “dichotic” differed to the same extent as they differed before in conditions “contra45” and “dichotic.” Thus the “counterbalance” explanation did not hold; performance in conditions “dichotic” and “ipsi” was similar, probably because in these conditions the NTCs were presented to the same ear as the target component.

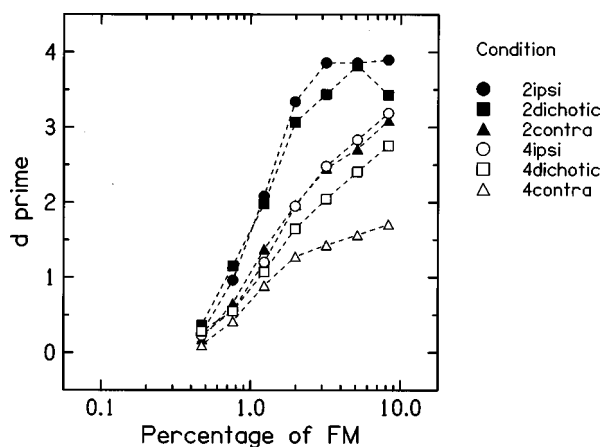


FIG. 5. Mean d' scores measured in experiment 3 as a function of percentage of frequency modulation. Circles correspond to condition “ipsi,” while squares and triangles correspond to conditions “dichotic” and “contra” respectively. Filled and open symbols indicate that the target component corresponded to the second and the fourth harmonic, respectively.

D. Possible within-channel cues

As mentioned in Secs. IV A and IV B, one possible interpretation of the difference in performance between the “dichotic” and “ipsi” conditions compared to the “contra” condition in experiment 3 is that for the former detection was mediated by within-channel interactions between the target

and other components. Two kinds of possible within-channel cues have been mentioned. Each of them will now be discussed in more detail.

(1) Amplitude modulation of the output of a filter tuned between the target and the next-highest component: the modulation depth (at the 5-Hz modulation rate) would be greater for incoherent than for coherent FM. To minimize the usefulness of such cues, the stimuli were presented at low levels and with a pink noise background. Nevertheless, to further test whether such a cue might have been used, we calculated excitation patterns (Glasberg and Moore, 1990) of the stimuli in the ipsilateral ear for a maximum mistuning of 1.98%, at which consistent differences were observed between the dichotic and contra conditions (Fig. 4). We measured the amount by which the excitation in the “valley” of the excitation pattern (that falling between the two peaks produced by the target and next-highest harmonic) exceeded that produced by the pink noise background. The amount of this “excess excitation” was approximately constant over stimulus duration (i.e., for different points during the modulation cycle) for coherent FM, although the frequency location of the “valley” moved. For incoherent FM, the amount of this excess excitation varied over the modulation cycle. When the second harmonic was the target, the amount of the excess excitation was between 0 and 0.5 dB for the standard stimulus (coherent FM) and varied between 0 dB and 3 dB for the signal stimulus (incoherent FM). The corresponding figures for the fourth harmonic were between 8 and 10 dB for the standard stimulus and between 4 and 13 dB for the signal stimulus, suggesting not only that the within-channel cue was more audible in this condition, but also that it differed more between the standard and signal stimuli. Thus although the amounts of excess excitation were often greater than zero, an explanation in terms of within-channel cues would predict that the difference in performance between the dichotic and contra conditions should be consistently greater when the fourth, rather than the second, harmonic was mistuned. As can be seen in Fig. 4, this was not the case. Furthermore, these rather weak within-channel cues are similar to those calculated for the study of Carlyon (1991), which measured the ability to discriminate coherent from incoherent FM of the center component relative to the flanking components of a 1500+2100+2500 Hz complex. The calculated excess excitation was around 6 dB for the standard stimulus (coherent FM) and varied between 0 dB and 10 dB for the signal stimulus (incoherent FM). Thus the output of a filter tuned in between the target and the next-highest harmonic was modulated in amplitude by 10 dB in Carlyon’s (1991) study and by 9 dB in the present study. Carlyon’s subjects could not perform the task. Clearly, if listeners could not use the within-channel cues in Carlyon’s study, it is unlikely that they could do so here.

(2) Envelope cue: Lee and Green (1994) concentrated their discussion of within-channel cues on envelope cues available at the output of the auditory filter centered on the target component. They estimated the strength of these cues by analyzing the power spectrum of the envelope of the output of a simulated auditory filter centered on this component. For a harmonic complex, the only component in the power

spectrum is the one at F_0 . If the target is mistuned by an amount of ΔF Hz, then lower components are present in the power spectrum of the envelope. The most dominant component is at $2\Delta F$ Hz and its magnitude increases with increase in harmonic number of the target component. The pink background noise used in the present experiment would have reduced the detectability of the low-frequency envelope components, since the envelope spectrum of the noise, after passing through the auditory filter, contained components which would partially mask the low-frequency components (Dau *et al.*, 1997). Furthermore, if this sort of envelope cue had been used in the present experiment, the difference between performance in conditions ipsi and contra would have been more pronounced for the fourth than for the second target component. This was not the case.

To summarize, it is quite unlikely that either of the two kinds of within-channel cues mentioned was used in the present experiment. Thus the present findings indicate that grouping by ear of presentation impairs performance in detection of mistuning.

V. DISCUSSION

A. Comparison with previous studies

The present experiments measured detection of inharmonicity in complex tones using the task of discrimination between coherent and incoherent frequency modulation of a single target component within an otherwise harmonic complex. Earlier findings that the detection of inharmonicity is impaired by presenting an asynchronous sinusoidal interferer which is capable of streaming out the target component (Carlyon, 1994a) were replicated. Different conditions of lateralization of the interferer (experiments 1 and 2) and lateralization of the nontarget components relative to the target (experiment 3) were investigated.

1. Lateralization of the interferer

Experiment 1 showed that an interferer presented to the contralateral side was able to stream out the target component, but to a lesser degree than for ipsilateral presentation. Experiment 2 showed that an interferer which was presented dichotically with an interaural level difference (ILD) of 10 dB, so that it was perceived contralaterally, had the same (large) effect as if it were presented ipsilaterally. The most parsimonious explanation for the data is that the strength of the effect of the interferer was determined by the ear of presentation, not by the perceived location. This result differs from that obtained by Darwin and Hukin (1997), who investigated the ability of a precursor tone, with a frequency equal to that of one of the components of a vowel, to reduce that component’s contribution to the vowel’s quality. They found the effect of the precursor to be larger when vowel and precursor were lateralized to opposite sides (due to ITD) than when they were lateralized to the same side; i.e., lateralization of the precursor was an effective factor. The apparent contradiction might be reconciled in the following way. In Darwin and Hukin’s study (experiment 4) the precursor consisted of a tone identical in duration to the duration of the vowel (56 ms), separated from the vowel (including the harmonic corresponding in frequency to the precursor) by a si-

lent interval of 160 ms. In this situation, the concurrent grouping of vowel and simultaneous harmonic was counteracted by sequential streaming of precursor and harmonic which might be governed by the repetition of two identical events. In the present study, the interferer was neither identical in duration to the main stimulus, nor separated by a silent interval from the main stimulus. In this situation, continuity of interferer and target could have been more important. It may be that streaming mediated by continuity is largely determined by ear of presentation, whereas that mediated by “repetition of identical events” is determined by perceived location. A lack of continuity of the interferer in the contralateral but not in the perceived contralateral condition might then lead to the dominance of the factor “ear” over the factor “perceived location.” The effect of onset asynchrony on concurrent sound segregation probably relies more on continuity of the sounds than does sequential streaming, which in turn might be more dependent on repetition of identical events. The same argument might be applied when comparing the present results with the evidence for lateralization effects (due to ITDs) in sequential streaming tasks (Hartmann and Johnson, 1991; Hukin and Darwin, 1995; Darwin and Hukin, in press). When subjects listen to a longer sequence of individual events, then repetition of the spatial characteristics (the perceived side) of these events may be more important.

There is another aspect which might be important. Bregman (1990) drew a distinction between primitive, data-driven segregation on the one hand and schema-based segregation on the other hand. Following this distinction, the present task—detection of mistuning—is a task which depends mainly on primitive (data-driven) grouping mechanisms, while Hartmann and Johnson’s (1991) task—recognition of well-known melodies—depends more on schema-based segregation mechanisms, which are influenced more by practice and attention. It is quite conceivable that the two mechanisms are affected differently by perceived location.

2. Lateralization of the target component

Experiment 3 showed that contralateral presentation of the target component impaired performance in detection of mistuning, but perceived contralateral location did not. This effect is distinct from a loss of within-channel cues reported for higher harmonics for contralateral presentation by Lee and Green (1994). These authors reported no difference between performance in detection of mistuning of low harmonics in steady tones for ipsilateral versus contralateral presentation of the target component relative to the remainder of the complex. Hence, the results of the two studies differ with respect to the presence or absence of effects due to ear of presentation of the target component. One possible explanation for this discrepancy is based on the fact that the present study examined a large range of percentages of FM, while Lee and Green measured thresholds corresponding to 79% correct responses in an adaptive procedure. At a d' of 1.1, which corresponds to $P(c)$ equal to 0.79, the present study shows only small differences between condition “contra” and conditions “ipsi” and “dichotic,” but these differences

become more pronounced for higher values of d' . Thus by measuring the psychometric functions, the present study revealed additional information leading to different conclusions with regard to segregation processes due to ear of presentation.

Another possible explanation is based on the fact that the present study used FM stimuli instead of steady tones. For our stimuli, inharmonicity occurred momentarily between components and could only be detected by a simultaneous across-channel comparison process. Sequential comparison in the course of (one) stimulus presentation, of the pitch of the target component with either the F_0 of the remainder of the complex or with the pitch of another component would not give any reliable information. In contrast, for steady tones a sequential pitch comparison process would result in reliable information about the presence of inharmonicity, even though the components were presented simultaneously (Demany and Semal, 1990). Lee and Green’s subjects may have used such a cue. This explanation is consistent with Lee and Green’s finding that, in the absence of within-channel cues, thresholds were similar for simultaneous and sequential presentation of the target component and the NTCs. The two explanations are not mutually exclusive.

Another informal observation should be mentioned at this point. Two of the subjects reported spontaneously that in condition “contra” they turned their eyes (and partly turned their head) in the direction of the NTCs in order to “listen mainly” to these NTCs. We hypothesize that doing this helped them focus attention on the NTCs, thereby reducing the salience of the target component at the opposite side. Evidence for the existence of such an influence of eye position on auditory selective attention has been reported repeatedly in the literature (Gopher, 1973; Reisberg *et al.*, 1981; Okita and Wei, 1993). In the present task this might be helpful because if the subjects were focusing on the side ipsilateral to the target component they would be more likely to hear the target out clearly in *both* intervals, and this would make the standard and the signal interval more similar. However, if subjects were focusing on the NTCs (contralateral side) then they would be less aware of the target component except in the signal interval, where it was segregated and perceived at the side where it was presented.

B. Role of ear of entry in simultaneous grouping

It is quite conceivable that, in tasks which crucially depend on simultaneous across-channel processes, the ear of entry is an important factor for segregation. This would be compatible with the finding that: (1) in profile analysis tasks, presentation of the target component to the contralateral side led to worse performance than ipsilateral presentation (Green and Kidd, 1983; Bernstein and Green, 1987); (2) contralateral presentation of a component reduced its contribution to vowel quality compared to ipsilateral presentation (Hukin and Darwin, 1995); and (3) presenting two simultaneous competing vowels to different ears improved vowel identification (Culling and Summerfield, 1995a).

In contrast, perceived location (due to ITD) has been found to be a rather ineffective cue in simultaneous grouping

(Culling and Summerfield, 1995a; Hukin and Darwin, 1995). The present results extend this finding to perceived location due to ILDs in detection of mistuning. For sequential grouping processes in speech, Darwin and Hukin (in press) reported a strong influence of interaural time differences but no influence of common F_0 . Thus there is some evidence that for *sequential* grouping the pattern of relative importance of cues might be reversed.

Hill and Darwin (1996) reported evidence that mistuning, as a cue for sound segregation, influences lateralization due to interaural time differences. They suggested that “spatial information may be combined selectively across frequency on the basis of auditory grouping cues.” The present results (experiment 3) are consistent with this idea, but they also indicate that the segregation mechanism receives (weaker) input from the other ear.

VI. SUMMARY AND CONCLUSIONS

The present study measured detection of inharmonicity in complex tones using a task requiring discrimination between coherent and incoherent frequency modulation of a single target component within an otherwise harmonic complex. The results replicated earlier findings that the detection of inharmonicity is impaired by presenting an asynchronous sinusoidal interferer which is capable of streaming out the target component (Carlyon, 1994a). Different conditions of lateralization of the interferer (experiments 1 and 2) and lateralization of the nontarget components relative to the target (experiment 3) were investigated. Experiment 1 showed that interferers presented to the contralateral side also impaired performance, although to a lesser degree. Experiment 2 showed that the strength of the interference effect was probably determined by the ear of presentation, not by the perceived location (due to ILDs). Experiment 3 showed that this was also true for the localization of the nontarget components relative to the target component; i.e., contralateral presentation of the nontarget components impaired detection performance, but perceived contralateral location (due to ILDs) did not.

The present results indicate that the mechanism underlying concurrent sound segregation is unlikely to be directly driven by the output of a localization mechanism (since different effects were observed for identical perceived locations depending on whether the perceived location resulted from a single ear of entry or resulted from an interaural level difference). Instead, the segregation mechanism is likely to get a strong input from one ear and a weaker input from the other ear, and to be located at a level at least as high as the first station of binaural interaction, namely the superior olive.

ACKNOWLEDGMENTS

The authors wish to thank Brian Glasberg and Brian Moore for providing us with the program for the calculation of excitation patterns. We also thank Brian Moore, Chris Darwin, and an anonymous reviewer for helpful comments on previous versions of this manuscript.

¹The 48-dB/octave attenuation applied to the nontarget components, whose

highest component had a frequency of 3500 Hz, meant that some aliased products attenuated by ≥ 32 dB were present at frequencies ≥ 6500 Hz. These components produced no information relevant to the task, and were masked by the noise background. Aliased components corresponding to the target, which was filtered at a rate of 100 dB/octave, were attenuated by approximately 93 dB.

²Before entering the data into the ANOVA, the individual thresholds were normalized with regard to the threshold of each subject obtained in the baseline condition. For that purpose the thresholds were transformed in the following way: transformed threshold = \log_2 (original threshold/baseline threshold).

³Comparable conditions—without the simultaneous part of the interferer—are available for the following conditions in the present experiment: (a) NONE; (b) ipsi39, sinusoidal interferer; (c) ipsi39, 0.33 complex interferer.

⁴In condition “I39C49,” the contralateral level was set 10 dB higher than the ipsilateral level, to ensure a strong lateralization of the dichotic interferer. The 4-dB difference in presentation level on the contralateral side between this dichotic interferer and the purely contralateral interferer in experiment 1 might lead to an increase in thresholds for the dichotic interferer compared to the purely contralateral interferer, because the level effect observed in experiment 1 was also present for the contralateral interferer.

⁵A repeated measures three-way ANOVA (harmonic no. \times lateralization \times percentage of FM) showed no significant main effect of harmonic number [$F(1,3) = 8.39, p = 0.063$], but did show a significant interaction between harmonic number and FM [$F(6,18) = 8.76, p < 0.001$].

Beerends, J. G., and Houtsma, A. J. M. (1989). “Pitch identification of simultaneous diotic and dichotic two-tone complexes,” *J. Acoust. Soc. Am.* **85**, 813–819.

Bernstein, L. R., and Green, D. M. (1987). “The profile-analysis bandwidth,” *J. Acoust. Soc. Am.* **81**, 1888–1895.

Blauert, J. (1983). *Spatial Hearing* (MIT, Cambridge, MA).

Bregman, A. S. (1990). *Auditory Scene Analysis: The Perceptual Organization of Sound* (MIT, Cambridge, MA).

Bregman, A. S., and Pinker, S. (1978). “Auditory streaming and the building of timbre,” *Can. J. Psychol.* **32**, 19–31.

Carlyon, R. P. (1991). “Discriminating between coherent and incoherent frequency modulation of complex tones,” *J. Acoust. Soc. Am.* **89**, 329–340.

Carlyon, R. P. (1992). “The psychophysics of concurrent sound segregation,” *Philos. Trans. R. Soc. London, Ser. B* **336**, 347–355.

Carlyon, R. P. (1994a). “Detecting mistuning in the presence of synchronous and asynchronous interfering sounds,” *J. Acoust. Soc. Am.* **95**, 2622–2630.

Carlyon, R. P. (1994b). “Further evidence against an across-frequency mechanism specific to the detection of frequency modulation (FM) incoherence between resolved frequency components,” *J. Acoust. Soc. Am.* **95**, 949–961.

Carlyon, R. P. (1996). “Masker asynchrony impairs the fundamental-frequency discrimination of unresolved harmonics,” *J. Acoust. Soc. Am.* **99**, 525–533.

Ciocca, V., and Darwin, C. J. (1993). “Effects of onset asynchrony on pitch perception: Adaptation or grouping?,” *J. Acoust. Soc. Am.* **93**, 2870–2878.

Culling, J. F., and Summerfield, Q. (1995a). “Perceptual separation of concurrent speech sounds: Absence of across-frequency grouping by common interaural delay,” *J. Acoust. Soc. Am.* **98**, 785–797.

Culling, J. F., and Summerfield, Q. (1995b). “The role of frequency modulation in the perceptual segregation of concurrent vowels,” *J. Acoust. Soc. Am.* **98**, 837–846.

Darwin, C. J. (1995). “Perceiving vowels in the presence of another sound: a quantitative test of the ‘Old-plus-New’ heuristic,” in *Levels in Speech Communication: Relations and Interactions: A Tribute to Max Wajskop*, edited by C. Sorin, J. Mariani, H. Méloni, and J. Schoentgen (Elsevier, Amsterdam), pp. 1–12.

Darwin, C. J., and Carlyon, R. P. (1995). “Auditory grouping,” in *Handbook of Perception and Cognition, Volume 6, Hearing*, edited by B. C. J. Moore (Academic, London), pp. 387–424.

Darwin, C. J., and Ciocca, V. (1992). “Grouping in pitch perception: Effects of onset asynchrony and ear of presentation of a mistuned component,” *J. Acoust. Soc. Am.* **91**, 3381–3390.

Darwin, C. J., and Hukin, R. W. (1997). “Perceptual segregation of a har-

- monic from a vowel by interaural time difference and frequency proximity," *J. Acoust. Soc. Am.* **102**, 2316–2324.
- Darwin, C. J., and Hukin, R. W. (in press). "Auditory objects of attention: The role of interaural time-differences," *J. Exp. Psychol. Hum. Percept. Perform.* (in press).
- Darwin, C. J., and Sutherland, N. S. (1984). "Grouping frequency components of vowels: When is a harmonic not a harmonic?," *Q. J. Exp. Psychol.* **36A**, 193–208.
- Dau, T., Kollmeier, B., and Kohlrausch, A. (1997). "Modeling auditory processing of amplitude modulation. I. Detection and masking with narrow-band carriers," *J. Acoust. Soc. Am.* **102**, 2892–2905.
- Demany, L., and Semal, C. (1988). "Dichotic fusion of two tones one octave apart: Evidence for internal octave templates," *J. Acoust. Soc. Am.* **83**, 687–695.
- Demany, L., and Semal, C. (1990). "Harmonic and melodic octave templates," *J. Acoust. Soc. Am.* **88**, 2126–2135.
- Deutsch, D. (1979). "Binaural integration of melodic patterns," *Percept. Psychophys.* **25**, 399–405.
- Glasberg, B. R., and Moore, B. C. J. (1990). "Derivation of auditory filter shapes from notched-noise data," *Hearing Res.* **47**, 103–138.
- Gopher, D. (1973). "Eye-movement patterns in selective listening tasks of focused attention," *Percept. Psychophys.* **14**, 259–264.
- Green, D. M., and Dai, H. (1992). "Temporal relations in profile comparisons," in *Auditory Physiology and Perception*, edited by Y. Cazals, L. Demany, and K. Horner (Pergamon, Oxford, England), pp. 471–477.
- Green, D. M., and Kidd, G. (1983). "Further studies of auditory profile analysis," *J. Acoust. Soc. Am.* **73**, 1260–1265.
- Hartmann, W. M., and Johnson, D. (1991). "Stream segregation and peripheral channeling," *Music Percept.* **9**, 155–184.
- Hartmann, W. M., McAdams, S., and Smith, B. K. (1990). "Hearing a mistuned harmonic in an otherwise periodic complex tone," *J. Acoust. Soc. Am.* **88**, 1712–1724.
- Hill, N. I., and Bailey, P. J. (1997). "Profile analysis with an asynchronous target: Evidence for auditory grouping," *J. Acoust. Soc. Am.* **102**, 477–481.
- Hill, N. I., and Darwin, C. J. (1996). "Lateralization of a perturbed harmonic: Effects of onset asynchrony and mistuning," *J. Acoust. Soc. Am.* **100**, 2352–2364.
- Houtsma, A. J. M., and Goldstein, J. L. (1972). "The central origin of the pitch of pure tones: Evidence from musical interval recognition," *J. Acoust. Soc. Am.* **51**, 520–529.
- Hukin, R. W., and Darwin, C. J. (1995). "Effects of contralateral presentation and of interaural time differences in segregating a harmonic from a vowel," *J. Acoust. Soc. Am.* **98**, 1380–1387.
- Lee, J., and Green, D. M. (1994). "Detection of a mistuned component in a harmonic complex," *J. Acoust. Soc. Am.* **96**, 716–725.
- Levitt, H. (1971). "Transformed up-down methods in psychoacoustics," *J. Acoust. Soc. Am.* **49**, 467–477.
- McAdams, S. (1989). "Segregation of concurrent sounds. I: Effects of frequency modulation coherence," *J. Acoust. Soc. Am.* **86**, 2148–2159.
- McAdams, S., Botte, M.-C., and Drake, C. (1998). "Auditory continuity and loudness computation," *J. Acoust. Soc. Am.* **103**, 1580–1591.
- Micheyl, C., and Carlyon, R. P. (1998). "Effects of temporal fringes on the fundamental-frequency discrimination," *J. Acoust. Soc. Am.* **104**, 3006–3018.
- Moore, B. C. J., Glasberg, B. R., and Peters, R. W. (1986). "Thresholds for hearing mistuned partials as separate tones in harmonic complexes," *J. Acoust. Soc. Am.* **80**, 479–483.
- Moore, B. C. J., Peters, R. W., and Glasberg, B. R. (1985). "Thresholds for the detection of inharmonicity in complex tones," *J. Acoust. Soc. Am.* **77**, 1861–1867.
- Okita, T., and Wei, J.-H. (1993). "Effects of eye position on event-related potentials during auditory selective attention," *Psychophysiology* **30**, 359–365.
- Reisberg, D., Scheiber, R., and Potemken, L. (1981). "Eye position and the control of auditory attention," *J. Exp. Psychol. Hum. Percept. Perform.* **7**, 318–323.
- Summerfield, Q., and Culling, J. F. (1992). "Auditory segregation of competing voices: Absence of effects of FM or AM coherence," *Philos. Trans. R. Soc. London, Ser. B* **336**, 357–366.
- Warren, R. M., Bashford, Jr., J. A., Healy, E. W., and Brubaker, B. S. (1994). "Auditory induction: Reciprocal changes in alternating sounds," *Percept. Psychophys.* **55**, 313–322.

On the source-identification method

William M. Hartmann,^{a)} Brad Rakerd,^{b)} and Joseph B. Gaalaas^{c)}
Michigan State University, East Lansing, Michigan 48824

(Received 8 June 1997; revised 25 August 1998; accepted 28 August 1998)

The source identification method is a standard psychophysical procedure for studying the ability of listeners to localize the source of a sound. The method can be described in terms of a statistical model in which listeners' responses are determined by the width and bias of an internal distribution. This article presents a theoretical study of the method, particularly the relationships between the average experimental observables, rms error and variability, and parameters of the internal distribution. The theory is tested against source-identification experiments, both easy and difficult. Of particular interest is the experimental dependence of observable statistics on the number of sources in the stimulus array, compared with theoretical predictions. It is found that the model gives a good account of several systematic features seen in the experiments. The model leads to guidelines for the design and analysis of source-identification experiments. © 1998 Acoustical Society of America. [S0001-4966(98)02712-X]

PACS numbers: 43.66.Qp, 43.66.Yw [RHD]

INTRODUCTION

The source-identification method is an experimental technique for studying the ability of human (or other) listeners to localize the source of a sound. The method is easy to describe. The listener is in an environment with a number, N , of sound sources. One source is caused to emit a signal, and it is the listener's task to identify the location of the source. The location may be identified by name, number, or by coordinates on a prearranged scale. Over trials the listener receives presentations from all the sources, typically many times.

The source-identification method, hereafter called the "SIM," is especially applicable for localization experiments in a room. Here, the experimenter may be interested in localization as a function of the signal, or the listener, or the room itself. However, because of standing waves in the room, an experiment done with a sound source in any one location may be special and not representative of the system of interest. By averaging performance over a number of source locations, the experimenter achieves greater generality. Therefore, SIM data are normally averaged over the source array.

The SIM is naturally modeled in terms of statistical decision theory (Searle *et al.*, 1975, 1976; Hartmann, 1983b). The present article is primarily a theoretical study of that model. It shows how observable variables, rms error and variability, averaged over the source array, are related to parameters of the model internal distribution. Therefore, this article provides a guide to the design of SIM experiments that are intended to discover the internal parameters. The article is concerned especially with the choice of the number of sources to be used in an experiment that measures localization ability over a fixed angular range.

The SIM experiments studied here are constrained by the following assumptions: First, it is assumed that the allowed response set is identical with the stimulus set. For example, there might be $N=24$ loudspeakers in front of a listener labeled 1 through 24. After presentation of a sound from one of the speakers, the listener must respond with a number from 1 to 24. Next, it is assumed that the sources are equally spaced by a common angle, A , measured in degrees along a single angular dimension, for example azimuth or elevation. For definiteness, the following discussion will be couched in terms of the azimuthal dimension, but the method is applicable to sources in any plane.

The decision theory model used for calculations below is one dimensional. Therefore, the model is inappropriate when the perceptual character of the localization task is multidimensional. It is assumed that sources are arranged over part of a circle, to be called the *span*, with angular extent $\Gamma=(N-1)A$, and with source number 1 at one extreme and source number N at the other.

A SIM experiment begins with a choice of statistics to describe localization error. Searle *et al.* (1975, 1976) used the absolute value of the discrepancy between response and target. Hartmann (1983b) used the root-mean-square (rms) error, which has theoretical advantages described below. The rms statistic is designated by the symbol \underline{D} , the square root of an average squared error, computed as follows:

$$\underline{D} = \sqrt{\underline{D}^2} = \sqrt{\sum_{k=1}^N W(k) D^2(k)}, \quad (1)$$

where $W(k)$ is the fraction of the trials on which source k was presented, and $D^2(k)$ is the mean square localization error for source k . This function is given by

$$D^2(k) = A^2 \frac{1}{M_k} \sum_{i=1}^{M_k} (R_i - k)^2, \quad (2)$$

where R_i is the listener's response—on the scale of source numbers—to the i th trial on which source k is presented.

^{a)}W.M.H. is at the Department of Physics and Astronomy.

^{b)}B.R. is at the Department of Audiology and Speech Sciences.

^{c)}J.B.G. is at the Department of Mechanical Engineering at the University of Texas at Austin.

There are a total of M_k of such trials. Equation (1) introduces the notation whereby a bar over a symbol indicates an average over sources and a bar under a symbol indicates the square root of that average.

Statistic \underline{D} includes both variability and constant error. A second statistic, \underline{s} , measures only variability by computing error with respect to the mean response. It is the square root of quantity $\overline{s^2}$ given by

$$\overline{s^2} = \sum_{k=1}^N W(k) s^2(k), \quad (3)$$

where the variability for source k is given by

$$s^2(k) = A^2 \frac{1}{M_k} \sum_{i=1}^{M_k} [R_i - R(k)]^2, \quad (4)$$

and $R(k)$ is the average response of the listener—in terms of source numbers—when a given source k is presented,

$$R(k) = \frac{1}{M_k} \sum_{i=1}^{M_k} R_i. \quad (5)$$

Statistic $s(k)$ is a biased estimate of response variability that tends to underestimate the actual standard deviation for small sample sizes. For comparison with the variability observed experimentally or in a Monte Carlo simulation $s(k)$ should be multiplied by $\sqrt{M_k/(M_k-1)}$, a factor which becomes important if the number of presentations is small.

In addition to variability, there is constant error. The constant error, $C(k)$, measured in degrees, is the difference between the true location of a source, k , and the mean perceived location of the source, $C(k) = A[R(k) - k]$. It may be positive or negative except when k is a well-defined extreme location. Rakerd and Hartmann (1986) noted a Pythagorean relationship among rms error, variability, and constant error:

$$D^2(k) = s^2(k) + C^2(k). \quad (6)$$

Therefore $D(k)$ was called the *overall* error. It follows that $\overline{D^2} = \overline{s^2} + \overline{C^2}$, where $\overline{C^2}$ is an average over sources analogous to $\overline{D^2}$ and $\overline{s^2}$. The calculations below are devoted to calculating these statistics, particularly \underline{D} and \underline{s} .

I. DECISION THEORY MODEL

The decision theory model for a listener's response, given a sound coming from source k , includes several basic assumptions. The first is that the listener has an internal coordinate θ for the source positions, undoubtedly established visually if the sources are visible, and that the presentation of source k leads to a normally distributed representation of location cues on that coordinate system. The probability density that source k leads to internal value θ is given by

$$P(\theta) = \frac{1}{\sigma_k \sqrt{2\pi}} e^{-(\theta - \theta_k - b_k)^2 / 2\sigma_k^2}. \quad (7)$$

Here, parameter θ_k is the location on the reference coordinate for source k , and b_k is a bias such that the acoustical cues for source k are not centered exactly on this referent.¹ Bias leads to constant error, $C(k)$, and increases the size of the overall error, $D(k)$.

A key parameter is the angular standard deviation, σ_k , called the *width of the internal distribution*, or, simply, *the width*. It depends on the listener, the type of sound that must be localized, the environment in which the experiment is performed, and the position of the source. The sound may be easy to localize (small σ_k), e.g., a broadband impulsive noise, or it may be difficult (large σ_k), e.g., a spectrally sparse tone without onset transient. Normally, the purpose of a SIM experiment is to determine the width as a function of experimental conditions.

Because the width is not zero the listener makes inconsistent responses to a given source. The width is generally a function of k because some sources are more difficult to localize than others. In the azimuthal plane sources to left and right are more difficult than sources in front, and in the median sagittal plane sources overhead are more difficult than others.

A second assumption of the model calculation is that responses are quantized; when a listener experiences internal coordinate θ , the listener responds by choosing the source with referent θ_k that is closest to θ . (Alternatively, listener responses on a continuum scale may be quantized in the process of recording the data.) There are two kinds of calculation, *terminated span* or *wrapped span*. For a terminated-span calculation, the span has well-defined ends, typical of a span that is much less than a complete circle. Here, the probability of making a particular response given a particular source is a simple monotonic function of the distance along the span between the two locations. By contrast, a wrapped-span calculation includes both errors along the span and error outside the span; it is defined in more detail below.

A. Calculations without bias

The present section examines statistics \underline{D} and \underline{s} when there is no bias ($b_k = 0$). The calculations were motivated by the conjecture that for a given source array span, the values of overall error, \underline{D} , and variability, \underline{s} , should be insensitive to the number of sources in the array. The logic was simple: As the number of sources is reduced the listener is less likely to make an error because the sources are farther apart. However, when the listener *does* make an incorrect choice, the contribution to the overall error sum is a larger number of degrees. The conjecture that \underline{D} and \underline{s} should be insensitive to N follows from the expectation that these two effects should largely cancel one another. One purpose of the calculations below was to test that conjecture.

The dependence of \underline{D} and \underline{s} on the number of sources was tested in a computation where each source is presented an equal number of times [$W(k) = 1/N$]. The calculation used an analytic form for the cumulative normal function to determine the probabilities of each possible response for each possible source.

1. The small-span limit

A source array with a small span extends over a limited range of azimuth values. Therefore, a small-span source-identification experiment can provide the same information

as a minimum audible angle experiment with the advantage that the source-identification method should be less sensitive to standing waves in the environment.

When the span is small, the width may be regarded as independent of the source number, i.e., σ_k becomes a constant, σ_0 . Calculations in the small-span limit are normally terminated-span calculations. From the structure of the equations it is possible to come to some general conclusions. There is reason to expect that function $D^2(k)$ should be approximately equal to σ_0^2 , because the second moment of a normal density is the variance. Function $D^2(k)$ resembles the second moment of density P . This is a theoretical advantage of the rms quantities \underline{D} and \underline{s} . However, $D^2(k)$ is not exactly equal to σ_0^2 , both because the formula is a discrete sum—not an integral—and because of end effects. In the limit that the width σ_0 becomes very small while the number of sources N becomes large, $D(k)$ approaches σ_0 , as long as k is not close to the edges of the source array. In those limits, the discrete sum approaches an integral, and end effects are not important because the distribution has little strength near the ends. Also, in those limits the value of \underline{D} approaches σ_0 because the fraction of sources near the end becomes small, and \underline{D} is determined primarily from values of $D(k)$ that are away from the ends.

A logical problem with terminated-span calculations is that when the width σ_0 becomes comparable to the source span Γ , the model sometimes predicts performance that is worse than random guessing. When this unreasonable result occurred in calculations below, the calculations were halted and the limiting point was noted in the graphical presentation of the results. The random guessing limits for \underline{D} and \underline{s} are given by Eqs. (A8) and (A12) of the Appendix, where they are derived.

The results of the calculations are given in scaled units, normalized to either the span Γ or the width σ_0 . Therefore, the calculations are not immediately applicable to any particular experiment, but, with a little work, they are applicable to *all* particular experiments. Parameter σ_0 is always given in units of the span. The work of Searle *et al.* (1976) suggests that the internal width σ_0 increases in proportion to the span. Therefore, the normalized parameter σ_0/Γ , as used here, is a convenient choice.²

Figure 1 shows the predictions of the analytic cumulative normal calculation for \underline{D} as a function of increasing number of sources, N . The figure shows that \underline{D} converges to the width when N is large and σ_0 is a small fraction of the span. For example, when $\sigma_0/\Gamma=0.025$, \underline{D} converges to within one percent of σ_0 when there are 50 sources. When σ_0/Γ is not small, \underline{D} always converges to a value that is less than σ_0 . The discrepancy is caused by end effects, but see Sec. I A below. Figure 1 also shows that the expected value of \underline{D} is close to its asymptotic value (for large N) when there are enough sources that the spacing between the sources is less than or equal to σ_0 . These *adequate values* of N are indicated with a filled star.

Although Fig. 1 shows that \underline{D}/σ_0 decreases with increasing σ_0 , in fact, \underline{D} itself increases monotonically with increasing σ_0 : the larger the width, the larger the rms error.

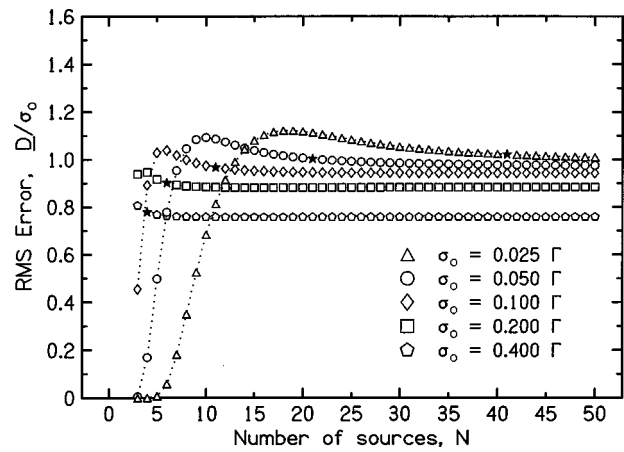


FIG. 1. rms error, \underline{D} , expressed in units of σ_0 , the width of the listener's localization probability density function. Statistic \underline{D} is presented as a function of the number of sources in the array, assuming that span Γ remains constant. The parameter is σ_0 in units of the span. A filled star indicates the value of N where the spacing between sources is equal to the width σ_0 .

The quantity \underline{D}/σ_0 decreases because \underline{D} increases less rapidly than linearly with increasing σ_0 .

For practical purposes, Fig. 1, and other figures in this article, must be used iteratively to find a self-consistent solution for the width. The experimenter begins by knowing Γ and N . The experimenter measures \underline{D} . The self-consistent calculation begins with the assumption that $\sigma_0 = \underline{D}$. This leads to a value of the graph parameter σ_0/Γ . The graph then leads to a predicted value of \underline{D}/σ_0 , and hence a revised value of σ_0 . Because the plots in Fig. 1 are smooth, one expects the calculation to converge to a stable value of σ_0 after only one or two iterations.

The insensitivity of \underline{D} to the number of sources is further demonstrated in Fig. 2, which shows \underline{D}/σ_0 as a continuous function of σ_0/Γ . The calculated value of \underline{D} varies by less than 10% as the number of sources is varied, provided that there are at least six sources and σ_0 is greater than 5% of the span. When σ_0 is greater than 20% of the span, \underline{D} becomes extremely insensitive to the number of sources.

Parallel calculations for variability, \underline{s} , for the case of no bias show that \underline{s} is very similar to \underline{D} , as would be expected.

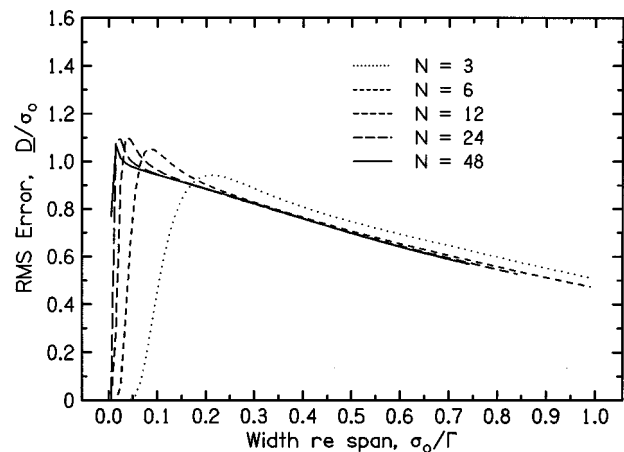


FIG. 2. rms error, as a function of the continuous variable σ_0/Γ , the width of the listener's internal distribution expressed as a fraction of the span. Each function is cut off at the random guessing limit.

Although $\underline{\sigma}$ is logically required to be smaller than \underline{D} , calculated plots of $\underline{\sigma}$ vs N or $\underline{\sigma}$ vs σ_0/Γ almost coincide with the corresponding plots for \underline{D} (Figs. 1 and 2) so long as the width is less than 10% of the span (i.e., $\sigma_0/\Gamma < 0.1$). The discrepancy between $\underline{\sigma}$ and \underline{D} grows as σ_0/Γ increases, but the difference is not more than 10%, even when σ_0/Γ is as large as 0.5.

2. Spans approaching 180 degrees

As the source span increases it becomes more important to take account of the dependence of the width on source location. For definiteness, we continue to assume that the sources are in the horizontal plane. The dependence of the width, σ_k , on the angular position of the source, θ_k , is modeled by assuming a constant difference limen for the interaural time difference. This model is known to capture some, but not all, of the azimuthal dependence of the width. In this model, the localization error is inversely proportional to the derivative of the interaural time difference with respect to angular position. For an azimuthal coordinate system, with $\theta=0^\circ$ directly in front of the listener, the interaural time difference is described by the Woodworth formula (1938),

$$\Delta t = \alpha(\theta + \sin \theta), \quad (8)$$

where θ is in radians and α is a constant equal to the head radius divided by the speed of sound. Differentiating with respect to θ and inverting gives

$$\frac{d\theta}{d(\Delta t)} = \frac{1}{\alpha(1 + \cos \theta)}. \quad (9)$$

Since σ_k is proportional to $d\theta_k$,

$$\sigma_k = \frac{2\sigma_0}{1 + |\cos \theta_k|}, \quad (10)$$

where σ_0 is the width directly in front of the listener. The absolute value in the denominator is necessary to account for the sign of $\cos \theta$ in the different quadrants.

As the span approaches 180° , there is a second, and structurally more important, effect that must be considered in the computations, namely ‘‘wrapped’’ probabilities. If, for example, the source is at 80° to the left of center, the probability of choosing a response that is 70° to the right of center is not just the probability of making an error of 150° ; one must add also the probability of making an error of 210° ($360 - 150 = 210$). The need to include wrapped probabilities signifies the departure from the terminated-span calculation considered in Sec. I A 1. For example, it is no longer necessary to consider the random guessing limit because large probabilities for responses off the ends of the array are correctly wrapped. The calculations shown in Figs. 3 and 4 below include both the effect of source-dependent width and wrapped probability.

Figure 3 illustrates how \underline{D} depends on span Γ when the array is centered on the forward direction and extends equally to the listener’s left and right by $\Gamma/2$. The figure shows the effect of the variation of σ with source angle for various values of σ_0 when the number of sources is large. If the span is small, σ is approximately constant. The fact that

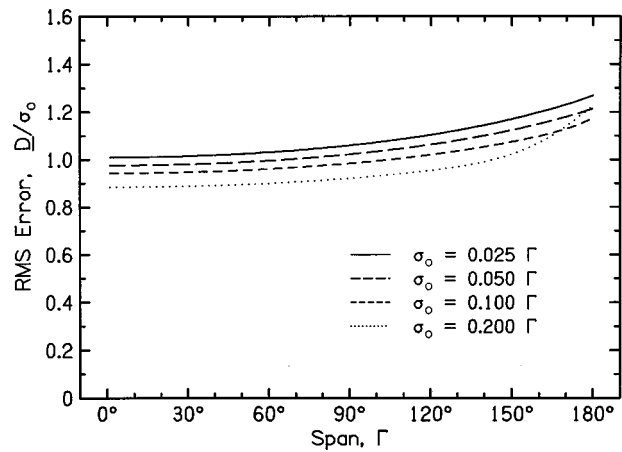


FIG. 3. rms error as a function of span Γ when width σ changes with source position such that the width expressed as interaural time difference remains constant. rms error \underline{D} is normalized to the width directly in front of the listener σ_0 . The number of sources in the calculation was $N=50$.

\underline{D}/σ changes by less than 10% as Γ increases to about 120° shows that the assumption of constant ITD is equivalent to a constant-sigma approximation even as a source span becomes as large as $\pm 60^\circ$. As the span increases beyond 120° \underline{D} begins to rise. When $\sigma_0 \leq 0.1\Gamma$ this rise is proportional to the increase in the average value of σ . Therefore, if the plot of \underline{D} is normalized to the value of σ averaged over the span the plot becomes almost a flat line, independent of Γ . The average value of σ from integrating Eq. (10) is

$$\bar{\sigma} = 4\sigma_0 \frac{\tan(\Gamma/4)}{\Gamma} \quad (\Gamma \leq \pi), \quad (11)$$

$$\bar{\sigma} = 4\sigma_0 \frac{2 - \tan(\pi/2 - \Gamma/4)}{\Gamma} \quad (\pi < \Gamma \leq 2\pi),$$

where Γ is expressed in radians.

For σ_0 greater than 10% of Γ , the average-sigma model is less successful. For a span greater than 160° , there is an anomalous curvature when $\sigma_0 = 0.2\Gamma$.

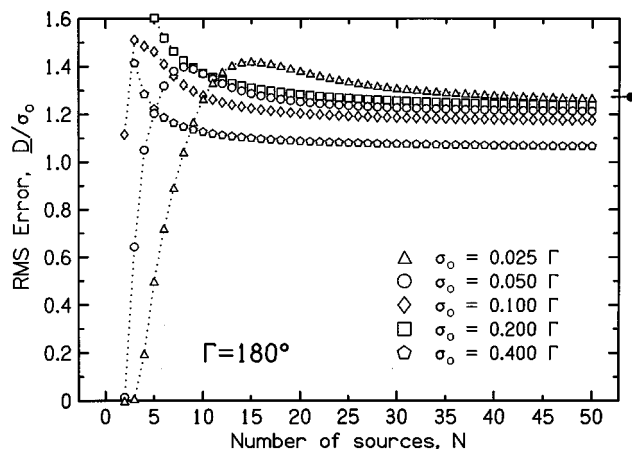


FIG. 4. rms error for source-dependent width as a function of the number of sources. The span is 180° centered on the forward direction. This figure can be compared with Fig. 1 to see the effects of source-dependent width and wrapped probability. The tick mark on the right axis shows the average width over 180° .

Figure 4 shows \underline{D} as a function of the number of sources for a span of 180° . As described in connection with Fig. 3, the asymptotic values in the large N limit are similar to Fig. 1 except that they are scaled by the average of σ/σ_0 . From Eq. (11) for $\Gamma=180^\circ$, this is equal to a scale factor $4/\pi$ or 1.27. Figure 4 shows that when N is not asymptotically large this simple scaling does not always apply. The figure also shows that \underline{D} does not vary monotonically with σ_0 ; the value for $\sigma_0=0.2\Gamma$ seems to be out of order. Figure 3 suggests that this nonmonotonic behavior is restricted to spans greater than about 160° . The curiously large curvature for the plot with $\sigma_0=0.2\Gamma$ occurs only for such large spans. The nonmonotonic behavior is the result of the combined effects of source-dependent width and wrapped probability. Calculations that exclude either one of these show only a monotonic dependence on width.

Calculations with a 180° span and wrapped probability were also done for a constant (source-independent) value of the width. The calculations led to a plot of \underline{D} vs N that was almost identical to the terminated-span calculation in Fig. 1, except for the extreme case, $\sigma_0=0.4\Gamma$. For both, \underline{D} systematically underestimated the width. For the terminated span the reason was end effects, as noted in Sec. I A 1. For the wrapped span the reason is the wrapped probabilities themselves.

If the width is less than 20% of the span, wrapped probability has a negligible effect on \underline{D} ($\leq 1\%$) when the span is not greater than 180° . Because wrapping complicates the analysis of data, an experimenter would do well to avoid spans approaching 180° if the experimental conditions promote large internal width, 30° or more.

3. Span greater than 180 degrees

When a span exceeds 180° , the source array cannot be entirely in front of the listener. Some sources must extend toward the rear, and this changes the perceptual nature of the localization task. Sources which differ considerably in azimuth may lie on the same cone of confusion and be perceptually similar. This multidimensional aspect of perception is not captured in our one-dimensional localization model. For purposes of illustration we proceed with the model anyway.

When Γ becomes greater than 180° , the array itself wraps around so that some sources are closer to each other across the gap between source 1 and source N than along the span. This possibility requires a new computational rule for scoring such that the maximum error charged against the listener is 180° . Any error that is found to be greater than 180° is replaced by its 360° complement. Thus for any pair of sources in the array, there is a unique magnitude and direction of the difference between them.

When the source array extends behind the listener, it is common to deal with the multidimensional character of the task by regarding confusions between front and back sources as separate from azimuthal confusions. Therefore azimuthal errors are computed by giving the listener the benefit of a reflection in the frontal plane (includes the points at $\pm 90^\circ$ azimuth and the point overhead) if that leads to a smaller error (Wightman and Kistler, 1989). Below, the calculations that employ that rule are called "reflection scoring." It is not

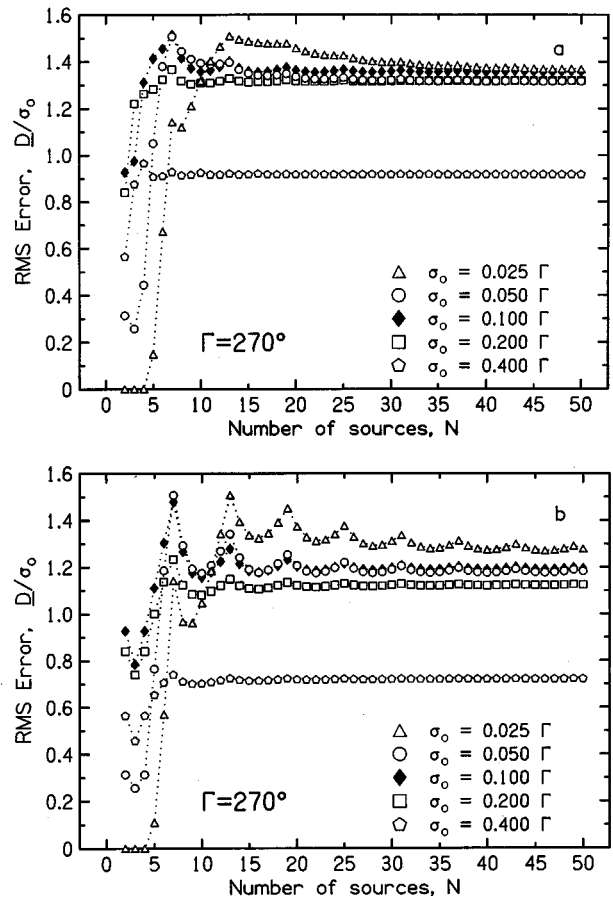


FIG. 5. rms error for source-dependent width, and for a large span, $\Gamma=270^\circ$. Part (a) does not give the subject the benefit of a front-to-back reflection; part (b) has reflection scoring.

necessary that an actual source be present at the site of the reflection. When reflection scoring is introduced, the final value of the error is the smallest of the listener's choice or its 360° complement, or the reflected choice or its 360° complement.

As an example of large spans, we chose a span $\Gamma=270^\circ$. The array was centered on the midline, with one end at -135° , the other end at $+135^\circ$, and the remaining sources ($N-2$) equally spaced in between. The internal width was taken to depend on source angle per Eq. (10).

Figure 5(a) shows the results without reflection scoring. As before, \underline{D}/σ_0 is quite insensitive to the number of sources. Upon careful observation, periodic variations can be observed in the \underline{D}/σ_0 data, especially for small σ_0 . This effect is due to the arrangement of the sources based on Γ and N . When $\Gamma=270^\circ$, there are sources located at $\theta = \pm 90^\circ$ whenever $N=6n+1$ (where $n=1,2,\dots$). This creates peaks because the average σ_k is increased. (The same effect occurs for circular spans whenever $N=4n$.) The analogous plot of \underline{s}/σ_0 is the same as \underline{D}/σ_0 in Fig. 5(a) within 10%, except when $\sigma_0/\Gamma=0.4$ where the discrepancy becomes about 15%.

Figure 5(b) shows the effect on \underline{D} when reflection scoring is introduced. The values of \underline{D} are generally reduced, of course. Further, the tendency for peaks at $N=6n+1$ is greatly enhanced. A better description of the effect is that

reflection scoring introduces a valley centered on N values given by $N=6n+4$. Valleys result from source placements in which the localization score benefits the most when the listener is given credit for a correct answer despite a front-to-back reversal.

According to Eq. (11), the average width, $\bar{\sigma}(270)$, is equal to $1.35\sigma_0$. In the limit of a large number of sources, \underline{D} agrees very well with the expectation $\underline{D}=1.35\sigma_0$ if reflection scoring is not used [Fig. 5(a)]. Only as the ratio of width to span grows to 0.4 is there appreciable departure. (For a 270° array a ratio of 0.4 means that the internal width is more than 100° , a case of extreme uncertainty.) Even if the number of sources is not large, the \underline{D} values in Fig. 5(a) do not differ from the expected value by more than about ten percent. The same statements cannot be made about the calculation with reflection scoring [Fig. 5(b)]. Then statistic \underline{D} is less stable both with respect to σ_0 and with respect to the number of sources. The peak and valley structure is, however, particularly apparent for a 270° span. For general span Γ ($\Gamma > 180^\circ$), peaks and valleys are not as frequent. A peak occurs for N sources when there are two integers N and k that satisfy the condition

$$N = \frac{2G(2k-1)+1}{2G+1}, \quad (12)$$

where G is the span fraction, $G=\Gamma/360$.

It is somewhat difficult to evaluate the significance of the structure observed for reflection scoring because we do not believe that our one-dimensional calculation is appropriate perceptually for sources that extend to the rear. However, this objection to the calculation is not fatal. The actual cause of the valleys in the structure is a series of source locations that particularly benefit the listener when reflection scoring is introduced. To some degree, this experimental artifact is bound to appear with reflection scoring. The precise size of the artifact depends on the perceptual model.

4. Summary

At the outset of this section on the SIM without bias, it was conjectured that the values of \underline{D} and \underline{s} might be insensitive to the number of sources. It was expected that the smaller probability of making an error when the number of sources is small would be compensated by the larger penalty when an error is actually made. Therefore, it was further conjectured that experimental values of \underline{D} and \underline{s} should provide reliable estimates of internal width σ . In the end, Secs. I A 1–3 above support these conjectures. The conjectures hold for a wide range of widths and source spans. However, the relationship between quantities \underline{D} and \underline{s} and the width parameter depends on the width parameter itself, in the form σ/Γ , as shown by Figs. 1–5. Therefore, an actual determination of the width from \underline{D} or \underline{s} may require some modest iteration. The functions in the figures are so well behaved that convergence is assured.

B. Calculations with bias

The model of Sec. I A described a listener without bias. When the sound originated from source k , the internal distri-

bution for auditory localization cues was centered at the location θ_k , corresponding to the reference position of the source as established visually. It is this reference coordinate that the listener uses in making responses. Therefore, the statistics of the responses to source k depended only on a single parameter, the width σ_k . The model without bias is, however, an idealization. Unfortunately, in sound localization, bias is the rule and not the exception. Bias is introduced by visual cues (ventriloquism) and by acoustical cues, such as the reflections from walls in an asymmetrical room environment. Bias can be introduced into an experiment deliberately; a large visual bias is caused by directing a listener's gaze to the end of a source array (Hartmann, 1983a). A large acoustical bias can be created by putting a single reflecting surface in an otherwise anechoic room (Rakerd and Hartmann, 1985). But although bias can be experimentally controlled, it cannot be entirely eliminated; it is normally present for any listener whether one wants it or not (Hartmann, 1983b).

Bias consists of a displacement of internal acoustical cues with respect to the angular reference coordinate system, θ_k . Therefore, bias can be seen in plots of $R(k)$, and it is measured for individual sources by constant error $C(k)$. An average measure of bias is \underline{C} . Because the rms error, \underline{D} , includes \underline{C} [Eq. (6)], the bias also appears in \underline{D} .

In this article we take the view that the goal of the experimenter is to use the source identification method to learn about the width of the internal distribution σ . The presence of bias poses a problem, and the purpose of the present section is to try to deal with it. Although σ can be determined from either \underline{s} or \underline{D} in the absence of bias, the presence of bias has a major direct effect on \underline{D} which makes it unreliable for estimating σ . By contrast, the variability \underline{s} should, in principle, be independent of bias because variability is calculated with respect to the mean response made by the listener and not with respect to a physical referent. In practice, however, \underline{s} is affected by bias, both because of effects at the ends of the arrays and because of the quantization of the responses. Therefore, statistic \underline{s} is the best statistic to use to estimate σ in the case of bias, but it is not without troubles of its own, as will be seen below. What makes it difficult to discuss bias is that bias can take many forms. Below, we deal with two types, constant bias and central bias. Calculations are presented in the small-span limit.

1. Constant bias

Constant bias means that the displacement of the acoustical cues with respect to the reference coordinate system is constant, independent of the source. Constant bias is a common occurrence, especially if the array of sources is small. The effect of directed gaze on the localization of sources in a 28° span was found to be modeled best by a constant bias (Hartmann, 1983a).

Numerical studies, using the decision theory model and constant width, on the effects of constant bias showed that bias can always be neglected if the number of sources is large enough. If the bias is large, it may not be practical to run as many sources as are needed for \underline{s} to give a good estimate of σ_0 , but large N is an important limit to keep in

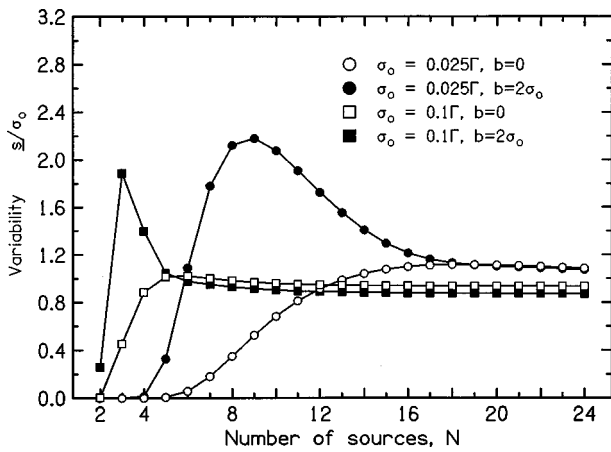


FIG. 6. The role of constant bias. Open symbols show variability \underline{s} when there is no bias. Filled symbols show the effect of making the bias, b , twice the width, σ_0 . Two values of σ_0/Γ are shown.

mind. The effect of bias on \underline{s} depends sensitively on the ratio of bias b to width σ_0 . Bias effects are shown in the plot of \underline{s} in Fig. 6 for the special case that the bias is twice the width. The filled-circle plot in Fig. 6 shows \underline{s} when the bias is 5% of the source span ($b/\Gamma=0.05$) and $\sigma_0/\Gamma=0.025$. It can be compared with \underline{s} in the absence of bias (open circles). When there is no bias, \underline{s} gives a good estimate of σ_0 if the number of sources is about $N=14$ or greater. Adding the bias has a dramatic effect on the variability, leading to a peak at $N=9$. The peak overestimates σ_0 by a factor of 2.

The behavior shown by the circles in Fig. 6 is typical. Whenever the bias is twice the width there is a peak (height $1.5 < \underline{s}/\sigma_0 < 2.5$) as a function of N . The peak occurs at $N=N_{\max}$, where $N_{\max} \approx \text{Int}(0.2\Gamma/\sigma_0) + 1$. Not surprisingly, a given bias has the largest effect for the smallest σ_0 , and the number of sources needed to eliminate that effect may become large. The square symbols in Fig. 6 check the above statements when the bias is $b/\Gamma=0.2$ and the width is $\sigma_0/\Gamma=0.1$.

If the bias becomes as large as $4\sigma_0$, \underline{s} becomes an oscillating function of N and cannot estimate σ_0 . On the other hand, if the bias is no larger than σ_0 itself then the effects of bias on \underline{s} are less than 10%, so long as there are four or more sources in the array and σ_0/Γ is larger than about 0.02. Then it is possible to ignore the bias in determining σ_0 as the large- N limit of \underline{s} .

2. Central bias

Whereas constant bias is necessarily directed toward one end of the source array or the other, central bias is directed toward the center of the array. In the common case of a symmetrical array with the subject looking at the center, a central bias may be a visual effect. In general, any central tendency, such as a reluctance to choose extreme responses, appears as a central bias.

The central bias function itself might take different forms: straight line, S-curve, step function, etc. The calculations of this section employ a step-function bias function because the experiments described below often found $R(k)$ functions approximately of this form. In a step-function bias

the auditory cues for all the sources to the left of center are biased toward the right by a constant (b_l) and all the sources to the right of center are biased toward the left by a constant (b_r). The bias can be characterized by a single central-bias parameter b_c if it is symmetrical ($b_l=b_c$ and $b_r=-b_c$).

Model calculations for small spans indicated that \underline{s} calculated with central bias was very similar to \underline{s} calculated with a constant bias of the same magnitude. Typical differences between the two kinds of bias were less than 10% for N large enough to provide a reasonable estimate of \underline{s} . The sign of the difference was always the same; central bias led to the larger \underline{s} . The difference grew with increasing bias magnitude. However, as long as the bias was not greater than twice the width, the difference was less than 33% even when the bias was as large as 80% of the span.

II. EXPERIMENTS

To test the model calculations we performed localization experiments. We were particularly interested in how \underline{D} and \underline{s} depend on the number of sources in a given span. Therefore, the experiments were performed using 3, 6, 12, and 24 sources.

A. Tasks

In order to test the computations in several ranges of σ_0 , we used two tasks, one in which the localization was easy and one in which it was difficult. Both tasks were performed in a reverberation room.

1. Easy (EL) experiment

In the easy localization (EL) task, listeners sat 3 m away from an array of speakers in the horizontal plane. The array extended 23° to the left and right of the midline ($\Gamma=46^\circ$). Broadband noise at a level of 55 dB SPL was given a step-function amplitude envelope and played through one of the speakers. The subjects' task was to declare which loudspeaker had sounded.

2. Difficult (DL) experiment

The difficult localization task (DL) was made much more difficult than the EL task. Listeners were 6 m away from the source array, again in a 46° span. Because of the larger distance to the source, incoherent reverberant sound was a larger fraction of the total sound power, making localization more difficult. The stimulus was broadband noise that had been low-pass filtered (corner frequency of 5 kHz, -48 dB/octave). Therefore, listeners could not use high-frequency interaural intensity cues that are especially helpful in this room. The SPL of the noise before filtering was identical to the EL experiment. The filtered noise was given a linearly rising amplitude envelope with a duration of 2 s. During the onset, uncorrelated broadband noise was played at a level of 85 dB through a speaker behind the subject's neck to mask the onset of the stimulus. Therefore, listeners gained no benefit from the precedence effect, further degrading localization ability. Again, the task was to declare which loudspeaker sounded.

B. Method

The reverberant room was rectangular with dimensions $7.67 \times 6.35 \times 3.58$ m high. It had a reverberation time of 4 s at midrange frequencies. The orientation of the array in the room is best described as a nonspecial geometry. The 24 loudspeakers were Realistic Minimus 3.5, consisting of a single driver in a sealed box. They had been chosen from a set of 85 based on similar on-axis frequency response in an anechoic environment.

The configurations for the different number of sources were as follows:

$$N = 24 \Rightarrow A = 2^\circ \Rightarrow \Gamma = 46^\circ,$$

$$N = 12 \Rightarrow A = 4^\circ \Rightarrow \Gamma = 44^\circ,$$

$$N = 6 \Rightarrow A = 8^\circ \Rightarrow \Gamma = 40^\circ,$$

$$N = 3 \Rightarrow A = 23^\circ \Rightarrow \Gamma = 46^\circ.$$

The loudspeakers were at ear level of a seated subject. A bar rested on the head of the subject to help the subject maintain a constant, forward facing position. Each source was labeled with a number, and the subject made a response by using a button box to increment a numerical display up or down. The display reading was then recorded by the computer running the experiment.

C. Subjects and procedure

Four subjects participated in these experiments. Subjects W, R, and G were males, ages 57, 45, and 21, respectively, and were the coauthors of this article. Subject J was a female of age 17. Subjects W and R had extensive experience in localization experiments and had high-frequency hearing losses typical of males their age. Subjects G and J had recent experience as subjects and had normal hearing.

The experiments were performed in blocks of runs for both easy (EL) and difficult (DL) tasks. A block consisted of a run for each source spacing condition for either the EL or the DL case. The runs of a given block were performed on the same day, and the order of the runs within a block was randomized. Each run consisted of 48 stimulus-response pairs and lasted 10–15 min. Within each run, all stimuli were presented an equal number of times in random order. Therefore, a particular source was presented twice for $N = 24$, four times for $N = 12$, eight times for $N = 6$, and 16 times for $N = 3$. There was no feedback, but a curious subject was allowed to view the results at the end of a run. Each subject did three blocks for both EL and DL conditions.

D. Results

The experimental results appear in their greatest detail in plots of $R(k)$, the average response of a listener to source k . For illustration, plots of $R(k)$ are shown for listener W in Fig. 7(a) and (b) for the EL and DL experiments, respectively. Perfect performance corresponds to an $R(k)$ plot that is a 45-degree line. It can be seen that Fig. 7(a) approximates a 45-degree line, although there is considerable central bias, as described above. The plot for the DL experiment in Fig. 7(b) shows enormous deviations from the 45-degree ideal as

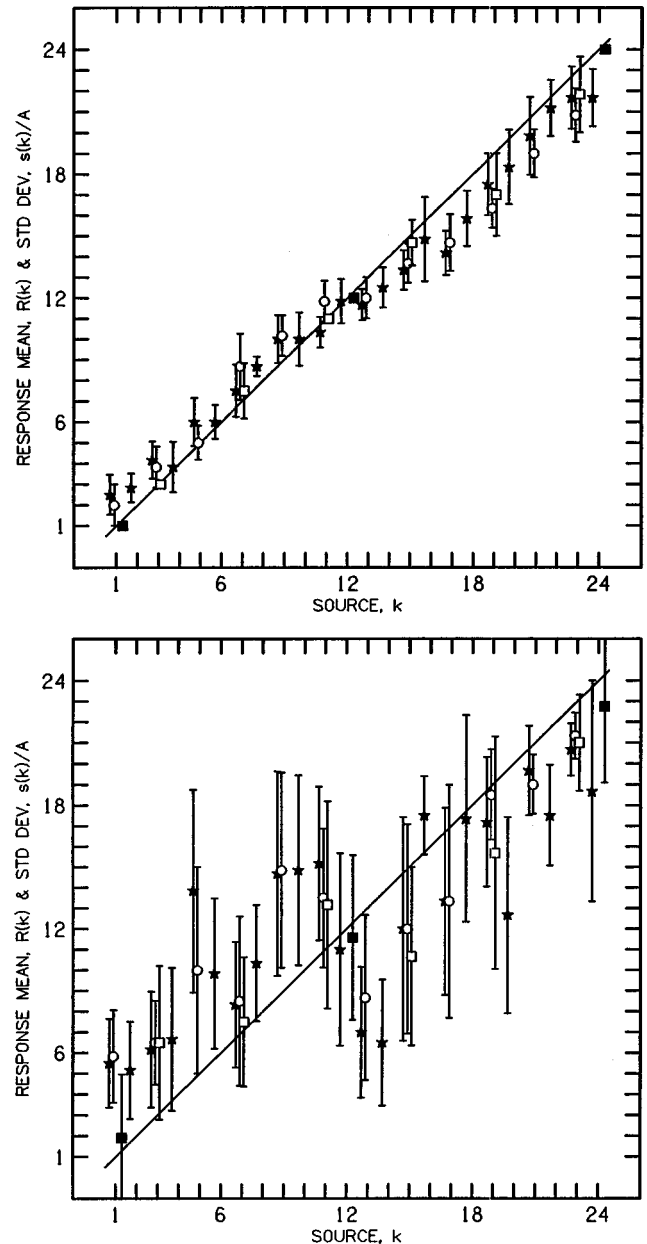


FIG. 7. Function $R(k)$, the average response of listener W to source number k . Error bars are plus and minus the variability, $s(k)$. Experiments with different numbers of sources (N) are plotted on the same graph: stars for $N = 24$, open circles for $N = 12$, open squares for $N = 6$, and filled squares for $N = 3$. Part (a) is for the EL experiment. Part (b) is for the DL experiment. Each small division on horizontal and vertical axes corresponds to 2° .

well as central bias. Figure 7(a) and (b) is typical of $R(k)$ plots for all the listeners, although different listeners had different forms of bias, some better approximated as constant bias, not central.

Of primary interest in the present article are the average quantities \underline{D} and \underline{s} for the eight different conditions ($N = 24, 12, 6$, and 3 for both the EL and DL experiments). These are given in Table I, averaged over the three runs for each listener. These averages and corresponding standard deviations ($n - 1$) over the three runs appear in Figs. 8 and 9.

III. COMPARISON—THEORY AND EXPERIMENT

The principal comparison between theory and experiment was a test of the prediction of the decision theory

TABLE I. Experimental values of rms error (\underline{D}), variability (\underline{s}), and constant error (\underline{C}) for four listeners in two source identification experiments, easy (EL) and difficult (DL). The arrays spanned 46 degrees and included $N=3, 6, 12,$ or 24 sources. Values of width and bias are model parameters determined from the asymptotic variability and constant error, respectively. The parameters were used for model calculations in the comparison plots that follow.

Listener	N	Experiment (degrees)			Model (degrees)	
		\underline{D}	\underline{s}	\underline{C}	width	bias
EL experiment						
G	3	0	0	0	1.21	1.60
	6	0	0	0		
	12	2.21	1.68	1.44		
	24	2.01	1.21	1.60		
J	3	0	0	0	1.26	2.73
	6	1.09	0.84	0.69		
	12	3.09	1.67	2.60		
	24	3.01	1.26	2.73		
R	3	0	0	0	1.64	2.67
	6	2.66	2.37	1.21		
	12	3.26	2.03	2.55		
	24	3.13	1.64	2.67		
W	3	0	0	0	1.43	3.29
	6	3.21	2.44	2.09		
	12	3.85	1.93	3.33		
	24	3.59	1.43	3.29		
DL experiment						
G	3	10.14	8.60	5.37	6.70	10.02
	6	8.54	6.88	5.06		
	12	11.39	6.73	9.19		
	24	11.70	6.04	10.02		
J	3	8.08	7.82	2.03	4.50	8.67
	6	8.70	6.48	5.81		
	12	9.21	6.79	6.22		
	24	9.61	4.14	8.67		
R	3	11.60	10.00	5.88	7.40	9.09
	6	9.70	8.29	5.04		
	12	11.46	6.56	9.40		
	24	11.13	6.42	9.09		
W	3	7.12	6.73	2.32	5.70	10.15
	6	10.00	6.13	7.90		
	12	10.27	5.94	8.38		
	24	11.37	5.13	10.15		

model for the dependence of \underline{s} and \underline{D} on the number of sources in the array. This dependence was the primary focus of model calculations themselves, for small and large spans, with and without bias.

Because the experimental span was only 46° the model calculation could be done in the small-span limit. The input parameters to the model were the width of the internal distribution and the bias. The bias was assumed to be of the constant type, or, equivalently, central. The biases observed experimentally were of both types, but, as described in Sec. I B 2, these two types of bias have similar effects on the average statistics of interest. It was assumed that the width and bias parameters depend only on the listener and the experimental conditions—EL or DL. Therefore, it was expected that the dependence on number of sources, for both \underline{D} and \underline{s} , should be predicted by the model.

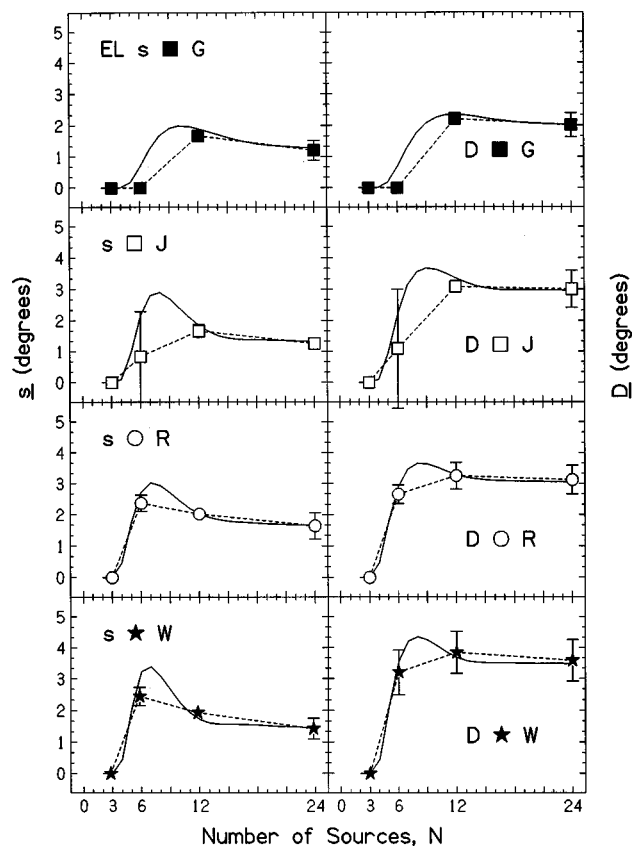


FIG. 8. Comparison between experiment (points) and model (solid lines) for the easy localization (EL) experiment. Each row is for a single listener, \underline{s} and \underline{D} . Error bars are two standard deviations ($n-1=2$ weight) in overall length. Dashed lines connect the experimental points.

The procedure for assigning model parameters was simple. We assumed that the width should be determined by the large- N limit of \underline{s} , i.e., $N=24$ in Table I. When the model width is small it is equal to $\underline{s}(24)$; when the width is not small, it must be taken to be somewhat larger than the experimental $\underline{s}(24)$ in order that $\underline{s}(N)$ agrees with experiment in the limit that $N=24$.

We also determined the bias parameter from the experimental constant error, $\underline{C}(24)$, in Table I. As a measure of bias, this constant error approximately agreed with the vertical shifts seen in plots of $R(k)$. For example, $\underline{C}(24)$ for listener W in Table I is 3.29° . This agrees with $R(k)$ in Fig. 7(a), which suggests a central bias averaging $1.5\text{--}2.0$ divisions, or $3^\circ\text{--}4^\circ$.

Therefore, the nature of the comparison was to determine the model parameters from the width and estimated bias for $N=24$ and to compare the model predictions, for both \underline{s} and \underline{D} , with the experimental results for $N=3$, $N=6$, and $N=12$. The model parameters are shown in the right two columns in Table I.

The comparisons between calculations and the EL experiments are shown in Fig. 8. The comparisons show that the model is in reasonable numerical agreement with experiment, even though the parameters were not chosen to provide an optimum fit. Further, the model captures a number of features seen in the experiments: There is a tendency for a

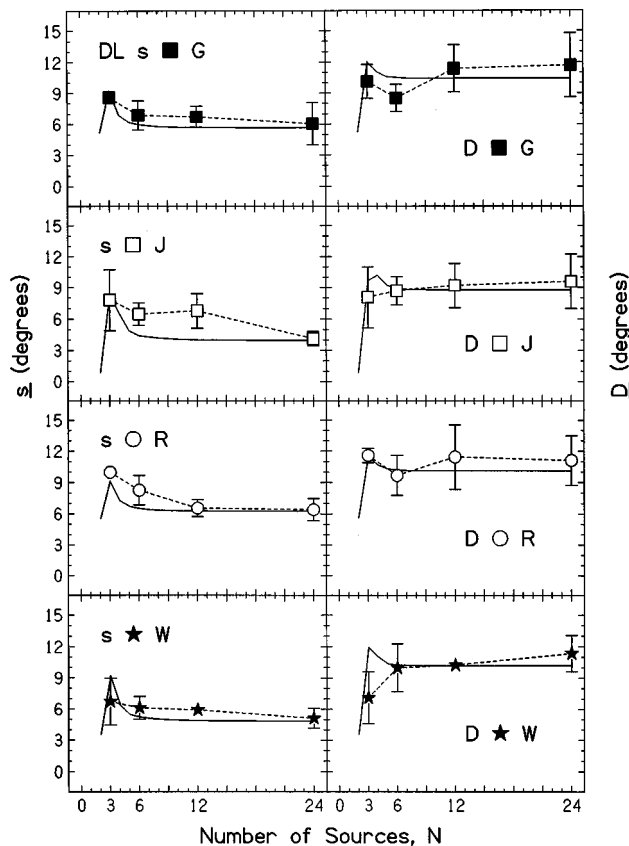


FIG. 9. Same as Fig. 8 but for the difficult localization (DL) experiment.

peak in \underline{s} and \underline{D} as a function of N when the width is small. However, theoretically the peak is less prominent for \underline{D} than for \underline{s} , and experimentally no significant peak appears in \underline{D} .

The comparisons between calculations and the DL experiments are shown in Fig. 9. In the DL experiments the width is large. For large width, theory and experiment agree that there is no peak for $3 \leq N \leq 24$; there is only a tendency for \underline{s} to decrease with increasing N . \underline{D} is also predicted to decrease in the region of small N , as observed experimentally for two of the listeners. Overall, the agreement between experiment and model is better for \underline{s} than for \underline{D} , and this result is not surprising given that \underline{D} is more sensitive to bias, which is treated only in the simplest possible way by the present model calculation.

IV. CONCLUSIONS

The source-identification method (SIM) is a standard technique used to measure the ability to localize a sound. The method uses an array of source positions, which is particularly useful when there is reason to expect that the perception of any one source would be special. Such conditions occur in rooms. The experimental data from this method are in the form of variability (theoretically insensitive to bias) and rms error (includes both variability and bias). The method can be analyzed with a decision theory model based on a coordinate system imagined to be internal to the listener. Sources from the physical world lead to distributions of localization cues on this internal coordinate, characterized

by a model *width* and a displacement *bias* of the mean. A similar model was used to analyze the minimum audible angle method (Hartmann and Rakerd, 1989).

Calculations are simplest for a terminated-span model. Here, the array is short enough that points on the internal coordinate that are to the left of the leftmost source must be assigned to the leftmost source; they do not wrap around and become confused with positions on the right. Terminated-span calculations find that if bias is negligible, both the rms error and the variability can provide good estimates of the average width of the internal distribution if there are enough sources in the array. The results are very insensitive to the number of sources if the spacing between the sources is less than or approximately equal to the width. The variability appears to be a good measure of the width even in the presence of bias if the bias is smaller than the width.

Bias that is larger than the width—a frequent occurrence—complicates the relationship between experimental results and the parameters of the internal distribution. The variability (not the rms error) may still be a reliable measure of the width if the number of sources is large enough. To determine the required number of sources, one must model the bias in some way and fit the experimental data to width and bias model parameters. Two simple bias models, constant and central, were found to give similar results.

When the angular span of the model is not terminated, probabilities are wrapped around a complete circle. Calculations indicate that the variability continues to provide a good measure of the internal width, as long as the width is not greater than 20% of the span.

When the angular span of the actual sources is wrapped beyond 180° , source localization becomes a multidimensional perceptual problem, and the perceptual distance between two sources is not a monotonic function of the azimuth difference. Therefore, our one-dimensional model is not applicable. Applying the model anyway reveals complicated effects that occur when localization scores are given the benefit of a front-to-back reversal. Similar effects are expected to occur independent of the model.

Finally, experiments with human listeners were done in order to test the model calculations. The experiments used a small span in which the number of sources varied from 3 to 24. To provide a stringent test, both easy localization (EL) and difficult localization (DL) experiments were done. The experiments were done in a reverberation room, and constant errors (biases) were a major component of the overall errors. It was found that the model gave a reasonable account of the experimental results, even though the model treatment of bias was simple. To improve on the methods used here would require a treatment of bias peculiar to each individual listener. The resulting model would lead to better agreement with experiment, at the cost of generality.

Because of its internal consistency and satisfactory experimental validation, the decision theory model in this article can serve as a guide to the design and analysis of source identification experiments. In the matter of experimental design, the model can determine the correct number of sources to use in an array, based on anticipated results. After the rms

error and variability data are experimentally known, the model can be used, first to decide whether a reliable value of the width of the internal distribution can be determined from the data, and second to calculate the actual values of the width and the bias.

ACKNOWLEDGMENTS

This research was supported by Grant No. DC00181 from the NIDCD of the NIH. Additional funding was provided by the National Science Foundation, which supported Joseph Gaalaas through its Research Experience for Undergraduates grant to the MSU Department of Physics and Astronomy. We are grateful to Joy Hsu for her participation in this study. Steve Colburn, Barbara Shinn-Cunningham, and Raymond Dye made many useful comments on a previous version of this article.

APPENDIX: LIMITS OF HIGH UNCERTAINTY

In the limit of high uncertainty, the width of the internal distribution becomes large compared to the span. In the extreme uncertainty limit, there is a negligible probability that the internal representation of the source lies within the span of allowed responses. Therefore, terminated-span model calculations find that all responses become extreme responses. In the absence of bias, sources 1 and N are chosen equally.

Then $\overline{D^2}$ is given by summing the squared differences between the N sources and the extremes. The two extreme sums get the same weight (1/2), and they are, in fact, equal. Therefore,

$$\overline{D^2} = \frac{A^2}{N} \sum_{k=1}^N (k-1)^2. \quad (\text{A1})$$

The finite sum can be done, and

$$\overline{D^2} = A^2 \frac{(2N-1)(N-1)}{6}. \quad (\text{A2})$$

Because the span is $\Gamma = (N-1)A$,

$$\underline{D} = \frac{\Gamma}{\sqrt{3}} \sqrt{1 + \frac{1}{2(N-1)}}. \quad (\text{A3})$$

The second term inside the square root can be neglected when the number of sources becomes large; even if there are as few as four sources, dropping this term makes less than a 10% change in \underline{D} .

In the limit that all responses are extreme responses, statistic \underline{s} can be calculated from the differences between the extremes and the mean. If there is no bias, the mean of the extremes is $(N+1)/2$, and

$$\overline{s^2} = A^2 \left[\frac{1}{2} \left(1 - \frac{N+1}{2} \right)^2 + \frac{1}{2} \left(N - \frac{N+1}{2} \right)^2 \right], \quad (\text{A4})$$

so that

$$\underline{s} = A \frac{N-1}{2} = \frac{\Gamma}{2}. \quad (\text{A5})$$

The extreme response results for \underline{D} and \underline{s} [Eqs. (A3) and (A5)] are the correct limits for the statistical technique used

in this article as the uncertainty becomes infinite. However, these limits are unreasonable because listeners can achieve better performance by guessing randomly among the sources. Better large uncertainty limits are the random guessing limits calculated below.

If the N sources are presented equally often, \underline{D} is the square root of

$$\overline{D^2} = \frac{A^2}{N} \sum_{k'=1}^N \sum_{k=1}^N P(k'|k)(k-k')^2, \quad (\text{A6})$$

where $P(k'|k)$ is the probability of choosing source k' given that source k was presented.

If listeners guess randomly then, in the absence of bias, they make each response k' equally often, independent of the source k , and $P(k'|k) = 1/N$. The double sum can be done and

$$\overline{D^2} = A^2 \frac{(N-1)(N+1)}{6}, \quad (\text{A7})$$

or, in terms of span Γ ,

$$\underline{D} = \frac{\Gamma}{\sqrt{6}} \sqrt{1 + \frac{2}{N-1}}. \quad (\text{A8})$$

Equation (A8) is less than (A3) as expected.

Similarly \underline{s} can be calculated from

$$\overline{s^2} = \frac{A^2}{N} \sum_{k'=1}^N \sum_{k=1}^N P(k'|k)[k' - R(k)]^2, \quad (\text{A9})$$

where $R(k)$ is the mean response given source k .

In the random guessing limit and in the absence of bias, the mean response to source k is the mean location, independent of k , $R(k) = (N+1)/2$. Therefore,

$$\overline{s^2} = \frac{A^2}{N} \sum_{k'=1}^N \left[k' - \frac{N+1}{2} \right]^2. \quad (\text{A10})$$

Doing the finite sum leads to

$$\overline{s^2} = A^2 \frac{N^2-1}{12}, \quad (\text{A11})$$

and in terms of span Γ ,

$$\underline{s} = \frac{\Gamma}{\sqrt{12}} \sqrt{1 + \frac{2}{N-1}}. \quad (\text{A12})$$

Equation (A12) is less than (A5) as expected.

From Eqs. (6), (A8), and (A12), $\underline{C} = \underline{s}$ and the overall rms error is equally divided between variability and central bias.

¹This kind of bias, depending on the source, was called "sensory" bias by Hartmann and Rakerd (1989). Mathematically, it behaves similarly to the "response bias" introduced by Braida and Durlach (1972), which, however, is a function of the response and not the source.

²Searle *et al.* (1976) concluded that the width of the internal distribution scales with the span of the sources. This conclusion paralleled the earlier discovery that the width for absolute identification of intensities scales with the range of intensities (Durlach and Braida, 1969; Braida and Durlach, 1972). A problem with this parallel is that the work by Searle *et al.* (also Shelton and Searle, 1978) failed to distinguish between width and bias. The more recent work by Koehnke and Durlach (1989), while not strictly in-

volving localization, may have remedied that problem. That work found incomplete scaling, as predicted by Hartmann and Rakerd (1989).

- Braida, L. D., and Durlach, N. I. (1972). "Intensity perception II. Resolution in one-interval paradigms," J. Acoust. Soc. Am. **51**, 483–502.
- Durlach, N. I., and Braida, L. D. (1969). "Intensity perception I. Preliminary theory of intensity resolution," J. Acoust. Soc. Am. **46**, 372–383.
- Hartmann, W. M. (1983a). "Localization of sound in rooms—The effect of a visual fixation" Proc. 11th ICA, 139–142.
- Hartmann, W. M. (1983b). "Localization of sound in rooms," J. Acoust. Soc. Am. **74**, 1380–1391.
- Hartmann, W. M., and Rakerd, B. (1989). "On the minimum audible angle—A decision theory approach," J. Acoust. Soc. Am. **85**, 2031–2041.
- Koehnke, J., and Durlach, N. I. (1989). "Range effects in the identification of lateral position," J. Acoust. Soc. Am. **86**, 1176–1178.
- Rakerd, B., and Hartmann, W. M. (1985). "Localization of sound in rooms. II: The effect of a single reflecting surface," J. Acoust. Soc. Am. **78**, 524–533.
- Rakerd, B., and Hartmann, W. M. (1986). "Localization of sound in rooms. III: Onset and duration effects," J. Acoust. Soc. Am. **80**, 1695–1706.
- Searle, C. L., Braida, L. D., Cuddy, D. R., and Davis, M. F. (1975). "Binaural pinna disparity: another auditory localization cue," J. Acoust. Soc. Am. **57**, 448–455.
- Searle, C. L., Braida, L. D., Davis, M. F., and Colburn, H. S. (1976). "Model for sound localization," J. Acoust. Soc. Am. **60**, 1164–1975.
- Shelton, B. R., and Searle, C. L. (1978). "Two determinants of localization acuity in the horizontal plane," J. Acoust. Soc. Am. **64**, 689–691.
- Wightman, F. L., and Kistler, D. (1989). "Headphone simulation of free-field listening. II: Psychophysical validation," J. Acoust. Soc. Am. **85**, 868–878.
- Woodworth, R. S. (1938). *Experimental Psychology* (Holt, New York).

Methods of interval selection, presence of noise and their effects on detectability of repetitions and prolongations

Peter Howell, Alison Staveley, Stevie Sackin, and Lena Rustin

Department of Psychology, University College London, Gower Street, London WC1E 6BT, England

(Received 25 March 1998; accepted for publication 3 August 1998)

Accurate methods for locating specific types of stuttering events are necessary for diagnosis, treatment, and prognosis. A factor that could add variability to assessment of stuttering is noise on recordings. The effects of noise were assessed by adding noise to intervals of speech containing all fluent material, fluent material with a repetition, or fluent material with a prolongation. These intervals allow a unique dysfluency response to be made. A statistical analysis of the occurrence of such intervals in spontaneous speech showed that only a limited number of intervals met these criteria. This demonstrated that selecting intervals at random from spontaneous speech (as in time interval analysis procedure) will infrequently lead to a unique and unambiguous dysfluency specification for the interval. Intervals were selected for testing from the intervals that met the stipulated criteria. These were presented for dysfluency judgment when the position of the stuttering within an interval was varied and with different amounts of added noise (no added noise, 3 dB, and 6 dB of noise relative to mean speech amplitude). Accuracy in detecting stuttering type depended on noise level and the stuttering's position in the interval, both of which also depended on the type of stuttering: Noise level affected detection of repetitions more than prolongations: Repetitions were more difficult to detect when they occurred at the end of an interval whereas prolongations were more difficult to detect when they were at the beginning of an interval. The findings underline the importance of adopting rigorous recording standards when speech is to be employed to make stuttering assessments. © 1998 Acoustical Society of America. [S0001-4966(98)04311-2]

PACS numbers: 43.70.Dn [AL]

INTRODUCTION

Measurements of the incidence of stuttering in samples of speech are required for a number of purposes: They are used to aid clinicians in deciding who to treat (diagnosis), to assess what changes in speech occur after treatment (treatment outcome), and to help establish which individuals are likely to be treated most successfully (prognosis). However, the measurement procedures that are traditionally used in clinics produce variable estimates of stuttering when different judges assess the same samples of speech (Kully and Boberg, 1988). Some approaches being investigated to improve assessments are motor metrics (Alfonso, 1990; Smith, 1997), automatic procedures (Howell *et al.*, 1997a; Howell, Sackin, Glenn, and Au-Yeung, 1997), and improved psychometric methods (Howell *et al.*, 1997b; Ingham *et al.*, 1993).

The audio recordings of speech used for assessment should also be made to high standards. However, it is not always easy to achieve good quality recordings in clinical environments. The effects noise introduced during recording has on assessments have not been investigated previously. The following study was conducted to ascertain how such noise affects the detectability of repetitions and prolongations. These types of stuttered dysfluency were selected as an increase in the proportion of prolongations to repetitions is an important diagnostic (Conture, 1990; Howell, 1993) and prognostic indicator (Conture, 1990). They can be reliably detected on words when recordings are made in controlled acoustic environments (Howell *et al.*, 1997b). For reasons given in the next section, assessments of the effects of noise have to be made in fixed-length intervals. In the final section,

background evidence concerning how noise affects detection of repetitions and prolongations is given.

A. Test interval selection criteria

Speech is listened to in continuous context when samples are assessed in clinics. Such procedures offer no control over whether judges give equal attention to all sections and whether speech in the surrounding context affects judgments about the stretch (Parducci, 1965). In the current study, experimental material was selected so: (a) The response to the test extract is unambiguous (fluent throughout, contains a repetition, contains a prolongation). (b) The material can be presented in equivalent contexts so that judgments are not biased. Though on the face of it these seem simple requirements, matters are somewhat complicated.

The first requirement is met by presenting speech for judgment that contains all fluent material, a single repetition or a single prolongation. Care has to be taken when selecting fluent material since some types of stuttered dysfluencies extend over groups of words [referred to by Howell, Au-Yeung, Sackin, Glenn, and Rustin (1997) as supralelexical dysfluencies]. Supralelexical dysfluencies include phrase repetitions, phrase revisions, and idea abandonments (Wingate, 1988). Words within supralelexical dysfluencies can appear perceptually fluent on superficial listening and would be judged accordingly when presented in isolation. However, they have different prosodic structure relative to fluent speech that is not part of a supralelexical dysfluency (Howell and Young, 1991). Supralelexical dysfluencies were identified and marked so that the words that occur in them can be

excluded when test material is selected. After this exclusion, the speech that remains has dysfluencies that occur within the bounds from the start of one word to the next (including repetitions and prolongations) usually on the first part of the first syllable in the word (Brown, 1945; Wingate, 1988). Dysfluencies like this are called lexical dysfluencies.

Syllables selected according to dysfluency type are presented in a fluent context to meet the second requirement, mentioned at the outset of this section. The reason a fluent context is necessary can be appreciated by considering what would happen if the syllable that contains a lexical dysfluency or a fluent syllable alone was presented. The syllables that contain a lexical dysfluency are usually longer than the fluent ones. The syllables are relatively easy to locate when noise on recordings is low. The duration of the syllables would be apparent when they are presented in isolation. The duration would remain apparent when noise is added to the syllable. Listeners could then use duration to decide what type the syllable is irrespective of whether noise on recordings prevents judges determining where a syllable starts and finishes in continuous context. Consequently, though it could be more difficult to extract syllable duration as information about dysfluency in noisy recordings, this would not be apparent if the syllables were extracted by the experimenter before the noise was added. A second feature of both repetitions and prolongations, already mentioned, is that they usually occur in initial position in a syllable. If a dysfluent syllable starts an extract, the position where the dysfluency occurs is provided to the listener. As with duration, noise might degrade listeners' ability to detect syllable position information yet listeners would be able to use it if syllables were spliced out of their context and presented for judgment.

By selecting test syllables that occur in a fluent context, all test intervals can have the same duration and the position where the test syllable occurs can be varied to obviate these problems. This proposal has some similarities with Ingham *et al.*'s (1993) procedure. There are, however, two differences between their procedure and the current one that needs highlighting: (a) Here the speech is processed so apparently fluent syllables that appear within supralexical dysfluencies are excluded. (b) All syllables in an interval are assessed from low noise recordings to see if they contain a lexical dysfluency prior to selection of test intervals. Intervals for noise tests are then selected so that they contain one and only one lexical dysfluency. In contrast, in Ingham *et al.*'s (1993) time interval procedure, intervals are selected at random. Consequently, in their procedure it is not known what dysfluencies the intervals contain and whether a dysfluency is completed within an interval. A by-product of the selection criteria applied in the current study is an indication of the extent to which intervals include multiple dysfluencies or have dysfluencies split between one or more test intervals. This topic is returned to in the Discussion when consideration is given to whether time interval analysis provides a satisfactory measure of stuttering.

B. Effects of noise on dysfluency assessment

Noise can originate in recording equipment and in the equipment used when the recordings are assessed subse-

quently as well as in external noise present in the recording environment. The ways the noise floor, frequency response, and response to transients of the equipment can lead to poor registration of the intensity-time profile of speech have been documented by Rosen and Howell (1981) when the speech is initially recorded, and by Scott and Howell (1992) when the sounds are reproduced for perceptual testing. The main source of room noise in clinics is extraneous sound. Some extraneous noises are relatively easy for the experimenter to control (e.g., clinical personnel speaking or corridor noises). Others, such as hum due to equipment in the building and traffic rumble, are not under direct experimental control. In addition to these sound sources, rooms with hard walls, like those in clinics, are reverberant and this also degrades recording quality (Watkins, 1992).

Noise from all these sources would make judges' decisions variable. It would be expected that judges would be less accurate when deciding about dysfluencies when noise level is high than when it is low. Some of the variability in Kully and Boberg's (1988) study that was attributed to variation between judges would arise from these sources. The design of the study did not allow control of reproduction equipment as the judges who acted as subjects were sent tapes that they played on their own equipment. The tapes judged on the poorest quality equipment would be more variable than those judged on equipment with better signal-to-noise ratio. In this way, inter-equipment variability would appear as interjudge variability. Generally speaking, without agreed recording standards, it is not possible to compare results obtained in different recording and test environments.

The preceding observations underline why care has to be taken when recording and reproducing speech for research purposes. However, scant attention has been given to the quality of recordings used in research publications aimed at improving methods to collect and assess samples of stuttered speech. The minimum requirements for control of recordings for this purpose are to employ a calibrated acoustic environment during the initial recording and the subsequent testing phases and to ensure comparable quality recording and reproduction equipment are used always: If the equipment used is referred to explicitly, manufacturers' catalogs can be consulted for specifications and, when different equipment is used in different parts of a study, those specifications can be compared. None of these requirements is met in the Ingham *et al.* (1993) study that uses different recording and reproduction equipment and where tests are performed in widely differing environments.

It is expected that repetitions and prolongations will be affected in different ways when noise is introduced onto recordings. Considering repetitions first, one salient property is how intensity fluctuates over time. Each successive attempt of the iterated sound is followed by an interval of relative silence. As noted earlier, poor quality acoustic environments affect intensity-time profiles. Consequently, detection of repetitions would be affected. In prolongations, where a sound is sustained, energy in the formant regions lasts for longer

and allows listeners more time to integrate this information through the background noise. Consequently, prolongations would be expected to be less affected by noise.

In the present study, sections of speech were selected on the basis of the responses of expert judges which started and ended with fluent syllables and contained either a fluent syllable or one and only one syllable that was either a repetition or a prolongation (Boehmler, 1959). The number of sections that it is possible to select according to these constraints is described. An important subsidiary issue about this analysis is that it shows that a high proportion of samples are heterogeneous with respect to their dysfluency composition if these constraints are not applied (for example, when intervals are selected at random). The selected sections of speech were judged with different amounts of room noise added. The type of syllable contained in the fluent context determined what response was appropriate. Listeners judged the interval type when different amounts of noise were added. The hypotheses tested are that noise will increase error rates of repetitions and prolongations and that decisions about repetitions will be affected by noise more than prolongations.

I. METHOD

A. Subjects

Twenty-nine children who stutter were recruited. Twenty-five were male and four were female. They ranged in age from 7 to 12 years (mean age 10.8 years). They were recorded when they were being assessed for treatment at a London clinic. The children had been referred to the clinic where they and their parents were seen by speech pathologists specializing in developmental stuttering. All the children employed were admitted to intensive therapy as a result of the assessments. The samples of speech were taken as part of their assessment.

B. Recordings

The speech material used in the current experiment was unscripted monologue speech samples, a minimum of two minutes long. A range of topics of conversation was suggested to the child before he or she started the monologue. Examples of topics are events on the way to the clinic, peer and sibling relationships, hobbies, and favorite TV programs. The choice of which of these topics was taken up was left to the child. These topics were suggested so that the child did not "dry up" during the recording (this was never a problem).

The speech was transduced with a Sennheiser K6 microphone positioned 6 in. in front of the speaker in direct line with the mouth. All speech was recorded on DAT tape. The recordings were made in an Amplisilence sound-attenuated booth. The noise floor during recording was determined with the apparatus set up as in the test recordings. The noise floor was recorded while the speaker remained silent. This was fed into an Onno-Soki dual-channel analyzer. Background noise was more than 80 dB down relative to peak speech value between 500 Hz and 10 kHz. Speech was transferred digitally to a computer for further processing. The speech from the DAT tapes was down-sampled during transfer to 20 kHz.

C. Location of fluent syllables, part-word repetitions, and prolongations by an expert panel

Expert judges were employed to assess the speech for selection of test material (details about the judges are given in Sec. I C 1). These judges provided two assessments of the speech. They located supralexic dysfluencies (Sec. I C 2). Speech was then syllabified and all syllables classified as being fluent or containing designated types of lexical dysfluencies (Sec. I C 3).

1. Expert judges

Three expert judges were employed in this part of the experiment. Two of them were the judges employed in Howell *et al.* (1997b). These judges are both male and have considerable experience in categorizing stuttered events (7 years and 2 years, respectively, each with 2 years experience using procedures similar to the ones used here). They are researchers involved full time in developing assessment techniques and assessing linguistic factors in stuttering. The more experienced judge has phonetic training up to masters level and the other a doctorate in computational linguistics. The performance of these judges in tasks like the ones here has been reported elsewhere (Howell *et al.*, 1997b). The other judge is female with phonetic training up to masters level. She has 1 year of experience with stuttered speech, using similar procedures to the current ones. Once she was trained, interjudge agreement was assessed by comparison with the other two judges. One of the expert judges from Howell *et al.* (1997b) only performed classification of syllables as lexical dysfluencies.

2. Location of supralexic dysfluencies

The speech was transcribed as the first step in location of supralexic dysfluencies. Two of the three judges transcribed the recordings independently. They did this by repeatedly listening to sections of the recording segmented into tone units. The transcription was in orthographic form with word attempts not indicated, e.g., k.k.Katy would be Katy. The agreement between transcribers was high (92% of all words) and so one transcriber's version was chosen at random for use in the subsequent assessments.

The two principal judges went through the transcriptions and located occurrences of phrase repetitions (e.g., "in the, in the morning"), phrase revisions (e.g., "my brother, er, no my uncle"), multiword interjections (e.g., "you know"), and idea abandonments where one topic was abandoned and another commenced [see Wingate (1988) for detailed descriptions of these types of dysfluency]. The extent of these supralexic dysfluencies was determined based on Levelt's (1983) work examining similar structures to these that occur in fluent speakers's speech (Howell *et al.*, 1997). Levelt identified several speech components around a dysfluency all of which occur in the phrase revision "You (turn left at the, no I mean, turn right at the) crossroads." The word "left" is in error (the reparandum) which is later substituted by the word "right" (the alteration). The speaker has an overshoot (the words "at the" after the reparandum). Before the speaker recommences, an interjection ("no I mean") is produced. When making the correction, the speaker backtracks

(i.e., says the word “turn” a second time). Retraces, overshoots, and interjections (multi- or single-word), all of which appear in this example, are optional parts of phrase revisions. Identification of these components allows speech to be parsed so supralexical dysfluencies can be located and their extent determined. In the example, the supralexical dysfluency involves all the words within ⟨ ⟩. The extent of a phrase repetition was determined in like manner (the only difference between a phrase revision and a phrase repetition is that the repetition does not contain altered words). Incomplete phrases were identified as semantic discontinuities. Any sequence of words that was incomplete semantically was marked as an incomplete phrase and these words were excluded from interval selection.

3. Location of lexical dysfluencies

The speech was syllabified to select the stretches of sound to be presented to judges for assessment of lexical dysfluencies. All the speech was syllabified (including syllables that occurred within supralexical dysfluencies). Syllables that were part of supralexical dysfluencies were excluded before statistical analysis for lexical dysfluency and for selection of test material. Syllabification is described followed by the procedure adopted for assessing lexical dysfluency.

a. *Syllabification.* Syllabification of speech was done by an artificial neural network. The network was used as it allowed the large amount of speech available to be processed quickly and reliably. The syllabification algorithm first located the vowels in the speech. The architecture for vowel detection consists of a two-layer recurrent Elman network with 13 inputs, eight hidden units, and one output unit, with backpropagation as the learning algorithm. The units in the input layer are fully connected to the units in the hidden layer (all of which have a single context unit) which are in turn fully connected to the output unit. The inputs to the network were the first 12 Mel Cepstral coefficients (10-ms frames, 10-ms step) plus one amplitude envelope parameter per frame. The envelope parameter was obtained by band-pass filtering the speech between 100 and 400 Hz using fourth-order Butterworth filters. The filter output was rectified and the resultant signal then smoothed with a 25-Hz low-pass, second-order Butterworth filter. The amplitude envelope was then summed over each 10-ms window and the base 10 logarithm of this taken. Each of the 13 input parameters was normalized to between -1 and $+1$ by subtracting the mean and dividing by twice the standard deviation. The networks were trained with the read speech from six male child stutterers reading “Arthur the Rat” that was used in Howell *et al.* (1997a). The children were aged between 8 and 12 years. The first 30 s of speech from each speaker was used for training. During training, the network had to activate the vowel output once on each vowel and to remain inactive during other phonemes. The peaks associated with vowels were obtained by smoothing the network output with a 5-Hz low-pass, second-order Butterworth filter.

The syllable boundaries were located by using the vowel markers located by the networks together with a speech-silence detector (Rabiner and Sambur, 1975). If the Rabiner

and Sambur (1975) algorithm detected silence between a pair of vowels the offset of the first syllable was placed at the start of the silence and the onset of the second syllable at the end of the silence. If there was no silence between a pair of vowels a single boundary was placed at the point of minimum energy between the pair of peaks. A voiceless repetition can be incorporated with the following syllable. After training the ANNs were tested on spontaneous speech from child stutterers. The networks correctly classified 95.6% of syllables in the spontaneous speech.

b. *Assessment procedure.* The procedure adopted for deciding about lexical dysfluencies by the experienced judges was developed from that employed by Howell *et al.* (1997b). Three independent assessments were made by each judge: In the first assessment, judges only indicated which syllables were fluent. Syllables were only considered fluent if all three judges labeled them fluent. These were not involved in subsequent assessments. For the remaining syllables there was some indication that the syllable was dysfluent. All the syllables that remained were assessed independently for category of dysfluency, once for repetition and once for prolongation. Note that since the second and third assessments were made independently and on the same material, a judge could give a prolongation response on one occasion and a repetition on another to a syllable (as would be appropriate in an example like “mmmm.m.mother”).

Other than the materials judged and the response allowed, the way the assessments were performed was common to all three of the assessments. The pool of syllables for making the judgment was specified (all syllables for fluent judgments or the dysfluent syllables for repetition and prolongation judgments). A random presentation order for the syllables in each pool was then computed so that the global context in which judgments were made was as constant as possible. The first randomly selected syllable and the syllable that followed were played to the judge. The pair of syllables had the same timing as they had had in the original recording so pauses were apparent as quiet sections between the two syllables in the pair. The response the judge made was whether the first syllable was fluent, repetition, or prolongation depending which assessment was being performed.¹ For fluent and prolonged syllables, the second syllable simply served to provide context. The second syllable also provided some context for deciding about repetitions. It is not possible to determine whether a repetition that is split between two syllables (because the initial attempt has a vowel) is occurring unless the adjacent syllable is heard. So, for example, “cat” has to be heard to ascertain that the first syllable in “cuh-cat” is repeated. Location of repetition across pairs of syllables allows more extensive iterations to be identified. For instance, in a sequence like “cuh-cuh-cat,” repetition would be detected on both the first and final pair of syllables. Though consecutive runs of repetition like this can be designated as iterations of a single repetition, they are long and tend to straddle test intervals (see 1.4 in Sec. I D below). The syllable pair being tested could be heard repeatedly (by pressing the return key on a keyboard) until the judge was ready to make his or her response. The judges were self-paced and could take a break whenever they wanted. Test

sounds were played over RS 250-924 headsets in the test booth. To check on noise level added to the signal from external and electrical sources, a speech signal was input at 75 dB SPL. Background noise with speech switched off was 40 dB SPL below the speech level.

D. Interval selection criteria

Once the syllables had been assessed, they were used to select test materials. Test material had to have a designated target syllable and fluent syllables around it. Moreover there had to be sufficient fluent syllable context to allow a range of starting positions to be used for the target syllable while at the same time overall duration had to be kept constant for the reasons given in the Introduction. These constraints required that the initial fluent context extended beyond the test interval duration. Intervals of the same duration where the target syllable has different starting positions can then be selected from the more extensive context. These more extensive contexts are referred to as super-intervals for brevity. Test intervals are the parts of super-intervals presented for assessment. In the following sections, selection criteria for target syllables and test intervals are described followed by the procedure for adding noise.

1. Target syllable

Each syllable was checked to establish whether it met the following criteria for designation as fluent, repetition, or prolongation:

- 1.1. A syllable was designated fluent if all judges gave it a fluent response.
- 1.2. For a repetition syllable, at least two of the judges had to call it a repetition. If only two judges considered the syllable to be a repetition, neither of these judges was allowed to give this syllable a prolongation response as well (this excluded dysfluencies like the “mmm.m.mother” example in Sec. I C 3 above). The response of the judge who did not designate the syllable as a repetition was not allowed to be “prolongation.”
- 1.3. The criteria for a prolongation syllable were the same as those for a repetition syllable given in 1.2 except that the dysfluency type specifications were reversed.
- 1.4. An additional criterion applied solely to repetitions. They could be part- or whole-syllable but they could contain only one repeated syllable (e.g., “ka Katy” not “ka ka ka Katy”). This restriction was applied so that repetitions were limited in extent to a single interval and so that the syllables in intervals of different target syllable types could be found which corresponded roughly in duration (see 3.1). Though this criterion could conceivably have been required for long prolongations, this was not necessary for the present speech material.
- 1.5. The “target” syllable was not allowed to occur within any part of a supralexical dysfluency.

Looser criteria were adopted in 1.2 and 1.3 because there were fewer syllables in repetition and prolongation classes than there were fluent syllables.

2. Interval construction criteria

Once target syllables that had a fluent, repetition, or prolongation designation had been obtained, they were checked to see whether they could be used to construct a super-interval. All appropriate target syllables were checked. The principal requirement behind selection of super-intervals was to provide a fluent surrounding context for the designated target syllable. The criteria for the super-intervals were:

- 2.1. A super-interval could contain one and only one syllable that was fluent, repetition, or prolongation and no syllable that was part of a supralexical dysfluency. All other syllables had to be agreed by all judges as fluent syllables.
- 2.2. Isolated interjections (including filled pauses such as “umm” or “err” could not occur within any of the super-intervals.
- 2.3. There had to be two unanimously agreed fluent syllables preceding the target syllable.
- 2.4. The target syllable had to have three unanimously agreed fluent syllables following it.

If the fluent fillers in super-intervals had a fluent context word which a majority but not all judges designated fluent (only two rather than three judges passing constraint 2.1 on one fluent context word), but passed all other selection criteria, they were retained as potential practice material for the test judges.

A super-interval might consist of the words “the black mmmouse sat on the” where “mmmouse” is a prolonged target syllable. From this super-interval, three test intervals were constructed. The first of these started at the first syllable in the super-interval and extended to the end of the fluent syllable after the prolonged syllable (in the example, the interval “the black mmmouse sat”). This interval could include silent pauses. The duration was measured and the subsequent two test intervals had to be close in duration to it. The second interval started on the second syllable (on “black” in the example) and extended at least one fluent syllable beyond that which ended the first test interval. The third test interval started on the target syllable itself and continued to at least one fluent syllable beyond the end of the second test interval.

3. Selection of fluent and repetition super-intervals to match prolongation super-intervals

After the restrictions outlined in Secs. I D 2 and I D 3 above, only ten prolongation super-intervals were available (with the three starting positions used in each super-interval, this allowed construction of 30 prolongation test intervals). Equal numbers of fluent and repetition super-intervals were chosen. The fluent and repetition super-intervals were selected so that they shared the same basic temporal features as the available prolongation intervals. The selection criteria for the repetition and prolongation super-intervals were:

- 3.1. The syllables in the fluent, repetition, and prolongation intervals had to have similar average durations.
- 3.2. Pauses, if they appeared, had to be in corresponding positions.

Unlike the previous criteria, these were applied manually. A breakdown about how the main selection criteria whittled down the instances is presented in the Results (Sec. II).

4. Addition of noise to test intervals

The ten super-intervals of each of the three target syllable types allowed 90 test intervals to be constructed when the three starting positions were applied. Three further stimuli were created from each of these 90 stimuli. The first had no noise added, the second 3 dB, and the third 6 dB of noise relative to the mean speech amplitude of each syllable.

Noise was real room noise recorded on DAT tape with the Sennheiser K6 microphone. The noise was recorded in a quiet office that had plaster walls with nothing on them and was 8×20 ft. It had a window at one of the narrow ends that was closed and a door at the opposite end that was also closed while the recording was made. The office was located in the center of London and there was background traffic noise. The recording equipment was in the room and it was switched on. The equipment and microphone were located in the center of the room. A section of the recorded noise was selected where there was no noise from the corridor and where there was no predominant sound such as traffic accelerating. The noise was typical of that which occurs in the best recordings made in similar rooms in clinics. To check this, the signal-to-noise (S/N) ratio was calculated on four recordings supplied by US clinics using the algorithm described by Sims (1985). Noise levels over 40-s extracts were between 2.7 and 6.7 dB.

The processing to add the noise to the speech samples was as follows:

- 4.1. The test intervals were scaled to the same maximum value.
- 4.2. The mean amplitude was calculated over the full length of the test interval.
- 4.3. Each test interval was processed separately for each desired noise level. The S/N ratio was equal to $10 \times \log_{10}$ (mean amplitude of S/mean amplitude of N).

The mean amplitude of N was calculated over the length of the interval to be processed (i.e., if the interval was 1200 samples long, the mean amplitude of the noise was calculated over the first 1200 samples and N for this interval stopped at this sample). A multiplier was applied to the noise to bring the desired mean amplitude of N to the value appropriate to give the required S/N ratio. The S and N were then added.

E. Experimental procedure for assessment of test intervals by test judges

Six test judges were employed for the experiment. These were all female students who were in their fourth (final) year of a full-time speech pathology course. They had received training on clinical methods of assessing dysfluency as part of their course and had experience in making such judgments in clinical practice. They were chosen as they had a homogeneous level of experience and were representative of the clinical judges who would be required to assess clients' recordings. These were used to perform psychometric assess-

ments. The playback apparatus for the test judges was the same as that described earlier. The 270 test intervals (the 90 test intervals described at the beginning of the previous section $\times 3$ for intervals at different noise levels) were selected at random without replacement and these were presented to the test judges to make their response. The response was whether the interval contained only fluent syllables or included either a repetition or a prolongation. Only one response was allowed to each interval heard. Each judge did the experiment in isolation. They pressed a mouse button and they heard each stimulus once over the RS 250-924 headset.

The subjects received practice before they did the proper assessments. Only three prolongations met all the selection criteria except that one of the fluent context syllables was not unanimously agreed to be fluent (criterion 2.1) during the assessment by the expert judges. Three fluent and repetition super-intervals (matched in the same way as the test super-intervals) were selected. Eighty-one practice test intervals were created from the original three fluent, prolongation, and repetition super-intervals. These were tested prior to collection of data on the experimental material in the same manner. Responses to the practice intervals were discarded before statistical analysis.

II. RESULTS

A. Effect on distribution of intervals of selection criteria

The way the selection criteria restricted the candidate super-intervals was examined. Each syllable was considered with respect to whether there was agreement across judges about whether the syllable was fluent, a repetition, or a prolongation according to criteria 1.1 to 1.4 specified in the Method (Sec. I). Syllables that met the agreement criteria were potential candidates for target syllables and, in the case of agreed fluent syllables, as filler items for the super-interval. Over all syllables, the proportion that did not meet these criteria was 18.2% (1699 syllables). Note that not all the syllables that failed to meet the agreement criteria are disagreements between judges. This 18.2% includes cases where the word was considered dysfluent by all judges but none of the judges considered it a repetition or prolongation and also cases where two or three of the judges agreed that a target syllable was both repetition and prolongation as in the "mmmm.m.mother" example given in Sec. I C 3. The number of agreed syllables is given separately for fluent, repetitions, and prolongations in row one of Table I.

The second row of Table I shows the number and percentages of super-intervals removed because the super-interval had a word that was part of a supralelexical dysfluency. Exclusions are classified by target syllable type even though the super-interval could be prohibited because the target syllable (criterion 1.5) and/or syllables in the super-interval filler context (criterion 2.1) occurred within a supralelexical dysfluency. Also note that these data do not include standalone interjections. The average over all target syllable types of super-intervals where the syllables in an interval overlapped with a supralelexical dysfluency was roughly 40%. A further factor of note about the number of target syllables

TABLE I. Breakdown of how super-intervals (determined by the type of target syllable shown along the top row) are reduced by the selection requirements indicated in the left column. The totals and percentages (in brackets) are given.

Target syllable type	Fluent	Repetition	Prolongation
Overall target syllables of the designated type	6767	796	86
One of the syllables in a super-interval occurs within a supralelexical dysfluency	1718 (25.4%)	459 (57.6%)	29 (33.7%)
Super-interval contains an interjection	1032 (15.3%)	76 (9.5%)	17 (19.8%)
Super-interval contains another lexical dysfluency or a nonagreed F, P, or R syllable	626 (27.1%)	192 (24.1%)	30 (34.9%)
Remainder	2186 (32.3%)	69 (8.7%)	10 (11.6%)

that occurred within a supralelexical dysfluency was that the probability that a repetition will be involved in a supralelexical dysfluency was higher than that for a prolongation. A chi square on the number of repetitions and prolongations that were part of a supralelexical dysfluency (459 and 29, respectively, as shown in row two) against those not part of a supralelexical dysfluency (the sum of the remaining columns in Table I, 337 and 57 for repetitions and prolongations, respectively) showed that there was a significant association (chi square=18.0, $df=1$, $p<0.001$).

The remaining analyses summarized in Table I examined the syllables around the target syllable to see whether they fulfilled the criteria for specification of a super-interval with the response designation of the target syllable. The third row of Table I shows the reduction in number of super-intervals caused by the occurrence of interjections that were not part of supralelexical dysfluencies (criterion 2.2). From the percentages of super-intervals that contained such an isolated interjection, it appears that these depend on target syllable type (15.3%, 9.5%, and 19.8% for fluent, repetition, and prolongation, respectively). This would support the view that there is relative inhibition of interjections around repetitions and a heightened chance around prolongations relative to fluent contexts. However, summing up the syllables in the remaining rows for the respective columns to estimate the number of these that did not contain an isolated interjection gives totals of 2812, 261, and 40 compared with 1032, 76, and 17 that contain an interjection. A chi square test showed that there was no association between target syllable type and whether the super-interval contained an interjection (chi square=3.25, $df=2$, $p>0.05$). This is particularly noteworthy bearing in mind the high number of fluent target syllables that would tend to lead to a significant result. The same chi square analysis using repetition and prolongation alone was also not significant (chi square=1.43, $df=1$, $p>0.05$). The relative reduction in the percentage of super-intervals constructed from repetition target syllables that contained an interjection was due to the higher likelihood of repetitions being associated with supralelexical dysfluencies that reduced the overall total. Thus the likelihood of an isolated interjection occurring in a super-interval was about the same whether the

target syllable was fluent, repetition, or prolongation.

Row four shows the reduction in super-intervals brought about because the interval contained a lexical dysfluency on a syllable other than the target syllable or because the super-interval contained a syllable other than the target syllable that was not agreed fluent (criteria 2.3 and 2.4). A similar analysis to that on isolated interjections was done on the lexical dysfluencies. Again the percentages suggest that prolongations are hit harder by lexical dysfluency prohibitions than are repetitions. The totals in the last two rows of Table I were entered into a contingency table where one row was whether the lexical dysfluency criteria prohibited the candidate super-interval being accepted (626, 192, and 30 for the fluent, repetition, and prolongation columns, respectively) and row two was not prohibited by lexical dysfluencies (2186, 69, and 10 for fluent, repetition, and prolongation). Chi square analyses showed that there was a significant association when fluent syllables were included (chi square=363.77, $df=2$, $p<0.001$) but not when repetitions and prolongations alone were considered (chi square=0.037, $df=1$, $p>0.05$). Reservations about the chi square analysis with fluent syllables need to be expressed given the sensitivity of this statistic to high numbers of observations that can lead to spurious significance as mentioned earlier. It would be more conservative, therefore, to conclude that there was no association between whether an interval contained a prohibited lexical dysfluency and repetition and prolongation dysfluency target syllable type. In summary, it appears, then, that the only factor leading to super-intervals being rejected in Table I that differentially affected target syllable types was the high proportion of repetitions that occurred as part of a supralelexical dysfluency.

A further factor of note is that the number of super-intervals was dramatically reduced by the specified criteria (bearing in mind that over an hour long speech, in total, was assessed). A response to an interval as stuttered or nonstuttered is only meaningful if the interval contains a specific type of dysfluency and the interval incorporates all the dysfluency. The other side of this analysis is, therefore, that it shows arbitrarily chosen intervals are not appropriate for assessing dysfluency type: If this is done, many intervals will

TABLE II. Proportion of errors and their standard deviations (in parentheses beneath) for test intervals. Target syllable type is given in the column on the left (labeled F for fluent, R for repetition, and P for prolongation). The three starting positions relative to the super-interval are indicated along the top row at the head and the three different noise levels are labeled in the following row.

	Start 1			Start 2			Start 3		
	No noise	3 dB	6 dB	No noise	3 dB	6 dB	No noise	3 dB	6 dB
F	13.3 (12.1)	11.7 (16.0)	18.3 (14.7)	3.3 (5.1)	8.3 (9.8)	13.3 (15.1)	8.3 (9.8)	6.7 (8.2)	11.7 (16.0)
P	28.3 (14.7)	36.7 (13.7)	48.3 (16.0)	28.3 (11.7)	35.0 (8.4)	43.3 (12.1)	18.3 (11.7)	28.3 (17.2)	33.3 (19.7)
R	26.7 (17.5)	50 (16.7)	65 (11.7)	35 (15.2)	58.3 (14.7)	68.3 (9.8)	36.7 (12.1)	55.0 (12.2)	68.3 (9.8)

contain multiple dysfluencies (lexical and supralexic) and syllables that expert judges do not agree about. The selection criteria also prevent a dysfluency from being split between different intervals (fragmentation). Minimizing the occurrence of multiple dysfluencies in an interval and prevention of fragmentation of dysfluencies between intervals make incompatible demands about choice of interval duration: Multiple dysfluencies can be reduced by choosing shorter intervals whereas fragmentation is reduced if intervals are made longer. Despite the restrictions on choice of super-intervals, some intervals were found that contained a target syllable of the designated type that occurred in the context of fluent syllables. The fluent syllable contexts, in turn, allowed test intervals to be constructed to establish how noise and starting position affected detectability of dysfluencies by test judges. The selection constraints also determined the duration of the super-intervals. The duration of super-intervals that passed all the tests was 2.71 s for fluent intervals, 2.64 s for prolongation intervals, and 2.60 s for repetition intervals.

B. Effects of noise on detectability of repetitions and prolongations

Error proportions and standard deviations for each target syllable type at the three starting positions and when the three levels of noise were added are shown in Table II averaged over judges. Error rates were relatively high even when there was no noise added to the test intervals because the test judges were only allowed to hear the sound once (when they signaled that they were ready). These data were analyzed by a three-way analysis of variance (ANOVA) with the factors starting position relative to the super-interval (three levels; two, one, or no fluent syllable lead in), noise level (three levels; no noise, 3 dB, and 6 dB), and target syllable type (three levels; fluent, repetition, or prolongation targets).

The main effect of noise level was significant ($F_{2,135} = 26.18, p < 0.001$). This arose, as expected, from higher error rates as noise level increased. Tukey simultaneous tests showed that error rate was significantly higher in the 3-dB ($T = 3.9, p < 0.001$) and 6-dB conditions ($T = 7.2, p < 0.0001$) after adjustment for error rate in the no noise condition and error rate was significantly higher in the 6-dB condition ($T = 3.3, p < 0.005$) after adjustment for error rate in the 3-dB condition. The main effect of target syllable type

was also significant ($F_{2,135} = 123.39, p < 0.001$) with more errors on repetitions than prolongations and more errors of prolongations than fluents. Tukey simultaneous tests showed that error rate was significantly higher for repetitions ($T = 8.8, p < 0.0001$) and prolongations ($T = 15.6, p < 0.0001$) after adjustment for fluent error rate and error rate for prolongations was significantly higher ($T = 6.9, p < 0.0001$) after adjustment for error rate on repetitions.

The hypothesis, presented in the Introduction, that repetitions will be more affected than prolongations by noise predicts an interaction between noise level and target syllable type. This interaction was significant ($F_{4,135} = 5.17, p = 0.001$). Inspection of the data in Table II shows that the percentage increase in errors with increasing noise level was biggest for repetitions for each of the three starting positions (the difference in percentages between no noise and 6 dB of noise was 38.3%, 33.3%, and 31.6%), next biggest for prolongations (20.0%, 15.0%, and 15.0%), and least of all for fluents (5.0%, 10.0%, and 3.4%). Thus it appears to be the case that repetitions are most affected by noise and prolongations are next-most affected, as hypothesized. The interaction between starting position and target syllable type was also significant ($F_{4,135} = 2.76, p = 0.03$). The data show that prolongations are least error prone when they appear late in the test interval (a bigger preview), whereas the converse is true of repetitions and fluents.

III. DISCUSSION

A. Effect on distribution of intervals of selection criteria

The findings have relevance for choice of an appropriate assessment procedure for research purposes on stuttering in general. The current study shows that intervals less than 3 s long that contain one and only one type of lexical dysfluency are rare in connected speech. More intervals would occur if longer lexical and supralexic dysfluencies (occupying up to the entire interval) were allowed. Such long dysfluencies are more likely to be fragmented between intervals when the intervals are randomly imposed (this can also happen even with short lexical dysfluencies). This can lead to one dysfluency affecting two adjacent intervals. It can also lead to dysfluencies being missed as when word or phrase repetitions consisting of a single repetition are split at the point where

the repetition recommences. These observations make application of time-interval analysis procedures to, for instance, assessing the effects of frequency-shifted feedback (Ingham *et al.*, 1997) problematic.

Time interval analysis procedures have the advantage that they are relatively quick and easy to perform in comparison with current assessments. It is not clear, however, how the results of such procedures should be interpreted. Though they appear to give an indication of treatment outcome, as discussed in the preceding paragraph (Ingham *et al.*, 1997) they bias these estimates by underestimating dysfluencies on some occasions and inflating them on others. The dominant effect appears to be to overestimate stuttering. Thus as seen in Ingham *et al.*'s (1997) data where 5-s randomly selected intervals were used, the vast majority of intervals are judged as dysfluent leading to ceiling effects. The problem with the use of this technique for diagnostic and prognostic indications is that it does not allow dysfluency types, known to be important for each of these topics, to be assessed. These indicators are discussed further in the following section.

B. Effects of noise on detectability of repetitions and prolongations

The effects of noise on assessments of repetition and prolongation show that comparison of performance across recording environments with different noise levels distorts fluency assessment. They also underline the fact that details of the recording environment (including microphones, test rooms, and so on) need to be as noise-free as possible. Without these precautions, it is likely that stuttering will be underestimated since the results show that repetitions, in particular, as well as prolongations to some extent tend to be designated fluent whereas fluent intervals are relatively infrequently called repetition or prolongation. There should also be agreed specifications about minimum recording standards that need to be met to conform to clinical and research requirements.

The first specific implication about noise affecting dysfluent classes differentially follows from the finding that noise leads to stuttering incidence being underestimated. This has significance for diagnosis as missed dysfluencies, by definition, would underestimate stuttering frequency. Similarly, if by chance noise level increases over recordings made during and after treatment, this could lead to spurious apparent improvements. It would also lead to prognostic indications being missed and distorted. So, for instance, Conture's (1990) view is that a change from a predominance of repetitions in a child's speech to a high proportion of prolongations is a sign that the disorder is worsening. This would appear to happen if speech recorded from a noisy environment was compared with one recorded in a quiet environment due to noise affecting repetitions more than prolongations. Alternatively if an initial assessment made in quiet was compared with one in noise, a judge might miss this telltale sign.

A second important finding in this study is that detectability of repetitions and prolongations in noise is affected by the position that they occupy in a test interval. For one thing,

if intervals are used, the differential detectability could affect diagnostic and prognostic indications in a similar way to that discussed in the previous paragraph. Also, the findings may have theoretical significance. A breakdown in fluency that results in a prolongation may arise from speech changes made in the prior context whereas a repetition breakdown may occur before a problematic word (Au-Yeung *et al.*, in press).

One difference between the stimuli used in Ingham *et al.*'s (1997) time interval analysis procedure and the current one is that the former authors used audiovisual rather than audio alone stimuli. This might be considered a limitation to the investigation of noise in the present study since audiovisual presentation is widely regarded as allowing judges to be more sensitive to stuttering than audio alone. However, this matter is not at all clear cut. Judgments of audiovisual synchrony are less sensitive when in the familiar task of viewing a face when speaking than the less familiar task of watching a person hammering (Dixon and Spitz, 1980). The well-known McGurk effect can also be interpreted as showing a lack of sensitivity to audio information when a face is viewed (McGurk and MacDonald, 1976). In this illusion, the presence of a facial view of a speaker producing a /b/ dubbed with the speaker's production of /g/ leads to perception of /d/. The McGurk effect appears to make a listener less sensitive to the auditory features responsible for perception of plosive stop consonants. A second limitation is that we have not examined the extent to which reduction in intervals due to the selection criteria are ameliorated by allowing more extensive dysfluencies that still occur within the confines of an interval of a specified duration. Though this would make the problem somewhat less acute, it would not remove the problem.

ACKNOWLEDGMENT

This research was supported by a grant from the Wellcome Trust.

¹Howell *et al.* (1997b) took ratings as well as categorizations of each word. Here, since a panel of judges is used, it is possible to dispense with ratings: Control experiments have shown that the results of the panel are monotonically related to ratings given to each syllable.

- Alfonso, P. (1990). "Subject definition and selection criteria for stuttering research in adult subjects," *ASHA Reports* **18**, 15–24.
- Au-Yeung, J., Howell, P., and Pilgrim, L. (in press). "Phonological words and stuttering on function words," *J. Speech. Language Hear. Res.*
- Boehmler, R. M. (1959). "Listener responses to non-fluencies," *J. Speech Hear. Res.* **1**, 132–141.
- Brown, S. F. (1945). "The loci of stuttering in the speech sequence," *J. Speech Disorders* **10**, 181–192.
- Conture, E. G. (1990). *Stuttering*, (Prentice-Hall, Englewood Cliffs, NJ), 2nd ed.
- Dixon, N. F., and Spitz, L. (1980). "The detection of auditory visual desynchrony," *Perception* **9**, 719–721.
- Howell, P. (1993). "Stuttering in childhood," *The Ciba Foundation Bulletin* **35**, 15–16.
- Howell, P., and Young, K. (1991). "The use of prosody in highlighting alteration in repairs from unrestricted speech," *Q. J. Exp. Psychol.* **43(A)**, 733–758.
- Howell, P., Au-Yeung, J., Sackin, S., Glenn, K., and Rustin, L. (1997). "Detection of supralexical dysfluencies in a text read by child stutterers," *J. Fluency Disorders* **22**, 299–307.

- Howell, P., Sackin, S., and Glenn, K. (1997a). "Development of a two-stage procedure for the automatic recognition of dysfluencies in the speech of children who stutter: II. ANN recognition of repetitions and prolongations with supplied word segment markers," *J. Speech, Language Hear. Res.* **40**, 1085–1096.
- Howell, P., Sackin, S., and Glenn, K. (1997b). "Development of a two-stage procedure for the automatic recognition of dysfluencies in the speech of children who stutter: I. Psychometric procedures appropriate for selection of training material for lexical dysfluency classifiers," *J. Speech, Language Hear. Res.* **40**, 1073–1084.
- Howell, P., Sackin, S., Glenn, K., and Au-Yeung, J. (1997). "Automatic stuttering frequency counts," in *Speech Motor Production and Fluency Disorders*, edited by H. Peters, W. Hulstijn, and P. van Lieshout (Elsevier, Amsterdam).
- Ingham, R. J., Cordes, A. K., and Gow, M. L. (1993). "Time-interval measurement of stuttering: Modifying interjudge agreement," *J. Speech Hear. Res.* **36**, 503–515.
- Ingham, R. J., Moglia, R. A., Frank, P., Ingham, J. C., and Cordes, A. K. (1997). "Experimental investigation of the effects of frequency-altered auditory feedback on the speech of adults who stutter," *J. Speech, Language Hear. Res.* **40**, 361–372.
- Kully, D., and Boberg, E. (1988). "An investigation of inter-clinic agreement in the identification of fluent and stuttered syllables," *J. Fluency Disorders* **13**, 309–318.
- Levelt, W. J. M. (1983). "Monitoring and self-repair in speech," *Cognition* **14**, 41–104.
- McGurk, H., and MacDonald, J. (1976). "Hearing lips and seeing voices," *Nature (London)* **264**, 746–748.
- Parducci, A. (1965). "Category judgment: A range-frequency model," *Psychol. Rev.* **17**, 9–16.
- Rabiner, L. R., and Sambur, M. R. (1975). "An algorithm for detecting the endpoints of isolated utterances," *Bell Syst. Tech. J.* **54**, 297–315.
- Rosen, S., and Howell, P. (1981). "Plucks and bows are not categorically perceived," *Percept. Psychophys.* **30**, 1256–1260.
- Scott, S., and Howell, P. (1992). "Infinitely peak clipping speech alters its P-center," in *Proceedings of the Fourth International Congress on Rhythm (C.N.R.S., Paris)*, pp. 151–156.
- Sims, J. T. (1985). "A speech-to-noise ratio measurement algorithm," *J. Acoust. Soc. Am.* **78**, 1671–1674.
- Smith, A. (1997). "A multilayered dynamic approach to stuttering," *Speech Motor Production and Fluency Disorders*, edited by H. Peters, W. Hulstijn, and P. van Lieshout (Elsevier, Amsterdam).
- Watkins, A. J. (1992). "Perceptual compensation for the effects of reverberation on amplitude envelopes—cues to the splay-splay distinction," *Proc. Inst. Acoust.* **14**, 125–132.
- Wingate, M. E. (1988). *The Structure of Stuttering: A Psycholinguistic Study* (Springer-Verlag, New York).

Role of experience for language-specific functional mappings of vowel sounds

Keith R. Kluender^{a)}

Department of Psychology, University of Wisconsin—Madison,
1202 West Johnson Street, Madison, Wisconsin 53706

Andrew J. Lotto

Department of Psychology and Parmly Hearing Institute, Loyola University—Chicago,
6525 North Sheridan Road, Chicago, Illinois 60626

Lori L. Holt

Department of Psychology, University of Wisconsin—Madison,
1202 West Johnson Street, Madison, Wisconsin 53706

Suzi L. Bloedel

Department of Audiology and Speech Pathology, VA Medical Center,
5000 West National Avenue, Milwaukee, Wisconsin 53295

(Received 28 January 1997; revised 16 July 1998; accepted 20 August 1998)

Studies involving human infants and monkeys suggest that experience plays a critical role in modifying how subjects respond to vowel sounds between and within phonemic classes. Experiments with human listeners were conducted to establish appropriate stimulus materials. Then, eight European starlings (*Sturnus vulgaris*) were trained to respond differentially to vowel tokens drawn from stylized distributions for the English vowels /i/ and /l/, or from two distributions of vowel sounds that were orthogonal in the $F1-F2$ plane. Following training, starlings' responses generalized with facility to novel stimuli drawn from these distributions. Responses could be predicted well on the bases of frequencies of the first two formants and distributional characteristics of experienced vowel sounds with a graded structure about the central "prototypical" vowel of the training distributions. Starling responses corresponded closely to adult human judgments of "goodness" for English vowel sounds. Finally, a simple linear association network model trained with vowels drawn from the avian training set provided a good account for the data. Findings suggest that little more than sensitivity to statistical regularities of language input (probability-density distributions) together with organizational processes that serve to enhance distinctiveness may accommodate much of what is known about the functional equivalence of vowel sounds. © 1998 Acoustical Society of America. [S0001-4966(98)00312-9]

PACS numbers: 43.71.An [WS]

INTRODUCTION

Two significant characteristics of the way listeners perceive speech sounds are that experience in a particular language environment has profound effects, and that some acoustic instantiations of a phoneme are perceptually more compelling or effective than others. Although this latter observation has been a common one ever since speech researchers first manipulated natural and synthetic speech signals, for a long while relatively little was made of this fact. Perhaps this was owing to the historical influence of "categorical perception" of speech sounds, by which within-category differences were considered largely irrelevant. A number of studies have revealed the importance of differences between different examples of the same phoneme. For example, some speech stimuli served as more effective adapters in selective adaptation studies (Miller *et al.*, 1983; Samuel, 1982), and some stimuli served as better competitors in dichotic competition experiments (Miller, 1977; Repp, 1977). More recent studies have incorporated explicit

judgments of the degree to which particular stimulus is perceived as a good example of a particular phonetic segment (Grieser and Kuhl, 1989; Iverson and Kuhl, 1995; Kuhl, 1991; Miller and Volaitis, 1989; Volaitis and Miller, 1992).

The research effort reported here concerns developmental aspects of responding to vowel-sound distributions in a graded and language-specific manner. By the age of 6 months, infants respond to vowel sounds in a language-appropriate fashion even when stimuli overlap considerably along acoustic dimensions that are less directly relevant to vowel identity (Kuhl, 1983). Using a reinforced head turn paradigm, Kuhl trained infants to turn their heads only when the phonemic quality of a repeating background stimulus changed between the relatively similar synthesized vowels /a/ and /ɔ/ modeled after male utterances. When tested on novel synthesized vowels /a/ and /ɔ/ modeled after utterances by women and children (adding variation in pitch contour in addition to shifting absolute frequency of formants), infants provided the correct response as defined by phonemic (functional) equivalence despite talker and fundamental-frequency (f_0) changes.

While this earlier study attests to the ability of infants to

^{a)}Electronic mail: kluender@mac.wisc.edu

respond equivalently to vowels in the face of phonemically irrelevant variation, more recent studies by Kuhl and her colleagues (Grieser and Kuhl, 1989; Iverson and Kuhl, 1995; Kuhl, 1991) have investigated how responses to vowel sounds vary across acoustic/auditory dimensions that are directly relevant phonemically. In these cases, instances of the same vowel differing in acoustic/auditory dimensions seem not to be perceptually equivalent for either 6-month olds or adults. Using a reinforced head-turn paradigm, Grieser and Kuhl (1989) examined the extent to which six-month-old infants responded to a change from a repeating background /i/ stimulus to another variant of /i/ drawn from a distribution of /i/ examples. They found that the degree to which infants responded to a change from the background stimulus to another variant of the vowel was less when the background stimulus was a vowel judged by adult listeners to be near ideal or “prototypical,” Kuhl (1991) conceptualized this as a “perceptual magnet effect” and suggested that infants come to internalize vowel category prototypes similar to those for adults, and that variants of the vowel category are perceptually assimilated to the prototype or “Native Language Magnet” (Kuhl, 1993) to a greater degree than could be explained by psychophysical distance alone.

As might be expected, whether one of the comparison stimuli was a “prototype” or not, greater acoustic/auditory distance resulted in greater discriminability, and infants were generally more likely to respond when acoustic/auditory differences were greater. This fact makes the results a bit more difficult to interpret with regard to the process by which infants respond differentially. In a sense, the paradigm pitted the infant’s ability to discriminate two vowel tokens against the infant’s tendency to respond equivalently to discriminably different vowels that share some functional equivalence. By analogy, one would not wish to suggest that infants were incapable of detecting gender and age differences in Kuhl’s (1983) experiments with the vowels /a/ and /ɔ/. In any event, these studies (Grieser and Kuhl, 1989; Kuhl, 1991) demonstrate that infants were less likely to respond (indicating a stimulus change) when the background stimulus represented a relatively good example of the vowel /i/. Kuhl (1991) took this as evidence that there is an internal organization of phonetic categories around prototypic members that is an ontogenetically early aspect of the speech code.

This conclusion is consonant with the ubiquitous finding in psychological studies of categorization that instances of categories or concepts, whether dogs or birds or automobiles, are not equally exemplary. If one infers the existence and nature of internal representations for categories from responses on a variety of tasks, such representations would seem to have a graded structure—often described as being centered around an ideal or “prototypical” instance of the category (Rosch, 1975, 1978). For now, the present authors are agnostic with regard to the existence of internal representations for categories and are not prepared to require their existence when the data mostly consist of differential responses to functionally near-equivalent instances. Some reservations regarding the utility of posting representations such as phonetic categories will be conveyed in later discussion in this report. Here, the term “category” will be used only

when it is necessary to portray the intentions of other investigators.¹ Also, the terms “prototype” and “prototypical” will be used only for consistency with formulation of these issues by others.² Instead, descriptions of stimulus materials will hew more closely to physical dimensions, and more neutral terminology such as “functional equivalence” or “functional mapping” will be used.

Considerations of terminology aside, Kuhl’s measurements of infants’ differential responses to contrasts between acoustically different instantiations of a given phoneme constitute an important step in understanding how infants come to perceptually organize sounds in a fashion appropriate to their language. More fine-grained analyses of the overall structure of infant functional mappings for vowel sounds (in contrast to establishing only the centroid or prototype) will be especially important, in part because, to a large extent, it is the hallmark of other studies of categorization that such equivalence classes have graded structures with some stimuli (not only prototypes) being better exemplars than others. Goodness judgments by adult listeners (Kuhl, 1991) suggest that, not only do equivalence classes for vowels have the appearance of being structured around a best example or prototype, but also that instances nearer to the best exemplar or prototype are “better” members of the category—an archetypal category structure. Analogous data has been collected for adult classification of consonants (e.g., Iverson and Kuhl, 1995; Massaro, 1987; Miller *et al.*, 1983; Miller and Volaitis, 1989; Samuel, 1982).

What has become apparent is that the degree to which infants treat instances of a vowel distribution equivalently is conditioned by their experience with a particular language. Evidence supporting a role for learning can be found in a study (Kuhl *et al.*, 1992) using the same paradigm as Grieser and Kuhl (1989; Kuhl, 1991) with infants from different language environments. Six-month-old infants raised in Swedish- and English-speaking environments exhibit quite different tendencies to respond to changes from a relatively good example to a relatively poor example of a vowel when tokens are drawn from a distribution corresponding to the Swedish high front rounded vowel /y/ versus a distribution corresponding to the English vowel /i/. Again, for both groups of infants, larger acoustic differences were detected more easily for both native and non-native³ vowel sets. Importantly, however, English infants were much more likely to respond to differences between the relatively good “prototype” high front rounded Swedish vowel /y/ and variants of /y/ than they were to respond to differences between the relatively good “prototype” English /i/ and its variants. The complementary pattern was found for Swedish infants’ responses. The fact that infants are less likely to respond differentially to examples of a vowel common within their language environment is taken as evidence that, by six months of age, infants have begun to treat similarly sounds that correspond to functional groupings in their native-language environment.

By contrast, Kuhl (1991) found that, for rhesus monkey subjects discriminating /i/ and /i/-like sounds in a task methodologically analogous to that used with infants, there was little or no evidence that relatively good /i/ stimuli are per-

ceived as any more similar to other vowel sounds drawn from a distribution of /i/ sounds than are relatively poor instances. Taken together, results with human infants and with monkeys have encouraged a number of researchers to propose that infants possess initial “language-universal” categories that are modified through exposure to the native language to become language-specific categories of adult language users (Miller and Eimas, 1996; for reviews, see Best, 1994; Werker, 1994). Most specifically, Eimas (1991) has argued that there exists an innately given, universal set of phonemes together with processes that enable the infant to map acoustic variants onto phonemic category representations. In addition to being consistent with traditional nativist accounts of language competence (e.g., Halle, 1990; Pinker and Bloom, 1990), innate phonetic categories may be congenial to some essentialist accounts of concepts more generally (Atran, 1987; Gelman and Wellman, 1991; Keil, 1987; Medin and Ortony, 1989).

Kuhl (1991) was initially circumspect with regard to such questions, presenting two potential explanations: “First, infants at birth could be biologically endowed with mechanisms that define vowel prototypes for certain vowels (e.g., the ‘quantal’ vowels) or for all of the vowels in all the languages of the world . . . A second alternative is that the effects are due to experience in listening to a specific language. (p. 105)” More recently, Kuhl (1993) suggests that native-language prototypes are most likely the product of early experience in a language environment. Relatively little has been revealed, however, about putative processes by which learning and experience would shape development of functional (phonemic) equivalence among vowel sounds if, in fact, functional equivalence can be learned. It is necessary to elucidate the processes by which functional equivalences for vowel sounds might arise through experience and learning if they are to arise *de novo*. If equivalence classes (phonetic categories) for different acoustic instantiations of vowels can be a function of experience and general processes of learning, what are the salient characteristics of the resulting response structure? In particular, do patterns of responses to learned vowel equivalence classes bear close resemblance to response patterns measured for infant and adult humans?

The use of nonhuman animal subjects afforded Kuhl (1991) the opportunity to assess vowel discrimination in a model unfettered by extensive experience with distributional properties of vowel sounds. In the present studies, animal models are used to address explicitly questions relating to experience with vowel sounds when language-specific properties are strictly controlled. The aim is to understand better the nature of explicitly learned equivalence classes for vowel sounds to afford comparison with extant measures from human infant and adult listeners. The nonhuman species used is European starlings (*Sturnus vulgaris*), a bird that has been demonstrated to have hearing comparable to humans within the frequency range of human vowel sounds (Dooling *et al.*, 1986; Kuhn *et al.*, 1980, 1982) and appears to share a common mechanism of spectral analysis with many other vertebrates including humans (Dooling *et al.*, 1986).

Because nonhuman animals have been shown to be reasonably adept at responding differentially when presented

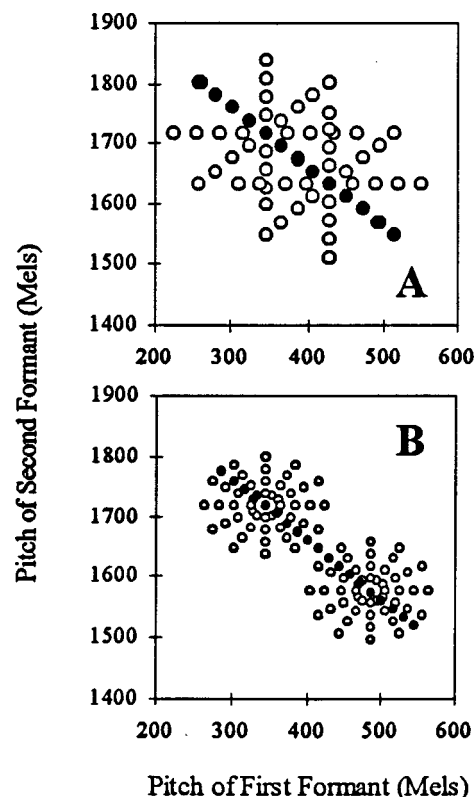


FIG. 1. In the top panel (a), 13 stimuli used in preliminary study (Lotto *et al.*, in press) are represented by filled circles and plotted in mel coordinates corresponding to synthesizer frequency values for F_1 and F_2 . All circles, filled and unfilled, correspond to stimuli used by Kuhl (1991). In the bottom panel (b), 19 vowel stimuli used in experiment 1 are plotted as filled circles in a mel-scaled F_1 – F_2 space. Unfilled circles correspond to F_1 and F_2 values for /i/ and /u/ stimuli used in experiments 2 and 3.

with contrasts between speech sounds (Kluender, 1991; Kluender *et al.*, 1987; Kluender and Lotto, 1994; Kuhl and Miller, 1975, 1978; Kuhl and Padden, 1982, 1983) including vowel sounds (Burdick and Miller, 1975; Kluender and Diehl, 1987), it is not enough simply to demonstrate that starlings can respond differentially to different vowel sounds. If general processes of learning serve to explain perceptual development of speech perception by human infants, then one needs to demonstrate that responses to vowel equivalence classes learned by nonhuman subjects bear close resemblance to response patterns measured for infant and adult humans.

I. EXPERIMENT 1

The present effort began with synthesis of stimuli in accord with the descriptions given by Grieser and Kuhl (1989) and Kuhl (1991). In a preliminary experiment (Lotto *et al.*, in press) a series of stimuli was drawn from their two overlapping distributions of vowel sounds. [See top panel (a) of Fig. 1.] With the exception of durational differences, stimuli were synthesized in accordance with their descriptions. Tokens for each of Kuhl’s (1991) distributions lay on eight spokes radiating from a centroid in a mel-scaled F_1 – F_2 space. Lotto *et al.* (in press) used only the 13 stimuli along the diagonal (filled symbols). Sixteen listeners were asked to judge the quality of these 13 vowel sounds with

respect to whether each sounded most like the vowel in “heat,” “hat,” “hate,” “hit,” “head,” “hood,” or “none of the above.” The most important feature of subjects’ reported percepts is that at least two of the stimuli from Grieser and Kuhl’s (1989) and Kuhl’s (1991) /i/ distribution [top panel (a) of Fig. 1] typically were not perceived as /i/ by this group of listeners. Much more common for these sounds were percepts of /ε/, /e/, and /ɪ/. Because stimuli were not included from other spokes from Kuhl’s (1991) distribution, these data do not address the degree of which other stimuli drawn from that distribution would be perceived as /i/. This observation that some of the tokens intended to be perceived as /i/ by Grieser and Kuhl (1989) and by Kuhl (1991) are not perceived as /i/ is consistent with earlier reports (Iverson and Kuhl, 1995; Lively, 1993; Sussman and Lauckner-Morano, 1995).

In the interest of employing a set of stimuli that would constitute a distribution of reasonably compelling instances of the vowel /i/, a second series of stimuli were synthesized. In order to better delineate a range of acceptable tokens of the vowel /i/, these stimuli were presented to naive listeners for identification.

A. Method

1. Subjects

Sixteen college-age adults served as subjects. For all experiments reported here involving human objects, individuals learned English as their first language and reported normal hearing. All subjects received Introductory Psychology class credit for their participation.

2. Stimuli

Nineteen five-formant vowel stimuli were synthesized using the cascade branch of the Klatt (1980) software synthesizer implemented in CSRE (CSYNTR16; Jamieson *et al.*, 1992) on a microcomputer with 12-bit resolution at a 10-kHz sampling rate and were stored on computer disk. Stimuli were synthesized with parameters chosen from along a diagonal in a mel-scaled $F1$ – $F2$ space [see filled circles in bottom panel (b) of Fig. 1]. In contrast to earlier efforts and in the interest of better circumscribing a region of perceptually acceptable instances of /i/, stimuli were spaced only 20 mel apart along the diagonal. The diagonal was at 45° relative to the mel-scaled $F1$ – $F2$ plane, so the $F1$ and $F2$ mel values of each stimulus were of equal increments or decrements relative to adjacent stimuli. The fifth stimulus from the most extreme (low $F1$, high $F2$) end of the diagonal shared the same $F1$ and $F2$ values as the centroid of the /i/ distribution used previously (Grieser and Kuhl, 1989; Kuhl, 1991) and conformed to mean values for male talkers measured by Peterson and Barney (1952). Center frequencies (Hz) and mel values for $F1$ and $F2$ are listed in Table I. Synthesizer values for $F3$, $F4$, and $F5$ were held constant at 2780, 3300, and 3850 Hz, respectively. Formant bandwidths, $B1$, $B2$, $B3$, $B4$, and $B5$, were 50, 70, 110, 250, and 200 Hz, respectively. Duration of each stimulus was 300 ms. Although Grieser and Kuhl (1989) and Kuhl (1991) used 500-ms stimuli, and Iverson and Kuhl (1995) used 435-ms stimuli, 300 ms was chosen as a reasonable compromise between those rather ex-

TABLE I. Synthesis parameters for first and second formants of stimuli used in experiment 2 depicted as both Hz and mel.

Hertz		mel	
$F1$	$F2$	$F1$	$F2$
221	2421	288	1775
233	2388	303	1760
246	2355	317	1746
258	2322	331	1732
270	2290	345	1718
283	2258	359	1704
295	2226	373	1690
308	2194	387	1676
321	2163	402	1661
334	2132	416	1647
347	2102	430	1633
360	2071	444	1619
374	2041	458	1605
387	2011	472	1590
401	1982	486	1576
415	1953	500	1562
429	1924	515	1548
443	1896	529	1534
457	1868	543	1520

trime durations and shorter more natural durations. Fundamental frequency was held constant at 120 Hz. A 25-ms linear amplitude ramp was imposed on the beginning and end of each stimulus.

3. Procedure

Given the intended application for these stimuli (experiment 2) and the present emphasis upon the range of acceptable /i/ stimuli, a forced-choice identification task was used. Subjects were asked to identify stimuli as /i/ or as /ɪ/. The choice of /ɪ/ as an alternative was based upon the authors’ perception of many of these shorter (300 vs 435 ms) stimuli being better examples of /ɪ/ than of /e/ or /ε/. Stimulus presentation was under control of a microcomputer. Following D/A conversion (Ariel DSP-16), stimuli were low-pass filtered (Frequency Devices 677, cutoff frequency 4.8 kHz) prior to being attenuated (Analog Devices AD7111 digital attenuator), amplified (Stewart HDA4), and played over headphones (Beyer DT-100) at 70 dB SPL. Calibration of presentation level was achieved by first matching the rms level of all stimuli to a 1-kHz tone prior to D/A conversion. Subjects were instructed to press either of two buttons labeled “heat” and “hit” to indicate which of these alternatives best characterized the vowel sound heard on a trial.

B. Results

Data pooled across 16 listeners are presented in Fig. 2. The first nine stimuli were labeled as /i/ quite reliably (greater than 85% of presentations). As $F1$ and $F2$ values increase and decrease, respectively, more stimuli are identified as /ɪ/, not /i/. Based upon this distribution of responses, it was now possible to construct with confidence distributions of /i/ and /ɪ/ exemplars for presentation in the following equivalence class learning experiment.

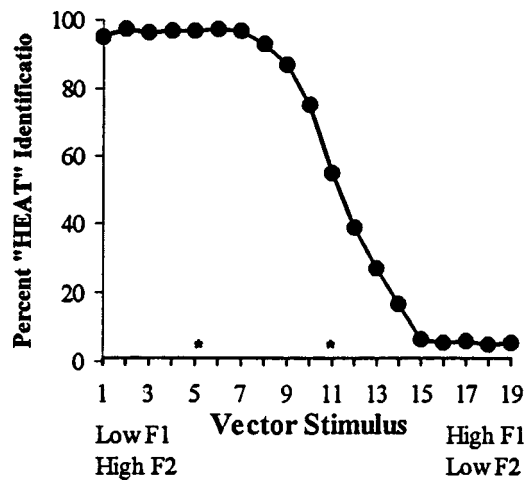


FIG. 2. Identification data from 16 listeners responding "heat" or "hit" when identifying 19 vowel stimuli in experiment 1 and depicted in the bottom panel (b) of Fig. 1. Stimuli 5 and 11 (indicated by *) share $F1$ and $F2$ values with "prototype /i/" and "nonprototype /i/" stimuli, respectively, used by Kuhl (1991).

II. EXPERIMENT 2

Experiment 2 was designed to answer the primary question addressed in this report. If equivalence classes for different acoustic instantiations of a given vowel can be a function of experience and learning, what are the salient characteristics of the resulting response structure? In particular, are response gradients acquired through learning comparable to response gradients measured for infant and adult human listeners? Animal studies of speech perception have been used to assess auditory processes without confounds of effects of experience (e.g., Dooling *et al.*, 1995; Kluender and Lotto, 1994; Kuhl, 1981, 1986, 1991). In contrast, the present study is designed explicitly to engage processes of learning in an animal for which experience with speech sounds can be precisely controlled. European starlings (*Sturnus vulgaris*) were trained to respond differentially to stimuli drawn from distributions of vowel sounds representative of English vowels, /i/ and /ɪ/, or from distributions constructed to be orthogonal to the /i/ and /ɪ/ distributions in a mel-scaled $F1$ - $F2$ plane. These orthogonal distributions roughly correspond to high front rounded vowel /y/ and high mid rounded vowel /ʉ/ like those occurring in Swedish. Half of the birds were assigned as /i-ɪ/ birds, and half were assigned as /y-ʉ/ birds.

A. Method

1. Subjects

Eight European starlings (*Sturnus vulgaris*) served as subjects in the learning experiment. Free-feed weights ranged from 66 to 102 g.

2. Stimuli

A total of 196 vowel stimuli were synthesized representing equal 49 token distributions of the English vowels /i/ and /ɪ/ and of the two orthogonal distributions /y/ and /ʉ/. Distributions for /i/ and /ɪ/ vowels alone are represented in the bottom panel (b) of Fig. 1, and distributions for all four

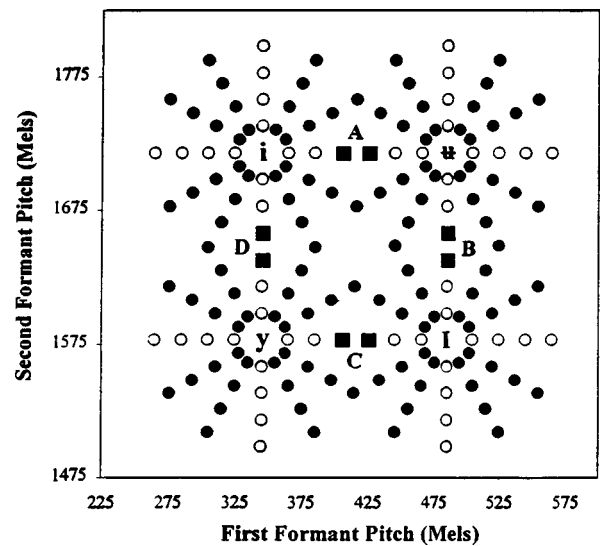


FIG. 3. Mel-scaled plot of 196 vowel stimuli synthesized for experiment 2 representing equal 49-token distributions of the English vowels /i/ and /ɪ/ and vowels approximate to /y/ and /ʉ/. Filled circles represent stimuli used in training. Unfilled circles, filled squares, and the symbols /i/, /ɪ/, /y/, and /ʉ/ (centroids) correspond to stimuli withheld until the testing phase of experiment 2. Squares labeled A, B, C, D correspond to pairs of stimuli used in comparison of between- and within-distribution response strengths.

vowels are shown in Fig. 3. From experiment 1, it is inferred that all 49 examples of /i/ were reasonably good versions of the English vowel /i/. The centroid of /i/ was synthesized with values very close to the mean values for /i/ measured by Peterson and Barney (1952), and the authors perceived all members of the /i/ distribution to be acceptable versions of the English vowel /i/. However, owing partially to the duration of the stimuli, a few instances were not particularly compelling versions of a lax vowel. Centroids for /y/ and /ʉ/ were determined on the basis of considerations other than appropriateness as exemplars of vowels from Swedish or any other language. Instead, centroids for /y/ and /ʉ/ were chosen so that the cluster of four distributions fulfilled a number of experimental desiderata including denser sampling, orthogonality, and evaluation of discrimination versus functional equivalence (categorization).

Of course, none of the vowels closely mimic realistic productions representative of infant experience. Steady-state vowels, with variations of only $F1$ and $F2$ and excluding diphthongal patterns, consonantal contexts, and durational differences, may be pale imitations of the real thing; however, static monophthongal vowels are consistent with previous studies addressing the same and related questions. Although formant values for /y/ closely approximate stimuli used for Kuhl *et al.* (1992), it is unlikely that any of the stimuli in this distribution would constitute particularly good examples of Swedish /y/ for two reasons. First, for Swedish, /y/ is heavily diphthongized, and these sounds are monophthongal. Second, high front rounded vowels have relatively low-frequency $F3$, and the range of $F2$ frequencies used across the distribution preclude the use of $F3$ values appropriate for a high front rounded vowel. Both of these reservations hold for the synthetic versions of Swedish /y/ used by Kuhl *et al.* (1992).

The four distributions of stimuli differed in several ways from the original Grieser and Kuhl (1989) and Kuhl (1991) stimuli. First, 12 spokes of stimuli, instead of 8, emanated from the centroids. Second, stimuli were synthesized along each spoke with $F1$ and $F2$ frequency values corresponding to four 20-mel increments. As seen from experiment 1, the smaller step size afforded a more realistic approximation of the perceptually acceptable area in the $F1$ – $F2$ plane for a given vowel sound. Half again as many spokes and the smaller step size together contributed to more compact distributions that provided a denser sampling of the perceptual space.

There are two other important aspects of these stimulus distributions that bear note. First, each pair of vowel distributions ($/i/-/ɪ/$, $/y/-/ʏ/$) is orthogonal to the other in a mel-scaled space. One virtue of this arrangement is that any confounds related to predispositions of the auditory system or to effects from experience with other sounds can be detected or eliminated.

Second, vowel pairs overlap sufficiently to assess separately the contributions of discrimination versus functional equivalence. This is because some subsets of stimuli that require differential responding by half the subjects do not require differential responding to the other half of the subjects. For example, one can see from stimuli marked by filled squares in Fig. 3 that stimuli to which $/i-ɪ/$ birds should respond differentially (A vs B and C vs D) do not require differential responding by $/y-ʏ/$ birds (A,B both $/ʏ/$ and C,D both $/y/$). These comparisons afford direct measurement of whether subjects respond similarly due to functional equivalence or due to lack of discriminability.

All stimuli for experiment 2 were synthesized with the same values for duration, amplitude contour, f_0 contour, formant bandwidth, $F3$, $F4$, and $F5$ as stimuli from experiment 1. Formant-frequency values for $F1$ and $F2$ at the centroids for the $/i/$ were 270 and 2290 Hz (344.8 and 1718.1 mels as in experiment 1), and 389 and 1986 Hz (484.8 and 1578.1 mels) for $/ɪ/$. First and second formant values for $/i/$ differ minimally from Peterson and Barney (1952) average values of 390 and 1990 Hz for men. Values of $F1$ and $F2$ at the centroids were 270 and 1986 Hz (344.8 and 1578.1 mels) for $/y/$, and 389 and 2290 Hz (484.8 and 1718.1 mels) for $/ʏ/$. Formant frequencies for the other 48 stimuli for each distribution were placed at 20-mel intervals measured from the centroid, 4 on each of the 12 spokes for each distribution.

3. Procedure

Birds were first trained by means of operant procedures to peck differentially to vowels either drawn from distributions for $/i/$ or $/ɪ/$, or drawn from distributions for $/y/$ and $/ʏ/$. Following 5 to 20 h of food deprivation (adjusted to each bird individually for optimal performance⁴), birds were placed in a sound-proof operant chamber (Industrial Acoustics Corp. AC1) inside a larger single-wall sound-proof booth (Suttle Acoustics Corp). In a go/no-go task, birds pecked a single lighted 1.2-cm-square key located 15 cm above the floor and centered below the speaker. For two of the $/i-ɪ/$ birds, pecks to $/i/$ were positively reinforced, while, for the other two, pecks to $/ɪ/$ were positively reinforced. For

two of the $/y-ʏ/$ birds, pecks to $/y/$ were positively reinforced, while, for the other two, pecks to $/ʏ/$ were positively reinforced. Stimuli were presented, responses were recorded, and reinforcement was controlled by a 80286 microcomputer with an Ariel DSP16 A/D–D/A board and custom parallel I/O.

On each trial, a single vowel sound was presented repeatedly once per 1.3 s at an average A-weighted peak level of 70 dB SPL measured at the approximate location of the bird's head (Bruel & Kjaer type 2232). Stimuli were equated for rms energy level prior to attenuation. On a trial-by-trial basis, the intensity of the sound was varied randomly from 70 dB by ± 0 –5 dB [mean=70 dB SPL] through a computer-controlled digital attenuator (Analog Devices 7111). This roving intensity level mitigated the opportunity for responding correctly on the basis of relative loudness. Average duration of each trial was 30 s, varying geometrically from 10 to 65 s. Intertrial interval was 15 s. No sound or light (other than normal chamber illumination) was presented during the intertrial interval. Responses to positive stimuli were reinforced on a variable interval schedule by 1.5–2.0 s access to food from a hopper beneath the peck key. Duration of hopper access was adjusted for each bird for consistent performance across a session. Average interval to reinforcement was 30 s (10 to 65 s), so that positive stimuli were reinforced on an average of once per trial. Note that when a trial was long (e.g., 57 or 65 s) and times to reinforcement were short (e.g., 10 or 12 s), reinforcement was available more than once. Likewise, on shorter positive trials, reinforcement did not become available if time to reinforcement was longer than the trial. Such intermittent reinforcement encouraged consistent peck rates during subsequent non-reinforced test trials. During negative trials, birds were required to refrain from pecking for 5 s in order for presentation of the stimulus to be terminated.

Following magazine training and autoshaping procedures, reinforcement contingencies were gradually introduced over a one-week period in sessions of 60 to 72 trials each. During that first week: mean amplitude of the stimuli was increased from 35 to 70 dB SPL in order to introduce the sound without startling the birds; average trial duration increased from 5 to 30 s; intertrial interval decreased from 40 to 15 s; average time to reinforcement was increased from 5 to 30 s; access to the food hopper was decreased from 4.0 to 2.0 s; and the ratio of positive to negative trials decreased from 4:1 to 1:1.

Birds were trained first to respond differentially to a subset of 64 of the sounds included in their respective pairs of vowel distributions. Training stimuli are represented as filled symbols in Fig. 3. Some stimuli (unfilled symbols and filled squares), including the centroids of the distributions, were withheld from presentation during the training phase of the study. These stimuli were reserved for the test phase in order to be used as novel exemplars to assess the degree of generalization to novel tokens and to assess the response structure in a way that is unconfounded with history of reinforcement. All birds learned quickly to respond correctly to training tokens of $/i/$ versus $/ɪ/$, or $/y/$ versus $/ʏ/$, pecking at least twice as often to positive stimuli versus negative stimuli

Starling Response Strength

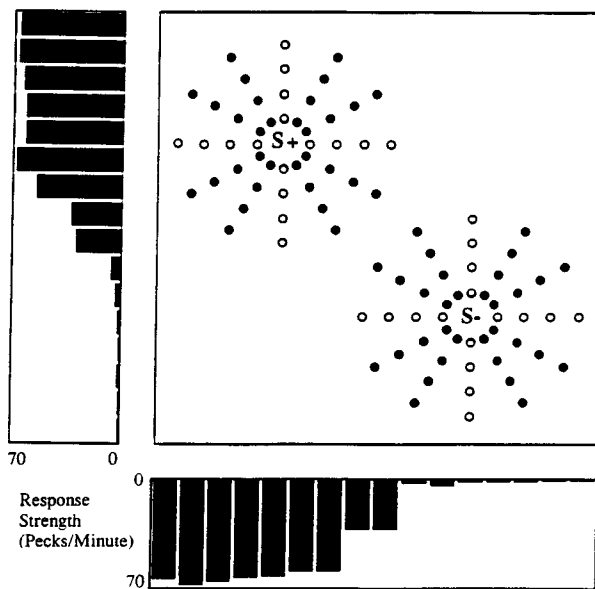


FIG. 4. From experiment 2, adjusted peck rates as a function of $F1$ and $F2$ values are plotted as histograms on x ($F1$) and y ($F2$) axes following rotation/reflections to align responses in the $/i/-/i/$ diagonal. Bar heights correspond to mean peck rates for stimuli with a given $F1$ or $F2$ value following scaling to each bird's maximum peck rate for any stimulus.

at the end of 80 days of training (5120 trials). Birds continued to be trained with the subset of representatives of their distributions for a total of 101 training sessions.

The eight birds were then tested on novel examples [the centroids and other stimuli that had not yet been presented from the birds' respective distributions ($/i/-/i/$, $/y/-/u/$)]. A subset of previously reinforced training stimuli (eight from each vowel-sound distribution) also were tested as test stimuli in this second stage of the experiment to make possible comparisons between experienced exemplars and novel instances of the distributions. Across 50 daily sessions, all 50 test stimuli (34 novel+16 non-novel) were presented 20 times each. During a single test session, 20 novel stimuli were presented individually in 30-s trials. During presentation of novel stimuli, no contingencies were in effect. Birds neither received food reinforcement nor needed to refrain from pecking in order for presentation to terminate after 30 s. Trials with novel stimuli were interspersed among the 64 reinforced trials using non-novel training stimuli. Test trials could not occur until after 15 non-novel stimulus trials had been presented. This assured that each bird "settled in" to the task before responding to test stimuli.

B. Results

Data for all birds across four conditions are displayed in Fig. 4. For each subject, the two highest and two lowest response rates to a given stimulus were not entered into the analyses.⁵ Whether birds were reinforced for pecking to $/i/$, $/l/$, $/y/$, or $/u/$, the same basic patterns of data were seen. There were no systematic differences between $/i/-/i/$ and $/y/-/u/$ birds, nor were there any systematic differences as a consequence of which vowel in a pair was designated positive. Consequently, in order to evaluate performance across

the eight avian subjects, data as a function of $F1$ and $F2$ values were reflected and/or rotated to align positive and negative vowel clusters in the $F1-F2$ plane. Data for cases when $/i/$ was positive were rotated 180 degrees to conform with data for cases when $/i/$ was positive. For $/y/$ and $/u/$, a reflection is required to meet the same end. Values from cases for which $/y/$ was positive were reflected over an $F2$ axis separating $/y/$ from $/i/$. Values from cases for which $/u/$ was positive were reflected over an $F1$ axis separating $/u/$ from $/i/$. Analogous reflections were performed prior to analysis for negative categories. Finally, in order to normalize for individual differences in peck rates, mean peck rates in pecks per minute were converted to percentages of the maximum mean peck rate measured for each bird in response to any test trial.

Multiple linear regression analyses were conducted separately for peck rates to novel positive stimuli and to novel negative stimuli. Three independent variables were entered into the multiple regression analyses: $F1$ value (mels); $F2$ value (mels); and distance from centroid of the distribution (mels). These dimensions are orthogonal, thus avoiding many of the usual concerns regarding multivariate measures. For stimuli to which birds were reinforced for pecking (positive), all three variables contributed significantly to prediction of peck rate. The three-variable regression was statistically significant ($F_{ratio_{3,132}} = 26.37$, $p < 0.0001$, multiple $R = 0.61$). The value of $F2$ had the greatest contribution ($r = 0.52$, $p < 0.001$) followed by $F1$ value ($r = -0.28$, $p < 0.001$) followed by distance from the centroid ($r = -0.14$, $p < 0.05$). Using as an example the two birds for which $/i/$ was the positive vowel, regression analysis indicates that birds pecked most vigorously in response to stimuli with higher $F2$ and lower $F1$, and overlaid upon this pattern is a tendency to peck more rapidly to stimuli closer to the centroid of the distribution of $/i/$ tokens. The same pattern was seen for each vowel distribution: highest rates for high $F1$ and low $F2$ for $/i/$, low $F1$ and low $F2$ for $/y/$, and for high $F1$ and high $F2$ for $/u/$, with enhanced responding near the centroid for all cases.

For stimuli to which birds were trained to refrain from pecking (negative), the same basic pattern was found with all three variables again contributing significantly to prediction of peck rate. The overall regression was significant ($F_{ratio_{3,132}} = 33.22$, $p < 0.0001$, multiple $R = 0.66$). The ordinal relation of the three variables predicting peck rates was the same as for the positive cases. The value of $F2$ had the greatest contribution ($r = 0.46$, $p < 0.001$) followed by $F1$ value ($r = -0.37$, $p < 0.001$) followed by distance from the centroid ($r = 0.28$, $p < 0.001$). Using the same example of the two birds for which $/i/$ was positive and $/i/$ was the negative vowel, the regression analysis indicates that birds pecked least in response to stimuli with lower $F2$ and higher $F1$, and overlaid upon this pattern is a tendency to peck relatively less to stimuli closer to the centroid of the distribution of $/i/$ tokens. The same pattern was seen for each vowel distribution: lowest rates for low $F1$ and high $F2$ for $/i/$, high $F1$ and high $F2$ for $/y/$, and for low $F1$ and low $F2$ for $/u/$, with diminished responding near the centroid for all cases. For both positive and negative stimuli, response rate

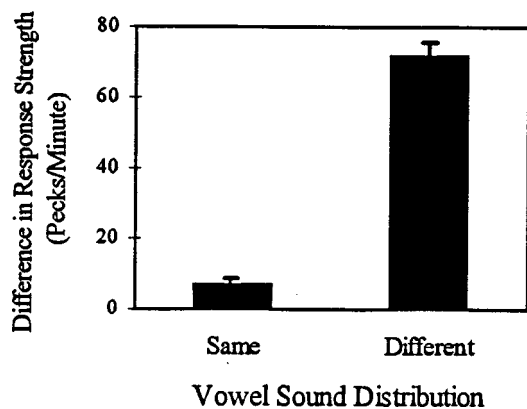


FIG. 5. Average differences in peck rates in response to pairs of stimuli when drawn from the same vowel sound distribution or from different distributions.

for any given stimulus can be reasonably well predicted on the bases of $F1$ and $F2$ values and on the distance from the centroids of the distributions.

The reader may recall that one of the difficulties in interpreting infant responses is that one cannot know whether infants fail to respond because they cannot discriminate two stimuli or because they are treating discriminably different stimuli equivalently. To address this question in the present experiment, distributions had been constructed to overlap in a manner such that some pairs of stimuli were included in a single distribution for one set of birds, but were divided between the two distributions for the other set of birds. Labels **A**, **B**, **C**, and **D** denoted these four pairs in Fig. 3. Analyses of peck rates for these pairs of stimuli indicate that pairs of vowels from the same distribution for one set of birds (e.g., /i–ɪ/) were, indeed, discriminably different for the other set of birds (e.g., /y–ʉ/). Average absolute-value differences in normalized peck rates are plotted in Fig. 5.

When stimuli were assigned to different distributions (**B–C** and **A–D** for /y–ʉ/; **A–B** and **C–D** for /i–ɪ/) the average difference was 71.94 pecks per minute, a significantly greater response difference ($t_{14} = 15.58$, $p < 0.0001$) as compared to an average difference of 7.14 pecks for minute when stimuli were drawn from the same distribution (**A–B** and **C–D** for /y–ʉ/; **B–C** and **A–D** for /i–ɪ/). The fact that differences in peck rates were so much greater for stimuli assigned to different distributions (/i/ vs /ɪ/, /y/ vs /ʉ/) compared to stimuli drawn from the same distribution (/i/, /ɪ/, /y/, or /ʉ/) can be taken as strong evidence that the degree to which stimuli elicit the same response cannot be explained simply as a lack of discriminability. It appears that birds learned to treat discriminably different stimuli as functionally equivalent.

C. Discussion

From the data for the eight birds, several observations can be made. First, relative frequencies of the two primary spectral prominences ($F1$ and $F2$) were good predictors of how these two-vowel spaces became organized for starling subjects. Within the context of general principles of learning, analogous effects are well established and may remind the reader of classical theories of discrimination learning (e.g.,

Spence, 1936, 1937, 1952, 1960). One of the essential facts that these early learning theorists wished to explain was that a positive response to one stimulus ($S+$) was affected by the nature of a second stimulus ($S-$) which discouraged responding. A classic experiment in this regard (Hanson, 1959) demonstrated that the peak of the discrimination function for responses by pigeons that were trained to respond to a visual stimulus at one wavelength ($S+$) would shift to a longer wavelength when $S-$ was a shorter wavelength. Basically, this “peak shift effect” consisted of the response pattern to $S+$ (excitatory) being skewed away from $S-$ (inhibitory).

In the present experiment, strength of responses to stimuli from positive distributions became greater as the frequencies of spectral prominences for $F1$ and $F2$ were more distant from those for the negative distributions. For the example of the vowels /i/ ($S+$) and /ɪ/ ($S-$), response strength increased with decreasing $F1$ and increasing $F2$ frequencies. This pattern is consistent with what one would expect on the basis of precedents in the learning literature. Lest one consider this point to be of significance only as it pertains to a trivial consistency between pigeon and starling performance, it bears note that such behavior is consistent with classic perspectives in phonetics. As Jakobson and Halle wrote in *The Fundamentals of Language* (1971, p. 22) “All phonemes denote nothing but mere otherness.” In this case, the degree to which a stimulus is treated as /i/, /ɪ/, /y/, or /ʉ/ depends considerably upon the degree to which the stimulus is not /ɪ/, /i/, /ʉ/, or /y/, respectively. This tradition was extended, for example, in the simulation studies by Liljencrantz and Lindblom (1972) and later by Lindblom (1986) in which many of the consistencies in vowel systems across languages could be explained by the principle of languages using vowel sounds that are as mutually distinctive as possible in acoustic and/or auditory space. When one considers the present experiment as one for which the task for subjects is to organize a very small vowel space, such “mere otherness” plays an influential role.

However consistent the data may be with regard to precedents in the learning and phonetics literature, there exists a potentially disquieting difference between starling response patterns and previous reports of adult human goodness ratings for distributions of /i/ tokens. Following the necessary reflections, all eight starlings exhibited graded response structures with increasing response strength as the frequencies of $F1$ and $F2$ became more distant from formant frequencies for the opposing vowel distribution. However, Kuhl (1991) found no strong evidence for this sort of anisotropy for goodness judgments by adult humans for stimuli distributed around the same centroid but with 30-mel step sizes. While it is true that the present experiment employed distributions of more densely packed stimuli relative to earlier efforts (e.g., Grieser and Kuhl, 1989; Kuhl, 1991), this difference between human and starling data bears note. Experiment 3 of this report provides adult human judgments of the stimuli used in Experiment 2, and discussion of these discrepancies will receive fuller attention.

Turning now to the third predictor of response strength, consider the fact that response rates were greater for positive distributions and lesser for negative distributions when

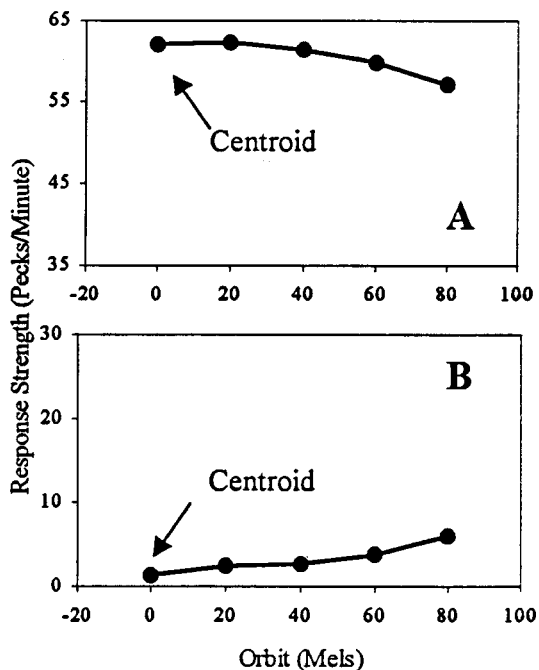


FIG. 6. From experiment 3, adjusted peck rate data averaged across conditions for stimuli at different distances from the centroids of positive (top A) and negative (bottom B) distributions.

stimuli were nearer to centroids of the distributions. Figure 6 displays adjusted peck rate data averaged across conditions for stimuli at different distances from the centroids of positive and negative distributions. Such response patterns—whether derived from ratings of “goodness,” response times in category judgment tasks, or response rates/probabilities—are frequently considered among the hallmarks of “category” structure.

Gradients present for starling data stand in contrast to Kuhl’s (1991) finding that rhesus monkeys showed no evidence of response differences beyond those predicted simply by acoustic/auditory distance. Monkeys were equally proficient discriminating pairs of vowel stimuli when one stimulus was the prototype /i/ as when one stimulus was the poorer rendition (nonprototype) of /i/. Despite the fact that distributions were more densely sampled in the present case, the centroids for /i/ distributions in both studies were near identical to those for Kuhl (1991). There are two reasons not to consider the present results to be at odds. First, Kuhl (1991) used a within-distribution discrimination task; monkeys were reinforced for responding to within-distribution stimulus differences. The present case is more akin to actual use of phonetic distinctions with starlings reinforced for responding to between-distribution differences with no encouragement to respond differentially to within-distribution differences. Second, monkeys did not have the benefit of extensive experience with the distributions of vowel sounds. Of course, this is not analogous to the case for starlings in the present study nor for the comparison case of six-month-old human infants who have been bathed in a half-year exposure to distributions of vowel sounds.

Overall, there is little to recommend a sensory account. The monkey data suggest that differential effects, *vis a vis* the centroid, are not a consequence of any general auditory

predeposition. The fact that starling data did not differ systematically as a function of vowel (/i/, /ɪ/, /y/, /ʌ/) suggests that none of these sounds is privileged in acoustic/auditory terms.

It is beyond the scope of the present report to review theories of categorization; however, it bears note that all theories of categorization strive, at least in part, to explain the ubiquitous finding of graded structure. This is true for the class of probabilistic models which include spreading activation (e.g., Collins and Loftus, 1975) or feature comparison (Smith *et al.*, 1974) and which often include hypothesis of some internal prototype with which particular instances are compared (see, e.g., Posner and Keele, 1968; Strange *et al.*, 1970). Others have proposed that graded structure can be accommodated in exemplar-based models by which stimuli are categorized with reference to stored exemplars of individual experienced instances (e.g., Hintzman and Ludlam, 1980; Medin and Schaffer, 1978). Finally, more recent connectionist models of distributed memory (e.g., Knapp and Anderson, 1984) also result in graded category structure.

One explanation offered for the results of the earlier studies by Kuhl and her colleagues (Grieser and Kuhl, 1989; Iverson and Kuhl, 1995; Kuhl, 1991, 1993) is that vowel “categories” could be conceptualized as being organized around an ideal or prototypical version of the vowel. Kuhl (1993) argues for experience-based versus innate prototypes, and the present data are consistent with this in as much as starlings would be unlikely genetic recipients of prototypes for the human vowel sounds /i/, /ɪ/, /y/, /ʌ/. With respect to humans, Kluender (1994) has made the argument that, in general, principles of natural selection would not encourage innate predispositions for speech sounds that are relatively infrequent among the world’s languages. In this respect, none of the vowels used in this study, with the exception of /i/, occurs with great frequency among languages. Even for very common /i/, acoustic properties can vary considerably across languages.

For the most part, theories of human categorization behavior do not rely upon endowment with innate prototypes or concepts; although, some essentialist accounts of concepts have been influential (Atran, 1987; Gelman and Wellman, 1991; Keil, 1987; Medin and Ortony, 1989). Instead, most attempts to explain categorization behavior make do with the assumption that the environment provides ample structure for experience to define and shape internalized category structure. In the present case with starlings, one would infer that experience with distributional properties of these vowel sounds served as the basis for development of the graded response structures. More specifically, behavior comes to reflect experienced probability-density functions in as much as vowel-sound distributions were more dense nearer to the centroid. Following experiment 3, a simple linear learning model will be presented that tests how, for starlings (and humans), experience with distributional properties of vowel sounds may give rise to graded response structures.

III. EXPERIMENT 3

Starling response gradients, both for /i-ɪ/ birds and for /y-ʌ/ birds, differed from the /i/ category gradient inferred

from adult goodness judgments in Kuhl (1991). In particular, the majority of the variance in human judgments measured in that earlier study by Kuhl could be attributed to distance from the centroid (prototype) with little observable influence of $F1$ and $F2$ frequency *per se*. In the present experiment, a goodness judgment task much like that used by Kuhl (1991) with adult human subjects was used to assess the pattern of relative “goodness” judgments of /i/ and /ɪ/ stimuli used in experiment 2.

A. Method

1. Subjects

Thirteen college-age adults served as subjects. All subjects learned English as their first language, reported normal hearing, and received Introductory Psychology class credit for their participation.

2. Stimuli

All 98 stimuli from the distributions for /i/ and /ɪ/ employed in experiment 2 were used in experiment 3.

3. Procedure

The subjects’ task was to judge all vowel tokens with regard to the extent to which each token constituted a “good” example of the vowel /i/ or the vowel /ɪ/. One to three subjects were tested concurrently in three single-subject sound-proof chambers (Suttle Equipment Corp.) during a single half-hour experimental session. Each of the 98 stimuli was presented six times in random order at an intensity level of 70 dB SPL at a rate of about one stimulus every 3 s. To avoid any bias being introduced by the particular pronunciation of the experimenter, all instructions were written. Subjects were instructed to press one of seven buttons labeled “1 good hit,” “2,” “3,” “4,” “5,” “6,” and “7 good heat” to indicate the degree to which each token sounded like a good example of /i/ or /ɪ/. After selecting one of the seven alternatives, subjects pressed an eighth button to indicate that they were satisfied with their selection. To make certain that subjects were familiar with the range and distribution of the stimulus tokens, the first two blocks of 98 responses were considered practice and were not subjected to further analysis.

B. Results

All subjects had no problems conforming with instructions and completing the task. Patterns of average ratings across the 13 subjects are displayed in Fig. 7. Analogous to the analysis for experiment 2, $F1$ value (mels), $F2$ value (mels), and distance from centroid of the distribution (mels) were entered into the multiple regression analyses. Regression analyses were run separately for responses to stimuli from the /i/ and /ɪ/ distributions. For responses to /i/ stimuli, regression on only two variables was statistically significant (F ratio_{3,634} = 30.20, $p < 0.0001$, multiple $R = 0.35$). The value of $F2$ had the greatest contribution ($r = 0.33$, $p < 0.001$) followed by distance from the centroid ($r = -0.13$, $p < 0.001$). The value of $F1$ did not contribute significantly to predicting the relative goodness of /i/ tokens ($r = -0.04$, $p = 0.34$).

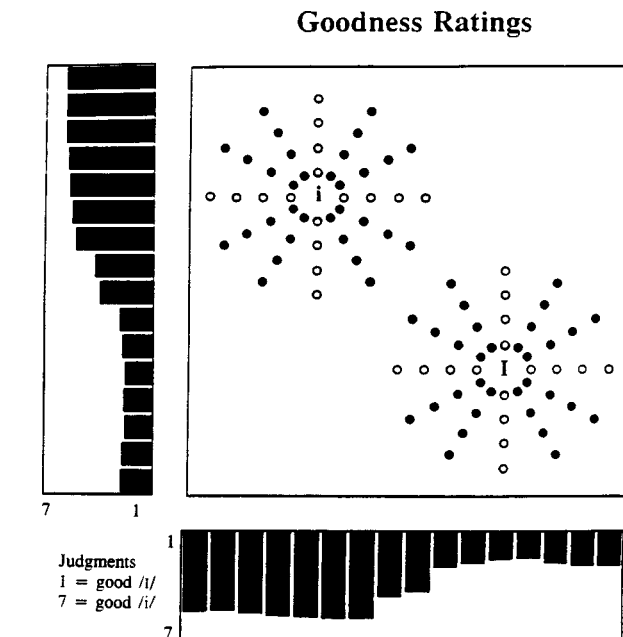


FIG. 7. From experiment 3, average ratings by 13 human listeners of good /i/ (7) to good /ɪ/ (1) for 34 stimuli presented to starlings as novel test stimuli. Histograms are as a function of $F1$ and $F2$ values.

For judgments of /ɪ/, all three variables contributed significantly to prediction of ratings. The three-variable regression was statistically significant (F ratio_{3,634} = 45.88, $p < 0.0001$, multiple $R = 0.42$). Distance from the centroid had the greatest contribution ($r = 0.30$, $p < 0.001$) followed by $F2$ value ($r = 0.24$, $p < 0.001$) followed by value of $F1$ ($r = -0.18$, $p < 0.001$).

Regression analyses were conducted to quantify the correspondence between starling responses to distributions for /i/, /ɪ/, /y/, and /ʉ/ and adult human goodness ratings for the /i/ and /ɪ/ distributions. For starlings, the data consisted of the responses to novel test tokens drawn from respective positive and negative distributions following reflections as before for /i/, /ɪ/, /y/, and /ʉ/. Response rates for these 34 tokens, 17 novel positive tokens and 17 negative, were compared with goodness ratings for corresponding tokens of /i/ and /ɪ/, respectively. The correlation between responses to tokens drawn from positive and negative distributions (for starlings) and goodness judgments of corresponding /i/ and /ɪ/ tokens (for humans) was extremely high ($r = 0.999$, $p < 0.0001$) indicating that, across the two distributions, starling responses and adult human judgments were in generally close correspondence.

Given the source of much of the variance in the data for both human and avian subjects, such substantial correlation may not be surprising. Much of the variance across response rates and across ratings for the two distributions is related to differential responses to two distributions of sounds. Starlings were trained to respond differentially to contrasts between /i/ vs /ɪ/ or /y/ vs /ʉ/, and humans were asked to rate instances of phonemically distinct classes of sounds /i/ and

/i/. Consequently, much of the total variance entered into the correlation analysis can be interpreted with respect to responses being of two distinct types owing to the use of two distinct distributions of sounds. As such, the extremely high degree of shared variance may have more to do with variance between vowel distributions than with variance within vowel distributions, a central focus of this effort.

In order to address correspondences between response patterns within individual vowel distributions, separate regression analyses were conducted for starling responses to novel positive tokens and human judgments of corresponding tokens of /i/, and for starling responses to negative tokens and human judgments of corresponding tokens of /i/. The correlation between starling peck rates to the 17 novel stimuli drawn from positive distributions and human goodness judgments of the corresponding stimuli drawn from the /i/ distribution was substantial ($r=0.671$, $p<0.01$). The correlation between starling peck rates to the 17 novel stimuli drawn from negative distributions and human goodness judgments of stimuli drawn from the /i/ distribution was still greater ($r=0.784$, $p<0.001$).

The choice of /i/ as the benchmark positive distribution was an arbitrary one; /i/ could have been used. Although the lack of systematic variation as a consequence of which vowel was designated positive suggests that this choice ought not matter, two additional regression analyses were conducted. One analysis compared responses to tokens drawn from positive distributions for starlings with goodness judgments for /i/, and one compared responses to tokens drawn from negative distributions for starlings with goodness judgments for /i/. Both of these correlations were comparable to those computed for the previous complementary relationships. The correlation between peck rates in response to novel positive tokens and goodness judgments for corresponding /i/ tokens was significant yielding $r=0.697$ ($p<0.002$). The correlation between responses to novel negative tokens and goodness judgments for corresponding /i/ tokens also was significant yielding $r=0.703$ ($p<0.002$).

Overall, there was a remarkable correspondence between human goodness judgments and starling peck rates. With the exception of the negligible contribution of $F1$ frequency on goodness judgments for /i/, overall pattern of human responses is quite consistent with the starling measures.

Figure 8 displays mean goodness ratings as a function of distance from the centroids of the distributions for /i/ and /ɪ/. This tendency to attribute a greater degree of “goodness” to tokens with formant-frequency values nearer the centroids of these distributions is consistent with Kuhl’s (1991) measurements for a broader distribution of tokens which shared the same /i/ centroid as used in these experiments. Although broad gradients corresponding to values of $F2$ for /i/ judgments and to $F1$ and $F2$ for /ɪ/ judgments do not correspond well to Kuhl’s data, the effects, particularly for /i/ were not unanticipated. Lively (1993) synthesized /i/ stimuli comparable (30-mel rings) to those used by Kuhl (1991), and while his adult human subjects demonstrated a significant effect of distance from the centroid for both “prototype” and “non-prototype” conditions, vowels with higher $F2$ values were given the highest goodness ratings. From Lively’s figures,

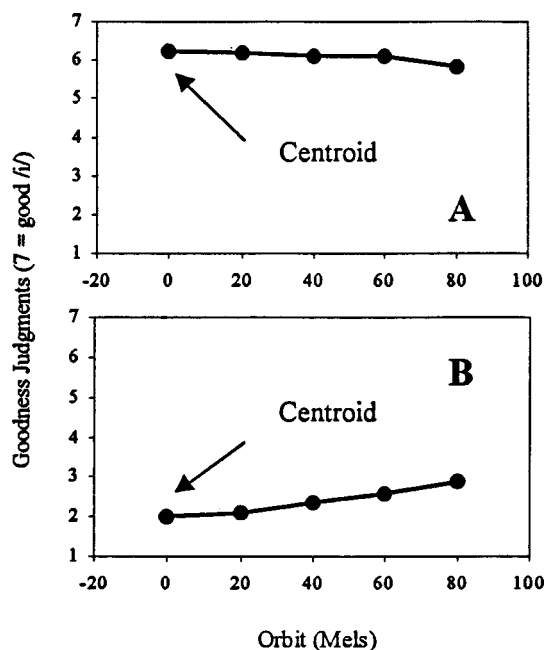


FIG. 8. From experiment 3, average goodness ratings from human listeners for 34 stimuli presented to starlings as novel test stimuli as a function of distance from the centroids of /i/ (top A) and /ɪ/ (bottom B) distributions.

one also can observe that the value of $F1$ played a negligible role in goodness ratings for /i/. Human goodness judgments elicited for tokens from tighter, denser distributions in experiment 3 correspond well with Lively’s (1993) measures of goodness for broader distributions (as used by Kuhl, 1991). Further, starling responses are in close accord with these findings.

One possible explanation for the sizable influence of $F2$ could be that, when $F2$ is relatively high and nearer $F3$, there is some auditory interaction creating a functional $F2$ ($F2'$) that serves to warp perceptual distance in a fashion not captured solely by mel distance (e.g., Johnson, 1989). Typically, the assumption is that $F2'$ can be described as the weighted average of $F2$ and $F3$, thus equal mel steps when $F2$ is near $F3$ result in disproportionately large perceptual distances.

One way in which starling and human performance differed is informative. For human listeners, $F2$ and, to a lesser extent, distance from the centroid accounted for much of the variance in goodness judgments of /i/. For the same listeners, variance in goodness judgments of /i/ was best described in terms of distance from the centroid followed by $F2$ and finally $F1$, all being statistically significant predictors. This contrasts with starling data for which distance from the centroid always is less predictive than $F2$ or $F1$. The more compelling effect of distance from the /i/ centroid for native-English listeners may be due to the fact that for /i/, but not /ɪ/, close neighbors (/ɛ/, /e/, /ɜ:/, and /i/) surround all sides in the $F1$ – $F2$ plane. There is a smaller effect of distance from the centroid for goodness judgments of /i/, which lies at an extreme corner of the vowel space with no neighboring vowels with lower $F1$ or higher $F2$. While extreme versions of /i/ (low $F1$, high $F2$) are most distinctive relative to other English vowel sounds, acoustic instances of /i/ that are most central to the distribution would be maximally distinctive from surrounding vowel sound distributions. What is the

same whether one considers either the minimalist two-vowel spaces presented to starlings or the more-populated English vowel space, a perceptual principle akin to “mere otherness” is observed much as it was suggested to exist in the postulation of “adaptive dispersion” (Lindblom, 1986) as a predictor of the structure of vowel inventories.⁶

C. Minimalist computational model

In order to better understand how a relatively simple organism such as a starling can come to learn a functional mapping of vowel sounds that is so similar to that for humans, a simple linear association network model was simulated using elementary matrix and vector operations. Because the data for starlings and for humans were fairly well accommodated in the linear operations of regression analysis, there was reason to believe that a learning model based solely upon linear operations might provide an adequate and potentially informative account for the data. The model used here can be considered an instantiation of the Hebbian synapse rule (Hebb, 1949), and is a tightly constrained model in which all operations are local and there is no need for the “back-propagation” of errors common to many current network models.

A linear network can be conceptualized as a system of linear algebra equations of the form:

$$\mathbf{A}\mathbf{w}=\mathbf{b}, \quad (1)$$

where \mathbf{A} is a matrix of input exemplars, \mathbf{w} is a vector of connection weights, and \mathbf{b} is a vector of output values. The weights of the network can then be solved for by

$$\mathbf{w}=\mathbf{A}^+\mathbf{b}, \quad (2)$$

where \mathbf{A}^+ is the pseudo-inverse of \mathbf{A} . (For review, see Jordan, 1986.)

Inputs to the network were synthesizer values for $F1$ and $F2$ for each English vowel (/i/ and /ɪ/). Thus, each vowel sound was described as a two-value vector. The 64 vectors for the training stimuli used for /i-ɪ/ birds in experiment 3 were entered into an array \mathbf{A} yielding a 64×2 element input matrix. A 64×1 output matrix \mathbf{b} was created by entering a “1” for the positive stimuli (/i/) and a “0” for the negative stimuli (/ɪ/). Then, Eq. (2) was solved for the 2×1 weight vector \mathbf{w} . This completed the “training” phase. This matrix-algebraic solution is formally equivalent to using a single-layer network for which weights are determined through multiple iterations of exposure to training tokens (Jordan, 1986). In this case, advantage was taken of the fact that the same weights can be derived by solving equations in closed form.

The model then was tested using the 34 novel test stimuli and 16 training stimuli that were presented to birds in trials without contingencies. This constituted a new input matrix \mathbf{A} of dimensions 50×2 . This matrix was multiplied by the 2×1 weight vector derived in the “training” phase to yield a 1×50 vector of values corresponding to the output values (between 0 and 1) for each of the test stimuli.

Comparisons between the model output for test stimuli and avian peck rates to the same stimuli reveal a number of similarities. As was the case for bird responses, model output

exhibited a gradient across values of $F1$ and $F2$ such that greater and lower outputs occur for those stimuli with extreme formant values. Also, there is a similar “prototype” effect in as much as output values respect the probability-density distribution of the input with relatively higher or lower values nearer the centroids of the positive and negative distributions, respectively. Correlation coefficients were computed comparing model output and peck rates for /i-ɪ/ birds reinforced for pecking either to /i/ or to /ɪ/. For the /i/ positive case, $r=0.926$, $p<0.0001$. For the /ɪ/ positive case, $r=0.919$, $p<0.0001$. As was the case for comparisons between avian responses and human goodness judgments, comparisons also were made between model outputs and avian responses to stimuli within individual vowel distributions. The correlation between starling peck rates to the 17 novel stimuli drawn from positive distributions and model predictions for the corresponding stimuli drawn from the /i/ distribution was $r=0.678$, $p<0.01$. The correlation between starling peck rates to the 17 novel stimuli drawn from negative distributions and model predictions for stimuli drawn from the /ɪ/ distribution was greater $r=0.730$, $p<0.01$. It appears that this minimalist perceptron model may provide respectable predictive power.

It should be emphasized that the purpose of this simulation exercise was not to propose that the learning process for either human infants or starlings must reduce to a simple model of this type. Although this model can be cast as a “neural network” model and could enjoy the allusion to neural processing, no such claims are being made here. It does bear note, however, that such a model engenders biologically plausible operations in the sense that connections are local and weight adjustments follow simple Hebbian rules. Nevertheless, the model is likely too simplistic and contextually isolated at present to be suggested as a model for neural activity in avian, let alone human brains. What is important is that there is reason to hope that the processes by which human infants (and starlings) come to organize vowel sounds in a language-specific fashion may be explainable by rather elegant and possibly linear processes.

IV. GENERAL DISCUSSION

The present effort began with the fundamental question of how perceptual behavior of human infants could come to respect language-specific equivalence classes for speech sounds through experience and learning if such classes were to arise *de novo*. Earlier findings (Kuhl, 1991) using nonhuman subjects suggested that, for vowel sounds at least, properties of mammalian auditory sensory systems do not, by themselves, give rise to functional equivalence classes appropriate to linguistic sound systems. This evidence, together with studies (Kuhl, 1983; Kuhl *et al.*, 1992) demonstrating that, by six months of age, infants respond to acoustically different vowel sounds in a fashion that respects their functional equivalence within a language environment, suggests an essential role of early experience. While Kuhl (1991) took advantage of animal subjects to minimize effects of experience with speech sounds in order to evaluate raw sensory

abilities, the present studies exploited the opportunity to embrace and control experience with approximations to natural distributions of speech sounds.

Following an experiment which established the appropriateness of stimulus materials for this effort, it was found that starlings could learn functional equivalence classes of vowel sounds that were representative of the English vowels /i/ and /ɪ/ as well as control stimuli /y/ and /u/. Starlings generalized to novel instances of these distributions, and there was evidence that equivalent responses to different tokens drawn from the same distributions of vowel sounds were not indicative of a lack of discriminative capacity. In fact, avian subjects that learned to treat orthogonal (in $F1-F2$ space) distributions equivalently were facile in responding differentially to the same pairs of stimuli treated equivalently by other subjects.

Both across and within vowel distributions, there was remarkable agreement between measures of starling response strength (peck rate) and human goodness judgments of the same English vowel sounds. To the extent that divergence between starling and human performance was found (greater effect of distance from centroid for /ɪ/), it is likely explainable on the basis of experience with vowel sounds encountered by native-English human listeners but not by starling subjects. Taken together, human and avian results suggest that the process of mapping a space of vowel sounds may be in accord with long-held principles of “mere otherness” and “adaptive dispersion.”

A very simple linear associative model was used to assess starling performance. When the model was permitted the same range of “experience” with distributions of vowel sounds as starlings were, response strengths to individual vowel sounds from the model and birds were in close agreement. Although no claims should be made about the verisimilitude of the computational simulation as compared with biological instantiations of these processes by humans or by birds, the model does present an existence proof that a simple linear system can result in functional mappings of vowel sounds in similarly graded and language-specific fashion. In particular, simulation results do suggest that relatively elegant solutions may exist to explain how subjects with brains of little volume come to exhibit response patterns that are strikingly like those measured for human subjects for the same vowel sounds. Avian and computational performances taken together, it may be appropriate to exhibit some caution before one either posits the requirement of innate specific predispositions for phonetic categories, or hypothesizes the existence of internal prototypes for phonetic categories through whatever process. Neither starlings nor perceptrons have the privilege of inheriting human phonetic categories, and peaks in response gradients allude to, but do not require, putative prototypes. In a similar spirit (Lacerda, 1998) has introduced an exemplar-based model inspired by neuronal group selection theory (Edelman, 1987) that further demonstrates that constructs such as prototypes are unnecessary to account for extent data for human adults and infants responding to vowel sounds.

It well may be the case that rather general processes of learning can accommodate much of what is known about the

functional equivalence of vowel sounds within the vowel space of a language environment. This demonstration of the efficacy of simple learning via distributional properties at the phonetic level is consonant with recent demonstrations that statistical relationships between neighboring speech sounds can be used by 8-month-old infants at the morphemic level for word segmentation (Saffran *et al.*, 1996). When one considers the task assigned to the infant language learner, it may be possible for young listeners to establish their nascent lexicons through little more than sensitivity to statistical regularities of language input together with organizational processes that serve to enhance distinctiveness of regions in that input.

ACKNOWLEDGMENTS

The authors thank Carol Fowler, Francisco Lacerda, Arthur Samuel, and Winifred Strange for thoughtful comments on an earlier draft of this manuscript. This work was supported by NIDCD Grant No. DC-00719 and NSF Young Investigator Award DBS-9258482 to the first author.

¹Among concerns one may have regarding the use of the term “category” is the fact that the term is used in at least three different ways. First, the term most commonly is used to refer to a group of objects or events in the world that more or less share some set of attributes. Second, the term “category” often is used to refer to a set of objects or events that give rise to similar behavior, i.e., functional equivalence. Third, the term is sometimes used with reference to some internal cognitive representation which may or may not be defined by a prototype. Putatively, this internal representation serves to mediate the relation between sensory information and behavior.

²Kuhl (1991) was similarly circumspect with regard to her use of “prototype” with respect to internal representations of phonetic categories. In the cognitive psychology categorization literature, behavior that has been attributed to the existence of prototypes also has been attributed to exemplar models that do not require categories to be defined by reference to a single representation of the category (see, e.g., Brooks, 1978; Knapp and Anderson, 1984; Medin and Schaffer, 1978; Nelson, 1974; Reed, 1972). While there are significant differences both within and between different prototype and exemplar models of categorization, for now, it will be adequate to understand that, for all of these theoretical approaches, categories are taken to exhibit structure such that not all instances of a category constitute equally good category members. Kuhl (1991, 1993) accepts both prototype and exemplar models as plausible with respect to phonetic categories.

³The Swedish vowel system does include a variant of the vowel [i]; however, Swedish /i/ is substantially different acoustically from English /i/ and the /i/ “prototype” used in Kuhl *et al.*'s (1992) study was not typical of Swedish /i/.

⁴Optimal performance was defined as the highest ratio of pecks to positive versus negative stimuli. Birds were idiosyncratic with regard to the amount of deprivation that resulted in the most stable performance, and weights ranged from 80% to 90% of free-feed weights at the time of training/testing.

⁵Extreme values were deleted to account for the fact that behavior of the birds can be affected by motivational factors irrelevant to the questions of interest. For example, a very hungry subject will peck more vigorously and indiscriminantly, often early in a test session, and relatively satiated birds will decrease peck rates overall toward the end of some sessions. Truncation of both extremes is an unbiased method of avoiding such aberrant data.

⁶One would expect that, if nonhuman subjects must respond differentially to more than two vowels (e.g., the four front vowels /i/, /ɪ/, /e/, and /æ/), a greater effect of distance from the centroid should be found for /ɪ/ and /e/ owing to the requirement of distinctiveness from flanking neighbors. The authors presently are conducting such an experiment.

Atran, S. (1987). “Folkbiological universals as common sense,” *Noam Chomsky: Consensus and Controversy*, edited by S. Modgil and C. Modgil (Falmer, Philadelphia).

- Best, C. T. (1994). "The emergence of native-language phonological influences in infants: A perceptual assimilation model," in *The Development of Speech Perception: The Transition from Speech Sounds to Spoken Words*, edited by J. V. Goodman and H. C. Nusbaum (MIT, Cambridge, MA), pp. 167–224.
- Brooks, L. (1978). "Non-analytical concept formation and memory for instances," in *Cognition and Categorization*, edited by E. Rosch and B. Lloyd (Erlbaum, Hillsdale, NJ), pp. 169–211.
- Burdick, C. K., and Miller, J. D. (1975). "Speech perception by the chinchilla: Discrimination of sustained /a/ and /i/," *J. Acoust. Soc. Am.* **58**, 415–427.
- Collins, A. M., and Loftus, E. F. (1975). "A spreading-activation theory of semantic processing," *Psychol. Rev.* **82**, 407–428.
- Dooling, R. J., Best, C. T., and Brown, S. D. (1995). "Discrimination of synthetic full-formant and sinewave /ra-la/ continua by budgerigars (*Melopsittacus undulatus*) and zebra finches (*Taeniopygia guttata*)," *J. Acoust. Soc. Am.* **97**, 1839–1846.
- Dooling, R. J., Okanoya, K., Dowling, J., and Hulse, S. (1986). "Hearing in the starling (*Sturnus vulgaris*): Absolute thresholds and critical ratios," *Bull. Psychonomic Soc.* **24**, 462–464.
- Edelman, G. (1987). *Neural Darwinism: The Theory of Neuronal Group Selection* (Basic Books, New York).
- Elimas, P. D. (1991). "Comment: Some effects of language acquisition on speech perception," in *Modularity and the Motor Theory of Speech Perception*, edited by I. G. Mattingly and M. Studdert-Kennedy (Erlbaum, Hillsdale, NJ), pp. 111–116.
- Gelman, S. A., and Wellman, H. M. (1991). "Insides and essences: Early understandings of the non-obvious," *Cognition* **23**, 183–209.
- Grieser, D., and Kuhl, P. K. (1989). "Categorization of speech by infants: Support for speech-sound prototypes," *Dev. Psych.* **25**, 577–588.
- Halle, M. (1990). "Phonology," in *An Invitation to Cognitive Science: Language*, edited by D. N. Osherson and H. Lasnik (MIT, Cambridge, MA), pp. 43–68.
- Hansen, H. M. (1959). "Effects of discrimination training on stimulus generalization," *J. Exp. Psychol.* **58**, 321–372.
- Hebb, D. O. (1949). *The Organization of Behavior* (Wiley, New York).
- Hintzman, D. L., and Ludlam, G. (1980). "Differential forgetting of prototypes and old instances: Simulation by an exemplar-based classification model," *Mem. Cog.* **8**, 378–382.
- Iverson, P., and Kuhl, P. (1995). "Mapping the perceptual magnet effect for speech using signal detection theory and multidimensional scaling," *J. Acoust. Soc. Am.* **97**, 553–562.
- Jakobson, R., and Halle, M. (1971). *The Fundamentals of Language* (Mouton, The Hague).
- Jamieson, D. J., Ramji, K. V., Kheirallah, I., and Nearey, T. M. (1992). "CSRE: A speech research environment," in *Proceedings ICSLP 92*, edited by J. Ohala, T. Nearey, B. Derwing, M. Hodge, and G. Wiebe (Univ. Alberta, Edmonton, AB), pp. 1127–1130.
- Johnson, K. (1989). "Higher formant normalization results from auditory integration of F2 and F3," *Percept. Psychophys.* **46**, 174–180.
- Jordan, M. I. (1986). "An introduction to linear algebra in parallel distributed processing," in *Distributed Processing: Explorations in the Microstructure of Cognition, Vol. 1: Foundations*, edited by D. E. Rumelhart and J. L. McClelland (MIT, Cambridge, MA), pp. 365–422.
- Keil, F. C. (1987). "Conceptual development and category structure," in *Concepts and Conceptual Development: Ecological and Intellectual Factors in Categorization*, edited by U. Neisser (Cambridge U. P., Cambridge), pp. 175–200.
- Klatt, D. H. (1980). "Software for a cascade/parallel formant synthesizer," *J. Acoust. Soc. Am.* **67**, 971–995.
- Kluender, K. R. (1991). "Effects of first formant onset properties on voicing judgments result from processes not specific to humans," *J. Acoust. Soc. Am.* **90**, 83–96.
- Kluender, K. R. (1994). "Speech perception as a tractable problem in cognitive science," in *Handbook of Psycholinguistics*, edited by M. A. Gernsbacher (Academic, San Diego, CA), pp. 173–217.
- Kluender, K. R., and Diehl, R. L. (1987). "Use of multiple speech dimensions in concept formation by Japanese quail," *J. Acoust. Soc. Am. Suppl.* **1** **82**, S84.
- Kluender, K. R., and Lotto, A. J. (1994). "Effects of first formant onset frequency on [-voice] judgments result from general auditory processes not specific to humans," *J. Acoust. Soc. Am.* **95**, 1044–1052.
- Kluender, K. R., Diehl, R. L., and Killeen, P. R. (1987). "Japanese Quail can learn phonetic categories," *Science* **237**, 1195–1197.
- Knapp, A. G., and Anderson, J. A. (1984). "Theory of categorization based on distributed memory storage," *J. Exp. Psychol.* **10**, 616–637.
- Kuhl, P. K. (1981). "Discrimination of speech by nonhuman animals: Basic sensitivities conducive to the perception of speech-sound categories," *J. Acoust. Soc. Am.* **70**, 340–349.
- Kuhl, P. K. (1983). "Perception of auditory equivalence classes for speech in early infancy," *Inf. Beh. Dev.* **6**, 263–285.
- Kuhl, P. K. (1986). "Theoretical contributions of tests on animals to the special-mechanisms debate in speech," *Exp. Biol.* **45**, 233–265.
- Kuhl, P. K. (1991). "Human adults and human infants show a 'perceptual magnet effect' for the prototypes of speech categories, monkeys do not," *Percept. Psychophys.* **50**, 93–107.
- Kuhl, P. K. (1993). "Innate predispositions and the effects of experience in speech perception: The Native Language Magnet Theory," in *Developmental Neurocognition: Speech and Face Processing in the First Year of Life*, edited by D. de Boysson-Bardies et al. (Kluwer Academic, The Hague), pp. 259–274.
- Kuhl, P. K., and Miller, J. D. (1975). "Speech perception by the chinchilla: Voiced-voiceless distinction in the alveolar-plosive consonants," *Science* **190**, 69–72.
- Kuhl, P. K., and Miller, J. D. (1978). "Speech perception by the chinchilla: Identification functions for synthetic VOT stimuli," *J. Acoust. Soc. Am.* **63**, 905–917.
- Kuhl, P. K., and Padden, D. M. (1982). "Enhanced discriminability at the phonetic boundaries for the voicing feature in macaques," *Percept. Psychophys.* **32**, 542–550.
- Kuhl, P. K., and Padden, D. M. (1983). "Enhanced discriminability at the phonetic boundaries for the place feature in macaques," *J. Acoust. Soc. Am.* **73**, 1003–1010.
- Kuhl, P. K., Williams, K. A., Lacerda, F., Stevens, K. N., and Lindblom, B. (1992). "Linguistic experience alters phonetic perception in infants six-months of age," *Science* **255**, 606–608.
- Kuhn, A., Leppelsack, H. J., and Schwartzkopff, J. (1980). "Measurement of frequency discrimination in the starling (*Sturnus vulgaris*) by conditioning of heart rate," *Naturwissenschaften* **67**, 102–103.
- Kuhn, A., Muller, C. M., Leppelsack, H. J., and Schwartzkopff, J. (1982). "Heart-rate conditioning used for determination of auditory threshold in the starling," *Naturwissenschaften* **69**, 245–246.
- Lacerda, F. (1998). "An exemplar-based account of emergent phonetic categories," *J. Acoust. Soc. Am.* **103**, 2980(A).
- Liljencrantz, J., and Lindblom, B. (1972). "Numerical stimulation of vowel quality systems: The role of perceptual contrast," *Language* **48**, 839–862.
- Lindblom, B. (1986). "Phonetic universals in vowel systems," in *Experimental Phonology*, edited by J. J. Ohala and J. J. Jaeger (Academic, Orlando, FL), pp. 13–44.
- Lively, S. E. (1993). "An examination of the perceptual magnet effect," *J. Acoust. Soc. Am.* **93**, 2423.
- Lotto, A. J., Kluender, K. R., and Holt, L. L. (in press). "Effects of language experience on perceptual organization of vowel sounds," in *Papers in Laboratory Phonology V*, edited by M. Broe and J. Pierrehumbert (Cambridge U. P., Cambridge).
- Massaro, D. W. (1987). "Categorical partition: A fuzzy logical model of categorization behavior," in *Categorical Perception*, edited by S. Harnad (Cambridge U. P., Cambridge), pp. 254–283.
- Medin, D. L., and Ortony, A. (1989). "Psychological essentialism," in *Similarity and Analogical Reasoning*, edited by S. Vosniadou and A. Ortony (Cambridge U. P., New York), pp. 179–195.
- Medin, D. L., and Schaffer, M. M. (1978). "A context theory of classification learning," *Psychol. Rev.* **85**, 207–238.
- Miller, J. L. (1977). "Properties of feature detectors for VOT: The voiceless channel of analysis," *J. Acoust. Soc. Am.* **62**, 641–648.
- Miller, J. L., and Eimas, P. D. (1996). "Internal structure of voicing categories in early infancy," *Percept. Psychophys.* **58**, 1157–1167.
- Miller, J. L., and Volaitis, L. E. (1989). "Effect of speaking rate on the perceptual structure of a phonetic category," *Percept. Psychophys.* **46**, 505–512.
- Miller, J. L., Connine, C. M., Schermer, T. M., and Kluender, K. R. (1983). "A possible auditory basis for internal structure of phonetic categories," *J. Acoust. Soc. Am.* **73**, 2124–2133.
- Nelson, K. (1974). "Concept, word, and sentence: Interrelations in acquisition and development," *Psychol. Rev.* **81**, 267–248.
- Peterson, G. E., and Barney, H. L. (1952). "Control methods used in a study of the vowels," *J. Acoust. Soc. Am.* **24**, 175–184.

- Pinker, S., and Bloom, P. (1990). "Natural language and natural selection," *Behav. Brain Sci.* **13**, 707–784.
- Posner, M. I., and Keele, S. W. (1968). "On the genesis of abstract ideas," *J. Exp. Psychol.* **77**, 28–38.
- Posner, M. I., and Keele, S. W. (1970). "Retention of abstract ideas," *J. Exp. Psychol.* **83**, 304–308.
- Reed, S. K. (1972). "Pattern recognition and categorization," *Cogn. Psychol.* **3**, 383–407.
- Repp, B. H. (1977). "Dichotic competition of speech sounds: The role of acoustic stimulus structure," *J. Exp. Psychol.* **3**, 37–50.
- Rosch, E. H. (1975). "Cognitive representations of semantic categories," *J. Exp. Psychol.* **3**, 193–233.
- Rosch, E. H. (1978). "Principles of categorization," in *Cognition and Categorization*, edited by E. Rosch and B. Lloyd (Erlbaum, Hillsdale, NJ).
- Saffran, J. R., Aslin, R. N., and Newport, E. L. (1996). "Statistical learning by 8-month-old infants," *Science* **274**, 1926–1928.
- Samuel, A. G. (1982). "Phonetic prototypes," *Percept. Psychophys.* **31**, 307–314.
- Smith, E. E., Shoben, E. J., and Rips, L. J. (1974). "Structure and processing in semantic memory: A feature model for semantic decision," *Psychol. Rev.* **81**, 214–241.
- Spence, K. W. (1936). "The nature of discrimination learning in animals," *Psychol. Rev.* **43**, 427–449.
- Spence, K. W. (1937). "The differential response in animals to stimuli varying within a single dimension," *Psychol. Rev.* **44**, 430–444.
- Spence, K. W. (1952). "The nature of the response in discrimination learning," *Psychol. Rev.* **59**, 89–93.
- Spence, K. W. (1960). *Behavior Theory and Learning* (Prentice–Hall, Englewood Cliffs, NJ).
- Strange, W., Keeney, T., Kessel, F. S., and Jenkins, J. J. (1970). "Abstraction over time from distortions of random dot patterns—a replication," *J. Exp. Psychol.* **83**, 508–510.
- Sussman, J., and Lauckner-Morano, V. (1995). "Further tests of the 'perceptual magnet effect' in the perception of [i]: Identification and change-no-change discrimination," *J. Acoust. Soc. Am.* **97**, 539–552.
- Volaitis, L. E., and Miller, J. L. (1992). "Phonetic prototypes: Influence of place of articulation and speaking rate on the internal structure of voicing categories," *J. Acoust. Soc. Am.* **92**, 723–735.
- Werker, J. F. (1994). "Cross-language speech perception: Developmental change does not involve loss," in *The Development of Speech Perception: The Transition from Speech Sounds to Spoken Words*, edited by J. V. Goodman and H. C. Nusbaum (MIT, Cambridge, MA), pp. 93–120.

The recognition of sentences in noise by normal-hearing listeners using simulations of cochlear-implant signal processors with 6–20 channels

Michael F. Dorman

*Department of Speech and Hearing Science, Arizona State University, Tempe, Arizona 85287-0102
and University of Utah Health Sciences Center, Salt Lake City, Utah 84132*

Philipos C. Loizou

Department of Applied Sciences, University of Arkansas at Little Rock, Little Rock, Arkansas 72204-1099

Jeanette Fitzke

Department of Speech and Hearing Science, Arizona State University, Tempe, Arizona 85287-0102

Zhemín Tu

Department of Applied Sciences, University of Arkansas at Little Rock, Little Rock, Arkansas 72204-1099

(Received 14 January 1998; accepted for publication 4 September 1998)

Sentences were processed through simulations of cochlear-implant signal processors with 6, 8, 12, 16, and 20 channels and were presented to normal-hearing listeners at +2 dB S/N and at -2 dB S/N. The signal-processing operations included bandpass filtering, rectification, and smoothing of the signal in each band, estimation of the rms energy of the signal in each band (computed every 4 ms), and generation of sinusoids with frequencies equal to the center frequencies of the bands and amplitudes equal to the rms levels in each band. The sinusoids were summed and presented to listeners for identification. At issue was the number of channels necessary to reach maximum performance on tests of sentence understanding. At +2 dB S/N, the performance maximum was reached with 12 channels of stimulation. At -2 dB S/N, the performance maximum was reached with 20 channels of stimulation. These results, in combination with the outcome that in quiet, asymptotic performance is reached with five channels of stimulation, demonstrate that more channels are needed in noise than in quiet to reach a high level of sentence understanding and that, as the S/N becomes poorer, more channels are needed to achieve a given level of performance.

© 1998 Acoustical Society of America. [S0001-4966(98)04912-1]

PACS numbers: 43.71.Es, 43.71.Ky, 43.66.Ts [WS]

INTRODUCTION

Cochlear implants currently use a minimum of 4 and a maximum of 24 electrodes. It is reasonable to assume that the greater the number of electrodes, the better the speech understanding. This, however, does not seem to be the case. Patients with 6-channel processors achieve scores on tests of speech understanding which are similar to the scores of patients using processors with many more channels (see Dorman *et al.*, in press; Fishman, Shannon, and Slattery, 1997; Wilson, 1997; Tyler *et al.*, 1996). Thus, the data from patients leave unanswered the question of how many electrodes, or channels, should be implemented in a cochlear implant.

Another approach to answering this question is to test normal-hearing listeners with signals which have been processed in the manner of a cochlear-implant signal processor. By using normal-hearing listeners as subjects, many sources of variability inherent in the testing of cochlear-implant patients, such as differences in electrical stimulation strategy, differences in the survival of cell bodies in the spiral ganglion, and differences in the location of electrodes relative to remaining neural tissue, are eliminated. Of course, "simulations" have their own set of limitations, the most notable being that auditory stimulation cannot replicate the mostly

unknown dynamics of current spread in the cochlea. Nonetheless, experiments with normal-hearing listeners give insight into the number of channels which, in the best case, would be needed to reproduce speech adequately for cochlear-implant patients.

In simulation experiments with normal-hearing listeners, signals are typically bandpass filtered into n channels and are rectified and smoothed. The root mean square (rms) energy of the envelope in each channel is computed and signals, either sinusoids with frequencies equal to the center frequencies of the bandpass filters, or noise bands the width of the analysis filters, are output to listeners. When processed in this manner, sentences, *in quiet*, can be understood with greater than 90% accuracy when as few as four channels are implemented (Shannon *et al.*, 1995; Dorman *et al.*, 1997). These data suggest that if electrical stimulation could reproduce the stimulation produced on the basilar membrane by a small number of fixed-frequency sine waves, or noise bands, then only a small number of channels would need to be implemented in a cochlear-implant signal processor to achieve a very high level of sentence understanding.

The results of experiments on sentence understanding in quiet most likely underestimate the number of channels necessary to achieve a high level of sentence understanding in

noisy, “real world” situations. If this were the case, then the view that only a small number of channels are necessary in a cochlear-implant signal processor would need to be modified. To determine whether this is the case, in the present experiment, sentences were processed into 6, 8, 12, 16, and 20 channels and were presented to normal-hearing listeners against a background of speech-shaped noise at +2 dB S/N and -2 dB S/N. The +2 dB S/N ratio was chosen because pilot experiments suggested that interpretation of the results would not be confounded by a ceiling effect on performance. The -2 dB S/N was chosen to assess whether the number of channels necessary to reach maximum performance increased as the signal to noise ratio decreased.

I. METHOD

A. Subjects

Twenty-one normal-hearing students at Arizona State University, who ranged in age from 22 to 55 years, participated in the experiment. The subjects were divided into two groups (of 11 and 10 subjects) for testing.

B. Speech material

The test signals were sentences taken from the H.I.N.T. lists (Nilsson, Soli, and Sullivan, 1994). Each sentence was composed of between four and seven words. Each word was counted in the calculation of percent-correct scores. The sentences were presented at +2 and -2 dB S/N. Twenty sentences were used in each of the five test conditions (i.e., for processors with 6, 8, 12, 16, and 20 channels) for each of the S/N ratios. The noise was spectrally shaped based on the averaged spectrum of the H.I.N.T. sentences (Nilsson *et al.*, 1994). For each S/N condition, the stimuli from all five channel conditions were randomized into a single test sequence. All test materials were stored on computer disk and were output via custom software routines using MATLAB (The MathWorks, Inc.) software and a 16-bit D/A converter.

C. Signal processing

A software version of a cochlear-implant signal processor, similar to that of the Med El Combi-40, was implemented using the MATLAB signal-processing toolbox. Signal processing was implemented in the following manner. Signals were first processed through a pre-emphasis filter (low pass below 1200 Hz, -6 dB per octave) and then bandpassed into n frequency bands (where n varied from 6 to 20) using sixth-order Butterworth filters. The envelope of the signal was extracted, using a 4-ms rectangular window, by full-wave rectification and low-pass filtering (second-order Butterworth) with a 400-Hz cutoff frequency. [A 400-Hz cutoff frequency was used to conform to the cutoff frequency commonly used in the Combi-40’s signal processor. Shannon *et al.* (1995) found no difference in patient performance with low-pass filters set at 160 Hz and above.] Sinusoids were generated with amplitudes equal to the root-mean-square (rms) energy of the envelopes (computed every 4 ms) and frequencies equal to the center frequencies of the bandpass

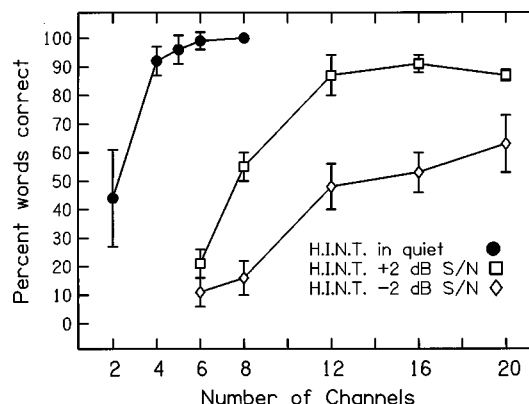


FIG. 1. Sentence intelligibility as a function of the number of channels of stimulation. The parameter is the signal-to-noise ratio. Error bars indicate ± 1 standard deviation.

filters. The sinusoids of each band were summed and presented to the listeners at 72 dB SPL (re: vowel peaks) through Sennheiser HMD 410 headphones.

Signal processors with 6, 8, 12, 16, and 20 channels were constructed. The center frequencies of the channels in the processors with 6 and 8 channels were equally spaced on a logarithmic scale. The center frequencies for the 6-channel processor were 394, 639, 1038, 1685, 2736, and 4444 Hz. For the 8-channel processor, the center frequencies were 366, 526, 757, 1089, 1566, 2253, 3241, and 4662 Hz. For processors with 12, 16, and 20 channels, the channel center frequencies were computed according to the equation: $1100 \log(f/800+1)$, where f is the frequency in Hz [this is similar to the technical mel scale of Fant (1973)]. The center frequencies for the 12-channel processor were 274, 453, 662, 905, 1190, 1521, 1908, 2359, 2885, 3499, 4215, and 5050 Hz. The center frequencies for the 16-channel processor were 216, 343, 486, 647, 828, 1031, 1260, 1518, 1808, 2134, 2501, 2914, 3378, 3901, 4489, and 5150 Hz. The center frequencies for the 20-channel processor were 182, 280, 388, 507, 638, 782, 940, 1114, 1306, 1517, 1749, 2004, 2284, 2593, 2932, 3306, 3717, 4169, 4666, and 5213 Hz.

D. Procedures

The subjects were tested in two groups. One group was tested with the sentence material at +2 dB S/N, and the other at -2 dB S/N. For practice, at each S/N the listeners were presented with 100 sentences from the TIMIT sentence database (Lamel *et al.*, 1986). Five blocks of 20 sentences were presented during practice. In each block the sentences were processed in the manner of one of the channel conditions (i.e., $n=6, 8, 12, 16,$ and 20). The words in each sentence were displayed on a computer screen following the presentation of the sentence. During the test, sentences were presented once and responses were entered, either by the subject, or by the third author, by typing on the computer keyboard. The test was self paced.

II. RESULTS

The results for sentences presented at +2 dB S/N are shown as the middle function in Fig. 1. The mean scores for

processors with 6, 8, 12, 16, and 20 channels were 21, 55, 87, 91, and 87 percent correct, respectively. A repeated-measures analysis of variance demonstrated a significant main effect for channels ($F_{4,10}=418$, $p<0.000\ 001$). *Post hoc* tests according to Scheffe, using an alpha of 0.05, indicated that eight channels allowed significantly better performance than six channels, and that 12 channels allowed significantly better performance than eight channels. Performance reached asymptote with 12 channels of stimulation, i.e., performance with 12-, 16-, and 20-channel processors did not differ.

The results for sentences presented at -2 dB S/N are shown as the right-most function in Fig. 1. The mean scores for processors with 6, 8, 12, 16, and 20 channels were 11, 16, 48, 53, and 62 percent correct, respectively. A repeated-measures analysis of variance demonstrated a significant main effect for channels ($F_{4,9}=100.0$, $p<0.000\ 01$). *Post hoc* tests according to Scheffe, using an alpha of 0.05, indicated that performance in the 6- and 8-channel conditions differed from that in the 12-, 16-, and 20-channel conditions, that performance in the 12-, and 16-channel conditions differed from that in the 6-, 8-, and 20-channel conditions, and that performance in the 20-channel condition differed from performance in all of the other conditions.

III. DISCUSSION

In the introduction we noted that, in quiet, only four channels of stimulation are necessary to allow sentences to be understood with greater than 90% accuracy. This is not the case in noise. At $+2$ dB S/N, where performance is not constrained by a ceiling effect, 12 channels are necessary to reach maximum performance. At -2 dB S/N, 20 channels are necessary to reach maximum performance. As the S/N ratio becomes poorer, more channels are needed to achieve a given level of performance. These findings are illustrated in Fig. 1, where the current data and data on the recognition of the H.I.N.T. sentences in quiet, from Dorman *et al.* (1997), are plotted. The 8-channel processor, which allowed a mean score of 100-percent correct in quiet, allowed a mean score of 55-percent correct at $+2$ dB S/N and allowed a mean score of 16-percent correct at -2 dB S/N. If speech in noise is to be understood, then signal processors for cochlear implants should have more than a few channels and, most generally, the more channels, the better.

Achieving the goal of transmitting information to implant patients through a large number of channels has proven difficult. For example, when the number of electrodes activated in a 22-electrode array has been systematically reduced and speech understanding has been measured in quiet, six or seven electrodes have provided the same intelligibility as 20 electrodes (Fishman *et al.*, 1997; Wilson, 1997). Or, put another way, increasing the number of electrodes beyond six or seven has not improved intelligibility. This outcome suggests that it may be some time before 20 independent, information-bearing channels can be realized for cochlear implant patients. If this is the case, then the goal of 12 chan-

nels is a reasonable one. As shown in Fig. 1, sentence intelligibility functions at $+2$ and -2 dB S/N show large increases in performance when the number of channels increases from 8 to 12, but show no significant improvement from 12 to 16. The large improvement in performance for the 12-channel processor relative to the 8-channel processor is due, most likely, to the increase in the number of filters, from three to five, allocated to the frequency domain of F_2 (i.e., between 900 and 2500 Hz). The increase in number of filters allows better resolution of F_2 frequency. Other factors which may underlie the improvement in performance for the 12-channel processor relative to the 8-channel processor are better spectral contrast within each channel and an increase in the number of channels with a high S/N. Both of these factors are a consequence of the decrease in filter width in the 12-channel condition.

If providing 12 channels of stimulation proves beyond the reach of current technology, then even a small increase in the number of effective channels of stimulation from current devices would be of great benefit. As shown in Fig. 1, at $+2$ dB S/N a 34-point improvement in intelligibility was obtained when the number of channels was increased from six to eight. In an unpublished experiment, we have found a 20-point improvement in intelligibility at $+6$ dB S/N when the number of channels was increased from six to eight. Thus, current implant devices need to be improved only a little, in terms of the effective channels of stimulation, in order to provide a large improvement in patient performance in noise.

ACKNOWLEDGMENT

This research was supported by grant No. DC RO 1 00654-7 from the National Institute on Deafness and Other Communication Disorders.

- Dorman, M. F., Loizou, P., and Rainey, D. (1997). "Speech intelligibility as a function of the number of channels of stimulation for signal processors using sine-wave and noise-band outputs," *J. Acoust. Soc. Am.* **102**, 2403-2411.
- Dorman, M., Loizou, P., Fitzke, J., and Tu, Z. (in press). "The recognition of NU-6 words by cochlear-implant patients and by normal-hearing subjects listening to NU-6 words processed in the manner of CIS and SPEAK strategies," *Ann. Otol. Rhinol. Laryngol.*
- Fant, G. (1973). *Speech Sounds and Features* (MIT, Cambridge, MA).
- Fishman, K., Shannon, B., and Slattery, W. (1997). "Speech recognition as a function of the number of electrodes used in the SPEAK cochlear implant speech processor," *J. Speech Hear. Res.* **40**(5), 1201-1215.
- Lamel, L., Kassel, R., and Seneff, S. (1986). "Speech database development: Design and analysis of the acoustic-phonetic corpus," *Proceedings of DARPA Speech Recognition Workshop*, pp. 100-109.
- Nilsson, M., Soli, S., and Sullivan, J. (1994). "Development of the Hearing in Noise Test for the measurement of speech reception thresholds in quiet and noise," *J. Acoust. Soc. Am.* **95**, 1085-1099.
- Shannon, R., Zeng, F.-G., Kamath, V., Wygonski, J., and Ekelid, M. (1995). "Speech recognition with primarily temporal cues," *Science* **270**, 303-304.
- Tyler, R., Gantz, B., Woodworth, G., Parkinson, A., Lowder, M., and Schum, L. (1996). "Initial independent results with the Clarion cochlear implant," *Ear and Hearing* **17**(6), 528-536.
- Wilson, B. (1997). "The future of cochlear implants," *British Journal of Audiology* **31**, 205-225.

Effects of noise and spectral resolution on vowel and consonant recognition: Acoustic and electric hearing

Qian-Jie Fu,^{a)} Robert V. Shannon, and Xiaosong Wang

Department of Auditory Implants and Perception, House Ear Institute, 2100 West Third Street, Los Angeles, California 90057

(Received 9 January 1998; revised 13 August 1998; accepted 14 September 1998)

Current multichannel cochlear implant devices provide high levels of speech performance in quiet. However, performance deteriorates rapidly with increasing levels of background noise. The goal of this study was to investigate whether the noise susceptibility of cochlear implant users is primarily due to the loss of fine spectral information. Recognition of vowels and consonants was measured as a function of signal-to-noise ratio in four normal-hearing listeners in conditions simulating cochlear implants with both CIS and SPEAK-like strategies. Six conditions were evaluated: 3-, 4-, 8-, and 16-band processors (CIS-like), a 6/20 band processor (SPEAK-like), and unprocessed speech. Recognition scores for vowels and consonants decreased as the S/N level worsened in all conditions, as expected. Phoneme recognition threshold (PRT) was defined as the S/N at which the recognition score fell to 50% of its level in quiet. The unprocessed speech had the best PRT, which worsened as the number of bands decreased. Recognition of vowels and consonants was further measured in three Nucleus-22 cochlear implant users using either their normal SPEAK speech processor or a custom processor with a four-channel CIS strategy. The best cochlear implant user showed similar performance with the CIS strategy in quiet and in noise to that of normal-hearing listeners when listening to correspondingly spectrally degraded speech. These findings suggest that the noise susceptibility of cochlear implant users is at least partly due to the loss of spectral resolution. Efforts to improve the effective number of spectral information channels should improve implant performance in noise. © 1998 Acoustical Society of America. [S0001-4966(98)05612-4]

PACS numbers: 43.71.Es, 43.71.Ky, 43.66.Ts [WS]

INTRODUCTION

Although normal-hearing listeners can recognize speech even in high levels of interfering noise, speech recognition of hearing-impaired listeners and cochlear implant listeners is much more susceptible to noise. Reduced spectral resolution is a possible cause of the reduced performance in noise. It has been widely observed that hearing-impaired listeners have broadened auditory tuning curves, and that the degree of broadening is correlated with speech recognition performance, especially in noise (e.g., Horst, 1987). Cochlear implant listeners are limited in spectral resolution by the number and location of electrodes arrayed along the tonotopic axis of the cochlea. It is theoretically and practically important to understand whether the limited spectral resolution is a key factor affecting speech performance in noise for cochlear implant users. The present study measures speech recognition as a function of signal-to-noise level for signals that are systematically varied in spectral resolution.

The effect of spectral resolution on speech recognition has received considerable attention in the last 20 years. Dubno and Dorman (1987) synthesized vowel stimuli with differing degrees of spectral contrast between formant peaks and troughs. They found that, for vowel stimuli with widened higher frequency formants, vowel recognition was unaffected until the first-formant bandwidth was six times wider than normal. This result is consistent with Shannon

et al. (1995) who demonstrated good vowel recognition in quiet with only four modulated bands of noise representing the speech spectrum.

The effect of noise on speech recognition was measured by ter Keurs *et al.* (1992, 1993) as a function of spectral smearing to simulate the loss of spectral resolution in hearing impairment. They used an FFT overlap-and-add technique to smear the spectral representation and measured recognition of sentences, vowels, and consonants as a function of signal-to-noise level. They found no significant decrease in performance until the spectrum was smeared by more than a critical band. Performance was reduced only moderately even for spectral smearing of an octave.

Moore and colleagues (Baer and Moore, 1993, 1994; Nejime and Moore, 1997) measured the effect of spectral smearing on sentence recognition as a function of the level of masking noise or interfering speech. They found no difference in performance in quiet between the intelligibility of the original speech, and conditions in which the spectral information had been smeared to simulate broadened perceptual bandwidths (Equivalent Rectangular Bandwidths: ERBs) by factors of 3 and 6. However, the difference in performance between the original speech and spectrally smeared conditions increased dramatically as the noise level was increased.

Boothroyd *et al.* (1996) smeared the spectrum of speech by multiplication with low-pass noise. In quiet listening conditions intelligibility was reduced to 50% only when spectral information was smeared by more than 1000 Hz. In noise,

^{a)}Electronic mail: qfu@hei.org

the signal-to-noise ratio at which performance dropped to half of its level in quiet (phoneme recognition threshold, PRT) worsened by 12.9 dB for 707-Hz smearing and 16.4 dB for 2000-Hz smearing. In general, these studies have demonstrated that reduction of spectral information by spectral smearing can reduce performance in quiet and increase susceptibility to noise.

The effects of background noise on speech performance in cochlear implant users with different speech processing strategies have been investigated by several researchers (Dowell *et al.*, 1987; Hochberg *et al.*, 1992; Kiefer *et al.*, 1996; Müller-Deiler *et al.*, 1995; Skinner *et al.*, 1994). Dowell *et al.* (1987) investigated 13 Nucleus-22 cochlear implant users with the $F0F2$ speech processing strategy and 9 Nucleus-22 cochlear implant users with $F0F1F2$ strategy, both of which were speech formant-extraction strategies. In these strategies the implant speech processor estimates the fundamental frequency of the voice ($F0$), and the frequencies of the first and second formants ($F1, F2$), and stimulates electrodes assigned to represent $F1$ and $F2$ with a pulse rate equal to $F0$. Their results for a closed set spondee test showed that speech recognition performance was reduced at a +10-dB S/N ratio when using the $F0F2$ strategy compared to quiet, but was not reduced at +10 dB with the $F0F1F2$ strategy. However, recognition scores were significantly lower for both $F0F1F2$ and $F0F2$ processing strategies when the signal-to-noise ratio was further reduced to +5 dB.

Hochberg *et al.* (1992) measured the effects of noise on speech performance in normal-hearing listeners and cochlear implant users. They measured phoneme recognition as a function of signal-to-noise (S/N) ratio in ten normal-hearing adults and ten successful adult users of the Nucleus cochlear implant using one of two formant-estimation speech processing strategies (MPEAK or $F0F1F2$). The MPEAK strategy estimates $F0$ and presents pulses at the $F0$ rate on electrodes assigned to represent $F1$ and $F2$. In addition, several electrodes in the high-frequency basal region are stimulated with pseudo random pulse rates for unvoiced sounds. The phoneme recognition threshold (PRT) was defined as the S/N at which the phoneme recognition score fell to 50% of its value in quiet (in that study recognition in quiet was 98% for normal hearing subjects and 42% for implant subjects). Their results showed that PRT was -2 dB for the average normal-hearing subject and +9 dB for the average implant listener. Hochberg *et al.* (1992) also demonstrated that a digital noise reduction algorithm (INTEL) improved the phoneme recognition threshold of the implant group by an average of 4.2 dB. Weiss (1993) found that additive noise resulted in substantial errors in formant frequency estimation by the Nucleus feature-extracting algorithm for $F2$. However, errors in the frequency estimates for $F2$ were substantially reduced when the noisy speech was preprocessed by the INTEL noise reduction algorithm.

More recently, the effects of noise on speech discrimination in cochlear implant patients were reported by Müller-Deiler *et al.* (1995). In their study, sentence recognition was measured in 18 cochlear implant users with the MPEAK formant-estimation speech processing strategy and 9 co-

chlear implant users with the SPEAK processing strategy. The SPEAK processor selects 6–10 spectral peaks every 4 ms and stimulates the 6–10 electrodes assigned to represent those spectral regions at rates up to 250 Hz (McDermott *et al.*, 1992a, b). Müller-Deiler *et al.* found that the noise suppression mode of the commercial device allowed significantly better discrimination in noise for both strategies and that the SPEAK strategy showed a significantly better performance in noise than MPEAK.

A more extensive comparison between the SPEAK and MPEAK processing strategies was done by Skinner *et al.* (1994). In their study, both SPEAK and MPEAK processing strategies were implemented on wearable speech processors of the Nucleus-22 cochlear implant system in 63 post-linguistically deaf adults. While there was no significant difference between processing strategies in quiet, the results showed marked improvement in recognition of sentences in noise with the SPEAK strategy.

Kiefer *et al.* (1996) compared recognition of sentences between MPEAK, SPEAK, and Continuous Interleaved Sampling (CIS: Wilson *et al.*, 1991) strategies. The CIS strategy presents pulses that represent speech envelope information to a fixed number of electrodes. No formant estimation is performed in CIS processing. They found SPEAK and CIS to be superior to MPEAK strategy, both in quiet and in noise, and found the CIS strategy to be less susceptible to noise than SPEAK.

These studies indicate that current speech processing strategies such as SPEAK not only provide high recognition levels in quiet, but also provide significantly better performance in noise when compared to previous feature-extraction strategies (Skinner *et al.*, 1994; Kiefer *et al.*, 1996). It is not clear if the improvements are due to the increased number of effective spectral channels or other aspects of improved speech processing. Furthermore, even for the latest SPEAK processing strategy, the performance for those cochlear implant listeners were still considerably poorer than normal-hearing subjects, especially in noisy environments (Müller-Deiler *et al.*, 1995). Unfortunately, none of previous studies illustrated the reason why speech recognition of cochlear implant users is susceptible to background noise.

The goal of the present study was to understand whether the noise susceptibility of cochlear implant users was due to the loss of fine-structure spectral information. Two experiments were conducted. In experiment 1, the effects of noise and spectral resolution on speech recognition were investigated in normal-hearing subjects. The intelligibility of vowels and consonants was measured in normal-hearing listeners as a function of signal-to-noise ratio, with the number of spectral channels as a parameter, when transmitted by modulated bands of noise, as in Shannon *et al.* (1995). In experiment 2, vowel and consonant recognition were measured as a function of signal-to-noise ratio in three cochlear implant listeners with either their original speech processor with the SPEAK processing strategy or a custom speech processor with a four-channel CIS speech processing strategy.

I. EXPERIMENT 1: ACOUSTIC SIMULATION

A. Methods

1. Subjects

Four normal-hearing acoustic listeners (two males and two females) between the ages of 25 and 35 years served as subjects. All subjects had thresholds better than 15 dB HL at audiometric test frequencies from 250 to 8000 Hz and all were native speakers of American English.

2. Test materials

Speech performance was assessed using two measures: vowels and consonants. Vowel recognition was measured in a 12-alternative identification paradigm, including 10 monophthongs and 2 diphthongs, presented in a /h/-vowel-/d/ context (heed: h/i/d, hawed: h/ɔ/d, head: h/ε/d, who'd: h/u/d, hid: h/i/d, hood: h/u/d, hud: h/ʌ/d, had: h/æ/d, heard: h/ɜ/d, hoed: h/o/d, hod: h/a/d, hayed: h/e/d). The tokens for these closed-set tests were digitized natural productions from five men, five women, three boys, and two girls, drawn from the material collected by Hillenbrand *et al.* (1995). Consonant recognition was measured in a 16-alternative identification paradigm, for the consonants /b d g p t k l m n f s ʃ v z dʒ θ/, presented in an /a/-consonant-/a/ context. Two repetitions of each of the 16 consonants were produced by three speakers (1 male, 2 female) for a total of 96 tokens (16 consonants* 3 talkers* 2 repeats).

All test materials were stored on computer disk and were output via custom software to a 16 bit D/A converter (TDT DD1) at a 16-kHz sampling rate. Speech sounds were presented in a completely randomized test sequence using a Tucker-Davis-Technologies (TDT) AP2 array processor in a host PC connected via an optical interface.

3. Signal processing

The speech signal was mixed with simplified speech spectrum-shaped noise (constant spectrum level below 800 Hz and 10-dB/octave roll-off above 800 Hz). The signal-to-noise ratio (S/N) was defined as the difference, in decibels, between the rms levels of the whole speech token and the noise. The speech signal was mixed with the noise at S/N levels of 24 dB, 18 dB, 12 dB, 6 dB, 0 dB, -3 dB, -6 dB, -9 dB, -12 dB, and -15 dB, for a total of 11 conditions in addition to the original speech.

Recognition performance was measured as a function of signal-to-noise ratio in four normal-hearing subjects in the unprocessed speech condition and in spectrally degraded speech, which was used to simulate cochlear implants with the current SPEAK and CIS speech processing strategies. A detailed description of the implementation of these spectrally degraded speech stimuli follows.

a. Sixteen-band speech. The unprocessed speech with the desired S/N level was first pre-emphasized using a first-order Butterworth high-pass filter with a cutoff frequency of 1200 Hz, and then bandpass filtered into 16 broad frequency bands using eighth-order Butterworth filters. The corner frequencies (3 dB down) of the bands were at 100, 379, 473, 583, 713, 866, 1046, 1259, 1509, 1804, 2152, 2561, 3043, 3612, 4281, 5070, and 6000 Hz. The envelope of the signal

in each band was extracted by half-wave rectification and low-pass filtering (eighth-order Butterworth) with a 500-Hz cutoff frequency. The envelope of each band was used to modulate a wide-band noise, which was then spectrally limited by the same bandpass filter used for the original analysis band. The A-weighted output from each band was then summed and presented to the listeners diotically through Sennheiser HDA200 headphones at 70 dB. This condition was labeled as 16-band speech, simulating a cochlear implant with a 16-channel CIS speech processing strategy.

b. Eight-band speech. The same processing method as sixteen-band speech was used, except that the whole spectrum of the speech was divided into eight bands. The corner frequencies of this processor were 100, 473, 713, 1046, 1509, 2152, 3043, 4281, and 6000 Hz. The output speech was labeled as eight-band speech, simulating a cochlear implant with an eight-channel CIS speech processing strategy.

c. Four-band speech. The same processing method as sixteen-band speech was used, except that the whole spectrum of the speech was divided into four broadbands. The corner frequencies of four-band processor were 100, 713, 1509, 3043, and 6000 Hz. The output speech was labeled as four-band speech, simulating a cochlear implant with a four-channel CIS speech processing strategy.

d. Three-band speech. The same processing method as sixteen-band speech was used, except that the whole spectrum of the speech was divided into three broadbands. The corner frequencies of the three-band processor were 100, 923, 2417, and 6000 Hz. The output speech was labeled as three-band speech, simulating a cochlear implant with a three-channel CIS speech processing strategy.

e. SPEAK-like speech. This processing strategy was similar to the Nucleus SPEAK strategy. The speech was divided into 20 narrow frequency bands. The corner frequencies were at 85, 200, 314, 428, 542, 657, 771, 885, 1010, 1160, 1333, 1531, 1759, 2040, 2390, 2801, 3282, 3845, 4505, 5278, and 6184 Hz (similar to frequency allocation table 3 in the Spectra-22 speech processor). The envelope of each band was extracted by half-wave rectification and low-pass filtering with a cutoff frequency of 100 Hz. Note that the envelope filter frequency is somewhat different from that used in the CIS-like acoustic processors. This lower envelope filter frequency was selected to avoid the aliasing effect caused by the 250-Hz resampling rate. Every 4 ms, the six bands with the highest amplitudes were selected to represent the spectral peaks. These peak values were each used to set the levels of six, 4-ms bursts of wide-band noise, and each burst was then spectrally limited by the same bandpass filter used for the original analysis band. The A-weighted outputs from all bands were then summed and presented to the listeners through headphones at 70 dB.

4. Procedure

Each test block included 180 tokens for vowel recognition or 96 tokens for consonant recognition. A stimulus token was randomly chosen from all 180 tokens in vowel recognition and from 96 tokens in consonant recognition and presented to the subject. Following the presentation of each token, the subject responded by pressing one of 12 buttons in

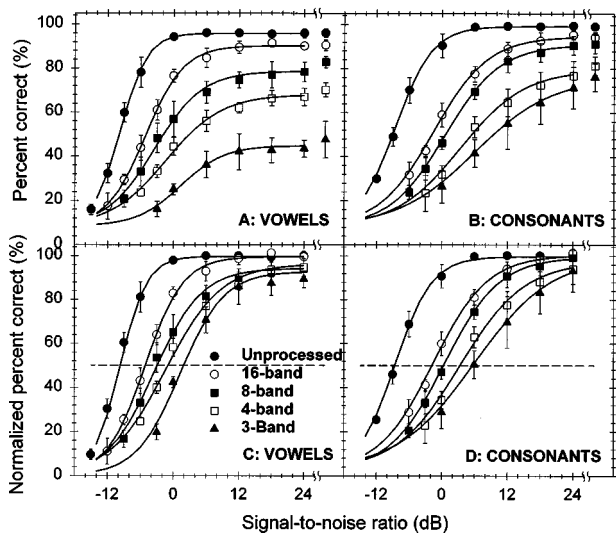


FIG. 1. Recognition of vowels and consonants as a function of signal-to-noise ratio for the unprocessed speech and 16-, 8-, 4-, and 3-band speech from four normal-hearing subjects. (A) Mean vowel scores. (B) Mean consonant scores. (C) Normalized mean vowel scores after correction for chance. (D) Normalized consonant scores after correction for chance. Error bars indicate \pm one standard deviation. Solid lines represent the best-fit curve based on Eq. (1). The dashed lines indicate 50% of the normalized score after correction for chance.

the vowel test or one of 16 buttons in the consonant test, each marked with one of the possible responses. No feedback was provided, and subjects were instructed to guess if they were not sure, although they were cautioned not to provide the same response for each guess. The subjects started the formal test without training and with no appreciable period of adjustment to the new processed sound. Our objective was to obtain a “snapshot” of phoneme recognition prior to any learning effects for a particular processor strategy or setting. However, all subjects were familiar with spectrally degraded speech sounds from recent previous studies. In all figures, each data point represents two runs by each subject, consisting of 30 presentations of each vowel and 12 presentations of each consonant. All test conditions, including number of channels, signal-to-noise ratio, as well as vowel/consonant tests, were randomized and counterbalanced across subjects.

B. Results

Figure 1(A) shows recognition scores of vowels as a function of S/N ratio for the unprocessed, and for the sixteen-, eight-, four-, and three-band speech. Vowel scores gradually decreased as signal-to-noise (S/N) ratio decreased for all conditions. A two-way ANOVA showed a significant effect of number of channels [$F(4,102)=729.43$, $p < 0.0001$], S/N ratio [$F(5,102)=54.11$, $p < 0.0001$], as well as a significant interaction [$F(20,102)=3.89$, $p < 0.0001$]. However, no significant difference was observed across subjects [$F(4,190)=0.604$, $p=0.66$], so only average data are shown for the acoustic experiments.

Figure 1(B) shows recognition scores for consonants as a function of S/N ratio in the same five conditions. Similar to the pattern obtained in vowel recognition, consonant scores gradually decreased as S/N ratio decreased. A two-way ANOVA showed a significant effect of number of channels [$F(4,102)=265.79$, $p < 0.0001$], S/N ratio [$F(5,102)=164.44$, $p < 0.0001$], as well as a significant interaction [$F(20,102)=8.21$, $p < 0.0001$]. No significant effect of subjects was observed [$F(4,164)=0.296$, $p=0.88$], so only average data are presented.

Figure 1(C) and (D) shows the normalized performance on vowels and consonants, respectively, as a function of S/N ratio, relative to the performance in quiet. The scores were first corrected for chance following Boothroyd *et al.* (1996). The dashed lines in Fig. 1(C) and (D) indicate 50% of the normalized score after correction for chance. The S/N level that produced this 50% level of performance was defined as the phoneme recognition threshold (PRT). Normalized performance functions shifted to higher S/N ratios for both vowels and consonants as the number of spectral bands decreased. Even the PRT for 16 bands of spectral information was noticeably poorer than unprocessed speech.

The data of Fig. 1 (and subsequent figures) were fit by a simple sigmoidal model (Boothroyd *et al.*, 1996):

$$\% C = P_0 + (Q - P_0) / (1 + e^{-\beta(x - \text{PRT})}), \quad (1)$$

where Q is the percent correct in quiet, PRT is the phoneme recognition threshold in dB, x is the S/N ratio in dB, P_0 is the chance level of performance (6.25% for consonants, 8.33% for vowels), and β is related to the slope of the func-

TABLE I. The model parameters of sigmoidal fitting for all vowel conditions.

Condition	Listener	Q (%)	PRT (dB)	β	Slope at PRT(%/dB)	R^2
Original	NH	95.9 \pm 0.9	-9.92 \pm 0.53	0.41 \pm 0.03	7.79 \pm 0.52	0.999
16-channel	NH	90.3 \pm 1.2	-5.14 \pm 0.44	0.29 \pm 0.04	5.45 \pm 0.79	0.998
8-channel	NH	78.7 \pm 3.1	-3.34 \pm 1.37	0.24 \pm 0.03	4.24 \pm 0.48	0.988
4-channel	NH	68.2 \pm 3.0	-1.26 \pm 0.83	0.21 \pm 0.06	3.52 \pm 0.96	0.991
3-channel	NH	46.3 \pm 4.8	2.31 \pm 2.64	0.24 \pm 0.09	3.28 \pm 1.24	0.990
SPEAK	NH	80.2 \pm 3.5	-6.08 \pm 1.01	0.37 \pm 0.10	6.71 \pm 1.69	0.988
4-CIS	N3	42.5	0.87	0.28	4.32	0.976
	N4	59.3	-2.86	0.25	4.51	0.980
	N7	54.2	4.73	0.21	3.56	0.996
SPEAK	N3	59.6	4.19	0.321	5.75	0.979
	N4	74.8	-2.51	0.355	6.79	0.990
	N7	63.2	8.06	0.361	6.59	0.993

TABLE II. The model parameters of sigmoidal fitting for all consonant conditions.

Condition	Listener	Q (%)	PRT (dB)	β	Slope at PRT(%/dB)	R^2
Original	NH	99.4±0.4	-8.41±0.54	0.30±0.05	6.11±1.00	0.999
16-channel	NH	94.7±2.7	-1.51±1.08	0.20±0.01	4.09±0.24	0.998
8-channel	NH	90.9±3.6	+0.55±0.66	0.21±0.03	4.20±0.53	1.000
4-channel	NH	79.6±5.1	+3.42±1.13	0.17±0.02	3.35±0.36	0.995
3-channel	NH	76.3±6.0	+6.35±1.99	0.14±0.01	2.73±0.31	0.996
SPEAK	NH	84.6±3.8	0.57±1.03	0.22±0.05	4.29±1.01	0.989
4-CIS	N3	63.0	0.79	0.173	3.15	0.988
	N4	75.6	0.87	0.237	4.54	0.995
	N7	77.8	1.65	0.166	3.20	0.994
SPEAK	N3	61.5	0.93	0.230	4.17	0.961
	N4	69.7	-1.14	0.233	4.38	0.991
	N7	75.6	3.48	0.152	2.90	0.973

tion at PRT. Tables I and II list the estimated values for these parameters for all conditions for vowels and consonants, respectively. The fits of this function to the data were uniformly excellent, with all R^2 values better than 0.96. For the performance in quiet (Q), scores dropped significantly as the number of spectral bands was reduced for both vowels [$F(4,20)=210.49, p<0.0001$] and consonants [$F(4,20)=26.06, p<0.0001$]. The slope of the function at PRT was significantly shallower for the noise-band conditions than for the unprocessed condition for both vowels [$F(4,20)=10.42, p<0.0001$] and consonants [$F(4,20)=19.07, p<0.0001$]. *Post hoc* tests according to Tukey indicated that there was no significant difference in slope (β) among the noise-band conditions. The PRT worsened significantly as the number of channels decreased for vowels [$F(4,20)=49.04, p<0.0001$] and consonants [$F(4,20)=98.76, p<0.0001$].

There was a high correlation between Q and PRTs for both vowels and consonants for the spectrally degraded speech (CIS-like speech only), shown in Fig. 2. The SPEAK-like and unprocessed speech are not included in this analysis. SPEAK-like speech emphasizes spectral information and discards amplitude information, and so is not strictly comparable to the CIS conditions, and the unprocessed results in

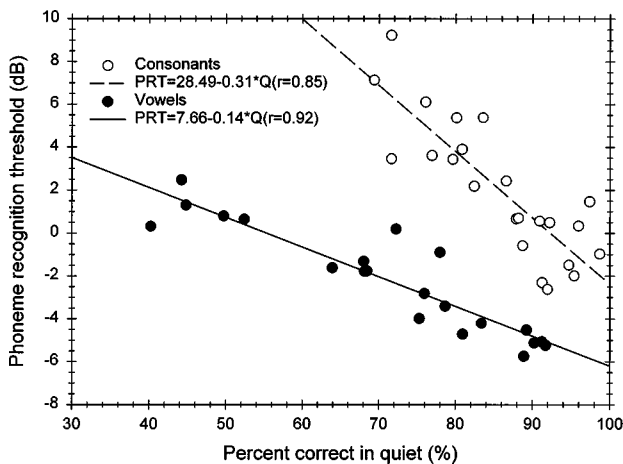


FIG. 2. Phoneme recognition thresholds from individual subjects as a function of performance in quiet for the spectrally degraded speech (16-, 8-, 4-, and 3-band) conditions in normal-hearing listeners. Error bars indicate \pm one standard deviation.

quiet were limited by ceiling effects. From Fig. 2 it is apparent that the PRT can be reasonably well predicted from Q , the performance in quiet, for CIS-like spectrally degraded speech. These results demonstrate that reduction of spectral information has two closely related effects: reducing the performance level in quiet, and also reducing the PRT in noise.

Figure 3(A) shows recognition scores of vowels and consonants as a function of signal-to-noise ratio for SPEAK-like speech. There was a significant effect of the signal-to-noise ratio on vowel recognition [$F(8,27)=37.65, p<0.0001$] as well as on consonant recognition [$F(7,24)=76.07, p<0.0001$]. *Post hoc* tests according to Tukey showed a significant performance drop in vowel recognition when the S/N level was 0 dB or lower. For consonants, a significant performance drop was observed when the S/N was 6 dB or lower. Figure 3(B) shows the normalized performance for vowels and consonants. The dashed line indicates 50% of the percent correct in quiet. Parameter values estimated from this data are also presented in Tables I and II.

C. Discussion

For normal-hearing subjects, the unprocessed speech had the lowest PRT: -9.92 dB for vowels and -8.41 dB for consonants. This confirms previous work showing the strong robustness of unprocessed speech in noise for normal-

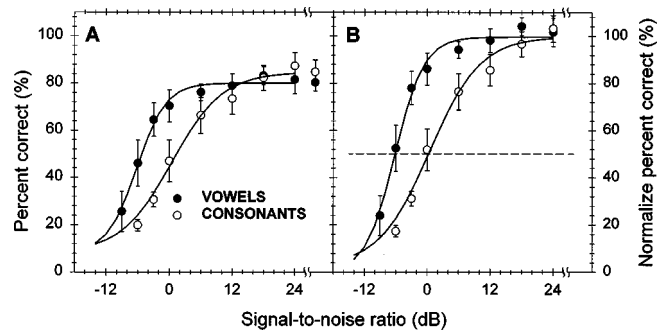


FIG. 3. Recognition of vowels and consonants from four normal-hearing subjects as a function of signal-to-noise ratio for spectrally degraded speech in conditions simulating SPEAK processing strategy in cochlear implants. (A) Mean recognition scores of vowels and consonants. (B) Normalized scores of vowels and consonants after correction for chance. Error bars indicate \pm one standard deviation. The dashed lines indicate 50% of the normalized score after correction for chance.

TABLE III. Subject information for three Nucleus-22 cochlear implant listeners who participated in the present study.

Subject	Age	Gender	Cause of deafness	Duration of implant use	Sentence score (CUNY)	Stimulation mode	Frequency table
N3	55	M	TRAUMA	6 years	68.2%	BP+1	7
N4	39	M	TRAUMA	4 years	95.1%	BP+1	9
N7	54	M	UNKNOWN	4 years	92.6%	BP+1	9

hearing subjects. These thresholds for normal-hearing subjects were lower (better) than previous results (Hochberg *et al.*, 1992), possibly due to the difference in test materials.

The manipulations for CIS-like speech preserved the temporal and amplitude cues in each spectral band, but removed the fine spectral detail within each band. The amount of available spectral information was systematically changed by varying the number of bands. Consistent with previous results (Shannon *et al.*, 1995; Dorman *et al.*, 1997), recognition performance in quiet increased as the number of bands increased. A relatively high level of vowel and consonant recognition was obtained with only four bands of spectral information in quiet. Note that the level of performance observed in the present study was lower than that observed by Shannon *et al.* with four bands due the use of more difficult, multi-talker materials. In the present study, nearly perfect recognition was achieved in quiet with 16 bands of spectral information. These results indicate that the loss of spectral information down to four bands only results in a minimal decrease in speech recognition in quiet. However, the loss of spectral information produced a larger reduction in speech recognition when noise was added. Although only a 5% difference was observed in the quiet condition between the sixteen-band speech and unprocessed speech, this difference increased dramatically to more than 30% at a S/N ratio of -6 dB (Fig. 1). This result indicates that fine spectral information may be important for speech recognition in noisy environments, which are typical of many listening conditions in everyday life. The loss of fine spectral information may cause the loss of some perceptual cues that might be used for sound source determination, such as harmonicity or coherent temporal modulation (Yost and Sheft, 1993), resulting in a strong noise susceptibility of speech.

Two major current speech processing strategies in cochlear implants are SPEAK and CIS strategies, which both use a filter-band processing strategy. The major difference between these two strategies is that the CIS strategy preserves temporal envelope information from all filter bands while the SPEAK strategy only preserves the temporal envelope information with the highest energy every 4 ms from a subset of bands (average of six bands) out of 20 total analysis filter bands. In the quiet condition, normal-hearing listeners achieved 80% correct on vowels and 85% correct on consonants for SPEAK-like speech. Both of these scores were lower than those of eight-band speech, but higher than those of four-band speech. The data from the present study showed that the PRT of vowels for SPEAK-like speech was -6.08 dB, which was somewhat better than the PRT for sixteen-band speech. However, the PRT for consonants was

$+0.57$ dB for SPEAK-like speech, which was slightly poorer than the PRT for eight-band speech. These results indicate that SPEAK processing is similar to 16-band processing for vowels, probably due to its fine spectral representation. However, SPEAK processing is more similar to eight-band speech for consonants, possibly because the temporal information rate is slow and sparsely distributed over the electrodes.

Another interesting factor is that the reduction of fine spectral information has a slightly different impact on vowel and consonant recognition in noise. The statistical analysis showed that the PRTs of vowels were significantly poorer than those of consonants in both the unprocessed speech and the spectrally degraded speech [$F(1,58) = 12.49$, $p = 0.001$]. For the unprocessed speech, the PRT for vowels was only 1.5 dB poorer than that of consonants. However, the PRTs for vowels were about 4 dB poorer than for in consonants spectrally degraded CIS-like speech, independent of the number of bands. The PRT difference between vowels and consonants was 6.7 dB in SPEAK-like speech, possibly because vowel recognition is more dependent on spectral information. The SPEAK processor selects only the six bands with the strongest energy in each 4-ms interval, so that temporal envelope information from all other bands is not represented in that 4-ms interval.

II. EXPERIMENT 2: ELECTRIC STIMULATION

A. Methods

1. Subjects

Cochlear implant subjects were three post-lingually deafened adults using the Nucleus-22 device. All had at least six months experience utilizing the SPEAK speech processing strategy and all were native speakers of American English. All implant subjects had 20 active electrodes available for use. Two subjects (N4 and N7) used frequency allocation table 9 (150–10 823 Hz) in their clinical implant processor and one subject (N3) used frequency allocation table 7 (120 Hz–8658 Hz). Subjects N4 and N7, based on their sentence and word recognition scores, were excellent users of the cochlear implants, and subject N3 was an average user. No poor users were chosen in this study to avoid floor effects. All implant participants had extensive experience in speech recognition experiments. Table III contains relevant information for the three subjects, including their most recent scores on the CUNY sentence test, presented without lipreading in the sound field.

2. Test materials and procedures

The same test materials as experiment 1 were used. For cochlear implant users, all signals were presented at comfortable audible levels through the Audio Input Selector (AIS) when using their own speech processor with SPEAK processing strategy. In the four-channel CIS processing strategy condition, all signals were presented at comfortable audible levels through a custom interface (Shannon *et al.*, 1990). The comfortable audible levels were adjusted by each individual subject in each listening session. Subjects were instructed to maintain the same loudness scale across all tests. There was a considerable difference in the familiarity of the subjects with the two processor strategies evaluated in this study: All subjects were somewhat familiar with the custom four-channel CIS speech processor from previous experiments, but all were highly familiar with the SPEAK processing strategy from daily experience for more than four years.

3. Signal processing

Speech recognition performance was also measured as a function of signal-to-noise ratio for three Nucleus-22 cochlear implant users with both the original SPEAK processing strategy and a custom four-channel CIS processing strategy. The implementation of these speech-processing strategies in Nucleus-22 cochlear implant users was described as follows.

a. SPEAK processor. The SPEAK processing strategy (McDermott *et al.*, 1992a) is the normal clinical speech processor provided by Cochlear Corporation and used by subjects everyday. The implementation of SPEAK processing strategy is briefly described as follows. Incoming sound is analyzed into 20 filters and the amplitude in each filter is extracted. The filter outputs are scanned to select an average of six maxima approximately every 4 ms (Cochlear Corporation, 1995). This scanning occurs continuously, and electrodes associated with the maxima are stimulated at the actual scanning rate from a basal-to-apical position in the cochlea. The average stimulation rate is 250 Hz, but it can vary by ± 100 Hz, depending on the subject's speech processor program as well as the incoming sound intensity and spectral composition. In the present study, the same frequency allocation map was used that each subject used in their everyday clinical processor. The noise suppression circuit of the speech processor was not activated.

b. CIS processor. The four-channel CIS processor was implemented through a custom interface (Shannon *et al.*, 1990) without using the patient's own Spectra-22 speech processor. The signal was first pre-emphasized using a first-order Butterworth high-pass filter with a cutoff frequency of 1200 Hz, and then bandpass filtered into four broad frequency bands using eighth-order Butterworth filters. The corner frequencies of the bands were at 100 Hz, 713 Hz, 1509 Hz, 3043 Hz, and 6000 Hz (the same filters used in the acoustic simulation). The envelope of the signal in each band was extracted by half-wave rectification and low-pass filtering (eight-order Butterworth) with a 160-Hz cutoff frequency. Note that this envelope filter frequency is somewhat lower than that used in the acoustic simulation due to the

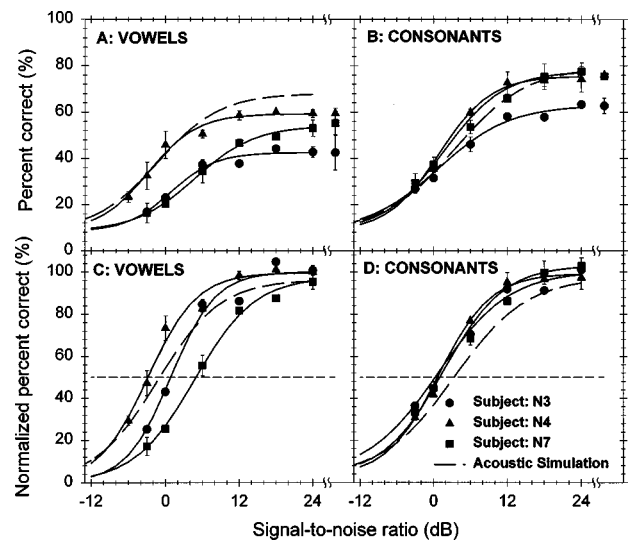


FIG. 4. Recognition of vowels and consonants from three Nucleus-22 cochlear implant users as a function of signal-to-noise ratio with a four-channel CIS processing strategy. (A) Individual vowel scores. (B) Individual consonant scores. (C) Normalized vowel scores after correction for chance. (D) Normalized consonant scores after correction for chance. Error bars indicate \pm one standard deviation. The long-dashed lines represent the results from four-band speech in normal-hearing listeners. The short-dashed lines indicate 50% of the normalized score after correction for chance.

lower re-sampling rate used in electric stimulation. Previous results with acoustic processors showed no significant difference for envelope filter frequencies of 160 Hz and 500 Hz (Shannon *et al.*, 1995). The acoustic amplitude (40-dB range) was transformed into electric amplitude by a power-law function with an exponent of 0.2 ($E=A^{0.2}$; Fu and Shannon, 1998) between each subject's threshold (T -level) and upper level of loudness (C -level). Then this transformed amplitude was used to modulate the amplitude of a continuous, 500-pulse/s biphasic pulse train with a 100- μ s/phase pulse duration, and delivered to electrode pairs (18,22), (13,17), (8,12), and (3,7).

B. Results

Figure 4(A) and (B) shows the recognition scores of vowels and consonants as a function of signal-to-noise ratio when the implant users listened to the four-channel CIS processing strategy. The long-dashed line re-plots the mean results from the four-band speech condition in the acoustic simulation from Fig. 1(A) and (B). Due to a significant effect of subjects on vowel recognition [$F(2,90) = 6.84$, $p = 0.002$], Fig. 4 plots the individual recognition score for all subjects instead of plotting the mean score. The performance-intensity functions (PIF) of subject N4, who had the best performance, were close to those from acoustic simulation in both vowel recognition [$F(1,34) = 3.23$, $p = 0.081$] and consonant recognition [$F(1,34) = 0.073$, $p = 0.789$]. For subject N7, the recognition scores of consonants were similar to those from acoustic simulation [$F(1,34) = 0.007$, $p = 0.935$], however, the vowel scores were significantly lower than those from acoustic simulation [$F(1,34) = 22.74$, $p < 0.001$]. For subject N3, the recognition scores of vowels were significantly lower than the results from the corresponding acoustic simulation conditions

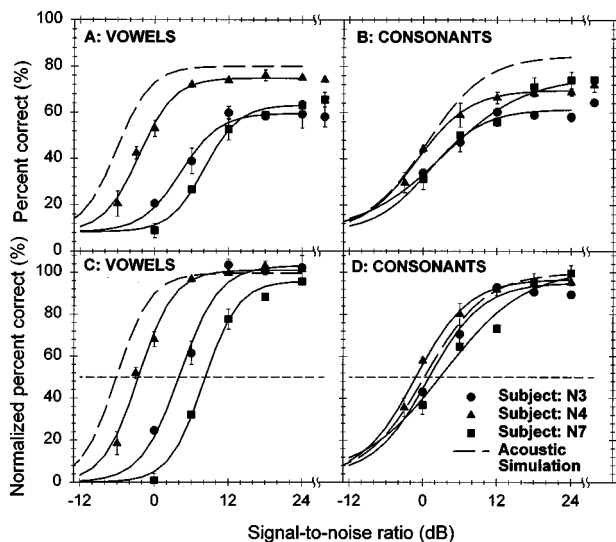


FIG. 5. Recognition of vowels and consonants from three Nucleus-22 cochlear implant users as a function of signal-to-noise ratio with SPEAK processing strategy. (A) Individual vowel scores. (B) Individual consonant scores. (C) Normalized vowel scores after correction for chance. (D) Normalized consonant scores after correction for chance. Error bars indicate \pm one standard deviation. The long-dashed lines represent the results with SPEAK-like speech in normal-hearing listeners. The short-dashed lines indicate 50% of the normalized score after correction for chance.

[$F(1,34) = 53.17, p < 0.001$] while consonants were slightly lower than the results from the corresponding acoustic simulation conditions [$F(1,34) = 3.32, p = 0.077$]. Figure 4(C) and (D) shows the normalized percent correct for vowel and consonant recognition, respectively. The short-dashed lines in Fig. 4(C) and (D) indicate 50% of the normalized score after correction for chance.

Figure 5(A) shows the recognition scores of vowels as a function of signal-to-noise ratio from three cochlear implant users with their own speech processor with SPEAK processing strategy. The long-dashed line shown in the figure represents the acoustic simulation results from SPEAK-like speech for comparison. Results were significantly poorer than the acoustic simulation results for subject N4 [$F(1,34) = 9.69, p = 0.004$], subject N3 [$F(1,34) = 65.33, p < 0.001$], and subject N7 [$F(1,34) = 46.22, p < 0.001$]. Figure 5(B) shows recognition scores for consonants as a function of signal-to-noise ratio for three cochlear implant subjects, with the medium-dashed line showing the acoustic simulation results for SPEAK-like speech. Results were slightly poorer than the acoustic simulation results for subject N4 [$F(1,34) = 4.52, p = 0.041$], but significantly poorer for subject N3 [$F(1,34) = 15.77, p < 0.001$] and subject N7 [$F(1,34) = 6.35, p = 0.017$]. Figure 5(C) and (D) shows normalized vowel and consonant scores relative to the recognition score in the quiet condition (and corrected for chance). The short-dashed lines in Fig. 4(C) and (D) indicate 50% of the normalized score after correction for chance. Figure 5(C) shows that all three implant subjects have steep P/I slopes for vowel stimuli which are similar to the slope of the simulation results. Note that the performance level in quiet was significantly different. PRTs for the three implant listeners ranged from +8.06 to -2.51 dB, compared to -6.14 dB for the normal-hearing subjects. However, the normalized consonant

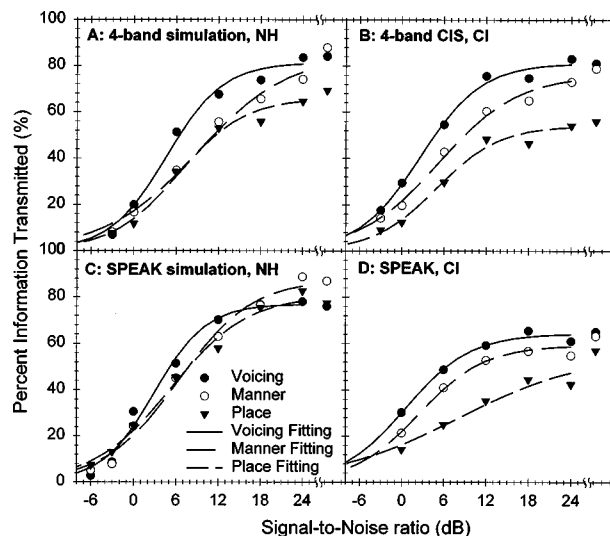


FIG. 6. Percent information received on voicing, manner, and place cues for CIS and SPEAK strategies in implant and normal-hearing listeners. (A) Normal-hearing subjects listening to four-band speech. (B) Cochlear implant listeners with four-channel CIS processing strategy. (C) Normal-hearing subjects listening to SPEAK-like speech. (D) Cochlear implant listeners with SPEAK processing strategy. The lines represent the best-fit curves based on Eq. (1).

P/I curves of all three cochlear implant users were similar to the average curve from the normal-hearing simulation, indicating that the primary difference was in the level of performance in quiet.

Figure 6 presents the consonant information received on the production-based categories of voicing, manner and place (Miller and Nicely, 1955). Panels (A)–(D) show information received as a function of S/N ratio for the four-band CIS condition and the SPEAK condition for both normal-hearing and implant listeners. For the four-band CIS condition note that implant listeners received approximately the same amount of information on voicing and manner cues as did the normal-hearing listeners. However, overall the implant listeners received less place information than the acoustic listeners. The implant patient with the best speech recognition (N4) received nearly the same amount of place information as acoustic listeners. However, for the SPEAK processor implant listeners did not receive as much information on any of the three categories as normal-hearing listeners with SPEAK-like speech.

Figure 7 shows the average phoneme recognition threshold (PRTs) of vowels and consonants from normal-hearing subjects listening to different acoustic simulation conditions and the individual phoneme recognition thresholds from the three cochlear implant users with both SPEAK and CIS processing strategies. For acoustic hearing, the unprocessed speech had the best PRT: -9.92 dB for vowels and -8.41 dB for consonants. The PRT for vowels deteriorated by 7.44 dB as the number of bands decreased from 16 to 3. The PRT for consonants deteriorated by 7.86 dB as the number of bands decreased from 16 to 3. The PRTs for SPEAK-like processing were similar to the 16-band processor for vowels and similar to the 8-band processor for consonants. Implant listeners had similar consonant PRTs to normal-hearing (NH) listeners in the SPEAK condition, and slightly better

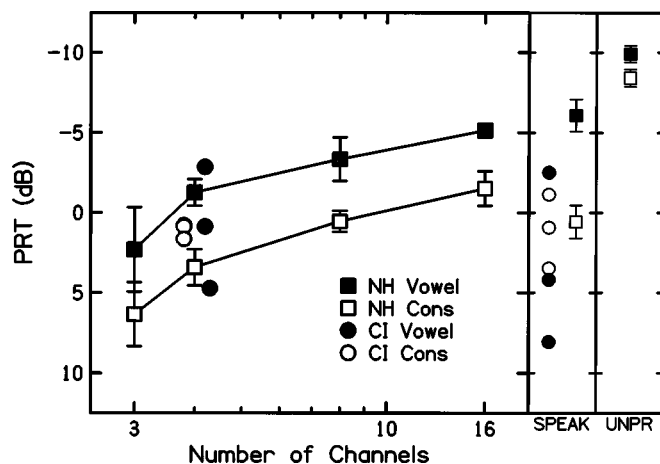


FIG. 7. Phoneme recognition thresholds for vowels and consonants as a function of experimental conditions. Phoneme recognition threshold was defined as the S/N at which the phoneme recognition score fell to 50% of its value when no noise was added (after correction for chance).

PRTs in the four-band condition. However, all three cochlear implant (CI) listeners had considerably poorer PRTs for vowels than NH listeners in the SPEAK condition, and only one CI listener had a vowel PRT that was in the normal range in the four-band condition.

C. Discussion

Speech recognition by the better cochlear implant listeners with four-band CIS processing was similar to that for NH listeners with the same processing strategy. This result is similar to the recent study by Dorman and Loizou (1997, 1998) which showed similar performance between seven CI patients with a six-channel CIS processor and NH listeners with a six-band processor. In their study four of the seven CI listeners had performance on multi-talker vowels that was similar to NH listeners and three CI listeners were poorer. In the present study two of the three CI listeners showed similar performance to NH listeners on vowel recognition and one of three was similar on consonant recognition. Information transmission analysis of the consonant results showed that reception of place information was the primary difference between CI and NH listeners: Similar levels of information were received by CI and NH listeners on voicing and manner cues. This result suggests that implant listeners were not able to fully utilize spectral place information even with four widely separated electrodes. In addition, the three CI listeners showed significantly different levels of performance, while the performance of NH listeners was more uniform. This pattern of results suggests that one factor contributing to the high variability of CI performance is the variability in the ability to integrate spectral cues in CI listeners.

One potential factor that might limit the cross-spectral integration of information in CI listeners is the interaction between electrodes. In the ideal case, implant listeners with completely independent electrodes would be able to use as many channels of spectral information as they have electrodes. If electrodes are highly interactive this might limit the effective number of information channels to less than the number of electrodes. In a separate series of experiments

(Hanekom and Shannon, 1996, 1998; Chatterjee and Shannon, 1998) that measured electrode interaction in these same three CI listeners, N4 did have the least cross-electrode interaction and the highest speech recognition performance. However, even CI listener N7 had essentially no interaction between the four electrodes used in the four-band CIS-like condition, although his PRT for vowels was poorer than the NH PRT for the three-band processor. So although these CI listeners have relatively little channel interaction, N3 was still not able to effectively utilize all four channels of spectral information. Thus simple interaction across electrodes does not appear to explain the difference in performance across CI subjects.

In general, for both CIS and SPEAK processing the PRT for CI and NH listeners was similar for consonants while CI listeners did worse on vowels. In the SPEAK processing scheme temporal resolution is reduced to provide more spectral information. Twenty electrodes (or carrier noise bands) are available to represent the spectral information. In the NH listeners this processing scheme produced PRTs that were similar to 16-band CIS for vowels and 8-band CIS for consonants. However, CI listeners with the SPEAK strategy performed similarly for consonants, but only at the three-band CIS level for vowels (Fig. 7). This result again suggests that implant listeners are not able to integrate speech information across electrodes as well as NH listeners can integrate the same cues across frequency. In addition, CI listeners with SPEAK perform more poorly than NH listeners on voicing and manner cues (Fig. 6). This suggests that the implant listeners with SPEAK processing are losing potential temporal cues as well. It may be that the strategy of SPEAK processing to trade off temporal resolution for increased spectral resolution may not be the best trade-off for CI listeners. While these three listeners did better in quiet with the SPEAK processor, in noise the SPEAK processing produced poorer vowel PRTs and poorer consonant place-of-articulation recognition than the four-band CIS processing, even though they had more than one year of experience with SPEAK processing and no experience with CIS processing.

While normal-hearing subjects showed a significant relation between the performance in quiet and PRTs (Fig. 2), cochlear implant users did not. Whereas subjects N4 and N7 had similar vowel recognition scores for the unprocessed and +24-dB S/N conditions (55%) in the four-band CIS condition, additional noise had a much more detrimental effect on performance for subject N7 than for N4 (Fig. 4), resulting in a difference of 7.6 dB in their PRTs. The individual variability in performance among cochlear implant users may be due to many factors, such as amplitude mapping, electrode interaction, as well as frequency-electrode mismatch. These factors might distort the relation between quiet performance and PRT due to differential contributions of these factors to speech performance in either quiet or in noise condition.

The slope of the performance in noise curves indicate the susceptibility of each processing condition to increasing levels of noise. This slope is dependent on the materials used, and can be as steep as 10%–20%/dB for sentence materials (Plomp and Mimpen, 1979; Nilsson *et al.*, 1998). The slope for normal-hearing subjects listening to the unproc-

essed speech was 7.8%/dB for vowels and 6.1%/dB for consonants, similar to previous results from normal-hearing listeners in speech-shaped noise (Studebaker *et al.*, 1994). Slopes were shallower in the acoustic simulation conditions in which spectral information was reduced; the slopes for vowels in all conditions were between 3.3% and 6.7%/dB, while the slopes for consonants were 2.7%–4.3%/dB. There was no significant difference in slope for implant listeners and for the corresponding acoustic simulation conditions. Thus the shallow slope observed in implant listeners appears to be due to the reduced spectral resolution.

A major concern when comparing the results from normal-hearing subjects and cochlear implant users is the effect of learning (Rosen *et al.*, 1997). In all conditions the subjects were given no experience with a particular speech processor prior to formal vowel and consonant testing. The only exception was the SPEAK processor for implant listeners, a processing strategy with which they had had at least one year of daily experience. However, the results in this condition were still poorer for CI listeners than for NH listeners. Without experience the difference in performance may have been even larger. NH listeners, who presumably have full access to spectral cues, had higher speech recognition even though they had no practice with the SPEAK processing strategy. This is additional evidence that the CI listeners are not achieving full use of the spectral information provided by the SPEAK processing strategy, even after prolonged experience.

III. GENERAL DISCUSSION

The data from the present study quantify the susceptibility of cochlear implant users with the current SPEAK and CIS speech processing strategies to interfering noise. The results from normal-hearing listeners simulating the loss of spectral resolution in implants indicate that the noise susceptibility is at least partly due to the loss of fine spectral structure caused by the number of electrodes used in the speech processing strategy. In addition, implant listeners may have other limitations due to their individual etiology of deafness that may further reduce performance.

In some respects, implant listeners are similar to hearing aid users in that they may be unable to recognize speech at signal-to-noise ratios (S/N) that are quite tolerable to normal-hearing listeners. Recent studies have demonstrated that individuals with sensorineural hearing loss often have markedly reduced speech recognition scores in noise compared to normal-hearing listeners (Cooper and Cutts, 1971; Cohen and Keith, 1976; Plomp and Mimpen, 1979; Dirks *et al.*, 1982; Van Tasell *et al.*, 1987, 1988). The PRT of cochlear implant users is similar to the PRT of hearing-impaired subjects listening to amplified speech (Dirks *et al.*, 1982). Moore (1997) suggested that the two most important causes of the noise susceptibility in hearing-impaired listeners were reduced frequency selectivity and loudness recruitment. The gain in hearing aids and the amplitude mapping functions in implants will partially correct for loudness recruitment, but both groups may be limited by their common problem: the lack of fine spectral information. For cochlear implants, the current speech processing strategies preserve only crude

spectral information because of the limitation of the number of electrodes; all detailed fine spectral information is lost. Some hearing-impaired listeners have reduced frequency selectivity (e.g., Stelmachowicz *et al.*, 1985; Horst, 1987; Turner and Henn, 1989), and so may not be able to utilize the fine spectral information.

The results of the present study showed that the noise susceptibility of cochlear implant users was similar to that of normal-hearing subjects listening to an acoustic simulation of cochlear implant speech processing. Although previous studies have shown that speech performance in quiet does not improve as the number of electrodes are increased (Fishman *et al.*, 1997; Dorman and Loizou, 1997, 1998; Brill *et al.*, 1997), the present study shows that a larger number of electrodes may enhance speech performance in noise. This suggests that improved performance by cochlear implant users in noise may be achieved by (1) improving the effective number of spectral channels by increasing the number of electrodes or by signal processing that allows more complete utilization of the existing electrodes, or (2) preprocessing with noise suppression algorithms (Weiss, 1993; van Hoesel *et al.*, 1993, 1995a, b, 1997). These pre-processing strategies work well at +10 dB to 0 dB S/N level, which is a S/N region where cochlear implant listeners can benefit.

IV. SUMMARY AND CONCLUSIONS

The susceptibility of cochlear implant users to the interfering effects of background noise is partly due to the loss of fine spectral information inherent in the current speech processing strategies. Levels of spectral reduction that have little effect in quiet conditions can still result in substantial performance decrements in noise. Some cochlear implant patients show performance in quiet and in noise that is similar to normal-hearing listeners with equivalent reduction in spectral resolution. However, other cochlear implant listeners show poorer performance than processor-matched normal-hearing subjects, suggesting that those implant listeners are not receiving as many spectral channels of information as electrodes. Better noise suppression methods prior to the actual speech processing should be considered and included in the future speech processor designs. Performance in noise could also be improved if speech processing methods could be developed to allow cochlear implant patients to utilize more spectral channels.

ACKNOWLEDGMENTS

We wish to thank Professor James Hillenbrand for allowing us to use the multi-talker vowel test materials, and also thank the three implant listeners and four normal-hearing subjects for their participation in the current experiments. This research was supported by NIDCD.

Baer, T., and Moore, B. C. J. (1993). "Effects of spectral smearing on the intelligibility of sentences in noise," *J. Acoust. Soc. Am.* **94**, 1229–1241.

Baer, T., and Moore, B. C. J. (1994). "Effects of spectral smearing on the intelligibility of sentences in the presence of interfering speech," *J. Acoust. Soc. Am.* **95**, 2277–2280.

Boothroyd, A., Mulhearn, B., Gong, J., and Ostroff, J. (1996). "Effects of spectral smearing on phoneme and word recognition," *J. Acoust. Soc. Am.* **100**, 1807–1818.

- Brill, S., Gstöttner, W., Helms, J., vIlberg, C., Baumgartener, W., Müller, J., and Keifer, J. (1997). "Optimization of channel number and stimulation rate for the fast continuous interleaved sampling strategy in the COMBI 40+," *American Journal of Otology* **18** (Suppl.), S104–S106.
- Chatterjee, M., and Shannon, R. V. (1998). "Forward masked excitation patterns in multielectrode cochlear implants," *J. Acoust. Soc. Am.* **103**, 2565–2572.
- Cochlear Corporation (1995). *Audiologist Handbook* (Englewood, CO).
- Cohen, R. L., and Keith, R. W. (1976). "Use of low-pass noise in word recognition," *J. Speech Hear. Res.* **19**, 48–54.
- Cooper, J. C., and Cutts, B. P. (1971). "Speech discrimination in noise," *J. Speech Hear. Res.* **14**, 332–337.
- Dirks, D. D., Morgan, D. E., and Dubno, J. R. (1982). "A procedure for quantifying the effects of noise on speech recognition," *J. Speech Hear. Disorders* **47**, 114–123.
- Dorman, M. F., and Loizou, P. C. (1997). "Speech intelligibility as a function of the number of channels of stimulation for normal-hearing listeners and patients with cochlear implants," *Am. J. Otol.* **18**, S113–S114.
- Dorman, M. F., and Loizou, P. C. (1998). "Identification of consonants and vowels by cochlear implant patients using a 6-channel continuous interleaved sampling processor and by normal-hearing subjects using simulations processors with two to nine channels," *Ear and Hearing* **19**, 162–166.
- Dorman, M. F., Loizou, P. C., and Rainey, D. (1997). "Speech understanding as a function of the number of channels of stimulation for processors using sine-wave and noise-band outputs," *J. Acoust. Soc. Am.* **102**, 2403–2411.
- Dowell, R. C., Seligman, P. M., Blamey, P. J., and Clark, G. M. (1987). "Speech perception using a two-formant 22-electrode cochlear prosthesis in quiet and in noise," *Acta Oto-Laryngol.* **104**, 439–446.
- Dubno, J. R., and Dorman, M. F. (1987). "Effects of spectral flattening on vowel identification," *J. Acoust. Soc. Am.* **82**, 1503–1511.
- Fishman, K., Shannon, R. V., and Slattery, W. H. (1997). "Speech recognition as a function of the number of electrodes used in the SPEAK cochlear implant speech processor," *J. Speech Hear. Res.* **40**, 1201–1215.
- Fu, Q.-J., and Shannon, R. V. (1998). "Effects of amplitude nonlinearities on speech recognition by cochlear implant users and normal-hearing listeners," *J. Acoust. Soc. Am.* **104**, 2570–2577.
- Hanekom J. J., and Shannon R. V. (1996). "Place pitch discrimination and speech recognition in cochlear implant users," *South African Journal of Communication Disorders*, **43**, 27–40.
- Hanekom, J. J., and Shannon, R. V. (1998). "Gap detection as a measure of electrode interaction in cochlear implants," *J. Acoust. Soc. Am.* **104**, 2372–2384.
- Hillenbrand, J., Getty, L. A., Clark, M. J., and Wheeler, K. (1995). "Acoustic characteristics of American English vowels," *J. Acoust. Soc. Am.* **97**, 3099–3111.
- Hochberg, I., Boothroyd, A., Weiss, M., and Hellman, S. (1992). "Effects of noise and noise suppression on speech perception by cochlear implant users," *Ear and Hearing* **13**, 263–271.
- Horst, J. W. (1987). "Frequency discrimination of complex signals, frequency selectivity, and speech perception in hearing-impaired subjects," *J. Acoust. Soc. Am.* **82**, 874–885.
- Kiefer, J., Müller, J., Pfennigdorf, T., Schön, F., Helms, J., von Ilberg, C., Gstöttner, W., Ehrenberger, K., Arnold, W., Stephan, K., Thumfart, W., and Baur, S. (1996). "Speech understanding in quiet and in noise with the CIS speech coding strategy (Med-El Combi-40) compared to the Multi-peak and Spectral peak strategies (Nucleus)," *ORL* **58**, 127–135.
- McDermott, H. J., McKay, C. M., and Vandali, A. E. (1992a). "A new portable sound processor for the University of Melbourne/Nucleus Limited Multichannel cochlear implant," *J. Acoust. Soc. Am.* **91**, 3367–3371.
- McDermott, H. J., McKay, C. M., Vandali, A. E., and Clark, G. M. (1992b). "A comparison of speech perception of cochlear implantees using the Spectral Maxima Sound Processor (SMSP) and the MSP (Multi-peak) processor," *Acta Oto-Laryngol.* **112**, 752–761.
- Miller, G., and Nicely, P. (1955). "An analysis of perceptual confusions among some English consonants," *J. Acoust. Soc. Am.* **27**, 338–352.
- Moore, B. C. J. (1995). *Perceptual Consequences of Cochlear Damage* (Oxford U.P., New York) (with accompanying CD of audio demonstrations).
- Müller-Deiler, J., Schmidt, B. J., and Rudert, H. (1995). "Effects of noise on speech discrimination in cochlear implant patients," *Ann. Otol. Rhinol. Laryngol.* **166**, 303–306.
- Nejime, Y., and Moore, B. C. J. (1997). "Simulation of the effect of threshold elevation and loudness recruitment combined with reduced frequency selectivity on the intelligibility of speech in noise," *J. Acoust. Soc. Am.* **102**, 603–615.
- Nilsson, M., Soli, S., and Masuda, A. (1998). "A definition of normal binaural sentence recognition in quiet and noise," *J. Am. Acad. Audiol.* (in press).
- Plomp, R., and Mimpen, A. M. (1979). "Speech-reception threshold for sentences as a function of age and noise level," *J. Acoust. Soc. Am.* **66**, 1333–1342.
- Rosen, S., Faulkner, A., and Wilkinson, L. (1997). "Perceptual adaptation by normal listeners to upward shifts of spectral information in speech and its relevance for users of cochlear implants," in *Speech, Hearing, and Language: Work in Progress* (Phonetics and Linguistics, University College, London), Vol. 10.
- Shannon, R. V., Adams, D. D., Ferrel, R. L., Palumbo, R. L., and Grandgenett, M. (1990). "A computer interface for psychophysical and speech research with the Nucleus cochlear implant," *J. Acoust. Soc. Am.* **87**, 905–907.
- Shannon, R. V., Zeng, F.-G., Kamath, V., Wygonski, J., and Ekelid, M. (1995). "Speech recognition with primarily temporal cues," *Science* **270**, 303–304.
- Skinner, M. W., Clark, G. M., Whitford, L. A., et al. (1994). "Evaluation of a new spectral peak coding strategy for the Nucleus-22 channel cochlear implant system," *Am J. Otol.* **15**, 15–27.
- Stelmachowicz, P. G., Jesteadt, W., Gorga, M. P., and Mott, J. (1985). "Speech perception ability and psychophysical tuning curves in hearing impaired listeners," *J. Acoust. Soc. Am.* **77**, 620–627.
- Studebaker, G. A., Taylor, R., and Sherbecoe, R. L. (1994). "The effect of noise spectrum on speech recognition performance-intensity functions," *J. Speech Hear. Res.* **37**, 439–448.
- ter Keurs, M., Festen, J. M., and Plomp, R. (1992). "Effect of spectral envelope smearing on speech reception. I," *J. Acoust. Soc. Am.* **91**, 2872–2880.
- ter Keurs, M., Festen, J. M., and Plomp, R. (1993). "Effect of spectral envelope smearing on speech reception. II," *J. Acoust. Soc. Am.* **93**, 1547–1552.
- Turner, C. W., and Henn, C. C. (1989). "The relation between vowel recognition and measures of frequency resolution," *J. Speech Hear. Res.* **32**, 49–58.
- Van Hoesel, R. J., and Clark, G. M. (1995a). "Evaluation of a portable two-microphone adaptive beamforming speech processor with cochlear implant patients," *J. Acoust. Soc. Am.* **97**, 2498–2503.
- Van Hoesel, R. J., and Clark, G. M. (1995b). "Manikin and cochlear implant patient test results with a portable adaptive beamforming processor to suppress the effect of noise," *Ann. Otol. Rhinol. Laryngol.* **166**, 144–146.
- Van Hoesel, R. J., and Clark, G. M. (1997). "Psychophysical studies with two binaural cochlear implant subjects," *J. Acoust. Soc. Am.* **102**, 495–507.
- Van Hoesel, R. J., Tong, Y. C., Hollow, R. D., and Clark, G. M. (1993). "Psychophysical and speech perception studies: A case report on a binaural cochlear implant subject," *J. Acoust. Soc. Am.* **94**, 3178–3189.
- Van Tasell, D. J., and Yanz, J. L. (1987). "Speech recognition threshold in noise: Effects of hearing loss, frequency response, and speech materials," *J. Speech Hear. Res.* **30**, 377–386.
- Van Tasell, D. J., Larsen, S. Y., and Fabry, D. A. (1988). "Effects of an adaptive filter hearing aid on speech recognition in noise by hearing-impaired subjects," *Ear and Hearing* **9**, 15–21.
- Weiss, M. R. (1993). "Effects of noise and noise reduction processing on the operation of the Nucleus-22 cochlear implant processor," *J. Rehab. Res. Develop.* **30**, 117–128.
- Wilson, B. S., Finley, C. C., Lawson, D. T., Wolford, R. D., Eddington, D. K., and Rabinowitz, W. M. (1991). "New levels of speech recognition with cochlear implants," *Nature* (London) **352**, 236–238.
- Yost, W. A., and Sheft, S. (1993). "Auditory perception," in *Human Psychophysics*, edited by W. A. Yost, A. N. Popper, and R. R. Fay (Springer-Verlag, New York), pp. 193–236.

The relation between identification and discrimination of vowels in young and elderly listeners^{a)}

Maureen Coughlin,^{b)} Diane Kewley-Port,^{c)} and Larry E. Humes^{d)}

Department of Speech and Hearing Sciences, Indiana University, Bloomington, Indiana 47405

(Received 22 April 1997; revised 5 August 1998; accepted 16 September 1998)

This study examined both the identification and discrimination of vowels by three listener groups: elderly hearing-impaired, elderly normal-hearing, and young normal-hearing. Each hearing-impaired listener had a longstanding symmetrical, sloping, mild-to-moderate sensorineural hearing loss. Two signal levels [70 and 95 dB sound-pressure level (SPL)] were selected to assess the effects of audibility on both tasks. The stimuli were four vowels, /i,e,ε,æ/, synthesized for a female talker. Difference limens (DLs) were estimated for both $F1$ and $F2$ formants using adaptive tracking. Discrimination DLs for $F1$ formants were the same across groups and levels. Discrimination DLs for $F2$ showed that the best formant resolution was for the young normal-hearing group, the poorest was for the elderly normal-hearing group, and resolution for the elderly hearing-impaired group fell in between the other two at both signal levels. Only the elderly hearing-impaired group had DLs that were significantly poorer than those of the young listeners at the lower, 70 dB, level. In the identification task at both levels, young normal-hearing listeners demonstrated near-perfect performance ($M = 95\%$), while both elderly groups were similar to one another and demonstrated lower performance ($M = 71\%$). The results were examined using correlational analysis of the performance of the hearing-impaired subjects relative to that of the normal-hearing groups. The results suggest that both age and hearing impairment contribute to decreased vowel perception performance in elderly hearing-impaired persons. © 1998 Acoustical Society of America. [S0001-4966(98)05112-1]

PACS numbers: 43.71.Ky, 43.66.Ts, 43.66.Fe [RHD]

INTRODUCTION

Very few studies have examined both identification and discrimination of speech by hearing-impaired listeners, with even fewer focusing exclusively on vowel perception (Nabelek *et al.*, 1992; Van Tasell *et al.*, 1987; Turner and Henn, 1989; Leek *et al.*, 1987; Summers and Leek, 1992). Moreover, elderly hearing-impaired subjects have seldom been the focus of vowel-perception studies. Given the primary importance of audiometric threshold elevation for other speech recognition tasks among this group (Humes, 1996), the present study examines vowel perception in elderly hearing-impaired listeners as compared to both elderly and young normal-hearing listeners. The purpose of this project was to extend ongoing work examining basic speech-perception capabilities and to investigate the impact of hearing impairment and age on a listener's ability to identify and discriminate vowels.

Since vowels have relatively higher amplitude and longer duration than consonants, they are believed to be more salient for persons with hearing impairment. Reports such as Pickett (1970) represent the common view that vowel-recognition performance is "grossly abnormal" only for a person with a profound hearing loss. Recent research, however, by Nabelek *et al.* (1992) has reported a range of

vowel-identification performance of 68% to 93% for subjects with only a modest hearing impairment, such as a mild-to-moderate sloping sensorineural hearing loss.

In the case of the young normal-hearing listener, natural vowels at audible levels are not usually confused with one another because the peripheral auditory system preserves the spectro-temporal differences between different vowels (Turner and Henn, 1989). Peterson and Barney (1952) reported that natural vowels spoken by men, women, and children are highly identifiable with an average score of 94%. In replications of that study, Hillenbrand *et al.* (1995) obtained an overall identification score of 95% for natural vowels, but for steady-state, synthetic vowels, a lower overall score of 73% was observed (Hillenbrand and Gayvert, 1993). However, higher identification scores (83%) have been observed for synthetic vowels modeled after one female talker (Kewley-Port, 1991). In general, natural vowels in isolation are identified correctly 85%–90% by young normal-hearing listeners (Jenkins *et al.*, 1994).

Vowel-formant discrimination in young normal-hearing listeners has also been studied and related to frequency discrimination of simpler sounds. Discrimination ability for the normal-hearing listener at a comfortable presentation level (60–70 dB SPL) for a 1000-Hz pure tone 200 ms in duration, for example, is approximately 2 Hz or a Weber fraction ($\Delta F/F$) of 0.002 or 0.2% (Moore, 1973), with a logarithmic increase in discrimination threshold as frequency increases logarithmically. Vowels are complex stimuli where threshold ΔF s for a change in formant frequency results in spectral differences in the intensity of the harmonics.

^{a)}Some material in this manuscript was presented at the 130th meeting of the Acoustical Society of America, St. Louis, MO, November 1995.

^{b)}Electronic mail: mcoughli@indiana.edu

^{c)}Electronic mail: kewley@indiana.edu

^{d)}Electronic mail: humes@indiana.edu

Kewley-Port and Watson (1994), for instance, used psychophysical procedures incorporating minimal-uncertainty training in a vowel-formant discrimination task. Threshold ΔF s were reported as approximately 14 Hz in the $F1$ region (<800 Hz) with thresholds increasing linearly in the $F2$ region as a function of frequency. These results suggested a Weber fraction of 1.5% that was better than previously reported thresholds of 3%–7% for vowel formants by Flanagan (1955) and Mermelstein (1978). Those investigators used less than optimal experimental procedures; namely, higher stimulus uncertainty and little subject training. The thresholds reported by Kewley-Port and Watson (1994) likely represent the optimal discrimination abilities of normal-hearing listeners at the limits of performance.

Most of the literature on identification and discrimination of speech by hearing-impaired listeners focuses on young hearing-impaired listeners. Hearing impairment, however, is of significant concern to the elderly. Elderly persons consider disabilities involving communication to be among the most severe (Jacobs-Condit, 1984). Despite its importance, the role of peripheral hearing loss on the speech communication process in the elderly has not always received careful attention. However, Humes and colleagues performed a series of experiments examining several proposed hypotheses thought to account for the decreased speech understanding abilities in the elderly hearing-impaired population. The series began by examining peripheral hearing loss (i.e., audibility or decreased spectral resolution) and found that indeed peripheral hearing loss, as opposed to central auditory processing or cognitive factors, accounted for approximately 80% of the variance in speech identification performance (Humes and Roberts, 1990; Humes and Christopherson, 1991). That is, the subjects with the poorest pure-tone thresholds consistently demonstrated the poorest speech recognition ability. To account for the remaining 20% of the variance, Humes and Christopherson (1991) examined four groups of subjects on a range of speech perception tasks. The groups were divided into ‘‘young–old’’ (age 65–75 years) hearing impaired, ‘‘old–old’’ (age 76–86 years) hearing impaired, young normal-hearing, and young simulated hearing-loss listeners. The results showed that the young–old hearing-impaired listeners performed less well than the young normal-hearing listeners, but not significantly different than the young simulated hearing-loss listeners. The old–old listeners performed significantly worse than all other groups. These results suggest that audibility is the primary factor in the decreased performance of the young–old group, which was consistent with the previous findings in the series (Humes and Roberts, 1990). Additional decreases in performance of the old–old group appeared to be related to factors other than audibility. In any hearing loss, central auditory processing problems and cognitive factors may be present in addition to the peripheral loss, and each factor’s role in speech understanding may be difficult to determine. However, it appears that hearing sensitivity is the factor most highly correlated with speech understanding ability among the elderly.

Recent work by Gordon-Salant and Fitzgibbons (1995), however, demonstrated age-related decreases in speech-

recognition performance in conditions of acoustic degradation, such as background noise or reverberation. These results applied to elderly normal-hearing listeners, as well as to those with a mild-to-moderate sensorineural hearing loss. They found age-related degradation in performance to be most notable in conditions of time compression when compared to young listeners. Fox *et al.* (1992) also reported a difference in performance between young and elderly listeners on a silent-center monosyllabic word identification task. The elderly listeners’ performance suggested a decreased ability to use dynamic acoustic information. The authors hypothesized that the difference in performance could possibly be greater with isolated vowels as stimuli, although this has yet to be examined.

Although the hearing-impaired listener demonstrates reduced spectral resolution (Nabelek, 1992; Van Tasell *et al.*, 1987; Turner and Henn, 1989; Leek *et al.*, 1987), it appears that the mild-to-moderately hearing-impaired listener’s identification and discrimination abilities may be reduced but adequate, in some cases. Nabelek (1992) reported similar vowel-identification errors among hearing-impaired subjects and normal-hearing listeners in a degraded listening condition, such as reverberation or noise. Van Tasell *et al.* (1987) found that vowel-masking patterns of the hearing-impaired subjects were compressed when compared to the patterns of the normal-hearing subjects, and that the peaks were less resolved and spectral details were not preserved. Despite the obvious alteration of the incoming speech signal, one of Van Tasell’s three hearing-impaired subjects recognized the majority of the seven synthetic vowel stimuli well (93%), while the other two performed near 70% accuracy. Turner and Henn (1989) found that speech-masking patterns indicated that subjects with sensorineural hearing loss do not preserve the spectral features of a speech sound as well as normal-hearing subjects. Leek *et al.* (1987) created a complex vowel-like sound with four amplitude peaks between 0.1 and 4.0 kHz. They measured identification ability in noise as a function of peak-to-trough differences in the spectrum of those complex stimuli. They reported that normal-hearing listeners could identify greater than 75% of the vowels with less than a 2-dB peak-to-trough difference, while the hearing-impaired listeners required approximately a 6–7-dB difference to achieve the same score. Although different peak-to-trough thresholds were obtained between groups, hearing-impaired subjects were able to score greater than 90% correct when the peak-to-trough difference was large (14 dB) and held constant. Leek *et al.* (1987) also reported that, for some natural vowels, peak-to-trough differences may be as high as 25–30 dB, and that may be an explanation as to why listeners with poor spectral resolution demonstrate reasonably accurate identification ability for some natural vowels. The question remains whether there is a relationship between listeners’ identification performance and their ability to discriminate underlying spectral differences, especially when a peripheral hearing loss is present.

The purpose of the present study was to examine the effects of hearing loss and age on a listener’s ability to discriminate and identify vowels. More specifically, this study examined the extent to which identification performance can

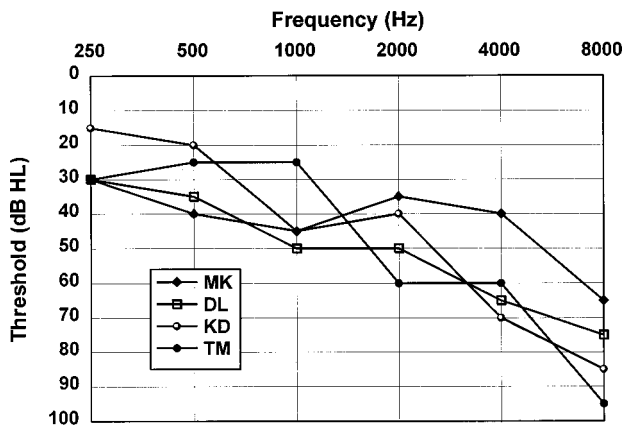


FIG. 1. Preferred ear pure-tone thresholds of the hearing-impaired subjects.

be predicted by discrimination performance and whether correlations between discrimination and identification performance and hearing loss or age exist.

I. METHOD

A. Subjects

Three subject groups, consisting of young normal-hearing ($N=4$), elderly normal-hearing ($N=4$), and elderly hearing-impaired ($N=4$), served as listeners for this study. Young normal-hearing subjects (YNH) ranged in age from 23 to 24 years ($M=23.5$ y), elderly normal-hearing (ENH) from 71 to 77 years ($M=73.75$ y), and elderly hearing-impaired (EHI) from 69 to 74 years ($M=71.5$ y). All normal-hearing subjects ($N=8$) had pure-tone thresholds of 20 dB HL or less at octave intervals from 250–4000 Hz, and no evidence of middle-ear pathology at the time of testing. Subjects in the YNH group were graduate students in the Department of Speech and Hearing Sciences at Indiana University, while the ENH and EHI subjects were recruited from a subject pool maintained by the Department of Speech and Hearing Sciences and were residents of Bloomington, Indiana. All subjects were paid for their participation.

Each hearing-impaired subject ($N=4$) had a long-standing, bilaterally symmetrical, moderate, sloping sensorineural hearing loss, believed to be of cochlear origin based on acoustic reflex testing, case history, and symmetry of air- and bone-conduction thresholds. Average air-conduction thresholds of the hearing-impaired group for 0.25, 0.5, 1, 2, and 4 kHz were 26, 30, 41, 46, and 59 dB HL (ANSI, 1996), respectively. Normal middle-ear status was determined for all subjects by tympanometric testing at the initial visit. Figure 1 shows individual pure-tone thresholds for the four

hearing-impaired subjects at octave intervals from 250 through 8000 Hz. This particular configuration of hearing loss was chosen based on literature reporting it as the most obvious and well-documented peripheral deficit in the elderly (Corso, 1959; Spoor, 1967). All hearing-impaired subjects were consistent users of amplification and demonstrated intelligible speech. Both groups of elderly listeners were found to be within normal limits for their age on two cognitive tests (WAIS-R and WMS-R).

B. Stimuli

The stimuli consisted of the four monophthongal English vowels, /i, e, ε, æ/, that had been used in earlier studies of detection thresholds (Kewley-Port, 1991) and formant discrimination (Kewley-Port and Watson, 1994). These vowels to be used in the identification and discrimination tasks were selected to maximize variability in performance as required for successful correlational analyses. A pilot study with an additional group of YNH subjects was administered to determine the identification accuracy for a larger set of ten English vowels (/i, i, e, ε, æ, a, ʌ, o, u, u/). The pilot study revealed a large variation in performance across the four target vowels used in the present study. Investigations of speech perception by hearing-impaired listeners also indicate that the four front vowels, /i/, /e/, /ε/, and /æ/, are easily confused (Nabelek *et al.*, 1992). Assmann (1982) reported that the same four vowels had a large number of errors in vowel confusion matrices, although /ʌ/ caused the most errors. The four acoustically similar front vowels, /i, e, ε, æ/, were selected for study.

The four target vowels were synthesized from spectrographic measurements of a female talker using the cascade branch of the KLTSYN synthesizer (Klatt, 1980). The steady-state formant values are shown in Table I. Fundamental frequency linearly fell from 220–180 Hz over the entire duration of the vowel. Vowel duration was set to 175 ms, the average of the talker's long and short vowels. The overall amplitude contour had a shallow rise/fall shape for naturalness. Bandwidths for the formants were constant across vowels at $BW1=70$, $BW2=90$, and $BW3=170$ Hz. The four vowels synthesized with these parameters are referred to as the standard vowels. RMS energy for standard vowels was measured at the maximum amplitude portion of the vowel (between 21–50 ms after onset) and a range of 9 dB was found for the four vowels. Previous research (Kewley-Port and Watson, 1994) has demonstrated that this range is typical for a constant gain in the glottal source that excites a full range of formant values. However, since hearing-impaired subjects were being used, it was important to assure that the

TABLE I. Frequencies in Hz for formants $F1$, $F2$, and $F3$ used in synthesizing the four vowels. The last two columns give the range of formant values in the test sets for $F1$ and $F2$ incremental changes (inc).

Vowel	Standard vowels			Range values	
	$F1$	$F2$	$F3$	$F1$ inc	$F2$ inc
i	450	2300	3000	455–522	2315–2513
e	550	2500	3100	555–621	2515–2712
ε	600	2200	3000	605–671	2210–2341
æ	1000	1950	3000	1007–1107	1960–2091

TABLE II. Procedures used for normal-hearing and hearing-impaired listeners.

Days	Experimental design	
	Task	Presentation level (dB SPL)
1–3	Minimal uncertainty training, /i/ F1	95
4–6	Medium uncertainty discrimination	95
7–8	Medium uncertainty discrimination	70
9	Identification	95 and 70

digital amplitude of the synthetic vowels was reasonably well equated to eliminate possible effects of intensity differences on the final results. Therefore, a median rms value was chosen and all vowels were adjusted to be within ± 1 dB of this value. As a result, the vowel /æ/ was resynthesized with an adjusted glottal output.

The standard vowels were used in both the identification and discrimination task. The test vowels to be discriminated from the standard vowels were synthesized in sets of 14 stimuli. Each set included test vowels for one of two conditions, namely an increment in $F1$ or $F2$ formant frequency for a total of eight separate sets of test stimuli. For each stimulus set, 14 step sizes in formant frequency were calculated using a log ratio such that steps 10–14 would be easily discriminable from the standard (Table I). Although steps 10–14 would be easily discriminable for the normal-hearing listeners (Kewley-Port and Watson, 1994), a second set of test stimuli were synthesized such that the largest step size was increased by 50% to allow a wider range of testing for the hearing-impaired subjects.

Two levels of signal presentation, 70 and 95 dB SPL, were chosen to assess the effect of audibility on speech perception performance for the elderly hearing-impaired subjects. A level of 95 dB SPL was chosen as a highly audible level and one that approached the upper limit of comfortable loudness for both the normal-hearing and elderly hearing-impaired listeners. Supra-threshold spectral information for the elderly hearing-impaired subjects was thought to be comparable to the normal-hearing subjects at this level. A second presentation level of 70 dB SPL was less audible for the elderly hearing-impaired, especially in the higher frequencies where the hearing loss was more significant. This level is also closer to the 77 dB SPL level used in the earlier studies with YNH by Kewley-Port and Watson (1994).

C. Overview of experimental design

The design of this experiment is mixed with a between-subjects factor of subject group (EHI, ENH, and YNH) and within-subjects factors of vowel (four target vowels), task (identification and discrimination), and presentation level (70 dB and 95 dB SPL). The order in which each condition of the experiment was presented is shown in Table II. Subjects participated in a total of nine testing sessions, each 90 min in length. Initial training under minimal uncertainty was provided for both groups of listeners in order to obtain low and

stable thresholds (Kewley-Port and Watson, 1994). Subsequently, discrimination testing of the first and second formants for four vowels was conducted under medium stimulus uncertainty (i.e., all four vowels and both formants mixed within a block). Discrimination testing required three sessions (4.5 h) at 95 dB SPL followed by two sessions (3 h) at 70 dB SPL to achieve stable thresholds. On the final day of testing, the identification task was administered at both presentation levels. The design presumed that the discrimination task would provide some training, or at least familiarity, with the vowels prior to the identification task.

D. Procedures

Two experimental tasks were selected, an identification and a discrimination task. The vowels for both tasks were output through a 16-bit D/A converter (Tucker-Davis Technologies DA-1) at a 10 000-Hz sample rate followed by a digital 4000-Hz low-pass filter with a 65-dB/octave rejection rate. The calibration /æ/ vowel was set to the signal level (70 dB or 95 dB SPL) as measured in a 6-cc coupler with a Larson-Davis sound-level meter (model 800B). The vowel was calibrated via a VU meter prior to each testing session. The subjects listened to stimuli under TDH-39 headphones, coupled to the right ear of the normal-hearing subjects and to the preferred ear for the hearing impaired subjects. Subjects indicated their responses on a keyboard. The identification task was a standard forced-choice classification task. Four one-word responses containing the four test vowels were displayed on a computer screen; subjects entered the responses directly into the computer. The training portion of the identification task consisted of one block (20 trials) of ordered presentation and one block (20 trials) of random presentation of the four target vowels, both with feedback. These two blocks were repeated, totaling four blocks (80 trials) of training at a 95 dB SPL presentation level. Subjects then listened to four blocks (80 trials) of stimuli, presented without feedback, at both presentation levels. Testing alternated in levels between 70 and 95 dB SPL on successive blocks.

Test procedures for the discrimination portion of this study followed those of Kewley-Port and Watson (1994), which involved psychophysical procedures designed to obtain optimal discrimination performance. An adaptive-tracking task was used to obtain the thresholds at 71% correct following Levitt (1971). In each trial, stimuli were presented in a modified, two-alternative, forced-choice task with feedback with a 400-ms interstimulus interval. The standard was presented in the first interval, and subjects pressed a key to indicate which of the next two intervals contained the “different” (test) stimulus.

Each formant condition was individually tested in 80-trial blocks. Kewley-Port and Watson (1994) found no difference in thresholds for incremental or decremental discrimination changes. As a result, all different (test) stimuli in this study consisted of an increment in formant frequency only. The $F1$ for /i/ was chosen as the training vowel for the discrimination task because the $F1$ formant shift is in the lower frequency regions and would presumably be easier to discriminate for our subjects with high-frequency hearing loss. After substantial training (>20 blocks) with the /i/

vowel (see Table II), the task then switched from minimal uncertainty to medium uncertainty, in which any of the eight formants was presented as the standard within a block. Adaptive tracks were separately maintained for each formant. For each block, a value of ΔF representing discrimination performance was calculated as the difference in formant frequency between the standard and the test vowels using the average of the formant frequencies of the reversals over the ten trials in a testing block. Discrimination results are referred to as difference limens (DLs). A formant-frequency DL for each subject was averaged from the ΔF values from the last four blocks, unless an outlier score appeared in the last four blocks, in which case the block immediately preceding the final four was substituted. Based on previous discrimination testing under medium uncertainty (Kewley-Port, 1992), it was estimated that reasonably stable DLs could be achieved with four-and-one-half h (>2000 trials) of testing. Subjects first participated in testing for the four-and-one-half hours at 95 dB, followed by three h of testing with the same stimuli at 70 dB SPL.

II. RESULTS

A. Discrimination task

Minimal uncertainty training using /i/ F1 (21 blocks consisting of 1680 trials) for all three subject groups suggested listeners were near asymptotic performance. In particular, ΔF decreased until a plateau was observed over at least four blocks. The average ΔF of the last four blocks of training sessions for the EHI group was 17.9 Hz. The averages of the YNH and ENH groups were 18.6 and 21.7 Hz, respectively. These results demonstrate that consistent thresholds for this low-frequency formant were obtained across groups after training.

Estimates of the DLs as ΔF averaged separately across each subject group are displayed in Fig. 2 as a function of formant frequency. DLs for the 95 dB SPL level are shown in Fig. 2(a) and for the 70 dB SPL level in Fig. 2(b). Data from the medium-uncertainty discrimination task (Table III) indicate large differences in DLs across presentation level in the F2 region, in contrast to small differences in the F1 region. Specifically, performance in the F1 region was similar for all groups in all conditions. In the F2 region (>1800 Hz), on the other hand, the hearing-impaired subjects' DLs were elevated by a factor of three, as compared to those for

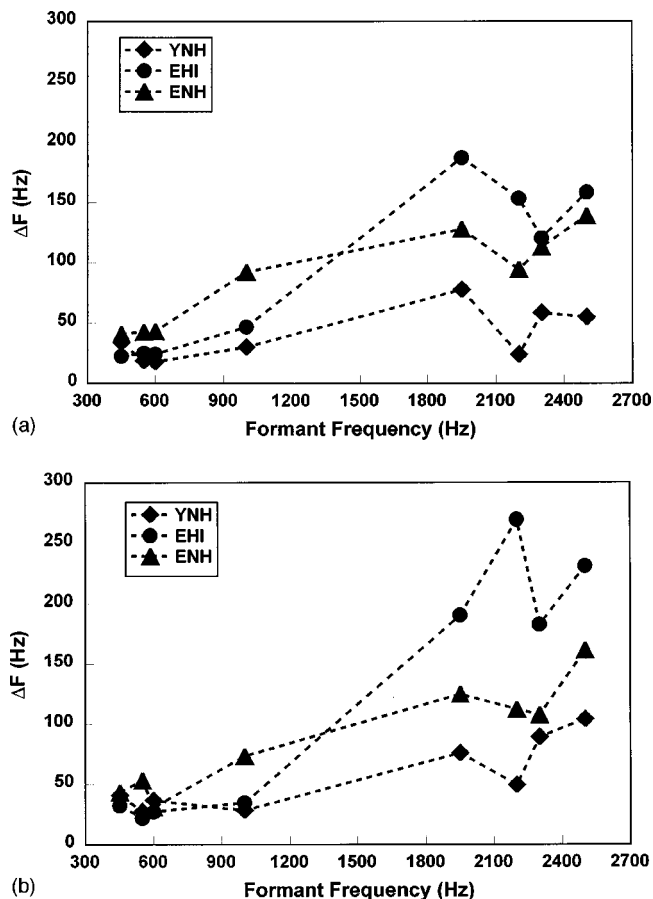


FIG. 2. Average discrimination performance for the three groups. Data points labeled 450–1000 Hz represent corresponding F1 changes for /i/, /e/, /ɛ/ and /æ/, respectively. Data points 1950–2500 Hz represent the F2 changes for the same vowels in the order of /æ/, /ɛ/, /i/, and /e/. The points in this figure are connected to illustrate the differences in performance between the different groups. (a) Displays data at 95 dB SPL, and (b) at 70 dB SPL.

YNH subjects, and by a factor of about 1.5 times higher than those for ENH subjects in the 95-dB condition [Fig. 2(a)]. A somewhat similar pattern of results was observed at the lower presentation level [Fig. 2(b)]. High variability in the F2 region was noted for the elderly-listener groups (Table III). Three-way analysis of variance performed on the DLs revealed significant main effects for group, level, and formant frequency across F1 and F2 [group: $F(2,9) = 8.91$, $p < 0.01$; level: $F(1,9) = 12.83$, $p < 0.01$; formant: $F(7,63) = 46.59$, $p < 0.001$]. The group by formant interaction was

TABLE III. Means and standard deviations of discrimination DLs demonstrating the high variability in performance for the elderly groups.

	F1								F2								
	I		e		ɛ		æ		I		e		ɛ		æ		
	\bar{x}	s.d.	\bar{x}	s.d.	\bar{x}	s.d.	\bar{x}	s.d.	\bar{x}	s.d.	\bar{x}	s.d.	\bar{x}	s.d.	\bar{x}	s.d.	
95 dB																	
YNH	33.83	10.36	18.76	7.90	17.88	3.31	30.02	12.65	58.45	34.04	54.85	2.47	23.88	7.70	77.71	34.24	
ENH	40.81	11.37	42.66	20.45	43.15	6.74	92.39	10.95	113.11	30.67	139.18	57.78	94.52	20.97	128.00	8.91	
EHI	22.64	15.37	25.14	5.21	24.24	16.43	46.75	22.38	120.63	61.33	158.82	103.71	153.61	60.93	187.39	18.99	
70 dB																	
YNH	40.84	19.45	27.43	14.43	36.77	13.02	28.43	9.17	89.11	15.34	103.93	27.95	49.46	18.37	75.81	26.51	
ENH	43.32	12.82	53.20	3.07	30.83	10.71	73.31	23.30	107.67	49.36	161.41	54.22	112.26	14.31	124.76	5.68	
EHI	32.36	14.37	22.00	19.15	27.24	14.59	34.75	26.78	182.82	24.50	231.33	121.95	269.68	101.41	190.53	19.37	

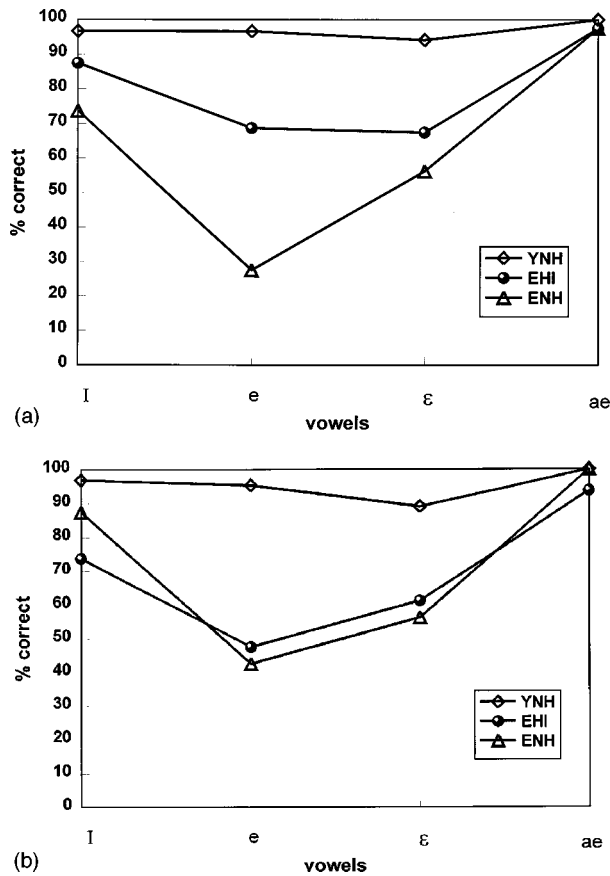


FIG. 3. Average identification scores for all three groups' presentation level. (a) Displays data at 95 dB SPL, and (b) at 70 dB SPL.

significant [$F(14,63)=9.21, p<0.001$], as well as level by formant [$F(7,63)=4.45, p<0.001$]. Group by level interaction was barely nonsignificant and no significant three-way interaction was present. A Scheffe *post-hoc* test for DLs for the main effect of group suggested that the YNH group was significantly different ($p<0.05$) from the EHI group, but neither the YNH nor the EHI were significantly different from the ENH group.

B. Identification task

Identification performance during training to learn the key-word responses for the four target vowels was monitored. Results of the training blocks showed that the sub-

jects' performance systematically improved by the end of the training session. An accuracy level of 80% correct was achieved by all listeners after training except subject MD of the ENH group, whose maximum score equaled 40%, and subject TM of the EHI group, whose high score reached 60% correct.

1. Group comparisons

Overall identification scores for the three groups were 97%, 80%, and 64% at the 95-dB presentation level and 95%, 69%, and 72% at the 70-dB level for the YNH, EHI, and ENH groups, respectively. Identification scores are shown for each vowel and level in Fig. 3(a) and (b) and Table IV. In general, vowels /e/ and /ε/ were more easily confused for subjects in identification, while the vowel /æ/ showed small differences between groups. Three-way analysis of variance for the arcsine transformed identification scores revealed a significant difference for vowel and group, but not level [vowel: $F(3,24)=13.03, p<0.001$; group: $F(2,8)=4.48, p<0.05$]. No significant interactions between the independent variables were present. Scheffe *post-hoc* analysis of group differences suggested there were no strong pair-wise differences between groups because of the high variability in the elderly groups.

2. Variability within groups

Identification scores for YNH subjects, for vowels or levels (Table IV), were near ceiling performance and therefore had low variability. Therefore, identification performance for the YNH group can be represented by a single grand-mean value of 97% averaged over subjects, levels, and vowels. The overall performance (97% correct) on these synthetic steady-state vowels was somewhat higher than expected. Hillenbrand and Gayvert (1993) and Kewley-Port (1991), for example, reported overall performance levels for ten-vowel sets of 73.8% and 83%, respectively. This high level of performance can likely be attributed to the small four-vowel set and training procedures. In contrast, one of the most notable results was the high variability in performance for both elderly groups. For the EHI group, the best subject's score equaled 93.1%-correct vowel identification

TABLE IV. Means and standard deviations for vowel identification in percent correct demonstrating high variability in performance for the elderly groups.

Identification	I		e		ε		æ	
	\bar{x}	s.d.	\bar{x}	s.d.	\bar{x}	s.d.	\bar{x}	s.d.
95 dB								
YNH	100	0	98.33	2.87	96.67	5.77	100	0
ENH	73.75	40.29	27.50	23.27	56.25	30.65	97.50	5
EHI	87.50	21.80	68.75	37.05	67.50	32.02	97.5	2.89
70 dB								
YNH	95	8.67	95	5	91.67	14.43	100	0
ENH	87.50	15	42.50	29.01	56.25	37.50	100	0
EHI	73.75	18.88	47.5	43.69	61.25	36.83	93.75	7.5

and the worst subject scored 51.75%. A similar range was found in the ENH group, as the best subject scored 84.4% while the worst subject scored 50.6%.

III. DISCUSSION

A. Discrimination results

The discrimination results for the YNH group were similar to those of Kewley-Port and Watson (1994). They reported a pattern for formant discrimination thresholds for normal-hearing subjects that was constant across frequency in the $F1$ range, with thresholds progressively increasing as a function of frequency in the $F2$ region. The average DL in the $F1$ region for the YNH group (as well as the ENH and EHI groups) in this study was approximately 30 Hz. This value is elevated compared to the discrimination thresholds of 14 Hz found in Kewley-Port and Watson, apparently due to the difference in stimulus uncertainty (medium versus minimal).

Vowels at the 95 dB SPL presentation level should have been audible for all groups, and therefore, no difference was expected between groups in discrimination ability. Both the normal-hearing groups showed no difference in discrimination performance on the basis of the presentation level for either 70 or 95 dB (Table III). The discrimination results at 70 dB should have demonstrated the poorest performance in the $F2$ region for hearing-impaired listeners. As expected, discrimination performance of the EHI group was elevated, but only for $F2$ frequencies greater than 1800 Hz, suggesting that high-frequency hearing loss affected discrimination performance. However, significantly poorer performance for $F2$ formants at the 95-dB level was also noted. A possible reason for the poorer performance at both levels could be audibility, on the assumption that $F2$ spectral information was still not sufficiently above hearing threshold in the higher-frequency region, even at 95 dB SPL. Alternatively, the poorer $F2$ -discrimination performance could be related to factors other than audibility that affect a hearing-impaired listener's ability to discriminate spectral changes, such as the broader auditory filters for vowels reported by Turner and Henn (1989) and Van Tasell *et al.* (1987).

A somewhat surprising result, however, was the similar performance in the $F1$ region by all groups in all conditions. Based on this result, it is reasonable to assume that the low-frequency hearing deficit was mild enough that the majority of the speech spectrum was audible in that region, resulting in near-normal performance for the $F1$ DLs at both levels. While the contributions of low $F1$ frequencies versus $F2$ frequencies to vowel identification are not known, the implication is that the correct recognition of vowels might be improved if the hearing-impaired listeners focused more attention on the $F1$ region with near-normal resolution than on the impaired $F2$ region. This strategy holds even more potential for improvement as listening levels approach those of normal conversation and $F2$ formants become inaudible. Training techniques, such as those used by Christensen and Humes (1996), to draw attention to different acoustic dimensions, may be worth pursuing for $F1$ versus $F2$ listening strategies. We should not overlook, however, that for the

crowded English vowel space, differences in formant frequencies for $F1$ may be very close to the DL, as it is for the 50-Hz difference for /e/-/ɛ/, which approaches the average 40.9-Hz $F1$ DL for elderly listeners.

As shown in the statistical analysis, subject age (ENH vs YNH) did not have a significant effect on performance for the discrimination task. $F2$ DL group means for the ENH group, although higher than those from the YNH group, did not differ significantly (see Table III for discrimination-group means and standard deviations). However, wide variation in individual performance for some $F2$ DLs was observed for the elderly normal-hearing listeners.

B. Identification results

Unlike the discrimination results, age-related decreases in performance appeared in the identification results. The ENH group performed significantly worse than the YNH group on vowel identification. The difference in performance between the two tasks may be due to increased cognitive requirements to identify vowels in a four-alternative, forced-choice task compared to those needed to discriminate auditory stimuli in a minimal stimulus uncertainty task. Identification requires perceiving the stimulus, matching it to a stored, central representation, and then attaching a label. In discrimination, on the other hand, perceptual comparisons can be made in short-term memory without labeling. Several studies have shown age-related identification performance differences for degraded listening situations (Nabelek, 1988; Fox *et al.*, 1992). Our isolated synthetic vowel stimuli represent a type of degraded speech signal, since they have no formant movement and lack other characteristics of natural speech. While no difference in identification performance between the two elderly groups was noted, both elderly groups performed significantly worse than the YNH group. The vowel /æ/ was consistently identified accurately by all groups, while /e/ and /ɛ/ presented the greatest difficulty for elderly listeners. The vowels /ɪ/ and /ɛ/ are short, lax vowels in English, and the fixed duration for all vowels may have interfered with correct identification. Probably, the unnatural steady-state, fixed-duration formants, in the otherwise diphthongized /e/ vowel, were responsible for reduced identification.

As noted by several other researchers, accurate identification of English vowels is dependent on combined information from three acoustic properties: spectral cues for the vowel target, vowel duration, and formant dynamics (Andruski and Nearey, 1992; Jenkins *et al.*, 1994; Hillenbrand *et al.*, 1995). In this experiment, the four synthetic vowels had reduced acoustic cues related primarily to the spectral targets of $F1$ and $F2$. Many studies with younger normal-hearing listeners have found that after minimal training, synthetic steady-state vowels can be identified at better than 80% accuracy (Assmann *et al.*, 1982; Kewley-Port, 1991). In the present study, the YNH listeners identified the four-vowel set with 95% accuracy. However, our two groups of elderly listeners had the same amount of training and obtained an average of 71% correct for the same four-vowel set. It is our hypothesis that younger listeners are able to adjust criteria used to categorize vowels when presented with

reduced acoustic information more quickly, and with less training, than elderly listeners. If this hypothesis is true, it has numerous implications for explaining difficulties encountered by elderly persons in deriving benefit from hearing aids, as well as exploring methods of aural rehabilitation to improve hearing-aid benefit.

C. Relation of identification performance to discrimination performance

Correlational analyses were undertaken to examine the hypothesis that as a listener's ability to discriminate the underlying spectral differences between vowels is degraded, identification accuracy should also decrease. Baseline data for the hearing-impaired group were compared to each of the normal-hearing groups (YNH and ENH) to facilitate examination of this relationship (essentially, discrimination "loss" was correlated with identification "loss"). YNH listeners were used as the standard of performance as representative of the most typical population of listeners. The ENH were chosen to compare with the EHI group in order to control for some factors related to age that might affect performance on the listening tasks, in addition to those associated with hearing impairment.

Since the focus of analysis was the loss or difference in abilities as a result of hearing impairment, the data evaluated in the correlations were difference scores. For discrimination, a difference in ΔF between EHI and the corresponding normal-hearing group was calculated, called ΔT . Because there was a significant difference for both normal-hearing groups across formant and level for discrimination, ΔT was calculated from ΔF for each formant and level by subtracting individually from the normal-hearing group ΔF the corresponding ΔF for each EHI subject. For identification, different procedures were followed. Based on the analysis of variance results, identification performance for the YNH group was represented by a single mean value of the four vowels ($M=97\%$). However, since formant frequency was a significant factor for the vowel identification in the ENH group, identification values for the ENH group were calculated separately for each formant and averaged across level. A "percent-difference identification" score, ΔP , was obtained by subtracting the normal-hearing mean scores from the individual EHI subject scores. Thus two sets of ΔT and ΔP difference scores were calculated, one each for either the YNH or the ENH group as the reference standard.

The goal of these correlational analyses was to see if identification could be predicted from discrimination for the EHI listeners. This is only meaningful where a difference in discrimination exists between the two presentation levels indicating a possible effect of hearing impairment. Little difference in performance across groups was observed for all $F1$ DLs and for $/\text{æ}/ F2$ at the two presentation levels (Table III). As a result, correlational analyses for the EHI listeners were conducted with only the three $F2$ formants ($/i, e, \text{ɛ}/$) that demonstrated a difference across groups. Correlations of differences in discrimination performance (ΔT) with differences in identification performance (ΔP), for each subject and presentation level, were significant for the young normal-hearing as standard (Fig. 4, $r = -0.55$, $p = 0.005$)

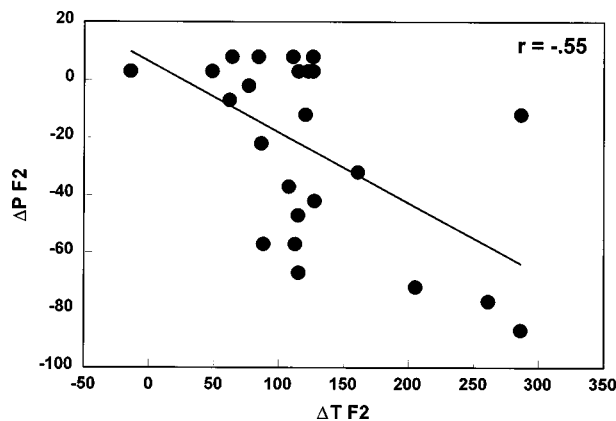


FIG. 4. Group correlation between the differences in DLs (ΔT) and percent identification (ΔP) for $F2$. DL differences were calculated by subtracting the YNH ΔF value for each $F2$ formant and level individually from each corresponding ΔF for the EHI listeners. Percent-difference identification is calculated by subtracting the raw EHI data from the average YNH performance.

and the elderly normal-hearing as standard (Fig. 5, $r = -0.46$, $p < 0.025$). Significant negative correlations are interpreted to mean that, as discrimination of formant frequency degrades with hearing impairment, these increased DLs predict a corresponding decrease in the ability to identify vowel quality.

The similarity of the significant correlation coefficients for both groups of normal listeners, young ($r = -0.55$) and elderly ($r = -0.46$), was not anticipated. The YNH group provides a baseline measure that represents excellent performance relative to the variables of age, hearing status, and testing competence, since these listeners were young, normal-hearing graduate students in speech and hearing sciences. It was expected that differences between them and the EHI group, therefore, would be sufficiently large to reveal a significant correlation. For the ENH, however, the two factors of age and testing competence were presumably similar to those of the EHI group, thereby reducing potential differences between the groups. Not only did this turn out to be true, but in the case of the identification task, the performance difference between elderly groups was neutralized,

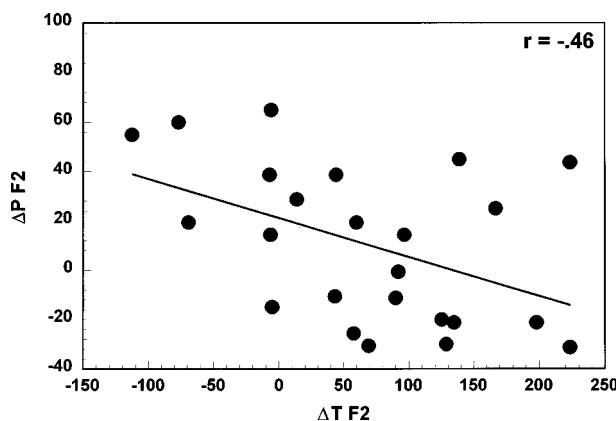


FIG. 5. Group correlation between the differences in DLs (ΔT) and percent identification (ΔP) for $F2$. DL difference and percent-difference identification were calculated between the EHI group and the ENH group similar to that for Fig. 4.

apparently by an age-related factor related to learning to label reduced-cue synthetic vowels. In spite of this, a significant negative correlation was obtained, one that was only slightly smaller than that for the YNH group.

This result was not an obvious outcome of these experiments for several reasons. Although other researchers have found reduced ability for hearing-impaired listeners to discriminate aspects of vowel spectra, the general conclusion of those studies is similar to that of Leek *et al.* (1987), who stated that spectral contrast in vowels is sufficient to provide useful cues to vowel identity for persons with moderate hearing impairment. This implies that there would be little systematic relation between discrimination and identification. In this experiment, a significant correlation was found between the two tasks on the basis of $F2$ alone. As previously mentioned, EHI subjects might be expected to identify vowels reasonably well using their near-normal ability to resolve differences in $F1$. Since this was not the case for just the four-vowel set studied here, other investigations of the relation between discrimination and identification are needed to determine the effects of impairment for all 11 monophthongal English vowels. We note, however, that in a pilot study using a set of ten English vowels and a group of YNH, only the four vowels used in this study showed anything other than near-perfect performance. Our focus has been on the most common configuration of hearing impairment, that of moderate-sloping sensorineural loss. Because wide variation is observed for many measures of audiometric function within this group, further investigation with a larger number of subjects is needed to establish the relation of degraded formant discrimination to actual speech recognition performance. Examining the predictability of identification from $F2$ discrimination, we note that the variance accounted for was about 25%. In the previous discussion, several other factors that may contribute to differences in individual performance on the two tasks have been identified, such as normal DLs for $F1$, cognitive abilities to learn task procedures, and ability to adapt perceptual strategies for the identification of reduced-cue vowels. In addition, detailed individual differences in auditory function undoubtedly played a role, and those revealed by the audiogram are discussed in the next section. Considering these potential sources of variability, the 25% level of variance accounted for by $F2$ alone appears to be a good first step towards improving our understanding of vowel perception by persons with mild-to-moderate hearing impairment.

D. Relation of vowel discrimination and hearing loss

Next, the correlational analysis of peripheral hearing loss on discrimination performance was examined. Since the discrimination results contained a natural split in thresholds between high- and low-frequency formants for these four vowels, correlational analysis was conducted based on the low-frequency and high-frequency pure-tone averages of the elderly hearing-impaired subjects. A sensation level (SL) for each subject was calculated by subtracting pure-tone averages separately, either low (LFSL=0.25, 0.5 and 1 kHz) or high (HFSL=2 and 4 kHz), from the presentation level. High or low SL was paired with the corresponding discrimi-

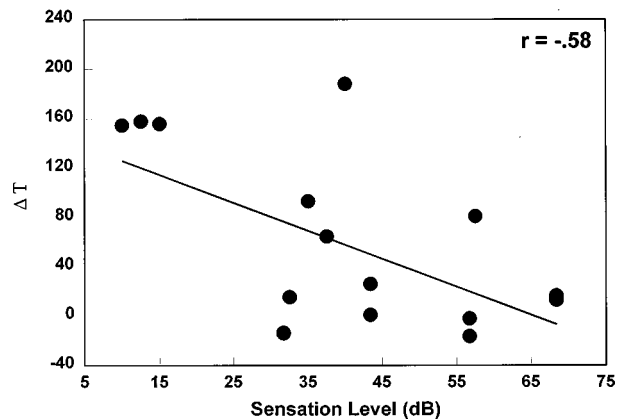


FIG. 6. Group correlation between sensation level and threshold differences for both low-frequency ($F1$) and high-frequency ($F2$) regions. Threshold differences were calculated as an average of the ΔT values for the EHI group subtracted from YNH over $F1$ and $F2$ separately. Sensation level was calculated from the pure-tone averages separately for the low- or high-frequency regions (see the text). $F1$'s are filled circles and $F2$'s are open circles.

nation differences (ΔT) for the YNH or ENH standards. Values were then averaged across $F1$ (low) or $F2$ (high) frequency regions, for a total of 16 pairs of values (4 subjects \times 2 levels \times 2 formants). Correlations for these 16 pairs for the YNH standard reached significance (Fig. 6, $r = -0.58$, $p < 0.02$), as well as the same comparison for the ENH standard (Fig. 7, $r = -0.71$, $p < 0.005$). Thus, degraded ability to discriminate among vowel formants is predictable, in part, on the basis of audibility. Moreover, when the age-related factors are comparable for the two elderly groups and hearing status is presumably the primary difference between groups, 50% of the variance is accounted for by audibility. This result supports the conclusion of other studies by Humes and colleagues (Humes, 1996) that reduced audibility is a primary factor for the decreased abilities to process speech observed for elderly persons with hearing loss.

IV. SUMMARY AND CONCLUSIONS

Three groups of subjects (elderly normal-hearing, elderly hearing-impaired, and young normal-hearing) partici-

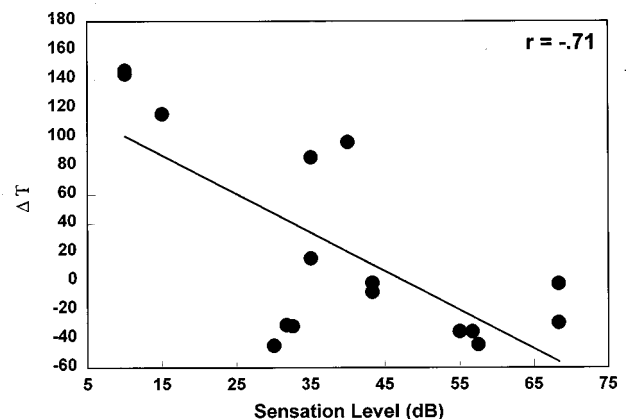


FIG. 7. Group correlation between sensation level and threshold differences for both low-frequency ($F1$) and high-frequency ($F2$) regions. Threshold differences were calculated for the EHI group subtracted from the YNH group similar to that in Fig. 6.

pated in the same experimental tasks (identification and discrimination) at two signal levels (70 and 95 dB SPL) to determine the role of hearing loss and age on a listener's ability to discriminate and identify vowels. The discrimination performance of the young normal-hearing listeners was typical of previous results for these stimuli (Kewley-Port and Watson, 1994). The young normal-hearing subjects demonstrated excellent vowel-identification scores at both presentation levels, an overall average of 97% for the four target vowels. Elderly normal-hearing discrimination performance was not significantly different from that of the young normal-hearing group. However, identification performance was different. Possible explanations for the difference may be cognitive load required for each task. Although some studies reference age-related performance deficits with identification (Nabelek, 1988; Fox *et al.*, 1992), further examination of age and auditory task may provide more conclusive evidence.

Large differences in performance within the hearing-impaired group, despite their similar audiometric configurations, suggest the heterogeneity of the group as a whole. As a result, one is cautioned against making individual predictions based on the results of the group performance. However, given the range of normal-to-impaired performance for discrimination in the *F2* region exhibited with this sample, group performance is probably representative of other groups of hearing-impaired subjects with similar losses. Elderly hearing-impaired *F2* discrimination performance was significantly worse at the lower presentation level (70 dB) than at the higher level (95 dB).

The final questions addressed in this study involved the various relations among an individual's identification performance, their underlying ability to discriminate spectral changes, and their peripheral hearing loss. The wide variability of performance over vowels exhibited by subjects across levels for *F2* allowed for correlational analyses. Analyses for three formants in the *F2* region that showed variability for the hearing-impaired group revealed a significant correlation between difference limens for formant discrimination and the ability to correctly identify the vowel. This correlation was significant when both young normal-hearing and elderly normal-hearing subject groups were used as standards of comparison. Therefore, it is concluded that vowel identification is partially predicted by reduced ability to discriminate spectral differences in the *F2* region (at higher frequencies). Also, the stimulus sensation level and subjects' discrimination performance were significantly correlated.

Overall, the results of this study suggest that while the hearing-impaired listener may attend to *F1* cues when identifying a vowel, the role of the *F2* cues is evident in the correlations. Based on these results, it appears that a hearing-impaired listener's ability to discriminate overall spectral changes in the high frequencies may be predictive of his or her ability to correctly identify the vowel sound. It appears that a mild-to-moderate high-frequency hearing loss for some subjects does have a significant effect on vowel identification, even in optimal listening conditions. Thus, even with normal discrimination in the *F1* region and when vowels are at apparently audible levels in the *F2* region, some

listeners have such elevated *F2* DLs that identification is impaired.

ACKNOWLEDGMENTS

This research was supported by the National Institutes of Health Grants No. NIHD02229 and NIHAG-08293 to Indiana University.

- Andruski, J., and Nearey, T. (1992). "On the sufficiency of compound target specification of isolated vowels and vowels in /bVb/ syllables," *J. Acoust. Soc. Am.* **91**, 390–410.
- ANSI (1996). ANSI S3.6-1996, "Specification for Audiometers" (American National Standards Institute, New York).
- Assmann, P. F., Nearey, T. M., and Hogan, J. T. (1982). "Vowel identification: Orthographic, perceptual, and acoustic aspects," *J. Acoust. Soc. Am.* **71**, 975–989.
- Christensen, L. A., and Humes, L. E. (1996). "Identification of multidimensional complex sounds having parallel dimensional structure," *J. Acoust. Soc. Am.* **99**, 2307–2315.
- Corso, J. (1959). "Age and sex differences in pure-tone thresholds," *J. Acoust. Soc. Am.* **31**, 498–507.
- Flanagan, J. (1955). "Difference limen for the intensity of a vowel sound," *J. Acoust. Soc. Am.* **27**, 288–291.
- Fox, R. A., Wall, L. G., and Gokcen, J. (1992). "Age-related differences in processing dynamic information to identify vowel quality," *J. Speech Hear. Res.* **35**, 892–902.
- Gordon-Salant, S., and Fitzgibbons, P. J. (1995). "Recognition of multiply degraded speech by young and elderly listeners," *J. Speech Hear. Res.* **38**, 1150–1156.
- Hillenbrand, J., and Gayvert, R. T. (1993). "Identification of steady-state vowels synthesized from the Peterson and Barney measurements," *J. Acoust. Soc. Am.* **94**, 668–674.
- Humes, L. E., and Christopherson, L. A. (1991). "Speech identification difficulties of hearing-impaired elderly persons: The contributions of auditory processing deficits," *J. Speech Hear. Res.* **34**, 686–693.
- Humes, L. E., and Roberts, L. (1990). "Speech-recognition difficulties of the hearing-impaired elderly: The contributions of audibility," *J. Speech Hear. Res.* **33**, 726–735.
- Humes, L. E. (1996). "Speech understanding in the elderly," *J. Am. Acad. Audiol.* **7**, 161–167.
- Jacobs-Condit, L., editor (1984). *Gerontology and Communication Disorders* (American Speech-Language-Hearing Association, Rockville, MD).
- Jenkins, J. J., Strange, W., and Miranda, S. (1994). "Vowel identification in mixed-speaker silent-center syllables," *J. Acoust. Soc. Am.* **95**, 1030–1043.
- Kewley-Port, D. (1991). "Detection thresholds for isolated vowels," *J. Acoust. Soc. Am.* **89**, 820–829.
- Kewley-Port, D. (1992). "Effect of levels of stimulus uncertainty and consonantal context on formant frequency discrimination," *J. Acoust. Soc. Am.* **89**, S1996.
- Kewley-Port, D., and Watson, C. S. (1994). "Formant-frequency discrimination for isolated English vowels," *J. Acoust. Soc. Am.* **95**, 485–496.
- Klatt, D. H. (1980). "Software for a cascade/parallel formant synthesizer," *J. Acoust. Soc. Am.* **67**, 971–995.
- Leek, M. R., Dorman, M. F., and Summerfield, Q. (1987). "Minimum spectral contrast for vowel identification by normal-hearing and hearing-impaired listeners," *J. Acoust. Soc. Am.* **81**, 148–154.
- Levitt, H. (1971). "Transformed up-down methods in psychoacoustics," *J. Acoust. Soc. Am.* **49**, 467–477.
- Mermelstein, P. (1978). "Difference limens for formant frequencies of steady-state and consonant-bound formants," *J. Acoust. Soc. Am.* **63**, 572–580.
- Moore, B. C. J. (1993). "Frequency difference limens for short-duration tones," *J. Acoust. Soc. Am.* **54**, 610–619.
- Nabelek, A. K. (1988). "Identification of vowels in quiet, noise, and reverberation: Relationships with age and hearing loss," *J. Acoust. Soc. Am.* **84**, 476–484.
- Nabelek, A. K., Czyzewski, Z., and Krishnan, L. A. (1992). "The influence of talker differences on vowel identification by normal-hearing and hearing-impaired listeners," *J. Acoust. Soc. Am.* **92**, 1228–1246.
- Peterson, G. E., and Barney, H. L. (1952). "Control methods used in a study of the vowels," *J. Acoust. Soc. Am.* **24**, 175–184.

- Pickett, J. M., Martin, E. S., Johnson, D., Smith, S. B., Daniel, Z., Willis, D., and Otis, W. (1970). "On patterns of speech feature reception by deaf listeners," in *Speech Communication Ability and Profound Deafness*, edited by G. Fant (Alexander Graham Bell Association for the Deaf, Washington, DC).
- Spoor, A. (1967). "Presbycusis values in relation to noise-induced hearing loss," *Int. Audiol.* **6**, 48–57.
- Summers, W. V., and Leek, M. R. (1992). "The role of spectral and temporal cues in vowel identification by listeners with impaired hearing," *J. Speech Hear. Res.* **35**, 1189–1199.
- Turner, C., and Henn, C. (1989). "The relation between vowel recognition and measures of frequency resolution," *J. Speech Hear. Res.* **32**, 49–58.
- Van Tasell, D., Fabry, D. A., and Thibodeau, L. M. (1987). "Vowel identification and vowel masking patterns of hearing-impaired subjects," *J. Acoust. Soc. Am.* **81**, 1586–1597.

A0 and A1 coupling, arching, rib height, and f -hole geometry dependence in the 2 degree-of-freedom network model of violin cavity modes

George Bissinger

Physics Department, East Carolina University, Greenville, North Carolina 27858

(Received 19 May 1998; revised 24 August 1998; accepted 25 August 1998)

Six free parameters in the 2 degree-of-freedom (2DOF) network model [E. A. G. Shaw, *J. Acoust. Soc. Am.* **87**, 398–410 (1990)] for the A0 and A1 cavity modes of the violin were optimized by fitting a 64-measurement database of frequencies and upper-/lower-bout pressure ratios obtained by varying volumes of water in a rigid, zero-arch aluminum violin cavity surrogate with various orientations. The optimized 2DOF model predicts an A0 frequency dependence on cavity volume of $f \sim V^{-0.25}$, quite different from the Helmholtz value of $V^{-0.50}$ but in excellent agreement with experiment, signaling substantial coupling between the A0 and A1 modes. After modifying the model to separate rib height and arching dependence, predicted frequencies and pressure ratios behaved similarly—all decreased with increasing rib height or arching—with the notable exception of A1 frequencies, which increased with arching. For 11 instruments ranging in size from a 1/16th size violin to violoncellos, the optimized 2DOF model predicted A0 frequencies consistently $\sim 11\%$ higher than experiment; similarly A1 frequency predictions were 15% high. The effects of sliding, flipping or rotating the f -holes were also investigated. © 1998 Acoustical Society of America. [S0001-4966(98)02912-9]

PACS numbers: 43.75.De [WJS]

INTRODUCTION

The importance of the lowest cavity air mode, A0, to violin sound was noted in the very earliest reports of violin research. This mode, the compliant wall version of the Helmholtz resonance, undoubtedly owes its preeminence to the fact that it is: (a) the only cavity mode that radiates strongly through the f -holes, and (b) the lowest frequency (~ 280 Hz) strongly radiating mode of any type in the violin (corpus modes usually don't appear until ~ 400 Hz), making it of the utmost importance for the violin sound on the lowest (G) string. In fact one of the main objectives in the scaling theory of the Hutchins–Schelleng violin octet was computing the frequency of A0 for various size instruments.¹ Higher cavity modes, labeled in order, A1, A2, etc., all must have a node in the region of the f -holes, and hence must owe whatever acoustic distinction they have achieved to secondary radiation from the cavity-mode-induced corpus motion, i.e., from coupling to the corpus. A1, the first longitudinal mode, has enjoyed considerable recent prominence because of its perceived relationship to the tone quality of the violin.² The A1 frequency, in combination with the upper first corpus bending mode frequency, has been used to compute a quantity called the A1–B1 Δ which was then used to help classify the violin quality.³

Although a substantial literature about cavity modes has accumulated over the past (almost) two centuries, there has also been considerable recent work arising from the usual evolution of technological and scientific techniques. Among these are scientific studies varying from Schelleng's seminal work for the A0 mode "The violin as a circuit,"⁴ Shaw's two-degree-of-freedom (2DOF) network model for A0 and A1,⁵ and Bissinger's boundary element method (BEM) cal-

culations for A1 and higher modes for a rigid, closed, violin cavity,⁶ to purely empirical,^{7–11} or semi-empirical^{12,13} investigations.

Shaw's 2DOF network analysis was the first to incorporate any air modes above A0 into the network representation. His extended conceptualization, combined with the number of assumptions and approximations needed to account for the complicated shape of the violin cavity with f -holes, introduced some accompanying uncertainty about the numerical values of the estimated circuit parameters. Since the 2DOF model has the capability to compute frequencies (and pressure ratios) for the A0 and A1 modes, it is of potential practical value to makers and designers of modified or redesigned bowed string instruments like the violin octet. The experiment presented here used varying amounts of water to alter specific partial volumes or cross sectional areas in an aluminum violin cavity surrogate to independently check the "free" parameters in the 2DOF model and to help understand the problems inherent in applying the 2DOF model to other bowed string instruments. After optimizing parameters on this data set, the model was used to investigate how various factors such as rib height, arching and cavity length, or sliding, rotating or flipping the f -holes, affect mode frequencies and pressure ratios. Finally, the model was used to make predictions for 11 instruments ranging from 1/16th violin to the violoncello.

I. EXPERIMENT

The surrogate cavity used to test the 2DOF model was a zero-arch aluminum violin-shaped cavity labeled *La Empierre* (the "metalled one") first described in detail in Refs. 10 and 11.

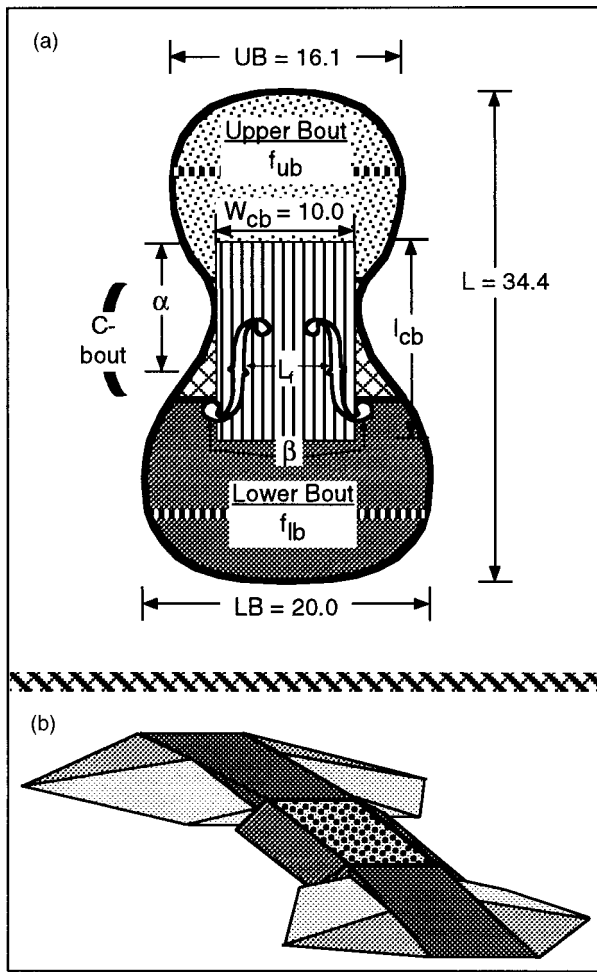


FIG. 1. (a) *La Empierre* cavity shape showing relevant geometry and fit parameters α , β , f_{ub} , f_{lb} , L_f , l_{cb} , (all dim. in cm). Dashed horizontal lines in UB and LB denote maximum fill lines; barred rectangle outlines f -hole inertance region with length l_{cb} . (b) Arching modules for top (and back) plate with block, wedge and (truncated) corner volumes.

A. Apparatus

La Empierre ensures experimental conditions unattainable with an actual violin, viz.: (1) elimination of wall compliance effects (especially important for A0); (2) accurate cavity height $H=3.5$ cm, in-plane area= 514 cm², and volume $V_0=1800$ cm³ due to flat top/bottom; (3) easy upper or lower bout (UB or LB, resp.) partial volume changes by changing cavity orientation after introducing measured amounts of water; and (4) quick f -hole replacement and f -hole motion over a 2-cm range via an insert region. Figure 1 presents an accurately scaled drawing of the cavity (showing maximal fill line positions for UB and LB). The cavity has no end blocks, a minor matter for A0 and A1.⁶ Also shown in Fig. 1 are the approximate position of the f -holes (spaced slightly closer than normal to accommodate translation of f -holes), and relevant cavity volume and inertance regions from Shaw⁵). For this experiment the f -holes had an area of 10.2 cm² and were placed at the normal position for a violin.

B. Experimental procedures

Measurements of A0 and A1 cavity mode frequencies $f(A0)$ and $f(A1)$ and UB/LB pressure ratios $R(A0)$ and

$R(A1)$ were made with two small calibrated microphones, tie-wrapped onto flexible wire supports, and slipped through the f -holes into the UB and LB regions of the violin cavity 1 cm below the top. The cavity was excited by pink noise alternately injected into the UB or LB regions of the cavity. A 100-measurement average (50 UB, 50 LB excitation) of Hanning-weighted 800 line FFTs over 0–2 kHz was acquired for both microphones simultaneously. UB/LB pressure ratios for *La Empierre* and a Roth machine-figured violin compare quite well with prior measurements.⁵ Typical UB and LB cavity microphone spectra clearly exhibited frequency and amplitude changes for horizontal, UB-filled, and LB-filled orientations for added water volumes ranging up to 252 cm³. In the horizontal orientation cavity height H ranged from 3.5 cm (empty) to 3.01 cm with 252 cm³ water added. Combined, the six volumes, three orientations, two frequencies and two pressure ratios gave 64 simultaneous independent measurements. Typical errors were $\pm 0.3\%$ for frequency and $\pm 7\%$ for R .

II. 2DOF MODEL OF A0 AND A1

Details of the intricate conceptualization required to produce the 2DOF model were given in Ref. 5. Only the briefest outline is offered here. The network impedance equations were originally expressed in terms of three impedances Z_1 , Z_2 , and Z_3 which were functions of: (i) the UB and LB capacitances C_1 and C_2 , resp.; (ii) the f -hole and C -bout inertance L_f and L_C , resp.; (iii) the division parameters α (fraction of C -bout inertance above f -hole center point) and β (fraction of f -hole inertance in lower bout volume). For ease in the applying the results to other instruments the UB and LB partial cavity volumes were written as $f_{ub}V_0$ and $f_{lb}V_0$, resp., i.e., as fractions of the original volume V_0 . For all calculations the width of the C -bout region W_{cb} was fixed at its actual minimum value of 10.0 cm, rather than an averaged value, and the cavity height H was fixed at its actual value for each added water volume. (All dimensions given are internal cavity dimensions.) Our fitting procedure optimized L_f , L_C , f_{ub} , f_{lb} , α , and β . The equations used to estimate various lumped parameters are noted below.

A. Capacitances

The network capacitances C_1 and C_2 depend on the UB and LB partial volumes, viz.,

$$C_1 = \frac{f_{ub} \cdot V}{\rho \cdot c^2}, \quad (1)$$

$$C_2 = \frac{f_{lb} \cdot V}{\rho \cdot c^2}. \quad (2)$$

When a water volume V_w was added to the cavity, V in Eqs. (1) and (2) was modified for each V_w /orientation condition as follows:

- UB fill—replace numerator with $f_{ub} \cdot V_0 - V_w$ in Eq. (1) and $f_{lb} \cdot V_0$ in Eq. (2),
- Hor. fill—replace numerator with $f_{ub} \cdot (V_0 - V_w)$ in Eq. (1) and $f_{lb} \cdot (V_0 - V_w)$ in Eq. (2),

- LB fill—replace numerator with $f_{ub} \cdot V_0$ in Eq. (1) and $f_{lb} \cdot V_0 - V_w$ in Eq. (2).

In Eqs. (1) and (2) only f_{ub} and f_{lb} were fit parameters.

B. Inertances

The C -bout inertance L_C , with C -bout region inertance length l_{cb} was calculated from

$$L_C = \frac{\rho \cdot l_{cb}}{W_{cb} \cdot H}. \quad (3)$$

In Eq. (3) only l_{cb} was a fit parameter.

The f -hole inertance L_f which can be estimated for a violin top plate of thickness t by summing inertances for an elliptical orifice L_{fe} (with major and minor axes a and b , resp.) and for two circular orifices L_{f1} and L_{f2} with radii r_1 and r_2 resp., after introducing a multiplicative fit coefficient c_f , using the equations

$$L_{fe} = \frac{\rho \cdot (t + 3.92 \cdot b)}{\pi \cdot a \cdot b}, \quad (4)$$

$$L_{f1} = \frac{\rho \cdot (t + 1.7 \cdot r_1)}{\pi \cdot r_1^2}, \quad (5)$$

$$L_{f2} = \frac{\rho \cdot (t + 1.7 \cdot r_2)}{\pi \cdot r_2^2}, \quad (6)$$

and the sum to give L_f

$$L_f = c_f \cdot 0.5 \cdot (L_{fe}^{-1} + L_{f1}^{-1} + L_{f2}^{-1})^{-1}. \quad (7)$$

C. Experimental simultaneous impedance equations

These various network parameters were conglomerated by Shaw into three impedances Z_1 , Z_2 , and Z_3 to generate the network impedance sum equation

$$Z_1 + Z_2 + Z_3 = 0. \quad (8)$$

The UB/LB pressure ratio R is computed from Z_1 and Z_2 ,

$$R = \frac{P_{ub}}{P_{lb}} = - \frac{Z_1}{Z_2} \Big|_{f=f(A0,A1)}. \quad (9)$$

The pressure ratios were incorporated into the set of simultaneous impedance equations by a straightforward rearrangement of the impedance sum equation, viz.,

$$R - 1 - \frac{Z_3}{Z_2} = 0. \quad (10)$$

Four simultaneous equations can be generated using the measured values for $f(A0)$, $f(A1)$, $R(A0)$ and $R(A1)$ for each (added water volume/orientation) measurement condition. It is not possible to extract the desired six parameters from just four equations, so the parameters L_f , L_C , f_{ub} , f_{lb} , α , and β common to all volumes and orientations (hereinafter labeled “global” parameters) were optimized with the aid of a standard nonlinear fitting program¹⁴ over the entire set of 64 simultaneous equations.

Although the six fit parameters ideally could be extracted simultaneously, attempts to do this resulted in erratic values dependent on the chosen initial values. There were number of possible reasons for this: (a) relatively slow variation in frequencies and pressure ratios as water volume was changed, combined with typical experimental errors; (b) local minima in the multiparameter χ^2 space; (c) the fit parameters were always present in products or ratios with other fit parameters; hence the ratio (or product) was a better value than either parameter singly. Other general aspects of the fitting procedure worth mentioning were the obvious physical limitations on some quantities—i.e., $0 \leq \alpha, \beta, f_{ub}, f_{lb} \leq 1$. Since l_{cb} and W_{cb} appear only as a ratio in L_C the smaller value of W_{cb} chosen here means our optimized l_{cb} value was correspondingly smaller than in Ref. 5. The fitting procedure that produced the best and most stable results cycled through parameter pairs (α, β) , (L_f, L_C) , and (f_{ub}, f_{lb}) , which were chosen because the equations generally had some terms with just one or the other. Each pair value was reset to the best fit results before indexing to the succeeding pair; occasionally it was valuable to vary just one parameter about these optimized values to minimize the overall fit error. All calculations used $\rho = 1.205 \times 10^{-3}$ g/cm³ and $c = 34\,300$ cm/s.

III. OPTIMIZED GLOBAL PARAMETERS

The final set of global parameters for *La Empierre*— $\alpha = 0.62$, $\beta = 0.19$, $f_{ub} = 0.36$, $f_{lb} = 0.44$, $L_C = 482 \mu\text{H}$, $l_{cb} = 14.0$ cm, and $L_f = 194 \mu\text{H}$ —was quite successful in predicting the measured experimental values for $f(A0)$, $R(A0)$ and $f(A1)$, $R(A1)$ presented in Fig. 2, except at the very largest volume changes. Also shown in Fig. 2 are 2DOF predictions using the “initial”, “preferred” and “alternate” parameter sets for an actual violin from Ref. 5. Although all parameter sets consistently follow experimental *trends* the “initial” and “alternate” parameter sets clearly do much poorer in predicting the magnitudes. Although the optimized parameters had a 31% smaller fit error than Shaw’s “preferred” set, the overall excellent agreement between parameter sets for surrogate and real violin cavities—with and without arching—gives one substantial confidence in the generality of the 2DOF model. Later calculations of arching and rib height effects on $A0$ and $A1$ frequencies and pressure ratios and applications to actual instruments will rely on this generality. Our optimized global parameter set is given in Table I along with those from Ref. 5.

A. C-bout inertance length

Shaw was faced with two alternatives in choosing the value for the C -bout inertance length: Was it better to be “...guided by the standing-wave viewpoint...where the inertance “occupies” 50% of the cavity length...,” hereinafter referred to as SW (empty cavity length $L \approx 34$ cm)?—or was l_{cb} related to the length of the C -bout region (≈ 8.5 cm+end corrections, hereinafter referred to as CB)? Since the SW prediction for $l_{cb} = L/2 \approx 17$ cm and the CB prediction was ~ 8.5 cm+end corrections, each alternative suggested similar l_{cb} values, ~ 15 – 16 cm. The experiment on *La Empierre* is an especially apt place to search for sug-

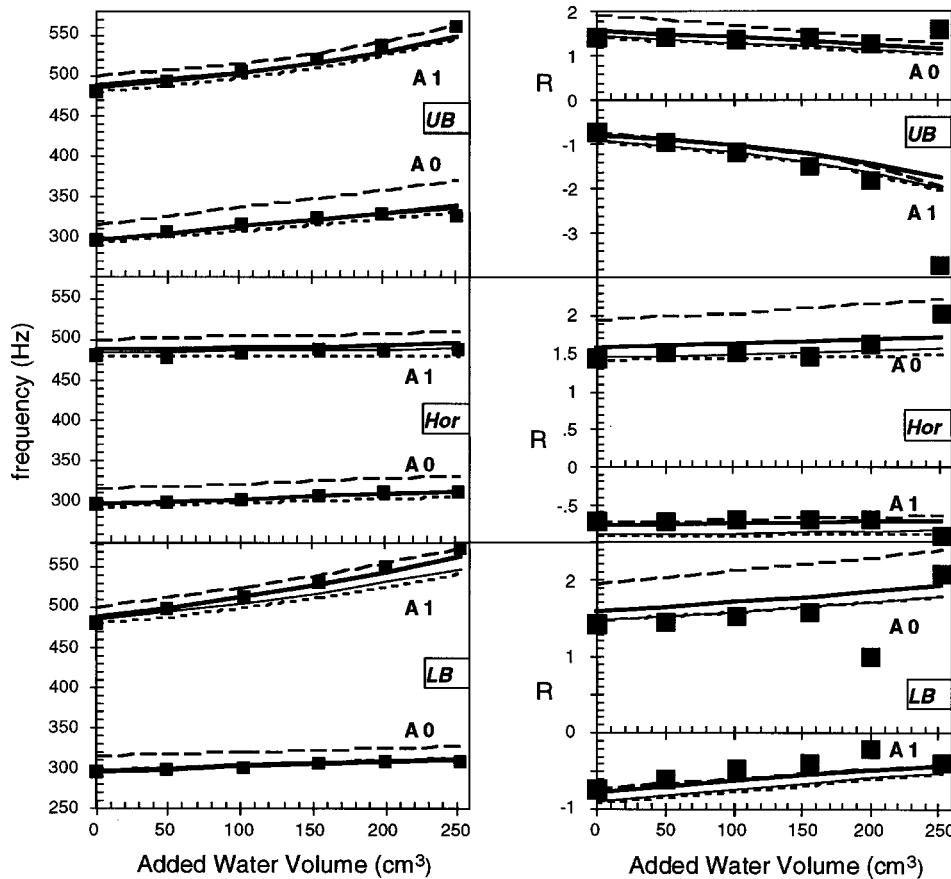


FIG. 2. A0 and A1 2DOF model calculations for Table I parameters versus experimental frequency (left column) and UB/LB pressure ratios (right column) for UB, hor. and LB fillings. [— (this work); Ref. 5: - - - (init.), — · — (pref.), - - - (alt.) parameter sets; ■ exp. pts.]

gestive trends in l_{cb} when water is introduced into the UB or LB regions, because these waterfills decrease the violin cavity length but cause little change in the C-bout region. An $L/2$ systematic variation in l_{cb} points to the SW alternative; conversely insensitivity to cavity length variations points to CB. Fixing all of the global parameters except l_{cb} , then fitting data for water in the UB only, LB only, and then UB and LB data fit simultaneously, gives the results shown in Fig. 3 for optimized l_{cb} vs cavity length, along with the SW and CB predictions (normalized at the $V_w=0$ point). Overall the CB alternative for l_{cb} appears to be favored.

IV. APPLICATIONS

Applications of the 2DOF model of scientific or practical interest are generally rapid and easy once the circuit parameters in the network model have been determined. The model will be applied first to understanding modifications to *La Empierre*, and then to actual instruments.

TABLE I. *La Empierre* 2DOF optimized global parameters compared with “initial”, “preferred” and “alternate” parameter sets from Ref. 5. For comparison l_{cb} has been isolated from L_C .

Ref.	α	β	$L_f(\mu H)$	f_{ub}	f_{lb}	l_{cb} (cm)
This work	0.62	0.19	194	0.36	0.44	14.0
5 (init.)	0.67	0.25	200	0.33	0.47	14.5 ^a
5 (pref.)	0.60	0.20	190	0.36	0.47	13.6 ^a
5 (alt.)	0.70	0	171	0.36	0.47	13.0 ^a

^aCorrected for 10% larger W_{cb} value.

A. La Empierre

1. Volume dependence of $f(A0)$ in a rigid cavity

The A0 mode is so important to the overall sound of bowed string instruments because its normal placement on the lower strings supports lower pitches where normal corpus modes do not radiate efficiently, hence it is of great practical value to be able to estimate $f(A0)$ from the geometry of the instrument. The traditional Helmholtz (rigid) cavity mode volume dependence is $f(A0) \sim V^{-0.50}$, and, prior to

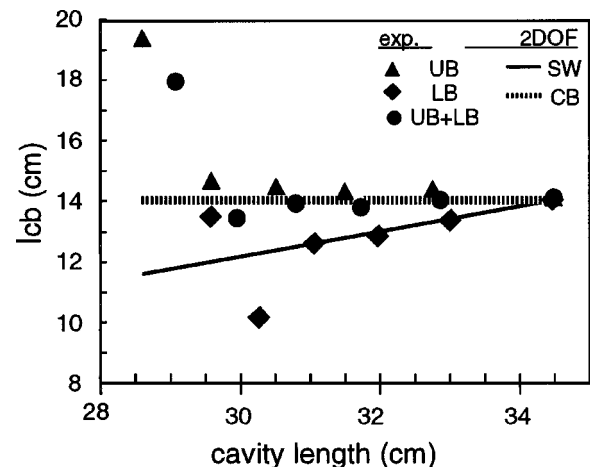


FIG. 3. Inertance length l_{cb} vs cavity length for fits to data for waterfill in UB, LB and UB and LB, compared to 2DOF SW and CB predictions normalized at 34.4 cm.

the 2DOF model, was estimated with no consideration of higher modes. In light of this it is natural to ask—does incorporating $A1$ affect $f(A0)$ significantly?

With all its simplifications *La Empierre* is the idealized cavity prototype for the 2DOF model. And it is significant that here, where most of the extraneous interactions that complicate actual violin cavity mode analysis have been eliminated, $A1$ most clearly demonstrates its strong effect on $A0$. In the 2DOF model the $A1$ mode can be “excited” by setting $l_{cb}=0$, and letting $\alpha \rightarrow 0$ and $\beta \rightarrow 1$. The volume dependence of $A0$ alone was determined by computing $f(A0)$ for volumes from 800 to 1800 cm³ in 100-cm³ steps. Fitting this data set gave $f(A0) \sim V^{-0.50}$, exactly as expected. When the 2DOF model *with A1 incorporated* was used to calculate the $A0$ volume dependence the result was $f(A0) \sim V^{-0.25}$. This result is in excellent agreement with the $f(A0) \sim V^{-0.27}$ fit result from an earlier (horizontal only) *La Empierre* waterfall experiment, over the same volume range.¹¹ The large change in the volume exponent from the Helmholtz value indicates substantial coupling between the $A0$ and $A1$ cavity modes.

An independent experimental verification of this surprising result comes from analysis of earlier measurements by Hutchins on the effect that major rib height changes in the four largest violin octet instruments had on $f(A0)$.¹ Such a modification should have a relatively small effect on the corpus compliance and none on f -hole geometry. Fitting this data set using f -hole, UB, C -bout and LB dimensions pertinent to these four instruments gave $f(A0) \sim V^{-0.33}$ (exponent range of -0.29 to -0.37 is consistent with precision of reported frequencies), quite similar to the $V^{-0.27}$ result for *La Empierre*.

Furthermore, $A0$ - $A1$ coupling also has significant consequences for the 2DOF UB/LB pressure ratio $R(A0)$: with $A1$, $R(A0) = 1.57$; without $A1$, $R(A0) = 1.00$. Measurements show that $R(A0) > 1$ for *La Empierre* (Fig. 2) and for violins (see later discussion) indicating that wall compliance is of little consequence in the $A0$ - $A1$ coupling, hence $R(A0) > 1$ appears to be a reliable indicator for $A0$ - $A1$ coupling.

2. f -hole modifications

The 2DOF model can easily compute the effect of f -hole position and orientation changes on frequencies and pressure ratios, but it cannot predict how top plate compliance in an actual instrument might be affected by such modifications. Comparing model predictions to the results of earlier experiments:

• Sliding or Rotating

An earlier *La Empierre* experiment investigated the effects of sliding the f -holes over a 2-cm range on frequencies of cavity modes below 2 kHz.¹⁰ From Fig. 1 it can be seen that sliding the f -holes primarily changes α (which decreases as the f -holes are slid upward), with only a minor effect on β (although one could not expect any actual C -bout inertance geometry to be such a regular rectangular shape). The 2-cm range of movement corresponds to α varying from ~ 0.55 to ~ 0.70 . Experimentally, sliding the f -holes toward the upper bout changed $f(A0)$ less than

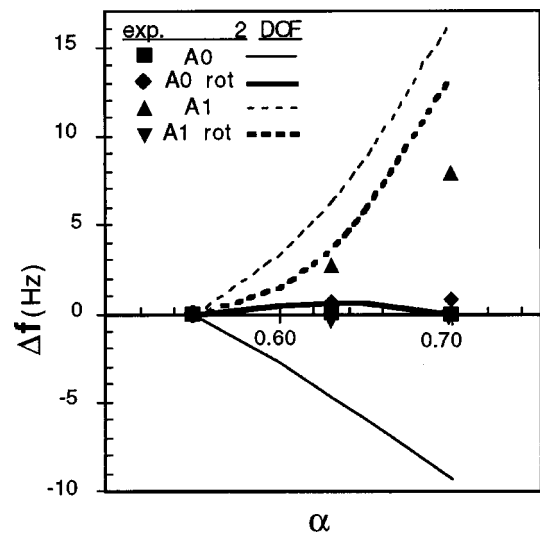


FIG. 4. 2DOF predictions for $A0$ and $A1$ frequency shifts Δf vs α , compared to experimental values for normal and rotated f -holes slid over a 2-cm range (α decreases as f -holes slid upward).

$\sim 0.3\%$, whereas $f(A1)$ increased by $\sim 2\%$. The 2DOF model predicted that $f(A0)$ would decrease by $\sim 3\%$, and that $f(A1)$ would increase by $\sim 15\%$.

Rotating the f -holes moves the lower circular apertures into the C -bout inertance region, hence $\beta \rightarrow 0$ (moving f -holes closer, or reducing size of the lower aperture produces similar effects). If the f -hole is rotated [cf Ref. 10, Fig. 2] so that the entire lower aperture moves into the C -bout inertance region, the 2DOF model can simulate this modification by letting $\beta \rightarrow 0$. Little effect on α , f_{ub} , f_{lb} , and l_{cb} would be expected, although L_f could be affected. For Stradivarius pattern f -holes, rotation (without sliding) raised $f(A0) \sim 5\%$ while lowering $f(A1)$ by 1%, whereas the 2DOF model predicted that both $A0$ and $A1$ would decrease by $\sim 5\%$.

• Sliding and Rotating

When the rotated f -holes were slid upward a small increase was observed in $f(A0)$ but not $f(A1)$; these changes were reproduced well for $A0$ but less well for $A1$ by the 2DOF model. It was predicted that rotating reduces the sensitivity of $f(A0)$ and $f(A1)$ to f -hole position along the corpus, in agreement with the $A1$ mode results but not $A0$. Figure 4 presents all of the sliding f -hole results.

• Flipping

As the final example of f -hole modifications, the effect of flipping the f -holes 180° was examined. A reasonable first approximation to this implausible modification is to interchange f_{ub} and f_{lb} values, essentially equivalent to switching upper and lower bout cavities. Assuming l_{cb} is probably unaffected by this flip since it appears to be governed by C -bout geometry (see earlier remarks) and α and β are kept constant (a crucial—if dubious—assumption for α), the calculated frequency shifts for 200 cm³ of added water are: horizontal fill— $\Delta f = -17$ Hz vs $\Delta f = -4$ Hz (exp.); UB filled— $\Delta f = -14$ Hz vs $\Delta f = -21$ Hz (exp.); and LB filled— $\Delta f = -16$ Hz vs $\Delta f = +16$ Hz (exp.). The agreement between measured and cal-

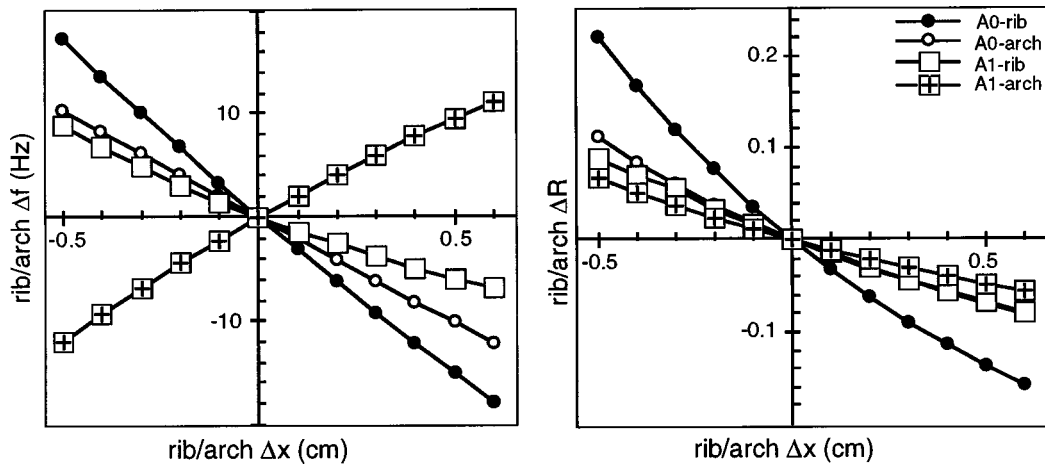


FIG. 5. Frequency (left) and UB/LB pressure ratio (right) differences for A0 and A1 vs changes from nominal values of $H_R=3.0$ cm ($H_A=0$ cm) and $H_A=1.0$ cm ($H_R=3.0$ cm). [For $H_R=3.0$ and $H_A=0$ cm, $f(A0)=315$ Hz, $f(A1)=496$ Hz, $R(A0)=1.67$, $R(A1)=-0.76$.]

culated Δf is only fair here, and highly dependent on the choice of α .

3. Arching and rib height

Since the original formulation of the 2DOF model did separate the contributions of rib height H_R and arch height H_A to the A0 and A1 frequencies and pressure ratios, it was straightforwardly modified to accomplish this. It is interesting to compare the 2DOF model predictions with a recent BEM calculation for a rigid, closed (eliminating A0) violin cavity that examined the effect varying H_R and H_A had on $f(A1)$. Since H_A variations change UB, CB, and LB volumes or areas in different proportions, but H_R changes do not, different trends in frequencies and pressure ratios for the two modes might be expected in the 2DOF model.

La Empierre geometry was entered into a calibrated graphics program to accurately outline the UB and LB areas linked to their respective partial volumes; e.g., for plate area of 514 cm², UB area $\approx f_{ub} \cdot 514$ cm² ≈ 180 cm², covering 12.7 cm of the overall 34.4 cm length. The LB and CB regions covered 13.1 cm and 8.6 cm, resp., defining the lengths used for the UB and LB wedge shapes that abut the CB rectangular block along the length; corner volumes (some truncated) comprise all the rest of the volumes, except for two additional wedges on either side of the *C*-bout block (see Fig. 1), 26 modular volumes in all, and all scaled to H_A . Using accurately known volumes and dimensions for eight instruments ranging from 1/16th size violin to 1/8th size cello, it was determined that a multiplicative factor of 0.70 was needed to make the arch volume agree with experiment. With $H_R=3.0$ cm and an average arch of 1.2 cm for each plate, typical for a violin, the computed volume was 2130 cm³, in good agreement with typical violin results.¹³

Modifications to H_R and H_A affect the *C*-bout inertance L_C through the cross sectional area, and the UB and LB capacitances C_1 and C_2 through the partial volume changes. The f_{ub} and f_{lb} values showed a negligible change after including arch contributions, hence we assume for all following calculations that changes in H_R and H_A have no significant effect on our global parameters.

The arching-rib height dependencies of the A0 and A1 frequencies and pressure ratios were scanned by letting $H_A=0$, and varying H_R from 2.5 to 3.6 cm, and then letting $H_R=3.0$ cm, and varying H_A from 0.5 to 1.6 cm. The results are plotted in Fig. 5 as differences from the $H_R=3.0$ cm, $H_A=0$ cm values. Pressure ratio trends are the same for A0 and A1, uniformly decreasing [i.e., $R(A1)$ gets more negative) as H_R or H_A increase. As expected $f(A0)$ decreases monotonically as H_R or H_A increase because of their link to the volumes, and, unsurprisingly, incremental rib height changes produce larger frequency changes than arch changes. However, there are opposite trends in $f(A1)$ between H_R and H_A changes—*increasing the arch increases $f(A1)$, increasing the rib height decreases it*. This is in agreement with BEM calculations for a rigid, closed cavity, and also observed in fit results on 11 instruments in the violin, viola and cello family.^{6,13}

4. Closing the *f*-holes

Jansson observed that $f(A1)$ dropped from 500 to 475 Hz, when the violin's *f*-holes were closed.¹² To calculate $f(A1)$ with A0 "excised" in the 2DOF model, the calculation was performed in the limit by letting the *f*-hole area $\rightarrow 0$, so that $L_f \rightarrow \infty$. The model predicted a drop in $f(A1)$ from 531 Hz to 521 Hz, in agreement with the observed trend, although smaller than observed.

B. Actual instruments

Certainly the most interesting applications are to musical instruments for which fortunately there are sufficient prior data to provide satisfactory tests of its capabilities.

1. $f(A0)$

The optimized 2DOF model with rib height and arching included can now be readily applied to calculate A0 and A1 mode frequencies for comparison with real bowed string instruments. The needed geometry data was available from an 11 instrument (1/16th and 1/4 violins, 3 violins, viola, alto violin, 1/8 and 1/4 cello, 2 cellos) database¹³ which had a wide range of *f*-hole areas ($\sim 6.7:1$), cavity volumes ($\sim 65:1$),

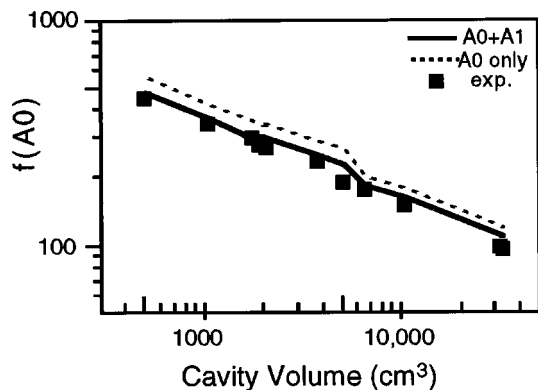


FIG. 6. 2DOF predictions of $f(A0)$ vs cavity volume for 11 instruments (individual instrument f -hole geometry and top plate thicknesses used). Also shown for comparison is prediction for A0 only.

and cavity lengths ($\sim 3.4:1$). The f -hole areas were calculated and scaled to make the *La Empierre* L_f value equal to our optimized value. L_C was computed using approximate C -bout arched cross sections (CB alternative adopted for calculation of l_{cb}). Approximate UB-LB partial volumes were computed for use in the impedance sum Eqs. (8) and (10).

The 2DOF calculations of A0 are compared with experimental results in Fig. 6. Agreement across the entire range of instruments was quite good both in trends and magnitude; the 2DOF predictions (which of course are for a rigid cavity) lie on the average $11(\pm 4)\%$ higher than experiment. Of note is the kink in the 2DOF curve that occurs at the transition from violins to cellos, which is also where the rib height/corpus length ratio makes an abrupt change from ~ 0.09 to ~ 0.16 . Since cavity compliance lowers $f(A0)$, it is not surprising that predicted values are uniformly high. Some idea of the magnitude of the compliance effect can be gotten from soundpost insertion in violin, which typically raises $f(A0)$ by 10%–15%. Because significantly induced corpus motion is still observed even with the soundpost acting as a local stiffener,^{15–18} an additional 10%–15% rise in $f(A0)$ would seem within reason when going to a perfectly rigid cavity [note, however, that $f(A0)$ for a violin buried in sand with additional padded lead weights on the top plate shows only a 1% increase compared with the unrestrained violin⁹]. Also included in Fig. 6 are $f(A0)$ calculations with A1 excised. The effect of excising A1 is to significantly worsen agreement between theory and experiment especially at the violin end of the curve.

2. $f(A1)$

The 2DOF predictions of $f(A1)$ versus cavity length for the same group of instruments are shown in Fig. 7. Although $f(A1)$ also depends on rib height and arching its primary dependence is on the length of the cavity. Again the model predicts the trends quite well over the entire cavity length range, although the predicted frequencies all lie $\sim 15\%$ high.

3. $R(A0)$ and $R(A1)$

The 2DOF predictions of UB/LB pressure ratio magnitudes for all 11 instruments are shown in Fig. 8 along with experimental results from this work and Ref. 5. An interest-

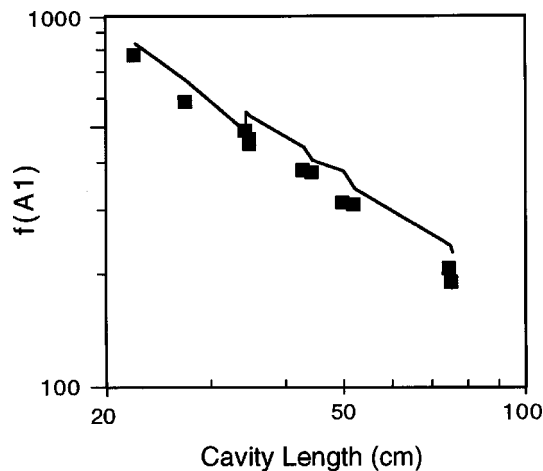


FIG. 7. 2DOF predictions of $f(A1)$ vs cavity length for 11 instruments.

ing linkage was seen between the R magnitudes for A0 and A1; if the A0 ratio decreased, the A1 magnitude increased, and vice versa (some of this is seen in Fig. 2), another sign of the coupling between A0 and A1. Although experimental R values are available only for violins now, the agreement is quite good considering that the model does not compensate for cavity compliance.

V. CONCLUSIONS

The 2DOF model of Shaw with optimized parameters successfully predicted the dependence of:

- $f(A0)$ on cavity volume, including the coupling effect of A1, offering for the first time a theoretical basis for the failure of the Helmholtz resonator equation to reproduce the *La Empierre* results.
- A0 and A1 frequencies and pressure ratios on arching-rib height changes as well as less successful predictions of sliding and/or rotating f -holes.

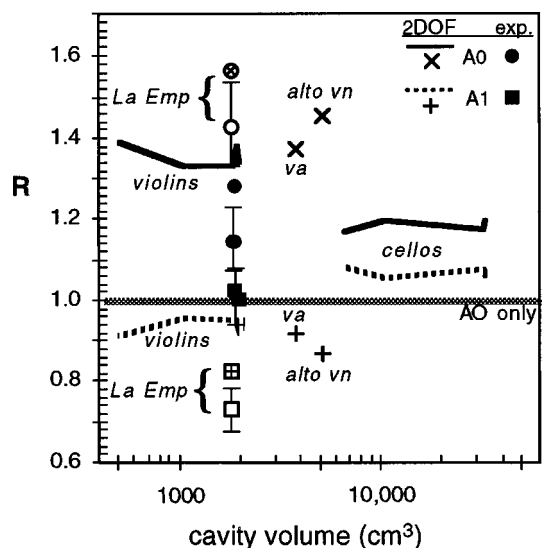


FIG. 8. 2DOF UB/LB pressure ratios for 11 instruments, plus *La Empierre* [only lines shown for violin and cello groups and (-) sign suppressed for $R(A1)$]. $R=1$ line is 2DOF prediction for A0 alone. Experimental measurements from this work and Ref. 5.

- (c) $f(A0)$, $f(A1)$, $R(A0)$ and $R(A1)$ on pertinent geometrical features of actual instruments over a very large volume, rib height, arching, length, and f -hole range.

The 2DOF model almost always reproduced experimental trends, pointing toward improved equations for the calculation of $f(A0)$ and $f(A1)$ frequencies (and pressure ratios). The global parameter set optimized for *La Empierre* was close to Shaw's "preferred" set (derived for actual violins) indicating the generality of the 2DOF model and showed clearly that the "alternate" and "initial" parameter sets were poorer choices.

On the other hand the 2DOF model presently does not consider the soundpost, corpus compliance or corpus-cavity coupling issues, nor does it incorporate higher cavity modes or show any particular sensitivity to actual cavity shape since it deals only in partial volumes and cross sectional areas. In fact the 2DOF model requires *prior* knowledge of the cavity mode shapes to assign regions to various parameters. In this regard it is clearly complementary to the BEM approach which by its very nature is quintessentially particular about cavity geometry. Of course problems such as this are inherent to any simple, approximate, conceptual network representation of modes of vibration. To some extent these weaknesses are balanced by the rapidity and ease of application of this model to changes in the cavity, e.g., how rib holes affect $f(A0)$.¹⁹

The *La Empierre* experiment presented here was able to validate a consistent set of 2DOF network model parameters capable of being used for a wide range of reasonably reliable predictions about the $A0$ and $A1$ cavity modes. The optimized model not only reproduced the *La Empierre* results but also showed its generality and power through its successful application to a wide range of actual musical instruments.

ACKNOWLEDGMENT

I would like to acknowledge a useful conversation with Edgar Shaw.

¹C. M. Hutchins, "A 30-year experiment in the acoustical and musical

development of violin-family instruments," J. Acoust. Soc. Am. **92**, 639–650 (1992).

²C. M. Hutchins, "A measurable controlling factor in the tone and playing qualities of violins," Catgut Acoust. Soc. J. **1** (Ser. II), 10–15 (1989); C. M. Hutchins, "The future of violin research," Catgut Acoust. Soc. J. **2** (Ser. II), 1–7 (1992).

³The value of the $A1-B1$ Δ in predicting violin quality is ambiguous because the original experimental procedure used to extract both frequencies could sometimes mistakenly produce a Δ for the lower first corpus bending mode instead. [G. Bissinger, "Ambiguity in $A1-B1$ Δ Criterion for violin tone and quality," Catgut Acoust. Soc. J. **3** (Ser. II), 13–16 (1996).]

⁴J. C. Schelleng, "The violin as a circuit," J. Acoust. Soc. Am. **35**, 326–338 (1963).

⁵E. A. G. Shaw, "Cavity resonance in the violin: Network representation and the effect of damped and undamped rib holes," J. Acoust. Soc. Am. **87**, 398–410 (1990).

⁶G. Bissinger, "Acoustic normal modes below 4 kHz for a rigid, closed violin-shaped cavity," J. Acoust. Soc. Am. **100**, 1835–1840 (1996).

⁷E. Jansson, "On higher air modes in the violin," Catgut Acoust. Soc. Newsletter, No. 19, 13–15 (1973).

⁸I. M. Firth, "Modal analysis of the air cavity of the violin," J. Catgut Acoust. Soc. **48**, 17–24 (1987).

⁹C. M. Hutchins, "A study of the cavity resonances of a violin and their effects on its tone and playing qualities," J. Acoust. Soc. Am. **87**, 392–397 (1990).

¹⁰G. Bissinger, "Effect of f -hole shape, area, and position on violin cavity modes below 2 kHz," Catgut Acoust. Soc. J. **2** (Ser. II), 12–17 (1992).

¹¹G. Bissinger, "The effect of violin cavity volume (height) changes on the cavity modes below 2 kHz," Catgut Acoust. Soc. J. **2** (Ser. II), 18–21 (1992).

¹²E. Jansson, "Acoustical properties of complex cavities. Prediction and measurements of resonance properties of violin-shaped and guitar-shaped cavities," Acustica **37**, 211–221 (1977).

¹³G. Bissinger, "Semiempirical relationships for $A0$ and $A1$ cavity mode frequencies for bowed string instruments of the violin, viola and cello family," Catgut Acoust. Soc. J. **2** (Ser. II), 8–12 (1992).

¹⁴Using *Minerr* function in Mathcad (Mathsoft, Inc., Cambridge, MA).

¹⁵K. D. Marshall, "Modal analysis of a violin," J. Acoust. Soc. Am. **77**, 695–709 (1985).

¹⁶G. Bissinger, "Some mechanical and acoustical consequences of the violin soundpost," J. Acoust. Soc. Am. **97**, 3154–3164 (1995).

¹⁷G. Bissinger, "Modal analysis comparison of new violin before and after ~250 hours of playing," Proc. 13th Intern. Modal Analysis Conf., Soc. Exp. Mechanics, Bethel, CT, 1995, pp. 822–827.

¹⁸G. Bissinger, "Vibro-acoustics in the violin: A gas-MAC attack on the corpus-cavity interaction," Proc. 15th Intern. Modal Analysis Conf., Soc. Exp. Mechanics, Bethel, CT, 1997, pp. 699–703.

¹⁹C. M. Hutchins, "A study of the cavity resonances of a violin and their effects on its tone and playing qualities," J. Acoust. Soc. Am. **87**, 392–397 (1990).

Long-range acoustic detection and localization of blue whale calls in the northeast Pacific Ocean

Kathleen M. Stafford^{a)}

Department of Fisheries and Wildlife, Oregon State University, Newport, Oregon 97365

Christopher G. Fox

NOAA, Pacific Marine Environmental Laboratory, Newport, Oregon 97365

David S. Clark

Naval Command, Control and Ocean Surveillance Center, San Diego, California 95152

(Received 14 February 1997; accepted for publication 24 August 1998)

Analysis of acoustic signals recorded from the U.S. Navy's SOund SURveillance System (SOSUS) was used to detect and locate blue whale (*Balaenoptera musculus*) calls offshore in the northeast Pacific. The long, low-frequency components of these calls are characteristic of calls recorded in the presence of blue whales elsewhere in the world. Mean values for frequency and time characteristics from field-recorded blue whale calls were used to develop a simple matched filter for detecting such calls in noisy time series. The matched filter was applied to signals from three different SOSUS arrays off the coast of the Pacific Northwest to detect and associate individual calls from the same animal on the different arrays. A U.S. Navy maritime patrol aircraft was directed to an area where blue whale calls had been detected on SOSUS using these methods, and the presence of a vocalizing blue whale was confirmed at the site with field recordings from sonobuoys.

[S0001-4966(98)01312-5]

PACS numbers: 43.80.Ka, 43.30.Sf, 43.30.Xm [FD]

INTRODUCTION

Blue whales (*Balaenoptera musculus*) have been protected internationally since 1965 (Leatherwood *et al.*, 1983). The numbers of these animals were greatly reduced by whaling and the current global population is not well known. Estimates of the blue whale population in the North Pacific range from about 1400 to 3500 (Mizroch *et al.*, 1984; Yochem and Leatherwood, 1985; Barlow, 1994), and the number of animals found along the coast of central California appears to be increasing (Calambokidis *et al.*, 1990; Barlow, 1994). Little is known about the numbers or distribution of blue whales off the Pacific Northwest. This population was exploited in limited numbers by whalers, particularly in the 1920s and 30s (Pike, 1954; Nishiwaki, 1967; Pike and MacAskie, 1969), but no specific regions of abundance have been described. Most recent work on blue whale distribution and behavior is conducted within accessible, near-shore habitats. In order to study migratory patterns and behavior in the open ocean, a new set of tools is required for long-range detection to allow efficient use of observation platforms and ultimately for indirect study using remote sensing methods.

The U.S. Navy has been recording "biologicals," which includes blue whale calls, on their SOund SURveillance System (SOSUS) arrays since the system was established in the mid-1950s to track submarines (Nishimura and Conlon, 1994). The SOSUS arrays consist of a series of bottom-mounted hydrophones that relay the received acoustic signals via underwater cables to shore-based facilities for signal pro-

cessing (Nishimura and Conlon, 1994; Fox *et al.*, 1995). The location of these arrays is currently classified and cannot be discussed here. Despite this restriction, the Navy's hydrophone system is useful for remotely studying whale calls. Because they are bottom mounted, the positions of the multiple hydrophone elements are fixed and the signals can be summed into acoustic beams providing significant signal gain. Given accurate sound-speed profiles, arrival time measurements on only three arrays are necessary for localizing the source of a sound (Watkins and Schevill, 1972). Since 1991 the SOSUS system has been used by the National Oceanic and Atmospheric Administration's Pacific Marine Environmental Laboratory (NOAA/PMEL) in Newport, Oregon, to study underwater earthquakes and volcanoes (Fox *et al.*, 1994). This collected data set, with the corresponding analysis methods developed for seismic studies, can be readily modified to study whale calls.

The approach taken in this study involved several sequential efforts. First, field recordings of calls were made in the presence of blue whales. These recordings were then digitized, analyzed in time-frequency space, and a matched filter kernel was developed to allow detection of the call beneath the ambient noise. The matched filter was then cross correlated with acoustic recordings from SOSUS arrays in the North Pacific to allow the calls to be detected at up to three receiver locations. Epicenter inversion techniques developed for seismic studies were then applied to the arrival times derived from the matched filter output to allow blue whale locations to be calculated at ranges of up to several hundred kilometers. Finally, the methods were applied to real-time recordings from SOSUS to direct a U.S. Navy patrol aircraft to an offshore location where a large whale was

^{a)}Current address: Cooperative Institute for Marine Resources Studies, Oregon State University, Hatfield Marine Science Center, Newport, OR 97365.

sighted and blue whale calls were detected with on-site sonobuoys. A match between the calls recorded by the patrol aircraft and SOSUS was confirmed as the same whale by comparison of the acoustic records from these two platforms.

I. BACKGROUND

Although the near-shore distribution of blue whales along California and the Baja peninsula, Mexico is documented (Calambokidis *et al.*, 1990; Barlow, 1994), very little is known about the animals offshore Oregon and Washington. A chart developed from Japanese whaling data shows blue whales distributed over the continental shelf from Baja up to the Gulf of Alaska (Nishiwaki, 1967). Only one blue whale was sighted 80 km west of Cascade Head, Oregon, during surveys from the 100-fa curve to 160-km offshore during winter months from 1959 to 1961 (Fiscus and Niggol, 1965). No blue whales were identified during aerial and ship-board surveys conducted on the outer continental shelf (to 185-km offshore) of Oregon and Washington between April 1989 and September 1990 (Green *et al.*, 1992). Data from Canadian whaling stations indicated that blue whales were found off Vancouver Island, Canada seasonally, with peak abundance (as indicated by catches) in June and September (Rice, 1974). The distribution of these animals has been described as "well offshore" (Pike and MacAskie, 1969). While there is some evidence from seismic recordings made at two sites on the Juan de Fuca Ridge (Jacobson *et al.*, 1987; McDonald *et al.*, 1995) that blue whales currently occur in deep water off Oregon, there are no defined regions that can be used as a target for vessels or aircraft interested in finding blue whales for behavioral or population studies.

Low-frequency acoustic signals propagating in deep ocean environments have low attenuation characteristics and thus are detectable over great distances via the deep sound channel (Urlick, 1983; Spiesberg and Fristrup, 1990; Spindel and Worcester, 1990). Mysticetes generally produce low-frequency signals that are probably used for communication (Reysenbach de Haan, 1966; Evans, 1967; Winn and Perkins, 1976; Thompson *et al.*, 1979). Calls of baleen whales have been classified into three groups by Clark (1990): (1) simple calls, which are usually low-frequency (<1000 Hz), frequency modulated signals; (2) complex calls which are broadband signals ranging from 500 to 5000 Hz; and (3) clicks, knocks, or grunts usually of short duration and variable frequency. Currently, most of what is known of blue whale calls consists of simple calls with fundamental frequency ranges reported from about 16 to 25 Hz. Such calls may be used for contact among conspecifics due in part to the low attenuation characteristics of subsonic frequencies (Payne and Webb, 1971; Clark, 1990). Blue whale calls have been reported in the literature for animals in the southeast Pacific (off Chile) (Cumplings and Thompson, 1971), the northwest Atlantic (Edds, 1982; Mellinger and Clark, 1995), the central Pacific (Thompson and Friedl, 1982) and the northeast Pacific (McDonald *et al.*, 1995; Thompson *et al.*, 1996; Clark and Fristrup, 1997; Rivers, 1997).

The use of acoustic techniques to determine numbers and distributions of calling whales has been particularly successful with migrating bowhead whales. Clark and Ellison

(1988, 1989) were able to provide an estimate of the number of calling whales passing a hydrophone array off Pt. Barrow, Alaska during the whales' spring migration. These authors report that a "sizeable" proportion of these animals were not in range of visual observation posts and could not, therefore, have been counted in visual censuses. Because not all bowhead whales call while migrating and a variety of factors affect the ability to reliably locate and track whales, visual and acoustic results were combined to provide a more accurate estimate of the population size.

II. FIELD RECORDINGS OF BLUE WHALE CALLS

In August–September, 1993, field recordings were collected in the presence of approximately 14 blue whales between 37–38 °N and 122.4–123.5 °W on five dates: 26 and 28 August and 6, 15, and 29 September, 1993. Recordings were made when blue whales were observed within 1000 m of the Oregon State University 18-m R/V 'Cille. During recording periods, the vessel was stopped and the engines shut down. Recordings were made on both channels of a TEAC Digital Audio Tape (DAT) Recorder; one channel was used to record underwater sounds received through a commercial hydrophone, while the other was used for commentary. The hydrophone had a flat response from 20 Hz to 2 kHz and was rolled off by 3 dB at 12 Hz.

The DAT tapes were redigitized at a sample rate of 256 Hz at NOAA/PMEL in Newport, Oregon using equipment identical to that used to record data from SOSUS hydrophones. This produced a format compatible with the software and hardware used by PMEL for the analysis of SOSUS data. The time series data were processed using a fast Fourier transform (FFT) of 1024 points (25% overlap) to produce spectrograms of the calls. Calls were seen in spectrograms from 10 of the 15 recording sessions (66.6%) or 232 of 322 min (72%). Fundamental frequencies were often difficult to identify from the spectrograms due to interference from local shipping noise, cable strumming, and the roll-off of the hydrophone. Harmonics, however, were clearly visible.

The calls were of two parts. Such multi-part sounds were often described as "20 c/s long pulses" and later as parts "A" and "B" (Thompson *et al.*, 1996). Figure 1 shows one AB call pair recorded off central California in September, 1993. As with the recording of Thompson *et al.* (1996), the field recordings had substantial low-frequency noise that, in all instances, precluded measurement of the lowest A call frequencies. The A calls preceding B calls were detected by their higher-frequency harmonics (Fig. 1). No other whale sounds were identified in these recordings.

In order to better quantify the nature and variability of the calls, time-frequency characteristics of individual calls were digitized from a graphic workstation. The beginning and ending frequencies and duration were measured for each of 303 B calls recorded, including measurements of the fundamental frequency (when visible) and second, third, and fourth harmonics. B calls were characterized by a down-sweep of ~1.6 Hz, from 18.9 to 17.3 Hz and lasted 16 s. Table I presents the characteristics of the analyzed blue whale calls, including frequency down-sweep and duration for the fundamental frequency and harmonics. Because the

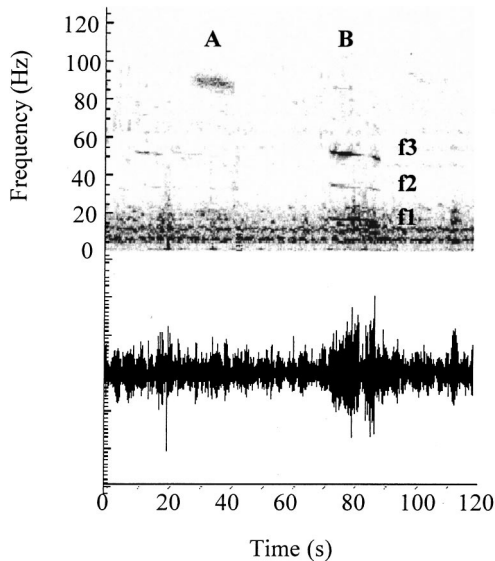


FIG. 1. Blue whale AB call pair from field recordings off California, September 1993. Recordings were collected on a portable hydrophone when blue whales were identified within 1000-m range. Three harmonics of the B call are visible. The A call fundamental is barely visible in the surrounding noise but elements of this call can be seen up to 90 Hz. (FFT size 128 points, 50% overlap.)

fundamentals were more masked by ambient noise, fewer fundamental frequencies were measured than second, third, and fourth harmonics.

III. MATCHED FILTER DEVELOPMENT

A. Background

As noted above, blue whale calls in the northeast Pacific occur near 20 Hz, which is also the range of much shipping noise (Payne and Webb, 1971; Urick, 1983), so the fundamental calls may be obscured by louder ambient noise. A filter that can extract the signal from the surrounding noise is useful for signal detection. Depending on duration and frequency bandwidth, the range at which whale calls can be detected increases by use of cross-correlation techniques (Spiesberger and Fristrup, 1990) such as are used in matched filtering. Matched filters maximize the signal-to-noise ratio of the output by condensing the amplitude of the signal into the output peak (Camp, 1970; Robinson and Treilt, 1980). The gain in signal-to-noise ratio obtained from a matched filter increases with the product of the bandwidth and the duration of a given signal.

TABLE I. Time and frequency characteristics of blue whale B calls used to create kernels for the matched filter. As stated in the text, the fundamental of the A part of the call was obscured by noise.

	B call		
	f_1	f_2	f_3
Duration (s)	16.2 ± 2.7	15.9 ± 2.3	14.9 ± 3.0
Begin frequency (Hz)	18.9 ± 0.4	37.2 ± 0.6	55.7 ± 0.8
End frequency (Hz)	17.3 ± 0.3	34.2 ± 0.7	51.7 ± 1.2
n	16	85	295

A matched filter may be implemented as the correlation of part of a known signal with a noisy time series. For instance, Freitag and Tyack (1993) used 100 μ s of a captive dolphin (*Tursiops truncatus*) click recorded on one channel and cross correlated this with input data from other channels to produce peaks in the output which indicated the presence of clicks. They found that this method worked well when the animal was held in a large pen, but when the animal was held in a tank, direct detection without matched filtering of the clicks produced better results. One disadvantage of this approach is that individual variation in calls may produce filters that are overly specific.

For this experiment, only part B of the blue whale call was used. The B call of northeast Pacific blue whales is an excellent signal to model because it is frequency modulated over a long duration. Although there is some variation in individual blue whale calls, all share the downsweep characteristic. A matched filter developed from average values of numerous blue whale calls should be more robust in detecting other calls than a kernel developed from a single call. Because the amplitude of the same call on different SOSUS arrays will differ based on the animal's distance from each array, applying the matched filter developed here will allow for detection of these calls in noisy data. It is then possible to match peaks of the same call on three different SOSUS hydrophone arrays and locate the source of the call. The distributions of calling animals can be extended beyond the range at which calls can be detected by visual examination of the spectrograms alone.

B. Filter design

Mathematical kernels simulating the first, second, and third harmonics were created from mean values of B call characteristics with an inverse Fourier transform. Given the desired sample rate, and estimates of upper and lower frequencies and duration, a complex time series was produced that simulated the Fourier spectrum of a simple linear sweep with these characteristics. The inverse Fourier transform of this model spectrum then produces the time-domain representation of the call.

As an initial test, these matched filters were cross correlated with the data recorded in the field to see if they detected known calls in the data time series. A time series of some of the field data from California that contains two blue whale calls with visible fundamentals and two other calls identified by the presence of harmonics is shown in Fig. 2(a). The results of cross correlating these data with a matched filter developed only from the fundamental (f_1) is shown in Fig. 2(b). For three of the calls, correlation peaks are produced in the output. When applied to the same data, the matched filter composed of the second harmonic identified the two "obvious" calls with correlation peaks that stand further above the noise than Fig. 2(b) [Fig. 2(c)]. The most useful kernel for this data set, however, was that which imitated the third harmonic only. Narrow peaks are produced for four calls and the background noise is reduced [Fig. 2(d)]. This is to be expected; the higher harmonics sweep a larger frequency range, therefore the time-bandwidth product is greater than

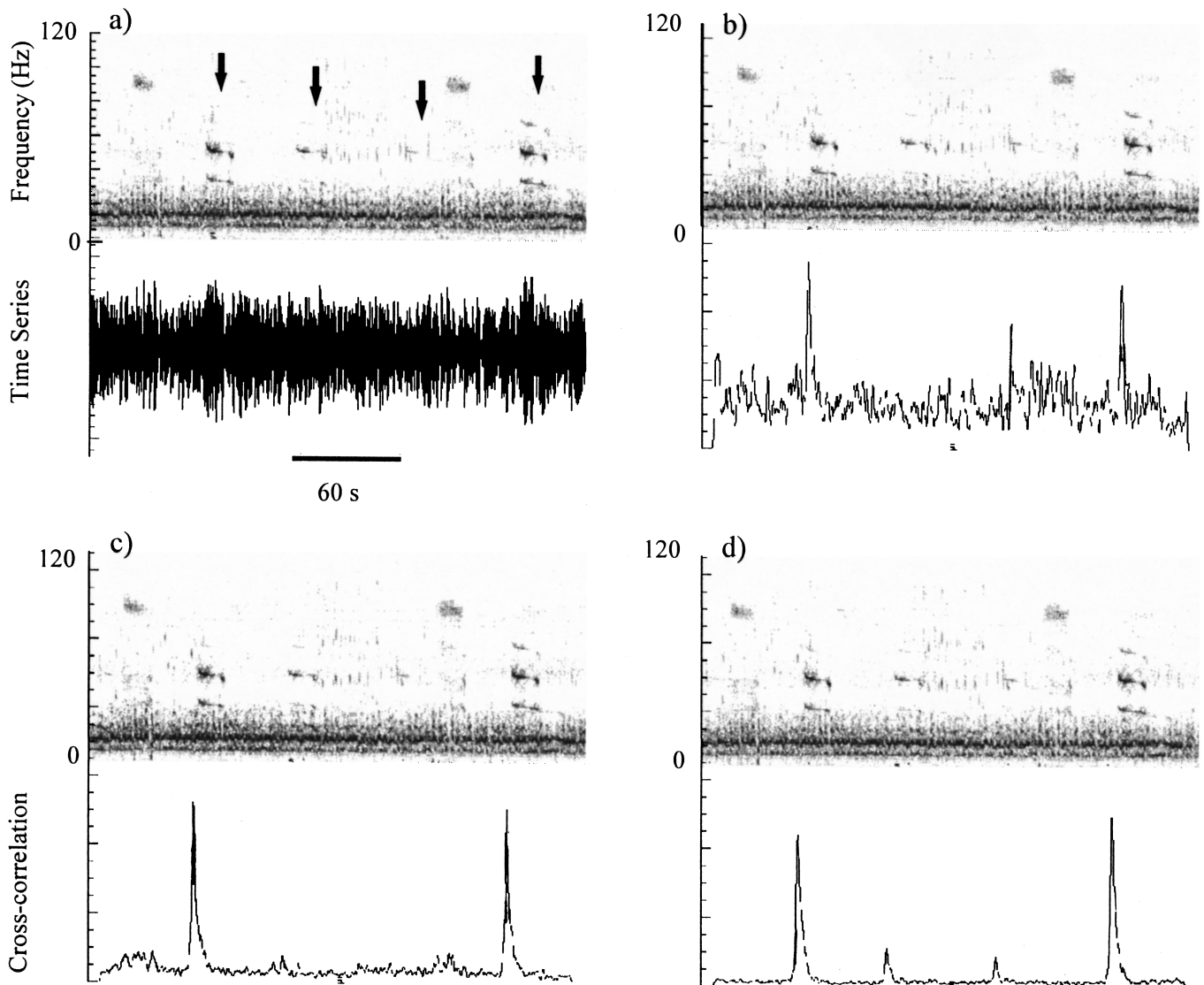


FIG. 2. Average call statistics were used to develop various matched filter kernels to improve signal detection. (a) Time series and spectrogram of four blue whale B calls recorded in the field using a portable hydrophone. Each call is indicated by an arrow; (b) Cross correlation of data from (a) with a matched filter modeled after the fundamental frequency alone; (c) Cross correlation of data from 2(a) with an f_2 kernel; (d) Same data correlated with a matched filter imitating the third harmonic alone. (FFT size 512 points, 75% overlap.)

for the fundamental. There is also less ambient noise in the 50-Hz range.

C. Application to SOSUS data

When it was determined that the matched filters successfully identified calls in the field data from which they were developed, the kernels were modified to match the 100-Hz sample rate of SOSUS beam-formed data collected at PMEL. These data were originally collected for a geophysical experiment, and were low-pass filtered at 40 Hz; therefore, harmonics above f_2 were eliminated. Future efforts will sample at 128 Hz and low pass at 60 Hz to avoid eliminating the useful third harmonic. The matched filter kernels were cross correlated with SOSUS data in which there were known blue whale calls, found by visually examining sonograms of archived data files. SOSUS data in which four AB call pairs are clearly visible in the spectrogram, and the results of cross

correlation of the f_1 kernel with these data, are shown in Fig. 3(a). For every B call, a peak is discernible in the output. There are also smaller amplitude peaks where there are A calls. This is probably due to these calls containing a slight downsweep in frequency as well as having a similar duration as the B call. The matched filter was then cross correlated with data from a hydrophone in which there were only faint blue whale calls to determine matched filter performance on low amplitude signals [Fig. 3(b)]. Although the three calls in Fig. 3(b) are not as readily discerned in the spectrogram and not at all in the time series, cross correlation with the f_1 matched filter produces clear peaks in the signal-to-noise ratio.

While harmonics were regularly seen in the field-recorded data, they were seen less often in the SOSUS data, so a complex kernel was no more successful at detecting whale calls than was the fundamental kernel. The ability of a

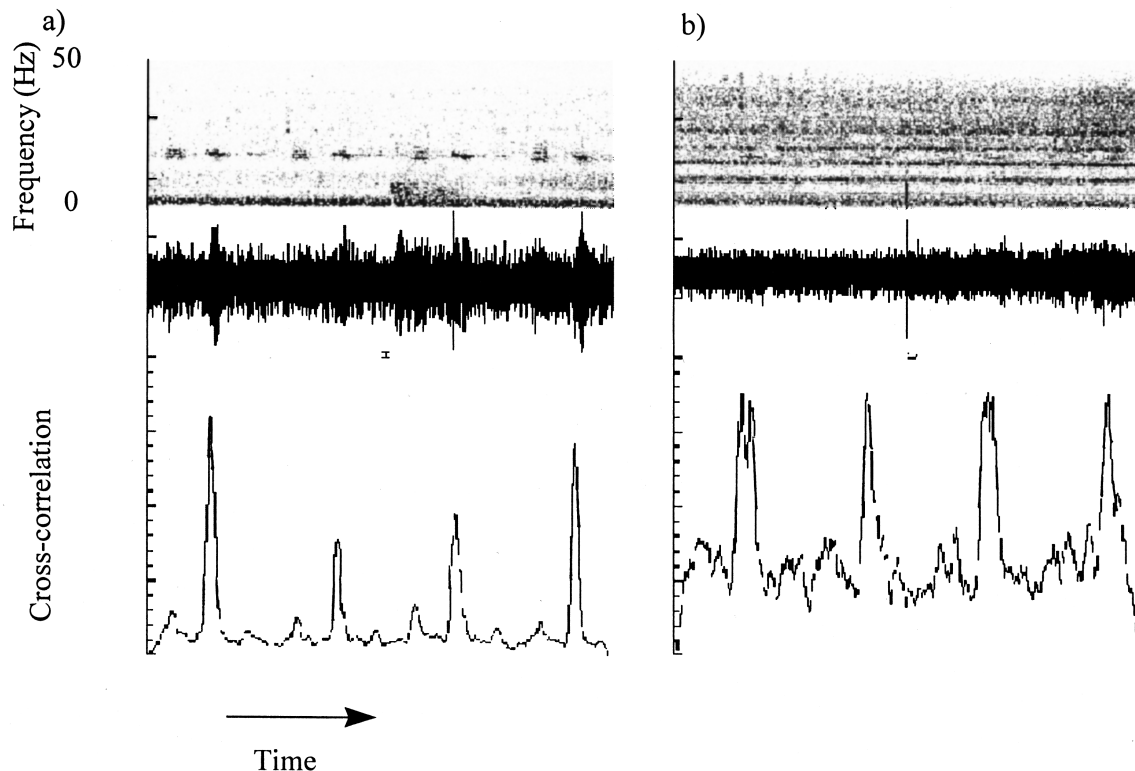


FIG. 3. (a) Spectrogram and time series of four blue whale calls recorded by SOSUS that have been cross correlated with a matched filter developed from portable hydrophone recordings based on the B call fundamental frequency alone; (b) faint blue whale calls from a different SOSUS array and cross correlation of its time series with the matched filter. Although the calls are not visible in either the time series or the spectrogram, the correlation peaks are clear and can be used for timing arrivals.

kernel to detect blue whale calls is determined by how closely the kernel approximates the calls. The matched filter that imitated f_1 detected calls on both the data from which it was generated and SOSUS data. This result shows that the kernel developed from the field data is general enough to be applied to data not used in the design of the kernel. The relative height and width of the correlation output is related to the amplitude of the call being detected.

It is possible that this kernel may not detect calls of blue whales recorded in different areas, but the procedures used above for northeast Pacific blue whales can be applied to other geographic regions. Cross correlation with artificial kernels such as those developed in this experiment may be better at detecting calls than would use of a single recorded call as a matched filter because the latter would include any ambient noise recorded with that call. Therefore, the output of a correlation with a matched filter would not be as successful if other data had different ambient noise characteristics from the filter.

The success of the matched filter on SOSUS data in which blue whale calls cannot be visually identified by an observer from a spectrogram shows that this method can be used to detect blue whale calls even in a noisy environment or when the calls are of low amplitude. Consequently, the range over which these calls can be detected is increased. It should be possible to create kernels for other low-frequency whale calls, such as finback whale (*Balaenoptera physalus*) calls, and thus increase the utility of matched filters in whale call detection.

Mellinger and Clark (1993, 1997) compared matched filtering with two other methods to determine which was optimal for the automatic detection of whale calls in large data sets. They determined that matched filtering worked less well than either spectrogram correlation or a hidden Markov model at automatically picking calls from data. A matched filter was used for this experiment because detection was only the first step in the two-part process of detecting and then localizing a call. While spectrogram correlation uses the spectrogram itself for detection, the matched filter here was cross correlated with the time series of the data in order that the time of the call could be determined for use in the time delay localization.

IV. LOCALIZATION OF BLUE WHALES

With the successful design of robust matched filters for northeast Pacific blue whale calls, seismic processing software developed by PMEL was modified to allow routine application of the filters to SOSUS data. Up to 15 min of data from three data channels, representing one formed beam from each of the three arrays, were displayed on a computer workstation. Whale calls had to be visible on one or two channels (arrays) for call localization to be attempted. The remaining channel was selected by determining which beam from the third array best intersected the other two beams. The matched filter was applied to all channels, resulting in a composite display of the cross-correlated signal and the spectrogram for each channel (Fig. 4).

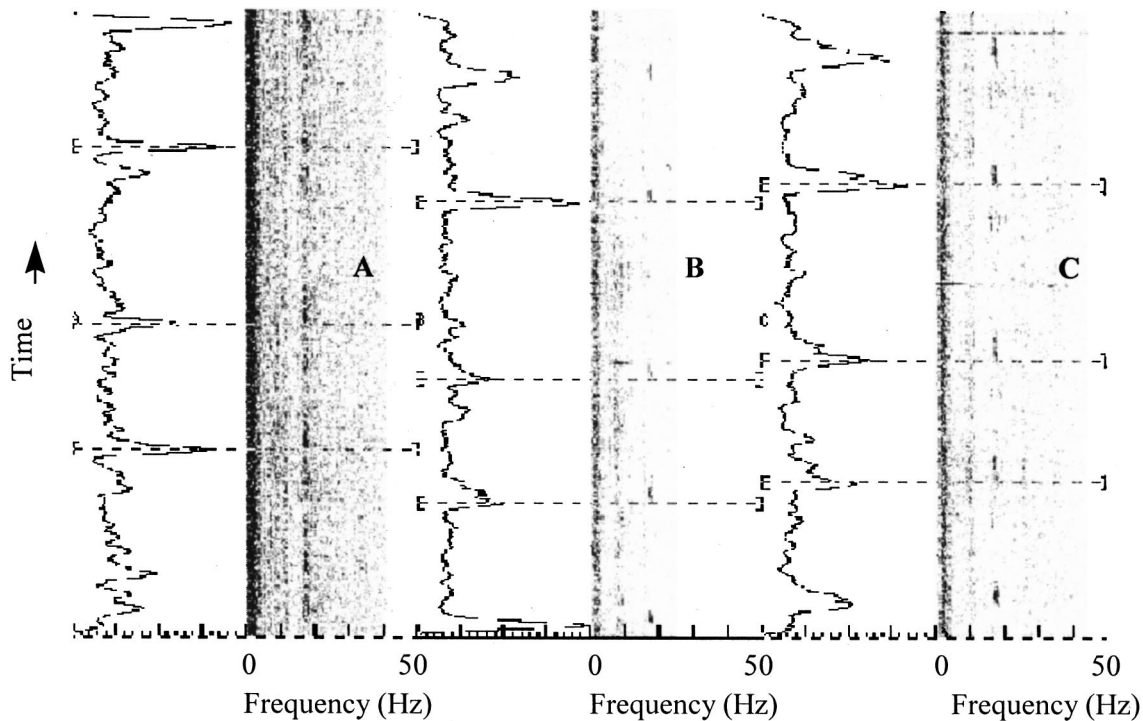


FIG. 4. SOSUS data from three different hydrophone arrays cross correlated with a matched filter based on the fundamental frequency of the B call. The same blue whale calls are visible on arrays A and B but can only be detected on array C when the matched filter is applied. Arrival time picks are labeled 1, 2, and 3. The calls arrive first on array B, then array C, then array A.

The pattern of peaks in the cross-correlated data were compared among channels to determine how the calls were associated. Because a call series often had pauses and variation in repetition rate, identifying the same call on different channels was generally straightforward. When a call was selected, its arrival time at each array was selected. A detailed plot of the matched filter output allows resolution for each pick down to 0.01 s. A display of three picks (1,2,3) is shown in Fig. 4.

The arrival times of the same call at three different array locations are combined with sound-speed models for the northeast Pacific and compared to an initial position of 46°N/129°W. A nonlinear least-squares technique is used to estimate source time, latitude, and longitude of the call. It is not possible to determine a quantitative measure of location accuracy with this method as there are no degrees of freedom for calculation of a standard error. However, a measure of the bias in the calculated localization for earthquakes was performed by dropping small explosive shots at known positions. The calculated locations were found to be 1.76 ± 0.76 km south and 0.46 ± 2.04 km west from the known explosive shot points which were deployed at the same range to the SOSUS arrays as the whale calls that were localized (Fox *et al.*, 1995). A Monte Carlo simulation was run using the three available arrays and assuming a rms error of 0.1 s per pick for each hydrophone. This simulation was run with a grid step of 0.75 degrees in latitude and longitude for the region around which whale calls had been localized. Assuming the ability to pick the cross-correlation peak to within 0.1 s, the rms errors for the small region around the blue whale localizations discussed here were $\pm 0.06^\circ$ latitude and $\pm 0.25^\circ$ longitude.

V. GROUND-TRUTH EXPERIMENT

To evaluate the fidelity of locations derived from SOSUS by use of these techniques, an experiment was undertaken to coordinate real-time localization of blue whales from SOSUS data with a Navy P-3C patrol flight operated by patrol squadron VP-46 at the Naval Air Station at Whidbey Island, Washington. Model AN/SSQ-53D sonobuoys were used to relay acoustic signals back to the aircraft via radio links. The P-3C's sonobuoy radio receivers were interfaced to a prototype acoustic tracking system, which provided multiple channels of acoustic data to a processing system. Positions of acoustic sources were determined by arrival time delay analysis. Figure 5 shows an example of the data display received from multiple sonobuoys. Both time-frequency spectrograms and a geographic display are provided to the operator. The locations of sonobuoys are labeled with their radio channels and the resulting source location hyperbolae are also displayed. Three or more buoys are used to form a series of hyperbolae and their intersection depicts the location of the acoustic source.

On 4 August, 1994, a P-3C flight was scheduled. Blue whale calls were seen in spectrograms from SOSUS and locations were determined by the methods described above. A position of 46°36'N by 129°07'W was calculated by NOAA/PMEL personnel in Newport, Oregon and radioed to the P-3C before the 1000 PDT take-off. The P-3C took off from the Naval Air Station at Whidbey Island, Washington at 0955 PDT and began operations at 1129 PDT in this area. Weather conditions were generally favorable with the exception of 25–30 knot surface winds. The aircraft initially dropped a bathy-thermograph buoy in the area of the detec-

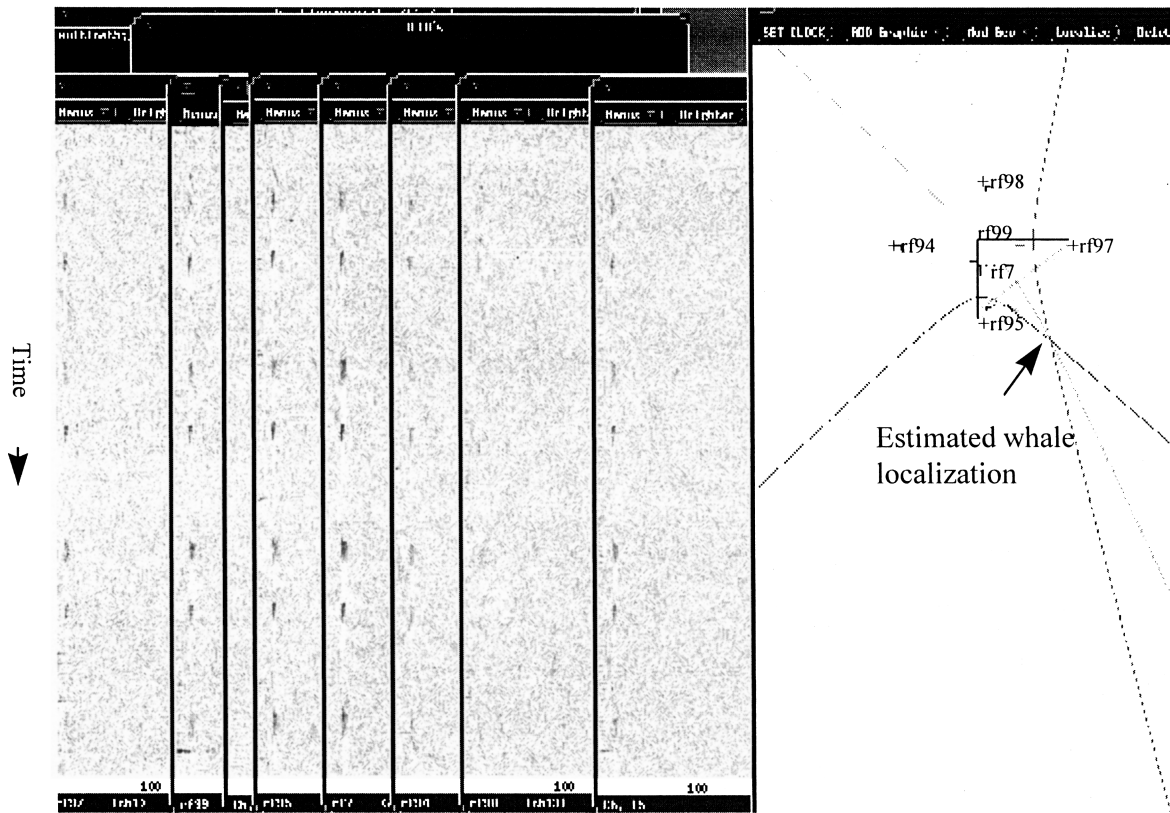


FIG. 5. P-3C sonobuoy display recorded at 1315 PDT. The location of this call series was estimated to be $46^{\circ}34.0'N/128^{\circ}51.9'W$. Relative sonobuoy positions and the derived call location are shown on the right side of the figure, while spectrograms of the acoustic signals received from the sonobuoys is shown on the left. Positions of the sonobuoys (in N latitude and W longitude) were as follows: rf7: $46^{\circ}34'55''/128^{\circ}59'06''$, rf94: $46^{\circ}35'03''/128^{\circ}59'06''$, rf95: $46^{\circ}31'15''/128^{\circ}53'01''$, rf97: $46^{\circ}35'04''/128^{\circ}47'27''$, rf98: $46^{\circ}39'27''/128^{\circ}53'03''$, rf99: $46^{\circ}35'02''/128^{\circ}53'16''$.

tion, and the measured sound velocity profile was used to determine the acoustic propagation characteristics of the area. These environmental characteristics were used to establish the appropriate hydrophone depth settings and geographic spacing for the sonobuoys. Sonobuoys were then deployed and signals from the sonobuoys were received aboard the aircraft. Immediately after the sonobuoy deployment was completed (1145 PDT), blue whale calls from a single individual were detected on all buoys and localized. Figure 5 shows an example of such a localization, made at 1315 PDT, in which the source of the calls was estimated to be at $46^{\circ}34.0'N/128^{\circ}51.9'W$. Since sonobuoys drift away from their original positions on the prevailing currents, the P-3C periodically resurveyed the sonobuoy field, allowing updated buoy positions to be used in the localization calculations.

Following the initial acoustic localization, an attempt was made to confirm the acoustic position by conducting a visual search. This was performed at an altitude of 1100 ft at an air speed of 195 knots. Unfortunately the high surface winds made a visual search for the whale very difficult, despite the known presence of an animal in the area. One of the flight crew briefly saw what he described as a large whale at the surface at 1251 PDT and marked its position as $46^{\circ}33.7'N/128^{\circ}51.4'W$. Attempts to resight the animal were not successful. The crewman was subsequently able to answer questions indicating that he had seen a large whale, but could not provide enough detail to allow positive species

identification. Throughout this phase of the acoustic survey, short-range calls from a single blue whale were detected; no calls from other species were detected.

During post-processing, 21 SOSUS localizations were determined for blue whale calls between 1200 and 1400 PDT. A comparison of the sighting location at 1251 with the

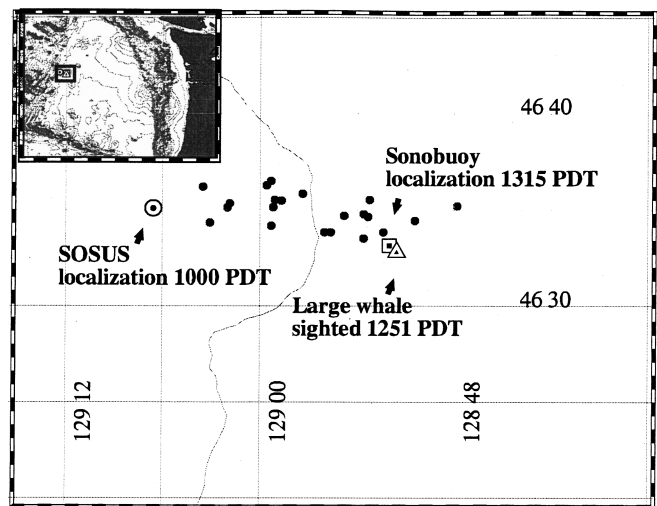


FIG. 6. Map of blue whale call localizations from SOSUS (initial location shown as \odot , post-processing localizations shown as \bullet), the Navy sonobuoy localization (\square), and the location of the sighting of a large whale (\triangle).

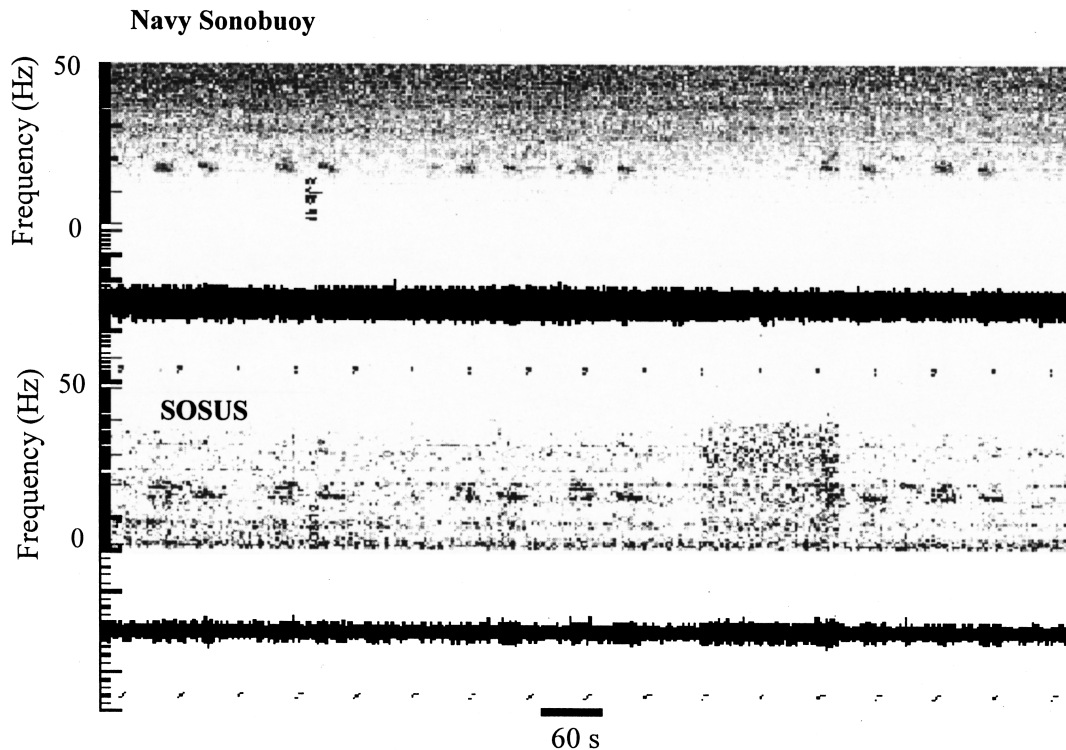


FIG. 7. Side-by-side comparison of six blue whale calls recorded on SOSUS (upper panel) and an air-dropped sonobuoy (lower panel). The spacing and repetition rate of these call series and suggest that they are from the same source, which was later confirmed by their derived locations.

closest time SOSUS localization (1247 PDT) gave a difference of 12.3 km while a comparison of the acoustic localization from the sonobuoys at 1315 with the same call on SOSUS gave a difference of only 2.2 km. A cubic spline was fitted through the 21 locations to generate “ideal” straight-line locations of calls. On average, the SOSUS-determined localizations were 2.45 ± 2.25 km from these locations (Fig. 6).

A comparison of the spectrograms from one of the sonobuoys and SOSUS suggests that the animal recorded on these two media was the same. Ninety minutes of available recordings from the sonobuoy with the loudest blue whale calls were compared with SOSUS data from the same time (1300–1430 PDT). Thirty-six AB pairs (72 calls total) were recorded with the sonobuoy array. During this time, 38 AB pairs (96 total calls) were recorded on SOSUS. The two additional calls from SOSUS overlap other calls, indicating that calls from at least two blue whales were detected by SOSUS, but not recorded on the sonobuoys, at this time. The pattern of call pairs from the sonobuoys is exactly matched with SOSUS data. Figure 7 shows six AB pairs from each medium. Range from the receivers varies between 400 and 600 km, suggesting that blue whale calls may be reliably detected at these distances under similar acoustic conditions using the matched filter technique.

VI. CONCLUSIONS

Passive localization of calling animals by use of fixed hydrophone arrays such as SOSUS has many advantages. SOSUS arrays can provide information on the locations of whales over a large area. The animals can be located without

being disturbed by nearby ship or aircraft and calls are not masked by noise from these vessels (Watkins and Schevill, 1972). Whale calls can be recorded and localized in poor weather conditions and seasons that are not conducive to visual surveys (Clark and Ellison, 1988, 1989). Additionally, short-term swim tracks generated from SOSUS and the associated gaps in calling may be used as an indication of their behavior and what percent of time animals can be expected to be near the surface and thus observable to visual surveys (Fristrup and Clark, 1997). The coordination of the P-3C flight with shore-based monitoring demonstrates the feasibility of locating an individual calling whale by use of the long-range capability of SOSUS. The direction of a rapid-response, medium-range acoustic search with sonobuoys was used as a proof of concept to validate the acoustic localizations determined by use of SOSUS. Cueing field observations from shore-based monitoring can greatly improve the efficiency of field studies.

Passive acoustic localization alone cannot provide a complete picture due to several shortcomings. First, because they are bottom-mounted in deep water, the SOSUS arrays have very poor coverage of waters over the continental shelf (Fox *et al.*, 1995), which is a primary habitat. Second, there is presently no means of determining other behaviors of the calling animal without visual observations. Third, acoustic data alone provide no information as to the numbers and distributions of noncalling whales. Finally, the individual differences in calls among blue whales have not been sufficiently studied to determine how many individuals are represented in a series of locations. Until some of these shortcomings are addressed, numbers and distributions of calling

animals from long-range acoustic monitoring will only provide part of the information necessary to estimate densities. Information resulting from the analyses of multi-mode survey data, such as combining acoustic, visual, and genetics, may be used to overcome some of these problems.

Recently, more effort has been placed on including acoustics in assessing regional concentrations of mysticetes, particularly blue whales, with the aim of better understanding the calling behavior of these animals (Clark and Fristrup, 1997; Teranishi *et al.*, 1997). A number of experiments in the southern California Bight region have combined visual and acoustic "sightings" to address some of the difficulties of censusing large whales. Several different combinations of acoustic methods have been coordinated with shipboard visual surveys including the use of towed arrays, local moored arrays, and SOSUS (Clark and Fristrup, 1997), and drifting sonobuoy arrays (Teranishi *et al.*, 1997). Fristrup and Clark (1997) address the advantages of these types of dual-mode surveys and suggest means by which they can best be used to estimate the densities of animals in an area. A combination of passive localization and on-site observations of whales should provide a more complete picture of the animals' behavior while calling as well as the proportion of calling animals in one area. This information is crucial for population estimates based solely on acoustic methods.

Unlike the relatively near-shore efforts in the southern California Bight region, the area monitored by SOSUS in the offshore northeast Pacific is less tractable because the animals occur far offshore. The concentration of blue whales is currently unknown, but may be too sparse to merit the expense of a large-scale visual survey. For the time being, however, localizing blue whale calls offshore of Oregon and Washington will help define regions where the animals do occur. As a database of whale call locations is built up, our understanding of blue whale habitat, relative abundance and seasonality will improve, which may lend itself to a dual-mode survey in the area offshore of Oregon and Washington.

ACKNOWLEDGMENTS

This work was performed as a partial requirement for a M.S. degree in Wildlife Sciences at Oregon State University. Supporting agencies include ONR (Program No. 9310834), the OSU Endowed Marine Mammal Program, and the NOAA VENTS program. Thanks are due to Dr. Bruce Mate for his guidance as K.M.S.' graduate adviser. Additionally, Dr. Christopher Clark of Cornell University loaned the hydrophone and DAT recorder used in the field portion of this experiment. Dr. Mark McDonald provided helpful comments on a previous draft of this manuscript. PMEL contribution #1832.

Barlow, J. (1994). "Abundance of large whales in California coastal waters: A comparison of ship surveys in 1979/1980 and in 1991," Reports of the International Whaling Commission **44**, 399–406.

Calambokidis, J., Steiger, G. H., Cabbage, J. C., Balcomb, K. C., Ewald, C., Kruse, S., Wells, R., and Sears, R. (1990). "Sightings and movements of blue whales off central California 1986–1988 from photo-identification of individuals," Reports of the International Whaling Commission Special Issue **12**, 343–348.

Camp, L. (1970). *Underwater Acoustics* (Wiley–Interscience, New York), 308 pp.

Clark, C. W. (1990). "Acoustic behavior of mysticete whales," in *Sensory Abilities of Cetaceans*, edited by J. Thomas and R. Kastelein (Plenum, New York), pp. 571–583.

Clark, C. W., and Ellison, W. T. (1988). "Numbers and distributions of bowhead whales, *Balaena mysticetus*, based on the 1985 acoustic study off Pt. Barrow, Alaska," Reports of the International Whaling Commission **38**, 365–370.

Clark, C. W., and Ellison, W. T. (1989). "Numbers and distributions of bowhead whales, *Balaena mysticetus*, based on the 1986 acoustic study off Pt. Barrow, Alaska," Reports of the International Whaling Commission **39**, 297–303.

Clark, C. W., and Fristrup, K. M. (1997). "Whales '95: A combined visual and acoustic survey of blue and fin whales off southern California," Reports of the International Whaling Commission **47**, 583–600.

Cummings, W. C., and Thompson, P. O. (1971). "Underwater sounds from the blue whale, *Balaenoptera musculus*," J. Acoust. Soc. Am. **50**, 1193–1198.

Edds, P. L. (1982). "Vocalizations of the blue whale, *Balaenoptera musculus*, in the St. Lawrence River," J. Mammal. **63**, 345–347.

Evans, W. E. (1967). "Vocalizations among marine mammals," in *Marine Bioacoustics*, edited by W. N. Tavolga (Pergamon, New York), Vol. 2, pp. 159–186.

Fiscus, C. H., and Niggol, K. (1965). "Observations of cetaceans off California, Oregon and Washington," U.S. Fish and Wildlife Service Special Scientific Report—Fisheries No. 498, 27 pp.

Fox, C. G., Dziak, R. P., Matsumoto, H., and Schreiner, A. E. (1994). "Potential for monitoring low level seismicity on the Juan de Fuca Ridge using military hydrophone arrays," Marine Tech. Soc. J. **27**, 22–30.

Fox, C. G., Radford, W. E., Dziak, R. P., Lau, T. K., Matsumoto, H., and Schreiner, A. E. (1995). "Acoustic detection of a seafloor spreading episode on the Juan de Fuca Ridge using military hydrophone arrays," Geophys. Res. Lett. **22**, 131–134.

Freitag, L. E., and Tyack, P. L. (1993). "Passive acoustic localization of the Atlantic bottlenose dolphin using whistles and echolocation clicks," J. Acoust. Soc. Am. **93**, 2197–2205.

Fristrup, K. M., and Clark, C. W. (1997). "Combining visual and acoustic survey data to enhance density estimation," Reports of the International Whaling Commission **47**, 933–936.

Green, G. A., Brueggeman, J. J., Grotefendt, R. A., Bowlby, C. E., Bonnell, M. L., and Balcomb, K. C. III (1992). "Cetacean distribution and abundance off Oregon and Washington, 1989–1990," Chapter 1 in *Oregon and Washington Marine Mammal and Seabird Surveys*, edited by J. J. Brueggeman, Final Report, OCS Study MMS 91-0093, pp. 1–100.

Jacobson, R. S., Bibee, L. D., Embley, R. W., and Hammond, S. R. (1987). "A microseismicity survey of Axial Seamount, Juan de Fuca Ridge," Bull. Seismol. Soc. Am. **77**, 160–172.

Leatherwood, S., Reeves, R. R., and Foster, L. (1983). *The Sierra Club Handbook of Whales and Dolphins* (Sierra Club, San Francisco), 302 pp.

McDonald, M. A., Hildebrand, J. A., and Webb, S. C. (1995). "Blue and fin whales observed on a seafloor array in the northeast Pacific," J. Acoust. Soc. Am. **98**, 712–721.

Mellinger, D. K., and Clark, C. W. (1993). "A method for filtering bioacoustic transients by spectrogram image convolution," Proceedings IEEE Oceans '93 **3**, 122–127.

Mellinger, D. K., and Clark, C. W. (1995). "Abstract. Characteristics of fin and blue whale vocalizations recorded from IUSS in the north and west Atlantic," 11th Biennial Conference on the Biology of Marine Mammals, December 1995, Orlando, FL.

Mellinger, D. K., and Clark, C. W. (1997). "Methods for automatic detection of mysticete sounds," Marine and Freshwater Behaviour and Physiology **29**, 163–181.

Mizroch, S. A., Rice, D. W., and Breiwick, J. M. (1984). "The blue whale, *Balaenoptera musculus*," Marine Fisheries Review **46**, 15–19.

Nishimura, C. E., and Conlon, D. M. (1994). "IUSS Dual Use: Monitoring whales and earthquakes using SOSUS," Marine Tech. Soc. J. **27**, 13–21.

Nishiwaki, M. (1967). "Distribution and migration of marine mammals in the North Pacific area," Bulletin of the Ocean Research Institute, University of Tokyo, pp. 1–64.

Payne, R., and Webb, D. (1971). "Orientation by means of long range acoustic signaling in baleen whales," Ann. (N.Y.) Acad. Sci. **188**, 110–142.

- Pike, G. C. (1954). "Whaling on the coast of British Columbia," *Norsk Hvalfangst-Tidende* **3**, 117–127.
- Pike, G. C., and MacAskie, I. B. (1969). "Marine Mammals of British Columbia," *Bull. Fisheries Res. Board of Canada* **171**, 1–54.
- Reysenbach de Haan, F. W. (1966). "Listening underwater: Thoughts on sound and cetacean hearing," *Whales, Dolphins and Porpoises*, edited by K. S. Norris (University of California Press, Berkeley), Chap. 26, pp. 583–596.
- Rice, D. W. (1974). "Whales and whale research in the eastern North Pacific," *The Whale Problem*, edited by W. E. Schevill (Harvard University Press, Cambridge, MA), Chap. 6, pp. 170–195.
- Rivers, J. A. (1997). "Blue whale, *Balaenoptera musculus*, vocalizations from the waters off central California," *Marine Mammal Science* **13**, 186–195.
- Robinson, E. A., and Treitel, S. (1980). *Geophysical Signal Analysis* (Prentice-Hall, Englewood Cliffs, NJ), 466 pp.
- Spindel, R. C., and Worcester, P. F. (1990). "Ocean acoustic tomography," *Sci. Am.*, October 1990, pp. 94–99.
- Spiesberger, J. L., and Fristrup, K. M. (1990). "Passive localization of calling animals and sensing of their acoustic environment using acoustic tomography," *Am. Nat.* **135**, 107–153.
- Teranishi, A. M., Hildebrand, J. A., McDonald, M. A., Moore, S. E., and Stafford, K. M. (1997). "Abstract. Acoustic and visual studies of blue whales near the California Channel Islands," *J. Acoust. Soc. Am.* **102**, 3121.
- Thompson, P. O., and Friedl, W. A. (1982). "A long term study of low frequency sound from several species of whales off Oahu, Hawaii," *Cetology* **45**, 1–19.
- Thompson, T. J., Winn, H. E., and Perkins, P. J. (1979). "Mysticete sounds," in *Behavior of Marine Animals: Current Perspectives in Research. Volume 3: Cetaceans*, edited by H. E. Winn and B. L. Olla (Harvard U.P., Cambridge, MA), pp. 403–431.
- Thompson, P. O., Findley, L. T., Vidal, O., and Cummings, W. C. (1996). "Underwater sounds of blue whales, *Balaenoptera musculus*, in the Gulf of California, Mexico," *Marine Mammal Science* **12**, 288–292.
- Urick, R. J. (1983). *Principles of Underwater Sound*, 3rd ed. (McGraw-Hill, New York), 423 pp.
- Watkins, W. A., and Schevill, W. A. (1972). "Sound source location by arrival-times on a non-rigid three-dimensional hydrophone array," *Deep-Sea Res.* **19**, 691–706.
- Winn, H. E., and Perkins, P. J. (1976). "Distribution and sounds of the minke whale, with a review of mysticete sounds," *Cetology* **19**, 1–12.
- Yochem, P. K., and Leatherwood, S. (1985). "Blue whale *Balaenoptera musculus* (Linnaeus, 1758)," in *Handbook of Marine Mammals*, edited by S. H. Ridgeway and R. J. Harrison (Academic, New York), Vol. 3, Chap. 8, pp. 193–240.

The neural network classification of false killer whale (*Pseudorca crassidens*) vocalizations

Scott O. Murray^{a)}

Institute of Theoretical Dynamics, 2201 Academic Surge, 1 Shields Avenue, University of California, Davis, California 95616

Eduardo Mercado

Center for Molecular and Behavioral Neuroscience, Rutgers University-Newark Campus, 197 University Avenue, Newark, New Jersey 07102

Herbert L. Roitblat

Department of Psychology, 2430 Campus Road, University of Hawaii, Honolulu, Hawaii 96822

(Received 16 April 1998; revised 10 July 1998; accepted 5 September 1998)

This study reports the use of unsupervised, self-organizing neural network to categorize the repertoire of false killer whale vocalizations. Self-organizing networks are capable of detecting patterns in their input and partitioning those patterns into categories without requiring that the number or types of categories be predefined. The inputs for the neural networks were two-dimensional characterization of false killer whale vocalizations, where each vocalization was characterized by a sequence of short-time measurements of duty cycle and peak frequency. The first neural network used competitive learning, where units in a competitive layer distributed themselves to recognize frequently presented input vectors. This network resulted in classes representing typical patterns in the vocalizations. The second network was a Kohonen feature map which organized the outputs topologically, providing a graphical organization of pattern relationships. The networks performed well as measured by (1) the average correlation between the input vectors and the weight vectors for each category, and (2) the ability of the networks to classify novel vocalizations. The techniques used in this study could easily be applied to other species and facilitate the development of objective, comprehensive repertoire models. © 1998 Acoustical Society of America. [S0001-4966(98)03312-8]

PACS numbers: 43.80.Ka [FD]

INTRODUCTION

Quantifying a species' repertoire is a fundamental challenge in the study of animal vocalizations. Many attempts have been made to characterize the various sounds produced by dolphin (*Delphinidae*) species. However, little progress has been made in developing objective, comprehensive repertoire models. The development of such models is important because they can facilitate comparisons both within and between species, aiding in the development of functional models. Currently, the field lacks an objective method capable of classifying the entire vocal repertoire of a dolphin species. Murray *et al.* (1998) describe a method capable of characterizing dolphin vocalizations that can be applied to all signal types (e.g., pulsed and continuous waveforms). This paper extends that work, demonstrating how self-organizing neural networks can classify the repertoire of false killer whale vocalizations.¹

Techniques that categorize dolphin vocalizations based on objective and quantitative analysis methods have recently been explored (e.g., Buck and Tyack, 1993; Dawson and Thorpe, 1990; McCowan, 1995). A dynamic time-warping method was used by Buck and Tyack (1993) to assess the similarity of bottlenosed dolphin (*Tursiops truncatus*) whistles. The method used an algorithm that first extracted

the frequency contour of the whistles through fundamental frequency analysis. The algorithm then performed a nonuniform time dilation to align the contours by minimizing the total square difference between the observed contour and a reference contour. Finally, the algorithm computed a distance measure between the observed contour and a library of reference contours. The observed contour was assigned to the closest reference contour. The technique was derived from speech recognition approaches (e.g., Itakura, 1975), and assumed that two whistles with similar contour shapes were the same, despite any differences in absolute length of the vocalization.

McCowan (1995) made similar assumptions about which features are most important in whistle analysis. In addition to generalizing across whistle length, she assumed that whistles that have been shifted up or down in absolute frequency, while maintaining the same "shape," should be categorized as the same. Twenty measurements of peak frequency were taken to represent each whistle. The frequency measurements were used to generate a correlation matrix, and principal component analysis was conducted using the correlation matrices. The factor scores from each data set of whistles were subjected to *K*-means cluster analysis to group whistles into clusters based on contour similarity. By using correlation matrices, the technique was able to cluster whistles that differed in absolute duration and frequency.

^{a)}Electronic mail: smurray@itd.ucdavis.edu

Both of these techniques (Buck and Tyack, 1993 and McCowan, 1995) are vast improvements over subjective judgment in that they ensure reliable classification performance. However, these techniques have only been applied to whistle-type vocalizations and they may, in fact, be limited in their ability to categorize other signal types. Both methods only consider frequency information and do not take into account changes in amplitude characteristics that occur with pulsed vocalizations.

A. Self-organizing neural networks

Neural networks are a promising technique in the analysis of animal vocalizations. Neural networks have been successful at classifying a number of complex signal types, including human speech (e.g., Kohonen, 1988; Huang and Kuh, 1992) and dolphin biosonar echoes (e.g., Au and Nachtigall, 1995; Roitblat *et al.*, 1989). The study reported here employs *unsupervised neural networks*. Unlike supervised neural networks (e.g., multilayer perceptrons), unsupervised networks require only weak assumptions about the number and type of potential categories. Unsupervised networks are capable of learning to detect regularities and correlations in their input, and adapting their responses to that input (Demuth and Beale, 1993). Unsupervised networks are called self-organizing because the organization is not imposed on them by an outside intelligent agent, but instead is learned as the outcome of the patterns to which they are exposed and the learning algorithm which adjusts their weight structure. Generally, unsupervised neural networks partition a given data set into disjoint subsets (i.e., categories), such that patterns in the same category are as alike as possible, and patterns in different clusters are as dissimilar as possible (Mehrotra *et al.*, 1997). While most unsupervised networks share this similar goal, they may differ in the specifics of their mathematical implementation.

Self-organizing neural networks, similar to the one presented in this paper, have been used previously to classify humpback whale song vocalizations (Walker *et al.*, 1996). Time-frequency representations (spectrograms) of humpback whale song units were used as inputs into a self-organizing feature map. The network classified the song units similarly to human visual and aural impressions and traditional statistical clustering algorithms.

The technique presented by Walker *et al.* (1996) can be applied to the entire song repertoire, but spectrograms may not be the best choice for neural network inputs. The time-bandwidth tradeoff inherent in all spectrogram-like representations can dramatically affect the representation of a signal and how it is classified. Very different spectrograms can result from the same signal following only slight changes in the window size. For example, a signal can appear to be a continuous whistle with a large window size, and appear to be a series of short pulses with a small window. In the absence of information about the animal's integration window, therefore, arbitrary window sizes and shapes may mislead categorization.

The inputs for the neural networks used in the study reported here were two-dimensional characterizations of

false killer whale vocalizations. Each vocalization was characterized by its simultaneous modulations in duty cycle and peak frequency (Murray *et al.*, 1998). The short-time duty-cycle measure compares the signal to a continuous sinusoid. As the signal approaches a continuous sinusoid, the duty-cycle measure begins to approach 1.00. Pulses are represented as lower duty-cycle values as a function of pulse repetition rate (Murray *et al.*, 1998). Consequently, high duty-cycle vocalizations are heard as whistles; lower duty-cycle values correspond to pulsed vocalizations. The duty cycle/peak frequency representational scheme presented here is not subject to the same constraints as spectrograms. With spectrograms, the time-frequency tradeoff can qualitatively alter the signal representation (or "type"). For example, a pulsed signal can appear to be continuous with the proper window size. Here, the time-frequency tradeoff only affects the resolution of the peak frequency measurements and does not affect the type of signal as represented by the duty cycle measurements.

The first neural network used in this study used *competitive learning*, where units in a competitive layer distributed themselves to recognize frequently presented input vectors. The result of this network was a set of classes representing typical patterns in the vocalizations. The second network used was a Kohonen feature map, which is similar to a competitive network in many respects. The additional aspect of a feature map is that the outputs are organized topologically. Similarity among patterns are mapped into closeness relationships on a grid, providing a graphical organization of pattern relationships (Dayhoff, 1990).

The primary advantages to the techniques used in this study are that all emitted vocalizations were characterized using a single method, and the outputs of the characterization were organized into patterns based on the features present in the vocalizations. Both types of neural networks (competitive and Kohonen feature map) require few *a priori* assumptions regarding the categorical structure of the vocalizations. Instead, the networks search for correlational structure in the data and form categories around these centers of correlation. Both networks were used in order to contrast their respective outputs.

I. METHODS

The 500-vocalization data set used in Murray *et al.* (1998) was used for this study. The vocalizations were from two false killer whales, one male and one female, located at Sea Life Park, Oahu, Hawaii. Recordings were made by isolating each animal in a distant portion of its tank while the other animal remained behind a gate in another portion of the tank. The minimum distance between the animal being recorded and the other animal behind the gate was approximately 30 m. While recording, the trainer positioned the animal's melon (forehead region of the animal from which it is believed sound emanates) underwater so that its head was about 1–2 m away from the hydrophone. This procedure ensured very high signal-to-noise ratios, as well as confidence concerning the identity of the animal making the sounds (Murray *et al.*, 1998).

All sounds were recorded with a Sony digital audio-tape recorder (DAT), TCD-D8, which uses a sampling rate of 44.1 kHz, for a frequency bandwidth to 22 kHz. A hydrophone (custom-built by W. Au) with a sensitivity of -185 dB and a bandwidth to 200 kHz was used for all recordings. Using a quasirandom procedure, 500 vocalizations were chosen for analysis and digitized onto a PC using a SoundBlaster-32 sound card.

A single vocalization was defined as an uninterrupted (in time) sound emission and could encompass multiple sound “types” (e.g., a whistle and pulse train). The data set included a random sample of 250 vocalizations from each of the two false killer whales. Each vocalization was sequenced into a series of short-duration (512 point—approximately 11.6 ms) nonoverlapping time windows and described along two dimensions: duty cycle and peak frequency. Duty cycle refers to the percentage of time a signal is “on” relative to the total length of the signal and in this context is relative to the 512-point window length. The duty cycle algorithm assigned a value between 0.0 (no signal—e.g., an interpulse interval) to 1.00 (a continuous signal—e.g., a whistle). In this way, the duty-cycle measure gave an approximation of the type of waveform (e.g., pulsed versus continuous) within each time window.

The characterization vectors (duty cycle and peak frequency) for each vocalization served as the inputs into a self-organizing, competitive neural network and a two-dimensional, self-organizing feature map. The input vectors for the networks must have the same number of elements; therefore, the characterization vectors for each vocalization were sampled 30 times at regular intervals. The average duration of each vocalization was 506 ms (s.d.=761 ms), meaning that most vocalizations had approximately 40 windows. The use of 30 samples was arbitrary, but preliminary analysis demonstrated it to be sufficient to capture the dynamics of most signals. When pulse trains were analyzed, the zero elements (representing interpulse intervals) and nonzero elements (representing individual pulses) were sampled separately. This was done to maintain the same relative spacing of zero and nonzero elements in the vectors.

Before presentation to the neural network, the input vectors were scaled to z scores, using the grand mean and standard deviation over all signals. The mean for the duty-cycle values was 0.46 (s.d.=0.34) and the mean for peak frequency was 7122 Hz (s.d.=2687 Hz). Signal vectors were then normalized to unit length by dividing each vector by its length, meaning that the input vectors lay on a unit hypersphere. The input values were normalized because the neural network algorithm used maximum dot product as a similarity measure. If two vectors are of unit length, the dot product is equal to the cosine of the angle between the two vectors (i.e., a “meaningful” measure of similarity). Normalizing to unit length removes magnitude information from the inputs and is important to consider when interpreting the results. For example, after normalization of z -scored feature vectors, a window which was 0.1 standard deviations above the mean in frequency and of mean duty cycle, [0.1 0], would be treated as equivalent to a window that was 3 s.d. above the mean in frequency and of mean duty cycle, [3 0]. (After normaliza-

tion both vectors equal [1 0].) What is preserved after normalization is the dynamics, or the change of the signal across time relative to the mean.

The inputs for the neural networks were a combination of duty cycle and peak frequency values. Input vectors were constructed by concatenating the two 30-element vectors into a single 60-element vector. To test the reliability of the categories formed by the network, a subset of 250 input vectors was chosen randomly from the set of 500 to serve as a training set. These vectors served as inputs to train the network. The remaining 250 vectors served as a test set. The performance of the network developed with the training set was compared with the test set. The neural networks were implemented using custom script-code accessing functions in MATLAB’s Neural Network Toolbox (The MathWorks, Inc.).

II. COMPETITIVE NETWORK

The units in the competitive network were initialized to random weight vectors with the number of elements in each weight vector equal to the number of elements in the input vectors (i.e., 60 elements). An input vector was presented to the network and the angle between the input vector and each of the unit’s weight vectors was computed. The unit with the smallest angular difference from the input vector was the “winner.” The weights of the winning unit were adjusted in the direction of the input vector. The size of the adjustment was controlled by a learning-rate parameter. Therefore, when the same input vector was presented again, the winning unit was more likely to win and its values were adjusted closer to the input vector. The weight vectors of each of the units, at the end of training, represented prototypes or category “centroids.”

To summarize, the competitive network worked as follows:

- (1) Apply an input vector \mathbf{X} .
- (2) Calculate the angular distance \mathbf{D}_j between \mathbf{X} and the weight vectors \mathbf{W}_j of each unit. Since normalized inputs and weight vectors were used, the cosine of the angle between \mathbf{X} and \mathbf{W} equals the dot product:

$$\mathbf{D}_j = \mathbf{X} \cdot \mathbf{W}_j$$

- (3) The unit that has the weight vector closest to \mathbf{X} (i.e., the largest dot product) is declared the winner. The winner’s weights are adjusted in the direction of \mathbf{X} by the formula:

$$\mathbf{W}_j[n+1] = \mathbf{W}_j[n] + \alpha(\mathbf{X} - \mathbf{W}_j[n]),$$

where n indicates the iteration number, and α the learning rate.

- (4) Perform steps (1) through (3), cycling through each input vector.

After training, each of the input vectors was assigned to the unit (category) whose weight vector (category centroid) was closest. The performance of the network was assessed by calculating the average cosine of the angle between each unit’s weight vector and the input vectors assigned to it. In

other words, the degree to which each input vector was related to its respective unit's weight vector was measured.

A. Results

The number of units in a winner-take-all network determines the maximum number of potential categories. The number of units ultimately used in training the network was arrived at through a trial-and-error procedure by first starting with a large number of units—i.e., many more than reasonably suspected categories—and then reducing the number. Forty units (possible categories) were first used. Presentation of the training vectors was iterated 20 000 times at learning rates of 0.05 and repeated with a rate of 0.10. In both cases, only five of the units learned—i.e., showed adjustments in their values. The number of units was subsequently reduced by one-half (from 20 to 10). In all cases, only five units adjusted their weights.

The network was trained with five units at a learning rate of 0.10 for 10 000 iterations. The weight vectors from each of the five units after training are shown in Fig. 1. The x axis represents each of the 60 elements of the vectors and the y axis represents normed z -score values. Zero represents the mean; values above and below zero represent deviations from the mean. The first 30 elements representing duty-cycle values are shown above the second 30 elements representing peak frequency.

Looking at weight vector 1 (W1) in Fig. 1, the first 30 elements (representing duty cycle) are constant and of relatively high value. The representation of peak frequency (dashed line) is ascending. This vector represents ascending whistle vocalizations. The false killer whales used in this study frequently made short-duration ascending whistles; these vocalizations are one of the most salient vocalizations when listening to the animals in almost any behavioral context. Because these vocalizations were so commonly observed, the observance of a weight vector that represented these vocalizations gave validity to the performance of the neural network.

Looking at weight vector 2 (W2) in Fig. 1, the first 30 elements (representing duty cycle) begin at relatively high values, then approximately halfway through (element 13 or 14) drop in value. This weight vector seems to represent the whistle→pulse-train vocalizations. These vocalizations begin as whistles, then switch to what sounds to us like a click train or a rapidly pulsed vocalization (Murray *et al.*, 1998). Looking at elements 31 to 60 (representing peak frequency), it appears that during the high duty-cycle portion (i.e., the whistle), peak frequency is ascending. During the pulse-train portion, the peak frequency of the end of the whistle is maintained at a relatively constant level throughout the duration of the pulse train, similar to the examples presented in Murray *et al.* (1998).

Weight vector 3 is straightforward to interpret. Both the duty cycle (first 30 elements) and the peak frequency (second 30 elements) are relatively constant and at low values. This vector is the result of low-frequency pulse trains. Weight vector 4 has a similarly straightforward interpretation. It has intermediate duty-cycle values and low peak-frequency values, and is likely the result of lower frequency, rapidly

pulsed vocalizations. Weight vector 5 has low duty-cycle values and high peak-frequency values and seems to represent high-frequency pulse trains.

The performance of the neural network was evaluated by first calculating how much of the input space was accounted for by each weight vector. The cosine of the angle between each input vector used for training and each unit's weight vectors were calculated. The input vectors were assigned to the category represented by the unit with the closest weight vector. Thus, there were five clusters of input vectors corresponding to the five units. A total of 94 of the training vectors clustered with the weight vector of unit 1 (W1), 25 with W2, 43 with W3, 27 with W4, and 61 with W5.

The average similarity (as measured by angular distance) across all training vectors and their respective category's weight vector was 0.72. Additionally, the average similarity was calculated between the members of each category and the four "unassociated" units. The average between-category similarity was -0.11 . The results reflect the general goal of an unsupervised network—to partition a data set into disjoint subsets (i.e., categories), such that patterns in the same category are as alike as possible, and patterns in different clusters are as dissimilar as possible. Referring to Table I, the average within-category similarity is shown in the main diagonal. The other cells in the table show between-category similarity.

The 250 vectors not used to train the network served as a novel test set. Each member of the test set was clustered with the nearest weight vector from each of the five units. A total of 93 of the test vectors clustered with W1, 20 with W2, 41 with W3, 28 with W4, and 68 with W5. The distribution of vocalizations among the weight vectors in the test set is closely aligned with the training set, suggesting representative samples for both the training and testing data set. The average similarity between each test input vector and its unit's respective weight vector was 0.69. Performance of the network with the test set (0.69) is comparable to that of the network using the training set (0.72). The average between-category similarity for the test set was -0.11 (see Table II).

The competitive neural network recognized five major categories in the false killer whale vocalizations analyzed. The within-category similarity was high, with an average correlation of 0.72. Additionally, the categories learned with the training set were able to be generalized to the novel test set, suggesting that the categories are reliable. The competitive network approximates the minimum number of categories present in the input patterns. The next network used, a Kohonen feature map, provides a different representation of the vocalizations.

III. FEATURE MAP

The two-dimensional feature map used in this study was similar to the competitive network described above. However, the competitive units were ordered topologically in a two-dimensional square grid. Each unit had neighbors on the grid where a neighborhood of diameter 1 included a specified unit and its immediately adjacent neighbors. A neighborhood

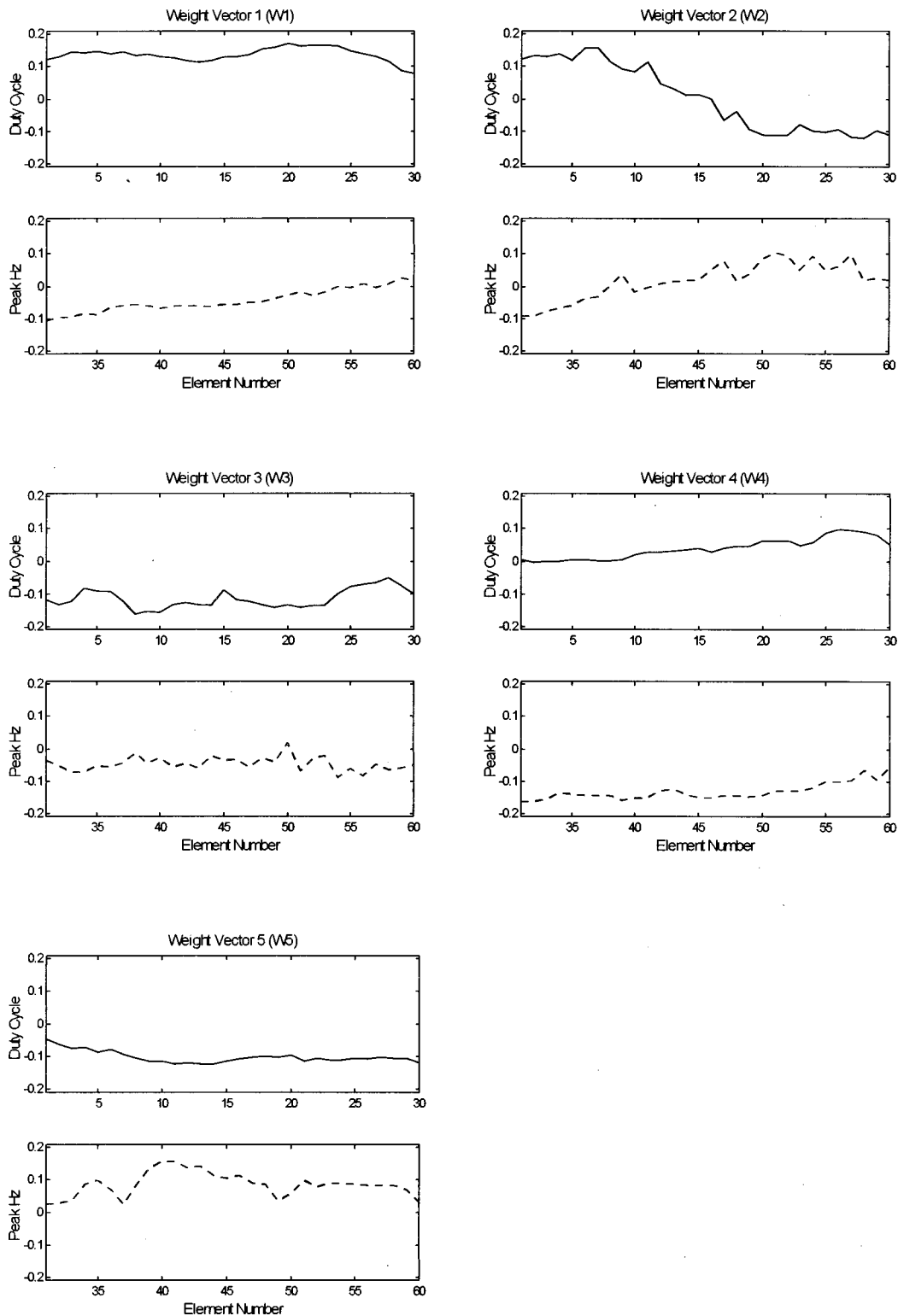


FIG. 1. The weight vectors of each of the five units after training with duty-cycle and peak-frequency inputs. The 60-element weight vectors are shown with the first 30 elements (duty cycle) plotted above the second 30 elements (peak frequency). Zero (y axis) represents the grand mean for each dimension (normed z scores). The weight vector from unit 1 (W1) has relatively high duty-cycle values and ascending peak frequency. This unit represents ascending whistle vocalizations. The other units can be interpreted similarly.

of diameter 2 included the diameter 1 units and their immediately adjacent neighbors. The feature map in this study used a 5×5 grid.

The feature map differed from the competitive network in terms of which units had their weights updated. In addition to updating the winner, the feature map updated the

winner's neighbors. The result was that neighboring units tended to have similar weight vectors (i.e., represent similar portions of the input space). During the initial stage of training, the neighborhood size encompassed the entire 5×5 grid (i.e., each unit adjusted its weights in response to each input vector) and was decreased linearly so that it reached a mini-

TABLE I. The mean similarity/correlation between each cluster of the training set and each of the five unit's weight vector. Within-category similarities are in the main diagonal; all other cells show between-category similarities. This table highlights the ability of the competitive neural network to form maximally distinct categories.

	Weight 1	Weight 2	Weight 3	Weight 4	Weight 5
Cluster 1	0.81	0.06	-0.58	0.45	-0.70
Cluster 2	0.06	0.63	-0.08	-0.11	0.05
Cluster 3	-0.53	-0.08	0.70	0.07	0.33
Cluster 4	0.42	-0.22	0.07	0.74	-0.59
Cluster 5	-0.67	0.07	0.33	-0.61	0.74

num of 1 after one-quarter of the training cycles and remained there for the rest of training. This allowed the entire feature map to move initially in the direction of the input space, then, as the neighborhood size decreased to 1, the map ordered itself topologically over the presented input vectors.

The first three steps outlined above for the competitive network apply to the feature map. The following are the additional properties of the feature map.

- (1) The winning unit, \mathbf{W}_c , is designated as the center of a group of units (i.e., a neighborhood) that lie within a distance D (neighborhood size) from \mathbf{W}_c .
- (2) Train this group of units according to the formula:

$$\mathbf{W}_j[n+1] = \mathbf{W}_j[n] + \alpha(\mathbf{X} - \mathbf{W}_j[n])$$

for all weight vectors within a distance D of \mathbf{W}_c .

As the training progresses, the values of D and α (the learning rate) are gradually reduced.

By assessing the number of input vectors that activated (clustered with) each unit, it was possible to examine the distribution of the input space across the topology represented by the network. Similar to the competitive network, a set of 250 vectors, randomly selected from the total pool of 500, were used as input vectors for training. The remaining 250 were used to test reliability. Reliability was measured by correlating the distributions across the topological map of the training vectors and the test vectors.

A. Results

The feature map was trained for 15 000 iterations at a learning rate of 0.15. The weight vectors after training are presented in Fig. 2. The first 30 elements in each plot represent duty-cycle values, and elements 31 through 60 represent peak frequency. Row and column notation (row, column), will be used to refer to specific units on the grid in Fig. 2.

TABLE II. The mean similarity/correlation between each cluster of the test set and each of the five unit's weight vector. When the trained network is presented with novel vocalizations, very similar patterns of similarity/dissimilarity are found as compared to the training set (Table I).

	Weight 1	Weight 2	Weight 3	Weight 4	Weight 5
Cluster 1	0.75	0.09	-0.60	0.35	-0.62
Cluster 2	0.07	0.59	-0.05	-0.07	0.01
Cluster 3	-0.52	-0.09	0.72	0.12	0.29
Cluster 4	0.41	-0.11	0.04	0.68	-0.58
Cluster 5	-0.66	0.07	0.31	-0.61	0.73

Referring to Fig. 2, units (2,4), (2,5), (3,4), and (3,5) (i.e., middle/right of grid) represent relatively high and constant duty cycles and gradually ascending peak frequencies. These weight vectors are similar to the weight vector of unit 1 (\mathbf{W}_1 in Fig. 1) in the competitive network and correspond to ascending whistle vocalizations. Similarly, units (4,1), (4,2), (5,1), and (5,2) (i.e., lower-left portion of the grid) represent low duty-cycle, high-frequency vocalizations. In the upper-left portion of the grid, units (1,1), (1,2), (2,1), and (2,2), represent whistle→pulse-train vocalizations. These units are similar to unit 2 (\mathbf{W}_2 in Fig. 1) of the competitive network.

The distribution of the training-set input space across the topology of the network is shown in Fig. 3 as “training set.” The input space is heavily distributed in the lower left (corresponding to high-frequency pulse trains) and middle right (corresponding to ascending whistles) of the topology. The distribution was also calculated for the novel test inputs and is depicted in Fig. 3 as “test set.” The two distributions are similar with a correlation of 0.89.

The categories developed by the feature map were consistent with those of the competitive neural network. Many of the patterns in the weight vectors that were seen in the competitive networks were evident in the feature map. Additionally, the input spaces in both the competitive and feature map networks seemed to distribute themselves similarly. For example, units representing constant/high duty cycle and ascending peak frequency (ascending whistles) attracted a large percentage of the input space in both the competitive network and the feature map.

IV. DISCUSSION

Two types of neural networks were used to classify the vocalizations: a competitive network and a two-dimensional feature map. Both networks were trained with a combination of duty-cycle and peak-frequency input values. The competitive network learned five different categories. The fact that the network learned the two obvious categories—whistles and click trains, reflected by both high and low duty-cycle weight vectors, respectively, attests to the validity of the network.

Based on interpretation of the five weight vectors from the competitive network, the main categories seem to be ascending whistles, low-frequency pulse trains, and high-frequency pulse trains. The network also recognized the whistle→pulse-train transitions as a significant category (see Fig. 1, \mathbf{W}_2). The peak frequency of the high duty-cycle portion (i.e., the whistle) of this category was ascending. The pulse-train component (low duty cycle) seemed to maintain the peak frequency of the end of the whistle.

It is important to point out that the ability of the neural network to learn these “combination” categories (categories with both continuous-wave and pulsed components) was facilitated by the use of a measure of waveform shape. Because of the aural and spectral distinctiveness of many pulsed versus continuous sounds, vocalizations that possess combinations may be arbitrarily separated into different components. Therefore, it is unlikely that the combination categories would have been arrived at through subjective

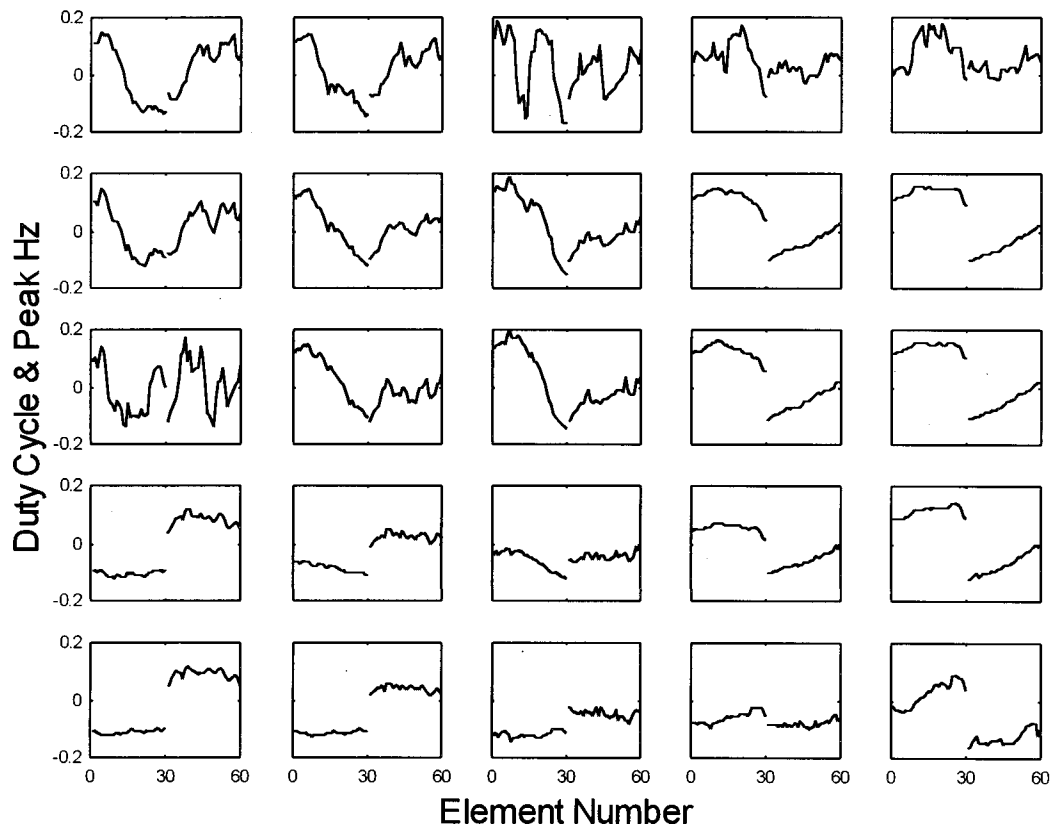


FIG. 2. The topology of the input space using duty-cycle and peak-frequency values. The x axis in each plot represents the element number of each weight vector. The first 30 elements represent duty cycle and the elements 31 to 60 represent peak frequency. The y axis represents scaled and normalized duty-cycle and peak-frequency values, where zero represents the grand mean. Units on the right/middle side of the topology have relatively high duty cycle and ascending peak frequency (ascending whistles). Units in the lower-left portion have low duty cycle and relatively high peak frequency (high-frequency pulse trains). Also, units that are close to each other have similar-looking weight vectors.

classification techniques such as aural analysis of visual analysis of spectrograms. For example, if aural analysis were used, a whistle that suddenly changed into a pulse train (see Murray *et al.*, 1998, for examples) might be classified into two separate vocalizations: a whistle immediately followed by a pulse train. However, with the short-time duty-cycle measure, the continuity of the vocalizations was preserved. The use of an objective measure of signal type allows for a different definition of a single vocalization: an uninterrupted (in time) sound emission as opposed to a certain subjective class of vocalization (e.g., whistle or pulse train). Such a definition is likely more functionally relevant because it is defined by the vocalizing animal and not by the subjective judgment of a human listener.

The categories developed by the self-organizing feature map complemented the results obtained with the competitive network. The types of weight vectors observed in the competitive network were also seen in the feature map. Additionally, the input distribution patterns (i.e., input clustering) were very similar in both the competitive and feature map networks. Both types of networks demonstrated that the self-organizing approach, using the two types of inputs (duty cycle and peak frequency), is a very effective way of categorizing dolphin vocalizations.

Though the results of the two types of networks were complementary, each has its own advantages. The competitive network was effective in finding the minimum number

of potential categories in the data set. Additional characteristics were revealed by the feature map, such as the relative distribution of the input space (through category redundancy) and the topological relationships between categories.

The neural network classification scheme presented here is easily amenable to different types of acoustic signal representations. For example, there may be other relevant dimensions, such as signal duration, which may be important to include in future implementations of these networks. Likewise, some investigators may only want to consider a certain duty-cycle category (e.g., whistles) in their analysis. Such networks could limit their inputs to relevant spectral features

Training Set					Test Set				
8	1	4	2	9	4	0	5	6	16
5	1	3	12	25	4	2	2	15	16
5	2	9	7	10	8	1	8	5	10
12	4	4	12	20	7	6	6	15	17
34	13	24	9	15	42	13	19	14	9

FIG. 3. The distribution of the duty-cycle and peak-frequency input space over the topology depicted in Fig. 2. Most of the input vectors of both the training set and test set clustered in the right-middle (ascending whistles) portion of the topology and in the lower-left portion (pulse trains). The two distributions have a Pearson's correlation of 0.89, meaning that the distribution of the input space in the trained network is generalizable to novel vocalizations.

(e.g., fundamental frequency). Overall, the networks are very flexible, and it is ultimately up to the investigator to determine which inputs are most relevant to his or her particular classification task.

In summary, the techniques used in this study provide a unique and objective method for classifying cetacean vocalizations. Forming simple categories using self-organizing networks can facilitate comparisons between different species and different behavioral contexts, as well as aid in the development of functional models of cetacean vocalizations. The ability of self-organizing networks to “search” for inherent relationships in the data and form categories based on those relationships makes them well-suited for classifying animal vocalizations.

ACKNOWLEDGMENTS

This study was conducted as part of an M.A. program at the University of Hawaii, and was made possible through the support of Marlee Breese, formerly of Sea Life Park, Oahu.

¹The use of the term “vocalization” in this paper is not meant to imply that vocal folds are necessarily the mechanism producing the sounds. It is used as a general term for dolphin sounds that are internally generated via air-flow in the head region.

Au, W. W. L., and Nachtigall, P. E. (1995). “Artificial neural network modeling of dolphin echolocation,” in *Sensory Systems of Aquatic Mam-*

mals, edited by R. A. Kastelein, J. A. Thomas, and J. A. Thomas (De Spil, The Netherlands), pp. 183–199.

Buck, J., and Tyack, P. (1993). “A quantitative measure of similarity for *Tursiops truncatus* signature whistles,” *J. Acoust. Soc. Am.* **94**, 2497–2506.

Dawson, S., and Thorpe, C. (1990). “A quantitative analysis of the sounds of Hector’s Dolphin,” *Ethology* **86**, 131–145.

Dayhoff, J. E. (1990). *Neural Network Architectures: An Introduction* (Van Nostrand Reinhold, New York).

Demuth, H., and Beale, M. (1993). *Neural Network Toolbox* (The Math-Works, Inc., Natick, Massachusetts).

Huang, Z., and Kuh, A. (1992). “A combined self-organizing feature map and multilayer perceptron for isolated word recognition,” *IEEE Trans. Signal Process.* **11**, 2651–2675.

Itakura, F. (1975). “Minimum prediction residual principle applied to speech recognition,” *IEEE Trans. Acoust., Speech, Signal Process.* **23**, 67–72.

Kohonen, T. (1988). “The ‘neural’ phonetic typewriter,” *Computer* **21**, 11–22.

McCowan, B. (1995). “A new quantitative technique for categorizing whistles using simulated signals and whistles from captive bottlenose dolphins (*Delphinidae, Tursiops truncatus*),” *Ethology* **100**, 177–193.

Mehrotra, K., Chilukuri, K. M., and Sanjay, R. (1997). *Elements of Artificial Neural Networks* (MIT, Cambridge, MA).

Murray, S. O., Mercado, E., and Roitblat, H. L. (1998). “Characterizing the graded structure of false killer whale (*Pseudorca crassidens*) vocalizations,” *J. Acoust. Soc. Am.* **104**, 1679–1688.

Roitblat, H. L., Moore, P. W. B., Nachtigall, P. E., Penner, R. H., and Au, W. W. L. (1989). “Natural echolocation with an artificial neural network,” *Int. J. Neural Syst.* **1**, 239–247.

Walker, A., Fisher, R. B., and Mitsakakis, N. (1996). “Singing maps: classification of whale-song units using a self-organizing feature mapping algorithm,” DAI Research Paper No. 833.

The effect of abdominal wall morphology on ultrasonic pulse distortion. Part I. Measurements

Laura M. Hinkelman^{a)}

Department of Electrical Engineering, University of Rochester, Rochester, New York 14627

T. Douglas Mast

Applied Research Laboratory, The Pennsylvania State University, University Park, Pennsylvania 16802

Leon A. Metlay

Department of Pathology and Laboratory Medicine, University of Rochester Medical School, Rochester, New York 14642

Robert C. Waag

Departments of Electrical Engineering and Radiology, University of Rochester, Rochester, New York 14627

(Received 14 December 1997; revised 13 July 1998; accepted 17 August 1998)

The relative importance of the fat and muscle layers of the human abdominal wall in producing ultrasonic wavefront distortion was assessed by means of direct measurements. Specimens employed included six whole abdominal wall specimens and twelve partial specimens obtained by dividing each whole specimen into a fat and a muscle layer. In the measurement technique employed, a hemispheric transducer transmitted a 3.75-MHz ultrasonic pulse through a tissue section. The received wavefront was measured by a linear array translated in the elevation direction to synthesize a two-dimensional aperture. Insertion loss was also measured at various locations on each specimen. Differences in arrival time and energy level between the measured waveforms and computed references that account for geometric delay and spreading were calculated. After correction for the effects of geometry, the received waveforms were synthetically focused. The characteristics of the distortion produced by each specimen and the quality of the resulting focus were analyzed and compared. The measurements show that muscle produces greater arrival time distortion than fat while fat produces greater energy level distortion than muscle, but that the distortion produced by the entire abdominal wall is not equivalent to a simple combination of distortion effects produced by the layers. The results also indicate that both fat and muscle layers contribute significantly to the distortion of ultrasonic beams by the abdominal wall. However, the spatial characteristics of the distortion produced by fat and muscle layers differ substantially. Distortion produced by muscle layers, as well as focal images aberrated by muscle layers, show considerable anisotropy associated with muscle fiber orientation. Distortion produced by fat layers shows smaller-scale, granular structure associated with scattering from the septa surrounding individual fat lobules. Thick layers of fat may be expected to cause poor image quality due to both scattering and bulk absorption effects, while thick muscle layers may be expected to cause focus aberration due to large arrival time fluctuations. Correction of aberrated focuses using time-shift compensation shows more complete correction for muscle sections than for fat sections, so that correction methods based on phase screen models may be more appropriate for muscle layers than for fat layers. © 1998 Acoustical Society of America. [S0001-4966(98)05911-6]

PACS numbers: 43.80.Cs, 43.80.Vj, 43.58.Ry, 43.20.Fn [FD]

INTRODUCTION

The relationship between abdominal wall tissue structure and image quality in transabdominal ultrasonography is a subject of considerable lore and speculation. For instance, a widely held belief among clinical ultrasonographers and ultrasound researchers is that poor ultrasonic image quality is primarily associated with obesity.¹⁻³ Although this belief has some scientific basis, at least because increased body wall thickness should cause greater attenuation of the ultrasound beam in transabdominal imaging, most of the evidence sup-

porting this theory is anecdotal. Some clinicians and researchers maintain that poor ultrasonic image quality does not directly correspond to obesity in general, that is, that image quality depends on the individual's body wall structure. For example, while many obese individuals are difficult to image, some thin but muscular individuals also produce poor ultrasonic image quality.^{4,5} Very little scientific study has been conducted to relate the characteristics of abdominal wall morphology to ultrasonic aberration.

In one clinical study,⁵ the quality of abdominal B-scans from 140 people was correlated with various body characteristics. Although obesity was associated with poor image quality in this study, it was not considered to be a direct cause of reduction in image quality. In most cases, the upper

^{a)}Current address: Department of Meteorology, The Pennsylvania State University, University Park, Pennsylvania 16802.

layers of the abdominal wall imaged well, even when the deeper organs were obscured in the images. For this reason, the authors suggested that muscle may contribute significantly to the formation of distortion. Other factors associated with poor images included atherosclerosis, lower limb paralysis, and the presence of ribs, intestinal gas, or an aponeurosis (tissue joining two muscle groups) in the acoustic path.

Several groups have studied the importance of fat and muscle layers by using pork tissue to simulate the human abdominal wall.^{3,6,7} In the study reported in Ref. 6, pork fat and a combination of pork fat and muscle were found to decrease mean grey level in ultrasonic images of a tissue-mimicking phantom. In addition, a thick layer of fat was observed to produce an “unsharp image,” while muscle alone seemed to have little effect on image quality. In a related study,⁷ signals were received from a disc transducer placed in the thoracic cavity of an anesthetized pig by a phased array outside the pig’s abdomen. The pig’s abdominal wall was removed in sequential layers, and images were made at each depth. Removal of the complete abdominal wall resulted in significant improvement of image quality, but no individual layer was found to cause the bulk of the image degradation. Instead, removal of each consecutive layer resulted in an incremental reduction of distortion.⁵ In a similar *in vitro* study,³ separate pork fat and muscle samples were found to slightly raise the sidelobe levels of an ultrasonic beam at human body temperature. Similar levels of distortion were measured for a larger sample, containing a layer of fairly homogeneous muscle and two layers of fat. Much higher levels of distortion were detected for another specimen in which the muscle was marbled with fat.

Some insight into the relationship between distortion caused by animal tissues and the human abdominal wall is provided by the study reported in Ref. 8. In this study, samples of pork muscle, pork fat, and a combination of these did not produce distortion similar to that measured for the human abdominal wall. However, heavily marbled beef did cause significant distortion, including both phase and wave shape aberrations. Simple time-shift compensation was unable to improve images subjected to distortion produced by heavily marbled beef or by the human abdominal wall. These results, considered together with those from Refs. 3, 6, and 7 above, show that studies of ultrasonic distortion caused by animal tissue should be interpreted with caution when characterization of ultrasonic distortion effects in humans is desired. The studies indicate that animal tissues may not, in general, accurately mimic ultrasonic distortion processes occurring in human tissues, but that certain animal tissues (e.g., muscle tissue that is marbled with fat^{3,8}) may provide reasonable approximations.

Taken together, published studies provide mixed experimental evidence that tissue structures other than fat significantly contribute to ultrasonic distortion in the human body wall. Since the prospects for adaptive correction of ultrasonic aberration depend on both the physical causes of the distortion and the locations at which the distortion is incurred, it is important that the source of wavefront distortion be accurately known. For example, if both fat and muscle layers

cause significant distortion, single phase screen models^{9–15} may be inappropriate for modeling distortion through the abdominal wall. Likewise, if internal structure within the layers of the human abdominal wall proves to be important to ultrasonic image degradation *in vivo*, correction algorithms based on homogeneous-layer models^{4,16,17} will provide suboptimal improvement in image quality.

One barrier to understanding wavefront distortion mechanisms has been an apparent lack of information regarding the structure of the human abdominal wall and the type of distortion this morphology could be expected to produce. For example, tissues such as fat and muscle are commonly assumed to be homogeneous rather than possessing internal structure.^{4,9,16,18–20} Both muscle and fat are, in fact, comprised of smaller tissue units organized together.^{20–22} For this reason, fat and muscle layers can both produce distortion. Since the structures are different, distortion produced by these two tissues may be expected to have different spatial characteristics. Such differences have been observed in some experimental studies involving sections of the human abdominal wall.²³ A related study of simulated ultrasonic propagation through human abdominal wall cross sections^{24,25} suggests that muscle and fat affect propagating ultrasonic wavefronts differently. This study also indicates that ultrasonic wavefront distortion is caused by a combination of strong scattering and large-scale sound-speed variations.

The present paper reports an experimental study of the relative effects of the muscle and fat layers of the abdominal wall on ultrasonic pulses. The purpose of this study was to investigate how specific morphologic features of the abdominal wall affect ultrasonic image quality. Answers to this question, provided in part by this paper and the companion simulation paper,²⁶ will help to determine the types of correction procedures that are most effective and the limitations of these procedures.

I. ABDOMINAL WALL ANATOMY

Most previous models of tissue structure employed in medical ultrasound have been based on oversimplifications of human anatomy. Accurate understanding of abdominal wall morphology is critical to the development of meaningful models for ultrasound–tissue interactions in the abdominal wall, as well as to the development of improved algorithms for aberration correction in ultrasonic imaging. For these reasons, the morphologic features of the abdominal wall relevant to medical ultrasonic imaging are summarized below. This description of the abdominal wall is employed in this study to interpret measured distortion from whole abdominal wall specimens as well as individual fat and muscle layers. The already noted companion paper²⁶ employs this description as the basis for the propagation model used in the simulations reported there. Further details can be found in standard references on human anatomy such as Refs. 21, 22, and 27.

A typical abdominal wall specimen used in this study (specimen 101a) is shown in Fig. 1. The skin, fat, and muscle sections are readily apparent in the view showing the skin surface [Fig. 1(a)]. In this case, the fat layer is more than

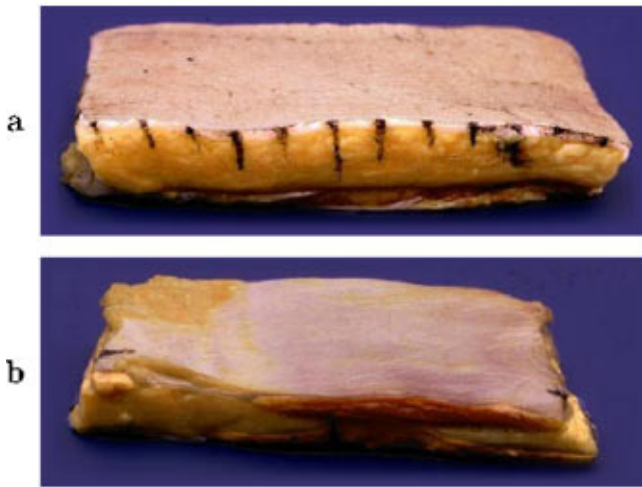


FIG. 1. Abdominal wall specimen 101a before dissection. (a) View with skin facing upward. (b) View with peritoneum and retroperitoneal fat facing upward. Markings are at intervals of 1 cm.

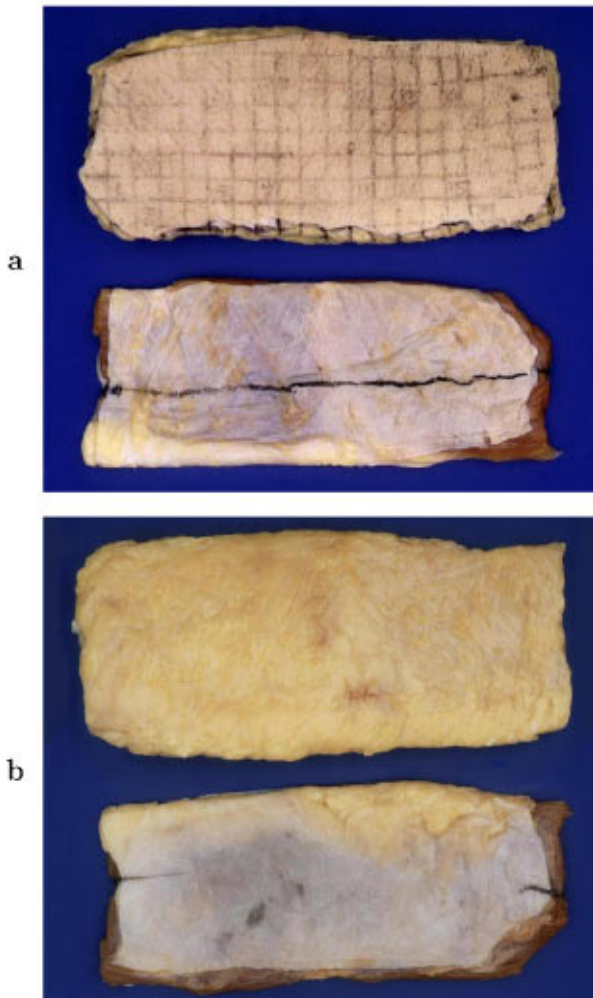


FIG. 2. Individual layers of abdominal wall specimen 113. (a) Views showing skin in the fat section (above) and fascia in the muscle section (below). (b) Views of the opposite sides of each layer, showing subcutaneous fat in the fat section (above) and the peritoneum with retroperitoneal fat in the muscle section (below).

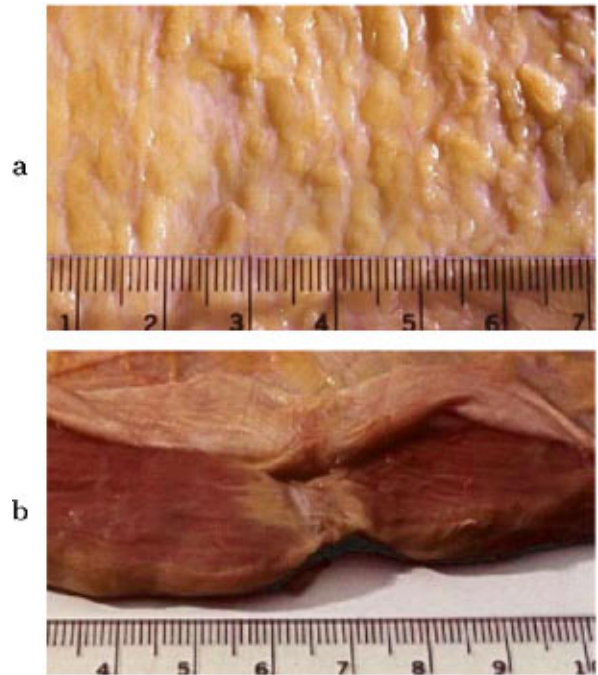


FIG. 3. Magnified view of abdominal wall features in specimen 65. (a) Subcutaneous fat lobules. (b) Muscle layer, with peritoneum drawn back to expose an aponeurosis.

twice the thickness of the muscle layer. The black lines are remnants of markings used to position the tissue in measurements. The opposite side of the same specimen [Fig. 1(b)] shows a clear view of the peritoneum, the thick membrane that lines the inner surface of the abdominal wall. It is also apparent that the muscle layer is not uniform. In this case, a portion of the muscle section consists largely of fat. Some retroperitoneal fat is also evident in the back left corner of the specimen. Even with this fat section attached under the peritoneal membrane, however, the peritoneal surface appears smooth, as does the skin surface.

The muscle and fat sections of specimen 113 are shown after separation in Fig. 2. Panel (a) shows the fat section with the skin facing upward and the muscle section in the same orientation, exposing the sheet of connective tissue that separated the layers. Since the surface of this membrane was originally attached to both the fat and muscle layers, the fat-muscle interface was smooth before dissection. Although the layers do not separate absolutely cleanly, the surface irregularities caused by the separation are small. An aponeurosis (sheet of tissue joining two muscle groups) appears as a light-colored vertical band visible through the membrane in the muscle section. Panel (b) depicts the underside of the fat layer, revealing lobules of subcutaneous fat, as well as the underside of the muscle section, showing the peritoneum and some retroperitoneal fat.

A closer view of fat structure in specimen 65 is given in panel (a) of Fig. 3. Although fat cells contain solidified drops of oil, fat tissue is shown in panel (a) to have additional structure. Subcutaneous fat is composed of loose fat cells held together in lobules by thin septa of fibrous tissue. The lobules are usually 2.5–7.5 mm across and are approximately ovoid or spherical. In the illustration, ovoid lobules

appear to be oriented with long axes parallel to each other. The subcutaneous fat layer of the human abdominal wall is commonly 0.5–6.0 cm thick. The thickness may vary slowly with position across the abdomen. As mentioned above, fat can also occur below the peritoneum or as deposits within muscle. The speed of sound in fat is about 1.48 mm/ μ s at body temperature.²⁴

Collagen-containing materials that connect and support organs and tissues of the body are termed connective tissue. The various connective tissue structures serve as surfaces to which the other tissues bind and thus give form to the body. The skin and aponeuroses are examples of dense connective tissue while the membranes that surround fat lobules are a form of loose connective tissue. The skin is composed of a lower layer, the dermis, which is composed of dense collagenous connective tissue, and a thin upper layer, the epidermis. The skin has approximately uniform thickness for each specimen but varies from 1–3 mm thick among individuals. Aponeuroses, which join muscle sections, are made up of highly organized dense collagenous connective tissue. The connective tissue fibers in aponeuroses run parallel to the lines of stress in the body. Tendinous intersections in the rectus abdominus, like that shown in Fig. 3(b), may be considered aponeuroses, although they tend to be less substantive. In the specimens we have examined, the connective

bands in the rectus abdominus have been dominated by fat, probably because of the age of the specimen donors. Other connective tissue in the abdominal wall includes extensive sheets known as fasciae that envelop bundles of muscle fibers and are somewhat looser than aponeuroses. The peritoneal lining also rests on a thin layer of dense connective tissue. A nominal sound speed value previously employed for skin, fascia, and membranes within the abdominal wall is 1.613 mm/ μ s.²⁴

Muscle cells, which are tubular and fluid filled, with complex fibrils, are bound into bundles by collagenous tissue. The fibrous structure of muscle tissue can be observed in Fig. 3(b). Small bundles of muscle fibers are bound together to form larger groups, including the rectus abdominus and the external, internal, and transverse obliques. Because of the arrangement of muscle groups and their segmentation, the overall muscular structure varies throughout the abdominal wall. In addition, muscles are not homogeneous as they can have fatty infiltrations (analogous to “marbling” in beef) and variable connective tissue content in addition to fasciae and aponeuroses. A typical sound speed for muscle, measured perpendicular to the fibers, is 1.547 mm/ μ s.²⁴

The relative positions and orientations of muscle groups appearing in the human abdominal wall are sketched in Fig. 4 and briefly described below. The rectus abdominus,

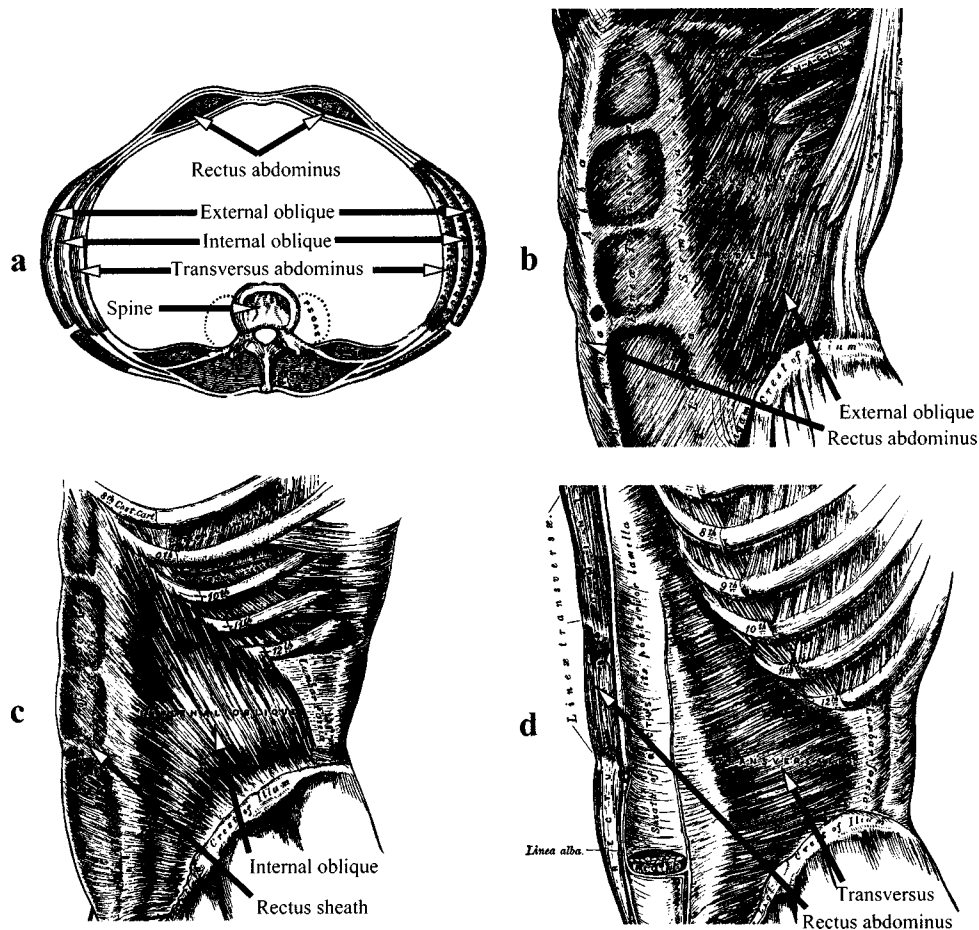


FIG. 4. Sketch of muscle groups in the human abdominal wall. (a) Cross section showing relative positions of all muscle groups. (b) External oblique and rectus abdominus. (c) Internal oblique and rectus sheath. (d) Transversus abdominus (transversalis), rectus sheath, and rectus abdominus (to left of linea alba). Adapted from Ref. 27.

which consists of two bands of muscle running vertically along the midline of the abdominal wall, is separated into sections by at least three horizontal or zigzagged aponeuroses. The rectus abdominus is enclosed by layers of connective tissue, called the rectus sheath. At both medial (outer) margins of the rectus muscles, the rectus sheath joins the aponeuroses of the internal and external oblique groups. Muscle fibers of the external oblique group run diagonally downward and inward from the side of the torso below the arm to their aponeurosis. The internal obliques, which lie beneath the external obliques, run diagonally upward and inward from the iliac crest to their own aponeurosis or to the ribs. The fibers of the external obliques are roughly perpendicular to those of the internal obliques. The transversus abdominus muscles lie below the internal obliques and are oriented approximately horizontally. At the midline of the body, between the rectus abdominus muscles, is the linea alba, where the peritoneum joins with the aponeuroses of the internal and external obliques and the transversus abdominus as well as with other connective fasciae. In this region and just beyond the medial margins of the rectus abdominus, there is usually no muscle present in the abdominal wall.

The abdominal wall also contains a variety of blood vessels which generally lie in the plane of the abdominal wall. Blood vessels are present in a range of sizes and are composed primarily of connective tissue and muscle. Other smaller components of the abdominal wall, such as nerves and hair follicles, are neglected in this study.

II. METHOD

A. Measurements

Six fresh unfixed specimens of the upper abdominal wall were obtained from autopsy and stored at -20°C . The six specimen donors ranged in age from 57 to 85 with an average age of 71 years. Four died of cardiac failure, one of stroke, and the last of Alzheimer's disease. Five of the donors were male and one was female. None of the donors was significantly overweight.

Each specimen was thawed by immersion in room-temperature saline solution and reference lines for positioning were ruled on the specimen surface with India ink. The specimen was then pressurized to 345 MPa (500 p.s.i.) for one half-hour to ensure that no air bubbles were present within the tissue. (This pressurization technique has previously been shown to remove bubbles that cause significant ultrasonic scattering.^{28,29}) The wavefront distortion produced by the whole specimen was then measured using the procedure and equipment detailed in Ref. 30 and highlighted here for convenience. The specimen was suspended with the skin upward between 7.5- μm -thick polyimide membranes in a water tank electronically maintained at 37.0°C . Ultrasonic pulses with a nominal center frequency of 3.75 MHz were emitted from a custom-made, 13-mm-diam hemispheric source placed approximately 165 mm below the specimen. Data were recorded on each of the 128 elements of a 3.75-MHz linear array positioned 5–10 mm above the specimen's skin surface. A foam mask was used to reduce the elevation dimension of the receiving array, so that the active area of

each element measured $0.72 \times 1.44 \text{ mm}^2$. The array was physically translated 32 times in the elevation direction to obtain data for a $92.16 \times 46.08 \text{ mm}^2$ aperture. The position of each measurement relative to the markings on the specimen's skin was noted. The peak-to-peak insertion loss of the specimen was also measured in several locations by comparing waveform maxima for signals recorded through the tissue and through a water path.

After distortion data had been collected for the entire specimen, the specimen was removed from the measurement chamber and separated into two sections. This was accomplished by carefully dividing the specimen at the septum between the subcutaneous fat and the muscle layer with a scalpel. In general, the distinction between those layers was quite clear. However, because the septum itself is thin, it was not divided but remained entirely with one of the layers, whichever proved easier at the time. During this dissection, care was taken not to disturb the markings on the skin. Additional markings were added on the top surface of the muscle layer corresponding to those on the skin. The first of the resulting sections contained the skin and subcutaneous fat, and will be referred to as the "fat" section. The other consisted of the remainder of the specimen from beneath the subcutaneous fat down to and including the parietal pleura. This section consisted mainly of muscle but also included fatty intrusions, blood vessels, and connective tissue. This section will be referred to as the "muscle" section.

Distortion measurements were made for the individual layers. The protocol used was the same as that described for the intact specimens. The muscle layer was measured first. It was inserted with the mount at the same height as was used for the whole specimen, so that the distance between the layer and each transducer was the same for this layer as when the muscle layer was part of the whole specimen. When the fat layer was measured, the mount was placed as before but the receiving transducer was lowered to ensure that the separation of the receiver and the skin surface was the same as in the original measurement. This allowed the configuration to be maintained as much as possible without requiring extensive changes between measurements. The resulting small reduction in distance between the source and specimen did not significantly affect the measurements because the hemispheric source transducer induced an incident field comparable to that of a point source far from the specimen. The India ink marks on the surface of each muscle and fat layer were used to align the layer laterally in the mount as it had been for the original whole specimen measurement.

Water path measurements were made before and after each specimen measurement series to serve as a reference and to characterize system effects.

B. Data processing

The received wavefronts were characterized as in previously reported measurements.³¹ The processing methods are briefly summarized here. A reference waveform was created for each set of data by averaging those waveforms that met a cross-correlation criterion for similarity. This reference pulse was cross-correlated with all the measured waveforms to produce an arrival time surface from which questionable out-

lying points were removed by smoothing. A two-dimensional fourth-order polynomial fit to the arrival time surface was used to window the original waveforms. A new arrival time surface was then obtained by repeating the arrival time estimation procedure using the windowed data. The effects of measurement geometry were removed by subtracting a best (least mean square error) fit two-dimensional fourth-order polynomial from the calculated arrival times to yield the arrival time fluctuations across the aperture. Energy level variations were calculated by integrating the squared amplitudes of the samples in each windowed waveform, converting the results to decibel units, and subtracting a fitted two-dimensional, fourth-order polynomial from the result. The waveform similarity factor¹² was computed using all the windowed waveforms throughout the aperture to provide a measure of the variability of waveform shape characteristics.

The arrival time and energy level variations determined for each data set, including the whole and sectioned specimens, were displayed as two-dimensional grayscale plots and their magnitude was described by computation of rms values. The spatial variability of the maps was described by the full-width half-maximum correlation lengths of the arrival time fluctuations and the energy level fluctuations in the array and elevation directions. To characterize anisotropy of wavefront distortion, aspect ratios were computed in each case as the ratio of the larger correlation length to the smaller correlation length. Average insertion loss values for the specimens were also computed.

Wavefronts were synthetically focused using a direct implementation of the time-domain Rayleigh integral. In this method, the time history of an ultrasonic pressure field is calculated in an image plane located 180 mm from the receiving aperture. Received wavefronts were spatially apodized using Hamming windows in elevation and azimuth. Waveforms from individual array elements, modeled as monopole sources on an infinite rigid baffle, were then combined according to the formula³²

$$p(x, y, t) = \frac{\rho}{2\pi} \iint \frac{\dot{v}_n(x_s, y_s, t - R/c + R_0/c)}{R} dx_s dy_s, \quad (1)$$

where $p(x, y, t)$ is the acoustic pressure in the image plane, ρ is the ambient density, $v_n(x_s, y_s, t)$ is the normal velocity in the source plane (defined here to be directly proportional to the waveform signal), and $R = \sqrt{(x - x_s)^2 + (y - y_s)^2 + z^2}$ is the distance from a point (x, y, z) in the image plane to a point $(x_s, y_s, 0)$ in the source plane. An additional delay, represented in Eq. (1) by the distance $R_0 = \sqrt{x_s^2 + y_s^2 + z^2}$, causes the wavefront to be focused at the center of the image plane at the time $t=0$. The geometry for the synthetic focusing implementation is essentially that sketched in Fig. 1 of Ref. 11.

In the numerical implementation of Eq. (1), the time derivative \dot{v} was evaluated using the second-order-accurate finite difference expression

$$\dot{v}(x_s, y_s, t) \approx \frac{v(x_s, y_s, t + \Delta t) - v(x_s, y_s, t - \Delta t)}{2\Delta t}, \quad (2)$$

where Δt is the sampling time of $0.05 \mu\text{s}$. Focal-plane waveforms were then computed by evaluating the integral in Eq. (1) as a discrete summation over all the aperture elements. Linear interpolation of source waveforms was employed to combine signals at common instants in the image plane. Pressure time histories were computed for 128 temporal samples, 120 image points in the aperture direction, and 80 image points in the array direction, using a time step of $0.05 \mu\text{s}$ and a spatial step of 0.4688 mm .

Focal quality was evaluated using effective widths in the array, azimuth, and time directions for levels -10 and -20 dB down from the peak amplitude. These effective widths were calculated using maximum-amplitude projections of analytic envelopes for the pressure signals, as in Ref. 11. Peripheral energy ratios, defined as the ratio between the integrated pulse energy outside a reference ellipsoid to the integrated pulse energy inside the ellipsoid,¹¹ were calculated for the -10 -dB effective widths. As in Ref. 11, the reference ellipsoid was defined to be centered at the position of peak amplitude and the ellipsoid width along each axis was equal to the -10 -dB effective width in the corresponding direction.

III. RESULTS

Arrival time and energy level fluctuation maps for the measured muscle, fat, and whole abdominal wall sections are shown in Fig. 5. The distortion produced by the fat and muscle layers have distinctly different spatial characteristics. The muscle layers produce distortion patterns having clearly oriented features. In most cases, a pattern of parallel striations is present. This is frequently overlaid with a few high-contrast curvilinear features, generally perpendicular to the underlying striations. The arrival time and energy level fluctuation maps for the fat layers, on the other hand, appear to consist almost entirely of small granular structures. On the scales used here, the energy level fluctuation maps display higher contrast when compared to the arrival time fluctuation maps. The maps for the whole specimens combine the characteristics of both layers in varying proportions. The striations and strong patterns of the muscle fluctuation maps are blended with the granular patterns caused by the fat layer. Shifts in locations of features in the whole and section distortion maps are mainly attributed to slight differences in specimen position in the sequential layer measurements.

The differences in the distortion maps produced by the different tissue sections are closely related to the differences in the structure of these layers. Inspection of the specimens indicated that most striations seen in the muscle layer distortion maps run parallel to muscle fibers. The white bands correspond to the positions of aponeuroses at the muscle connection points. Similarly, the granular patterns of the fat distortion maps are reminiscent of the arrangement of fat lobules. The results for the whole specimens contain features present in the results for each of the corresponding individual sections. These observations lead to the simple conclusion that the spatial characteristics of distortion produced by tissue structures resemble projections of the structures themselves.

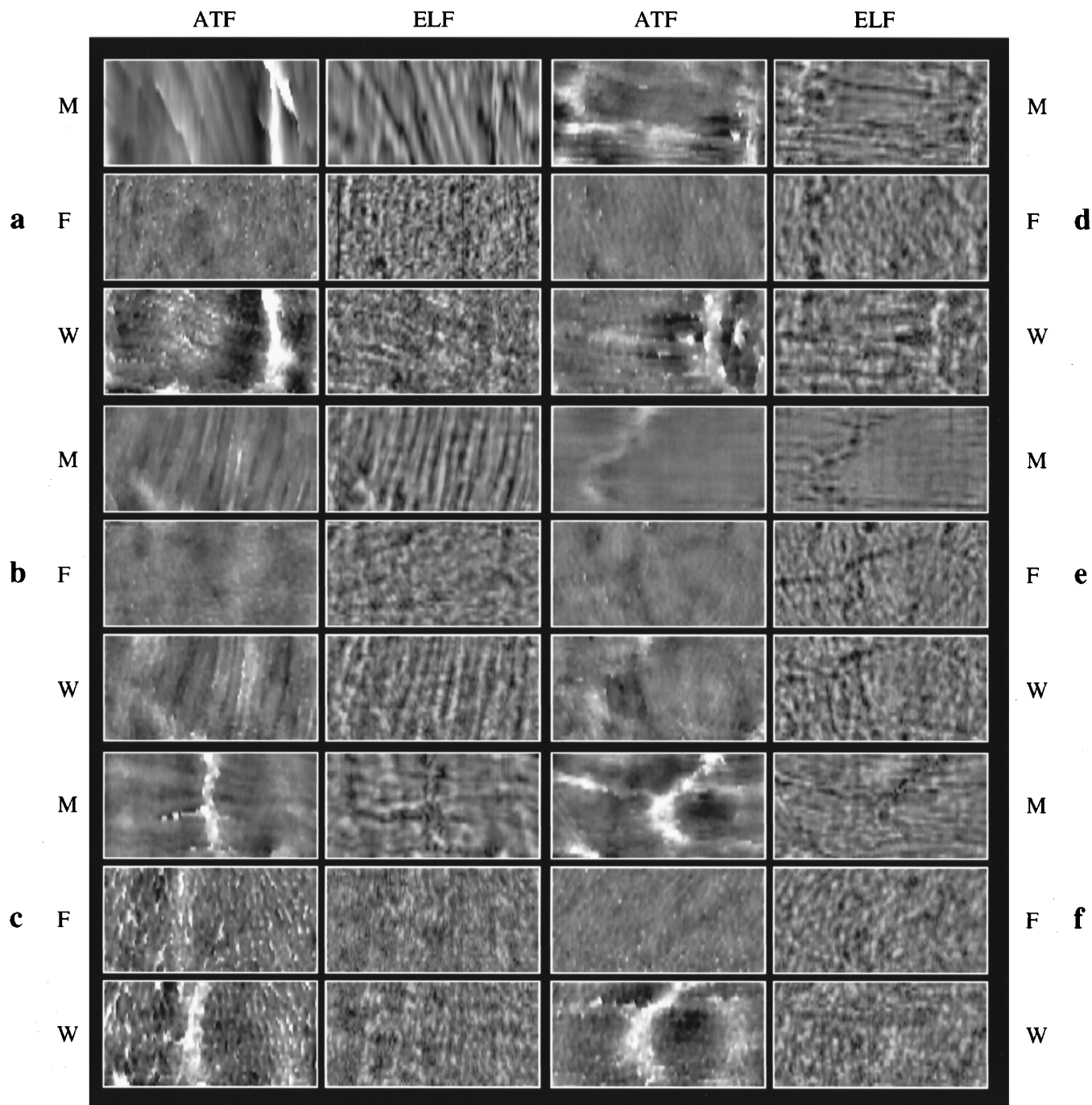


FIG. 5. Distortion maps for six abdominal wall specimens and their individual muscle and fat layers. Energy level fluctuations (ELF) and arrival time fluctuations (ATF) are shown for the muscle layers (M), fat layers (F), and whole specimens (W). The ATFs are shown on a linear gray scale with white indicating a delay of 150 ns and black indicating an advance of 150 ns. Log-compressed ELFs are shown on a gray scale with white indicating an increase of 10 dB and black indicating a decrease of 10 dB. Each panel spans 128 elements (92.16 mm) in the horizontal (array) direction and 32 elements (46.08 mm) in the vertical (elevation) direction. (a) Specimen 65. (b) Specimen 101. (c) Specimen 113. (d) Specimen 114. (e) Specimen 116. (f) Specimen 118.

The statistics given in Table I quantitatively describe the distortion illustrated in Fig. 5. Mean distortion values for five water path measurements, which characterize the influence of the measurement system, are also given for comparison. The aspect ratios of the distortion produced by the muscle layers (mean values 1.84 for arrival time fluctuations and 2.50 for energy level fluctuations) reflect the anisotropy evident in the distortion maps. The correlation lengths for arrival time fluctuations produced by the muscle sections are greater than those for the energy level variations. The distor-

tion maps produced by the fat layers are also somewhat anisotropic: average aspect ratios for the arrival time and energy level fluctuations are 1.54 and 1.45, respectively. Although some anisotropy may result from the element dimensions (the array direction pitch was half the elevation direction pitch), the computed aspect ratios are consistent with the ovoid appearance of fat lobules seen in Fig. 3. Correlation lengths for fat layers are significantly smaller than those for the muscle layers and are not preferentially aligned with respect to the muscle fibers. This decrease in correlation

TABLE I. Wavefront distortion statistics for measured propagation. Statistics shown include specimen thicknesses, rms arrival time and energy level fluctuations, correlation lengths (CL) of fluctuations in the array (x) and elevation (y) directions, aspect ratios (AR) of correlation lengths, and waveform similarity factors. The mean and standard deviation values shown for correlation lengths (marked with asterisks) are statistics for the larger and smaller correlation lengths, respectively, in each measurement.

Specimen	Layer	Thickness (mm)	Arrival time fluctuations				Energy level fluctuations				Waveform similarity factor
			rms (ns)	CL _x (mm)	CL _y (mm)	AR	rms (dB)	CL _x (mm)	CL _y (mm)	AR	
65	muscle	8.5	60.3	5.40	17.18	3.18	3.07	2.45	8.41	3.43	0.951
	fat	9.8	31.1	1.51	2.17	1.44	3.85	1.55	2.14	1.38	0.946
	whole	18.3	75.9	6.35	11.78	1.86	3.45	2.15	1.95	1.10	0.887
101	muscle	7.8	28.5	3.31	7.16	2.16	2.94	2.08	5.28	2.54	0.939
	fat	13.0	26.8	6.07	5.53	1.10	2.78	2.86	2.00	1.43	0.947
	whole	20.8	39.0	5.12	8.86	1.73	3.05	2.13	3.34	1.57	0.912
113	muscle	12.0	44.5	6.51	7.87	1.21	2.91	4.20	2.84	1.48	0.931
	fat	17.8	51.6	1.38	2.57	1.86	2.68	1.30	2.30	1.77	0.802
	whole	29.8	70.3	2.60	4.67	1.80	3.01	1.58	2.44	1.54	0.807
114	muscle	10.0	55.8	7.98	6.18	1.29	3.19	4.41	1.85	2.38	0.921
	fat	17.5	21.5	1.96	3.94	2.01	2.85	2.26	3.71	1.64	0.956
	whole	27.5	54.0	4.43	5.86	1.32	3.35	3.23	2.51	1.29	0.880
116	muscle	8.3	18.9	8.58	5.22	1.64	1.86	4.77	1.63	2.93	0.981
	fat	9.5	21.9	3.18	4.90	1.54	2.88	1.99	2.53	1.27	0.965
	whole	17.8	35.6	6.01	6.19	1.03	3.09	2.23	2.43	1.09	0.949
118	muscle	18.0	61.9	10.15	6.49	1.56	2.75	3.94	1.76	2.24	0.919
	fat	14.3	23.5	1.65	2.11	1.28	2.71	2.07	2.46	1.19	0.914
	whole	32.3	61.4	9.46	7.56	1.26	2.95	2.09	2.29	1.10	0.862
Mean	muscle	10.8	45.0	9.82*	5.52*	1.84	2.79	5.17*	2.10*	2.50	0.940
	fat	13.7	29.4	3.63*	2.54*	1.54	2.96	2.67*	1.86*	1.45	0.922
	whole	24.4	56.0	7.81*	5.35*	1.50	3.15	2.65*	2.08*	1.28	0.883
	water	...	6.0	0.70	0.991
Standard deviation	muscle	3.9	17.8	3.74*	1.21*	0.74	0.48	1.66*	0.46*	0.66	0.023
	fat	3.6	11.5	1.63*	1.61*	0.35	0.44	0.57*	0.36*	0.22	0.061
	whole	6.2	16.4	2.68*	1.72*	0.34	0.20	0.51*	0.31*	0.23	0.048
	water	...	0.8	0.07	0.001

length reflects the relative size and shape of fat lobules and muscle fibers as well as the absence of strong linear distortion features, such as those produced by aponeuroses in the muscle layer, from the fat layer distortion maps.

The data in Table I indicate that arrival time fluctuations caused by muscle layers are significantly more severe than those caused by fat layers. The average rms arrival time fluctuation for muscle layers is 45.0 ns versus 29.4 ns for fat. Fat layers produce slightly more energy level distortion than the muscle layers. The arrival time and energy level distortion produced by whole specimens is generally greater than that produced by the individual layers. The arrival time fluctuations are typically comparable to the geometric sum of the rms arrival time distortion values of the individual layers. However, in several cases, the arrival time or energy level fluctuation for the whole specimen is smaller than one of the fluctuations for the individual sections. Discussion of the cause of this phenomenon, with support from simulation results, is given in the companion paper.²⁶

The values of the waveform similarity factor for each tissue specimen are also given in Table I. The values given

indicate that propagation through fat causes greater wave shape distortion than does passage through muscle. The average wave shape distortion produced by propagation through the whole specimens is significantly greater than that found for one layer alone. Differences in arrival time or overall pulse amplitude do not significantly affect the waveform similarity factor; however, the waveform similarity factor decreases when frequency components are selectively removed from portions of the wavefront, as when energy is scattered out of the direct path during propagation. Thus, the increased wave shape distortion for fat layers suggests that more energy is scattered away from the main propagation direction by the fat layer than by the muscle layer.

Insertion losses for the measured specimens and their subsections are reported in Table II. Both the average total insertion loss and average loss per unit thickness (obtained by dividing the average insertion loss by the average thickness from Table I) are given for each specimen. These values indicate the power loss that can be expected on each passage of an ultrasonic beam through the abdominal wall or one of its layers in medical imaging. An average insertion loss of

TABLE II. Measured insertion loss values. The average and standard deviation for each specimen are shown together with values per unit thickness, obtained by dividing the average insertion loss by the average thickness from Table I.

Specimen	Layer	Average (dB)	Standard deviation (dB)	Average/Thickness (dB/cm)
101	muscle	2.33	3.23	2.99
	fat	4.61	1.97	3.55
	whole	10.19	4.14	4.90
113	muscle	5.62	3.42	4.68
	fat	16.68	1.81	9.37
	whole	15.91	3.59	5.34
114	muscle	7.10	3.15	7.10
	fat	6.71	2.71	3.83
	whole	8.16	2.12	2.97
116	muscle	2.04	1.77	2.46
	fat	4.20	2.71	4.42
	whole	7.57	3.69	4.25
118	muscle	7.40	2.85	4.11
	fat	8.52	2.82	5.96
	whole	11.94	0.92	3.70
Mean	muscle	4.90	2.88	4.27
	fat	8.14	2.40	5.43
	whole	10.75	2.89	4.23
Standard deviation	muscle	2.57	0.66	1.81
	fat	5.08	0.47	2.39
	whole	3.36	1.34	0.94

10.75 dB was measured for the six whole specimens. This amounts to a loss of 4.23 dB for each centimeter of tissue. Although the muscle and fat layers were nearly equally thick, on average, the fat layers caused a mean loss of 8.14 dB while the muscle layers reduced the power by 4.90 dB. The loss rate measured for the fat layers, at 5.43 dB/cm, was 27% higher than the rate of 4.27 dB/cm measured for the muscle sections.

The effect of the measured distortion on focal quality is evident in Fig. 6, which shows cross-sectional x - y images of the three-dimensional focal envelope along the plane of maximum amplitude in the axial (z) direction. These images are analogous to C-scan images of the effective point source employed in the distortion measurements. All focuses shown in Fig. 6 are much more aberrated than the corresponding water-path focus, shown in Fig. 7. The water-path focuses still show different focal widths in the array and elevation directions because the synthesized aperture is larger in the array direction than in the elevation direction. The corresponding B-scan images, shown for comparison in Fig. 8, show little aberration in the axial direction. In Fig. 6, both muscle and fat sections are seen to cause significant degradation of focus quality. The primary difference between focuses obtained through muscle layers and through fat layers is that significant anisotropy appears in the muscle-layer images. This anisotropy is associated with the preferred direction of muscle fibers relative to the receiving aperture;

greater aberration generally occurs in the direction perpendicular to the muscle fibers. The focus images obtained through entire abdominal wall specimens show greater aberration, including features caused by both the muscle and fat sections.

Corrected focal images, obtained using time-shift compensation of delay profiles determined with the reference waveform method, are also shown in Figs. 6–8. Most of the focal images aberrated by muscle layers are improved by time-shift compensation more than those aberrated by fat layers. In particular, time-shift compensation appears to reduce sidelobe levels more dramatically for muscle layers than for fat layers. However, artifacts remaining in the corrected images for the entire abdominal wall are associated with aberrations due to both the muscle and fat layers. Time-shift compensation has little effect on the axial characteristics of the aberrated focuses or on any aspect of the water-path focuses.

The characteristics of the synthetically computed focuses are summarized in Table III. Data is included for focal images computed from wavefronts measured after propagation through each muscle layer, fat layer, and whole specimen. The average results for five water paths are also listed for comparison. In each case, results are given for both the original and time-shift compensated waveforms. Point resolution is characterized by the -10 - and -20 -dB effective widths in the x (azimuth), y (array), and z (axial) directions, while contrast resolution is characterized by the -10 -dB peripheral energy ratio. The focal effective widths are generally greater in the y direction than the x direction because of the smaller size of the receiving array in the elevation direction. Focuses are also wider in both directions parallel to aperture than in the axial (time) direction, because the axial resolution depends on the pulse length rather than the aperture size.

Differences in focal spot size between the different specimens are small at -10 dB, but clearly evident at -20 dB. Focus aberration produced by muscle is, on the average, far greater than that produced by fat, although this distortion is considerably greater in directions perpendicular to the muscle fiber orientation. Aberration for the whole specimens is somewhat greater than for the muscle layers. However, time-shift compensation is much more effective for the waveforms distorted by muscle layers than for those that passed through only the fat. On the average, time-shift compensation improved the -20 -dB widths for the muscle paths by 70.3% and 57.4% in the array and elevation directions, respectively. The corresponding improvements for the fat-layer paths were 48.1% and 13.1%, respectively. Time-shift compensation was so effective for the muscle layers that, although muscle layers exhibited greater time-shift distortion, the average x and y effective widths for corrected focuses were smaller for the muscle layers than the fat layers. Focuses obtained through water paths were affected only slightly by time-shift compensation, indicating that any time-delay differences associated with nonuniformities in the elements or electronics were small.

Time-shift compensation was also effective in reducing the size of the focuses obtained for the waveforms that had passed through the whole specimens. An average improve-

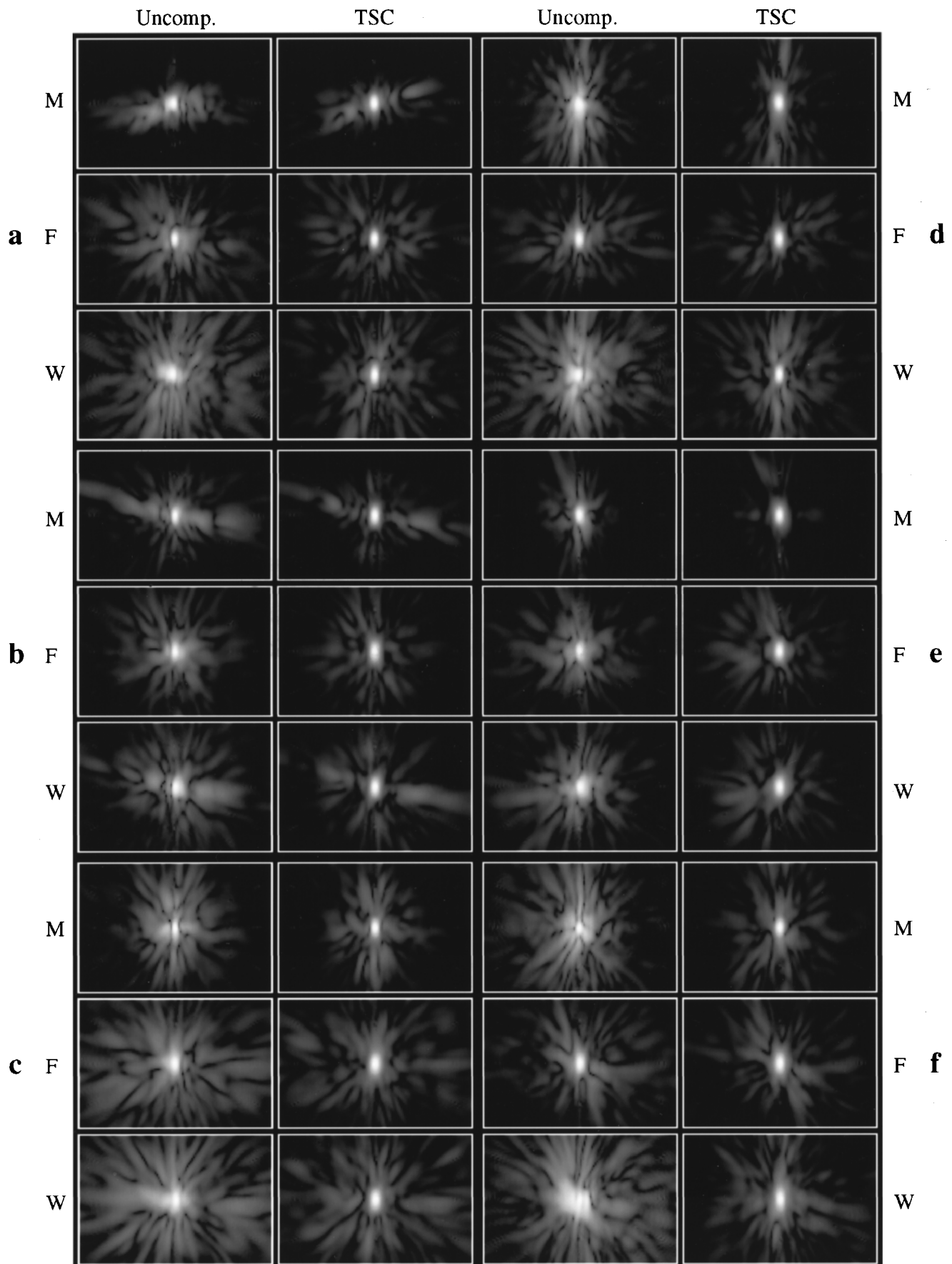


FIG. 6. Axial cross section (C-scan) images of synthetic focuses obtained from each entire specimen and its fat and muscle sections. Log-compressed analytic envelopes of each C-scan are shown on a 50-dB dynamic range for muscle layers (M), fat layers (F), and whole specimens (W). Both uncompensated (Uncomp.) and time-shift compensated (TSC) images are shown. Each panel spans 56.26 mm in the horizontal (array) direction and 37.50 mm in the vertical (elevation) direction. (a) Specimen 65. (b) Specimen 101. (c) Specimen 113. (d) Specimen 114. (e) Specimen 116. (f) Specimen 118.

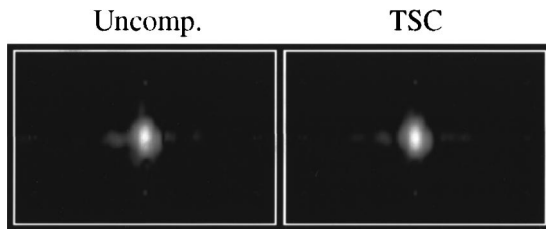


FIG. 7. Axial (C-scan) cross section images of synthetic focuses obtained through a representative water path. Images are shown in a format analogous to that of Fig. 6.

ment of about 73% was obtained in the array direction and 64% in the elevation direction. However, time-shift compensation alone is not sufficient to reduce the focus size of waveforms affected by whole specimens to the water-path limit. The -20 -dB effective widths of the corrected focuses for the whole specimens average 12.1%, 18.0%, and 0.6% larger than the water path focuses in the array, elevation, and azimuth directions, respectively, so that the point resolution of these images was not corrected to the limits associated with the finite aperture size.

The -10 -dB peripheral energy ratio is a measure of contrast resolution that can be used to compare the quality of focuses that are similar in width. Trends in these values generally follow the trends in focus size. That is, the average peripheral energy ratio is larger (indicating a greater portion of energy outside the main focal lobe) for the muscle layers than the fat layers, but whole specimens exhibit a larger peripheral energy ratio than either group of individual layers. After correction, the peripheral energy ratios for muscle layers and fat layers are comparable. However, the peripheral energy ratios for all tissue specimens are still significantly larger than those for the water paths before correction. Specifically, the peripheral energy ratios for the time-shift compensated muscle, fat, and whole specimens average 41.0%, 35.9%, and 76.9% larger than the average value for the uncompensated water paths.

IV. DISCUSSION

The effects of specific tissue features, noted also in the case of the chest wall,³³ are evident in the distortion maps shown here. Most notable are the white streaks (corresponding to locally delayed arrival of the wavefront) in the arrival time fluctuation maps that correspond to aponeuroses or fibrous connections in the rectus muscles. These features are

apparent in the distortion maps of both the muscle and total specimens. The association of wavefront delays with these aponeuroses is explained by staining and pathological inspection, which indicate that these tissue structures are composed largely of fat in the specimens employed in this study. This is probably due to the age of the specimen donors in the current study; aponeuroses occurring in younger individuals may cause different distortion effects because more connective tissue and less fat may occur in these structures. Time-shift fluctuations associated with these aponeuroses clearly affect the focal images shown in Fig. 6. Aponeuroses were also found to degrade image quality in Ref. 5.

Other tissue features that clearly affect distortion characteristics and focus quality include fibrous muscle and septated fat. Muscle fibers cause anisotropy clearly visible in arrival time and energy level distortion maps; these maps appear similar to projections of the muscle fibers themselves. Aberrated focuses show analogous anisotropy, with greater distortion appearing perpendicular to the orientation of the muscle fibers. Fat layers caused distortion with granular characteristics similar to speckle in ultrasonic images, suggesting that the distortion is primarily caused by inhomogeneities such as high-contrast septa within the subcutaneous fat. This conclusion is supported by simulation results that have shown arrival time variations and scattering associated with septa²⁴⁻²⁶ and by experimental results³⁴ that showed a strong correspondence between connective-tissue content and echogenicity in fatty tissue. Other connective tissue structures, such as the fibers that compose fascia and membranes between tissue layers, may also cause specific distortion features, but full understanding of these effects requires more complete analysis of dissected specimens.

Measured insertion losses were often significantly higher than attenuation values available in the literature (at 3.75 MHz, typically 1.8 dB/cm for fat, 4.1 dB/cm for muscle, and 5.9 dB/cm for connective tissue²⁴). This was particularly true for the fat layers, for which an average insertion loss of 5.43 dB/cm was obtained. The values were also about two to three times higher than the estimated attenuation of 0.5 dB/cm/MHz commonly used in ultrasonic imaging of tissue. These discrepancies are most likely due to contributions of scattering to the measured insertion losses. Since insertion loss was determined from the peak value of the received waveform within a short time window, scattered energy that arrived after the initial wavefront was effectively

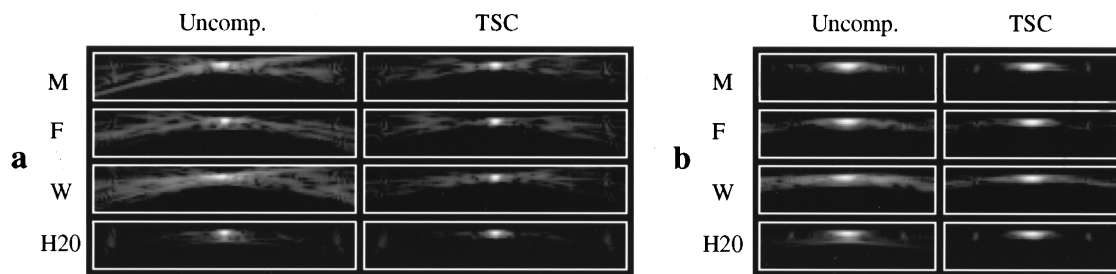


FIG. 8. Cross-section (B-scan) images of synthetic focuses obtained from specimen 65 and a representative water path measurement. (a) Cross section taken along the array direction, spanning 56.26 mm in width. (b) Cross section taken along elevation direction, spanning 37.50 mm in width. The vertical dimension in each panel spans 9.75 mm in the depth (axial) direction. Log-compressed analytic envelopes of focal waveforms are shown on a gray scale with a 50-dB dynamic range.

TABLE III. Focus properties for measured propagation. Effective widths are shown for the array (x), elevation (y), and axial (z) directions at levels of -10 and -20 dB. The peripheral energy ratios shown were computed using the -10 -dB widths.

Specimen	Processing	Layer	-10 -dB width (mm)			-20 -dB width (mm)			Peripheral energy ratio
			x	y	z	x	y	z	
65	uncompensated	muscle	3.37	4.09	1.17	14.10	7.85	2.10	1.02
		fat	2.30	4.27	1.17	7.41	6.77	1.65	1.13
		whole	6.62	5.68	1.18	18.69	23.41	2.94	1.95
	tsc	muscle	2.30	4.09	1.19	4.54	6.15	1.63	0.59
		fat	2.18	4.20	1.18	3.20	6.08	1.58	0.52
		whole	2.21	4.65	1.22	4.12	7.16	1.68	0.72
101	uncompensated	muscle	2.45	4.51	0.99	8.50	6.98	1.40	1.11
		fat	3.20	4.71	0.97	7.94	8.17	1.40	0.76
		whole	3.28	4.98	0.91	5.86	8.18	1.48	1.38
	tsc	muscle	2.21	4.31	1.06	3.31	6.29	1.46	0.58
		fat	2.32	4.59	1.02	3.57	6.97	1.41	0.45
		whole	2.30	4.56	1.08	3.65	6.75	1.48	0.66
113	uncompensated	muscle	2.08	5.12	1.01	18.12	24.30	1.57	2.88
		fat	3.56	5.58	0.77	10.93	10.94	1.51	1.72
		whole	5.94	5.79	0.79	20.42	20.38	1.91	2.71
	tsc	muscle	2.12	4.29	1.07	3.48	6.72	1.47	0.70
		fat	2.73	4.99	1.11	4.44	8.52	1.52	0.72
		whole	2.62	4.86	1.11	4.10	7.72	1.50	0.81
114	uncompensated	muscle	3.74	6.90	0.87	7.88	22.51	1.40	0.96
		fat	2.34	4.57	1.01	4.72	7.18	1.58	0.67
		whole	4.06	8.50	0.87	13.21	36.72	2.67	2.72
	tsc	muscle	2.50	4.40	1.01	3.91	7.45	1.43	0.43
		fat	2.26	4.50	1.05	3.36	6.78	1.55	0.44
		whole	2.16	4.31	1.12	3.38	6.64	1.54	0.84
116	uncompensated	muscle	2.32	4.44	1.02	4.37	7.10	1.43	0.47
		fat	2.44	4.54	1.00	7.45	7.42	1.40	0.74
		whole	3.17	4.87	0.97	9.05	8.28	1.40	0.96
	tsc	muscle	2.24	4.21	1.02	3.47	6.27	1.43	0.32
		fat	2.30	4.31	1.01	3.86	6.45	1.41	0.44
		whole	2.45	4.50	1.02	4.15	6.81	1.42	0.44
118	uncompensated	muscle	8.10	6.41	0.90	22.13	28.21	1.98	3.08
		fat	2.46	4.98	0.74	4.91	8.26	1.87	0.97
		whole	10.15	8.96	1.18	18.56	22.86	2.49	1.25
	tsc	muscle	2.25	4.42	0.76	3.61	8.42	1.34	0.70
		fat	2.39	4.80	0.76	4.07	7.54	1.70	0.60
		whole	2.29	5.02	1.12	3.91	8.67	1.52	0.69
Mean	uncompensated	muscle	3.68	5.25	0.99	12.52	16.16	1.65	1.59
		fat	2.72	4.78	0.94	7.23	8.12	1.57	1.00
		whole	5.54	6.46	0.98	14.30	19.97	2.15	1.83
	tsc	muscle	2.22	4.18	1.04	3.47	6.18	1.51	0.39
		water	2.27	4.29	1.02	3.72	6.88	1.46	0.55
		fat	2.53	4.57	1.02	3.75	7.06	1.53	0.53
Standard deviation	uncompensated	whole	2.34	4.73	1.11	3.89	7.29	1.52	0.69
		water	2.22	4.18	1.04	3.41	6.14	1.48	0.32
		muscle	2.26	1.15	0.11	6.79	9.87	0.31	1.10
	tsc	fat	0.53	0.46	0.16	2.28	1.50	0.18	0.39
		whole	2.66	1.80	0.16	5.91	10.74	0.65	0.76
		water	0.03	0.03	0.02	0.08	0.07	0.09	0.03
Standard deviation	tsc	muscle	0.13	0.12	0.14	0.45	0.89	0.95	0.15
		fat	0.43	0.30	0.14	0.46	0.87	0.11	0.12
		whole	0.17	0.20	0.07	0.31	0.78	0.09	0.14
		water	0.03	0.04	0.02	0.10	0.08	0.06	0.01

lost. Small inhomogeneities such as septa scatter higher frequencies more strongly, so that the peak value used for the insertion loss measurement was further decreased by loss of high-frequency components from the incident pulse. The present method of measuring insertion loss is different from common *in vitro* methods for measuring frequency-dependent attenuation in tissue, which often employ long time windows.^{28,35–37} In such measurements, the effect of scattering on the measured attenuation is reduced because time integration allows scattered energy arriving after the main pulse to contribute to the measured transmitted power, while in the current measurements, only energy scattered very near the forward direction can contribute to the measured peak waveform amplitude.

The importance of scattering effects to the measured insertion loss is further suggested by the large standard deviations in the measured insertion loss for each specimen; since the large-scale tissue structure of each specimen is largely uniform, absorption effects do not explain these spatial variations. Absorption effects also do not explain the result that the average insertion loss per unit thickness is smaller for whole specimens than for either muscle or fat layers. This phenomenon is likely to be associated with cumulative effects that occurred only in the case of whole specimens. The muscle layer, like most human tissues, exhibits frequency-dependent scattering and absorption effects, so that the wavefront exiting the muscle layer may have fewer temporal high-frequency components than the corresponding water-path wavefront. Since attenuation in the fat layer (due both to absorption and scattering) is smaller when high-frequency components are removed from the incident wavefront, the overall insertion loss per unit length can be lower for whole specimens than for either of the individual layers. Results shown in the companion simulation paper²⁶ provide quantitative estimates of the relative contributions of scattering and absorption to total attenuation.

Some previous workers have suggested that the subcutaneous fat layer^{2,15,18} constitutes the main source of degradation in abdominal ultrasound imaging, while others^{3,8,38,39} have shown that the abdominal muscle layer produces substantial distortion. The present study indicates that both layers significantly contribute to ultrasonic aberration, both through wavefront distortion and attenuation. However, the distortions produced by these layers have different characteristics and different implications for adaptive aberration correction. Distortion caused by fat layers was found here to be smaller than that caused by muscle layers, but the distortion caused by fat layers proved more difficult to correct by time-shift compensation. The negative effects of fat layers on ultrasonic images are exacerbated in obese patients, where thick layers of subcutaneous fat can cause much greater attenuation and distortion. On the average, muscle layers were found to produce greater arrival time fluctuations than fat layers. However, the measured muscle layers caused distortion with smaller energy level fluctuations and greater waveform similarity factors. These observations suggest that muscle layers scatter less than fat layers, and further imply that phase-screen models may be more appropriate for abdominal muscle layers than for the subcutaneous fat.

Another common assumption about ultrasonic aberration in the abdomen is that irregularly shaped boundaries between tissue layers are an important cause of wavefront distortion.^{19,40} The results of the present study suggest that irregular boundaries are of less importance than internal tissue structures. As seen in Figs. 1 and 2, interfaces between muscle and fat layers are typically smooth rather than rough or rippled. Substantial distortion was measured here from both individual muscle and fat layers, even though these specimens contained no fat–muscle interfaces and lay flat in the tissue mount due to the natural weight and pliability of warm tissue. The features observed in time-shift and energy level distortion maps do not correspond to small variations that may occur in skin–fat or fat–muscle boundaries, but clearly resemble the internal structure of muscle and fat. More direct evidence regarding the relative importance of tissue-layer boundaries has been obtained using simulations and is presented in the companion paper.²⁶

The characteristics of the experimental population require further comment. As noted above, the specimens used in this study came from older (mean age 71 years), nonobese individuals. It is therefore likely that the muscle in these specimens was poorly toned and that the subcutaneous fat layers were thinner than is common among the general population. This suggests that the distortion measured here for both the muscle and fat layers is lower than might be found in general. Therefore, the results described here should be considered a lower bound for distortion produced by the general population. Since fat seems to scatter more ultrasonic energy than does muscle, distortion produced by extremely obese patients can be expected not only to be greater but also more difficult to correct than the distortion produced by non-obese patients. Although the signal power could be increased to compensate for the absorption of ultrasound in fat, aberration caused by scattering effects presents a more challenging problem for adaptive imaging. More complicated algorithms than simple time-shift compensation in the aperture are most likely required if the effects of scattering are to be removed.

Distortion measured in the current study may be somewhat different from that which occurs *in vivo*, in part because of the finite distance between the tissue and receiver. Propagation in a homogeneous medium such as water causes a spatial low-pass filtering effect,⁴¹ so that some spatial fluctuations in the wavefront are smoothed during propagation from the specimen to the receiving transducer array. The result of this effect, which is unrelated to any frequency-dependent absorption that may occur, is that distortion may be somewhat underestimated by the current measurements. However, *in vivo* wavefront distortion may also be reduced by the common clinical practice of pressing the ultrasonic probe tightly against the body wall. Since the static behavior of tissue is similar to that of an incompressible fluid surrounded by a pliable boundary, the applied pressure decreases the ultrasonic propagation path length through the abdominal wall and may also move some fat lobules and septa outside the acoustic path, reducing wavefront distortion caused by scattering. This pressure may also anisotropically align structures such as septa so that scattering effects are

further decreased (less scattering occurs, for instance, when septa are aligned perpendicular to the direction of propagation²⁴).

The present results for correction of aberrated focal images have strong implications for the design of adaptive ultrasonic imaging methods. The results show that both fat and muscle layers cause aberration that cannot be completely corrected by simple time-shift compensation of received wavefronts, so that neither layer can be accurately modeled as a phase screen at the receiving aperture. Aberration caused by the muscle layers was correctable to a greater extent than that caused by the fat layers, implying that the phase screen model is more appropriate for muscle layers. The muscle layer may be more appropriately modeled by a phase screen some distance from the aperture,^{12,14} but the fat layer is unlikely to be accurately modeled by any single phase screen because of the strong, distributed, depth-dependent scattering that occurs within the subcutaneous fat. Models employing multiple phase screens may model propagation through the abdominal wall more accurately; however, it remains to be seen whether application of such models can significantly improve correction algorithms without introducing computational complexity comparable to full-wave propagation models.

V. CONCLUSIONS

Measurements of distortion made using human abdominal wall specimens and their individual fat and muscle layers have shown that both fat and muscle cause significant wavefront and focus distortion. The spatial characteristics of the resulting distortion are directly related to internal tissue structure. The results imply that distortion caused by ultrasonic propagation through the abdominal wall is due to a more complex combination of effects than previously supposed by many researchers and clinicians.

On the whole, muscle layers cause greater arrival time distortion but less energy level and waveform distortion than fat layers. The ordered, fibrous structure of muscle causes greater anisotropy in observed distortion patterns and aberrated focal images. Distortion caused by muscle layers is corrected fairly well by time-shift compensation, implying that phase-screen models may be useful in correction of aberration caused by muscle layers.

Fat layers cause smaller arrival time distortion but greater energy level and waveform distortion. These results, as well as the random isotropic appearance of distortion patterns and the highly variable insertion loss measured for fat layers, imply that scattering from septa is the primary cause of wavefront distortion in the subcutaneous fat. Focus aberration caused by fat layers is corrected less completely by time-shift compensation than is distortion caused by muscle layers. For these reasons, phase-screen models and homogeneous-layer models are both insufficient to depict distortion caused by fat layers of the abdominal wall.

Distortion caused by entire abdominal wall specimens has been shown to be a combination, but not a simple summation, of distortion effects caused by muscle and fat layers. This result suggests that aberration correction algorithms based on single phase-screen models do not provide opti-

um compensation for distortion caused by the human abdominal wall. Likewise, algorithms that employ homogeneous-layer models of tissue layers cannot effectively correct for structure-dependent effects that cause much of the distortion observed here.

ACKNOWLEDGMENTS

Michael J. Orr is thanked for assisting with the measurements and data analysis. Dong-Lai Liu is thanked for providing the distortion estimation software using the reference waveform method and for significantly improving the measurement control software. Funding for this investigation was provided by the University of Rochester Diagnostic Ultrasound Research Laboratory Industrial Associates, NIH Grants DK 45533, HL 50855, and CA 74050, and US Army Grant DAMD-17-94-J-4384. Computations were performed in part at the Center for Academic Computing of the Pennsylvania State University and at the Cornell National Supercomputing Facility, which was supported in part by the National Science Foundation, New York State, and the IBM Corporation.

¹Frederick Kremkau, personal communication, August 1997.

²W. Fiegler, R. Felix, M. Langer, and E. Schultz, "Fat as a factor affecting resolution in diagnostic ultrasound: possibilities for improving picture quality," *Eur. J. Radiol.* **5**, 304–309 (1985).

³L. A. Ødegaard, "Phase aberration correction in medical ultrasound imaging," Ph.D. thesis, University of Trondheim, Trondheim, Sweden, 1995.

⁴D. A. Carpenter, G. Kossoff, and K. A. Griffiths, "Correction of distortion in US images caused by subcutaneous tissues: results in tissue phantoms and human subjects," *Radiology* **195**, 563–567 (1995).

⁵A. Shmulewitz, S. A. Teefey, and B. S. Robinson, "Factors affecting image quality and diagnostic efficacy in abdominal sonography: a prospective study of 140 patients," *J. Clin. Ultrasound* **21**, 623–630 (1993).

⁶U. Haberkorn, G. Layer, V. Rudat, I. Zuna, A. Lorenz, and G. van Kaick, "Ultrasound image properties influenced by abdominal wall thickness and composition," *J. Clin. Ultrasound* **21**, 423–429 (1993).

⁷B. S. Robinson, A. Shmulewitz, and T. M. Burke, "Waveform aberrations in an animal model," 1994 IEEE Ultrason. Symp. Proc. **3**, 1619–1624 (1994).

⁸T. Noda, A. Iida, K. Murakami, and T. Shimura, "Basic investigation of a wavefront distortion correction method due to velocity inhomogeneities," *Jpn. J. Medical Elect. Biol. Eng.* **32** (Supplement), 119 (1994) (abstract, in Japanese).

⁹M. O'Donnell and S. W. Flax, "Phase-aberration correction using signals from point reflectors and diffuse scatterers: Measurements," *IEEE Trans. Ultrason. Ferroelectr. Freq. Control* **35**, 768–774 (1988).

¹⁰D. Rachlin, "Direct estimation of aberrating delays in pulse-echo imaging systems," *J. Acoust. Soc. Am.* **88**, 191–198 (1990).

¹¹D.-L. Liu and R. C. Waag, "Time-shift compensation of ultrasonic pulse force degradation using least-mean-square error estimates of arrival time," *J. Acoust. Soc. Am.* **95**, 542–555 (1994).

¹²D.-L. Liu and R. C. Waag, "Correction of ultrasonic wavefront distortion using backpropagation and a reference waveform method for time-shift compensation," *J. Acoust. Soc. Am.* **96**, 649–660 (1994).

¹³C. Dorme and M. Fink, "Ultrasonic beam steering through inhomogeneous layers with a time reversal mirror," *IEEE Trans. Ultrason. Ferroelectr. Freq. Control* **43**(1), 167–175 (1996).

¹⁴A. P. Berkhoff and J. M. Thijssen, "Correction of concentrated and distributed aberrations in medical ultrasound imaging," 1996 IEEE Ultrasonics Symp. Proc. **2**, 1405–1410 (1996).

¹⁵G. C. Ng, P. D. Freiburger, W. F. Walker, and G. E. Trahey, "A speckle target adaptive imaging technique in the presence of distributed aberrations," *IEEE Trans. Ultrason. Ferroelectr. Freq. Control* **44**(1), 140–151 (1997).

¹⁶S. W. Smith, G. E. Trahey, and O. T. von Ramm, "Phased array ultra-

- sound imaging through planar tissue layers," *Ultrasound Med. Biol.* **12**(3), 229–243 (1986).
- ¹⁷G. Kossoff, D. A. Carpenter, D. E. Robinson, D. Ostry, and P. L. Ho, "A sonographic technique to reduce beam distortion by curved interfaces," *Ultrasound Med. Biol.* **15**(4), 375–382 (1989).
- ¹⁸L. Nock, G. E. Trahey, S. W. Smith, "Phase aberration correction in medical ultrasound using speckle brightness as a quality factor," *J. Acoust. Soc. Am.* **85**, 1819–1833 (1989).
- ¹⁹L. A. Ledoux, A. P. Berkhoff, and J. M. Thijssen, "Ultrasonic wave propagation through aberrating layers: experimental verification of the conjugate gradient Rayleigh method," *IEEE Trans. Ultrason. Ferroelectr. Freq. Control* **43**(1), 158–166 (1996).
- ²⁰M. Kunin, "Bridging septa of the perinephric space: anatomic, pathologic, and diagnostic considerations," *Radiology* **158**, 361–365 (1986).
- ²¹R. Warwick and P. L. Williams (eds.), *Gray's Anatomy* (Saunders, Philadelphia, 1973), 35th ed. pp. 488–490, 519–527.
- ²²J. L. Matthews and J. H. Martin, *Atlas of Human Histology and Ultrastructure* (Lea & Febiger, Philadelphia, 1971), pp. 54–55, 102–119.
- ²³L. M. Hinkelman, "Ultrasonic pulse wavefront distortion produced by abdominal and chest wall," *Proc. 10th Ann. Univ. Rochester Diagnostic Ultras. Res. Lab. Indust. Assoc. Mtg.* 8–25 (1993).
- ²⁴T. D. Mast, L. M. Hinkelman, M. J. Orr, V. W. Sparrow, and R. C. Waag, "Simulation of ultrasonic pulse propagation through the abdominal wall," *J. Acoust. Soc. Am.* **102**, 1177–1190 (1997).
- ²⁵T. D. Mast, L. M. Hinkelman, M. J. Orr, V. W. Sparrow, and R. C. Waag, "Erratum: 'Simulation of ultrasonic pulse propagation through the abdominal wall' [*J. Acoust. Soc. Am.* **102**, 1177–1190 (1997)]," *J. Acoust. Soc. Am.* **104**, 1124–1125 (1998).
- ²⁶T. D. Mast, L. M. Hinkelman, M. J. Orr, and R. C. Waag, "The effect of abdominal wall morphology on ultrasonic pulse distortion, Part II. Simulations," *J. Acoust. Soc. Am.* **104**, 3651–3664 (1998).
- ²⁷H. Gray, *Gray's Anatomy*, edited by T. P. Pick and R. Howden (Gramercy, New York, 1977), pp. 358–364 (facsimile of 1901 American edition of *Anatomy, Descriptive and Surgical*).
- ²⁸J. A. Campbell, "Measurements of Ultrasonic Differential and Total Scattering Cross Sections for Tissue Characterization," Ph.D. thesis, University of Rochester, 1984.
- ²⁹Y. Sumino and R. C. Waag, "Measurements of ultrasonic pulse arrival time differences produced by abdominal wall specimens," *J. Acoust. Soc. Am.* **90**, 2924–2930 (1991).
- ³⁰L. M. Hinkelman, D.-L. Liu, L. A. Metlay, and R. C. Waag, "Measurements of ultrasonic pulse arrival time and energy level variations produced by propagation through abdominal wall," *J. Acoust. Soc. Am.* **95**, 530–541 (1994).
- ³¹L. M. Hinkelman, D.-L. Liu, R. C. Waag, Q. Zhu, and B. D. Steinberg, "Measurement and correction of ultrasonic pulse distortion produced by the human breast," *J. Acoust. Soc. Am.* **97**, 1958–1969 (1995).
- ³²A. D. Pierce, *Acoustics: an Introduction to its Physical Principles and Applications* (Acoustical Society of America, Woodbury, NY, 1989), 2nd ed.
- ³³L. M. Hinkelman, T. L. Szabo, and R. C. Waag, "Measurements of ultrasonic pulse distortion produced by the human chest wall," *J. Acoust. Soc. Am.* **101**, 2365–2373 (1997).
- ³⁴R. C. Sanders, "Sonography of Fat," in *Ultrasound Annual 1984*, edited by R. C. Sanders and M. Hill (Raven, New York, 1984), pp. 71–94.
- ³⁵R. C. Chivers and R. J. Parry, "Ultrasonic velocity and attenuation in mammalian tissues," *J. Acoust. Soc. Am.* **63**, 940–953 (1978).
- ³⁶S. A. Goss, R. L. Johnston, and F. Dunn, "Comprehensive compilation of empirical ultrasonic properties of mammalian tissues," *J. Acoust. Soc. Am.* **64**, 423–457 (1978).
- ³⁷S. A. Goss, R. L. Johnston, and F. Dunn, "Compilation of empirical ultrasonic properties of mammalian tissues II," *J. Acoust. Soc. Am.* **68**, 93–108 (1980).
- ³⁸P. Krämmmer and D. Hassler, "Measurements of spatial time-of-flight fluctuations of; ultrasound pulses passing through inhomogeneous layers," 1987 IEEE Ultrasonics Symp. Proc. **2**, 939–942 (1987).
- ³⁹M. Van den Aarsen, W. A. Verhoef, and J. M. Thijssen, "Influence of absorbing and scattering media on the propagation of ultrasound," *J. Acoust. Soc. Am.* **85**, 567–575 (1989).
- ⁴⁰H. Wang, E. S. Ebbini, M. O'Donnell, and C. A. Cain, "Phase aberration correction and motion correction for ultrasonic hyperthermia phased arrays: experimental results," *IEEE Trans. Ultrason. Ferroelectr. Freq. Control* **41**(1), 34–43 (1994).
- ⁴¹J. W. Goodman, *Introduction to Fourier Optics* (McGraw-Hill, San Francisco, 1968), Chap. 3.

The effect of abdominal wall morphology on ultrasonic pulse distortion. Part II. Simulations

T. Douglas Mast

Applied Research Laboratory, The Pennsylvania State University, University Park, Pennsylvania 16802

Laura M. Hinkelman^{a)}

Department of Electrical Engineering, University of Rochester, Rochester, New York 14627

Michael J. Orr

Department of Electrical Engineering, University of Rochester, Rochester, New York 14627

Robert C. Waag

Departments of Electrical Engineering and Radiology, University of Rochester, Rochester, New York 14627

(Received 14 December 1997; revised 13 July 1998; accepted 17 August 1998)

Wavefront propagation through the abdominal wall was simulated using a finite-difference time-domain implementation of the linearized wave propagation equations for a lossless, inhomogeneous, two-dimensional fluid as well as a simplified straight-ray model for a two-dimensional absorbing medium. Scanned images of six human abdominal wall cross sections provided the data for the propagation media in the simulations. The images were mapped into regions of fat, muscle, and connective tissue, each of which was assigned uniform sound speed, density, and absorption values. Propagation was simulated through each whole specimen as well as through each fat layer and muscle layer individually. Wavefronts computed by the finite-difference method contained arrival time, energy level, and wave shape distortion similar to that in measurements. Straight-ray simulations produced arrival time fluctuations similar to measurements but produced much smaller energy level fluctuations. These simulations confirm that both fat and muscle produce significant wavefront distortion and that distortion produced by fat sections differs from that produced by muscle sections. Spatial correlation of distortion with tissue composition suggests that most major arrival time fluctuations are caused by propagation through large-scale inhomogeneities such as fatty regions within muscle layers, while most amplitude and waveform variations are the result of scattering from smaller inhomogeneities such as septa within the subcutaneous fat. Additional finite-difference simulations performed using uniform-layer models of the abdominal wall indicate that wavefront distortion is primarily caused by tissue structures and inhomogeneities rather than by refraction at layer interfaces or by variations in layer thicknesses. © 1998 Acoustical Society of America. [S0001-4966(98)06011-1]

PACS numbers: 43.80.Cs, 43.80.Vj, 43.20.Fn, 43.58.Ta [FD]

INTRODUCTION

Wavefront distortion is considered to be a significant obstacle to improved ultrasonic image quality. However, little is known about its actual cause. Some direct measurements have been made to characterize the distortion produced by various tissues.¹⁻⁶ These measurements have yielded parameters describing wavefront distortion from these tissues, but have provided limited insight into the actual causes of the distortion.

Because basic knowledge about the physical causes of wavefront distortion is lacking, researchers have relied on a variety of assumptions to develop wavefront distortion correction algorithms. Several early algorithms were based on the assumption that wavefront distortion produced by propagation through soft tissue consisted solely of phase aberrations that could be modeled as the result of a phase screen in the measurement aperture.⁷⁻¹⁰ This model of wavefront dis-

ortion was supported by the results of an experimental study¹¹ in which poor ultrasonic image quality was found to correlate with the presence of phase errors while little amplitude distortion was detected. However, later studies indicated that amplitude and wave shape distortion occur as well.^{2,4-6,12} To accommodate this finding, distortion has been modeled as the result of a phase screen some distance from the aperture¹³⁻¹⁵ or as a phase screen and an amplitude screen at the aperture.^{16,17}

A greater knowledge of the mechanisms that cause wavefront distortion would improve understanding of what is required for successful distortion compensation. Several investigators have attempted to improve this understanding by calculating distortion using ray-tracing or other simplified models.¹⁸⁻²² However, these simulations have also been based on simple assumptions about the structure of the body wall and the causes of wavefront distortion. For example, one study¹⁸ employed measured scattering from liver tissue and model random media to estimate wavefront distortion using a weak scattering approximation. Ødegaard^{19,20} used a ray-tracing technique that was limited to refraction effects,

^{a)}Current address: Department of Meteorology, The Pennsylvania State University, University Park, Pennsylvania 16802.

and assumed a very simple tissue geometry. Manry,²¹ in a model of propagation through breast tissue, applied a finite-difference time-domain method to a similarly simple tissue model so that refraction dominated the effects observed. Berkhoff *et al.*,²² in computations employing conjugate gradient techniques to evaluate the Rayleigh integral, concerned themselves only with the effect of propagation through an irregular interface. In other computations from the same group,¹⁵ tissue has been modeled as succession of random phase screens.

In a recent study,^{23,24} a full-wave simulation technique was applied to tissue models based on images of actual human abdominal wall cross sections. Results of that study demonstrated that this finite-difference time-domain simulation produced arrival time, energy level, and wave shape distortion similar to that measured for large abdominal wall specimens. The study also showed that amplitude distortion produced by the abdominal wall can be described as the result of strong scattering.

The purpose of the present study is to use the simulation technique described in Ref. 23 to examine the causes of ultrasonic wavefront distortion in the abdominal wall. In particular, questions concerning the relative contributions of the fat and muscle layers to distortion and the importance of the interface between these layers are investigated. Quantitative correlation methods are employed to relate specific tissue structures to computed wavefront distortion features. Distortion predicted by finite-difference simulations is also compared with results of simulations employing more idealized models of ultrasound-tissue interactions. The simulation results are qualitatively compared with experimental results reported in the companion paper.²⁵

I. METHOD

Propagation of ultrasonic pulses through the fat and muscle layers of the abdominal wall was simulated in two dimensions using the tissue modeling technique and the lossless finite-difference time-domain (FDTD) algorithm described in Ref. 23. The six tissue maps of abdominal wall cross sections employed in the previous study were again used as input to the FDTD program. However, in this case the tissue maps were also separated into fat and muscle layers along the center of the septum dividing the layers, and the propagation of an ultrasonic pulse through each layer was calculated individually.

The tissue maps were made by processing scanned images of abdominal wall cross sections which had been stained to distinguish tissue types according to the procedure described in Ref. 26. Regions of the images containing connective tissue (e.g., skin, tendon, and septa), muscle, and fat were color coded. Density and sound speed arrays for the finite-difference computation, as well as absorption arrays used in the straight-ray computations discussed below, were created from these images by mapping the various colors to representative density and sound speed values obtained from the literature for each tissue type. The values employed are the same as those reported in Ref. 23, and are shown in Table I for reference. The 12 tissue maps employed are shown in Fig. 1.

TABLE I. Sound speed, density, and attenuation parameters employed in finite-difference and straight-ray simulations. Attenuation values shown are those appropriate for a center frequency of 3.75 MHz. These values were compiled in Ref. 23.

Medium	Sound speed (mm/ μ s)	Density (g/cm ³)	Attenuation (dB/cm)
Water	1.524	0.993	0.02
Fat	1.478	0.950	1.8
Muscle	1.547	1.050	4.1
Skin/CT	1.613	1.120	5.9

The general appearance of the cross sections is consistent with descriptions from standard anatomical texts²⁷⁻²⁹ and the human specimens shown in Ref. 25. The fat sections are composed primarily of subcutaneous fat lobules separated by thin connective tissue membranes (septa). Inhomogeneities, mainly consisting of fat, are present in all the muscle sections. Boundaries between muscle, fat, skin, and water (exterior to the specimen) in this figure are not entirely smooth. The roughness seen in these boundaries is substantially greater than that occurring *in vivo* or in measurements²⁵ because the cross sections were fixed in formalin while still stiff from being frozen for the cutting procedure.

Specific anatomical features can also be observed in each of the tissue maps in Fig. 1. Cross section 75hi (a) shows a cross section of the rectus muscle cut perpendicular to the midline of the body. The thick connective tissue to the right is the linea alba. Cross section 77ba (b) shows the rectus muscle on the right. At the left side of the cross section, muscle layers shown are the external and internal obliques, cut diagonally to the cross section, as well as the transversus abdominus, cut parallel to the cross section. Cross section 87de (c) is cut along the rectus muscle parallel to the midline of the body. A fibrous connection, or aponeurosis, is shown, but is mostly composed of fat.²⁵ A fatty region is evident within the muscle layer to the left. The skin is also thicker than in the other cross sections. Cross section 102gh (d) is cut perpendicular to the rectus muscle. Blood vessels are evident both within the subcutaneous fat and in a fatty region that occurs within the thin muscle section. Both cross sections 120de (e) and 120fe (f) are cut along the rectus muscle from the same abdominal wall specimen. An aponeurosis, which does not extend through the entire muscle layer in the vertical direction,²⁷ is evident in both sections.

The simulation parameters were chosen to emulate the measurement configuration described in Refs. 2 and 25. Propagation of a plane-wave pulse through each layer was computed. The pulse had a center frequency of 3.75 MHz and a -6 -dB bandwidth of 1.6 MHz. The waveforms exiting each cross section were recorded at a sampling rate of 225 MHz for 7.3 μ s by 128 simulated receivers 0.72 mm in width placed about 8 mm from the skin surface.

A one-dimensional version of the reference waveform method²³ was used to calculate the arrival time of the pulse at each receiving position in the simulation data. The arrival time fluctuations across the receiving aperture caused by each whole or layer cross section were calculated by sub-

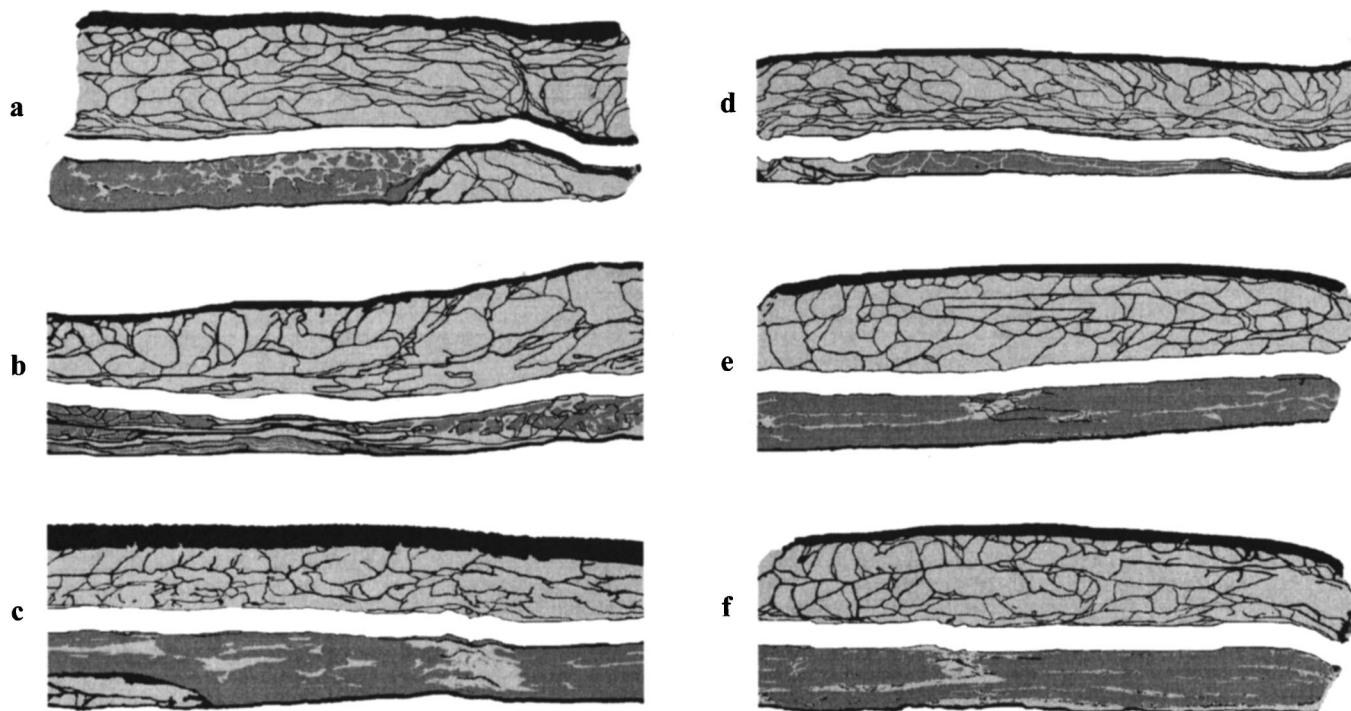


FIG. 1. Muscle-layer and fat-layer tissue maps employed in simulations. Black denotes connective tissue, dark gray denotes muscle, and light gray denotes fat. The fat layers (above) and the muscle layers (below) are obtained in each case from the whole-specimen maps shown in Ref. 23. The actual width of each map shown is 110 mm. (a) Cross section 75hi. (b) Cross section 77ba. (c) Cross section 87de. (d) Cross section 102gh. (e) Cross section 120de. (f) Cross section 120fe.

tracting a linear fit from these calculated arrival times. This fit, when applied to the one-dimensional fluctuations, compensated for gross changes in tissue thickness in a manner similar to higher-order fits previously employed for two-dimensional fluctuations.^{1,2,5,6,23} Energy level fluctuations in the wavefronts were calculated by summing the squared amplitudes of each waveform over a $2.4\text{-}\mu\text{s}$ window that isolated the main pulse, converting to decibel units, and subtracting the best linear fit from the resulting values. Variations in pulse shape across the aperture were evaluated using the waveform similarity factor.¹³

Insertion losses were also calculated from the finite-difference time-domain results. Water path results computed by the methods described above, using a constant sound speed of $1.524\text{ mm}/\mu\text{s}$ and a constant density of $0.993\text{ g}/\text{cm}^3$, were used as reference amplitude values. Insertion loss values were then determined by comparing peak amplitudes of analytic envelopes for tissue-path and water-path signals for each simulated receiver. Since no explicit absorption was included in the finite-difference simulation, and since any numerical absorption due to finite-difference discretization appeared in both tissue- and water-path computations, the resulting attenuation was due only to effects of propagation through the inhomogeneous tissue.

Arrival time fluctuations, energy level fluctuations, and insertion loss were also computed for the modeled cross sections using the asymptotic technique described in Ref. 23. In this case, ultrasonic rays were assumed to pass directly through the tissue without deviation from their initial direction of propagation. The arrival time for rays spaced 0.0847 mm apart was calculated by summing the travel time

along the path of propagation. Likewise, the relative energy level of each ray was computed by integrating the spatially dependent absorption coefficient from Table I along the ray paths. Arrival time and energy level surfaces were determined for the 128-element simulated aperture by averaging arrival times and energy levels for rays occurring within the span of each simulated element (eight or nine rays were averaged for each element). Arrival time and energy level fluctuations were then computed by subtracting the best linear fit from the results of each simulation. The output waveforms were assumed to be identically shaped (waveform similarity factor equal to 1) for the asymptotic straight-ray computation since no mechanism for wave-shape distortion was included in the model. Average bulk attenuation values were also computed for each whole and partial cross section as a function of position along the simulated aperture by integrating absorption values along each ray path. No water-path results were computed for the straight-ray method.

For each ray path employed in the straight-ray computations, the total propagation length within individual tissue types (including fat, muscle, connective tissue, and water) was determined by simple summation. These lengths were then normalized by the total propagation path to obtain the fractional contribution of each tissue type to each ray path. As with the arrival time and attenuation values, tissue fractions for each tissue type were averaged for rays occurring within the span of each element to obtain tissue-fraction curves.

For whole and sectioned maps and both straight-ray and finite-difference simulations, correlation coefficients between the arrival time and energy level curves and the tissue-

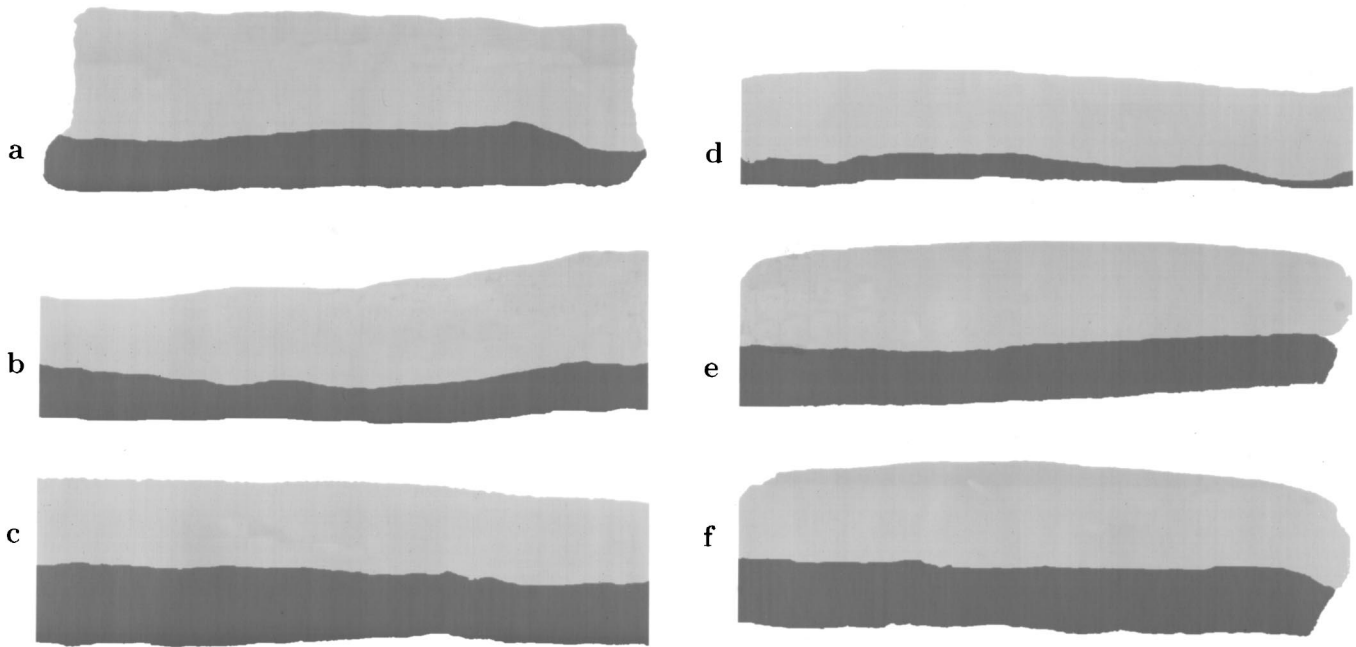


FIG. 2. Solid-layer tissue maps employed in simulations. Cross sections are mapped and ordered as in Fig. 1.

fraction curves were computed. In each case, the correlated curves were 128-point functions corresponding to the 128-element simulated aperture. In addition, arrival time fluctuation and energy level fluctuation curves were summed for the fat and muscle sections of all simulations for comparison with the whole-specimen results.

In order to evaluate the relative importance of tissue

boundaries and layer-thickness variations in producing wavefront distortion, finite-difference and straight-ray simulations were also performed for tissue maps composed of uniform layers. These maps were obtained by altering the layers from Fig. 1 so that the upper layer contained only homogeneous fat and the lower layer contained only homogeneous muscle. The uniform-layer tissue maps are shown in Fig. 2. Data obtained using uniform-layer simulations were processed in the same manner as the data from the simulations employing full tissue structure.

II. RESULTS

Waveforms simulated by the finite-difference method for cross section 120fe are shown in Fig. 3. The waveforms appear similar to measured waveforms recorded for the same abdominal wall specimen,²³ and show several characteristics common to data from the cross sections studied here. Specifically, the muscle-layer wavefront shows substantial arrival time variation that is primarily associated with propagation through a large-scale inhomogeneity (in this case, a fatty aponeurosis), while energy level fluctuations and waveform variations are small. The fat-layer wavefront shows smaller-scale arrival time variations as well as waveform distortion and localized amplitude dropouts. The full-specimen wavefront roughly appears to be a combination of the two layer wavefronts, containing both the large-scale features of the muscle-layer wavefront and the smaller-scale aberrations of the fat-layer wavefront.

Arrival time and energy level distortion simulated using the finite-difference method for whole abdominal wall cross sections, muscle layers, and fat layers are graphically summarized in Figs. 4 and 5, respectively. Panel (f) of each figure shows distortion curves obtained from the waveforms shown in Fig. 3. Although Figs. 4 and 5 show individual variations in the relative contributions of tissue layers to

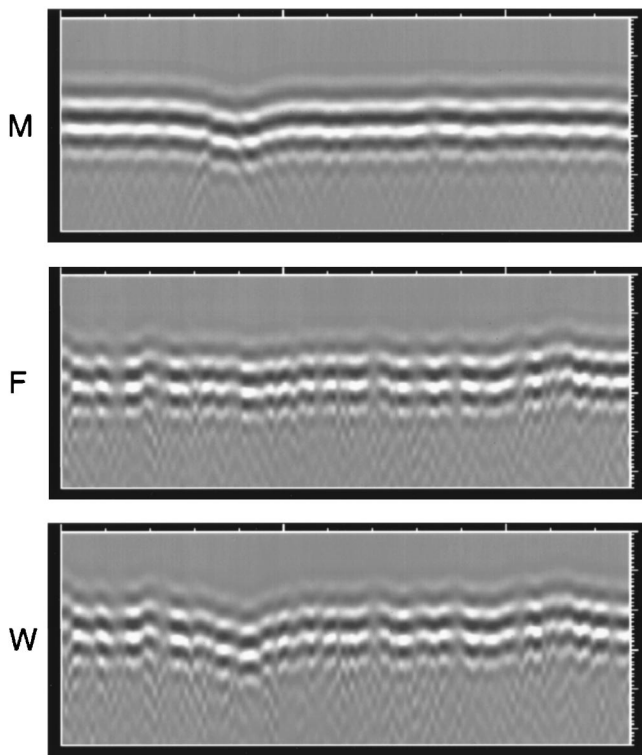


FIG. 3. Simulated waveforms for cross section 120fe (W) and its muscle (M) and fat (F) layers. Waveforms are shown on a linear gray scale with time as the vertical axis and element number as the horizontal axis. The temporal range shown is $2.3 \mu\text{s}$ for 128 elements.

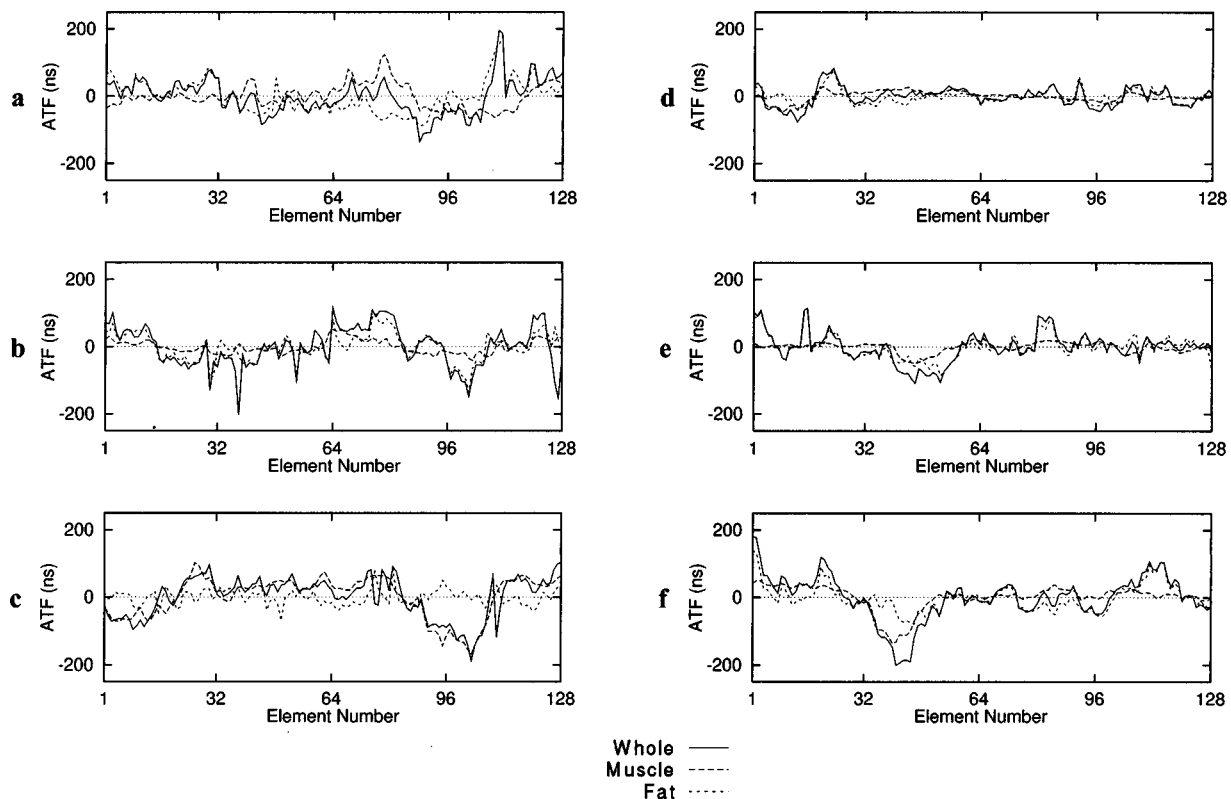


FIG. 4. Arrival time fluctuations (ATF) calculated using the finite-difference, time-domain method for whole specimens, muscle layers, and fat layers. (a) Cross section 75hi. (b) Cross section 77ba. (c) Cross section 87de. (d) Cross section 102gh. (e) Cross section 120de. (f) Cross section 120fe.

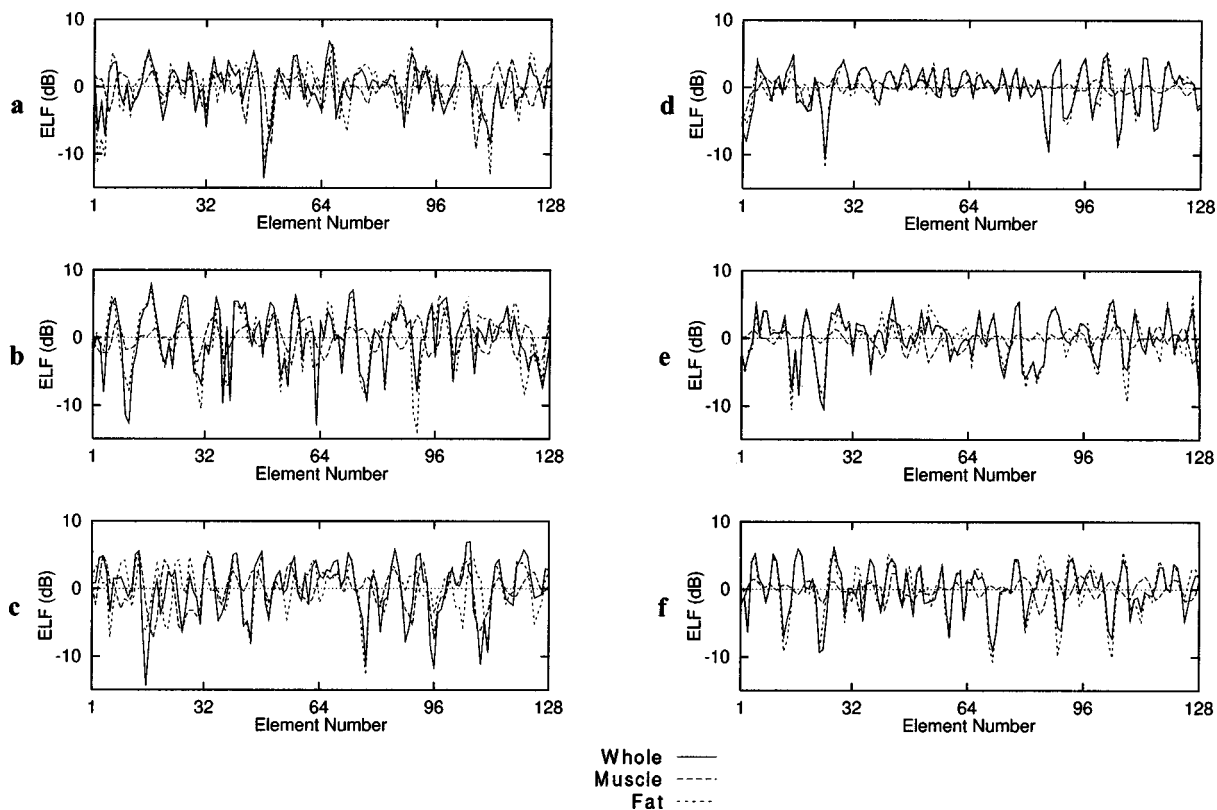


FIG. 5. Energy level fluctuations (ELF) calculated using the finite-difference, time-domain method for whole specimens, muscle layers, and fat layers. (a) Cross section 75hi. (b) Cross section 77ba. (c) Cross section 87de. (d) Cross section 102gh. (e) Cross section 120de. (f) Cross section 120fe.

TABLE II. Wavefront distortion statistics for simulated propagation. Statistics shown include the rms arrival time and energy level fluctuations, correlation lengths (CL) of these fluctuations, and waveform similarity factors for finite-difference, time domain (FDTD) and straight-ray (S-R) simulations employing muscle sections, fat sections and whole specimens.

Specimen	Simulation	Layer	Thickness (mm)	Arrival time fluctuations		Energy level fluctuations		Waveform similarity factor
				rms (ns)	CL (mm)	rms (dB)	CL (mm)	
75hi	FDTD	muscle	9.8	36.5	8.37	2.39	1.60	0.986
		fat	21.3	49.2	8.00	3.45	1.43	0.989
		whole	31.1	53.0	4.70	3.29	1.25	0.957
	S-R	muscle	9.8	38.0	3.55	0.36	5.45	1.000
		fat	21.3	60.6	6.08	0.48	4.79	1.000
		whole	31.1	62.3	2.40	0.42	1.92	1.000
77ba	FDTD	muscle	7.4	19.7	8.59	1.88	1.77	0.996
		fat	17.6	42.5	3.76	4.29	1.61	0.965
		whole	25.0	59.9	4.05	4.44	1.17	0.951
	S-R	muscle	7.4	23.2	2.91	0.35	12.51	1.000
		fat	17.6	51.7	1.52	0.44	2.46	1.000
		whole	25.0	61.6	2.00	0.46	2.09	1.000
87de	FDTD	muscle	12.5	61.3	10.22	2.70	1.97	0.995
		fat	15.9	22.5	1.35	3.26	1.31	0.982
		whole	28.4	60.9	8.68	4.18	1.46	0.948
	S-R	muscle	12.5	62.9	10.54	0.55	13.15	1.000
		fat	15.9	29.7	1.16	0.23	1.18	1.000
		whole	28.4	66.4	6.89	0.60	10.76	1.000
102gh	FDTD	muscle	3.5	15.2	7.99	0.87	1.75	0.999
		fat	15.4	21.6	2.68	2.96	1.31	0.993
		whole	18.9	28.4	3.72	3.10	1.37	0.986
	S-R	muscle	3.5	15.9	7.45	0.24	10.03	1.000
		fat	15.4	26.8	1.73	0.25	2.74	1.000
		whole	18.9	31.9	2.44	0.25	2.83	1.000
120de	FDTD	muscle	9.8	15.2	6.53	1.17	1.77	0.999
		fat	17.8	36.4	2.84	3.37	1.30	0.977
		whole	27.7	43.6	4.88	3.28	1.38	0.980
	S-R	muscle	9.8	16.8	4.63	0.19	8.69	1.000
		fat	17.8	39.8	2.35	0.29	2.58	1.000
		whole	27.7	47.3	3.43	0.38	4.65	1.000
120fe	FDTD	muscle	11.5	38.4	10.32	1.17	1.66	0.999
		fat	17.6	40.2	4.84	3.65	1.45	0.987
		whole	29.1	67.1	8.19	3.41	1.30	0.983
	S-R	muscle	11.5	40.1	10.55	0.42	13.89	1.000
		fat	17.6	45.9	2.13	0.37	2.68	1.000
		whole	29.1	71.3	8.72	0.51	6.11	1.000
Mean	FDTD	muscle	9.1	31.1	8.67	1.70	1.75	0.996
		fat	17.6	35.4	3.91	3.50	1.40	0.982
		whole	26.7	52.2	5.70	3.62	1.32	0.968
	S-R	muscle	9.1	32.8	6.61	0.35	10.62	1.000
		fat	17.6	42.4	2.50	0.34	2.74	1.000
		whole	26.7	56.8	4.31	0.44	4.73	1.000
Standard deviation	FDTD	muscle	3.2	18.1	1.43	0.74	0.13	0.005
		fat	2.1	11.2	2.32	0.45	0.12	0.010
		whole	4.3	14.1	2.16	0.55	0.10	0.017
	S-R	muscle	3.2	18.0	3.42	0.13	3.21	0.000
		fat	2.1	13.0	1.81	0.10	1.16	0.000
		whole	4.3	14.6	2.81	0.12	3.37	0.000

TABLE III. Correlation of finite-difference, time-domain results (FDTD) with straight-ray results (S-R) and with tissue composition.

Specimen	Layer	Arrival time fluctuations				Energy level fluctuations			
		S-R	Muscle	Fat	CT	S-R	Muscle	Fat	CT
75hi	muscle	0.762	0.355	-0.445	-0.241	0.355	-0.074	0.088	-0.141
	fat	0.776	...	-0.445	0.738	0.422	...	0.349	-0.518
	whole	0.666	0.076	-0.570	0.363	0.363	0.005	0.207	-0.258
77ba	muscle	0.719	0.051	-0.460	0.550	0.353	-0.200	0.365	-0.305
	fat	0.454	...	-0.238	0.388	0.518	...	0.240	-0.568
	whole	0.501	-0.213	-0.221	0.524	0.572	-0.070	0.246	-0.500
87de	muscle	0.957	0.896	-0.917	-0.429	0.065	0.022	0.067	-0.261
	fat	0.368	...	-0.353	0.331	0.617	...	0.497	-0.630
	whole	0.783	0.821	-0.821	-0.310	0.190	0.042	0.113	-0.439
102gh	muscle	0.914	0.753	-0.651	-0.290	0.067	0.151	-0.003	-0.402
	fat	0.710	0.433	-0.599	0.590	0.585	-0.282	0.520	-0.644
	whole	0.810	0.426	-0.722	0.250	0.498	0.116	0.274	-0.548
120de	muscle	0.884	0.794	-0.827	-0.323	0.161	0.072	0.087	-0.355
	fat	0.706	...	-0.507	0.527	0.471	...	0.357	-0.643
	whole	0.787	0.727	-0.620	0.243	0.489	-0.186	0.306	-0.565
120fe	muscle	0.952	0.928	-0.955	-0.597	-0.015	0.054	0.028	-0.259
	fat	0.686	-0.074	-0.653	0.464	0.553	-0.159	0.307	-0.645
	whole	0.872	0.823	-0.842	0.214	0.444	-0.078	0.205	-0.575
Mean	muscle	0.865	0.630	-0.803	-0.222	0.164	0.004	0.013	-0.287
	fat	0.617	...	-0.626	0.506	0.528	...	0.414	-0.608
	whole	0.737	0.443	-0.782	0.214	0.426	-0.029	0.240	-0.406
Standard deviation	muscle	0.101	0.350	0.215	0.399	0.157	0.124	0.022	0.090
	fat	0.164	...	0.038	0.147	0.073	...	0.151	0.053
	whole	0.133	0.432	0.085	0.281	0.135	0.106	0.049	0.212

overall distortion, some tissue-specific distortion is seen. For instance, most panels of Fig. 4 show that large-scale arrival time fluctuations from muscle layers and whole abdominal wall cross sections match well. These large-scale time-shift features are generally correlated with positions of large-scale inhomogeneities such as the fatty aponeuroses that occur in cross sections 87de, 120de, and 120fe. Likewise, many large, rapidly varying energy level fluctuations appearing in Fig. 5 are very similar in results for fat layers and whole cross sections, but do not appear in results for muscle layers.

Statistics describing the distortion produced by the six tissue maps using finite-difference simulations are presented in Table II. As with measurements (taken on different specimens) reported in the companion paper,²⁵ the whole specimens usually cause distortion greater than either of the two component layer distortions and comparable to the geometric sum of the layer distortions. However, in contrast to measurements, the muscle sections usually produce arrival time distortion of lower amplitude (mean rms value 31.1 ns) than the corresponding fat layers (mean 35.4 ns). The rms energy level fluctuations, in agreement with measurements,²⁵ are substantially greater for fat sections (mean 3.50 dB) than for muscle sections (mean 1.70 dB). Waveform similarity factors for simulations are generally higher (indicating smaller waveform distortion) than those for measured data using the same specimens—the mean waveform similarity factor was 0.968 for finite-difference simulations employing whole cross sections, as opposed to 0.899 for analogous measurements.^{23,24}

The straight-ray results reported in Table II show the same trends as those from straight-ray simulations reported in Refs. 23 and 24 using whole abdominal wall cross sections. That is, for each cross section, the rms straight-ray arrival time fluctuation is close to that for the finite-difference computation, so that magnitudes of arrival time fluctuations are predicted fairly well by this simple model. However, the rms energy level fluctuation is considerably less than that for the finite-difference computation, implying that tissue-dependent absorption contributes little to ultrasonic amplitude distortion in the abdominal wall.

Coefficients from correlation of the finite-difference arrival time and energy level fluctuations with the corresponding straight-ray results as well as with the tissue-fraction curves are shown in Table III. In general, finite-difference and straight-ray results correlate more highly for arrival time fluctuations than for energy level fluctuations. This observation is consistent with the differences in fluctuation statistics seen in Table II. The highest mean correlation between finite-difference and straight-ray arrival time fluctuations (0.865) occurs for the muscle sections, implying that phase screen models may be more appropriate for muscle layers than for fat layers. The highest mean correlation between finite-difference and straight-ray energy level fluctuations (0.528) occurs for the fat sections, indicating that amplitude dropouts due to scattering (in the finite-difference simulation) occurred in similar positions to dropouts due to absorption (in the straight-ray simulation). Both effects are associated with connective tissue content because of the high

TABLE IV. Correlation of layer distortion results and summed layer results with whole-specimen results for finite-difference, time-domain (FDTD) and straight-ray (S-R) simulations.

Specimen	Layer	Whole Specimen			
		FDTD		S-R	
		ATF	ELF	ATF	ELF
75hi	Muscle	0.257	0.358	0.347	0.232
	Fat	0.734	0.768	0.809	0.692
	Muscle + Fat	0.942	0.833	1.000	1.000
77ba	Muscle	0.558	0.279	0.571	0.414
	Fat	0.815	0.817	0.932	0.697
	Muscle + Fat	0.826	0.846	0.999	0.999
87de	Muscle	0.890	0.604	0.896	0.926
	Fat	0.048	0.610	0.336	0.359
	Muscle + Fat	0.888	0.870	1.000	1.000
102gh	Muscle	0.652	0.295	0.546	0.495
	Fat	0.828	0.944	0.868	0.510
	Muscle + Fat	0.991	0.977	1.000	1.000
120de	Muscle	0.661	0.133	0.588	0.652
	Fat	0.933	0.914	0.940	0.868
	Muscle + Fat	0.987	0.961	1.000	1.000
120fe	Muscle	0.840	0.094	0.797	0.694
	Fat	0.838	0.899	0.851	0.584
	Muscle + Fat	0.993	0.940	1.000	0.999
Mean	Muscle	0.643	0.294	0.624	0.569
	Fat	0.699	0.825	0.789	0.618
	Muscle + Fat	0.938	0.905	1.000	1.000
Standard deviation	Muscle	0.226	0.182	0.195	0.242
	Fat	0.325	0.124	0.228	0.176
	Muscle + Fat	0.068	0.062	0.000	0.001

acoustic contrast and absorption of connective tissue.

The tissue-fraction correlation coefficients reported in Table III indicate clear relationships between tissue constituents and ultrasonic wavefront distortion components. For the muscle sections, both muscle and fat fractions correlate significantly with arrival time fluctuations (mean correlations 0.630 and -0.803 respectively), while the corresponding coefficient for the connective-tissue fraction (-0.222) does not indicate a significant correlation. (For 128 samples of a random signal, a correlation coefficient with magnitude greater than 0.2875 is significant to a 99.9% confidence level.³⁰) Arrival time correlation coefficients are positive for muscle fractions and negative for fat fractions because muscle tissue causes an advance, or positive arrival time fluctuation, in the wavefront, while fat tissue causes a delay, or negative arrival time fluctuation. The large negative correlation (-0.803) between fat content and arrival time fluctuations indicates that fatty inhomogeneities within muscle layers are a major cause of arrival time fluctuations in the abdominal wall. Energy level fluctuations do not correlate well with tissue fractions for the muscle section, although the correlation between energy level fluctuation and connective-tissue fraction is marginally significant (0.287).

For the fat sections, both fat fractions and connective tissue fractions correlate significantly with the arrival time and energy level fluctuations computed by the finite-difference method. The significant negative correlation coefficient (-0.608) between energy level fluctuations and connective tissue fraction indicates that amplitude dropouts occur at positions of high connective tissue content within the subcutaneous fat. Visualization of propagation through cross sections²³ has shown that such dropouts occur when septa scatter energy outside the main direction of propagation. This scattering, which occurs because of the high sound speed and density contrast between connective tissue and fat, is greatest for septa oriented nearly perpendicular to the direction of propagation. Also notable is the effect of a blood vessel (with vessel wall modeled as muscle and connective tissue) in the fat section of cross section 102gh. This vessel causes a significant correlation (0.433) between the muscle fraction and the arrival time fluctuation and a marginal correlation between the muscle fraction and the energy level fluctuation. This large effect of a single blood vessel is similar to that found for a blood vessel in the chest wall in Ref. 6.

Further evidence of the relative contribution of individual layers to wavefront distortion in the abdominal wall is provided by Table IV, which shows correlation coefficients between layer results and whole-specimen results for arrival time and energy level fluctuations. In general, results for both the muscle and fat sections correlate significantly with the whole-specimen results. However, for the finite-difference simulations, the energy level fluctuations for the whole specimen correlate much more highly with those calculated for fat sections (0.825) than with those for muscle sections (0.294). The rows marked "muscle + fat" in Table IV refer to correlations between distortion curves for whole cross sections and distortion curves obtained by summing the curves for the corresponding muscle and fat layers. In all cases, the summed section results correlate fairly highly (mean correlation coefficients 0.938 for arrival time fluctuations, 0.905 for energy level fluctuations) with whole-section results for the finite-difference simulations, while the corresponding correlations averaged 1.000 for the straight-ray simulations. Thus, for the finite-difference computations, the wavefront distortion produced by whole cross sections is similar but not equivalent to the sum of distortions caused by their individual layers.

Computed insertion loss values for the whole and layer tissue maps are listed in Table V along with the insertion losses measured for the whole specimens before dissection using the method described in the companion paper.²⁵ In each case, the loss per unit length is greater for muscle than fat in the straight-ray simulation but greater for fat than muscle in the finite-difference simulation. Since insertion loss effects in the finite-difference simulation were only due to scattering, this observation provides further evidence that fat sections caused more scattering than muscle sections.

In every case shown in Table V, measured insertion losses are greater than insertion losses calculated by either the finite-difference or straight-ray method. However, the measured insertion losses (mean 4.88 dB/cm) agree well with values (mean 4.96 dB/cm) obtained by summing the

TABLE V. Computed and measured insertion loss values. Means and standard deviations of insertion losses are shown for measurements employing whole specimens from which the cross sections were taken as well as straight-ray (S-R) and finite-difference (FDTD) simulations using the cross sections. Also shown is the sum of calculated insertion loss rates for straight-ray and finite-difference simulations (SR + FDTD).

Specimen	Layer	Measured			S-R			FDTD			S-R+ FDTD (dB/cm)
		Average (dB)	Standard deviation (dB)	Rate (dB/cm)	Average (dB)	Standard deviation (dB)	Rate (dB/cm)	Average (dB)	Standard deviation (dB)	Rate (dB/cm)	
75hi	muscle	3.50	0.48	3.57	1.84	2.49	1.88	5.45
	fat	6.27	0.52	2.94	4.25	3.51	2.00	4.94
	whole	14.08	7.66	4.52	9.72	0.67	3.13	5.38	3.30	1.73	4.86
77ba	muscle	2.88	0.36	3.90	1.63	1.91	2.20	6.10
	fat	4.78	0.60	2.71	4.41	4.06	2.51	5.22
	whole	12.87	3.38	5.15	7.61	0.57	3.04	5.69	4.44	2.28	5.32
87de	muscle	4.77	0.72	3.82	1.32	2.75	1.06	4.88
	fat	5.26	0.23	3.31	3.14	3.28	1.97	5.28
	whole	15.68	2.93	5.49	9.99	0.77	3.52	4.14	4.29	1.46	4.98
102gh	muscle	1.41	0.42	4.01	0.60	0.90	1.71	5.72
	fat	4.32	0.27	2.81	3.58	2.99	2.32	5.13
	whole	9.52	4.09	5.04	5.69	0.50	3.01	4.07	3.13	2.15	5.16
120de	muscle	4.05	0.20	4.12	0.61	1.21	0.62	4.74
	fat	4.91	0.31	2.75	3.61	3.42	2.03	4.78
	whole	11.89	3.22	4.22	8.92	0.40	3.22	3.94	3.36	1.42	4.64
120fe	muscle	4.42	0.42	3.85	0.93	1.21	0.81	4.66
	fat	5.08	0.37	2.88	3.98	3.63	2.26	5.14
	whole	11.89	3.22	4.22	9.45	0.51	3.25	4.52	3.37	1.55	4.80
Mean	muscle	3.51	0.43	3.88	1.16	1.75	1.38	5.26
	fat	5.10	0.38	2.90	3.83	3.48	2.18	5.08
	whole	12.81	4.26	4.88	8.56	0.57	3.20	4.62	3.65	1.77	4.96
Standard deviation	muscle	1.23	0.17	0.19	0.52	0.76	0.64	0.59
	fat	0.65	0.15	0.22	0.47	0.36	0.22	0.19
	whole	2.32	1.95	0.51	1.64	0.13	0.19	0.74	0.56	0.37	0.25

insertion losses from the finite-difference computation (due only to scattering effects) and from the straight-ray computation (due only to bulk absorption effects). This result suggests that energy loss from wideband ultrasonic pulses in the abdominal wall may be explained as a combination of bulk absorption effects and scattering effects.

Figures 6 and 7, respectively, show arrival time fluctuations and energy level fluctuations for the finite-difference uniform-layer simulations. For comparison, fluctuation curves for finite-difference simulations with abdominal wall cross sections including full internal structure (identical to the whole-specimen results shown in Figs. 4 and 5) are also shown. Both arrival time and energy level fluctuations are seen to be considerably smaller in the uniform-layer simulations than in the full-structure simulations.

Quantitative results for the simulations employing uniform fat and muscle layers are summarized in Table VI. The mean arrival time fluctuations shown there are less than half those for “full” finite-difference and straight-ray simulations that included internal tissue structure (Table II). The correlation lengths of the arrival time fluctuations are much larger than those reported in Table II for the simulations that included full tissue structure. Arrival time fluctuations computed from the finite-difference uniform-layer simulations correlate very well with straight-ray simulations employing

the same uniform layers (mean correlation coefficient 0.991), so that time-shift aberration caused in the uniform layer simulations is almost entirely due to large-scale thickness variations rather than refraction at interfaces. These large-scale layer thickness variations, however, do not explain arrival time fluctuations computed from finite-difference simulations employing full tissue structure, because arrival time fluctuations in the uniform layer simulations did not correlate significantly with fluctuations from the full finite-difference simulations (mean correlation coefficient 0.262).

Energy level fluctuations reported for the uniform-layer FDTD simulations provide an indication of the importance of refraction and scattering at tissue interfaces, since other possible causes of energy level fluctuations (i.e., scattering from small structures and tissue-dependent absorption) were absent from these simulations. The energy level fluctuations from the finite-difference uniform-layer simulations are comparable in magnitude to those for the full straight-ray simulations, but much smaller than those observed in the full finite-difference simulations. Energy level fluctuations from the finite-difference uniform-layer simulations did not correlate significantly with energy level fluctuations obtained in either of the simulations employing full tissue structure. Computed waveform similarity factors for all six finite-difference uniform-layer simulations are indistinguishable

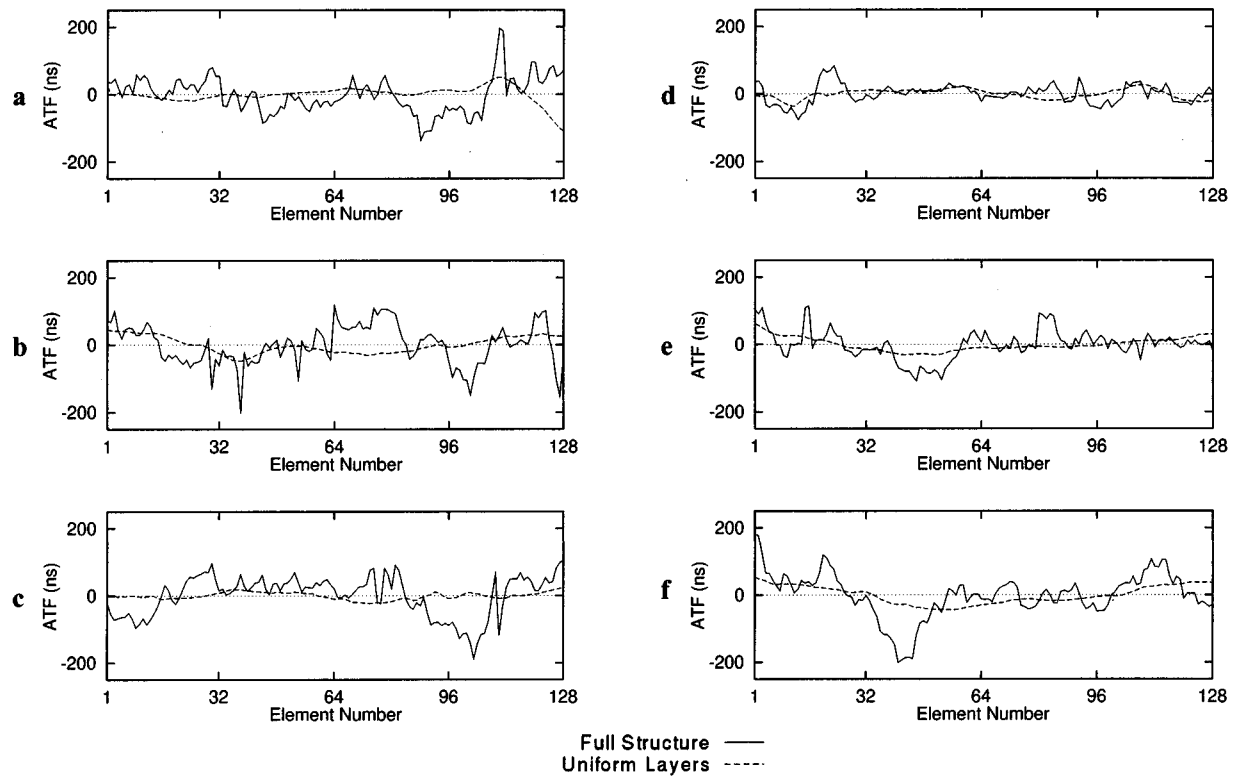


FIG. 6. Arrival time fluctuations (ATF) calculated using the finite-difference, time-domain method for whole specimens with full internal structure and with uniform-tissue fat and muscle layers. (a) Cross section 75hi. (b) Cross section 77ba. (c) Cross section 87de. (d) Cross section 102gh. (e) Cross section 120de. (f) Cross section 120fe.

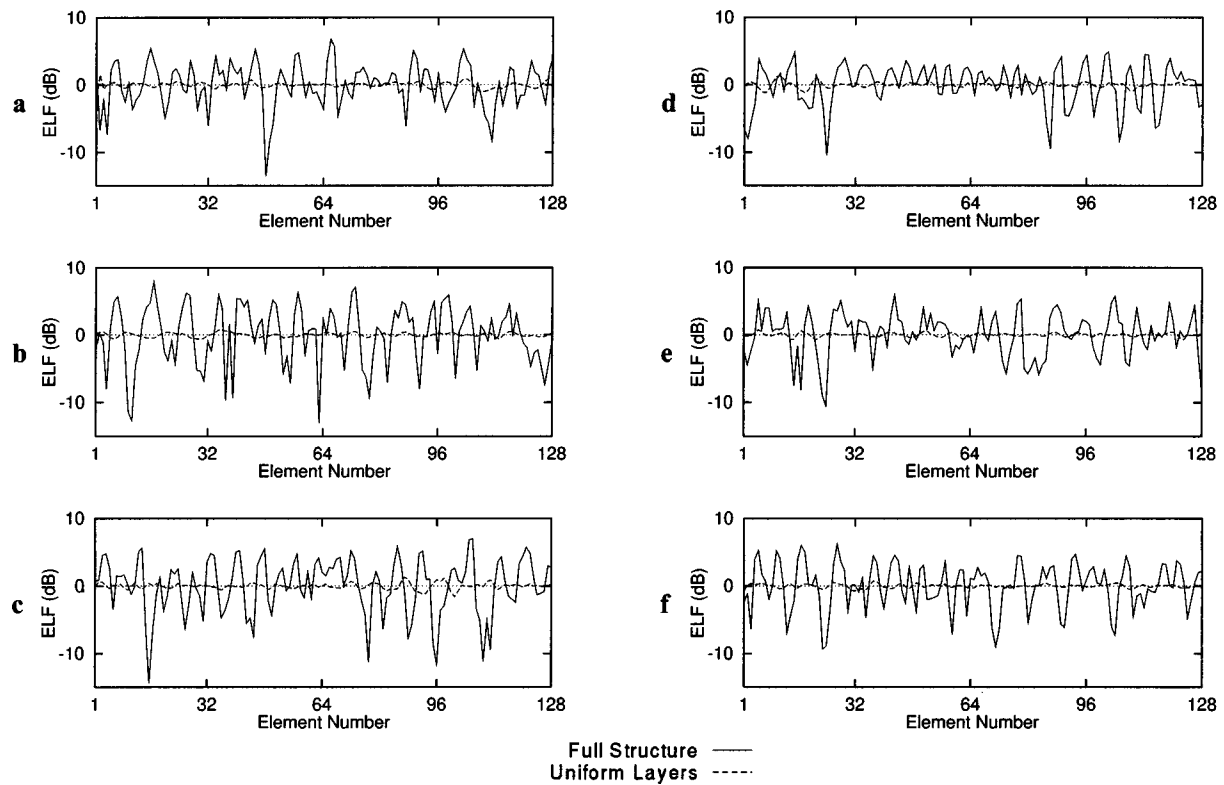


FIG. 7. Energy level fluctuations (ELF) calculated using the finite-difference, time-domain method for whole specimens with full internal structure and with uniform-tissue fat and muscle layers. (a) Cross section 75hi. (b) Cross section 77ba. (c) Cross section 87de. (d) Cross section 102gh. (e) Cross section 120de. (f) Cross section 120fe.

TABLE VI. Wavefront distortion statistics for finite-difference simulation of propagation through uniform fat and muscle layers.

Specimen	Arrival time fluctuations		Energy level fluctuations		Waveform similarity factor	Correlation Coefficient versus S-R (uniform)		Correlation Coefficient versus FDTD (whole)	
	rms (ns)	CL (mm)	rms (dB)	CL (mm)		ATF	ELF	ATF	ELF
75hi	24.2	6.51	0.46	0.97	1.000	0.994	0.183	-0.156	0.086
77ba	24.2	15.01	0.30	2.23	1.000	0.997	0.170	0.145	0.098
87de	10.6	10.88	0.42	1.63	1.000	0.971	0.130	0.064	-0.281
102gh	14.3	9.00	0.39	1.86	1.000	0.991	0.289	0.374	0.020
120de	19.7	16.71	0.27	1.61	1.000	0.996	0.092	0.563	0.146
120fe	26.9	20.33	0.26	1.63	1.000	0.997	0.159	0.581	0.171
Mean	20.0	13.07	0.35	1.66	1.000	0.991	0.171	0.262	0.040
Standard deviation	6.4	5.18	0.08	0.41	0.000	0.010	0.067	0.294	0.166

from unity to four significant figures, indicating that negligible frequency-dependent scattering occurred in these simulations. These small energy level fluctuations, low correlations, and high waveform similarity factors suggest that scattering and refraction at muscle-fat interfaces is not a significant source of amplitude and waveform aberrations observed in ultrasonic propagation through the abdominal wall.

III. DISCUSSION

The results of the simulations reported here provide additional support to the findings reported in the companion measurement paper²⁵ and add insight regarding the characteristics and causes of ultrasonic wavefront distortion by abdominal wall tissue. As in the measurements,²⁵ both muscle and fat sections were found to cause substantial wavefront distortion and attenuation. The simulations performed here indicate causes for the different characteristics of distortion produced by each section.

Simulations suggest that muscle sections primarily cause time-shift aberration due to large-scale variations in the amounts of fat, muscle and connective tissue components within muscle layers. In all cases, correlations between finite-difference and straight-ray arrival time fluctuations for the muscle sections were higher than the corresponding correlations for the fat sections, indicating that muscle layers are more appropriately modeled as phase screens than are fat layers. However, arrival time fluctuations for both muscle layers and fat layers had comparable magnitude and correlated significantly with arrival time fluctuations for whole cross sections, so that both layers should be considered important sources of time-shift aberration in transabdominal ultrasonic imaging.

The simulations also suggest that scattering from inhomogeneities within the subcutaneous fat is a major cause of amplitude and waveform distortion in ultrasonic propagation through the abdominal wall. Energy level fluctuations for fat layers were highly correlated with those for whole cross sections, indicating that most amplitude fluctuation features originated in the fat section. High negative correlations between connective-tissue fraction and energy level fluctuations suggest that these amplitude fluctuations are primarily explained by scattering from septa within fatty tissue. This

conclusion agrees with qualitative analysis of simulated propagation within abdominal wall cross sections, as reported in Ref. 23. It may also be noted that scattering from septa may become more important for large septa or short ultrasonic wavelengths; in such cases, scattering can cause large fluctuations that are sometimes referred to as diffraction, reflection, or refraction.

The simulations provide insight into the manner in which distortions produced by individual layers combine into distortion produced by whole specimens. For both the simulations presented here and the measurements presented in the companion paper,²⁵ arrival time fluctuations (ATF) produced by whole specimens are usually comparable to the geometric sum of the fluctuations produced by the individual layers, i.e.,

$$ATF_{total} \sim \sqrt{ATF_{muscle}^2 + ATF_{fat}^2}.$$

For arrival time fluctuations measured in Ref. 25 as well as those simulated here by finite-difference and straight-ray methods, the geometric sum of the rms fluctuations caused by individual layers is within 30% of the rms fluctuation for whole specimens. Since fluctuations caused by two independent random processes should add geometrically, this result suggests that distortion produced by fat layers is roughly independent of that produced by muscle layers, and that both layers can approximately be considered random aberrators. However, some anomalous results appear in both measurements and simulations; in some cases, the rms arrival time or energy level fluctuation for a whole specimen is less than the rms fluctuation for one or both of the individual layers.

Such differences are possible because, in the case of the whole specimen, the wavefront impinging on the fat layer has already been distorted by propagation through the muscle layer. If the distortion-producing features of the muscle and fat layers are not truly independent of each other, the aberrated wavefront may interact with the structures in the fat layer in ways that reduce or exaggerate the overall distortion level. For instance, Fig. 4(c) shows that near the center of cross section 87de, large-scale arrival time fluctuations occurring in the fat layer partially cancel those that arise in the muscle layer. This occurs in part because, as can be seen in Fig. 1, the fat layer is thicker (causing a large-scale delay in the wavefront) in this region of the cross sec-

tion where the muscle layer contains little fat (causing a relative advance in the wavefront). Because of the importance of large-scale, ordered structure in causing cumulative effects such as this, it may be noted that the human abdominal wall is not fully represented by simple random-process models. In general, the manner in which distortions caused by individual layers combine will be influenced by the specific structure of the tissue being studied.

Results for the insertion loss, or the attenuation in the wavefront amplitude, have shown that both scattering effects (as modeled in finite-difference simulations) and absorption effects (as modeled in straight-ray simulations) make significant contributions to the total insertion loss. Insertion losses estimated by summing results from these two simulations agree well with measured insertion losses for the same specimens. This result suggests that procedures for estimating attenuation by the human abdominal wall, whether for correction of amplitude aberration or quantitative estimation of scattering properties, should consider scattering effects as well as absorption effects. Relative contributions of absorption and scattering to total attenuation, however, can be different in tissues having structure different from the abdominal wall. For instance, some experimental results have suggested that scattering accounts for 2%–18% of attenuation in liver tissue for frequencies between 1.2 MHz and 7 MHz,^{31,32} while the current experimental and simulated results suggest that scattering accounts for about 36% of total insertion loss in the human abdominal wall for pulses centered at 3.75 MHz. This discrepancy is likely associated with differences in morphology between human abdominal wall and liver tissue.

Simulations performed using straight-ray and uniform-layer approximations allow comparison of the present tissue model to others previously employed in medical ultrasound. The straight-ray simulation method is analogous to modeling the abdominal wall as a single phase and amplitude screen at the receiving aperture. Previous results^{23,24} have shown that this model incompletely describes wavefront distortion from the human abdominal wall. The current study, while confirming this conclusion, also indicates that single-phase-screen models describe distortion produced by muscle layers more accurately than distortion produced by fat layers. This result suggests that aberration correction techniques employing single-phase-screen models may provide greater gains when wavefront distortion is due to thick muscle layers than when distortion is associated with obesity.

Others have modeled human tissue as a series of layers of nominally homogeneous properties. Such uniform layers can cause ultrasonic aberration either by variations in thickness^{7,8,33} or by refraction and scattering at interfaces between layers.^{4,15,34,35} The uniform-layer FDTD simulations performed in the present study provide a test of the appropriateness of these models. Arrival time fluctuations from uniform-layer simulations were considerably smaller than those for simulations including full internal structure and were also uncorrelated with full-structure simulations, so that thickness variations of nominally uniform layers appear to be a minor cause of wavefront distortion. The small energy level fluctuations and high waveform similarity factors com-

puted for uniform-layer simulations suggest that refraction and scattering at muscle–fat interfaces is not a significant source of wavefront distortion observed in the abdominal wall. Since comparable sound-speed and impedance mismatches occur between other tissue layers such as skin and fat, the present results suggest that scattering from internal tissue structures contributes more strongly to observed wavefront distortion than do refraction and scattering from any interfaces between tissue layers. Thus, although models assuming uniform tissue layers have successfully corrected image artifacts associated with refraction caused by specific anatomic features,^{34,36} such models may not provide optimal correction for focus degradation in transabdominal ultrasonic imaging.

A third model sometimes used in simulation studies of ultrasonic imaging includes single or multiple phase screens synthesized using measured or estimated aberration statistics. Typically, a few parameters such as rms distortion values and correlation lengths are employed as parameters for realization of a simple random distribution.^{13,15,37,38} These models, by design, produce distortion that is statistically similar to aberration caused by tissues. However, tissue-specific features of ultrasonic wavefront distortion are not depicted by simple stochastic models because tissue is not a true random medium. The ordered, anisotropic distortion induced by muscle fibers is one example of a distortion feature important to ultrasonic imaging that is not accounted for by simple random aberrator models. Another example is the distortion caused by septa aligned close to the propagation direction within the subcutaneous fat, including scattering and arrival-time variations that increase cumulatively with propagation through the fat layer. Because tissue structure determines the wavefront distortion encountered in clinical practice, statistical representations of tissue are also of little use for distortion correction methods. Since tissue structure on scales important to medical ultrasound (~ 1 – 20 mm) varies widely among individuals, effective aberration correction will require compensation specific to each patient and view.

Worthy of comment are differences between the specimens employed here for tissue-type mapping and those used in Ref. 25 for two-dimensional wavefront distortion measurements of whole specimens and individual sections. The relative thicknesses of the specimens employed were comparable, having a mean of 26.6 mm for the mapped specimens, and a mean of 24.4 mm for the measured specimens. However, the muscle layer was usually about half the thickness of the fat layer for the mapped specimens, while muscle layer thicknesses were typically close to fat layer thicknesses for the measured specimens. The muscle layer was actually thicker than the fat layer for one specimen (118) measured in Ref. 25.

The discrepancy in muscle thickness between the two specimen groups may partially explain the relatively low distortion values found for simulated propagation through muscle sections in the present paper. Another possible reason for the low distortion associated with muscle sections in the present paper may be the result of inaccuracies in tissue mapping. In particular, the fibrous microstructure of muscle was not mapped in the present study, and some connective tissue

occurring in the muscle layers was not accurately mapped, since the staining technique employed provided less contrast between muscle and connective tissue than between fat and connective tissue. Finally, another likely cause of disagreement between the simulations reported here and the measurements reported in Ref. 25 is that the present simulations were performed in two dimensions. Further discussion of this limitation is given in Ref. 23.

The absence of frequency-dependent absorption is a possible source of error in estimates of total tissue attenuation and energy level fluctuations from the straight-ray computations. However, since absorption in tissue increases approximately linearly with frequency, lower absorption for frequency components below the pulse center frequency would nearly cancel higher absorption for frequency components above the center frequency. For this reason, the neglect of frequency-dependent absorption is not considered to be a significant source of error in the attenuation or energy level fluctuation curves computed using the straight-ray method. Still, inclusion of frequency-dependent absorption could result in some waveform distortion effects. Therefore, if actual waveforms were employed in this simulation, the peak-to-peak insertion losses could deviate from the bulk absorption calculated above and waveform similarity factors could deviate from unity even in the absence of scattering.

Likewise, the absence of any tissue-specific absorption from the finite-difference computations is a possible source of inaccuracy when using the present finite-difference method to estimate waveform and energy level distortion. Because frequency-dependent absorption would cause additional waveform distortion, the absence of frequency-dependent absorption may be a partial explanation for the large waveform similarity factors computed from simulated wavefronts. However, since energy level fluctuations obtained from the straight-ray simulation using tissue-dependent absorption are much smaller than energy level fluctuations from the finite-difference simulations, inclusion of absorption in the finite-difference simulations would have only a small effect on the computed energy level distortion.

More detailed discussion of limitations and sources of error for the simulation methods employed is given in Ref. 23.

IV. CONCLUSIONS

Simulation results have been presented to provide quantifiable correlation between tissue morphology and ultrasonic wavefront distortion produced by the human abdominal wall.

The results support conclusions based on measurements²⁵ that used whole abdominal specimens and their individual fat and muscle layers. Specifically, the finite-difference simulation results show that both fat and muscle layers cause significant distortion. Correlation of distortion curves with tissue composition indicates that inhomogeneous regions such as fatty inclusions within muscle layers cause significant arrival time fluctuations, while amplitude aberration is predominantly caused by scattering from septa within the subcutaneous fat. One difference between the finite-difference and measurement results is that although muscle layers produced more arrival time variation in the measure-

ments, comparable arrival time fluctuation was caused by muscle and fat layers in the simulations. However, in both cases, fat layers caused greater energy level distortion.

Additional simulations performed using a straight-ray model suggest that phase-screen models are more appropriate for muscle layers of the abdominal wall than for the subcutaneous fat, but that single phase-screen models incompletely describe aberration caused by the human abdominal wall. Simulations performed using a uniform-layer model indicate that refraction at interfaces between tissue layers, as well as varying thickness of muscle and fat sections of the abdominal wall, are minor sources of ultrasonic wavefront distortion compared to large-scale inhomogeneities and effects caused by internal structure. The importance of specific ordered tissue structures to cumulative distortion effects within layers, as well as to the combination of wavefront distortion by fat and muscle layers, suggests that tissue models employing simple random processes incompletely depict wavefront distortion caused by the abdominal wall.

In summary, these results suggest that models of ultrasonic propagation within human soft tissues, whether employed within aberration correction algorithms or imaging simulations, should include realistic depictions of tissue morphology to obtain accurate results. Models of tissue morphology for aberration correction should also accurately depict tissue structures specific to the individual and location of interest.

ACKNOWLEDGMENTS

The authors thank Dr. Leon A. Metlay for advice during construction of the tissue maps and for other consultation regarding abdominal wall morphology. Dong-Lai Liu is thanked for providing the original two-dimensional version of the distortion estimation code. Funding for this investigation was provided by the University of Rochester Diagnostic Ultrasound Research Laboratory Industrial Associates, NIH Grants DK 45533, HL 50855, and CA 74050, and US Army Grant DAMD-17-94-J-4384. Computations were performed at the Cornell National Supercomputing Facility, which was supported in part by the National Science Foundation, New York State, and the IBM Corporation, and at the Center for Academic Computing of the Pennsylvania State University.

¹Y. Sumino and R. C. Waag, "Measurements of ultrasonic pulse arrival time differences produced by abdominal wall specimens," *J. Acoust. Soc. Am.* **90**, 2924–2930 (1991).

²L. M. Hinkelman, D.-L. Liu, L. A. Metlay, and R. C. Waag, "Measurements of ultrasonic pulse arrival time and energy level variations produced by propagation through abdominal wall," *J. Acoust. Soc. Am.* **95**, 530–541 (1994).

³P. D. Freiburger, D. C. Sullivan, B. H. LeBlanc, S. W. Smith, and G. E. Trahey, "Two dimensional ultrasonic beam distortion in the breast: In vivo measurements and effects," *Ultrason. Imaging* **14**(4), 398–414 (1992).

⁴Q. Zhu and B. D. Steinberg, "Large-transducer measurements of wavefront distortion in the female breast," *Ultrason. Imaging* **14**(3), 276–299 (1992).

⁵L. M. Hinkelman, D.-L. Liu, R. C. Waag, Q. Zhu, and B. D. Steinberg, "Measurement and correction of ultrasonic pulse distortion produced by the human breast," *J. Acoust. Soc. Am.* **97**, 1958–1969 (1995).

⁶L. M. Hinkelman, T. L. Szabo, and R. C. Waag, "Measurements of ul-

- trasonic pulse distortion produced by the human chest wall," *J. Acoust. Soc. Am.* **101**, 2365–2373 (1997).
- ⁷M. O'Donnell and S. W. Flax, "Phase-aberration correction using signals from point reflectors and diffuse scatterers: Measurements," *IEEE Trans. Ultrason. Ferroelectr. Freq. Control* **35**(6), 768–774 (1988).
- ⁸L. Nock, G. E. Trahey, and S. W. Smith, "Phase aberration correction in medical ultrasound using speckle brightness as a quality factor," *J. Acoust. Soc. Am.* **85**, 1819–1833 (1989).
- ⁹D. Rachlin, "Direct estimation of aberrating delays in pulse-echo imaging systems," *J. Acoust. Soc. Am.* **88**, 191–198 (1990).
- ¹⁰D.-L. Liu and R. C. Waag, "Time-shift compensation of ultrasonic pulse focus degradation using least-mean-square error estimates of arrival time," *J. Acoust. Soc. Am.* **95**, 542–555 (1994).
- ¹¹M. O'Donnell and S. W. Flax, "Phase aberration measurements in medical ultrasound: Human studies," *Ultrason. Imaging* **10**(1), 1–11 (1988).
- ¹²B. S. Robinson, A. Shmulewitz, and T. M. Burke, "Waveform aberrations in an animal model," 1994 *IEEE Ultrason. Symp. Proc.* **3**, 1619–1624 (1994).
- ¹³D.-L. Liu and R. C. Waag, "Correction of ultrasonic wavefront distortion using backpropagation and a reference waveform method for time-shift compensation," *J. Acoust. Soc. Am.* **96**, 649–660 (1994).
- ¹⁴C. Dorne and M. Fink, "Ultrasonic beam steering through inhomogeneous layers with a time reversal mirror," *IEEE Trans. Ultrason. Ferroelectr. Freq. Control* **43**(1), 167–175 (1996).
- ¹⁵A. P. Berkhoff and J. M. Thijssen, "Correction of concentrated and distributed aberrations in medical ultrasound imaging," 1996 *IEEE Ultrasonics Symp. Proc.* **2**, 1405–1410 (1996).
- ¹⁶S. Krishnan, P.-C. Li, and M. O'Donnell, "Adaptive compensation for phase and magnitude aberrations," *IEEE Trans. Ultrason. Ferroelectr. Freq. Control* **43**(1), 44–55 (1996).
- ¹⁷Q. Zhu and B. D. Steinberg, "Deabberation of incoherent wavefront distortion: an approach toward inverse filtering," *IEEE Trans. Ultrason. Ferroelectr. Freq. Control* **44**(3), 575–589 (1997).
- ¹⁸R. C. Waag, D. Dalecki, and W. A. Smith, "Estimates of wave front distortion from measurements of scattering by model random media and calf liver," *J. Acoust. Soc. Am.* **85**, 406–415 (1989).
- ¹⁹L. A. Ødegaard, "Phase Aberration Correction in Medical Ultrasound Imaging," Ph.D. thesis, University of Trondheim, Trondheim, Sweden, 1995.
- ²⁰L. Ødegaard, E. Halvorsen, B. Ystad, H. G. Torp, and B. Angelsen, "Delay and amplitude focusing through the body wall; A simulation study," 1996 *IEEE Ultrason. Symp. Proc.* **2**, 1411–1414 (1996).
- ²¹C. W. Manry, Jr., and S. L. Broschat, "FDTD simulations for ultrasound propagation in a 2-D breast model," *Ultrason. Imaging* **18**(1), 25–34 (1996).
- ²²A. P. Berkhoff, P. M. van den Berg, and J. M. Thijssen, "Simulation of wave propagation through aberrating layers of biological media," 1994 *IEEE Ultrason. Symp. Proc.* **3**, 1797–1800 (1994).
- ²³T. D. Mast, L. M. Hinkelman, M. J. Orr, V. W. Sparrow, and R. C. Waag, "Simulation of ultrasonic pulse propagation through the abdominal wall," *J. Acoust. Soc. Am.* **102**, 1177–1190 (1998).
- ²⁴T. D. Mast, L. M. Hinkelman, M. J. Orr, V. W. Sparrow, and R. C. Waag, "Erratum: 'Simulation of ultrasonic pulse propagation through the abdominal wall' [*J. Acoust. Soc. Am.* **102**, 1177–1190 (1997)]," *J. Acoust. Soc. Am.* **104**, 1124–1125 (1998).
- ²⁵L. M. Hinkelman, T. D. Mast, L. A. Metlay, and R. C. Waag, "The effect of abdominal wall morphology on ultrasonic pulse distortion. Part I. Measurements," *J. Acoust. Soc. Am.* **104**, 3635–3649 (1998).
- ²⁶L. M. Hinkelman, L. A. Metlay, C. J. Churukian, and R. C. Waag, "Modified Gomori trichrome stain for macroscopic tissue slices," *J. Histotech.* **19**(4), 321–323 (1996).
- ²⁷R. Warwick and P. L. Williams (eds.), *Gray's Anatomy* (Saunders, Philadelphia, 1973), 35th ed., pp. 488–490, 519–527.
- ²⁸H. Gray, *Gray's Anatomy*, edited by T. P. Pick and R. Howden (Gramercy, New York, 1977), pp. 358–364 (facsimile of 1901 American edition of *Anatomy, Descriptive and Surgical*).
- ²⁹J. L. Matthews and J. H. Martin, *Atlas of Human Histology and Ultrastructure* (Lea & Febiger, Philadelphia, 1971), pp. 54–55, 102–119.
- ³⁰P. R. Bevington, *Data Reduction and Error Analysis for the Physical Sciences* (McGraw-Hill, New York, 1969), pp. 310–311.
- ³¹K. J. Parker, "Ultrasonic attenuation and absorption in liver tissue," *Ultrason. Med. Biol.* **9**, 363–369 (1983).
- ³²J. A. Campbell, "Measurements of ultrasonic differential and total scattering cross sections for tissue characterization," Ph. D. thesis, University of Rochester, Rochester, New York, 1984.
- ³³H. Wang, E. S. Ebbini, M. O'Donnell, and C. A. Cain, "Phase aberration correction and motion correction for ultrasonic hyperthermia phased arrays: experimental results," *IEEE Trans. Ultrason. Ferroelectr. Freq. Control* **41**(1), 34–43 (1994).
- ³⁴G. Kossoff, D. A. Carpenter, D. E. Robinson, D. Ostry, and P. L. Ho, "A sonographic technique to reduce beam distortion by curved interfaces," *Ultrason. Med. Biol.* **15**(4), 375–382 (1989).
- ³⁵L. A. Ledoux, A. P. Berkhoff, and J. M. Thijssen, "Ultrasonic wave propagation through aberrating layers: experimental verification of the conjugate gradient Rayleigh method," *IEEE Trans. Ultrason. Ferroelectr. Freq. Control* **43**(1), 158–166 (1996).
- ³⁶D. A. Carpenter, G. Kossoff, and K. A. Griffiths, "Correction of distortion in US images caused by subcutaneous tissues: results in tissue phantoms and human subjects," *Radiology* **195**, 563–567 (1995).
- ³⁷L. A. Ødegaard, "Using signals scattered from diffuse inhomogeneities to correct for phase aberrations caused by a phase-screen far from the transducer," 1995 *IEEE Ultrason. Symp. Proc.* **2**, 1443–1447 (1995).
- ³⁸W. E. Walker and G. E. Trahey, "Aberrator integration error in adaptive imaging," *IEEE Trans. Ultrason. Ferroelectr. Freq. Control* **44**(4), 780–791 (1997).

***In vitro* characterization of a novel, tissue-targeted ultrasonic contrast system with acoustic microscopy**

Gregory M. Lanza

Department of Medicine, Division of Cardiology, Barnes-Jewish Hospital, Washington University, St. Louis, Missouri 63110

Rebecca L. Trousil and Kirk D. Wallace

Department of Physics, Washington University, St. Louis, Missouri 63130

James H. Rose

Department of Physics and Astronomy and Ames Laboratory, Iowa State University, Ames, Iowa 50011

Christopher S. Hall and Michael J. Scott

Department of Medicine, Division of Cardiology, Barnes-Jewish Hospital, Washington University, St. Louis, Missouri 63110

James G. Miller

Department of Physics, Washington University, St. Louis, Missouri 63130

Paul R. Eisenberg

Department of Medicine, Division of Cardiology, Barnes-Jewish Hospital, Washington University, St. Louis, Missouri 63110

Patrick J. Gaffney

Division of Hematology, National Institute for Biological Standards and Control, Blanche Lane, South Mimms, Potters Bar, Hertfordshire EN6 3QG, United Kingdom

Samuel A. Wickline

Department of Medicine, Division of Cardiology, Barnes-Jewish Hospital, Washington University, St. Louis, Missouri 63110 and Department of Physics, Washington University, St. Louis, Missouri 63130

(Received 17 March 1997; accepted for publication 22 August 1998)

Targeted ultrasonic contrast systems are designed to enhance the reflectivity of selected tissues *in vivo* [Lanza *et al.*, *Circulation* **94**, 3334 (1996)]. In particular, these agents hold promise for the minimally invasive diagnosis and treatment of a wide array of pathologies, most notably tumors, thromboses, and inflamed tissues. In the present study, acoustic microscopy was used to assess the efficacy of a novel, perfluorocarbon based contrast agent to enhance the inherent acoustic reflectivity of biological and synthetic substrates. Data from these experiments were used to postulate a simple model describing the observed enhancements. Frequency averaged reflectivity (30–55 MHz) was shown to increase 7.0 ± 1.1 dB for nitrocellulose membranes with targeted contrast. Enhancements of 36.0 ± 2.3 dB and 8.5 ± 0.9 dB for plasma and whole blood clots, respectively, were measured between 20 and 35 MHz. A proposed acoustic transmission line model predicted the targeted contrast system would increase the acoustic reflectivity of the nitrocellulose membrane, whole blood clot, and fibrin plasma clot by 2.6, 8.0, and 31.8 dB, respectively. These predictions were in reasonable agreement with the experimental results of this paper. In conclusion, acoustic microscopy provides a rapid and sensitive approach for *in vitro* characterization, development, and testing of mathematical models of targeted contrast systems. Given the current demand for targeted contrast systems for medical diagnostic and therapeutic use, the use of acoustic microscopy may provide a useful tool in the development of these agents. © 1998 Acoustical Society of America. [S0001-4966(98)01412-X]

PACS numbers: 43.80.Qf, 43.20.Fn, 43.35.Ns [FD]

INTRODUCTION

Gramiak and Shah¹ first introduced the concept of acoustic contrast agents as tools for enhancing ultrasound and Doppler sensitivity. The preponderance of systemic contrast agents are microbubble formulations designed to enhance the acoustic appearance of the blood pool and to define its distribution and integrity.^{2–4} Unlike blood pool agents, site-directed ultrasonic contrast agents are intended to specifically and sensitively enhance the acoustic reflectiv-

ity of a pathological tissue which would otherwise be difficult to distinguish from surrounding normal tissue. Burgeoning discoveries of clinically important pathological markers and the rapid production of monoclonal antibodies against these epitopes are expected to broadly expand the diagnostic capability and utility of ligand targeted ultrasonic contrast agents to improve the specificity and sensitivity of ultrasonic diagnoses.

In the past, “passive targeting” has been employed to

target contrast agents to the liver or spleen by virtue of non-specific clearance mechanisms of the reticular endothelial system. Tumors have been similarly nonspecifically targeted by taking advantage of delayed contrast washout from neovascular tissue beds surrounding and penetrating into the pathology. However, “active targeting” involves the use of a molecular epitope-specific ligand to concentrate contrast particles on an *a priori* selected tissue. Until recently,⁵ development of ligand-directed particulate agents has suffered from a general inability to overcome the rapidity of normal physiologic clearance functions which have profoundly limited their accumulation at target sites and precluded efficacious signal enhancement.

In the present study, a novel, nongaseous, ultrasound contrast agent invented in our laboratory is investigated with acoustic microscopy to measure the increase in ultrasonic reflectivity from biological and synthetic surfaces targeted with the contrast agent. We have recently reported a ligand-targeted ultrasonic contrast agent that specifically binds and enhances the acoustic reflectivity of thrombi *in vitro* and *in vivo* when administered either *in situ* or intravenously.⁵⁻¹⁰ Unlike traditional ultrasonic microbubble contrast agents, this particle is nongaseous, approximately 250 nm in diameter, and exhibits low acoustic reflectivity unless bound to a surface. The acoustic reflectivity of thrombi is significantly enhanced with this agent when imaged with either a conventional clinical vascular echocardiographic (7.5 MHz)⁵ or high frequency intravascular imaging (30 MHz) systems.¹¹ Its small size, typically 1000 times less volume than most microbubble formulations has allowed the contrast agent to not only localize thrombi, but also to penetrate and acoustically enhance the internal recesses of the thrombi, resulting in a clearer depiction of morphology.⁵ Moreover, the bound particles provide stable and prolonged visualization of the target pathology without need for special techniques, such as transient and/or second harmonic imaging, frequently required when insonifying power-sensitive, microbubble-based, blood pool contrast agents.

In this report, we utilize acoustic microscopy and *in vitro* methods to provide quantitative estimates of enhanced reflectivity derived from our targeted, lipid encapsulated, perfluorocarbon contrast system. Over the last 25 years, acoustic microscopy has been used to visualize tissues,^{12,13} cells,¹⁴ and subcellular organelles^{15,16} and to characterize their material¹⁷⁻¹⁹ and acoustic properties.^{20,21} Our laboratory has utilized acoustic microscopy to quantify atherosclerotic plaque composition,²² to define ventricular architectural remodeling in cardiomyopathies,²³⁻²⁵ and to physically characterize the disorganization and composition of aortic tissue in Marfan’s syndrome.²⁶

Three different substrates were targeted for enhancement of reflectivity after contrast binding: (1) nitrocellulose, a homogeneous, chemically modifiable substrate; (2) red blood cell; and (3) fibrin clot, *in vitro* analogues of venous and arterial thrombi, respectively. Thrombi were chosen as an initial pathological target in view of its dominant role in cardiovascular morbidity and mortality.

In Sec. I, a simple acoustic transmission line model, proposed as an explanation for the acoustic reflectivity of the

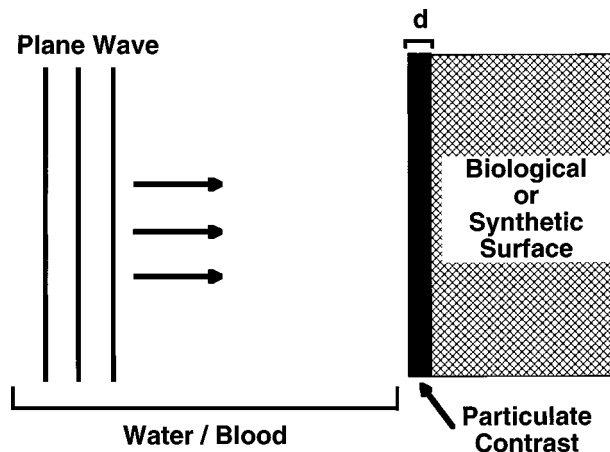


FIG. 1. Three layer model intended to describe the observed enhancement of the reflectivity due to the targeted contrast agent. The half-space reflection coefficient is calculated for a normally incident plane wave that enters from the left (water or blood) and is reflected from the layered half-space (sample covered by the contrast agent).

contrast system, is discussed. In Sec. II, methods for the production of the contrast agent, the experimental substrates, and acoustic microscopy are presented. In Sec. III, the experimental acoustic reflectivities from the various substrates are presented and compared with model predictions. In Sec. IV, the potential impact of the acoustic contrast system and model on medical ultrasonography is discussed.

I. MODEL

A. Proposed mechanism for contrast enhancement

A simple acoustic transmission line model was developed to explain the observed increase in acoustic reflectivity of a targeted substrate.²⁷ The experimental system was modeled as a three-layer system of a host medium, a thin (250-nm) contrast layer, and the substrate (Fig. 1). The complex frequency-dependent reflection coefficient [$R(k)$] at the surface of the substrate of a normally incident pressure plane wave is described by

$$R(k) = R_{12} + \frac{T_{12}R_{23}T_{21}e^{2ikd}}{1 - R_{21}R_{23}e^{2ikd}}. \quad (1)$$

Here, $k = 2\pi/\lambda$ and is the wave number in bulk perfluorocarbon, and d is the thickness of the perfluorocarbon contrast agent layer. R_{xy} and T_{xy} represent the reflection and transmission coefficients at joined half-spaces of materials x and y (from x to y). The increase in acoustic reflectivity can be expressed on a logarithmic scale as

$$\text{Increase} = 20 \text{Log}_{10} R(k)/R_{13}, \quad (2)$$

where R_{13} is the reflection coefficient at the water/specimen interface with no contrast. The effect of the targeted enhancement agent on the loss was calculated from Eq. (2) for the thrombi and nitrocellulose membrane described in detail earlier. For the nitrocellulose membrane, the following nominal acoustic values were inserted for the perfluorocarbon contrast agent (density = 1.8 g/cm³, sound velocity = 600 m/s), the nitrocellulose substrate (density = 1.12

g/cm^3 , sound velocity=1490 m/s), and for deionized room temperature water (density=1.0 g/cm^3 , velocity=1490 m/s).

II. METHOD

A. Preparation of control and targeted emulsion contrast systems

The targeted contrast system was produced by incorporating biotinylated phosphatidylethanolamine into the outer lipid monolayer of a nongaseous perfluorocarbon emulsion as previously described.⁵ Briefly, the emulsion was comprised of perfluorodichlorooctane (40% v/v, PFDCO, Minnesota Manufacturing and Mining, St. Paul, MN), safflower oil (2.0%, w/v), a surfactant comixture (2.0%, w/v), and glycerin (1.7%, w/v). The surfactant comixture included 64 mole% lecithin (Pharmacia, Inc., Clayton, NC), 35 mole% cholesterol (Sigma Chemical Co., St. Louis, MO) and 1 mole% *[N-(6-(biotinoyl)amino)hexanoyl]-dipalmitoyl-L-alpha-phosphatidyl-ethanolamine* (Pierce, Rockford, IL) which were dissolved in chloroform, evaporated under reduced pressure, dried in a 50 °C vacuum oven overnight and dispersed into water by sonication, resulting in a liposome suspension. The liposome suspension was transferred into a blender cup (Dynamics Corporation of America, New Hartford, CT) with perfluorodichlorooctane, safflower oil, and distilled, deionized water and emulsified for 30–60 s. The emulsified mixture was transferred to an S110 Microfluidics emulsifier (Microfluidics, Newton, MA) and continuously processed at 10 000 PSI for 3 min. The completed emulsion was placed in stopper crimp sealed vials and blanketed with nitrogen until use. A control emulsion was prepared identically except that a nonbiotinylated phosphatidylethanolamine was substituted into the outer surfactant layer. Biotinylated and control perfluorocarbon emulsion particle sizes were determined in triplicate at 37 °C with a Brookhaven BI-90 laser light scatter submicron particle size analyzer (Brookhaven Instruments Corporation, Holtsville, NY) and the average diameters [\pm standard error of the mean (SEM)] were found to be 222.0 ± 6.7 nm and 261.7 ± 3.7 nm, respectively (90% of the particles had diameters less than 380 nm).

B. Targeting ligands

In the development of a thrombus-targeted contrast system, we evaluated a highly specific, high affinity monoclonal $F_{(ab)}$ fragment against D-dimer, DD-3B6.²⁸ Briefly, D-dimer, a fibrin degradation fragment, was bound to the center of a nitrocellulose membrane surface modified with a six-carbon spacer and activated with glutaraldehyde. The periphery of the nitrocellulose membrane was blocked with bovine serum albumin to preclude nonspecific binding. No data were generated with acoustic microscopy when the D-dimer was selected as a clot targeting epitope *in vitro*. Clots doped with plasminogen were exposed to various concentrations of tissue plasminogen activator in order to generate D-dimer. Unfortunately, clot integrity was lost in virtually all instances by rapid thrombolytic dissolution. Subsequently, the targeting ligands for fibrin and red blood cell thrombi were changed to monoclonal antibodies, NIB 1H10 and/or NIB

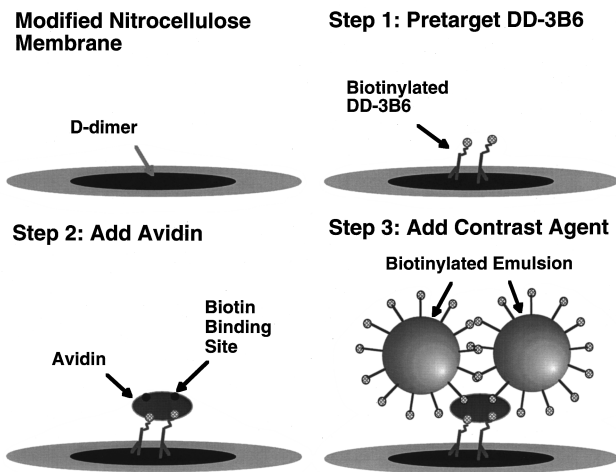


FIG. 2. A graphic depiction of the three step targeted contrast system as applied to a D-dimer bound to nitrocellulose membranes and targeted with DD-3B6.

5F3,^{29,30} directed against a stable fibrin epitope within the intact ϵ -domain of the protein. NIB 1H10 and NIB 5F3 were used interchangeably.

C. Preparation of the nitrocellulose membrane

Nitrocellulose disks ($n=12$) were modified with a six-carbon spacer arm and activated with glutaraldehyde for conjugation with protein or peptide epitopes.³¹ Nitrocellulose disks (2.5 cm diameter) were immersed in 1,6 diaminohexane (2.5% w/v, pH 11.9) for 60 min under constant rotary agitation. The membranes were next washed under constant agitation for approximately 12 h in 1-*M* acetic acid followed by 12 h in ultrapure water with several changes of each medium. The diaminoalkane-modified nitrocellulose membranes were then exposed to 1% glutaraldehyde in 0.5-*M* $\text{NaHCO}_3/\text{Na}_2\text{CO}_3$, pH 10, for 15 min followed by a 3-h wash in several changes of ultrapure water. The diaminohexane-modified, glutaraldehyde-activated nitrocellulose membranes were stored dry at 4 °C until use.

D-dimer (50- μg) dissolved in 0.1-*M* phosphate buffered saline (PBS) (pH 7.2–7.4) was spotted and dried dropwise onto the center of each of six membranes with a microliter syringe and allowed to dry. Next, each membrane was washed with three, 5-min changes of PBS-0.1% Tween 20. Crystalline bovine serum albumin (3% w/v) in PBS-0.1% Tween 20 was used to block glutaraldehyde activated protein binding sites left unoccupied after the application of D-dimer for 20 min. Excess bovine serum albumin was removed with three, 5-min isotonic, PBS washes.

The contrast system comprised three independent steps and utilized avidin to couple a pretargeted biotinylated ligand with a biotinylated emulsion particle (Fig. 2). In step 1, each membrane was incubated at ambient temperature with 12.5- μg DD-3B6, a D-dimer directed biotinylated monoclonal $F_{(ab)}$ fragment, for 2 h.²⁸ The membranes were washed repeatedly with PBS then incubated with 250- μg avidin in PBS for 30 min (step 2). The nitrocellulose membranes were rewashed with PBS and then exposed to targeted (biotinylated, $n=6$) or control (nonbiotinylated, $n=6$)

emulsion (75- $\mu\text{l}/\text{ml}$ PBS) for 20 min with mild agitation (step 3). After rewashing the nitrocellulose with PBS, steps 2 and 3 were repeated to ensure more uniform surface coverage. Each nitrocellulose disk was secured in a polystyrene holder for acoustic imaging above a polished stainless steel reflector. The mounted specimen was immersed in isotonic, phosphate buffered saline (pH 7.2–7.4) at room temperature for ultrasonic insonification with the acoustic microscope.

D. Preparation of human plasma clots

Plasma clots ($n=6$) were produced on nitrocellulose by combining human citrated plasma (300 μl) and 100-mM calcium chloride (100 μl) with five units of thrombin in a plastic mould placed on the membranes. The plasma was allowed to coagulate slowly at ambient temperature and the clots were transferred to PBS until exposure to the control or targeted contrast system. Targeted plasma clots ($n=3$) were incubated individually with 150- μg biotinylated antifibrin monoclonal antibody (15- $\mu\text{g}/\text{ml}$ PBS; NIB 1H10)^{29,30} for 2 h at ambient temperature; the remaining control clots ($n=3$) were maintained in PBS with 1% bovine serum albumin. The antibody treated clots were repeatedly washed with PBS, then incubated with 0.5 mg of avidin (50- $\mu\text{g}/\text{ml}$ PBS) for 30 min. After washing excess avidin from the clots in three changes of PBS, fibrin-targeted plasma clots were exposed to the targeted emulsion for 30 min with gentle, continuous agitation. Targeted clots were again washed extensively with PBS and reexposed to avidin and the biotinylated contrast to maximize surface coverage. Control clots were incubated with the nonbiotinylated control emulsion without the ligand-avidin targeting system to assess nonspecific acoustic enhancement. All clots were maintained in PBS until acoustic microscopy was performed.

E. Preparation of whole blood thrombi

Whole blood clots ($n=12$) were produced by combining fresh citrated human blood (300 μl) and 100-mM calcium chloride (100 μl) with five units of thrombin in a plastic mould placed above a nitrocellulose membrane. The plasma was allowed to coagulate slowly at ambient temperature, and the clots were maintained in PBS until exposure to the control or targeted contrast system. Control ($n=6$) and fibrin-targeted ($n=6$) contrast systems were applied in a three-step procedure as previously described for plasma clots.

F. Acoustic microscopy

Acoustic microscopy (Fig. 3) was performed on peptide modified nitrocellulose membranes as well as plasma or whole blood thrombi.³² Ultrasonic imaging was performed with a 25- or 50-MHz nominal center frequency broadband transducer (V324, 0.25-in. diameter, 1-in. point target focus and V309, 0.25-in. diameter, 0.5-in. point target focus, respectively, Panametrics Company, Waltham, MA) operated in a pulse-echo mode. A Tektronix DSA 601 digitizing oscilloscope (Beaverton, OR) was used to digitize backscattered radiofrequency (rf) data at 500 megasamples per second with 8-bit resolution. A variable gain system was used to

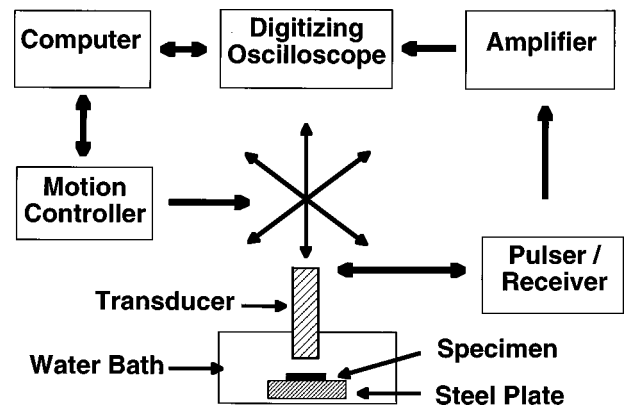


FIG. 3. Schematic of equipment and electronics.

increase the effective dynamic range of the digitizer. The focus of the ultrasonic beam was placed at the front surface of each sample. Preliminary peak detected images of specimen surfaces were acquired to reveal contrast-targeted and control regions. Radiofrequency (rf) data were acquired from the contrast-targeted and nontargeted regions by raster scanning approximately 400 independent sites from each specimen.

Radiofrequency data were stored and analyzed with custom software. A 400-ns Hamming window centered on the front surface of the sample was applied to each rf line. The power spectra of the gated rf lines were computed by fast Fourier transformation and referenced to the power spectrum returned from a near-perfect steel planar reflector.^{33,34} The average bandlimited reflected power was computed in the logarithmic domain from the frequency-dependent reflected power transfer function across the useful bandwidth of the transducer and expressed in decibels relative to the scattering from a polished steel reflector.

G. Statistics

Differences in frequency averaged reflectivity power between control and targeted treatments were statistically analyzed using the Statistical Analysis System software (SAS Institute, Inc., Cary, NC). Control ($n=6$) and targeted ($n=6$) regions of peptide-modified nitrocellulose membranes were compared using paired T -tests. Studies involving plasma and whole blood cell clots were designed and analyzed as randomized complete block, where the block effect was equated with day of study. Differences between means, presented as averages \pm standard error of the mean (SEM), were considered significant at $p < 0.05$.

III. RESULTS

The enhancement of acoustic reflectivity imparted by the targeted perfluorocarbon emulsion system on synthetic (nitrocellulose) and biological surfaces (thrombi) was quantitatively determined using acoustic microscopy. Based on these data, a simple theoretical model was proposed to provide a conceptual and mathematical framework for understanding the basis of the enhanced acoustic reflectivity imparted by this system.

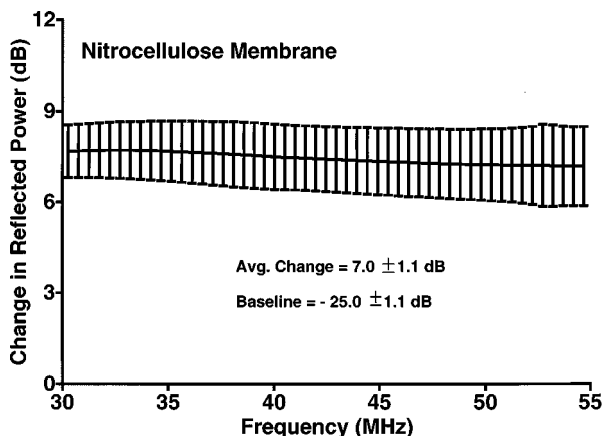


FIG. 4. The change in reflected power from D-dimer coupled membranes following ultrasonic enhancement with D-dimer-targeted contrast system using 50-MHz acoustic microscopy.

1. Nitrocellulose substrate

The change in the reflected power for the front wall specular reflection was determined for both targeted and nontargeted independent regions and their difference as a function of frequency is presented in Fig. 4. The average baseline acoustic reflectivity (\pm SEM) for the nitrocellulose membrane was -25.0 ± 1.1 dB relative to a near perfect (~ 0.5 dB) planar steel reflector. The binding of the D-dimer-targeted contrast system increased the reflected power from the central portion of the membrane by $+7.0 \pm 1.1$ dB to -18.0 ± 0.7 dB ($p < 0.05$).

2. Plasma thrombi

The acoustic enhancement of plasma clots supported on nitrocellulose following treatment with the targeted contrast system was evaluated with acoustic microscopy using anti-human fibrin monoclonal antibodies targeted against *e*-domain epitopes of intact fibrin (Fig. 5). All plasma clots were insonified nominally at 25 MHz. The control plasma clot backscatter exhibited inherently low backscatter although it was 7–10 dB above the noise floor (-75 dB steel plate reflection) of the electronics associated with the experi-

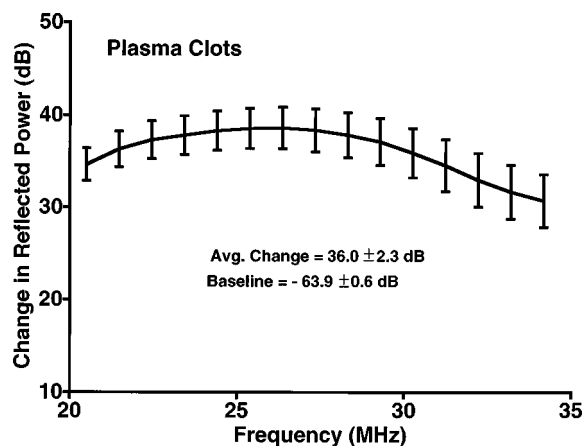


FIG. 5. The change in reflected power from plasma clots following ultrasonic enhancement with a fibrin-targeted contrast system using 25-MHz acoustic microscopy.

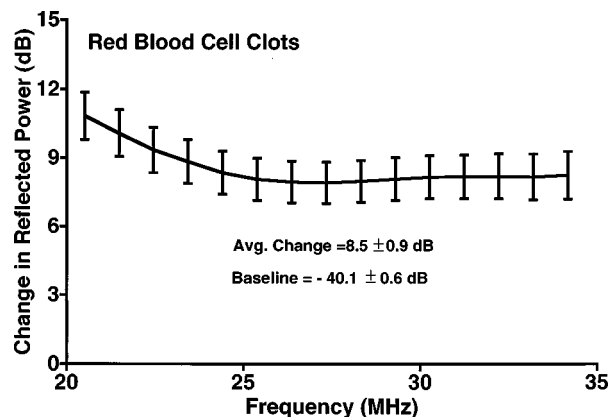


FIG. 6. The change in reflected power from whole blood cell clots following ultrasonic enhancement with a fibrin-targeted contrast system using 25-MHz acoustic microscopy.

mental apparatus. The fibrin-targeted contrast agent increased the frequency averaged reflected power from the plasma clot surface from -63.9 ± 0.6 dB to -27.9 ± 0.2 dB, a change of 36.0 ± 2.3 dB ($p < 0.05$).

3. Red blood cell thrombi

Unlike plasma clots *in vitro*, actual thrombi *in vivo* are cellular and have a higher background acoustic reflectivity (-40.1 ± 0.6 dB). Therefore, whole human blood clots were prepared, treated with the fibrin-targeted contrast system and insonified nominally at 25 MHz in a manner similar to the human plasma clots (Fig. 6). The targeted contrast system significantly increased the acoustic reflectivity of the clot surface 8.5 ± 0.9 dB to -31.6 ± 1.2 dB ($p < 0.05$).

The detailed physics that accounts for the acoustic enhancement imparted by this novel, perfluorocarbon-based, targeted contrast system has not been established. However, using reasonable assumptions, the measured enhancement of the reflectivity observed was consistent with predictions of a simple linear acoustics transmission line model (Table I). In this approach, the reflection coefficient is calculated for a three layer fluid model. The acoustic transmission line model predicted the targeted contrast system would increase the acoustic reflectivity of the nitrocellulose membrane, whole blood clot and fibrin plasma clot by 2.6, 8.0, and 31.8 dB, respectively. These calculations demonstrate reasonable, first-order agreement with our experimentally determined enhancements, i.e., 7.0, 8.5, and 36.0 dB, respectively.

IV. DISCUSSION

Our laboratory has recently demonstrated the first successful *in vivo* application of a ligand-targeted contrast agent. The acoustic agent is a biotinylated, lipid encapsulated, nongaseous perfluorocarbon emulsion which utilizes avidin-biotin interactions to couple a pretargeted biotinylated ligand to the acoustic particle.³⁵ The particle has 1/1000th the volume of a typical microbubble used for perfusion contrast imaging and exhibits low intrinsic echogenicity except when bound to a target or to itself. Since our initial report, other targeted acoustic contrast agents have begun to emerge. A nongaseous, inherently echogenic liposome coupled directly

TABLE I. Summary of acoustic transmission model assumptions and predicted and measured ultrasonic reflectivities.^a

Material	Density (g/cm ³)	Velocity (mm/μs)	Ratio of material to water impedance	Measured baseline reflectivity (dB)	Measured enhanced reflectivity (dB)	Predicted enhanced reflectivity (dB)
Plasma clot	1.01	1.49	1.01	-63.9±0.6	-27.9±0.2	-32.1±1.4
RBC clot ^b	1.01	1.49	1.01	-40.1±0.6	-31.6±1.2	-32.1±1.4
Nitrocellulose	1.12	1.49	1.12	-25.0±1.1	-18.0±0.7	-22.4±0.5
Water	1.00	1.49	1.00	NA ^d	NA	NA
PFDCO ^c	1.80	0.60	0.72	NA	NA	NA

^aLayer thickness=250 nm.

^bRBC=red blood cell.

^cPFDCO=perfluorodichlorooctane.

^dNA=not applicable.

to monoclonal antibodies and demonstrated to bind targeted molecular epitopes, *in vitro* and *in vivo* (when administered directly upstream of the target) has been reported.³⁶ Commercial pharmaceutical companies currently developing perfusional microbubble formulations have begun to modify their perfusional agents for targeted applications. McCreey *et al.*³⁷ recently reported a stabilized liposomal microbubble which has been modified to utilize a RGD domain for targeting thrombi. Klivanov *et al.*³⁸ has also reported the development of a similar, stabilized lipid microbubble which utilizes avidin-biotin interactions.

In the present study, we have described the use of acoustic microscopy to assess the acoustic reflectivity enhancement created by targeted contrast agents bound to a variety of substrates, including thrombi created *in vitro*. Acoustic microscopy provides a stable system for evaluating the efficacy of contrast agents and for potentially comparing the utility of different targeting antibodies or formulation changes. Such studies may be performed relatively rapidly and with very modest expenditures for formulation materials and monoclonal antibodies.

In general, the specificity and dissociation constants of the various monoclonal antibody ligands commercially produced are well known. The dissociation constant for avidin-biotin is well known ($k_d = 10^{-15} M$); But the distribution of targeted epitopes along biological tissue surfaces and planes is unknown. The proposed acoustic microscopy method provides a unique opportunity to assess the distribution of molecular epitopes over a biological surface. Each step of the acoustic contrast system (antibody, avidin, and emulsion) is applied in excess in order to saturate all binding sites and maximize acoustic signal. If the selected epitope has inadequate surface density and/or distribution to provide efficacious surface coverage with the contrast agent, then combinations of targeted markers may be considered to increase the number of binding sites and improve acoustic enhancement. Performing these studies *in vitro* provides a relatively inexpensive and rapid approach to screen potential targeting ligand systems before progressing to complicated *in vivo* models.

Our targeted ultrasonic contrast agent has demonstrated a remarkable versatility to significantly enhance the reflectivity of substrates with both high and low inherent acoustic

reflectivity. The magnitude of acoustic enhancement was greatest when the inherent echogenicity of the substrate was very low, as for the plasma clots, and least when the inherent acoustic reflectivity of the substrate was high. Since the integrated backscatter from normal tissues at similar frequencies to those used in this study is approximately -45 to -55 dB below a planar steel reflector,^{24,39} these data suggest that targeted pathologic tissues could be enhanced around 8.5 dB for a 250-nm single layer application. For multi-layered tissues with increased effective layer thickness, such as neovasculature capillary beds in solid tumors, the targeted contrast system would be expected to increase the overall reflected signal more.

Quantification of the acoustic reflectivity created by the targeted contrast system and measured from specific substrates is consistent with the physical mechanism of a simple acoustic transmission line model. The enhanced acoustic reflectivity predicted by this model appears to provide a reasonable first-order approximation to the experimental results reported in this study. The modest differences between predicted and experimental results reflect, in part, our lack of specific knowledge of both the spatial distribution of the targeted contrast agent over the targeted surface as well as the true acoustic properties of the substrate. The hypothesized layer model is simple and, if substantially correct, suggests that careful selection of the emulsified perfluorocarbon's sound velocity and/or density⁴⁰ may enhance the magnitude of acoustic reflectivity. Furthermore, the layer model implies that the aggregation and concentration of contrast particles might be best described as a reflective surface. Careful consideration must be paid to the distribution of molecular epitopes and tissues in order to generate an effectively smooth and reflective contrast surface layer(s). Because the acoustic transmission line model predicts a frequency independent increase in reflectivity, contrast agents that are well described by this model should be useful at clinical imaging frequencies as well. We have observed this qualitatively in our laboratory.⁵

In the case of red blood cell thrombi, the contrast agent was targeted to the *e*-domain epitopes of fibrin which created a loosely interwoven network entrapping the cellular elements of blood, predominantly erythrocytes. Since erythrocytes are 6–8 μm in diameter and the contrast particles are

250 nm in diameter, heterogeneous contrast enhancement was noted with both high frequency acoustic microscopy and previously with routine echocardiography. The acoustic transmission line model implicitly suggests that the best acoustic enhancement will occur when the the alignment of bound contrast particles approximates a continuous layer. Thus the tight fibrin network of arterial thrombi (i.e., "white clots") which have a platelet predominance and a paucity of erythrocytes would have better acoustic enhancement than venous thrombi (i.e., "red clots") which have a loose fibrin architecture interspersed with red blood cells. In this manner, the acoustic transmission line model provides an intellectual framework for systematically selecting, designing, and improving targeted contrast systems.

Several limitations of the current work will be addressed in future reports. Quantitative acoustic microscopy and the acoustic transmission line model has furthered our understanding of targeted perfluorocarbon contrast agents, but more refined studies are required to confirm and refine the model. In particular, several reasonable assumptions required to obtain predicted estimates of acoustic reflectivity will require formal, experimentally derived confirmation.

Although the methodologies described represent a valuable adjunct in the development of our nongaseous, perfluorocarbon contrast system, these approaches may have limitations for other contrast systems. Principally, the sensitivity of typical microbubbles to the preparation steps or to the sound pressures involved with routine scanning is unclear and untested in our laboratory.

V. SUMMARY

In summary, *in vitro* techniques that facilitate the rapid and inexpensive development and deployment of novel, nongaseous, perfluorocarbon-based, targeted acoustic contrast systems have been developed. The methods rely on the use of acoustic microscopy and allow development of targeted contrast systems and/or their components *in vitro*. The degree of acoustic enhancement expected *in vivo* relative to the inherent echogenicity of the target tissue may be estimated by these *in vitro* studies as well as by means of a simple acoustic transmission line model. The data suggest that a nongaseous, perfluorocarbon contrast system can improve the acoustic reflectivity of biological and synthetic surfaces that differ broadly in their intrinsic echogenicities. Thus this contrast agent appears to possess broad functionality against pathological tissues of key concern to the medical community.

ACKNOWLEDGMENTS

We thank Dr. Tracey A. Edgell and Dr. Sanj Raut at the National Institute for Biological Standards and Control, U.K. for assistance in purification and preparation of the biotinylated antifibrin monoclonal antibodies. This work was supported by Grant No. HL-59865. Dr. Wickline is an Established Investigator of the American Heart Association, Dallas, TX. Dr. Lanza is an American Heart Association, Missouri Affiliate Fellow.

- ¹R. Gramiak and P. Shah, "Echocardiography of the aortic root," *Invest. Radiol.* **3**, 356–366 (1968).
- ²H. Bleeker and K. Shung, "Ultrasonic characterization of Albunex[®], a new contrast agent," *J. Acoust. Soc. Am.* **87**, 1792–1797 (1990).
- ³N. De Jong, F. Ten Cate, C. Lancée, J. Roelandt, and N. Bom, "Principles and recent developments in ultrasound contrast agents," *Ultrasonics* **29**, 324–330 (1991).
- ⁴S. Feinstein, "New developments in ultrasonic contrast techniques: Transpulmonary passage of contrast agent and diagnostic implications," *Echocardiography* **6**, 27–33 (1989).
- ⁵G. Lanza, K. Wallace, M. Scott, W. Cacheris, D. Abendschein, D. Christy, A. Sharkey, J. Miller, P. Gaffney, and S. Wickline, "A novel site-targeted ultrasonic contrast agent with broad biomedical application," *Circulation* **94**, 3334–3340 (1996).
- ⁶D. Christy, K. Wallace, G. Lanza, M. Holland, C. Hall, M. Scott, W. Cacheris, P. Gaffney, J. Miller, and S. Wickline, "Quantitative intravascular ultrasound: demonstration using a novel site targeted acoustic contrast agent," *Proc. IEEE Ultrason. Symp.* **95CH35844**, 1125–1128 (1995).
- ⁷G. Lanza, K. Wallace, D. Abendschein, M. Scott, C. Sheehan, W. Cacheris, D. Christy, A. Sharkey, J. Miller, P. J. Gaffney, and S. Wickline, "Specific acoustic enhancement of vascular thrombi *in vivo* with a novel site targeted ultrasonic contrast agent," *Circulation* **92**, (Suppl. I), I-260 (1995).
- ⁸G. Lanza, K. Wallace, M. Scott, C. Sheehan, W. Cacheris, D. Christy, A. Sharkey, J. Miller, and S. Wickline, "Initial description and validation of a novel site targeted ultrasonic contrast agent," *Circulation* **92**, (Suppl. I), I-260 (1995).
- ⁹G. Lanza, K. Wallace, D. Abendschein, R. Trousil, M. Scott, C. Sheehan, J. Miller, P. Gaffney, and S. Wickline, "Acoustic enhancement of arterial thrombi *in vivo* following intravenous injection," *Circulation* **94**, (Suppl. I), I-319 (1996).
- ¹⁰G. Lanza, K. Wallace, J. Miller, and S. Wickline, "Development of a novel site-targeted ultrasonic contrast agent" in *Advances in Echo Imaging Using Contrast Enhancement*, edited by N. Nanda, R. Schlieff, and B. Goldberg (Kluwer Academic, Dordrecht, 1996).
- ¹¹K. Wallace, G. Lanza, M. Scott, M. Holland, D. Christy, C. Sheehan, W. Cacheris, P. Gaffney, J. Miller, and S. Wickline, "Intravascular ultrasound detection of thrombi after enhancement with a novel site targeted acoustic contrast agent," *Circulation* **92**, (Suppl. I), I-585 (1995).
- ¹²L. Kessler, A. Korpel, and P. Palermo, "Simultaneous acoustic and optical microscopy of biological specimens," *Nature (London)* **239**, 111–112 (1972).
- ¹³L. Kessler, S. Fields, and F. Dunn, "Acoustic microscopy of mammalian kidney," *J. Clin. Ultrasound* **2**(4), 317–320 (1974).
- ¹⁴J. Hildebrand, D. Rugar, R. Johnston, and C. Quate, "Acoustic microscopy of living cells," *Proc. Natl. Acad. Sci. USA* **78**, 1656–1660 (1981).
- ¹⁵R. Johnston, A. Atalar, J. Heiserman, V. Jipson, and C. Quate, "Acoustic microscopy: Resolution of subcellular detail," *Proc. Natl. Acad. Sci. USA* **76**, 3325–3329 (1979).
- ¹⁶D. Rugar, J. Heiserman, S. Minden, and C. Quate, "Acoustic microscopy of human metaphase chromosomes," *J. Microsc.* **120**, 193–199 (1980).
- ¹⁷J. Hildebrand and D. Rugar, "Measurement of cellular elastic properties by acoustic microscopy," *J. Microsc.* **134**, 245–260 (1984).
- ¹⁸K. Kameyama and G. Asano, "Evaluation of elastic structural change in coronary atherosclerosis using scanning acoustic microscopy," *Atherosclerosis* **94**(2-3), 191–200 (1992).
- ¹⁹J. Katz and A. Meunier, "Scanning acoustic microscope studies of the elastic properties of osteons and osteon lamellae," *J. Biomech. Eng.* **115**, 543–548 (1993).
- ²⁰W. O'Brien, Jr., J. Olerud, K. Shung, and J. Reid, "Quantitative acoustical assessment of wound maturation with acoustic microscopy," *J. Acoust. Soc. Am.* **69**, 575–579 (1981).
- ²¹R. Waag, P. Lee, H. Persson, E. Schenk, and R. Gramiak, "Frequency-dependent angle scattering of ultrasound by liver," *J. Acoust. Soc. Am.* **72**, 343–352 (1982).
- ²²R. K. Shepard, J. G. Miller, and S. A. Wickline, "Quantification of atherosclerotic plaque composition in cholesterol-fed rabbits with 50-Mhz acoustic microscopy," *Arterioscler. Thromb.* **12**, 1227–1234 (1992).
- ²³A. Wong, T. Osborn, J. Miller, and S. Wickline, "Quantification of ventricular remodeling in the tight-skin mouse cardiomyopathy with acoustic microscopy," *Ultrasound Med. Biol.* **19**, 365–374 (1993).
- ²⁴G. Davison, C. Hall, J. Miller, M. Scott, and S. Wickline, "Cellular

- mechanisms of captopril-induced matrix remodeling in Syrian hamster cardiomyopathy," *Circulation* **90**, 1334–1342 (1994).
- ²⁵G. Davison, C. Hall, J. Miller, M. Scott, and S. Wickline, "Ultrasonic tissue characterization of end-stage dilated cardiomyopathy," *Ultrasound Med. Biol.* **21**, 853–860 (1995).
- ²⁶D. Recchia, A. Sharkey, M. Bosner, N. Kouchoukos, and S. Wickline, "Sensitive detection of abnormal aortic architecture in Marfan syndrome with high-frequency ultrasonic tissue characterization," *Circulation* **91**, 1036–1043 (1995).
- ²⁷P. Morse and K. Ingard, "Acoustic transmission lines," in *Theoretical Acoustics* (Princeton U. P., Princeton, NJ, 1986), pp. 467–491.
- ²⁸F. Lee, G. Boniface, R. Lambrecht, D. Rylatt, and P. Bundesen, "Technetium-99 m labelling of DD-3B6/22 antifibrin monoclonal antibody fragment Fab' for thrombus imaging," *Immunol. Cell Biol.* **71**(Pt. 2), 117–124 (1993).
- ²⁹S. Raut and P. Gaffney, "Evaluation of fibrin binding profile of two antifibrin monoclonal antibodies," *Thromb. Haemostasis* **76**, 56–64 (1996).
- ³⁰T. Edgell, F. McEnvoy, P. Webbon, and P. Gaffney, "Monoclonal antibodies to human fibrin: interaction with other animal fibrins," *Thromb. Haemostasis* **75**, 595–599 (1996).
- ³¹M. Masson, E. Lauritzen, and A. Holm, "Chemical activation of nitrocellulose membranes for peptide antigen-antibody binding studies: direct substitution of the nitrate group with diaminoalkane," *Electrophoresis* **14**, 860–865 (1993).
- ³²A. Wong, E. Verdonk, B. Hoffmeister, J. Miller, and S. Wickline, "Detection of unique transmural architecture of human idiopathic cardiomyopathy by ultrasonic tissue characterization," *Circulation* **86**, 1108–1115 (1992).
- ³³S. Wickline, E. Verdonk, and J. Miller, "Quantification of the transmural shift of myofiber orientation in normal human hearts with ultrasonic integrated backscatter," *J. Clin. Invest.* **88**, 438–446 (1991).
- ³⁴S. Wickline, E. Verdonk, B. Sobel, and J. Miller, "Identification of human myocardial infarction in vitro based on the frequency dependence of ultrasonic backscatter," *J. Acoust. Soc. Am.* **91**, 3018–3025 (1992).
- ³⁵G. Paganelli, P. Magnani, F. Zito, E. Villa, F. Sudati, L. Lopalco, C. Rossetti, M. Malcovati, F. Chiolerio, E. Seccamani, and F. Fazio, "Three-step monoclonal antibody tumor targeting in carcinoembryonic antigen-positive patients," *Cancer Res.* **51**, 5960–5966 (1991).
- ³⁶S. Demos, K. Ramani, B. Kane, R. Greene, A. Nagara, H. Alkan-Onyuksel, D. McPherson, and M. Klegerman, "Targeted acoustic liposomes for atherosclerotic enhancement during intravascular and transvascular ultrasonic imaging," *Circulation* **94**, I-209 (1996).
- ³⁷T. McCreery, R. Sweitzer, G. Wu, D. Shen, D. Yellowhair, and E. Unger, "Targeted ultrasound contrast agents for detection of thrombosis," *Circulation* **94**, (Suppl. I), I-654 (1996).
- ³⁸A. Klivanov, M. Hughes, J. Marsh, C. Hall, J. Miller, J. Wible, and G. Brandenburger, "Targeting of ultrasound contrast material: An *in vitro* feasibility study," *Acta Radiol.* **38**(Suppl. 412), 113–120 (1997).
- ³⁹G. Lanza, M. Scott, G. Davison, C. Hall, D. Christy, J. Miller, and S. Wickline, "Angiotensin II receptor blockade in Syrian hamster (TO-2) cardiomyopathy does not affect microscopic cardiac material properties: implications for mechanisms of tissue remodeling," *Cardiovasc. Drugs Ther.* **11**(4), 521–529 (1997).
- ⁴⁰C. Hall, J. Rose, R. Kaufman, R. Fuhrhop, S. Handley, K. Waters, and S. Wickline, "Experimental determination of phase velocity of perfluorocarbons: Applications to targeted contrast agents," edited by S. Schneider, M. Levy, and B. McAvoy (Institute of Electrical and Electronic Engineers, Ontario, Canada, 1997), Vol. 97ch36118, pp. 1605–1608.

LETTERS TO THE EDITOR

This Letters section is for publishing (a) brief acoustical research or applied acoustical reports, (b) comments on articles or letters previously published in this Journal, and (c) a reply by the article author to criticism by the Letter author in (b). Extensive reports should be submitted as articles, not in a letter series. Letters are peer-reviewed on the same basis as articles, but usually require less review time before acceptance. Letters cannot exceed four printed pages (approximately 3000–4000 words) including figures, tables, references, and a required abstract of about 100 words.

Does hearing aid benefit increase over time?

Christopher W. Turner and Ruth A. Bentler

Department of Speech Pathology and Audiology, The University of Iowa, Iowa City, Iowa 52242

(Received 5 May 1998; accepted for publication 21 August 1998)

In a recent tutorial for the journal, Palmer *et al.* [J. Acoust. Soc. Am. **103**, 1705–1721 (1998)] reviewed the literature on the potential for increases in hearing aid benefit over time (acclimatization). Their review might leave some readers with the impression that acclimatization has implications for the fitting and selection of hearing aids today. We (Turner and Bentler), along with two other researchers in the field (Humes and Cox), conducted a similar review of the literature a few years earlier [Turner *et al.*, *Ear and Hearing* **17**, 14S–28S (1996)] and found little evidence of a robust effect. The bulk of the existing evidence, including the most recent studies on this topic, support earlier conclusions, i.e., that there is no evidence for the existence of a strong acclimatization effect in current hearing aid use. © 1998 Acoustical Society of America. [S0001-4966(98)01712-3]

PACS numbers: 43.10.Ln, 43.66.Ts, 43.66.Ba, 43.64.Bt [JWH]

Clinical audiologists and hearing aid manufacturers, as well as patients themselves, would be greatly pleased if one could say with confidence that the benefit received by a patient arising from a newly fitted hearing aid would improve over time. Such an increase in hearing aid benefit over time has been termed “acclimatization” or “auditory learning.” This increase in measured benefit over time would be the result of an improvement in auditory capabilities following the provision of hearing aid amplification. These acclimatization effects must be separated from any task-specific learning involved in the measurement procedures, such as learning to take a test. In their recent review of this topic, Palmer *et al.* (1998, p. 1718) state that “...data in each area support the notion of auditory learning...” They also state that the extent and rate of the effect is unclear at this time. Unfortunately, only a small or nonexistent extent and rate of acclimatization has been reported in the numerous published studies to date. This view is explained in considerable detail in Turner *et al.* (1996). The four most recent studies with large numbers of subjects (Humes *et al.*, 1997; Saunders and Cienkowski, 1997; Holte, 1997; Neuman, 1997) failed to show any increase in hearing aid benefit over time. It would seem that if acclimatization was an important and strong effect upon current clinical practices, the evidence for it would be much clearer.

In each of the numerous studies (at least 18) on this topic, subjects were people who normally use hearing aids, and therefore their results should generalize to the hearing aid user population as a whole. The experiments typically

measured speech recognition using syllable, word or sentence lists at several intervals following the initial fitting of the hearing aid, and examined if the scores increased over time. Palmer *et al.* (1998) do not comment on the size of the effect and the variability across and within subjects. This is an unfortunate omission, as the casual reader of that review might mistakenly conclude that acclimatization is sometimes a robust effect and that the various studies reviewed in the tutorial found very different results. The overwhelming characteristic of the data obtained in all the studies is that the size of the increase was very small (0–7 percentage points) in speech recognition score. The standard deviation across subjects was at best equal to the size of the effect and more typically many times as large as the effect. Thus some subjects in these experiments actually showed “decreases” in hearing aid benefit over time. Within-subject variability for speech recognition testing is dependent upon the number of test items, and to state with confidence that improvement of a few percent does or does not occur in an individual subject would require many hundreds of test items. For example, to show an improvement of 7 percentage points in a typical patient would require over 600 independent test items; smaller improvements would require even longer lists. Thus individual acclimatization, if it occurs, would be difficult to demonstrate, requiring large experiments with many subjects and long test sessions in order to find a small effect. And when one attempts to measure a small effect with large variability, it is not surprising that studies with small numbers of subjects can show different results. The simplest explanation

of the data as a whole is that the effects to be measured are small or nonexistent and that the measurements are obscured by large variability. Even if confounding sources of variability were tightly controlled, one would not expect the mean values obtained in the studies to show an increase. And if such factors as task-specific learning, which might be confused with acclimatization, were eliminated, one might expect any observed increases in hearing aid benefit over time to be even smaller.

Certainly it is impossible for us to prove the null hypothesis, i.e., that acclimatization does not occur for hearing aid use, and no one can know if acclimatization will occur for new signal-processing hearing aids that have not yet been invented. Nonetheless, the massive amounts of evidence collected so far indicate that as of today, either it does not occur, or if it does, it is so small that it is very hard to measure. While it is possible that experimental circumstances could be designed that might maximize measured acclimatization effects, these kinds of situations may not be realistic for current hearing aid users. If acclimatization only exists under unrealistic conditions (if it exists at all), then it may have little relevance to hearing aid manufacturing and dispensing.

In summary, the recent review of Palmer *et al.* (1998) may mislead some researchers, clinicians, and hearing aid manufacturers by suggesting that hearing aid benefit may increase over time in a manner that has consequences for

today's hearing aids. When the small or nonexistent magnitude of the acclimatization effect is considered, we feel that the review of Palmer *et al.* (1998) should not be taken casually as support for the importance of acclimatization in hearing aid use. The literature to date is very clear on one aspect of acclimatization. It is a small effect at best. If the increase in hearing aid benefit over time cannot be reliably demonstrated in typical hearing aid users under normal circumstances (albeit under controlled conditions) in nearly 20 studies to date, then the most logical conclusion for the hearing and audiology community is that it is not a large or important effect.

- Holte, L. (1997). "Acclimatization in hearing aids," presented at the Iowa City Hearing Aid Conference, Iowa City, IA (unpublished).
- Humes, L. E., Halling, D., and Coughlin, M. (1996). "Reliability and stability of various hearing-aid outcome measures in a group of elderly hearing aid users," *J. Speech Hear. Res.* **39**, 923-935.
- Neuman, A. C. (1997). "Acclimatization to hearing aids," presented at the Second Biennial Hearing Aid Research and Development Conference, NIDCD and DVA, Bethesda, Maryland (unpublished).
- Palmer, C. V., Nelson, C. T., and Lindley, G. A. (1998). "The functionally and physiologically plastic adult auditory system," *J. Acoust. Soc. Am.* **103**, 1705-1721.
- Saunders, G. H., and Cienkowski, K. M. (1997). "Acclimatization to hearing aids," *Ear and Hearing* **18**, 129-139.
- Turner, C. W., Humes, L. E., Bentler, R. A., and Cox, R. M. (1996). "A review of the literature on hearing aid benefit as a function of time," *Ear and Hearing* **17**, 14S-28S.

Representation of the displacement in terms of scalar functions for use in transversely isotropic materials

A. Rahman and F. Ahmad

Department of Mathematics, Quaid-i-Azam University, Islamabad, Pakistan

(Received 29 May 1998; revised 22 July 1998; accepted 20 August 1998)

Comments are presented on two recent papers [J. Acoust. Soc. Am. **96**, 2546 (1994), J. Acoust. Soc. Am. **100**, 57 (1996)]. Their results can be obtained with much economy of work by employing an alternative representation for the decomposition of the displacement. This decomposition is useful whenever transversely isotropic materials are being studied. © 1998 Acoustical Society of America. [S0001-4966(98)00712-7]

PACS numbers: 43.20.Ks, 43.20.Tb, 43.40.Cw [ANN]

INTRODUCTION

Recently Honarvar and Sinclair,¹ subsequently referred to as HS, have studied scattering of an acoustic wave from a cylinder of transversely isotropic material immersed in a fluid. They have generalized earlier work of Faran² and Flax *et al.*³ on scattering from isotropic cylinders. B. Zhang, H. Dong, and K. Wang,⁴ subsequently referred to as ZDW, have studied the acoustic field excited by multipole sources in a fluid-filled borehole surrounded by a transversely isotropic elastic solid.

In this short note we wish to comment on the representation of the displacement in terms of scalar functions used by HS and ZDW. We suggest an alternative representation which produces simpler equations, although it leads to the same final results. Our purpose is to bring to the notice of workers dealing with transverse isotropy, a representation which is very useful, has been present in the literature for a long time, but seems to have been overlooked by researchers who have done recent work in this field.

I. REPRESENTATION OF THE DISPLACEMENT

HS and ZDW have decomposed the displacement \mathbf{u} in terms of three potential functions φ , ψ , and χ in the following manner:

$$\mathbf{u} = \nabla\varphi + \nabla \times (\chi \hat{e}_z) + a \nabla \times \nabla \times (\psi \hat{e}_z). \quad (1)$$

In cylindrical coordinates, the above representation implies

$$U_r = \frac{\partial\varphi}{\partial r} + \frac{1}{r} \frac{\partial\chi}{\partial\theta} + a \frac{\partial^2\psi}{\partial r \partial z}, \quad (2a)$$

$$U_\theta = \frac{1}{r} \frac{\partial\varphi}{\partial\theta} - \frac{\partial\chi}{\partial r} + \frac{a}{r} \frac{\partial^2\psi}{\partial\theta \partial z}, \quad (2b)$$

$$U_z = \frac{\partial\varphi}{\partial z} - a \left(\frac{\partial^2\psi}{\partial r^2} + \frac{1}{r} \frac{\partial\psi}{\partial r} + \frac{1}{r^2} \frac{\partial^2\psi}{\partial\theta^2} \right). \quad (2c)$$

When U_r , U_θ , and U_z are substituted in the equation of motion for \mathbf{u} , the following equations result for the potential functions φ , ψ , and χ . These are Eqs. (12)–(14) of HS and Eqs. (6) of ZDW. These are reproduced here for comparison with Eqs. (6) of the present note:

$$\left(\nabla^2 - \frac{\partial^2}{\partial z^2} \right) \left[c_{11} \nabla^2 \varphi + (c_{13} + 2c_{44} - c_{11}) \frac{\partial^2 \varphi}{\partial z^2} - \rho_c \frac{\partial^2 \varphi}{\partial t^2} \right. \\ \left. + a \frac{\partial}{\partial z} \left\{ (c_{11} - c_{13} - c_{44}) \nabla^2 \psi + (c_{13} + 2c_{44} - c_{11}) \frac{\partial^2 \psi}{\partial z^2} \right. \right. \\ \left. \left. - \rho_c \frac{\partial^2 \psi}{\partial t^2} \right\} \right] = 0, \quad (3a)$$

$$\frac{\partial}{\partial z} \left\{ (c_{13} + 2c_{44}) \nabla^2 \varphi + (c_{33} - c_{13} - 2c_{44}) \frac{\partial^2 \varphi}{\partial z^2} - \rho_c \frac{\partial^2 \varphi}{\partial t^2} \right\} \\ + a \left(\frac{\partial^2}{\partial z^2} - \nabla^2 \right) \left\{ c_{44} \nabla^2 \psi + (c_{33} - c_{13} - 2c_{44}) \frac{\partial^2 \psi}{\partial z^2} \right. \\ \left. - \rho_c \frac{\partial^2 \psi}{\partial t^2} \right\} = 0, \quad (3b)$$

$$\left(\nabla^2 - \frac{\partial^2}{\partial z^2} \right) \left\{ \frac{c_{11} - c_{12}}{2} \nabla^2 \chi + \left(c_{44} - \frac{c_{11} - c_{12}}{2} \right) \frac{\partial^2 \chi}{\partial z^2} \right. \\ \left. - \rho_c \frac{\partial^2 \chi}{\partial t^2} \right\} = 0. \quad (3c)$$

If an alternative representation for \mathbf{u} is used, the resulting equations, i.e., the counterparts of Eqs. (2) and (3) above, are much simplified. This representation was first used by Buchwald⁵ and has also been employed by others.^{6,7} The displacement is decomposed in the following manner:

$$\mathbf{u} = \nabla\varphi + \nabla \times (\chi \hat{e}_z) + \left(\frac{\partial\psi}{\partial z} - \frac{\partial\varphi}{\partial z} \right) \hat{e}_z. \quad (4)$$

The components of \mathbf{u} , in cylindrical polar coordinates, are

$$U_r = \frac{\partial\varphi}{\partial r} + \frac{1}{r} \frac{\partial\chi}{\partial\theta}, \quad (5a)$$

$$U_\theta = \frac{1}{r} \frac{\partial\varphi}{\partial\theta} - \frac{\partial\chi}{\partial r}, \quad (5b)$$

$$U_z = \frac{\partial\psi}{\partial z}. \quad (5c)$$

A comparison of Eqs. (2) and (5) indicates that the Buchwald representation (4) as contrasted with (1) will lead to much economy of labor. A distinct advantage of Eqs. (5) is that

they contain derivatives of only the first order. We find that the Buchwald representation also accomplishes the desired goal of separating the *SH* wave from the rest of the displacement. The resulting equations are

$$c_{11} \left(\nabla^2 - \frac{\partial^2}{\partial z^2} \right) \varphi + c_{44} \frac{\partial^2 \varphi}{\partial z^2} + (c_{13} + c_{44}) \frac{\partial^2 \psi}{\partial z^2} - \rho_c \frac{\partial^2 \varphi}{\partial t^2} = 0, \quad (6a)$$

$$(c_{13} + c_{44}) \left(\nabla^2 - \frac{\partial^2}{\partial z^2} \right) \varphi + c_{44} \left(\nabla^2 - \frac{\partial^2}{\partial z^2} \right) \psi + c_{33} \frac{\partial^2 \psi}{\partial z^2} - \rho_c \frac{\partial^2 \psi}{\partial t^2} = 0, \quad (6b)$$

$$\frac{1}{2} (c_{11} - c_{12}) \left(\nabla^2 - \frac{\partial^2}{\partial z^2} \right) \chi + c_{44} \frac{\partial^2 \chi}{\partial z^2} - \rho_c \frac{\partial^2 \chi}{\partial t^2} = 0. \quad (6c)$$

A comparison of Eqs. (3) and (6) indicates that representation (4) has indeed produced simpler equations.

The two representations lead to identical characteristic equations. We assume

$$\varphi = \sum_{n=0}^{\infty} B_n J_n(sr) \cos(n\theta) \exp\{i(k_z z - \omega t)\}, \quad (7a)$$

$$\psi = \sum_{n=0}^{\infty} C_n J_n(sr) \cos(n\theta) \exp\{i(k_z z - \omega t)\}, \quad (7b)$$

$$\chi = \sum_{n=0}^{\infty} D_n J_n(sr) \sin(n\theta) \exp\{i(k_z z - \omega t)\}. \quad (7c)$$

Substitution of (7a) and (7b) in Eqs. (3a) and (3b) leads to the following characteristic equation;

$$s^2(s^2 + k_z^2)(c_{11}c_{44}s^4 - \xi s^2 + \zeta) = 0,$$

where ξ and ζ have been defined in HS, Eqs. (20) and (21). HS and ZDW have dropped the factors s^2 and $s^2 + k_z^2$ to obtain

$$c_{11}c_{44}s^4 - \xi s^2 + \zeta = 0. \quad (8)$$

However, when we substitute (7a) and (7b) in Eqs. (6a) and (6b), Eq. (8) immediately results. An advantage of the Buchwald representation is that it does not lead to extraneous factors.

Finally we remark that the Buchwald representation gives simplified expressions for the matrix elements defined in Eq. (36) of HS and Eq. (9) of ZDW.

¹F. Honarvar and A. N. Sinclair, *J. Acoust. Soc. Am.* **100**, 57 (1996).

²J. J. Faran, *J. Acoust. Soc. Am.* **23**, 405 (1951).

³L. Fax, V. K. Varadan, and V. V. Varadan, *J. Acoust. Soc. Am.* **68**, 1832 (1980).

⁴B. Zhang, H. Dong, and K. Wang, *J. Acoust. Soc. Am.* **96**, 2546 (1994).

⁵V. T. Buchwald, *Q. J. Mech. Appl. Math.* **14**, 293 (1961).

⁶P. Chadwick and L. T. C. Seet, *Mathematika* **17**, 255 (1970).

⁷F. Ahmad and A. Rahman, submitted for publication to *Int. J. Eng. Sci.*

Response to “Representation of the displacement in terms of scalar functions for use in transversely isotropic materials” [J. Acoust. Soc. Am. 104, 3675 (1998)]

F. Honarvar

K. N. Toosi University of Technology, P.O. Box 16765-3381, Tehran 16579, Iran

A. N. Sinclair

Mechanical and Industrial Engineering, University of Toronto, Toronto, Ontario M5S 3G8, Canada

(Received 8 July 1998; accepted for publication 20 August 1998)

The authors comment on Rahman and Ahmad’s discussion on the representation of displacement fields by scalar potential functions. © 1998 Acoustical Society of America.

[S0001-4966(98)00812-1]

PACS numbers: 43.20.Ks [ANN]

Rahman and Ahmad have reminded us of Buchwald’s solution to problems involving transversely isotropic materials. While we acknowledge the simpler form of Buchwald’s solution, we would like to mention the reason we chose the more difficult approach¹ despite our awareness of simpler ones.

We had not completely overlooked Buchwald’s approach, and a rather simpler version of it, used by Mirsky, is referenced in our paper. We think that in Buchwald’s approach the physical meaning of the potential functions is sacrificed for the sake of mathematical simplicity. The potential functions ϕ , ψ , and χ used in our solution each have a

physical (acoustical) meaning. They represent P , SH , and SV waves, respectively. This makes the interpretation of results easier and allows one to investigate the effect of each type of wave separately in the mathematical model. This physical meaning does not seem to exist for all three potential functions used in Buchwald’s solution.

Therefore, while we acknowledge the correctness and simpler form of Buchwald’s approach, we still believe that our solution has a stronger physical basis.

¹F. Honarvar and A. N. Sinclair, “Acoustic wave scattering from transversely isotropic cylinders,” *J. Acoust. Soc. Am.* **100**, 57–63 (1996).

Observation of flexural Lamb waves (A_0 mode) on water-filled cylindrical shells

J. D. N. Cheeke, X. Li, and Z. Wang

Department of Physics, Concordia University, Montreal, Quebec, H3G 1M8 Canada

(Received 15 February 1998; accepted for publication 22 August 1998)

Results are presented for the propagation of circumferential acoustic waves around a thin-walled stainless steel tube. Sol gel lead titanate-zirconate (PZT) films and chirp interdigital transducer (IDT) electrodes were used to generate the A_0 mode from 0.8 to 6.0 MHz. Group and phase velocity measurements are in good agreement with the theory for the empty tube. When the tube is filled with water a large decrease of 21% in group velocity is observed. While there is as yet no theoretical explanation for this effect, the results show promise for liquid sensing applications. © 1998 Acoustical Society of America. [S0001-4966(98)00612-2]

PACS numbers: 43.40.Dx [CBB]

INTRODUCTION

There have been many theoretical¹⁻⁵ and experimental⁶⁻¹¹ studies of circumferential elastic waves in cylindrical shells immersed in a liquid, mostly in the context of underwater acoustics. In analogy with the case of a thin plate, the theoretically possible circumferential modes are Lamb type (A_0 and S_0) and Scholte–Stoneley type (**A** and **S**). A major concern of this previous work has been the identification of the modes corresponding to the observed echoes or resonances in a particular experimental configuration.

Talmant *et al.*⁶⁻⁸ irradiated thin cylindrical shells immersed in water with short acoustic pulses and measured group velocities of waves circumnavigating the cylinder. A “fast” wave was identified as being S_0 while a “slow” wave was associated with a Scholte interface wave **A**. The A_0 mode was not observed, the reason given being that radiation damping is much stronger for this mode. A third weak circumferential mode with a group velocity of 2450 m/s was observed but not identified. Izbicki *et al.*⁹⁻¹¹ used a different geometry where the transducer was placed on the inside wall of an empty cylindrical shell and the receiving transducer was placed in the liquid. The results were compatible with those of Talmant *et al.* for excitation external to the tube; S_0 and **A** modes were observed but no A_0 mode was identified.

In the present work we have used a different experimental configuration which is complementary to those mentioned above. A chirp interdigital transducer (IDT) was placed on the outer surface of a water-filled tube. This allowed scanning over a wide frequency range under constant conditions in the same experiment. Furthermore, by the nature of the configuration, we are able to detect only tube-borne waves (S_0 or A_0) and not the Scholte–Stoneley waves which are propagated at the solid–fluid interface inside the tube. Thus there can be no ambiguity in the assignment of waves to either A_0 or **A** modes in our experiment; the observed modes must be A_0 . Results for S_0 modes are easily distinguishable from A_0 by travel time; these were reported previously¹² and will not be considered here. In this communication we concentrate on results for the A_0 mode in the region $fd \sim 1$ for a

thin-walled stainless steel tube where $f=0.8$ to 6.0 MHz, and $d=0.25$ mm. Liu and Lynnworth¹³ also studied the A_0 mode in cylindrical tanks but in a quite different regime where $fd \ll 1$.

I. EXPERIMENTAL METHODS

The measurement setup and the tube configuration are shown in Fig. 1. The experimental sample was a stainless steel tube with a wall thickness of 0.25 mm and a radius of 5.0 mm. A layer of PZT film was coated on the outer surface and an IDT was made along the circumferential direction. The pulse-echo technique was used to measure the time delay with a Ritec-10000 system. Tone-burst pulses were applied to the chirp IDT which served as both the transmitter and receiver. The output was connected to a digital oscilloscope and the wave forms were acquired by a computer using LABVIEW. The measurement was carried out at different frequencies with steps of 0.05 MHz. The frequency range was between 0.8 and 6.0 MHz, i.e., $fd=0.20$ to 1.5 mm-MHz, which covers all the sensitive fd range of the lowest flexural modes. The received echo train is shown in Fig. 2. The interval between the echoes is the travel time for a complete circumference, which is determined by using the cross-correlation method, and the group velocity can be obtained directly by knowing the radius of the shell. The phase velocity dispersion curve can be obtained by integrating the group velocity dispersion curve. The integration constant is experimentally determined in the following way. Because of the special property of the circumferential wave, which propagates round and round along the circumference, a pseudo-standing wave is easily formed for the output signals when the duration of the input tone-burst pulse is long enough, for example, more than one circumference. By measuring the adjacent frequencies f_n and f_{n+1} , where the signals are in maximum or minimum (constructive or destructive interference), the phase velocity can be estimated by $V \approx 2\pi R \cdot (f_{n+1} - f_n)$. Thus the phase velocity values can be measured at certain discrete frequencies. Those values can be taken as the integration constant and the phase velocity dispersion curve was thus obtained. For technical reasons it was

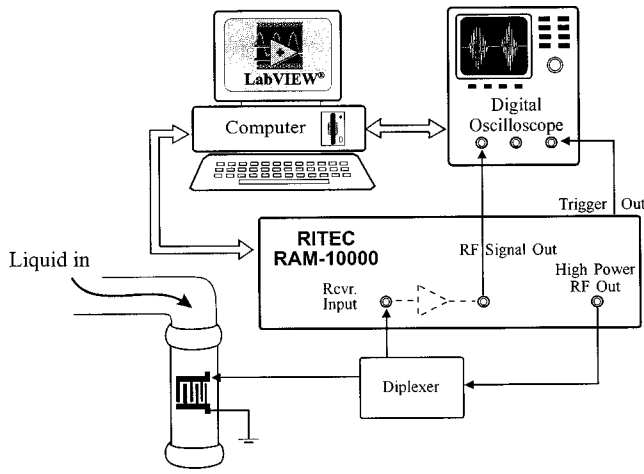


FIG. 1. Schematic configuration of the sample and measurement arrangement.

not possible to observe these resonances for the water-filled tube, so an experimental phase velocity curve is not available for this case.

While echoes could be obtained over the full range 0.8–6.0 MHz for the empty tube, signals could only be observed in the range 0.85–2.4 MHz for the water-filled case. Representative echo trains for the two are shown in Fig. 3. It is clear by inspection that water loading decreases v_g significantly at the higher frequencies while it has a much smaller effect at 1 MHz. Comparison between experiment and theory for v_g of the empty and filled tubes as a function of fd is made in Fig. 4. It is seen that v_g has a plateau at about 2400 m/s over the accessible experimental range of fd and that there is a 21% decrease in v_g at the higher frequencies. Our

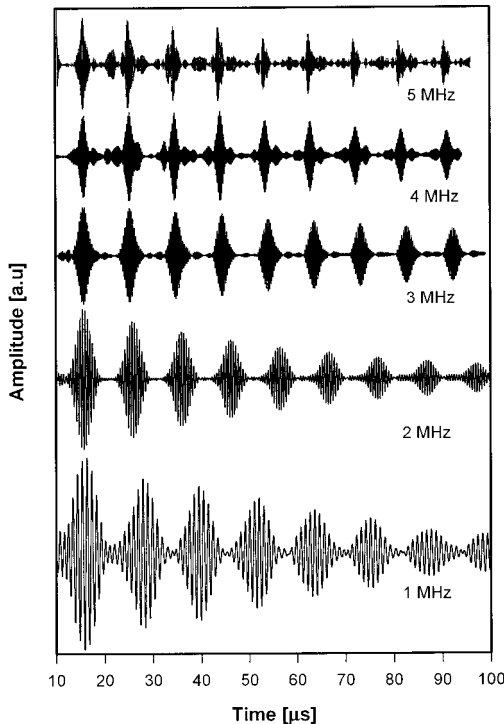


FIG. 2. Received echo trains at different frequencies for an empty stainless steel shell ($R=5$ mm, $d=0.25$ mm).

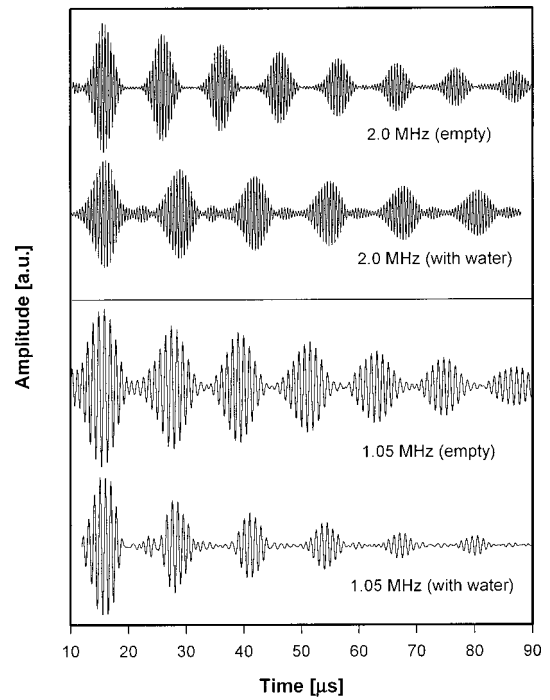


FIG. 3. Time delay signals of the A_0 mode in the empty and water-filled tube.

previously reported work¹² showed good agreement between theory and experiment for the empty tube, so this surprising decrease remains to be explained.

II. DISCUSSION

While it is clear, as mentioned above, that we measure the A_0 and not the \mathbf{A} mode, a third possibility must also be considered. This involves leakage of the A_0 mode into the liquid, propagation as a bulk wave in water, and reconversion to the A_0 mode before the pulse arrives at the transducer. This possibility is, however, excluded because the shortest possible flight path would lead to a longer transit time than that observed experimentally. We also confirmed this experimentally by inserting co-axially an empty tube

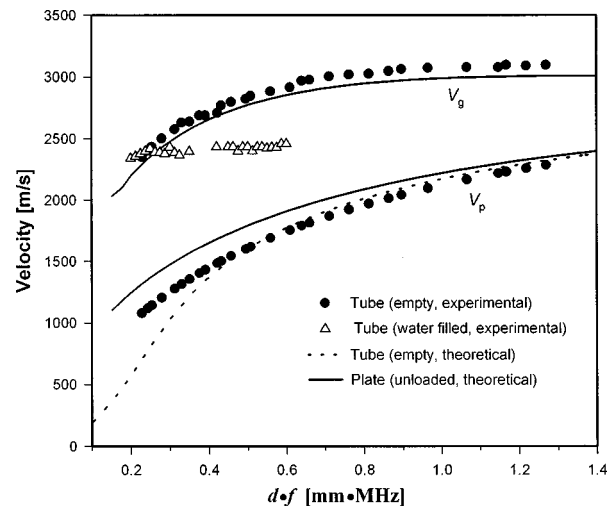


FIG. 4. Experimental and theoretical results for the A_0 mode for empty and water-filled shell.

with an outer radius close to the inner radius of the water-filled tube. This structure would profoundly modify, delay, or smear out any bulk wave travelling in the water. No change in either the delay time or the amplitude of the echoes was observed, from which we conclude that the observed signals were tube-borne over the entirety of their propagation path.

It is difficult to make detailed comparisons with the work of Talmant *et al.*,^{6,7} who observed principally the **A** mode. Our results do, however, strongly suggest that the third circumferential mode that they observe, highly attenuated and with $v_g = 2450$ m/s, corresponds to the A_0 mode studied here. Apart from this, the situation is paradoxical. Talmant *et al.* observe experimentally and theoretically a plateau in v_g for the **A** mode in stainless steel, with $v_g \leq 2000$ m/s for $0.2 < fd < 0.3$. Their calculated curve for the water-loaded A_0 mode is almost identical to that we obtain for the unloaded tube, with a value of about 2400 m/s for this range of fd . Experimentally we observe a plateau for the water-loaded tube, with $v_g = 2400$ m/s, well below Talmant's theoretical curve at the higher frequencies. Thus, while both **A** and A_0 modes demonstrate a plateau experimentally (although with significantly different values of v_g) in the same range of fd , the A_0 result is in marked disagreement with theory. It should be noted, however, that the values calculated by Talmant *et al.* are for air inside and water outside the tube, which is the opposite of our experimental arrangement. Resolution of this discrepancy must await development of the theory for the water-filled tube. Finally, loss of signal for $fd > 0.5$ is probably due to the A_0 mode becoming leaky at high phase velocities, similar to the case of fluid-loaded thin plates.

III. CONCLUSIONS

In this work we have unambiguously observed propagation of the A_0 mode in a fluid-loaded thin cylindrical shell, which has not hitherto been observed in other experimental configurations. At the highest accessible frequencies we see a dramatic decrease of about 21% in v_g compared to the

empty cylinder. The observation of a plateau in v_g is similar to observations for the **A** mode observed by Talmant *et al.*, but there is as yet no theoretical explanation of this behavior for the A_0 mode.

ACKNOWLEDGMENTS

This work was supported by the Natural Sciences and Engineering Research Council (NSERC) of Canada. One of us (Xing Li) is grateful to FCAR for financial support.

- ¹N. D. Veksler, "The analysis of peripheral waves in the problem of plane acoustic pressure wave scattering by a circular cylindrical shell," *Acustica* **69**, 63–72 (1989).
- ²G. C. Gaunard and D. Brill, "Acoustic spectrogram and complex frequency poles of a resonantly excited elastic tube," *J. Acoust. Soc. Am.* **75**, 1680–1693 (1984).
- ³E. D. Breitenbach, H. Überall, and K. B. Yoo, "Resonant scattering from elastic cylindrical shells," *J. Acoust. Soc. Am.* **74**, 1267–1273 (1983).
- ⁴S. G. Solomon, H. Überall, and K. B. Yoo, "Mode conversion and resonant scattering of elastic waves from a cylindrical fluid-filled cavity," *Acustica* **55**, 147–159 (1984).
- ⁵L. Fax, L. R. Dragonette, and H. Überall, "Theory of elastic resonance excitation by sound scattering," *J. Acoust. Soc. Am.* **63**, 723–731 (1978).
- ⁶M. Talmant and G. Quentin, "Backscattering of short ultrasonic pulse from thin cylindrical shells," *J. Appl. Phys.* **63**, 1857–1863 (1988).
- ⁷M. Talmant, G. Quentin, J. L. Rousselot, J. V. Subrahmanyam, and H. Überall, "Acoustic resonances of thin cylindrical shells and the resonance scattering theory," *J. Acoust. Soc. Am.* **84**, 681–688 (1988).
- ⁸M. Talmant, H. Überall, R. D. Miller, M. F. Werby, and J. W. Dickey, "Lamb waves and fluid-borne waves on water-loaded, air-filled thin spherical shells," *J. Acoust. Soc. Am.* **86**, 278–289 (1989).
- ⁹L. Izbicki, G. Maze, and J. Ripoche, "Diffusion acoustique par des tubes immergés dans l'eau: Nouvelles resonances observees en basse fréquence," *Acustica* **61**, 137–139 (1986).
- ¹⁰P. Pareige, G. Maze, and J. Ripoche, "Resonances d'un tube élastique: source d'émission acoustique interne," *Rev. Phys. Appl.* **22**, 83–88 (1987).
- ¹¹A. Gerard, J. L. Rousselot, L. Izbicki, G. Maze, and J. Ripoche, "Resonances d'ondes d'interface de coques cylindriques minces immergés: détermination et interpretation," *Rev. Phys. Appl.* **23**, 289–299 (1988).
- ¹²J. D. N. Cheeke, X. Li, and Z. Wang, *1995 IEEE Ultrasonics Symposium Proceedings* (November, 1995, San Antonio), pp. 441–444.
- ¹³Y. Liu and X. Lynnworth, "Flexural wave sidewall sensor for noninvasive measurement of discrete liquid levels in large storage tanks," *1993 IEEE Ultrasonics Symposium Proceedings*, pp. 385–390.

Atmospheric propagation transfer function determination using an adaptive filter

Jonathan W. Benson

Wave Propagation Laboratory, Department of Electrical and Computer Engineering, University of Illinois, Urbana, Illinois 61801

(Received 31 March 1998; accepted for publication 21 August 1998)

In this Letter an alternative method for the experimental determination of the complex acoustic propagation transfer function is presented. The method uses an adaptive filter in system identification mode. The inputs to the system are the source and received signals. The transfer function is represented by finite impulse response filter coefficients. Good results were obtained using filter lengths in the range from 100 to 250 with a sampling rate of 12 k samples/s. The method is outlined and some representative results with experimental field data are given. © 1998 Acoustical Society of America. [S0001-4966(98)01112-6]

PACS numbers: 43.60.Lq, 43.28.Fp, 43.28.Vd [JCB]

INTRODUCTION

The propagation of acoustic waves is affected by the presence of such factors as wind, temperature gradients, ground reflections, and turbulence. The combination of these factors creates a complex time varying propagation transfer function. Determination of this transfer function in both magnitude and phase can be accomplished in many ways. The adaptive filtering method outlined here is presented as an alternative to other methods, some of which are mentioned below. The adaptive method described here allows for the modeling of the propagation transfer function using a finite impulse response (FIR) filter which is continuously adapted, on a sample by sample basis, to track the transfer function variation with time. The filter coefficients may be inspected at any instant to compute the magnitude and phase of the transfer function via the z transform. The method permits one to easily view an accurate evolution of the transfer function with time, allowing for a wealth of analysis possibilities. The method is relatively simple, computationally inexpensive, and can be used in real-time applications.

There are many other methods of transfer function computation. Standard Fourier methods can give good results with careful choice of parameters such as window and FFT size. Berkhout *et al.* describe a visualization method where a source wavelet is transmitted and received by an array of microphones.¹ The method visually describes the complex behavior of the wave as it is received by the array. It also allows for the computation of the full relative transfer function of the propagation. Heutschi and Rosenheck describe a method of computing the impulse response of the propagation via the use of maximum length sequences (MLS).²

The adaptive method will be described and then some example results using the method will be presented. The performance of the method will not be compared to any other method, as this would be complex and beyond the scope of this letter.

I. METHOD DESCRIPTION

For the purpose of this discussion we will consider the situation where a source emits an acoustic signal which is then received at a remote location. The source and received signals are sampled and input to an adaptive filtering system which is arranged in what is known as a system identification configuration. A good treatment of adaptive signal processing can be found in Windrow and Stearns.³ A block diagram of the system is presented in Fig. 1. The output of the adaptive filter is subtracted from the actual received signal to form the error signal. The error signal is fed back to the adaptive filter and is used to control the adaptation process. Several different adaptive filter algorithms were tested including the basic least mean squares (LMS), the transform domain LMS, the data-reusing LMS, the recursive least-squares (RLS), and the RLS lattice. The best results for this application came when using the RLS lattice algorithm⁴ or the data-reusing LMS,⁵ but good performance might be achieved with other adaptive algorithms as well.

At any time instant, the transfer function is modeled as a linear time-invariant system. Accordingly, one must be aware of the limitations inherent to this type of representation, such as the inability to account for doppler effects. The length of the FIR filter used will set the complexity of the transfer function that can be modeled.

The parameters of the adaptive algorithms should be chosen with care. The length of the filter must be chosen long enough to adequately represent the transfer function while not being so long as to lessen the ability of the adaptive algorithm to adjust the coefficients fast enough to keep up with the changing propagation conditions. A general guideline for choosing the maximum filter length is the fact that the transfer function should remain essentially unchanged over the period of time equivalent to the length of the filter. The variability in the transfer function is related to the variability of the propagation conditions. Various filter lengths were tried and good results were obtained with 100 to 250 taps (using a 12-kHz sampling rate) depending on the specific propagation conditions (wind speed, etc.). The adaptation constant μ must also be chosen for good performance.

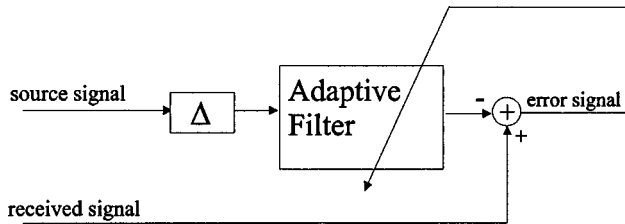


FIG. 1. Block diagram of the transfer function determination system. The Δ delay block accounts for most of the propagation delay.

The value of μ should be chosen according to guidelines used in the adaptive filtering literature.³ The Δ delay block shown in Fig. 1 should be used to account for an expected minimum propagation delay. The adaptive filter can then account for the variations in the delay. The variation in the delay will be a function of the propagation distance and the wind speed fluctuations. Expected standard deviations of the propagation delay⁶ suggest that the filter lengths mentioned above are adequate to account for the variations.

II. EXAMPLE RESULTS

In this section some results will be given which serve to illustrate the method. The layout of the field experiments from which the data used in these examples were obtained is shown graphically in Fig. 2. The source was a large loudspeaker to which white noise bandlimited from 100 to 5500 Hz was fed. In general, the SPL at 1 m in front of the speaker was measured to be above 132 dB (*re*: 20 μ Pa). The center of the speaker was 0.75 m above the ground. Propagation was from west to east over very flat terrain consisting of 10–12-cm tall grass and slightly moist soil. The receiver was 0.36 m above the ground and was 105 m from the source. Data from two different wind speed and direction conditions will be presented. The first set was taken when the wind was from the NE at 0.5 m/s and the second with SSE winds at 4.5 m/s as measured 1.5 m above the ground. The signal generated by the loudspeaker was recorded using a microphone placed 1 m in front of the loudspeaker and at the center point of the face grating. The loudspeaker was an Electro-Voice MTH-4, which utilizes multiple conventional and horn transducers. Because of the difficulty in accurately measuring the actual sound field radiated by the loudspeaker, it should be noted that what is actually being computed here is a transfer function from reference to receiver and not necessarily from source to receiver. Careful experimental setup can lead to a reference signal that is a good estimate of the actual source

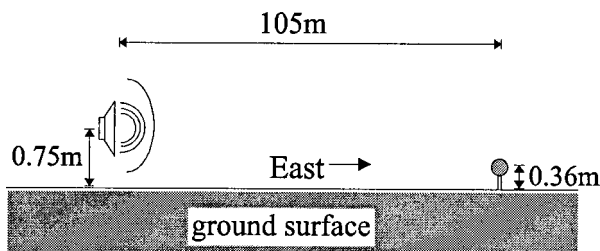


FIG. 2. Diagram of the propagation experiment. Propagation was from west to east over dry grass with slightly moist soil.

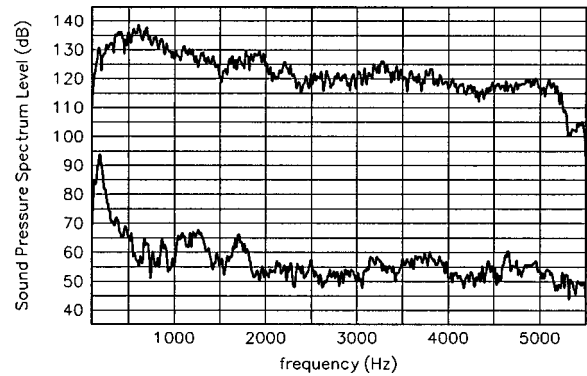


FIG. 3. Magnitudes of the power spectra of a 1-s segment of data for the source (upper trace) and the received (lower trace) signals. Data shown from 100 to 5500 Hz. Level in decibels *re*: 20 μ Pa, bandwidth=1.47 Hz.

signal. The reference and received signals were recorded together on digital audio tape using a sampling rate of 12 k samples per second. The digital data were taken directly from the tape and transferred to a computer for the transfer function computations.

A. Results from the first set of data: low wind speed conditions

The power spectra of the reference and received signals for the first set of data are shown in Fig. 3. The spectra were computed using one second of data. The data set was then input to the adaptive system for transfer function computation. The data-reusing LMS algorithm was employed with four reuses, a filter length of 250, a μ value of 0.7, and a constant Δ (delay) of 3550 samples. The filter weights representing the transfer function were saved for inspection every 600 samples (1/20 s). These saved weights were the average weights over each 600 sample segment. Shown in Fig. 4 are the magnitude and phase of the average transfer function over the 1 s of data from which the power spectrum was computed in Fig. 3. It should be noted that one expects 40 dB of attenuation due to spherical spreading for this propagation distance. This attenuation is further altered by effects such as ground shadows, ground waves, refraction, turbulence, and absorption. The pronounced dip centered at about 600 Hz in the transfer function response is most likely due to ground effects and agrees with results found in Piercy *et al.*⁷

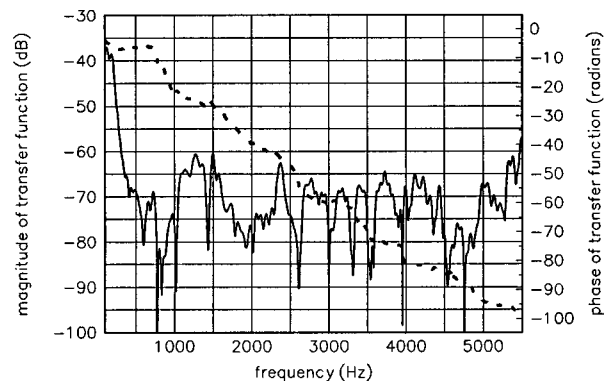


FIG. 4. The average transfer function found using the adaptive system over the 1-s data segment with 0.5-m/s wind. The magnitude (solid line) and phase (dashed line) are shown. Bandwidth for both=3 Hz.

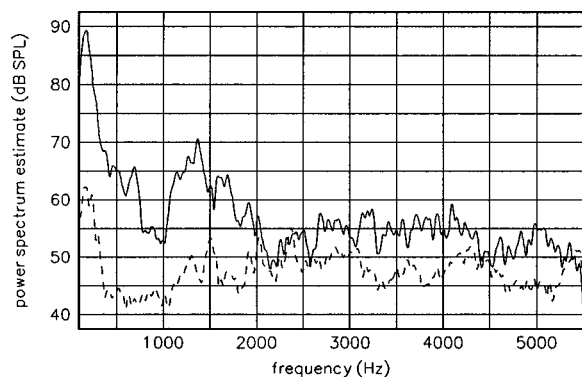


FIG. 5. Estimated power spectra of the received signal (solid line) and the error signal (dashed line) over the 1-s segment of data with 0.5-m/s wind. Level in decibels *re*: 20 μ Pa, bandwidth for both=3 Hz.

The quality of the model is perhaps best measured by observing the power spectra of the received signal and the error (difference) signals. Figure 5 shows these estimated power spectra for the same 1-s segment of data. The model seems to be accurate out to nearly 2 kHz. The time evolution of the magnitude of the transfer function is displayed in Fig. 6 for frequencies from 100 to 2000 Hz, and is an example of the many illustrative pictures one can construct using this method.

B. Results from the second set of data: greater wind speed

As the wind speed increases one would expect that the propagation transfer function would vary more quickly and more severely with time due to the increase in turbulence. This is illustrated in the results from the second set of data in which the wind averaged 4.5 m/s. Figure 7 shows the time evolution of the computed transfer function over a 1-s segment of data for this higher wind speed case. The data-reusing LMS algorithm was again used. However, this time the best performance was obtained with a filter of length 128. In comparison to that shown in Fig. 6, the structure of the magnitude of the transfer function appears much more ran-

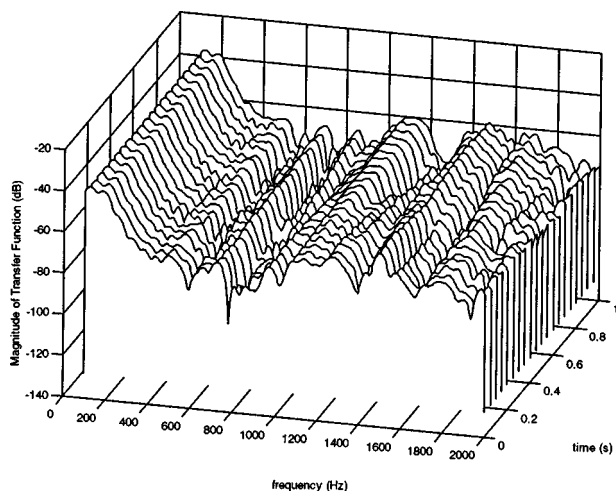


FIG. 6. The time evolution of the magnitude of the computed transfer function from 100 to 2000 Hz for the 1-s data segment with 0.5-m/s wind. Bandwidth=4 Hz.

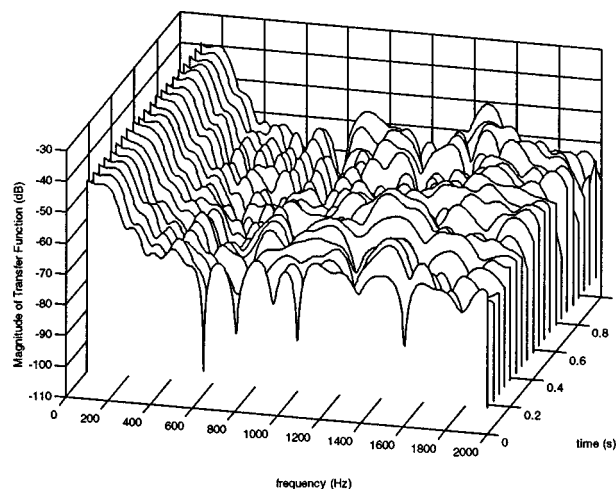


FIG. 7. The time evolution of the magnitude of the computed transfer function from 100 to 2000 Hz for the 1-s data segment with 4.5-m/s wind. Bandwidth=4 Hz.

dom in nature. The shorter filter length was the result of the tradeoff mentioned earlier between filter length and the tracking speed of the adaptive system. The system still provides good transfer function estimates in this case. The error signal power spectrum shows good performance to 2 kHz in a manner similar to that shown in Fig. 5. As the rate of transfer function variability becomes faster, the method may not be able to provide good performance. The variability rate at which the performance becomes unacceptable will be a function of the transfer function complexity.

III. CONCLUSIONS

The alternative method of calculating the acoustic propagation transfer function outlined in this paper provides an accurate model of the effects of propagation. The model takes the form of a FIR filter whose coefficients are continuously adapted using an adaptive filter system in the system identification mode. The system adapts such that the output of the adaptive filter, which has the source signal as its input, mimics the actual received signal as closely as possible. The data-reusing LMS and the recursive least-squares lattice gave the best results of the algorithms tested. It was found that filter lengths from 100 to 250 provided good performance for the propagation conditions analyzed in this paper. The length of the filter used will be a function of the speed of evolution and complexity of the transfer function, with the maximum filter length being given by the equivalent time of relative stability in the transfer function. Example results for two different wind speed situations were presented. The method provides accurate time-evolution transfer function data with low complexity and computational expense. It should prove useful in the continuing study of acoustic propagation.

ACKNOWLEDGMENTS

The author would like to thank Professor George W. Swenson, Jr., Professor W. Kenneth Jenkins, and Dr. Michael White for their support. This work was funded by the U.S. Army Construction Engineering Research Labs under Contract No. DACA-88-97-M-0262.

- ¹A. J. Berkhout, M. M. Boone, and P. J. M. Valks, "Multichannel impulse responses for outdoor sound propagation," *J. Acoust. Soc. Am.* **98**, 1169–1177 (1995).
- ²K. Heutschi and A. Rosenheck, "Outdoor sound propagation measurements using an MLS technique," *Appl. Acoust.* **51**, 13–32 (1997).
- ³B. Widrow and S. D. Stearns, *Adaptive Signal Processing* (Prentice-Hall, Englewood Cliffs, NJ, 1985).
- ⁴S. Haykin, *Adaptive Filter Theory* (Prentice-Hall, Englewood Cliffs, NJ, 1986), pp. 482–483.
- ⁵W. K. Jenkins, A. W. Hull, J. C. Strait, B. A. Schnauffer, and X. Li, *Advanced Concepts in Adaptive Signal Processing* (Kluwer, Boston, 1996), pp. 54–68.
- ⁶D. K. Wilson and D. W. Thomson, "Acoustic propagation through anisotropic, surface-layer turbulence," *J. Acoust. Soc. Am.* **96**, 1080–1095 (1994).
- ⁷J. E. Piercy, T. F. W. Embleton, and L. C. Sutherland, "Review of noise propagation in the atmosphere," *J. Acoust. Soc. Am.* **61**, 1403–1418 (1977).